Advances in Geophysical and Environmental Mechanics and Mathematics

Series Editor: Professor Kolumban Hutter

For further volumes:
http://www.springer.com/series/7540

Board of Editors

Kolumban Hutter • Yongqi Wang
Irina P. Chubarenko

Physics of Lakes

Volume 2: Lakes as Oscillators

Springer

Prof. Dr. Kolumban Hutter
ETH Zürich
c/o Versuchsanstalt für Wasserbau
Hydrologie und Glaziologie
Gloriastr. 37/39
8092 Zürich
ETH-Zentrum
Switzerland
hutter@vaw.baug.ethz.ch

PD. Dr. Yongqi Wang
Chair of Fluid Dynamics
Department of Mechanical Engineering
Darmstadt University of Technology
Petersenstr. 30
64287 Darmstadt
Germany
wang@fdy.tu-darmstadt.de

Dr. Irina P. Chubarenko
Russian Academy of Sciences
P.P. Shirshov Institute of
Oceanology
prospect Mira 1
236000 Kaliningrad
Russia
irina_chubarenko@mail.ru

ISSN 1866-8348
ISBN 978-3-642-19111-4 e-ISBN 978-3-642-19112-1
DOI 10.1007/978-3-642-19112-1
Springer Heidelberg Dordrecht London New York

Library of Congress Control Number: 2011933562

Cover design: deblik, Berlin

Printed on acid-free paper

Springer is part of Springer Science+Business Media (www.springer.com)

This book series on Physics
of Lakes is dedicated
in memoriam to
Professor Clifford H. Mortimer (1911–2010)
and to
Professor Lawrence A. Mysak
mentors, teachers and friends

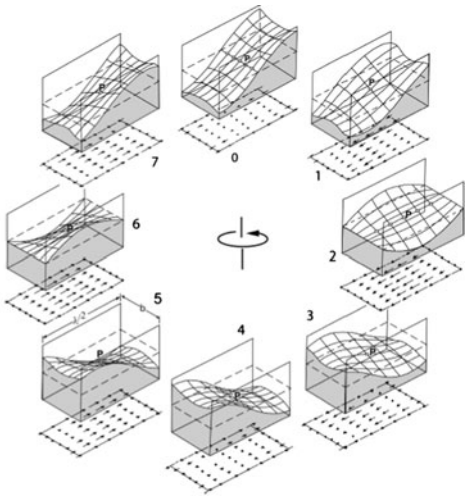

Clifford H. Mortimer (1911–2010), Founding Director of Center for Great Lakes Studies, Distinguished Professor Emeritus, Biological Sciences, University of Wisconsin–Milwaukee (photo from http://www.glwi.uwm.edu/profiles/chmortimer/).

Biography of Clifford H. Mortimer and some reminiscences.

Clifford H. Mortimer was born in Bristol, England on 27 February 1911 and died on 11 May 2010. He received his basic education in the UK. He earned a B.S. degree in zoology from Manchester University in 1932 and a Ph.D. in genetics from the Humboldt University in Berlin in 1935. He subsequently held a research position at the Fresh Water Biological Association (FBA) on Lake Windermere in England until 1941. During World War II he was recruited by the *Royal Naval Scientific Service*, from 1941–1946, working in the Oceanographic Group of the Admiralty Research Laboratory, where he studied waves and tides. In 1946, Mortimer returned to the FBA and remained there until becoming the director of the *Scottish Marine Biological Station* in 1956, a position, which he held for 10 years until taking the Distinguished Professorship at the University of Wisconsin–Milwaukee (UWM) and directorship of the Center of Great Lakes Studies (CGLS) (today the Great Lakes WATER (Wisconsin Aquatic Technology and Environmental Research) Institute and School of Fresh water Sciences) in 1966. He retired from his administrative post in 1978 and his academic role at UWM in 1981, when he was appointed Distinguished Professor Emeritus.

In 1958 Prof Mortimer was elected a Fellow of the *Royal Society, London*. He was proud about this and once emphasized that he received this honour even though he was not, as he said, a member of the 'Oxridge community'. In 1981 and 1995, respectively, he was granted a lifetime membership of the American Society of Limnology and Oceanography (ASLO) and was honoured with ASLO's lifetime Achievement Award in recognition of his contributions to lake biology, chemistry and physics and his leadership and general commitment to excellence. In 1985 and 1987 the UWM and École Polytechnique Féderale de Lausanne (Switzerland) awarded him each the Dr. honoris causa.

Professor Mortimer's earliest works were on the genetics of Cladocera and on water chemistry at the sediment–water interface and its influence on seasonal processes in lakes. However, he is best known for his research on internal waves. Surprisingly, trained as a zoologist, he acquired during World War II sufficient knowledge in dynamic oceanography to rise to the world's leading position as an interpreter of temperature and velocity data of internal waves

in lakes. His paper on internal seiches of Lake Windermere (1952) as a 2- (and 3-) layer baroclinic response and his Kelvin wave analysis of Lake Geneva (1963) are landmarks of the physical understanding of internal wave dynamics, later perfected by him in many subsequent reports and articles and summarized in his culminating book *Lake Michigan in Motion: Responses of an Inland Sea to Weather, Earth-Spin, and Human Activities* (2004).

A landmark on wave dynamics is his Lake Hydrodynamics, Limnol Oceanogr 20, 124–197 (1974); his last publication *Internal oscillations and related beat pulsations and surges in Lakes Michigan and Ontario* appeared in Limnol Oceanogr 51, 1914–1955 (2006), and he was still working on a study of the thermal equation of state of water the days before he died.

Professor Mortimer was an expert in collecting lake surface oscillation data and using these in the best possible way for his interpretation of the physical processes lying behind the data. He used in 1963 e.g. records of nine limnigraph stations of the Swiss Hydrological Service positioned in 1950 around Lake Geneva, smoothed these data to filter-out the barotropic signal and so made the baroclinic oscillations visible to identify the Kelvin-type wave movement. Moreover, he even incorporated in the figure data from instruments which had failed episodically and thus demonstrated that statistical time series analysis may well ignore important information of the original data. He maintained this view despite the recognition of the power of the statistical techniques, which he himself with his collaborators was expertly using.

The content of the present book reflects the strong influence, which Prof. Mortimer exercised in the 1970s and 1980s on the Swiss Water Scientists, and in particular on one of the authors (KH) of the book 'Physics of Lakes'. In 1975 the Swiss National Science Foundation (SNF) had initiated a 5-year national program 'Fundamental Problems of the Water Cycle in Switzerland' with several funded proposals, among others those by W. Graf (EPFL), K. Hutter (VAW), D. Imboden (EAWAG) and F. Zamboni (IFT). Prof. Mortimer was a member of the funding committee. This SNF-program and Prof. Mortimer's ensuing support provided a big incentive to Swiss Physical Limnology. He spent many days and weeks in the groups of the individual projects, collaborating with us, providing advice and criticism to the extent of caring about many details when we were launching our field programs and correcting the structure and English wording of our drafted manuscripts. During such weeks KH and Prof. Mortimer shared an office with desks opposite to one another. It is in these situations that I learned how to draft drawings from temperature and velocity data and to combine these elements to a meaningful picture explaining the underlying physics. No explanations were needed. One only had to look how he was doing it. If KH became an acceptable physical oceanographer it is largely through this association.

Even though I had strong intellectual interactions with Professor Mortimer on physical limnology of Lake Zürich, there is no paper in which we both appear as authors. Clifford saw me as a 'geometer', as he said, and put himself aside from it, saying that 'he is dealing with God's models' (while I was apparently dealing just with equations – human inventions). Nevertheless, he freely used mathematical results from all of us who were able to produce them, incidentally with skill to just use what aided him for the purpose at hand.

Prof. Mortimer was also a very hard worker with unusual strength. The following incident explains this: On a summer Sunday in 1981 or 1982, he, Dave Schwab and I went for a long walk to and along the crest of Albis Mountain near Zürich and back down again. The walk was more than 5 h and after returning to Zürich in the evening and saying good-bye to Clifford, Dave and I finally admitted to one another to be exhausted, needing a long night's sleep. On Monday morning around 9 or 10 o'clock Clifford came to the office with a few sheets which he had generated in the evening, asking me to look at them. He was then more than 70, between 30 to 40 years older than Dave and I.

This book shows many results of this collaboration and the research which emerged as a fruitful derivative of it.

The following fact may also be of interest, even though it probably had merely a tangible influence on Professor Mortimer; but we spoke on several occasions about it. When Professor Mortimer was working in the Oceanographic Group of the Admiralty Research Laboratory, he was also participating in the experimental determination of Fourier transforms of time series of a given period. To this end a paper stripe of the length of the circumference of a large wheel was pasted onto the outside periphery of the wheel. On this stripe the fluctuating time series was drawn, scaled to fit the time period to be analysed. If the wheel is rotated with a certain period of revolution and a stroboscopic light source illuminates the moving time series at a point with a period which is the nth fraction of the period of revolution, then the illuminated points select processes which have periods which equal twice the period of the entire stripe length divided by n. Mortimer tells that this was how the spectra of ocean waves were determined in the Oceanographic Group of the Admiralty Research Laboratory during World War II, see N.F. Barber et al. (1946). Professor Mortimer's knowledge and deep understanding of statistical time series analysis has been amazing to me and is likely due to this experience.

Professor Mortimer and his wife Inge Closs (1913–2000), of German origin, Stuttgart in Baden Würtemberg, had two daughters, Christine and Alison, who have two sons and a daughter and two sons, respectively. They reside in Emden, Friesland, Germany and in Wisconsin, USA. Professor Mortimer passed away in Milwaukee, Wisconsin on May 11 2010.

K. Hutter (KH)

This text is partly based on http://www4.uwm.edu/freshwater/news/20100604-clifford-h-mortimer-1911-2010.cfm http://www.limnology.org/news/silnews56.pdf and personal correspondence with Ch. Heimann, V. Klump, A. Brooks, D. Schwab and U. Lemmin.

N.F. Barber, F. Ursell, J. Darbyshire and M.J. Tucke: A frequency analysis used in the study of ocean waves. Nature, 158, September 7, 329–332 (1946).

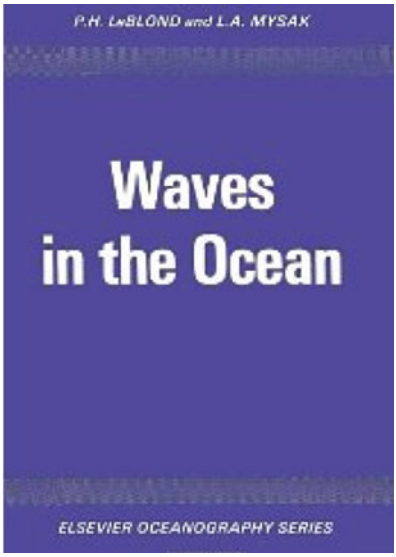

Lawrence Alexander Mysak and front cover of his book 'Waves in the ocean' (photo by Alain Désilets, from http://www.mdeie.gouv.qc.ca/).

Lawrence Alexander Mysak, born 22 January 1940 in Saskatoon, Saskatchewan, Canada, earned a flute performance diploma (1960) from the University of Alberta, Edmonton, a BSc degree (1961) in applied mathematics from the University of Alberta, an MSc degree (1963) in mathematics from the University of Adelaide, South Australia with a thesis in general relativity, and a Ph.D. degree (1967) in applied mathematics from Harvard University, Cambridge, MA, USA, with a dissertation on 'Continental Shelf Waves'. After a brief postdoctoral position in Geophysical Fluid Dynamics at Harvard, he commenced a professorial career at the University of British Columbia, Vancouver, first as Assistant Professor of Mathematics (1967–1970), then as Associate Professor of Mathematics and Oceanography (1970–1976), and finally as Professor of Mathematics and Oceanography (1976–1986). In 1986 Professor Mysak moved to Montreal to McGill University, where he was appointed the Atmospheric Environment Service/NSERC Chair Professor of Climate Research and Director of the Climate Research Group within the Department of Meteorology (now Department of Atmospheric and Oceanic Sciences). In 1990 he became founding Director of the McGill Centre for Climate and Global Change Research (C^2GCR), a position he held until 1996. He remained at McGill as Canada Steamship Lines Professor of Meteorology (in 1989–2010) and served on many departmental and university committees until May 31 2010, when he was appointed Canada Steamship Lines Professor Emeritus of Meteorology.

Professor Mysak was a dedicated and very successful university professor. At UBC and McGill he taught a wide range of mathematics, oceanography and climate dynamics courses, and he supervised or co-supervised 45 MSc and Ph.D. theses and 33 postdoctoral fellows and research assistants. Today, 21 of his former graduate and postdoctoral students are professors in 11 countries. In appreciation of his outstanding contributions to McGill and beyond, he was awarded at the Science Convocation in May 2010 an inaugural 'McGill University Medal for Exceptional Academic Achievement'.

Professor Mysak has traveled widely throughout his professional career, has held many visiting academic positions around the world, and has offered hundreds of lectures and seminars at numerous academic, government and research institutions. He took sabbaticals and short term visits at Cambridge University (Cambridge, England), NCAR (Boulder, CO, USA), the Naval Postgraduate School (Monterey, CA, USA) and the Laboratory of Hydraulics, Hydrology and Glaciology (VAW) at the Swiss Federal Institute of Technology (ETH), Zürich, Switzerland. While in Zürich during 1982–1983, he devoted much of his time to joint work on modeling baroclinic gravity and topographic waves in the Lake of Lugano, which is amply demonstrated in this volume 2 of *Physics of Lakes*. His impetus contributed immensely to the scientific flourishing of the Physical Limnology Group (at VAW) in 1982–1983, then led by K. Hutter. Further sabbaticals followed in 2000–2001, at the Institute for Atmospheric and Climate Science at ETH, Zürich and the National Institute of Geophysics and Volcanology, Bologna, and in 2007–2008 again at ETH, Zürich and the University of Stockholm, Sweden.

Professor Mysak has been (and still is) a prolific scientific author, and he is well known for the book *Waves in the Ocean* (co-authored with Paul LeBLOND in 1978). He has authored or co-authored more than 165 peer reviewed journal articles on a wide range of topics in oceanography, climatology and paleoclimates. In the first part of his professional career, the focus of his activities was mostly on applied mathematics and physical oceanography; later his research work became very broad, encompassing many aspects of climate science, including interactions between the atmosphere, the cryosphere, the oceans and the biosphere; his studies on climate ranged from decadal to million-year time scales. He has held editorial responsibilities for, among others, the Journal of Physical Oceanography, Geophysical and Astrophysical Fluid Dynamics, Atmosphere-Ocean, and the book series Coastal and Estuarine Studies (Springer, now AGU). He is currently Editor-in-Chief (for oceans) for the Atmospheric and Oceanographic Sciences Library (Springer). In recognition of his various achievements Professor Mysak has been honored by many awards and appointments in scholarly societies. In 1986 he was elected a Fellow of the Royal Society of Canada (FRSC); from 1993–1996 he was the President of the Academy of Science, one of the three academies that comprises the RSC. Moreover, in 1996 he was appointed a member of the Order of Canada for his pioneering research work and his accomplishments as a team builder as Director of the McGill C^2GCR and as President of the Academy of Science. In the year 2000 he was elected a Foreign Member of the Academia Europaea. He is a Fellow of the American Meteorological Society and of the American Geophysical Union, and is also an Honorary Member of the European Geosciences Union. During 2007–2011 he served as President of the International Association for the Physical Sciences of the Oceans, which is part of IUGG.

Professor Mysak is married to D. Mary Eeles, and they have two children, Paul Alexander, born 1975 and Claire Anastasia, born 1978. An accomplished musician, Professor Mysak plays flute in the I Medici di McGill symphony orchestra.

This text, written by KH, is based on a Curriculum Vitae of LAM and a personal biographical sketch by LAM.

Preface to the Book Series

An integrated view of *Physics of Lakes* requires expert knowledge in different specialities which are hardly found in single scientists. Even in a team the overall subject must be restricted; this has also been done here, as we only treat in this book series the *geophysical aspects of fluid dynamics*. Being applied to very complicated natural objects and phenomena, this science traditionally uses three main complementary approaches: *theoretical description*, *field observation* and (numerical, laboratory and other kinds of) *modelling*. The present work extensively uses all three approaches, this way providing to the reader an opportunity to build a coherent view of the entire subject at once – from the introduction of governing equations to various field phenomena, observed in real lakes. Several features, we believe, will make the series of especial interest for a wide range of students and scientists of geophysical interest as well as specialists in physical limnology. Before plunging into the main focus of lake physics we start with a detailed introduction of the main mathematical rules and the basic laws of classical physics; this makes further work with equations and their solutions much easier for readers without solid knowledge in the common trade of the background of mathematics and physics of continuous systems – biologists, chemists, ecologists. These sciences are today the most active branches in limnology and are utterly needed for the development of modern society; thus, an easily available physical background for them cannot be overestimated. A feature of this treatise is a consolidated view expressed in its three books of a wide panoramic overlook of various lake phenomena, inherent in physical oceanography and a fairly thorough theoretical treatment of fluid mechanics. This way, the reader will find here both the mathematical background and general physical laws and considerations of natural phenomena with their driving mechanisms (waves, turbulence, wind action, convection, etc.), and also a zoo of field examples from many lakes on our Globe. Special attention is devoted to the dynamic response of lakes on their free surface and in their interior, perhaps best coined as the climatology in response to external driving mechanisms – wind action and seasonal input of solar energy. These subjects reflect the many-years of professional interests of the authors.

The content of the books and the manner of the presentation are, of course, significantly influenced by the composition of the authors' team. Being professionals of slightly different branches of the same science (limnology, fluid dynamics

and oceanography), we tried to present lake physics in the most coherent way, extracting important kernels from all the mentioned fields. The differences in opinions, what procedure might be the optimal approach in presenting a certain topic have occasionally been quite extensive, requiring compromises, but we believe that the interference, rather than simple sum, of our knowledge contributed to an enhancement of the present product than would have been reached otherwise. An additional joy for us is national composition of our international team; translation of this Preface from the English into our native languages can be directly understood by more than 70% of the Earth population.

The subjects of this treatise on *Physics of Lakes*, divided into three volumes, cover the following topics:

VOLUME 1: Physics of Lakes: Formulation of the Mathematical and Physical Background

It commences in the introduction with a general, word-only motivation by describing some striking phenomena, which characterize the motion of lake water on the surface, in the interior of lakes and then relate these motions to the density distribution. It lists a large number of lakes on Earth and describes their morphology and the causes of their response to the driving environment.

Because physics of lakes can not be described without the language used in mathematics and only limited college knowledge calculus and classical Newtonian physics is pre-assumed, these subjects are introduced first by using the most simple approach with utmost care, and continuing with increasing complexity and elegance. This process leads to the presentation of the fundamental equations of Lake Hydrodynamics in the form of 'primitive equations', to a detailed treatment of angular momentum and vorticity. A chapter on linear water waves then opens the forum to the dynamics in water bodies with free surface. Stratification is the cause of large internal motions; this is demonstrated in a chapter discussing the role of the distribution of mass in bounded water bodies. Stratification is chiefly governed by the seasonal variation of the solar irradiation and its transformation by turbulence. The latter and the circulation dynamics are built on input of wind shear at the surface. The early theory of circulation dynamics with and without the effect of the rotation of the Earth rounds-off this first book into the dynamics of lakes. A chapter on turbulence modelling and a further chapter collecting the phenomenological coefficients of water complete this book on the foundations of the mathematics and physics of lakes.

VOLUME 2: Physics of Lakes: Lakes as Oscillators

The overwhelming focus in this volume of the treatise is on linear waves in homogeneous and stratified lakes on the rotating Earth. It comprises 12 chapters, starting with rotating linear shallow-water waves and demonstrating their classification into gravity and Rossby waves for homogeneous and stratified water bodies. This leads

naturally to the analysis of gravity waves in unbounded, semi-bounded and bounded domains of constant depth: Kelvin, inertial and Poincaré waves, reflection of such waves at the end of a gulf and their description in sealed basins as so-called 'inertial waves proper'. The particular application to gravity waves in circular and elliptical basins of constant depth then builds further confidence towards the treatment of barotropic and baroclinic basin wide wave dynamics affected by the rotation of the Earth. The classical analytical approach to the baroclinic motion in lakes is done using the two layer approximation. Recent observations have focused on higher order baroclinicity, a topic dealt with in two chapters. Whole lake responses are illustrated in barotropic and baroclinic wave analyses in Lake Onega[1] and Lake Lugano, respectively, with detailed comparisons of field data. The final four chapters are then devoted to a detailed presentation of topographic Rossby waves and the generalized Chrystal equations and their identification by field observations.

VOLUME 3: Physics of Lakes: Methods of Understanding Lakes as Components of the Geophysical Environment

Red line of this volume is the presentation of different methods of investigation of processes taking place in real lakes. Part I is devoted to numerical modeling approaches and techniques, applied to demonstrate the response of a lake to wind forcing. Numerical methods for convectively-dominated problems are compared, as well as different numerical treatments of advection terms and subgrid turbulence parameterization. Methods and tools of field measurements are laid down in Part II, including the presentation of principles of operation of commonly used current, temperature, conductivity, pressure and other sensors, along with modern techniques of measurement in the field. Basic rules of time series analysis are summarized. Laboratory experimentation, presented in Part III, is introduced by an account of dimensional analysis. Results of laboratory experiments on large amplitude nonlinear oscillations, wave transformation and meromixis and convective exchange flows in basins with sloping bottom are presented. Combined presentations of field, numerical and laboratory approaches build a general view of present-day methods of physical investigations in limnology.

Lake physics is a boundless subject embracing a great variety of questions. Some material on the seasonal water cycle, stratification and various mixing and stirring mechanisms has been collected by us but is still not included in the treatise. It may hopefully be summarized in a fourth volume.

Zürich, Switzerland — *Kolumban Hutter*
Darmstadt, Germany — *Yongqi Wang*
Kaliningrad, Russia — *Irina Chubarenko*
June 2010

[1] In today's Russian 'Onega' and 'Onego' are both in use. In this book we use 'Onega'.

Vorwort zur Buchreihe

Eine übergeordnete Betrachtungsweise von **Physik der Seen** verlangt überdurchschnittliche Kenntnisse in unterschiedlichsten Spezialgebieten, die man kaum in einer einzelnen Person vereinigt findet. Selbst innerhalb eines Teams muss das übergeordnete Thema eingeschränkt werden; das ist auch hier getan worden, da wir in diesen Bänden der Seenphysik nur *geophysikalische Belange* der *Fluiddynamik* behandeln. Dieses Gebiet der Strömungsmechnik, hier angewendet auf ziemlich komplizierte natürliche Objekte und Phänomene, verwendet traditionell drei unterschiedliche, aber komplementäre Vorgehensweisen: *Theoretische Beschreibungen, Feldbeobachtungen* und (numerische, Labor oder anderweitige) *Modellierung*. Das vorliegende Werk macht ausgedehnt Gebrauch von all diesen Methoden und gibt dem Leser so die Gelegenheit, eine kohärente Sichtweise über das gesamte Gebiet zu erarbeiten von einer Einführung in die Grundgleichungen bis zu den unterschiedlichsten Phänomenen, die man in realen Seen beobachten kann. Wir glauben, dass verschiedene Merkmale dieses Werk von speziellem Interesse macht für eine breite Leserschaft von Studierenden und Wissenschaftlern mit geophysikalischem Interesse, wie auch für Spezialisten der physikalischen Limnologie. Bevor wir jedoch eintauchen in das Zentrum der Seenphysik, starten wir mit einer detaillierten Einführung in die mathematischen Voraussetzungen und die grundlegenden Gesetze der klassischen Physik; dieses Vorgehen macht das Arbeiten mit Gleichungen und ihren Lösungen wesentlich leichter für all jene Leser, welche keine gründlichen Kenntnisse in der üblichen Anwendung der Mathematik und Physik von kontinuierlichen Systemen mitbringen, in der Regel angewandte Biologen, Chemiker und Ökologen. Diese Wissensgebiete gehören heute zu den aktivsten Gruppen der Limnologie und bilden daher die Spezialwissensgebiete, die für die Entwicklung der modernen Gesellschaft von großer Bedeutung sind. Eine leicht zugängliche Darbietung des physikalischen Hintergrundes kann nicht überschätzt werden. Ein Hauptzug dieses Werkes ist eine über drei Bände verteilte Betrachtungsweise, welche eine Übersicht über verschiedene Phänomene in Seen schafft, welche der physikalischen Ozeanographie zugeordnet sind und auf einer streng theoretischen Handhabung der Methoden der Fluidmechanik beruhen. So findet der Leser hier sowohl den mathematischen Hintergrund, die allgemeinen physikalischen Gesetze und deren Anwendung auf die natürlichen Phänomene der Seenphysik mit ihren Anregungsmechanismen (Wellen, Turbulenz, Windantrieb, Konvektion, etc.),

wie auch eine ganze Palette von Feldbeispielen vieler Seen dieser Erde. Spezielle Beachtung findet die dynamische Reaktion von Seen auf ihrer freien Oberfläche und in ihrem Innern, das Klima des Sees als Antwort der äusseren Antriebsmechanismen: Wind-Antrieb, jahreszeitlicher Eintrag der Sonnenenergie. Diese Thematik umfasst die jahrelange Erfahrung der beruflichen Interessen der Autoren.

Der Inhalt der Bücher und die Art und Weise der Darstellung des Stoffes sind offensichtlich stark von der Zusammensetzung des Autorenteams beeinflußt. Als Repräsentanten von (leicht) unterschiedlichen Spezialgebieten derselben Wissenschaft (Limnologie, Fluiddynamik und Ozeanographie), haben wir uns bemüht, die Seenphysik in kohärenter Weise darzustellen und wichtige Elemente aller oben erwähnten Gebiete zu extrahieren. Meinungsunterschiede, wie ein Thema am optimalsten darzustellen sei, waren gelegentlich recht heftig und verlangten Kompromisse; wir glauben hingegen, dass die Interferenz unseres Wissens im Gegensatz zu einer einfachen Summe mehr zur Qualität des gegenwärtigen Produktes beigetragen hat als dies andernfalls der Fall gewesen wäre. Ein zusätzlicher Gewinn für uns ist die internationale Zusammensetzung des Teams. Die Übersetzung dieses Vorwortes aus dem Englischen in unsere Muttersprachen kann direkt verstanden werden von mehr als 70% der professionellen angesprochenen Bevölkerung dieser Erde.

Der Inhalt dieser Abhandlung über Seenphysik, aufgeteilt in drei Bände, umfasst die folgenden Themen:

BAND 1: Physik der Seen: Formulierung des mathematischen und physikalischen Hintergrundes

Der Band beginnt in der Einführung mit einer allgemeinen, formelfreien Motivation durch Beschreibung von gewissen, treffenden Phänomenen, welche die Bewegung des Seewassers an der Oberfläche und im Seeinnern betreffen, und ordnen letztere der Verteilung der Dichte des Seewassers zu. Es wird zudem eine große Zahl von Seen auf dieser Erde gelistet und ihre Morphometrie charakterisiert, einschließlich der Beschreibung ihrer Verhaltensweise auf Grund der Reaktion auf die antreibenden Mechanismen.

Da die Physik von Seen nicht ohne die mathematische Sprache beschrieben werden kann, und da nur gerade die einfachsten Kenntnisse der Hochschulanalysis und der klassischen Physik vorausgesetzt werden, erfolgt eine Einführung in diese Themen anfänglich in der einfachsten möglichen Art und mit gößter Sorgfalt; mit wachsender Gewöhnung und fortschreitender Komplexität wird dann aber schrittweise auf eine elegantere Schreibweise übergegangen. Dieser Prozess führt so (1) zur Darstellung der Grundgleichungen der Seen-Hydrodynamik in Form der primitiven Gleichungen, die direkt den physikalischen Bilanzen entsprechen, und (2) zu einer detaillierten Behandlung des Drehimpulssatzes und der Wirbelbilanzgleichungen. Ein Kapitel über lineare Wasserwellen öffnet danach das Forum für die Dynamik von wassergefüllten Becken mit freier Oberfläche. Die Dichteschichtung ist Ursache für große interne Bewegungen, was in einem Kapitel demonstriert wird, in welchem die Rolle der Verteilung der Masse in endlichen Becken untersucht wird.

Schichtung wird hauptsächlich durch die jahreszeitliche Variation der Sonneneinstrahlung und deren Umformung durch Turbulenz gesteuert. Letztere sowie die Zirkulationsdynamik werden durch den Eintrag von Windschub an der Seeoberfläche gesteuert. Die frühe Theorie der Zirkulationsdynamik mit dem, bzw. ohne den, Einfluß der Erdrotation schließen dann den Themenkreis dieses ersten Bandes der Seendynamik. Ein Kapitel über turbulente Modellierung und ein weiteres Kapitel, das die phänomenologischen Koeffizienten von Wasser behandelt, vervollkommnen diesen ersten Band über die Grundlagen der mathematischen und physikalischen Behandlung der Physik von Seen.

BAND 2: Physik der Seen: Seen als Oszillatoren

Das hauptsächliche Thema in diesem zweiten Band der Monographie **Pysik der Seen** betrifft lineare Wellen in homogenen und geschichteten Seen auf der rotierenden Erde. Er umfasst zwölf Kapitel und beginnt mit linearen Wasserwellen auf der rotierenden Erde. Es werden Klassifikationen eingeführt, welche die Schwerewellen und Rossby-Wellen im begrenzten homogenen und im Schichtmedium charakterisieren. Dies führt in natürlicher Weise zur mathematischen Analyse von Schwerewellen im unbegrenzten und endlichen Medium mit konstanter Tiefe: Kelvin, Inertial- und Poincaré Wellen, Reflektion solcher Wellen am Ende eines Golfes und deren Beschreibung in vollkommen geschlossenen Becken als sogenannte eigentliche Inertialwellen (inertial waves proper). Die Anwendung von Gravitationswellen in kreisförmigen und elliptischen Becken konstanter Tiefe führt in natürlicher Weise zur interpretationsgerechten Behandlung von barotroper und barokliner beckenweiter Wellendynamik auf der rotierenden Erde. Das klassische analytische Vorgehen zur Beschreibung der baroklinen Bewegung in Seen wird mit der Zweischichten-Approximation gemacht. Neuere Beobachtungen an Seen haben sich jedoch auf das Erfassen der höheren Baroklinizität konzentriert. Diesem Thema werden zwei Kapitel gewidmet. Beckenweite Dynamik wird anhand von barotropen und baroklinen Studien des Onega Sees und Luganersees vorgenommen und mit ausgedehnten in-situ Messungen verglichen. Die letzten vier Kapitel werden der detaillierten Darstellung topographischer Rossby Wellen und den verallgemeinerten Chrystal Gleichungen und deren Identifikation anhand von Feldmessungen gewidmet.

BAND 3: Physik der Seen: Methoden, die Seen als Komponenten des geophysikalischen Umfeldes verstehen

Der rote Faden in diesem Band ist die Entwicklung unterschiedlicher Methoden zur Charakterisierung von physikalischen Prozessen in natürlichen Seen. Teil I ist numerischen Modellierungsmethoden und -techniken gewidmet, welche die Reaktion eines Sees auf die äusseren Windkräfte bestimmen. Numerische Methoden für verschiedene, von Konvektion dominierten Problemen, werden untereinander verglichen. Desgleichen werden unterschiedliche Schemata für

die advektiven Terme in den bestimmenden partiellen Differezialgleichungen und die Subgrid-Parametrisierung der Turbulenz getestet. In Teil II werden Methoden und Werkzeuge für Feldmessungen erläutert, und es werden die Arbeitsweisen von üblichen Strömungs-, Temperatur-, Leitfähigkeits-, Druck- und anderen Messgeräten vorgestellt bis hin zu den modernen Messtechniken, welche bei Feldmessungen eingesetzt werden. Die Grundregeln der Zeitreihenanalyse und statistischen Datenauswertung werden ebenfalls zusammengefaßt. Laborexperimentiertechniken werden im Teil III dargelegt und auf die Grundlage der Dimensionsanalyse abgestützt. Es werden Resultate vorgestellt von Laborexperimenten betreffend nichtlineare Schwingungen mit großer Amplitude, und es wird ihre Instabilität und Umwandlung durch Meromixis und konvektiven Austausch in Becken mit geneigten Topographien entlang ihrer Küstenlinien behandelt. Kombinierte Darstellung von Feldbeobachtungen, numerischen und Labormessdaten-Analysen stellen heute ganz allgemein den methodischen Zugang zur Interpretation von physikalischen Prozessen der Limnophysik her.

Physik der Seen ist ein sehr breites Gebiet, welches ein großes Spektrum von Fragestellungen umfasst. Gewisse Besonderheiten des jahreszeitlichen Wasserzyklus, Schichtung und unterschiedliche Mischungs- und Vermengungsmechanismen sind von uns studiert und angegangen worden, aber in diesem Werk noch nicht enthalten. Es ist zu wünschen, dass wir die Zeit und Energie aufbringen, diese in einem vierten Band zusammen zu fassen.

Zürich, Switzerland — *Kolumban Hutter*
Darmstadt, Germany — *Yongqi Wang*
Kaliningrad, Russia — *Irina Chubarenko*
June 2010

Предисловие к серии

Интегральное представление физики озер требует глубокого знания целого ряда различных специальностей, что вряд ли может быть достигнуто одним ученым. Даже коллективу авторов столь общую тему пришлось ограничить: в этой монографии рассматриваются только *геофизические* аспекты *динамики жидкости*. Имея дело со сложными природными объектами и явлениями, физическая лимнология традиционно использует три взаимодополняющих подхода: *теоретическое описание, натурные наблюдения* и (численное, лабораторное и другие виды) *моделирования*. Представленная работа в значительной степени использует все три подхода, давая читателю таким образом возможность построить максимально полное и согласованное представление о предмете – от вывода основных уравнений до исследования разнообразных явлений, наблюдаемых в реальных озерах.

Некоторые особенности этой серии, мы надеемся, сделают ее особенно привлекательной для широкого круга студентов, исследователей геофизической гидродинамики, специалистов в физической лимнологии. Прежде чем погрузиться в описание собственно физики озер, мы начинаем с детального введения основных математических правил и основополагающих законов классической физики; это облегчит дальнейшую работу с уравнениями тем читателям, у кого нет специального образования в математике и физике сплошных сред – биологов, химиков, экологов. Именно эти области лимнологии сегодня развиваются наиболее активно и особенно нужны для развития современного общества; следовательно, доступность изложения для них физических основ трудно переоценить.

Характерной чертой этой серии является обобщенный подход к изложению материала, сочетающий широкий панорамный обзор явлений, присущий физической океанографии, с глубоким и тщательным теоретическим рассмотрением, свойственным механике жидкости. Таким образом, читатель найдет здесь и математические основы, и основополагающие физические законы, и рассмотрение конкретных природных явлений вместе с их движущими механизмами (волны, турбулентность, действие ветра, конвекция и т.д.), и широкий спектр примеров натурных наблюдений во многих озерах нашей планеты. Особое внимание уделяется динамическому отклику озер и их свободной

поверхности на внешние факторы – действие ветра и сезонное поступление солнечной энергии, что обусловлено многолетним профессиональным интересом авторов.

Содержание книг и манера представления материала, конечно, существенно зависит от состава авторского коллектива. Будучи представителями разных школ и профессионалами в несколько различных аспектах одной и той же науки – в лимнологии, механике жидкости и океанологии – мы пытались представить физику озер наиболее гармоничным образом, извлекая ценные зерна из каждой области знаний. Разница мнений о том, какой путь мог бы быть оптимальнее в представлении того или иного материала, была иногда довольно значительна, требуя компромиссов; мы искренне надеемся, что результатом явилась не простая сумма, а реальная интерференция наших знаний, и финальный продукт от этого заметно выиграл. Еще один штрих к возникающей объемной картине добавляет национальный состав нашего интернационального коллектива: перевод этого Предисловия с английского на наши родные языки может быть непосредственно понят более чем 70% населения Земли.

Материал, изложенный в монографии **Физика Озер,** разделен на три тома:

ТОМ 1: Физика Озер – Математические и Физические Основы

Введение начинается с описания поразительных явлений, связанных с движением воды в озере и на его поверхности; затем эти движения соотносятся с распределением плотности. Далее перечисляются наиболее крупные озера Земли, описывается их морфология и характеризуются основные причины их отклика на воздействие окружающей среды.

Поскольку физика озер не может быть описана без языка математики, а у читателя предполагаются только ограниченные школьные знания об исчислении и классической НЬЮТОНовой физике, эти области вводятся сначала максимально просто, а затем исследование продолжается с нарастающей сложностью и элегантностью. Этот процесс приводит к представлению фундаментальных уравнений Гидродинамики Озер в форме так называемых `примитивных уравнений', вплоть до детального описания вращательного момента и завихренности. Затем обсуждение динамики вод в бассейнах со свободной поверхностью открывается главой о свойствах линейных волн. Присутствие стратификации является основным условием возникновения движений вод внутри озера; это демонстрируется в главе, обсуждающей роль распределения масс в ограниченных бассейнах. Стратификация вод в значительной степени управляется сезонными вариациями солнечной радиации и ее трансформацией турбулентностью.

Последняя, так же как циркуляция вод, обусловлена главным образом действием ветра на поверхность. Изложение основ теории циркуляции вод с учетом и без учета влияния вращения Земли заключает рассмотрение динамики вод в озерах. Главы о методах моделирования турбулентности и феноменологических свойствах воды заканчивают эту книгу об основах математики и физики озер.

ТОМ 2: Физика Озер – Озера как Осцилляторы

Основная тема этого тома серии – линейные волны в однородных и стратифицированных озерах на вращающейся Земле. Он содержит 12 глав. Сначала рассматриваются линейные волны на мелкой воде во вращающейся жидкости и дается их классификация на гравитационные волны и волны РОССБИ в однородных и стратифицированных бассейнах. Это естественным образом приводит к анализу гравитационных волн в неограниченных, полуограниченных и ограниченных бассейнах с постоянной глубиной: волн КЕЛЬВИНа, инерционных волн и волн ПУАНКАРЕ, отражения этих волн от закрытого конца залива и их описания в закрытых бассейнах как так называемых ‘собственно инерционных волн’. Приложение к гравитационным волнам в круглых и эллиптических бассейнах постоянной глубины продолжает обсуждение баротропной и бароклинной динамики волн во вращающемся бассейне. Классический аналитический подход к бароклинным движениям в озерах продемонстрирован с использованием двухслойной аппроксимации. Современные работы фокусируются на исследовании бароклинности более высоких порядков, что рассматривается в последующих двух главах. Отклик озера как целого проиллюстрирован анализом баротропных и бароклинных волн в озерах Онежском и Лугано и сопровожден детальным сравнением с натурными данными. Последние четыре главы посвящены подробному анализу топографических волн РОССБИ и обобщенных уравнений КРИСТАЛа и их идентификации в натурных данных.

Том 3: Физика Озер – Методы Исследования Озер в их Геофизическом Окружении

Представление различных *методов исследования* процессов, протекающих в реальных озерах, является основной темой этого тома. Часть I посвящена подходам и техникам *численного моделирования*, используемым для демонстрации отклика озер на действие ветра. Сравниваются численные методы, используемые для описания движений, доминируемых конвекцией; рассматриваются разные численные алгоритмы для расчета адвективного члена и параметризация подсеточной турбулентности. Методы и средства

натурных измерений изложены в Части II, включая описание принципов действия типичных сенсоров для измерения течений, температуры, электропроводности, давления и других, а также современные техники полевых измерений. Отдельная глава суммирует основные правила анализа временных рядов. *Лабораторное моделирование,* представленное в Части III, вводится началами анализа размерностей. Представлены результаты лабораторных экспериментов по нелинейным колебаниям большой амплитуды, трансформации волн и частичному перемешиванию, обменным течениям конвективной природы в бассейнах с наклонным дном. Совместное представление натурных, численных и лабораторных подходов позволяет в результате выстроить общий вид современных методов физических исследований в лимнологии.

Физика озер – тема, не имеющая границ, охватывающая огромный круг разнообразных вопросов. Собранный нами материал о сезонном цикле, различных механизмах перемешивания, размешивания и установления стратификации не включен в трехтомник, и, мы надеемся, может быть суммирован в четвертом томе серии.

Цюрих, Швейцария — Колумбан Хуттер
Вена, Австрия — Йонгки Ванг
Калининград, Россия — Ирина Чубаренко
июнь 2010

本书系列序言

湖泊物理学的综述，需要本领域不同专业的知识，这对于一个单独著述的学者是很难兼备的。甚至对于三人作者团队，我们也必须限制所著述研究的范围。本书系列专注于地球物理学的流体动力学研究。目前科学界对复杂自然现象的研究，通常采用三种互补的研究方法，即: 理论描述，场观测和 (数值的，试验的和其它方式的) 模拟。本专著亦充分运用这三种方法，以期提供给读者一个机会，从理论方程的引入到真实湖泊中所观看到的各种自然现象，建立一套对该领域清晰连贯的看法。我们相信本书系列的一些特色主题将吸引湖泊物理学专家们，以及众多对地球物理学有特别兴趣的学生和学者。

在进入湖泊物理的核心之前，我们先从详细的数学前提和基本物理定律的引入开始，这将使进一步的方程建立及求解变得容易理解，特别是对生物学家，化学家，生态学家而言，而他们从事的正是目前湖泊物理学研究中最具活力并对现代社会的发展深具影响的领域。在这些科研学者看来是高深的物理知识应成为容易利用的工具。本书系列分为三部，目的是要获得对湖泊中各种物理现象的一个全面了解。所采用的方法是建立在对流体力学精确的理论基础上。读者可以从中找到相关的数学基础，普遍的物理定律，也包括他们在湖泊物理中对自然现象上的应用和理解，以及这些现象产生的力学原理 (比如: 水波，湍流，风驱动，对流等)，从而得到对湖泊物理场的一个宏观印象。湖泊对其自由表面和内部特性的动力学响应，以及对外部驱动，如风力和太阳能的季节性摄入气象现象的反应也会被专门讨论。这些方面均涉及作者多年的相关工作经验和兴趣。

本系列所涉及的内容及描述的方式受到作者组合的深刻影响。由于各自不尽相同的专业背景(湖泊动力学，流体力学和海洋力学)，我们尝试以一个协调一致的方式介绍湖泊物理学和萃取所有上面提及领域的重要基础。作者因意见不同，比如怎样更好地描述一个相关的主题，有时甚至会有激烈的争辩，亦需要相互妥协。然而我们相信与所有作者知识的简单叠加相比，这样的交叉互补对本专著的质量是一个重要的贡献。对我们来说，这其中一个更大的乐趣是一个国际合作团队的形成。本序言从英语到我们各自母语的翻译将使得地球上超过 70%的人们可以直接理解。

这个三部书的系列将涵盖湖泊物理学的以下方面:

第一部: 湖泊物理学 ------ 数学和物理学基础的构成

本书将从一些相关现象的描述开始。这些现象与湖水在表面和内部的运动及水密度分布紧密相关。地球上许多湖泊被一一罗列，它们的地貌特征及对驱动力的响应特点也会被描述。

由于不通过数学语言，人们无法描述湖泊物理特性，并且我们假设读者仅具备最基本的大学数学解析和牛顿物理学基础，湖泊物理描述首先以一种尽可能简单的方式小心地被引入，其理论描述的复杂性将逐步增加。湖泊水力学的基本方程，物理学平衡和角动量守恒及涡流守恒方程随之被导出。关于线性波的章节将引出含有自由表面水体的动力学讨论。水的密度分层是产生强烈内部运动的原因，一个讨论在水体中质量分布影响的章节将论证这个特性。这样的水密度分层主要是由于太阳辐射的季节性变化以及由湍流产生的输运所控制，后者以及水环流动力学是由风力在水表面的作用而产生。早期环流动力学理论的引入，包括和不包括地球自转影响，将带领读者进入这本书的湖泊动力学部分。本系列书的第一部将以阐述湍流模拟和水的表征参数为结束。

第二部: 湖泊物理学 ------ 作为振荡器的湖泊

本书系列第二部将主要涉及受地球自传影响的匀质和密度分层湖泊中的线性波。包括 12 个章节，从在转动地球上的线性浅水波的讨论开始，引入波的分类，以便描述在均质和分层水体中的重力波和 Rossby 波。这将自然引出在无限大，半有限和有限的等深水域中重力波的分析: Kelvin，惯性 Poincare 波。也包括波在港湾端部的反射和在全封闭水域里惯性波的描述。重力波在圆形或椭圆形等深水域中的应用自然引入了在旋转地球上正压和斜压波的动力学处理。在湖泊中斜压运动将首先用二层近似这种经典方法来分析。观测主要集中在高阶斜压性的捕捉上。两个章节将涉及此内容。湖泊作为一个整体的特性，将通过在 Onega 湖和 Luganer 湖的正压和斜压运动的研究来讨论，相关测量数据将被仔细地对比。本部书最后四章将讨论地貌产生的 Rossby 以及它们在场观测中的识别。

第三部 : 湖泊物理学 ------ 了解湖泊的方法

本部书聚焦于介绍研究天然湖泊物理过程的不同方法。第一部分涉及数值方法和技术。这些被用来研究湖泊对外部风力的响应。针对各种对流起主导作用的问题，不同的数值方法被加以对比，不同的数值格式将被应用到给定偏微分方程的对流项和湍流的模拟上，并加以测试。第二部分包括有关测量的

方法和仪器。传统的在大规模场观测中使用的流速，温度，传导，压力和其它测量仪器的操作原理将会被介绍。其中也包括一些现代的测量仪器。时间序列分析和统计数据处理的基本规则将被总结。第三部分阐述了一些建立在量纲分析基础上的实验室试验技术。该部分也介绍和讨论了与大幅值的非线性波动相关的实验结果，以及与其相关的稳定性，在倾斜底部的局部混合和对流等。场观测，数值和实验数据分析构成了当今理解湖泊物理现象的一个通用方法。

湖泊物理学是一个广泛的学科，我们也搜集了比如季节性循环，密度分层及各种混合机制等的相关材料。但是本书系列没有包括这些内容。我们希望，在有时间和精力的基础上，能出版这个系列的第四部书，以期对这些内容加以总结。

瑞士 Zurich, K. Hutter
德国 Darmstadt 王永奇
俄罗斯 Kaliningrad I. Chubarenko
2010 年 6 月

Acknowledgments

This book series is an outgrowth of more than 3 decades of research and teaching activities, and so, the institutions which supported these activities deserve an early word of appreciation. The precursors to the books started as lecture notes on hydrodynamics of lakes, in particular 'Waves in the Ocean and Lakes' which KH held since the early 1980s of the last century in the Department of Mechanics of Darmstadt University of Technology and for some years also at the Swiss Federal Institute of Technology (ETH) in Zurich to upper level students of Earth Sciences, Physics, Engineering and Mathematics. Advanced courses, addressed to graduate students and postdoctoral fellows were also held on subtopics of lake physics at the International Centre for Mechanical Sciences (CISM) in Udine, Italy (1983) and published as 'Lake Hydrodynamics' [1] and as an Article in the Encyclopedia of Fluid Mechanics [2]. During the teaching and research years 1987–2006 considerable activity was devoted to physics of lakes, which is documented in the reference list for diploma theses [9–18], doctoral dissertations [19–21, 24, 26–28] and habilitation theses [29, 30]. Out of this grew a particularly fruitful collaboration with Dr.-Ing. habil Yongqi Wang (YW), who serves as second author of this book series. The incentive to write a broader text on the subject grew during a research project in the years 2001–2004 in the Physical Limnology Group of the Limnology Institute of Constance University, Germany in its Collaborative Research Projects 'Transport Processes in Lake Constance' and 'Littoral of Lake Constance'. In the field campaigns conducted by the Limnological Institute external research Institutes were also involved. Collaboration was initiated with Drs. Irina (IC) and Boris Chubarenko from the Atlantic Branch of the P. P. Shirshov Institute of Oceanology of the Russian Academy of Sciences, Kaliningrad, who were leading in the conduction of systematic experiments, data analysis and interpretation, mostly executed by IC, who joined the book series as third author.

In the mid 1970s of the last century KHs activities within the Laboratory of Hydraulics, Hydrology and Glaciology (VAW), at the Swiss Federal Institute of Technology, Zurich were shifted from glaciology to physical limnology. A new small research unit, dealing with Hydrodynamics of Lakes, was created. Generous financial support was provided. The group received expert advise from Prof. J. Sündermann at the University of Hannover (later Centre for Ocean and Climate Research, University of Hamburg), the late Prof. W. Krauss, formerly at

the Leibnitz Institute for Ocean Sciences, University of Kiel, and in particular, Prof. C.H. Mortimer, Centre for Great Lakes Studies, the University of Wisconsin, Milwaukee. The synoptic field campaigns, conducted in Lake Zurich, 1978; Lake of Lugano, 1979 and 1984; Lake Constance, 1993 were greatly influenced by them. In the late 1970s and early 1980s Prof. Mortimer spent several visiting assignments with the group, looking at the Lake Zurich data of 1978 and teaching us his outstanding graphical and statistical methods by which time series data, taken synoptically at several moorings with thermistor chains and current meters. could be combined to extract the physics and thus find an understanding of the underlying physical processes. Later, during the academic year 1982/1983, Prof. L.A. Mysak, now Department of Atmospheric and Ocean Sciences at McGill University, Montreal, spent his sabbatical with the group; his influence was of equal significance as that of Prof. C.H. Mortimer, but complementary. The papers on barotropic, baroclinic gravity and Rossby wave dynamics in Alpine lakes, summarised in this book, owe much to Profs. C.H. Mortimers and Mysaks advise. The work of the lake group at VAW has also greatly benefited from Dr. D.J. Schwab of NOAA's Great Lakes Environmental Research Laboratory (GLERL), Ann Arbor, Michigan, and from associations with doctoral students (now Dr.) Gabriel Raggio [22], (now Dr. Prof.) Thomas Stocker [6, 7, 25], (now Dr.) Johannes Sander [23] and research assistant Gordon Oman [3, 5] as well as Dr. Mike Laska [4] with whom gravity waves, topographic Rossby-waves, non-linear internal waves in channels and wind induced currents in stratified and homogeneous Lake Zurich were studied. Moreover, a long and very fruitful early collaboration ought to be mentioned with a group of community college teachers in Lugano and Melide in the South (Italian) Canton of Switzerland: Dr. F. Zamboni, Dr. C. Spinedi and Mr. G. Salvadè, with whom a very active collaboration existed between 1978 and 1987 on research of physical limnology in Lake of Lugano. It is seldom that such a collaboration between research professionals and 'hobby scientists' leads to a considerable surge of substantial results. Volume 2 of this treatise will demonstrate in several chapters that this collaboration has been very fruitful.

In the Department of Mechanics at Darmstadt University of Technology in (1987–2006), the focus of lake research was on laboratory experimental techniques and theoretical-numerical methods of non-linear internal waves and barotropic and baroclinic circulation dynamics. A fortunate association with the Limnological Institute of the University of Constance initiated by Prof. M. Tilzer, first casually and later more formally, within the collaborative research programs 'Transport Processes in Lake Constance' and 'Littoral of Lake Constance', led by Profs. P. Böger and K.O. Rothhaupt, made it possible that field work could be pursued, though at a somewhat moderate pace. Much of the fundamental work, which was done in Darmstadt in diploma (M.Sc), Ph.D. and Habilitation dissertations (cf. the mentioned references), has been motivated by this collaboration, as well as collaboration within this program with Drs. B. and I. Chubarenko from the Atlantic Branch of the P. P. Shirshov Institute of Oceanology, Russian Academy of Sciences, Kaliningrad, who had visiting assignments within this program. Throughout this 'Constance Period' Dr. E. Bäuerle and (until 1997) Dr. K. Jöhnk [29] were very supportive through their

own work, but also in many helping discussions, field work planning and measuring assignments.

In addition to all the above mentioned scientists Drs. N. Stashchuk and V. Vlasenko, now at the School of Earth, Ocean and Environmental Sciences, Plymouth University, UK, ought to be mentioned as well. They spent more than 4 years, from 1999 to 2003, in the fluid mechanics research group within the Department of Mechanics at Darmstadt University of Technology, working on a project funded by the Deutsche Forschungsgemeinschaft, mainly concentrating on nonlinear wave dynamics and convection in the baroclinic ocean. Their work, which was begun already in their Ph.D. dissertations and V. Vlasenko's doctoral thesis (corresponding to the Habilitation or D. Sc. in the West) in the Institute of Oceanology, Ukrainian Academy of Sciences, Sevastopol, provided a substantial boost to the lake research of the small group at that time. Apart from a number of important peer reviewed papers in oceanographic periodicals the collaboration with them led to the book 'Baroclinic Tides – Theoretical Modeling and Observational Evidence' [8]. V. Vlasenko also took the initiative to formulate with KH an INTAS project (funded from 03.2004 to 02.2007, grant Nr. 03-51-37 28) on 'Strongly nonlinear internal waves in lakes: generation, transformation, meromixis' with collaboration of KH from Darmstadt, V. Vlasenko & N. Stashchuk from Plymouth, Prof. V. Maderich and associates (from the Institute of Mathematical Machine and System Problems) and Prof. V. Nikishov and associates (from the Institute of Hydrodynamics), both of the Ukrainian Academy of Sciences in Kiev, Prof. N. Filatov (and associates) from the Northern Water Problems Institute, Russian Academy of Sciences, Petrozavodsk, Prof. E. Pelinovsky (and associates), Institute of Applied Physics, Russian Academy of Sciences, Nizhny Novgorod. The work of this INTAS project will be reviewed in a separate book, co-authored by the above mentioned scientists, one reason why topics covered in that book are treated less systematically in this book series.

Our work has generously been supported through the years by the Institutions by which we were applied. KH and YW were additionally funded by the Swiss National Science foundation (KH, 1975–1987); by the German Research Foundation (Deutsche Forschungsgemeinschaft) (KH and YW, 1987–2006); German Academic Research Exchange Service (Deutscher Akademischer Austauschdienst), Alexander von Humboldt Foundation (1987–2006); INTAS, Brussels (2004–2007). B. and I. Ch.'s visits to the Limnological Institute, Constance University were funded by the German Research Foundation; further collaboration was supported by the German Academic Exchange Service, by a Collaborative Linkage Grant by NATO and the Russian Foundation for Basic Research. To all these funding agencies we express our sincere thanks. Only such sources make it possible that research ideas can effectively and efficiently be put into practice.

In writing this treatise, KH as a retired member of Darmstadt University of Technology, wishes to acknowledge the generosity offered by Profs H.-E. Minor and R. Boes for the free access to the institute's facilities at VAW-ETH, of which KH is not a member. He also thanks all the other members of VAW for their endurance to cope with his presence. He particularly acknowledges the help received from

Bruno Nedela, who drew a great many of the illustrations in the second volume from hand-drafted and scanned 'originals'. His input is explicitly visible in the quality of these illustrations. Moreover, Drs. E. Vasilieva and S. Ktitareva helped in TEXing some manuscript elements and the production of Indices.

Finally, we all thank Springer for the support, in particular Dr. C. Bendall and A. Oelschläger for their efforts in the publication process of the books.

Zürich, Switzerland — *Kolumban Hutter*
Darmstadt, Germany — *Yongqi Wang*
Kaliningrad, Russia — *Irina Chubarenko*
June 2010

References

Books, Reports

1. Hutter, K.: *Lake Hydrodynamics*. CISM Courses and Lectures No 286, Springer Verlag Vienna-New York 341 pp. (1984)
2. Hutter, K.: Hydrodynamic modeling of lakes. Chap. 22 in: *Encyclopedia of Fluid Mechanics* (Ed: Cheremesinoff). Gulf Publ. Comp. Houston, 6 , 897–998 (1987)
3. Hutter, K. Oman G. and Ramming, H.-G.: *Wind-bedingte Strömungen des homogenen Zürichsees.* Mitteilung Nr 60 der Versuchsanstalt für Wasserbau, Hydrologie und Glaziologie and der ETHZ, 123 p. (1982)
4. Laska, M.: *Characteristics and modelling of the physical limnology processes*. Mitteilung Nr 54, der Versuchsanstalt für Wasserbau, Hydrologie und Glaziologie and der ETHZ 290 p. (1982)
5. Oman, G.: *Das Verhalten des geschichteten Zürichsees unter äusseren Windlasten. Resultate eines numerischen Modells. Sein Vergleich mit Beobachtungen.* Mitteilung Nr 61, der Versuchsanstalt für Wasserbau, Hydrologie und Glaziologie and der ETHZ 185 p. (1982)
6. Stocker, T. and Hutter, K.: *A model for topographic Rossby waves in channels and lakes.* Mitteilungen der Versuchsanstalt für Wasserbau, Hydrologie und Glaziologie, ETH Zürich, No 76, 1–154 (1985)
7. Stocker, T. and Hutter, K.: *Topographic waves in channels and lakes on the f-plane*. Lecture Notes on Coastal and Estuarine Studies, Vol. 9, Springer Verlag, Berlin, etc. (1987)
8. Vlasenko, V., Stashchuk, N. and Hutter, K.: *Baroclinic Tides – Theoretical Modelling and Observational Evidence*. Cambridge University Press, Cambridge, (2004)

Diploma (M. Sc.) Theses

9. Bauer, G.: *Windangeregte Strömungen im geschichteten Bodensee–Modellrechnungen und Feldbeobachtungen*. Diplomarbeit am Fachbereich Mechanik, Darmstadt University of Technology, 169 p. Juli 1993
10. Franke, V. *Physikalisch-biologische Kopplung zur Modellierung des Algenwachstums in Seen.* Diplomarbeit am Fachbereich Mechanik, Darmstadt University of Technology, 112 p. November 1996

11. Güting, P.: *Windgetriebene Strömungen und Diffusion eines Tracers* Diplomarbeit am Fachbereich Mechanik, Darmstadt University of Technology, 61 p. Februar 1994
12. Hüttemann, H.: *Modulation interner Wasserwellen durch Variation der Bodentopographie* Diplomarbeit am Fachbereich Mechanik, Darmstadt University of Technology, 110 p. September 1997
13. Maurer, J.: *Skaleneffekte bei internen Wellen im Zweischichtenfluid mit topographischen Erhebungen.* Diplomarbeit am Fachbereich Mechanik, Darmstadt University of Technology, 112 p. November 1993
14. Salzner, E.: *Energieeinträge in Seen*. Diplomarbeit am Fachbereich Mechanik, Darmstadt University of Technology, 98 p. Dezember 1996.
15. Umlauf, L: *Strömungsdynamik im Ammersee.* Diplomarbeit am Fachbereich Mechanik, Darmstadt University of Technology 151 p. November 1993
16. Wessels, F.: *Wechselwirkung interner Wellen im Zweischichtenfluid mit topographischen Erhebungen.* Diplomarbeit am Fachbereich Mechanik, Darmstadt University of Technology, 69 p. November 1993
17. Weimar, V.: *Nichtlineare, durch Randoszillation angeregte Wellen im Zweischichtenfluid.* Diplomarbeit am Fachbereich Mechanik, Darmstadt University of Technology, 65 p. April 1995
18. Zeitler, M.: *Vergleich zweier eindimensionaler Turbulenzmodelle der Seenphysik* Diplomarbeit am Fachbereich Mechanik, Darmstadt University of Technology, 112 p. November 1996

Doctoral Dissertations

19. Diebels, S.: *Interne Wellen – Ein Modell, das Nichtlinearität, Dispersion, Corioliseffekte und variable Topographie berücksichtigt.* Doctoral Dissertation, TH Darmstadt, 1–173, TH Darmstadt (1991)
20. Güting, P.: *Dreidimensionale Berechnung windgetriebener Strömungen mit einem $k-\epsilon$-Modell in idealisierten Becken und dem Bodensee*. Doctoral Dissertation, TU Darmstadt, 1–343 (1998)
21. Lorke, A.: *Turbulenz und Mischung in einem polymiktischen See – Untersuchungen auf der Basis von Mikrostrukturmessungen*. Doctoral Dissertation, TU Darmstadt 1–85 (1998)
22. Raggio, G.: *A channel model for curved elongated homogeneous lakes.* Mitteilung Nr 49 der Versuchsanstalt für Wasserbau, Hydrologie und Glaziologie and der ETHZ, 1–222 (1981)
23. Sander, J.: *Weakly nonlinear unidirectional shallow water waves generated by a moving boundary.* Mitteilung Nr 105 der Versuchsanstalt für Wasserbau, Hydrologie und Glaziologie and der ETHZ, 1–199 (1990)
24. Schuster, B.: *Experimente zu nichtlinearen internen Wellen großer Amplitude in einem Rechteckkanal mit variabler Bodentopographie*. Doctoral Dissertation, TH Darmstadt vii + (1–165) (1991)
25. Stocker, T. *Topographic Waves. Eigenmodes and reflection in lakes and semi-infinete channels.* Mitteilung Nr 93 der Versuchsanstalt für Wasserbau, Hydrologie und Glaziologie an der ETHZ, 1–170 (1987)
26. Umlauf, L.: *Turbulence parameterisation in hydrobiological models for natural waters*. Doctoral Disseertation, TU Darmstadt, XVI + 1–228 p. (2001)
27. Wang, Y.: *Windgetriebene Strömungen in einem Rechteckbecken und im Bodensee.* Band I: Text 1–186, Band II: Abbildungen 187–432, Doctoral Dissertation, TH Darmstadt (1995)
28. Weis, J.: *Ein algebraisches Reynoldsspannungsmodell*. Doctoral Dissertation, TU Darmstadt, 1–111 (2001)

Habilitation Theses

29. Jöhnk, K. D.: *Ein-dimensionale hydrodynamische Modelle in der Limnophysik. Turbulenz-Meromixis-Sauerstoff.* Fachbereich Mechanik, TU Darmstadt, XII + 1–235 (2000)
30. Wang, Y.: *From lake dynamics to granular materials – Two aspects of environmental mechanics.* Department of Mechanics, Darmstadt University of Technology, 277 p. (2001)

Preface to Volume II

This second volume to the treatise *Physics of Lakes* is dedicated to a single topic, namely *Lakes as Oscillators*. There are several reasons why this topic plays such a prominent role.

First, oscillations in lakes belong to those subjects, which were already studied by the pioneers in the seventeenth century. As Mortimer writes: "Readily observed, rhythmic fluctuations in lake level have long exercised a fascination and have stimulated mathematical modeling, but often with a longtime gap between observation and theoretical resolution [20]. The first detailed set of observations ([9], on Léman, 1730, introducing the local name 'seiche') and recognition of their occurrences in many lakes [26] were, it is interesting to note, preceded by systematic observations and conjectures by a Jesuit missionary [3] in 1671, describing the large but irregular 'tides' at the head of Green Bay (a gulf which opens onto Lake Michigan) and attributing to a combination of lunar tidal influence and to the main influence of the lake. Three centuries elapsed before those conjectures were confirmed by spectral analysis and numerical modelling [12, 13, 19]", from [20].

Mortimer continues: "With early observations and conjectures as a prelude, physical limnology was launched as a distinct branch of geophysical fluid mechanics (L' océanographie des lacs) by Forel's lifetime study of Léman seiches and temperature regime [10]. But again, in one respect priority must go to Lake Michigan, i.e. to a US Army surveyor's 1872 interpretation [8] of the conspicuous 2.2 h seiche at Milwaukee as a standing wave, thereby antedating Forel's similar interpretation [11] by 3 years and providing yet another example of an original idea occurring to two persons at about the same time. Mathematical modelling of this seiche (as the first transverse mode [23]) confirmed the 1872 interpretation. In fact, hydrodynamic modelling may be said to have 'cut its teeth' on seiches . . .", from [20].

Second, since the availability of electronic computation and the development of electronically based measuring techniques, which permitted relatively long term recording of detailed time series of density (via temperature and electrical conductivity) and velocity, the internal motion of the water in lakes became 'observable' via the construction of isotherm-depth or isopycnal time series at fixed mooring positions. Fast Fourier and more recently wavelet transforms and cross correlation analyses of such time series between synoptically recorded quantities became key working techniques to interpret whole-basin or localized internal processes. These

findings could be compared with predictions of theoretically deduced models. These measuring techniques did not only disclose the lake interior to our 'eyes', they made the internal whole-basin dynamics interpretable as the baroclinic variants of the surface or barotropic seiches observed already in the eighteenth and nineteenth century.

Parallel with the development of the electronic measuring techniques, software was developed by which such internal motions could be computed with much better adjustment of the lake geometry than was possible heretofore. This development took place in the 1970s and 1980s and allowed theoretical numerical interpretation of field observations; however, storage limitations often prevented optimal coincidence which had to await more sophisticated hardware. In this phase of development *numerical* modeling of lake hydrodynamics may reasonably be said to have 'cut its teeth' on *internal* seiches.

Third, it is a simple fact that, starting in the 1960s and 1970s of the last century, the dynamic response of lakes under barotropic and baroclinic conditions became the principal focus of research activities of a number of lake research centers all over the world: Among these mention might be made of the Center of Great Lakes Studies (CGLS), University of Wisconsin-Milwaukee, the NOAA Great Lakes Environmental Research Laboratory (GLERL), Ann Arbor Michigan, the Canadian Centre for Inland Waters (CCIW), Burlington, Ontario, the Centre for Water Research (CWR) at the University of Western Australia, Perth. In 1972 the International Field Year of the Great Lakes Studies was in operation. In the same year the Institut für Meereskunde at the University of Kiel conducted with the support of the Government of Baden-Würtemberg, a synoptic field campaign in Lake Constance (including Lake Überlingen) and deployed a number of moored thermistor chains and current meters [15, 17]. This was the first serious European lake campaign of physical limnology, in which experimental techniques known in physical oceanography were 'copied' for research of lake physics. In 1976 in Switzerland, the 5 year National Programme of the Swiss Science Foundation on Fundamental Problems of the Water Cycle in Switzerland (Grundlegende Probleme des Schweizerischen Wasserhaushaltes), 1977–81, was created with field studies similar to those above in Lake Zurich in 1978 [17, 18], Lake of Lugano in 1979 [1, 25] and 1984 [24], with scientists of the Laboratorio di Fisica Terrestre, ICTS, Lugano-Trevano, in Lake Geneva during the same 1977-81 period by the Laboratoire d' Hydraulique (LHYDREP) at Ecole Polytechnique Fédérale, Lausanne [21,22], and again in Lake Constance in 1993 by the Laboratory of Hydraulics, Hydrology and Glaciology (VAW) [14] at the Swiss Federal Institute of Technology and the Swiss Federal Institute for Water Resources and Water Pollution (EAWAG), in part with the support of the Limnological Institute at the University of Constance, and the Landesamt für Umweltschutz, Baden-Würtemberg, Germany. Many similar measuring campaigns, generally somewhat smaller in scope than the large synoptic programmes above, followed in the years to come by scientists of these and other institutions. A 1 month whole-basin synoptic programme in Lake Constance was again conducted in 2001 by the Limnological Institute at the University of Constance and the CWR, at the University of Western Australia and further support from the Institute of Mechanics

at Darmstadt University of Technology and the Atlantic Branch of the Shirshov Institute of Oceanology, Russian Academy of Sciences at Kaliningrad. The measurements, taken with moored and towed instruments recording temperature, current and atmospheric wind, temperature and humidity are collected in internal reports [4, 5, 7]. In these field measurements free and whole basin-scale analyses of the internal wave motion were made using the linear and non-linear surface and internal waves, and wave induced circulation dynamics were numerically implemented with software apt to describe these processes in detail.

In this Volume 2 of *Physics of Lakes* the external and internal dynamics of many lakes worldwide are studied with the focus on oscillations and comparison of measured data with the 'reproduced' model results. We start with the description of the theory and its simplifications under various conditions. Attention is devoted to the role played by the rotation of the Earth as it modifies gravity modes of barotropic and baroclinic motions and how it contributes to the independent formation of topographic Rossby waves, a subject which is treated by itself in three chapters. We study the influence of the density stratification when it is implemented by more than just a two-layer model. Such higher order baroclinicity was seldom analyzed in the past but has been the subject of more intense studies in recent years. The theoretical findings are verified either with results obtained by laboratory experiments or more frequently by the data collected in field campaigns. We close this book with an analysis of internal waves in lakes by a systematic derivation of channel models, which generalize the classical Chrystal model, and remove the somewhat biased approach in using 'Kelvin-wave dynamics' when incorporating the rotation of the Earth.

We assume the reader to be familiar with the subjects of Volume 1. Moreover, the statistical methods to handle data from time series of synoptically recorded temperature, salinity and velocity time series are equally assumed known, and will be used and demonstrated, but not separately explained.

Zürich, Switzerland — *Kolumban Hutter*
Darmstadt, Germany — *Yongqi Wang*
Kaliningrad, Russia — *Irina Chubarenko*
December 2010

References

1. Anonymous 82: *Hydrologische Messungen mit verankerten Instrumenten im Nordbecken des Luganersees während der Monate Juli/August 1979.* Gemeinsamer Bericht der Versuchsanstalt für Wasserbau, Hydrologie und Glaziologie an der ETH Zürich und des Laboratorio di Physica Terrestre, Lugano-Trevano (unpublished) (1981)
2. Anonymous 83: *Misure Idriologiche Lago di Lugano.* Gemeinsamer Bericht des Laboratorio di Physica Terrestre, Lugano-Trevano und der Versuchsanstalt für Wasserbau, Hydrologie und Glaziologie an der ETH Zürich (unpublished) (1983)
3. André, Father Louis; quoted and translated in Relation of 1671-72, and in Relation of 1676-77; In: Thwaites, R. G.: *The Jesuit Relations and other Documents*, **60**, Burrow, Cleveland, Ohio, 1671, 1676

4. Appt, J.: *Analysis of basin-scale Internal Waves in Upper Lake Constance*. Mitteilungen des Institutes für Wasserbau, Universität Stuttgart, **123**, XXXIV + (1–177), (2003)
5. Appt, J. and Stump, S.: *Die Bodensee-Messkampagne 2001, IWS/CWR Lake Constance Measuring Program 2001*. Mitteilungen des Institutes für Wasserbau, Universität Stuttgart, **111**, 67 pp. (2002)
6. Aubert, E. J. and Richards, T. L: (Eds.) *IFYGL – The International Field Year for the Great Lakes*. U. S. Dept. Commerce, National Oceanic and Atmospheric Administration. Great Lakes Environ. Res. Lab., U.S. Dept. Commerce, Ann Arbor, MI, U.S.A. 48104, 410 pp (1981)
7. Bäuerle, E., Chubarenko, B., Chubarenko, I., Halder, J., Hutter, K. and Wang, Y.: *Experimental campaign in the Mainau Island Littoral Zone of Lake Constance*. Report on field experiments 12 October – 19 November 2001. Darmstadt University of Technology and University of Constance, 1–85 (unpublished) (2002)
8. Comstock, C.B.: Tides at Milwankee, Wisconsin [and] Irregular oscillations in surface of Lake Michigan at Milwaukee. Rpt. Secy. War to 42nd Congress, Vol. 3. *Ann. Rpt. Survey of the Northern and Northwestern Lakes*, App. A., g-14, App. B 14-15, Washington, D.C. **14**, (1872)
9. Duillier, F. de: Remarques sur l' histoire du lac de Genève in Spon. *Histoire de Genève* **2**, 463 (1730)
10. Forel, F.A.: *Lac Léman*. Monographie Limnologique, Vol. 2, Lausanne Ronge (1895) Facsimile Ed: Slatkine Reprints genève (1969)
11. Forel, F.A.: Les seiches, vagues d' oscillation fixe des lacs, 1^{er} discours, *Actes Soc. Helvétique Sci. Nat.*, Andermatt, 575 (1875)
12. Heaps, N.S.: Resonant tidal co-oscillations in a narrow gulf. *Arch. Met. Geophys. Bioklim.* Ser A, **24**, 361 (1975)
13. Heaps, N.S., Mortimer, C.H. and Fee, E.J.: Numerical models and observations of water motion in Green Bay, Lake Michigan. *Phil. Trans. Roy. Soc.* A, **306**, 371 (1982)
14. Heinz, G.: *Strömungen im Bodensee. Ergebnisse einer Messkampagne im Herbst 1993* Mitteilungen der Versuchsanstalt für Wasserbau, Hydrologie und Glaziologie an der ETH Zürich, **135**, 1–237 (1995)
15. Hollan, E.: Strömungen am Bodensee. *Bericht AWBR*, **6**, 111–187 (1974)
16. Hollan, E., Rao, D.B. and Bäuerle, E.: Free surface oscillations in Lake Constance with an interpretation of the 'wonder of the rising water' at Constance in 1549. *Arch. Met. Geophys. Biokl.*, Ser A, **29**, 301–325 (1980)
17. Horn, W.: *Seeströmungen im Zürichsee. Ein Einblick in physikalisch-limnologische Prozesse und ihre messtechnische Erfassung*. Versuchsanstalt für Wasserbau, Hydrologie und Glaziologie an der ETH Zürich,VAW, Internal Report I/4 (1978)
18. Horn, W.: *Zürichsee 1978. Physikalisch-limnologisches Messprogramm und Datensammlung*. Versuchsanstalt für Wasserbau, Hydrologie und Glaziologie an der ETH Zürich, VAW, Internal Report I50 (1981)
19. Mortimer, C.H.: Spectra of long surface waves and tides in Lake Michigan and Green Bay, Wisconsin. *Great Lakes Res. Div. Univ. Mich.*, Publ. No. **13**, 304–325 (1965)
20. Mortimer, C.H.: Measurements and Models in Physical Limnology. In: Hutter, K.: Ed. *Hydrodynamics of Lakes* CISM Courses and Lectures No. 286 Springer Verlag Wien-New York, 287–319 (1984)
21. Prost, J.-P., Bauer, S.W., Graf, W.H. and Girod, H.: Campagne de mesures des courants dans Le Léman *Bull. Tech. Suisse Romande* **103**, 19 (1977)
22. Prost, J.-P., Perrinjaquet, C. and Beguin, Ph.: Campagne des mesures de la basse couche atmosphérique sur le Léman *Bull. Tech. Suisse Romande* **106**, 23 (1980)
23. Rao, D.B., Mortimer, C.H. and Schwab, D.: Surface normal modes of Lake Michigan: Calculations compared with spectra of observed water level fluctuations. *J. Phys. Oceanogr.* **6**, 575 (1976)
24. Stocker, T. and Salvadè, G.: *Interne Wellen im Luganersee*. Interner Bericht Nr. I/85 der Versuchsanstalt für Wasserbau, Hydrologie und Glaziologie an der ETH Zürich (unpublished) (1986)

25. Salvadè, G., Zamboni, F. and Hutter, K.: Physikalisch limnologische Felddmessungen im Luganersee. Interner Bericht des Laboratorio di Physica Terrestre, Lugano-Trevano und der Versuchsanstalt für Wasserbau, Hydrologie und Glaziologie an der ETH Zürich (unpublished) (1982)
26. Vaucher, J.P.E. : Mémoire sur les seiches due Lac de Genève, composé de 1803 à 1804. *Mem. Soc. Phys. Genéve*, **6**, 35 (1833)

Acknowledgements for Copyright Permission

Grateful acknowledgement is made to the following publishers, organizations and authors for permission to use previously published copyrighted figures and texts. Most figures were scanned and redesigned, sometimes with slight changes. Some figures are compositions of several figures of the source manuscripts.

American Meteorologiocal Society
Journal of Physical Oceanography
Figs. 19.2–19.5 – reproduced from J. H. SAYLOR et al. (1980)
Figs. 21.19, 21.20 – reproduced from T. STOCKER (1990)

American Society of Limnology & Oceanography
Figs 13.2–13.4 – reproduced from J. P. ANTENUCCI et al. (2000)
Fig. 13.9 – reproduced from J.P. ANTENUCCI & J. IMBERGER (2001)
Figs. 14.4, 14.9–14.13 – reproduced from U. LEMMIN et al. (2005)
Fig. 14.22 – composed from Figures of A. SAGGIO & J. IMBERGER (1998) and K. SHIMIZU et al. (2007)
Fig. 14.23 – reproduced from K. SHIMIZU et al. (2007)
Fig. 16.4 – reproduced from M. MÜNNICH et al. (1992)
Figs. 16.5–16.10 – reproduced from E. ROGET et al. (1997)
Figs. 16.11, 16.12, 16.14 – reproduced from A. SAGGIO & J. IMBERGER (1998)
Figs. 16.15, 16.17–16.21 – reproduced from J. APPT et al. (2004)
Figs. 22.3, 22.4 – reproduced from C.H. MORTIMER and U. LEMMIN (1956)

Aquatic Sciences, Schweizerische Zeitschrift für Hydrologie, Birkhuser Verlag, Basel
Figs. 14.14–14.16, 14.18–14.21 – reproduced from E. BÄUERLE (1994)
Fig. 18.22 – reproduced from J. TRÖSCH et al. (1987)

Arbeitsgemeinschaft Bodensee Rhein, Deutschland
Fig. 14.17 – reproduced from E. HOLLAN (1974)

Cambridge University Press, Cambridge, UK
Figs. 12.14–12.20 – reproduced from D. B. RAO (1966)
Figs. 15.14–15.18 – reproduced from V. VLASENKO et al. (2005)
Fig. 20.6 – reproduced from K. F. BALL (1965)

Figs. 20.17–20.19 – reproduced from E.R. JOHNSON (1987)
Figs. 21.39–21.44 – reproduced from T. STOCKER & E.R. JOHNSON (1989)
Figs. 22.6, 22.10, 22.23 – reproduced from G. RAGGIO & K. HUTTER (1982a)
Figs. 22.7–22.9, 22.11–22.14 – reproduced from G. RAGGIO & K. HUTTER (1982b)
Figs. 22.18, 22.20–22.22 – reproduced from G. RAGGIO & K. HUTTER (1982c)

Center for Great Lakes Studies (now Great Lakes WATER Institute) University of Wisconsin at Milwaukee
Figs. 11.9, 12.9 – reproduced from Report 32 by C. H. MORTIMER (1977)
Figs. 11.6, 12.2, 12.8, 12.10 – reproduced from Report 37 by C.H. MORTIMER (1980)

CRC-Press, Boca Raton, USA
Figs. 21.22, 21.23, 21.25, 21.26, 21.28, 21.29 – reproduced from T. STOCKER & K. HUTTER (1990)

European Sciences Union
Reproduction of
RUDNEV, S.F., SALVADÈ, G., HUTTER, K., ZAMBONI, F.: External gravity oscillations in Lake Onega, *Ann. Geophysicae*, **13**, 893–906 (1995) including Figs 17.1–17.9

Fluid Dynamics Research, published by IOP
Figs. 12.21, 12.22, 12.24–12.26 – reproduced from L.R.M. MAAS (2003)

Gebrüder Bornträger, E. Schweizerbartsche Verlagsbuchhandlung OHG, Stuttgart
http://www.schweizerbart.de
Fig. 12.3 – reproduced from C.H. MORTIMER (1974)
Fig. 12.4 – reproduced from W. KRAUSS (1966)

Journal of Marine Research, Yale University
Fig. 12.13 – reproduced from P.J. BROWN (1973)

London Mathematical Society
Fig. 12.12 – reproduced from the Proc. Lond. Math. Soc. G.I. TAYLOR (1920)

National Cheng Kung University Press, Tainan, Taiwan
Fig. 19.10 – reproduced from J. TRÖSCH (1986)

Prof. Y.-H. PAO, *National Taiwan University, Taipei, Taiwan*
Fig. 13.6 – reproduced from Y.-H. PAO & C.C. Mow (1973)

Royal Astronomical Society
Monthly Notes (Geophys. Suppl.)
Figs. 13.8, 13.10–13.12 – reproduced from S. GOLDSTEIN (1929)

Royal Society London
Fig. 20.12 – reproduced from V.T. BUCHWALD & J.K. ADAMS (1968)

Dr.-Ing. B. Schuster

Figs. 15.1–15.3, 15.6–15.8 – reproduced from the doctoral dissertation (1991)

Springer Verlag, Berlin, etc., Vienna, etc.
Figs. 14.5–14.8 – reproduced from E. BÄUERLE (1985)
Figs. 15.4, 15.9–15.13 – reproduced from H. HÜTTEMANN & K. HUTTER (2001)
Figs. 15.19–15.22, 15.24–15.34 – reproduced from G. SALVADÈ et al. (1988)
Figs. 19.6, 19.7, 20.4, 20.7, 20.10, 20.13, 20.15, 20.16, 21.7, 21.8, 21.30–21.36 – reproduced from T. STOCKER & K. HUTTER (1987)
Fig. 19.13 – reproduced from K. HUTTER (1984)
Fig. 21.14 – reproduced from E. BÄUERLE (1986)
Fig. 21.10–21.12 – reproduced from T. STOCKER & K. HUTTER (1985)
Figs. 22.15–22.17 – reproduced from K. HUTTER & G. RAGGIO (1982)

G. Raggio
Fig. 22.19 – reproduced from his dissertation (1980)

Taylor and Francis, www.informaworld.com
Fig. 16.16 – reproduced from G. BAUER et al. (1994)
Fig. 19.8 – reproduced from K. HUTTER et al. (1983)
Figs. 19.9, 20.9 – reproduced from E.R. JOHNSON (1987)
Figs. 20.1, 20.8 – reproduced from L.A. MYSAK (1983)
Fig. 21.45 – reproduced from E.R. JOHNSON & G. KAOULLAS (2010)
Reproduction of
STOCKER, K., HUTTER, K., SALVADÈ, G., TRÖSCH, J. ZAMBONI, F.: Observations and analysis of internal seiches in the Southern Basin of Lake of Lugano. *Ann. Geophysicae*, **5B**, 107–120 (1987), including Figs. 18.1–18.21

The University of Wisconsin Press
Figs. 14.1–14.3 – reproduced from C.H. MORTIMER (2004)

Versuchsanstalt für Wasserbau, Hydrologie und Glaziologie an der Eidgen. Techn. Hochschule, Zürich
Figs. 19.12, 20.2, 20.3, 21.10–21.13, 21.15–21.17 – reproduced from T. STOCKER & K. HUTTER (1985)
Figs. 20.11, 21.1, 21.4–21.6, 21.18, 21.21, 21.27 – reproduced from T. STOCKER (1987)

Wiley-Blackwell, Tellus
Fig. 19.11 – reproduced with additions from J. SIMONS (1978)

Zürich, Switzerland — *Kolumban Hutter*
Darmstadt, Germany — *Yongqi Wang*
Kaliningrad, Russia — *Irina Chubarenko*

June 2011

Contents of Volume I

Contents

Notation

We employ the common mathematical notation used in the Applied Sciences, but do not systematically use the same notation for analogous operations and/or the same physical variables throughout the volume. For instance,

- Derivatives of a univariate function $f(x)$ are denoted as $\mathrm{d}f/\mathrm{d}x$ or f'.
- Partial derivatives of a function $f(x_j)$, $j = 1, 2, \ldots, n$ with respect to x_k are denoted by
$$\frac{\partial f}{\partial x_k} \quad \text{or} \quad f_{,k} \quad \text{or} \quad f_{x_k}.$$
We generally prefer $\partial f/\partial x_k$ over $f_{,k}$ or f_{x_k}, but when the formulae are complicated, the graphical display of the short-hand notations often facilitates the interpretation of the formulae.
- Within chapters, we have consistently used one symbol for a physical variable, but from chapter to chapter, the symbols may change. In this spirit, we use, e.g. $\boldsymbol{u}$ and $\boldsymbol{v}$ to designate the three-dimensional fluid velocity field and $\boldsymbol{V}$, $\boldsymbol{M}$ for the depth integrated volume transport.

In the list below, only the principal symbols are listed. A scalar is generally written in italic type, a vector generally in lower case italic bold type, whilst a second rank tensor is written in upper case italic bold type.

Roman Symbols

$A(x, y)$	Amplitude distribution of the free surface or interface displacement function in a rectangular basin of constant depth on the rotating Earth
$A(x, t)$	Progressing wave function (Chap. 15)
$\mathbf{A}$	6×6-matrix, defining a first-order barotropic linear motion (Chap. 22)
$\mathbf{A}_s$	Special form of $\mathbf{A}$ for a first-order rectangular channel with straight lake axis (Chap. 22)

$\mathbf{A}_{\mathrm{R}}$ ..... Special form of $\mathbf{A}$ for a circular channel with constant cross section

a ..... Radius of a circular basin, parameter measuring the eccentricity of an ellipse

a ..... Major semi-axis of an ellipse

$\boldsymbol{a}$ ..... General vector

a_j ..... Physical components of a vector $\boldsymbol{a}$

$a_j^{(n)}$ ..... Natural components of a vector $\boldsymbol{a}$

$\mathbf{A}, \mathbf{B}, \mathbf{C}, \mathbf{D}, \mathbf{E}$ ..... $2N \times 2N$ complex valued matrices of a linear N^{th}-order seiche model (in Chap. 22, see (22.178)–(22.180))

B ..... Width or breadth of a channel

$\mathbb{B}$ ..... Boundary operator

B, B_1 ..... Breadth of the free surface of a cross section perpendicular to the lake axis (Chap. 22)

B_2 ..... Breadth of the thermocline interface of the cross-section perpendicular to the lake axis

$\mathbf{B}_c$ ..... 6×6-matrix, describing the no-flux boundary condition in a first order channel model (Chap. 22)

$\mathbf{B}_{\square}$ ..... 6×6-matrix to construct the barotropic seiche response in a first order theory for a rectangle of constant depth

$b(x, z, t)$ ..... Reduced gravity, buoyancy parameter ($= g\tilde{\rho}/\tilde{\rho}_0$)

b ..... Minor semi-axis of an ellipse

c ..... Wave speed (general)

$c_{\mathrm{ph}}, c_{\mathrm{gr}}$ ..... Phase velocity, group velocity

$c_{\mathrm{ext}}, c_{\mathrm{int}}$ ..... External (barotropic) wave speed, internal (baroclinic) wave speed

$c_0 (= HN_p)$ ..... Baroclinic wave speed

ce_{2m}, ce_{2m+1} ..... Cosine-elliptic Mathieu functions of even an odd order

Ce_{2m}, Ce_{2m+1} ..... Modified Mathieu functions; hyperbolic elliptic cosine functions of even and odd order; Cosh-elliptic Mathieu functions

$\mathbf{C}^{(m)}, \hat{\mathbf{C}}^{(m)}, \mathbf{C}_{\phi_j}^{(m)}, \hat{\mathbf{C}}_{\phi_j}^{(m)}$ .. Curvature dependent cross-sectional matrices defined in Appendix 22.A of Chap. 22

D ..... Constant water depth; discriminant of a bi-quadratic dispersion relation (22.142)

$D_{1,2}$ ..... Epilimnion, hypolimnion reference depths

$\mathcal{D}$ ..... Bounded or unbounded region in $\mathbb{R}^n, n = 2, 3$

$\mathbb{D}$ ..... Partial differential operator

$\mathrm{d}\boldsymbol{a}, \mathrm{d}\boldsymbol{a}_s, \mathrm{d}\boldsymbol{a}_l$ ..... Areal increments of the mantle surface of a shaft-like body, Appendix 22.B of Chap. 22

$\mathrm{d}a$ ..... Modulus of $\mathrm{d}\boldsymbol{a}$

d	Thickness of metalimnion – of diffuse interface
d	Ordinary differential operator
$\mathrm{d}\boldsymbol{\ell}$	Differential vector line element
$\mathrm{d}\boldsymbol{a}/\mathrm{d}t$	Total derivative of $\boldsymbol{a}$
$\mathrm{d}A$	Areal increment
$\mathrm{d}\boldsymbol{x}$	Vector valued position increment of x
$\mathrm{d}\boldsymbol{y}$	Vector valued position increment of y
div	Divergence operator
div_H	Horizontal (2-dimensional) divergence operator
$E[\Psi]$	Elliptic operator of the topographic wave equation ($= \nabla_H \cdot \{H^{-1}\nabla_H(\partial\Psi/\partial t)\}$)
$\boldsymbol{E}$	Matrix operator for ordinary differential equation of the first order (Chap. 21)
$\boldsymbol{\mathcal{E}}^{(m)}_{,j}, \hat{\boldsymbol{\mathcal{E}}}^{(m)}, \hat{\boldsymbol{\mathcal{E}}}_{,j}$	Curvature dependent cross-sectional third order tensors defined in Appendix 22.B of Chap. 22
$\boldsymbol{e}_i, \hat{\boldsymbol{e}}_i$	Basis vectors ($i = 1, 2, 3$) of length 1 and orthogonal to one another
F	Hypergeometric polynomial, elliptical radial stream function for the topographic wave equation
$\boldsymbol{F}$	Depth integrated body force beyond the contribution of the external pressure (Chap. 19), deformation gradient
$F(\boldsymbol{x}, t) = 0$	Equation defining a surface in $\mathbb{R}^3$
$\mathbf{F}(s, \omega)$	4×4-matrix for the linear channel equation describing seiche motions (Chap. 22), see (22.191)
f	First Coriolis parameter ($= 2\Omega \sin\phi$)
f_0	Reference value for first Coriolis parameter for $\phi = \phi_0$
$\tilde{f}$	Second Coriolis parameter ($= 2\Omega \cos\phi$)
G	Symbol for a general function
$G(\eta)$	Elliptical-azimuthal part of the stream function for the TW-equation
$G_n(\cdot, \cdot, x)$	Jacobi polynomial of order n (Chap. 19)
$g, \boldsymbol{g}$	Gravity constant, gravity vector
g'	Reduced gravity constant ($= g(\Delta\rho/\rho) = g(\rho_2 - \rho_1)/\rho_2$)
$\boldsymbol{g}(\boldsymbol{x})$	Metric tensor
grad	Gradient operator in 3 dimensions
grad_H	Horizontal gradient operator in 2 dimensions
H, H_0	Water depth, reference water depth
H_1, H_2	Upper and lower layer water depths (in a 2-layer model)
H_E	Equivalent depth of the 2-layer model ($= H_1 H_2/(H_1 + H_2)$)

$\mathcal{H}$	Isotroph depth
$\bar{\mathcal{H}}$	Scaled isotroph depth
H_{eq}	Equivalent depth
$\mathbf{H}^{(m)}, \mathbf{H}_{s,n}^{(m)}$	Curvature dependent cross-sectional matrices, defined in Appendix 22.A of Chap. 22
h_{bar}	Equivalent depth for barotropic processes
h_1, h_2, h_3	Parameters of the 3-layer shallow water model (Chap. 13)
I_ℓ	Modified Bessel function of first kind and ℓ-th order
$\boldsymbol{I}_3, \boldsymbol{I}_6$	Three- and six-dimensional unit matrices
$\mathrm{i} = \sqrt{-1}$	Imaginary unit
i	Counting index
$J[a,b]$	Dimensional Jacobi-operator ($= \frac{\partial a}{\partial x}\frac{\partial b}{\partial y} - \frac{\partial a}{\partial y}\frac{\partial b}{\partial x}$)
$\mathcal{J}[a,b]$	Non-dimensional Jacobi operator
$\mathcal{J}_\ell$	Wave solution of the shallow water equations in a circular basin of constant depth
j	Counting index
K, K^ϕ, K^ψ	Kinetic energy (general), kinetic energy for velocity potential, kinetic energy for stream function potential (Chap. 12)
K_ℓ	Modified Bessel function of second kind and ℓ-th order
$K(s)$	Curvature of the lake axis as a function of arc length
k	Counting index, x-component of the horizontal wave number
$\boldsymbol{k}$	Wave number vector, generally in three dimensions
$\boldsymbol{k}_h$	Horizontal wave number vector
$\hat{\boldsymbol{k}}$	Unit vector in the z-direction, against gravity $\boldsymbol{g}$
L, L_0	Typical horizontal dimension of a lake, reference length of a lake
$\mathcal{L} = \frac{\partial^2}{\partial t^2} + f^2$	Dimensional operator expressing the Coriolis corrected time derivative on the rotating Earth
$\mathcal{L} = \frac{\partial^2}{\partial t^2} + 1$	Dimensionless operator expressing the Coriolis corrected time derivative on the rotating Earth
ℓ	Azimuthal mode number
ℓ_m	Along-channel wave number of order m
$\boldsymbol{M}, \boldsymbol{M}_1, \boldsymbol{M}_2$	Mass or volume flux of the entire water column, of the top and bottom layers, and of a 2-layer model, respectively
$\mathbb{M}_{\alpha\beta}(s)$	Ordinary differential matrix operator used in the method of weighted residuals for the one-dimensional solution of the topographic wave equation
$\mathbb{M}$	Matrix operator corresponding to $\mathbb{M}_{\alpha\beta}(s)$
m	Counting index of eigenmodes, mode number

m_{crit}	Critical value of m
N	Buoyancy frequency, Brunt–Väisälä frequency $\left(N = -\frac{g}{\rho_0(z)}\frac{\mathrm{d}\rho_0(z)}{\mathrm{d}z}\right)$
N_p	Maximum value of the buoyancy frequency in the water column
$\hat{N}$	Dimensionless buoyancy frequency
$n(=1,2,...,\infty)$	counting index
$\boldsymbol{n}, \boldsymbol{b}^s, \boldsymbol{b}^b$	Unit normal vector (general) and on the free and basal surfaces
$n-D$	n-Dimensional
$\mathcal{O}$	Order symbol
P, p, p_0	Pressure, reference pressure
p'	Perturbation pressure
p_e, p_i	External pressure, internal pressure
$PE(t)$	Potential energy ($\int_0^{\mathcal{D}} gz\rho(z,t)\mathrm{d}z$)
$P_\alpha(s,n)$	Shape functions of stream function of the topographic wave equation in the method of weighted residuals
$\mathbf{P}_\alpha^{*(m)}$	Macroscopic atmospheric pressure gradient (vector), defined in Chap. 22
Q	Cross-section
∂Q	Boundary of a cross-section
$Q_\alpha(s,n)$	Shape functions for the method of weighted residuals for the topographic wave operator
q	Exponent of the radial depth variation of a circular lake ($h = (1-(r/a)^q)$)
R, R_D	Rossby radius of deformation ($= c_{ph}/f$)
$R_{\text{ext}}, R_{\text{int}}$	External, internal Rossby radius of deformation
R	Friction coefficient
$\mathbf{R}^{(m)}$	Macroscopic friction coefficient
$\boldsymbol{R}_\Omega = \mathbf{0}, \boldsymbol{R}_{\partial\Omega_\alpha} = \mathbf{0}$	Field equations in Ω and $\partial\Omega_\alpha$
$\mathcal{R}_3$	Three-dimensional matrix characterizing waves in the full 2-layer model
$\mathcal{R}_6$	Six-dimensional matrix characterizing waves in the equivalent depth 2-layer model
$\mathbb{R}^n$	Real Cartesian space of dimension n
r	Radial distance in polar coordinates
$r = \frac{H_2/H_1}{(1+H_2/H_1)}$	For the 2-layer model (Chap. 12)
$r = B/A$	Aspect ratio of an ellipse (Chap. 20)
r_0	Outer radius of a circular basin
S	Cross-sectional area perpendicular to the lake axis
S_1, S_2	Cross-sectional area of the epilimnion and hypolimnion layers, respectively
$S_n(=R_n/r_0)$	Dimensionless n-th order Rossby radius (Burger number in a circular basin with radius r_0)

$S_i = \frac{c_i}{(2L)f}$	Classical Burger number
T	Period (of a seiche)
$T[\Psi]$	Topographic wave operator ($= E[\Psi_t] + J[\Psi, fH^{-1}]$)
$\boldsymbol{T}^* = \boldsymbol{T} - (\boldsymbol{n} \cdot \boldsymbol{T}\boldsymbol{n})\mathbf{1}$	Tangential traction on a surface with unit normal vector $\boldsymbol{n}$
t, t_0	Time, reference time
$\boldsymbol{t}, \boldsymbol{t}_{\text{dyn}}$	Cauchy stress tensor, dynamic Cauchy stress tensor
U	x-component of the volume flow $\boldsymbol{V}$ ($U = \int_{-H}^{0} u(x, y, z, t)\mathrm{d}z$), characteristic horizontal velocity
U_0	Amplitude of U
u	x-component of the velocity field
$\boldsymbol{u}$	Velocity field vector
V	y-component of the volume flow $\boldsymbol{V}$ ($V = \int_{-H}^{0} v(x, y, z, t)\mathrm{d}z$)
V_0	Amplitude of V
$\boldsymbol{V}$	Volume (mass) transport vector
$\boldsymbol{V}_1, \boldsymbol{V}_2$	Volume transport vectors of a 2-layer model
$\boldsymbol{v}$	Velocity vector
v	y-component of the velocity field
v_{ph}	Phase velocity
$\boldsymbol{v}^{**}(s, n, z)$	Velocity function, describing the initial velocity field
$\mathbf{v}_s, \mathbf{v}_n, \mathbf{v}_z$	Sets of shape functions for v_s, v_n, v_z
W_i	Orthogonal functions of the Lanczos procedure (Chap. 17)
w	z-component of the velocity field
$w_n(x, y, t)$	(x, y, t)-dependent part of $w(x, y, z, t)$
$w_\alpha^{*(n)}$	Macroscopic wind load vector, defined in Chap. 22
$\boldsymbol{X}$	Position vector in 2D or 3D space of the reference configuration
$\boldsymbol{x}$	Position vector in 2D or 3D space of the present configuration
x	x-component of the Cartesian coordinates $\boldsymbol{x} \hat{=} (x, y, z)$
$\mid \boldsymbol{x} \mid$	Euclidean norm of $\boldsymbol{x}$:$\mid \boldsymbol{x} \mid = \sqrt{\boldsymbol{x} \cdot \boldsymbol{x}}$
$\underset{\sim}{\mathrm{x}}$	A set of independent variables
$\boldsymbol{Y}, \boldsymbol{y}$	Position vector in 2D or 3D space in the reference and present configuration, respectively
Y_ℓ	Bessel function of the second kind and ℓ-th order
$\hat{\mathbf{y}}_{\mathbf{s}}$	Lake axis as a function of the arc length along the channel axis
$Z_n^w(z)$	z-dependent part of the function $w(x, y, z, t)$ in a separation of variables expansion
$\mathbf{Z}^{(m)}, \hat{\mathbf{Z}}^{(m)}$	Curvature dependent cross-sectional matrices, defined in Appendix 22.A of Chap. 22
z	z-component of the Cartesian coordinates (x, y, z)

Greek Symbols

α, α_1	Coefficients of the non-linear terms of the K-dV equation
α_{gr}	Group velocity correcting factor, Chap. 22
$\beta = \mathrm{d}f/\mathrm{d}y$	β-plane parameter (y is the direction towards North on the Earth's surface)
β	Dispersion coefficient of the K-dV equation
$\boldsymbol{\Gamma}$	xy-components of the dynamical Cauchy stress (Chap. 19)
γ	Parameter arising in the 3-layer shallow water model (Chap. 13)
$\boldsymbol{\gamma}$	$(13, 23) = (xz, yz)$-components of the dynamic Cauchy stress (Chap. 19)
$\gamma = \frac{f}{\kappa\sqrt{gH}}$	Dimensionless rotation factor
Δ	Laplace operator, symbol for difference
$\Delta\rho$	Density difference
δ	Symbol for a small positive number
$\delta_{ij}, \delta_{\alpha\beta}$	Kronecker Delta ($\delta_{ij} = 1$ if $i = j$, else $\delta_{ij} = 0$; $\delta_{\alpha,\beta} = 1$ for $\alpha = \beta$, else $\delta_{\alpha\beta} = 0$)
$\delta = \frac{\rho_1}{\rho_2}$ or $= \frac{\rho_1}{\rho_*}$	Density ratio of the 2- and 3-layer model
$\delta\phi_\alpha$	Weighting function in the method of weighted residuals
$\delta I, \delta I_1 \delta I_6$	Functionals, defining the weak forms of an initial value problem (Chap. 22)
$\delta \boldsymbol{v}_1$	Weighting function for the momentum balance equation (Chap. 22)
$\delta \boldsymbol{v}_2$	Weighting function for the stress boundary condition at the free surface (Chap. 22)
$\delta \boldsymbol{v}_3$	Weighting function for the basal sliding law (Chap. 22)
$\delta \mathbf{v}_1, \delta \mathbf{v}_2, \delta \mathbf{v}_3$	Shape functions for $\delta\boldsymbol{v}_1$, $\delta\boldsymbol{v}_2$, and $\delta\boldsymbol{v}_3$
$\delta\mathbf{w}$	Set of shape functions for the weighting functions $\delta\boldsymbol{w}$
$\delta \lambda_1$	Weighting function for the mass balance equation (Chap. 22)
$\delta \lambda_2$	Weighting function for the kinematic equation of the free surface (Chap. 22)
$\delta \lambda_3$	Weighting function for the kinematic boundary condition at the free surface (Chap. 22)
$\delta\lambda_{1,2,3}$	Shape functions for $\delta\lambda_{1,2,3}$
$\delta \boldsymbol{w}_\Omega$	Weighting function for $\boldsymbol{w}$ defined in Ω
$\delta\boldsymbol{w}_{\partial\Omega_\alpha}$	Weighting function for $\boldsymbol{w}$ defined in $\partial\Omega_\alpha$
ε	Symbol for a small positive number, depth along shore (Chaps. 19–21)
ε	Scaled dimensionless density difference in the 2-layer model ($= \frac{\rho_2-\rho_1}{\rho_*}$ or $= \frac{\rho_2-\rho_1}{\rho_2}$)

$\varepsilon_{ij} = \frac{\rho_j - \rho_i}{\rho_j}$	Dimensionless density differences arising in the $n\ (>2)$ layer model
$\varepsilon = a_\xi / H$	Amplitude–water depth ratio
ε_{ijk}	Levi–Cività tensor, alternating symbol
ζ	Vertical displacement of an isolated water particle in a stratified still fluid
ζ	$(z = \zeta(x, y, t))$, function defining the free surface of a lake in $\mathbb{R}^3$
ζ	z-component of the vorticity vector
$\zeta_{1,2}$	$(z = \zeta_{1,2}(x, y, t))$, function defining the free surface and the thermocline surface of a 2-layer model
$\zeta*$	Conjugate complex of ζ
$\zeta(s, n, t)$	Vertical displacement of the free surface
$\zeta^{**}(s, n)$	Surface displacement, describing the initial elevation field $z = \zeta^{**}(s, n)$
$\eta, \eta_1, ..., \eta_n$	Vertical displacements of the free surface and the interfaces in an n-layer model
θ	Azimuth angle in cylindrical coordinates
θ	Angle between wave vector $\boldsymbol{k}$ and its projection into the (x, y)-plane (Chap. 11)
$\theta(x, y)$	Phase angle of a 2D wave of a fluid in a rectangle
κ	Modulus of the horizontal wave number
κ^2	$= k^2 + \ell^2$
$\lambda = \mathrm{i}\kappa$	Exponential decay factor (Chap. 22)
λ_α	Eigenvalues of the velocity potential (Chap. 12, Sect. 12.9)
λ_n	Eigenvalues of the Lanczos procedure (Chap. 17)
μ	Dynamic viscosity of water
$\mu = (h/\lambda)^2$	Squared ratio of the water depth H to the wave length λ
$\mu^{-1} = B/L$	Aspect ratio of the rectangular channel with breadth B and length L
$\nu^2 = \frac{1}{3}a^2 = \frac{1}{3}\frac{B^2}{4R_m^2}$	Squared aspect ratio in a circular ring of rectangular cross-section with width B and mean radius R_m
$\nu = \mu/\rho$	Kinematic viscosity of water
$\nu_\alpha, \nu_{\text{ext}}, \nu_{\text{int}}$	'Separation parameters' of the equivalent depth models
ν_1, ν_2	Angular velocities of the slowest longitudinal and transverse modes of the seiches in a non-rotating rectangle
$\Xi_n(z/H)$	Shape functions in the method or weighted residuals
Π_{bt}	Barotropic potential vorticity
π	$= 3.1415926...$

ρ	Dimensionless radial distance, mass density per unit volume
ρ_*	Reference mass density (of water at 4°C)
$\rho', \tilde{\rho}$	Density perturbations
$\rho_{1,2}$	Mass density per unit volume in layers 1 and 2
σ	(Mostly) dimensionless frequency
$\sigma = \frac{\rho - \rho_*}{\rho_*}$	Density anomaly
$\boldsymbol{\tau}_w, \boldsymbol{\tau}_{\text{wind}}$	Wind shear stress (traction) on the free surface
$\boldsymbol{\tau}_b, \boldsymbol{\tau}_{\text{bottom}}$	Basal shear stress (traction)
$\Phi(y)$	Transverse dependence of ζ and U in Kelvin waves
$\Phi(z)$	Vertical variation of the horizontal velocity profile in internal waves
ϕ	Latitude angle
$\phi_n(z/H)$	Shape functions used in the method of weighted residuals
ϕ, ϕ_n	General harmonic functions
ϕ, ψ	Shape, basis or trial functions
χ	Diffusivity
$\chi_n(z/H)$	Shape functions used in the method of weighted residuals
$\boldsymbol{\chi}(\boldsymbol{X}, t)$	Motion function
Ψ	Mass transport stream function
$\Psi_n(z)$	z-dependent contribution of $\psi(x, y, z, t)$
$\psi(x, y, z, t)$	General function, stream function
$\psi_n(x, y, t)$	(x, y, t)-dependent contribution of $\psi(x, y, z, t)$
$\psi_n(z/H)$	Shape functions in the method of weighted residuals
$\boldsymbol{\Omega}, \lvert\boldsymbol{\Omega}\rvert = \Omega$	Angular velocity of the rotating frame of the Earth, modulus of the angular velocity $\boldsymbol{\Omega}$
ω	Circular frequency
ω_z	z-component of the vorticity vector

Miscellaneous Symbols

∇	Nabla operator, del-operator, generally in three dimensions
∇_H	Nabla operator in two dimensions
$\nabla f, \nabla_H g$	Gradient of f in 3D, gradient of g in 2D
$\nabla \cdot f$	Divergence of f in 3D
$\nabla_H \cdot g$	Divergence of g in 2D
$(\cdot, \cdot)$	General inner product in 2D or 3D $(\boldsymbol{f}, \boldsymbol{g}) = \int_{\mathcal{D}_3} \boldsymbol{f}(\boldsymbol{x}) \cdot \boldsymbol{g}(\boldsymbol{x}) \mathrm{d}\boldsymbol{x}^3,$ $(\boldsymbol{f}, \boldsymbol{g}) = \int_{\mathcal{D}_2} \boldsymbol{f}(Vx) \cdot \boldsymbol{g}(\boldsymbol{x}) \mathrm{d}\boldsymbol{x}^2$

$\langle \cdot, \cdot \rangle$	$= \int_0^1 f(\xi) g(\xi) \mathrm{d}\xi$
$\langle\langle \cdot, \cdot \rangle\rangle$	$= \int_{-H}^0 f(z/H) g(z/H) \mathrm{d}z$
$[A]$	Scale (= typical magnitude) of variable A
$[\![A]\!] = A^+ - A^-$	Jump of A across a singular surface
$\frac{\mathrm{d}(\cdot)}{\mathrm{d}t} = (\cdot)^{\cdot}$	Total or material time derivative, keeping the Lagrangean position fixed
$\frac{\partial(\cdot)}{\partial t}$	Partial time derivative, or local time derivative, keeping the spatial position fixed
$\times$	Multiplication sign
$\boldsymbol{a} \times \boldsymbol{b}$	Vector product of $\boldsymbol{a}$ and $\boldsymbol{b}$, also called cross product
$\boldsymbol{a} \otimes \boldsymbol{b}$	Dyadic (exterior) product between two vectors $\boldsymbol{a}$ and $\boldsymbol{b}$ $((\boldsymbol{a} \otimes \boldsymbol{b})_{ij} = a_i b_j)$
$\mathrm{tr}(\boldsymbol{A})$	Trace of the tensor $\boldsymbol{A}$: $\mathrm{tr}\boldsymbol{A} = A_{ii}$.

List of Acronyms

ADCP	Acoustic Doppler Current Profiler
a. s. l.	Above sea level
ATSIT	Automatic Digital Current Meter of Russian production
BITEX	Biwako Transport Experiment (in Lake Biwa 1992–1994)
CTD	Current–Temperature–Depth
E	East
EW	East–West
ELCOM	Estuary, Lake, and Coastal Ocean Model
eK-dV(e)	extended Korteweg–de Vries (equation)
FD	Finite Difference
FE	Finite Element
FV	Finite Volume
Hm	Seiche mode in the shallow water approximation of horizontal order m
HmVn	Seiche mode of the shallow water equations in enclosed basins of horizontal order m and vertical order n (they also occur separately as Hm and Vn)
IW	Internal Wave
K-dV(e)	Korteweg–de Vries (equation)
LDS	Lake Diagnostic Systems sampling station
MEZ	Mitteleuropäische Zeit (Middle European Time) (= UTC + 1)
MWR	Method of Weighted Residuals
N	North
NE	North–East
NW	North–West
NS	North–South
N. H.	Northern Hemisphere
RCM	Recording Current Meter of Aanderaa, Norway
SE	South–East
SFE	Swiss Service Féderale des Eaux
S. H.	Southern Hemisphere

SMA	Schweiz. Meteorologische Anstalt (Swiss Meteorological Service)
SW	South–West
TCD(M)	Two-Layer Constant Depth (model) (both layers have constant depth)
TDP	Two-Layer Defant Procedure
TED(M)	Two-Layer Equivalent Depth (model)
THCD(M)	Three-Layer Constant Depth (model) (all three layers have constant depth)
THED(M)	Three-Layer Equivalent Depth (model)
THVD(M)	Three-Layer Variable Depth (model)
THVD(M)C	Three-Layer Variable Depth (model) Complete
TVD(M)	Two-Layer Variable Depth (model)
TVD(M)C	Two-Layer Variable Depth (model) complete
TW	Topographic Wave
UTC	Coordinated Universal Time (= MEZ + 1)
VAW	Versuchsanstalt für Wasserbau, Hydrologie und Glaziologie an der Eidgenössischen Technischen Hochschule, Zürich (Laboratory of Hydraulics, Hydrology and Glaciology at the Federal Institute of Technology, Zurich)
W	West
WE	West–East
WLR	Water Level Recorder

Chapter 11
The Role of the Earth's Rotation: Fundamentals – Rotation and Stratification Influenced Dynamics

In Chaps. 7 and 8 of Volume I, an introduction was given to the mathematical treatment of linear waves in general and to water waves in particular. To isolate the specific properties of water waves with a free surface, the influence of the rotation of the reference frame was not considered. Here, our aim is to elucidate the role played by the rotation of the reference frame – the Earth – in the dynamics of large water masses such as ponds, lakes, and the ocean.

11.1 Estimations by Dimensional Reasoning

The rotation of the Earth manifests itself in almost all flow configurations that occur in large water bodies, but depending upon the type of process modifications implied by this rotation the effects are either

- *Large* – they cause a flow qualitatively completely different from the corresponding flow without rotation – or
- *Moderate* – they modify quantitatively the flow that would develop without rotation – or
- *Small* – they lead to very small alterations that may simply be ignored in comparison with the flow without rotation.

There are certain thumb rules, which are based on theoretical analyses and have been corroborated by observations; they tell us, under which physical conditions the rotation of the Earth is likely to exercise an influence on the physical process under investigation. The *size and bathymetry of a basin* primarily dictate whether the rotation of the Earth must be accounted for or can be ignored. Very roughly, three classes of processes can be characterized to be influenced by the rotation of the Earth, and they scale according to the sizes of the water body. In general, *the smaller a basin, the less important the role of the rotation of the Earth*. However, this rule is not sufficient. The size of a basin above which the rotation may exercise an effect depends also on the *processes under study*, and here experience tells us to differentiate as follows:

K. Hutter et al., *Physics of Lakes*, *Volume 2: Lakes as Oscillators*, Advances in Geophysical and Environmental Mechanics and Mathematics,
DOI 10.1007/978-3-642-19112-1_11, © Springer-Verlag Berlin Heidelberg 2011

11.1.1 Tributary Affected Advection

Because the Coriolis force is perpendicular to the particle velocity, Coriolis effects divert the path of a moving water mass within a water body to the right (left) on the Northern (Southern) hemisphere. This can be observed even in reservoirs and ponds of only 1 km horizontal extent and is measurable in mountainous lakes with large tributaries (such as, e.g. the river Rhine in Lake Constance). An estimate when this rotational effect may be significant can easily be given, if a water parcel from the fluid of a jet-like moving water mass is considered in isolation, see Fig. 11.1, which shows a top view of such a parcel together with a portion of its curved trajectory, the local radius of curvature being R. Assume that the motion is purely horizontal. Then, for an observer moving with the fluid parcel, the forces acting on the fluid parcel perpendicular to the trajectory are the Coriolis[1] force mfv pointing towards the centre of curvature and the centrifugal force, mv^2/R, in which m is the mass of the parcel. Equating the two forces, $mfv = mv^2/R$, shows that the mass cancels out and so

$$R = \frac{v}{f}. \tag{11.1}$$

The radius of curvature of the trajectory of a fluid parcel that is unaffected by boundaries is of the order of v/f, where v is its velocity and f the Coriolis parameter. With $v \simeq 10^{-2} - 10^{0}\,\mathrm{ms}^{-1}$ and $f \sim 10^{-5}\,\mathrm{s}^{-1}$, this yields $R \sim 10^{3} - 10^{5}$ m. So, if a jet from a tributary moves with a velocity of $1\,\mathrm{ms}^{-1}$ or less and the water body in which it moves has an extent of one to a few kilometers, it is likely that the motion of this jet will be affected by the rotation of the Earth: The jet will likely be found

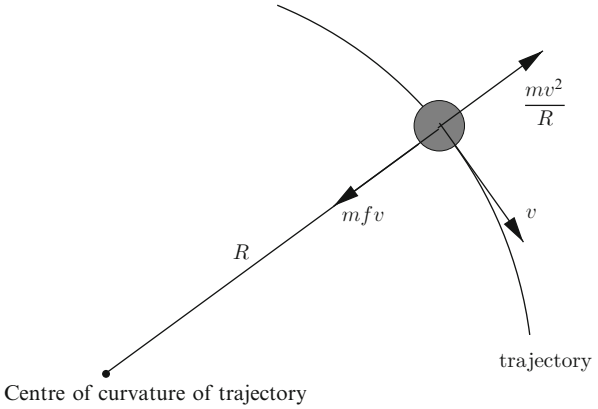

Fig. 11.1 Fluid parcel within the jet flow from a tributary, *top view*. The velocity v is tangential to the trajectory, and the forces perpendicular to it are the Coriolis and the centrifugal forces. The graph applies to a situation on the Northern hemisphere

[1] For a portrait of Coriolis and a short biography, see Volume I, Fig. 4.5, p. 98.

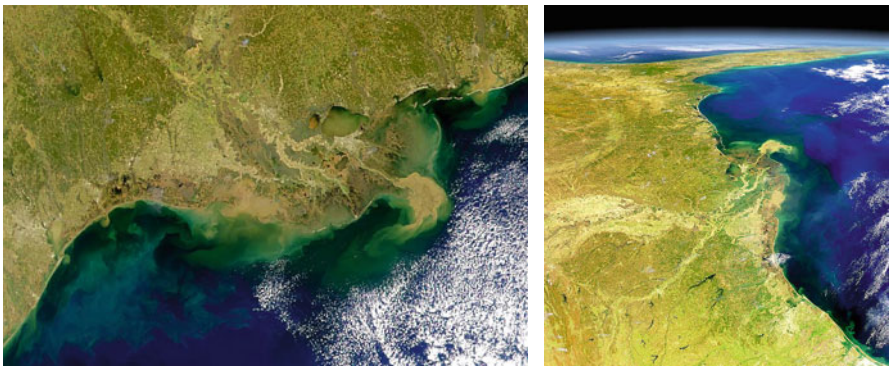

Fig. 11.2 Example of the jet found along the right shore on the Northern hemisphere. The sediment plume of the Mississippi River is quite visible in this SeaWiFS image as it empties into the Gulf of Mexico (from http://visibleearth.nasa.gov)

along the right (left) shore on the Northern (Southern) hemisphere. An example is given in the photo of Fig. 11.2.

11.1.2 Wind-Induced Circulation

Wind acts as a momentum source; it establishes a shear stress at the free surface which triggers the horizontal water motion that is carried to depth due to diffusion of momentum. The Coriolis effects cause the horizontal current to rotate with increasing depth, in the (counter) clockwise direction on the Northern (Southern) hemisphere. Therefore, two processes are of main importance for the general structure of the water currents here: the *transfer* of momentum into deeper layers due to molecular and turbulent viscosity, and the *turning* due to the Coriolis force. The momentum decreases with depth because of the dissipation due to friction; hence, the velocity decreases with increasing depth but the Coriolis effect is maintained. Such layers arise near the lake surface and for sufficiently deep lakes also near the bottom boundary, where the penetration of momentum is coupled with the rotation of the Earth; in natural reservoirs, they are widely observed and are called *Ekman boundary layers*. The corresponding depth, within which the described mechanism is significant for the current field formation is called the *Ekman depth*. A detailed analysis of wind-induced currents, including the *Ekman* layer and its generalization has been given in Chap. 9 (Volume I) of this treatise.

Let us estimate the thickness D of the Ekman layer by dimensional reasoning. Evidently, the value of D will depend on how effectively the water transmits the momentum from layer to layer. A measure for this is the kinematic viscosity of the water, $\nu\,[\mathrm{m^2 s^{-1}}]$. The second mechanism is the rotation of the Earth, expressed by the Coriolis parameter, $f\,[\mathrm{s^{-1}}]$. These two quantities combine to a length $D \sim (\nu/f)^{1/2}$, viz.,

$$D = \sqrt{\frac{2\nu}{f}}\,\pi, \tag{11.2}$$

where the factor $\sqrt{2}\pi$ is inserted for reasons that become apparent in the respective theory, see Chap. 9 (Volume I).

Of course, values for D depend on the substituted values for ν. Flows in natural basins and reservoirs are turbulent, of which the values for the viscosity depend on the scale of the flow under consideration. Moreover, measurements of vertical profiles of the kinematic turbulent viscosities show that they are relatively small in the epi- and hypoliminion and can be one to two orders larger in the thermocline region. For the estimates here an average value is sufficient. For turbulent flows in nature these are $\nu \in [10^{-2};\, 10^{-1}]\,\mathrm{m^2\,s^{-1}}$ and $f \sim 10^{-4}\,\mathrm{s^{-1}}$, so $D \in [45, 140]\,\mathrm{m}$. For lakes the value at the lower end is more appropriate; $D \in [100, 140]\,\mathrm{m}$ is used for the open ocean. So, here we see: *it is not so much the horizontal extent of a basin, but its depth which dictates whether the rotation of the Earth affects the circulation dynamics of a water body*. Of course, the horizontal extent of a basin must be sufficiently large that the rotational flow can be formed: 50 m depth and a few kilometers horizontal extent (or more) suffice to make it important.

11.1.3 Barotropic and Baroclinic Wave Dynamics

Water waves are also influenced by the rotation of the Earth via the Coriolis force. If we consider the channel solutions of surface gravity waves without rotation as, e.g. displayed in the graphs of Figs. 6.12–6.14 (Volume I), these waves will be modified by the Coriolis force, simply because, due to its action, water particles experience a force to the right (left) on the Northern (Southern) hemisphere. This must modify the types of waves insofar, as for 'longitudinal modes' wave heights can no longer be constant across the channel width but must vary, with wave height maxima to the right (left) of the wave propagation direction on the Northern (Southern) hemisphere. Analogously, for 'transverse modes' a variation of the wave amplitude in the long direction must necessarily be established, and in an infinitely long channel this can only be accomplished, if *cell structures develop*, for otherwise the wave amplitude would go to infinity at some place in the channel which would physically be inadmissible. The free-surface-water-wave equations indeed generate these bounded solutions, they are the so-called Kelvin and Poincaré *waves*, respectively, as we shall soon see.

We can also estimate when the rotation of the Earth will affect the propagation of waves in a body of water. The argument follows again that of Fig. 11.1 with the difference that the parcel is now a wave packet and $R = v/f$ is built with the phase speed of the wave.[2] The length

[2] At this point of the development it may not become clear to the reader, why the parcel should be able to be replaced by a wave-packet. However, in a first approach, we may accept this as an analogy and investigate its consequences. Later formulas will corroborate this.

$$R_{\mathrm{D}} = \frac{v_{\mathrm{ph}}}{f} \tag{11.3}$$

is called the *Rossby radius of deformation* or simply the *Rossby radius*. A typical numerical value for the phase velocity in the water waves is its value in the shallow water approximation in which we have seen in Chaps. 4 and 7 (Volume I), respectively, that

$$v_{\mathrm{ph}} = \begin{cases} \sqrt{gH} & \text{homogeneous barotropic case,} \\ \sqrt{g\,\dfrac{\Delta\rho}{\rho}\,\dfrac{H_1 H_2}{H_1 + H_2}} & \text{two-layer baroclinic case,} \end{cases} \tag{11.4}$$

in which H is the total water depth and H_1 and H_2 are the thicknesses of the upper and lower layers, so $H = H_1 + H_2$. Moreover, $\Delta\rho/\rho$ is the relative density difference of the two layers. A few representative values of the Rossby radius of deformation, evaluated according to (11.3) and (11.4), have been computed and are collected in Table 11.1. As can be seen from this table, Rossby radii for barotropic flows are perhaps between 200 and 500 km. This implies that for barotropic gravity waves the rotation of the Earth ought to be accounted for whenever the horizontal extent of a basin is about half the Rossby radius or more, i.e. 100–250 km. This means that barotropic wave dynamics will be influenced by the rotation of the Earth in large lakes like the Great Lakes, Lake Ladoga (210/128 km largest length/width), Lake Onega (240/80 km largest length/width), Lake Victoria and Lake Tanganyika, the Baltic Sea, the Caspian Sea, but hardly in Lake Constance (60 km long), Lake Geneva (100 km long) whose widths are both small, just a few km and certainly not in even smaller lakes. On the other hand, for baroclinic wave processes in a two-layer approximation the Rossby radius of deformation is just a few kilometers. Here, the effects of the rotation of the Earth are visible in much smaller basins of the extent of 10–30 km, say. There are many mountainous lakes, 10–30 km long and a few kilometers wide. Their gravity wave dynamics is affected by the rotation of the Earth mostly only marginally, but at weak stratification, the corresponding Rossby radii of deformation may become so small (e.g. in autumn) that the rotation of the Earth may be negligible in summer but important in late autumn.

The reader should also be aware of the fact that for the stratified case Table 11.1 contains only results for a two layer model and thus only lists Rossby radii for the first baroclinic mode of a typical summer stratification. There are higher baroclinic

Table 11.1 Rossby radii of deformation R_{D} in kilometre for a one-layer, barotropic and a two-layer, baroclinic fluid when v_{ph} is given by (11.4) and $\Delta\rho/\rho = 10^{-3}$, $f = 10^{-4}\,\mathrm{s}^{-1}$, $g = 10\,\mathrm{ms}^{-2}$. $H = H_1 + H_2$

Water depth		H (m)	50	200	1,000
Barotropic case	R_{D} (km)		224	447	1,000
Baroclinic case	R_{D} (km)	$H_1 = 10\,\mathrm{m}$	2.83	3.08	3.14
		$H_1 = 40\,\mathrm{m}$	2.83	5.66	6.20

modes (e.g. for a three layer model, compare with the results obtained in Chap. 8 in Volume I of this book series). We explain there that, the higher the baroclinic mode is, the smaller will be the corresponding phase speed and, consequently, the smaller the Rossby radius belonging to it. The reader may show by himself/herself that for a realistic summer stratification this next higher order Rossby radius is of the order of 1 km.

All these facts will be theoretically substantiated, but it is interesting to realize that relatively simple arguments of dimensional analysis and physical reasoning have led us to these important inferences regarding the dynamical behaviour of water bodies. This concerns *gravity waves*. There is, however, one additional wave phenomenon which we have not been able to describe so far. These are the so-called *Rossby waves* or *geostrophic* or *vorticity waves*. In a frame of reference which is inertial, such waves are not excited. Their existence cannot easily be explained by arguments of dimensional reasoning. We have to await the presentation of the governing equations to make this clear. This will be done by using the shallow water equations and not the finite or infinite depth equations, the reason being that the essential properties can be extracted with less heavy mathematical formulae.

11.2 Rotation Influenced Shallow Water Waves

We consider small amplitude linear water waves in a layer of variable depth of a fluid on the rotating Earth. We suppose conditions of an ideal fluid with negligible viscous or turbulent stresses and vanishingly small heat flux, negligible dissipation and vanishing radiation. Such assumptions are in oceanography often referred to as conditions of *adiabaticity*.[3] We further impose the *shallow water approximation* which implies that the vertical momentum equation reduces to a balance between the vertical derivative of the pressure and the gravity forces (known as the *hydrostatic pressure assumption*). We shall momentarily also restrict considerations to *barotropicity* (i.e. the density is constant) and to *linearity* implying that convective accelerations are ignored and free surface elevations above the rest positions are small. Later we will see that restriction to conditions of barotropicity can be lifted provided the water depth is constant.

All these assumptions are made to arrive at a simple system of equations which can be handled analytically but still captures the essential physics, and complications can be added later on. Nevertheless, the simplifications mentioned above can also be justified, which we shall now do: In doing so, we let ourselves be motivated by the fact that wave motion is in focus. Its existence is based on variations of the free surface and density (see Chap. 8 in Volume I). Viscous and turbulent

[3] The classical definition of adiabaticity is that a body is thermally isolated from its environment. This means that in this case heat flux and radiation sources are zero. Our weaker interpretation includes in the definition all those terms which are associated with dissipation, through species, momentum, and heat diffusion.

stresses and the presence of heat flow, dissipation and radiation will attenuate the wave amplitudes as the waves progress. The imposition of the shallow water approximation is tantamount to assuming that wavelengths are much larger than wave heights and the hydrostatic pressure assumption accounts for the fact that vertical accelerations are small in comparison to the acceleration due to gravity. All these assumptions can rigorously be made by non-dimensionalizing the governing equations with a proper scaling of the physical variables.

Balances of mass and momentum imply

$$\left.\begin{aligned} &\frac{\partial u}{\partial x}+\frac{\partial v}{\partial y}+\frac{\partial w}{\partial z}=0,\\ &\frac{\partial u}{\partial t}-fv=-\frac{1}{\rho}\frac{\partial p}{\partial x},\\ &\frac{\partial v}{\partial t}+fu=-\frac{1}{\rho}\frac{\partial p}{\partial y},\\ &0=-\frac{\partial p}{\partial z}-\rho g, \end{aligned}\right\} \quad \begin{aligned} &z\in[\zeta(x,t),-H(x)],\\ &(x,y)\in\mathcal{D}\subset\mathbb{R}^2, \end{aligned} \tag{11.5}$$

where $\mathcal{D}$ is the horizontal domain over which the water is distributed, sometimes identified with $\mathbb{R}^2$. These equations must be solved subject to the boundary conditions

$$\left.\begin{aligned} &\frac{\partial \zeta}{\partial t}+\frac{\partial \zeta}{\partial x}u+\frac{\partial \zeta}{\partial y}v-w=0,\\ &p=p_0=\text{const.}, \end{aligned}\right\} \quad \begin{aligned} &z=\zeta(x,y,t),\\ &(x,y)\in\mathcal{D} \end{aligned} \tag{11.6}$$

which assumes constant atmospheric pressure and

$$\frac{\partial H}{\partial x}u+\frac{\partial H}{\partial y}v+w=0, \quad \text{at} \quad z=-H(x,y), \quad (x,y)\in\mathcal{D}. \tag{11.7}$$

In a first step, we integrate the continuity equation from $z=-H(x,y)$ to $z=\zeta(x,y,t)$ as follows:

$$\int_{-H(x,y)}^{\zeta(x,y,t)}\frac{\partial u}{\partial x}\mathrm{d}z+\int_{-H(x,y)}^{\zeta(x,y,t)}\frac{\partial v}{\partial y}\mathrm{d}z+w(x,y,\zeta,t)-w(x,y,-H,t)=0. \tag{11.8}$$

The result (i.e. right-hand side) is still zero since the definite integral of the zero function yields zero. The next step consists of interchanging the order of performance of the differentiations and integrations in (11.8) viz.,

$$\int_{-H(x,y)}^{\zeta(x,y,t)}\frac{\partial u}{\partial x}\mathrm{d}z=\frac{\partial}{\partial x}\int_{-H(x,y)}^{\zeta(x,y,t)}u\,\mathrm{d}z-u(x,y,\zeta,t)\frac{\partial \zeta}{\partial x}-u(x,y,-H,t)\frac{\partial H}{\partial x} \tag{11.9}$$

and a similar formula for v

$$\int_{-H(x,y)}^{\zeta(x,y,t)} \frac{\partial v}{\partial y}\mathrm{d}z = \frac{\partial}{\partial y}\int_{-H(x,y)}^{\zeta(x,y,t)} v\,\mathrm{d}z - v(x,y,\zeta,t)\frac{\partial \zeta}{\partial y} - v(x,y,-H,t)\frac{\partial H}{\partial y}. \tag{11.10}$$

These formulae reflect the explicit application of the Leibniz rule of differentiation of an integral whose upper and lower limits are themselves functions of the variable with respect to which the integral is differentiated. Substituting (11.9), (11.10) into (11.8) yields

$$\frac{\partial}{\partial x}\underbrace{\int_{-H(x,y)}^{\zeta(x,y,t)} u\,\mathrm{d}z}_{:=U} + \frac{\partial}{\partial y}\underbrace{\int_{-H(x,y)}^{\zeta(x,y,t)} v\,\mathrm{d}z}_{:=V} - \underbrace{\left\{u\frac{\partial \zeta}{\partial x} + v\frac{\partial \zeta}{\partial y} - w\right\}_{z=\zeta}}_{=-\partial\zeta/\partial t,\ \text{see (11.6)}} - \underbrace{\left\{u\frac{\partial H}{\partial x} + v\frac{\partial H}{\partial y} + w\right\}_{z=-H}}_{=0,\ \text{see (11.7)}} = 0, \tag{11.11}$$

which, in view of the identifications expressed below the curly brackets, reduces to

$$\frac{\partial \zeta}{\partial t} + \frac{\partial U}{\partial x} + \frac{\partial V}{\partial y} = 0. \tag{11.12}$$

U and V are the *volume fluxes* in the x- and y-directions, respectively. In the linear approximation, they are representable as

$$U \cong \int_{-H(x,y)}^{0} u(x,y,z,t)\,\mathrm{d}z, \qquad V \cong \int_{-H(x,y)}^{0} v(x,y,z,t)\,\mathrm{d}z. \tag{11.13}$$

Problem 11.1 *By formulating the mass balance for a water column element of cross section* $\mathrm{d}x\,\mathrm{d}y$ *and height* $H + \zeta$*, show that (11.12) is obtained. Convince yourself that with the exact definitions of the volume fluxes, (11.12) is exact.*

◆

Next, we return to $(11.5)_4$ and integrate it subject to the boundary condition $(11.6)_2$. This yields

$$p(x,y,z,t) = \rho g(\zeta(x,y,t) - z) + p_0, \tag{11.14}$$

from which, since $p_0 =$ constant,[4]

[4] The physical interpretation of p_0 is atmospheric pressure at $z = \zeta$ which obviously is a function of x, y and t : $p_0 = p_0(x,y,t)$. However, typical length scales over which atmospheric pressures vary, are, in general, larger than the horizontal extent of common lakes, implying that p_0 may be assumed to be constant. When atmospheric *fronts* move across a lake, then p_0 should not be treated as constant. In this more general case atmospheric pressure gradients would enter (11.15) and (11.17) as driving forces of the motion.

$$\frac{\partial p}{\partial x}(x,y,t) = \rho g \frac{\partial \zeta}{\partial x}(x,y,t), \quad \frac{\partial p}{\partial y}(x,y,t) = \rho g \frac{\partial \zeta}{\partial y}(x,y,t) \tag{11.15}$$

is deduced. The horizontal components of the pressure gradient are, therefore, only functions of x, y, and t but not z, making the right-hand sides of $(11.5)_{2,3}$ z-independent and implying that also the left-hand sides are z-independent. It follows: *In a linearized barotropic fluid model which obeys the hydrostatic pressure and the adiabaticity assumptions, the horizontal velocity components are independent of the vertical coordinate. Moreover, the vertical velocity component must be a linear function of the z-coordinate*; it is given by

$$w(x,y,z,t) = \frac{(z+H)}{H} \frac{\partial \zeta(x,y,t)}{\partial t}, \tag{11.16}$$

which is zero at the bottom and reaches a maximum at the free surface.[5] Furthermore, in this linear approximation $U = Hu$ and $V = Hv$, so that

$$\begin{aligned} \frac{\partial u}{\partial t} - fv = -g \frac{\partial \zeta}{\partial x}, \quad \frac{\partial v}{\partial t} + fu = -g \frac{\partial \zeta}{\partial y}, \\ \frac{\partial \zeta}{\partial t} + \frac{\partial}{\partial x}(Hu) + \frac{\partial}{\partial y}(Hv) = 0. \end{aligned} \tag{11.17}$$

An alternative way of writing these would also be

$$\begin{aligned} \frac{\partial U}{\partial t} - fV = -gH \frac{\partial \zeta}{\partial x}, \quad \frac{\partial V}{\partial t} + fU = -gH \frac{\partial \zeta}{\partial y}, \\ \frac{\partial \zeta}{\partial t} + \frac{\partial}{\partial x}(U) + \frac{\partial}{\partial y}(V) = 0. \end{aligned} \tag{11.18}$$

Here, volume fluxes (U, V) have replaced the horizontal velocities (u, v) as basic variables. This form of the governing equations is better suited for computation. Horizontal, depth averaged velocities are then obtained a posteriori from $(u, v) = \frac{1}{H}(U, V)$.

Equations (11.17) comprise the governing equations for free long waves in a basin of finite depth $H(x, y)$. To find out which kind of motions they describe, it is more convenient to transform them to a single equation in just one variable. We shall do this here for the surface elevation ζ as follows (the steps are not entirely straightforward which is one reason for the demonstration). First, we differentiate

[5] Actually, with the linearized boundary condition (11.6), $\partial\zeta/\partial t = w$, at $z = 0$ and the full boundary condition (11.7), (11.16) reads

$$w(x,y,z,t) = \frac{(z+H)}{H} \frac{\partial \zeta(x,y,t)}{\partial t} + \left[\frac{1}{H} \frac{\partial H}{\partial x} \frac{U}{H} + \frac{1}{H} \frac{\partial H}{\partial y} \frac{U}{H} \right] z$$

in which the second bracketed is dropped in the shallow water approximation.

$(11.17)_1$ with respect to time and substitute $(11.17)_2$. Similarly, we differentiate $(11.17)_2$ and substitute $(11.17)_1$. These two steps yield

$$\mathcal{L}[u] = -fg\frac{\partial \zeta}{\partial y} - g\,\frac{\partial^2 \zeta}{\partial t \partial x},\quad \mathcal{L}[v] = fg\,\frac{\partial \zeta}{\partial x} - g\,\frac{\partial^2 \zeta}{\partial t \partial y}, \tag{11.19}$$

where

$$\mathcal{L} = \frac{\partial^2}{\partial t^2} + f^2. \tag{11.20}$$

Second, we take the integrated mass balance, $(11.17)_3$, and apply $\mathcal{L}$ to it

$$\mathcal{L}\left[\frac{\partial \zeta}{\partial t}\right] + \frac{\partial}{\partial x}\left(\mathcal{L}\left[Hu\right]\right) + \frac{\partial}{\partial y}\left(\mathcal{L}\left[Hv\right]\right) = 0. \tag{11.21}$$

Since H is only a function of x and y, we have $\mathcal{L}[Hu] = H\mathcal{L}[u]$ and $\mathcal{L}\left[Hv\right] = H\mathcal{L}[v]$. Thus, upon substitution of (11.19) into (11.21) and some transformations the resulting single variable equation for ζ

$$\begin{gathered}\nabla_H \cdot \left\{H \nabla_H \frac{\partial \zeta}{\partial t}\right\} + J\left[fH, \zeta\right] - \frac{1}{g}\left(\frac{\partial^2}{\partial t^2} + f^2\right)\frac{\partial \zeta}{\partial t} = 0,\\ J\left[a, b\right] := \frac{\partial a}{\partial x}\,\frac{\partial b}{\partial y} - \frac{\partial a}{\partial y}\,\frac{\partial b}{\partial x}\end{gathered} \tag{11.22}$$

is obtained. This partial differential equation is of third order in time and of second order in space. ∇_H is the two-dimensional horizontal gradient operator. The operator J is called the Jacobian operator, and the Coriolis parameter does not need be constant.

This last remark requires qualification. When a Cartesian coordinate system is chosen on the Earth, with the x-axis pointing towards East, the y-axis pointing towards North and the z-axis pointing towards the zenith, then the origin of this coordinate system fixes the geographical latitude and, therefore, the Coriolis parameter f; it does not vary. If a basin has a large North–South extent, such that the curvature of the Earth may be of some significance, then one may no longer be allowed to use Cartesian coordinates but must use spherical coordinates for which f varies in the North–South direction. It turns out that the simplest extension of (11.22) is to apply still (11.22) but now with variable f. In the chosen coordinate system (x, y, z), the only nontrivial component of $(\mathrm{grad}\, f)$ is the change of f with y, $\beta := \mathrm{d}f/\mathrm{d}y$. The use of the letter β is standard in geophysics and the two approximations, (1) $f =$ constant and (2) $f = f_0 + \beta y$ are called the *f-plane approximation* and the *β-plane approximation*, respectively.

Returning to (11.22), we may say that it holds true both for the f-plane and β-plane approximations. The differential equation (11.22), because it is third order

in time, possesses in general three different wave solutions;[6] however, these belong only to two classes as we shall now see:

- *Waves of the first class*. When $J[fH, \zeta] = 0$ then (11.22) reduces to an equation of the second order in $\partial\zeta/\partial t$. Since these waves obviously depend on gravity (the constant g arises explicitly in the resulting equation), and because the waves do also exist when $f = 0$ (non-rotating frame of reference), they are called *surface gravity waves*. It is easy to show that for $H =$ constant the dispersion relation is given by $(\omega^2 - f^2)/k^2 = gH$ in this case. In the limit of no rotation, these waves agree with the long wave-length shallow-water waves. They are non-dispersive. When the rotation of the Earth is present these surface gravity waves are *modified* – perhaps slightly, perhaps substantially – by the presence of the Coriolis parameter f. They are non-dispersive.
- *Waves of the second class, Rossby waves or quasi-geostrophic waves or vorticity waves*. These waves are governed by the third solution of the wave equation (11.22) and only exist when the Jacobian operator does not identically vanish, and they are approximately obtained from (11.22) by balancing the first two terms (and ignoring the third, gravity dependent term),

$$\nabla_H \cdot \left\{ H \nabla_H \frac{\partial \zeta}{\partial t} \right\} + J[fH, \zeta] = 0. \tag{11.23}$$

  This is the famous *Rossby wave equation*. The reader may prove by himself/herself that it may be obtained from $(11.17)_{1,2,3}$ by ignoring in $(11.17)_3$ the time derivative $\partial\zeta/\partial t$, which is tantamount to the *rigid lid assumption*. This explanation makes equally clear that *the rigid lid assumption eliminates surface gravity waves*; indeed in (11.23) the gravity term is missing. Furthermore, Rossby waves do only exist when $\partial(fH)/\partial x$ and $\partial(fH)/\partial y$ do not both simultaneously vanish. This demonstrates that they only exist in a fluid on a rotating non-inertial frame of reference; thus, they necessarily possess non-vanishing absolute vorticity for which reason they are sometimes also called *vorticity waves*. Depending upon whether $\beta = \partial f/\partial y = 0$ or $\beta \neq 0$ and $H =$ constant, $H \neq$ constant there are several special cases which we shall discuss below.

From a conceptual point of view the fact that a new type of wave was found in a fluid on a rotating non-inertial frame is significant. In such a fluid system there arise phenomena that do not exist in a system referred to an inertial frame of reference. The effect of the rotation of the Earth has here not modified but, rather, created a new phenomenon, not existing otherwise. It will be interesting to see how these waves look like and whether they are of importance in physical limnology.

In the above analysis, the surface gravity waves and the Rossby waves were obtained from (11.22) by balancing the appropriate two of the three terms of

[6] This statement assumes that of the three solutions for the wave frequency all are real. Without explicit analysis this is not guaranteed. We here anticipate this fact.

the differential equation. These balances can be obtained more formally by non-dimensionalizing equation (11.22). To this end, let L_0 and H_0 be typical horizontal and vertical length scales and let time and Coriolis parameter be scaled by f_0^{-1} such that

$$H = H_0 h, \quad x = L_0 \bar{x}, \quad t = \frac{1}{f_0}\bar{t}, \quad f = f_0 \bar{f}.$$

With these, (11.22) assumes the form

$$\bar{\nabla}_H \cdot \left\{ h \bar{\nabla}_H \frac{\partial \bar{\zeta}}{\partial \bar{t}} \right\} + J\left[\bar{f} h, \bar{\zeta}\right] - \frac{L_0^2}{R_D^2} \left(\frac{\partial^2}{\partial \bar{t}^2} + \bar{f}^2 \right) \frac{\partial \bar{\zeta}}{\partial \bar{t}} = 0, \tag{11.24}$$

in which

$$R_D := \frac{\sqrt{g H_0}}{f_0} \tag{11.25}$$

is the *Rossby radius of deformation*.[7] For $f_0 = 10^{-4}\,\mathrm{s}^{-1}$, $H_0 = 5{,}000\,\mathrm{m}$ it is of the order of 2,300 km; when $H_0 = 100\,\mathrm{m}$ one obtains $R_D \simeq 330\,\mathrm{km}$. Rotational and gravity effects uncouple when corresponding typical wave lengths are sufficiently separate. In particular, the effects of the rotation of the Earth upon surface gravity waves are significant if the horizontal length scale L_0 is comparable to the Rossby radius of deformation. For barotropic waves this is the case for lake and ocean basins of the magnitude of the Great Lakes, Lake Baikal, the Baltic Sea, but certainly neither for Lake Constance nor Lake Geneva nor smaller basins.

Equation (11.24) also provides the conditions when second class waves uncouple from first class waves as stipulated by (11.23). This is so when $R_D \gg L_0$, which is certainly the case in many ocean basins and all lakes under barotropic conditions. Barotropic Rossby waves can almost always be described by the reduced equation (11.23).[8] Baroclinic Rossby waves may well be influenced by gravity waves unless $L_0 \ll R_D$, the internal Rossby radius of deformation.

Equation (11.24) also discloses a *scale invariance* of the original Rossby wave equation (11.23). Indeed, when the last term in (11.24) is omitted and when $\bar{f} = 1$

[7] Later, we shall also introduce an *internal* Rossby radius of deformation. For a two-layer system (upper layer depth H_1, density ρ_1; lower layer depth H_2, density ρ_2) it is given by

$$R_D = \frac{\sqrt{g' H_E}}{f_0}, \quad g' = g\,\frac{\rho_2 - \rho_1}{\rho_2}, \quad H_E = \frac{H_1 H_2}{H_1 + H_2}.$$

This internal Rossby radius is exactly what we have introduced in (11.3), (11.4) in the baroclinic case with methods of dimensional analysis; it applies for a stratified fluid in two layers and is much smaller than its external counterpart. So, whereas in certain lake basins the effects of the rotation of the Earth may be ignored for *surface waves* this is not so for *internal waves*. We shall come back to this property later on.

[8] An exception may be the Caspian Sea which has a very deep (>1,000 m) Southern part for which $R_D \simeq 1{,}000\,\mathrm{km}$ and $L_0 \simeq 250\,\mathrm{km}$ and a shallow middle and Northern part, where $R_D \simeq 70\,\mathrm{km}$, and the same L_0-value. A thorough analysis of this has, however, not been done.

(f-plane approximation), then its remainder is independent of any horizontal length scale. As a consequence, the solutions for the scaled variables of the reduced equation (11.24) with $\bar{f} = 1$ will be the same for all geometrically similar basin bathymetries (irrespective of their size). This is not so when the last term in (11.24) is kept because it then contains the factor L_0^2/R_D^2 which introduces a dependence on size.

11.3 A Brief Classification of Rossby Waves

Equation (11.23) is written for the free surface elevation ζ; more convenient and better suited for applications is an equation for the mass transport stream function. To introduce it, consider $(11.17)_3$ subject to the *rigid lid assumption* so that

$$\frac{\partial}{\partial x}(Hu) + \frac{\partial}{\partial y}(Hv) = 0. \tag{11.26}$$

It follows that the volume transport $H\boldsymbol{v}$ is derivable from the relations

$$Hu = -\frac{\partial \Psi}{\partial y}, \quad Hv = \frac{\partial \Psi}{\partial x}. \tag{11.27}$$

Ψ is called the *mass transport stream function*. If (11.27) is substituted into $(11.17)_{1,2}$ and the surface elevation ζ is eliminated from the emerging equations, what results reads as follows:

$$\nabla_H \cdot \left\{ \frac{1}{H} \nabla_H \frac{\partial \Psi}{\partial t} \right\} + J\left[\Psi, \frac{f}{H}\right] = 0. \tag{11.28}$$

In form, (11.28) is identical to the Rossby wave equation (11.23).[9] Introducing the (elliptic) operator

$$E[\Psi] = \nabla_H \cdot \left\{ \frac{1}{H} \nabla_H \Psi \right\}, \tag{11.29}$$

we now write (11.28) as

$$T[\Psi] := \frac{\partial}{\partial t} E[\Psi] + J\left[\Psi, \frac{f}{H}\right] = 0. \tag{11.30}$$

As one might surmise, this is a free wave equation, in which external driving forces have been omitted. In an ocean or lake domain $\mathcal{D}$, it is generally solved subject to the boundary condition of vanishing flow through the basin boundary $\partial\mathcal{D}$. In

[9] For a portrait of Karl Gustav Rossby and a biographical sketch, see Fig. 19.1 in Chap. 19.

other words, the shore line is a mass transport streamline. Now, since mass transport streamlines are the lines along which Ψ = constant, and absolute values of Ψ are insignificant, a solution of the Rossby wave equation is determined by solving the boundary value problem[10]

$$T[\Psi] = 0, \quad \text{in} \quad \mathcal{D}, \quad \text{with } \Psi = 0, \quad \text{along } \partial\mathcal{D}. \tag{11.31}$$

We close this section with a few remarks and a *classification of Rossby waves*:

- The Rossby wave equation in the f-plane approximation is scale invariant, as already mentioned before. This scale invariance is physically valid when there is a sufficient separation of the length scales of the surface gravity and the Rossby waves.
- It can be shown that the Rossby wave equation is invariant under *conformal transformations*. This property can constructively be used to determine a great variety of solutions from any other one. However, because the depth distribution is transformed along with the domain, this invariance property is less useful from a practical viewpoint than a first sight might surmise.
- If the Jacobian $J[\Psi, f/H] = 0$, then (11.31) reduces to $\partial E[\Psi]/\partial t = 0$, which implies after an integration by time, since we are looking for free wave solutions, that

$$E[\Psi] = 0, \quad \text{in} \quad \mathcal{D}, \quad \text{with } \Psi = 0, \quad \text{on} \quad \partial\mathcal{D}. \tag{11.32}$$

  It follows from this, because $E[\cdot]$ is an elliptic operator that Ψ must assume its maximum and its minimum at the boundary where $\Psi = 0$.[11] So, (11.32) possesses only the zero solution; there are no Rossby waves when $J[\Psi, f/H] \equiv 0$.

Evidently, the condition that $J[\cdot] \neq 0$ can only be fulfilled for $f \neq 0$. Depending upon the variations of f and/or H the following *classification of the (general) Rossby waves* is made:

- If $\nabla_H H = 0$, i.e. if the layer depth is constant, then necessarily $\beta \neq 0$ must hold in order that (11.30) possesses a non-trivial solution. In a constant depth atmosphere, ocean or lake, Rossby waves exist in the β-plane, but not in the f-plane approximation. Such waves can develop provided the NS-extent of a basin with constant depth is large such that $\beta L_0 \simeq \mathcal{O}(f)$ implying $L_0 \geq 500$–1,000 km. These waves cover a large portion of the Globe and are thus called *planetary Rossby waves*. They are primarily seen in the atmosphere and the deep ocean.

[10] The boundary condition is in general $\Psi = C_\alpha$ = const along each boundary with vanishing flow of water through it. Each boundary has a different value of C_α. If a lake has no island, then only a single C arises which may be set to zero, because the stream function can accordingly be normalized.

[11] This fact is stated here without proof.

- In the f-plane approximation ($\beta = 0$), at mid to high latitudes ($f \simeq 10^{-4}$), the Jacobian operator differs from zero when $\nabla_H H \neq 0$. In this case, Rossby waves can only exist because of the variable topography. These waves are called *topographic (Rossby) waves*. Because the variation of the topography is much richer than that of the Coriolis parameter, topographic waves are more complex in structure than planetary Rossby waves. Signals are particularly pronounced where topographic slopes are large, in the atmosphere near mountains, in the ocean in the vicinity of the shelf- and shore regions and near sea mountains. When waves travelling along the continental shelves are addressed, then they are referred to as *shelf-waves*.

The planetary and the topographic Rossby waves are the two main Rossby wave types; there are special cases of these which, frequently, bear their own names:

- When topographic waves cover large NS-distances they may be called *planetary topographic waves*. Shelf waves travelling through the entire Atlantic or Pacific Ocean are of this type.
- Close to the Equator (to within $\pm 5°$ latitude) f is so small that it may be ignored in comparison to βL_0. The corresponding waves enjoy special features and are called *equatorial planetary* (Rossby) *waves* or *equatorial topographic* (Rossby) *waves*.

A first physical grasp of the Rossby wave equation is gained if time-independent *steady solutions* to $T[\Psi] = 0$ are sought. These are given by

$$J\left[\Psi, \frac{f}{H}\right] = 0,$$

which can also be written as

$$\nabla_H \Psi \times \nabla_H \left(\frac{f}{H}\right) = 0. \tag{11.33}$$

This equation states that the two vectors, $\nabla_H \Psi$ and $\nabla_H (f/H)$ are parallel. Since $\nabla_H \Psi$ is at every point perpendicular to the lines of constant volume transport Ψ, (11.33) states that the volume-transport streamlines are parallel to the lines of constant f/H, which are called *isotrophs*. On the f-plane they are simply the isobaths. They can immediately be constructed if the bathymetry to a basin is given together with the location of the basin on the Globe. Equation (11.33) now tells us that the streamlines of a steady Rossby current must be parallel to the isotrophs: *the isotrophs are necessarily the streamlines of the steady vorticity motions*. Alternatively, whenever the streamlines are not parallel to the isotrophs, then a Rossby wave must develop. In fact, if we envisage the topographic wave equation, $T[\Psi] = 0$, as a simple oscillator model, then the Jacobian $J[\Psi, f/H]$, whose value is a measure of the angle between streamlines and isotrophs, acts as a 'restoring force' that drives the system back to this 'equilibrium flow configuration'. Rossby waves arise because of the fluid particles tendency to follow the isotrophs as much as possible.

This fact is indication where in a particular situation one should look for Rossby wave motion, e.g. if an ocean or lake basin has a strong variation in its bathymetry. Seamounts and -troughs are particular candidates for this.

The lake with the largest North–South extent on the Globe is the Caspian Sea. It is nearly 1,200 km long and between 300 and 400 km wide, and its depth spans over a tremendous range: only 5 m or less in the Northern most third part, about 700 m in the middle portion and 1,000 m in its Southern third, see Fig. 11.3a, which shows a depth chart. So, this basin is an ideal test case for β-effects. Let H and $\mathcal{H} = H/f$ be the bathymetric depth and *isotroph depth*,[12] respectively. With

$$\begin{aligned} f &= 2\Omega \sin\phi = f_0 \bar{f} = (2\Omega \sin\phi_0)\frac{\sin\phi}{\sin\phi_0}, \\ \Omega &= 7.272 \times 10^{-5}\ \mathrm{s}^{-1}, \quad \phi_0 = 42^\circ, \end{aligned} \tag{11.34}$$

we may then write

$$\mathcal{H} = \frac{1}{f_0}\frac{H}{\bar{f}} = \frac{1}{f_0}\bar{\mathcal{H}}, \qquad \bar{\mathcal{H}} = \frac{H}{\bar{f}}. \tag{11.35}$$

We shall call $\bar{\mathcal{H}}$ the *scaled isotroph depth*. The reference geographical latitude is $\phi_0 = 42^\circ$, and the lake stretches from $\phi_{\min} = 36^\circ 30'$ at $y = -600$ km to $\phi_{\max} = 47^\circ$ at $y = 600$ km. Panel (b) of Fig. 11.3 displays the scaled inverse isotrophs. The graph shows that in the entire Northern basin of perhaps 6,000 km^2 the inverse isotrophs do not reach 5 m, whilst in the Southern basin $\bar{\mathcal{H}}$ reaches 1,100 m (see the deep red spot in panel (b)) of Fig. 11.3. Comparing the two charts also indicates that their horizontal distribution is slightly different. Of particular interest is, therefore, the difference

$$\bar{\mathcal{H}} - H = \frac{1-\bar{f}}{\bar{f}} H. \tag{11.36}$$

Its distribution is shown in Fig. 11.3c. It proves that depth differences between the scaled inverse isotrophs $\bar{\mathcal{H}}$ and the water depth H are small in the Northern half of the lake, but as large as 90 m in the Southern part. This makes it likely that β-effects may be of significance in the basin wide wave response.

Another very informative example is obtained, when we consider planetary waves in a constant depth ocean or atmosphere; in this case, equation (11.30) takes the form

$$\nabla_H^2 \frac{\partial \Psi}{\partial t} + \beta \frac{\partial \Psi}{\partial x} = 0, \tag{11.37}$$

(H drops out from the equation). Assuming harmonic wave propagation in the x-direction $\Psi = \Psi_0\, \mathrm{e}^{i(kx-\omega t)}$, yields the dispersion relation

[12] The lines of constant f/H are called isotrophs. We choose here to name isolines of H/f 'isotroph depths', but mention that this is not an official denotation.

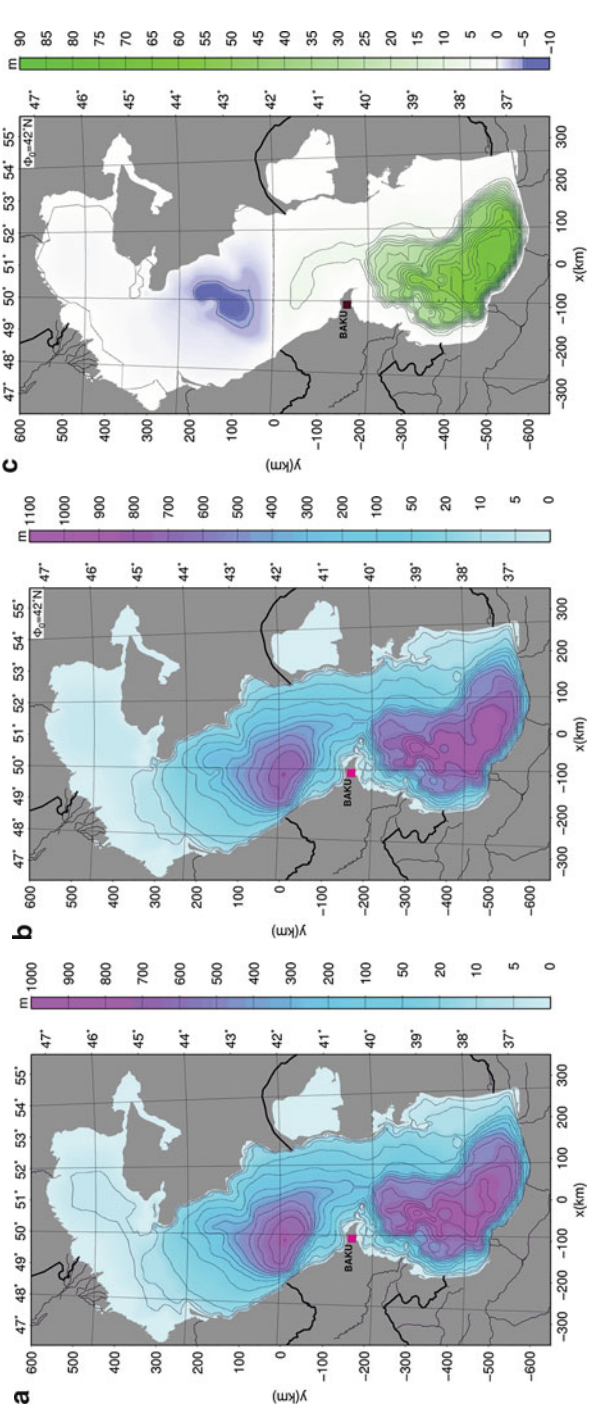

Fig. 11.3 (**a**) Bathymetric contours H of the Caspian Sea. Note the strong North–South gradient from a large Northern basin of less than 5 m depth to a 700-m deep middle region and a 1,000-m deep Southern part. (**b**) Scaled inverse isotroph contours $\bar{\mathcal{H}} = H/\bar{f}$. (**c**) Distribution of the difference depth $\bar{\mathcal{H}} - H = (1 - \bar{f})H/\bar{f}$, for the Caspian Sea indicating that β-effects may be important

$$\omega = -\frac{\beta}{k}, \tag{11.38}$$

from which we may deduce

$$c_{\mathrm{ph}} = -c_{\mathrm{gr}} = -\frac{\beta}{k^2}. \tag{11.39}$$

These equations state that the phase necessarily travels from East to West whereas the group does so from West to East.[13] Thus, on the Northern hemisphere the energy of planetary Rossby waves travels across the mid to northern Atlantic from the American coast towards Europe with a group speed which equals in magnitude the phase speed that travels in the opposite direction.

At mid-latitudes typical diameters of a gyre of a storm-low are 10^5 m (so $k \sim 10^{-6}\,\mathrm{m}^{-1}$ and $\beta \simeq 10^{-11}\,\mathrm{s}^{-1}\,\mathrm{m}^{-1}$ implying $|c_{\mathrm{ph}}| = |c_{\mathrm{gr}}| \simeq 10\,\mathrm{ms}^{-1}$). Thus, such a wave propagates approximately $10^6\,\mathrm{md}^{-1}$. So, it takes such a weather front roughly four days to cross the Atlantic ocean. This may explain field observations: the so-called synoptical scale at mid latitudes lasts about 5–7 days. This means that, if the weather is bad in a given region, it is bad for the duration of a few days; after these days, the global weather system over this area will be replaced by another one. This applies as much to the ocean as it does to the atmosphere.

Remark 11.1. Planetary vorticity waves occur in the atmosphere persistently and exhibit special features, but their existence is not only due to the non-inertial reference frame but also simply because of the topological peculiarity of the sphere-like geometry of the Earth. About 97% of the mass of the Earth's atmosphere is concentrated within the 30 lowest most kilometers, whilst the Earth's radius is approximately 6,400 km. Hence, the Earth's atmosphere is, naturally, a very thin layer, and dominant winds are primarily tangential to the Globe. Owing to the irregularity of the solar heating on land and over the ocean in the Equatorial and Polar Regions, during summer and winter in the different hemispheres, the atmosphere is in perpetual motion – wind fields are formed out of necessity!

Consider a global wind field that is everywhere tangential to the Earth's surface (which we think to be spherical) and imagine the Earth to be a fur ball with every hair line representing a director of the wind vector at the given point. How can we comb the hairs on the ball? All our attempts will show that it is impossible to comb 'wind hairs' smoothly (i.e. with continuous tangents); at least two 'gyres' have to be formed, one of clockwise, the other of anti-clockwise rotation. The centre of each gyre is a singular point insofar, as it is a point from which 'wind hairs' of any direction emerge. Incidentally, if the Earth were of toroidal shape, 'wind hair' could everywhere smoothly be combed, without the formation of such gyres. Points of the singularity in the orientation of the tangents to the horizontal currents are called *disclinations*. They are either sources or sinks of mass, which in the atmosphere or

[13] With $\mathrm{e}^{i(kx-\omega t)}$ a positive ω means propagation into the positive x-direction.

ocean are maintained by concentrated upward and downward convective flow, much like the flow in a chimney. These are the regions where mass between different layers of fluid is exchanged.

The fact that surface parallel flows on the exterior of a spherical like Earth necessarily require the formation of at least one pair of counter rotating gyres is a topological property of the sphere. It implies that tangential flows on the outside of sphere-like bodies have always non-vanishing local vorticity (which in an inviscid fluid is globally balanced). It is evident that this kind of vorticity wave exists independently of the classical Rossby wave, which assumes a rotating frame of reference. Moreover, in an inviscid spherical fluid layer no motion can start from a state of rest, so single layered atmospheric circulation cannot be formed, in principle. Cells must be formed, which allow mass and vorticity (and energy) exchanges between the layers through convection.

Remark 11.2. The rotation of the Earth manifests itself in the atmosphere and the ocean through several effects.

- *Trade winds:* Because the Earth rotates towards East, the wind in the equatorial belt between 30° North and South of the Equator moves westward, remaining behind the speed of the solid Earth due to its rotation. These so-called trade winds are basically steady and powerful with speeds of approximately 16–25 $\mathrm{km\,h^{-1}}$ and are used for navigation all-the-year-round since ancient times.
- At mid-latitudes (between 30° and 60° where the β-effect is appreciable) planetary Rossby waves transport energy to the West (on the Northern hemisphere) with a group speed given by (11.39).
- All motions are turned to the right (left) on the Northern (Southern) hemisphere.
- A difference in the intensity of cyclonic and anti-cyclonic gyres is observed. Cyclones, which rotate in both hemispheres in the same direction as the planet are more powerful than anti-cyclones. When they cross the Equator, they are rapidly destroyed.

11.4 Plane Linear Waves in a Rotating Stratified Fluid

In the preceding sections, rotationally influenced shallow water waves in a homogeneous fluid were briefly analyzed. It was shown that two classes of waves exist, first class waves, which persist also when the frame of reference is inertial, and second class waves, which exist exclusively because of the rotation of the frame of reference. We shall demonstrate in this section that both types of waves also exist in a stratified fluid. To this end linear waves *in an unbounded domain* of a general Boussinesq fluid will be studied. It will be shown that such waves are generally elliptically polarized, and that they exist only in regions for which

$$f < \omega < N,$$

where f is the Coriolis parameter and N the buoyancy frequency, whilst ω is the circular frequency of the wave. Attention will be focussed on the propagation of free waves in a shallow layer of a Boussinesq fluid on the f-plane. It will be demonstrated that such waves are describable as a linear combination of waves having different speeds and different vertical structures both of which are determined by the vertical distribution of the Brunt–Väisälä frequency.[14] This vertical mode structure has already been studied in Chap. 8, Sect. 8.5 in Volume I, however, a re-analysis is worthwhile as it will shed light on a subtle point not touched upon in the earlier analysis.

11.4.1 Waves in a Linearly Stratified Rotating Unbounded Boussinesq Fluid

Consider the linearized equations of motion in which the Boussinesq and adiabaticity assumptions are invoked but no shallowness assumption is made. The pertinent equations are (4.235)–(4.237) in Chap. 4 in Volume I, which are repeated here as

$$\operatorname{div} \boldsymbol{v} = 0, \tag{11.40}$$

$$\rho^* \left\{ \frac{\partial \boldsymbol{v}}{\partial t} + 2\boldsymbol{\Omega} \times \boldsymbol{v} \right\} = -\operatorname{grad} p' + \rho' \boldsymbol{g}, \tag{11.41}$$

$$\frac{\partial \rho'}{\partial t} - \rho^* \frac{N^2}{g} w = 0, \tag{11.42}$$

in which $\boldsymbol{v} = (u, v, w)$,

$$N^2(z) = -\frac{g}{\rho^*} \frac{\mathrm{d}\rho_0(z)}{\mathrm{d}z}, \tag{11.43}$$

and $N(z)$ is the buoyancy or Brunt–Väisälä frequency , see Definition 8.2 in Volume I. Equations (11.40)–(11.42) are the continuity equation, the three components of the momentum equation and a combination of energy and tracer-mass conservation under adiabatic conditions. The pressure p' can be eliminated from (11.41) by deriving the vorticity transport equation, i.e. taking the curl of (11.41). Taking a further time derivative of the emerging equation and then eliminating ρ' with the aid of (11.42), yields the pair of equations

$$\operatorname{div} \boldsymbol{v} = 0, \tag{11.44}$$

$$\operatorname{curl} \frac{\partial^2 \boldsymbol{v}}{\partial t^2} - 2 \left(\operatorname{grad} \frac{\partial \boldsymbol{v}}{\partial t} \right) \boldsymbol{\Omega} = \operatorname{curl} \left\{ \frac{N^2}{g} \boldsymbol{g} w \right\}. \tag{11.45}$$

[14] For portraits and biographical sketches of Sir David Brunt and Vilho Väisälä see Fig. 8.13 of Volume I.

These are a scalar and vector valued equation for the velocity field $\boldsymbol{v}$ as a function of space and time.

The ensuing analysis will now be restricted to *constant* N corresponding to *linear stratification*. This makes transformations of the right-hand side of (11.45) easier, but still allows qualitative inferences from deduceable results. Plane wave solutions of (11.44) and (11.45) are sought in the form

$$\boldsymbol{v} = \boldsymbol{V} \exp\left(i(\boldsymbol{k}\cdot\boldsymbol{x} - \omega t)\right). \tag{11.46}$$

$\boldsymbol{V} \mathrel{\hat{=}} (U, V, W)$, $\boldsymbol{k}$ and ω are the constant amplitude vector, the wavenumber vector and the circular frequency, and i is the imaginary unit. Physically realizable solutions are obtained by taking the real or imaginary part of (11.46). Substituting (11.46) into (11.44) and (11.45) yields

$$\begin{aligned} &\boldsymbol{k}\cdot\boldsymbol{V} = 0, \\ &\omega^2\boldsymbol{k}\times\boldsymbol{V} - i(2\boldsymbol{\Omega}\cdot\boldsymbol{k})\omega\boldsymbol{V} + \frac{N^2 W}{g}\boldsymbol{k}\times\boldsymbol{g} = \boldsymbol{0}. \end{aligned} \tag{11.47}$$

This system of equations may be regarded as a homogeneous linear system of equations for the components of the amplitude vector $\boldsymbol{V}$, and it thus possesses a solution only if its determinant vanishes. The derivation of this condition is facilitated, if it is recognized that $\boldsymbol{k}\cdot\boldsymbol{V} = 0$ implies that *in a Boussinesq (or density preserving) fluid in an infinite domain all motion is transverse to the direction of wave propagation. There can be no longitudinal plane waves in such a fluid.*[15] It follows that $\boldsymbol{V}$ is orthogonal to the vector $\boldsymbol{k}$, and it possesses only two independent components perpendicular to $\boldsymbol{k}$. To account for this fact, let (x, y, z) be a Cartesian coordinate system with the z-axis vertical opposite to the direction of gravity, see Fig. 11.4. The wavenumber vector may have any direction in this space, but $\boldsymbol{g}$ and $\boldsymbol{k}$ together define a vertical plane. Let $\{\boldsymbol{e}_1, \boldsymbol{e}_2, \boldsymbol{e}_3\}$ be an orthonormal basis with $\boldsymbol{e}_3$ parallel to $\boldsymbol{k}$, $\boldsymbol{e}_1$ perpendicular to $\boldsymbol{k}$ and in the vertical plane formed by $\boldsymbol{g}$ and $\boldsymbol{k}$, and $\boldsymbol{e}_2$ perpendicular to $\boldsymbol{e}_1$ and $\boldsymbol{e}_3$ such that $\{\boldsymbol{e}_1, \boldsymbol{e}_2, \boldsymbol{e}_3\}$ form a right handed system. It is obvious that $\boldsymbol{e}_2$ lies in the xy-plane, and it is equally obvious that

$$\begin{aligned} \boldsymbol{V} &= U_1\boldsymbol{e}_1 + U_2\boldsymbol{e}_2, \\ W &= -U_1 \sin\theta', \\ \boldsymbol{g} &= -g\left(\sin\theta\boldsymbol{e}_3 - \sin\theta'\boldsymbol{e}_1\right). \end{aligned} \tag{11.48}$$

Substituting (11.48) into (11.47)$_2$ yields two equations for U_1 and U_2 which can be written as (k is equal to $|\boldsymbol{k}|$)

[15] Any model for which the mass balance equation reduces to the continuity equation $\operatorname{div}\boldsymbol{v} = 0$ does not permit acoustic waves, which are longitudinal as we have seen.

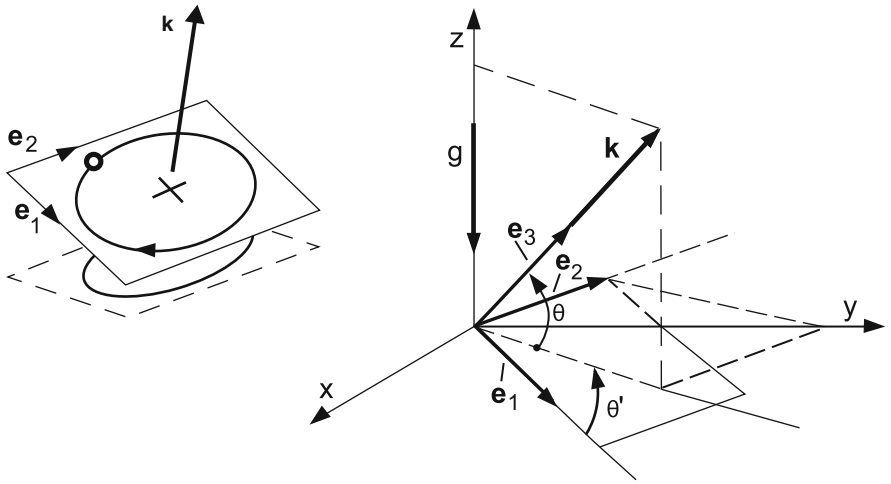

Fig. 11.4 The wavenumber vector $\boldsymbol{k}$ and the gravity vector $\boldsymbol{g}$ define together a vertical plane in a Cartesian coordinate system (x, y, z). $\{\boldsymbol{e}_1, \boldsymbol{e}_2, \boldsymbol{e}_3\}$ is an orthonormal basis with $\boldsymbol{e}_3$ parallel to $\boldsymbol{k}$ and $\boldsymbol{e}_1, \boldsymbol{e}_2$ perpendicular to it, $\boldsymbol{e}_1$ being in the vertical plane; so $\boldsymbol{e}_2$ is in the xy-plane. Two angles θ' and θ in the vertical plane define the orientations of $\boldsymbol{e}_1$ and $\boldsymbol{e}_3$ in the vertical plane relative to the intersection line between the vertical plane formed by $\boldsymbol{g}$ and $\boldsymbol{k}$ and the xy-plane. Obviously, $\theta + \theta' = 90°$. The inset shows the orbital plane spanned by $\{\boldsymbol{e}_1, \boldsymbol{e}_2\}$ with a particle and its elliptical orbit when $N \neq 0$ and $\boldsymbol{\Omega} \neq \boldsymbol{0}$

$$\begin{pmatrix} 2i(\boldsymbol{\Omega}\cdot\boldsymbol{k})\omega & \omega^2 k \\ (\omega^2 - N^2\cos^2\theta)k & -2i(\boldsymbol{\Omega}\cdot\boldsymbol{k})\omega \end{pmatrix} \begin{pmatrix} U_1 \\ U_2 \end{pmatrix} = 0. \tag{11.49}$$

This is a homogeneous system for U_1 and U_2 which has nontrivial solutions provided that

$$\omega^2 \left\{ k^2 \left(\omega^2 - N^2\cos^2\theta \right) - 4(\boldsymbol{\Omega}\cdot\boldsymbol{k})^2 \right\} = 0. \tag{11.50}$$

This equation establishes a relation between ω and $\boldsymbol{k}$ and thus constitutes the *dispersion relation* for plane waves in an unbounded linearly stratified and rotating fluid. A double solution $\omega = 0$ corresponds to no wave at all. The remaining solutions take the form

$$\omega^2 = N^2\cos^2\theta + 4\Omega^2\cos^2\alpha, \tag{11.51}$$

in which α is the angle between $\boldsymbol{\Omega}$ and $\boldsymbol{k}$. *Evidently, for the squared frequency the effects of stratification and rotation are additive*. Given the wavenumber vector $\boldsymbol{k}$ and the frequency ω, the phase and group velocities follow from (11.51), and the velocity amplitudes U_1, U_2 can be computed from (11.49). Qualitatively, the behaviour is as follows:

- When there is *no rotation*, $\boldsymbol{\Omega} = \mathbf{0}$, then $\omega = N \cos\theta$; this does not mean that the frequency is independent of $\boldsymbol{k}$, because $\cos\theta = \{(k_1^2 + k_2^2)/(k_1^2 + k_2^2 + k_3^2)\}^{\frac{1}{2}}$. Here, the indices $1, 2, 3$ refer to the x-, y- and z-directions, respectively. With $\boldsymbol{\Omega} = \mathbf{0}$ and (11.51) satisfied, (11.49) can be solved for the velocity amplitudes with the solution $U_2 = 0$, $U_1 =$ arbitrary. The fluid particles move persistently in the same direction: *Internal waves in a stratified fluid on an inertial frame are linearly polarized*.
- In a *non-stratified* ($N = 0$) *rotating* fluid straightforward calculations using (11.50) show that

$$\omega = 2\boldsymbol{\Omega} \cdot \hat{\boldsymbol{k}}, \quad c_{\text{ph}} = 2\boldsymbol{\Omega} \cdot \frac{\hat{\boldsymbol{k}}}{k}, \quad \boldsymbol{c}_{\text{gr}} = \frac{2}{k}\left\{\boldsymbol{\Omega} - (\boldsymbol{\Omega} \cdot \hat{\boldsymbol{k}})\hat{\boldsymbol{k}}\right\}, \tag{11.52}$$

  in which $\hat{\boldsymbol{k}}$ is the unit vector in the direction of $\boldsymbol{k}$ ($\hat{\boldsymbol{k}} = \boldsymbol{e}_3$). This implies that true rotational waves propagate only when the direction of propagation is not perpendicular to $\boldsymbol{\Omega}$: If $\boldsymbol{k} \perp \boldsymbol{\Omega}$, then $\omega = 0$ and $c_{\text{ph}} = 0$.
  Moreover, substituting $(11.52)_1$ into (11.49) (in which $N = 0$) yields $U_2 = -iU_1$, so that

$$\boldsymbol{v} = U_1(\boldsymbol{e}_1 - i\boldsymbol{e}_2)\exp\left(i\,(\boldsymbol{k} \cdot \boldsymbol{x} - \omega t)\right). \tag{11.53}$$

  After separating real and imaginary parts this becomes

$$\begin{aligned} &\boldsymbol{v} = U_1\{\cos(\boldsymbol{k} \cdot \boldsymbol{x} - \omega t)\boldsymbol{e}_1 + \sin(\boldsymbol{k} \cdot \boldsymbol{x} - \omega t)\boldsymbol{e}_2\} \quad \text{(real part)} \\ &\boldsymbol{v} = U_1\{\sin(\boldsymbol{k} \cdot \boldsymbol{x} - \omega t)\boldsymbol{e}_1 - \cos(\boldsymbol{k} \cdot \boldsymbol{x} - \omega t)\boldsymbol{e}_2\} \quad \text{(imaginary part)}. \end{aligned} \tag{11.54}$$

  Both are acceptable solutions to the wave equation, and it is easy to prove that for $\boldsymbol{\Omega} \cdot \boldsymbol{k} > 0$, corresponding to $\omega > 0$ the velocity vector at fixed x traces, in the course of the motion, *a circle in the clockwise direction*, performing a complete revolution in the period $2\pi/\omega$; see Fig. 11.5. *The waves are circularly polarized*.
- In the general case when the fluid is stratified ($N \neq 0$) and the frame of reference is rotating ($\boldsymbol{\Omega} \neq \mathbf{0}$), the polarization is a combination of the linear and circular polarization. The waves are now *elliptically polarized* and the sense of revolution is – as above – against that of the circular frequency, see inset in Fig. 11.4.

These properties can be tested with ocean and lake current measurements from stationary buoys moored on submerged chains. These moorings perform the motion of the projection into the horizontal plane of the orbital trajectory. Of course, the real motion is not purely harmonic in these cases and translational motions are, in general, superimposed on oscillatory ones. Velocity vectors of these wave motions when viewed from above rotate in the clockwise (anticlockwise) direction on the Northern (Southern) hemisphere. This is a direct consequence of the properties of such rotational waves. If stratification is ignored, then gravity plays no role and only the direction of the triad $\{\boldsymbol{e}_1, \boldsymbol{e}_2, \boldsymbol{e}_3\}$ relative to that of $\boldsymbol{\Omega}$ is significant. For $\omega > 0$, $\boldsymbol{k}$ points in the upper halfspace on the Northern hemisphere and the rotation of the

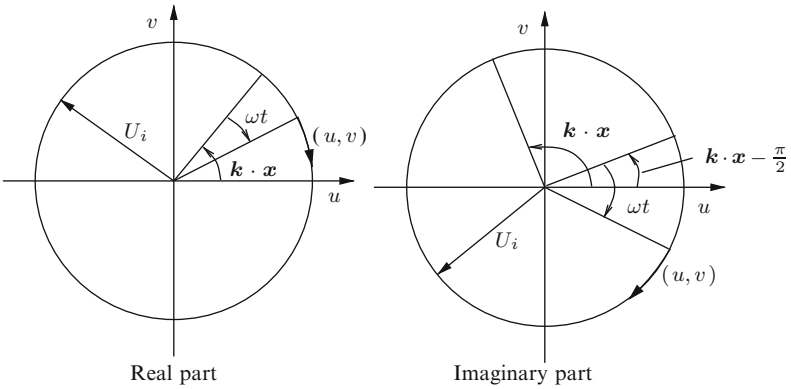

Fig. 11.5 Polar diagrams (hodographs) of the velocity vectors (11.54) representing a harmonic travelling wave. *Left panel* for $(11.54)_1$, *right panel* for $(11.54)_2$

velocity vector seen from above is clockwise. For $\omega < 0$, $\boldsymbol{k}$ points into the Southern halfspace and thus seen from below the velocity vector rotates counterclockwise (corresponding to clockwise rotation seen from above). A similar argument holds for the Southern hemisphere where the rotation is in the opposite direction. Progressive vector diagrams[16] constructed from time series of horizontal velocity vectors of such current measurements will thus form loops and be traversed in the clockwise (anticlockwise on the Southern hemisphere) direction. In small basins, such as mountainous lakes, the relative narrowness of the shore will inhibit the circular component of these 'garlandes', and loops may not close and be pointed, see Fig. 11.6 showing examples from various lake and ocean basins. Additional examples of garlandic trajectories of freely moving buoys are also, e.g. given by Mortimer [15].

A further physically very useful result also emerges from (11.50) if $\boldsymbol{\Omega}$ and $\boldsymbol{k}$ are expressed in their component form of the x, y, z coordinate system of Fig. 11.4. In this system

$$\boldsymbol{\Omega} \hat{=} \tfrac{1}{2}(0, \tilde{f}, f), \quad f = 2\Omega \sin\phi, \quad \tilde{f} = 2\Omega \cos\phi, \tag{11.55}$$

[16] Progressive vector diagrams are 'displacement' plots from current meter measurements at fixed positions. If Δt is the temporal increment at which the velocity vector $\boldsymbol{v}_i$ (i =number of the time increment) is measured, then

$$\boldsymbol{s}_n = \sum_{i=0}^{n} \boldsymbol{v}_i \Delta t, \quad (n = 0, 1, 2, \ldots)$$

determines the trajectory of a 'virtual particle' that passed the current meter at $n = 0$, see Volume 3, Chapter 'Instruments and sensors'. The particle is not real, because the current meter does not follow it (Eulerian description). An alternative is to follow a marker (e.g. freely moving drifter buoy) through time (Lagrangean description).

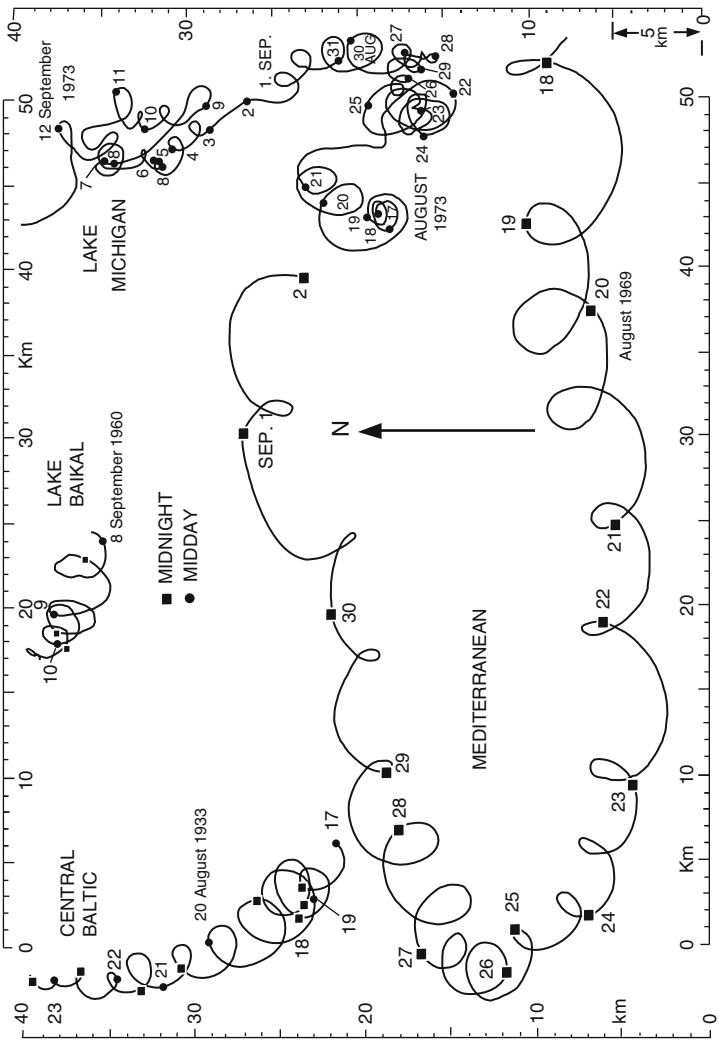

Fig. 11.6 Examples of looping current tracks, observed in different basins and plotted on a common scale: Central Baltic (distance from shore 31 km, local depths 14 m, from Gustafson and Kullenberg 1936 [6]); Lake Baikal (6 km, 10 m, Galazii 1969 [3]); Lake Michigan (12 km, 12 m, Sato and Mortimer 1975 [18]) and Mediterranean (100 km, 10 m, Gonella 1974 [5]), from [13]. © Center for Great Lakes Studies, now Great Lakes WATER Institute, reproduced with permission

where ϕ is the geographical latitude, and

$$\boldsymbol{k} \hat{=} (k_1, k_2, k_3). \tag{11.56}$$

With these, and recognizing that $k^2 \cos^2\theta = k_1^2 + k_2^2$, (11.50) takes the form

$$(k_1^2 + k_2^2)(\omega^2 - N^2) + k_3^2(\omega^2 - f^2) - k_2^2 \tilde{f}^2 - 2k_2 k_3 \tilde{f} f = 0. \tag{11.57}$$

In the shallow water approximation, $\tilde{f}$ may be ignored (see Definition 4.20 in Chap. 4 in Volume I and its consequences); then (11.57) reduces to

$$\frac{k_1^2 + k_2^2}{k_3^2} = \frac{\omega^2 - f^2}{N^2 - \omega^2}. \tag{11.58}$$

This is the dispersion relation in the shallow water approximation for a fluid on the rotating Earth which is linearly stratified in the z-direction. It discloses significant physical results: k_1 and k_2 are the x- and y-components of the wavenumber vector, and the left-hand side of equation (11.58) is necessarily positive; thus, the right-hand side must also be positive. Two cases can be distinguished:

- When $N^2 > \omega^2$, then one must also have $\omega^2 > f^2$ implying $f < |\omega| < N$. f forms a lower bound for internal waves to exist and N is the corresponding upper bound. For constant f all waves that are not influenced by bottom topography or boundaries are thus superinertial. Should ω be larger than N or smaller than f then the right-hand side of (11.58) is negative, and this requires the wavenumbers to be complex-valued. Their imaginary parts will give rise to exponential behaviour in the x-direction (attenuation). The existence of an upper bound N and a lower bound f for ω thus explains why the metalimnion in a stably stratified lake may serve as a wave guide to internal waves. Figure 8.16 in Chap. 8 in Volume I shows an N-profile obtained from density measurements in Lake Zurich. Often, N-distributions are as shown schematically in the inset map. A more detailed sketch of this is shown in Fig. 11.7. For the selected value of ω, plane unbounded internal waves can only propagate in the indicated band of the metalimnion.
  The transition from the wave guide regime to the regimes outside of it must be special. It is characterized by $|\omega| \sim N$. It will be shown below that whenever $|\omega| \sim N$ then the conditions of the shallow water approximation are not satisfied. Hence, (11.58) should be replaced in these instances by (11.57). These transition regions are known in the literature as *critical layers*. They are particularly prone to instabilities and are the locations where localized overturning and circulating motions may arise, since vertical convective motion may there be comparable to the horizontal motion, Fig. 11.7b.
- There is another, and less important, frequency range for which (11.58) admits real solutions for frequency and wavenumbers: $N < \omega < f$. Here, waves must be *subinertial* and stratification is extremely weak. This is the reason why such

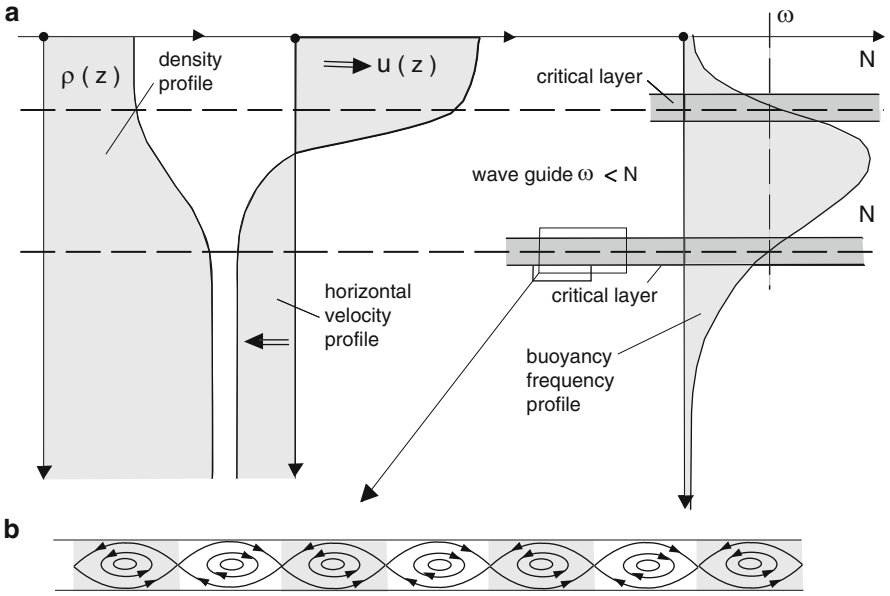

Fig. 11.7 (**a**) Density, horizontal velocity and buoyancy frequency profiles in a lake subject to summer stratification. For a given frequency ω a wave guide is singled out, in which shallow water waves can propagate. Above and below this wave guide, wave tails accompany the wave in the guide, which decay as one moves away from the wave guide boundaries. In the immediate vicinity of these boundaries, the shallow water assumption does no longer hold. In this thin layer, convective motions may arise, giving rise to a structure of the local motion as shown in panel (**b**)

subinertial plane free waves are less frequent. They can equally be ruled out in the shallow water approximation.

The above analysis may suggest that only waves with superinertial frequencies, $\omega > f$, exist, at least in a linearly stratified fluid and when the shallow water approximation is involved. This is not so; in fact waves with subinertial frequencies, $\omega < f$, also exist when β-effects or topographic variations are significant, or when the region in which they propagate is bounded. The former are the Rossby waves and thus of second class, the latter are the Kelvin waves and are of first class and may have sub- or superinertial frequencies. Both will be dealt with in greater detail in subsequent chapters.

Such waves in bounded regions generally do not have constant crests perpendicular to the direction of wave progression, but crests decay or grow exponentially. These other waves form the largest body of dynamic activity in the atmosphere, ocean and lakes. Some authors single out plane waves (with constant crests perpendicular to the direction of wave propagation) and reserve a separate name for them: *Sverdrup waves*, in honor of the Norwegian geophysicist and oceanographer: Harald Ulrik Sverdrup (1988–1957) who dealt with them first.

11.4.2 Waves in a Stably Stratified Shallow Layer of a Boussinesq Fluid

The preceding discussion pertains to waves with arbitrary wave length, arbitrary orientation and linear stratification *in an unbounded domain*. These are all rather severe restrictions. In particular, whereas the ocean and lakes may for certain processes be regarded as infinitely large in the horizontal direction, they are bounded from above by the free surface and from below by the *bathymetry*. Thus to address such more realistic situations, we shall focus attention to a horizontal layer of a stably stratified Boussinesq[17] fluid on the rotating Earth, subject to a constant Coriolis parameter (f-plane approximation). In principle, our approach is similar to what has already been analyzed in Sects. 7.2 and 8.5 in Volume I of this book series, but here the effects of rotation and stratification will be combined and the role of the shallow water approximation will be somewhat scrutinized.

11.4.2.1 Validity of the Shallow Water Equations[18]

In this section, we confine our attention to long waves but before concentrating on those, consider the linearized Boussinesq equations

$$\begin{aligned}
&\nabla_H \cdot \boldsymbol{v} + \frac{\partial w}{\partial z} = 0,\\
&\rho^* \frac{\partial \boldsymbol{v}}{\partial t} + f\rho^* \hat{\boldsymbol{k}} \times \boldsymbol{v} + \nabla_H p' = 0,\\
&\underline{\rho^* \left(\frac{\partial w}{\partial t} - \tilde{f} u \right)} + \frac{\partial p'}{\partial z} + \rho' g = 0,\\
&\frac{\partial \rho'}{\partial t} - \rho^* \frac{N^2}{g} w = 0.
\end{aligned} \tag{11.59}$$

The first is the continuity equation, the second are the horizontal components of the momentum equation, the third is the vertical component of the momentum balance in which the underlined terms are absent when the shallow water approximation is made, and the last equation is the adiabatic form of the energy equation.

These equations have been written in such a way that $\boldsymbol{v} \hat{=} (u, v)$ are the two-dimensional horizontal velocity components and ∇_H is the two-dimensional horizontal gradient operator. Analogously, $(11.59)_2$ are the two horizontal components of the momentum balance, whilst $(11.59)_3$ is the vertical counterpart. The underlined terms are the time rate of change of the vertical momentum and the vertical Coriolis acceleration. From a combination of the last two equations (11.59), on

[17] For a portrait and biographical sketch of Boussinesq see Fig. 11.8.

[18] Consult also Sects. 4.6 and 4.7 of Chap. 4 in Volume I of this book series for a general discussion of these properties.

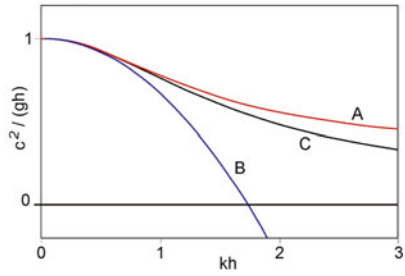

Fig. 11.8 Joseph Valentin Boussinesq (1842–1929), French mathematician and physicist. Photo from http://en.wikipedia.org/, after Bastiaan Willink, Geschiedenis: De samenwerking tussen Korteweg en de Vries – Een speurtocht naar persoonlijkheden, pp 179–185 (NAW 6/7 nr. 1 maart 2007). The graph illustrates the Boussinesq approximation for water waves (Boussinesq, 1872), which is valid for weakly non-linear and fairly long waves. The linear phase speed squared $c^2/(gh)$ is shown as a function of relative wave number kh. A and B are Boussinesq's solutions, while C is the solution of the full linear wave theory (after http://en.wikipedia.org/).

Joseph Valentin Boussinesq (15 March 1842–19 February 1929) was a self taught French mathematician and physicist who made significant contributions to the theory of hydrodynamics, vibrations, light and heat. He started his career as a college teacher and commenced his scientific writings in 1865. From 1872 to 1886 he was appointed professor at the Faculty of Sciences of the University at Lille, where he lectured on differential and integral calculus. From 1886 to his retirement in 1918 (at the age of 76) he was professor at the Faculty of Sciences at the University of Paris (Sorbonne), holding, until 1896 the chair of Mechanics and thereafter that of Mathematical Physics.

Boussinesq had an early collaboration (from 1867 to 1886) with Barré de Saint Venant. Out of this activity sprang his monumental 'Essai sur la théorie des eaux currantes' (Essay on the theory of flowing water), 1877, which presents a general theory of steady and unsteady channel flows accounting for non-hydrostatic pressures. A precursor to this work had already been published by Boussinesq in 1871; it supported John Scott Russel's great solitary wave of translation observed in 1834.

In 1897, Boussinesq published his 'Théorie d' écoulement tourbillonnant et tumultueux des liquides', a work that greatly contributed to the study of turbulence and hydrodynamics.

In fluid dynamics, several approximations or parameters are named after Boussinesq. Among these, the 'Boussinesq approximation' characterizes buoyancy driven flows in which density differences are only accounted for when they occur multiplied with the gravity constant g. So, in a Boussinesq fluid the velocity field is solenoidal and propagation of sound cannot be captured. Moreover, the Boussinesq approximated equations look the same under inversion, i.e. a rising oil bubble in water with density only slightly smaller than that of water looks the same as a falling water drop in a bath of the same oil. This is not so for an air bubble rising in water and a water drop falling in air (in a rain), since $\Delta\rho/\rho$ is of order unity.

The famous 'eddy viscosity' to parameterize the turbulent shear stress has been introduced by Boussinesq, as were the 'shallow water equations'.

Ref:

Boussinesq, J.V.: Théorie des ondes et des remous qui se propagent le long d'un canal rectangulaire horizontal, en communiquant au liquide contenu dans ce canal des vitesses sensiblement pareilles de la surface au fond. Journal de Mathématique Pures et Appliquées, Deuxième Série 17, 55–108 (1872).
Boussinesq, J.V.: 'Essai sur la théorie des eaux currantes' Mémoires présentées par divers savants á l' Académie des Scienes, Paris 23, 1–660; 24, 1–60 (1877).

The text is based on: http://en.wikipedia.org/wiki/Joseph-Valentin-Boussinesq and

W.H. Hager: Hydraulicians in Europe 1800–2000, Int. Assoc. Hydr. Engr. Res. (IAHR) Monograph, 2003, p 774

eliminating the perturbation density ρ', one may deduce the relation

$$\left(\underline{\frac{\partial^2}{\partial t^2}} + N^2\right) w - \underline{\tilde{f}\frac{\partial u}{\partial t}} = -\frac{1}{\rho^*}\frac{\partial^2 p'}{\partial t\,\partial z}, \tag{11.60}$$

of which the underlined terms would be missing if the hydrostatic pressure assumption (the full shallow water approximation) had been used. From a harmonic ansatz $p' = p_0 \exp(i\omega t)$, $u = u_0 \exp(i\omega t)$, $w = w_0 \exp(i\omega t)$ it then follows that necessarily

$$\omega^2 \ll N^2 \text{ for the hydrostatic limit to be valid.}$$

As is seen from Fig. 11.7 such an assumption is not valid at the upper and lower edges of the wave guide where these regions are the critical layers mentioned above. Moreover, omitting the underlined terms in (11.60) implies that in order for the shallow water approximation to be valid, the processes must have long periods as well as large length scales. These conditions are obviously not satisfied in the critical layers. Furthermore, the vertical acceleration term in (11.60) is $\mathcal{O}(\mathcal{A}^2)$, whilst the Coriolis term is $\mathcal{O}(\mathcal{A})$ ($\mathcal{A}$ is the aspect ratio of the vertical to the horizontal scales, see Sect. 4.7 of Chap. 4 in Volume I). Thus, the long time-scale approximation breaks down before the large length approximation becomes invalid in the shallow water approximation. In spite of this, the term $\tilde{f}u$ in $(11.59)_3$ is generally dropped whilst the vertical acceleration may be kept. The reason is that $\rho^* \tilde{f} u$ is thought to be absorbed in the gravity term. We shall subsequently follow this custom and thus will systematically drop $\tilde{f}u$.

The derivation of this result has been the reason for keeping the vertical acceleration terms in $(11.59)_3$.

11.4.2.2 Free Waves in a Shallow Stratified Boussinesq Fluid on the f-Plane

It is somewhat cumbersome to work with equations (11.59) that contain the variables u, v, w, p' and ρ'. For this reason one may ask whether a single equation for one of these unknowns would be advantageous. Furthermore, for a vertically stratified fluid it would be natural to separate the vertical from the horizontal dependencies and to write for any of the above variables

$$\psi(x, y, z, t) = \Psi_n(z)\psi_n(x, y, t) \tag{11.61}$$

and to uncouple the equations for $\Psi_n(z)$ and $\psi_n(x, y, t)$. Such a decoupling was already performed in Sect. 8.5 in Volume I in which internal oscillations in a stratified fluid, referred to an inertial frame, were analyzed. On the background of that knowledge it is anticipated that the variables $\Psi_n(z)$ in (11.61) will follow from a one-dimensional boundary value problem in the z-direction with boundary conditions

imposed on the free surface $z = 0$ and at the bottom $z = -H$. Obviously, for $\Psi_n(z)$ not to be x, y and t dependent, H must be constant. This already demonstrates that the decoupling (11.61) with the indicated dependencies is only possible for constant depth layers. In the light of Sect. 11.3 where second class waves were briefly studied, this means that in the f-plane approximation the decoupling (11.61) automatically eliminates topographic Rossby waves.

Note also that a separation of the form (11.61) is only helpful, if it is achieved for disturbance fields of arbitrary composed frequencies (such waves are called *polychromatic*). Would the separation only be possible for mono-chromatic waves, then each frequency would require its own separation equations to be solved; the advantage of the separation (11.61) would in such a case undoubtly be lost. Moreover in an attempt to reduce (11.59) to a higher order partial differential equation for a single variable, it may happen that the anticipated separation of the original four-dimensional problem into separable problems in one, z, and then three, x, y, t, dimensions may not be possible. Note that besides the differential equations, also the boundary conditions must be separable to achieve this goal. For a constant depth fluid the perturbation pressure p' or a horizontal velocity component must be taken to be the governing field variables.[19] Combination of the hydrostatic version of (11.59) permits this elimination of all but one variable. This elimination is rather cumbersome even though it is straightforward. Here we merely quote the result and ask the reader to perform the computations himself/herself. For the shallow water equations in the f-plane the following alternatives are obtained:

$$\begin{aligned}
\nabla_H^2 v + \mathcal{L}\frac{\partial}{\partial z}\left(N^{-2}\frac{\partial v}{\partial z}\right) &= 0, \quad (v = \text{a horizontal velocity component}),\\
\nabla_H^2 p' + \mathcal{L}\frac{\partial}{\partial z}\left(N^{-2}\frac{\partial p'}{\partial z}\right) &= 0, \quad (p' = \text{pressure}),\\
N^2\nabla_H^2 w + \mathcal{L}\frac{\partial^2 w}{\partial z^2} &= 0, \quad (w = \text{vertical velocity component}),
\end{aligned} \tag{11.62}$$

in which

$$\mathcal{L} = \frac{\partial^2}{\partial t^2} + f^2. \tag{11.63}$$

Had we kept the underlined term in $(11.59)_3$ (recall, we have dropped $\tilde{f}u$ already), then the equation for the vertical velocity component would be instead

$$\left(N^2 + \underline{\frac{\partial^2}{\partial t^2}}\right)\nabla_H^2 w + \underline{\tilde{f}\frac{\partial}{\partial t}(\nabla_H^2 u)} + \mathcal{L}\frac{\partial^2 w}{\partial z^2} = 0. \tag{11.64}$$

[19] This separation also works in the β-plane approximation, if the perturbation pressure or the y-component of the velocity field are taken as the independent fields, see [8].

We emphasize once more that the underlined terms are ignored in the shallow water approximation. These terms destroy two properties that make the separation of variables technique so convenient in the shallow water approximation. If the term involving $\tilde{f}$ is kept, (11.64) contains two variables, w and u; elimination of u with the aid of (11.59) and (11.62) is difficult and not worthy to achieve for the present arguments. If this term is dropped, the first underlined term involving the second time derivative, explicitly introduces the frequency in a harmonic analysis. The resulting equation must then be solved for each fixed ω separately. This implies that the poly-chromatic validity of (11.64) is lost in this case.

Problem 11.2 *Equations (11.59) are also valid in the β-plane approximation. One must only assume that the x, y-axes point towards East and North, respectively and that $\beta = \mathrm{d}f/\mathrm{d}y \neq 0$. Show that in the shallow water approximation (11.59) can be transformed into the single differential equation*

$$\frac{\partial}{\partial t}\nabla_H^2 v + \beta\frac{\partial v}{\partial x} + \left(\frac{\partial^3}{\partial t^3} + f^2\frac{\partial}{\partial t}\right)\frac{\partial}{\partial z}\left\{\frac{1}{N^2}\left(\frac{\partial v}{\partial z} - \underline{\frac{N^2}{g}v}\right)\right\} = 0 \qquad (11.65)$$

for v (the North–South component of the horizontal velocity). Actually, the underlined term is only obtained for a non-Boussinesq fluid for which ρ^* is replaced by ρ_0 in (11.59). ◆

The derivation of the above equation shows that (11.65) is the x-derivative of the vorticity balance (curl of the momentum balance). It describes how temporal changes of the relative vorticity may be compensated by latitudinal repositioning ($\beta\partial v/\partial x$) and by vertical stretching of interior vortex lines (the last term). Clearly, the latter two terms are due, respectively, to the variability of f and the presence of a non-constant mean density field.

When the Boussinesq assumption is made, the last underlined term is ignored. This is justified provided $|\partial v/\partial z| \gg N^2 v/g$, or

$$\frac{g}{N^2} \gg \frac{v}{\partial v/\partial z} = [\mathcal{H}] \quad \Rightarrow \quad 10^4 - 10^6\ \mathrm{m} \gg [\mathcal{H}],$$

where $[\mathcal{H}]$ is a typical depth scale, a condition that is always satisfied. Moreover, (11.65) is a partial differential equation, third order in time, and thus contains gravity *and* planetary Rossby waves. When the β-term can be ignored, then (11.65) is becoming second order in time ($\partial/\partial t$ is then a common factor of the equation) and the second class waves reduce to steady currents, whilst gravity waves are maintained.

In a constant depth basin solutions of (11.62) are sought by *separation of variables* in the form

$$[u, v, w, p'](x, y, z, t) = Z_n^{(u,v,w,p')}(z)[u_n, v_n, w_n, p'_n](x, y, t), \qquad (11.66)$$

in which the subscript n is a counting index whose meaning will become apparent in a moment.

It is straightforward to show that the vertical and horizontal problems then become

Vertical problems

$$\left.\begin{aligned} &\frac{\mathrm{d}^2 Z_n^{(w)}(z)}{\mathrm{d}z^2} + \frac{N^2(z)}{gh_n} Z_n^{(w)}(z) = 0, \\ &\frac{\mathrm{d}}{\mathrm{d}z}\left(\frac{1}{N^2(z)} \frac{\mathrm{d}Z_n^{(u,v,p')}(z)}{\mathrm{d}z}\right) + \frac{Z_n^{(u,v,p')}(z)}{gh_n} = 0, \end{aligned}\right\} -H < z < 0, \qquad (11.67)$$

Horizontal problems

$$\begin{aligned} \mathcal{L}[(u, v, w, p')(x, y, t)] - gh_n \nabla_H^2 [(u_n, v_n, w_n, p'_n)(x, y, t)] = 0, \\ (x, y, t) \in \mathcal{D} \times [0, \infty), \end{aligned} \qquad (11.68)$$

in which $(gh_n)^{-1}$ is a *separation constant* and h_n has the dimension of a length, called the nth *equivalent depth*. By virtue of the separation of variables, the original spatially three-dimensional equations (11.62), which must be solved in a lake domain, have been split into two separate problems, a spatially one-dimensional vertical problem and a spatially two-dimensional horizontal problem. It is rather obvious that solving two lower dimensional problems is economically more efficient than doing this for the original problem, but the simplification has been bought by limiting the geometry to *basins of constant depth*. Furthermore, yet unknown separation constants gh_n have been introduced, of which the values are a priori unknown.

Interesting to observe is also that the vertical problem (11.67) for the vertical velocity w differs from those for the horizontal velocity components u, v and the perturbation p', whilst the differential equations (11.68) for the horizontal parts are the same for all variables u, v, w, p'. Moreover, since (11.67) only exhibits a z-dependence and (11.68) only enjoys (x, y, t)-dependences, but no z-dependence the separation of variables has been achieved as far as the differential equations are concerned.

The reader may convince himself/herself of all these facts by solving

Problem 11.3 *Show that a separation of variable solution can also be constructed for (11.65). Indeed, substitution of*

$$v(x, y, z, t) = Z_n^{(v)}(z) v_n(x, y, t) \qquad (11.69)$$

into (11.65) leads to the equations

$$\begin{aligned}
&\frac{\mathrm{d}}{\mathrm{d}z}\left\{\frac{1}{N^2}\left(\frac{\mathrm{d}Z_n^{(v)}(z)}{\mathrm{d}z}-\frac{N^2}{g}Z_n^{(v)}(z)\right)\right\}+\frac{1}{gh_n}Z_n^{(v)}(z)=0,\\
&\nabla_H^2\frac{\partial v_n(x,y,t)}{\partial t}+\beta\frac{\partial v_n(x,y,t)}{\partial x}-\frac{1}{gh_n}\mathcal{L}\frac{\partial v_n(x,y,t)}{\partial t}=0
\end{aligned}\tag{11.70}$$

for the vertical and horizontal problems, respectively. ◆

Remark 11.3. Notice that when $\beta = 0$, $(11.70)_2$ is isotropic in the horizontal coordinates, i.e. v_n no longer needs to be the North–South component of the velocity field, but can be any horizontal velocity component one pleases. In other words, the coordinate system can be arbitrarily rotated about the vertical (to the zenith) without altering the equation.

If any one of the differential equations (11.67) is complemented by boundary conditions at $z = 0$ and $z = -H$, the emerging two-point-boundary-value problem will form an eigenvalue problem for the eigenvalue gh_n. Of course, depending upon which of the variables u, v, w, p' are used, these boundary conditions need be formulated in terms of the same variable for which the differential equation is written down. The method of separation of variables is, however, only complete, if the boundary conditions are equally separable. In physical terms these are

$$\begin{aligned}
p'(x,y,0,t)-\rho_0 g\zeta(x,y,t)&=0,\quad \text{at } z=0,\\
w(x,y,0,t)-\frac{\partial\zeta}{\partial t}(x,y,t)&=0,\quad \text{at } z=0,\\
w(x,y,-H,t)&=0,\quad \text{at } z=-H,
\end{aligned}\tag{11.71}$$

The first says that the perturbation pressure at $z = 0$ equals the weight of the water column above the free surface. The second is the linearized kinematic boundary condition of the free surface, and the third condition expresses impermeability of the basal surface. Conditions (11.71) must be reduced to other, alternative, conditions, expressed in one variable – u, v, w or p – only. The corresponding expressions for v are awkward but when ζ is eliminated from $(11.71)_{1,2}$ and (11.60) is used, the pressure boundary conditions take the form

$$\begin{aligned}
&\left(\underline{\frac{\partial^2}{\partial t^2}}+N^2\right)p'+g\frac{\partial p'}{\partial z}=0,\quad \text{at } z=0,\\
&\frac{\partial p'}{\partial z}=0,\quad \text{at } z=-H,
\end{aligned}\tag{11.72}$$

in which we have set $\rho_0 \simeq \rho_*$ and the underlined term is not present when the shallow water approximation is invoked.

Problem 11.4 *Using (11.60) and $\tilde{f}=0$, show that the boundary conditions (11.71), expressed in the vertical velocity are given by*

$$\left(\underline{\frac{\partial^2}{\partial t^2}} + N^2\right) w + g\frac{\partial w}{\partial z} = 0, \quad at\ z = 0,$$
$$w = 0, \quad at\ z = -H, \tag{11.73}$$

where, again, the underlined term is dropped in the shallow water approximation. ◆

Substituting (11.66) into (11.73) and (11.72), respectively, corroborates that the boundary conditions expressed in terms of the pressure or vertical velocity are only separable in the shallow water approximation and then read

$$\frac{\mathrm{d}Z_n^{(w)}(0)}{\mathrm{d}z} + \frac{N^2(0)}{g} Z_n^{(w)}(0) = 0, \quad Z_n^{(w)}(-H) = 0,$$
$$\frac{\mathrm{d}Z_n^{(p')}(0)}{\mathrm{d}z} + \frac{N^2(0)}{g} Z_n^{(p')}(0) = 0, \quad \frac{\mathrm{d}Z_n^{(p')}}{\mathrm{d}z}(-H) = 0, \tag{11.74}$$

respectively. We shall not write down the boundary conditions in terms of the variables $Z_n^{(u,v)}$.

Equations $(11.67)_1$, $(11.74)_1$, [or $(11.67)_2$, $(11.74)_2$ for the perturbation pressure p'] define a two-point-boundary-value problem for the function $Z_n^{(w)}$ [or $Z_n^{(p')}$] and the eigenvalue gh_n. Notice that this boundary value problem depends only on the (equilibrium) stratification defined by $\rho_0(z)$. Therefore, the same vertical eigenfunctions and eigenvalues apply for any wave, whatever its temporal and spatially horizontal scales may be. In other words, the same vertical eigenfunctions and eigenvalues apply for both classes of *polychromatic* waves. This is so because the equations are those of the shallow water approximation. Had we not implemented it, then separation into a vertical and horizontal problem would still be possible, but only for *monochromatic* waves. It would imply that for each frequency the vertical eigenfunctions would be different.

Problem 11.5 *If the vertical acceleration terms in the vertical momentum equation are accounted for, but* $\tilde{f} = 0$*, then the linear wave problem is defined by (11.64) and (11.73), or*

$$\left(N^2 + \frac{\partial^2}{\partial t^2}\right) \nabla_H^2 w + \mathcal{L}\frac{\partial^2 w}{\partial z^2} = 0, \quad (\boldsymbol{x}, t) \in \mathbb{R}^2 \times \mathbb{R}^+,$$
$$\left(N^2 + \frac{\partial^2}{\partial t^2}\right) w + g\frac{\partial w}{\partial z} = 0, \quad at\ z = 0,$$
$$w = 0, \quad at\ z = -H. \tag{11.75}$$

Assuming the plane wave

$$w(x, y, z, t) = Z_n^{(w)}(z)\exp\left[i\left(\boldsymbol{k}_h \cdot \boldsymbol{x}_h - \omega t\right)\right],$$

in which $\boldsymbol{k}_h \hat{=} (k_x, k_y)$ *is the horizontal wavenumber vector and* $\boldsymbol{x}_h \hat{=} (x, y)$*, it may be shown that* $Z_n^{(w)}(z)$ *is given by the following eigenvalue problem:*

$$\begin{aligned} \frac{\mathrm{d}^2 Z_n^{(w)}(z)}{\mathrm{d}z^2} + \frac{N^2 - \omega^2}{\omega^2 - f^2} k_h^2 Z_n^{(w)}(z) &= 0, \quad -H < z < 0, \\ (N^2 - \omega^2) Z_n^{(w)}(0) + g\frac{\mathrm{d}Z_n^{(w)}(0)}{\mathrm{d}z} &= 0, \quad z = 0, \\ Z_n^{(w)}(-H) &= 0, \quad z = -H. \end{aligned} \tag{11.76}$$

◆

The eigenvalue problem (11.76) shows that the frequency ω arises in the differential equation and one boundary condition. Thus, (11.76) is not of Sturm–Liouville type. Moreover, for each frequency the eigenvalue problem possesses its own solution.

The eigenvalue problem (11.76) can be somewhat simplified by making use of the fact that internal waves give rise to very small surface displacements, but large interior deformation. This then justifies to request $Z_n^{(w)}(0) = 0$ as free surface boundary condition. If this is used instead of $(11.76)_2$, the emerging eigenvalue problem is again of Sturm–Liouville type, but the barotropic eigenmodes are eliminated this way, and only the baroclinic eigenmodes are obtained. Their solutions are discussed in Sect. 8.5 of Chap. 8 in Volume I. In that section, the properties of eigenvalue problems of Sturm–Liouville type were listed. It was stated there that they possess countably infinite eigenvalues which can be ordered by size, so that the counting index n may be used to enumerate these. The eigenvalue problems emerging from the incomplete separation of variables procedure (e.g. the boundary value problem (11.76)) also show countably infinite eigenvalues that can be ordered by size, in general, but a strict proof that continuous spectral regimes do not exist has not been given in these cases.

The above separation of variables solutions have been constructed for waves on the f-plane ($f = \text{const}$). Similar attempts to construct separation of variables solutions have also been undertaken for waves on the β-plane, i.e. when $\mathrm{d}f/\mathrm{d}y = \beta \neq 0$. A detailed account on this is given in Chaps. 10–15 of LeBlond and Mysak's 'Waves in the Ocean' [8]. There, it is proved that the true separation of the vertical and horizontal poly-chromatic waves on the β-plane is possible, if (1) the perturbation pressure is the field variable for which the vertical eigenvalue problem is formulated and (2) provided the shallow water approximation is invoked. All other cases result in a form of the vertical eigenvalue problem in which either in the differential equation or the boundary conditions or both the frequency ω arises. There is even a situation for which a separation of the motion into a vertical and a horizontal problem does not exist.

Problem 11.6 *Show that (11.59) with* $\tilde{f} \neq 0$ *do not allow separation of variables in the above sense, not even for mono-chromatic waves.* ◆

The eigenvalue problem for the vertical distribution of the variables u, v, w or p' gives no information on the role of the rotation of the Earth, if the frequency and/or the wavenumber do not arise in the differential equations and/or boundary conditions. This information is provided by the dispersion relation[20] and can be obtained via the horizontal problem described by (11.68) for all variables u_n, v_n, w_n and p'_n. If the horizontal domain is unbounded, a plane wave ansatz

$$\phi_n = \phi_n^{(0)} \exp\left[i\left(\boldsymbol{k}_h \cdot \boldsymbol{x}_h - \omega t\right)\right], \qquad \phi_n = \{u_n, v_n, w_n, p'_n\} \tag{11.77}$$

is adequate for its solution. $\boldsymbol{k}_h$ is the horizontal wavenumber vector with norm k_h and ω the frequency and both are real. Substituting (11.77) into (11.68) shows (11.77) to be a solution, provided the *dispersion relation*

$$\omega_n^2 = f^2 + g h_n k_h^2 \tag{11.78}$$

is satisfied (we have indexed the frequency, because for each eigenvalue of the vertical problem gh_n (11.78) is its own dispersion relation). Waves obeying the dispersion relation (11.78) are dispersive, even though they are shallow water waves, and have phase and group velocities

$$\boldsymbol{c}_{\mathrm{ph}} = \frac{\omega_n}{k_h^2} \boldsymbol{k}_h, \qquad \boldsymbol{c}_{\mathrm{gr}} = \frac{g h_n}{\omega_n} \boldsymbol{k}_h. \tag{11.79}$$

They are parallel to each other and obey the chain of inequalities

$$|\boldsymbol{c}_{\mathrm{gr}}| < \sqrt{g h_n} < |c_{\mathrm{ph}}|. \tag{11.80}$$

Waves obeying the dispersion relation (11.78) were first mentioned by Poincaré [17] in his 'Méchanique célèste' and are for this reason today called Poincaré waves. For real wavenumbers k_n and real ω_n (the only possibilities in infinite space), they satisfy the obvious inequality $|\omega_n| > f$. It follows, Poincaré *waves have always superinertial frequencies*. Of course, (11.78) allows also solutions with complex valued frequencies and wavenumbers, but they can, obviously, not exist in infinite (x, y)-space because they would become unbounded or evanescent as $(x, y) \to (\pm\infty, \pm\infty)$. For such waves to exist, the domains must be bounded. We shall discuss such solutions of the shallow water equations on the rotating Earth in Chap. 12.

[20] This argument shows that in vertical eigenvalue problems for problems not based on the shallow water approximation the eigenvalues gh_n depend on the rotation of the Earth since the evaluation of gh_n is constrained to the satisfaction of the dispersion relation (11.78).

We close this subsection with the following remarks: There is no unanimous nomenclature of rotation affected waves. The plane waves in a horizontally unbounded region treated above have uniform amplitudes in the direction perpendicular to the direction of wave propagation. Following LeBlond and Mysak [8] or Gill [4] we call them Poincaré waves, whilst, e.g. Mortimer [13, 15] and Platzman [16] refer to the rotation affected homogeneous plane progressive waves (with constant crests perpendicular to the wave-number vector) as Sverdrup waves and reserve the name Poincaré waves to combinations of them, of which particular forms meet the boundary conditions of rectangular channels and basins with vertical side walls. The unifying property of all these waves is the dispersion relation (11.78), as we shall see in the next chapter. For further details, see [15].

It is not difficult to see that plane progressive Poincaré waves have in general non-trivial velocity components in all three space directions. The orbital motion of the particles, however is plane, as we have seen in Sect. 11.4.1, with the orbital plane being tilted from the vertical, Fig. 11.9. According to Mortimer [14], as the wave length increases 'the orbital plane leans more and more (to the left in the Northern hemisphere); the celerity rises above $c_{\mathrm{ph}} = \sqrt{gh}$, see (11.80); the group velocity (at which wave energy is propagated) falls below c_{ph}; the orbital plane increasingly tilts toward the horizontal; and the wave period approaches the inertial period [as is easily seen from (11.78)]. At the long wave length limit (infinity) the orbital plane is entirely horizontal, and particle motion is indistinguishable from the inertial motion in a circle. This is the basis of frequent references to inertial or near-inertial oscillations, viewed as limiting cases of Poincaré waves, in which energy is entirely or nearly all kinetic'.

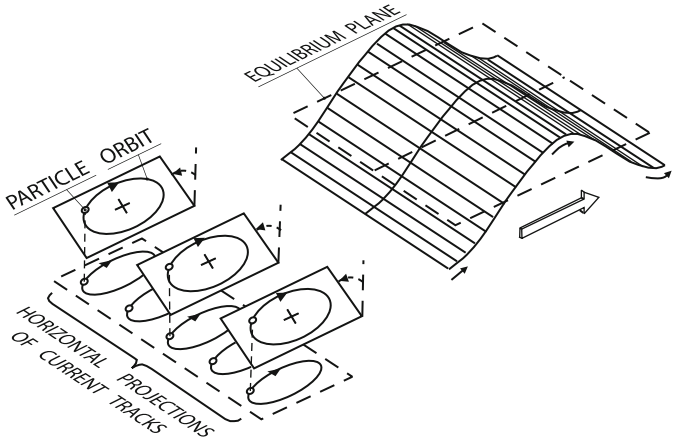

Fig. 11.9 Sketch of a homogeneous sinusoidal Poincaré (Sverdrup) wave in unbounded horizontal space. The height of the wave does not change along the wave crest, the orbit planes are tilted away from the vertical (to the left in the Northern hemisphere when looking in the direction of wave progress). The horizontal projections of those orbits are clockwise traversed ellipses, Mortimer [12]. © Center for Great Lakes Studies (now Great Lakes WATER Institute), reproduced with permission

11.4.3 The Two-Layer Model

A severe disadvantage of the separation of variables solutions in the last subsection is the restriction of the basin to constant depth with vertical shores. On the f-plane it automatically eliminates topographic Rossby waves and will also falsify the wave structure due to topographic variations. A separation of variables into vertical and horizontal modes is strictly not possible, but owing to the typical monotonous stratification of lakes during the summer months (see Sect. 8.5 of Chap. 8 in Volume I) with nearly constant densities in the epi- and hypolimnia and a rapid transition in the metalimnion, the buoyancy frequency differs appreciably from zero only in the regions of these rapid density changes. The density may thus be considered to be constant in each layer. The buoyancy frequency is then zero everywhere except at the layer interfaces with density jumps, where it forms a Dirac pulse. In the two layer approximation, the upper layer has constant depth H_1 and constant density ρ_1, and the second layer with $\rho_2 > \rho_1$, has variable depth H_2, see Fig. 11.10. It is physically obvious, and this was demonstrated in Sect. 8.5.2.3 in Volume I. Example c, that with a metalimnion of vanishing extent, there can be no oscillatory part of the solution within the metalimnetic wave band (which has zero thickness anyhow); in other words, in a two-layer system, there can be only *one barotropic* and *one baroclinic* vertical mode.

The division of the lake domain into several layers (here two) implies for variable bathymetry that each layer fills in the (x, y)-space different regions, so that the layer equations will hold in different regions. In many mountainous lakes with steep shores for which the two-layer model will form a valid approximation, the difference region may be small and then negligible for wave dynamic analyses. The

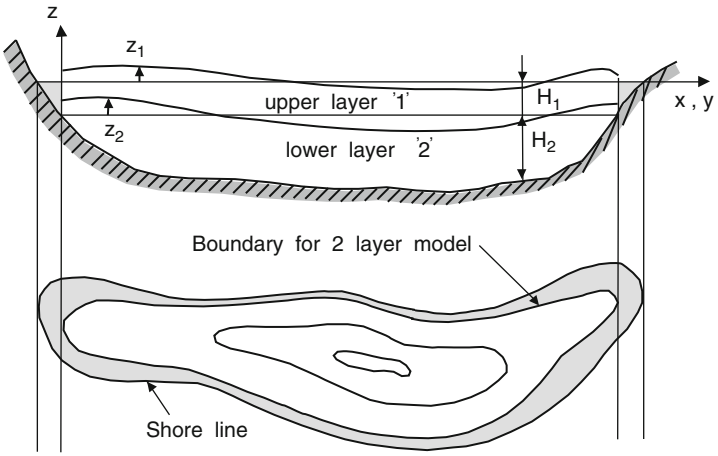

Fig. 11.10 Two-layer model with upper layer depth H_1 and lower depth H_2. The mathematical models often use a vertical wall as boundary at the depth contour of H_1. The *shaded portion* is then ignored in the model calculations

computational domain is then defined by the 'thermocline shore line', the intersection between the bathymetry and the interface depth of the upper with the lower layer. In Fig. 11.10, this corresponds to ignoring the triangular torus-type region that is shaded. We are only aware of a few wave dynamic analyses – and they are numerical – in which layer equations would be solved in different regions. Therefore, we confine attention in the following to the situation where the computational domain is restricted to the region where both layers exist.

Let us begin by stating the linearized adiabatic field equations on the f-plane,

$$\left.\begin{aligned} &\nabla_H \cdot \boldsymbol{v} + \frac{\partial w}{\partial z} = 0, \\ &\rho^* \left(\frac{\partial \boldsymbol{v}}{\partial t} + f \hat{\boldsymbol{k}} \times \boldsymbol{v} \right) = -\nabla_H p, \end{aligned} \right\} \quad (\boldsymbol{x}, t) \in (\mathcal{D} \subset \mathbb{R}^2) \times [0, \infty). \tag{11.81}$$

These comprise of the continuity and horizontal momentum equations and must be subject to the conditions

$$\left.\begin{aligned} &\frac{\partial \zeta_1}{\partial t} + (\nabla_H \zeta_1) \cdot \boldsymbol{v}_1 - w_1 = 0, \\ &p = 0, \end{aligned} \right\} \quad \text{at } z = \zeta_1, \tag{11.82}$$

$$\left.\begin{aligned} &\frac{\partial \zeta_2}{\partial t} + (\nabla_H \zeta_2) \cdot \boldsymbol{v}_1 - w_1 = 0, \text{ or} \\ &\frac{\partial \zeta_2}{\partial t} + (\nabla_H \zeta_2) \cdot \boldsymbol{v}_2 - w_2 = 0, \\ &p_1 = p_2, \end{aligned} \right\} \quad \text{at } z = -H_1 + \zeta_2, \tag{11.83}$$

$$(\nabla_H H_2) \cdot \boldsymbol{v}_2 - w_2 = 0, \qquad \text{at } z = -(H_1 + H_2) \tag{11.84}$$

at the free surface, the layer interface and the bottom topography, respectively. These equations shall now be reduced to a set of two-layer equations. To this end we first integrate the continuity equation over the upper and lower layers, respectively. In the upper layer, this yields (we omit writing the dependencies on x, y and t)

$$\int_{-H_1+\zeta_2}^{\zeta_1} (\nabla_H \cdot \boldsymbol{v}_1) \mathrm{d}z + w_1(\zeta_1) - w_1(-H_1 + \zeta_2) = 0, \tag{11.85}$$

where the subscript notation follows from Fig. 11.10. Interchanging in the first integral the integration and differentiation and using Leibniz's rule yields

$$\begin{aligned} \nabla_H \cdot \int_{-H_1+\zeta_2}^{\zeta_1} \boldsymbol{v}_1 \mathrm{d}z - \{(\nabla_H \zeta_1) \cdot \boldsymbol{v}_1 - w_1\}_{z=\zeta_1} \\ + \{(\nabla_H \zeta_2) \cdot \boldsymbol{v}_1 - w_1\}_{z=-H_1+\zeta_2} = 0. \end{aligned} \tag{11.86}$$

In view of $(11.82)_1$ and $(11.83)_1$, the last two terms in (11.86) can be replaced by $-\partial\zeta_1/\partial t$ and $-\partial\zeta_2/\partial t$, respectively. Defining by

$$\boldsymbol{M}_1 = \int_{-H_1+\zeta_2}^{\zeta_1} \boldsymbol{v}_1 \mathrm{d}z \cong H_1\boldsymbol{v}_1, \quad \boldsymbol{M}_2 = \int_{-(H_1+H_2)}^{-H_1+\zeta_2} \boldsymbol{v}_2 \mathrm{d}z \cong H_2\boldsymbol{v}_2, \tag{11.87}$$

the volume transports in the upper and lower layers, (11.86) reduces to

$$\frac{\partial(\zeta_1-\zeta_2)}{\partial t} + \nabla_H \cdot \boldsymbol{M}_1 = 0. \tag{11.88}$$

Similarly, for the second layer

$$\frac{\partial\zeta_2}{\partial t} + \nabla_H \cdot \boldsymbol{M}_2 = 0. \tag{11.89}$$

These equations are exact and express the mass balance in the upper and lower layers, respectively.

Problem 11.7 *Consider a water column through the upper and lower layers of cross section* $\mathrm{d}x\mathrm{d}y$. *By performing a balance of mass for the column in the upper and lower layer separately, derive (11.88), (11.89) in an alternative way.* ◆

Next, we integrate the hydrostatic pressure equations, $\partial p_{1,2}/\partial z = -\rho_{1,2}g$, from the top surface to an arbitrary depth, z. This yields

$$\begin{aligned} p_1 &= -\rho_1 g(z-\zeta_1), \\ p_2 &= -\rho_2 g(z+H_1-\zeta_2) + \rho_1 g(H_1-\zeta_2+\zeta_1). \end{aligned} \tag{11.90}$$

Taking the horizontal gradient of each of these and substituting the resulting expressions into $(11.81)_2$ leads to the equations

$$\begin{aligned} \frac{\partial\boldsymbol{v}_1}{\partial t} + f\hat{\boldsymbol{k}}\times\boldsymbol{v}_1 &= -g\nabla_H\zeta_1, \\ \frac{\partial\boldsymbol{v}_2}{\partial t} + f\hat{\boldsymbol{k}}\times\boldsymbol{v}_2 &= -g'\nabla_H(\zeta_2-\zeta_1) - g\delta\nabla_H\zeta_1, \end{aligned} \tag{11.91}$$

in the derivation of which we have set $\rho_2 = \rho^*$. The constants

$$g' = g\varepsilon,\ \varepsilon := \frac{\rho_2-\rho_1}{\rho_*},\ \delta = \frac{\rho_1}{\rho_*} \cong 1 \tag{11.92}$$

are called the *reduced gravity constant*, *relative density difference* and *layer density ratio*, respectively. In common summer stratifications, we have $\varepsilon = 10^{-3} \div 10^{-2}$. In view of (11.87), (11.91) can also be written in terms of $\boldsymbol{M}_1$ and $\boldsymbol{M}_2$. When complemented by (11.88) and (11.89), the following linear system is obtained:

$$\begin{aligned}
&\frac{\partial(\zeta_1-\zeta_2)}{\partial t}+\nabla_H\cdot\boldsymbol{M}_1=0,\\
&\frac{\partial\boldsymbol{M}_1}{\partial t}+f\hat{\boldsymbol{k}}\times\boldsymbol{M}_1=-gH_1\nabla_H\zeta_1,\\
&\frac{\partial\zeta_2}{\partial t}+\nabla_H\cdot\boldsymbol{M}_2=0,\\
&\frac{\partial\boldsymbol{M}_2}{\partial t}+f\hat{\boldsymbol{k}}\times\boldsymbol{M}_2=-g'H_2\nabla_H(\zeta_2-\zeta_1)-gH_2\delta\nabla_H\zeta_1
\end{aligned}\tag{11.93}$$

for $(\boldsymbol{x}_h,t)\in\left(\mathcal{D}\subset\mathbb{R}^2\right)\times\mathbb{R}^+$. These equations together comprise the governing equations for the *two-layer variable depth model* (**TVDM**). They lie at the centre of linear wave analysis in physical limnology as they include barotropic and first mode baroclinic processes in a stratified water body with a strong thermocline positioned at the interface between the two layers. The equations include first and second class wave motions on the f or β-plane, but restricted to the shallow water approximation. The equations have been solved numerically for a large number of enclosed basins from the Great Lakes to relatively small mountainous lakes, and the eigenvectors and eigenmodes have been tested against field data. Among these are time series of surface elevations measured at shore positions, temperature and velocity from thermistor chains and current meters moored at various positions, within the lake, generally with great success. In subsequent chapters, we will provide detailed corroboration for these facts.

When the rotation of the Earth is ignored, then $f=0$, and (11.93), after elimination of $\boldsymbol{M}_1$ and $\boldsymbol{M}_2$, become

$$\begin{aligned}
&\frac{\partial^2(\zeta_1-\zeta_2)}{\partial t^2}-\nabla_H\cdot(gH_1\nabla_H\zeta_1)=0,\\
&\frac{\partial^2\zeta_2}{\partial t^2}-\nabla_H\cdot\left\{g'H_2\nabla_H(\zeta_2-\zeta_1)+gH_2\nabla_H\zeta_1\right\}=0
\end{aligned}\tag{11.94}$$

for $(\boldsymbol{x}_h,t)\in\left(\mathcal{D}\subset\mathbb{R}^2\right)\times\mathbb{R}^+$, in which the second term in the first equation could also be written as $gH_1\nabla_H^2\zeta_1$, but this will not be done to preserve the structural symmetry of the equations.

Finally, the one layer, exclusive barotropic model is obtained from (11.93) and (11.94) by adding the layer equations and setting $\varepsilon=0$. This then yields generally

$$\begin{aligned}
&\frac{\partial\zeta}{\partial t}+\nabla_H\cdot\boldsymbol{M}=0,\\
&\frac{\partial\boldsymbol{M}}{\partial t}+f\hat{\boldsymbol{k}}\times\boldsymbol{M}=-gH\nabla_H\zeta
\end{aligned}\tag{11.95}$$

with

$$\boldsymbol{M}=\boldsymbol{M}_1+\boldsymbol{M}_2,\qquad\zeta=\zeta_1$$

and

$$\frac{\partial^2 \zeta}{\partial t^2} - \nabla_H \cdot (gH \nabla_H \zeta) = 0, \tag{11.96}$$

when the rotation of the Earth is ignored.

It is interesting to note that for constant depth of the basin, $H_1 + H_2 = H = \text{const}$, (11.93) will now be reduced to two separate one-layer models. The computations will demonstrate that the TVDM contains the barotropic and first mode baroclinic processes. Beyond this, the analysis will give information as to the structure and order of magnitude of the barotropic and first baroclinic field variables. Toward this end, we add ν_α times the lower layer continuity and momentum equations to the corresponding upper layer equations, define auxiliary variables according to

$$\boldsymbol{M}_\alpha = \boldsymbol{M}_1 + \nu_\alpha \boldsymbol{M}_2, \qquad \zeta_\alpha = \zeta_1 + (\nu_\alpha - 1)\zeta_2 \tag{11.97}$$

and require that the emerging equations have the same form as the one layer equations, i.e.

$$\begin{aligned} \frac{\partial \zeta_\alpha}{\partial t} + \nabla_H \cdot \boldsymbol{M}_\alpha &= 0, \\ \frac{\partial \boldsymbol{M}_\alpha}{\partial t} + f \hat{\boldsymbol{k}} \times \boldsymbol{M}_\alpha &= -g h_\alpha \nabla_H \zeta_\alpha \end{aligned} \tag{11.98}$$

with still unknown ν_α and h_α. Performing the above combination of the layer momentum equations $(11.93)_{3,4}$ yields

$$\begin{aligned} \frac{\partial \boldsymbol{M}_\alpha}{\partial t} + f \hat{\boldsymbol{k}} \times \boldsymbol{M}_\alpha &= -g \nabla_H \left\{ [H_1 + \nu_\alpha (1-\varepsilon) H_2] \zeta_1 + \varepsilon \nu_\alpha H_2 \zeta_2 \right\} \\ &\stackrel{!}{=} -g h_\alpha \nabla_H \zeta_\alpha \stackrel{(11.97)}{=} -g \left(h_\alpha \nabla_H \zeta_1 + h_\alpha (\nu_\alpha - 1) \nabla_H \zeta_2 \right). \end{aligned}$$

(It is at this point where H_1 and H_2 must be assumed to be constant.) Since the second and the last expressions must be identities in ζ_1 and ζ_2, the following two equations for ν_α and h_α emerge:

$$H_1 + \nu_\alpha (1-\varepsilon) H_2 = h_\alpha, \qquad H_2 \varepsilon \nu_\alpha = h_\alpha (\nu_\alpha - 1). \tag{11.99}$$

On eliminating h_α, the following quadratic equation for ν_α is obtained:

$$\nu_\alpha^2 + \frac{H_1 - H_2}{(1-\varepsilon) H_2} \nu_\alpha - \frac{1}{1-\varepsilon} \frac{H_1}{H_2} = 0, \tag{11.100}$$

of which the solution is

$$\nu_\alpha = -\frac{H_1 - H_2}{2(1-\varepsilon)H_2} \pm \left\{ \frac{(H_1 - H_2)^2}{4(1-\varepsilon)^2 H_2^2} + \frac{H_1}{(1-\varepsilon)H_2} \right\}^{1/2}. \tag{11.101}$$

When pursuing the computations with this exact formula, little if anything can be extracted. However, because for common stratifications $\varepsilon = \mathcal{O}(10^{-3})$, Taylor series expansions of (11.101) in terms of ε and truncating this expansion at the linear term suffices. Then with $H := H_1 + H_2$

$$\begin{aligned} \nu_\alpha &= \frac{-(H_1 - H_2) \pm (H_1 + H_2)}{2H_2} + \frac{-(H_1^2 - H_2^2) \pm (H_1^2 + H_2^2)}{2H_2(H_1 + H_2)}\varepsilon + \mathcal{O}(\varepsilon^2) \\ &= -\frac{H_1 - H_2}{2H_2}(1+\varepsilon) \pm \frac{H}{2H_2}\left(1 + \frac{H_1^2 + H_2^2}{H^2}\varepsilon\right) + \mathcal{O}(\varepsilon^2). \end{aligned} \tag{11.102}$$

Problem 11.8 *Show that with (11.102) formulae (11.97), (11.99) and (11.101) lead to the following two sets of solutions:*

- *Barotropic, external mode:* $\nu_{\text{ext}} := \nu_\alpha$ *(upper signs in (11.101))*

$$\begin{aligned} \nu_{\text{ext}} &= 1 + \frac{H_2}{H}\varepsilon + \mathcal{O}(\varepsilon^2), \\ h_{\text{ext}} &= H - \frac{H_1 H_2}{H}\varepsilon + \mathcal{O}(\varepsilon^2), \\ \boldsymbol{M}_{\text{ext}} &= \boldsymbol{M}_1 + \boldsymbol{M}_2 + \frac{H_2}{H}\boldsymbol{M}_2\varepsilon + \mathcal{O}(\varepsilon^2), \\ \zeta_{\text{ext}} &= \zeta_1 + \frac{H_2}{H}\zeta_2\varepsilon + \mathcal{O}(\varepsilon^2), \end{aligned} \tag{11.103}$$

- *Baroclinic, internal mode:* $\nu_{\text{int}} := \nu_\alpha$ *(lower signs in (11.101))*

$$\begin{aligned} \nu_{\text{int}} &= -\frac{H_1}{H_2}\left\{1 + \frac{H_1}{H}\varepsilon\right\} + \mathcal{O}(\varepsilon^2), \\ h_{\text{int}} &= \frac{H_1 H_2}{H}\varepsilon + \mathcal{O}(\varepsilon^2), \\ \boldsymbol{M}_{\text{int}} &= \boldsymbol{M}_1 - \frac{H_1}{H_2}\boldsymbol{M}_2 - \frac{H_1^2}{H_2 H}\boldsymbol{M}_2\varepsilon + \mathcal{O}(\varepsilon^2), \\ \zeta_{\text{int}} &= \zeta_1 - \frac{H}{H_2}\zeta_2 - \frac{H_1^2}{H_2 H}\zeta_2\varepsilon + \mathcal{O}(\varepsilon^2). \end{aligned} \tag{11.104}$$

Moreover, from these equations deduce the lowest (zeroth) order inverted relations

$$
\begin{aligned}
\boldsymbol{M}_1 &= \frac{H_1}{H}\left(\boldsymbol{M}_{\text{ext}} + \frac{H_2}{H_1}\boldsymbol{M}_{\text{int}}\right) + \mathcal{O}(\varepsilon),\\
\boldsymbol{M}_2 &= \frac{H_2}{H}\left(\boldsymbol{M}_{\text{ext}} - \boldsymbol{M}_{\text{int}}\right) + \mathcal{O}(\varepsilon),\\
\zeta_1 &= \left(1 - \frac{H_2^2}{H^2}\varepsilon\right)\zeta_{\text{ext}} + \frac{H_2^2}{H^2}\varepsilon\zeta_{\text{int}} + \mathcal{O}(\varepsilon^2),\\
\zeta_2 &= -\frac{H_2}{H}\left(\zeta_{\text{int}} - \zeta_{\text{ext}}\right) + \mathcal{O}(\varepsilon).
\end{aligned}
\tag{11.105}
$$

◆

The results of Problem 11.8 allow the following inferences to be drawn: For the barotropic mode, the equivalent depth, h_{ext}, see $(11.103)_2$, very nearly equals the water depth, whilst for the baroclinic mode, the equivalent depth, h_{int}, see $(11.104)_2$, is nearly that of the two layer model, (see (8.103) in Chap. 8 in Volume I).

Suppose next that $\boldsymbol{M}_{\text{int}} = \boldsymbol{0}$, $\zeta_{\text{int}} = 0$ (no baroclinic motion), then from (11.105)

$$
\frac{\boldsymbol{M}_1}{H_1} = \frac{\boldsymbol{M}_{\text{ext}}}{H} = \frac{\boldsymbol{M}_2}{H_2}, \quad \zeta_1 = \zeta_{\text{ext}}, \quad \zeta_2 = \frac{H_2}{H}\zeta_{\text{ext}}. \tag{11.106}
$$

These formulae imply that the velocities are the same in the two layers by magnitude and direction. Moreover, the ratio $\zeta_2/\zeta_1 = H_2/H$, which means that the interface displacement is the depth fraction of the surface displacement. For a very thin upper layer, $\zeta_1 \sim \zeta_2$ but for a very thin lower layer ζ_2 is small. All this is reminiscent of barotropic behaviour.

Next, if we take $\boldsymbol{M}_{\text{ext}} = \boldsymbol{0}$ and $\zeta_{\text{ext}} = 0$, then we have

$$
\boldsymbol{M}_1 = \frac{H_2}{H}\boldsymbol{M}_{\text{int}} = -\boldsymbol{M}_2, \quad \zeta_1 = \frac{H_2^2}{H^2}\varepsilon\zeta_{\text{int}}, \quad \zeta_2 = -\frac{H_2}{H}\zeta_{\text{int}}. \tag{11.107}
$$

Here the horizontal volume flux in the two layers is the same, but in opposite directions and the free surface elevation is of the order $\mathcal{O}(\varepsilon\zeta_{\text{int}})$ which is a very small fraction of the interface displacement. This explains why the rigid lid assumption is a defendable approximation for analyses of the internal motion.

This one-layer version of the original two layer model is due to Charney [2]; it is called in the literature the *two-layer equivalent depth model* (**TEDM**). As the above derivation has shown, it is only valid for constant depth. It also eliminates all higher order baroclinic waves. For many situations this is justified, but occasionally, higher order baroclinic modes are observed. This is, e.g. the case when the buoyancy profile has two or more relative maxima. For this reason Longuet–Higgins in Mortimer [11] and Heaps [7] introduced a three layer model and Lighthill [9] showed, how an N-layer model can be reduced to equivalent depth form.[21]

[21] Because of the boundedness of lakes, n-layer equivalent depth models for $n > 2$ are not very useful, because they require the same domain boundary for each n. This is becoming unrealistic, when $n > 2$. For an ocean, where boundaries are far away, such models are better suited.

Often in ensuing developments we shall discuss barotropic or baroclinic behaviours simultaneously. In these instances, we generally think of an equivalent depth model or a separation of variables procedure and will distinguish between barotropic and baroclinic processes according to whether h_α is the water depth or an equivalent depth belonging to a certain stratification, which was made explicit by Monismith [10] and applied by Antenucci and Imberger [1].

11.5 Concluding Discussion

The focus in this chapter has been to see how the rotation of the Earth and the stratification of the water exercise an influence on the dynamics of the water motion in lakes (and the ocean). This was achieved by pointing at observational facts which illustrate seemingly 'unusual' behaviour and by explaining them by simple physics through dimensional reasoning. In a second approach, these first explanations were subsequently deepened with the aid of a mathematical analysis of the rotationally influenced linear shallow water equations and the discussion of gravity and geostrophic Rossby waves. This is done for homogeneous and stably stratified water bodies, whereby stratification is implemented through continuous vertical density variations or through horizontal layers of different densities.

A typical manifestation of the rotation of the Earth in lakes is the deviation of the progression of velocity and displacement disturbances of a wave or current signal from a more or less straight path. Rivers which enter a large basin approximately perpendicular to the shore line are diverted to the right (left) on the Northern (Southern) hemisphere and follow a right (left) bounded motion in the otherwise still basin. Wind stress, exerted on the lake surface, gives rise to a near surface current structure, which rotates (to the right on the Northern hemisphere) around the vertical centre line with decreasing amplitude, which becomes nearly negligible at the so-called Ekman-depth (see Sect. 11.1.2). The presence of the Coriolis force implies in this case, that a boat subject to no other external 'forces' than the surface current drifts in a direction to the right of the wind.

The same Coriolis forces are also responsible for the fact that linear waves are differently structured with rotation than without rotation of the frame of reference. Longitudinal plane waves in a channel which have constant amplitude across the channel when they are referred to an inertial frame, experience transverse exponential decay of the amplitude to the left on the Northern hemisphere (NH) and to the right on the Southern hemisphere (SH). The e-folding length of this decay is the Rossby radius of deformation, v_{ph}/f in which v_{ph} is the phase speed and f the Coriolis parameter. These waves are shore bound and have large phase speeds for the barotropic and approximately up to 100 times smaller Rossby radii of deformation for baroclinic processes (see Table 11.1).

The linear wave equation is third order in time and therefore has also three different roots (of which all can be real). Solutions can be split into two classes, the *gravity* waves, of which the existence persists when the rotation of the Earth is ignored, and

the *quasi-geostrophic* or *vorticity* or Rossby waves which only exist because of the rotation of the Earth. The gravity waves are therefore modified by the rotation of the Earth: It will be shown that those longitudinal waves become Kelvin waves, and transversal waves turn into Poincaré waves.

The second class waves are obtained as the third solution of the general wave equation (11.24). For length scales which are large as compared to the Rossby radius of deformation they are described by a partial differential equation of the first order (e.g. (11.28)) and have been shown to exist only when $J[\psi, f/H] \neq 0$ where $J[a, b]$ is defined in (11.22). So, necessarily $f \neq 0$, and for constant water depth f must have non-vanishing spatial gradient or else, H must vary with position. This leads to a classification of Rossby waves, of which the *topographic* Rossby waves are nearly the only ones which are important for lakes.

We also discuss plane linear waves of a Boussinesq-fluid in infinite three dimensional space and show that they are confined to a wave guide in which

$$\frac{\omega^2 - f^2}{N^2 - \omega^2} > 0.$$

For these waves particle trajectories are ellipses which lie on inclined planes perpendicular to the wave vector (see Fig. 11.4) and thus in vertical planes for horizontal wave propagation. When rotation is absent, the elliptical trajectory reduces to a double line; the waves are then linearly polarized. On the other hand, when $N = 0$ (no stratification) waves are inertial ($\omega^2 = f^2$) and they are circularly polarized with the velocity vector turning in the clockwise direction when looking from above. When to this motion a translation is added, orbital trajectories become garlanded, and are traversed in the clockwise direction, when looked from above. Such motions are closely mimicked by buoys, whose position is followed in time. (Fig. 11.7).

When the domain is bounded from above by a free surface – this is the situation in the ocean and in lakes – it turns out that a separation of variables technique can be used to decouple the vertical from the horizontal motion. This separation is strictly only possible for constant water depth and must be performed in both the differential equations and boundary conditions. Such a separation of the horizontal from the vertical problem is possible, when the shallow water approximation is imposed and the boundary value problem is formulated for the perturbation pressure. When other variables (e.g. the vertical velocity component) are used, additional simplifying assumptions (e.g. the rigid lid assumption) may be needed. Else, the separation is only possible for monochromatic waves. A disadvantage of this method is that a true separation is not possible for variable depth basins. In this case, the lake is divided into layers of constant density. This procedure is not tied to the assumption of constant depth; but now the disadvantage is that for variable depth, the individual layers encompass different regions in the horizontal plane. This procedure is particularly popular in physical limnology for lakes which are stably stratified in layers of constant density.

References

1. Antenucci, J.P. and Imberger, J.: Energetics of long internal gravity waves in large lakes *Limnol. Oceanogr.*, **46** (7) 1760–1773 (2001)
2. Charney, J.G.: Generation of ocean currents by wind *J. Marine Research*, **14** 477–498 (1955)
3. Galazii, G.I., ed.: *Baikal Atlas*. Limnological Institute Acad. Sci. U.S.S.R., Siberian Section. Publ by Govt. Dept. Geodesy and Cartography, Irkutsk & Moscow, 30 p. (1969)
4. Gill, A.E.: *Atmosphere and Ocean Dynamics* Academic Press, London 662 p. (1982)
5. Gonella, J.A.: Effet d'écran d' une thermocline observations faites sur la bouée-laboratoire, *La Houille Blanche*, **7/8**, 607–613 (1974)
6. Gustafson, T. and Kullenberg B.: *Untersuchungen von Trägheitsströmungen in der Ostsee* Svensk. Hydrogr.-Biol. Komm. Skr. (New Series) Hydrogr, **13**, 28 p. (1936)
7. Heaps, N.S.: Seiches in a narrow lake, uniformly stratified in three layers. *Geophys. Suppl., J. Roy. Astronom. Soc.* **5**, 134–156 (1961)
8. LeBlond, P.H. and Mysak, L.A.: *Waves in the Ocean* Elsevier Sci. Publ, Amsterdam 602 p.(1978)
9. Lighthill, M.J. Sir: Dynamic response of the Indian Ocean to onset of the Southwest monsoon *Phil. Trans. Roy. Soc.* **A265**, 45–92 (1969)
10. Monismith, S.G.: Wind-forced motions in stratified lakes and their effect on mixed-layer shear. *Limnol. Oceanogr.*, **30**, 771–783 (1985)
11. Mortimer, C.H.: Water movement in lakes during summer stratification. Evidence from the distribution of temperature in Windermere. *Phil. Trans. R. Soc. Lond.*, **B236**, 355–404 (1952)
12. Mortimer, C.H.: *Internal waves observed in Lake Ontario during the International Field Year for the Great Lakes (IFYGL), 1972: I Descriptive survey and preliminary interpretations of near-inertial oscillations in terms of linear channel-wave models.* Center for Great Lakes Studies, Spec. Report. No 32, University of Wisconsin-Milwaukee, 122 p. (1977)
13. Mortimer, C.H.: *Internal motion and related internal waves in Lake Michigan and Lake Ontario as responses to impulsive wind stress. I Introduction, descriptive narrative and archive of IFYGL data.* Center for Great Lakes Studies, Spec. Report No 37, University Wisconsin-Milwaukee, 192 p. (1980),
14. Mortimer, C.H.: *Long internal waves in lakes: Review of a century of research.* Center for Great Lakes Studies, Spec. Report No 42, University Wisconsin-Milwaukee, 92 p. (1993)
15. Mortimer, C.H.: *Lake Michigan in Motion. Responses of an Inland Sea to Weather, Earth-Spin, and Human Activities*. The University of Wisconsin Press, 311 p. (2004)
16. Platzman, G.: Ocean Tides and Related Waves *Amer. Math. Soc. Lectures in Applied Mathematics* **14**, 239–291 (1971)
17. Poincaré, H.: Sur la precession des corps deformables. *Bull. Astronom.*, **27**, 321 p. (1910)
18. Sato, G.K. and Mortimer C.H. : *Lake currents and temperatures near the Western shore of Lake Michigan* Center for Great Lakes Studies, Spec. Report No 22, University Wisconsin-Milwaukee, 98 p. (1975)

Chapter 12
The Role of the Earth's Rotation: Oscillations in Semi-bounded and Bounded Basins of Constant Depth

12.1 Motivation

In Chap. 7 of Volume I, the propagation of surface waves in a layer of a homogeneous fluid referred to an inertial frame was studied. It was shown that superposing the fields of two waves, with the same frequency propagating in opposite directions with the same amplitude can be combined to a standing wave. These standing waves appear as localized oscillations between fixed nodal lines of which the distance defines the semi-wave length with wave humps and wave troughs arising inbetween. Under frictionless conditions imaginary walls can be placed at any position parallel to the wave direction to confine a channel without physically violating any boundary conditions. Similarly, the locations of the nodal lines across the channel turned out to be the positions of standing waves where the longitudinal velocity component vanishes for all time so that vertical walls can equally be inserted at these positions without disturbing the solution. This then formally yields the surface wave solution for the unidirectional motion in a basin of rectangular form and constant depth, see Figs. 7.9 and 7.12 in Chap. 7 of Volume I. These standing wave solutions were subsequently generalized to two-dimensional oscillations in rectangular cells of constant depth in which non-vanishing horizontal velocity components are allowed within the cell that only persistently vanish at the four side walls, thus forming oscillations of true cellular structure (see Figs. 7.14 and 7.15 in Chap. 7 in Volume I). How does the structure of these waves change when the fluid is rotating?

In Chap. 11, a first analysis of the role of the influence of the rotation of the Earth was provided. It was shown that in constant depth basins the water motion in a stratified fluid layer can in the shallow water approximation be split into a vertical problem defining the barotropic and baroclinic components (due to stratification) and a horizontal problem. It is the latter which chiefly describes the role of the rotation of the Earth via the dispersion relation and the Coriolis-acceleration terms in the horizontal momentum equations. The stratification enters this dispersion relation through the eigenvalues of the vertical problem but a feed back of the rotation of the Earth to the vertical problem does not arise. Therefore, in the shallow water approximation the baroclinic mode structure is not influenced by the rotation of the Earth,

K. Hutter et al., *Physics of Lakes*, *Volume 2: Lakes as Oscillators*, Advances in Geophysical and Environmental Mechanics and Mathematics,
DOI 10.1007/978-3-642-19112-1_12,

whilst the horizontal problem is affected by the former.[1] We determined in Chap. 11 also the harmonic wave solution to the horizontal problem by using a plane wave ansatz for a wave propagating in the infinite horizontal plane. The corresponding waves have super inertial frequencies, are called Poincaré-(Sverdrup)-waves, and only have real frequency and real wavenumber in infinite space. Complex valued wavenumbers and frequencies will yield exponential growth or decay in space and time and then require bounded domains.

In this chapter, we focus attention on the role played by the rotation of the Earth in the horizontal problem. In other words, we address the question how the rotation of the Earth alters the solutions as constructed in Chap. 7 in Volume I and Chap. 11.

Whereas the theory has been developed by prominent mathematicians, of the 19th century and the first half of the 20th century (Kelvin, Poincaré, Sverdrup, Taylor, Helmholtz, Goldstein, Rossby...) the graphical interpretation of the results has chiefly been done by Mortimer [24–27].

12.2 Kelvin Waves

Consider a water layer of constant depth bounded at $y = 0$ by a vertical wall. We shall see later on that, alternatively, we may equivalently consider an infinitely long canal with vertical side walls parallel to the x-axis positioned at $y = 0$ and $y = B$. In the shallow water approximation, the governing equations of the free water motion are given by the layer averaged mass and momentum balances,

$$\left.\begin{aligned} &\frac{\partial \zeta}{\partial t} + \frac{\partial U}{\partial x} + \frac{\partial V}{\partial y} = 0, \\ &\frac{\partial U}{\partial t} - fV = -gh_{\text{bar}}\frac{\partial \zeta}{\partial x}, \\ &\frac{\partial V}{\partial t} + fU = -gh_{\text{bar}}\frac{\partial \zeta}{\partial y}, \end{aligned}\right\} (x, y, t) \in (-\infty, \infty) \cup [0, \infty) \cup \mathbb{R}^+, \tag{12.1}$$

in which $\boldsymbol{M} \hat{=} (U, V)$, ζ is the displacement of the free surface from the un-deformed surface at rest, and $h_{\text{bar}} = H$ is the constant water depth.

We have seen in Chap. 7 in Volume I that plane waves in a non-rotating infinitely long channel propagate parallel to the side walls and have vanishing transverse velocity ($V \equiv 0$) throughout the channel. It is, therefore, tempting to assume that also (12.1) possess such a solution. Therefore, we let

$$\left.\begin{aligned} &\zeta = \zeta_0 \Phi(y) \exp\left[i(kx - \omega t)\right], \\ &U = u_0 h_{\text{bar}} \Phi(y) \exp\left[i(kx - \omega t)\right] \\ &V \equiv 0, \end{aligned}\right\} (x, y, t) \in (-\infty, \infty) \cup [0, \infty) \cup \mathbb{R}^+, \tag{12.2}$$

[1] Recall that in formulations which are not based on the shallow water approximation the coupling can be shown to be two-sided.

in which k is the wavenumber and ω the circular frequency. In (12.2), we assumed that ζ and U propagate harmonically into the positive x-direction with phase speed $c_{\mathrm{ph}} = \omega/k$. Both, ζ and U have the same transverse behaviour $\Phi(y)$; this is a direct consequence of (12.1); ζ_0 and U_0 are constant amplitudes. Since V vanishes throughout, the side boundary conditions are automatically satisfied. Substituting (12.2) into (12.1) yields

$$\left.\begin{aligned} c_{\mathrm{ph}} &= \frac{\omega}{k} = \pm\sqrt{g h_{\mathrm{bar}}}, \\ \zeta_0 &= \sqrt{\frac{h_{\mathrm{bar}}}{g}}\, u_0, \\ \frac{\mathrm{d}\Phi}{\mathrm{d}y} + \frac{f}{c_{\mathrm{ph}}}\Phi = 0 \quad &\Rightarrow \quad \Phi = \exp\left(-fy/c_{\mathrm{ph}}\right). \end{aligned}\right\} \tag{12.3}$$

The first is the shallow water dispersion relation whose frequencies may be sub- or super-inertial, the second relates the amplitude of the free surface displacement with that of the x-velocity component, and the third yields the transverse variation of ζ and U. It follows that the amplitudes of ζ and U decay exponentially as one moves away from the side boundary. The decay rate is given by the *Rossby radius of deformation* or in brief the *Rossby radius*

$$R = \frac{c_{\mathrm{ph}}}{f} = \frac{\sqrt{g h_{\mathrm{bar}}}}{f} = \frac{\sqrt{g h_{\mathrm{bar}}}}{2\Omega \sin\phi}. \tag{12.4}$$

Its value depends on the Coriolis parameter and the size of the phase speed c_{ph}, which in turn itself depends on $h_{\mathrm{bar}} = H$ (for barotropic waves). Typical values are given in Table 12.1. R grows according to a square root law with the water depth, and it decays with $\sin^{-1}\phi$, where ϕ is the geographical latitude. These waves are called *Kelvin waves* in honor of Lord Kelvin,[2] who in 1879 [12] in a paper entitled

Table 12.1 Typical values of the Rossby *radius of deformation* (in km) for *barotropic* motions depending on water depth and geographical latitude to the North or South, values in (km)

$\Phi(^\circ)$ \ H(m)	20	50	100	200	500	1,000	2,000
10	553	874	1,236	1,749	2,765	3,910	5,530
20	280	444	627	888	1,404	1,985	2,808
30	192	303	429	607	960	1,358	1,920
40	149	236	334	472	747	1,056	1,494
50	125	198	280	396	626	886	1,253
60	110	175	247	350	554	784	1,109
70	102	161	228	323	511	722	1,022
80	97	154	218	308	487	689	975

[2] For a biographical sketch see Fig. 12.1.

'On gravitational oscillations of rotating water' provided the basis for all rotation affected waves on the f-plane.

We have mentioned above that the regions of applicability of the above solution can also be channels with constant water depth and constant width B. This is now clear from the solution (12.2), (12.3), since $V \equiv 0$ identically vanishes. At any position $y = B$ a vertical wall may be inserted that is parallel to the x-axis without violating the solution. The exponential decay of ζ and U in the transverse direction with an e-folding width of the size of the Rossby radius of deformation thus requires a channel to have a width of the size of this Rossby radius of deformation or larger in order that such a decay may become observable by measurement. The Great Lakes in US/Canada, the Caspian Sea and the Baltic Sea are of this size but Lake Ladoga and Lake Onega – the two largest lakes in Europe – are perhaps a bit too small.

Figure 12.2 depicts the behaviour of the solution (12.2) and (12.3). These waves are non-dispersive and propagate with the same phase speed as do shallow water waves without rotation. They are *coastal trapped* and have boundary layer structure if the basin width is sufficiently large relative to the Rossby radius of deformation. At small channel widths relative to the Rossby radius of deformation we have $\Phi(y) \approx 1$, and the Kelvin wave becomes an ordinary long gravity wave. Furthermore, since there are only x- and z-components of the velocity vector, the fluid particle trajectories traverse elliptical orbits in vertical planes. Finally, if the wave propagates in the negative x-direction ($\omega < 0$), then the phase speed is $c_{\mathrm{ph}} = -\sqrt{gh_{\mathrm{bar}}}$, and so, the attenuation is in the negative y-direction. Both situations can be described as follows: The Kelvin *wave amplitudes of ζ and U are transversely attenuated to the right (left) on the Northern (Southern) hemisphere when looking into the direction of propagation of the wave.*

Problem 12.1 *Consider (12.1) with $V \equiv 0$. From $(12.1)_{1,2}$, which we write now as*

$$\frac{\partial \zeta}{\partial t} + \frac{\partial U}{\partial x} = 0, \quad \frac{\partial U}{\partial t} = -gh_{\mathrm{bar}} \frac{\partial \zeta}{\partial x} \tag{12.5}$$

the zeroth order approximation ζ_0, U_0

$$\begin{aligned} U_0 &= A_0 \exp\left[i(kx - \omega t)\right], \\ \zeta_0 &= B_0 \exp\left[i(kx - \omega t)\right] \end{aligned} \tag{12.6}$$

in which

$$B_0 = \frac{k}{\omega} A_0, \qquad \frac{\omega^2}{k^2} = c_{\mathrm{ph}}^2 = gh_{\mathrm{bar}} \tag{12.7}$$

can be derived. Here, A_0 and B_0 do not show any y-dependence. Equation $(12.1)_3$ allows to use the above solution for U_0 to derive the equation

$$\frac{\partial \zeta_1}{\partial y} = -\frac{f}{gh_{\mathrm{bar}}} U_0 \tag{12.8}$$

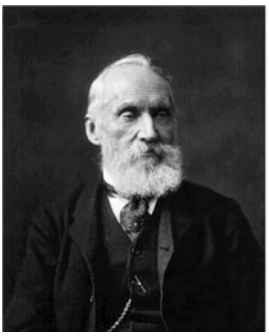

Fig. 12.1 William Thomson, first Baron Kelvin (1824–1907). A Kelvin–Helmholtz instability rendered visible by clouds over Mount Duval in Australia. Photos from http://en.wikipedia.org/.

William Thomson, first Baron Kelvin or Lord Kelvin, or Kelvin of Largs (26 June 1824, Belfast, Northern Ireland, 17 December 1907, Netherhall at Largs) was a mathematical physicist and engineer. He was professor of Natural Philosophy at Glasgow University for more than 50 years and did important work in the mathematical analysis of electricity and the formulation of the first and second law of thermodynamics. He also had a successful career as an electrical telegraph engineer which propelled him into the public eye and ensured his wealth, fame and honour. Largely for this work he was knighted by Queen Victoria (1866), becoming Sir Willliam. Moreover, for his scientific key role in developing the basis of the absolute temperature and the Kelvin temperature scale, and because of his opposition to the Irish Home Rule, he received ennoblement as Baron Kelvin of Largs or Lord Kelvin (1892).

As a child William Thomson lost his mother at the age of 6 years (1830). The four boys and two girls who survived infancy were educated by their father who was a mathematics and engineering teacher at the Royal Belfast Academic Institution. In 1834, the father became professor at Glasgow University. So, son William started his university education in Glasgow at the age of 10. In the academic year 1839–1840, he won the class prize in Astronomy for his essay on the figure of the Earth, which showed an early talent for mathematical analysis and creativity. When coming across Fourier's *Théorie analytique de la chaleur* he committed himself to study continental mathematics. Between 1841 and 1842 he wrote under the pseudonym P.Q.R. three papers on the theory of heat and its connection with electricity. He left Glasgow University in 1841 without a degree and went with his father's strong support to Cambridge, where he graduated in 1845 in second place and also won the Smith's Prize. In the same year, he also became a fellow of Peterhouse but left Cambridge in 1846, when, at the age of 22, he was appointed to the chair of Natural Philosophy in the University of Glasgow, a position he kept until 1899.

William Thomson's important work on the first and second law of thermodynamics was done in the years from 1847 onwards during about 10 years. Besides his fundamental work on absolute zero, he and James Prescott Joule collaborated, one result being the Joule–Thomson effect. He also phrased the second law in the form: *It is impossible, by means of inanimate material agency, to derive mechanical effect from any portion of matter by cooling it below the temperature of the coldest of the surrounding objects*.

Thomson did also major work on electricity and developed his Thomson bridge, Kelvin generator, mirror galvanometer and many more. He was deeply involved in the proper build-up of the telegraph cable across the Atlantic, involving serious professional disputes with Wildman Whitehouse, the electrician of the Atlantic Telegraph Company and his eventual triumph and Whitehouse's disaster and dismissal. Thomson was also an enthusiastic yachtsman and contributed to the perfection to many marine instruments. His interest in tides led to the description of Kelvin waves and the Thomson tide predicting machine.

Thomson published more than 600 scientific papers and filed 70 patents. His book 'Treatise on Natural Philosophy' (1867) with Peter Guthrie Tait did much in unifying the modern physics of that time.

The text is based on:

http://de.wikipedia.org/wiki/Lord_Kelvin

http://en.wikipedia.org/wiki/Lord_Kelvin.

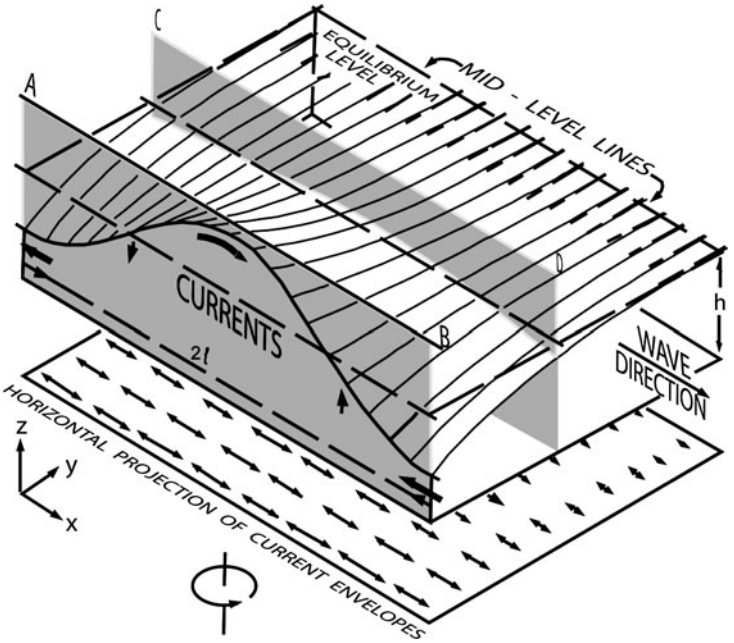

Fig. 12.2 Long Kelvin wave in a semi-infinite half space x, y, propagating in the positive x-direction in an uniform depth model. The vertical plane AB defines the shore of a layer of infinite width. The vertical plane CD parallel to AB may also form a shore line adapted from [27], with changes. © Center for Great Lake Studies (now Great Lakes WATER Institute), reproduced with permission

from which

$$\zeta_1 = -\frac{f}{gh_{\text{bar}}} U_0 y \tag{12.9}$$

is obtained. This demonstrates that for longitudinal motions the free surface must be transversely inclined in order that the transverse pressure gradient can balance the Coriolis force. Show that by continuing this iteration procedure, the following expressions are obtained:

$$\begin{aligned} U &= A_0 \left\{ 1 - \left(\frac{y}{R}\right) + \frac{1}{2!}\left(\frac{y}{R}\right)^2 - \frac{1}{3!}\left(\frac{y}{R}\right)^3 \pm \cdots \right\} \exp\left[i\left(kx - \omega t\right)\right] \\ &= A_0 \exp\left(-\frac{y}{R}\right) \exp\left[i\left(kx - \omega t\right)\right], \\ \zeta_0 &= B_0 \left\{ 1 - \left(\frac{y}{R}\right) + \frac{1}{2!}\left(\frac{y}{R}\right)^2 - \frac{1}{3!}\left(\frac{y}{R}\right)^3 \pm \cdots \right\} \exp\left[i\left(kx - \omega t\right)\right] \\ &= B_0 \exp\left(-\frac{y}{R}\right) \exp\left[i\left(kx - \omega t\right)\right], \end{aligned} \tag{12.10}$$

which is the same as (12.2) and (12.3). Here $R = c_{\text{ph}}/f$. ◆

This iterative construction has been pursued in practice only to first order in y. It is called *Kelvin wave dynamics*, has been introduced by Defant [9] and applied by him in the seiche analysis of Lake Michigan and later by Platzman and Rao [28] in an analysis of surface seiches of Lake Erie.

The method of Kelvin wave dynamics has found its ultimate application in the construction of extended channel models of Raggio and Hutter [35–37], and Hutter and Raggio [38], a kind of Chrystal-equations for elongated lakes on the rotating Earth. In these models the governing equations (12.1) are written in curvilinear coordinates, in which one axis follows the long direction of the lake (approximately the thalweg), whilst the other axis is perpendicular and transverse to this long axis. Raggio and Hutter perfected this method by a formal procedure using the method of weighted residuals, which allows determination of as many transverse elements of the analogue representations to (12.10) as desired. A full account on this class of channel modes is given in Chap. 22.

12.2.1 Pseudo-Standing Kelvin Waves

In a non-rotating fluid layer of constant depth, standing waves do exist. In fact such standing waves were constructed in Sects. 7.2 and 7.3, see Figs. 7.9, 7.12 of Volume I. Their distinctive feature is that spatially fixed nodal lines x=const. do exist, across which no water will move at any one time. In an infinite channel of constant width, exact standing Kelvin waves (in a rotating channel) *do not exist*. What exists is something 'close to standing waves': they will subsequently be called *pseudo-standing Kelvin waves*.[3] To construct their solution, consider a forward propagating Kelvin wave with large amplitudes at $y = 0$ and decaying as y grows, and a backward moving Kelvin wave with large amplitudes at $y = B$ and decaying as $(B - y)$ decreases. These waves are given by

$$(\zeta, u)_{\text{forward}} = \left(\frac{c_{\text{ph}}}{g}u_0, u_0\right) \exp\left(-\frac{fy}{c_{\text{ph}}}\right) \exp\left[i\left(kx - \omega t\right)\right],$$
$$(\zeta, u)_{\text{backward}} = \left(\frac{c_{\text{ph}}}{g}u_0, -u_0\right) \exp\left(-\frac{f(B-y)}{c_{\text{ph}}}\right) \exp\left[i\left(kx + \omega t\right)\right]. \tag{12.11}$$

Adding the two waves and taking real parts yields

[3] In the literature such pseudo-standing waves are for brevity often simply called standing waves; we believe this convention is more confusing than convenient.

$$\begin{aligned}\zeta &= \Re e\{\zeta_{\text{forward}} + \zeta_{\text{backward}}\} \\ &= \frac{2c_{\text{ph}}}{g} u_0 \exp\left(-\frac{fB}{2c_{\text{ph}}}\right)\left\{\cosh\left[\frac{f}{c_{\text{ph}}}\left(\frac{B}{2}-y\right)\right]\cos kx\cos\omega t\right. \\ &\qquad \left. + \sinh\left[\frac{f}{c_{\text{ph}}}\left(\frac{B}{2}-y\right)\right]\sin kx\sin\omega t\right\}, \\ u &= \Re e\{u_{\text{forward}} + u_{\text{backward}}\} \\ &= 2u_0 \exp\left(-\frac{fB}{2c_{\text{ph}}}\right)\left\{\sinh\left[\frac{f}{c_{\text{ph}}}\left(\frac{B}{2}-y\right)\right]\cos kx\cos\omega t\right. \\ &\qquad \left. + \cosh\left[\frac{f}{c_{\text{ph}}}\left(\frac{B}{2}-y\right)\right]\sin kx\sin\omega t\right\}.\end{aligned} \tag{12.12}$$

The solution (12.12) enjoys the following properties (compare Figs. 12.3 and 12.4).

- For $y = B/2$ and $x = (2n+1)\pi/(2k)$, $\zeta = 0$ for all time. Any of these points, called *amphidromic points* or *amphidromes*, is characterized by the fact that the surface never experiences any elevation from its equilibrium level.
- For $y = B/2$ and $x = n\pi/k$ (these are the points on the centre line between two amphidromic points) the velocity vanishes at all times.
- At times $t = n\pi/\omega$ the surface elevation ζ (velocity u) is symmetrically (anti-symmetrically) distributed across the channel width with maximum velocities arising at the shore lines at positions x midway between the amphidromic points. Similarly, for $t = ((2n+1)\pi/(2\omega))$, ζ is anti-symmetrically distributed, whilst u is symmetrically distributed across the channel.
- Lines of *constant elevation amplitudes* – the so-called *co-range lines* – are given by

$$\cosh^2\left[\frac{f}{c}\left(\frac{B}{2}-y\right)\right]\cos^2(kx) + \sinh^2\left[\frac{f}{c}\left(\frac{B}{2}-y\right)\right]\sin^2(kx) = \text{const.} \tag{12.13}$$

  These lines are dashed in Fig. 12.4. In the vicinity of the amphidrome they encircle the amphidromic point, farther away they are oscillatory.
- Lines of *constant phase* – the so-called *co-tidal lines* – are described instead by

$$\tan\phi = \tan(kx)\tanh\left[\frac{f}{c}\left(\frac{B}{2}-y\right)\right] = \text{const.} \tag{12.14}$$

  It is easily seen that these are lines through the amphidromic points. Co-tidal lines which differ in phase from one another by the angle π are centro- symmetrically arranged with respect to the amphidromic point.

All these properties can with little effort be deduced from the respective formulae, and they are easily corroborated in Figs. 12.3 and 12.4. The former

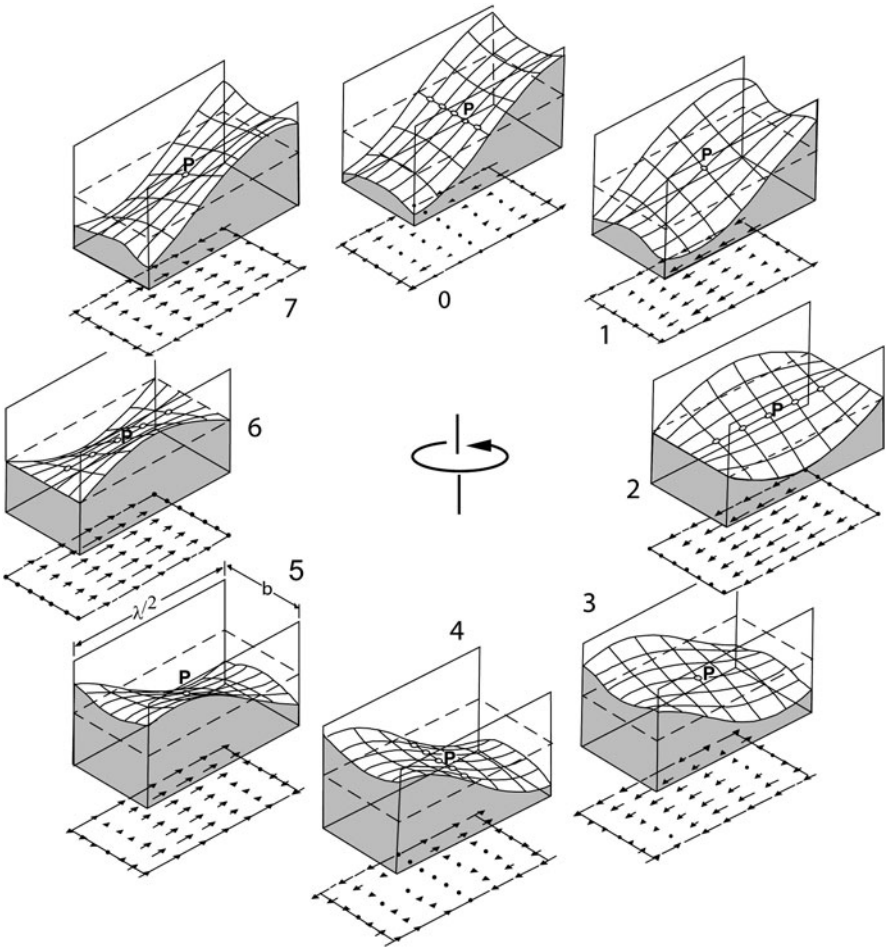

Fig. 12.3 Successive phases (1/8 cycle) of a long, standing, amphidromic wave in a straight rotating channel of rectangular cross section. Horizontal components of the wave current are projected on the plane below the channel. The amphidromic point P of zero elevation change, around which the wave rotates counter-clockwise, is in the centre (redrawn from Mortimer, 1974 [24]. © Int. Ver. Theor. Angew. Limnol., http://www.schweizerbart.de)

of these displays the distribution of the surface elevation and longitudinal velocity in successive phases of (1/8)-cycle of such an amphidromic wave. The figure illustrates the cyclonic (anticlockwise on the Northern Hemisphere) propagation of the wave: In one period of its motion, the wave crest moves around the amphidromic point and the velocity moves forth and back along the channel. The velocities are weakest along lines transverse to the channel and midway between the amphidromic points; however *there is no line across the channel at which the longitudinal velocity would vanish for all time*. It follows that gravity waves in a gulf or a closed basin cannot simply be obtained by superimposing Kelvin waves. We shall soon return to this point.

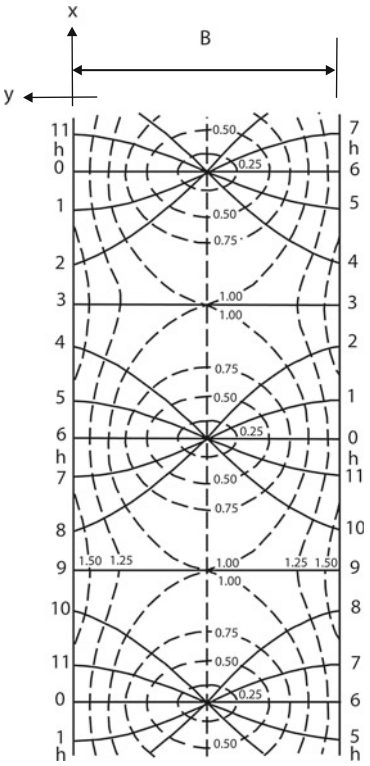

Fig. 12.4 Amphidromic system in an infinitely long canal, resulting from superposition of two Kelvin waves of 12-h period, traveling in opposite directions. *Full lines*: co-tidal lines in hours: *broken lines*: co-range lines (Z_0=0.5, $k = 1$, $f/c = 0.7$, corresponding to a canal width of 400 km, $H = 40$ m). © Courtesy W. Krauss (1966) [14], http://www.schweizerbart.de

12.2.2 Baroclinic Kelvin Waves

So far in this chapter only barotropic Kelvin waves were studied. In Chap. 11 it was, however, shown that in a *strictly vertically stratified fluid layer of constant depth in the shallow water approximation* the horizontal and the vertical problem can be separated such that the vertical eigenvalue problem, formulated, say, for the vertical velocity component, determines the equivalent depths h_n, where n is a counting index which identifies the baroclinic mode number. This equivalent depth then enters the horizontal problem which determines the propagation properties in the horizontal direction.

For instance, in the *two layer variable depth model*, the baroclinic analogue of the linearized governing equations are given by (11.98). The equations are exactly the same equations as (12.1) with gh_{bar} replaced by gh_{int}, where

$$h_\alpha = \begin{cases} h_{\text{ext}} = H, & \text{barotropic case,} \\ h_{\text{int}} = \varepsilon \dfrac{H_1 H_2}{H_1 + H_2}, & \text{2-layer, baroclinic case} \end{cases} \tag{12.15}$$

Table 12.2 Equivalent depth factors r and $\sqrt{r}$ for the first baroclinic mode for a selected number of ratios H_2/H_1

H_2/H_1	r	$\sqrt{r}$	H_2/H_1	r	$\sqrt{r}$
0.1	0.0909	0.3015	5.0	0.8333	0.9129
0.5	0.3333	0.5774	10.0	0.9091	0.9535
1.0	0.5000	0.7071	100.0	0.9901	0.9950
			∞	1.000	1.000

is the equivalent depth of the two layer model in the barotropic and baroclinic modes, respectively and $\varepsilon = \Delta\rho/\rho$. So, the Kelvin wave solutions are equally analogous and given by

$$\begin{aligned} \zeta_\alpha &= \sqrt{\frac{h_\alpha}{g}} u_0 \exp\left(-\frac{f}{\sqrt{gh_\alpha}} y\right) \exp\left[i\left(kx - \omega t\right)\right], \\ U_\alpha &= u_0 h_\alpha \exp\left(-\frac{f}{\sqrt{gh_\alpha}} y\right) \exp\left[i\left(kx - \omega t\right)\right] \end{aligned} \tag{12.16}$$

with the corresponding Rossby radius of deformation

$$R_{\text{eq}} = \begin{cases} R_{\text{ext}} = \sqrt{gH}/f, & \text{barotropic case,} \\ R_{\text{int}} = \sqrt{gh_{\text{int}}}/f, & \text{baroclinic case.} \end{cases} \tag{12.17}$$

Writing

$$h_{\text{int}} = \frac{1}{1 + H_1/H_2} H_1\varepsilon = rH_1\varepsilon, \quad r = \frac{H_2/H_1}{H_2/H_1 + 1}, \quad \varepsilon = \frac{\rho_2 - \rho_1}{\rho_*}, \tag{12.18}$$

the equivalent depth, h_{int} is written as a quantity proportional to $H_1\varepsilon$. Table 12.2 lists a few values of r and $r^{1/2}$; $H_1\varepsilon$ is the equivalent depth, h_{int} in the limit as $H_2/H_1 \to \infty$.

So, for rough estimates we may set

$$\begin{aligned} h_{\text{int}} &= rH_1\varepsilon, \\ c_{\text{ph}}^{\text{int}} &= \sqrt{rgH_1\varepsilon} = \sqrt{r}\sqrt{gH_1\varepsilon} = \sqrt{r}(c_{\text{ph}}^{\text{int}})_{\max}, \\ R_{\text{int}} &= \frac{\sqrt{rgH_1\varepsilon}}{f} = \sqrt{r}\frac{\sqrt{gH_1\varepsilon}}{f} = \sqrt{r}R_{\text{int}}^{\max}, \end{aligned} \tag{12.19}$$

in which $R_{\text{int}}^{\max}$ is the internal Rossby radius of deformation. Values of $(c_{\text{ph}}^{\text{int}})_{\max}$ lie in the interval between approximately $10^{-2}\,\text{ms}^{-1}$ and $10\,\text{ms}^{-1}$. Figure 12.5 displays $R_{\text{int}}^{\max}$ as a function of the maximum phase speed $(c_{\text{ph}}^{\text{int}})_{\max} = \sqrt{gH_1\varepsilon}$ for various

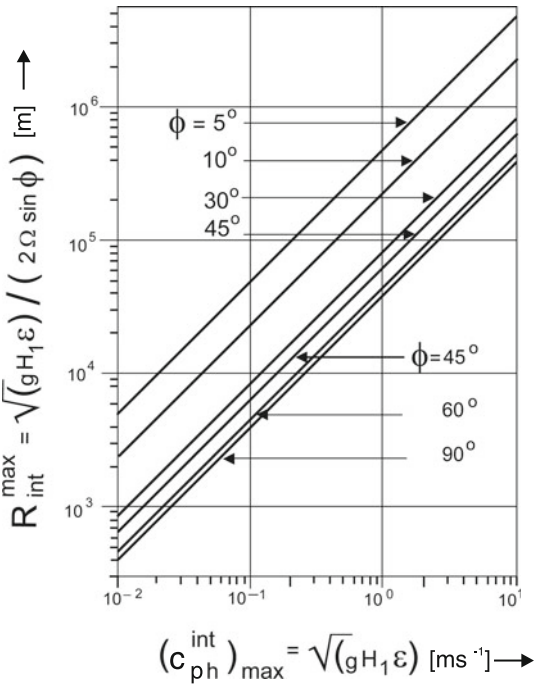

Fig. 12.5 Maximum internal Rossby radius of deformation as a function of the maximum internal phase speed $\sqrt{gH_1\varepsilon}$ for various latitude angles

values of the geographical latitude. For a specific two-layer stratification with depth ratio H_2/H_1, the adequate phase speeds and Rossby radii of deformation are then obtained by multiplication with $\sqrt{r}$.

12.3 Inertial Waves

Kelvin waves are long shallow water waves on the rotating Earth whose horizontal projection of the particle motion is purely longitudinal. Because of the Coriolis forces such an unidirectional motion can only be maintained when the surface elevation experiences an inclination in the direction perpendicular to the wave propagation. This transverse variation of the surface elevation, due to geostrophic adjustment, is exponentially evanescent as one moves away from the boundary. In an infinite basin, there are no boundaries that can sustain a deviation of ζ from its position at rest. Plane waves in infinite three-dimensional space (with constant wave amplitude perpendicular to the direction of wave propagation) were treated in Chap. 11, Sect. 11.4. A special case of these waves are the *inertial waves*. Their properties can be deduced from (12.1) by imposing the condition that their surface elevation vanishes, $\zeta \equiv 0$; so, all motion is purely horizontal. With $\zeta = 0$, (12.1) take the forms

$$\left.\begin{aligned} \frac{\partial U}{\partial x} + \frac{\partial V}{\partial y} &= 0, \\ \frac{\partial U}{\partial t} - fV &= 0, \\ \frac{\partial V}{\partial t} + fU &= 0, \end{aligned}\right\} (x, y, t) \in \mathbb{R}^2 \cup \mathbb{R}^+. \tag{12.20}$$

With the harmonic representation

$$(U, V) = (U_0, V_0)\exp\left[i(\boldsymbol{k} \cdot \boldsymbol{x} - \omega t)\right] \tag{12.21}$$

it is then readily shown that

$$\begin{aligned} &kx + ly = 0, \qquad \text{where} \quad \boldsymbol{k} = (k, l), \\ &-i\omega U_0 - fV_0 = 0, \; -i\omega V_0 + fU_0 = 0, \end{aligned} \tag{12.22}$$

from which one concludes that $\omega = f$, (independent of $\boldsymbol{k}$); hence, the wavenumber is arbitrary ($\boldsymbol{k}$ is perpendicular to the horizontal position vector (x, y)). This also implies that the phase speed $c = \omega/|\boldsymbol{k}|$ is arbitrary. Moreover,

$$\begin{aligned} U &= \Re e\{U_0 \exp\left[i(\boldsymbol{k} \cdot \boldsymbol{x} - \omega t)\right]\}, \\ V &= \Re e\{-iU_0 \exp\left[i(\boldsymbol{k} \cdot \boldsymbol{x} - \omega t)\right]\}, \\ \text{or} \qquad & \\ U &= \Im m\{U_0 \exp\left[i(\boldsymbol{k} \cdot \boldsymbol{x} - \omega t)\right]\}, \\ V &= \Im m\{-iU_0 \exp\left[i(\boldsymbol{k} \cdot \boldsymbol{x} - \omega t)\right]\}. \end{aligned} \tag{12.23}$$

This shows that particle motions are horizontal and circular with clockwise propagation in the Northern hemisphere, and the trajectory radius is $R = c/f$. These results may be summarized as follows:

Properties of Inertial Waves

- *The angular frequency equals the inertial frequency: $\omega = f$. This fact explains why these waves are called inertial waves.*
- *The wave speed is not restricted, i.e. these waves may have arbitrary wavenumber.*
- *Particle trajectories are horizontal circles with diameter $R = c_{\text{ph}}/f$ where c_{ph} is the phase speed; this radius is akin to the Rossby radius of deformation, its difference to the latter being that here c_{ph} is not explicitly specified, but may have any value.*

12.4 Poincaré Waves

Kelvin waves have the property that water particle displacements are strictly longitudinal, whilst inertial waves are circular. There are many other solutions of (12.1) which, when conveniently combined, fit particular boundary conditions [27, 29]. These solutions are described by the harmonic representation

$$(\zeta, U, V) = (\zeta_0, U_0, V_0)\exp\left[i\left(\boldsymbol{k}\cdot\boldsymbol{x} - \omega t\right)\right] \tag{12.24}$$

with the horizontal wavenumber vector $\boldsymbol{k}\hat{=}(k,l)$. Substituting (12.24) into (12.1) leads to a homogeneous linear system of equations for (ζ_0, U_0, V_0) which possesses the solution

$$\begin{aligned} U_0 &= -\frac{gh_n}{\omega^2 - f^2}(-k\omega + ifl)\zeta_0, \\ V_0 &= -\frac{gh_n}{\omega^2 - f^2}(-ikf - l\omega)\zeta_0, \end{aligned} \tag{12.25}$$

for arbitrary ζ_0, provided its determinant vanishes, which is the case, if

$$\omega^2 = f^2 + gh_n(k^2 + l^2). \tag{12.26}$$

'The general solution (12.25) and (12.26) is formally valid when k and l are complex valued; k and l can be real or imaginary, subject to the condition for pure harmonic waves that ω and $(k^2 + l^2)$ must be real. If, for a wave travelling in the x-direction k is real and positive and l is purely imaginary [to make this explicit, we may replace l by il'] a special class of progressive wave solutions appears [...], characterized by a sinusoidal variation of the wave amplitude in the x-direction and an exponential variation in the y-direction. But, if both k and l are real, and for convenience the direction of propagation is made to coincide with the x-axis, so that $k = k_h$ and $l = 0$ in a plane wave) the Sverdrup wave emerges with sinusoidal amplitude variation along x and no amplitude variation along y $(l = 0)$', after Mortimer [27]. All these solutions are summarized in Fig. 12.6 and the following problem.

Problem 12.2 *Show that the dispersion relation (12.26) can, alternatively, be written as*

$$y = (x^2 + 1 - a^2)^{1/2}, \tag{12.27}$$

$$y := \left|\frac{\omega}{f}\right|, \quad x := \frac{\sqrt{gh_n}k}{f}, \quad a^2 := \frac{gh_n l'^2}{f^2}. \tag{12.28}$$

Show, moreover, that for different values of the transverse wavenumber parameter a^2, the graphs of (12.27) are as shown in Fig. 12.6.

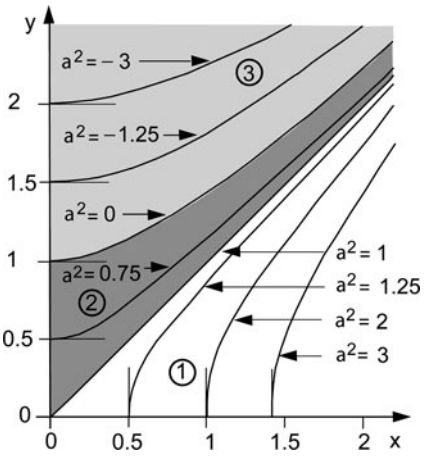

Fig. 12.6 Frequency, $y = |\omega/f|$ vs. wavenumber, $x = \sqrt{gh_n}k/f$, diagram. Regions (1)+(2) are the regime of transversely exponentially growing or evanescing waves, regime (3) is the regime of oscillatory waves, see also main text

- *Regime (1),* $1 < a^2$*: Graphs of (12.27) are branches of hyperbolas with vertices on the x-axis and asymptote* $y = x$ *(white triangle bounded by* $y = 0$ *and* $y = x$ *in Fig. 12.6.*
- *Regime (2),* $0 < a^2 < 1$*: Graphs of (12.27) are branches by hyperbolas with vertices on the y-axis and asymptote* $y = x$ *(dark-shaded region bounded by* $y = x$ *and the hyperbola for* $a^2 = 0$*. Note that in regimes (1) and (2) the transverse wavenumbers* l' *are real and corresponding waves transversely exponentially growing or evanescing.*
- *Regime (3),* $a^2 < 0$*: Graphs of (12.27) are branches of hyperbolas as shown in the light gray region of Fig. 12.6. In this region, wave crests are transversely harmonically varying* $(a^2 < 0)$*, but constant for* $a^2 = 0$*.* ◆

Platzman [29] and Mortimer [27] call waves in regime (3) Sverdrup waves; they have $l'^2 < 0$ (or $l^2 > 0$) and are, therefore, transversely oscillatory. It is obvious that by rotation of the coordinate system from (x, y) to $(\bar{x}, \bar{y})$ the direction of increasing $\bar{x}$ can be made to agree with the direction of wave progress, in which case $\bar{k} > 0$ and $\bar{l} = 0$. The corresponding solution for the surface elevation ζ and horizontal transports U, V can be obtained from (12.24) to (12.26). (We use overbars to indicate that the rotated coordinates $(\bar{x}, \bar{y})$ are used, for which $\bar{l} = 0$). Results are collected in Problem 12.3.

Problem 12.3 *Write (12.24)–(12.26) in a Cartesian coordinate system* $(\bar{x}, \bar{y})$ *for which wave progression is in the* $\bar{x}$*-direction* ($\bar{l} = 0$)*, and prove that*

$$
\begin{aligned}
&(\bar{\zeta}, \bar{U}, \bar{V}) = (\bar{\zeta}_0, \bar{U}_0, \bar{V}_0)\exp[i(kx - \omega t)],\\
&\bar{U}_0 = \frac{\omega}{k}\bar{\zeta}_0, \quad V_0 = -i\frac{f}{k}\bar{\zeta}_0,\\
&\omega^2 = f^2 + gh_n k^2.
\end{aligned}
\tag{12.29}
$$

Taking real or imaginary values, (12.29) take the forms

$$\begin{aligned}\bar{\zeta} &= \bar{\zeta}_0[\cos(kx-\omega t),\ \sin(kx-\omega t)],\\ \bar{U} &= \frac{\omega}{k}\bar{\zeta}_0[\cos(kx-\omega t),\ \sin(kx-\omega t)],\\ \bar{V} &= \frac{f}{k}\bar{\zeta}_0[\sin(kx-\omega t),\ -\cos(kx-\omega t)],\end{aligned} \tag{12.30}$$

where the brackets $[\alpha\,,\beta]$ *are obtained from the real and imaginary parts, respectively. Using* $\bar{U} = H\bar{u}$, $\bar{V} = H\bar{v}$, *where* H *is the water depth, and the continuity equation*

$$\frac{\partial \bar{U}}{\partial x} + \frac{\partial}{\partial z}(H\bar{w}) = 0 \tag{12.31}$$

show, moreover, that for $n = 1$

$$\bar{w} = -\frac{\omega}{H}(z+H)\bar{\zeta}_0[\sin(kx-\omega t),\ -\cos(kx-\omega t)], \tag{12.32}$$

satisfying the boundary conditions $\bar{w}(z=-H) = 0$ *and* $\bar{w}(z=0) = \partial\zeta/\partial t$. *The linear variation of* $\bar{w}$ *with* z *over the depth is a consequence of the shallow water approximation.* ◆

Beyond this problem solution it can also be shown that particle trajectories are as shown for the more general stratified case in Fig. 11.9. Here, we mention once more that the Sverdrup wave, comprising regime (3) of Fig. 12.6 is a member of a more general class, treated by Poincaré [31],[4] and has been referred to as a Poincaré wave, e.g. by LeBlond and Mysak [18] as are all super-inertial waves covered in Fig. 12.6. Mortimer [27] writes 'However, others [22, 23, 29] find it convenient to confine the designation 'Poincaré' to waves which satisfy the boundary conditions at a straight vertical wall or walls in rotating uniform-depth models', and he demonstrates in a careful analysis that Poincaré waves so defined can be constructed as combinations of Sverdrup waves.

This is exactly, what we are now going to do. More specifically, we construct wave solutions of (12.1) which satisfy the boundary conditions $V = 0$ at the channel walls, but may have non-trivial transverse velocity component inside the channel. To this end, we eliminate U and ζ from (12.1) and seek plane wave solutions for

$$V = V_0(y)\exp[i(kx-\omega t)]. \tag{12.33}$$

The reader may verify that elimination of U and ζ from (12.1) yields

$$\left(\frac{\partial V}{\partial x^2} + \frac{\partial^2 V}{\partial y^2}\right) - \frac{1}{gh_n}\left(\frac{\partial^2}{\partial t^2} + f^2\right)V = 0 \tag{12.34}$$

[4] For a biographical sketch see Fig. 12.7.


COURS DE LA FACULTÉ DES SCIENCES DE PARIS.

LEÇONS

DE

MÉCANIQUE CÉLESTE

PROFESSÉES A LA SORBONNE

PAR

H. POINCARÉ,

TOME I.

THÉORIE GÉNÉRALE DES PERTURBATIONS PLANÉTAIRES.

PARIS,

GAUTHIER-VILLARS, IMPRIMEUR-LIBRAIRE

1905

Fig. 12.7 Jules Henri Poincaré (1854–1912), photographic portrait by Henri Manuel (from http://en.wikipedia.org/), and the front page of his 'Lectures on Celestial Mechanics' (image from Cornell University Library http://dlxs2.library.cornell.edu/).

Jules Henri Poincaré (29 April 1854, Meurthe-et-Moselle, near Nancy; 17 July 1912, Paris) was a French mathematician, theoretical physicist, mining engineer and philosopher of Science. During his childhood, he was seriously ill for a time with diphtheria. He received his first education from his mother. From 1862 to 1873 he attended the Lycée in Nancy, where his outstanding talents in all fields except music and physical education were noted, in particular the superiority in mathematics. Henri Poincaré spent the Franco-Prussian war of 1870 with his father in the Ambulance Corps. In 1873, he entered École Polytechnique, where he became a student of Charles Hermite. He graduated in 1875 (or 1876), but went on to study at the École des Mines, continuing with his mathematical studies in addition to the mining engineering syllabus, receiving the engineering degree in 1879. At the same time Poincaré was preparing for his doctorate in mathematics under Hermite. His thesis is in the field of differential equations, and the University of Paris (Sorbonne) granted him the Ph.D. in 1879. In 1881, he married Miss Poulain d'Andecy, and they had four children.

Poincaré started his professional career as a mathematics lecturer at Caen University, while simultaneously also working at the Ministry of Public Service from 1881 to 1885. He climbed up the latter as a mining engineer to chief engineer in 1893 and inspector general in 1910. Beginning in 1881 and for the remainder of his career he taught at the Sorbonne, where he eventually held the chairs of Physical and Experimental Mechanics, Mathematical Physics, Theory of Probability and Celestial Mechanics and Astronomy.

In 1887, Poincaré was elected to the French Academy of Sciences. He became its president in 1906, and was elected to the Académie Française. In 1887, he also won Oscar II, King of Sweden's mathematical competition for a resolution of the three-body problem concerning the free motion of multiple orbiting bodies, and in 1893 he joined the French Bureau des Longitudes, which engaged him in the synchronization of the time around the world. On 17 July 1912, Poincaré died of an embolism after prostate surgery.

Henri Poincaré is considered 'The Last Universalist', since he excelled in all fields of the discipline as it existed in his time. He worked not only on many subjects of pure mathematics but also other subjects of mathematical physics. He was the first to present the Lorentz transformation of the theory of special relativity (1896). A nice detailed reference to his work is given in the URL address below. The fluid waves named after him are briefly mentioned in a footnote of his book 'Celestial Mechanics'; they form now an important class of waves in meteorology, oceanography and limnology.

The text is based on: http://en.wikipedia.org/wiki/Jules_Henri_Poincare

and substitution of (12.33) in (12.34) leads to the eigenvalue problem

$$\begin{aligned} &V_0'' + \left(\frac{\omega^2 - f^2}{gh_n} - k^2\right) V_0 = 0, \quad 0 \leqslant y < B, \\ &V_0 = 0, \quad \text{at} \quad y = 0 \quad \text{and} \quad y = B. \end{aligned} \tag{12.35}$$

for the distribution of V across the channel. In the above, the prime denotes differentiation with respect to y, and B is the channel width. Depending on the value of h_n ($=H$ for the barotropic mode, $=h_n$ for the baroclinic mode) (12.33), (12.35) describe the barotropic and baroclinic progressing Poincaré waves. The solution of (12.35) is

$$V_0 = \bar{V} \sin\left(\frac{m\pi y}{B}\right), \qquad (m = 1, 2, 3, \ldots) \tag{12.36}$$

with the dispersion relation

$$k^2 = \frac{\omega^2 - f^2}{gh_n} - \frac{m^2\pi^2}{B^2}, \qquad (m = 1, 2, 3, \ldots), \quad (n = 0, 1, 2, \ldots), \tag{12.37}$$

or, alternatively,

$$\omega^2 = f^2 + gh_n\left(k^2 + \frac{m^2\pi^2}{B^2}\right) > f^2 + gh_n\frac{m^2\pi^2}{B^2} =: \omega_c^2. \tag{12.38}$$

This shows that, even though ω may continuously vary, there are quantized branches of k depending upon the horizontal (m) and vertical (n) mode structure. Obviously, for real m the elevation and the velocities across the channel are oscillatory, but depending on the value of m, the squared longitudinal wavenumber k^2 may be positive or negative, and solutions in the x-direction be oscillatory or exponential; in fact, with

$$m_{\text{crit}}^2 := \frac{B^2}{\pi^2}\frac{\omega^2 - f^2}{gh_n}, \tag{12.39}$$

one has for $m < m_{\text{crit}}$ oscillatory progressive waves and for $m > m_{\text{crit}}$ exponential variation of the fields in the x-direction.

Problem 12.4 *Using (12.1) and the solution for V, given by (12.33) and (12.34) to (12.35), show that ζ and U are given by*

$$\begin{aligned} \zeta &= \left\{\alpha_m \sin\left(\frac{m\pi y}{B}\right) - \beta_m \cos\left(\frac{m\pi y}{B}\right)\right\} \mathrm{e}^{i(kx - \omega t + \pi/2)}, \\ \alpha_m &= \phi_{mn}\frac{k}{f}\bar{V}, \qquad \beta_m = \phi_{mn}\frac{m\pi}{Bf}\frac{\omega}{f}\bar{V}, \end{aligned} \tag{12.40}$$

$$U = \left\{\bar{\alpha}_m \sin\left(\frac{m\pi y}{B}\right) - \bar{\beta}_m \cos\left(\frac{m\pi y}{B}\right)\right\} e^{i(kx-\omega t+\pi/2)},$$
$$\bar{\alpha}_m = \phi_{mn}\frac{\omega}{f}\bar{V}, \qquad \bar{\beta}_m = \frac{gh}{f}\phi_{mn}\frac{m\pi}{Bf}\frac{k}{f}\bar{V}, \tag{12.41}$$

with

$$\phi_{mn} = \frac{f^2}{\omega^2 - gh_n k^2} = \frac{f^2}{f^2 + \frac{m^2\pi^2}{B^2}gh_n}. \tag{12.42}$$

Hint*: Assume (12.40)$_1$ and (12.41)$_1$ to be correct and verify the coefficients.* ◆

The results of Problem 12.4, expressed by the formulae (12.40) and (12.41) are needed to deduce the following inferences:

- For given frequency the squared wavenumber, k^2, is only positive, provided the transverse modenumber, m is sufficiently small. Thus, for

$$m < m_{\text{crit}} := \frac{B}{\pi}\sqrt{\frac{\omega^2 - f^2}{gh_n}} \quad \rightarrow \quad k^2 > 0,$$

  the Poincaré waves are oscillatory in the x-direction. On the other hand, modes with mode number

$$m > m_{\text{crit}} \quad \rightarrow \quad k^2 < 0,$$

  are exponentially evanescent as $x \rightarrow \infty$ or $x \rightarrow -\infty$. Such waves can only exist in a semi-infinite channel or a channel of finite length. These are important in the solution of the reflection problem. This point will be taken up later again.
- Poincaré waves are necessarily *super-inertial*, i.e. their frequency ω is larger than the inertial frequency f. A fortiori, in an infinite channel (for which $k^2 > 0$) ω must be larger than the *cut-off frequency*, ω_c, whose square is the sum of f^2 and the square of the frequency of the transverse oscillation, ω_c^2, in a non-rotating channel.
- In the direction of wave progression the variable V lags behind ζ and U by $\pi/2$; so, the motion is purely transverse where U and ζ vanish and purely longitudinal where ζ experiences the largest transverse variations. This can also be inferred from Fig. 12.8a.
- The progressive Poincaré wave is asymmetric across the channel width. It possesses nodal lines of ζ where

$$\tan\left(\frac{m\pi y}{B}\right) = \frac{m\pi}{B}\frac{\omega}{k}. \tag{12.43}$$

  This equation is easily seen to have no solution for $y = B/2$. A fortiori, for the uninodal case (Fig. 12.8a, $m = 1$) the nodal line must lie in the interval $0 \leq y \leq B/2$. The asymmetry increases with decreasing ω and m and increasing

wavenumber k. In Fig. 12.8a the symmetry line is denoted by CCL and the nodal line by NL.[5]

- If the U and V components are combined to form vectors, then their vector diagram is as shown in the lower panel of Fig. 12.8a. This graph also shows an asymmetry in the velocity profile with the maximum velocities arising at the position indicated by MCL. For a stationary observer, as the wave is passing his position in the direction of wave progression, the velocity vector rotates in the *clockwise direction* in the Northern hemisphere, performing a full revolution as one wavelength passes the observer.

These properties, as well as snapshots of the elevation and velocity distributions of an uninodal ($m = 1$) and trinodal ($m = 3$) Poincaré wave are shown in Fig. 12.8, panels (a) and (b), respectively. These graphs are copied from Mortimer [27]; they are direct consequences of the formulae (12.33), (12.36)–(12.38), (12.40) and (12.41). The reader is encouraged to verify with these formulae the graphs, the figure caption and the properties spelled out in the above epitomized statements.

The structure of these solutions indicates that progressive Poincaré waves, if they exist at all in lakes (we shall provide evidence in later chapters), that they may be best measured when current meters are moored at off-shore positions. At such positions one may likely catch a strong current signal. Its clockwise rotation (on the Northern hemisphere) is then a first indication for Poincaré wave behaviour, the super-inertial frequency, $\omega > f$, being a second one.

A pseudo-standing wave pattern can also be produced along the channel, if two identical, but oppositely-propagating, Poincaré waves are combined:

$$V = V_0(y)\left\{e^{i(kx-\omega t)} + e^{-i(kx-\omega t)}\right\} = 2V_0(y)\cos(kx)e^{-i\omega t}, \qquad (12.44)$$

with $V_0(y)$ given by (12.36) and corresponding formulae for ζ and U that can easily be deduced from (12.40)–(12.42). We discuss the qualitative behaviour with the aid of Figs. 12.9 and 12.10.[6] Taking the cross-channel uninodal example from Fig. 12.8a, half-wavelength portions of two such oppositely-propagating Poincaré waves are shown in Fig. 12.9a. Eight phases in one oscillation cycle of the combined wave which they produce are numbered in sequence in Fig. 12.9b. Several features are evident: The cross channel standing wave structure is maintained, but the asymmetry, described earlier for the progressive Poincaré wave (i.e. the displacement of NL and MCL from CCL), is cancelled out: an along channel 'quasi-standing' pattern emerges, dividing the wave structure into cells; clockwise rotation of the current vectors is maintained with highest speeds at the centre of the cell; the solid boundary conditions are met at the channel sides (this is simply so by construction) but

[5] This follows from the simple fact that the equation $\tan x = c$ (=constant) has a solution x_s in the interval $[0, \pi/2]$. For growing c it is obvious (make a graph!) that x_s decreases; this is equivalent to increasing asymmetry.

[6] These beautiful figures are again redrawn from Mortimer. The discussion also parallels that of Mortimer, but is not an exact quotation.

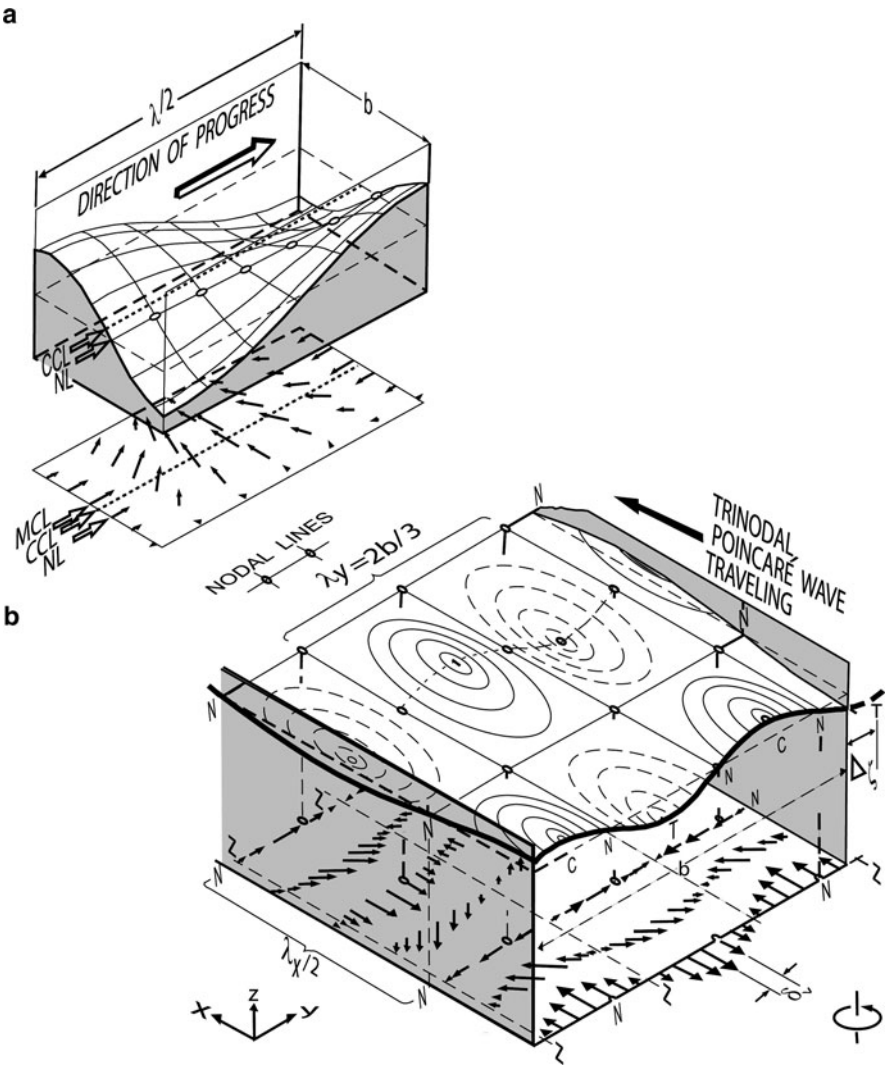

Fig. 12.8 (**a**) Progressing Poincaré wave with a uninodal ($m = 1$) cross channel distribution of the elevation ζ. Shown is a semi-period (length $\lambda/2$) with the velocity distribution in the lower *rectangle*. The *dotted line* (CCL) indicates the middle line of the channel, NL indicates the along channel nodal line shifted towards the wall to the right of the wave progression (on the Northern hemisphere); MCL marks the maximum current line. The currents along shore are sinusoidally distributed (with asymmetry) where the surface elevation shows the strongest transverse variations; it is transverse where $\zeta = 0$ across the entire channel. (**b**) Same for a trinodal progressive Poincaré wave. The nodal line of the elevation is shifted $\Delta\zeta$ to the right of the channel line, while MCL is shifted δ_v to the left of the nodal line (N) (adapted from Mortimes (1977) [27]). © Center for Great Lakes Studies (now Great Lakes WATER Institute), reproduced with permission

not at the cell ends (therefore, this is not a true standing wave, such as would be produced by a pair of oppositely-propagating plane waves in the absence of rotation); the current component in the along-shore direction at the cell end walls is small (increasingly smaller as the channel width increases) but does not fall to zero except at the centre point; the wave elevation pattern progresses clockwise around the cell-centre point (the amphidromic point P). An amphidromic point is also located at each cell corner.

Figure 12.10 illustrates four phases in one oscillation cycle of the third cross channel mode ($m = 3$) of such a pseudo-standing wave. As before, the motion has cell structure. For $t = 0$, each cell with horizontal wave lengths λ_x and λ_y is subdivided into four sub-cells in which the elevation has a high and a low, respectively, and velocities are longitudinal 'to-and-fro' as shown in the figure. A quarter period later, $t = T/4$, locations of elevation highs and lows are shifted as shown, and the current is transverse and again 'to-and-fro'. At time $t = T/2$, the elevation and velocity distributions are again as shown for $t = 0$ but with highs and lows interchanged and velocity directions reversed; a similar behaviour is seen at $t = 3T/4$ when compared with the graph for $t = T/4$. As time progresses the current vectors rotate in the clockwise direction (on the Northern hemisphere) and particle paths for a harmonic oscillation are elliptical and are traced once within a period. Finally, as before, the side boundary conditions are met, but there is no line across the channel at which the longitudinal velocity would vanish at all points for all time. Such pseudo-standing Poincaré wave solutions can therefore not hold for a closed basin.

12.5 Reflection from the End of a Channel Wall

Neither the quasi-standing Kelvin waves, see Figs. 12.3 and 12.4, nor the quasi-standing Poincaré waves, see Figs. 12.9 and 12.10, have cross channel positions at which the longitudinal velocity components would vanish at all time. So, a Kelvin wave entering a semi-infinite channel cannot be reflected at the channel end by an oppositely-propagating Kelvin wave of the same frequency. A similar statement also holds for Poincaré waves. However, it was discovered by Taylor [45] that a quasi-standing Kelvin-wave solution plus an countably infinite spectrum of reflected (backward) moving Poincaré waves allows the no-through flux condition at a transverse wall to be met.

The reflection of a Kelvin wave incident onto the end of a gulf is solved by adding to this wave a backward moving Kelvin wave of the same frequency and same wavenumber and an infinite number of backward moving, i.e. reflected Poincaré waves of the same frequency:

$$U_{\text{tot}}(x, y, \omega) = \Bigg[\left(U^{\text{in}}_{\text{Kelvin}}(x, y, \omega) + U^{\text{out}}_{\text{Kelvin}}(x, y, \omega) \right) + \sum_{m=1}^{\infty} a_m \left(U^{\text{reflected}}_{\text{Poincaré}} \right)_m (x, y, \omega) \Bigg]. \tag{12.45}$$

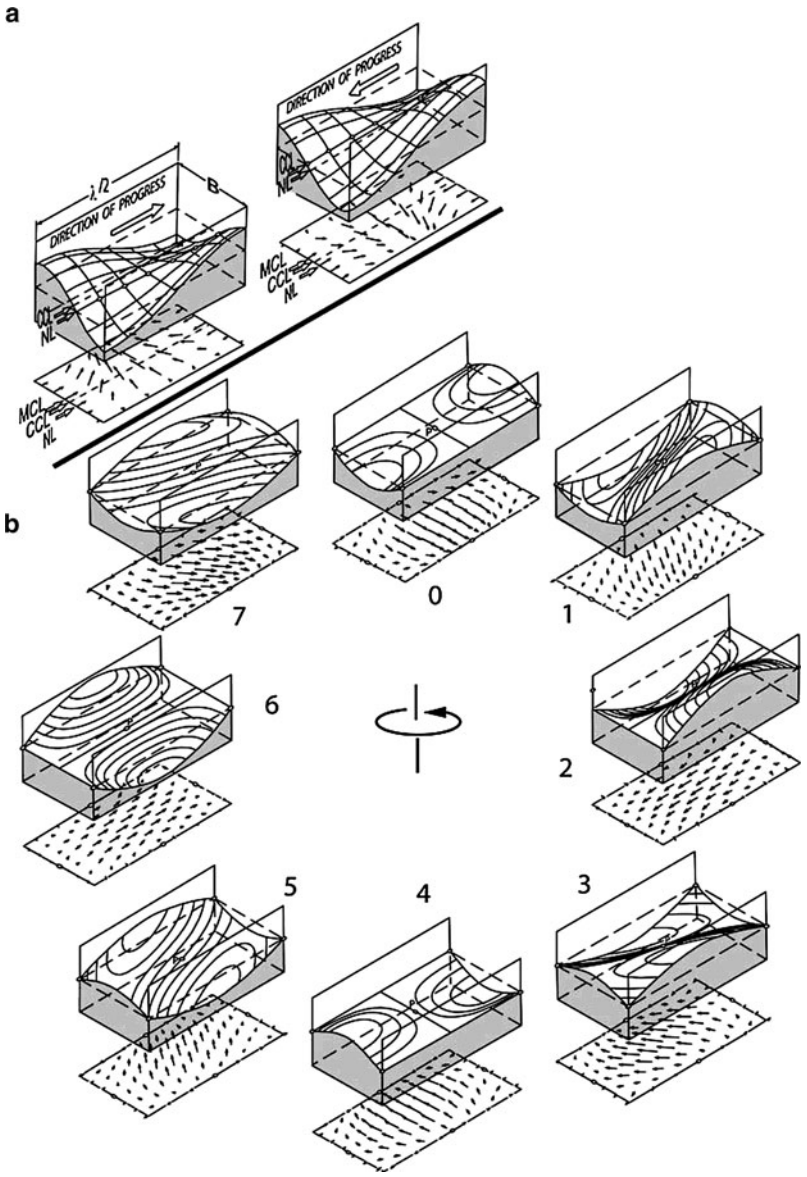

Fig. 12.9 Two oppositely-propagating but otherwise identical progressive Poincaré waves, from Fig. 12.8a and shown here in (**a**), combine to produce the amphidromic 'standing' Poincaré wave. Half-wavelength cells of the combined pseudo-standing wave are illustrated at 1/8-cycle intervals in (**b**). The combined wave, with amphidromic point P at the cell-centre, is truly standing (with one node in this case) across, but quasi-standing along the channel, as explained in the text. Wave topography can be viewed either as that of a water surface or as that of a 'thermocline' interface in a two-layered model, in which case the horizontal current vectors (illustrated beneath each cell) are those in the lower layer (adapted from Mortimer (1977) [26]). © Center for Great Lakes Studies (now Great Lakes WATER Institute), reproduced with permission

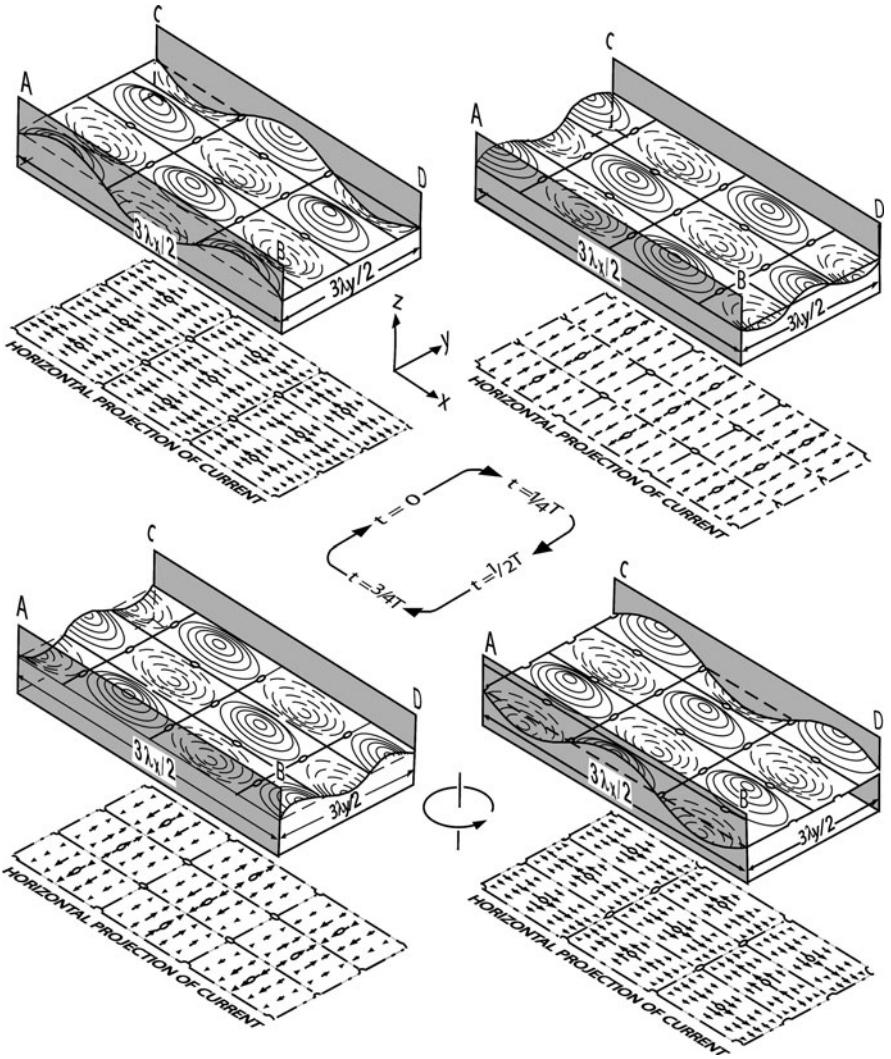

Fig. 12.10 A 'standing' Poincaré wave of cross-channel nodality 3, i.e. a trinodal equivalent of Fig. 12.9b, but with only 4 phases of the oscillation cycle shown. The same legend as for Fig. 12.9 applies; and the progressive Poincaré wave component, contributing to this combination, is illustrated in Fig. 12.9 (lower part) (adapted from Mortimer (1980) [27]). © Center for Great Lakes Studies (now Great Lakes WATER Institute), reproduced with permission

The free amplitudes, a_m, of these Poincaré waves are determined by the condition that there is no-flux through the channel wall:

$$U_{\text{tot}}(x_{\text{wall}}, y, \omega) = 0, \qquad y \in [0, B]. \tag{12.46}$$

in which the amplitude of $U^{\text{in}}_{\text{Kelvin}}$ is explicitly known. Before this equation can be exploited, the functions $U^{\text{in}}_{\text{Kelvin}}(x_{\text{wall}}, y, \omega)$ and $U^{\text{out}}_{\text{Kelvin}}(x_{\text{wall}}, y, \omega)$, which

are exponentials, must be expanded in Fourier-sine series with the elements $\sin(m\pi y/B)$, which describe the transverse variability of the functions $(U_{\text{Poincaré}}^{\text{reflected}})_m$, $m = 1, \ldots, \infty$. This then makes the right-hand side of (12.45) an infinite linear combination of $\sin(m\pi y/B)$, $m = 1, \ldots, \infty$, that must be zero. This yields an infinite number of equations for the coefficients a_m. By truncating the number of quasi-standing Poincaré modes to $m = 1, 2, \ldots, M < \infty$, the problem of the reflection of a Kelvin wave at the end of a gulf can explicitly be solved. This has been done by Taylor in 1920 [45], see Fig. 12.11.

If the incoming Kelvin wave has a frequency below the cut-off frequency, ω_c, of Poincaré waves, then the Poincaré modes are all evanescent as one moves away from the end wall. Although they are important for the satisfaction of the boundary condition, their presence is felt only near the end wall. For this reason, this type of reflection is called *complete reflection*. Figure 12.12 shows the amphidromic system and the current ellipses in a rectangular basin closed at one end as determined by Taylor.[7] The influence of the Poincaré waves is only seen near the channel end. When the frequency of the incoming wave is above the cut-off frequency, then this incoming Kelvin wave is reflected by a backward moving Kelvin wave and a finite number of reflected Poincaré waves, of which the presence is recognized in the *entire* basin, plus an infinite number of Poincaré waves, which are exponentially evanescent. Reflections are then called *incomplete*.

An example of the amphidrome modification near the closed end is shown for this case in Fig. 12.13 for higher frequencies, the amplitude pattern diverges from that due to a pair of Kelvin waves, acquiring more and more lateral structure as more and more Poincaré modes are reflected from the closed end of the channel. Figure 12.13, taken from [2] shows the distortion of the amphidromes with increasing frequencies.

12.6 Shallow Water Waves in a Rectangle of Constant Depth

The above description also makes clear, in principle, how quasi-standing shallow water waves can be treated in a (alongated) rectangular basin of constant depth. The longitudinal velocity U could be composed of a pair of a forward and backward moving Kelvin waves plus two infinite sums of Poincaré waves, of which one set is reflected at the front wall, $x = x_{\text{front}}$, the other at the back wall, $x = x_{\text{back}}$. Consequently,

$$U_{\text{tot}}(x, y, \omega) = U_{\text{Kelvin}}^{\text{forward}}(x, y, \omega) + U_{\text{Kelvin}}^{\text{backward}}(x, y, \omega) + \sum_{m=1}^{\infty} a_m \left(U_{\text{Poincaré}}^{\text{reflected}}\right)_m^{\text{front}} + \sum_{m=1}^{\infty} b_m \left(U_{\text{Poincaré}}^{\text{reflected}}\right)_m^{\text{back}} \tag{12.47}$$

[7] For a biographical sketch see Fig. 12.11.

Fig. 12.11 Geoffrey Ingram Taylor (1886–1975) (portrait from http://en.wikipedia.org/) and wavy Taylor vortices in the gap between concentrical cylinders, reproduced in laboratory (photo: K.G. Roesner, http://www.kgroesner.de/).

Geoffrey Ingram Taylor (7 March 1886, St. John's Wood, London; 27 June 1975, Cambridge, England) was an applied mathematician and physicist specialized in fluid dynamics and wave theory. His father was an artist, and his mother, Margaret Boole, came from a family of mathematicians. Taylor followed her footsteps studying mathematics at Trinity College, Cambridge University. With work on shock waves, 1909, he won the Smith's Prize and was elected a fellow at Trinity College in 1910 and a Reader in Dynamical Meteorology in the following year. His publication 'Turbulent motion in fluids' won him the Adams Prize in 1915.

During World War II Taylor was sent to the Royal Aircraft Factory in Farnborough to apply his knowledge in aerodynamics and meteorology to aircraft design; there he worked on stress in propeller shafts, learned to fly airplanes and made parachute jumps. After World War I, he returned to Cambridge, where he worked on rotating fluids. It is at this time when his paper on the reflection of a Kelvin wave at the end of a gulf with rectangular cross-section was written, which required a combination of the incoming Kelvin wave with an outgoing Kelvin wave and an infinite number of Poincaré waves. In 1915, Taylor was appointed a Royal Society research professorship. This freed him from teaching and led to a period of very active research on both fluid and solid mechanics (also of crystalline materials), including statistical approaches to turbulence. In 1934, Taylor realized – almost simultaneously with Polanyi and Orovan – that the plastic deformation of ductile material could be explained with the theory of dislocations.

During World War II Taylor worked on applications of his expertise to military problems, among others the propagation of blast waves in air and water. His prediction of the strength of the atomic explosion performed as part of the Manhattan Project in the desert of New Mexico is well known. In 1944, he was also knighted.

Taylor continued his research after the war, working on the development of supersonic aircraft. He officially retired in 1952 from active duty; he continued to work for twenty more years. He wrote his final paper on electrical activity in thunderstorms in 1969, when he was 83. He suffered a stroke in 1972 and died on 27 June 1975.

The text is based on: http://en.wikipedia.org/wiki/Geoffrey-Ingram_Taylor

Further references:

B. Pippard: Sir Geoffrey Taylor, Physics Today, Sept 1975, p 67
G. Batchelor. The life and legacy of G.I. Taylor. Cambridge University Press, 1994. ISBN 0-521-46121-9.

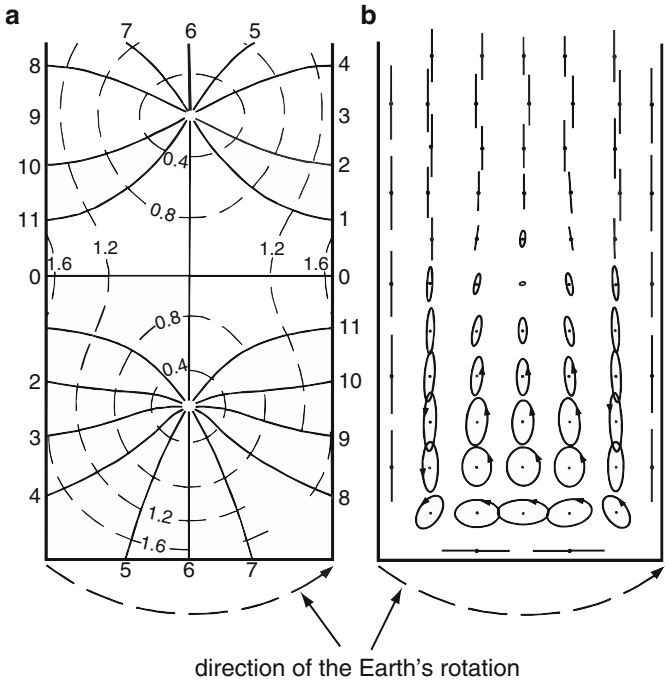

Fig. 12.12 Amphidromic system in a rectangular basin closed at one end. (**a**) co-tidal and co-range lines; (**b**) current ellipses, illustrating pure reflection. The *arrow* at the *bottom* indicates the rotation of the Earth, after G.I. Taylor [45] (1920). © London Mathematical Society, reproduced with permission

must hold, subject to the reflection conditions

$$U_{\text{tot}}(x_{\text{front}}, y, \omega) = 0, \qquad U_{\text{tot}}(x_{\text{back}}, y, \omega) = 0. \tag{12.48}$$

In addition, the periodicity condition

$$|x_{\text{back}} - x_{\text{front}}| = p\pi \qquad (p = 1, 2, \dots)$$

must hold. This defines the dispersion relation and hence the frequencies which are now quantized and isolated.

Upon Fourier expansion of $U_{\text{Kelvin}}^{\text{forward}}(x, y, \omega)$ and $U_{\text{Kelvin}}^{\text{backward}}(x, y, \omega)$ in y at $x = x_{\text{front}}$ and $x = x_{\text{back}}$, equations (12.48) form a linear homogeneous set of $2M$ ($M \to \infty$) equations for the amplitude coefficients a_m and b_m ($m = 1, \dots, M$). Setting the determinant of this system of equations equal to zero guarantees non-trivial solutions and determines the eigenfrequencies ω_{mp}, which are now quantized and isolated (m gives the mode number in the y-direction, p that in the x-direction). The eigenfrequencies carry three integer indices ω_{nmp}, $n = 0, 1, 2, \dots$ to identify

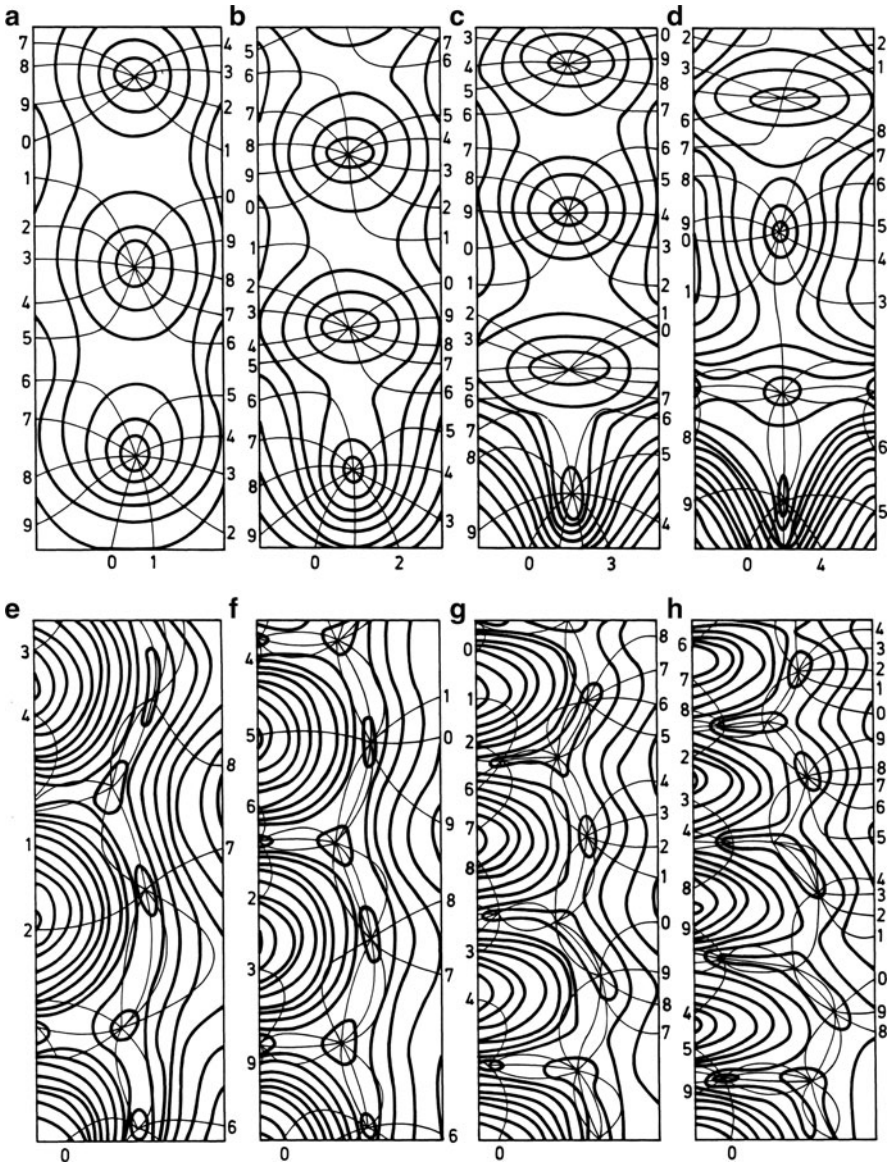

Fig. 12.13 Influence of the frequency on the amphidromic pattern for Kelvin waves reflected from the closed end of a channel. The closed end of the channel is at the *bottom* of the panels, and lines of constant phase and amplitude are labeled as *thin* and *heavy solid lines*. The width of the channel is $B = 500\,\mathrm{km}$, the latitude 54.46°N and the cut-off period is $T_c = 2\pi/\omega_c$ is equal to 8.46 h for $m = 1$. The Kelvin wave period decreases from panels (**a**)–(**h**) as follows: (**a**): 12.0 h; (**b**): 10.0 h; (**c**): 9.0 h; (**d**): 8.6 h; (**e**): 8.1 h; (**f**): 8.0 h; (**g**): 7.0 h; (**h**): 6.0 h. In panels (**a**)–(**d**), all Poincaré waves are evanescent, and at sufficiently large distance from the reflecting end the interference pattern becomes that of a pair of Kelvin waves travelling in opposite directions. In the last four panels (**e**)–(**h**), the $m = 1$ Poincaré mode propagates and the field far from the reflecting end consists of two Kelvin waves and a Poincaré wave. The asymmetry introduced by the reflected Poincaré wave is evident in the four panels (adapted from Brown (1973) [2]). © J. Marine Research, reproduced with permission

the barotropic vertical mode, and an infinity of baroclinic vertical modes, $m = 1, 2, 3, \ldots$ to identify the transverse and $p = 1, 2, 3, \ldots$ the longitudinal basin-scale modes.

Of course, such a solution technique is complicated for practical applications. But it is at least helpful to physically interpret free wave dynamics in oblong basins, strictly only for a homogeneous fluid in a rectangular basin. If this rectangle is long, then the eigenfrequency is below the cut-off frequency, at least for some of the lowest order modes. The quasi-standing Kelvin waves at these frequencies are complemented by Poincaré waves that are reflected at the two end cross sections and are evanescent as one moves away from these cross sections into the interior of the basin. These waves can be termed *Kelvin-like*, because 'Poincaré-type perturbations' are only appreciably excited at the long ends. Any eigenfrequency above the cut-off frequency $\omega_{mp} > \omega_c$ will generate Poincaré solutions which are oscillatory throughout the basin. Current measurements at off-shore moorings will most likely have the potential to record these Poincaré-type solutions. For more compact rectangles, say squares, the mode structure generally fills the entire rectangle and Kelvin- and Poincaré-type wave forms are intermixed.

12.6.1 Frequency Relation

The mathematical construction of eigensolutions for homogeneous water in rotating rectangles of constant depth has a relatively long history beginning with Lord Rayleigh [41, 42] and culminating with the doctoral dissertation by Rao [39] and its condensed version 'Free gravity oscillations in rotating rectangular basins', published in the Journal of Fluid Mechanics [40]. Rao writes: "Rayleigh's treatment was restricted to the case where the rotation speed[8] Ω was small compared with the speed ω of the oscillation and was later corrected by Proudman [34]. Taylor [45] gave the first complete solution (valid for any Ω) for the free oscillations in a rectangular basin. Some of his conclusions were criticized by Jeffreys [11], who pointed out that there was a double infinity of modes in the rotating case and that there might be modes travelling in both directions of the basin (with and against the rotation [Ω]). Defant [8] subsequently gave an approximate method of simplifying Taylor's analysis.

Lamb [16] gave an approximation to the slowest speed by a different method. His result is

$$(\omega^2 - \nu_1^2)(\omega^2 - \nu_2^2) = \left(\frac{4}{\pi}\right)^4 \Omega^2 \omega^2, \tag{12.49}$$

where ν_1 and ν_2 are the speeds of the slowest longitudinal and slowest transverse modes in the zero-rotation case (see, Chap. 7, Sect. 7.3 in Volume I).[9] In the special

[8] Rao calls 'angular velocity' 'rotation speed' or simply 'speed'.

[9] The frequency ν_j in the zero-rotation limit, $\Omega = 0$, is

case of a square, $\nu_1 = \nu_2$, and (12.49) reduces to

$$\omega - \nu_1 = \pm \frac{8}{\pi^2} \Omega. \tag{12.50}$$

This agrees with the result of Rayleigh [41] as corrected by Proudman [34].[10] Lamb also showed that there are wave systems travelling in both directions around the basin. Goldsbrough [10] solved the problem formally for any Ω, but approximated results to small Ω. He confirmed Lamb's results.

Corkan and Doodson [7] treated the case of a square sea by direct numerical integration of the dynamic equations and obtained frequency values at a few rotation speeds for the slowest positively (in the same direction as the rotation) and negatively (opposite the direction of rotation) propagating anti-symmetric modes. [...]. They found that negative waves are 'unstable' in the sense that these waves are transformed into positive waves at high rotations.

[...] Van Danzig and Lauwerier [46] [...] obtained a solution valid for any Ω but approximated the results to small values of Ω. The explicit results obtained by them are

$$\frac{\omega}{\nu_1} = 1 \pm \left(\frac{4}{\pi^2}\right) \frac{2\Omega}{\nu_1} + 0.138 \left(\frac{2\Omega}{\nu_1}\right)^2 + \cdots \tag{12.53}$$

for a square. The minus sign refers to the slowest positive anti-symmetric mode and the plus sign to the negative mode. This extends the approximation (12.50) of Lamb and Rayleigh by one more order in Ω. For a (2×1)-rectangle Van␣Danzig and Lauwerier give an explicit result only for the lowest order in Ω for the slowest positive anti-symmetric mode

$$\nu_{kl} = \pi \left\{ \left[(k/a)^2 + (l/b)^2 \right] g h_n \right\}^{1/2}, \quad \nu_1 := \min_{(k,l)} \nu_{kl},$$

where a and b are the side lengths of the rectangle. For $a > b$, ν_1 is obtained for $(k, l) = (1, 0)$; g is the acceleration due to gravity and h_n the equivalent depth for barotropic ($h_n = H$) or baroclinc modes.

[10] Rao is not very precise here. The result (12.50) is an approximation to (12.49) if $\nu_1 = \nu_2$. Indeed, for $\nu_1 = \nu_2$, (12.49) becomes

$$(\omega^2 - \nu_1^2) = \pm (\tfrac{4}{\pi})^2 \Omega \omega, \tag{12.51}$$

which, for $\Omega \to 0$ allows construction of the iterative solution

$$\omega_n = \nu_1 \sqrt{1 \pm (\tfrac{4}{\pi})^2 \tfrac{\Omega \omega_{n-1}}{\nu_1^2}}$$

with the first two iterates

$$\omega_0 = \nu_1, \quad \omega_1 = \nu_1 \sqrt{1 \pm (\tfrac{4}{\pi})^2 \tfrac{\Omega}{\nu_1}} \sim \nu_1 \pm \tfrac{8}{\pi^2} \Omega. \tag{12.52}$$

Lamb [17] (1932, p. 313, (22)) writes that (12.52) is approximate for $\Omega \to 0$.

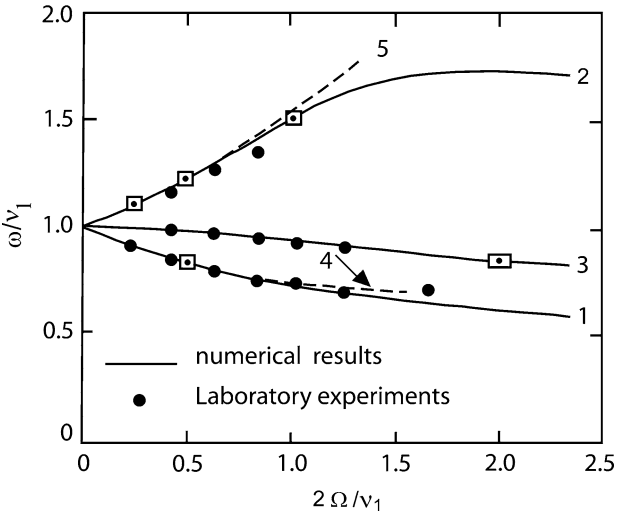

Fig. 12.14 Dimensionless frequency of oscillation (ω/ν_1) in *square* and *rectangular* basins of uniform depth, as a function of the dimensionless rotation speed ($2\,\Omega/\nu_1$). The *solid curves* are the results of Rao [40]: curves 1 and 2 correspond to the slowest positive and negative modes in a square and curve 3 to the slowest positive mode in a (2 × 1)-rectangle. Also shown are Corkan and Doodson's [7] results for the *square* (⊡) and Taylor's [45] results for a (2 × 1)-rectangle (⊡). Curves 4 and 5 show the results of Van Danzig and Lauwerier's [46] perturbation analysis for the slowest positive and negative modes in a square, valid to second order terms in ($2\,\Omega/\nu_1$). *Full circles* are obtained from laboratory experiments. The figure is a combination of two figures by Rao [40]. © J. Fluid Mech. Cambridge University Press, reproduced with permission

$$\frac{\omega}{\nu_1} = 1 - 0.302\left(\frac{2\Omega}{\nu_1}\right)^2, \tag{12.54}$$

which agrees with the result of Rayleigh [42] as corrected by Proudman [34], when specialized to the case of a (2 × 1)-rectangle", [40].

This is Rao's summary of the history of the problem prior to his work. He [40] determined the eigenfrequencies of the gravitational oscillations of a homogeneous fluid in a rectangle for any value of the rotation frequency. He conducted computations for the frequencies and modal structures of several of the lowest symmetric and anti-symmetric modes in a square and a (2 × 1)-rectangle. Figure 12.14 is a combined reproduction of two of his figures showing the frequency results for the slowest positive and negative modes in a square and the slowest positive anti-symmetric mode in a (2 × 1)-rectangle. In this diagram, the frequencies ω and Ω are non-dimensionalized by ν_1, the slowest zero-rotation frequency. For detailed explanations we refer to the figure caption.

Rao also determined the modal frequencies for other modes higher than those shown in Fig. 12.14. A number of these are shown in Fig. 12.15 for squares on the left and (2 × 1)-rectangles on the right. 'This diagram exhibits the effect of rotation on all modes of the zero-rotation spectrum with frequencies in the range $\omega/\nu_1 < 4$

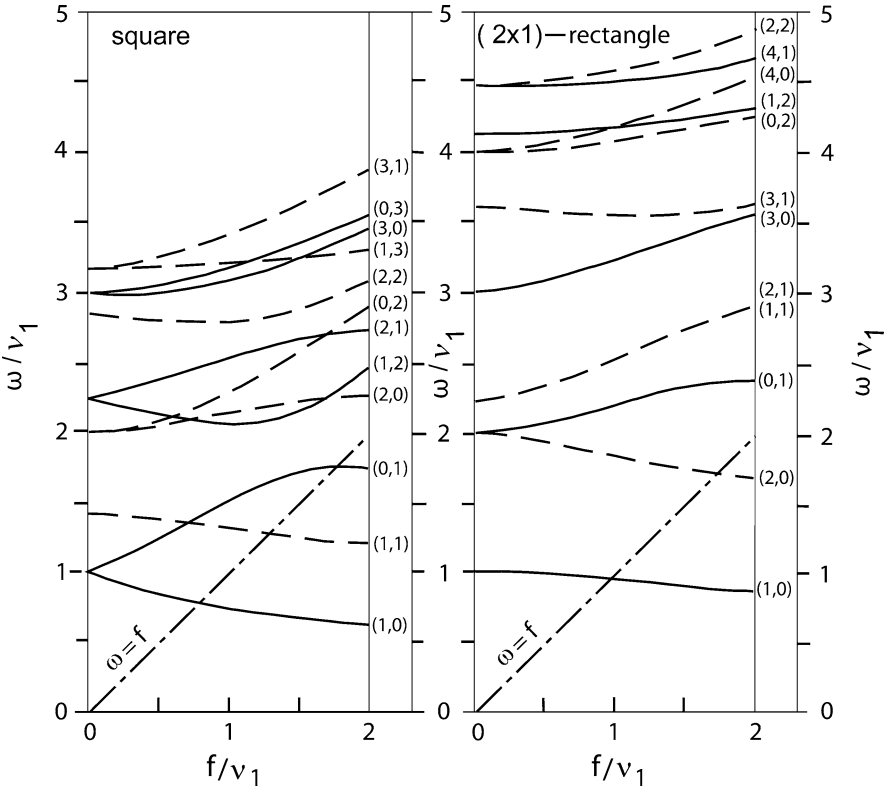

Fig. 12.15 Frequency (ω/ν_1) vs. rotation speed (f/ν_1) ($f = 2\,\Omega \sin\phi$) for various modes in a *square* (*left*) and (2×1)-rectangular (*right*) basin. *Solid* (*dashed*) *lines* correspond to anti-symmetric (symmetric) modes. Modes are identified by (k, l). For *squares*, in the non-rotation limit, some are doubly valued. The *dashed-dotted lines* separate the regimes of sub- and super-inertial frequencies (redrawn from [40]). © J. Fluid Mech. Cambridge University Press, reproduced with permission

for the square and $\omega/\nu_1 < 5$ for the rectangle. The solid lines correspond to anti-symmetric modes and the dashed lines to symmetric modes. The slowest mode of all is the anti-symmetric mode $(1, 0)$ which consists of one wave travelling in the positive direction of the basin; that is, in the same direction as that of rotation' [40]. The figure shows the $[(1, 0), (0, 1)]$, $[(1, 2), (2, 1)]$, $[(3, 0), (0, 3)]$ modes in a square; these are examples of doublets in the zero-rotation frequency spectrum for anti-symmetric modes. Similarly, the $[(2, 0), (0, 2)]$, $[(1, 3), (3, 1)]$ modes in a square are such doublets for anti-symmetric modes. These multiplets in the zero-rotation spectrum are split into distinct frequencies on the introduction of rotation. For the modes of the (2×1)-rectangle the zero-rotation limits of the frequencies are, however, all singlets. Moreover, note that square and (2×1)-rectangle have certain modes whose eigenfrequencies are sub-inertial ($\omega < f$) if the rotation speed Ω is sufficiently

large. Most frequencies are, however, super-inertial. Rao also demonstrates that with increasing aspect ratio of the rectangle

- The effect of the rotation on the frequencies of the few lowest longitudinal oscillations becomes less important and in the limit as $a/b \to \infty$, these oscillations are transformed into Kelvin waves,
- Purely transverse modes assume the form of waves with horizontal crests and, thus, approach in the limit as $a/b \to \infty$ Sverdrup waves, for which $\omega^2 = \nu^2 + f^2$.

12.6.2 Modal Structure

The elevation field of the free surface (or the displacement in an equivalent depth model) ζ may be written as

$$\zeta(x, y, t) = A(x, y) \cos[\omega t - \theta(x, y)]. \tag{12.55}$$

Here, $A(x, y)$ is the amplitude and $\theta(x, y)$ is the phase of high water at a point (x, y). Graphical representations of the modal structure are usually given in terms of co-amplitude lines (contours of A) and co-tidal lines (contours of θ) with a particular normalization of the amplitude function. Rao put the average value of A^2 over the basin equal to 100 in all cases. (It is generally more customary in practice to set the maximum value of A equal to 100.) In Figs. 12.16–12.19, the co-tidal lines are drawn at one-twelfth period, i.e. in θ-increments of 30° through the range $0 \leq \theta \leq 360°$. In what follows, we take $\Omega > 0$, that is the rotation of the basin is positive (on the Northern hemisphere, counterclockwise) and each figure shows results for a square and for a (2×1)-rectangle.

"The slowest positively propagating mode $(1, 0)$ is presented in Fig. 12.16, for rotation speed $f/\nu_1 = 2$. This mode, in both basins, consists of one wave travelling in the positive (counter-clockwise) direction about an amphidromic point at the centre of the basin. The amplitude of oscillation is zero at the amphidromic point and increases outward; it reaches a maximum value at the corners. This structure of the mode remains essentially unchanged with increasing rotation. In the sequel we refer to an amphidromic point as positive or negative according as the associated wave system rotates in the positive (counter-clockwise) or negative (clockwise sense). Open circles represent positive amphidromes, full circles will identify negative amphidromes.

Figure 12.17a–c represent the slowest negative mode at different values of f/ν_1 (note they are not the same for squares and (2×1)-rectangles). Taking first the case of a square, we see that for low rotation this mode consists of one wave travelling in the clockwise direction about an amphidromic point at the centre of the basin, as shown in Fig. 12.17a. As the rotation increases, the structure of the mode changes, in marked contrast to the slowest positive mode. In particular, for a certain value of f/ν_1, (not precisely determined [...] but in the range $1.0 < f/\nu_1 < 1.1$) a

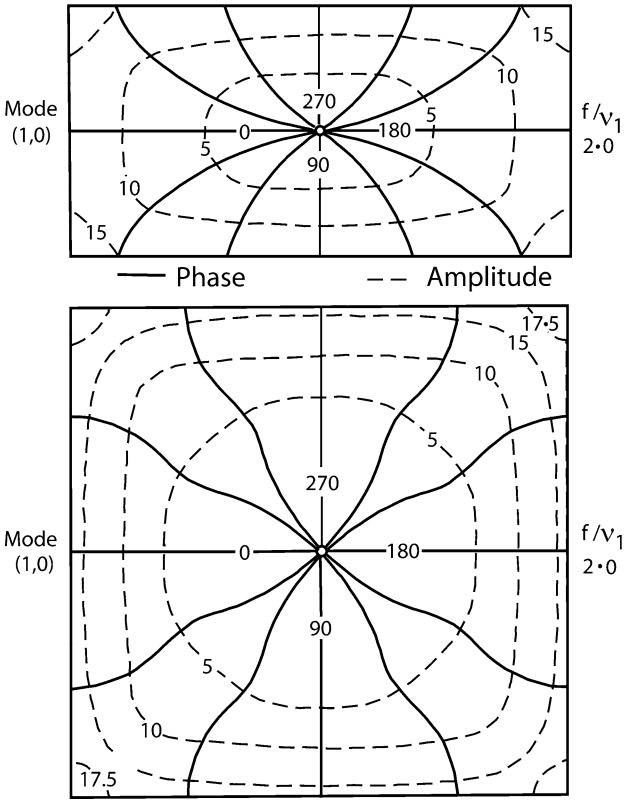

Fig. 12.16 Structure of the slowest positive amphidromic mode in a (2 × 1)-rectangle and in a *square*. In this and the following diagrams, *open circles* represent a positive amphidromic point, whilst *full circles* represent a negative amphidromic system (redrawn from [40]). © J. Fluid Mech. Cambridge University Press, reproduced with permission

system of four amphidromic points enters the basin from the boundaries as shown in Fig. 12.17b. As the rotation increases, these points move towards the centre of the basin, and the positive wave systems associated with them eventually dominate over the central negative wave. Even though there are five amphidromic points, the arrangement is such that the central negative-wave region is surrounded by a system of three waves which travel around the boundaries in a positive direction, as can be seen by careful examination of the co-tidal lines of Fig. 12.17b. As the rotation increases, the inner negative wave region contracts and the amplitude of this wave decreases. At $f/\nu_1 = 1.5$ (Fig. 12.17c) the amplitude of the negative wave is practically zero [...].

The upper parts of Fig. 12.17a–c show the slowest amphidromic mode in a (2 × 1)-rectangle. In this case, even at the low rotation $f/\nu_1 = 0.1$, there is one negative wave system (Fig. 12.17a) at the centre of the basin and two positive wave systems with amphidromic points located one on either side of the centre

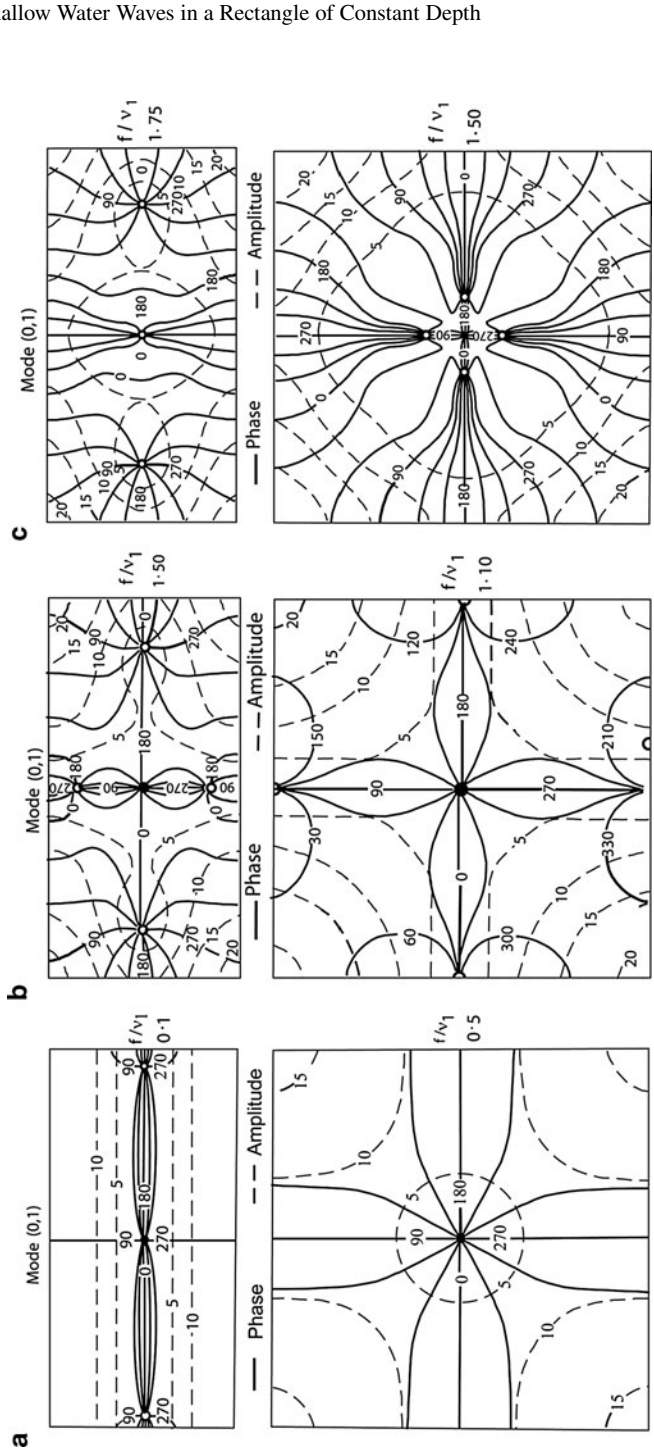

Fig. 12.17 The slowest negative anti-symmetric mode (0, 1) at the rotation speed $f/\nu_1 = (0.5, 0.1)$ (**a**), $f/\nu_1 = (1.10, 1.50)$ (**b**) and $f/\nu_1 = (1.50, 1.75)$ (**c**), for a *square* and (2×1)-rectangle, respectively (redrawn from [40]). © J. Fluid Mech. Cambridge University Press, reproduced with permission

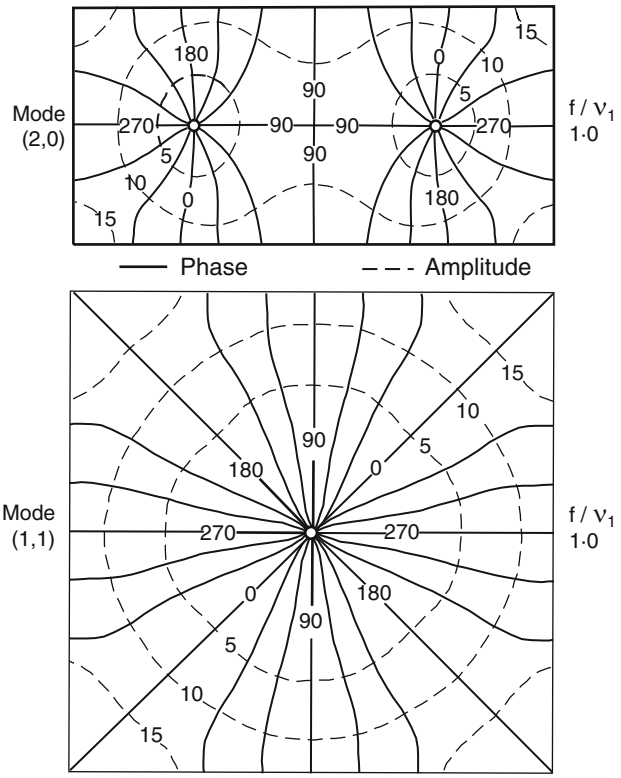

Fig. 12.18 The slowest positive symmetric mode for a *square* and a (2×1) – real angle and $f/\nu_1 = 1.0$ (redrawn from [40]). © J. Fluid Mech. Cambridge University Press, reproduced with permission

of the longitudinal axis. As the rotation is increased (Fig. 12.17b), two more positive amphidromic systems enter the basin, one on either side of the centre on the transversal axis, for a value of f/ν_1 in the range $1.4 < f/\nu_1 < 1.5$. Finally, by $f/\nu_1 = 1.75$ (Fig. 12.17c) the central negative amphidromic system disappears and one has three positive waves in the basin with amphidromic points located on the longitudinal axis" [40].

Next, consider the symmetric modes. In Fig. 12.18, we have displayed the slowest positive modes belonging to this family in a square and a (2×1)-rectangle for $f/\nu_1 = 1.0$. "The system consists of two waves travelling in the positive direction and the structure remains unchanged with increasing rotation. In the square, both waves travel around an amphidromic point at the centre of the basin, whereas in the (2×1)-rectangle, each wave has a separate amphidromic point located symmetrically with respect to the centre on the longitudinal axis. At $f/\nu_1 = 1.0$, Fig. 12.19a shows that the corresponding negatively propagating modes also consist of two waves. Just as [for] the first negative anti-symmetric mode, these modes undergo a

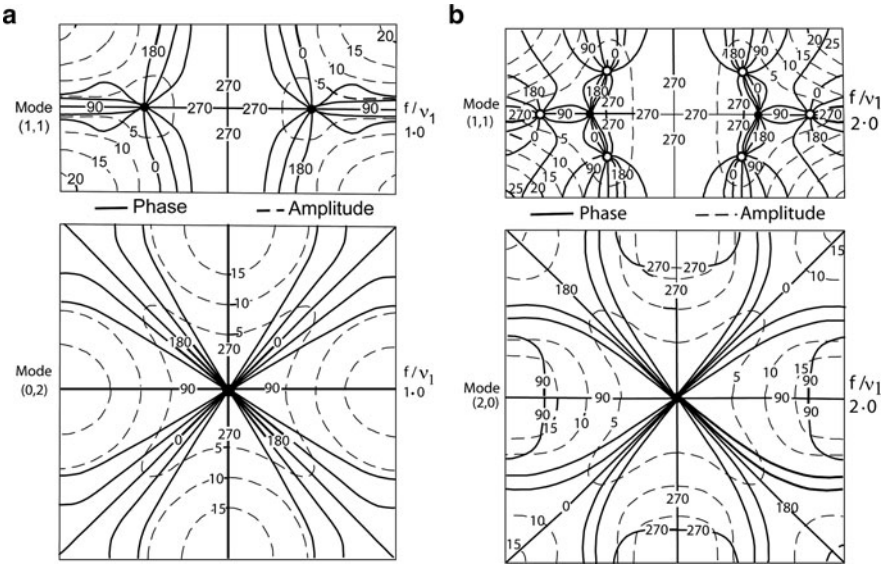

Fig. 12.19 The slowest negative symmetric mode at the rotation speeds $f/\nu_1 = 1.0$ (**a**) and $f/\nu_1 = 2.0$ (**b**) (redrawn from [40]). © J. Fluid Mech. Cambridge University Press, reproduced with permission

change in structure with increase in rotation: positive amphidromic points external to the basin gradually move across the boundary into the basin. The situation when $f/\nu_1 = 2.0$ is shown in Fig. 12.19b" [40].

The higher modes become very complicated in their structure, so we refrain from presenting them in any detail here, except to mention that negative amphidromic systems always appear to be 'unstable', that is, to give way to positive amphidromic systems.

12.6.3 Additional Results

Rao [40] also demonstrated that in long rectangles the determination of the (1, 0)-amphidromic system by 'Kelvin-wave dynamics' is a good approximation to the exact solution, see Problem 12.1. The surface displacement can be written as shown in (12.55) with

$$A(x,y) \equiv \left[\cos^2\left(\frac{\pi x}{a}\right) + \frac{f^2}{gh_n}\left(y-\frac{b}{2}\right)^2 \sin^2\left(\frac{\pi x}{a}\right)\right]^{1/2},$$
$$\theta(x,y) \equiv \arctan\left[\frac{f}{gh_n}\left(y-\frac{b}{2}\right)\tan\left(\frac{\pi x}{a}\right)\right]. \tag{12.56}$$

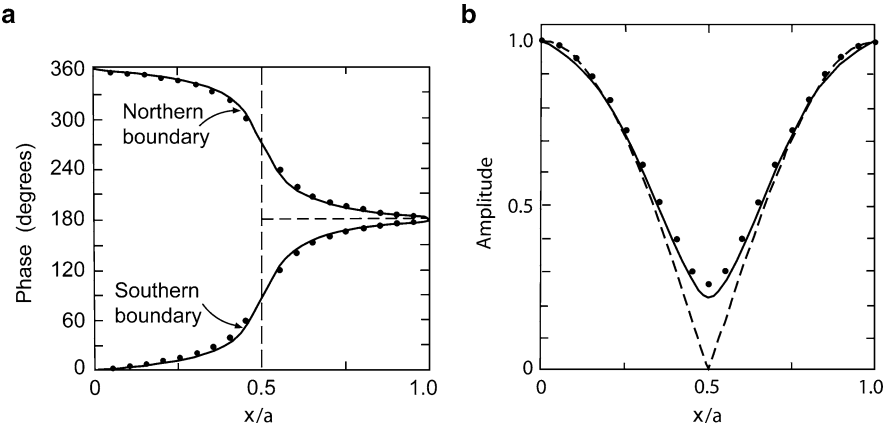

Fig. 12.20 Amplitude (**a**) and phase of high water (**b**) for the slowest longitudinal oscillation on the boundaries of a (6×1)-rectangular basin with rotation speed $f/\nu_1 = 1$. The *solid line* is the exact calculation, the *dots* are the results of applying the Kelvin-wave hypothesis and the *dashed line* is the situation with zero rotation (redrawn from two figures of [40]). © J. Fluid Mech. Cambridge University Press, reproduced with permission

Rao [40] plotted the amplitudes and phases of high water along the North and South boundaries (parallel to the x-axis) of the basin obtained from the exact analysis of the problem and from the above Kelvin-wave approximation for a (6×1)-rectangle with a rotation speed $f/\nu_1 = 1.0$, see Fig. 12.20. The figure also shows the situation in the non-rotating case. It provides ample demonstration of the accuracy of the approximate solution obtained by Kelvin-wave dynamics.

Rao also presented an analysis of the energy partition. In the zero-rotation case, the total energy is partitioned equally between potential and kinetic energy (i.e. the integrals of these energy densities over the rectangle and over a time period are the same. The motion is in this case irrotational. In the rotating case, the kinetic energy of the motion is resolved into two additive contributions due to irrotational and rotational motion, and the equipartition property is lost.

Rao also performed laboratory experiments with a rotating square tank of dimensions $a = b = 48.69\,\text{cm}$ and a water depth $H = 0.125\,a$. Distilled water was used with an organic tracer of 10^{-3} concentration added to reduce surface tension. Rao measured upper and lower bounds for the frequency (ω/ν) at rotation speeds of the tank $\Omega = 0, 0.5, 1.0, \ldots, 4.0\,\text{rad}\,\text{s}^{-1}$. The full circles in Fig. 12.20 are the results for the slowest negative anti-symmetric mode $(1, 0)$, the slowest positive anti-symmetric mode $(0, 1)$ and the slowest positive symmetric mode $(1, 1)$. Agreement between the experimental and the theoretical frequency is very good; 'the maximum error obtained is 6% for the $(1, 0)$ mode at $\Omega = 4\,\text{rad}\,\text{s}^{-1}$. However, at this speed of rotation the free surface assumes a very pronounced parabolic shape, and it is not surprising that results of the planar theory (which ignores the free surface curvature) do not (in this case) agree well with experimental results'.

It may, further, be mentioned that the solutions for the gravitational oscillations of a homogeneous fluid in a rectangular basin of constant depth have been numerically determined by Rao [39] by a method, originally designed by Proudman [33]. The method is to additively decompose the horizontal transport vector $\boldsymbol{V}$ into two contributions, $\boldsymbol{V} = \boldsymbol{V}^{\phi} + \boldsymbol{V}^{\psi}$, such that $\boldsymbol{V}^{\phi} = -\nabla\phi$ is irrotational and $\boldsymbol{V}^{\psi} = h^{-1}\boldsymbol{k} \times \nabla\psi$, is solenoidal. (Here, $\boldsymbol{k}$ is a unit normal vector pointing into the z-direction and $h = H/\bar{H}$ is the non-dimensional ratio of the actual depth H and the basin mean depth). Two selfadjoint boundary value problems for the potential ϕ and the stream function ψ then define function sets $\{\phi_\alpha\}$ and $\{\psi_\alpha\}$ ($\alpha = 1, 2, \ldots, \infty$) which satisfy the no-flux condition through the boundary, are complete in the set of square integrable functions and can be used to define expansions for $\boldsymbol{V}^{\phi}$, $\boldsymbol{V}^{\psi}$ and ζ. The governing equations (12.1) are, finally, used to derive an infinite system of ordinary differential equations for the three-times-infinite expansion coefficients, which are only functions of the time. This elegant integration procedure is in principle applicable to any closed geometry and was applied by Rao to computationally determine the solutions for rectangular basins of constant depth. For details see [33, 39, 40] and the Appendix to this chapter.

12.7 A 'Second-Class' of Inertial Waves: 'Inertial Waves Proper'

In the preceding analysis, gravity waves on the rotating Earth were studied as plane waves in an infinite medium, as bounded waves in a semi-infinite space, in channels and enclosed basins. The construction of solutions to these waves was attributed to Sverdrup, Kelvin, Taylor, and Poincaré. Gravity was important in their description. It entered the equations for a homogeneous fluid via the deformation of the free surface, as the associated water column establishes via gravity the necessary pressure gradient that drives the oscillations. When applying the rigid lid assumption, this gravity-induced pressure is absent and these barotropic waves cannot exist.

The loss of existence of these waves when the fluid is confined to a rigid container is due to the assumption that the pressure is decomposed into the gravity dependent quasistatic external contribution plus a dynamic contribution induced by the internal motion, which is ignored. Another class of long Sverdrup, Kelvin and Poincaré waves should, therefore, also exist when the rigid lid assumption is imposed (the container is rigid and completely filled by the fluid of uniform density), but these internal dynamic pressure gradients are not ignored in the momentum equations. These waves are also long, but they are considerably shorter than the gravity waves, with wave lengths of the container dimensions (the depth) or shorter. In a homogeneous fluid in a basin of constant depth, these waves and oscillations have been thoroughly studied by Maas [21]. His work also gives an extensive literature review. These waves are also called 'inertial waves', because they are only driven by the rotation of the container, which, in the application here is vertical

to the confining container bottom and lid.[11] They have a frequency which may be different from the rotation frequency f. (Note that in Sect. 12.6.3 oscillations were called inertial when the circular frequency agreed with the inertial frequency.) This is the reason, why we use the attribute 'second class'. Maas occasionally uses the term 'inertial waves proper', which is probably more appropriate, since the attribute 'second class' is commonly an identifier for Rossby-type vorticity waves. He also states: 'Inertial waves proper are often neglected in thin-fluid systems as ocean and atmosphere because they have small wave lengths, and because of the stratification of these media. The scale length of inertial waves is the depth-scale of the vertical mode considered, which is therefore small, making the wave more susceptible to viscous degradation. Relative to this length scale, long waves thus appear only when their frequencies approach the inertial frequency f. However, for 'fat bodies' [20], like the Earth's core [and] stellar interiors [...] it is natural to consider these waves over a broader subinertial frequency range'. Suggestions on the oceanic relevance appeared in the literature, so that their occurrence in spectra of current meters and thermistor registrations for lake measurements is worth being scrutinized. Most probable is their observation in large and deep ice covered lakes such as Lake Vostok or Lake Baikal in winter.

Very briefly, solutions for the axial cylinder were found by Kelvin [13]. Bryan [3] gave the analysis of exact solutions in an axial spheroid to which Rieutord et al. [43] constructed the toroidal modes, lacking radial displacements. Maas analyzed infinite and semi-infinite channels of constant width and depth and rectangular boxes, all with the angular velocity parallel to the edges, see Fig. 12.21.

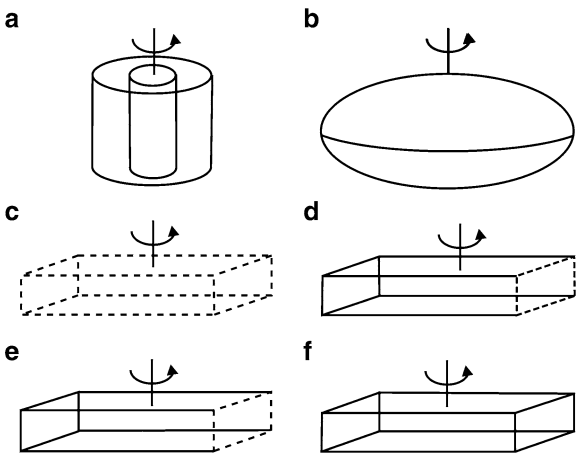

Fig. 12.21 Geometries for which 'inertial waves proper' have been constructed (**a**) axial cylindrical can or annulus, (**b**) axial spheroid, (**c**) infinite layer compressed between two parallel planes, (**d**) infinite channel, (**e**) semi-infinite duct, and (**f**) rectangular box. In all these cases, the rotation axis is a geometric symmetry axis. From [21]). © Fluid Dynamics Research, reproduced with permission

[11] For the geophysical application here the second Coriolis parameter $\tilde{f}$ is still ignored. So these inertial waves are long.

12.7.1 Governing Equations

Small amplitude waves in a homogeneous fluid that is rotating with angular frequency $\bar{\Omega}$ about a vertical axis aligned in the $\bar{z}$-direction (overbars denote dimensional quantities) are governed by the linearized, inviscid equations of motion on an $\bar{f}$-plane (where $\bar{f} = 2\bar{\Omega}$)

$$\begin{aligned}
&\frac{\partial \bar{u}}{\partial \bar{t}} - \bar{f}\bar{v} = -\frac{1}{\bar{\rho}}\frac{\partial \bar{p}}{\partial \bar{x}},\\
&\frac{\partial \bar{v}}{\partial \bar{t}} + \bar{f}\bar{u} = -\frac{1}{\bar{\rho}}\frac{\partial \bar{p}}{\partial \bar{y}},\\
&\frac{\partial \bar{w}}{\partial \bar{t}} = -\frac{1}{\bar{\rho}}\frac{\partial \bar{p}}{\partial \bar{t}},\\
&\frac{\partial \bar{u}}{\partial \bar{t}} + \frac{\partial \bar{v}}{\partial \bar{y}} + \frac{\partial \bar{w}}{\partial \bar{t}} = 0,
\end{aligned} \tag{12.57}$$

in which the usual notation has been used and $\bar{\rho} = \text{const.}$ (Note that in $(12.57)_3$ the hydrostatic assumption cannot be made since no gravity term is present.) In an infinite medium, the variables $(\bar{u}, \bar{v}, \bar{w})$ and $\bar{p}$ can be written as mono-chromatic waves, viz.,

$$(\bar{u}, \bar{v}, \bar{w}, \bar{p}) = (\bar{\tilde{u}}, \bar{\tilde{v}}, \bar{\tilde{w}}, \bar{\tilde{p}})\exp(-i\bar{\omega}\bar{t}), \tag{12.58}$$

leading to equations equivalent to (12.57) with $\partial(\cdot)/\partial\bar{t}$ replaced by $(-i\bar{\omega})$. If in these equations all velocity variables are eliminated, the so-called Poincaré equation [30, 31]

$$\frac{\partial^2 \bar{\tilde{p}}}{\partial \bar{x}^2} + \frac{\partial^2 \bar{\tilde{p}}}{\partial \bar{y}^2} - \left(\frac{\bar{f}^2}{\bar{\omega}^2} - 1\right)\frac{\partial^2 \bar{\tilde{p}}}{\partial \bar{z}^2} = 0 \tag{12.59}$$

for the pressure is obtained. For $\bar{\omega}^2 < \bar{f}^2$ this is a (hyperbolic) wave equation; for $\bar{\omega}^2 > \bar{f}^2$ it is elliptic instead. Plane waves are of the form

$$\bar{\tilde{p}}(\bar{x}, \bar{y}, \bar{z}) = \check{p}\,\exp(i\bar{\mathbf{k}}\cdot\bar{\boldsymbol{x}}), \tag{12.60}$$

where the wavenumber vector is $\bar{\mathbf{k}} \hat{=} (\bar{k}, \bar{\ell}, \bar{n})$. With (12.60), (12.59) implies the dispersion relation

$$\frac{\bar{\omega}}{\bar{f}} = \pm\frac{\bar{n}}{(\bar{k}^2 + \bar{l}^2 + \bar{n}^2)^{1/2}} = \pm\sin\phi, \tag{12.61}$$

where ϕ is the angle between $\bar{\mathbf{k}}$ and the plane perpendicular to the rotation axis. For $\bar{\omega}^2 < \bar{f}^2$, these waves are truly plane, not boundary trapped, with particle displacements which are largest in the interior of the fluid domain, resulting in a cellular wave pattern [1]. In the terminology of Platzman [29] and Mortimer [26],

they would be called Sverdrup-waves; however, they were already constructed by Poincaré [30] and are, therefore, called Poincaré waves by Maas [21].

For a layer with rigid bottom at $\bar{z} = -\bar{H}$ and rigid lid at $\bar{z} = 0$, it is readily seen that equations (12.57) enforce standing waves in the vertical with $\bar{w} = 0$ at $\bar{z} = (0, -\bar{H})$. Thus, we make the dynamically consistent ansatz

$$\begin{aligned} \bar{w} &= \sum_{n=1}^{\infty} \frac{\partial \bar{\zeta}_n}{\partial \bar{t}} \sin\left(\frac{n\pi\bar{z}}{\bar{H}}\right), \\ (\bar{u}, \bar{v}, \bar{p}) &= \sum_{n=1}^{\infty} (\bar{u}_n, \bar{v}_n, \bar{p}_n) \cos\left(\frac{n\pi\bar{z}}{\bar{H}}\right). \end{aligned} \tag{12.62}$$

Here, the subscript n refers to the n^{th} vertical mode. When substituting (12.62) into (12.57), it is straightforward to show that the amplitude functions satisfy the equations

$$\begin{aligned} \frac{\partial \bar{u}_n}{\partial \bar{t}} - \bar{f}\bar{v}_n &= -\bar{H}_n \frac{\partial^3 \bar{\zeta}_n}{\partial \bar{x} \partial \bar{t}^2}, \\ \frac{\partial \bar{v}_n}{\partial \bar{t}} + \bar{f}\bar{u}_n &= -\bar{H}_n \frac{\partial^3 \bar{\zeta}_n}{\partial \bar{y} \partial \bar{t}^2}, \\ \frac{\partial \bar{\zeta}_n}{\partial \bar{t}} + \bar{H}_n \left(\frac{\partial \bar{u}_n}{\partial \bar{x}} + \frac{\partial \bar{v}_n}{\partial \bar{y}}\right) &= 0, \end{aligned} \tag{12.63}$$

where

$$\bar{H}_n := \frac{\bar{H}}{n\pi}, \quad \bar{p}_n := \bar{\rho}\bar{H}_n \frac{\partial^2 \bar{\zeta}_n}{\partial \bar{t}^2}. \tag{12.64}$$

Formally, these equations agree with (12.1) except that the wave acceleration $\bar{H}_n \partial^2(\zeta_n)/\partial \bar{t}^2$ replaces the acceleration $\bar{g}$.

We now scale (12.63) and (12.64) by introducing the following dimensionless variables:

$$(x, y) = \frac{1}{\bar{H}_n}(\bar{x}, \bar{y}), \quad (u, v, \zeta) = \frac{1}{\bar{H}_n}(\bar{u}_n, \bar{v}_n, \bar{\zeta}_n), \quad (t, \omega^{-1}) = \bar{f}(\bar{t}, \bar{\omega}^{-1}). \tag{12.65}$$

With these relations (12.63) take the forms

$$\begin{aligned} \frac{\partial u}{\partial t} - v + \frac{\partial^3 \zeta}{\partial t^2 \partial x} &= 0, \\ \frac{\partial v}{\partial t} + u + \frac{\partial \zeta}{\partial t^2 \partial y} &= 0, \\ \frac{\partial \zeta}{\partial t} + \frac{\partial u}{\partial x} + \frac{\partial v}{\partial y} &= 0. \end{aligned} \tag{12.66}$$

Differentiation of $(12.66)_{1,2}$ with respect to t and elimination of u and v, respectively, yields the polarization equations, relating the velocity and elevation fields via

$$\begin{aligned} \mathcal{L}u &= \frac{\partial^2}{\partial t^2}\left(\frac{\partial^2 \zeta}{\partial t \partial x} + \frac{\partial \zeta}{\partial y}\right), \\ \mathcal{L}v &= \frac{\partial^2}{\partial t^2}\left(\frac{\partial^2 \zeta}{\partial t \partial y} - \frac{\partial \zeta}{\partial x}\right), \end{aligned} \tag{12.67}$$

where

$$\mathcal{L} := -\left(\frac{\partial^2}{\partial t^2} + 1\right). \tag{12.68}$$

These equations, when combined with $(12.66)_3$, imply the single differential equation

$$\left[1 + \left(1 - \nabla_H^2\right)\frac{\partial^2}{\partial t^2}\right]\frac{\partial \zeta}{\partial t} = 0 \tag{12.69}$$

for the vertical displacement field, where ∇_H^2 is the horizontal Laplace operator. With

$$(u, v, \zeta) = (\check{u}, \check{v}, \check{\zeta})\exp(-\mathrm{i}\omega t), \tag{12.70}$$

Equation (12.69) implies that $\check{\zeta}$ satisfies the Helmholtz equation

$$(\nabla_H^2 + \kappa^2)\check{\zeta} = 0, \qquad \kappa^2 := \frac{1 - \omega^2}{\omega^2}, \tag{12.71}$$

where $\omega \langle 1$ for $\kappa^2 \rangle 0$. Moreover, with (12.66) and representations (12.70) the spatial part of the horizontal velocities is given by

$$\check{u} = \frac{1}{\kappa^2}\left(-\mathrm{i}\omega\frac{\partial \check{\zeta}}{\partial x} + \frac{\partial \check{\zeta}}{\partial y}\right), \quad \check{v} = \frac{1}{\kappa^2}\left(-\mathrm{i}\omega\frac{\partial \check{\zeta}}{\partial y} - \frac{\partial \check{\zeta}}{\partial x}\right). \tag{12.72}$$

It is noteworthy that these waves exist as plane waves in $\mathbb{R}^2$, when they have subinertial frequencies $\omega^2 < 1$ ($\bar{\omega}^2 < \bar{f}^2$). For $\omega^2 > 1$, they are exponentially amplified or evanescent and thus can only exist in bounded regions. We shall now briefly discuss the various cases.

12.7.2 Plane Inertial Sverdrup (Poincaré) Waves

A vertically standing mode of the form (12.62) may propagate horizontally as a plane wave of the form

$$(u, v, \zeta) = (\hat{u}, \hat{v}, \hat{\zeta})\exp[\mathrm{i}(kx + \ell y - \omega t)] \tag{12.73}$$

with

$$(\breve{u}, \breve{v}, \breve{\zeta}) = (\hat{u}, \hat{v}, \hat{\zeta}) \exp\left[\mathrm{i}(kx + \ell y)\right]. \tag{12.74}$$

Owing to $(12.71)_2$ these waves satisfy the dispersion relation

$$\kappa^2 = \frac{1-\omega^2}{\omega^2} = k^2 + l^2 \quad \rightarrow \quad \omega = \frac{1}{\sqrt{1+k^2+\ell^2}} = \frac{1}{\sqrt{1+\kappa^2}}. \tag{12.75}$$

This leads to the following expressions for the phase and group speeds, c_{ph} and c_{gr}, respectively:

$$c_{\mathrm{ph}} = \frac{\omega}{\kappa} = \frac{1}{\kappa\sqrt{1+\kappa^2}}, \qquad c_{\mathrm{gr}} = \frac{\mathrm{d}\omega}{\mathrm{d}\kappa} = -\frac{\kappa}{(1+\kappa^2)^{3/2}}, \tag{12.76}$$

which shows that phase and group move in opposite directions parallel and anti-parallel to the wave vector $\mathbf{k} \mathrel{\hat{=}} (k, \ell)$. Figure 12.22 displays graphs of the dispersion relation and the two speeds.

12.7.3 Inertial Kelvin Waves

By definition, Kelvin waves are rotation influenced motions for which the velocity component in one horizontal spatial direction vanishes. To see whether (12.66) permits such solutions, we assume $v(x, y, t) \equiv 0$ but $u(x, y, t) \neq 0$. Then, (12.66) takes the forms

$$\frac{\partial u}{\partial t} + \frac{\partial^3 \zeta}{\partial t^2 \partial x} = 0, \quad u + \frac{\partial^3 \zeta}{\partial t^2 \partial y} = 0, \quad \frac{\partial \zeta}{\partial t} + \frac{\partial u}{\partial x} = 0. \tag{12.77}$$

From $(12.77)_{1,3}$ there follows

$$\frac{\partial}{\partial t}(u - u_{xx}) = 0. \tag{12.78}$$

This shows that along-wall velocities u either grow or decay as $\exp(\pm x)$ with along wall distance. The general solution of (12.77) with $v \equiv 0$ is seen to be

$$(u, v, \zeta) = (\breve{u}, 0, \breve{\zeta}) \exp\left[-x + \mathrm{i}(ky - \omega t)\right] \tag{12.79}$$

with

$$\breve{\zeta} = \frac{\mathrm{i}}{\omega}\breve{u}, \tag{12.80}$$

the dispersion relation

$$\omega = -\frac{1}{k} \tag{12.81}$$

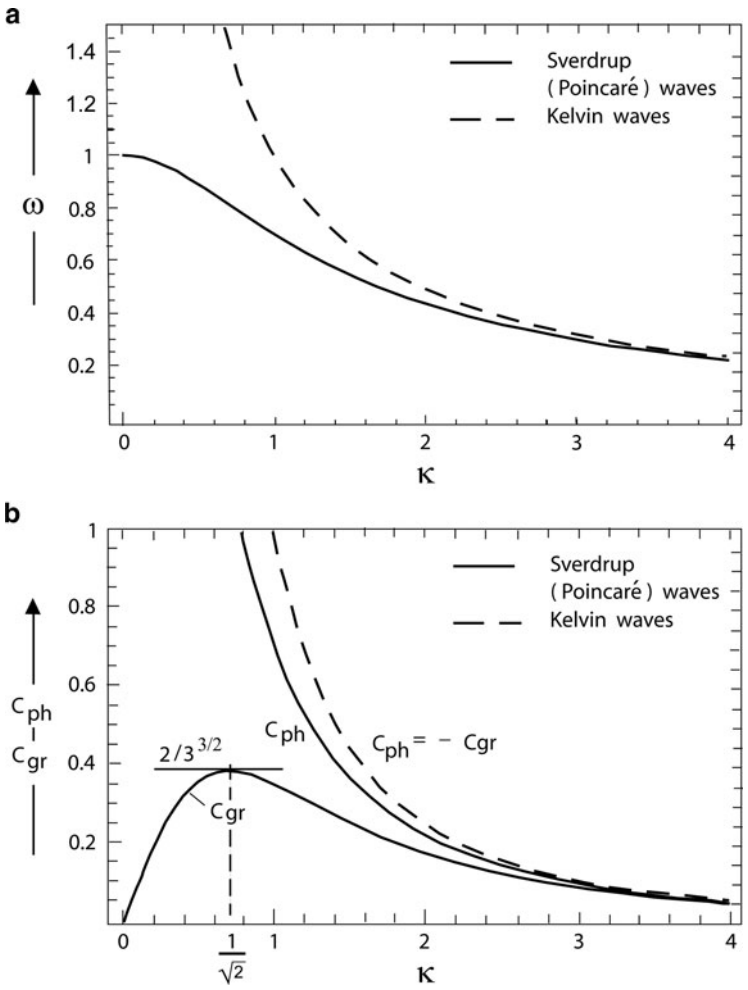

Fig. 12.22 (**a**) Dispersion relation for inertial Sverdrup (Poincaré) (*solid*) and inertial Kelvin (*dashed*) waves giving frequency ω vs. wavenumber amplitude κ. (**b**) Corresponding phase velocity (c_{ph}) and group velocity (c_{gr}) as functions of κ. For inertial Kelvin waves $c_{\mathrm{ph}} = -c_{\mathrm{gr}}$ (adapted from [21]). © Fluid Dynamics Research, reproduced with permission

and the phase, c_{ph}, and group, c_{gr}, velocities given by $c_{\mathrm{ph}} = -1/k^2$ and $c_{\mathrm{gr}} = 1/k^2$, respectively, see Fig. 12.22. Hence, energy propagates in a direction opposite to the phase. Inertial Kelvin waves thus decay in the direction of increasing x, while propagating their phase in the direction of decreasing y (more generally: the phase propagates to the right of decreasing wave amplitude (on the Northern hemisphere)). With reference to Fig. 12.23 this wave is trapped to the boundary at $x = 0$, and its energy propagates in the positive y-direction. However, since there are no lines parallel to the x-axis at which the u-velocity component would vanish, these Kelvin

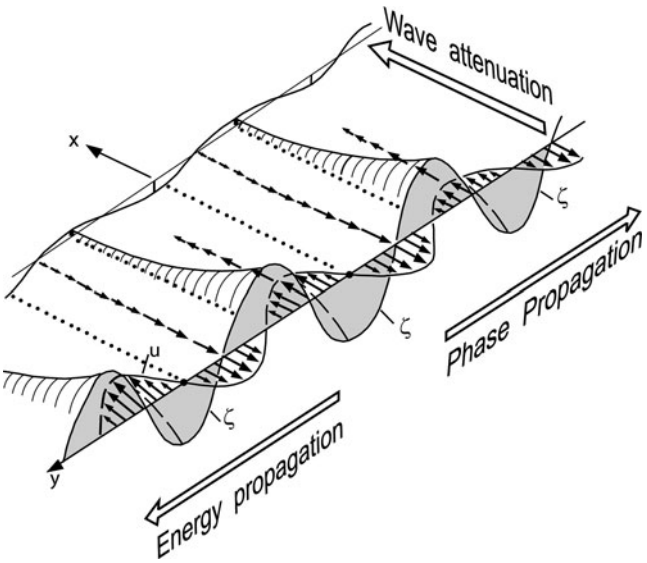

Fig. 12.23 In an inertial Kelvin wave with horizontal velocities in the x-direction, this velocity and the vertical displacements decay in the positive x-direction, whilst the phase propagates in the negative and the energy in the positive y-direction. The variables u and ζ are out of phase by $\pi/2$

waves do not exist in infinite space per se. They play, however, an essential role when Poincaré waves are reflected at a channel end.

12.7.4 Inertial Poincaré Waves in a Channel

If we assume the existence of a wall at $x = 0$ with no through-flux, then $u = 0$ at $x = 0$, implying from $(12.67)_1$

$$\frac{\partial^2 \zeta}{\partial t \partial x} + \frac{\partial \zeta}{\partial y} = 0 \qquad \text{at} \qquad x = 0. \tag{12.82}$$

A pair of incoming and reflected waves with identical frequency ω and along-wall wavenumber ℓ is given by

$$\zeta = Z_i \exp\left[\mathrm{i}(-kx + \ell y - \omega t + \phi)\right] + Z_r \exp\left[\mathrm{i}(kx + \ell y - \omega t - \phi)\right] \tag{12.83}$$

and needs to satisfy $(12.82)_1$ or

$$-\omega \frac{\partial \zeta}{\partial x} + \ell \zeta = 0 \qquad \text{at} \qquad x = 0, \tag{12.84}$$

implying, in view of (12.83),

$$Z_i(\mathrm{i}k\omega + \ell)\exp(\mathrm{i}\phi) + Z_r(-\mathrm{i}k\omega + \ell)\exp(-\mathrm{i}\phi) = 0.$$

This can also be written as

$$\frac{Z_i}{Z_r} = \frac{(k\omega + \mathrm{i}\ell)}{(k\omega - \mathrm{i}\ell)}\frac{\exp(-\mathrm{i}\phi)}{\exp(\mathrm{i}\phi)}. \tag{12.85}$$

In this expression, the denominator is the complex conjugate of the numerator, say, $r\exp(i\theta)/\,r\exp(-i\theta) = \exp(2i\theta)$ for some amplitude r and angle θ. This also shows that the reflected wave has the same amplitude as the incoming wave, so we may set $Z_i = Z_r = Z/2$. The two waves only suffer a phase shift. With $Z_i/Z_r = 1$, (12.85) implies

$$\exp(-2\mathrm{i}\phi) = \frac{k\omega - \mathrm{i}\ell}{k\omega + \mathrm{i}\ell} \quad \Rightarrow \quad \tan\phi = \frac{\ell}{k\omega}. \tag{12.86}$$

Moreover, perpendicular to the wall the resulting wave is standing; we may thus rewrite (12.83) as

$$\begin{aligned}\zeta &= Z\cos(kx - \phi)\exp[\mathrm{i}(\ell y - \omega t)] \\ &= Z\{\cos(kx)\cos\phi + \sin(kx)\sin\phi\}\exp[\mathrm{i}(\ell y - \omega t)] \\ &= \underbrace{Z\cos\phi}_{\mathcal{Z}}\{\cos(kx) + \frac{\ell}{k\omega}\sin kx\}\exp[\mathrm{i}(\ell y - \omega t)]\end{aligned} \tag{12.87}$$

with the newly defined amplitude $\mathcal{Z} = Z\cos\phi$. With the form (12.87) of the vertical displacement function, $(12.72)_1$ can be used to compute the cross-wall and along-channel velocity components. This straightforward computation yields for the *cross-wall velocity component*

$$u = \mathrm{i}k\mathcal{Z}\frac{\omega^3}{1-\omega^2}\left(1 + \left(\frac{\ell}{\omega k}\right)^2\right)\sin kx\ \exp[\mathrm{i}(\ell y - \omega t)] \tag{12.88}$$

and for the *along-channel velocity component*

$$v = \mathcal{Z}\left(-\ell\omega\cos kx + \frac{1}{k}\sin kx\right)\exp[\mathrm{i}(\ell y - \omega t)]. \tag{12.89}$$

It is evident from (12.88) that the cross-wall wavenumber k can be quantized when a second wall is erected at $x = L$. Then

$$k \in \left\{k_m = \frac{m\pi}{L}, \quad m = 1, 2, 3, \ldots\right\}. \tag{12.90}$$

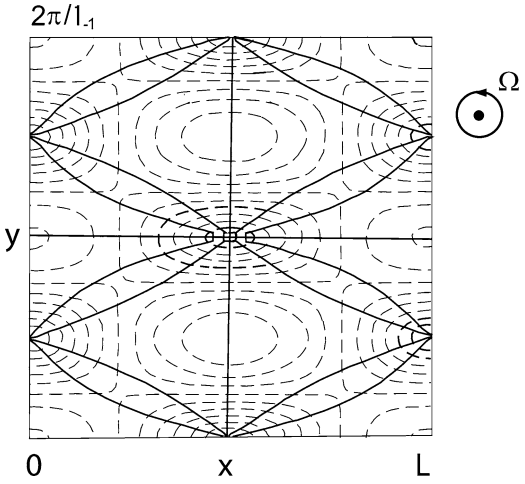

Fig. 12.24 Top view of one wave length segment of a channel which is infinitely long in the y-direction and of dimensionless width $L = 4$ in x-direction. It shows phase (*solid*) and amplitude (*dashed*) lines of the vertical displacement field of a pair of equal amplitude, mode-1, up and down channel propagating Poincaré modes of frequency $\omega = 0.7$. Amplitudes are maximal at the saddle nodes of phase lines, located on the channel axis, at $1/4$ and $3/4$ wave length. The rotation axis, designated Ω, points out of the paper (redrawn from [21]). © Fluid Dynamics Research, reproduced with permission

So, inertial Poincaré waves exist in infinitely long channels as isolated countable infinite modes.

The up- and down-channel solutions (12.87)–(12.90) of inertial Poincaré waves develop amphidromic structures similar to gravity driven Poincaré waves. Figure 12.24 shows this amphidromic system for such a mode-1 quasi-standing wave as constructed by Maas [21]. The mode structure is characterized by phase lines circling anti-cyclonically (i.e. clockwise) around nodal points where vertical elevation vanishes. According to Maas 'such phase pattern was first suggested long ago by Whewell [47] to comprehensively describe observed tidal elevation patterns, see [4]'.

12.7.5 Inertial Poincaré Channel Waves Reflecting from a Vertical Wall

Recall that classical gravity (externally) driven Kelvin waves can be combined by equal-amplitude forward and backward moving propagating Kelvin waves with the same frequency to form quasi-standing Kelvin waves in an infinite channel. Per se, these could not form a solution in a channel bounded from one side, because the no-flux condition through such an (imaginary) wall could not be satisfied. To achieve

such a no-flux condition through the end-wall, an infinite number of backward moving (reflected) Poincaré waves with the same frequency had to be added and adequately combined. This was Taylor's solution [45].

Such a solution cannot be found with inertial Kelvin waves. However, an inertial Poincaré wave entering a channel can be combined with a trapped inertial Kelvin wave and an infinite number of backward moving inertial Poincaré channel waves. Let us assume that the wave propagates in the y-direction and the across-channel wavenumber is $k_m = m\pi/L$. Then, the along-channel wavenumber ℓ_m can be deduced from $(12.71)_2$ to yield

$$\ell_m = \pm\left(\frac{1}{\omega^2} - (1 + k_m^2)\right)^{1/2} = \pm\left(\frac{1}{\omega^2} - \frac{1}{\omega_m^2}\right)^{1/2}, \tag{12.91}$$

where

$$\omega_m := (1 + k_m^2)^{-1/2} < 1 \tag{12.92}$$

is the cut-off frequency. For $|\ \omega\ | < |\ \omega_m\ |$, ℓ_m is real and inertial Poincaré waves exist as propagating waves; for $|\ \omega\ | > |\ \omega_m\ |$, they are exponentially evanescent or growing.

Consider a reflection at $y = 0$ for a mode-1 ($m = 1$) Poincaré wave approaching the wall at $y = 0$ from positions with $y > 0$. The total along channel velocity is thus composed of an incoming Poincaré wave (of given amplitude, here chosen to be unity, (12.89), $\mathcal{Z} = 1$) and having along channel wavenumber $+\ell_1$,

$$v^{\text{in}}_{\text{Poincaré}}(x, y, t) = \{-\ell_1\omega\cos k_1 x + \frac{1}{k_1}\sin k_1 x\} \times \exp(\mathrm{i}\ell_1 y), \tag{12.93}$$

plus a trapped inertial Kelvin wave ((12.79), but in the y-direction)

$$v^{\text{trapped}}_{\text{Kelvin}}(x, y, t) = v_0 \exp\left(-y + \frac{\mathrm{i}}{\omega}x\right), \tag{12.94}$$

plus an infinite sum of reflected inertial Poincaré waves, again of the form (12.89), but with a negative sign of the along-channel wavenumber

$$v^{\text{out}}_{\text{Poincaré}}(x, y, t) = \sum_{m=1}^{\infty} v_m\{\ell_m\omega\cos k_m x + \frac{1}{k_m}\sin k_m x\} \times \exp(-\mathrm{i}\ell_m y). \tag{12.95}$$

In (12.93)–(12.95), a common exponential factor $\exp(-i\omega t)$ has been dropped. The unknown complex valued amplitudes $v_0, v_1, v_2, \ldots$ follow from the no-flux condition at $y = 0$

$$\begin{aligned} &v^{\text{in}}_{\text{Poincaré}}(x, 0) + v^{\text{trapped}}_{\text{Kelvin}}(x, 0) + v^{\text{out}}_{\text{Poincaré}}(x, 0) \\ &= \left[\left(-\ell_1\omega\cos k_1 x + \frac{1}{k_1}\sin k_1 x\right)\exp(\mathrm{i}\ell_1 y) + v_0\exp\left(-y + \frac{\mathrm{i}x}{\omega}\right)\right. \end{aligned}$$

$$+\sum_{m=1}^{\infty} v_m \left\{ \ell_m \omega \cos k_m x + \frac{1}{k_m} \sin k_m x \right\} \exp(-\mathrm{i}\ell_m y) \Big]_{y=0}$$
$$= -\ell_1 \omega \cos k_1 x + \frac{1}{k_1} \sin k_1 x + v_0 \exp\left(\frac{\mathrm{i}x}{\omega}\right)$$
$$+\sum_{m=1}^{\infty} v_m \left\{ \ell_m \omega \cos k_m x + \frac{1}{k_m} \sin k_m x \right\} = 0. \tag{12.96}$$

Note that the inertial Poincaré waves with mode numbers $m > 1$ are all trapped (exponentially evanescent for $y > 0$). So, we define

$$\ell_m = -\mathrm{i}\left(\frac{1}{\omega_m^2} - \frac{1}{\omega^2}\right)^{1/2} = -\mathrm{i}s_m \quad (s_m > 1). \tag{12.97}$$

Equation (12.96) has been solved by Maas [21] using the collocation method. In this method, the infinite sum is truncated at $M - 1$. Writing (12.96) then for M different values of $x \in [0, L]$ yields a linear system of equations for the amplitudes $v_0, v_1, v_2, \ldots, v_{(M-1)}$. Figure 12.25 is based on a solution constructed with $M = 21$. It shows in panel (a) the amplitude (dashed) and phase (solid) of the vertical displacement field ζ. The phase propagates in the clockwise direction, whilst the energy does so in the anti-clockwise direction. Panel (b) in Fig. 12.25 shows corresponding horizontal velocity ellipses at a number of positions. These are traversed in the clockwise direction, and are very thin and along the channel sides at the boundaries, so that the velocity component perpendicular to the boundary vanishes.

12.7.6 Inertial Waves in Rectangular Basin of Constant Depth

Inertial waves also exist in fully enclosed basins as has been demonstrated by Maas [21] for rectangles by using the spectral method of Proudman [33] and Rao [40] (see Appendix to this chapter). This solution method uses a Helmholtz decomposition of the velocity field $\mathbf{v} = \mathbf{v}^{\phi} + \mathbf{v}^{\psi}$ with $\mathbf{v}^{\phi} = -\nabla\phi$, $\mathbf{v}^{\psi} = \hat{\mathbf{k}} \times \nabla\psi$, where $\hat{\mathbf{k}}$ is a unit vector aligned with the rotation axis. The no-flux condition at the boundary with unit normal vector $\mathbf{n}$ is then transformed to the statements

$$(\mathrm{grad}\,\phi) \cdot \mathbf{n} = 0, \qquad \psi = 0 \qquad \text{along} \quad \partial\mathcal{D}. \tag{12.98}$$

The velocity potential ϕ, the stream function ψ and the elevation field ζ are then represented as

$$(\phi, \psi, \zeta) = \sum_{\alpha} (p_\alpha \phi_\alpha,\ q_\alpha \psi_\alpha,\ r_\alpha \zeta_\alpha) \tag{12.99}$$

in terms of complete function sets $\{\phi_\alpha\}$, $\{\psi_\alpha\}$ (with $\zeta_\alpha \propto \phi_\alpha$), where α is a binary index ($\alpha = (k, \ell)$ for the (k, ℓ)-mode). These functions follow from suitably

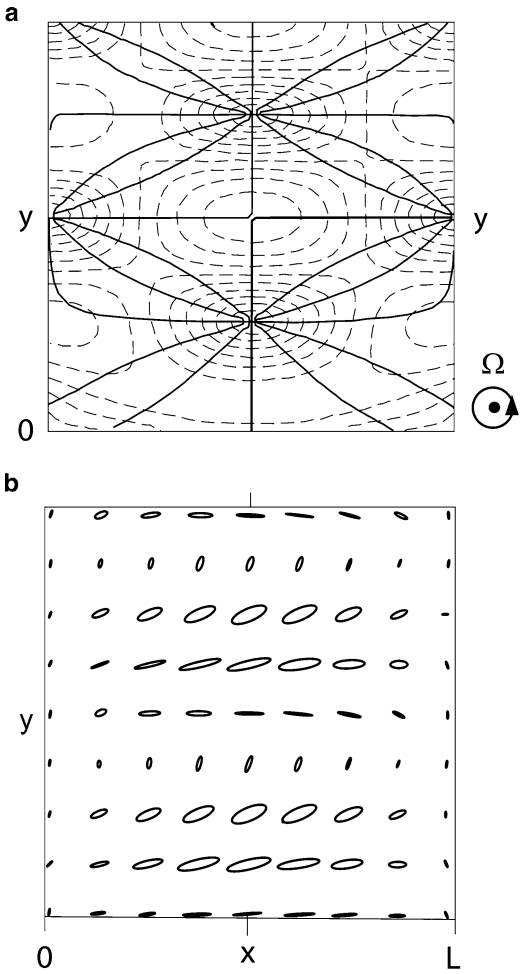

Fig. 12.25 Top view of (**a**) phase (*solid*) and amplitude (*dashed*) of the vertical displacement field of a mode-1, down-channel propagating inertial Poincaré mode of frequency $\omega = 0.7$ in a channel of dimensionless width $L = 4$, reflecting from a vertical wall at $y = 0$. During reflection inertial Kelvin and inertial Poincaré waves are excited, that are trapped in the y-direction. Phase lines are given every 30° which rotate anti-cyclonically around the amphidromes at the central axis (the rotation axis, Ω, is out of the paper; (**b**) horizontal current ellipses once traversed clockwise for $\omega > 0$ during one period (redrawn from [21]). © Fluid Dynamics Research, reproduced with permission

chosen selfadjoint elliptic eigenvalue problems, adjusted to the geometry of the fluid domain but not related to the dynamical equations except the flux condition through the boundary. The coefficients $p_\alpha, q_\alpha, r_\alpha$ are functions of time only. By substituting the representations (12.99) into the dynamical equations (here (12.106) and (12.107) in the Appendix) then yields a system of ordinary differential equations

for them. Some details of this method are presented in the Appendix to this chapter. This method of integration seems to be economical only for simple geometries. Proudman [33] suggested it and used it for the axial cylinder of uniform and parabolic depth shape, Rao [40] used the method to retrieve and extend Taylor's [45] results for rotational gravity waves in rectangles, and Maas [21] applied it to oscillations of 'inertial waves proper' in the rectangle. For the difficult particulars of the application of the method to rectangles we refer to Rao [40] and Maas [21].

In what follows, we shall only present the elevation and velocity fields of the first three modes in a rectangle of dimensionless size $2\pi \times \pi$. Maas needed 91 Fourier modes ($\alpha = 1, 2, 3, \ldots, 91$) to obtain five digits accuracy in the elevation and velocity fields. He writes [21]:

"When a vertical mode is picked, say $n = 1$, and the basin is scaled with the corresponding vertical scale, the eigenfrequencies are determined, and the corresponding elevation amplitude and velocity fields can be plotted. (Note that the actual vertical elevation is depth dependent, due to the vertical mode dependence, as in $(12.62)_1$.) Counting from the top-down, the first three modes are shown in Fig. 12.26 in a rectangular horizontal cross-section of the $2\pi \times \pi$ rectangular parallelepiped. Modes 1 and 3 have antisymmetric elevation (left) and symmetric velocity fields (right), and vice versa for mode 2. The pictures present the following information. In the elevation field ζ (at the left), colouring and dashed lines represent elevation amplitudes. Deep blue corresponds with zero elevation, red with maximum amplitudes. Phase lines (every 30°) are solid. They end in nodal (zero elevation) points and show that phase is circling around the amphidromes in either clockwise or anti-clockwise direction. All amphidromes on the middle axis ($y = \pi/2$) are traversed in a clockwise sense, all others (close to $y = 0$ and π) in anti-clockwise sense. Orthogonal crossings of phase lines (as, e.g. in the centre of the rectangle for mode 2) imply equal phases on all four branches, implying that the whole real central region of mode 2 rises and sinks in unison. Anti-symmetry of the elevation field of, e.g. mode-1 is evident from a 180° phase change between mirror images about the centre point.

The velocity field (u, v) (at the right side of Fig. 12.26) contains, in principle, four independent parameters. Each component has an amplitude and a phase. At each individual location these can be represented in terms of a velocity ellipse, as e.g. in [45], expressed in terms of four other parameters: maximum amplitude, $u_{\max}$, ellipticity $u_{\min}/u_{\max}$, orientation of the main axis, Ψ and phase (with respect to this local orientation Φ) [32]. The ellipticity varies between -1 (circular clockwise, deep blue) and $+1$ (circular anti-clockwise, red), whilst it represents rectilinear motion when it is zero (green). The green colour at the boundary tells that the velocity is rectilinear there. Separate consideration of the inclination shows the velocity vector to be everywhere parallel to the sides. Maximum velocity $u_{\max}$ is represented by dashed lines".

Further discussions, including results concerning the frequency properties and the first four modes of a $(\pi \times \pi)$-square are given by Maas [21].

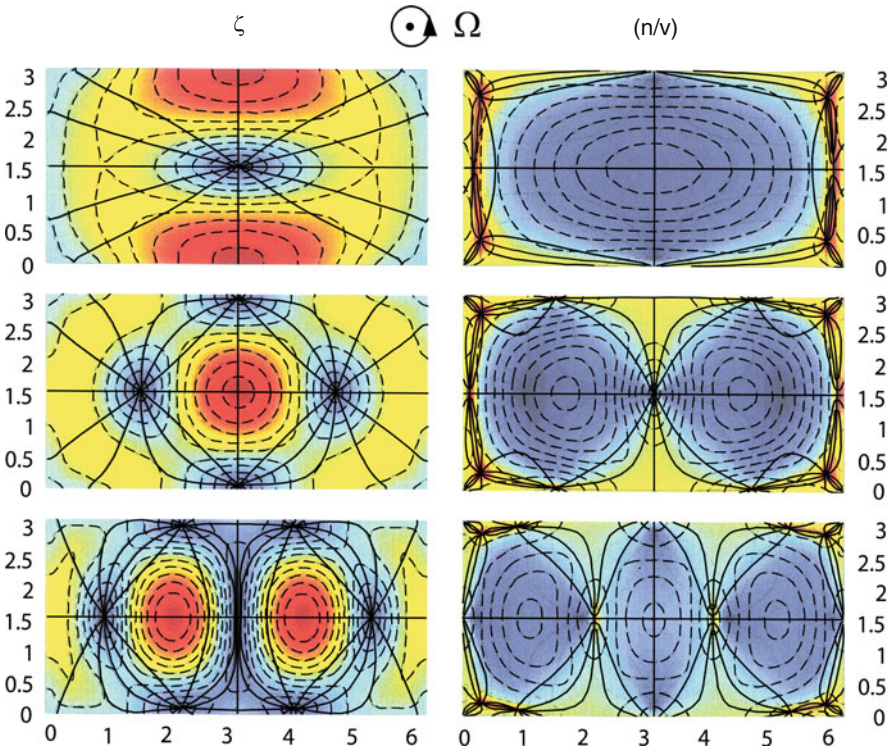

Fig. 12.26 Top view of elevation (*left*) and horizontal velocity (*right*) fields of a $2\pi \times \pi$ rectangle for mode 1, $\omega \approx 0.657$ (*top*); mode 2, $\omega \approx 0.564$ (*middle*); and mode 3, $\omega \approx 0.477$ (*bottom*). The rotation vector points out of the paper towards the reader; the tank thus moves anti-clockwise. For further explanation, see main text. Redrawn from [21]. © Fluid Dynamics Research, reproduced with permission

12.7.7 Discussion

In this section, inertial waves – better called 'inertial waves proper' or 'second class inertial waves' – were discussed, which are not supported by gravity but, apart from Coriolis effects, by dynamical pressure. Equations which are rather similar to the long wave equations, are obtained for each of the vertical modes that exist in a fluid layer having top and bottom perpendicular to the rotation axis. Acceleration due to gravity is replaced here by vertical acceleration in the wave field. The resulting horizontal problem was solved in the unbounded domain, in the infinite and semi-infinite channel and in rectangular basins.

Waves in the infinite plane are sub-inertial and known as inertial Sverdrup (or, according to a different nomenclature, Poincaré) waves. With one vertical boundary, along a straight line in the (x, y)-plane two plane waves can be combined into an inertial Poincaré wave whose velocity component normal to this wall vanishes.

This velocity component then vanishes also at an infinite number of other positions parallel to this wall, so that an additional wall can be placed at such a position, thus forming a channel. Inertial Kelvin waves have also been found as solutions having vanishing velocity component in one spatial direction. These waves then propagate the phase (energy) in a direction which is 90° to the right (to the left on the Southern hemisphere) of the direction of non-zero horizontal velocity (see Fig. 12.23), and this velocity as well as the corresponding particle motion decay exponentially with the velocity, making it incompatible with the existence of a solid boundary. So, free inertial Kelvin-waves proper do not exist.

The reflection of a channel inertial Poincaré wave from the end wall requires mathematically the addition of a trapped inertial Kelvin wave proper and an infinite number of reflected inertial Poincaré waves proper to achieve zero flux of fluid through the end wall. This implies that the inertial wave system in an enclosed rectangle consists of an additive combination of an infinite set of channel inertial Poincaré waves proper together with two inertial Kelvin waves proper, but we have expressed it as a combination of two intertwined infinite sets of spatial Fourier modes.

Maas [21], in his closing statements, mentions that 'the existence of (linear) wave solutions does not guarantee their stability'. He quotes for the axial can a proof of instability of inertial waves to short wavelength perturbations of oblique orientation [19] and muses that such instability results may extend also to rectangles.

The presentation of these waves in this book has been given, because under unusual circumstances it may not be unlikely that inertial waves proper may be observable in the field. This is likely the case in fully ice covered lakes under homogeneous conditions, when gravity driven motions in the water beneath the ice are considerably damped out, or non-existent at all. In those circumstances, also turbulent pulsations are effectively damped out. So, if inertial waves proper are excited, then they should be best observable in ice covered lakes. Of course, with wind forces being essentially absent, earthquakes then are the only remaining substantial triggering mechanisms of these waves. These give rise to a temporal Dirac-type displacement field of the solid boundary, which dies quickly out to zero. The induced motion in the aftermath of the earthquake within the lake region may then establish a resonant response of basin scale inertial waves proper.

Moreover, according to Maas [21], 'there seems to be no intrinsic reason to neglect these waves completely, despite their small-scale (order of the water depth) and to enforce solutions by the hydrostatic approximation. Krauss [15] observes that the hydrostatic approximation has been made ever since Laplace, but that a real motivation (except for the tautological statement that it applies to waves that are long compared with the water depth) is absent. Indeed, for this reason the approximation has been criticized by Solberg [44] when looking into these inertial 'cellular' waves, [...]. The failure of Laplace's Tidal Equations to even adequately model long surface waves in the presence of topographic variations was addressed by Chapman [5] and Chapman and Hendershott [6]'.

12.8 Concluding Discussion

In this chapter, the analysis of linear waves in a Boussinesq fluid on a permanently rotating frame was continued by studying such waves in semi-bounded and bounded basins of constant depth. By excluding depth variations, Rossby waves on the f-plane are automatically excluded. The goal of the chapter was twofold: (1) to construct gravity wave solutions of the linearized shallow water equations when the rotation of the Earth is included and (2) to present solutions for 'inertial waves proper' for barotropic fluids in domains with rigid boundaries. Concerning (1), this led to propagating and quasi-standing Kelvin and Poincaré waves in channels of constant width and constant depth. The impossibility of the existence of pure Kelvin and Poincaré waves in a semi-infinite gulf of a long rectangular basin led to Taylor's reflection problem, which showed that a pair of quasi-standing Kelvin waves had to be complemented by an infinite number of Poincaré waves with the same frequency and wavelengths of an integer fraction of the channel width in order to match the zero velocity condition across the channel width. If all the amplitudes of these infinite Poincaré waves are exponentially evanescent in the distance variable along the channel axis, then far from the gulf wall only the standing Kelvin wave survives and the reflection is called *complete*. Else, the quasi-standing Kelvin wave at large distances from the gulf wall is hidden in the 'noise' of the non-evanescent Poincaré waves; in this case, the reflection is called *incomplete*. Figure 12.13 shows in its eight panels a transition from complete to noisy incomplete reflection.

A quasi-standing oscillation of gravity waves in a rectangular basin of constant depth can be constructed by a superposition of a pair of standing Kelvin waves with two infinite numbers of propagating Poincaré waves with the same frequency, which move away from the respective walls. Identifying complete and incomplete reflection is only possible in oblong rectangles, because close to the bounding walls of the rectangle Kelvin and Poincaré activities are comparable.

It has, therefore, been desirable to employ a different solution technique for the seiche motion in (compact) rectangular basins of constant depth. This problem has a long history, starting with Lord Rayleigh at the beginning of the twentieth century and culminating with Rao's Ph.D dissertation in 1965. A historical account based on his work has been given in Sect. 12.6.1. The crucial idea, which allowed evaluation of the frequency relation with the least approximations (among the many) was the solution procedure proposed by Proudman in 1916, which is illustrated in the Appendix to this chapter. In essence, by using Helmholtz's theorem of additively decomposing a vector function into an irrotational and a solenoidal part, selfadjoint eigenvalue problems could be formulated, which Rao solved numerically by electronic computation. He also compared his frequency relation for a (1×1) and a (1×2) rectangle with experiments and demonstrated excellent agreement with the corresponding results obtained with a (1×1) and a (1×2) rectangle filled with a homogeneous fluid placed on a rotating table. His figures on the structure of amphidromies for various modes at varied rotation speeds demonstrate the complexities which seiches in a simple rectangle can take, certainly hardly predictable without a computational analysis.

The above analysis was conducted for linear gravity waves, i.e. waves which only exist when gravity is operating. In the mathematical approximation dealt with in this case, the pressure is purely hydrostatic. This means, in a homogeneous water mass, in which none of the surfaces bounding the water mass move (rigid lid), and no wind shear applies, the hydrostatic pressure drops out of the governing equations; the emerging gravity-free shallow water equations have only the zero solution. This is too restrictive; indeed, non-vanishing solutions of the shallow water equations can be reconstructed by adding the dynamical pressure gradients, see (12.57). Wave solutions of these equations are of another class and have been coined 'inertial waves proper'. They may be excited, e.g. in ice covered large lakes. Such waves have so far only been analyzed for simple geometries (see Fig. 12.21). Our presentation follows Maas [21], who constructed solutions for infinite channels and a homogeneous fluid in a rectangular box.

Plane inertial Sverdrup, inertial Kelvin and Poincaré waves do exist but exhibit physical behaviour which differs considerably from that of the corresponding gravity waves. Phase and group speeds of inertial Sverdrup and Kelvin waves propagate in different directions, see Fig. 12.23. Inertial quasi-standing Poincaré waves develop amphidromic systems similar to those of the classical standing Poincaré. Reflection of an inertial Kelvin wave at the end wall of a semi-infinite gulf does not exist; however, an incoming inertial Poincaré wave can be combined with a trapped Kelvin wave and an infinite number of outgoing Poincaré waves. So, inertial waves in rectangular basins of constant depth must also exist, and have indeed been constructed by Maas [21] using the Proudman–Rao decomposition technique explained in the Appendix to this chapter.

These wave types have not been applied to real ice covered lakes yet but indicate some promising potential of identification, say in Lake Baikal and Lake Vostok, etc.

12.9 Appendix: Solution Scheme of Proudman–Rao to Solve (12.1)

Proudman [33] suggested an elegant method to solve the equations describing the free linear oscillations of homogeneous water in an enclosed basin with variable depth and no inflow or outflow along the shore. It is assumed that the tidal motion takes place in a basin $\mathcal{D}$ completely enclosed by a rigid boundary, $\partial\mathcal{D}$, at which the no-through flow condition applies. The boundary value problem is given by (12.1) or

$$\begin{aligned} &\frac{\partial \zeta}{\partial t} + \nabla \cdot \mathbf{v} = 0, \\ &\frac{\partial \mathbf{v}}{\partial t} + f\hat{\mathbf{k}} \times \mathbf{v} = -g\nabla\zeta, \end{aligned} \qquad (x, y) \in \mathcal{D} \qquad (12.100)$$

subject to the boundary conditions

$$H\mathbf{v} \cdot \mathbf{N} = 0. \qquad (x, y) \in \partial\mathcal{D}. \qquad (12.101)$$

Here, all variables have their physical dimensions; furthermore, $\mathbf{v}, \zeta$ are functions of x, y, t; $\hat{\mathbf{k}}$ is a unit vector pointing in the $+z$-direction, g is the gravity constant, $H(x, y)$ the depth function and $\mathbf{N}$ is a unit vector in the (x, y)-plane perpendicular to the boundary $\partial\mathcal{D}$. It is further assumed that the region $\mathcal{D}$ is simply connected.

According to Helmholtz's theorem, the vector field $\mathbf{v}$ can be additively decomposed into two contributions, $\mathbf{v} = \mathbf{v}^{\phi} + \mathbf{v}^{\psi}$, such that

1. The kinetic energy is partitioned according to $K = K^{\Phi} + K^{\psi}$,

$$\underbrace{\frac{1}{2}\rho\int_{\mathcal{D}} \mathbf{v}\cdot\mathbf{v}H dA}_{K} = \underbrace{\frac{1}{2}\rho\int_{\mathcal{D}} \mathbf{v}^{\phi}\cdot\mathbf{v}^{\phi}H dA}_{K^{\phi}} + \underbrace{\frac{1}{2}\rho\int_{\mathcal{D}} \mathbf{v}^{\psi}\cdot\mathbf{v}^{\psi}H dA}_{K^{\psi}}, \tag{12.102}$$

   where dA is the increment of the surface area and ϕ, ψ have the meaning of a velocity potential and a stream function, respectively.
2. $\mathbf{v}^{\phi}$ and $\mathbf{v}^{\psi}$ are given by the relations

$$\mathbf{v}^{\phi} = -\nabla\phi, \qquad \mathbf{v}^{\psi} = h^{-1}\hat{\mathbf{k}}\times\nabla\psi, \tag{12.103}$$

   where $h = H/\bar{H}$ is the non-dimensional ratio of the actual depth $H(x, y)$ and the basin mean depth $\bar{H} = \frac{1}{A}\int_{\mathcal{D}} H(x, y)dA$.
3. At the boundary, the no-flux conditions imply the following Neumann and Dirichlet conditions

$$h\frac{\partial\phi}{\partial N} = h\nabla\phi\cdot\mathbf{N} = 0, \quad \psi = 0 \qquad (x, y) \in \partial\mathcal{D}, \tag{12.104}$$

   where $\partial(\cdot)/\partial N$ is the derivative normal to the boundary.
4. $\mathbf{v}^{\phi}$ and $\mathbf{v}^{\psi}$ are determined as functions of $\mathbf{v}$ by constructing from (12.103) the following inhomogeneous elliptic equations:

$$\begin{aligned} \nabla\cdot(h\nabla\phi) &= -\nabla\cdot(h\mathbf{v}^{\phi}) \stackrel{!}{=} -\nabla\cdot(h\mathbf{v}), \\ \nabla\cdot(h^{-1}\nabla\psi) &= -\nabla\cdot(\hat{\mathbf{k}}\times\mathbf{v}^{\psi}) \stackrel{!}{=} -\nabla\cdot(\hat{\mathbf{k}}\times\mathbf{v}). \end{aligned} \tag{12.105}$$

   (The expressions on the far right hold, since (12.103) implies $\nabla\cdot(h\mathbf{v}^{\psi}) \equiv 0$ and $\nabla\cdot(\hat{\mathbf{k}}\times\mathbf{v}^{\phi}) \equiv 0$, as can easily be proved).
5. Since $\mathbf{v}$ is unknown, the inhomogeneous equations (12.105) are not very helpful in that form. However, since $\mathbf{v}$ must satisfy (12.100) and (12.101), the procedure is to convert (12.105) into dynamical equations on ϕ and ψ, and, having determined ϕ and ψ in this way, to reconstruct $\mathbf{v}$ by means of (12.103). To this end, we represent ϕ and ψ in terms of the spectral functions of the following elliptic boundary value problems:

$$\left.\begin{aligned} -\nabla\cdot(h\nabla\phi_\alpha) &= \lambda_\alpha\phi_\alpha,\ (x,y)\in\mathcal{D},\\ h\frac{\partial\phi_\alpha}{\partial N} &= 0, \qquad\qquad (x,y)\in\partial\mathcal{D}, \end{aligned}\right\} \tag{12.106}$$

$$\left.\begin{aligned} -\nabla\cdot(h^{-1}\nabla\psi_\alpha) &= \mu_\alpha\psi_\alpha,\ (x,y)\in\mathcal{D},\\ h^{-1}\psi_\alpha &= 0, \qquad\qquad (x,y)\in\partial\mathcal{D} \end{aligned}\right\} \tag{12.107}$$

Here, α is a counting index, $\alpha = 1,2,\ldots,\infty$, and $\lambda_\alpha, \mu_\alpha$ are eigenvalues of the Neumann problem (12.106) and the Dirichlet problem (12.107) respectively. Note that the eigenvalue problems (12.106) and (12.107) do not involve the time and are defined once the basin geometry is prescribed.

6. Along with the functions ϕ_α and ψ_α we may also define the functions

$$\mathbf{v}_\alpha^\phi := -\nabla\phi_\alpha, \qquad \mathbf{v}_\alpha^\psi := h^{-1}\hat{\mathbf{k}}\times\nabla\psi_\alpha, \tag{12.108}$$

provided the functions ϕ_α and ψ_α are uniquely defined by (12.106) and (12.107).

It is not difficult to show that the problems (12.106) and (12.107) are selfadjoint. Therefore, the eigenvalues are real, the spectra are discrete and the eigenfunctions internally[12] orthogonal and can be normalized; moreover, ϕ_α and ψ_α are square integrable. To prove orthogonality, we multiply $(12.106)_1$ with ϕ_β and integrate over $\mathcal{D}$. This yields

$$\begin{aligned} &-\int_{\mathcal{D}}[\nabla\cdot(h\nabla\phi_\alpha)]\phi_\beta\,dA\\ &\quad= -\int_{\mathcal{D}}\nabla\cdot(h\nabla\phi_\alpha\phi_\beta)dA + \int_{\mathcal{D}} h\nabla\phi_\alpha\cdot\nabla\phi_\beta\,dA\\ &\quad= -\int_{\partial\mathcal{D}}\phi_\beta\underbrace{h\nabla\phi_\alpha\cdot N}_{=0}d(A) + \int_{\mathcal{D}} h\nabla\phi_\alpha\cdot\nabla\phi_\beta\,dA\\ &\quad= \lambda_\alpha\int_{\mathcal{D}}\phi_\alpha\phi_\beta\,dA. \end{aligned} \tag{12.109}$$

Here, the divergence theorem has been applied. Hence,

$$\int_{\mathcal{D}} h\nabla\phi_\alpha\cdot\nabla\phi_\beta\,dA = \lambda_\alpha\int_{\mathcal{D}}\phi_\alpha\phi_\beta\,dA \tag{12.110}$$

and by interchanging the roles of α and β

$$\int_{\mathcal{D}} h\nabla\phi_\beta\cdot\nabla\phi_\alpha\,dA = \lambda_\beta\int_{\mathcal{D}}\phi_\beta\phi_\alpha\,dA \tag{12.111}$$

[12] This means that any two functions ϕ_α, ϕ_β or ψ_α, ψ_β are orthogonal but not ϕ_α with ψ_β.

Subtracting (12.111) from (12.110) yields

$$0 = (\lambda_\alpha - \lambda_\beta) \int_{\mathcal{D}} \phi_\alpha \phi_\beta \, dA \qquad \forall\ \alpha, \beta. \tag{12.112}$$

For different eigenvalues, $\lambda_\alpha \neq \lambda_\beta$, if $\alpha \neq \beta$, this implies $\int_{\mathcal{D}} \phi_\alpha \phi_\beta \, dA = 0$ proving orthogonality of the function set $\{\phi_\alpha\}$. An analogous proof can also be established for the functions $\{\psi_\alpha\}$. The analogous relation to (12.110) is

$$\begin{aligned} \int_{\mathcal{D}} h^{-1} \nabla \psi_\alpha \cdot \nabla \psi_\beta \, dA &= \int_{\mathcal{D}} h^{-1} (\hat{\mathbf{k}} \times \nabla \psi_\alpha) \cdot (\hat{\mathbf{k}} \times \nabla \psi_\beta) dA \\ &= \mu_\alpha \int_{\mathcal{D}} \psi_\alpha \psi_\beta \, dA. \end{aligned} \tag{12.113}$$

Writing this for α and β interchanged, we conclude as above, if $\mu_\alpha \neq \mu_\beta$, $\alpha \neq \beta$, that $\int_D \psi_\alpha \psi_\beta \, dA = 0$, proving orthogonality of the function set $\{\psi_\alpha\}$. Alternatively, relations (12.111) and (12.113), combined with (12.108), yield

$$\begin{aligned} \int_{\mathcal{D}} h \mathbf{v}_\alpha^\phi \cdot \mathbf{v}_\beta^\phi \, dA &= \lambda_\alpha \int_{\mathcal{D}} \phi_\alpha \phi_\beta \, dA = c^2 A \delta_{\alpha\beta}, \\ \int_{\mathcal{D}} h \mathbf{v}_\alpha^\psi \cdot \mathbf{v}_\beta^\psi \, dA &= \mu_\alpha \int_{\mathcal{D}} \psi_\alpha \psi_\beta \, dA = c^2 A \delta_{\alpha\beta}, \end{aligned} \tag{12.114}$$

in which $c^2 = g\bar{H}$, A is the area of $\mathcal{D}$ and $\delta_{\alpha\beta} = 1$, if $\alpha = \beta$ and $\delta_{\alpha\beta} = 0$, if $\alpha \neq \beta$. The expressions on the far right of (12.114) are the normalization conditions for the functions ϕ_α, ψ_α or $\mathbf{v}_\alpha^\phi$, $\mathbf{v}_\alpha^\psi$, $\alpha = 1, 2, \ldots, \infty$. Note that the construction of the function sets $\{\phi_\alpha\}$, $\{\psi_\alpha\}$ or $\{\mathbf{v}_\alpha^\phi\}$, $\{\mathbf{v}_\alpha^\psi\}$ is all based on the solution of the time-independent self-adjoint boundary value problems (12.106) and (12.107); thus, these functions can be determined prior to the solution of the dynamical problem (12.100) and (12.101). In a first step towards that purpose, we now proceed to express $\mathbf{v}^\phi$, $\mathbf{v}^\psi$ in terms of $\{\mathbf{v}_\alpha^\phi\}$, $\{\mathbf{v}_\alpha^\psi\}$. Using the ansatz

$$(\mathbf{v}^\phi, \mathbf{v}^\psi) = \sum_{\alpha=1}^{\infty} (p_\alpha \mathbf{v}_\alpha^\phi, q_\alpha \mathbf{v}_\alpha^\psi) \tag{12.115}$$

it is easily shown with the aid of (12.114) that

$$\begin{aligned} p_\alpha &= \frac{1}{c^2 A} \int_{\mathcal{D}} h \mathbf{v}_\alpha^\phi \cdot \mathbf{v}^\phi \, dA \overset{!}{=} \frac{1}{c^2 A} \int_{\mathcal{D}} h \mathbf{v}_\alpha^\phi \cdot \mathbf{v} dA, \\ q_\alpha &= \frac{1}{c^2 A} \int_{\mathcal{D}} h \mathbf{v}_\alpha^\psi \cdot \mathbf{v}^\psi \, dA \overset{!}{=} \frac{1}{c^2 A} = \int_{\mathcal{D}} h \mathbf{v}_\alpha^\psi \cdot \mathbf{v} dA. \end{aligned} \tag{12.116}$$

We remark that p_α and q_α are time dependent, since $\mathbf{v}^\phi$ and $\mathbf{v}^\psi$ are time dependent.

Having obtained orthogonal bases for $\mathbf{v}^\phi$ and $\mathbf{v}^\psi$, we must now establish a basis for the height field ζ. It follows from the mass balance equation $(12.100)_1$ that ζ can be expressed in terms of $\{\phi_\alpha\}$ alone, since the functions $\mathbf{v}_\alpha^\psi$ are solenoidal. Therefore, we write

$$\zeta_\alpha = \gamma_\alpha \phi_\alpha \tag{12.117}$$

and determine the normalization by the condition that

$$\underbrace{\int_{\mathcal{D}} \zeta_\alpha \zeta_\beta \, dA}_{\bar{H}^2 A \delta_{\alpha\beta}} = \gamma_\alpha \gamma_\beta \int_{\mathcal{D}} \phi_\alpha \phi_\beta \, dA \overset{(12.114)_1}{=} \gamma_\alpha \gamma_\beta c^2 A \lambda_\alpha^{-1} \delta_{\alpha\beta}, \tag{12.118}$$

where the choice $\bar{H}^2 A \delta_{\alpha\beta}$ for the integration of the left-hand side is based only on reasons of dimensionality. This implies

$$\gamma_\alpha = \bar{H} \sqrt{\lambda_\alpha} c^{-1}, \qquad \zeta_\alpha = \bar{H} \sqrt{\lambda_\alpha} c^{-1} \phi_\alpha, \tag{12.119}$$

$$\int_{\mathcal{D}} \zeta_\alpha \zeta_\beta \, dA = \bar{H}^2 A \delta_{\alpha\beta}. \tag{12.120}$$

With this normalization the expansion

$$\zeta = \sum_{\alpha=1}^{\infty} r_\alpha \zeta_\alpha \tag{12.121}$$

and relation (12.120) imply

$$r_\alpha \equiv \frac{1}{\bar{H}^2 A} \int_{\mathcal{D}} \zeta_\alpha \zeta \, dA, \tag{12.122}$$

which is dimensionless.

Associated with the expansions (12.115) and (12.120) are the so-called Parceval relations

$$\begin{aligned} K^\phi &= \frac{1}{2} \rho \bar{H} \int_{\mathcal{D}} h \mathbf{v}^\phi \cdot \mathbf{v}^\phi \, dA \\ &= \frac{1}{2} \rho \bar{H} \int_{\mathcal{D}} h \left(\sum_\alpha p_\alpha \mathbf{v}_\alpha^\phi \right) \cdot \left(\sum_\beta p_\beta \mathbf{v}_\beta^\phi \right) dA \end{aligned}$$

$$= \frac{1}{2}\rho\bar{H}\sum_{\alpha,\beta} p_\alpha p_\beta \underbrace{\int_{\mathcal{D}} h\mathbf{v}_\alpha^\phi \cdot \mathbf{v}_\beta^\phi dA}_{c^2 A\delta_{\alpha\beta}\ (12.114)_1}$$

$$= \frac{1}{2}\underbrace{(\rho\bar{H}A)}_{M} c^2 \sum_\alpha p_\alpha^2 = \frac{1}{2}Mc^2\sum_\alpha p_\alpha^2, \tag{12.123}$$

$$K^\psi = \frac{1}{2}\rho\bar{H}\int_{\mathcal{D}} h\mathbf{v}^\psi \cdot \mathbf{v}^\psi dA$$

$$= \frac{1}{2}\rho\bar{H}\int_{\mathcal{D}} h\left(\sum_\alpha q_\alpha \mathbf{v}_\alpha^\psi\right)\cdot\left(\sum_\beta q_\beta \mathbf{v}_\beta^\psi\right) dA$$

$$= \frac{1}{2}\rho\bar{H}\sum_{\alpha,\beta} q_\alpha q_\beta \underbrace{\int_{\mathcal{D}} h\mathbf{v}_\alpha^\psi \cdot \mathbf{v}_\beta^\psi dA}_{c^2 A\delta_{\alpha\beta}\ (12.114)_2}$$

$$= \frac{1}{2}\underbrace{(\rho\bar{H}A)}_{M} c^2 \sum_\alpha q_\alpha^2 = \frac{1}{2}Mc^2\sum_\alpha q_\alpha^2, \tag{12.124}$$

$$P = \frac{1}{2}\rho g\int_{\mathcal{D}} \zeta^2 dA = \frac{1}{2}\rho g\int_{\mathcal{D}}\sum_{\alpha,\beta} r_\alpha r_\beta \zeta_\alpha\zeta_\beta dA$$

$$= \frac{1}{2}\rho g\sum_{\alpha,\beta} r_\alpha r_\beta \underbrace{\int_{\mathcal{D}} \zeta_\alpha\zeta_\beta dA}_{\bar{H}^2 A\delta_{\alpha\beta}\ (12.120)}$$

$$= \frac{1}{2}\underbrace{(\rho\bar{H}A)}_{M}\underbrace{(g\bar{H})}_{c^2}\sum_\alpha r_\alpha^2 = \frac{1}{2}Mc^2\sum_\alpha r_\alpha^2. \tag{12.125}$$

Here, K^ϕ and K^ψ are the kinetic energies of the irrotational and solenoidal motion fields and P is the (gravitational) potential energy. Evidently,

$$K^\phi + K^\psi + P = \frac{1}{2}Mc^2\sum_\alpha\left(p_\alpha^2 + q_\alpha^2 + r_\alpha^2\right) \tag{12.126}$$

is the total energy.

Having established spectral representations of $\mathbf{v}$ and ζ in terms of p_α, q_α, and r_α ($\alpha = 1, 2, \ldots, \infty$), we must now explore (12.100) to find a system of ordinary differential equations for these coefficients. First, we differentiate p_α, q_α as given in (12.116) and r_α in (12.122) with respect to time. Since the limits of integrations (the basin boundaries) are assumed independent of time, and since the characteristic functions $\mathbf{v}_\alpha^\phi$, $\mathbf{v}_\alpha^\psi$, ζ_α are also time independent, the result of this differentiation is merely to introduce $\partial\mathbf{v}/\partial t$ in place of $\mathbf{v}$ in (12.116) and $\partial\zeta/\partial t$ in place of ζ in (12.122):

$$\begin{aligned}
\frac{dp_\alpha}{dt} &= \frac{1}{c^2 A}\int_{\mathcal{D}} h\mathbf{v}_\alpha^\phi \cdot \frac{\partial \mathbf{v}}{\partial t} dA,\\
\frac{dq_\alpha}{dt} &= \frac{1}{c^2 A}\int_{\mathcal{D}} h\mathbf{v}_\alpha^\psi \cdot \frac{\partial \mathbf{v}}{\partial t} dA,\\
\frac{dr_\alpha}{d} &= \frac{1}{\bar{H}^2 A}\int_{\mathcal{D}} \zeta_\alpha \frac{\partial \zeta}{\partial t} dA.
\end{aligned} \tag{12.127}$$

In these relations, $\partial\mathbf{v}/\partial t$, $\partial\zeta/\partial t$ are next eliminated with the aid of (12.100). In doing this and making use of (12.106)–(12.108), (12.115), (12.116), and $(12.119)_2$, the resulting equations can be put into the form

$$\left.\begin{aligned}
\frac{dp_\alpha}{dt} &= \nu_\alpha \frac{d^2 r_\alpha}{dt} + f\sum_\beta \left(a_{\alpha\beta} p_\beta + b_{\alpha\beta} q_\beta\right),\\
\frac{dq_\alpha}{dt} &= f\sum_\beta \left(c_{\alpha\beta} p_\beta + \underbrace{d_{\alpha\beta}}_{0} q_\beta\right),\\
\frac{dr_\alpha}{dt} &= -\nu_\alpha p_\alpha,
\end{aligned}\right\} \tag{12.128}$$

in which the constant coefficients $\nu_\alpha, a_{\alpha\beta}, \ldots, d_{\alpha\beta}$ are defined as

$$\left.\begin{aligned}
&\nu_\alpha := \sqrt{c^2\lambda_\alpha},\\
&a_{\alpha\beta} := \langle \mathbf{v}_\alpha^\phi, -\hat{\mathbf{k}}\times\mathbf{v}_\beta^\phi\rangle, \quad b_{\alpha\beta} := \langle \mathbf{v}_\alpha^\phi, -\hat{\mathbf{k}}\times\mathbf{v}_\beta^\psi\rangle,\\
&c_{\alpha\beta} := \langle \mathbf{v}_\alpha^\psi, -\hat{\mathbf{k}}\times\mathbf{v}_\beta^\phi\rangle, \quad d_{\alpha\beta} := \langle \mathbf{v}_\alpha^\psi, -\hat{\mathbf{k}}\times\mathbf{v}_\beta^\psi\rangle,
\end{aligned}\right\} \tag{12.129}$$

where the inner product $\langle \mathbf{f}, \mathbf{g}\rangle$ is defined as

$$\langle \mathbf{f}, \mathbf{g}\rangle := \frac{1}{c^2 A}\int_{\mathcal{D}} h\mathbf{f}\cdot\mathbf{g} dA. \tag{12.130}$$

Note that the coupling coefficients depend only on the basin geometry and the functions ϕ_α, ψ_α which are also known, if the geometry is prescribed. Moreover, it follows from the definitions (12.129), (12.130) that

$$a_{\alpha\beta} = -a_{\beta\alpha}, \quad b_{\alpha\beta} = -c_{\beta\alpha}, \quad d_{\alpha\beta} = 0. \tag{12.131}$$

It is apparent from (12.128) that ν_α is the frequency of the normal modes in the zero-rotation case ($f = 0$). Rotation introduces a coupling between the p_α's and q_α's so that, when $f \neq 0$, the normal modes can only be built through linear combinations of $p_\alpha, q_\alpha, r_\alpha$. This spectral-type solution method is due to Proudman [33].

The ordinary differential equations (12.128) are homogeneous and linear with constant coefficients. They can, in principle, be solved by assuming solutions of the form

$$(p_\alpha, q_\alpha, r_\alpha) = (\check{p}_\alpha, \check{q}_\alpha, \check{r}_\alpha)\exp(-i\omega t) \tag{12.132}$$

and truncating the number of characteristic functions at $\alpha = M_p + M_q + M_\zeta$. Substituting (12.132) into (12.128) yields a matrix equation of the form

$$M_{\alpha\beta}(\omega)x_\beta = 0 \qquad \alpha, \beta = 1, 2, M_p + M_q + M_\zeta, \tag{12.133}$$

with a frequency dependent square matrix $\mathbf{M}$ of dimension $(M_p + M_q + M_\zeta) \times (M_p + M_q + M_\zeta)$ and vector $\mathbf{x}$, collecting all amplitudes $(\check{p}_\alpha, \check{q}_\alpha, \check{r}_\alpha)$. Admissible values of ω then follow from the solvability condition

$$\det \mathbf{M}(\omega) = 0. \tag{12.134}$$

This is essentially the procedure that was taken by Proudman [33] to determine the eigenfrequencies of the gravity induced rotational modes in a cylindrical basin with constant and parabolic bottom. Rao [40] employed it to find the oscillations of the fluid in a rotating rectangle of constant depth and free surface, whilst Maas [21] did the same for the inertial waves proper. The corresponding computations are not easy and still rather involved. The reader is asked to consult the literature.

The method is ideally suited to lake geometries and bathymetries of regular shape. In principle, however, it is applicable to any given basic geometry. Each lake then will give rise to its own function sets $\{\phi_\alpha\}$ and $\{\psi_\alpha\}$. These can be determined once and for all. When this is done, the solution procedure is to solve a system of ordinary differential equations in time. To our knowledge this has so far not been tried with real lakes.

References

1. Bjerknes, V., Bjerknes, J., Solberg, H. and Bergeron, T.T.: *Physikalische Hydrodynamik*, Springer, Berlin, etc. (1933)
2. Brown, P.J.: Kelvin wave reflection in a semi-infinite canal. *J. Mar. Res.*, **31**, 1–10 (1973)

3. Bryan, G.: The waves on a rotating liquid spheroid of finite ellipticity. *Phil. Trans. Royal Soc. Lond.*, **180**, 187–219 (1889)
4. Cartwright, D.: *Tides, a Scientific History*. Cambridge University Press, Cambridge (1999)
5. Chapman, D.: On the failure of Laplace's tidal equations to model sub-inertial motions at a discontinuity in depth. *Dyn. Atmos. Oceans*, **7**, 1–16 (1982)
6. Chapman, D. and Hendershott, M.: Shelf wave dispersion in a geophysical ocean. *Dyn Atmos. Oceans*, **7**, 17–31 (1982)
7. Corkan, R.H. and Doodson, A.T.: Free oscillations in a rotating square sea. *Proc. Roy. Soc. London A*, **21**, 147 (1952)
8. Defant, A.: *Gezeitenprobleme des Meeres in Landnähe*. (published in "Probleme der kosmischen Physik", Vol. 6) Hamburg, Henri Grand, p 80 (1925)
9. Defant, F.: Theorie der Seiches des Michigansees und ihre Abwandlung durch Wirkung der Corioliskraft. *Arch. Met. Geophys. Biokl.*, **A 6**, 218–241 (1953)
10. Goldsbrough, G.R.: The tidal oscillations in rectangular basins. *Proc. Roy. Soc. London A*, **132**, 689 (1931)
11. Jeffreys, H.: The free oscillations of water in an elliptical lake. *Proc. Lond. Math. Soc.*, **23**, 455–476 (1925)
12. Kelvin, L. (William Thomson): On the gravitational oscillations of rotating water. *Proc. Roy. Soc. Edinburgh*, **10**, 92–100, (1979); reprinted *Phil. Mag.*, **10**, 109–116 (1880)
13. Kelvin, L.: Vibrations of a columnar vortex. *Philos. Mag.*, **10**, 155–168 (1880)
14. Krauss, W.: *Interne Wellen*. Gebrüder Bornträger, Berlin, Nikolassee (1966)
15. Krauss, W.: *Methods and Results of Theoretical Oceanography I, Dynamics of the homogeneous and the quasi-homogeneous Ocean*. Gebr. Bornträger (1973)
16. Lamb, H.: *Hydrodynamics*. Cambridge University Press (1924)
17. Lamb, H.: *Hydrodynamics*. 6th edition, Cambridge University Press (1932)
18. LeBlond, P.H. and Mysak, L. A.: *Waves in the Ocean* Elsevier Sci. Publ, Amsterdam 602 p.(1978)
19. Lifschitz, A. and Fabijonas, B.: A new class of instabilities of rotating fluids. *Phys. Fluids*, **8**, 2239–2241 (1996)
20. Lighthill, S.M.J.: Dynamics of rotating fluids: a survey. *J. Fluid Mech.*, **26**, 411–431 (1966)
21. Maas, L.R.M.: On the amphidromic structure of inertial waves in a rectangular parallelepiped. *Fluid Dynamics Research*, **33**, 373–401 (2003)
22. Mortimer, C. H.: Frontiers in physical limnology with particular reference to long waves in rotating basins. *Proc. 5th Conf. Great Lakes Res., Great Lakes Res. Div. Univ. Michigan*, **9**, 9–42 (1963)
23. Mortimer, C. H.: *Large scale oscillatory motions and seasonal temperature changes in Lake Michigan and Lake Ontario* Special Report No 12, **Part I**, 11 p.: Text, **Part II**, 106 p.: Illustrations, Center for Great Lakes Studies, The University of Wisconsin-Milwaukee (1971)
24. Mortimer, C. H.: Lake Hydrodynamics *Mitt. Int. Ver. Theor. Angew. Limnol.*, **20**, 124–197 (1974)
25. Mortimer, C. H.: Substantive corrections to SIL Communications (IVL Mitteilungen) Nrs 6 and 20. *Mitt. Int. Ver. Theor. Angew. Limnol.*, **19**, 60–72 (1975)
26. Mortimer, C. H.: *Internal waves observed in Lake Ontario during the International Field Year for the Great Lakes (IFYGL), 1977: descriptive theory and preliminary interpretations of near-inertial oscillations in terms of linear channel models*. Special Report no 32, Center for Great Lakes Studies, The University of Wisconsin-Milwaukee, 122 p. (1977)
27. Mortimer, C. H.: *Internal motion and related internal waves in Lake Michigan and Lake Ontario as responses to impulsive wind stresses*. Special Report no 37, Center for Great Lakes Studies, The University of Wisconsin-Milwaukee, 192 p. (1980)
28. Platzman, G. and Rao, D.B.: The free oscillations of Lake Erie. In: *Studies on Oceanography* (Hidaka Volume) (ed. K. Yoshida), 359–382, University of Washington Press (1964)
29. Platzman, G. : Ocean Tides and Related Waves *Amer. Math. Soc. Lectures in Applied Mathematics*, **14**, 239–291 (1971)
30. Poincaré, H.: Sur l'équilibre d'une masse de fluide animee d'un movement de rotation. *Acta Mathematica*, VII, 259–380 (1885)

31. Poincaré, H.: Sur la precession des corps deformables. *Bull. Astronom.*, **27**, 321 (1910)
32. Prandle, D.: The vertical structure of tidal currents. *Geophys. Astrophys. Fluid Dyn.*, **22**, 29–49 (1982)
33. Proudman, J.: On the dynamical theory of tides. Part (ii): flat seas. *Proc. London Math. Soc.*, 2nd Series, **18**, 21–50 (1916)
34. Proudman, J.: Note on the free tidal oscillations of a sea with slow rotation. *Proc. Lond. Math. Soc.*, (2nd series), **35**, 75 (1933)
35. Raggio, G. and Hutter, K.: An extended channel model for the prediction of motion in elongated homogeneous lakes. Part 1. Theoretical introduction. *J. Fluid Mech.*, **121**, 231-255 (1982)
36. Raggio, G. and Hutter, K.: An extended channel model for the prediction of motion in elongated homogeneous lakes. Part 2. First order model applied to ideal geometry: rectangular basins with flat bottom. *J. Fluid Mech.*, **121**, 257-281 (1982)
37. Raggio, G. and Hutter, K.: An extended channel model for the prediction of motion in elongated homogeneous lakes. Part 3. Free oscillations in natural basins *J. Fluid Mech.*, **121**, 283-299 (1982)
38. Hutter, K. and Raggio, G.: A Chrystal-model describing gravitational barotropic motion in elongated lakes *Arch. Met. Geophys. Biokl.*, **Ser A, 31**, 361-378 (1982)
39. Rao, D.B.: *Free gravitational oscillations in rotating rectangular basins*. Ph.D Thesis, Department of Geophysical Sciences, The University of Chicago (1965)
40. Rao, D.B.: Free gravitational oscillations in rotating rectangular basins. *J. Fluid Mech.*, **25**, 523–555 (1966)
41. Rayleigh, L.: On the vibrations of a rectangular sheet of rotating liquid. *Phil. Mag.*, **5**, 297 (1903)
42. Rayleigh, L.: Notes concerning tidal oscillations upon a rotating globe. *Proc. Roy. Soc. A*, **82**, 448 (1909)
43. Rieutord, M., Georgeot, B. and Valdettaro, L.: Wave attractors in rotating fluids: a paradigm for ill-posed Cauchy problems. *Phys. Rev. Lett.*, **85**, 4277–4280, (2000)
44. Solberg, H.: Über die freien Schwingungen einer homogenen Flüssigkeitsschicht auf der rotierenden Erde. *I. Astophys. Norv.*, **1**, 237–340 (1936)
45. Taylor, G.I.: Tidal oscillations in gulfs and basins. *Proc. London Math. Soc.*, Series 2, XX, 148–181 (1920)
46. Van Danzig, D. and Lauwerier, H.A.: The North Sea Problem. IV. Free oscillations of a rotating rectangular sea. *Proc. K. ned. Akad. Wet.* (Series A), **63**, 339 (1960)
47. Whewell: Essay towards a first approximation to a map of co-tidal lines. *Phil. Trans. Royal Soc. London*, **123**, 147–236 (1833)

Chapter 13
Basin-Scale Gravity Waves in Circular and Elliptical Containers on the Rotating Earth

13.1 Motivation

We have learned so far that the oscillations in an incompressible fluid with free surface in a rotating container can arise as vorticity waves and as gravity waves. The former exist only because of the rotation of the container, the latter are 'modulated' by the rotation. On the f-plane, vorticity waves require depth variations to exist, whilst gravity dominated waves are driven by the deformation of the domain boundary, i.e. the deformation of the free surface and the pressure variations induced thereby as well as by the density variations throughout the fluid. Using the linearized equations of motion in the adiabatic and hydrostatic approximations for a Boussinesq fluid, it was shown in Chap. 11 that boundary affected gravity waves existed in straight channels with vertical side walls and constant depth as so-called Kelvin and Poincaré waves.

Kelvin waves have an unidirectional horizontal velocity field parallel to the straight side walls with maximum amplitudes at the side walls which are exponentially decaying away from them perpendicular and to the left of the propagating direction in the Northern hemisphere (N.H.). Combined as forward and backward moving monochromatic waves they form quasi-standing Kelvin waves whose surface or pycnocline elevations rotate counter-clockwise (on the N.H.) around the amphidromic point – the point with zero pycnocline displacement amplitude for all time. However, a combination of monochromatic Kelvin waves with fixed nodal lines of vanishing longitudinal velocity for all time does not exist.

For Poincaré waves the horizontal velocity field is bi-directional i.e. with components parallel and perpendicular to the channel axis and vanishing transverse velocity component at the side walls. Inside the channel, the horizontal velocity vector rotates at any fixed point with elliptical trajectory that is traversed in the clockwise direction on the N.H. Two monochromatic Poincaré waves, propagating forward and backward in the channel, combine to a quasi-standing Poincaré wave. Similar to Kelvin waves, such quasi-standing Poincaré waves possess no transverse nodal lines where longitudinal velocities would vanish for all time. They, therefore, only exist in infinitely long channels, as do quasi-standing Kelvin waves;

K. Hutter et al., *Physics of Lakes*, *Volume 2: Lakes as Oscillators*, Advances in Geophysical and Environmental Mechanics and Mathematics,
DOI 10.1007/978-3-642-19112-1_13,

however, unlike Kelvin waves, the wave activity of Poincaré waves is generally in the off-shore regions of the channel.

We have seen also that a boundary affected wave in a rectangular basin of constant depth is always a combination of a Kelvin wave plus a countable infinite number of Poincaré waves with the same frequency. If the frequency is sufficiently small (i.e. sub-inertial), then the Poincaré waves are of appreciable influence only close to the long ends of the rectangle, but become exponentially small as one moves inside the basin. In this case, one speaks of complete reflection. The appearance of the mode structure is Kelvin-like with progression of interfaces (free surface, pycnoclines) counter-clockwise (on the N.H.). If the frequency is larger (e.g. super-inertial), then the reflection is incomplete: a finite number of Poincaré waves is fully developed throughout the basin, whilst the others are exponentially decaying as one moves away from shore. Since the Kelvin wave is always exponentially evanescent far from shore, the appearance of the wave mode is Poincaré-like, and the rotation of the displacement surfaces and velocities is clockwise around the amphidromic points.

This interplay between Kelvin and Poincaré waves in rectangles of constant depth is generally assumed also to operate in enclosed basins of arbitrary geometry and bathymetry, and experience with realistic basins proves this interpretation to be basically correct. Indeed, basin-scale modes of gravity seiches have either primarily shore-bound activity with phase propagation counter-clockwise (on the N.H.) around the basin or the amphidromic point, if the eigenfrequency is small, or they have dominant off-shore activity with clockwise rotation around the amphidromic point (on the N.H.) and clockwise rotation of the horizontal velocity vector. In the former case, limnologists call the behaviour *Kelvin-like* or *Kelvin-type*; in the latter, they refer to it as *Poincaré-like* or *Poincaré-type*.[1] With this denotation we wish to express that Kelvin-type behaviour signifies primarily shore-bound activity with counter-clockwise phase propagation (on the N.H.) and that Poincaré-type behaviour means primarily off-shore activity with clockwise phase propagation (on the N.H.)

The above understanding is usually tacitly transferred to the dynamics of basin-scale gravity motions in lakes of arbitrary shape. We shall see when reporting results obtained for gravity waves in cylindrical containers of circular and elliptical shapes that this understanding requires modification.

In what follows, we shall discuss basin-scale modes of gravity seiches for circular and elliptical basins of constant depth which are sufficiently large that the rotation of the Earth exercises a sizeable influence on the mode structure. For barotropic processes, this requires horizontal basin dimensions of several 100 km extent – the external Rossby radius is of the order of 300–600 km, depending on water depth – for baroclinic modes i.e. lakes whose water is stratified by temperature and/or salt, the horizontal basin sizes can be as small as a few kilometres, depending on

[1] Most authors of scientific papers call the above behaviour simply Kelvin behaviour or Poincaré behaviour, which is overemphasizing these authors contribution, because neither Kelvin nor Poincaré have conducted work on gravity seiches *in arbitrary basins*.

horizontal and vertical mode structure.[2] A rough estimate for a two-layer system is obtained as follows:

$$R_{\text{int}} = \frac{1}{f}\sqrt{\frac{\Delta\rho}{\rho} g \frac{H_1 H_2}{H_1 + H_2}} \cong \frac{1}{f}\sqrt{\frac{\Delta\rho}{\rho} g H_1}, \qquad \text{for} \quad H_1 \ll H_2, \quad (13.1)$$

where $\Delta\rho$ is the density difference between the upper and lower layer, H_1 and H_2 are the upper and lower layer thicknesses. With $\Delta\rho/\rho = 10^{-2}$, $H_1/H = 10^{-1}$ this gives $R_{\text{int}} = 10^{-2} \times R_{\text{ext}}$, 3–6 km.

13.2 Conceptual Prerequisites

In constant depth containers, linear gravity waves can be decomposed by the separation of variable technique into vertical and horizontal wave structures. For instance, if any field variable $f(x, y, z, t)$ is written as

$$f(x, y, z, t) = F_n(z) f_n(x, y, t),$$

then $f = p$ is the perturbation pressure, and P_n satisfies the vertical eigenvalue problem

$$\left.\begin{aligned} &\frac{\mathrm{d}}{\mathrm{d}z}\left(\frac{1}{N^2(z)}\frac{\mathrm{d}P_n(z)}{\mathrm{d}z}\right) + \frac{1}{g h_n} P_n = 0, \\ &\frac{\mathrm{d}P_n}{\mathrm{d}z} = 0, \qquad \text{at} \qquad z = -H, \\ &\frac{\mathrm{d}P_n}{\mathrm{d}z} + \frac{N^2(z)}{g} P_n = 0, \qquad \text{at} \qquad z = 0, \end{aligned}\right\} \quad (13.2)$$

in which $N(z) = -g[\mathrm{d}\rho/\mathrm{d}z]/\rho_*$ is the buoyancy frequency and h_n the separation constant, the eigenvalue of (13.2), called the *equivalent depth*. Moreover, n is the counting index of the eigenmodes. In an approximate solution of (13.2), the second term in $(13.2)_3$ may be dropped. This then corresponds to the imposition of the rigid lid assumption.

Alternatively, the equation for the horizontal variation of the pressure, $f = p_n(x, y, t)$ is given by the differential equation

$$\mathcal{L} p_n - g h_n \Delta_H^2 p_n = 0, \qquad \mathcal{L} := \left(\frac{\partial^2}{\partial t^2} + f^2\right), \qquad f = 2\Omega \sin\phi, \quad (13.3)$$

[2] Internal Rossby radii for a two-layer system are about a factor 20–40 times smaller than external Rossby radii.

in which Ω is the angular velocity of the Earth, ϕ is the geographical latitude and which must be solved subject to the boundary condition of no flux through the vertical shore boundary.[3]

The temporal evolution of the horizontal velocities of the nth vertical mode is described by the linearized horizontal momentum equation in the adiabatic and hydrostatic approximations,

$$\frac{\partial \boldsymbol{v}_n}{\partial t} + f\boldsymbol{k} \times \boldsymbol{v}_n = -gh_n \mathrm{grad}_H\, p, \tag{13.4}$$

where $\boldsymbol{k} = (0, 0, 1)^{\mathrm{T}}$, and must be solved subject to the boundary condition

$$\frac{\partial \boldsymbol{v}_n}{\partial \boldsymbol{n}} = 0 \qquad \text{along the container wall,} \tag{13.5}$$

in which $\boldsymbol{n}$ is the unit vector perpendicular to the container wall.

Strictly, such normal mode solutions are not applicable to realistic basins for lakes, because they require constant depth and vertical bounding walls. However, when applied to circular or elliptical containers, they allow us to see how the terms 'Kelvin-type' and 'Poincaré-type' can be understood.

The answer to this was given by Antenucci et al. [3] and Antenucci and Imberger [4] by solving (13.3)–(13.5) for *circular* and *elliptical* containers with constant depth and restricting the stratification to three layers with constant density. In doing so, they could rely on solutions of the analogous problems for homogeneous fluids in circular and elliptical cylindrical containers by Thomson (Lord Kelvin) [19], Jeffreys [8] and Goldstein [7] and complementary work by Lamb [9].[4]

13.3 Circular Cylindrical Geometry

In *polar coordinates* (r, θ), for a cylindrical basin (13.3)–(13.5) take the forms

$$\left.\begin{aligned}
&\mathcal{L}p_n - gh_n \left\{ \frac{\partial^2 p_n}{\partial r^2} + \frac{1}{r}\frac{\partial p_n}{\partial r} + \frac{1}{r^2}\frac{\partial^2 p_n}{\partial \theta^2} \right\} = 0,\\
&\frac{\partial u_n}{\partial t} - f v_n = -gh_n \frac{\partial p_n}{\partial r},\\
&\frac{\partial v_n}{\partial t} + f u_n = -gh_n \frac{\partial p_n}{\partial \theta},\\
&u_n = 0, \quad \text{at} \quad r = r_0,
\end{aligned}\right\} \tag{13.6}$$

[3] Equations $(13.2)_1$ and (13.3) have been derived in Chap. 11 and are listed as $(11.67)_2$ and (11.68). Moreover, the boundary conditions are stated in $(11.74)_{3,4}$.

[4] For a biographical sketch see Fig. 13.1.

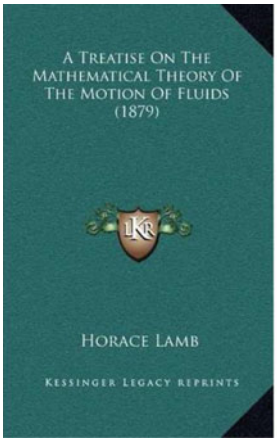

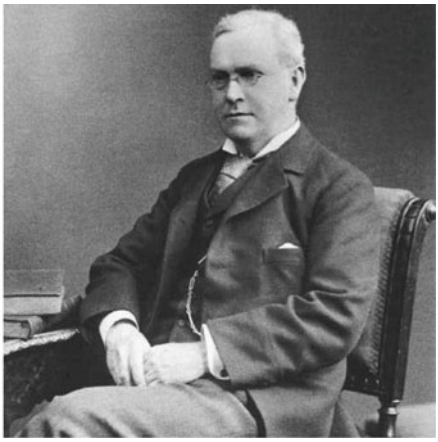

Fig. 13.1 Horace Lamb (1849–1934), a British applied mathematician and author of several influential texts on classical physics (http://en.wikipedia.org/) and the front page of his first book 'A treatise on the mathematical theory of the motion of fluids' which he wrote at the age before 30 (http://www.amazon.de/).

Horace Lamb (27 November 1849 at Stockport, England; 4 December 1934, Cambridge, England), the son of John Lamb, a foreman of a cotton mill, and his wife Elisabeth, née Rangley. After the early death of his father and the re-marriage of his mother, he was raised by his mother's sister Mrs. Holland. He studied at Stockport German School, Owens College, Manchester, and Trinity College, Cambridge, where he was second wrangler (meaning that he was second in the ranked list of mathematics students awarded a first class degree). In Cambridge, Lamb was student of George Gabriel Stokes and James Clerk Maxwell, received the Smith's Prize 1872 and was elected a Fellow of Trinity College in the same year. In 1875, he was appointed to the chair of mathematics at the Adelaide University, Australia where he lectures for 10 years. In 1885, he returned back to England as mathematics professor of the Victoria University (now University of Manchester), where he stayed until 1920 when he retired. Thereafter, he went to Cambridge, England where the honorary Rayleigh lectureship was created for him. He continued to work on his research.

Lamb worked primarily on hydrodynamics; however, he was extremely broad with contributions in elasticity, electrodynamics, dynamics and waves in plates. He was particularly esteemed as author of books (see below) and as a dedicated teacher. In the context of this book he contributed to the theory of tides. In 1884, Lamb was elected a Fellow of the Royal Society, London, which honored him in 1902 with the Royal Medal and in 1923 with the Copley medal. He was twice president of the Royal Society and from 1902–1904 president of the London Mathematical Society of which he received the De Morgan Medal in 1911. He earned seven honorary doctorates and became a member of the Academia Lincei in 1931. Horace Lamb was married with Elisabeth Foot and they had seven children.

Books:
A treatise on the mathematical theory of the motion of fluids. 1879, Kessinger Legacy Reprints 2010;
Hydrodynamics. Cambridge University Press 1895, 6th edn. 1933, reprinted by Dover;
An elementary course of infinitesimal calculus. Cambridge 1997, 3rd edn. 1919, reissued by Cambridge 2009;
Propagation of tremors over the surface of an elastic solid. Cambridge 1904;
The dynamical theory of sound. Cambridge 1910, 2nd edn. 1925, Dover 2004;
Higher mechanics. Cambridge 1920, 2nd edn. 1929;
Statics: Including hydrostatics and the elements of the theory of elasticity. Cambridge 1928, reissued Cambridge 2009;
Dynamics. Cambridge 1914, 2nd edn. 1923–1961.

The text is based on: http://de.wikipedia.org/wiki/Horace_Lamb, but see also http://www-history.msc.st-andrews.ac.uk/Biographies/Lamb.html.

in which u_n, v_n are now the radial and azimuthal components of $\boldsymbol{v}_n$, and r_0 is the radius of the cylindrical wall. Solutions of (13.6), representing propagating waves around the basin must have the forms[5]

$$\left.\begin{aligned} p_n(r,\theta,t) &= p^*_{\ell n}(r)\cos(\ell\theta+\omega_{\ell n}t),\\ u_n(r,\theta,t) &= u^*_{\ell n}(r)\sin(\ell\theta+\omega_{\ell n}t),\\ v_n(r,\theta,t) &= v^*_{\ell n}(r)\cos(\ell\theta+\omega_{\ell n}t). \end{aligned}\right\} \tag{13.7}$$

If this is substituted into (13.6), it is easily seen that $p^*_{\ell n}$ must satisfy the equation

$$p^{\star\prime\prime}_{\ell n}+\frac{1}{r}p^{\star\prime}_{\ell n}\left(\frac{\omega^2_{\ell n}-f^2}{gh_n}-\frac{\ell^2}{r^2}\right)p^{\star}_{\ell n}=0, \tag{13.8}$$

whilst

$$\left.\begin{aligned} u^{\star}_{\ell n}(r) &= -\frac{gh_n}{\omega^2_{\ell n}-f^2}\left\{\omega_{\ell n}p^{\star\prime}_{\ell n}(r)+\frac{f\ell}{r}p^{\star}_{\ell n}(r)\right\},\\ v^{\star}_{\ell n}(r) &= -\frac{gh_n}{\omega^2_{\ell n}-f^2}\left\{fp^{\star\prime}_{\ell n}(r)+\frac{\ell\omega_{\ell n}}{r}p^{\star}_{\ell n}(r)\right\}. \end{aligned}\right\} \tag{13.9}$$

Here, primes denote differentiation with respect to r. The boundary condition $(13.6)_4$ implies

$$\omega_{\ell n}p^{\star\prime}_{\ell n}(r_0)+\frac{f\ell}{r_0}p^{\star}_{\ell n}(r_0)=0. \tag{13.10}$$

In these equations, ℓ is the azimuthal mode number. The solution is obtained by solving the eigenvalue problem (13.8) and (13.10) first and then using the resulting expression for $p_{\ell n}$ in the right-hand side of (13.9). This then yields the radial dependence of the velocity components $u^*_{\ell n}(r)$ and $v^*_{\ell n}(r)$.

Equation (13.8) is Bessel's differential equation; by the transformation

$$\rho=|\lambda|r,\quad \lambda^2=\pm\frac{\omega^2_{\ell n}-f^2}{gh_n},\qquad \begin{matrix}\text{if}\quad \omega^2_{\ell n}>f^2,\\ \text{if}\quad \omega^2_{\ell n}<f^2,\end{matrix} \tag{13.11}$$

it can be put into the standard form

$$\frac{\mathrm{d}^2p^{\star}_{\ell n}(\rho)}{\mathrm{d}\rho^2}+\frac{1}{\rho}\frac{\mathrm{d}p^{\star}_{\ell n}(\rho)}{\mathrm{d}\rho}+\left(\pm1-\frac{\ell^2}{\rho^2}\right)p^{\star}_{\ell n}(\rho)=0,\quad \omega^2_{\ell n}\gtrless f^2. \tag{13.12}$$

[5] Antenucci and Imberger [4] write instead $p_n = p^*_n(r)\cos(\ell\theta)\cos(\omega_{\ell n}t)$ which is a rather annoying misprint if one attempts to verify the formulae, which we did.

For *superinertial* frequencies ($\omega_{\ell n}^2 > f^2$) its solutions are the Bessel functions $J_\ell(\rho)$ and $Y_\ell(\rho)$ of order ℓ; for *subinertial* frequencies ($\omega_{\ell n}^2 < f^2$) its solutions are the *modified* Bessel functions $I_\ell(\rho)$ and $K_\ell(\rho)$ of order ℓ. The functions $J_\ell(\rho)$ and $I_\ell(\rho)$ are bounded and regular at $\rho = 0$, but $Y_\ell(\rho)$ and $K_\ell(\rho)$ are singular there, Abramowitz and Stegun [1]. In a basin for which the centre $r = 0$ belongs to the basin domain, $Y_\ell(\rho)$ and $K_\ell(\rho)$ can, therefore, not occur in the expression of the solution for reasons of regularity. Solutions are thus of the form

$$p^\star_{\ell n}(r) = \left\{ J_\ell\left(\sqrt{\frac{|\omega_{\ell n}^2 - f^2|}{g h_n}} r\right), I_\ell\left(\sqrt{\frac{|\omega_{\ell n}^2 - f^2|}{g h_n}} r\right) \right\} \tag{13.13}$$

for super- and sub-inertial frequencies, respectively. In what follows, we shall use the common symbol $\mathcal{J}_\ell$ if either J_ℓ or I_ℓ are meant. Next, noting that (Abramowitz and Stegun [1])

$$\frac{\mathrm{d}\mathcal{J}_\ell(\rho)}{\mathrm{d}\rho} = \mathcal{J}_{\ell-1}(\rho) - \frac{\ell}{\rho}\mathcal{J}_\ell(\rho), \tag{13.14}$$

one may easily deduce that

$$\begin{aligned} \left.\frac{\mathrm{d}p^\star_{\ell n}}{\mathrm{d}r}\right|_{r=r_0} &= \frac{\mathrm{d}\mathcal{J}_\ell}{\mathrm{d}\rho}\frac{\mathrm{d}\rho}{\mathrm{d}r} = \frac{\mathrm{d}\mathcal{J}_\ell}{\mathrm{d}\rho}\sqrt{\frac{|\omega_{\ell n}^2 - f^2|}{g h_n}} \\ &= \sqrt{\frac{|\omega_{\ell n}^2 - f^2|}{g h_n}} \left(\mathcal{J}_{\ell-1} - \frac{\ell}{\sqrt{\frac{|\omega_{\ell n}^2 - f^2|}{g h_n}} r} \mathcal{J}_\ell \right)_{r=r_0} \end{aligned} \tag{13.15}$$

Using this formula in (13.10) yields the dispersion relation in the following dimensionless form

$$\begin{aligned} &\Sigma_{\ell n}\mathcal{J}_{\ell-1}(\Sigma_{\ell n}) + \ell\left(\frac{1}{\sigma_{\ell n}} - 1\right)\mathcal{J}_\ell(\Sigma_{\ell n}) = 0, \\ &\Sigma_{\ell n} := \frac{\sqrt{|\sigma_{\ell n}^2 - 1|}}{S_n}, \quad \sigma_{\ell n} := \frac{\omega_{\ell n}}{f}, \quad S_n = \frac{\sqrt{g h_n}}{r_0 f}, \end{aligned} \tag{13.16}$$

where

$$\mathcal{J}_\ell := \begin{cases} J_\ell, & \text{if} \quad \sigma_{\ell n} > 1, \\ I_\ell, & \text{if} \quad \sigma_{\ell n} < 1. \end{cases} \tag{13.17}$$

In the limnological context, this equation, for superinertial waves, is due to Csanady [5]. Solutions of (13.16) can be found for any values of f, r_0, gh_n and ℓ, if $|\sigma_{\ell n}| > |f|$; however, for subinertial waves, solutions are only real for a limited subset of ℓ, because of the exponential structure of $I_\ell(\rho)$. Lamb [9] (paragraph 210) showed that for a subinertial wave solution of azimuthal mode ℓ to exist, the condition

$$S_n < (\ell(\ell+1))^{-1/2} \tag{13.18}$$

must hold. Solutions have been constructed by Antenucci et al. [3] and Antenucci and Imberger [4].

The transcendental equation (13.16) possesses, in general, a countable infinite number of real solutions $\sigma_{\ell mn}$ $(m = 1, 2, 3, \ldots)$, which are positive or negative and correspond to waves which rotate clockwise and counter-clockwise, respectively, around the basin. The equation holds for all possible modes in the horizontal and vertical directions, which shall be characterized by the acronym $H\ell mVn$. $H\ell m$ typifies the horizontal azimuthal (ℓ) and radial (m) modes, whilst n denotes the vertical modes. Apart from the quantized frequencies $\sigma_{\ell mn}$, the modal pressures $p^*_{\ell mn}$ and velocities $v^*_{\ell mn}$ are of particular interest; they are now all identified by a ternary index $(\cdot)_{\ell mn}$. Specifically, the eigenvalue problem is solved as follows:

1. For given vertical density distribution, the buoyancy frequency $N(z)$ is determined, and then the vertical eigenvalue problem (13.2) is solved. This yields a sequence of wave speeds $c_n^2 = gh_n$ and Burger numbers S_n, $(n = 0, 1, 2, \ldots)$.
2. The roots of (13.16) are determined in conformity with the condition (13.18) and the selection (13.17) of the Bessel functions I_ℓ and J_ℓ.
3. This then fixes the radial distribution, of the pressure $p^*_{\ell mn}(r)$ according to (13.13) and radial derivative $\mathrm{d}p^*_{\ell mn}(r)/\mathrm{d}r$ according to (13.15).
4. The pressure functions obtained in item (3) are then used in the right-hand side of (13.9); they determine the radial distribution of the velocity components $u^*_{\ell mn}(r)$ and $v^*_{\ell mn}(r)$.
5. These results are then used in (13.7) to obtain the complete spatial and temporal distributions

$$\begin{aligned} u_{\ell mn}(r,\theta,t) &= u^\star_{\ell mn}(r)\sin(\ell\theta + \omega_{\ell mn}t), \\ v_{\ell mn}(r,\theta,t) &= v^\star_{\ell mn}(r)\cos(\ell\theta + \omega_{\ell mn}t), \\ p_{\ell mn}(r,\theta,t) &= p^\star_{\ell mn}(r)\cos(\ell\theta + \omega_{\ell mn}t), \end{aligned} \tag{13.19}$$

   which can be computed for any particular time slice.

The above analysis is based on work by Thomson (Lord Kelvin) [19] and Lamb [9] on gravity seiches in a homogeneous fluid in a circular basin of constant depth[6]; its two-layer version of the equations was first given by Csanady [6] and the modal

[6] For portraits and biographical sketches of Lord Kelvin and H.Lamb, see Figs. 12.1 and 13.1.

analysis for the three-layer fluid by Monismith [11]. The application of this circular wave problem to a real lake – Lake Kinneret (Israel) – was presented by Antenucci et al. [3]. In the ensuing description, we follow, with modifications, their approach.

13.4 Three-Layer Stratification – Lake Kinneret Treated as a Circular Cylinder of Constant Depth

The radius r_0 of the circular cylinder modeling Lake Kinneret was taken to be $r_0 = 6\,\text{km}$ and the three-homogeneous layer approximation to the stratification of the field campaigns performed in 1997/1998 (for details see Antenucci et al. [3]) is found to be as stated in Table 13.1.The authors also chose the vertical V1- and V2-phase speeds corresponding to the stratification of Table 13.1 and obtained the speeds of Table 13.2. Their results are explicitly presented for the first analysis period with $c_1 = 0.33\,\text{ms}^{-1}$.

Two classes of solutions are possible: In the subsequent analysis, we will show that for superinertial frequencies the solutions are reminiscent of Poincaré waves and will for this reason call them Poincaré-*type*. Correspondingly, for subinertial frequencies, the solutions are similar to Kelvin waves and will for this reason be called Kelvin-*type*.[7]

Poincaré-type waves exist for all f, r_0, c_n and horizontal mode number (recall, ℓmn is a counting index for the azimuthal (ℓ), radial (m), and vertical (n) modes), but Kelvin-type waves only exist, if (13.18) is satisfied.

In circular basins, the distinction between mode types is better made on the basis of the magnitude of the horizontal velocity vector. The criterion is (13.18). If $\ell(\ell+1) < S_n^{-2}$, then Kelvin-type behaviour means that the horizontal velocities are large close to the shore and smaller in the centre, perhaps very small if the radius of the cylinder is very large as compared to the internal Rossby radius of deformation. Alternatively, if $\ell(\ell+1) > S_n^{-2}$, then velocities tend to be larger in the centre than close to the shore. *Complete* reflection for the rectangular basin corresponds here to the solutions expressed in terms of *modified* Bessel functions, and *incomplete* is the analogue to the solutions expressed here in terms of (*ordinary*) Bessel functions.

For $\ell = 1$ and $c = c_1 = 0.33\,\text{ms}^{-1}$ (analysis period I), inequality (13.18) is satisfied for the model Lake Kinneret; therefore, there are solutions of the dispersion relation (13.16) for I_1 and J_1. The smallest values of the frequency σ for these

[7] We, here, do not follow the habit of Antenucci et al. [3] to call the two waves simply Kelvin and Poincaré waves, because these waves are denoted thus for straight infinite channels. Moreover, Taylor [18] showed that the seiches in a *rectangular* basin are composed of a pair of Kelvin and an infinite number of Poincaré waves of the same frequency, of which all are either exponentially evanescent as one moves away from the long end boundaries or some are oscillatory. If only evanescent Poincaré modes are present, then the behaviour is Kelvin-type and the reflection is called complete, else, mixed behaviour is present throughout the rectangular basin and the reflection is called incomplete.

Table 13.1 Three-homogeneous layer approximation to the stratified Lake Kinneret for three measuring periods in 1998, after Antenucci et al. [3]

Period	H_1 [m]	H_2 [m]	H_3 [m]	T_1 [°C]	T_2 [°C]	T_3 [°C]
(I) 98179–192	12.5	8.0	6.0	27.0	21.1	16.6
(II) 98205–218	12.5	10.0	5.5	28.8	22.4	16.6
(III) 98262–275	14.5	8.5	5.5	28.3	21.3	16.7

Table 13.2 Vertical mode V1- and V2-phase speeds $c_n = \sqrt{gh_n}, n = 1, 2$ for the three analysis periods of Table 13.1

Period	c_1 [ms^{-1}]	c_2 [ms^{-1}]
(I) 98179–192	0.33	0.16
(II) 98205–218	0.36	0.19
(III) 98262–275	0.37	0.16

Table 13.3 Mode numbers and wave types for the three-layer approximation (for measuring period I, see Tables 13.1 and 13.2) and corresponding seiche periods according to (13.16). Note that the radial mode number m_K, m_P is differentiated according to mode type (results by Antenucci et al. [3])

ℓ	m_K	m_P	n	Period (h)	Mode-type
1	1	–	1	22.5	Kelvin
1	–	1	1	12.5	Poincaré
1	–	1	2	17.5	Poincaré

yield a Kelvin-type and a Poincaré-type seiche as listed in Table 13.3. Alternatively, for $c = c_2 = 0.16\,\text{ms}^{-1}$, there exist only Poincaré-type seiches with J_1-solutions of (13.16) with period also listed in Table 13.3. With these, the modal velocities (13.19) can be calculated and from these the layer velocities computed as in [6]. The results are summarized in Fig. 13.2. This figure shows in column (i) the vertical displacements of the two internal interfaces of the three-layer fluid along the WE section; panels in columns (ii), (iii) show the upper, (lower) internal interface, with warm colours representing depression and cold colours representing elevations; panels (iv), (v) and (vi) represent the horizontal velocities in the upper, (middle) and (bottom) layer, respectively. The velocity vectors are normalized by the maximum velocity for each wave and represent the relative contribution to the velocity field in each layer by each wave.

Kelvin-type behaviour $[(\ell, m_K, n) = (1, 1, 1)]$ is demonstrated in rows (a) and (b) of Fig. 13.2. Row (a) shows the seiche mode at $t = 0$, row (b) a quarter period later, $t = T/4$. From panels [(ii)(iii)(a)(b)] we deduce a counter-clockwise rotation of both interior interfaces. Moreover, the layer-velocity plots in panels [(iv)(a)(b)], [(v)(a)(b)], and [(vi)(a)(b)] indicate large near shore velocities and smaller velocities towards the centre, but the decay is not substantial as is often the case, certainly because the internal Rossby radius of deformation is approximately equal to the basin radius. This behaviour is reminiscent of Kelvin-type wave behaviour.

Furthermore, because of the moderate decay of the amplitudes of the velocity (in this case) as one moves from shore towards the centre, one sees that the horizontal velocity also rotates anti-clockwise, a full revolution during the seiche period.

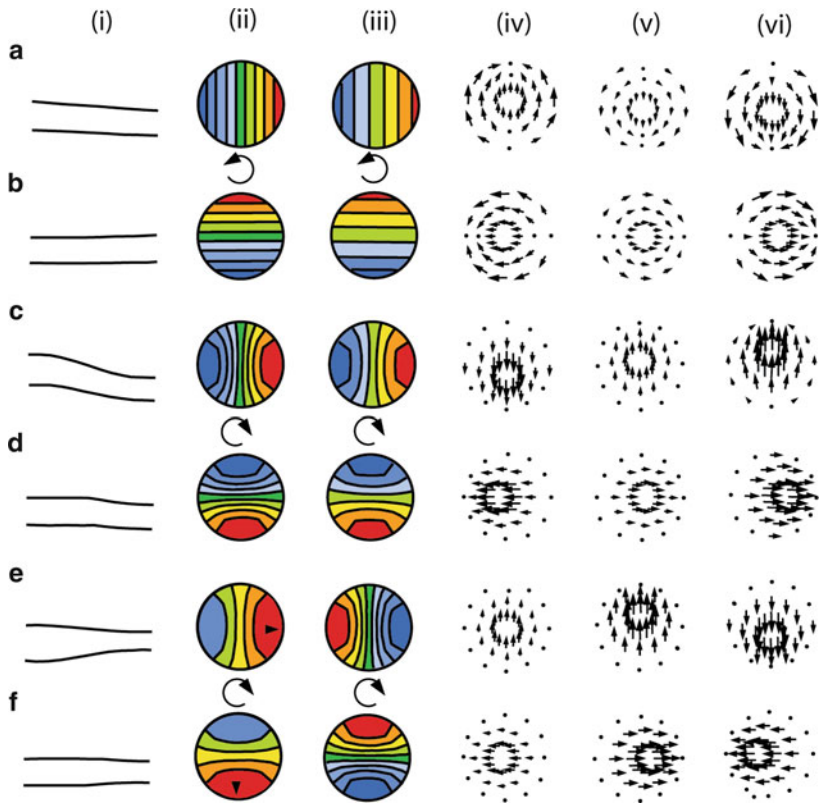

Fig. 13.2 Baroclinic wave characteristics for the three-layer fluid in a uniform-depth circular basin of 6 km radius situated at 32.5°N as listed in Tables 13.1–13.3 for period I. Rows [(**a**), (**b**)] show Kelvin-type V1-behaviour $(\ell, m_{\mathrm{K}}, n) = (1, 1_K, 1)$, rows [(**c**), (**d**)] display Poincaré-type V1 behaviour $(\ell, m_{\mathrm{P}}, n) = (1, 1_{\mathrm{P}}, 1)$ and [(**e**), (**f**)] show Poincaré-type V2 behaviour $(\ell, m_{\mathrm{P}}, n) = (1, 1_{\mathrm{P}}, 2)$. The velocity vectors are normalized by the maximum velocity for each wave and represent the relative contribution to the velocity field in each layer by each wave (redrawn from Antenucci et al. [3], with changes). Copyright 2000 by the American Society of Limnology and Oceanography, Inc, reproduced with permission

This is different from what is usually associated with Kelvin behaviour. Associated particle trajectories are small circles in the centre, become ellipses with major axes parallel to concentric circles, growing in size and eccentricity as one moves radially towards the shore circle, where the ellipses have collapsed to double lines (not shown). In current meter experiments, this should in principle be observable. The reason for this anti-clockwise current rotation is certainly the compactness of the basin geometry.[8]

[8] Recall that horizontal velocity vectors also rotate in the counter-clockwise direction (on the N.H.). So, when basin geometries are compact and horizontal extents are comparable to the internal

V1- and V2-mode Poincaré solutions – $(\ell m_{\mathrm{P}} n) = (111)$ and $(\ell m_{\mathrm{P}} n) = (112)$ – are displayed in rows [(c), (d)] and [(e), (f)] of Fig. 13.2, in which again the panels in rows [(c), (d)] and [(e), (f)] are time slices which are a quarter period apart. It is evident for both cases that displacement and layer velocities rotate clockwise. Interface displacement maxima are at the shore, whilst velocity maxima are in the centre. Horizontal velocities at the boundary are tangential to the shore, but close to the centre they are essentially parallel to the interface level lines. The velocity amplitudes of the $(11_{\mathrm{P}}1)$ Poincaré mode are greatest in the top and bottom layers, whilst those of the $(11_{\mathrm{P}}2)$-Poincaré mode are largest in the middle and bottom layers. It is also seen for this V2-mode that the middle layer thickens parallel to the steepest gradient of the interfaces. The velocity vectors are normalized by the maximum velocity for each wave and represent the relative contribution to the velocity field in each layer by each wave.

Antenucci et al. [3] also raise the question of whether there is a critical condition at the inertial frequency for basin-scale Kelvin-type waves. They mention that, as S_n increases, because the heating increases the phase speed, see (13.16), one would conceivably have a case in which the Kelvin-type wave is no longer supported (i.e. $S_n > (\ell(\ell+1) > -1/2)$). This critical condition is simply a function of the circular basin solution and will become clear, when we look at solutions of an elliptical basin.

Antenucci et al. [3] present a detailed analysis of data of their 1997/1998 field campaigns, conducted in Lake Kinneret. Figure 13.3 shows the lake bathymetry with isobaths at 5-m intervals and indicated sampling stations T1–T10 in June 1997 (open circles) and June to October 1998 (full circles), acoustic doppler current profiler (ADCPs) were deployed at T3, T8, and T10, and thermistor chains were deployed at all stations except T8 and T10. Power spectra of the integrated potential energy[9] for all three analysis periods I, II, III during 1998 showed significant peaks in the energy spectra at 24, 12, and 6 h. The authors conclude, because the energy peak at 6 h was not detected at all stations (not at T4 or T7b), it was not a coherent basin-scale signal. The V1-Kelvin-type wave at 24 h has been previously identified already by Ou and [12]. This period is a combination of a Kelvin-type free response amplified and slightly altered in structure by the strong daily WE-sea breeze. The V1 Poincaré seiche with a 12 h period has been isolated from isotherm depth time series deduced from the thermistor chain temperature data of the 1998 campaign, but has also been identified from earlier measurements conducted by Serruya [16].

Rossby radius of that wave mode, counter-clockwise rotation of the centre velocity may signify Kelvin-type wave behaviour.

[9] The integrated potential energy at a given position is defined by Antenucci et al. [3] as

$$PE(t) = g \int_{z_0}^{H} z\,[\rho(z,t)]\,\mathrm{d}z\,,$$

where integration is from the still water surface to the depth H. The formula computes the gravity potential for the instantaneous density distribution.

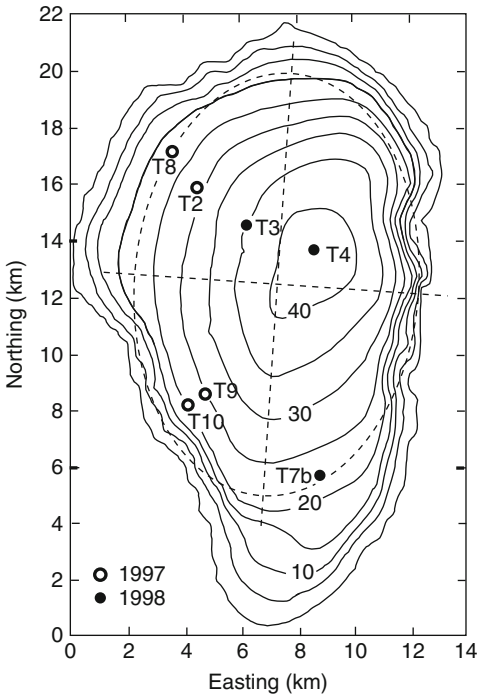

Fig. 13.3 Lake Kinneret bathymetry with isobaths at 5-m intervals and relevant sampling stations in 1997/1998. The ellipse fitted to the topography has an aspect ratio of $b/a = 2/3$. For details see main text. Redrawn from Antenucci et al. [3]. Copyright 2000 by the American Society of Limnology and Oceanography, Inc, reproduced with permission

The thermistor chains in the field campaigns were not ideally deployed to be able to identify a complete cycle of the 24-h Kelvin-type and 12-h Poincaré-type waves.

However, the isotherm–depth–time series from the thermistor chains at T2 and T9 both positioned along the 25-m isobath, see Fig. 13.3, give strong hints for the interpretation of anti-clockwise progression of the 24-h Kelvin-type wave and clockwise progression of the 12-h Poincaré-type wave. Figure 13.4 shows four days data from the 1997 campaign at stations T2 (top panel) and T9 (bottom panel). During this time, the crests of the 24-h Kelvin-type wave and the 12-h wave were in phase, so the second crest of the 12-h signal occurred during the trough of the 24-h signal. The figure shows that the clockwise phase progression of the 12-h wave from T9 to T2 occurred during 2–3 h, when the wind was not acting. The upward facing arrows indicate the clockwise phase progression of the 24-h Kelvin-type wave. True, these data are no more than a strong indication for the claimed behaviour, because no complete cycle is covered by the data, but Antenucci et al. [3] provide also other support for this interpretation. One of these is the evaluation of rotary power spectra of isopycnal vertical speeds, which they decompose into clockwise and anti-clockwise rotating components.

Poincaré-type V2 and V3 modes can hardly be determined from temperature measurements alone. Antenucci et al. [3], therefore, used velocity signals from ADCP measurements at T3 during the 1998 campaign. These are better interpreted with a more realistic model in which geometry and stratification is better adjusted to the real situation.

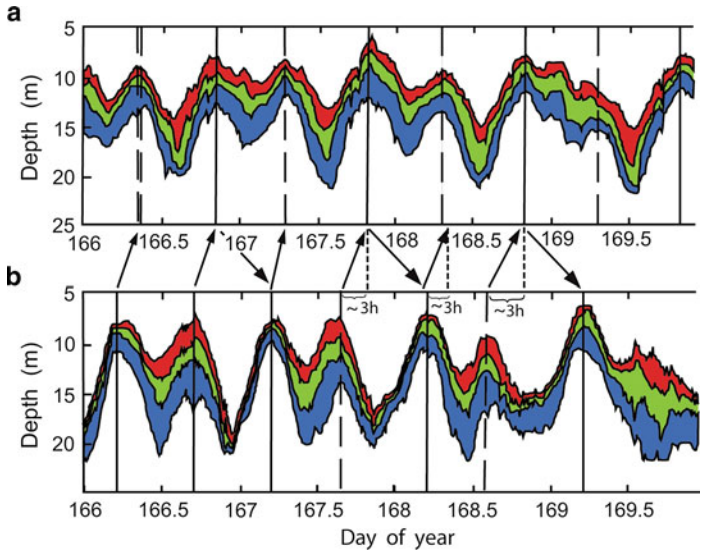

Fig. 13.4 Isotherm–depth–time series from T2 (**a**) and T9 (**b**) from the 1997 campaign in Lake Kinneret. Crests of the 24-h V1 Kelvin-type wave are indicated with solid vertical lines. Crests of the 12-h V1 Poincaré-type wave are indicated by both *dashed* and *solid lines*. Crest locations are chosen by visual inspection of the isotherm record. *Upward-facing arrows* show clockwise phase progression of the 12-h Poincaré-type wave, whilst *downward-facing arrows* show the anti-clockwise phase progression of the 24-h Kelvin-type wave (redrawn from Antenucci et al. [3], with changes). Copyright 2000 by the American Society of Limnology and Oceanography, Inc, reproduced with permission

Table 13.4 Lake Kinneret baroclinic wave summary

Period		ℓ	m_K	m_P	n	Wave type
Field	Three-layer model					
24	22.5	1	1	–	1	Kelvin
12	12.2	1	–	1	1	Poincaré
20 ± 2	17.5	1	–	1	2	Poincaré
20 ± 2	–	1	–	1	3	Poincaré

In summary, Antenucci et al. [3] conclude that the data of the horizontal velocity components suggest the simultaneous presence of V2 and V3 modes as collected in Table 13.4.

There is nearly perfect agreement between the periods of the $(1,1_K,1)$ Kelvin and $(1,1_P,1)$ Poincaré-type modes as obtained by the circular cylinder model and the thermistor chain data. However, this coincidence for the $(1,1_P,1)$-mode is less convincing. The field data suggest that the activated (20 ± 2) h modes are combined V2 plus V3 modes, but the V2 mode does not satisfactorily agree with the predicted 17.5 h period. A theoretical prediction of the V3 mode would need a four-layer model to make a prediction possible. However, it is likely that the value of this period would deviate from the observed (20 ± 2) h even more than for the V2

mode. Improvements can be achieved by better adjustment of the geometry as well as increased number of layers with correspondingly adjusted densities. In the subsequent sections Lake Kinneret will be modeled by an elliptical basin of constant depth. Apart from some practical applicability the elliptical basin will also yield a deeper understanding of Kelvin-type and Poincaré-type behaviour of waves in elongated basins.

13.5 Elliptical Cylindrical Container[10]

Equations (13.3)–(13.5) have also been solved for elliptical containers with vertical walls. Solutions for the homogeneous fluid layer were constructed by Jeffreys [8] and Goldstein [7] with additions by Lamb [9], and the application to the modal formulation (13.3)–(13.5) was presented by Antenucci and Imberger [4].

Let (x, y, z) be Cartesian and (ξ, η, ζ) elliptical cylindrical coordinates. They are related to one another by

$$\left.\begin{array}{l} x = \rho \cosh\xi \cos\eta, \\ y = \rho \sinh\xi \sin\eta, \\ z = z, \end{array}\right\}, \tag{13.20}$$

where $\rho = \sqrt{\mathsf{a}^2 - \mathsf{b}^2} > 0$ is a constant, and $\mathsf{a} > \mathsf{b}$ may be interpreted as major and minor semi-axes of an ellipse. Lines of constant ξ are ellipses and lines of constant η hyperbolas, which are perpendicular to the ellipses, see Fig. 13.5. Let (u_n, v_n) be the physical components of the modal velocity vector tangential to the hyperbolas and ellipses, respectively. Then, it can be shown that[11]

[10] In this section, we drop the index n characterizing the vertical mode. We shall also use counting indices m and n, which are used only here but have no relation to those indices used later in the text when solving the seiche eigenvalue problem.

[11] The literature on mathematical equations in elliptical coordinates seems to be fraught with errors (typos). The standard reference which one tends to trust unquestioned is Abramowitz and Stegun [1]. On p. 722 the Laplace operator in elliptical coordinates was found to be incorrectly printed, and the formulae, corresponding to (13.23) in Antenucci and Imberger [4] are also wrong. Pao and Mow [13] state on their p. 436

$$\mathrm{grad}_H\, f = \frac{1}{\rho J}\left(\frac{\partial f}{\partial \xi}, \frac{\partial f}{\partial \eta}\right) \tag{13.21}$$

$$\left.\begin{array}{l} \mathrm{div}_H \mathrm{grad}_H\, f = \dfrac{1}{\rho^2 J^2}\left(\dfrac{\partial^2 f}{\partial \xi^2} + \dfrac{\partial^2 f}{\partial \eta^2}\right), \\ J^2 := \cosh^2\xi - \cos^2\eta = \frac{1}{2}(\cosh 2\xi - \cos 2\eta) \end{array}\right\} \tag{13.22}$$

for the gradient and the Laplacean of a scalar f. These formulae were counterchecked against general formulae of differential operators in lecture notes on 'Theoretical Aerodynamics' by

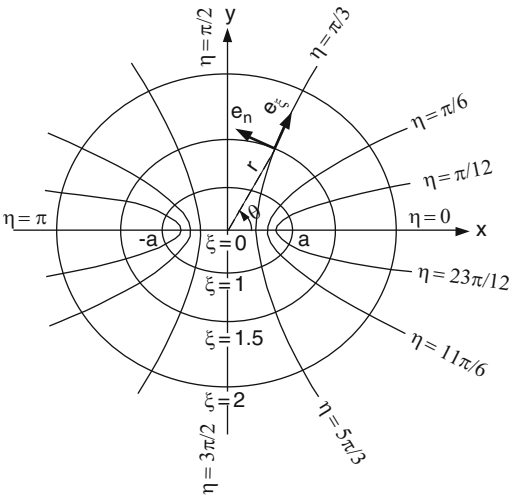

Fig. 13.5 Elliptic coordinate system. A family of confocal ellipses with focal length ρ. Intersecting the ellipses is a family of confocal hyperbolas. Note, $\xi \in [0, \infty)$ and $\eta \in [0, 2\pi]$. The length of the semi-major axis is $\rho \cosh \xi$, whilst that of the semi-minor axis is $\rho \sinh \eta$. Note also that across the line connecting the two focal points, the variable η experiences a jump $[[\eta]]$ between 0 and π

$$\begin{aligned} \text{grad}_H\, p_n &= \frac{\sqrt{2}}{\rho\sqrt{\cosh 2\xi - \cos 2\eta}} \left(\frac{\partial p_n}{\partial \xi}, \frac{\partial p_n}{\partial \eta} \right), \\ \text{div}_H \text{grad}_H\, p_n &= \frac{2}{\rho^2(\cosh 2\xi - \cos 2\eta)} \left\{ \frac{\partial^2 p_n}{\partial \xi^2} + \frac{\partial^2 p_n}{\partial \eta^2} \right\}. \end{aligned} \tag{13.23}$$

Substituting these expressions into (13.3)–(13.5) yields

$$\left.\begin{aligned} &\mathcal{L} p_n - \frac{2gh_n}{\rho^2(\cosh 2\xi - \cos 2\eta)} \left(\frac{\partial^2 p_n}{\partial \xi^2} + \frac{\partial^2 p_n}{\partial \eta^2} \right) = 0, \\ &\frac{\partial u_n}{\partial t} - f v_n = -\frac{\sqrt{2}gh_n}{\rho\sqrt{\cosh 2\xi - \cos 2\eta}} \frac{\partial p_n}{\partial \xi}, \\ &\frac{\partial v_n}{\partial t} + f u_n = -\frac{\sqrt{2}gh_n}{\rho\sqrt{\cosh 2\xi - \cos 2\eta}} \frac{\partial p_n}{\partial \xi}, \\ &u_n = 0, \qquad \text{at} \qquad \xi = \xi_0 \end{aligned}\right\} \tag{13.24}$$

for the nth modal pressure $p_n(\xi, \eta, t)$ and the velocity components $u_n(\xi, \eta, t)$ and $v_n(\xi, \eta, t)$, respectively. Equation (13.24) correspond to (13.6) in polar coordinates.

It is straightforward to see that (13.24) has solutions of the form

$$p_n(\xi, \eta, t) = p_n^*(\xi, \eta) \exp(i\omega_n t), \tag{13.25}$$

Sears [15]. Formulae for differential operators are derived there for general orthogonal coordinates and revealed (13.22) as well. Antenucci and Imberger's [4] Laplace operator agrees with (13.22), but not their use of $\text{grad}_H\, f$ with (13.21).

where p_n^* satisfies, the equation

$$(\omega_n^2 - f^2)\, p_n^* + \frac{2gh_n}{\rho^2(\cosh 2\xi - \cos 2\eta)} \left(\frac{\partial^2 p_n^*}{\partial \xi^2} + \frac{\partial^2 p_n^*}{\partial \eta^2} \right) = 0, \tag{13.26}$$

or after non-dimensionalization

$$\frac{\partial^2 p_n^*}{\partial \xi^2} + \frac{\partial^2 p_n^*}{\partial \eta^2} + 2q_n(\cosh 2\xi - \cos 2\eta)\, p_n^* = 0, \tag{13.27}$$

in which

$$\begin{aligned} q_n &= \frac{1 - \mathsf{b}^2/\mathsf{a}^2}{4} \quad \frac{\sigma_n^2 - 1}{S_n^2}, \quad \sigma_n = \frac{\omega_n}{f}, \quad S_n^2 = \frac{gh_n}{f\mathsf{a}}, \\ \rho^2 &= \mathsf{a}^2 - \mathsf{b}^2, \qquad \mathsf{a} > \mathsf{b}. \end{aligned} \tag{13.28}$$

Equations (13.27) and (13.28) agree with corresponding equations of Antenucci and Imberger [4]. By separation of variables

$$p_n^*(\xi, \eta) = \Xi_n(\xi) H_n(\eta) \tag{13.29}$$

one finds that $\Xi_n(\xi)$ and $H_n(\eta)$ satisfy the equations

$$\begin{aligned} \Xi_n''(\xi) - (b - 2q_n \cosh(\xi))\, \Xi_n(\xi) &= 0, \\ H_n''(\eta) + (b - 2q_n \cos(\eta))\, H_n(\eta) &= 0, \end{aligned} \tag{13.30}$$

where b is the separation constant and the prime denotes univariate differentiation with respect to ξ and η, respectively. The second of (13.30) is the canonical form of the *Mathieu equation*, the first is known as *modified Mathieu equation* and can be reduced to the Mathieu equation by setting $\xi = \pm i\eta$. In what follows, we drop the indices $(\cdot)_n$ in the functions Ξ_n, η_n and parameter q_n until further noticed. Let us discuss $(13.30)_2$ first.

13.6 Mathieu Functions

In this section, we drop the index n characterizing the vertical mode. We shall also use counting indices m and n, but they have nothing in common with such indices used later in the context when solving the seiche eigenvalue problem.

Depending upon the values of b and $q > 0$ in $(13.30)_2$, solutions for $H(\eta)$, may be bounded or unbounded as η increases, or they may be periodic with periods π or 2π. Because we look at fluid flow in the interior of the ellipse, in order to have

a unique single valued solution, $H(\eta)$ must return to the same value as η increases by 2π.

If the periodicity is π, then[12]

$$H(\eta) = \sum_{r=0}^{\infty} (A_{2r} \cos(2r\eta) + B_{2r} \sin(2r\eta)) . \tag{13.31}$$

Substituting this series into $(13.30)_2$ and collecting the coefficients of the cosine and sine functions, one obtains two infinite sets of homogeneous equations as follows:

- Coefficients of $\cos(2r\eta)$:

$$\left.\begin{aligned} & bA_0 - qA_2 = 0, \\ & (b-4)A_2 - q(A_4 + 2A_0) = 0, \\ & (b-4r^2)A_{2r} - q(A_{2r+2} + A_{2r-2}) = 0, \quad r \geqslant 2, \\ & \vdots \end{aligned}\right\} \tag{13.32}$$

- Coefficients of $\sin(2r\eta)$:

$$\left.\begin{aligned} & B_0 = 0, \\ & (b-4)B_2 - qB_4 = 0, \\ & (b-4r^2)B_{2r} - q(B_{2r+2} + B_{2r-2}) = 0, \quad r \geqslant 2, \\ & \vdots \end{aligned}\right\} \tag{13.33}$$

These (twice) infinite equations possess countable nontrivial solutions for their unknowns $A_0, A_2, \ldots, B_2, B_4, \ldots$ only, provided the determinants of the corresponding matrices vanish. These determinants are functions of b and q, and their roots may be written as

$$\begin{aligned} b &= a_{2m}(q), \quad m = 0, 1, 2, 3, \ldots, \\ b &= b_{2m}(q), \quad m = 1, 2, 3, 4, \ldots, \end{aligned} \tag{13.34}$$

The subscript integer m is a counting index for the respective roots. If these values for b are back substituted in (13.32) and (13.33), then $A_0^{(2m)}, A_2^{(2m)}, A_4^{(2m)}, \ldots$ and $B_2^{(2m)}, B_4^{(2m)}, \ldots$ can be evaluated except for a scaling factor, which is deter-

[12] We are following in this section Pao and Mow [13].

mined by an adequate normalization. The coefficients a_{2m} and b_{2m} are known as the *characteristic numbers of the* Mathieu *equations*. They are tabulated in [2] and by Stratton et al. [17], see also Abramowitz and Stegun [1] or Pao and Mow [13] for graphs of the characteristic numbers as functions of q.

Solutions with the period 2π are also expressible in series

$$H(\eta) = \sum_{r=0}^{\infty} \left(A_{2r+1} \cos((2r+1)\eta) + B_{2r+1} \sin((2r+1)\eta)\right). \tag{13.35}$$

Again, there exists a set of characteristic numbers $a_{2m+1}(q)$, $(m = 1, 2, 3, \ldots)$, and for each characteristic number the coefficients $A_{(2r+1)}^{(2m+1)}(q), \ldots, B_{(2r+1)}^{(2m+1)}(q)$ can be calculated.

The periodic solutions of the Mathieu equation, when b is given by the characteristic numbers a_m or b_m are called Mathieu functions, which are designated as $ce_m(\eta, q)$ and $se_m(\eta, q)$, they are also called *sine-elliptic* and *cosine-elliptic* Mathieu functions with counting index $m = 0, 1, 2, \ldots$. This yields the following four types of Mathieu functions

$$\begin{aligned}
ce_{2m}(\eta, q) &= \sum_{r=0}^{\infty} A_{2r}^{(2m)}(q) \cos 2r\eta, \qquad \text{when} \quad b = a_{2m}, \\
se_{2m+2}(\eta, q) &= \sum_{r=0}^{\infty} B_{2r}^{(2m+2)}(q) \sin 2r\eta, \qquad b = b_{2m+2}, \\
ce_{2m+1}(\eta, q) &= \sum_{r=0}^{\infty} A_{2r+1}^{(2m+1)}(q) \cos((2r+1)\eta), \qquad b = a_{2m+1}, \\
se_{2m+1}(\eta, q) &= \sum_{r=0}^{\infty} B_{2r+1}^{(2m+1)}(q) \sin((2r+1)\eta), \qquad b = b_{2m+1}.
\end{aligned} \tag{13.36}$$

From these, we deduce for $\eta = (0, \pi/2)$

$$\begin{aligned}
ce_m(0, q) &= \sum_{r=0}^{\infty} A_r^{(m)} \neq 0, \quad se_m(0, q) = 0, \\
ce_{2m}(\pi/2, q) &= \sum_{r=0}^{\infty} (-1)^r A_{2r}^{(2m)} \neq 0, \\
ce_{2m+1}(\pi/2, q) &= 0, \qquad se_{2m}(\pi/2, q) = 0, \\
se_{2m+1}(\pi/2, q) &= \sum_{r=0}^{\infty} (-1)^r B_{2r+1}^{(2m+1)} \neq 0.
\end{aligned} \tag{13.37}$$

Values for the coefficients $A_r^{(m)}$, $B_r^{(m)}$ for a few small values of m are tabulated e.g. in [2] and by Stratton et al. [17].

The even and odd order Mathieu functions satisfy the orthogonality conditions (n and m are positive integers)

$$\begin{aligned}
&\int_0^{2\pi} ce_m(\eta,q)ce_n(\eta,q)\mathrm{d}\eta = 0, \quad n \neq m,\\
&\int_0^{2\pi} se_m(\eta,q)se_n(\eta,q)\mathrm{d}\eta = 0, \quad n \neq m,\\
&\int_0^{2\pi} ce_m(\eta,q)se_n(\eta,q)\mathrm{d}\eta = 0, \quad n \neq m.
\end{aligned} \tag{13.38}$$

For $m = n$, the first two integrals have non-zero values, whilst the last vanishes also for $m = n$, because ce_m is even, and se_m is odd in η. A popular normalization is

$$\int_0^{2\pi} ce_m^2(\eta,q)\mathrm{d}\eta = \int_0^{2\pi} se_m^2(\eta,q)\mathrm{d}\eta = \pi. \tag{13.39}$$

These relations imply the following scaling conditions for the coefficients

$$\begin{aligned}
2\left[A_0^{(2m)}\right]^2 + \sum_{r=1}^{\infty}\left[A_{2r}^{(2m)}\right]^2 &= \sum_{r=0}^{\infty}\left[A_{2r+1}^{(2m+1)}\right]^2\\
&= \sum_{r=0}^{\infty}\left[B_{2r+1}^{(2m+1)}\right]^2 = \sum_{r=0}^{\infty}\left[B_{2r+2}^{(2m+2)}\right]^2 = 1.
\end{aligned} \tag{13.40}$$

Generally today, even and odd periodic Mathieu functions are based on this scaling. For orders $m = 0$ and $m = 1$ they are displayed in Fig. 13.6.

Next, consider the modified Mathieu equation $(13.30)_1$ of which so far a solution has not been determined. Since, however, $(13.30)_1$ transforms into $(13.30)_2$, if $\xi = \pm i\,\eta$ is substituted, the modified Mathieu functions can simply be written as the Mathieu functions of imaginary arguments. The solutions are now expressible in series of *hyperbolic elliptic cosine* and *hyperbolic elliptic sine* functions rather than circular elliptic cosine and sine functions. Denoting the modified Mathieu functions by $Ce_m(\xi,q)$ and $Se_m(\xi,q)$, we have, when $b = a_m$ and $b = b_m$, respectively

$$\begin{aligned}
Ce_m(\xi,q) &= ce(\mathrm{i}\xi,q) = \sum_{r=0}^{\infty} A_r^{(m)}\cosh r\xi, \qquad (b = a_m),\\
Se_m(\xi,q) &= (-\mathrm{i})se(\mathrm{i}\xi,q) = \sum_{r=1}^{\infty} B_r^{(m)}\sinh r\xi, \ (b = b_m).
\end{aligned} \tag{13.41}$$

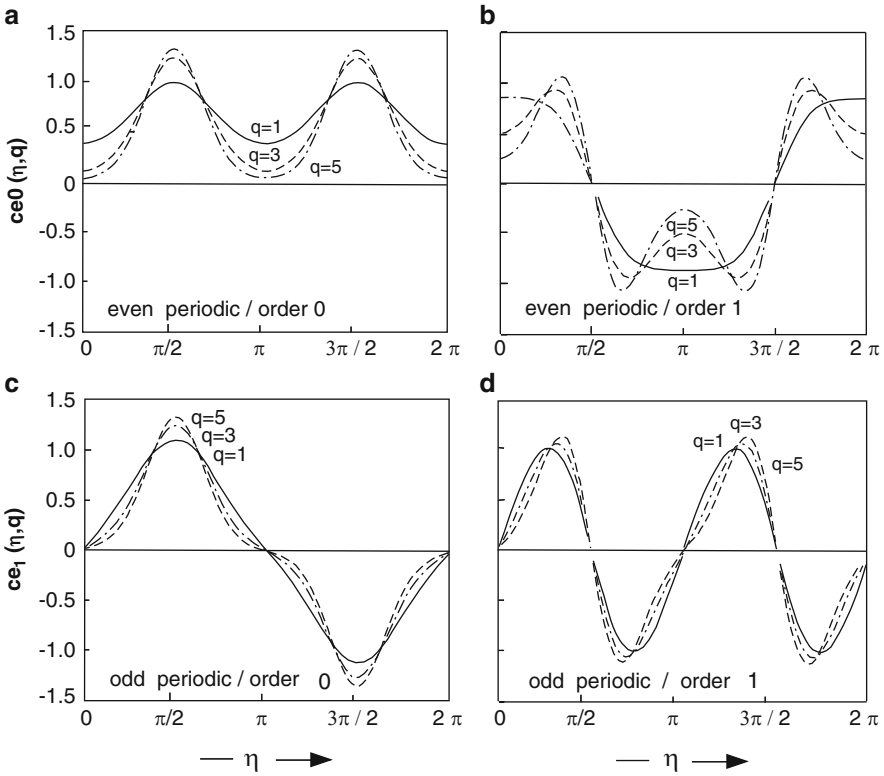

Fig. 13.6 Even and odd periodic Mathieu functions of order zero and one. (**a**) even, order zero; (**b**) even, order one; (**c**) odd, order zero; (**d**) odd, order one (from Pao and Mow [13], reproduced with permission)

These functions are no longer periodic and are sometimes also referred to as *cosh-elliptic* and *sinh-elliptic* functions.

13.7 Elliptical Basin: Normal Mode Analysis[13]

We now return to the earlier notation and revert to q_n instead of q. The intention is still the solution of (13.27), in which q_n is given by (13.28). Solutions of $(13.30)_1$ are the modified Mathieu functions $Ce(\eta)$ and $Se(\eta)$; $Ce(\eta)$ is an even function in η, whilst $Se(\eta)$ is odd. Similarly, solutions of $(13.30)_2$ are the (ordinary) Mathieu functions $ce(\xi)$, and $se(\xi)$, where $ce(\xi)$ is even in ξ, whilst $se(\xi)$ is odd. The general solution of (13.27) has the form $\Xi(\xi) \times H(\eta)$, so that p^* is composed as follows

[13] In this section, we follow Goldstein [7].

$$\begin{aligned} p^* &= \alpha Ce(\xi)ce(\eta) + \beta Se(\xi)ce(\eta) \\ &\quad + \gamma Ce(\xi)se(\eta) + \delta Se(\xi)se(\eta) \end{aligned} \tag{13.42}$$

for some α, β, γ and δ.

The transformation (13.20) implies

$$\begin{aligned} \mathrm{d}x &= \rho \sinh\xi \cos\eta \ \mathrm{d}\xi - \rho \cosh\xi \sin\eta \ \mathrm{d}\eta, \\ \mathrm{d}y &= \rho \cosh\xi \sin\eta \ \mathrm{d}\xi + \rho \sinh\xi \cos\eta \ \mathrm{d}\eta. \end{aligned} \tag{13.43}$$

from which in the limits $\xi \to 0$ and $y \to 0$ one may deduce

$$\frac{\partial}{\partial x} = -\frac{1}{\rho \sin\eta}\frac{\partial}{\partial \eta}, \qquad \frac{\partial}{\partial y} = \frac{1}{\rho \sin\eta}\frac{\partial}{\partial \xi}. \tag{13.44}$$

The parameters $\alpha, \ldots, \delta$ in (13.42) must be selected according to the satisfaction of regularity requirements and boundary conditions. For the confocal ellipses and hyperbolas of Fig. 13.5 the pressure p^* and the velocity components u^*, v^* must be continuous and differentiable as one moves across the line connecting the two foci of the ellipses with focal distance 2ρ. When this line segment is crossed, η will change to $2\pi - \eta$. So, e.g. $\sin(\eta)$ changes to $\sin(2\pi - \eta) = -\sin(\eta)$, but $\cos(\eta) = \cos(2\pi - \eta)$ keeps its value. Now, for reasons of physics, u^*, v^* and $p^*, \partial p^*/\partial x, \partial p^*/\partial y$ must not change when the line segment between the foci is crossed, unless they vanish. It then follows from (13.42) and (13.44) and the fact that $\sin\eta$ and $\partial(\cdot)/\partial\eta$ change sign, when $\eta \to (2\pi - \eta)$, that

$$\begin{aligned} &\left.\frac{\partial p^*}{\partial \xi}\right|_{\eta \to 2\pi - \eta} \quad \text{must change sign,} \\ &\left.\frac{\partial p^*}{\partial \eta}\right|_{\eta \to 2\pi - \eta} \quad \text{must change sign.} \end{aligned} \tag{13.45}$$

Now,

$$\begin{aligned} \frac{\partial p^*}{\partial \xi} &= \alpha Ce'(\xi)ce(\eta) + \beta Se'(\xi)ce(\eta) \\ &\quad + \gamma Ce'(\xi)se(\eta) + \delta Se'(\xi)se(\eta), \\ \frac{\partial p^*}{\partial \eta} &= \alpha Ce(\xi)ce'(\eta) + \beta Se(\xi)ce'(\eta) \\ &\quad + \gamma Ce(\xi)se'(\eta) + \delta Se(\xi)se'(\eta), \end{aligned} \tag{13.46}$$

where $(\cdot)'$ denotes univariate differentiation. In the limit as $\xi \to 0$, we have $Ce'(\xi) = 0$ since $Ce(\xi)$ is even in ξ; furthermore, $Se(0) = 0$. Moreover, when the segment connecting the foci is crossed, the second term in $(13.47)_1$ does not

change the sign, in conflict with $(13.45)_1$, so we necessarily have $\beta = 0$. Similarly, at $\xi = 0$ only the third term in $(13.47)_2$ survives, since $Se(0) = 0$, and $ce'(\eta) = -ce'(2\pi - \eta)$ because $ce(\eta) = ce(2\pi - \eta)$, implying $ce'(\eta) = 0$ at $\xi = 0$. Thus, one also must have $\gamma = 0$. These results show that

$$p^* = \alpha Ce(\xi)ce(\eta) + \delta Se(\xi)se(\eta). \tag{13.47}$$

Therefore, any solution of (13.27) must be either even in both ξ and η or odd in both ξ and η.[14]

The condition at the outer boundary is that the normal velocity is zero. If the exponential ansatz

$$\begin{aligned} u_n(\xi, \eta, t) &= u_n^*(\xi, \eta)\exp(\mathrm{i}\omega_n t), \\ v_n(\xi, \eta, t) &= v_n^*(\xi, \eta)\exp(\mathrm{i}\omega_n t) \end{aligned} \tag{13.48}$$

is used along with (13.25) for the pressure, then $(13.24)_{2,3}$ imply

$$\begin{aligned} u_n^*(\xi, \eta) &= u^*_{\mathrm{Ref}_n}\left(\mathrm{i}\omega_n \frac{\partial p_n^*}{\partial \xi} + f\frac{\partial p_n^*}{\partial \eta}\right), \\ v_n^*(\xi, \eta) &= u^*_{\mathrm{Ref}_n}\left(-f\frac{\partial p_n^*}{\partial \xi} + \mathrm{i}\omega_n \frac{\partial p_n^*}{\partial \eta}\right), \end{aligned} \tag{13.49}$$

where

$$u^*_{\mathrm{Ref}_n} := \frac{\sqrt{2}gh_n}{(\omega_n^2 - f^2)\rho\sqrt{\cosh 2\xi - \cos 2\eta}}. \tag{13.50}$$

The no-flux condition through the boundary ellipse $\xi = \xi_0$, $(13.24)_4$, thus leads to the requirement

$$\mathrm{i}\omega_n \frac{\partial p_n^*}{\partial \xi} + f\frac{\partial p_n^*}{\partial \eta} = 0, \quad \text{at} \quad \xi = \xi_0 \tag{13.51}$$

for all modes n. If $f = 0$ (no rotation of the Earth), then this implies

$$\frac{\partial p_n^*}{\partial \xi} = 0, \quad \text{at} \quad \xi = \xi_0. \tag{13.52}$$

The above analysis has made only the vertical mode (index n) visible, but by analogy with the circular cylindrical case, all equations derived so far in this subsection exhibit hidden azimuthal (variable ξ, mode number ℓ) and radial (variable η, mode

[14] This result was already obtained by Jeffreys [8].

number m) mode behaviour. If in (13.47) the azimuthal mode number ℓ is made explicit,

$$\begin{aligned} p^*_{\ell n} &= \alpha_{\ell n} Ce_{\ell n}(\xi, q_{\ell n}) ce_\ell(\eta, q_{\ell n}) \\ &\quad + \delta_{\ell n} Se_{\ell n}(\xi, q_{\ell n}) se_{\ell n}(\eta, q_{\ell n}), \end{aligned} \tag{13.53}$$

and then summed over ℓ, we have

$$\begin{aligned} p^*_n &= \sum_{\ell=0}^{\infty} \alpha_{\ell n} Ce_{\ell n}(\xi, q_{\ell n}) ce_{\ell n}(\eta, q_{\ell n}) \\ &\quad + \sum_{\ell=1}^{\infty} \delta_{\ell n} Se_{\ell n}(\xi, q_{\ell n}) se_{\ell n}(\eta, q_{\ell n}). \end{aligned} \tag{13.54}$$

If this is substituted into (13.51), it is recognized, owing to symmetry, that it is necessary to consider merely solutions, in which ℓ assumes odd values only or in which ℓ assumes even values only. The slowest mode belongs to those, in which ℓ is odd, so we take

$$\begin{aligned} p^*_n = \sum_{\ell=1,\text{odd}}^{\infty} &\{\alpha_{\ell n} Ce_{\ell n}(\xi, q_{\ell n}) ce_{\ell n}(\eta, q_{\ell n}) \\ &+ \delta_{\ell n} Se_{\ell n}(\xi, q_{\ell n}) se_{\ell n}(\eta, q_{\ell n})\}. \end{aligned} \tag{13.55}$$

(The analysis for ℓ even is similar.) Substitution of (13.55) in (13.51) gives

$$\begin{aligned} &\mathrm{i}\sigma \sum_{\ell,\text{odd}}^{\infty} \left\{\alpha_\ell Ce'_\ell(\xi_0, q) ce_\ell(\eta, q) + \delta_\ell Se'_\ell(\xi_0, q) se_\ell(\eta, q)\right\} \\ &+ \sum_{\ell,\text{odd}}^{\infty} \left\{\alpha_\ell Ce_\ell(\xi_0, q) ce'_\ell(\eta, q) + \delta_\ell Se'_\ell(\xi_0, q) se_\ell(\eta, q)\right\} = 0, \end{aligned} \tag{13.56}$$

in which the prime denotes univariate differentiation, and $\sigma = \omega/f$. (A remark may be in order regarding σ arising outside the first summation in (13.56). We have not written σ_ℓ, the reason being that the sum in (13.55) defines the pressure for any value of σ.) Equation (13.56) is the dispersion relation, which determines quantized values for σ. Expressing $ce_\ell(\eta, q_\ell)$ and $se_\ell(\eta, q_\ell)$ in the Fourier series

$$ce(\eta, q_\ell) = \sum_{\ell,\text{odd}}^{\infty} A_{r,\ell} \cos(r\eta), \qquad se(\eta, q_\ell) = \sum_{\ell,\text{odd}}^{\infty} B_{r,\ell} \sin(r\eta), \tag{13.57}$$

wherein $A_{r,\ell}$ and $B_{r,\ell}$ are functions of q_ℓ, splits (13.56) into the equations (the coefficients of the sine and cosine functions are set separately to zero)

$$\left.\begin{aligned}\sum_{\ell,\text{odd}}^{\infty}\{\mathrm{i}\sigma\alpha_\ell A_{r,\ell}Ce'(\xi_0,q_\ell)+r\delta_\ell B_{r,\ell}Se(\xi_0,q_\ell)\}=0,\\ \sum_{\ell,\text{odd}}^{\infty}\{\mathrm{i}\sigma\delta_\ell B_{r,\ell}Se'(\xi_0,q_\ell)-r\alpha_\ell A_{r,\ell}Ce(\xi_0,q_\ell)\}=0.\end{aligned}\right\} \tag{13.58}$$

In this (and earlier equations) the indices m and n have been omitted. (Recall, ℓ is the azimuthal, m the radial and n the vertical mode number.) For n fixed, (13.58) solves for the frequencies (and thus gives the mode numbers m). (13.58) is a different form of the dispersion relation (13.56). Equations (13.58) hold for odd values of r and constitute two infinite homogeneous linear equations for the coefficients α_ℓ, δ_ℓ. Nontrivial solutions exist, provided the infinite determinant of the linear system (13.58) vanishes. With the notation

$$\beta = S_n^{-2} = \frac{f^2\mathsf{a}^2}{gh_n}, \quad (ka)^2 = \frac{\sigma^2-1}{S_n^2} \tag{13.59}$$

(a is the major semi-axis, S_n the Burger number) this determinant is given by

$$\begin{Vmatrix} \mathrm{i}\sigma A_{1,1}Ce'_1, & B_{1,1}Se_1, & \mathrm{i}\sigma A_{1,3}Ce'_3, & B_{1,3}Se_3, & \dots \\ A_{1,1}Ce_1, & \mathrm{i}\sigma B_{1,1}Se'_1, & A_{1,3}Ce_3, & \mathrm{i}\sigma B_{1,3}Se'_3, & \dots \\ \mathrm{i}\sigma A_{3,1}Ce'_1, & 3B_{3,1}Se_1, & \mathrm{i}\sigma A_{3,3}Ce'_3, & 3B_{3,3}Se_3, & \dots \\ 3A_{3,1}Ce_1, & \mathrm{i}\sigma B_{3,1}Se'_1, & 3A_{3,3}Ce_3, & \mathrm{i}\sigma B_{3,3}Se'_3, & \dots \\ \vdots & \vdots & \vdots & \vdots & \vdots \end{Vmatrix} = 0, \tag{13.60}$$

where the indices m, n have been omitted as before. This is yet a third form of the dispersion relation from which the frequency is computed. This is Goldstein's [7] method to compute the eigenfrequencies of the gravitational seiche in an elliptical container of constant depth. The method is directly applicable to the modal equations of the stratified fluid, if the subscript n is recovered in the notation.

Goldstein[15] describes briefly the way, how approximations to the solutions of (13.60) are obtained. The computations – all done by hand and without tables of the Mathieu functions being available – must have been enormous, and the author and his wife, who participated, deserve our greatest admiration for the results achieved. If Δ_m is the determinant formed from the first $2m$ rows and columns of (13.60), successive approximations for $\kappa\mathsf{a}$ are obtained by putting $\Delta_1 = 0, \Delta_2 = 0, \dots$. Values for $\beta = S_n^{-2}$ and b/a, the ratio of the major to the minor semi-axis, were chosen. (Note, with $\mathsf{b}/\mathsf{a} = \tanh\xi_0$ also ξ_0 is fixed and with it $\varepsilon = \operatorname{sech}\xi_0$ and

[15] For a biographical sketch see Fig. 13.7.

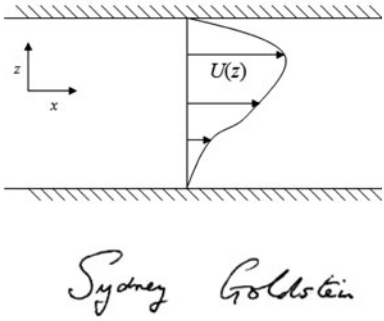

Sydney Goldstein

Fig. 13.7 Sydney Goldstein (1903–1989) (photo from http://www.annualreviews.org/). *Left*: The Taylor-Goldstein equation describes the dynamics of internal waves in the presence of a (continuous) density stratification and shear flow. A schematic diagram shows the base flow which is parallel to x axis, subject to a small perturbation away from this state which has components in both x and z directions (http://en.wikipedia.org/).

Sydney Goldstein (3 December 1903, Kingston-upon-Hull; 22 January 1989, Cambridge, USA) took his basic education at Bede School in Sunderland. He started his higher education at the University of Leeds in 1921, where he studied mathematics, but moved to St. John's College, Cambridge, graduating from the mathematical Tripos 1925 and gaining the Smith's Prize in 1927. He was awarded an Isaac Newton Studentship to continue research in applied mathematics and completed his Ph.D under Harold Jeffreys with a thesis entitled 'The theory and application of Mathieu functions' in 1928. With a Rockefeller Research Fellowship he then spent a year at the University of Göttingen with Ludwig , where he performed laboratory experiments of a fluid in a rotating elliptical container described in this book.

In 1929, Goldstein returned to Cambridge, but accepted in the same year a lectureship in mathematics at the University of Manchester. Manchester had a profound influence on Goldstein through the heritage of Osborne Reynolds and Horace Lamb. He moved to Cambridge again in 1931 and took over, on Lamb's death, the edition of 'Modern Developments in Fluid Dynamics' which appeared in 1938. He was elected Fellow of the Royal Society in London in 1937. During World War II, Goldstein worked at the National Physical Laboratory where he worked on boundary layer theory. In 1945, Goldstein moved again to the University of Manchester, where he assumed the chair of Applied Mathematics.

In 1950, Goldstein, who was of strong Jewish belief, accepted the chairmanship of the mathematics department of the Technion at Haifa, but resigned 1955, owing to the administrative overload, and took the chair of Applied Mathematics at Harvard University, Cambridge, USA.

Goldstein was a very influential fluid dynamicist and best known for his work on steady flow laminar boundary layers and turbulent resistance to rotation of a disk in a fluid. His work in aerodynamics and its influence led Sir James Lighthill to say that he was one of those who most influenced progress in fluid dynamics during the twentieth century'.

The text is based on:

http://en.wikipedia.org/wiki/Sydney_Goldstein and

J. Lighthill: Sydney Goldstein, Biographical Memoirs of Fellows of the Royal Society of London, 36, 175–197 (1990).

Table 13.5 Eigenvalues κ obtained by putting $\Delta_2 = 0$ for the indicated values of β and $\mathsf{b/a}$ (from Goldstein [7])

β	$\mathsf{b/a}$	1	$\frac{2}{3}$	$\frac{1}{3}$	0
	$\kappa\mathsf{a}$	1.59	1.75	1.81	1.83
0.225	$\frac{\omega}{f}$	3.50	3.82	3.94	3.98
	$\frac{\omega\mathsf{a}}{\sqrt{gh_n}}$	1.66	1.81	1.87	1.89
	$\kappa\mathsf{a}$	0	0.925	1.20	1.25
2.0	$\frac{\omega}{f}$	1.0	1.19	1.31	1.33
	$\frac{\omega\mathsf{a}}{\sqrt{gh_n}}$	1.41	1.69	1.86	1.89
	$\kappa\mathsf{a}$		0		
2.728	$\frac{\omega}{f}$		1.00		
	$\frac{\omega\mathsf{a}}{\sqrt{gh_n}}$		1.65		
	$\kappa\mathsf{a}$			0	
3.356	$\frac{\omega}{f}$			1.00	
	$\frac{\omega\mathsf{a}}{\sqrt{gh_n}}$			1.89	
	$\kappa\mathsf{a}$				0
3.556	$\frac{\omega}{f}$				1.00
	$\frac{\omega\mathsf{a}}{\sqrt{gh_n}}$				1.89
	$\kappa\mathsf{a}$	2.10i	1.90i	1.70i	1.56i
6	$\frac{\omega}{f}$	0.51	0.63	0.72	0.77
	$\frac{\omega\mathsf{a}}{\sqrt{gh_n}}$	1.26	1.55	1.76	1.89

therefore $q = \kappa^2\mathsf{a}^2\varepsilon^2/32$.) A selection of solutions, obtained by evaluating $\Delta_2 = 0$, is collected in Table 13.5.

For $\beta = 2$ and $\mathsf{b/a} = 2/3$, the solution of $\Delta_2 = 0$ gave $\kappa\mathsf{a} = 0.9252, \sigma = \omega/f = 1.19$ and $\omega\mathsf{a}/\sqrt{gh_n} = 1.69$. This also led to $\kappa\mathsf{a}\varepsilon = 0.69$, and then $\kappa\mathsf{a}\varepsilon \times \cosh\xi$ varies from 0.69 to 0.925 in the basin. The pressure p^* which, for the homogeneous fluid, is proportional to the surface displacement can then be calculated (modulo an arbitrary factor).

Having determined the eigenfrequencies, (13.58) can be used to determine for each σ_ℓ the coefficients α_ℓ and δ_ℓ (up to a scaling factor), and once these are known,

the pressure p_ℓ^* can be computed. For the homogeneous fluid this pressure equals the surface displacement (modulo a scaling factor). This function was plotted by Goldstein for $\kappa \mathsf{a}\sigma \cosh \xi = 0.7, 0.8, 0.9, 0.925$ and $\eta = 0, 15, 30, \ldots, 90°$. If p is written as

$$p = \zeta \times \exp(-\mathrm{i}\theta), \tag{13.61}$$

then $\zeta_\ell \cos(\omega_\ell t - \theta)$ is the surface elevation (modulo a scale factor). 'The corange lines[16] are $\zeta_\ell = $ const. and the cotidal lines are the lines $\theta = $ const. The corange and cotidal lines were plotted by Goldstein for the above values of ξ and η. They are shown in Fig. 13.8, in panel (a) for the first positive wave and in panel (b) for the first negative wave. For a circular basin they are circles and straight lines. For vanishingly small breadth the range is zero on the minor axis, the co-range lines are hyperbolas across the canal, and each half of the canal is cotidal (i.e. the two sides of the minor axis are in counter phase).

Panel (b) of Fig. 13.8 shows the corange and cotidal lines for the first negative mode (i.e. a mode propagating clockwise around the amphidromic point in the centre of the ellipse). (This mode has $\kappa \mathsf{a} = 2.8180$, $\omega/f = 2.23$, $\omega \mathsf{a}/(gh_n)^{1/2} = 3.15$, $\kappa \mathsf{a}\varepsilon \cosh \xi \in (2.1036, 2.8180)$). For this mode the tendency, with decreasing breadth, is for the amplitude at the end of the major axis to vanish, for the co-range lines to stretch along the basin, and for the co-tidal lines to crowd towards the major axis. The amplitude at the end of the minor axis is already more than three times as big as that at the end of the major axis'.

With the pressure p_ℓ^* determined by (13.53), the velocity components (parallel to the coordinate hyperbolas and ellipses) can be obtained with the aid of (13.49) and (13.50). This process then yields

$$\begin{aligned}
u_{\ell n}^*(\xi,\eta) &= (u_{\mathrm{Ref}}^*)_n \{\mathrm{i}\omega [\alpha_{\ell n} Ce'_{\ell n}(\xi, q_{\ell n}) ce_{\ell n}(\eta, q_{\ell n}) \\
&\quad + \delta_{\ell n} Se'_\ell(\xi, q_{\ell n}) se_{\ell n}(\eta, q_{\ell n})] + f[\alpha_{\ell n} Ce_{\ell n}(\xi, q_{\ell n}) ce'_{\ell n}(\xi, q_{\ell n}) \\
&\quad + \delta_{\ell n} Se(\xi, q_{\ell n}) se'(\eta, q_{\ell n})]\}, \\
v_{\ell n}^*(\xi,\eta) &= (u_{\mathrm{Ref}}^*)_n \{-f [\alpha_{\ell n} Ce'_{\ell n}(\xi, q_{\ell n}) ce_{\ell n}(\eta, q_{\ell n}) \\
&\quad + \delta_{\ell n} Se'_{\ell n}(\xi, q_{\ell n}) se_{\ell n}(\eta, q_{\ell n})] + \mathrm{i}\omega[\alpha_{\ell n} Ce_{\ell n}(\xi, q_{\ell n}) ce'_{\ell n}(\xi, q_{\ell n}) \\
&\quad + \delta_{\ell n} Se(\xi, q_{\ell n}) se'(\eta, q_{\ell n})]\},
\end{aligned} \tag{13.62}$$

where

$$(u_{\mathrm{Ref}}^*)_n = \frac{\sqrt{2} g h_n}{(\omega^2 - 1)\rho \sqrt{\cosh 2\xi - \cos 2\eta}}. \tag{13.63}$$

The transformation of these modal variables (subscript n) to the layer variables (subscript j) is given by Lighthill [10] for a n-layer model and for $n = 3$ by Antenucci

[16] This text follows Goldstein [7], but not in all details word by word.

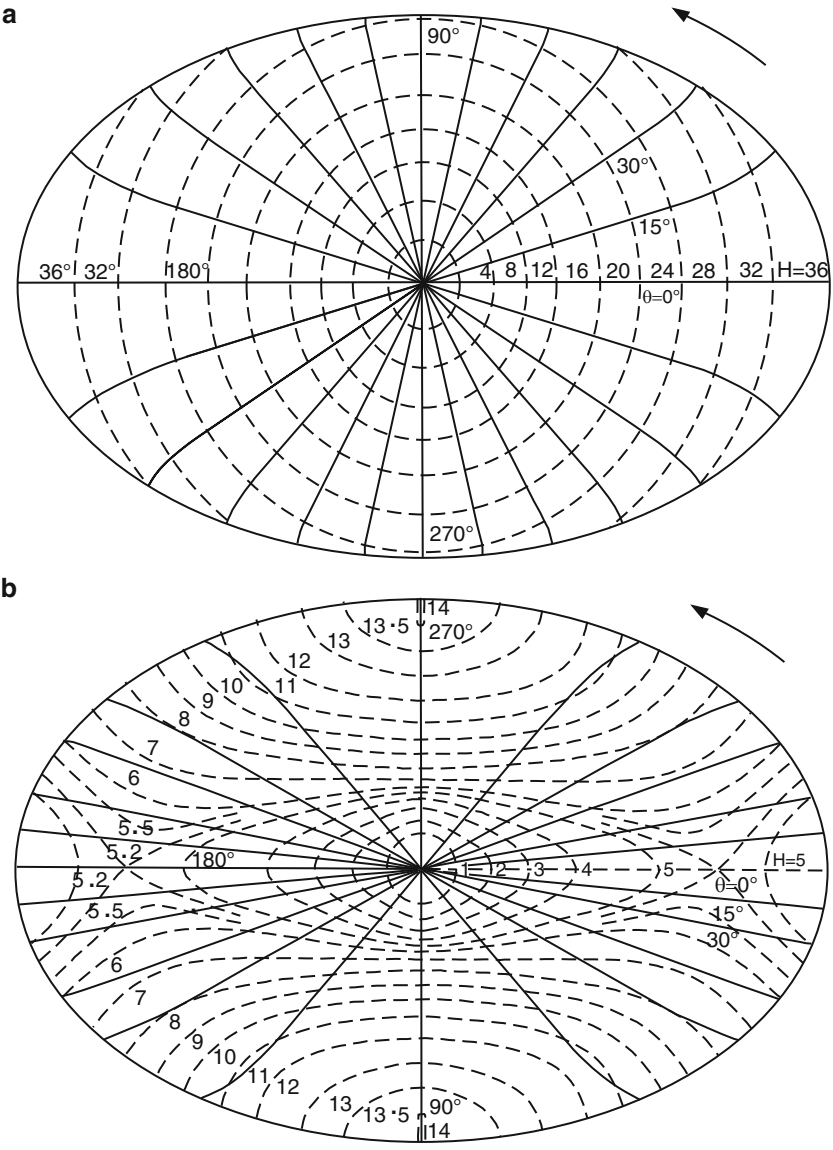

Fig. 13.8 Elliptical container of constant depth. (**a**) Corange and cotidal lines for the first positive wave. The *full lines* give the cotidal lines $\theta = \text{const.}$ and the *dashed lines* the corange lines $\zeta = \text{const.}$, where $\zeta \cos(\omega t - \theta)$ is the tide height. The cotidal lines are drawn at intervals of 15°, as shown. Figures near the corange lines give the relative amplitude. The *arrow* shows the direction of the rotation of the basin. The figure is drawn for $\mathsf{b}/\mathsf{a} = 2/3$, where a is the major semi-axis, b is the minor semi-axis, $\beta = S_n^2 = (f\mathsf{a})^2/(gh_n)$, f is the Coriolis parameter, g the acceleration due to gravity, and h_n the equivalent depth ($= H$ for a homogeneous fluid). (**b**) Corange and cotidal lines for the first negative wave. As in **(a)**, the *full lines* give the cotidal lines and the *dashed lines* the corange lines as before (redrawn from Goldstein [7]). © Royal Astronom. Soc., reproduced with permission

and Imberger [4], following earlier work by Csanady [6] and Monismith [11]

$$
\begin{aligned}
{}^{L}u_j^* &= \sum_{n=1}^{3} \frac{A_{nj}}{\det(a_{nj})} u_n^*, \\
{}^{L}v_j^* &= \sum_{n=1}^{3} \frac{A_{nj}}{\det(a_{nj})} v_n^*, \\
\zeta_j^* &= \sum_{n=1}^{3} \frac{B_{nj}}{\det(b_{nj})} p_n^*,
\end{aligned}
\tag{13.64}
$$

of the velocity vector in layer j, and ζ_j, which is the upper interface displacement of layer j. Furthermore, (a_{nj}) and (b_{nj}) are square matrices (as given below) and A_{nj}, B_{nj} are the cofactors of (a_{nj}) and (b_{nj}). The index $i = 1$ refers to the barotropic solution and ζ_1 is the surface displacement; $i = 2, 3$ refer to the first and second vertical baroclinic modes. For the three-layer model, the matrices (a_{nj}) and (b_{nj}) are given by

$$
(\boldsymbol{a}) = \begin{bmatrix}
-H_2 - H_3 + \varepsilon_{23}\dfrac{H_2 H_3}{h_1} + h_1 & H_2 - \varepsilon_{23}\dfrac{H_2 H_3}{h_1} & H_3 \\
-H_2 - H_3 + \varepsilon_{23}\dfrac{H_2 H_3}{h_2} + h_2 & H_2 - \varepsilon_{23}\dfrac{H_2 H_3}{h_2} & H_3 \\
-H_2 - H_3 + \varepsilon_{23}\dfrac{H_2 H_3}{h_3} + h_3 & H_2 - \varepsilon_{23}\dfrac{H_2 H_3}{h_3} & H_3
\end{bmatrix}
\tag{13.65}
$$

$$
(\boldsymbol{b}) = \begin{bmatrix}
\dfrac{a_{11}}{H_1} & \dfrac{a_{12}}{H_2} - \dfrac{a_{11}}{H_1} & \dfrac{a_{13}}{H_3} - \dfrac{a_{12}}{H_2} \\
\dfrac{a_{21}}{H_1} & \dfrac{a_{22}}{H_2} - \dfrac{a_{21}}{H_1} & \dfrac{a_{23}}{H_3} - \dfrac{a_{22}}{H_2} \\
\dfrac{a_{31}}{H_1} & \dfrac{a_{32}}{H_2} - \dfrac{a_{31}}{H_1} & \dfrac{a_{33}}{H_3} - \dfrac{a_{32}}{H_2}
\end{bmatrix},
\tag{13.66}
$$

where

$$
\varepsilon_{ij} = 1 - \frac{\rho_i}{\rho_j}, \quad (i, j, = 1, 2, 3, i \neq j)
\tag{13.67}
$$

and

$$
\begin{aligned}
h_1 &= H, h_2 = \frac{H}{2}[\gamma + (\gamma^2 - 4\delta)^{1/2}], \\
h_3 &= \frac{H}{2}[\gamma - (\gamma^2 - 4\delta)^{1/2}],
\end{aligned}
$$

$$\gamma = \frac{1}{H^2}(\varepsilon_{12}H_1H_2 + \varepsilon_{23}H_2H_3 + \varepsilon_{13}H_1H_3).$$
$$\delta = \frac{1}{H^3}\varepsilon_{12}\varepsilon_{23}(H_1H_2H_3). \tag{13.68}$$

H is the total depth, H_j, $(j = 1, 2, 3)$, are the layer depths and h_n are the equivalent model depths.

For a two-layer model

$$(\boldsymbol{a}) = \begin{bmatrix} H_1 - \varepsilon_{12}\dfrac{H_1H_2}{h_1} & H_2 \\ H_1 - \varepsilon_{12}\dfrac{H_1H_2}{h_2} & H_2 \end{bmatrix},$$
$$(\boldsymbol{b}) = \begin{bmatrix} \dfrac{a_{11}}{H_1} & \dfrac{a_{12}}{H_2} - \dfrac{a_{11}}{H_1} \\ \dfrac{a_{21}}{H_1} & \dfrac{a_{22}}{H_2} - \dfrac{a_{21}}{H_1} \end{bmatrix}, \tag{13.69}$$

$$h_1 = H = H_1 + H_2, \qquad h_2 = \varepsilon_{12}\frac{H_1H_2}{H_1 + H_2}. \tag{13.70}$$

Antenucci and Imberger [4] determined explicitly two layer solutions for an elliptical container, which approximates the geometry and stratification of Lake Kinneret. The ellipse best matching the lake bathymetry has $\mathsf{a} = 7.5\,\text{km}$, $\mathsf{b} = 5.0\,\text{km}$, as shown in Fig. 13.3; it has its central point at (35.51°N, 32.70°E), for which $f = 7.81 \times 10^{-5}\,\text{rads}^{-1}$. Antenucci and Imberger [4] also list the layer depths and temperatures inferred from the measuring periods I–III in 1998, and the phase speeds c_1 and c_2 of the V1 Kelvin-type and V1 Poincaré-type seiches, see Tables 13.1 and 13.2. Figure 13.9 displays the isopycnal displacements and velocity distributions for these two seiche modes. Rows [(a), (b)] and [(c), (d)] in column (i) show the interface displacements at an (initial) time and a quarter period later, the intensity of the shading indicating the magnitude of the displacement on a scale as indicated on the scale bar. In columns (ii) and (iii), the corresponding velocities in the top and bottom layers are displayed, in the rows [(a), (b)] and [(c), (d)] a quarter period apart from one another. In the panels of the top two rows, the largest velocities are near the boundaries and essentially parallel to these, and the motion is cyclonic (counter-clockwise on the N.H.) both for the interface and the off-shore velocities. This cyclonic rotation is easily seen in the interface displacements; in the velocity snapshots it is conspicuously seen close to the minor axis but not at the long ends of the ellipses. Here, at the long ends, the velocity snapshots suggest closed elliptical particle orbits. When comparing this with the Taylor solution [18] in long rectangles a close analogy to Kelvin-type behaviour away from the long ends and Poincaré-type behaviour close to the long ends seems to prevail.

In rows [(c), (d)] of Fig. 13.9, the analogous results are shown for the vertical mode one, azimuthal and radial mode one Poincaré seiche. Column (i) again displays the interface displacement (scaled to sizes from -1.5 to $+1.5$) one quarter

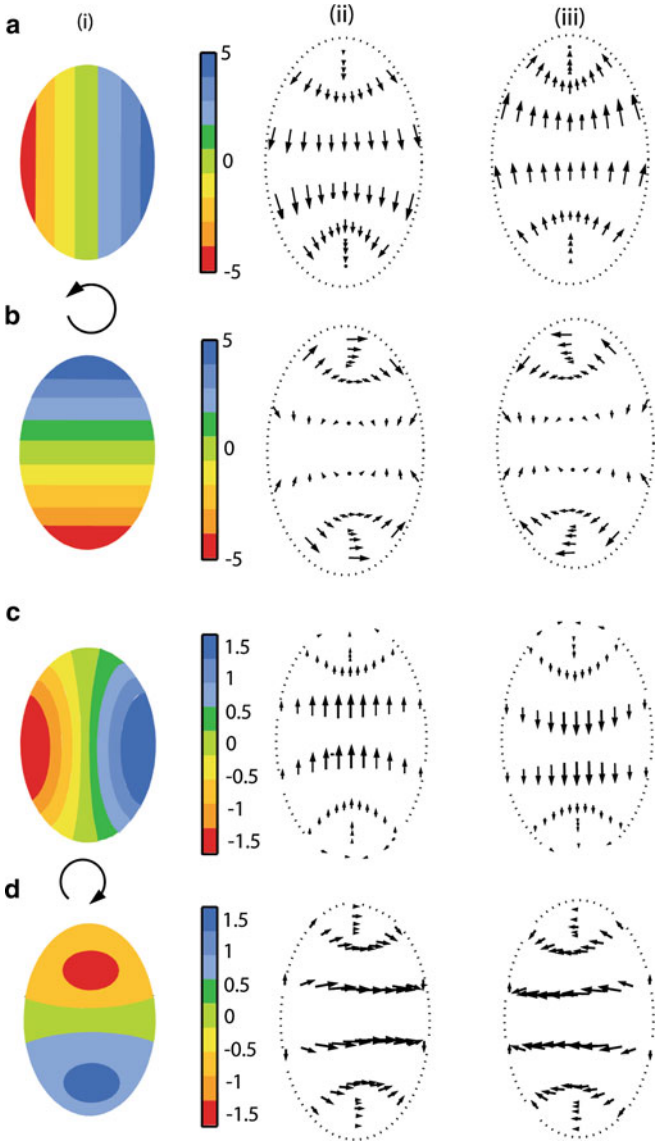

Fig. 13.9 Interface displacements (column (i)) and velocity distributions in the *top* layer (column (ii)) and the *bottom* layer (column (iii)) of a two-layer fluid in an elliptical container with constant depth. Rows [(a), (b)] show the vertical mode one, and azimuthal and radial mode one $(\ell, m_{\mathrm{K}}, n) = (1, 1_{\mathrm{K}}, 1)$ interface and velocity distributions at an initial time and a quarter period $T/4$ later, reminiscent of Kelvin-type behaviour. Rows [(c), (d)] show the same for the vertical mode one, azimuthal and radial mode one $(\ell, m_{\mathrm{P}}, n) = (1, 1_{\mathrm{P}}, 1)$ lowest order Poincaré-type seiche (redrawn from Antenucci and Imberger [4]). Copyright 2000 by the American Society of Limnology and Oceanography, Inc, reproduced with permission

period apart from one another. These now indicate anticyclonic (clockwise) rotation. The corresponding velocity distributions, displayed in columns (ii) and (iii), have the largest magnitude in the middle of the basin and equally show an anticyclonic rotation and counter-phase behaviour in the top and bottom layers. The velocities at the boundaries are small and parallel to the shore. This behaviour is reminiscent of Poincaré behaviour and is therefore justly called Poincaré-type.

13.8 Experimental Verification

Matching the periods and phase speeds of the $(\ell, m, n) = [(1, 1_{\mathrm{K}}, 1), (1, 1_{\mathrm{P}}, 1)]$ modes for Lake Kinneret has been done by Antenucci and Imberger [4] for both the circular and elliptical containers. This was shown already in Sect. 13.4 by comparing observations of isotherm–depth–time series with corresponding results from the circular basin adjusted to Lake Kinneret. Comparing this with results obtained with the elliptical model of Lake Kinneret corroborated *qualitatively* the same behaviour, but did not indicate any substantial improvement. In a way, this is no great surprise, since the simple circular and elliptical containers were both designed to best reproduce the measurements with computed information, postulated to correspond to some measured information collected at isolated points. Given this experimental evidence, which is still limited when measured on the complexity of the phenomena, marginal improvement with the only slightly more complex geometry is to be expected. To obtain a *quantitatively* better coincidence, a better adjustment to the geometry of the lake, and probably also better resolution of the stratification as well as denser deployment of instrumentation is necessary. The latter may often be economically impossible, the former requires computational expertise.

An independent experiment for a homogeneous fluid in an elliptical container with vertical side walls was conducted by Goldstein himself and is reported in 1929 [7]. In the following, his text is reproduced below, since it is so unusual for the time more than 80 years ago and reports verification of the model by a simple laboratory experiment. Goldstein, after describing the mathematical solution of the gravity seiche problem with the help of Mathieu functions essentially in the above form – continues and states:

> 'The calculations above were completed while I was at the Kaiser Wilhelm Institut für Strömungsforschung in Göttingen, and an experimental test of the results for free oscillations was possible by making observations in the rotating chamber there.[17]
>
> A wooden bath of elliptical shape with vertical walls was used. The length was 91.1 cm and the breadth 60.5 cm, so that the ratio of the axes was nearly 2:3. The bath, which stood on three legs, was placed with its centre on the axis of revolution of the chamber. (All apparatus must, of course, be screwed down fast.) It was filled with water to the required depth, the chamber was set in rotation, and when the water was at relative rest the oscillation to be

[17] The rotating chamber has been described by Prandtl in *Die Naturwissenschaften* [14]. It gives me much pleasure to record here my thanks to Professor Prandtl for permission to use this chamber.

studied was produced by gentle up-and-down motion (by hand) of a bottle with a flat bottom of diameter of 15 cm. With a little practice it became easy to bring the motion of the bottle into resonance with the oscillation to be studied, and waves of quite large amplitude could be obtained by a very gentle motion. (The method was suggested by Professor Prandtl.) In this way the first positive and the first negative wave could be produced.

Observations were taken with two different depths and, in addition to those made with the chamber at rest, at five different speeds of rotation (roughly 5, 10, 15, 20 and 25 revolutions a minute), the period of the positive wave only being observed at the highest speed. The periods of the positive and negative waves were measured, and also, by means of scales fastened vertically to the walls at the ends of the axes, the ratio of the amplitude at the end of the major axis to that at the end of the minor axis.

The bath had not been specially prepared for the experiment and its shape was not exactly elliptical. The main influence of the slight departure from the elliptical shape is on the ratio of the amplitude at the ends of the axes, the observation of which was in any case rough, and not on the period. On the other hand the depth was not constant (to have constant depth a special bottom, following the curvature of the free surface, would be necessary for each speed of revolution), and this may have an appreciable effect on the period. Actually, the depth was not constant even when the chamber did not rotate, but varied by as much as 1 cm. The dynamically equivalent constant depth is not necessarily the same as the mean depth over the whole area. The procedure adopted was to choose that value of the depth which makes the observed period (after reduction to allow for finite depth, as below) agree with the theoretically calculated period for the slowest of all the normal oscillations when the chamber was at rest; and then to calculate with this depth throughout. The depths as calculated in this way were 10.5 cm and 7.2 cm for the two series of observations, respectively.

The period of rotation of the chamber could be obtained as accurately as desired by means of a stop-watch and a bell striking once in every revolution. The periods of the oscillations were found by timing 30 oscillations on the stop-watch, and not less than three sets of observations were taken. The difference between two observations did not exceed 0.5%. for no rotation, and 2%. at the higher speeds. The values of β were calculated from the observed periods of rotation of the chamber, and the values of $\sigma \mathsf{a}/(gD)^{1/2}$ from the observed periods of oscillation.

The values calculated from tidal theory hold on the assumption that $(D/\mathsf{a})^2$ can be neglected, and some correction is necessary for finite depth. For no rotation, this is a simple matter. If, according to tidal theory, $\sigma/(gD)^{1/2}$ is k, then for finite depth

$$\sigma^2 = gk \tanh(kD), \tag{1}$$

where k has the same value as before.[18] Hence, approximately,

$$\sigma^2/(gD) = k^2(1 - \tfrac{1}{3}k^2D^2), \tag{2}$$

and

$$\sigma/(gD)^{1/2} = k(1 - \tfrac{1}{6}k^2D^2). \tag{3}$$

Hence, if f denote the value of $\sigma \mathsf{a}/(gD)^{1/2}$ as found from observation for finite depth, the value, ka, of $\sigma \mathsf{a}/(gD)^{1/2}$ according to tidal theory will be approximately[19]

[18] Lamb [9]: Hydrodynamics, chap IX, p 440, 6th edition (1932).

[19] The above text is reproduced as exactly as possible from Goldstein. In the terminology of this book 'tidal theory' can be identified with the 'shallow water theory', and Goldstein's (β, σ, D) are our $((f\mathsf{a})^2/(gh_n), \omega, h_n)$. Furthermore, his ω is our $f/2$ and his wavenumber k is our κ. To avoid

$$k\mathsf{a} = f(1 + \tfrac{1}{6} f^2 D^2/\mathsf{a}^2). \tag{4}$$

When the free surface is curved, the matter is not so simple even when the bottom follows the curvature of the free surface. If

$$p' = p - \frac{f^2}{8}(x^2 + y^2) + g\rho z, \tag{5}$$

where p is the pressure, then u and v are given by

$$\frac{\rho\sqrt{\cosh 2\xi - \cos 2\eta}}{\sqrt{2}gD} u = \frac{1}{\sigma^2 - f^2}\left(\mathrm{i}\sigma \frac{\partial p'}{\partial \xi} + f \frac{\partial p'}{\partial \eta}\right),$$

$$\frac{\rho\sqrt{\cosh 2\xi - \cos 2\eta}}{\sqrt{2}gD} v = \frac{1}{\sigma^2 - f^2}\left(-f \frac{\partial p'}{\partial \xi} + \mathrm{i}\sigma \frac{\partial p'}{\partial \eta}\right),$$

[in which p' replaces the surface displacement ζ] and p' satisfies the equation

$$\frac{\partial^2 p'}{\partial x^2} + \frac{\partial^2 p'}{\partial y^2} + \frac{\omega^2 - f^2}{\omega^2} \frac{\partial^2 p}{\partial z^2} = 0. \tag{6}$$

The boundary conditions are

$$\frac{\partial p'}{\partial z} = 0, \qquad \text{at} \quad z = -D + \frac{f^2}{8g}(x^2 + y^2), \tag{7}$$

and

$$\sigma^2 p' = g \frac{\partial p'}{\partial z}, \quad \text{at} \quad z = \frac{f^2}{8g}(x^2 + y^2), \tag{8}$$

together with the vanishing of the normal velocity at the bounding walls. If we neglect the curvature of the surface, then we may take p' proportional to $\cosh(k(z + D))$, and p' satisfies the same equation and boundary condition as ζ in tidal theory, with $k = \sigma/(gD)^{1/2}$. Also, (8) then leads to the same (1) as for no rotation, and we have the same correction formula as before.

---

confusion we shall write Goldstein's formulae with ω replaced by $f/2$. His formulae (2) and (3) are obtained from two-term Taylor series expansions of $\tanh(kD)$ in (1), which is the dispersion relation of a plane wave in a finite depth fluid on an inertial frame. Moreover, solving (3) for $k\mathsf{a}$ yields

$$k\mathsf{a} = \frac{\sigma\mathsf{a}}{\sqrt{gD}} \frac{1}{(1 - \frac{1}{6}k^2D^2)} \cong \frac{\sigma\mathsf{a}}{\sqrt{gD}}\left(1 + \frac{1}{6}k^2\mathsf{a}^2 \frac{D^2}{\mathsf{a}^2}\right).$$

One solution to this quadratic equation can be obtained by the recurrence relation

$$(k\mathsf{a})_{n+1} = f\left(1 + \tfrac{1}{6}(k\mathsf{a})_n^2 \frac{D^2}{\mathsf{a}^2}\right), \quad (k\mathsf{a})_0 = f$$

$(k\mathsf{a})_1$ then corresponds to formula (4).

To understand formula (5), it must be recognized that a steady free surface in the rotating chamber possesses the form of an axisymmetric paraboloid. The free surface is therefore positioned at $z = (2f/g)(x^2 + y^2)$, and the overburden pressure is given by $\rho g z - 2(f/g)(x^2 + y^2)$. ($z$ is measured upward from the position of the free surface at the rotation axis.) Thus, the dynamical pressure is as given in (5).

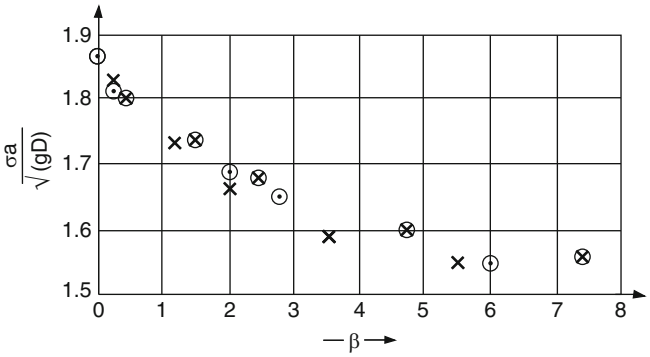

Fig. 13.10 Speeds of the first positive (Kelvin-type) wave. ⊙, calculated values: ×, observed values (corrected for the effect of finite depth) for $D = 10.5$ cm.; ⊗ observed values (corrected for the effect of finite depth) for $D = 7.8$ cm. The ordinates are $\sigma \mathsf{a}/(gD)^{1/2}$, the abscissas are β. D is the depth, supposed constant, which makes the calculated and observed periods of the slowest wave agree when there is no rotation (redrawn from Goldstein [7]). © Royal Astronom. Soc., reproduced with permission

> The formula (4) was then used in all cases to correct for the influence of finite depth. The results are shown in Figs. 13.10–13.12. For the positive wave the agreement between the observed and calculated values is quite as good as could be expected. Comparison of the single calculated value for the negative wave with the experimental values suggests that the method of calculating the depth leads to an error of about 3–5%. Apart from this the results give satisfactory support to the theory.
>
> Another supposition of tidal theory is that the amplitude is small compared with the depth. Observations of the period with different amplitudes showed no systematic change.
>
> For the first positive wave the ratios of amplitudes at the ends of the axes are shown in Fig. 13.11. The observations are in any case difficult, and are made more difficult by the feeling of dizziness consequent upon moving the head in the rotating chamber. Two observers were necessary, so that the amplitudes at the end of the axes could be observed simultaneously. The possible experimental error is about 6%. The agreement between the observed and calculated results is certainly as good as could be expected.
>
> Small pieces of paper at the bottom of the bath near the centre could be observed to describe elliptic orbits in the same direction as the wave, and the orbits gradually opened out as the rotation was increased, but no measurements were attempted'.

This is Goldstein's description of his laboratory experiments on lowest mode gravity seiches in an elliptical container of constant depth. Apart from the conscientious determination of the frequencies of the slowest positive (Kelvin-type) and negative (Poincaré-type) frequencies and amplitude ratios of the surface elevations at the boundaries of the major and minor axes, he states one additional significant observation in the very last paragraph above: To repeat, particle orbits close to the bottom in the centre are elliptical, and they are traversed in the direction of the wave, i.e. cyclonically for the one-mode Kelvin-type waves and anti-cyclonically for the mode-one Poincaré-type waves. This parallels the similar behaviour already mentioned for Kelvin-type and Poincaré-type waves when treating such waves in the

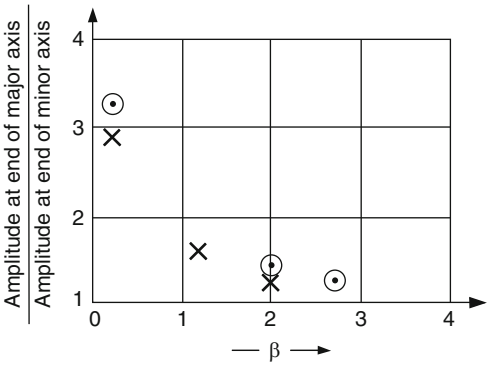

Fig. 13.11 Ratio of amplitudes at ends of major and minor axes in first positive wave. ⊙, calculated values; ×, observed values (redrawn from Goldstein [7]). © Royal Astronom. Soc., reproduced with permission

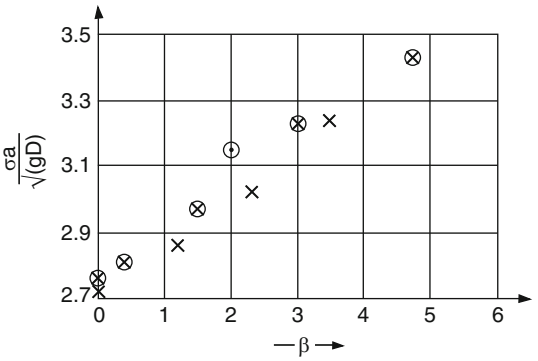

Fig. 13.12 Speeds for first negative Poincaré-type wave. The meaning of the symbols and signs for observed and calculated points are the same as in Fig. 13.10 (redrawn from Goldstein [7]). © Royal Astronom. Soc., reproduced with permission

circular cylindrical basin. Particle motions for Kelvin-type waves are only to-and-fro in a basin whose aspect ratio fulfils the limit $b/a \to 0$.

13.9 Discussion

Gravity driven oscillations in rotating circular and elliptical basins of uniform depth were studied on the basis of the shallow water theory. One of the aims was to see whether wave structures similar to Kelvin and Poincaré waves in constant depth channels were also exhibited by the governing shallow water equations in closed basins of cylindrical and elliptical shape. A second goal was to verify the corresponding mathematical solutions by some laboratory and field experiments. Considerations were limited to constant depth basins (and vorticity waves were thereby excluded), since the vertical and horizontal motions could be separated this way by solving the eigenvalue problem for the vertical motion first (and so charac-

terizing the barotropic and baroclinic dynamics due to the stratification), followed in a second step by the horizontal wave problem leading to a second eigenvalue problem for the horizontal modal structure. This separation of variables procedure is best formulated in terms of the perturbation pressure as independent variable.

Starting with the circular cylindrical geometry, the horizontal eigenvalue problem could be expressed in terms of ordinary and modified Bessel functions. Ordinary Bessel functions apply if the eigenfrequencies are super-inertial, $\omega^2 > f^2$, whilst modified Bessel functions are solutions for sub-inertial frequencies, $\omega^2 < f^2$. However, Lamb has shown that sub-inertial wave solutions only exist if the azimuthal mode number ℓ satisfies the inequality

$$\frac{r_0^2 f^2}{g h_n} > \ell(\ell + 1). \tag{13.71}$$

This is tantamount to exponentially decaying behaviour of the radial structure as one moves away from the container wall towards the cylinder centre. When (13.71) is not valid, solutions are expressed in terms of ordinary Bessel functions which are oscillatory in the radial direction. This property is reminiscent of complete and incomplete reflection in Taylor's patching of gravity wave solutions in oblong rectangles. Kelvin-type and Poincaré-type behaviour is indeed also borne out by the velocity distribution in the two cases and the parity of the rotation of the gyring flow: if (13.71) is satisfied, the largest azimuthal velocities arise close to the cylinder wall with cyclonic (counter-clockwise in the N.H.) rotation of the surface (interface) elevation and the central velocity vectors. On the other hand, if (13.71) is violated, the largest velocities arise in the central region and the surface (interface) elevation and central velocity vectors rotate anti-cyclonically (clockwise on the N.H.), see Fig. 13.2. However, when tracing fluid particle trajectories, these trajectories are compact closed curves, circular in the centre and elliptical with decreasing semi-minor axis as one move from the centre of the container towards the outer wall. This is unlike Kelvin behaviour in straight channels. Analogously, similar closed trajectories are exhibited by super-inertial modes, but the particles now traverse them in the clockwise direction. It is certainly the compactness of the container geometry that is responsible for this behaviour.

This Kelvin-type and Poincaré-type behaviour can also be observed in gravity modes in *elliptical* containers with constant depth. The horizontal eigenvalue problem can now be formulated in terms of Mathieu functions and the eigenvalue problem is expressed in terms of a structurally complex characteristic equation (a determinant of an infinite square matrix must be set to zero). For a homogeneous fluid in an elliptical container of aspect ratio $\mathsf{b}/\mathsf{a} = 2/3$ (b semi-minor axis, a semi-major axis), the first positive and first negative amphidromes are plotted in Fig. 13.8 as computed by Goldstein [7]. Antenucci and Imberger [4] determined the interface elevation and layer velocity distributions in a two layer fluid for the baroclinic first positive and first negative mode solutions. Figure 13.9 corroborates the same qualitative results as obtained for the corresponding solutions in the circular basin. The Kelvin-type mode exhibits high amplitudes and large velocities close to the

container wall, and both rotate cyclonically (counter clockwise on the N.H.). Alternatively, the Poincaré-type mode has large velocities close to the container centre, smaller velocities near the outer boundaries and anti-cyclonic rotation (clockwise on the N.H.) of velocity and interface elevation. Furthermore, particle trajectories are now elliptical with eccentricity influenced by the aspect ratio of the container geometry, relatively fat in the centre and reduced to a double line at the boundary. This behaviour has not been characteristic for Kelvin waves in straight channels. The denotations Kelvin-*type* and Poincaré-*type* account for exactly this difference.

The application of this elliptical mode analysis to Lake Kinneret is not an attempt of corroboration of the correctness of the model; this is assumed, and use of the elliptical seiche model for this lake is an attempt of perhaps reasonable fitting. A proof of its adequacy must be performed with an elliptical container of constant depth on a rotating table. This corroboration has been nearly (the container was only nearly elliptical and the water depth was only nearly constant) provided by Goldstein [7] by laboratory experiments in the rotating chamber of the Kaiser Wilhelm Institut in Göttingen. Goldstein used a container with a $2/3$ aspect ratio and measured for a homogeneous fluid the period of the first positive Kelvin-type and first negative Poincaré-type modes and the surface elevation amplitudes for different rotation speeds and compared these with his theoretical results. These are given in Figs. 13.10–13.12 and are convincing.

References

1. Abramowitz, M. and Stegun, I.A. (Eds.): *Handbook of Mathematical Functions* Dover Publ, New York (1965)
2. Anonymous, U.S. National Bureau of Standards: *Tables Relating to Mathieu Functions*, Columbia University Press, New York (1951)
3. Antenucci, J.P., Imberger, J. and Saggio, A.: Seasonal evolution of the basin-scale internal wave field in a large stratified lake. *Limnol. Oceanagr.*, **45**, (7), 1621–1638 (2000)
4. Antenucci J.P. and Imberger, J.: Energetics of long internal gravity waves in large lakes. *Limnol. Oceanogr.*, **46**, (7), 1760–1773 (2001)
5. Csanady, G.T.: Large-scale motion in the Great Lakes. *J. Geophys. Res.* **72**, 4151–4142 (1967)
6. Csanady, G.T.:Transverse internal seiches in large oblong lakes and marginal seas. *J. Phys. Oceanogr.* **12**, 84–96 (1982)
7. Goldstein, S.: Tidal motion in rotating elliptic basin of constant depth. *Monthly Notes Royal Astronom. Soc. (Geophys. Suppl.)*, **2**, 213–231 (1929)
8. Jeffreys, H.: The free oscillations of water in an elliptical lake. *Proc. Lond. Math. Soc.*, **23**, 455–476 (1925)
9. Lamb, H.: *Hydrodynamics*, 6^{th} edition, Cambridge University Press (1932)
10. Lighthill, S.M.J.: Dynamic response of the Indian Ocean to onset of the Southwest monsoon. *Phil. Trans. Roy. Soc. London*, **A 265**, (1159) 45–92 (1969)
11. Monismith, S.G.: Wind-forced motions in stratified lakes and their effect on mixed layer shear. *Limnol. Oceanogr.*, **30**, 771–783 (1985)
12. Ou, H.W. & Bennet, J.R.: A theory of the mean flow driven by long internal waves in a rotating basin, with application to Lake Kinneret, *J. Phys. Oceanogr.* **9**, 1112–1125 (1979)
13. Pao, Y.-H. and Mow, C.-C.: *Diffraction of Elastic Waves and Dynamic Stress Concentrations*, Crane Russak, New York and Adam Hilger, London (1973)

14. Prandtl, L.: Erste Erfahrungen mit dem rotierenden Laboratorium. *Die Naturwissenschaften* **19**, 425–427 (1926)
15. Sears, W.R.: *Theoretical Aerodynamics*, Part 1: Introduction to Theoretical Hydrodynamics. Graduate School of Aeronautical Engineering, Lecture Notes at Cornell University (1960)
16. Serruya, S.: Wind, water temperature and motions in Lake Kinneret: eneral pattern *Verh. Int. Ver. Limnol.*, **19**, 73–87 (1975)
17. Stratton, J.A., Morse, P.M., Chu, L.J. and Hutner, R.: *Elliptic Cylinder and Spheriodal Wave Functions*, John Wiley & Sons, New York (1941)
18. Taylor, G.I.: Tidal oscillations in gulfs and basins. *Proc. London Math. Soc.*, Series 2, XX, 148–181 (1920)
19. Thomson, Sir. W. (Lord Kelvin): On gravitational oscillations of rotating water. *Proc. R. Soc. Edinb.*, **10**, 92–100 (1879)

Chapter 14
Barotropic and Baroclinic Basin-Scale Wave Dynamics Affected by the Rotation of the Earth

14.1 Introduction

We have already given a detailed description of rotation affected external and internal waves in idealized containers of constant depth: straight channels, gulfs, rectangles and circular and elliptical cylinders. Pure Kelvin and Poincaré waves were shown to describe the oscillating motion in straight channels and their combination yielded the solution of the reflection of the rotation affected waves at the end wall of a rectangular gulf. The typical characterizations of Kelvin and Poincaré waves were seen to prevail (with some modification) in the fluid motion of rotating circular and elliptical cylinders with constant depth. The behaviour was termed Kelvin-type if for basin-scale dynamics the amplitudes of the surface and isopycnal displacements and velocities are shore-bound (i.e. large close to the boundaries and smaller in the interior of the basin), the motion cyclonic (that is counter-clockwise on the N.H.) and frequencies sub- or (less often) superinertial. Alternatively, for Poincaré-type behaviour, the surface and isopycnal displacements and velocities have large amplitudes in off-shore regions, their motion is anti-cyclonic and frequencies are strictly superinertial.

In this chapter, we will demonstrate that such behaviour can be seen in all lakes which are sufficiently large, that the rotation of the Earth can exercise a modulating effect on the oscillating gravity affected motion. We will treat both surface seiches in homogeneous lakes and internal basin-scale oscillations of stratified lakes and concentrate on field data which demonstrate convincingly the role played by the rotation of the Earth. Along with this, results obtained from models are presented and compared with the data; these then provide validation of the model in use, generally not completely because either the model is over-simplifying the physical situation or the data are insufficient to verify with certainty a certain claim of behaviour. In general, inferences derived from such comparisons of models and observations provide *probabilities* for certain interpretations, not exact facts.

On the *observational side*, one almost always has insufficient information, be this lack of instrumentation, insufficient planning of field campaigns, or lack of availability of obvious data, e.g. incomplete knowledge of the bathymetry, wind field which is insufficiently resolved in space and time, failures in correctly deploying

K. Hutter et al., *Physics of Lakes*, *Volume 2: Lakes as Oscillators*, Advances in Geophysical and Environmental Mechanics and Mathematics,
DOI 10.1007/978-3-642-19112-1_14,

instruments or failures in recording data, let alone unexpected general weather conditions that may turn out not to be ideal for the intended measurements, etc. These conditions are the usual constraints with which field limnologists must cope. Failures in this regard cannot be avoided; they must be minimized by adequate planning. Very often, data at different positions are taken episodically and not synoptically, which makes correlation of measured quantities in form of time series difficult or doubtful. Synoptic measurements which cover entire lake basins with sufficiently dense deployment of instruments are expensive and therefore rare. A few synoptic field campaigns have been performed in the last 40 years or so, but often, one is forced to work with data which only provide partial information for the corroboration of a certain conjectured behaviour.

On the *modeling side* the simplifying assumptions affect and, perhaps, falsify the interpretation of, and comparison with, the data. External and internal oscillations in lakes are mostly modeled with field equations in the adiabatic and Boussinesq assumptions; they then ignore dissipation and cannot provide information about decay rates of, e.g. pycnocline-displacement-time series. Moreover, the parameterization of the ground stratification is generally fraught with rather drastic simplifying assumptions. The continuous vertical density variation is nearly always replaced by dividing the lake into horizontal layers, each having its own constant density, sometimes paired with the assumption of a constant total depth. In a two-layer model, only the barotropic and the fundamental baroclinic wave modes can be reproduced; in an n-layer model only $(n-1)$ baroclinic wave modes can be determined. The decision for the choice of n (usually $n=2$, seldom $n=3$ or even more) and whether the variable depth bathymetry is approximated by a mean constant depth are a priori *estimates*, which can be, and for $n=2$, have occasionally been, shown to oversimplify the situation. A similar simplification is often introduced in n-layer models when the lake region with fewer than n layers is ignored, and the lake boundary is identified with the intersection of the upper surface of the deepest layer with the bottom surface.[1] It seems to be clear that for these a priori estimates, because they are subjective, no rational measures for error estimates can be defined.

On the *numerical side*, further errors are introduced simply by the selection of the numerical scheme (FD, FV, FE, spectral) and the choice of the approximation (grid size, order of approximation). The accuracy of these is generally well defined by the functional setting of the numerical model in relation to the initial boundary-value problem that is approximated. In concrete cases of failure of an adequate matching

[1] These various approximations are sometimes denoted by acronyms: Two-layer variable depth model (TVDM); two-layer equivalent depth model (TEDM), when both layers have constant depth and the computation domain is bounded by the (vertical) thermocline shore, which is the intersection of the interface between the epilimnion and hypolimnion layers (with constant densities) and the bathymetric surface. In this case, the barotropic and baroclinic responses follow from single layer models with equivalent depth. If this equivalent depth description is not introduced, and the primitive equations of the two-layer constant depth model are solved, then the TCDM is used. If the regions of the two-layer model with only one layer are included in the model, then the model is called TVDMC, in which the 'C' stands for 'complete'. Similarly, for three-layer models the acronyms THVDM, THEDM, THCDM and THVDMC are used.

of theory, numerics and observation, scrutiny of the cause(s) is vital. It may be any of the three above named classes, perhaps several of them.

The literature on gravitational surface seiches is abundant and proper reference can hardly be made. Most lakes are, however, not sufficiently large that the rotation of the Earth would in any even marginal form, play a role in the oscillation characteristics of homogeneous lakes.[2]

The Great Lakes, the Baltic Sea, the (semi)-bounded ocean basins (say, Adriatic Sea in the Mediterranean Sea, Black Sea, Lake Baikal, the Caspian Sea) are safe candidates where the rotation of the Earth plays a significant role. References on these are by Mortimer [35, 37, 38], in particular with emphasis on Lakes Michigan and Superior by Mortimer and Fee [42] and Mortimer [41], on Lake Erie by Platzman [44] and Platzman and Rao [50], on Lakes Ontario and Superior by Rao and Schwab [52] and on Lake Huron by Schwab and Rao [57]. Platzman [48] reports on a barotropic seiche analysis of the Atlantic and Indian Oceans and [49] and on gravitational seiches of the entire World Ocean.

14.2 Barotropic Basin-Wide Oscillations of Lake Michigan

The likely most thorough analysis of free surface motions of a lake is Mortimer and Fee's 1976 [42] analysis of the 'Free surface oscillations and tides of Lakes Michigan and Superior'. The strengths of this paper are the most carefully conducted spectral analyses 'from records of water levels at nineteen shoreline stations on Lakes Michigan, Huron and Superior. Power spectra from 95 station data sets and 128 spectra of interstation coherence and phase difference were prepared. These spectra have been used to (1) identify the first five free gravitational, barotropic modes (surface seiches) of the three basins; (2) estimate the corresponding seiche frequencies for the three lakes; (3) determine for some modes, the phase progression around the basin imposed by the Earth's rotation; and (4) speculate on the structure of other oscillations, including diurnal and semi-diurnal tides', Mortimer and Fee [35]. This work, complemented by theoretical-computational analyses of the barotropic seiches on the rotating Earth was later summarized in the book 'Lake Michigan in Motion' by Mortimer [41], in which many of the above mentioned papers are referenced.

The computational possibilities in the 1950–1970s of the twentieth century, the times when this kind of research was primarily conducted, were in their beginnings.

[2] The pioneering work on seiches in which the rotation of the Earth does or does not play a role is that of Forel [16] on Lac Léman (Lake Geneva); it stimulated the work of Chrystal [10, 11]. A very detailed early bibliography is given by Tison and Tison [64] with over 200 references. More recent surface seiche papers, in which the rotation of the Earth does not play a role, are by Bäuerle et al. [5] Hamblin and Hollan [19], Hollan [21, 22], Hutter et al. [27, 28] and Hutter [25, 26]. For further information, consult Chaps. 15–18. Surveys are given by Mortimer [40] and Platzman [46, 47].

Computation of the eigenvalue problems for the barotropic seiches on the rotating Earth for natural basins was virtually impossible in the 1950s – Defant's Kelvin wave dynamic solutions were the only approach to construct the amphidromies in (only elongated) basins, see Defant's, [14], construction of the amphidromies of the lowest two barotropic modes for Lake Michigan, Fig. 14.1 – and difficult and likely inaccurate in the seventies, because of the rather coarse resolution of the numerical grid.

Figure 14.1 illustrates Defant's [14] construction of the first two modes of Lake Michigan's surface seiches with periods of 9.05 and 4.88 h, respectively. These modes possess one and two positive amphidromes, and the rotation of the Earth produces a cross basin oscillation that processes together with the longitudinal motion but lags behind the latter by a quarter period, together forming a counter-clockwise

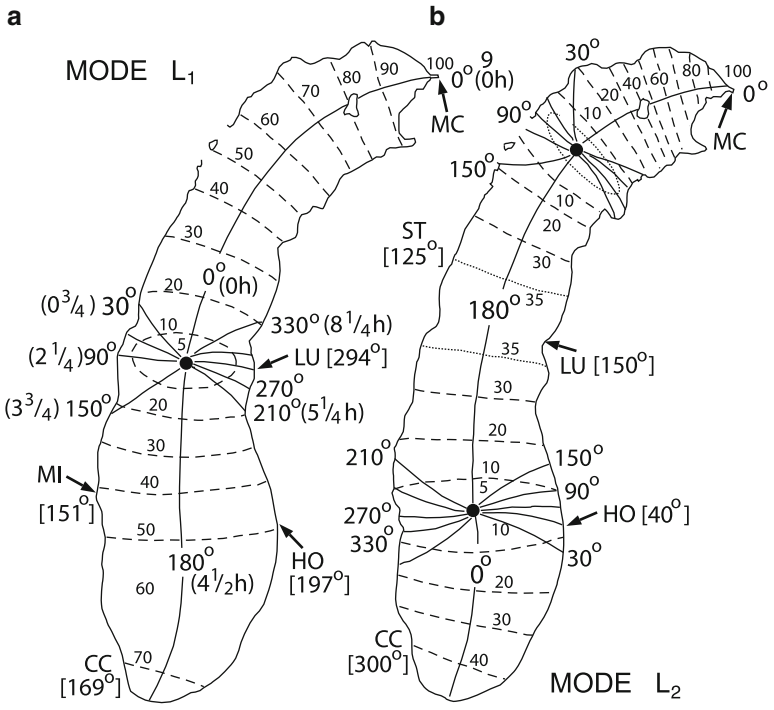

Fig. 14.1 Lake Michigan surface seiches. Amphidromic systems of the fundamental, L_1, and second, L_2, longitudinal modes, illustrated by Defant's model [14] with model predicted periods 9.05 and 4.88 h. *Dashed co-range lines* display surface elevation ranges relative to 100 at MC. *Solid co-phase lines*, radiating from the amphidromic points (*black spots*) of zero elevation change show the counter-clockwise progression of high water at 30° intervals relative to 0° at MC. Note, the Lake bathymetry here ignores the basin appended Green Bay. Corresponding progression in hours, for the 9-h L1 seiche mode, is shown within *round parentheses*. The *square bracketed angles*, relative to 0° at MC and placed against certain level recorder locations, represent *observed* phase progressions, derived from cross spectral analysis, Mortimer and Fee [42], of pairs of records. From Mortimer (2004) [41].

rotation (on the N.H.) of the high water around the amphidromic points. Co-range lines (dashed in the figure) display the surface elevation amplitudes in percentages of the maximum at MC and co-phase (co-tidal) lines (solid) radiating from the black dots (the amphidromic centres) illustrate the counter-clockwise phase propagation of high water at (1/12) cycle (30°) intervals relative to 0° at MC.

'In Fig. 14.1a the progression in hours from MC is shown in parentheses around the lake shore. The square-bracketed angles, relative to 0° at MC and representative for water level stations at positions, indicated by arrows, represent *observed* phase progression, derived from cross-spectral analysis by Mortimer and Fee [42] of pairs of records'.

The above follows Mortimer [41], who continues by stating 'that Defant assumed that the seiche currents, predicted by his father's model, Defant [13], were modified by the Earth's rotation and were in geostrophic equilibrium. The resulting patterns (displayed in Fig. 14.1) exhibit similarities with the double (quasi-standing) Kelvin wave in the rotating channel model (see Fig. 12.4 in Chap. 12)...'.

'The periods of the two surface seiche modes, modeled in Fig. 14.1, differed little from those calculated (but without rotation) by Rockwell [54]. Surprisingly, however, Defant did not look at the recorded lake levels to test his model. [...], that test came in 1965 with my (Mortimer's) spectral analysis of long series of water level records [36]. These came from several stations around the Lake and were kindly provided by the US Lake Survey, Army Corps of Engineers ...'.

The level records from six stations around Lake Michigan – one on Lake Huron, and one (Mackinaw City, MC) common to both basins – were either continuous charts, from which I (Mortimer) derived 15 min averages, or levels read hourly and tabulated by the US Lake Survey. The charts trace the motions of a float in a stilling well connected to the Lake by a narrow pipe. [...] each recorder, [...], displays its characteristic signature which depends on the design of the stilling well and on exposure to local [...] oscillations. Inspite of those differences, lower frequency oscillations can sometimes be picked out by eye beneath the irregular fluctuations. [...] For most times, however, oscillatory signals remain hidden, obscured by noise and one must call in the help of *spectral analysis* to reveal them. However, that powerful tool has its limitations, of which one must be aware to properly interpret spectra of Lake level fluctuations', Mortimer [41].

This cautious spectral analysis was performed by Mortimer and Fee [42] in a most impressive memoir, and a highlighting summary of it is presented by Mortimer [41]. Cross spectral analyses of station pairs surface-elevation-time series allow identification of peaks in the periodograms of the surface-elevation energies, phase shifts and coherences of such cross spectra. The authors paid special attention to the presence of spurious peaks, masquerading as *aliases*. The periods of the mode 1 and mode 2 seiches in Fig. 14.1 were determined this way, as are the phase angles in square braces identifying the phase propagation.

The two lowest longitudinal seiche modes of Lake Michigan using Defant's [14] method of Kelvin wave dynamics for the determination of the seiche periods and the mode structures as determined by Mortimer [36] and Rockwell [54] were again determined a decade later in a paper by Rao, Mortimer and Schwab

[53] . In this paper Lake Michigan, now including Green Bay, was discretized by a $14.4 \times 14.4\,\mathrm{km}^2$ grid with WE-SN orientation, and taking a bathymetry in which to each grid mid point a mean depth was assigned. The mean depth for the whole grid array was 84.2 m, 1.3% lower than that derived from chart contours; this makes basin-wide mode periods somewhat larger than had been determined earlier.

The lowest three longitudinal modes are displayed in Fig. 14.2. Signatures for the co-range and co-phase lines are the same as in Fig. 14.1, see also figure caption. In Fig. 14.2 'angles quoted in square brackets placed near some recorder locations are the 'observed' phase angles (relative to 0° at MC) for that mode and recorder, derived from inter-station phase and coherence information yielded by co-spectral analysis, according to Mortimer and Fee [42]. Asterisk codes indicate, for each mode and recorder, whether the corresponding spectral peaks are: *** very large, ** large, *⁻ present, * present but small, *° not visible. Locations of water-level recorders are coded as MC, LU, HO, CC, CW, WA, MI, GB, ST' (after Mortimer [41]).

The first longitudinal seiche mode (L_1, computed period 9.27 h) has two amphidromic points. The principal amphidrome occupies the whole of the main basin; the second is at the mouth of Green Bay. This is evidence of the forcing of the Bay oscillation by the main Lake seiche L_1 [...].

Mode L_2 (computed period 5.25 h) displays four positive amphidromes, two within the main basin, one at the mouth of Green Bay, and one in the inner Bay. [....] Mode L_3 (computed period 3.81 h) exhibits three positive amphidromes in the main basin and three in Green Bay [...]' [41]. Positive (negative) amphidromes exhibit counter-clockwise (clockwise) progression of the co-phase lines for the Northern (Southern) Hemisphere and are reminiscent of Kelvin-type behaviour.

'As described above, the modeled phase structure of each mode is displayed by co-phase lines drawn at 30° intervals, relative to 0° at the Northern end of the basin, MC. The phase relationships, 'observed' at water-level recorder locations by co-spectral analysis [...] are entered (as is also the observed frequency) as square-bracketed phase angles at those locations, all relative to 0° at MC. The agreement between calculated and observed phase angles is satisfactory for L_1 and L_2. For higher modes there is less agreement. For L_2, the amplitude at Milwaukee (MI) was too small to measure phase angles between those station pairs which include MI.

It is of interest at this point to compare the L_1 and L_2 structures in Fig. 14.2 with those predicted by Defant's [14] one dimensional model. Both models (in which the latter does not include Green Bay) place the amphidromic point and amplitude distributions in similar positions. The main differences are in the rates of phase progression around those points. They are more abrupt (i.e. the effect of the Earth's rotation is less conspicuous) in Fig. 14.2 than in the Fig. 14.1-model. Nevertheless, the similarities are remarkable and justify the use of Defant's [13] method[3] to account for the rotation of the Earth' [41].

[3] This statement may have to be revised now (2011) as computations can now be economically performed in a much more refined way. Moreover, a full two-dimensional computation and the inclusion of island do no longer present an obstacle for more accurate computations. The differences in the co-phase lines of the panels in Figs. 14.1 and 14.2 in fact call for a

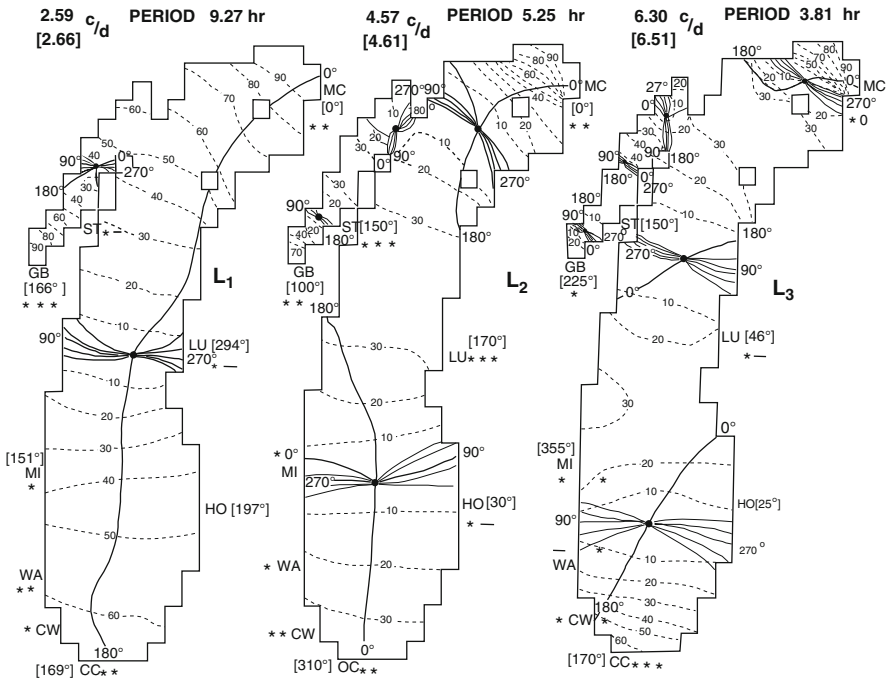

Fig. 14.2 Lake Michigan surface seiches. Calculated frequency/period and structures of the first three longitudinal amphidromic seiche modes L_1, L_2, L_3 of the main Lake Michigan basin as computed by Rao et al. [53]. Phase progression is shown (by *solid lines*) relative to 0° at MC. Elevation of the water surface is shown by *dashed co-range lines*, scaled in percent of the maximum of 100 in each mode. The bracketed 'observed' frequency in the *top left* of each panel is that of the corresponding peak, attributed to the mode, in spectra of observed water level fluctuations not shown here – see in Mortimer (2004) [41], Chap. 7. From Mortimer (2004) [41]. © University of Wisconsin Press, Milwaukee, reproduced with permission

We have seen already that positive amphidromes are reminiscent of Kelvin-type behaviour, whilst negative amphidromes exhibit Poincaré-type behaviour, which is often also referred to as *transverse* mode behaviour. Such seiche behaviour has also been observed in Lake Michigan at a high frequency (period ∼2.28 h) by Comstock [9]; it is readily excited in the Southern end of the main basin with largest amplitudes at WA, see Fig. 14.3a. This mode, called T_1 by Mortimer [41], has been also computed by Rao et al. [53] and was revealed as an extensive *negative* amphidrome with clockwise phase progression, which occupies most of the Southern basin as a predominant cross-basin oscillation. This is characteristic of Poincaré-type behaviour. The Northern part of the main basin has four positive amphidromes, but amplitudes are only large at the very Northern end and not

refined computation simply in order to see how the amphidromic structure is influenced by mesh refinement.

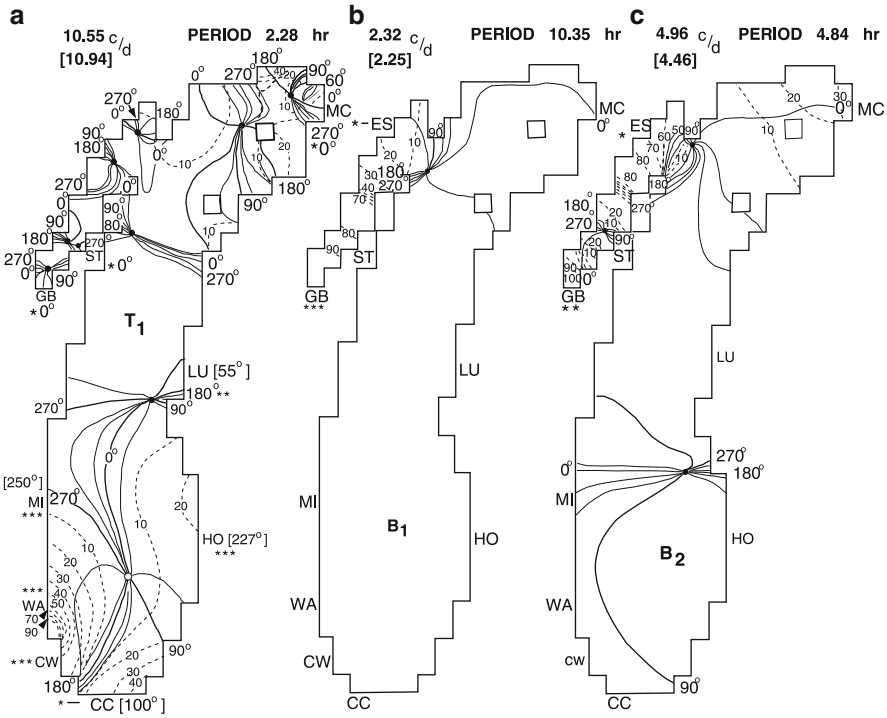

Fig. 14.3 Lake Michigan surface seiches. Calculated frequency/period and structures of the first transverse mode, T_1, panel (**a**), of the Southern basin and the first two longitudinal or resonance modes, B_1 and B_2, panels (**b**) and (**c**), of Green Bay. Phase progression is shown (by *solid lines*) relative to 0° at MC. Elevation of the water surface is shown by *dashed co-range lines*, scaled in percent of the maximum of 100 in each mode. The bracketed 'observed' frequency in the *top left* of each panel is that of the corresponding peak, attributed to the mode, in spectra of observed water level fluctuations not shown here – see [41], Chap. 7. Computations are by Rao et al. [53]. Angles quoted in square brackets placed near some recorder locations are the observed phase angles (relative to 0° at MC) for that mode and recorder, derived from interstation phase and coherence information yielded by co-spectral analysis. Asterisk code is the same as in Fig. 14.2 as are the recorder codes for the stations. From Mortimer (2004) [41]. © University of Wisconsin Press, Milwaukee, reproduced with permission

elsewhere. Thus, it is unlikely that this mode could be identified in surface-elevation recorders positioned in Green Bay or anywhere in the main basin, except, perhaps, at the Northern tip.

Bay resonances or *bay modes* are whole lake modes which possess appreciable amplitudes only within the bay, but generate motions of the free surface elevation within the main basin, which are very small (to the extent not to be measurable). The Green Bay modes B_1 and B_2 have periods of 10.35 and 4.84 h, respectively. B_1 is confined almost entirely to within the Bay, with maximum amplitude at the head of Green Bay (Fig. 14.3b). Mode B_2 (Fig. 14.3c) exhibits three positive amphidromes – one at the Northern mouth, one within the Bay, and one (with near zero amplitude)

Table 14.1 Lake Michigan: Frequencies and periods of the first five longitudinal seiche modes with positive amphidromies and counter-clockwise phase progression (Kelvin-type behaviour) and the first 'transverse' mode, T_1, with one negative amphidrome, exhibiting clockwise phase progression which is reminiscent of Poincaré-type behaviour, identified from inter-station coherences and compared with computed estimates. For details see main text, from [42], with simplifying modifications and additions

Mode no.	Observed		Computed (h)				
	Frequency [c/d]	Period [h]	Mortimer [36] (a)	Mortimer [36] (b)	Rockwell [54] (c)	Rockwell [54] (d)	Rao et al. [53]
1	2.69	8.92	9.2	9.1	9.09	8.83	9.27
2	4.76	5.04	5.5	4.9	4.92	4.87	5.25
3	6.60	3.64	4.1	3.6	3.58	3.54	3.81
4	7.68	3.12	3.2	2.9	2.91	2.86	
5	9.68	2.48	2.5	2.4	2.42	2.39	
T_1	10.96	2.19					2.28

in the Southern part of the main Lake. These modes have also been measured and are described in detail by Mortimer. These results indicate that the Green Bay modes B_1 and B_2 could also approximately be determined by restricting computations to a region, slightly larger than Green Bay with the mouth sealed for through flow.

Table 14.1 collects the frequencies and periods of the first five longitudinal and the first 'transverse' seiche modes and compares them with computed estimates. The five longitudinal modes have all positive amphidromes with counter-clockwise phase progression of the surface elevation, typical of Kelvin-type behaviour. The periods were computed by Mortimer [36] with Defant's [13], method, using 23 sections (column (a) in Table 14.1) and 56 sections (column (b) in Table 14.1) along the main lake axis, respectively. Rockwell [54], on the other hand, used Platzman and Rao's [50] method, excluding the rotation of the Earth with 85 sections, assuming that the straits of Mackinaw (between Lake Michigan and Lake Huron) are closed (c) and open (d), respectively. Rao et al. [53] discretized the linearized seiche equations on the finite difference grid of $14.4 \times 14.4\,\mathrm{km}^2$ mesh size. Only this more sophisticated integration procedure allowed identification of negative amphidromes. The mode T_1 is the longest mode with clockwise phase progression (on the Northern hemisphere), and with an extent covering about half of the Southern main basin of Lake Michigan, see Fig. 14.3a. This amphidrome exhibits Poincaré-type structure.

The above description comprises only a partial and incomplete report of what is known about the response of the homogeneous Great Lakes free oscillations. To our knowledge, the scientific memoirs, written by Mortimer and associates, in particular Mortimer and Fee [42], Rao et al. [53], Rao and Schwab [52] and Schwab [57], offer the most detailed comparison of the whole-basin seiche modes inferred from surface-elevation-time series at recorder stations with computational results. Such comparisons have also been made elsewhere, for instance for the internal wave dynamics in Lake Geneva, but generally in these situations the available whole-basin synoptic surface elevation recordings are known in much lesser detail. Generally, the periods of the few lowest seiche modes can relatively easily

be computed and the computed results compared with periods from spectra of (even isolated) surface-elevation-time series. Synoptic measurements are, however, generally not made at a sufficiently large number of recorder stations that cross-spectral analysis would allow reliable identification of mode phase progression. This is the distinctive feature of the Great Lakes data.

14.3 Internal Seiche Dynamics in Lake Geneva

14.3.1 Introduction

The study of basin wide oscillations in lakes originates from the Lake Geneva region, and the term 'seiche' has been introduced into the natural sciences by Forel [16] in his three volumes treating Limnology of Lac Léman.[4] In fact the term 'seiche' exists since the eighteenth century and has first appeared in a paper by Fatio-de-Duillier in 1730 [12]. Forel was studying the seiches of Lac Léman as a phenomenon of surface oscillations along the lake shore, not particularly paying attention to the effects played by the rotation of the Earth. The possibility of the manifestation of rotation-affected internal oscillations was brought by the Swiss Service Féderale des Eaux (SFE, 1954 [59]) when in 1950 12 high precision water level recorders were spaced around the lake to measure time series of the free surface, see Fig. 14.4. It should be noted that internal oscillations – manifest as pycnocline displacements – are accompanied by oscillations at the lake surface level, which are in counter-phase to one another and typically about 100 to 1000 times smaller in amplitude than the oscillations at the thermocline level. If these time series of surface displacements are filtered such that the barotropic modes are eliminated, it is possible to follow the progress of the internal baroclinic motions (Caloi et al. (1961) [8], Sinkes (1987) [62]). This method was used by Mortimer [35], see Fig. 1.2 in Chap. 1 in Volume I; he plotted the SFE-surface-level-time series in cyclonic order around the basin for eight stations and set in evidence the nearly constant counterclockwise progression of two cycles of an 80 h wave with a speed of progress close to $c_i = 0.45\,\mathrm{ms}^{-1}$.

Later measurements of the stratified Lake Geneva by thermistor chains and current meters were episodic and covered the years 1976–1979 and 1982–1983. These measurements are reported in Graf et al. [17] and Mortimer [39] in a conference book edited by Graf and Mortimer [18], in which Bohle-Carbonell [6] and Bohle-Carbonell and van Senden [7] have contributions on the dynamics of Lake Geneva.

[4] Lac Léman is the French counterpart of Lake Geneva. We use them as synonymous.

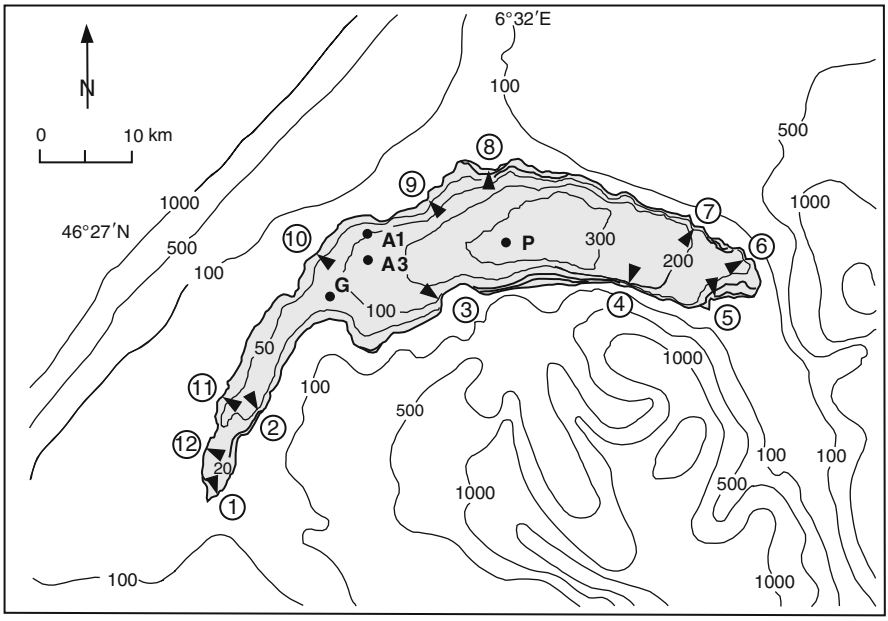

Fig. 14.4 Sketch of Lake Geneva and its surrounding topography and positions of the 12 SFE water level recording stations. Indicated are also the positions of mooring stations A1, A3, G, and P within the lake. Elevations of the surrounding land and lake depths are given in metres, with respect to the water surface of the lake. From Lemmin et al. (2005) [32], with changes. Copyright 2000 by the American Society of Limnology and Oceanography, Inc, reproduced with permission

Table 14.2 Lake Geneva hydrographic data

	Grand lac	Petit lac
Maximum depth (m)	310	70
Mean depth (m)	157	–
Maximum width (km)	13.8	5
Mean width (km)	10	4

14.3.2 Lake Morphology and Data Handling

Lake Geneva is composed of two basins, a deep central basin, sometimes called Grand Lac, covering more than two-thirds of its total area, and a narrow section in the West, called Petit Lac, see Table 14.2. Under typical summer stratification the internal Rossby radius is about 5.5 km, less than half the maximum width of the central basin. Given the Alpine surrounding landforms, with high mountains in the South and hills in the North, the wind field is largely affected by the topography: the Eastern part of the lake is sheltered from most strong winds. The central and Western parts of the lake are primarily subject to winds from Northeast and Southwest of duration from several hours to several days. Winds from Northeast are prone to generate large thermocline depressions of more than 20 m (Lemmin and D'Adamo, 1996 [33]).

Using the water-level data (4 June–30 November 1950), 6 h mean levels were tabulated by the SFE at 3 h intervals. For their analysis, Lemmin et al. [32] interpolated occasionally missing points over 5–6 neighboring points. Moreover, for the analysis the SFE data set was divided into a summer period (4 June–24 August) and an autumn period (28 August–30 November 1950). Changes in mean lake-water levels were eliminated by subtracting the corresponding mean value from each observation, but wind effects were not eliminated. For spectral analysis of records, a standard Fast Fourier Transform (FFT) with segment overlap was used. The analysis for all stations was carried out separately for the summer and autumn periods. Cross spectral analysis, applied to station pairs, was used to determine inter-station coherence and phase. These were compared with the spatial structures of seiche modes, simulated with the two-layer constant depth model (TCDM). Alternative computations were also conducted with the TEDM.

14.3.3 Model Equations

It is assumed that basin-scale internal wave dynamics in Lake Geneva is describable with sufficient accuracy by using a linear TCDM of the adiabatic Boussinesq-approximated dynamical equations. They are given

- For the upper layer ($H_1 = const.$) by

$$\begin{aligned} &\frac{\partial \boldsymbol{M}_1}{\partial t} + f\boldsymbol{k} \times \boldsymbol{M}_1 = -gH_1 \mathrm{grad}_H \zeta_1 + \frac{\boldsymbol{\tau}_\mathrm{W}}{\rho_1}, \\ &\mathrm{div}_H \boldsymbol{M}_1 + \frac{\partial \zeta_1}{\partial t} - \frac{\partial \zeta_2}{\partial t} = 0, \end{aligned} \tag{14.1}$$

- For the lower layer ($H_2 = H_2(x, y)$) by

$$\begin{aligned} &\frac{\partial \boldsymbol{M}_2}{\partial t} + f\boldsymbol{k} \times \boldsymbol{M}_2 = -g\delta H_2 \mathrm{grad}_H \zeta_1 - g\varepsilon H_2 \mathrm{grad}_H \zeta_2 - \frac{\boldsymbol{\tau}_\mathrm{B}}{\rho_2}, \\ &\mathrm{div}_H \boldsymbol{M}_2 + \frac{\partial \zeta_2}{\partial t} = 0. \end{aligned} \tag{14.2}$$

Here, ζ_1 and ζ_2 are the free surface and thermocline displacements, $\boldsymbol{M}_1, \boldsymbol{M}_2$ are the depth integrated layer fluxes $\boldsymbol{M}_i = H_i \boldsymbol{v}_i$, $i = 1, 2$, and $\rho_1 < \rho_2$ are the densities of the top and bottom layers, respectively. $\boldsymbol{\tau}_\mathrm{W}$ and $\boldsymbol{\tau}_\mathrm{B}$ are the wind stress and bottom friction stress fields and

$$\delta = \rho_1/\rho^*, \qquad \varepsilon = (\rho_2 - \rho_1)/\rho^*. \tag{14.3}$$

Moreover, the thermocline interface $z = \zeta_2(x, y, t)$ is assumed to be material (no layer mixing). Equations (14.1)–(14.3) agree with (11.92) and (11.93).

Ignoring bottom friction ($\boldsymbol{\tau}_{\mathrm{B}} = \mathbf{0}$) and restricting considerations to free waves ($\boldsymbol{\tau}_{\mathrm{W}} = \mathbf{0}$), solutions of (14.1), (14.2) are sought in the harmonic form

$$(\boldsymbol{M}_i, \zeta_i) = (\boldsymbol{Q}_i, Z_i) \times \exp(i\omega t) \tag{14.4}$$

so that the complex-valued vector-matrix differential eigenvalue equation

$$\left.\begin{aligned} &(i\omega \boldsymbol{\mathcal{M}}_6 + \boldsymbol{\mathcal{R}}_6)\boldsymbol{a} = \mathbf{0}, \ \text{in } \mathcal{D}, \\ &\boldsymbol{a} \cdot \boldsymbol{N} = 0, \qquad \text{along } \partial\mathcal{D} \end{aligned}\right\} \tag{14.5}$$

must be solved, where[5]

$$\boldsymbol{a} = (U_1, V_1, Z_1, U_2, V_2, Z_2)^{\mathrm{T}}, \qquad \boldsymbol{N} = (n_1, n_2, 0, n_1, n_2, 0)^{\mathrm{T}}$$

$$\boldsymbol{\mathcal{M}}_6 = \begin{pmatrix} 1 & 0 & 0 & 0 & 0 & 0 \\ 0 & 1 & 0 & 0 & 0 & 0 \\ 0 & 0 & 1 & 0 & 0 & -1 \\ 0 & 0 & 0 & 1 & 0 & 0 \\ 0 & 0 & 0 & 0 & 1 & 0 \\ 0 & 0 & 0 & 0 & 0 & 1 \end{pmatrix}, \tag{14.6}$$

$$\boldsymbol{\mathcal{R}}_6 = \begin{pmatrix} 0 & -f & gH_1\dfrac{\partial}{\partial x} & 0 & 0 & 0 \\ f & 0 & gH_1\dfrac{\partial}{\partial y} & 0 & 0 & 0 \\ \dfrac{\partial}{\partial x} & \dfrac{\partial}{\partial y} & 0 & 0 & 0 & 0 \\ 0 & 0 & g\delta H_2\dfrac{\partial}{\partial x} & 0 & -f & g\varepsilon H_2\dfrac{\partial}{\partial x} \\ 0 & 0 & g\delta H_2\dfrac{\partial}{\partial y} & f & 0 & g\varepsilon H_2\dfrac{\partial}{\partial y} \\ 0 & 0 & 0 & \dfrac{\partial}{\partial x} & \dfrac{\partial}{\partial y} & 0 \end{pmatrix}.$$

This system suffers from the fact that the mass matrix $\boldsymbol{\mathcal{M}}_6$ is not diagonal. Such a diagonalization can be achieved by introducing the new variable $z = Z_1 - Z_2$ and eliminating Z_1. The system of differential equations which then emerges is given by

[5] It appears that the corresponding equation in Lemmin et al. [32] suffers from misprints.

$$\left.\begin{aligned} &(i\omega\mathcal{I}_6 + \mathcal{R}_6^*)\boldsymbol{a}^* = \mathbf{0}, \text{ in } \mathcal{D}, \\ &\boldsymbol{a}^* \cdot \boldsymbol{N} = 0, \qquad \text{along } \partial\mathcal{D}, \end{aligned}\right\} \tag{14.7}$$

in which $\mathcal{I}_6$ is the 6-dimensional unit matrix and

$$\begin{aligned} \boldsymbol{a}^* &= (U_1, V_1, z, U_2, V_2, Z_2), \\ \mathcal{R}_6 &= \begin{pmatrix} 0 & -f & gH_1\dfrac{\partial}{\partial x} & 0 & 0 & gH_1\dfrac{\partial}{\partial x} \\ f & 0 & gH_1\dfrac{\partial}{\partial y} & 0 & 0 & gH_1\dfrac{\partial}{\partial y} \\ \dfrac{\partial}{\partial x} & \dfrac{\partial}{\partial y} & 0 & 0 & 0 & 0 \\ 0 & 0 & g\dfrac{\rho_1}{\rho^*}H_2\dfrac{\partial}{\partial x} & 0 & -f & g\dfrac{\rho_2}{\rho^*}H_2\dfrac{\partial}{\partial x} \\ 0 & 0 & g\dfrac{\rho_1}{\rho^*}H_2\dfrac{\partial}{\partial y} & f & 0 & g\dfrac{\rho_2}{\rho^*}H_2\dfrac{\partial}{\partial y} \\ 0 & 0 & 0 & \dfrac{\partial}{\partial x} & \dfrac{\partial}{\partial y} & 0 \end{pmatrix}, \end{aligned} \tag{14.8}$$

in which the definitions (14.3) have been used.[6]

When the TEDM is used, the equations corresponding to (14.5) and (14.6) are

$$\left.\begin{aligned} &(i\omega\mathcal{I}_3 + \mathcal{R}_3)\boldsymbol{b} = \mathbf{0}, \text{ in } \mathcal{D}, \\ &\boldsymbol{b} \cdot \boldsymbol{N} = 0, \qquad \text{along } \partial\mathcal{D}, \end{aligned}\right\} \tag{14.9}$$

$$\left.\begin{aligned} &\boldsymbol{b} = (U, V, Z)^{\mathrm{T}}, \quad \boldsymbol{N} = (n_x, n_y, 0)^{\mathrm{T}}, \\ &\mathcal{R}_3 = \begin{pmatrix} 0 & -f & gh_{\mathrm{E}}\dfrac{\partial}{\partial x} \\ f & 0 & gh_{\mathrm{E}}\dfrac{\partial}{\partial y} \\ \dfrac{\partial}{\partial x} & \dfrac{\partial}{\partial y} & 0 \end{pmatrix}, \end{aligned}\right\} \tag{14.10}$$

and h_{E} is the constant equivalent depth $h_{\mathrm{E}} = H_1 H_2/(H_1 + H_2)$.

For the numerical finite difference scheme an Arakawa-C grid (see Volume 3) was employed, using a rectangular grid with a mesh size of $500 \times 500\,\mathrm{m}^2$. The computational domain is defined as the region closest to the interior of the thermocline shore at the 15-m depth and is shown in Fig. 14.5.

[6] It is likely that Lemmin et al. [32] wished to use this latter description.

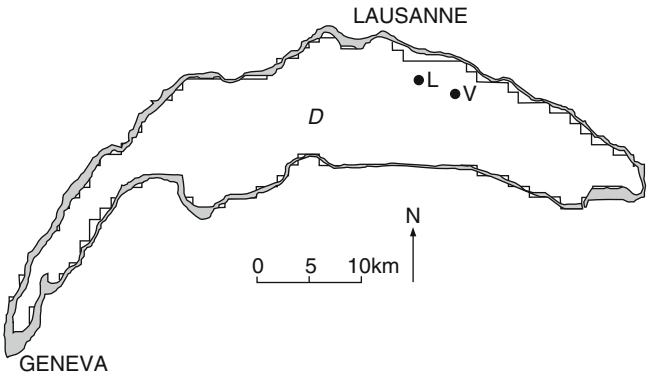

Fig. 14.5 Discretization of the Lake Geneva with a $500 \times 500\,\mathrm{m}^2$ grid approximation. $\mathcal{D}$ is the region with depth larger than 15 m. The *solid line* outlines the 22 m depth and the step-like closed curve is the numerical boundary. From Bäuerle [3]. © Springer, Berlin, reproduced with permission

Table 14.3 Calculated frequencies and periods of 12 internal oscillations of a TEDM for Lake Geneva using an equivalent depth of 13.53 m yielding a phase speed of $43.3\,\mathrm{ms}^{-1}$ and a discretization as shown in Fig. 14.5 (from Bäuerle [3])

Mode number	Frequency $[\mathrm{s}^{-1}]$	ω/f	Period [h]	Number of amphidromic systems	
				Positive	Negative
1	2.239×10^{-5}	0.2083	77.95	1	–
2	3.672	0.3416	47.53	2	–
3	5.481	0.5099	31.84	3	–
4	7.614	0.7083	22.92	4	–
5	9.241	0.8596	18.89	5	–
	10.750	1.000	16.24		Inertial frequency
6	10.765	1.001	16.21	6	–
7	12.352	1.1490	14.13	7	–
8	13.922	1.2951	12.54	8	–
9	15.182	1.4123	11.50	9	–
10	16.694	1.5529	10.45	10	2
11	16.823	1.5649	10.37	8	2
12	17.243	1.6040	10.12	9	2[a]

[a]Bäuerle [3] writes that mode 12 has only one negative amphidromy; however, this is in conflict with Figs. 14.11 and 14.12 which clearly show 2.

14.3.4 Modal Analysis for the TEDM

Computed frequencies ω_m of the first 12 modes of the discretized model of Lake Geneva with equivalent depth were first given by Bäuerle [3] and are listed in Table 14.3. This table is based on a mean depth of $H_1 + H_2 = 152.7\,\mathrm{m}$, $\varepsilon = 1.41 \times 10^{-3}$, and $H_1 = 15\,\mathrm{m}$, corresponding to $h_\mathrm{E} = 13.53\,\mathrm{m}$ and $c_i = \sqrt{g h_\mathrm{E}} = 43.3\,\mathrm{ms}^{-1}$.

The structure of the fundamental horizontal mode, H1, with period, $T = 77.95\,\mathrm{h}$, is laid out in Fig. 14.6, in panel (a) showing the amphidromic point and the co-range lines (dashed), scaled to a maximum of value 100, and co-phase (co-tidal) lines (solid) in 30° intervals. Panels (b–e) display the amplitudes of the interface deflection

$$\zeta(x, y, t) = A(x, y)\cos(\omega t - \Phi) \tag{14.11}$$

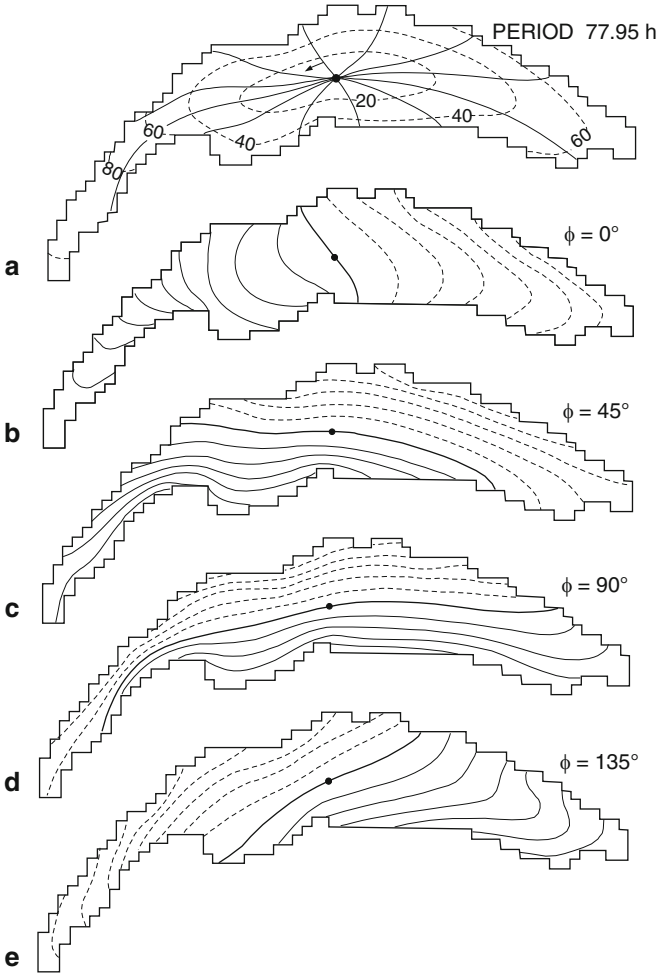

Fig. 14.6 H1-mode of an internal Kelvin-type wave in Lake Geneva computed with the TED-Model. (**a**) Amphidromic system showing co-range lines (*dashed*), scaled to a maximum of value 100 in 20% steps, and co-phase (co-tidal) lines (*solid*), showing zero vertical displacement lines in (1/8)-cycle time intervals. (**b**)–(**e**): Interface displacements drawn in 10% steps of the maximum amplitude plotted for the phase angles $\Phi = 0°, 45°, 90°$, and 135°. The zero amplitude line is drawn heavily; *solid* and *dashed lines* are in counter-phase (*solid* for positive displacements; *dashed* for negative displacements). From Bäuerle [3].

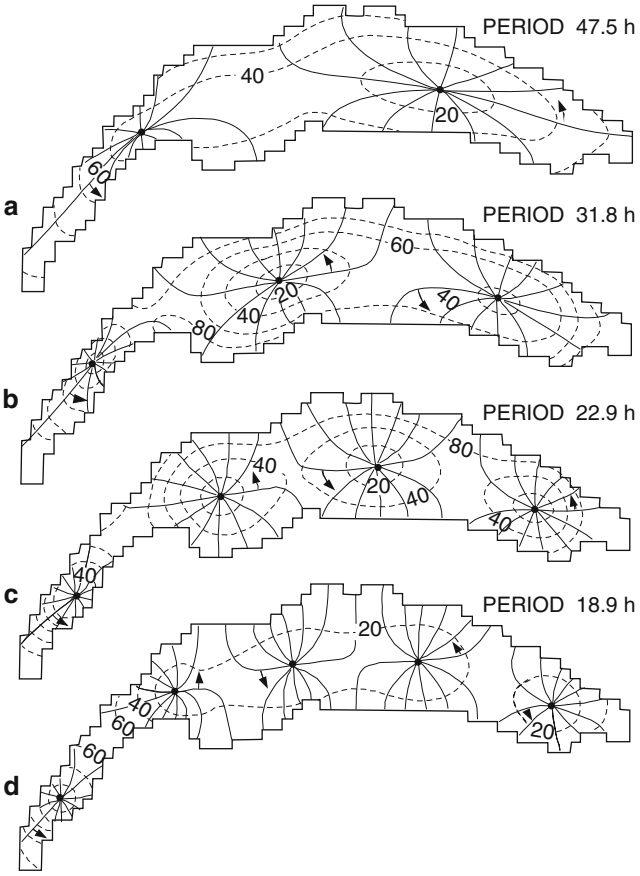

Fig. 14.7 Lake Geneva amplitude and phase distributions for modes 2–5. Co-range lines (*dashed*) are plotted in 20% steps of the maximum value 100, and co-phase lines (*solid*) showing the zero vertical displacement lines in 1/8 cycles of the full periods. (**a**) mode 2 (47.5 h); (**b**) mode 3 (31.8 h); (**c**) mode 4 (22.9 h); (**d**) mode 5 (18.9 h). From Bäuerle [3]. © Springer, Berlin, reproduced with permission

in steps of 30°, starting arbitrarily with the distribution at $\Phi = 0$, shown in panel (b). The rotation is counter-clockwise (cyclonic), the mode is therefore Kelvin-type. The next four internal modes predicted by the model and presented in Fig. 14.7 have from two to five amphidromic systems, all of which have cyclonic rotation (i.e. counter-clockwise in the N.H.). According to Table 14.3, all these modes have sub-inertial frequencies ($\omega_i < f$) and are therefore of Kelvin-type.

The next four modes (6–9) all have also a growing number (6–9) of positive amphidromic systems (see Table 14.3) and are therefore of Kelvin-type. This is so, even though their eigenfrequencies are superinertial ($\omega > f$). However, modes 10 and 11 are mixed-type, i.e. they have positive (anti-clockwise rotating in the N.H.) and negative (clockwise rotating in the N.H.) amphidromic systems (indicated

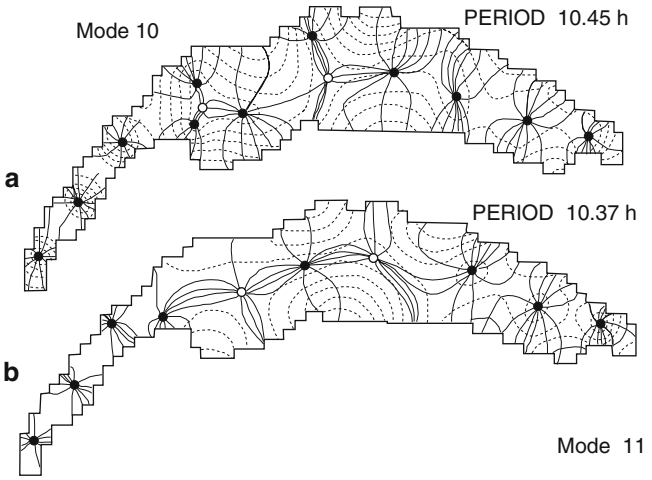

Fig. 14.8 Amphidromic systems for the 10th and 11th internal seiche modes for Lake Geneva showing positive (negative) amphidromic points as *full* (*open*) *circles*. Co-range lines are only shown where they are 20% or more of the maximum amplitude in the entire lake. Co-phase lines are plotted as zero displacement lines in (1/8)th of the full period. (**a**) mode 10 with period 10.45 h, (**b**) mode 11 with period 10.37 h. From Bäuerle [3]. © Springer, Berlin, reproduced with permission

by full and open circles for the amphidromic point, respectively). If the counting is in the direction of decreasing frequency in Table 14.3, the 10th mode has 12 amphidromic systems, ten positive and two negative ones, suggesting ten modes with Kelvin-type and two with Poincaré-type behaviour, respectively. The 11th mode has eight positive and two negative amphidromic systems but with smaller period than mode 10, see Fig. 14.8. These findings show that for mixed behaviour a particular mode can be detailed as (1) Kelvin-type where the velocity vectors rotate in the counter-clockwise direction and (2) Poincaré-type when this rotation is clockwise, and transverse velocities take appreciable values (often simply identified with transverse oscillations).

14.3.5 Modal Analysis for the TCDM

Lemmin et al. [32] determined the eigenfrequencies and eigenmodes of the systems (14.5) and (14.6) for the summer and autumn episodes in 1950, as defined earlier. These modes are characterized by the layer parameters listed in Table 14.3. In direct numerical simulations for conditions of the summer episode and a wind pulse of 18 h duration and 5 ms^{-1} strength from the Northeast and tapering off from the centre of the lake toward the Eastern end, the computations show that only modes

Table 14.4 Model parameters for the TCDM for the thermal stratification during the two measuring periods of the SFE in 1950 and the inferred modal periods for the modes H1, H3, and H12 for Lake Geneva

	Summer episode (4 June–24 August)	Autumn episode (28 August–30 November)
Epilimnion depth H_1 (m)	15	25
Hypolimnion mean depth H_2 (m)	175	165
Epilimnion temperature (°C)	19	8
Hypolimnion temperature (°C)	5.5	5.5
Mode H1 period (h)	81.5	130
Mode H3 period (h)	33.3	∼50
Mode H12 period (h)	10.7	13.5

H1, H3 and H12 have amplitudes that reach over 60% of the initial thermocline excursion in significant parts of the near shore area. This is why only these modes are subsequently discussed (see Table 14.4).

14.3.6 Internal Wave Dynamics Revealed by Surface Level Data

Lemmin et al. [32], investigated the wave-like response by plotting the pattern of the SFE-surface excursions around the basin during a typical forcing event. Figure 14.9 is a copy from their paper, and Fig. 14.10 displays the spectra of the SFE water fluctuations at stations (2) and (7) during the summer interval, from 4 June to 24 August 1950. It shows in the lower right corner of Fig. 14.9 a 5-day wind episode from Southwest growing during the first 2 days in a roughly linear fashion and then abruptly falling to negligible strength (note the logarithmic scale of the ordinate) in slightly more than half a day. When looking at the corresponding episodes of the filtered time series of the surface elevations at the limnigraph stations (1)–(11) around the lake, it is seen that, as soon as the strong wind from the Southwest sets in, the whole lake responds by a depression at the West end (stations 1, 11, and 2) and a rise at the East end (stations 4–6). The response to the rapid secession of the wind is considerably slower in the surface-elevation-time series; it takes place during 1.5–2 days, as is clearly seen in the elevation plots of the limnigraphs 4–7, say. The peak at 5 and the subsequent fall to nearly zero occurs at the beginning of day 3 and lasts beyond mid-day of the fourth day. This peak arises at stations 6 through 11 and consecutively continues to stations 1 and 2, marking a typical cyclonic motion around the basin, which is reminiscent of Kelvin-type behaviour. The amplitudes of the peaks decay consistently, but the widths of the shoulders of the peaks remain approximately the same.

Lemmin et al. further writes: ‘Spectral analysis revealed that independent of season and station location only certain modes were excited. The most prominent is the first, H1-mode, Fig. 14.11a. Its period is near 81.5 h in summer, increasing to

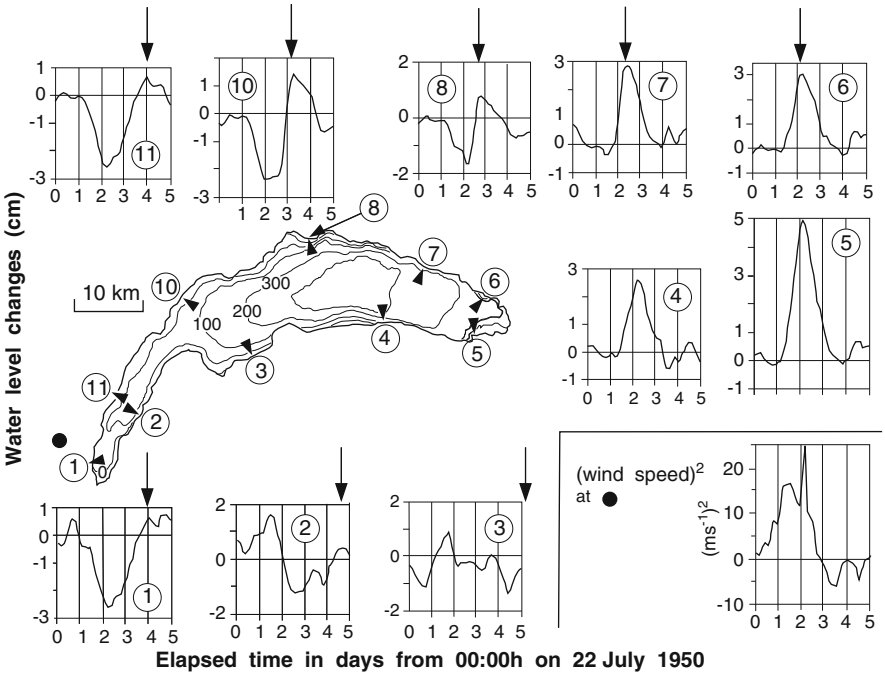

Fig. 14.9 Response of the water level around lake Geneva to an episode of southwest wind starting at 0000 h on 22 July 1950. Wind is shown (at *bottom right*) as speed squared of the component directed 40° East of North, which peaked at 5 ms^{-1} (18 $km\,h^{-1}$) 2 days and 6 h from the start. *Arrows* show the time of arrival of the peaks of the wind at the various stations. From Lemmin et al. [32]. Copyright 2000 by the American Society of Limnology and Oceanography, Inc, reproduced with permission

above 130 h in fall, as the density structure of the water column changes and c_i decreases. Spectra from the narrow Western end of the lake always showed the H1 mode response most clearly. A weak second mode (H2) signal could be detected in the spectra of some stations in the central part of the lake (stations 3 and 8), but not at other stations. The H3 mode, with periods of 33.3 h and near 50 h during summer and fall, respectively, was found at all stations around the lake, Fig. 14.11. A weak mode H4 seiche was found in some summer spectra but not those for the fall. Modes H5–H9 were not observed in any spectra. Mode H10 is interpreted as the first cross or transverse mode with summer and fall periods of 10.7 and 13.5 h, respectively. Modes H11 and H12, which are also transverse mode waves, are very close to the H10 period and cannot be distinguished in the spectra. [...] it is [also] found that the H1-mode occurs the most often [...]. Modes higher than H12 cannot be detected with certainty because of the cut-off imposed by the SFE filter'.

Cross spectral analysis of the free surface time series at stations 2 and 7 was performed, and energy, coherence and phase angle spectra are shown in Fig. 14.10. For mode H1 the amplitude is more than 20% larger near station 2 than near station

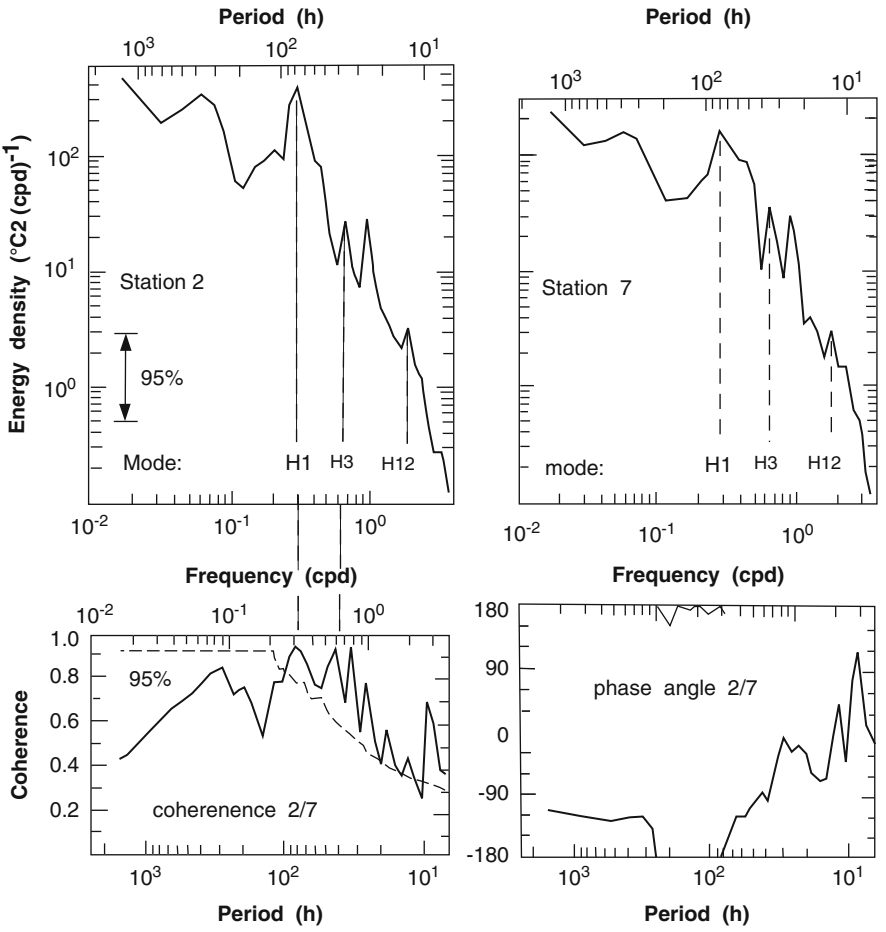

Fig. 14.10 *Top*: Lake Geneva spectra of SFE water-level fluctuations at stations 2 and 7 during the summer interval 4 June–24August 1950. *Bottom*: coherence and phase angle between stations 2 and 7. From Lemmin et al. [32]. Copyright 2000 by the American Society of Limnology and Oceanography, Inc, reproduced with permission

7, which is also visible in the energy spectral peaks in the top panels of the figure. Cross spectral analyses were also performed for all station pairs, and coherence was in most cases found to be well above the 95% confidence limit. The top panel in Fig. 14.11 displays for the indicated stations the coherences and phase angles as inferred from these cross spectral analyses relative to station 2 as a basis. 'Coherence is high for most station pairs, decreasing from West to East along the Southern shore. For the stations along the Northern shore coherence increased again from East to West and became high for the stations in the narrow West basin. The phase angles calculated from the data can be compared with those predicted by the numerical model, as indicated by the co-range lines. Along the South shore, satisfactory

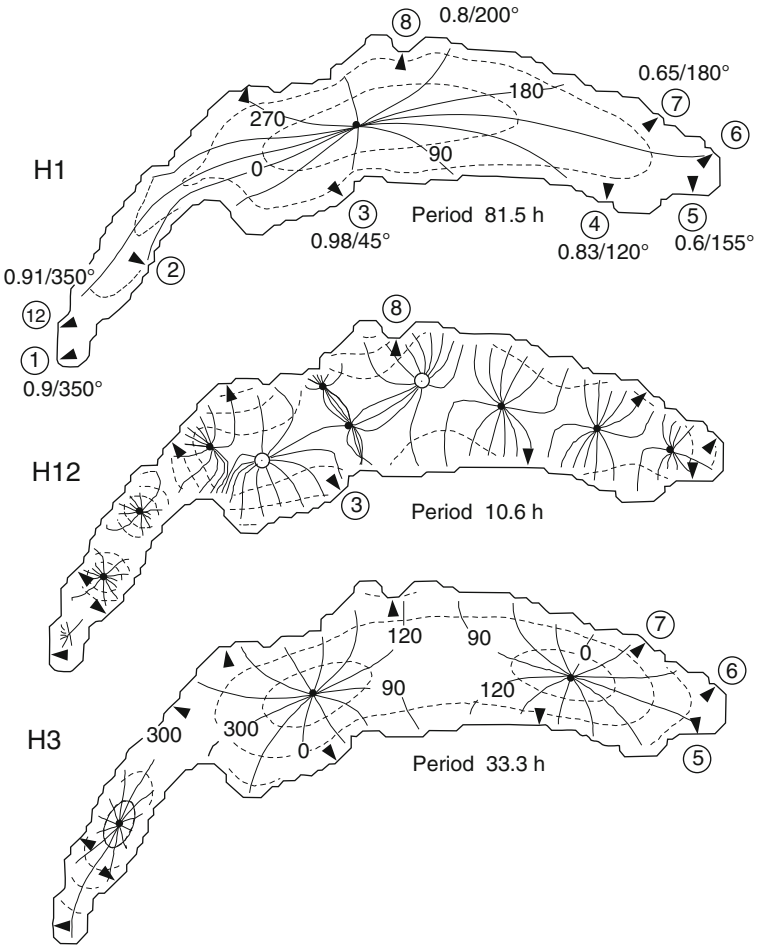

Fig. 14.11 Amphidromic structure and seiche periods for three different seiche modes for lake Geneva, predicted by the model. Results are presented as *co-range lines* (*dashed*) in 20% steps of the maximum and *co-phase* (co-tidal) *lines* in 30° increments. Some phase angles are written on the co-phase lines in order to indicate the sense of the rotation and the relation between the cells. Seiche periods relate to the summer situation. *Top*: H1 mode. At each station, phase and coherence relative to station 2 obtained from the SFE data are also indicated; for details see text. *Centre*: H12 mode, *Bottom*: H3 mode. From Lemmin et al. [32]. Copyright 2000 by the American Society of Limnology and Oceanography, Inc, reproduced with permission

agreement in phase angle is found. Agreement is less satisfactory on the Northern shore, in particular, at the entrance to the West basin at stations 10 and 11, even though coherence is high. At the West end of the lake, agreement improved again. The cyclonic progression of this seiche is clearly established' [32].

Lemmin et al. [32] provide also other evidence supporting the Kelvin-type behaviour of the H1-mode. These involve temperature measurements from

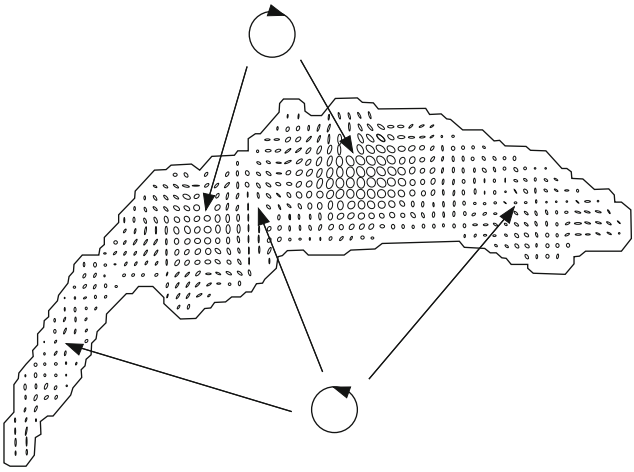

Fig. 14.12 Current pattern (particle trajectories) for the H12 seiche mode for lake Geneva, calculated with the numerical model for the bottom layer. The orientation of the particle rotations in the different regions of the lake is indicated. From Lemmin et al. [32]. Copyright 2000 by the American Society of Limnology and Oceanography, Inc, reproduced with permission

December 1982 to January 1983 campaign with thermistor chains moored at A1, A3 and G (Fig. 14.4). In view of the weak stratification, these measurements allow disclosure of a relatively long period of 136 h of the fundamental H1-mode. Moreover, the authors also provide hints that the Petit Lac is not participating in the H1-motion, so that this Kelvin-type seiche is confined to the Grand Lac, only.

For the H12 mode, sufficiently large coherences are only found in time series of station pairs that are part of the same amphidromic cell. The current pattern for this mode, integrated over one wave cycle, is presented in Fig. 14.12. It shows the closed trajectories of particles at grid positions which are traversed cyclonically (counter-clockwise on the N.H.) and anti-cyclonically (clockwise on the N.H.), as indicated in the figure. The current ellipses are 'fat' in the interior of the central basin and become increasingly elongated towards the shores and to the far West and East ends of the lake.

The two regions with clockwise rotating particles in the central part of the lake are reminiscent of Poincaré-type behaviour. This interpretation is supported by current records taken during summer 2001 at station P (Fig. 14.4) at 304 m depth, 5 m above the lake bottom, using an Aanderaa RCM9 current meter. The station is located in the centre of the central clockwise rotating cell (Fig. 14.4). Spectra of the North and East current components show at the H12-frequency a relatively sharp peak with the energy of the two components being nearly equal, at very high coherence and 45° phase difference. Moreover, progressive vector diagrams derived from the data also show the clockwise looping pattern characteristic for Poincaré waves (not shown here) and results from numerical simulations using the same wind

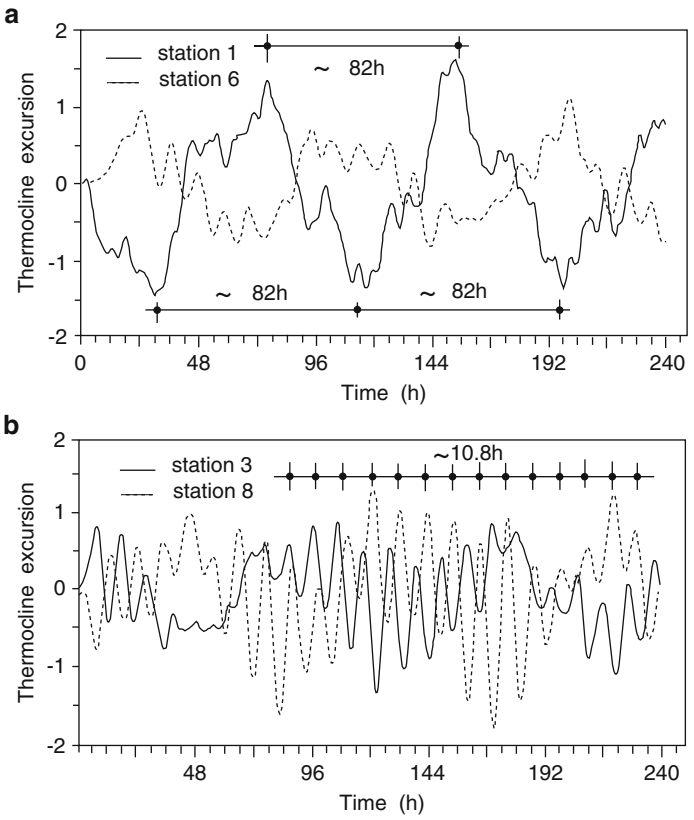

Fig. 14.13 Time series of thermocline excursions resulting from a numerical simulation for lake Geneva as detailed in the main text, (**a**) for the stations 1 and 6 and (**b**) for the stations 3 and 8. Period fitting by eye yields 82 and 10.8 h, for the H1 and H12 modes, respectively. From Lemmin et al. [32], with changes. Copyright 2000 by the American Society of Limnology and Oceanography, Inc, reproduced with permission

field which produced clear H1-signals at stations 1 and 6 generate a combination of H1 and H12 signals at stations 3 and 8, Fig. 14.13. All these facts make the interpretation as a Poincaré-type mode for H12 very likely.

Lemmin et al. [32] also give evidence of the H3-mode behaviour by performing a cross spectral analysis for the SFE surface elevations of the station pairs 6/5 and 6/7. In the Eastern part of the basin, these stations fall into the same amphidromic cell of the H3-mode (Fig. 14.11). The cyclonic progression is revealed by the phase angles of stations 5 and 7 with respect to the central station 6. The phase angle spectra (not shown here) indicate a cyclonic phase propagation and thus support the interpretation of the H3-mode as a Kelvin-type wave mode.

14.4 Transverse Internal Wave Motion in Lake Überlingen

14.4.1 Statement of the Problem

In the following we report on Poincaré-type basin-wide transverse baroclinic oscillations in a small lake of only a few kilometers width, analyzed by Bäuerle [4] from data taken in 1972 by Hollan [20] in a synoptic field campaign of Lake Constance. The paper is interesting, because it is didactically well posed and demonstrates that effects of the rotation of the Earth are of physical relevance even in basins of fairly small size.

Lake Überlingen is the Western most arm of the Upper Lake Constance, Fig. 14.14; it is approximately 17 km long and 2.5 km wide and, because of the hilly surroundings on either side of its long shore line, it is a deep channel-like basin, open at its East end to the proper Upper Lake Constance, with a maximum depth of 147 m at position S_1 in Fig. 14.14 and a mean depth of 80 m. Close to the Eastern end, but still to the West of the Island Mainau, because of the subsurface sill there, it is hydrodynamically partly separated from the remaining Upper Lake Constance. The common summer stratification consists of a light and warm epilimnion and a heavy cold hypolimnion with a relatively thin metalimnion. It can be approximated by a two layered structure with a sharp interface at the thermocline as shown in Fig. 14.15 for the episode from 1 to 7 October 1972.

Since the intensive measuring campaign in 1972, Lake Constance has been the subject of extensive studies of physical limnology.[7] Here, we report on relatively high-frequency transverse baroclinic oscillations of Lake Überlingen. In particular, it will be shown that the lowest transverse (uni-nodal) baroclinic mode response at a mid-basin position exhibits Poincaré-type structure and can be properly reproduced by a two-layered linear model.

14.4.2 Observations During the Bodensee-Experiment 1972[8]

Internal waves in Lake Überlingen occur relatively frequently, are generated also by moderate winds, which prevail from Northwest, and persist (with decaying amplitudes) for several days beyond the onsetting wind event. An example of transverse

[7] Hollan and Simons (1978) [23], Hamblin and Hollan (1978) [19], Hollan, Rao and Bäuerle (1980) [24], Bäuerle (1981), [2], Serruya, Hollan and Bitsch (1984), [58], Stewart and Hollan (1984) [63], Appt, Imberger and Kobus (2004) [1].

[8] 'Bodensee' is the German denotation of 'Lake Constance', see Fig. 14.14. It is divided into the 'obere Bodensee', the 'Upper Lake Constance', which constitutes the lake basin cutting off the 'Lower Lake Constance' basin at the town Constance where the River Rhine leaves the Upper Lake. The Upper Lake Constance is additionally divided into the true 'Upper Lake Constance' and 'Lake Überlingen'.

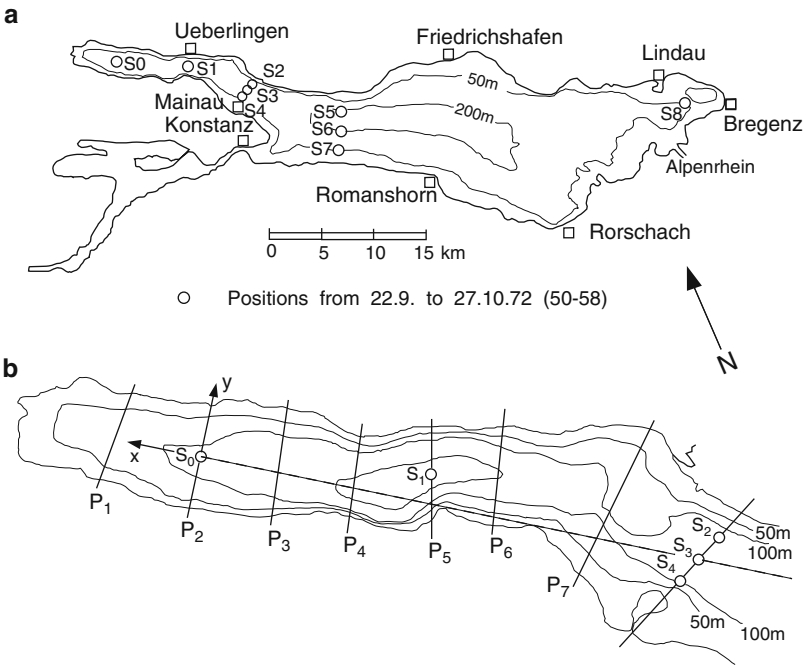

Fig. 14.14 (**a**) Bathymetry and topographic map of Lake Constance indicating the mooring sites S_0 through S_8 at which current meters and thermistor chains were installed from 22 September to 27 October 1972, see [20]. (**b**) Bathymetric chart of lake Überlingen, showing 50 m contour lines and stations $S_0 - S_4$, where current meters and thermistor chains were moored. Shown is also the (x, y) coordinate system, defining the along-channel and the transverse directions of the basin and the positive directions of the u- and v-velocity components of the horizontal velocity at S_0. From Bäuerle [4]. © Aquatic Sciences, reproduced with permission

oscillations is shown in Fig. 14.16, where the across-basin components of the horizontal velocity vector at station S_0 in 6-m depth (panel (a)) and at station S_1 in 5.5-m depth (panel (b)) are shown for a 7-day episode in early October 1972. Little imagination is needed to see that in the S_0 time series a 4-h period can be identified, whilst this is not possible in the S_1 time series. These, and subsequent data are taken from the data band of the Bodensee-Experiment 1972, [20]; it follows from scrutiny of these data that the time series of Fig. 14.16 reflect a composition of direct wind forcing, free transverse oscillations and other, less significant, processes. To isolate the free oscillations, the time-series were low-pass filtered. Figure 14.17 shows such filtered time-series of the u- (dashed) and v- (solid) components of the horizontal velocity vector at 6 m depth in S_0; the 4 h period is evident, as is the highly rotary behaviour of the current vector, since the transverse and longitudinal components are of similar scale, and have a persistent phase shift of approximately a quarter period: Maxima and minima of the longitudinal components arrive approximately a quarter period earlier than those of the transverse component, which is indicative

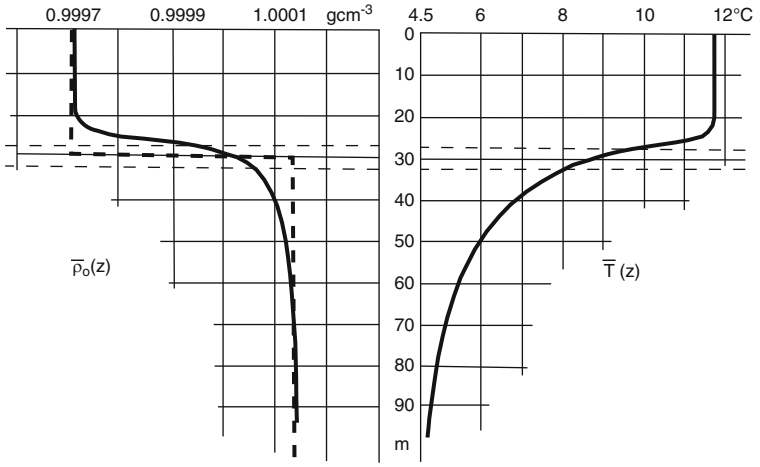

Fig. 14.15 Lake Constance vertical profile of the mean temperature $\bar{T}(z)$ (*right*) and mean density $\bar{\rho}(z)$ (*left*) plotted against depth. The two-layer approximation (*dashed*) is also shown with the interface at 8.5°C and the layer densities $\rho_1 = 0.9997\,\mathrm{g\,cm^{-3}}$ and $\rho_2 = 1.00013\,\mathrm{g\,cm^{-3}}$. From Bäuerle [4]. © Aquatic Sciences, reproduced with permission

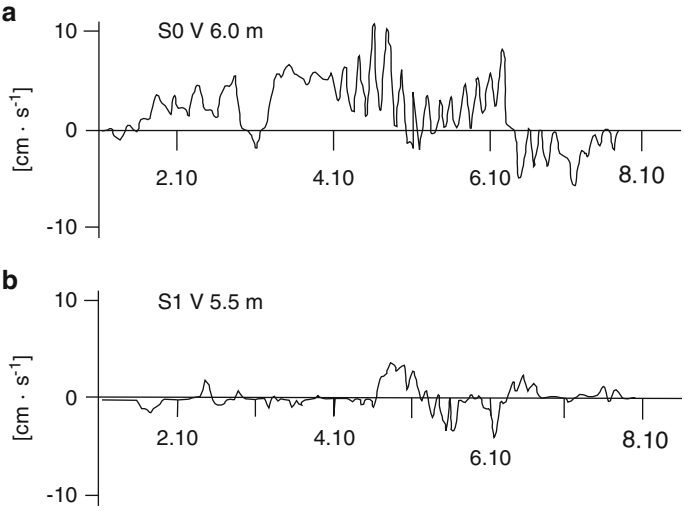

Fig. 14.16 Unfiltered time series of the transverse velocity component v (in $\mathrm{cm\,s^{-1}}$) in Lake Überlingen at S_0 in 6-m depth (panel (**a**)) and at S_1 in 5.5-m depth (panel (**b**)), respectively, plotted against time from 1 to 7 October 1972. (From Hollan [20])

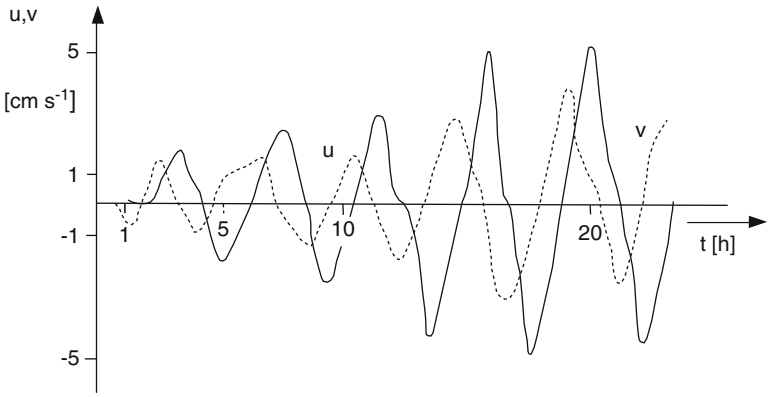

Fig. 14.17 Low-passed filtered longitudinal (*dashed*) and transverse (*solid*) components of the current in lake Überlingen at S_0 in 6 m depth in cm s^{-1}, plotted against time (in h) for an event starting on 4 October 00:00 h MET. (From Hollan [20])

of a clockwise rotation of the horizontal velocity vector. This is very convincingly shown in Fig. 14.18.

14.4.3 Numerical Solution for the TVD Model with Realistic Bottom Topography

The two-layer equations which must be solved for the two-layer variable depth model are stated as (14.1)–(14.6), and they are applied here for

$$f = 1.07 \times 10^{-4} (\mathrm{s}^{-1}), \quad H_1 = 30\,(\mathrm{m}), \quad \varepsilon = 5 \times 10^{-4},$$
$$\rho_1 = 0.999608\,(\mathrm{g\,cm}^{-3}), \quad \rho_2 = 1.000138\,(\mathrm{g\,cm}^{-3}).$$

For the numerical solution the correct approach would be to solve the eigenvalue problem (14.5) for the entire Upper Lake Constances; however, because a fine grid resolution of $50 \times 50\,\mathrm{m}^2$ is needed in Lake Überlingen, this would for the Upper Lake Constance lead to a very large matrix eigenvalue problem, too large to solve it adequately with common PCs. Variable mesh size with small meshes in Lake Überlingen and large meshes in the large basin of Upper Lake Constance would be ideal, but the corresponding software was not available. The alternative, employed by Bäuerle, was to assume that there is likely no or at most a small mass exchange between Lake Überlingen and the large basin of Upper Lake Constance. This conjecture is likely close to reality, because the relatively high frequency response of Lake Überlingen is hardly influenced by the motion of the water masses in the proper Upper Lake Constance. This conjecture is further supported by the very topography of Lake Überlingen. The sill West of the Island Mainau and the island

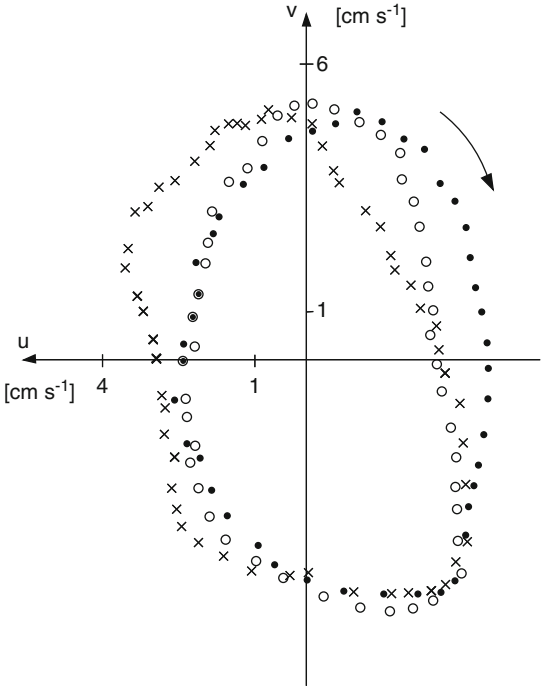

Fig. 14.18 Hodograph of the horizontal current shown in Fig. 14.17. The horizontal velocity is plotted during three periods. Symbols •, ×, ∘ mark the first, second, and third period in succession. The *arrow* indicates progression in time. From Bäuerle [4]. © Aquatic Sciences, reproduced with permission

itself form a natural barrier to the water masses entering the lake from the East. Bäuerle also hastens to note 'that this argument does not apply, if we were to study the longitudinal oscillations of the lake'.

A critical point of this procedure is the choice of the location of the boundary section at the entrance to Lake Überlingen at its Eastern end. Two artificial boundaries were introduced (see Fig. 14.19, cross sections marked A and B) at which the no-through-flow condition was applied. To the West of these transects the lake geometry was discretized by the $50 \times 50\,\mathrm{m}^2$ grid shown in Fig. 14.19a, and the computational domain was bounded by the thermocline depth of 30 m. It is obvious that this domain is somewhat smaller than the lake domain, a fact which will make the periods somewhat smaller than in reality. The application of the no-flow-through condition at the cross sections A or B will influence the solution in the interior of Lake Überlingen, however, it will be seen that the wave pattern in the vicinity of station S_0 is stable (or robust) against the two versions of the no-flow-through boundaries. This is indication, if not corroboration, that the restriction of the numerical solution of the transverse eigenmode to the region of Lake Überlingen yields robust results.

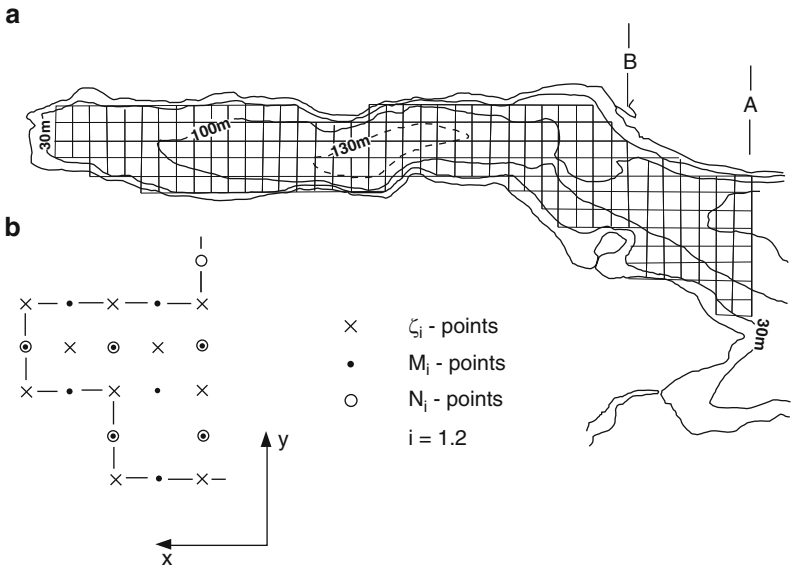

Fig. 14.19 (**a**) Bathymetry of Lake Überlingen overlain by a 50 m square grid as a basis of the two-layer model. The grid is so selected that each grid midpoint has a depth greater than 30 m. Cross sections A and B mark two possible entrance transects at which the no-flow-through boundary condition applies. (**b**) Selected staggered grid for the finite difference approximation of (14.5). *Symbols* indicate where respective variables are computed. Along the boundaries the normal transport is set to zero. Coriolis terms are incorporated into the scheme without averaging. From Bäuerle [4]. © Aquatic Sciences, reproduced with permission

Bäuerle confined attention to the mode with a period closest to 4 h. For the regions with no-flow-through boundary condition at transects A and B, the periods are $T = 3.931$ h and $T = 3.952$ h, respectively. For transects A and B, Fig. 14.20 shows the vertical interface displacements for the two selected boundaries. Panel (b) displays the interface displacement distributions at three different times through half the period T ($t = 0, t = T/4, t = T/2$). 'Elevation highs are shown as solid lines and instantaneous nodal lines are shown dashed-dotted. Horizontal velocities are directed along the orthogonal trajectories of these lines and point in the lower layer from highs to lows. As can be clearly seen from Fig. 14.20a, b the different discretizations with a mass transport cut-off at A and B, respectively, affect the true mode structure at the Eastern end of the lake, but hardly in its Western half, where the interface displacements are very similar. At position S_0 it is also clearly seen that the horizontal velocity vector does indeed rotate in the clockwise direction, a feature that is reminiscent of typical Poincaré-type behaviour.

An alternative way to demonstrate this behaviour is shown in Fig. 14.21 which displays the particle trajectories through one revolution. These trajectories are elongated ellipses. The longer and thinner the ellipses are, the more linearly polarized are the corresponding harmonic waves and the less significant is the effect of the

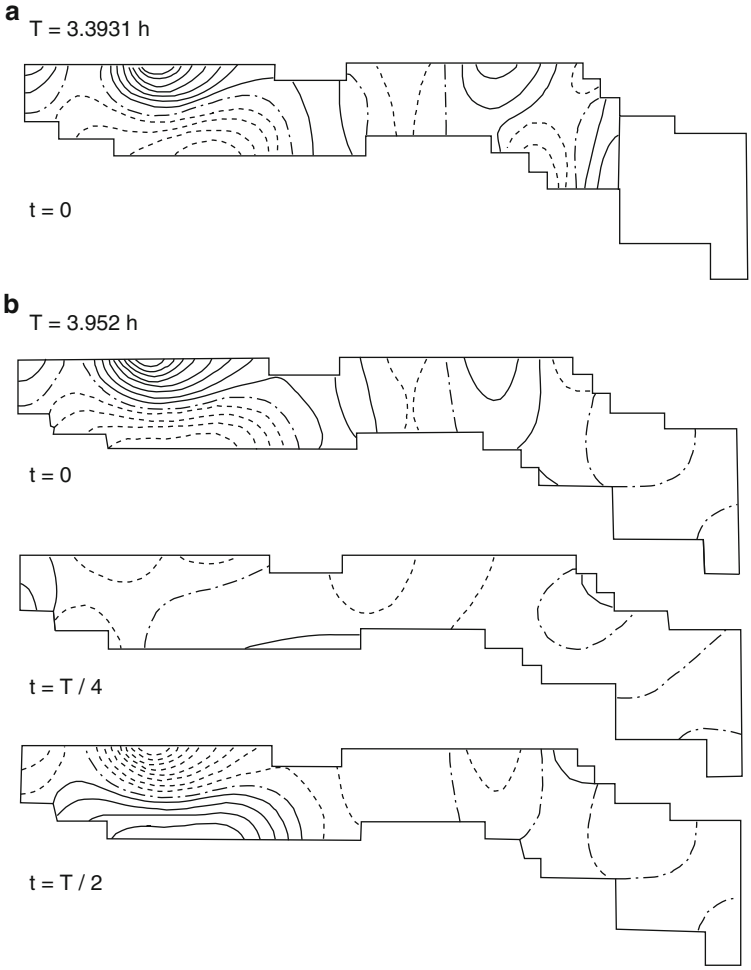

Fig. 14.20 Vertical interface displacement of the first internal transverse mode in Lake Überlingen, plotted in (**a**) for a basin, sealed at transect B, for the moment of maximum amplitude and in (**b**) at transect A for one half period in quarter period steps. *Dashed lines* indicate down-welling, *solid lines* up-welling. *Dashed-dotted lines* show zero-displacement curves. The *periods* are as shown in the insets. From Bäuerle [4]. © Aquatic Sciences, reproduced with permission

rotation of the Earth. In Fig. 14.21, 'these elliptical trajectories [...] show that in this mode at S_0 rotational effects are clearly present and not negligible. This was already seen in Fig. 14.18 and inferred there from observations. Comparison of Figs. 14.20 and 14.21 also makes clear that the 4 h signal of first transverse baroclinic oscillation could only have been observed at station S_0, but not [. . .] at the other stations S_1 to S_4. The Poincaré character of the mode response is an indication that in more detailed studies of the baroclinic processes in Lake Überlingen, the effects of the rotation of the Earth should not be ignored', from Bäuerle (1994) [4].

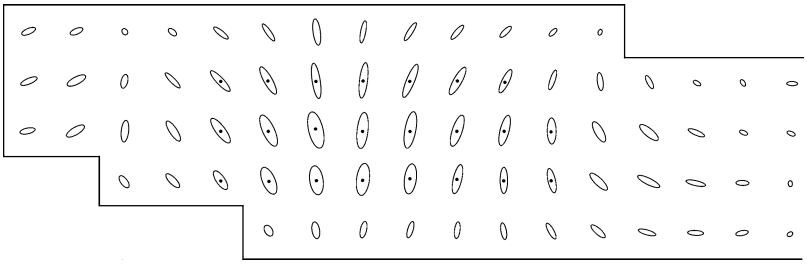

Fig. 14.21 Calculated elliptical fluid particle trajectories for the first internal transverse mode ($T = 3.95$ h) in the western part of Lake Überlingen. The current vectors in the region close to station S_0 are rotating in the clockwise direction, see also Fig. 14.18, from Bäuerle [4]. © Aquatic Sciences, reproduced with permission

14.5 Lake Biwa

Lake Biwa is the largest lake in Japan and is located on the main island of Honshu immediately adjacent to the city of Kyoto. It consists of two basins, the North Basin is approximately 55 km long, 17 km wide and more than 90 m deep, see Fig. 14.22. This basin is connected to the much smaller South Basin, which can be regarded as being dynamically essentially disconnected from the North Basin. Here, we shall only be concerned with the North Basin. Shimizu et al. [60] studied the horizontal structure and excitation of primary motions in the strongly stratified North Basin of this lake. They used field data collected in 1993 and 1994 for wind speed and direction, temperature profile and velocity structure in the summer water of this basin. The description of the data, which were collected, is given by Saggio and Imberger [55]. For the purposes of this section the temperature profiles measured by a thermistor chain at BN 50 during BYTEX93 and as part of biweekly routine measurements at Sta. 17B in 1994 are important. The thermistor chains had 20 thermistors spaced every 1 m in the metalimnion, extending up to 5 m apart near the surface and the bottom (see [55] for details). Vertical profiles of water velocity were measured by a shipboard acoustic Doppler current profiler (ADCP) on a monthly basis in 1994 along 11 transects in a W–E direction covering the whole North Basin (see [31]).

Shimizu et al. [60, 61] employed a modal analysis, which is based on the linearized shallow water equations for a layer-stratified system using the Boussinesq and hydrostatic approximations as is presented in Sect. 14.3.3 and is based on the previous analyses of e.g. Monismith [34] and Lemmin et al. [32]. The authors write the equations in complex notation such that the stiffness matrix of the forced linear equation is Hermitean[9] and thus, allow a modal decomposition of the inhomogeneous wind driven motion. We shall, here, primarily present results of the eigenvalue

[9] In this method they are following the procedure already employed earlier by Proudman [51] and Platzman [45].

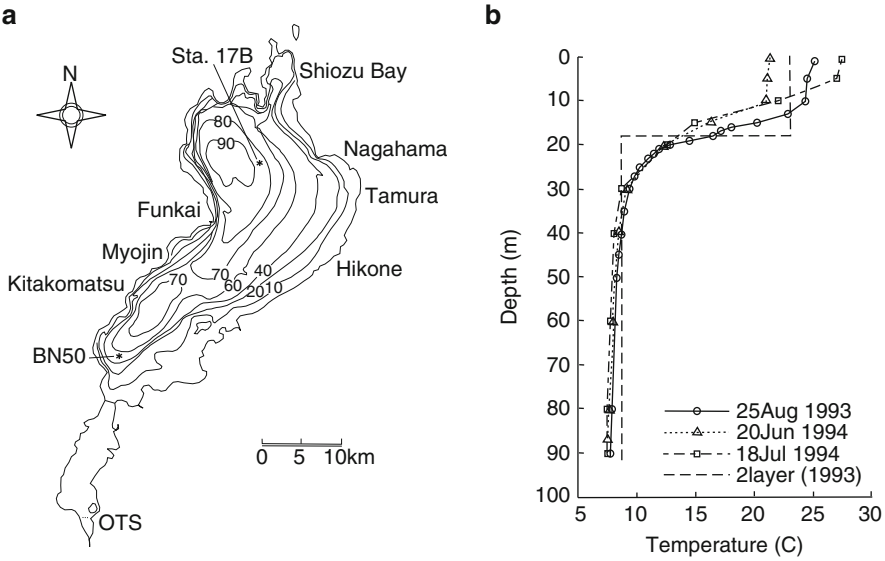

Fig. 14.22 (**a**) Lake Biwa (35°N, 136°E) bathymetry with 10 m isobaths and locations of relevant measurement stations. Thermistor chains were deployed near station BN50 during 1992. (**b**) Temperature profiles used for the modal analysis. The profiles in 1993 and 1994 were measured at BN50 and Station 17B. For the modal analysis with two-layer stratification, the depth of the interface was set at 18 m; figures composed from figures in Saggio and Imberger [55] and Shimizu et al. [60], with changes. © 2000 by the American Society of Limnology and Oceanography, Inc, reproduced with permission

problem as proposed by Shimizu et al., which is not solved as described by Bäuerle in Sect. 14.3.3, but by a slightly different procedure which is equivalent to it.

Its numerical solution for the irregularly shaped Lake Biwa was constructed using the finite difference method. A rectangular grid with horizontal spacing of approximately $460\,\mathrm{m} \times 570\,\mathrm{m}$ was used, in which surface and interface displacements are defined in the middle of each grid, and velocity components are defined on each face in the direction of the velocity, known as Arakawa C-grid, see Volume 3. The Coriolis force term was discretized with the method as suggested by Platzman [45] to keep the discretized stiffness operator Hermitean; this is important in order to retain the orthogonality and completeness of the modes in the discrete space. The thermocline depth of the two-layer model was set to 18 m and $\rho_2 - \rho_1 = 2.27\,\mathrm{kg\,m^{-3}}$. This is suggested by the measurements, see Fig. 14.22b. The phase of all waves was arbitrarily set to zero when the total volume transport of water in the upper layer was from North to South. In the numerical solution procedure, the shallow regions of the two-layer model with only one layer are included in the discretized model with application of the adequate flux condition along the 'thermocline shore' as previously suggested and applied by Salvadè et al. [56] (compare also Chap. 5, Sect. 5.6). Thus, this numerical model corresponds to the class

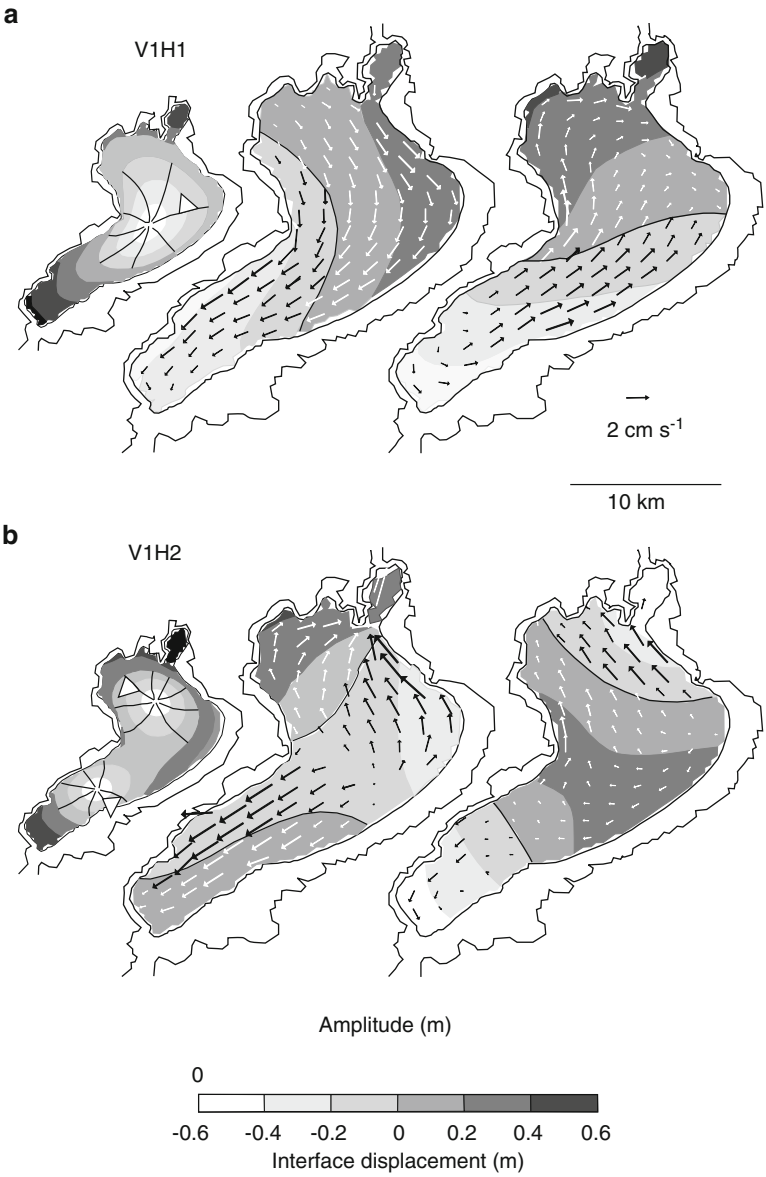

Fig. 14.23 Internal waves in Lake Biwa. (**a**) V1H1, (**b**) V1H2 (**c**) V1H4, (**d**) V1H6. The *middle graphs* in each panel correspond to the phase when the rates of energy input from spatially uniform winds are largest, and the *right graphs* correspond of a quarter period after the *left*. *Shading* and vectors show the interface displacement and the average velocity in the upper layer, respectively. In the smaller *left graphs*, *shading* and *lines*, respectively, show co-range contours and co-phase lines of wave trough with 45° interval. The *co-phase lines* with *white triangles* correspond to the phase shown in the *middle graph*, and the *triangles* show the direction of rotation. From Shimizu et al. [60], with changes.

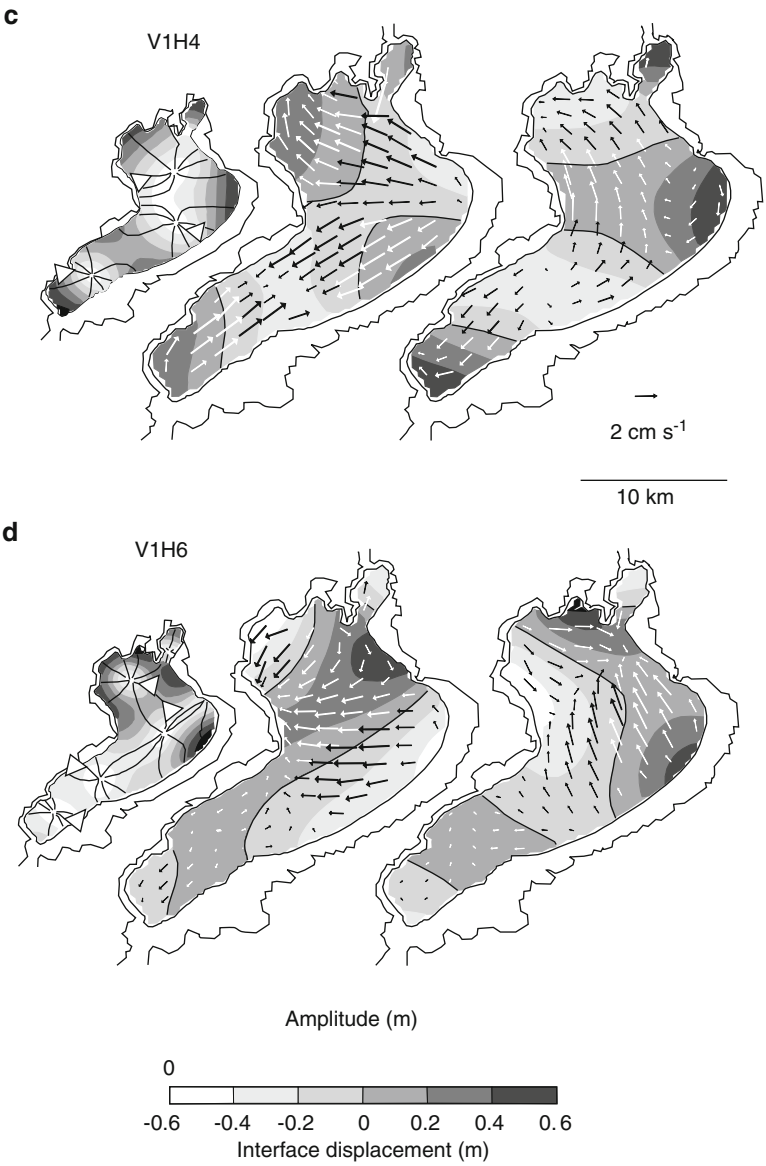

Fig. 14.23 (**Continued**)

TVDMC, the 'Two-layer Variable Depth Models – Complete' in the terminology of Mortimer (see footnote 1 to this chapter).

The ensuing discussion follows Shimizu et al. [60]. As elsewhere in this book, modes are characterized by the acronym VmHn, where Vm identifies the vertical mode with mode number m, whilst Hn identifies the horizontal mode with number n. Here, since only a two-layer model was employed, comparison with observed modes can only be made for V1Hm. Moreover, a wave mode or amphidrome will be called Kelvin-type, if the phase of the interface displacement rotates cyclonically (counter clockwise on the N.H.). On the other hand, if the rotation of the interface displacement is clockwise, the corresponding mode will be called Poincaré-type.

Figures 14.23a–d collect excerpts of results obtained from the numerical solution of the eigenvalue problem. Each panel consists of three graphs: the small ones show the co-range contours in grey shading with light grey showing small interface displacement amplitudes and co-phase lines as dark solid lines in 45° intervals. The white triangular arrow at one of these co-phase lines indicates the direction of rotation around the amphidromic point. The middle graphs correspond to the phase when the rates of wind energy input from spatially uniform wind are the largest, whilst the right panels correspond to a quarter period after the left. Grey shadings in these larger graphs mimic snapshots of the interface displacements, and arrows show corresponding snapshots of the average epilimnion currents.

Shimizu et al. [60] write: 'The vertical mode 1, horizontal mode 1 (hereafter $V1H1$) internal wave was a Kelvin[-type] wave that rotated cyclonically around the basin, the largest interface displacement occurred at the Northern and Southern ends, and the water velocity was nearly parallel to the thalweg (Fig. 14.23a). The V1H2 and V1H4 internal waves, respectively, had two and three cells where the crests and troughs of the interface rotated cyclonically. The particle orbits were nearly parallel to the thalweg except [in] the middle of the basin in V1H4, where the velocity vectors appeared to rotate anti-cyclonically (Fig. 14.23b,c); note the velocity vectors of a cyclonic wave of higher horizontal mode direction [...]. In V1H2, [the] resonance in Shiozu Bay made the interface displacement in the bay larger than in the main part of the lake. V1H3 had a similar structure to V1H2, except that the phase was opposite in [the] Shiozu bay (not shown). V1H6 was the lowest mode with an anti-cyclonic cell located in the middle of the North Basin (Fig. 14.23d). Field data have shown an anti-cyclonic rotation of the current vectors in the middle of the North Basin with period of 11 h in summer [15], confirming existence of this mode. Overall, the frequencies and horizontal structure of these modes matched well with previous studies (see Table 14.5)'.

14.6 Concluding Discussion

In this chapter, the focus has been to collect some convincing evidence that wind generated, but otherwise free gravity oscillations in lakes may be affected by the rotation of the Earth.

Table 14.5 Some characteristics of the internal [IW] and surface [SW] waves in lake Biwa. These waves are numbered in decreasing order of their natural periods. Abbreviations: Hm, horizontal mode; CC, cyclonic cell; AC, anti-cyclonic cell; NL, nodal line; NB, north basin; N, north; S, south; M, middle. (Excerpt of Table 1 from Shimizu et al. [60])

Class	Hm	Period[a] (Shimizu et al. [60])	Period[a] (other study)	Horizontal structure[b]
IW	1	42.1 h	45 h[c], 46 h[d]	Kelvin-type[a,e]
	2	23.9 h	23 h[d]	2 CCs[e], resonance in Shiozu Bay[f]
	3	18.6 h	–	2 CCs, resonance in Shiozu Bay[f]
	4	15.3 h	16 h[d]	3 CCs[e]
	5	11.9 h	12 h[d]	4 CCs
	6	10.5 h	11 h[g]	1 AC in N of NB and 3 CCs
	7	9.6 h	–	1 AC in N of NB and 5 CCs
	8	8.7 h	–	2 ACs in N of M and 2 CCs in S of NB
SW	1	220 min	270 min[e]	1 NL in S and of NB[e]
	2	62.1 min	78 min[e]	2 NLs in M of NB and SB[e]

[a]Inertial period is 20.7 h.
[b]References in the last column indicate report of similar structure.
[c]Kanari [30].
[d]Saggio and Imberger [55].
[e]Kanari [29].
[f]Okamoto and Endoh [43].
[g]Endoh et al. [15].

Homogeneous water bodies give rise to *barotropic* wave motions, in which the water in the entire water column moves unison, whilst in stratified waters *baroclinic* motions are manifested by a layering, in which the motion of the water in neighboring layers is essentially to-and-fro with largest amplitude signals at depths where the vertical density gradients are appreciable. In barotropic processes the most conspicuous signals of the water motion generally occur at the free surface as vertical surface elevation variations that can be measured by near-shore limnigraphs, arranged around the lake. From synoptically recorded elevation time series the progression of wave crests (or troughs) can be determined by the linearized, depth integrated, Boussinesq approximated shallow water equations, which, apart from the mode periods, also define for each mode the amphidromic systems covering the lake. These have been shown here for Lake Michigan and display the distribution of the oscillation amplitude in terms of level lines with its maximum representing the (normed) value 100, and the zero value identifying the centre of the amphidrome. These co-range lines are complemented by the co-phase lines, which radiate from the amphidromic point like spikes and describe the phase progression, essentially how an elevation high (or low) moves around the amphidromic point. If such rotations are counter-clockwise (on the N.H.), then the corresponding amphidromic system exhibits so-called Kelvin-type structure with relatively large horizontal velocities close to shore and smaller ones in the interior; the horizontal

velocity is essentially parallel to the border. If the rotations are clockwise (on the N.H.), then the behaviour is Poincaré-like, with relatively large horizontal velocities in both directions, but with a quarter period phase shift between the two, such that a clockwise rotation of the horizontal velocity vector emerges. The 'particles' move in elliptical orbits with 'fat' ellipses in the interior and 'thin' ones close to shore and major semi-axes parallel to the shore. The results obtained by Mortimer and associates and described in Sect. 14.2 show the computed first few seiche modes fit the inferences from measurements reasonably well; at higher order modes eigenfrequencies or eigenperiods can still be rather well predicted, but corroboration of the computed mode structure via identifications of elevation amplitudes and phase differences of cross spectra of station-pair elevation time series is less accurate because data may be too scarce or the linearized equations too much simplified.

When the lake water is stratified, the dominant dynamics takes place in the interior of the lake. To identify the baroclinic basin-wide wave structure, several methods have been used. One model is to use time series of free surface elevations from limnigraphs placed at isolated points around the lake shore and to filter these time series such that rapid barotropic signals are eliminated and to subject the filtered time series to spectral analysis as done for the unfiltered time series for identification of the barotropic oscillations. Such synoptic information could be obtained for Lake Geneva from 12 limnigraph recorders placed around the Lake by the Swiss Service Féderale des Eaux in 1949/1950 and disclosed the basin-scale internal seiche structure, verifying the lowest few modes in stratified Lake Geneva by using two-layer depth models (TCDM; TVDM) by Lemmin et al. [32].

More effective than measuring surface elevations are synoptic deployments of judiciously distributed thermistor chains with (generally equally) spaced thermistors, which record at fixed positions the fluctuating temperature. These data can (and have been) transformed to variables which are reminiscent of time series of vertical displacements of the water masses, e.g. the variation of the pycnocline elevation. Temperature measurements are more popular and, indeed, they have been more often used to record baroclinic oscillations in lakes than any other method. It should, however, also be emphasized that velocity measurements from instruments, moored at fixed stations both near-shore and off-shore are and have been helpful in the identification of Kelvin- and Poincaré-type behaviour. Rotary spectra or progressive (velocity) vector diagrams may support a suspected Kelvin- or Poincaré-type mode behaviour on the basis of phase progression from mass spectra of station-pair elevation time series.

References

1. Appt, J., Imberger, J. and Kobus, H.: Basin-scale motion in stratified Upper Lake Constance. *Limnol Oceanogr.*, **49**(4), 919–933 (2004)
2. Bäuerle, E.: Die Eigenschwingungen abgeschlossener, zweigeschichteter Wasserbecken bei variabler Bodentopographie. *Bericht aus dem Institut für Meereskunde*, Christian Albrechts Universität (1981)

3. Bäuerle, E.: Internal free oscillations in the Lake of Geneva. *Annales Geophysicae*, **3**, 199–206 (1985)
4. Bäuerle, E.: Transverse baroclinic oscillations in Lake Überlingen. *Aquatic Sciences*, **56** (2), 145–149 (1994)
5. Bäuerle, E., Ollinger, D. and Ilmberger , J.: Some meteorological, and hydrodynamical asects of Upper Lake Constance. *Arch. Hydrobiol.. Spec. Issues Adv. Limnol.*, **53**, 31–83 (1998)
6. Bohle-Carbonell, M.: Currents in Lake Geneva. *Limnol. Ocenaogr.* **31**, 1255–1266 (1986)
7. Bohle-Carbonell, M. and van Senden, D.: On internal seiches and noisy current fields – Theoretcal concepts versus observations, p. 81–105. In : *Large Lakes*, Tilzer, M. and Seruya Eds., Springer Verlag, Berlin etc., (1990)
8. Caloi, P., Migani, M. and Pannocchia, G.: Ancora sulle onde interne del lagoi Bracciano e sui fenomeni ad esse collegati. *Annales Geophyica*, Roma, **14**, 345–355 (1961)
9. Comstock, C. B.: Tides at Milwaukee, Wisconsin and irregular oscillations in surface of Lake Michigan at Milwaukee. *Rpt. Secy. War to 42nd Congress*, Vol **2**. *Ann. Rtp. Survey Northern and Northwestern Lakes*, App. A, 9–14, App. B, 14–15, Washington, D.C (1872)
10. Chrystal, G.: Some results in the mathematical theory of seiches. *Proc. Roy. Soc. Edinburgh*, **25**, 328–337 (1904)
11. Chrystal, G.: On the hydrodynamical theory of seiches (with a biographical sketch). *Trans. Roy. Soc. Edinburgh*, **41**, 599, (1905)
12. De Duillier, Fatio J.-C.: Remarques sur l'histoire du Lac de Genève in Spon. *Histoire de Genève*, T. II, 463 (1730)
13. Defant, A. : Neue Methode zur Ermittlung der Eigenschwingungen (Seiches) von abgeschlossenen Wassermassen (Seen, Buchten u. s. w.). *Ann. Hydrogr.* (Berlin) **46**, 78–85 (1918)
14. Defant, F. : Theorie der Seiches des Michigansees und ihre Abwandlung durch Wirkung der Corioliskraft. *Arch. Meteorol. Geophys. Bioklimatol.* (Wien) **A6**, 218–241 (1953)
15. Endoh, S., Okumura, Y. and Okamoto, I.: Field Observations in the North Basin. In: *Physical Processes in a Large Lake: Lake Biwa, Japan*, Okuda, S., Imberger, J. and Kumagai, K, eds., American Geophysical Union, 15–29 (1995)
16. Forel, F. A.: *Le Léman : Monographie Limnologique*, three volumes, Rouge, Lausanne (1895)
17. Graf, W.H., Perrinjaquet, C., Bauer, S.W., Prost, J.P. and Girod, H.: Measuring on Lake Geneva. p 123–147. In *Hydrodynamics of Lakes*, Graf, W.H. and Mortimer, C.H., eds. Elsevier, Amsterdam (1979)
18. Graf, W.H. and Mortimer, C.H., (eds).: *Hydrodynamics of Lakes*. Elsevier, Amsterdam (1979)
19. Hamblin, P.F. and Hollan, E.: On the gravitational seiches of Lake Constance and their Generation. *Schweiz. Z. Hydrol.*, **40**, 119–154 (1978)
20. Hollan, E.: Wind-induced motions in Lake Constance. *Bericht der AWBR.* **6**, 111–187 (1974)
21. Hollan, E.: Hydrodynamische Modellrechnungen über die Eigenschwingungen des Bodensee-Obersees mit einer Deutung des Wasserwunders von Konstanz im Jahre 1549. *Schw. Verein. für Geschichte des Bodensees und Umgebung*, Heft 97, 157–192 (1979)
22. Hollan, E.: Die Eigenschwingungen des Bodensee-Obersees und eine Deutung des Wasserwunders von Konstanz' im Jahre 1549, *Deutsches gewässerkundliches Jahrbuch*, ISSN 0344-0788, Abflussjahr 1979 (1980)
23. Hollan, E. and Simons, T.J.: Wind induced changes of temperature and currents in Lake Constance. *Arch. Met. Geophys. Bioclim.*, Ser. A. **27**, 333-373 (1978)
24. Hollan, E., Rao, D.B. and Bäuerle, E.: Free surface oscillations in Lake Constance with an interpretation of the 'Wonder of the rising water at Konstnz' in 1549. *Arch Met. Geophys and Miokl*. **A 29** 301–325 (1980)
25. Hutter, K.: Strömungsdynamische Untersuchungen im Zürich- und im Luganersee. Ein Vergleich von Feldmessungen mit Resultaten theoretischer Modelle. *Schweiz. Z. Hydr.* **45**, 101-144 (1983)
26. Hutter, K.: Fundamental Equations and Approximations. In: *Hydrodynamics of Lakes. CISM Courses and Lectures, No.286*, Springer, New York, 1–76 (1984)
27. Hutter, K., Raggio, G., Bucher, C. and Salvadè, C.: The surface seiches of Lake of Zürich, *Schweiz. Z. Hydrol.*, **44**, 423–454 (1982)

28. Hutter, K., Raggio, G., Bucher, C., Salvadè, C. and Zamboni, F.: The surface seiches of Lake of Lugano, *Schweiz. Z. Hydrol.*, **44**, 455–484 (1982)
29. Kanari, S.: On the study of numerical experiments of two-layer Lake Biwa. *Jpn. J. Limnology*, **35**, 1–17 (1974)
30. Kanari, S.: The long-period internal waves in Lake Biwa. *Limnol. Oceanogr.*, **20**, 544–553 (1975)
31. Kumagai, M., Asada, Y and Nakano, S.: Gyres measured by ADCP in Lake Biwa. In: *Physical Processes in Lakes and Oceans* Ed. J. Imberger. American Geophysical Union 199–208 (1998)
32. Lemmin, U., Mortimer, C.H. and Bäuerle, E.: Internal seiche dynamics in Lake Geneva *Limnol. Oceanogr*, **50**(1), 207–216 (2005)
33. Lemmin, U. and D'Adamo, N.: Summertime winds and direct cyclonic circulation: Observations from Lake Geneva, *Ann. Geophysicae*, **14**, 1207–1220 (1996)
34. Monismith, S.G.: Wind induced-motions in stratified lakes and their effect on mixed-layer shear. *Limnol. Oceanogr.* **15**, 94–151 (1985)
35. Mortimer, C.H.: Frontiers in physical limnology with particular reference to long waves in rotating basins. *Proc. 5th Conf. Great Lakes res. Div.*, University Michigan, 9–42 (1963)
36. Mortimer, C.H.: Spectra of long surface waves and tides in Lake Michigan and at Green Bay, Wisconsin. *Proc. 8th Conf. Gt. Lakes Res.*, University Michigan Gt. Lakes Res. Div., Publ. no. **13**, 304–325 (1965)
37. Mortimer, C.H.: Lake Hydrodynamics. *Mitt. Int. Vereinig. Limnol.*, **20**, 124–197 (1974)
38. Mortimer, C.H.: *Internal waves observed in Lake Ontario during the International Field Year for the Great Lakes (IFYGL), 1972: I descriptive survey and preliminary interpretations of near-inertial oscillations in terms of linear channel-wave models*. Center for Great Lakes Studies, Special report Nr 32, University of Wisconsin-Milwaukee, 122 pp. (1977)
39. Mortimer, C.H.: Strategies for coupling data collection and analysis with dynamic modeling of lake motions, 183–277. In: *Lake Hydrodynamics*, W. H. Graf and C. H. Mortimer, eds. Elsevier, Amsterdam, (1979)
40. Mortimer, C.H.: *Long internal waves in lakes: Review of a century of research*. Special report Nr. 42, University Wisconsin-Milwaukee, Center for Great Lakes Studies, 117 p. (1993)
41. Mortimer, C.H.: *Lake Michigan in Motion – Responses of an Inland Sea to Weather, Earth-Spin, and Human Activities*, University of Wisconsin Press (2004)
42. Mortimer, C.H. and Fee, E.J.: Free surface oscillations and tides of Lakes Michigan and Superior, *Phil. Trans. Roy. Soc. London*, **A281**, 1–61 (1976)
43. Okamoto, I and Endoh, S.: Water mass exchange between the main basin and Shiozu Bay. In: *Physical Processes in a Large Lake: Lake Biwa, Japan*, Okuda, S., Imberger, J. and Kumagai, K, eds. American Geophysical Union, 31–42 (1995)
44. Platzman, G.W.: The dynamic prediction of wind tides on Lake Erie. *Meteorol. Monogr.* **4** (26), 44p. (1963)
45. Platzman, G.W.: Two-dimensional free oscillations in natural basins. *J. Phys. Oceanogr.*, **2**, 117–138 (1972)
46. Platzman, G.W.: Ocean tides and related waves. *Amer. Math. Soc., Lectures in Appl. Math.*, **14**, 239 (1970)
47. Platzman, G.W.: Two-dimensional free oscillations in natural basins. *J. Phys. Oceanogr.*, **2**, 117–138 (1972)
48. Platzman, G.W.: Normal modes of the Atlantic and Indian Ocean. *J. Phys. Oceanogr.*, **5**, 201–221 (1975)
49. Platzman, G.W.: Normal modes of the world ocean. Part III: A procedure fro tidal synthesis. *J. Phys. Oceanogr.*, **14**, 1521–1531 (1984)
50. Platzman, G. and Rao, D.B.: The free oscillations of Lake Erie. In: *Studies on Oceanography* (Hidaka Volume) (ed. K. Yoshida), p. 359–382, University of Washington Press (1964)
51. Proudman, J.: On a general expansion in the theory of the tides. *Proc. Lond. Math. Soc.* **29**, 527–236 (1928)
52. Rao, D.B. and Schwab D.J.: Two-dimensional normal modes in arbitrary enclosed basins on the rotating Earth: Applications to Lakes Ontario and Superior. *Phil. Trans. Roy. Soc. London*, **A 281**, 63–96 (1976)

53. Rao, D.B., Mortimer, C.H. and Schwab D.J.: Surface normal modes of Lake Michigan: calculations compared with spectra of observed water level fluctuations. *J. Phys. Oceanogr.* **6**, 575–588 (1976)
54. Rockwell, D.C.: Theoretical free oscillations of the Great Lakes. *9th Conf. Great Lakes Res.*, Publ. no. **11**, Gt. Lakes Res. Div., Univ. Michigan, 302–368 (1966)
55. Saggio, A and Imberger J.: Internal wave weather in a stratified lake *Limnol. Oceanogr.*, **43** (8), 1780-1795 (1998)
56. Salvadè, G. Zamboni, F. and Barbieri, A.: Three-layer model of the north basin of Lake of Lugano. *Annales Geophysica* **5B**, 247–259 (1988)
57. Schwab, D.J.: Internal free oscillations in Lake Ontario. *Limnol. & Oceanogr.* **22**, 700–708 (1977)
58. Serruya, S., Hollan, E. and Bitsch, B.: Steady winter circulations in Lake Constance and Kinneret driven by wind and main tributaries. *Arch. Hydrobiol./Suppl.* **70**, (1), 33–100 (1984)
59. Service Féderal des Eaux; SFE.: *Les dénivellations du Lac Léman*. Département féderal des postes et des chemins de fer, Report, maps, figures (1954)
60. Shimizu, K., Imberger, J. and Kumagai, M.: Horizontal structure and excitation of primary motions in a strongly stratified lake *Limnol. Oceanogr.*, **52** (6), 2641-2655 (2007)
61. Shimizu, K. and Imberger, J.: Energetics and damping of basin-scale waves in a strongly stratified lake *Limnol. Oceanogr.*, **52** (6), 2641–2655 (2009)
62. Sirkes, Z.: Surface manifestations of internal oscillations in a highly saline lake (the Dead Sea), *Limnol. & Oceanogr.*, **32**, 76–82 (1987)
63. Stewart, K.M. and Hollan, E.: Physical model study of Lake Constance *Schweiz. Z. Hydrol.*, **46**, (1), 5–40 (1984)
64. Tison, L.J. and Tison, G.Jr.: Seiches et dénivellations causées par le vent dans les lacs, baies, estuaries, Note Technique Nr. 2102, Organisation Météorologiques Mondiale, Genève, Suisse (1969)

Chapter 15
Higher-Order Baroclinicity (I): Two Fluid Layers with Diffuse Interface – Three Fluid Layers with Sharp Interfaces[1]

15.1 Motivation and Review

Internal oscillations in the atmosphere, the ocean and lakes are due to density variations that may exist due to the (basically vertical) temperature and, in the ocean, salinity distributions. A frequently encountered stratification occurs in summer when the lake water is warm in the uppermost layer (epilimnion) and cold at depth (hypolimnion) with a more or less continuous transition layer (metalimnion) with often fairly abrupt temperature changes. Baroclinic, i.e. internal waves are manifest, in particular, in the metalimnion with largest amplitudes at the location of the largest (mean) vertical temperature gradient (thermocline).

A common approximation to this continuously stratified fluid system is a two-layer configuration with a constant-depth upper layer (epilimnion) of a light fluid with constant density overlaying a variable depth constant density heavy fluid (hypolimnion) with a density-jump interface at the location of the thermocline. The wave motion of the interface then mimics the baroclinic wave in the metalimnion. As we know, this two-layer approximation yields only one baroclinic mode and eliminates all others.

This two layer model has been successful in modeling dominant oscillating process in real mountainous lakes at mid latitudes. It allows identification of the barotropic and *first* baroclinic mode structure; these have been verified with data from many lakes.[2] Higher order baroclinic waves, i.e. waves whose mode structure is due to a continuous variation in the density with depth, are also observed, but much less frequently; the reason is likely that they carry less energy and are often hidden behind wind induced smaller scale water motions. However, their existence is often due to the deviation of the diffuse metalimnion from a sharp interface. In

[1] This chapter and the next chapter belong intellectually together; they are separated for reasons of length.

[2] Schwab [49], Mortimer [39, 40], Mortimer and Horn [41], Hutter et al. [28], Bäuerle [4], Horn et al. [23], Stocker et al. [54], Hutter [27], Stevens and Lawrence [53], Saggio and Imberger [46], Antenucci and Imberger [1, 2], Boegman et al. [8], Gòmes-Giraldo et al. [16], Shimizu and Imberger [50–52].

K. Hutter et al., *Physics of Lakes*, *Volume 2: Lakes as Oscillators*, Advances in Geophysical and Environmental Mechanics and Mathematics,
DOI 10.1007/978-3-642-19112-1_15, © Springer-Verlag Berlin Heidelberg 2011

the past, we believe, the lack of the observation of higher-order baroclinic waves in lakes and the ocean is not so much due to the fact that they are not excited, but rather (1) because measuring techniques may have been insufficiently detailed to capture them and (2) that the two-layer approximation prevents theory to identify them computationally. Mortimer [38] has given observational evidence of a higher baroclinic wave response in Windermere, and Salvadè et al. [47] have approximated the density profile measured on March 18 1987 at a mooring in the northern basin of Lake of Lugano and identified peaks in the velocity spectra with eigenperiods of a three-layer model, whilst our own laboratory experiments [24, 25, 57] identified first and second baroclinic modes. The experimental set-up was such that a single internal soliton, riding on the interface and approaching a topographic obstruction is split into two pairs of reflected and transmitted internal solitary waves that can be identified with the first and second order baroclinic modes belonging to the sharp interface configuration and its diffuse regularization, respectively. In more recent years, higher-order baroclinic mode structures have been more systematically analyzed in stratified mountainous lakes by a number of researchers, see e.g. [3, 7, 8, 15, 42, 45] and others.

In this chapter, we shall first present measurements of higher order solitary internal waves, performed in the laboratory and compare the data with results from theoretical modeling. The focus will be the interaction of the solitary wave with a sill and the demonstration how the second-mode solitary signals are generated during the interactions. It will be demonstrated that a diffusive interface is essential in order that transmission and reflection processes of an approaching first-order baroclinic soliton is accompanied by a fissure of the transmitted and reflected wave signals from first to higher-order baroclinic modes. Second, first and second-order baroclinic waves will then be studied in the Northern basin of Lake of Lugano on the basis of a three-layer approximation of the summer vertical density profile with two idealized interfaces, a thermocline at 10 m depth and a chemocline at 100 m depth, which marks the different mineralizations of the waters at intermediate and great depths. Third, results will be reported on field measurements – mostly from thermistor chains – of internal oscillations in various lakes which can clearly be identified as higher-order baroclinic mode behaviour. In all these instances, the effects of the rotation of the Earth will be ignored even though internal Rossby radii of the second-baroclinic mode are not in all cases sufficiently large to justify this simplification.

Finally, it should be mentioned that a great number of *non-linear* internal wave studies have been conducted and were also applied to the ocean and to lakes. However, we are not aware that they are looked at in the spirit addressed in this chapter.

In what follows, this chapter will be divided into two parts: Part A will be dealing with a two-layer fluid system with diffusive interface, Part B will analyse a three-layer model of the North basin of Lake of Lugano.

A. Laboratory Experiments on Baroclinic Solitary Waves in a Two-Layer Fluid System with Diffusive Interface

The experiments were conducted in the Laboratory of the (former) Department of Mechanics of the Darmstadt University of Technology in a number of M.Sc. and Ph.D. dissertations and post doctoral work, see [10, 11, 24, 34, 35, 48, 59, 60]. Here we follow Hüttemann and Hutter [25] and Vlasenko and Hutter [57].

15.2 Experimental Set-Up and Wave Generation

15.2.1 The Wave Channel

The wave channel consists of four Plexiglas modules, 2.5 m in length; its cross-section is 33 cm wide and 35 cm high (Fig. 15.1). The channel is filled with de-aerated fresh water of density $10^3\,\mathrm{kg\,m^{-3}}$ which is underlain by de-aerated saltwater of density $1{,}025\,\mathrm{kg\,m^{-3}}$. The filling is done cautiously through 24 diffusers at the bottom plate to minimize mixing of the two fluids during the filling process. The result is a two-layered configuration with an abrupt but continuous density transition through a diffusive interface (Fig. 15.2). The propagation of the wave and its transformation by a built-in sill is recorded by six electrical resistivity gauges P1–P6, positioned along the channel. A seventh gauge is installed to measure the vertical displacement of the free surface and to ensure that no significant surface motion is established by the generated baroclinic wave.

The details of the filling operations of the fresh and salty water that make the diffusive boundary layer (Fig. 15.2) as thin as possible, is described in Schuster [48]. Here, it may suffice to mention that by each passage of an internal solitary wave through the flume the interface layer became thicker, barely measurable from one experiment to the next, but with visible accumulation after 7–10 repetitions. Furthermore, on time scales of an hour and more, molecular diffusion of salt from the lower to the upper layer widened the diffusive interface (by app. 4 mm per hour), an extent that affected the internal dynamics. So, repetitions of identical experiments yielded reproducible interface deflections provided they were done within less than an hour.

15.2.2 Solitary Wave Generation and Measuring Technique

Given the two-layer analysis of wave propagation in Chap. 11 the generation of a soliton-like displacement curve of the interface with negligible barotropicity can be achieved by moving the two pistons of the wave generator in opposite directions such that the displaced volumes in the two layers are the same: $u_1 h_1 = -u_2 h_2$. It was found by trial and error that the piston had to follow a ramp function in time to control the piston movement (Fig. 15.3a) and to generate a nearly soliton-like wave hump (see [11, 48, 59, 60] for further details). In the region of the wave generator,

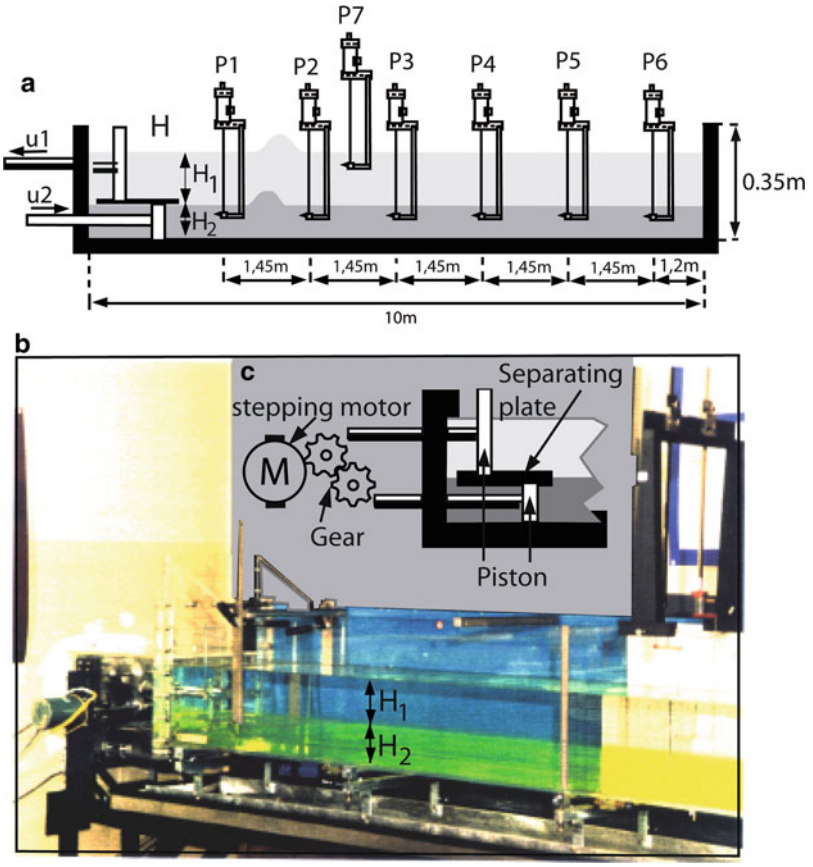

Fig. 15.1 (**a**) Sketch of the experimental arrangement (frontal view). On the *left* there are two pistons, separated by a thin plate at the interface level, which simultaneously move in opposite directions and displace the same volume of water. Six electrical resistivity gauges, P1–P6, record the interface elevation. A seventh gauge P7 records the free surface motion. (**b**) Wave channel with wave generator at the left end. (**c**) sketch of the wave generator. Composed from figures of B. Schuster (1991) [48]

the two pistons are separated by a thin Plexiglas plate to avoid mixing of water from the two layers, and to reduce the vortices that always form in the wake of the strong shearing at the interface surface because of the viscous behaviour of the fluid (formation of a vortex sheet!). The electrical resistivity gauges consist of two parallel wires subjected to an alternating voltage (Fig. 15.3b). The 5-kHz alternating current that is established avoids formation of electrolysis at the wires. The signal is amplified and digitized for computational analysis. Temporal resolution of 10 samples per second is sufficient to detect all effects related to the propagation of internal waves. Vertical adjustment of the gauge position is possible with an accuracy of 0.1 mm. This measuring arrangement suffers from an almost linear temporal drift because of

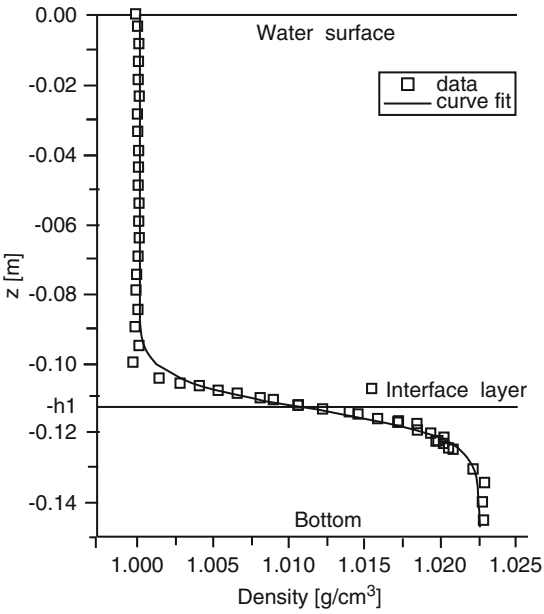

Fig. 15.2 Typical density profile in the channel. The measured data points (*squares*) were fitted by a sigmoidal transition function (*solid line*). From [48]

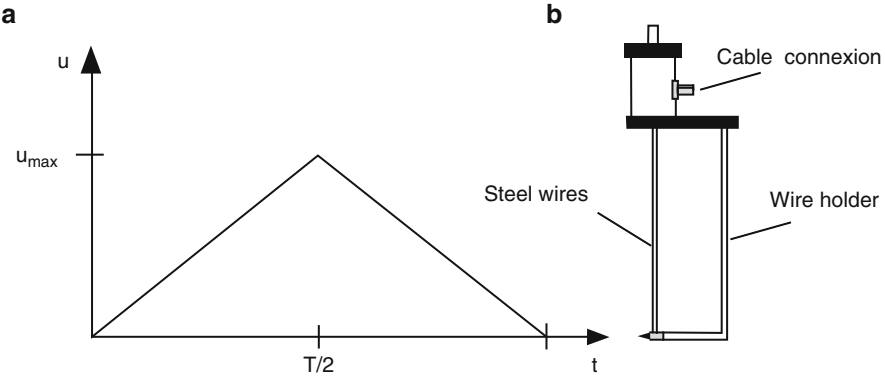

Fig. 15.3 Sketches of piston movement and gauge: (**a**) time-displacement curve of the piston of the wave generator; (**b**) conductivity gauge, consisting of two parallel wires subjected to an alternating current and connectable to an A/D convertor, from [48]

a galvanic coupling of the amplifiers and the water. This drift is manually corrected by subtracting an appropriate base value from the recorded time series, see Fig. 15.4. Moreover, because the reproduction accuracy of acceptable repeated experiments is sufficiently high, the spatial distance between the gauges can be made arbitrarily small by repeating experiments with the same system parameters after relocating the gauge along the channel.

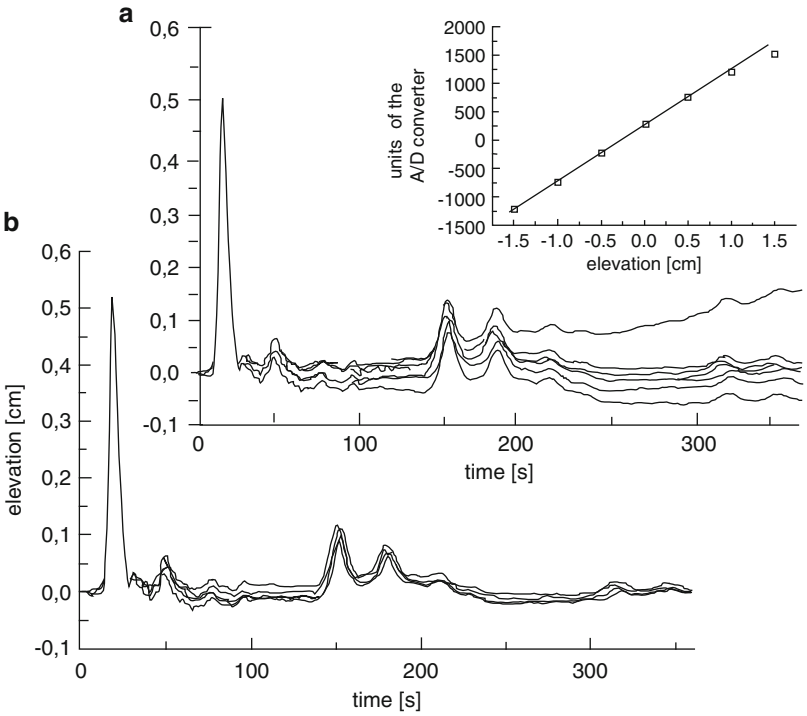

Fig. 15.4 Drift correction and reproduction accuracy. Reproduction accuracy of repeated experiments showing time series of elevation of the interface at one gauge: (**a**) before and (**b**) after drift correction. The inset in (**a**) shows a typical calibration curve of the gauges (after Hüttemann and Hutter (2001) [25]). © Springer, Berlin, reproduced with permission

15.2.3 Error Estimation

The major sources of errors in the measurements are those of calibration (approx. ± 0.1 mm), drift correction (approx. ± 0.2 mm) and noise in the electrical circuits (10 A/D converter units, which is about approx. ± 0.1 mm). The temporal error in the sampling rate of the A/D converter is said to be negligible. Thus, the overall error is smaller than approx. ± 0.5 mm. Because for most investigations in this section only the phase speed is of interest, one needs only relative changes in the signal and can ignore the absolute errors in the calibration and drift correction. This provides the possibility of evaluating even very small interface elevations.

15.3 The Experiments

The purpose of the experiments was to investigate the interaction of solitary waves with (1) the end walls to guarantee that the reflected waves would also exhibit solitary character and (2) sills, built-in at the floor of the channel. When partially

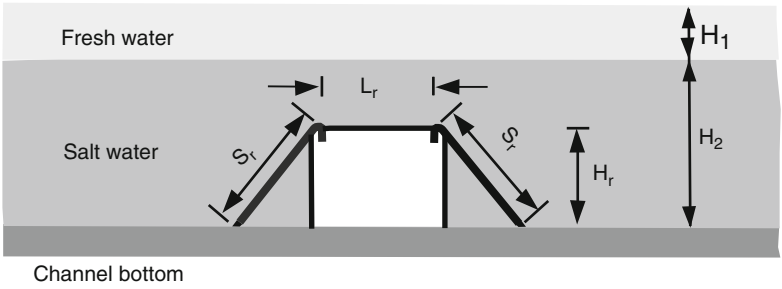

Fig. 15.5 Set-up of the sill and definition of the degree of blocking $B := H_r/H_2$

blocking the lower layer, a sill may split an incoming solitary wave into a reflected and a transmitted part. Depending on the degree of blocking $B = H_r/H_2$, see Fig. 15.5, the fissured forward and backward moving waves either keep the solitary character or are changed to oscillatory wave trains, see [11, 35, 48]. In ideal situations, we observed the excitation of a second transmitted solitary wave following the first at lower speed; more common was the formation of a transmitted wave train. Similar second reflected waves were also found in some experiments, but these had generally very small amplitudes and could often not be reliably reproduced.

There are two main parameters which characterize the system: the soliton amplitude and the degree of blocking. The amplitude is described by the Froude number $Fr = u_{\max}/c_{\text{lin}}$, which is the maximum piston velocity of the wave generator normalized by the linear phase speed c_{lin}. In the range $Fr \in [0.1, 0.8]$ the best results for soliton excitation were found with $Fr = 0.2$. This value generated an elevation amplitude of approximately 5 mm. Larger Froude numbers produce more oscillating wave trains in the back of the solitary wave, especially when interacting with the sill. The degree of blocking B was varied from 0.5 to 1.0. Smaller values of B do not have an observable effect on the transmitted wave, while higher values will break down the transmitted soliton to a simple oscillating wave train. Best results in the sense that the incoming soliton was split in two parts while keeping the solitary character, were achieved with $B \in [0, 7, 0.9]$. Two other parameters, the sill length and the steepness of the ramps of the sill are equally of significance for the reflection characteristics and the transmission of waves across the sill, but these are not in focus here, where attention is restricted to one and only one sill geometry with negligibly small L_r, for further scrutiny, see [35, 48].

15.3.1 Typical Experimental Data

Figures 15.6 and 15.7 show typical data sheets obtained from the experiments [48]. The layer depths are of the ratio 2 (top) : 1 (bottom) and 1 (top) : 2 (bottom) and the piston movement was such that almost perfect solitons were generated. The individual panels are plotted at equal distances, corresponding to a gauge

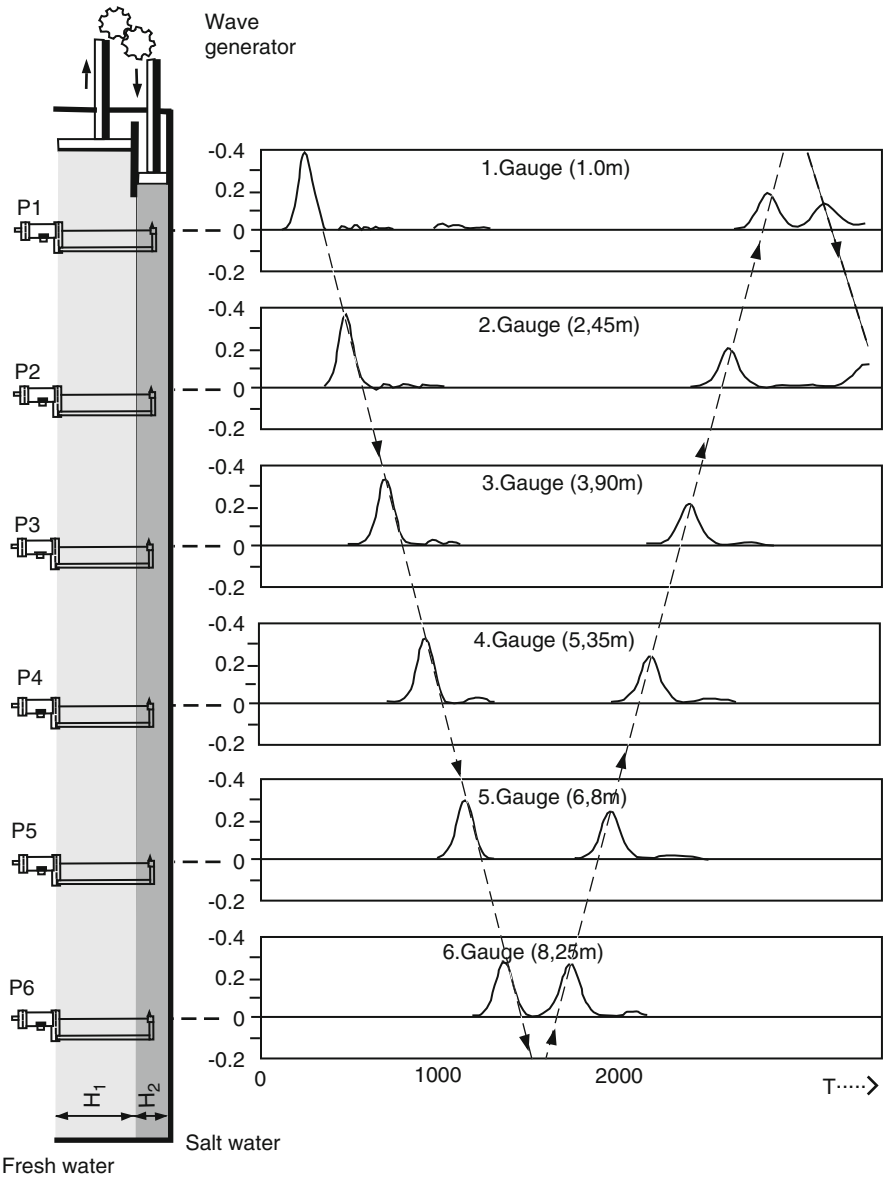

Fig. 15.6 Typical experimental data. Time series of the interface deflection at the six gauge positions, P1–P6, for a layer-thickness ratio $H_1/H_2 = 2:1$. On the *left* of the figure, the wave channel is shown with the locations of the gauges P1–P6. The time axis of the individual gauges is at the position of the respective gauges in the channel on the *left* of the figure. *Dotted lines* with *arrows* mark the propagation of the (fundamental) baroclinic mode of the two-layered system. Amplitudes are scaled with the equivalent water depth $H = H_1H_2/(H_1 + H_2)$ and time is made dimensionless with $T = t/\sqrt{g/H}$. The Froude number is $Fr = 0.88$ (From Schuster [48], with changes)

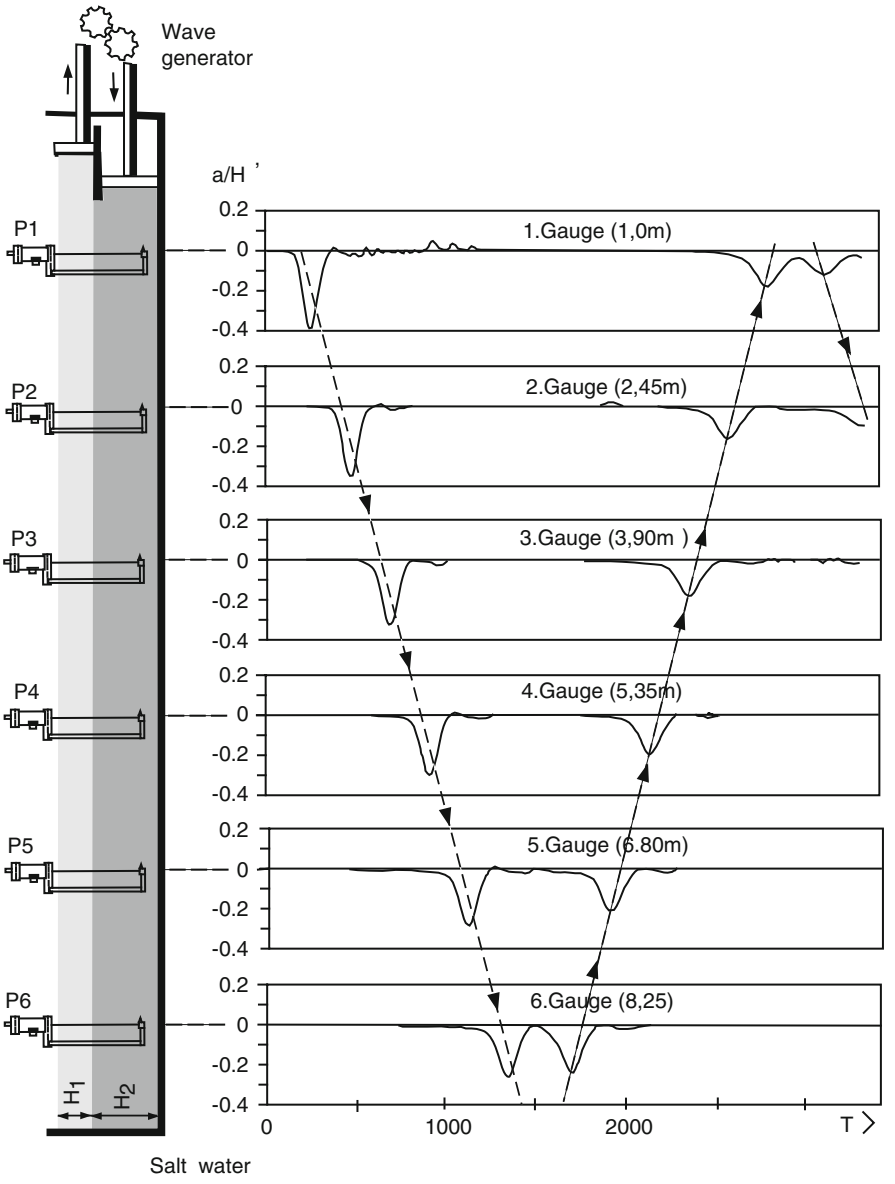

Fig. 15.7 Same as Fig. 15.6, but for a layer-thickness ratio $H_1/H_2 = 1 : 2$ (From [48], with changes).
Note: The small trailing oscillations behind the large solitary signal also seen in Figs. 15.6 and 15.8 could not be avoided in the experiments, but have been minimized by trial and error by moving the piston accordingly

distance of 1.45 m and the amplitudes are scaled with the equivalent water depth $H = H_1 H_2/(H_1 + H_2)$. In the early experiments, no sill was installed in the channel as only the reflection mechanism was tested at the end wall and at the generator wall that was erected after the passage of the generated wave. The initial wave signal, even though optically close to a perfect soliton signal, carried with it a very small trailing oscillating chain that was attenuated as the wave moved along the channel. Evidently, the main wave hump (Fig. 15.6) and trough (Fig. 15.7), respectively, are also considerably attenuated along the channel but the reflection at the end and generator walls preserves the soliton character of the wave signal well. The stability of the solitary wave hump and wave trough in Figs. 15.6 and 15.7, respectively, is in line with theoretical claims. Figure 15.8 shows the first peak signals,

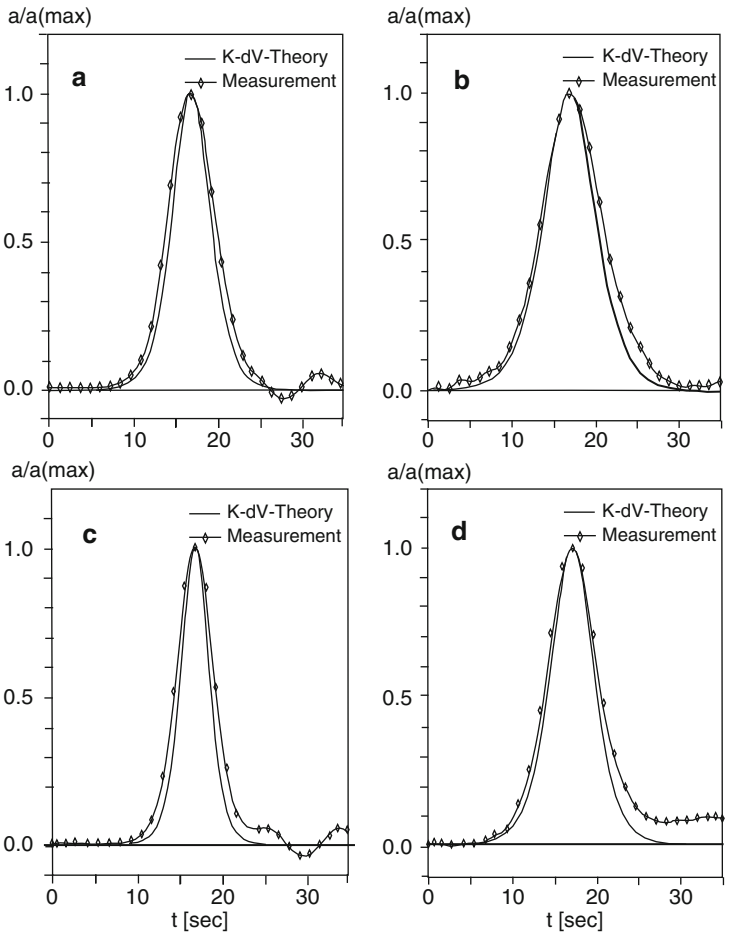

Fig. 15.8 Comparison of measured and theoretical soliton forms for layer thickness ratios $H_1/H_2 = 2 : 1$ (panels (**a**), (**b**)) and $H_1/H_2 = 3 : 1$ (panels (**c**), (**d**)) after the first (panels (**a**), (**c**)) and the second return passage (panels (**b**), (**d**)) of the gauge P1 for travel distances 2.45 and 16.45 m, respectively (composed from figures in [48])

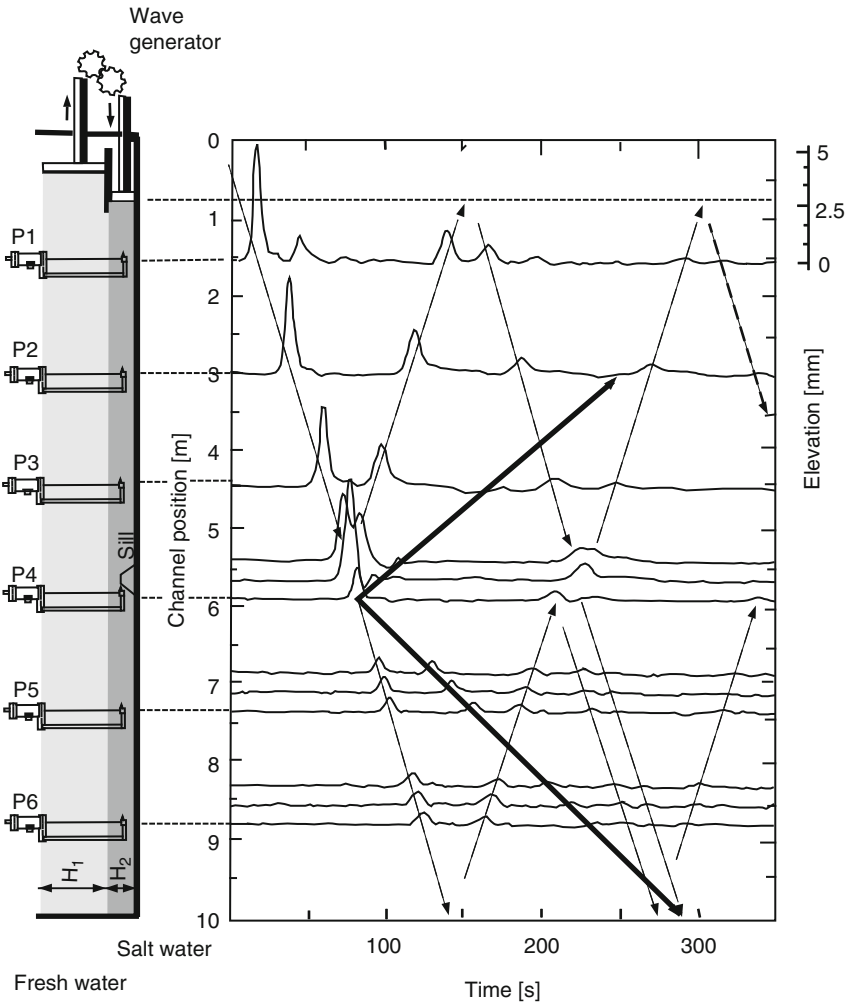

Fig. 15.9 Typical experimental data. Time series of the interface deflection at the six gauge positions P1–P6 (at gauges P4, P5, and P6, by repeating the experiment under identical conditions, three different positions are shown). On the *left*, the wave channel is shown with the exact location of the sill. The time axis of the individual gauges is at the vertical position of the respective gauges in the channel on the left. *Dashed lines* with *arrows* mark the propagation of the first vertical mode; *solid lines* show that of the first higher mode. Parameters are $Fr = 0.19$, $D = 2.67$, $B = 0.92$ (From [25]). © Springer, Berlin, reproduced with permission

measured at P1 after its first forward and second return passage and compares these with the sech^2-profile of the Korteweg-de-Vries (K-dV) equation for the 2:1 and 3:1 layering. Apart from the differences at the tail, the agreement is very good.

Figure 15.9 shows a typical data sheet with a built-in triangular sill between P3 and P4 and closer to P4. Interface elevations are now given in millimetre and

for each curve the same elevation scale, indicated in the upper right corner, is used, while the vertical position of the curve corresponds to the gauge position. The initial peak was approximately 5 mm high, decaying to about 1 mm while propagating all the way down to the end of the channel. The sketch on the left of the picture explains the position of the sill and the gauges along the channel length. The dotted lines and arrows mark the path of the fundamental-mode soliton; the gradient of the line gives the velocity of approximately $70\,\mathrm{mm\,s^{-1}}$. One easily sees the split at the sill in the middle of the channel and several reflections at both channel ends. The solid lines and arrows show the propagation of the suspected second higher-order baroclinic mode, generated by the sill. Here, the speed is only $20\,\mathrm{mm\,s^{-1}}$, even though the amplitude is almost equal to the transmitted fundamental-mode peak. We also indicate in Fig. 15.9 a reflected higher-mode wave, but owing to the smallness of the signal, we can presently only muse about its existence.

The propagation of the fundamental baroclinic mode solitary wave is already well known; so, this section will concentrate on the higher-mode peak. This higher mode signal has also solitary wave character, so, its wave form only follows from a weakly nonlinear theory, whilst its speed can be computed from a linear eigenvalue problem.

15.3.2 Results

This section presents some analysis of the experimental data with first interpretations.

15.3.2.1 Wave Signal

The shape of a typical K-dV soliton is given by the sech^2-profile. As we have seen in Fig. 15.8, the sech^2-profile is very well reproduced. Figure 15.10 compares the theoretical profiles with the measured data points in greater detail. Fundamental (Fig. 15.10a) and first higher mode (Fig. 15.10b) curves match the theoretical profile well except in the tails, where small deviations occur, that could, experimentally, never be avoided. Agreement between the sech^2-profile and the experimental data is well known [20,44]. The point here is, however, to demonstrate that the interaction of a fundamental mode solitary wave with the sill generates for these experimental conditions in addition higher order modes of the reflected signal (here only mode-2 is detectable), which is equally solitary and not simply an oscillating wave train. Evidently, the data in panel (a) are more accurate with less scatter than the data in panel (b).

15.3.2.2 Wave Speed

The most significant difference between the two observed wave modes is their travelling speed. Theoretically, the wave speed of the first higher mode c_1 can be

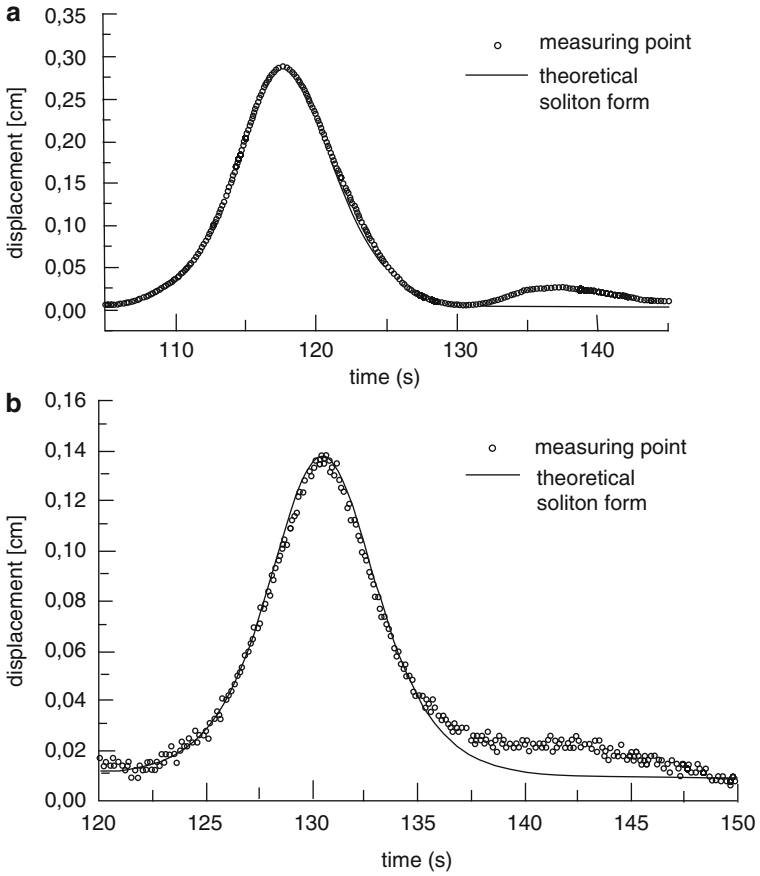

Fig. 15.10 Solitary wave signals. Comparison between the theoretical (*solid lines* and experimental soliton-type interface displacements; (**a**) for the fundamental baroclinic mode and (**b**) for the first higher order baroclinic mode (From Hüttemann (1977) [24]. Hüttemann and Hutter (2001) [25])

estimated to be about a third of the ground-mode solitary-wave speed c_0. Table 15.1 compares the calculated and measured wave speeds of a sample experiment. The blank spaces in the columns 'Experiments' occur, because no further higher mode was observable, whilst blanks in the two-layered solitary theory column are obvious because no higher modes exist in the two-layer theories. Agreement of the experimental with the theoretical results is remarkably good.

15.3.2.3 Influence of the Height of the Transition Layer

The longer a particular set-up is used for measurement, the thicker the transition area will become and the slower the fundamental mode wave will travel. Theoretically,

Table 15.1 Measured and computed wave speeds ($n = 0, 1, 2$ denote the fundamental and first and second higher baroclinic modes)

n	Experiments		Linear theory		
	c_n [cm s^{-1}]	c_n/c_0	c_n [cm s^{-1}]	c_n/c_0	Two-layer c_n [cm s^{-1}]
0	7.0	1	7.3	1	7.9
1	2.0	0.29	2.2	0.30	
2			1.3	0.18	
n	Solitary theory				
	Piecewise linear ρ_0		Sigmoidal ρ_0		
	c_n [cm s^{-1}]	c_n/c_0	c_n [cm s^{-1}]	c_n/c_0	
0	7.2	1	7.1	1	
1	2.1	0.29	2.1	0.30	
2	1.4	0.19	1.3	0.18	

the wave speed is given as a function of the thickness of the transition layer d, whilst in the experiments we could only observe changes in the wave speed depending on the time passed since the wave channel was filled with the two fluids. The channel set-up does not allow measurement of the density gradient while performing measurements of the transition surface elevation. To allow comparison of theory and experiments, the dependence of the thickness of the transition region d on the set-up lifetime T is assumed to be of the linear form

$$d(T) = \delta T + d_0, \tag{15.1}$$

where δ is a linear mixing constant, which is empirically determined and d_0 is the mixing offset caused by the filling process. δ was found to be approximately $4\,\mathrm{mm\,h^{-1}}$, and the values obtained for d_0 range from 13 to 17 mm. This seems to be reasonable in view of the sensitive filling operation. Using the values for δ and d_0, one can plot the wave speeds against the interface thickness d and compare the experimental data with the computational results. Lines A and B in Fig. 15.11 are plotted using the theory with a piecewise linear temperature profile, whilst C and D represent experimental data for the incoming solitary wave before reaching the sill, and the transmitted fundamental-mode solitary wave (D), respectively. The speeds of the line D in the graph of Fig. 15.11 are smaller than those of line C, because of the smaller amplitude of the transmitted wave. The points on line E show the measured wave speed of the transmitted first higher-mode soliton.

For inviscid systems, one would expect the measured speeds to be larger than the theoretical ones because the nonlinear amplitude correction is not incorporated in the theory. In spite of this, all experimental wave speeds are smaller than the corresponding theoretical values. We suppose that the neglect of viscosity and interactions with the flume boundaries cause the deviations. They obviously disappear when the ratio c_1/c_0 is considered, rather than the absolute wave

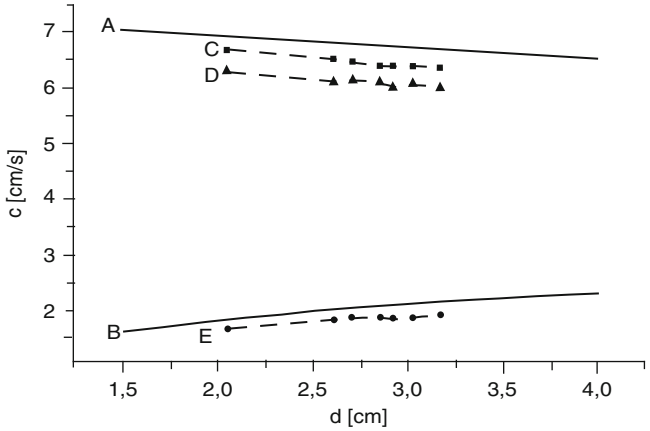

Fig. 15.11 Wave speed plotted against interface thickness d – Lines A and B show the theoretical results for this set-up. The data points of line C were obtained for the incoming solitary wave, those of line D for the transmitted fundamental-mode wave. Line E shows the measured values for the transmitted first-higher mode peak (From [24, 25]). © Springer, Berlin, reproduced with permission

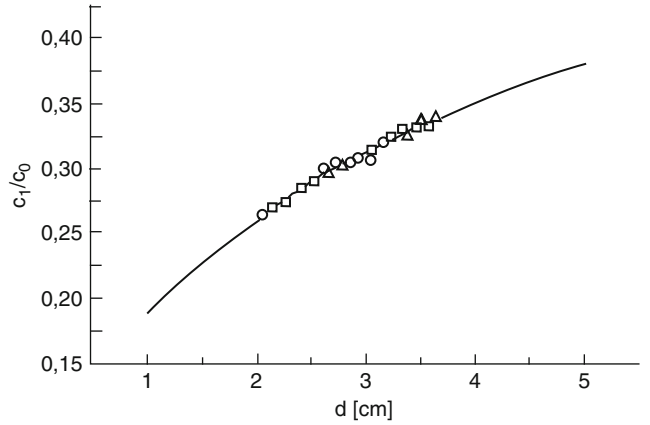

Fig. 15.12 Ratio c_1/c_0 plotted against d. The *solid line* gives the theoretical result for the piecewise linear temperature profile. Equation (15.1) was used to fit the experimental data given by the symbols (From [24, 25]). © Springer, Berlin, reproduced with permission

speeds. Figure 15.12 shows the near-perfect agreement of the ratio c_1/c_0 from the experiments and the theoretical values for the piecewise linear temperature profile (solid line). Equation (15.1) was used to fit the experimental data. The symbols (squares, triangles, circles) belong each to the same set of experiments using the same parameter values for δ and d_0.

15.4 Analytical Models for the Evolution of Baroclinic Waves

15.4.1 Equations

Consider a quiescent stratified fluid layer resting on a horizontal plane bottom and having a flat free surface. Let Oxz be a Cartesian coordinate system fixed with the fluid at rest. Its origin O and the x and y-axes pointing along and across the channel, are chosen to lie on the free surface, whilst the z-axis is pointing upward against the direction of gravity. Initially, the analysis will be confined to three dimensions: along and across the channel and vertically to it. The governing equations will be written relative to a rotating system of coordinates, but later the rotation of the Earth will be ignored and the across channel variations will be dropped, because in the small scale laboratory experiments the direction across the channel gives no contributions to the mode structure and is omitted. Let (u, v, w) be the Cartesian velocity components in the (x, y, z)-directions, respectively. They are in general functions of the position and time: $u = u(x, y, z, t)$, $v = v(x, y, z, t)$, $w = w(x, y, z, t)$. The total water depth is H and, for variable topography, the total water depth H is a function of x, y: $H = H(x, y)$. Assume, moreover, that the density of the undisturbed system varies with depth only, $\rho_0 = \rho(z)$. This function is assumed to model a light upper layer (epilimnion) of constant density that is continuously connected with a lower, heavier, layer (hypolimnion), also of constant density. The transition thickness d is assumed to be small in comparison to the total depth H. There are several possibilities to parameterize this smooth transition from the epilimnion to the hypolimnion density, and here, we shall treat essentially two: (1) a piecewise linear transition (Fig. 15.13a) and (2) a so-called sigmoidal fit (Fig. 15.13b). A sharp interface can be obtained mathematically in the limit $d \to 0$, but in reality the interface will always be diffuse. With $d = 0$, only one baroclinic wave mode exists, whilst for $d > 0$, there is a countable infinite set of baroclinic modes, the first two of which have been identified in the experiments.

Different weakly nonlinear theories of internal waves in a continuously stratified fluid are based on the balance laws of mass, momentum and energy of an ideal fluid under adiabatic conditions and the assumption of a solenoidal (divergence free) velocity field,

$$\begin{aligned} &\operatorname{div} \boldsymbol{v} = 0, \\ &\frac{\partial \boldsymbol{v}}{\partial t} + (\operatorname{grad} \boldsymbol{v})\boldsymbol{v} + 2\boldsymbol{\Omega} \times \boldsymbol{v} = -\frac{1}{\rho}\operatorname{grad} p - \boldsymbol{g}, \\ &\frac{\partial \rho}{\partial t} + \operatorname{grad} \rho \cdot \boldsymbol{v} = 0, \end{aligned} \tag{15.2}$$

where $\boldsymbol{v} \hat{=} (u, v, w)$, $\boldsymbol{\Omega} \hat{=} \Omega(0, \cos\phi, \sin\phi)$, $\boldsymbol{g}$ is the acceleration vector due to gravity and $\rho = \rho_0(z) + \tilde{\rho}$. If the rotation of the Earth is accounted for, then the second Coriolis parameter is generally ignored (see, however, [11]). In Cartesian co-ordinates and in the convective approximation, (15.2) takes the forms

$$
\begin{aligned}
\frac{\partial u}{\partial x}+\frac{\partial v}{\partial y}+\frac{\partial w}{\partial z}&=0,\\
\frac{\partial u}{\partial t}+\frac{\partial u}{\partial x}u+\frac{\partial u}{\partial y}v+\frac{\partial u}{\partial z}w-fv&=-\frac{1}{\rho_0}\frac{\partial p}{\partial x},\\
\frac{\partial v}{\partial t}+\frac{\partial v}{\partial x}u+\frac{\partial v}{\partial y}v+\frac{\partial v}{\partial z}w+fu&=-\frac{1}{\rho_0}\frac{\partial p}{\partial y},\\
\frac{\partial w}{\partial t}+\frac{\partial w}{\partial x}u+\frac{\partial w}{\partial y}v+\frac{\partial w}{\partial z}w&=-\frac{1}{\rho_0}\frac{\partial p}{\partial z}+\frac{g\tilde{\rho}}{\rho_0},\\
\frac{\partial \tilde{\rho}}{\partial t}+\frac{\partial \tilde{\rho}}{\partial x}u+\frac{\partial \tilde{\rho}}{\partial y}v+\frac{\partial \tilde{\rho}}{\partial z}w+\frac{\mathrm{d}\rho_0}{\mathrm{d}z}w&=0.
\end{aligned}
\tag{15.3}
$$

One of the more difficult problems in solving these equations is the prescription of the boundary conditions for the pressure. We, therefore, eliminate the pressure from (15.3) by taking the curl of the momentum equations. If attention is restricted to the situation when $\partial(\cdot)/\partial y = 0$, and when the stream function ψ is introduced according to

$$
u=\frac{\partial \psi}{\partial z},\quad w=-\frac{\partial \psi}{\partial x},
\tag{15.4}
$$

then, the continuity equation is satisfied identically and equations $(15.3)_{2,4}$ combine to the vorticity equation, whilst $(15.3)_{3,5}$ are simplified, but remain unchanged. The equations read in the Boussinesq approximation[3] ($\bar{\rho}_0 = \rho_0 = \text{const}$)

$$
\begin{aligned}
\frac{\partial \omega}{\partial t}+J[\omega,\psi]-f\frac{\partial v}{\partial z}&=\frac{\partial b}{\partial x},\\
\frac{\partial v}{\partial t}+J[v,\psi]+f\frac{\partial \psi}{\partial z}&=0,\\
\frac{\partial b}{\partial t}+J[b,\psi]+N^2(z)\frac{\partial \psi}{\partial x}&=0,\\
\omega:=\frac{\partial^2\psi}{\partial x^2}+\frac{\partial^2\psi}{\partial z^2},&
\end{aligned}
\tag{15.5}
$$

in which ω is the z-component of the vorticity vector curl $\boldsymbol{v}$ and

$$
J[a,c]:=\frac{\partial a}{\partial x}\frac{\partial c}{\partial z}-\frac{\partial a}{\partial z}\frac{\partial c}{\partial x},
$$

$$
b:=\frac{g}{\bar{\rho}_0}\tilde{\rho},
\tag{15.6}
$$

$$
N^2(z):=\frac{g}{\rho_0}\left(-\frac{\mathrm{d}\rho_0}{\mathrm{d}z}\right)
\tag{15.7}
$$

[3] We follow Vlasenko et al. (2005) [58], Chap. 5, p. 182.

are the Jacobian operator, the buoyancy force and squared buoyancy frequency.

Next, we non-dimensionalize (15.5) by introducing the scales

$$\begin{aligned}(x,z,t) &= \left(\lambda x^*, Hz^*, (\lambda/c_0)t^*\right),\\ (\psi,b,v) &= \left((-a_\xi c_0)\psi^*, (a_\xi c_0^2/H)b^*, (a_\xi c_0/H)v^*\right).\end{aligned} \tag{15.8}$$

Here, H and λ are length scales in the vertical and horizontal directions, $c_0 := HN_p$ is the scale for the baroclinic wave speed, with N_p the maximum value of the buoyancy frequency: $N_p = \max_{z\in(0,H)} N(z)$. Moreover, a_ξ is a typical wave amplitude. The dimensionless variants of (15.5) then take the forms

$$\begin{aligned}&\psi_{zzt} + \mu\psi_{xxt} + \varepsilon J(\psi_{zz},\psi) + \varepsilon\mu J(\psi_{xx},\psi) - (\lambda f/c_0)v_z = b_x,\\ &v_t + \varepsilon J(v,\psi) + (\lambda f/c_0)\psi_z = 0,\\ &b_t + \varepsilon J(b,\psi) + \bar{N}^2(z)\psi_x = 0,\end{aligned} \tag{15.9}$$

in which asterisks as identifiers of the dimensionless variables have been dropped. Two parameters

$$\varepsilon := \frac{a_\xi}{H} \quad \text{and} \quad \mu := \left(\frac{H}{\lambda}\right)^2 \tag{15.10}$$

represent a measure for the ratio of the wave amplitude to the total depth and a squared aspect ratio of the depth scale to the wave length scale, which constitutes a measure of *dispersion*. The remaining parameter $\lambda f/c_0$ is the ratio of the wave length to the Rossby radius of deformation, which defines the effects of rotational dispersion.

On the assumption that

$$\varepsilon \ll 1, \quad \mu \ll 1 \tag{15.11}$$

are small, an asymptotic two-parameter expansion can be performed with (15.9), which then reduces to the Korteweg-de Vries (K-dV) equation. This expansion, pursued to first order is due to Benney (1966) [5] and to second order due to Lee and Beardsley (1974) [33]. For the non-rotational case ($f = 0$) the asymptotic solution can be shown to be expressible as

$$\begin{aligned}\psi(x,z,t) = {} & A(x,t)\Phi(z) + \varepsilon A^2(x,t)\Phi^{(1,0)}(z) + \mu A_{xx}(x,t)\Phi^{(0,1)}(z)\\ & \varepsilon\mu\left[\left(A(x,t)A_{xx}(x,t) - \tfrac{1}{2}A_x^2(x,t)\right)\Phi_a^{(1,1)}(z) + \tfrac{1}{2}A_x^2(x,t)\Phi_b^{(1,1)}(z)\right]\\ & + \varepsilon^2 A^3(x,t)\Phi^{(2,0)}(z) + \mu^2 A_{xxxx}(x,t)\Phi^{(0,2)}(z) + \cdots,\end{aligned} \tag{15.12}$$

$$b(x,z,t) = A(x,t)\frac{N^2(z)}{c}\Phi(z) + \varepsilon A^2(x,t)B^{(1,0)}(z) + \mu A_{xx}(x,t)B^{(0,1)}(z)$$
$$\varepsilon\mu\left[\left(A(x,t)A_{xx}(x,t) - \tfrac{1}{2}A_x^2(x,t)\right)B_a^{(1,1)}(z) + \tfrac{1}{2}A_x^2(x,t)B_b^{(1,1)}(z)\right]$$
$$+ \varepsilon^2 A^3(x,t)B^{(2,0)}(z) + \mu^2 A_{xxxx}(x,t)B^{(0,2)}(z) + \cdots, \qquad (15.13)$$

in which $A(x,t)$ describes the progressing wave and Φ the vertical profile. The superscript (m,n) identifies the (ε^m, μ^n)-order of the term $\Phi^{(m,n)}$ in the expansion. To second order, the terms related to $O(\varepsilon,\mu)$ consist of two parts, denoted by subscripts a and b. The linear eigenvalue problem for $\Phi(z)$

$$\Phi_{zz} + \frac{N^2(z)}{c^2}\Phi = 0, \qquad (15.14)$$
$$\Phi(-H) = \Phi(0) = 0 \qquad (15.15)$$

defines a set of solutions $(\Phi(z)_j, c_j)$, where j is the number of the baroclinic mode.

If only the first order terms in the expansions (15.12), (15.13) are retained, then for $f = 0, \nu = 0$, and with an accuracy of $O(\varepsilon,\mu)$, the K-dV-equation

$$A_t + cA_x + \alpha_1 AA_x + \beta A_{xxx} = 0 \qquad (15.16)$$

can be derived from (15.9), which describes all possible unidirectional waves. The parameters α_1, β and c are coefficients of nonlinearity, dispersion, and linear phase speed of long internal waves, respectively. In the Boussinesq approximation, α_1 and β are determined as

$$\alpha_1 = \frac{3}{2}c\frac{\int_{-H}^{0}(\mathrm{d}\Phi/\mathrm{d}z)^3\mathrm{d}z}{\int_{-H}^{0}(\mathrm{d}\Phi/\mathrm{d}z)^2\mathrm{d}z}, \quad \beta = \frac{c}{2}\frac{\int_{-H}^{0}\Phi^2\mathrm{d}z}{\int_{-H}^{0}(\mathrm{d}\Phi/\mathrm{d}z)^2\mathrm{d}z}. \qquad (15.17)$$

In the more common case, when the amplitudes of the internal waves are relatively large, the second order terms in the expansions (15.12) and (15.13) can introduce essential corrections to the first order solution. For instance in a two-layer model of fluid stratification the coefficient of quadratic non-linearity in the K-dV equation, α_1 is positive when $H_1 < H_2$, but negative when $H_1 > H_2$. In this case, the next cubic non-linearity becomes the major source of non-linearity. In the second order shallow water theories[4] the K-dV equation for A is replaced by the *extended* Korteweg-de Vries (*eK-dV*) *equation*, in which the coefficient of the cubic non-linearity can be explicitly computed, if $\Phi(z)$ is known, see [58].

[4] For the two-layer stratified case see Djordjevic and Redercopp [12], Gear and Grimshaw [14], Miles [36], Choi and Camassa [9], Ostrovsky and Grue [44], and for the continuous stratification Grimshaw [17], Grimshaw et al. [18], Grimshaw [19], Ivanov et al. [29], Lamb and Yan [32].

15.4.2 Baroclinic Modes for a Two-Layer System with Diffuse Interface

According to the theory outlined in the last section, the analysis of weakly non-linear baroclinic waves consists of two steps, (1) the determination of the z-profiles of the various modes for Φ by solution of the eigenvalue problem (15.14) and (15.15) and (2) the solution of the K-dV equation for the signal propagation. Here, we shall be concerned with the determination of the baroclinic modes for the critical velocity (which is proportional to Φ).

Step 1 is the parameterization of the measured density profile by a functional relation. The following profiles allow satisfactory reproduction of the measured density distribution.

15.4.2.1 Piecewise Linear Density Profile

This can parametrically be given as (Fig. 15.13a)

$$\rho_0(z) = \begin{cases} \rho_1, & \text{for } -h^+ < z < 0, \\ \rho_1 - \dfrac{\Delta\rho}{d}\left(h^+ + z\right), & \text{for } -h^- < z < -h^+, \\ \rho_2, & \text{for } -H < z < -h^-, \end{cases} \tag{15.18}$$

and yields

$$N^2(z) = \begin{cases} 0, & \text{for } -h^+ < z < 0, \\ -\dfrac{g\Delta\rho}{\rho_0 d} \simeq -\dfrac{g\Delta\rho}{d\rho_2}, & \text{for } -h^- < z < -h^+, \\ 0, & \text{for } -H < z < -h^-. \end{cases} \tag{15.19}$$

This choice of the density profile allows exact solution of the eigenvalue problem (15.14) and(15.15), see [24]. The eigenvalue problem (15.14) and (15.15) can, however, equally be solved numerically. Figure 15.13c displays the vertical distribution of the vertical fluid velocity for modes $n = 0, 1, 2$ for conditions as stated in the figure caption, and wave speeds are listed in Table 15.1.

15.4.2.2 Sigmoidal Density Profile

A better approximation of the transition of the density profile from the upper to the lower layer is the sigmoidal density function [30] (Fig. 15.13b,d)

$$\rho_0(z) = \bar{\rho}_0 \exp\left\{\frac{\Delta\rho}{2\bar{\rho}_0}\tanh\left(-\frac{2}{d}(z + h_1)\right)\right\}, \tag{15.20}$$

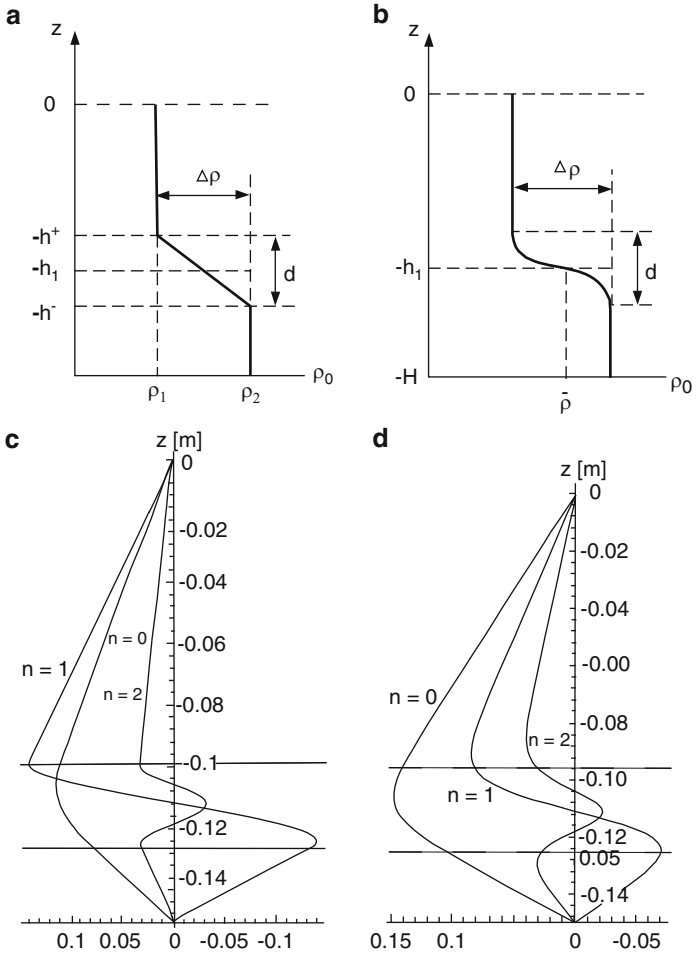

Fig. 15.13 Piecewise linear (**a**) and sigmoidal (**b**) density profiles in a two-layer fluid system with diffuse interface between the two layers. Baroclinic modes for $n = 0, 1, 2$, computed for a 15-cm thick two-fluid system with $H_1 = 3.8\,\text{cm}$, $H_2 = 11.2\,\text{cm}$ and $d = 2.65\,\text{cm}$ for piecewise linear (**c**) and sigmoidal **(d)** density structure (Composed from figures in [24, 25]). © Springer, Berlin, reproduced with permission

which is sketched in Fig. 15.13b and of which a fit to the measured data is given in Fig. 15.2. The eigenvalue problem (15.14) and (15.15) for Φ reads in this case

$$\begin{aligned} &\frac{\mathrm{d}^2\Phi}{\mathrm{d}z^2} + \frac{g}{c^2}\frac{\Delta\rho}{d\,\bar{\rho}_0}\mathrm{sech}^2\left(-\frac{2}{d}(z+h_1)\right)\Phi = 0, \\ &\Phi(0) = \Phi(-H) = 0, \end{aligned} \tag{15.21}$$

with exact solutions in terms of hypergeometric functions [24] which, however, possess poor numerical convergence properties. It is easier to solve (15.21) numerically with a commercial software. The corresponding mode structure and the computed phase speeds are given in panel (d) of Fig. 15.13, and Table 15.1, respectively, again for the layer particulars as listed in the figure caption.

The fundamental baroclinic speed has also been computed for the two-layer model with abrupt density change across the interface ($d = 0$). Its phase speed is also listed in Table 15.1.

Remarks:

- Starting from the linearized adiabatic equations in two dimensions, (15.3) with $v = 0$, $\partial(\cdot)/\partial y = 0$ and $f = 0$, Hüttemann (1997) [24] also determined the following equation for the vertical velocity component

$$\frac{\partial^4 w}{\partial z^2 \partial t^2} + \frac{\partial^4 w}{\partial x^2 \partial t^2} + \frac{1}{\rho_o}\frac{\mathrm{d}\rho_0}{\mathrm{d}z}\frac{\partial^3 w}{\partial z \partial t^2} - \frac{g}{\rho_0}\frac{\mathrm{d}\rho_0}{\mathrm{d}z}\frac{\partial^2 w}{\partial x^2} = 0 \tag{15.22}$$

  subject to the rigid lid boundary conditions $w(0) = w(-H) = 0$. He assumed travelling waves of the form

$$w = A(x - ct)\Phi(z). \tag{15.23}$$

  The function $A(x-ct)$ describes the horizontal form of the vertical velocity with time, whilst $\Phi(z)$ gives the vertical structure. With the substitution $y = x - ct$, (15.22) and (15.23) imply

$$-\frac{\dfrac{\mathrm{d}^4\Phi}{\mathrm{d}y^4}}{\dfrac{\mathrm{d}^2 A}{\mathrm{d}y^2}} = \frac{\dfrac{\mathrm{d}^2\Phi}{\mathrm{d}z^2} + \dfrac{1}{\rho_0}\dfrac{\mathrm{d}\rho_0}{\mathrm{d}z}\dfrac{\mathrm{d}\Phi}{\mathrm{d}z} - \dfrac{g}{c^2}\dfrac{1}{\rho_0}\dfrac{\mathrm{d}\rho_0}{\mathrm{d}z}}{\Phi} = k^2 \tag{15.24}$$

  with separation parameter k. This yields the differential equation

$$\frac{\mathrm{d}^4 A}{\mathrm{d}y^4} + k^2\frac{\mathrm{d}^2 A}{\mathrm{d}y^2} = 0 \tag{15.25}$$

  and the eigenvalue problem for $\Phi(z)$

$$\begin{aligned} &\frac{\mathrm{d}^2\Phi}{\mathrm{d}z^2} + \frac{1}{\rho_0}\frac{\mathrm{d}\rho_0}{\mathrm{d}z}\frac{\mathrm{d}\Phi}{\mathrm{d}z} - \left(\frac{g}{c^2}\frac{1}{\rho_0}\frac{\mathrm{d}\rho_0}{\mathrm{d}z} + k^2\right)\Phi = 0, \\ &\Phi(0) = \Phi(-H) = 0. \end{aligned} \tag{15.26}$$

  Using the sigmoidal density profile (15.19) and ignoring the second term on the left-hand side of (15.26), Hüttemann then solved the eigenvalue problem (15.26) approximately. For the same experimental conditions as those used in Fig. 15.13, he obtained the phase speeds listed in Table 15.1 under the heading

'linear theory': the $\Phi(z)$-profiles (not shown here) deviate sharply from those of Fig. 15.13.

- There are other parameterizations of the buoyancy frequency, which approximate sigmoidal density profiles. For instance, Vlasenko [55] and Vlasenko et al. [56, 58] suggest to use

$$N(z) = \frac{N_p}{1 + \left(\dfrac{2(z + H_p)}{\Delta H_p}\right)^2}, \tag{15.27}$$

in which H_p is the depth at which N possesses its maximum value N_p and ΔH_p is the width of the $N(z)$-profile at the mean value $0.5N_p$. Figure 5.1 in [58] demonstrates that the parameterization (15.27) allows representation of a great variety of density profiles arising in lakes and the ocean.

15.4.3 Results of the Numerical Modeling

In the previous section, the baroclinic linear eigenvalue problem (15.14) and (15.15) was solved for the piecewise linear and sigmoidal density profiles (15.18) and (15.20), respectively. It yielded the vertical distributions of the vertical velocity component of the three basic baroclinic modes ($n = 0, 1, 2$) and the corresponding wave speeds, see Fig. 15.13 and Table 15.1, and corroborated the high probability of the interpretation of the measured peaks of the interface displacements as the trace of the lowest three baroclinic solitons. Such solitons are idealized interpretations of the waves that are generated by the interaction of the approaching solitary wave with the sill, and theoretically only emerge asymptotically for large distances after reflection and transmission. Numerical solution of the governing primitive equations (15.5) subject to the appropriate initial conditions provides better insight into this problem. This was done by Vlasenko and Hutter [57], see also Vlasenko et al. [58], of which we here report some excerpts.

To reproduce the laboratory experiment, the amplitude of the incident wave was taken to be 5 mm, corresponding to a laboratory Froude number $Fr = u/c_p^{(0)} = 0.13$, where u is the horizontal orbital velocity of the incident wave and $c_p^{(0)}$ the linear wave speed. The height of the sill was $H_r = 3.2$ cm, corresponding to a degree of blocking $B = 0.92$ ($H_2 = 3.5$ cm) and the sill length was 60 cm as in the laboratory experiment. For a description of the numerical scheme to integrate (15.5), we refer the reader to Chap. 4, Sect. 2 of [58].

Figure 15.14 shows the interaction of a solitary wave with the triangular sill. The individual panels show how the wave interaction proceeds for an incident wave from the right to the left. The snapshots are for the times $T_0 \times (5, 6, 9, 17)$, where $T_0 = \lambda_{(0)}/c_{(0)} = 4.2$ s is the ratio of the incident soliton wave length λ_0 to the fundamental linear phase velocity c_0. The panels from top to bottom show the time slices when the incident wave hits the sill ($t = 5T_0$), has just passed

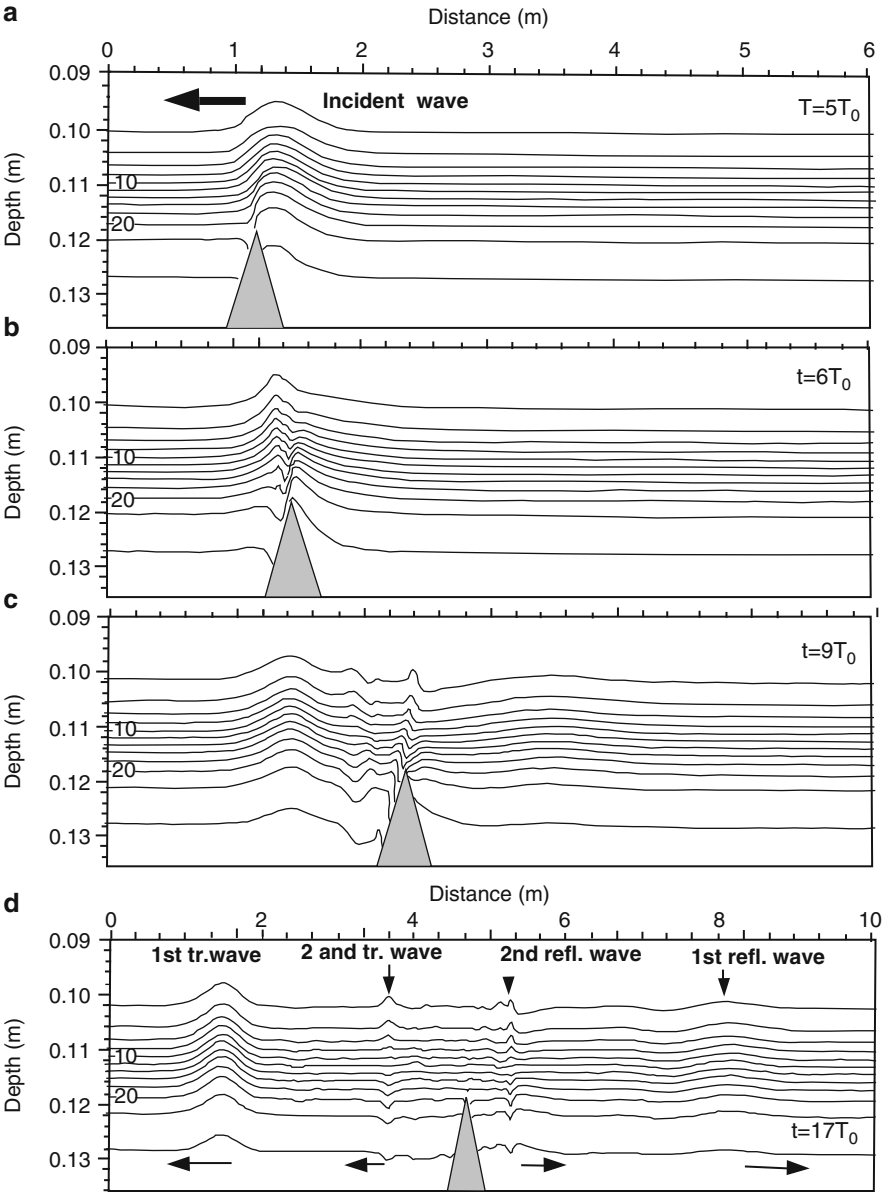

Fig. 15.14 Evolution of the density field (density anomaly $(\rho(z) - \rho(0))$ relative to the density at the free surface in $\mathrm{kg\,m^{-3}}$) during the interaction of a fundamental mode solitary wave with the sill. The figure shows the development of the fundamental and first higher order modes of the transmitted and reflected signals in panel (**d**) (Courtesy Vlasenko et al. (2005) [58]). © Cambridge University Press, reproduced with permission

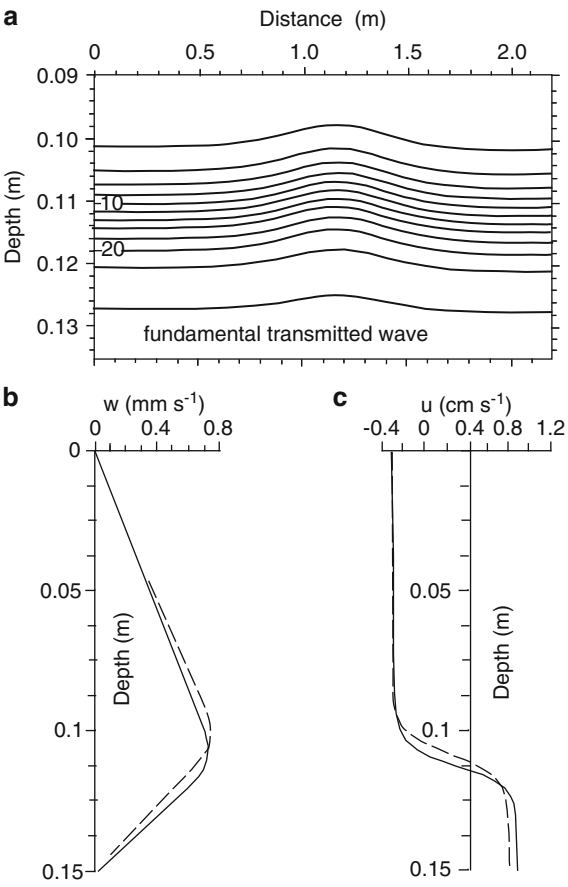

Fig. 15.15 Density anomaly field ($\rho(z) - \rho(0)$, kg m^{-3}) of the fundamental transmitted wave (**a**) and vertical profiles of the vertical, w (**b**), and horizontal, u (**c**), velocity, computed for the sigmoidal density profile and shown as *dashed lines*. For comparison, the vertical profiles of the K-dV soliton of the same amplitude are shown by *solid lines*, for $t = 35T_0$ (Composed from figures of [58]). © Cambridge University Press, reproduced with permission

the sill ($t = 6T_0$), when a transmitted fundamental soliton seems to have formed and higher order modes(s) are forming ($t = 9T_0$), and when clearly identified signals of the fundamental and first higher baroclinic transmitted and reflected waves ($t = 17T_0$) have formed. The direction of propagation of the waves is indicated by the arrows in panel (d). Computations have been performed for much larger times and the following discussion and Figs. 15.15–15.18 are based on the results at the time slice $t = 35T_0$.

The fundamental transmitted (Fig. 15.15) and reflected (Fig. 15.16) waves at $t = 35T_0$ look qualitatively just like the fundamental soliton with isopycnal displacements all pointing upward throughout the entire depth from the surface to the bottom, the amplitudes of the isopycnals of the transmitted signals being larger than those of the reflected signals (see panels (b) and (c) in Figs. 15.15 and 15.16). Panels (b) and (c) in the figures show the depth profiles of the vertical, w, and horizontal, u, velocity components (dashed). For comparison, the vertical profiles of the K-dV soliton with the same amplitude are also shown by the solid lines. The difference

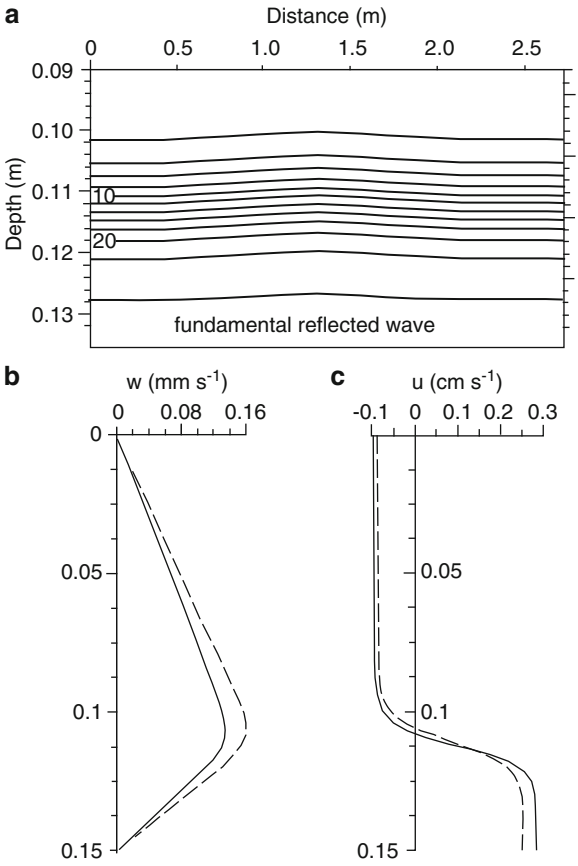

Fig. 15.16 The fundamental reflected baroclinic wave. Notations are the same as in Fig. 15.15, for $t = 35T_0$ (Composed from figures of [58]). © Cambridge University Press, reproduced with permission

between the dashed and solid profiles is a measure of deviation from the asymptotic soliton. Figure 15.17 shows the isopycnal displacements and the w- and u-velocities for the transmitted first higher order wave also for $t = 35T_0$. Here, the vertical isopycnal displacements in the upper and lower parts of the fluid are in opposite directions, forming humps in the upper layer and troughs in the lower layer with nearly zero amplitude in the diffusive interface. Correspondingly, the vertical velocity w is up- and downward in the upper and lower parts (panel (b)) with a sign change at the interface. Along with this, the horizontal velocity, u, is directed in a to–fro–to manner (panel (c)) from top to bottom with zero values where w is going through a maximum, and a relative maximum where w is zero. The difference between the numerical profiles (dashed) and the profiles of the steady solitons (solid) is still small, so that identification of the transmitted wave signal is indeed essentially the first higher mode baroclinic wave. This is different for the reflected higher mode signal displayed in Fig. 15.18. Panel (a) in this figure indicates with the counter-phase isopycnal displacements that first higher mode behaviour must be dominant, but the oscillating portions of the wave signal point also at the presence of

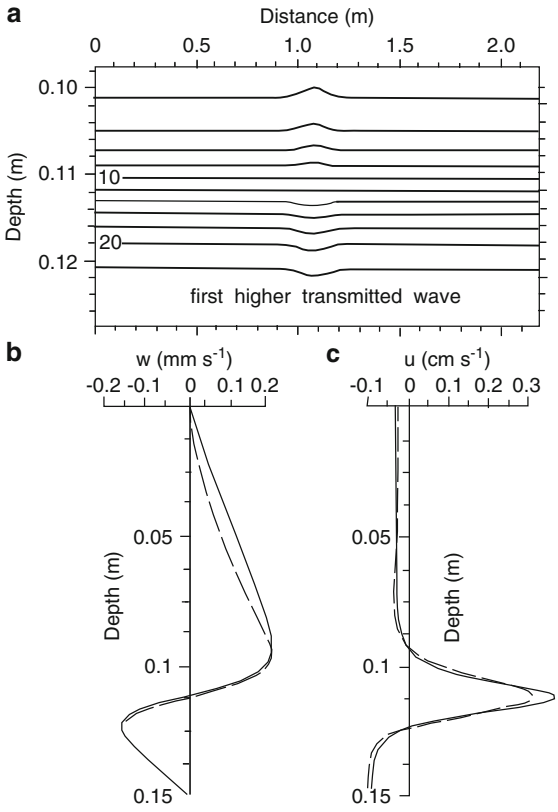

Fig. 15.17 The first transmitted baroclinic wave. Notations are the same as in Fig. 15.15, for $t = 35T_0$ (Composed from figures of [58]). © Cambridge University Press, reproduced with permission

second, third and higher mode behaviour. This interpretation is supported by the w- and u-profiles shown in panels (b) and (c) in Fig. 15.18 when the numerical profiles (dashed) deviate substantially from the analytical K-dV solitons (solid).

The experiments and numerical computations reported above show that a nearly perfect K-dV soliton that is approaching a sill in an otherwise constant depth channel may at the sill be broken up into transmitted and reflected wave signals which constitute a combination of fundamental and higher order baroclinic waves. The experiments were performed such that the lowest two baroclinic modes were the dominant contributors to these signals, but for the reflected wave even higher order modes could not be ignored in the interpretation of the signal even though this was not done explicitly. Of course, the outcome of this fission to higher order baroclinicity by the sill depends on the height of the sill relative to the thickness of the lower layer of the fluid system. Vlasenko and Hutter [57], Vlasenko et al. [58] also study the dependence of this interaction process on the degree of blocking and on the Froude number of the generated incident wave. What can be learnt here is that *topographic features, if sufficiently strong may be cause for the transfer of baroclinic energy from lower mode to higher mode behaviour.*

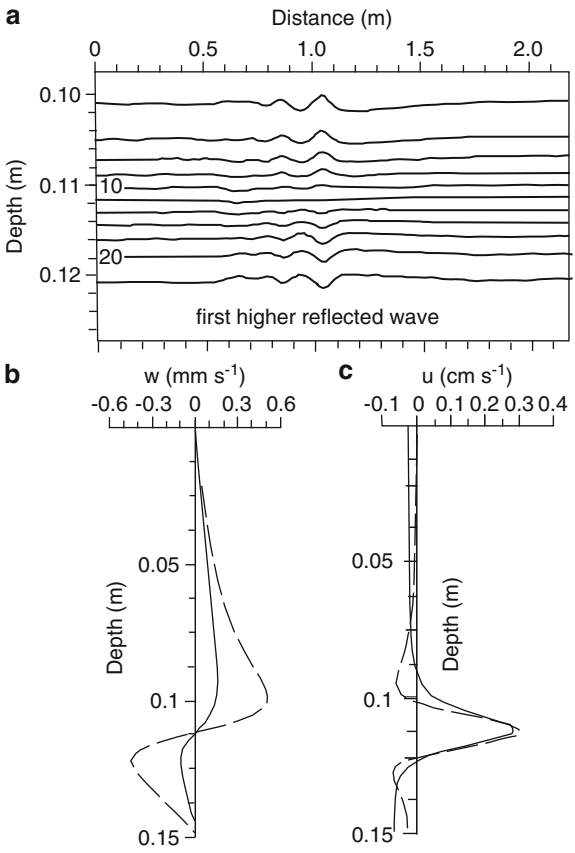

Fig. 15.18 The first reflected baroclinic wave. Notations are the same as in Fig. 15.15, for $t = 35T_0$ (Composed from figures of [58]). © Cambridge University Press, reproduced with permission

B. Three-Layer Model of the North Basin of Lake of Lugano

Even though higher order baroclinicity in most lakes is likely due to the diffusive interface between the epilimnion and the hypolimnion through a metalimnion of finite thickness, there are occasionally depth variations of the mineralization of the water, especially in very deep eutrophic lakes with meromixis. In such circumstances, oxygen depletion and a relative surplus of, e.g. sulphate may occur at depth to the extent that the chemical concentration and therefore electrical conductivity increase abruptly as one moves down through this *chemocline*. This situation exists in the North basin of Lake of Lugano and contributes, together with a density jump due to the (diffusive) thermocline interface, to an additional higher order baroclincity. In this case, it is, however, not clear, which of the two interface motions, that of the thermocline or that of the chemocline, generate the fundamental mode behaviour of a basin wide oscillation. We shall see in this case that the largest phase speed, and therefore shortest internal seiche period is due to the motion of the chemocline, and the next to the largest phase speed and therefore the next to the

shortest seiche period is due to the thermocline motion. This assumes that the two interfaces are sharp, and so, we ignore their diffusive thicknesses which are always present.

In the ensuing study, we report on an analysis that was conducted by Salvadè et al. [47] who used data, recorded by the Laboratorio di Studi Ambientali, Lugano, Switzerland in 1987 and physical experiments of a summer campaign of 1979 (unpublished),[5] performed jointly by the Laboratory of Hydraulics, Hydrology and Glaciology at ETH, Zürich and the Laboratorio di Fisica Terrestre, Lugano.

15.5 The Thermo-Chemical Density Structure of the North Basin of Lake of Lugano

Lake of Lugano consists of three basins; the North basin (Fig. 15.19) is an L-shaped channel of about 17 km length with a mean width of 1,500 m and mean and maximum depths of 170 and 288 m, respectively. The South basin and the pond at Ponte Tresa are not the subject here; see, however, Chap. 18 for a detailed study of the

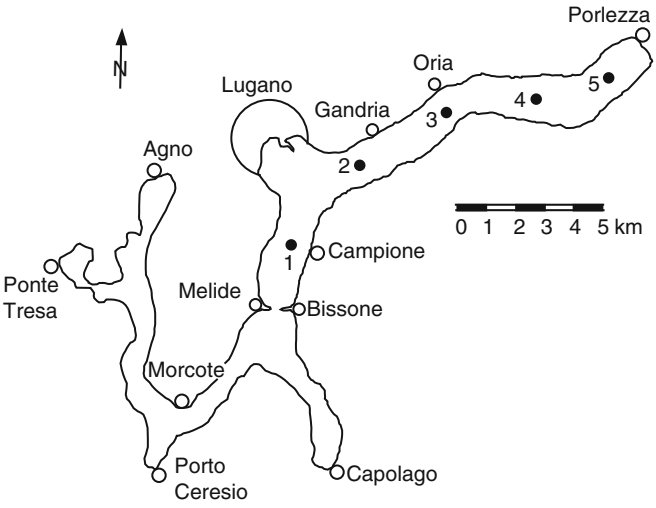

Fig. 15.19 Map of the Lake of Lugano. The North basin extends from Porlezza to Melide Bissone. Positions 1–5 indicate measuring stations of the field campaign on December 1984. The South basin is roughly S-shaped and extends from Capolago to Agno, but without the Pond at Ponte Tresa which is separated from it by the channel at Lavena (From Salvadè et al. [47]). © European Geosciences Union, reproduced with permission

[5] All these measurements are listed in the annual reports of the International Commission for the protection of the Italo-Swiss waters (Laboratorio Studi Ambientali 1980–1986) [31].

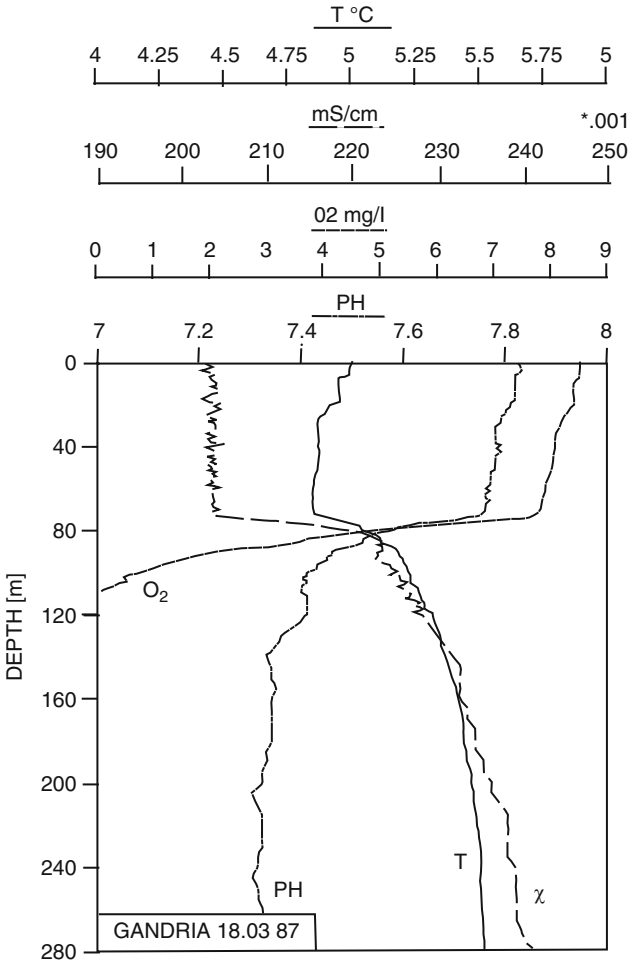

Fig. 15.20 Vertical profiles of temperature, conductivity, dissolved oxygen and pH-value, measured near Gandria at the end of the winter water circulation on March 18, 1987 (From [47]). © European Geosciences Union, reproduced with permission

baroclinic dynamics in the South basin of Lake of Lugano. The water transport is from the North basin to the South basin through the channel of Melide and from the South basin to the pond of Ponte Tresa through the channel of Lavena. The entire outflow is all from the pond at Ponte Tresa into the Tresa river to the Lago Maggiore.

Since 1980, regular field programs were carried out by the Laboratorio di Studi Ambietali at Lugano, measuring vertical profiles of temperature, electrical conductivity, dissolved oxygen and pH value by means of multi-parameter probes. Figure 15.20 shows profiles of the temperature (T) electrical conductivity (χ), dissolved oxygen (O_2) and pH-value, recorded on March 18 1987 near Gandria (Fig. 15.19). For all measured parameters a strong gradient is visible at a depth

between 80 and 100 m. This figure represents the species profiles at the end of the winter circulation, which is also typical for profiles observed in former years. It is evident that the circulation does not penetrate below the 100 m depth, corroborating the meromixis for this lake with a chemocline at 100 m depth.

Salvadè et al. [47] note: 'From December 3–7 1984 the Laboratorio di Studi Ambientali carried out a measurement campaign, using a multi-parameter probe MSE: Temperature and conductivity profiles were measured twice a day, in five different positions along the thalweg of the North basin as indicated in Fig. 15.19. From all the conductivity measurements a mean profile was calculated and the part between 80 and 150 m was approximated by a third order polynomial with a correlation coefficient of 0.999. The vertical $\bar{z}$-shifting of the mean profile $\bar{\chi}$ necessary to fit each measured profile was then calculated. In essence the equation

$$\sum_{i=1}^{N}[\chi(z_i) - \bar{\chi}(z_i - \bar{z})]^2 = \text{Min} \tag{15.28}$$

was solved for $\bar{z}$. Here, z_i is the ith depth where resistivity measurements were made and N is the number of measurements performed at a given position'.

Figure 15.21a shows the $\bar{z}$-values during the measuring campaign at stations 1 and 5, situated at the two ends of the lake. One can note vertical variations of the profiles over more than 10 m. The two time series appear to be in counter phase, and this suggests the development of internal waves related to the density change at 100 m. Figure 15.21b shows the vertical shift $\bar{z}$ as a function of the station position at two instances approximately 20 h apart, suggesting that even horizontally the basin is not uniform.

No continuous measurements over longer periods are available during the winter time, but we do have some recorded time series during a summer measuring campaign; and Salvadè et al. have attempted to verify the possibility of internal wave formation at 100 m depth by developing a three-layer model that also simulates the summer stratification.

Figure 15.22 shows the vertical profile of conductivity at 20°C, measured at Gandria on 20 August 1987; the three suggested layers and the mean values of the conductivity for each layer are indicated. Heaps [21, 22] already developed a three-layer model with constant or linear variable density; the layers represent the epilimnion, the thermocline zone and the hypolimnion. He used a spectral method to solve the equations in a rectangular basin with constant depth. Mortimer [38] analyzed the internal water movements of Windermere by means of a three-layer model of a rectangular basin worked out by Longuet–Higgins and inferred that some features of the movement in the lake could not be explained on the basis of a simple two-layer theory.

The aim here is to verify the occurrence of oscillations in the deep layer of the hypolimnion. Therefore, the basin is subdivided into three layers which correspond to the epilimnion, the upper part of the hypolimnion down to 100 m depth and its lower part.

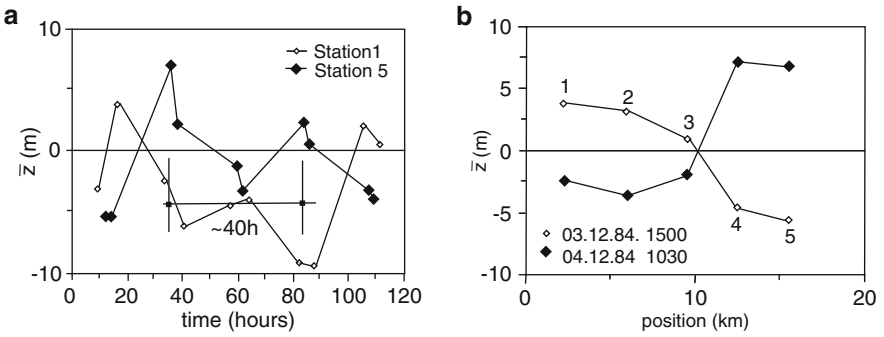

Fig. 15.21 (**a**) Time series of the mean vertical displacement of χ, relative to the stations at the two ends of the North basin of Lake of Lugano. Time is measured from 0 h of December 1984 onwards. Stipulated periods of approximately 40 h are also indicated; (**b**) Mean vertical displacement of χ along the thalweg of the North basin of Lake of Lugano, measured in the afternoon of 3 December 1984 and the following day. The two *curves* are snapshots which are 20.5 h apart, suggesting a period of 41 h (Courtesy [47]). © European Geosciences Union, reproduced with permission

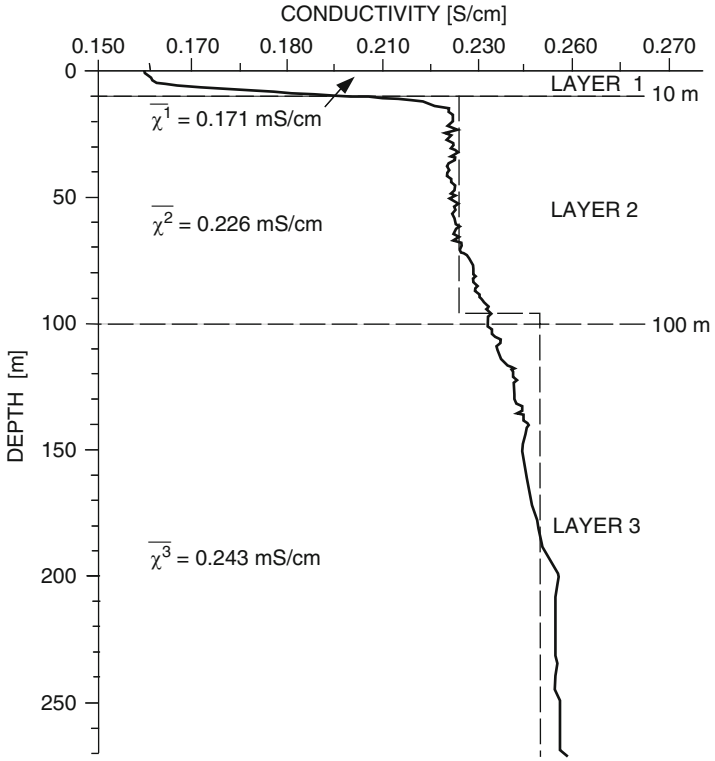

Fig. 15.22 Vertical profile of conductivity reduced to 20°C, measured in the North basin of Lake of Lugano on 20 Aug 1987. The three-layer approximation assumed in the calculations is also shown in *dashed lines* (Courtesy [47]). © European Geosciences Union, reproduced with permission

15.6 Linear Wave Dynamics of the Three-Layer Model

The three-layer model used here is depicted in Fig. 15.23. It constitutes two layers in the upper parts of the basin of constant depth and constant densities of different values $\rho_1 < \rho_2$. The interface between the upper most and middle layer is interpreted as the thermocline positioned at 10 m depth. The interface between the middle layer and the bottom layer defines the chemocline at 100 m depth. Moreover, the density ρ_3 differs from ρ_2, and for stable stratification we have $\rho_3 > \rho_2$. The interfaces are treated as impermeable, and their intersections with the basal topography define, in the vertical projection, annuli-type regions, in which only two, respectively, only one layer exist, see Fig. 15.23b.

We call H_1 and H_2 the constant thicknesses of the upper and middle layers and $H_3(x, y)$ the variable thickness of the third layer. Similarly, η_1, η_2, and η_3 denote the vertical displacements of the free surface and the interfaces, respectively; they are considered small in comparison to the layer thicknesses, so that in a linear treatment, the differences of the intersections of the functions $\eta_i(x, y, t)$ and the intersections at rest $\eta_i = 0$ $(i = 1, 2, 3)$ with the bathymetry are negligible. This implies that H_1, H_2, and H_3 are all time independent.

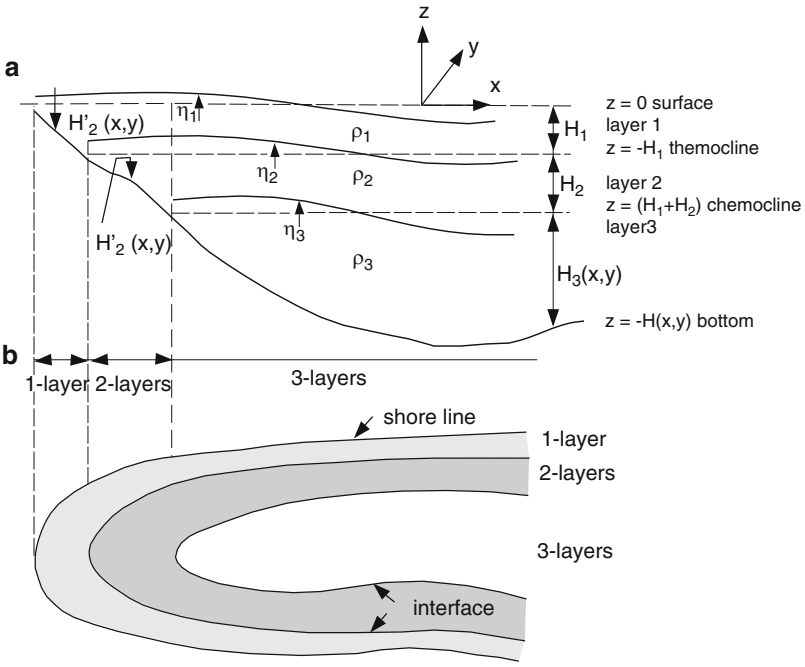

Fig. 15.23 (**a**) Vertical configuration of the three-layer model. (**b**) Intersections of the free surface with the ground (shoreline), of the mean thermocline with the bottom profile (thermocline shore) and of the mean chemocline (chemocline shore) with the ground

The linearized governing equations in the adiabatic and hydrostatic approximation are in each layer given by the continuity equation, the horizontal momentum equation and the hydrostatic pressure equation, viz.,

$$\left.\begin{aligned} &\mathrm{div}_H \boldsymbol{v}_i + \frac{\partial w}{\partial z} = 0, \\ &\frac{\partial \boldsymbol{v}_i}{\partial t} + \frac{1}{\rho_i}\,\mathrm{grad}_H\, p_i = 0, \\ &\frac{\partial p_i}{\partial z} = -\rho_i g. \end{aligned}\right\} \; i = 1, 2, 3. \tag{15.29}$$

Here, div_H and grad_H are horizontal operators and $\boldsymbol{v}_i$ is the horizontal velocity vector, p_i the pressure, ρ_i the density in the ith layer, and g the gravity constant. Boundary and transition conditions at the interfaces require the pressure to be continuous; so,

$$p = \begin{cases} 0, & \text{at } z = \eta_1(x, y, t), \\ \rho_1 g(H_1 + \eta_1 - \eta_2), & \text{at } z = -H_1 + \eta_2(x, y, t), \\ \rho_1 g(H_1 + \eta_1 - \eta_2) & \\ \quad + \rho_2 g(H_2 + \eta_2 - \eta_3), & \text{at } z = -(H_1 + H_2) + \eta_3(x, y, t). \end{cases} \tag{15.30}$$

These are simply the weights of the water columns above the respective interfaces. Integrating the layer pressure equations $(15.29)_3$ subject to the boundary conditions (15.30) and eliminating the pressure from the emerging relations and $(15.29)_2$ yields the horizontal momentum equations in the three layers in the form

$$\frac{\partial \boldsymbol{v}_i}{\partial t} + \begin{cases} g\,\mathrm{grad}_H \eta_1 = 0, & i = 1, \\ g\{\mathrm{grad}_H \eta_1 + \varepsilon_{21}\mathrm{grad}_H(\eta_2 - \eta_1)\} = 0, & i = 2, \\ g\{\mathrm{grad}_H \eta_1 + \varepsilon_{31}\mathrm{grad}_H(\eta_2 - \eta_1) + \varepsilon_{32}\mathrm{grad}_H(\eta_3 - \eta_2)\} = 0, & i = 3, \end{cases} \tag{15.31}$$

where

$$\varepsilon_{ij} = \frac{\rho_i - \rho_j}{\rho_j}, \;\; i, j = 1, 2, 3, \;\; j < i. \tag{15.32}$$

Because none of the variables η_i in (15.31) depends on z, the velocities in each layer are independent of z.

Next, we wish to integrate the continuity equation $(15.29)_1$ in each layer over the layer depth. To this end, the kinematic boundary conditions are needed at each interface. The resulting kinematic conditions are then used in the horizontal depth-integrated momentum equations. The derivation of the emerging depth-integrated equations is given as (15.34) below and left to the reader to verify in the following

Problem 15.1 *With reference to Fig. 15.23, show that the kinematic equations at the free surface and the layer interfaces take the forms,*

- *At the free surface* $$\frac{\partial \eta_1}{\partial t} + (\mathrm{grad}_H \eta_1) \cdot \boldsymbol{v}_1 - w_1 = 0, \tag{15.33a}$$
- *At the thermocline* $$\frac{\partial \eta_2}{\partial t} + (\mathrm{grad}_H \eta_2) \cdot \begin{Bmatrix} \boldsymbol{v}_1 \\ \boldsymbol{v}_2 \end{Bmatrix} - \begin{Bmatrix} w_1 \\ w_2 \end{Bmatrix} = 0, \tag{15.33b}$$
- *And at the chemocline* $$\frac{\partial \eta_3}{\partial t} + (\mathrm{grad}_H \eta_3) \cdot \begin{Bmatrix} \boldsymbol{v}_2 \\ \boldsymbol{v}_3 \end{Bmatrix} - \begin{Bmatrix} w_2 \\ w_3 \end{Bmatrix} = 0. \tag{15.33c}$$

Use these relations in the depth-integrated continuity equations to derive the following integrated balance of mass equations

$$\begin{aligned} &\frac{\partial(\eta_1 - \eta_2)}{\partial t} + \mathrm{div}_H \{\boldsymbol{v}_1(\eta_1 - \eta_2 + H_1)\} = 0, \\ &\frac{\partial(\eta_2 - \eta_3)}{\partial t} + \mathrm{div}_H \{\boldsymbol{v}_2(\eta_2 - \eta_3 + H_3)\} = 0, \\ &\frac{\partial \eta_3}{\partial t} + \mathrm{div}_H \{\boldsymbol{v}_3(\eta_3 + H_3)\} = 0. \end{aligned} \tag{15.34}$$

Verify these equations also by formulating mass balances for infinitesimal layer columns by assuming density preserving conditions. ◆

Equations (15.31) and (15.34) form together $6 + 3 = 9$ partial differential equations for the unknowns $\boldsymbol{v}_i$ (6) and η_i (3). They hold for a three-layer fluid system with free surface when effects of the rotation of the Earth are ignored and, therefore, can only hold for small lakes. They hold in the interior regions of a small lake when the water depth exceeds $H_1 + H_2$. In Fig. 15.23b, this is the un-shaded interior region. In the outer annulus-type regions, the two-layer and one-layer analogues must hold. Furthermore, the various regions with one, two and three layers must be connected by transition conditions. The formulation of these additional equations will be postponed. Here, we only add the remark that the usual procedure is to restrict computations to the region with the largest number of layers and to define the computational shore line as the intersection of the deepest layer surface with the bathymetric profile. However, this eliminates in the multi-layer case a large part of the near shore water mass and falsifies the results unduly.

Assuming harmonic oscillations

$$(\eta_i, \boldsymbol{v}_i) = (\bar{\eta}_i, \bar{\boldsymbol{v}}_i) \exp(i\omega t), \quad (i = 1, 2, 3), \tag{15.35}$$

Equation (15.31) can be solved for $\boldsymbol{v}_i$ and then the resulting relations substituted into (15.34).

Problem 15.2 *Show that this substitution leads to equations which, after dropping non-linear terms, take the forms*

$$\begin{aligned}
\mathrm{div}_H\left\{H_1 \mathrm{grad}_H\left(\eta+\eta'+\eta_3\right)\right\} &= -\frac{\omega^2}{g}\eta,\\
\mathrm{div}_H\left\{H_2 \mathrm{grad}_H\left(\delta_1\eta+\eta'+\eta_3\right)\right\} &= -\frac{\omega^2}{g}\eta',\\
\mathrm{div}_H\left\{H_3 \mathrm{grad}_H\left(\delta_2\eta+\delta_3\eta'+\eta_3\right)\right\} &= -\frac{\omega^2}{g}\eta_3,
\end{aligned} \tag{15.36}$$

where overhead bars have been dropped and

$$\begin{aligned}
&\eta := \eta_1-\eta_2, \quad \eta' := \eta_2-\eta_3,\\
&\delta_1 := 1-\varepsilon_{21}, \quad \delta_2 := 1-\varepsilon_{31}, \quad \delta_3 := 1-\varepsilon_{32}.
\end{aligned} \tag{15.37}$$

◆

These equations slightly generalize Longuet–Higgins' equations to variable depth and general geometry, see his equations in [38].

We now demonstrate how the annuli regions are handeled. To this end, (15.36) must be complemented by adding equations for the zones which have only one or two layers. These equations are easily derived by imposing adequate restrictions to (15.36).

- In the two-layer zone, we drop $(15.36)_3$, set $\eta_3 = 0$ and $\eta = \eta_2$ and replace the constant H_2 by the function $H_2(x, y)$. This leads to

$$\begin{aligned}
\mathrm{div}_H\left\{H_1 \mathrm{grad}_H\left(\eta+\eta_2\right)\right\} &= -\frac{\omega^2}{g}\eta,\\
\mathrm{div}_H\left\{H_2' \mathrm{grad}_H\left(\delta_1\eta+\eta_2\right)\right\} &= -\frac{\omega^2}{g}\eta_2.
\end{aligned} \tag{15.38}$$

- In the one-layer zone we drop $(15.36)_{2,3}$, set $\eta_3 = \eta_2 = 0$ and $H_1 = H_1(x, y)$ and then obtain from $(15.36)_1$

$$\mathrm{div}_H\left\{H_1' \mathrm{grad}_H \eta_1\right\} = -\frac{\omega^2}{g}\eta_1. \tag{15.39}$$

The complete system of partial differential equations to be solved, are now (15.36), (15.38), and (15.39). They must be complemented by adequate boundary conditions. These conditions will be chosen first as the no-flux condition of water through the lake bottom at the location of the free surface and interface intersections with the bathymetry. Second, in layers 1 and 2 the fluxes of water from the interior of the chemocline boundary to its exterior must be continuous. Similarly, in layer 1, continuity of the fluxes must also be observed in the upper-layer transition

through the thermocline boundary. These conditions are usually implemented by requesting that

$$\begin{aligned} \frac{\partial \eta_1}{\partial \boldsymbol{n}} &= 0, && \text{along the outer shore,} \\ \frac{\partial \eta_2}{\partial \boldsymbol{n}} = \frac{\partial \eta}{\partial \boldsymbol{n}} &= 0, && \text{along the intersection} \\ & && \text{of the chemocline with the ground,} \\ \frac{\partial \eta_3}{\partial \boldsymbol{n}} = \frac{\partial \eta}{\partial \boldsymbol{n}} = \frac{\partial \eta'}{\partial \boldsymbol{n}} &= 0, && \text{along the intersection,} \\ & && \text{of the chemocline with the ground,} \end{aligned} \tag{15.40}$$

in which $\partial(\cdot)\partial \boldsymbol{n}$ denotes the derivative of $(\cdot)$ normal to the respective boundary line. This formulation is due to Salvadè et al. [47]. They call it the THree-layer Variable Depth Complete model (THVDC).

15.7 Computational Results and Their Comparison with Field Data

Salvadè et al. [47] are not very explicit, how the eigenvalue problem (15.36), (15.38)–(15.40) was solved. They state: 'The THVDC-model-equation system has been discretized using the finite difference method ...'. The eigenvalues and eigenvectors of the final matrix have been calculated according to the method of Martin, Parlett, Peters, Reinsch Wilkinson, see [13], introducing some modifications to reduce the computer memory occupation. For the North basin of the Lake of Lugano the bathymetric grid already used by Hutter et al. [28] was utilized. It is a rectangular grid with 23×66 squared cells having 250 m side-length. The depths η_1, η_2, η_3 and η are defined in the centre of each square cell, whereas the velocity $\boldsymbol{v}\,(u, v)$ is defined in the middle of the cell sides. This corresponds to an Aracawa C-grid.

Assuming $H_1 = 10$ m and $H_2 = 100$ m, there are 309 three-layer cells, 145 two-layer cells and only 2 one-layer cells, since the basin has very steep shores. The resulting eigenvalue system has therefore 1,219 unknowns. It is interesting to note that, if the choice of the two-layer model described by Hutter [26] would have been followed, i.e. if the zones with less than three layers would have been neglected, then 13% of the total basin volume would have been neglected.

Table 15.2 collects the parameter values used in the model. The thermocline is assumed to be at 10 m and the chemocline at 100 m depth; the other parameters correspond to the average values measured in August 1985. The mineralization has been obtained from conductivity measurements through a calibration plot determined by the Laboratorio di Studi Ambientali and the density has been calculated according to the Wilson–Bradley formula, see Chap. 10 in Volume I. Table 15.3 lists the values of the periods calculated by the THVDC model and, as a comparison, those obtained by Hutter et al. [28] using the two-layer model (10 m thick first layer with a mean temperature of 21°C, $\varepsilon_{12} = 0.194 \times 10^{-2}$).

Table 15.2 Parameters used in the model for the three layers, where ρ is the density and ε_{ij} are defined in (15.32) for the North basin of Lake of Lugano

Layer	1	2	3
Depth (m)	0–10	10–100	Variable
Conductivity at 20°C [$\mu s\,cm^{-1}$]	157	216	232
Salinity [$mg\,l^{-1}$]	140	201	217
Temperature [°C]	21.0	8.1	5.4
$\rho\,[kg\,m^{-3}] - 1{,}000$	-1.8210	8.2890×10^{-2}	2.1610×10^{-1}
$\varepsilon_{ij} = (\rho_i - \rho_j)/\rho_j$	$\varepsilon_{21} = 0.1904 \times 10^{-2}$	$\varepsilon_{31} = 0.2037 \times 10^{-2}$	$\varepsilon_{32} = 0.1331 \times 10^{-3}$

Table 15.3 Periods of the first ten modes of oscillation for the North basin of Lake of Lugano predicted by the THVDC model, compared with the values obtained by the two-layer TVD model stated in Hutter et al. [28]

Mode	Period (h) THVDC	Period (h) TVD
1	35.1	
2	25.1	26
3	16.7	
4	11.4	11.6
5	11.0	
6	9.5	
7	8.1	8.4
8	7.6	
9	6.5	6.7
10	6.2	

15.7.1 Mode 1[6]

Figure 15.24 displays free surface and interface elevations of the first mode of oscillation with a period of 35 h. The amplitudes are normalized to a 1 m maximum of the thermocline. The solid lines represent points which oscillate with the same amplitude (isolines); the dashed lines oscillate with a phase opposite to the solid lines. Therefore, the chemocline and the thermocline oscillate with opposite phases. The oscillation amplitude of the chemocline is about 10 times greater than that of the thermocline. Mode 1 is, therefore, the resonant oscillation mode of the chemocline. Large water oscillations at depths much deeper than the thermocline have already been observed by Mortimer [37] and calculated by Heaps [21]. They can explain the eddy diffusion of heat and salt content in deep waters during the summer thermal stratification.

If we consider the basin as a rectangular channel with constant depth and apply the relations of Longuet–Higgins in [38] with the parameters of Table 15.2, we

[6] The ensuing text follows very closely that of Salvadè et al. [47].

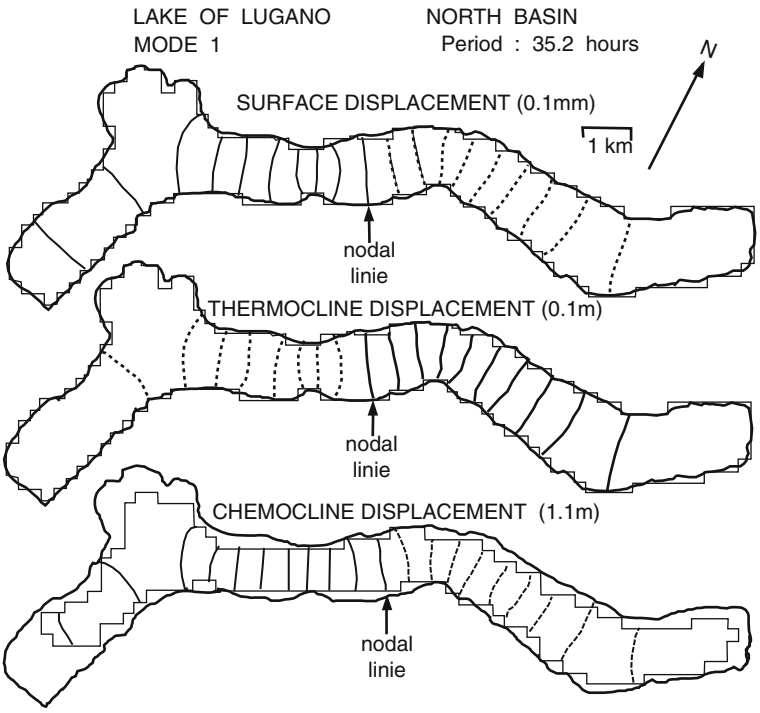

Fig. 15.24 Isolines of elevation amplitude predicted for mode 1 of the three-layered North basin of lake of Lugano. *Solid lines* and *dotted lines* indicate elevations which are in counter phase relative to each other. The amplitude value between two successive isolines is given in parentheses. Note also the areal reduction of the third layer (Courtesy [47]). © European Geosciences Union, reproduced with permission

obtain a period of about 39 h and a ratio between the oscillation amplitudes of the chemocline and the thermocline of about −20 (the negative sign indicates the phase opposition). These values are of the correct order of magnitude but not in very close proximity to those of the present model: The higher value of the period obtained this way (39 h vs. 35.1 h in Table 15.3) is obtained because we assumed as channel length that at the surface, rather than that at the depth of the chemocline, which is shorter. The mean depth of the third layer is, however, not well defined: estimation of a proper length for the analytical model is thus difficult. To treat the basin as if it were a rectangular channel is therefore a rough approximation. Notice also that first and second-order vertical baroclinic modes have Rossby radii of 4.1 and 2.5 km; therefore, having neglected the rotation of the Earth at the depth of the chemocline (mean width ca. 1 km) can somewhat modify the values of the period.

In 1979, a field campaign was carried out in the North basin of the Lake of Lugano. Figure 15.25 shows the positions of the measuring stations and the layout

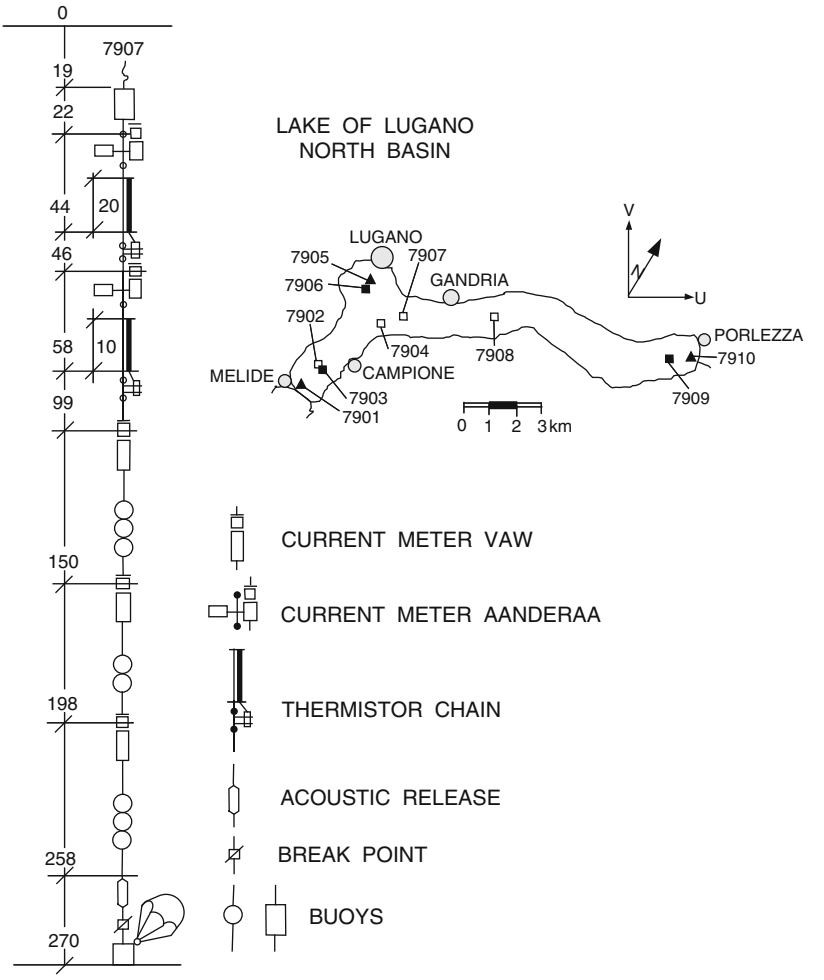

Fig. 15.25 Example of a measuring station moored in the field campaign of the North basin of Lake of Lugano in 1979. The instrument depths are indicated and the map shows the station positions (Courtesy [47]). © European Geosciences Union, reproduced with permission

of station No. 7907. The measurements were discussed by Hutter et al. [28] and by Mysak et al. [43]. Figure 15.26 shows some spectra of the temperature measured at different depths at station 7902 moored near the south end and station 7907 toward the middle of the basin.[7]

[7] For the spectral analysis the method suggested by Bloomfield [6] was followed: from the time series the best linear trend was subtracted, to avoid leakage, its extremes were rounded by a cosine bell window which covers 10% of the time series at each side; after applying the Fourier transform, the periodogram calculation was carried out through a Daniell spectral window developed over 13

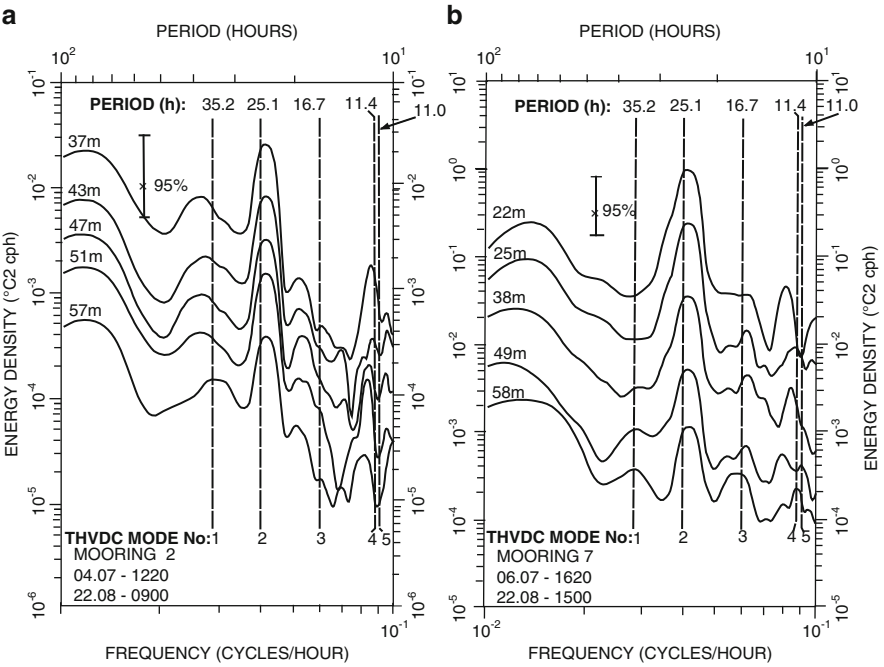

Fig. 15.26 (**a**) Spectral plots of temperature time series measured in the North basin of Lake of Lugano at different depths, recorded at station 7902 from 4 July to 22 August 1979. *Vertical lines* indicate the periods predicted by the model. (**b**) Same as panel (**a**), but for station 7907 from 6 July to 22 August. The time series at depth indicate the occurrence of an oscillation with a period of 35 h (Courtesy [47]). © European Geosciences Union, reproduced with permission

Beside the 24 h main peak, interpreted by Hutter et al. [28] as the period of the fundamental mode of thermocline oscillation, one can well see a peak at roughly 35 h which corresponds to the first mode of oscillation of the THVDC model. The peak width could be due to a variation of density and stratification with consequent period variation. In the spectral analysis reported by Hutter et al. [28], this peak is not present as the time series were filtered to remove the oscillations which had a period greater than 30 h. On the other hand, Mysak et al. [43] considered oscillations with greater periods (= 75 h).

The spectral analysis of temperatures measured at station No. 7907, (Fig. 15.26b) moored near the nodal line, shows that the 35 h peak becomes greater with increasing depth, as predicted by the model. Unfortunately, these are the deepest measurements carried out in 1979: they reach only a depth of 58 m, which corresponds to

terms. The 95% limits of the confidence interval turn out to be those corresponding to 15 degrees of freedom of the χ^2-distribution. Moreover, one must consider in the spectral analysis that the temperature sensors were at their sensitivity limit for detecting small variations, especially for the time series at depth.

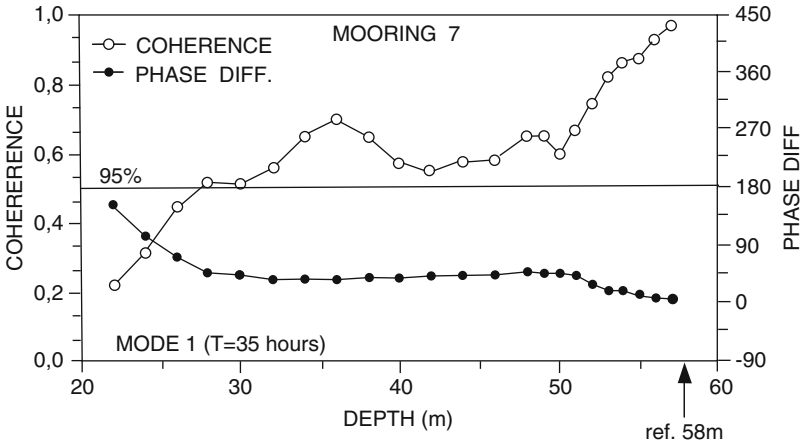

Fig. 15.27 Coherence and phase difference for mode 1, between the temperature time series measured in the North basin of Lake of Lugano at 58 m depth and the other series measured at smaller depths. The deeper series and those close to the thermocline tend to oscillate at counter phases (Courtesy [47]). © European Geosciences Union, reproduced with permission

about half of the assumed middle layer. Figure 15.27 shows the coherence and the phase difference between the temperatures measured at the deepest point of the thermistor chain (58 m) and that at different depths. The phase difference tends to 180° as predicted by the model. One should note, however, that the coherence gives low values and therefore this value of the phase difference is not reliable with a high degree of statistical confidence. To obtain more reliable conclusions we should not only analyze temperature measurements, but also conductivity measurements over the whole depth. This would enable us to build and to analyze time series of constant density surfaces, which better represent the internal wave oscillations.

The free surface displacement, which is in counter phase with respect to the thermocline displacement is of the order of 1 mm (in agreement with the model of Longuet–Higgins which gives $(\eta_1/\eta_2 = -0.0006)$ and therefore analysis of possible limnigraph recordings to detect this oscillation mode is practically impossible with presently available instruments. Figure 15.28 displays the velocity distribution for mode 1 over the three layers. It shows the instant of maximum displacement. Plots of Figs. 15.28 and 15.24 correspond therefore to times which are a quarter period apart. The maximum velocity arises close to the displacements nodal line. The middle layer is in counter phase relative to the other two layers.

The only reliable velocity measurements recorded in the 1979 campaign were those of the current meters of station No. 7908 (Fig. 15.25) which was moored near the nodal line of mode 1. The upper most current meter of this station was at a depth of 15 m, i.e. in the lower metalimnion zone (unfortunately the depth values are not reliable; they could have an error of as much as 5 m). We assume that it shows the current of the upper layer. The second current meter was placed at a depth of 39 m which corresponds to the middle zone of the second layer. The third current meter

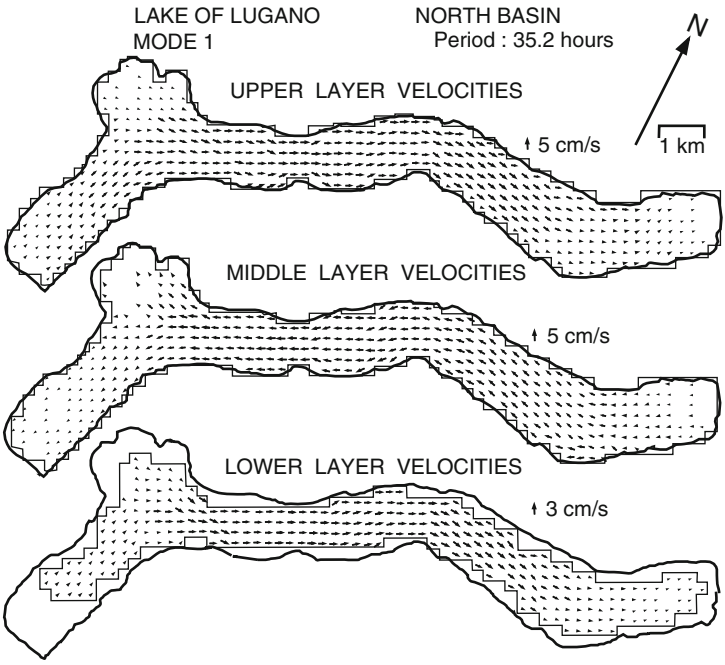

Fig. 15.28 Calculated mean velocity distributions in the three layers of the North basin of Lake of Lugano for mode 1. *Top* and *bottom* velocities are opposite to the current in the middle layer, but velocity amplitudes are comparable in magnitude (Courtesy [47]). © European Geosciences Union, reproduced with permission

was placed at 146 m and the fourth at 267 m. As the instruments are sensitive only to a velocity greater than 2 cm s^{-1}, we obtained continuous measurements for the first current meter, but only intermitted ones for the second and sporadic recordings for the other two. Unfortunately, due to a mechanical failure we were able to obtain only 21 days of measurements.

Figure 15.29 shows the velocity vectors measured on July 23 1979 (u is directed along the thalweg). As predicted by the model, the current in the middle layer is in counter phase with respect to the other two layers. The deepest current meter (267 m) did not record a current on that day, as its value was probably below its sensitivity limit. However, there must have been a small current, as the direction detected by the instrument vane was not constant. The arrow in Fig. 15.29 at 267 m depth indicates the current direction at 12 h. Within certain limits the current value at this depth is in phase with respect to that detected by the instrument placed at 146 m and therefore the whole lower layer moves in the same direction, as the model predicts. It must, however, be noted that the direction shown by the current meter placed at 267 m also has the same value after 18 h. This does not agree with the prediction of the model, but it could also be due to the small current value which did not succeed in rotating the vane. Figure 15.30a shows the spectral analysis of the

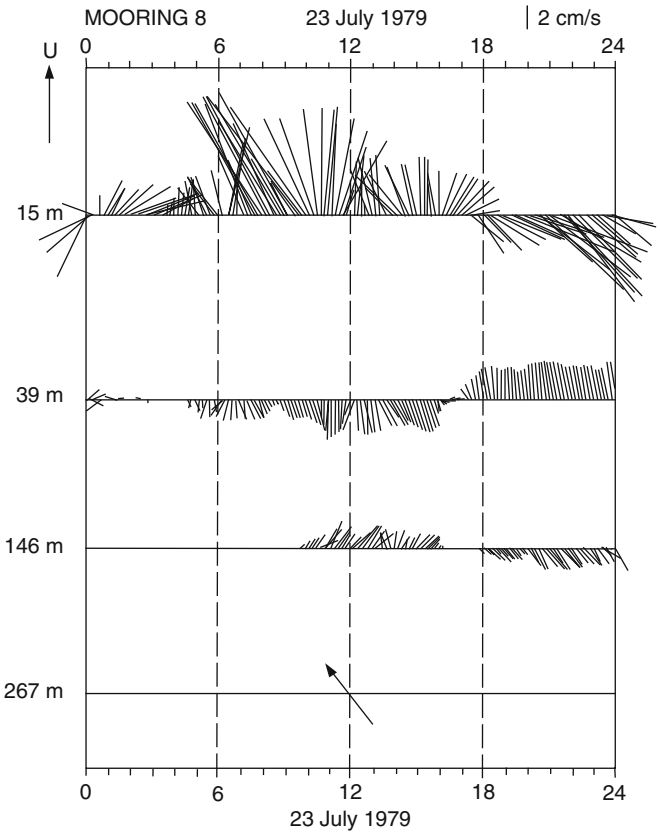

Fig. 15.29 Stick plot diagrams of the velocities measured at mooring 7908 in the North basin of Lake of Lugano at Gandria on 23 July 1979. The *arrow* at 267 m indicates the current direction at 12 h; the current speed there was below the instrument threshold. The three-layer structure is evident (Courtesy [47]). © European Geosciences Union, reproduced with permission

u velocity component, at the depths of 15 and 39 m. The confidence interval limits of 95% are clearly very large due to the short lengths of the time series. In spite of this, the 35 h peak is still clearly visible. As shown in Fig. 15.30b, the coherence value between the time series relative to the 35 h period is above the 95% limit of the confidence interval. Even the phase difference is in agreement with the model prediction.

15.7.2 Mode 2

Figure 15.31 shows the lines of equal amplitude for mode 2 with a 25-h period. The oscillation amplitude of the chemocline is only twice that of the thermocline. This

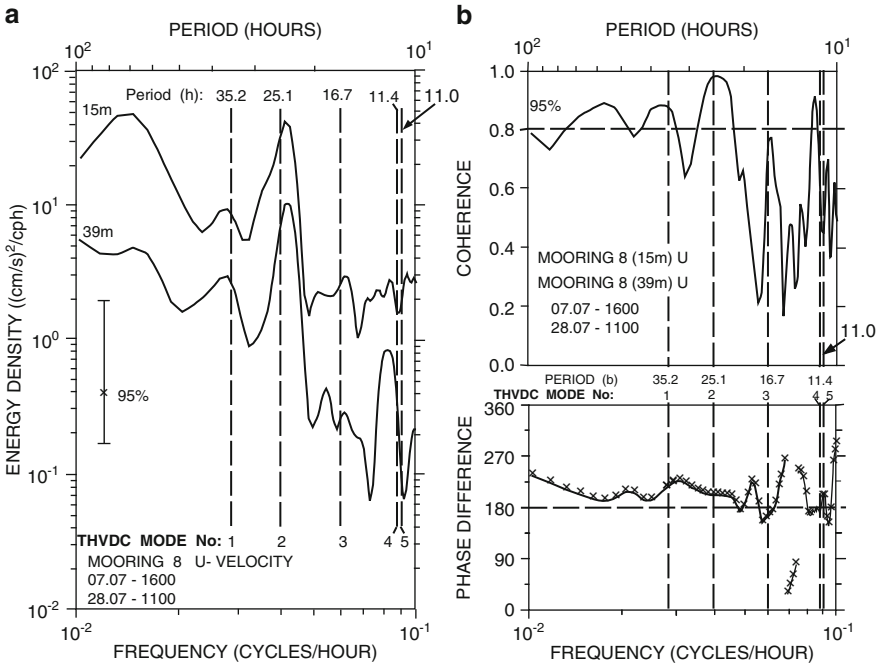

Fig. 15.30 (**a**) Spectral plot of the velocity components along the thalweg of the North basin of Lake of Lugano, measured at two different depths at mooring 7908 at Gandria, from 7 July to 28 July 1979. The confidence limit is broader than in Fig. 15.26 because the time series is shorter. The model predicts correctly the 35-h peak at 39-m depth. (**b**) Coherence and phase difference between the two velocity components analyzed in panel (**a**) (Courtesy [47]). © European Geosciences Union, reproduced with permission

mode can be considered as the resonant oscillation mode of the thermocline, as it has a single nodal line. Thermocline and chemocline oscillate with the same phase but are in counter phase with the free surface. The temperature oscillation measured by the deepest thermistor (58 m) of Station 7907 and the temperature measured at different depths (not illustrated here), relative to the same period, demonstrate in-phase relations, in agreement with the model predictions. This oscillation mode is described in detail by Hutter et al. [28]. The period value calculated by THVDC is smaller than that calculated for the two-layer model and therefore nearer to the value obtained by the spectral analysis of temperatures near the thermocline. Figure 15.26 shows a dominant peak at the 24-h period, which is slightly smaller than the value predicted by the models. In all probability, this is forced oscillation due to the relatively strong daily wind cycle setting-in in the mid afternoons, to which the lake responds with large amplitude oscillations as its period is near resonance (see [26]).

As already mentioned when discussing mode 1, by applying the rectangular channel model of Longuet–Higgins in [38], we obtain a value of 22 h for the period, with an oscillation of the thermocline in phase with that of the chemocline and

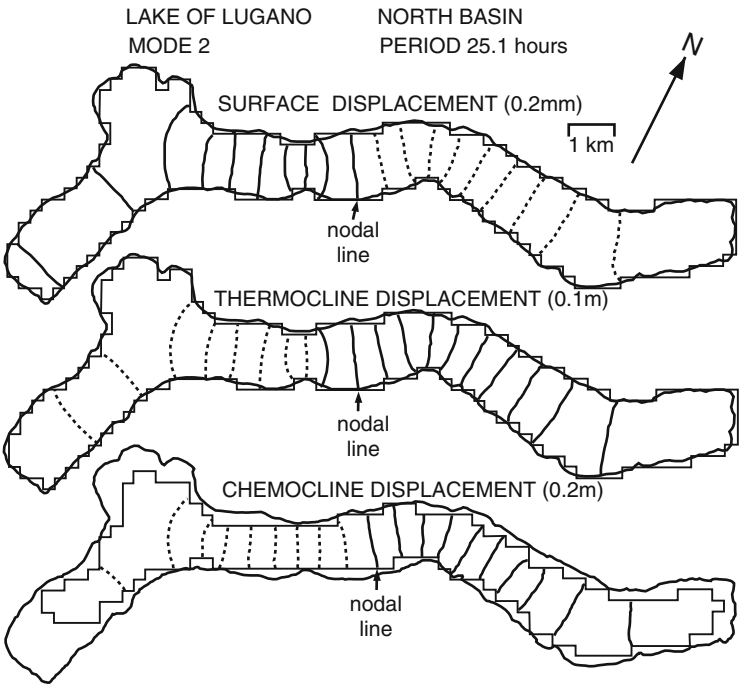

Fig. 15.31 Calculated isolines of elevation amplitude for mode 2 in the North basin of stratified Lake of Lugano at the free surface, the thermocline and the chemocline. The lake responds with large amplitude oscillations as its period is near resonance (see [26]) of a periodic 24-h wind signal (Courtesy [47]). © European Geosciences Union, reproduced with permission

with a ratio $\eta_2/\eta_3 \simeq 1$ (according to the THVDC model the ratio is about 0.5). Figure 15.32 shows the velocity distribution for this mode. The middle layer velocities in the central part of the lake are in phase with those of the epilimnion, but they contrast with those of Fig. 15.30b. Moreover, the model predicts very small velocities in this layer, about 30 times smaller than the epilimnion velocities, and this is in contrast with the spectral analysis shown in Fig. 15.30a. It is likely that the model could correctly predict velocities pointing in the opposite direction in the second layer, if consistent density values and thicknesses of the layers were adopted. (Recall that because of lack of data a complete set of data was composed from observations at different times, even different years).

15.7.3 Mode 3

The isolines of elevation amplitudes for the free surface and the thermo- and chemoclines as predicted by the model have two nodal lines for each oscillating surface,

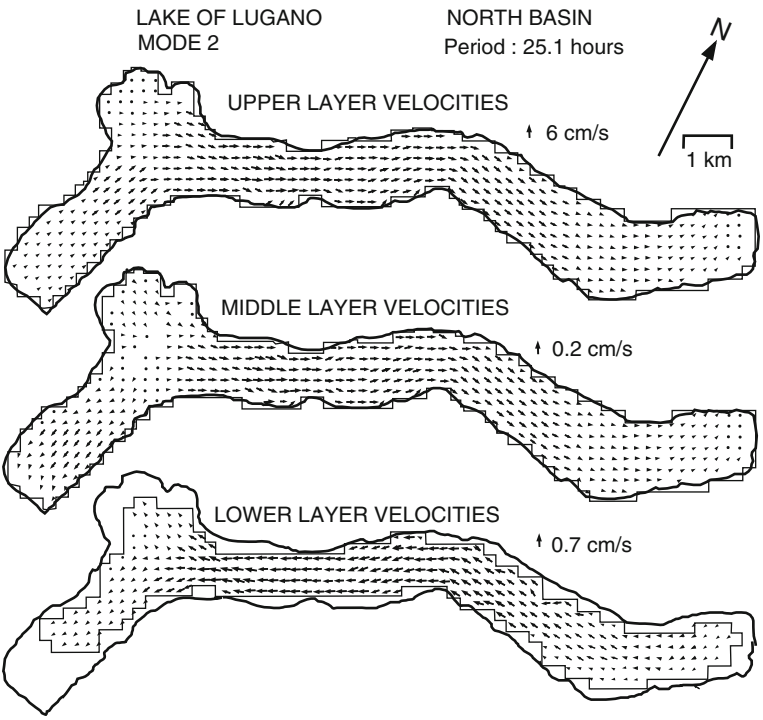

Fig. 15.32 Calculated mean velocity distributions in the three layers for mode 2 in the North basin of stratified Lake of Lugano. *Top* and *middle* layer velocities are opposite to the current in the *bottom* layer, but the velocities in the *top* layer are 16–20 times larger than in the lower layers (Courtesy [47]). © European Geosciences Union, reproduced with permission

and it is interesting to note that they are not exactly at the same position (Fig. 15.33). This relative shift of the nodal lines is likely due to the fact that the three layers have different boundaries defined by the shore, the thermocline shore and the chemocline shore, respectively, see Fig. 15.23. Chemocline and thermocline, and thermocline and free surface, oscillate in counter phase. As the oscillation amplitude of the chemocline is more than 10 times larger than that of the thermocline and the free surface amplitude is even a factor of 1,000 smaller, this oscillation mode can be considered as the second resonant mode of the chemocline. It is, therefore, an oscillation which increases its amplitude with increasing depth; the observations seem to confirm this, as shown in Fig. 15.26b, but not in Fig. 15.26a (the spectral analysis of the temperature at 58 m of station 7907 shows a relative maximum which corresponds to that of mode 3). Figure 15.34 shows the calculated velocity distribution. Station 7908 was placed in the nodal zone for the velocities of this mode, and this may explain the absence of the corresponding peak in the observations, as shown in Fig. 15.30a.

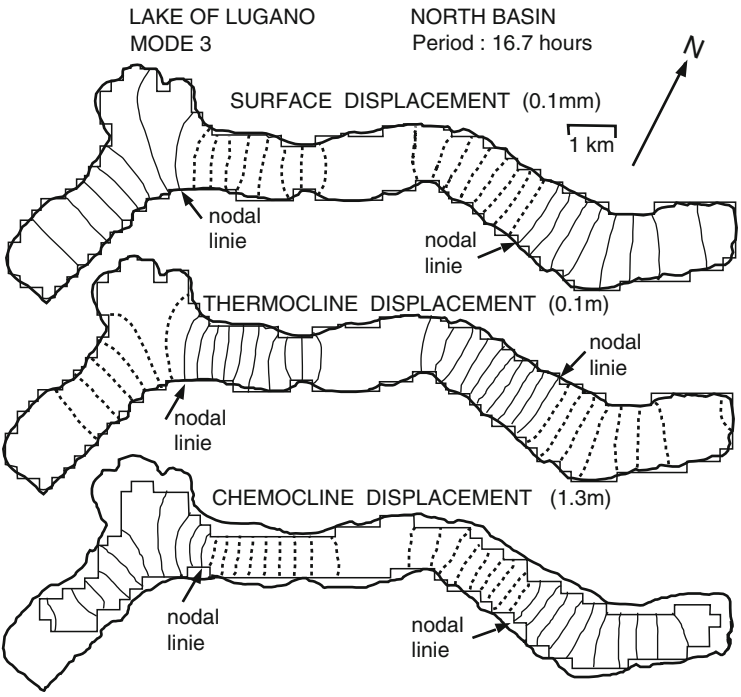

Fig. 15.33 Calculated isolines of elevation amplitude for mode 3 in the North basin of stratified Lake of Lugano at the free surface, the thermocline and the chemocline. Note, the number of nodal lines in the three layers is the same, but their positions vary (Courtesy [47]). © European Geosciences Union, reproduced with permission

15.7.4 Modes 4 and 5

In mode 4, the free surface and the thermocline have two nodal lines, but the chemocline oscillates with three nodal lines. In mode 5, also the thermocline shows three nodal lines (these modes are not illustrated). The positions of the nodal lines of the three surfaces are no longer the same. This should be due to the different extensions of the three interfaces: in a test of the model performed on a basin having three layers over the whole computation zone (same extension of the three interfaces), the locations of the nodal lines are the same.

According to the model, the two oscillation modes have very similar periods. Mode 4 should, however, correspond to the second resonant mode of the thermocline, and it is nearly coincident with the value calculated by Hutter [27] and Hutter et al. [28]; mode 5 should correspond to the third resonant mode of the chemocline. In mode 4, the model predicts a period value of about 11.4 h. The spectral analysis of the observations shows a distinct 12-h peak which could be the first higher harmonic response of the 24-h resonance: because of its large amplitude, this wave should be non-linear (see [23]). The high 12-h peak may also hide the 11.4 h peak.

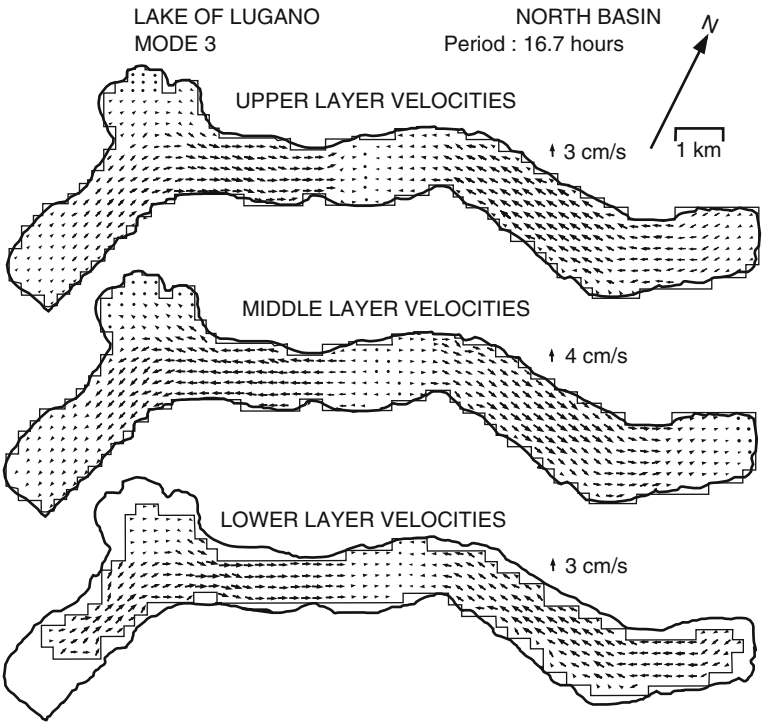

Fig. 15.34 Calculated mean velocity distributions in the three layers of the North basin of stratified Lake of Lugano for mode 3. *Top* and *bottom* velocities are opposite to the current in the middle layer, but their magnitude in all three layers is approximately the same (Courtesy [47]). © European Geosciences Union, reproduced with permission

Another source of the disagreement between the model predictions and the observations could also be the choice of the parameters, the relatively coarse discretization process and the neglect of the effects of the rotation of the Earth. Figure 15.30b shows a well pronounced peak at about 12 h of the velocity measured at 39 m, which has no correspondence in the measurements of the current meter at 15 m but which seems to be in agreement with the velocity distribution of mode 4 (not illustrated).

15.8 Model Sensitivity

The results reported in the last section are based on a specific selection of system parameters. Whilst these are generally chosen according to judicious evaluation, it became apparent that often different choices may be similarly justified. It is, therefore, recommended that parameters are slightly varied about their most probable values to see, how the system reacts to such variations. This will be done now. The

Table 15.4 Calculated seiche periods of the three-layer North basin of the Lake of Lugano for various different parameter selections. The parameter selection of the basic run is given in Table 15.2. The ten largest computed periods (in hours) are listed when the parameters in row 2 deviate from the conditions of Tables 15.2 and 15.3. Column 2 lists the periods of the basic run (see Table 15.3).

Model		Calculated periods [h]				
	Parameters Table 15.3	$H_1 = 12$ $H_2 = 88$ [m]	$H_1 = 10$ $H_2 = 100$ [m]	$T_1 = 22$ [°C]	$T_1 = 8.5$ [°C]	$S_3 = 230$ [mg l^{-1}]
1	35.1	35.2	34.0	34.9	33.0	34.1
2	25.1	23.1	25.1	23.9	24.8	24.9
3	16.7	16.7	16.2	16.6	15.6	16.1
4	11.4	11.1	11.4	11.1	11.3	11.3
5	11.0	10.4	10.7	10.7	10.4	10.7
6	9.5	9.5	9.2	9.4	8.9	9.2
7	8.1	7.6	8.1	7.7	8.0	8.0
8	7.6	7.5	7.4	7.5	7.1	7.3
9	6.5	6.2	6.5	6.2	6.5	6.5
10	6.2	6.0	6.0	6.1	5.8	6.0

periods that are predicted by the model when modifying the parameter values are listed in Table 15.4. In column 2, the values calculated when using the parameters of Table 15.2 are listed for reference. On the top of each column the value of the modified parameters are indicated. Note that the parameter modifications are not always consistent because, for example, a change of the upper layer thickness would involve also a change of mean temperature, of salinity and therefore also of the density value. This was not done, since our aim was to test the model sensitivity to the change of single parameters. One can see, for example, that if one increases the epilimnion thickness or its temperature, the periods of modes 2 and 4 decrease, as they are typical oscillation modes of the thermocline. On the other hand, if one increases the thickness of the middle layer, the periods of modes 1 and 3 decrease as they correspond to the oscillation modes related to the chemocline. The period of mode 2 (fundamental mode of the thermocline) is almost independent of the parameter modifications which concern the lower zones of the hypolimnion; as asserted by Mortimer [38] the measurement of this period cannot give any information about what happens at greater depth.

15.9 Inferences

Knowledge of the behaviour of the chemical stratification, assumed to change the density at about 100-m depth in the North basin of the Lake of Lugano, is fundamental for the restoration projects of the eutrophic state of the lake. The vertical oscillations may infer inaccurate values of the mean salt contents of the basin, when calculated from single measured profiles. The model predicts oscillation amplitudes

of the chemical stratification of more than 10 m, if they are normalized to 1 m amplitude of the thermocline oscillations. However, the measurements of the 1979 field campaign show thermocline oscillations larger than 5 m. It is, therefore, easy to infer that deep oscillations should reach very large amplitudes, which the model cannot describe, as it makes use of linearized equations. These deep oscillations could influence the eddy diffusion of heat and substances, which makes it difficult to determine the value of the vertical eddy diffusion coefficient necessary for restoration models. The chemical stratification indicates that the winter water circulation of the North basin is limited to the upper 100 m. It is not clear what might be the effects on the lake of a deeper mixing and under what meteorological conditions they might occur.

As described above, some experimental data can be well interpreted by a three-layer model. Other data, however, indicate a behaviour which does not seem to be correlated with the chemical stratification. Moreover, it is not clear how the meteorological conditions influence the chemocline.

More detailed knowledge of the chemical stratification of the basin should involve the simultaneous measurements of the temperature and conductivity profiles, recorded at several places and over long periods of time.

15.10 Summary

In this chapter, conditions of the generation and persistence of higher order baroclinic dynamics in lake systems were in focus. The influence of the rotation of the Earth was ignored as the vertical mode structure due to vertical density stratification was primarily studied. Two qualitatively distinct stratifications were looked at:

- A two-layer fluid system, in which the density jump between two homogeneous fluid layers with different densities was smoothed by a continuous, but relatively abrupt density change from the lighter, upper fluid layer to the heavier, lower layer. Laboratory experiments were conducted in which vertical interface–displacement–time series were measured. An initially solitary wave signal was impinging a triangular obstruction, which was fissured into a reflected and a transmitted signal and both signals were recorded in the respective regions. These signals were compared with computational results obtained from a weakly nonlinear wave theory. Both theory and experiments showed that a pure soliton of the fundamental vertical mode – the only existing baroclinic mode in a two-layer system with sharp interface – could be split into several vertical modes; in the experiment, the fundamental and first higher order baroclinic modes were clearly identified. This implies that *a continuous transition of the density through the metalimnion from a lighter epilimnion to a heavier hypolimnion in a lake gives rise to a distribution of the fundamental baroclinic motion among several, also higher order modes*. Two layers are too coarse to capture these.
- A lake may be stratified approximately in three layers, not simply because of a better resolution of the density variation through the metalimnion, but because of a distinct mineralization of the water in different layers. This happens in Lake

of Lugano, which is 'dead' below 50 m and exhibits a small but abrupt density change at the 100-m depth. Here, a theoretical model on the basis of a three layer model with sharp thermo- and chemoclines gives rise to two baroclinic vertical modes. Special in this situation is that the three different layers extend in the projection into the horizontal plane over distinct regions, which implies that the distributions of the interface displacement eigenfunctions of the chemocline and thermocline are rather distinct from one another. Verification of the computational results by field experiment is not easy because of likely incomplete deployment of instruments, but in the Lake of Lugano case sufficient coincidences were found that the computed model response was convincingly substantiated.

As mentioned above, the influence of the rotation of the Earth was ignored and did not play a role in the examples considered. In the next chapter, we shall show examples where higher order baroclinicity and rotation dependent horizontal dynamics interplay with one another.

References

1. Antenucci, J.P. and Imberger, J.: Energetics of long internal gravity waves in large lakes. *Limnol. Oceanogr.* **46**(7), 1760–1773 (2001)
2. Antenucci, J.P. and Imberger, J.: On internal waves near the high-frequency limit in an enclosed basin. *J. Geophys. Res*, **106**, C10, 22465–22474 (2001)
3. Appt, J., Imberger, J. and Kobus, H.: Basin-scale motion in stratified Upper Lake Constance. *Limnol. Oceanogr.*, **49**(4), 919–933 (2004)
4. Bäuerle, E.: Internal free oscillations in the Lake of Geneva. *Ann. Geophysicae*, **3**, 199–206 (1985)
5. Benney, D.J.: Long non-linear waves in fluid flows. *J. Math. Phys.*, **45**, 52–63 (1966)
6. Bloomfield, P.: *Fourier analysis of time series: An introduction*. John Wiley, New York (1976)
7. Boegman, L., Imberger, J. Ivey, G.N. and Antenucci, J.P.: High-frequency internal waves in large stratified lakes. *Limnol.Oceanogr.*, **48**(2), 895–919 (2003)
8. Boegman, L., Ivey, G.N. and Imberger, J.: The energetics of large-scale internal wave degeneration in lakes. *J. Fluid. Mech.*, **531**, 159–180 (2005)
9. Choi, W. and Camassa, R.: Fully nonlinear internal waves in a two-fluid system *J. Fluid Mech.*, **396**, 1–36 (1999)
10. Diebels, S.: *Nichtlineare, interne Wellen im Zweischichtenfluid auf der f-Ebene: Theorie und numerische Berechnungen*. Diploma Thesis, Tech. University Darmstadt (1991)
11. Diebels, S., Schuster, B. and Hutter, K.: Nonlinear internal waves over variable topography. *Geophys. Astrophys. Fluid Dyn.*, **76**, 165–192 (1994)
12. Djordjevic, V.D. and Redercopp, L.G.: The fission and disintegration of interval solitary waves moving over two dimensional topography. *J. Phys. Oceanogr.*, **8**, 1016–1033 (1978)
13. Engeln-Müllges, G. and Reuter, F.: *Formelsammlung zur numerischen Mathematik mit Standard-FORTRAN-Programme*, Bibliographisches Institut Mannheim (1984)
14. Gear, J.A. and Grimshaw, R.: A second-order theory for solitary waves in shallow-fluids. *Physics of Fluids*, **26**, 14–29 (1983)
15. Gloor, M., Wüest, A. and Münnich, M.: Benthic boundary mixing and resuspension induced by internal seiches. *Hydrobiologia*, **284**, 59–68 (1994)
16. Gòmes-Giraldo, A.J., Imberger, J. and Antenucci, J.P.: Spatial structure of the dominant basin-scale internal waves in Lake Kinneret. *Limnol.Oceanogr.*, **51**(1), 229–246 (2006)

17. Grimshaw, R.: Evolution equations for weakly nonlinear, long internal waves in a rotating fluid. *Studies in Applied Mathematics*, **73**, 1–33 (1985)
18. Grimshaw, R., Pelinovsky, E. and Talipova, T.: The modified Korteweg-de Vries equation in the theory of large-amplitude internal waves. *Nonlinear Processes in Geophysics*, **4**, 237–250 (1997)
19. Grimshaw, R., Pelinovsky, E. and Talipova, T.: Solitary wave transformation in a medium with sign-variable quadratic nonlinearity and cubic nonlinearity. *Physica D*, **4**, 237–250 (1999)
20. Grue, J., Jensen, A., Rusas, P.O. and Sveen, J.K.: Properties of large amplitude internal waves. *J. Fluid Mech.*, **380**, 257–278 (1999)
21. Heaps, N.S.: Seiches in a narrow lake, uniformly stratified in three layers. *Geophys. Suppp. R. Astron. Soc.*, **5**, 134–156 (1961)
22. Heaps, N.S.: Development of a three-layered spectral model for the motion of a stratified shelf sea. I. Basic equations. In:*Physical Oceanography of Coastal and Shelf Seas* (ed.: B. Johns). Amsterdam Elsevier, 386–400 (1983)
23. Horn, W., Mortimer, C.H. and Schwab, D.J.: Wind-induced internal seiches in the Lake of Zürich observed and modelled. *Limnol. Oceanogr.*, **31**(6), 1230–1252 (1986)
24. Hüttemann, H.: *Modulation interner Wasserwellen durch Variation der Bodentopographie*. Master thesis, Fachbereich Mechanik Technische Hochschule Darmstadt (1997)
25. Hüttemann, H. and Hutter, K.: Baroclinic solitary water waves in two-layer fluid system with diffuse interface. *Experiments in Fluids*, **30**, 317–326 (2001)
26. Hutter, K.: Fundamental Equations and Approximations. In: *Hydrodynamics of Lakes. CISM Courses and Lectures, No.286*, Springer, New York, 1–76 (1984)
27. Hutter, K. (with contributions by Bäuerle, E., Salvadè, G., Spinedi, C. and Zamboni, F.): Large scale water movements in lakes. *Aquatic Sciences*, **53**, 100–135 (1991)
28. Hutter, K., Salvadè, G. and Schwab, D.J.: On internal wave dynamics in the Northern Basin of the Lake of Lugano. *Geophys. Astrophys. Fluid Dyn.*, **27**, 299–336 (1983)
29. Ivanov, V.A., Konyaev, K.V. and Serebryany, A.N.: Group of intense internal waves in the shelf zone of the sea. *Izvestiya Atmospheric & Oceanic Physics*, **17**(12), 1302–1309 (1981)
30. Krauss, W.: *Interne Wellen*. Gebrüder Bornträger, Berlin, Nikolassee (1966)
31. Laboratorio Studi Ambientali: Richerche sull'evoluzione del lago di Lugano. *Commissione internationale oper la protezione delle aque italo-svizzere*. Dip. Ambiente, CH-Bellinzona (1980–1986)
32. Lamb, K.G. and Yan, L.: The evolution of internal wave undular bores: comparisons of a fully nonlinear numerical model with weakly nonlinear theories. *J. Phys. Oceanogr.*, **26**, 2712–2734 (1996)
33. Lee, C.-Y. and Beardsley, R.C.: The generation of long internal waves in a weakly stratified shear flow. *J. Geophys. Res.*, **79**, 453–462 (1974)
34. Maurer, J.: *Skaleneffekte bei internen Wellen im Zweischichtenfluid mit topographischen Erhebungen*. Diploma Thesis, Tech University Darmstadt, 112p (1993)
35. Maurer, J., Hutter, K. and Diebels, S.: Viscous effects in internal waves of two-layered fluids with variabe depth. *Eur. J. Mech. B/Fluids*, **15**(4), 445–470 (1996)
36. Miles, J.W.: On internal solitary waves II. *Tellus*, **31**, 456-462 (1979)
37. Mortimer, C.H.: The use of models in the study of water movements in stratified lakes. *Verh. Int. Vereing. Limnol.* (Proc. Int. Limnol. Ass., Stuttgart), **11**, 254–260 (1951)
38. Mortimer, C.H.: Water movement in lakes during summer stratification. Evidence from the distribution of temperature in Windermere. *Phil. Trans. R. Soc. Lond.*, **B236**, 355–404 (1952)
39. Mortimer, C.H.: Lake Hydrodynamics. *Mitt. Int. V. Theor. Angew. Limnol.*, **20**, 124–197 (1953)
40. Mortimer, C. H.: The resonant responses of stratified lakes to wind. *Schweiz. Z. Hydrol.*, **15**, 94–151 (1953)
41. Mortimer, C.H. and Horn, W.: Internal wave dynamics and their implications for plankton biology in the Lake of Zürich. *Vierteljahresschr. Naturforsch. Ges., Zürich*, **137**, 299–318 (1982)
42. Münnich, M., Wüest, A. and Imboden, D.M.: Observations of the second vertical mode of the internal seiche in an alpine lake. *Limnol. Oceanogr.*, **37**(8), 1705–1719 (1992)

43. Mysak, L.A., Salvadè, G., Hutter, K. and Scheiwiller, T.: Topographic waves in a stratified elliptical basin with application in the basin of Lugano. *Phil. Trans. R. Soc. Lond. A*, **316**, 1–55 (1985)
44. Ostrovsky, L.A. and Grue, J.: Evolution equation for strongly nonlinear internal waves. *Physics of Fluids*, **15**(10), 2934–2948 (2003)
45. Roget, E., Salvadè, G. and Zamboni, F.: Internal seiche climatology in a small lake where transversal and second vertical modes are usually observed. *Limnol.Oceanogr.*, **42**(4), 663–673 (1997)
46. Saggio, A. and Imberger, J.: Internal wave weather in a stratified lake. *Limnol. Oceanogr.*, **43**(8), 1780–1795 (1998)
47. Salvadè, G., Zamboni, F. and Barbieri, A.: Three-layer model of the North Basin of Lake of Lugano. *Annales Geophysicae*, **5B**, 247–259 (1988)
48. Schuster, B.: *Experimentelle Studie zur Interaktion nichtlinearer, interner Wellen mit variabler Bodentopographie in einem Rechteckkanal*. PhD Thesis, Fachbereich Mechnik, TH Darmstadt (1991)
49. Schwab, D.J.: Internal free oscillations in Lake Ontario. *Limnol. Oceanogr.*, **22**, 700–708 (1977)
50. Shimizu, K., Imberger, J. and Kumagai, M.: Horizontal structure and excitation of primary motions in a strongly stratified lake. *Limnol. Oceanogr.*, **52**(6), 2641–2655 (2007)
51. Shimizu, K. and Imberger, J.: Damping mechanisms of internal waves in continuously stratified rotating basins. *J. Fluid. Mech*. **637**, 137–172 (2009)
52. Shimizu, K. and Imberger, J.: Energetics and damping of basin-scale internal waves in a strongly stratified lake. *Limnol. Oceanogr.*, **53**(4), 1574–1588 (2008)
53. Stevens, C.L. and Lawrence, G.A.: Estimation of wind-forced internal seiche amplitudes in lakes and reservoirs, with data from British Columbia, Canada. *Aquatic Sci.*, **59**, 115–134 (1997)
54. Stocker, K., Hutter, K., Salvadè, G., Trösch, J. and Zamboni, F.: Observations and analysis of internal seiches in the Southern Basin of Lake of Lugano. *Ann Geophysicae*, **5B**, 553–568 (1987)
55. Vlasenko, V.I.: Multimodal soliton of internal waves. *Izvestiya Atmospheric and Oceanic Physics*, **30**(2), 161–169 (1994)
56. Vlasenko, V.I., Brandt, P. and Rubino, A.: On the structure of large-amplitude internal solitary waves. *J. Phys. Oceanogr.*, **30**, 2172–2185 (2000)
57. Vlasenko, V. and Hutter, K.: Generation of second mode solitary waves by the interaction of a first mode soliton with a sill. *Nonlinear Processes in Geophysics*, **8**, 223–239 (2001)
58. Vlasenko, V., Stashcuk, N. and Hutter, K.: *Baroclinc Tides – Theoretical Modeling and Observational Evidence*. Cambridge University Press, 351 pp. (2005)
59. Wessels F.: *Wechselwirkung interner Wellen im Zweischichtenfluid mit topographischen Erhebungen*. Diploma Thesis, Tech University Darmstadt 69p (1993)
60. Wessels, F. and Hutter, K.: Interaction of internal waves with a topographic sill in a two-layered fluid. *J. Phys. Oceanogr.*, **26**(1), 5–20 (1996)

Chapter 16
Higher-Order Baroclinicity (II) Interpretation of Lake Data with Rotating and Non-rotating Models

In parts A and B of the last chapter, two sources of higher order baroclinicity were looked at (1) a two-layer fluid system with a diffusive interface and (2) a three-layer configuration with two sharp interfaces due to the presence of a thermocline and a chemocline. In this chapter we give further field evidences of higher order baroclinicity. Both cases are to a certain extent idealized; in a realistic situation, density changes are generally less abrupt and should be represented by using a thermal equation of state $\rho = \rho(T, s)$ from measured temperature and electrical conductivity profiles. If this argument is consistently adopted, this would, strictly, mean that a numerical model for a stratified lake should be based on a multi-layer model, e.g. with linear density variation across each layer. For reasons of accurate determination of the phase speeds of the higher baroclinic seiche, this should be done so, even if only fundamental (V1) and first higher order (V2) modes[1] are of interest.

In the majority of cases of baroclinic seiche analyses in enclosed basins, the two-layer approximation is employed (Hutter et al. [26], Horn et al. [24], Bäuerle [8], Stocker et al. [49], Lemmin et al. [34], Shimizu et al. [50, 52] and many others) and with them, most phenomena of internal wave dynamics can be explained. The continuous transition of the density profile from the epilimnion to the hypolimnion gives way for the existence of all higher order baroclinic wave modes, and these are often measurable if external forcing excites them with sufficient energy.

According to Münnich et al. [41], higher vertical modes are rarely reported. These authors quote LaZerta [30] and Wiegand and Chamberlain [54] who study V2-mode behaviour, and the authors themselves provide observational evidence for the excitation of the V2-mode in Lake Alpnach, a basin of the Lake of the four Cantons in Switzerland. This quotation overlooks the very early recognition of higher order baroclinic wave signals by Mortimer [36] in Windermere and his and Heaps' [17–19] attempts to characterize V2-signals by the three-layer model. The likely most detailed study of higher order baroclinic water dynamics is the experimental and theoretical study of Lake Banyoles in Catalonia (Spain) by Roget

[1] V1 and V2, etc., stand for vertical mode 1, mode 2, etc.; similarly, H_1, H_2, etc., stand for horizontal mode 1, mode 2, etc.

K. Hutter et al., *Physics of Lakes*, *Volume 2: Lakes as Oscillators*, Advances in Geophysical and Environmental Mechanics and Mathematics,
DOI 10.1007/978-3-642-19112-1_16,

et al. [45]. Nowadays, physical limnologists are better aware of these wave signals; higher order baroclinicity is touched upon, among others, by Appt et al. [4], Boegman et al. [11] and Shimizu et al. [50, 52].

16.1 V2-Vertical Mode of the Internal Seiche in Lake Alpnach (Switzerland)

Figure 16.1 gives sketches of V1 and V2 behaviour. For the fundamental V1-mode of a solitary wave, all pycnoclines are bent in the same direction, which means that vertical components of particle displacements or velocities have the same sign over the entire depth, through the epi-, meta- and hypolimnion. Alternatively, for the first higher order baroclinic mode V2 of the solitary wave, pycnoclines are bent upward in the upper layer and downward in the lower layer, resulting in a thickening of the metalimnion during the passage of the wave. For linear seiche analysis, this has been qualitatively interpreted by Münnich et al. [41] by the sketches of Fig. 16.1. Panels (a) and (b) show V1 and panels (c) and (d) V2-modes. Alternatively, panels (a) and (c) show first horizontal, H1, modes and panels (b) and (d) second horizontal, H2, modes. Of course, such an interpretation is no more than a stipulation with high likelihood of correctness. Without synoptic observations of temperature and velocity at different stations and depths, its corroboration is not possible with certainty.

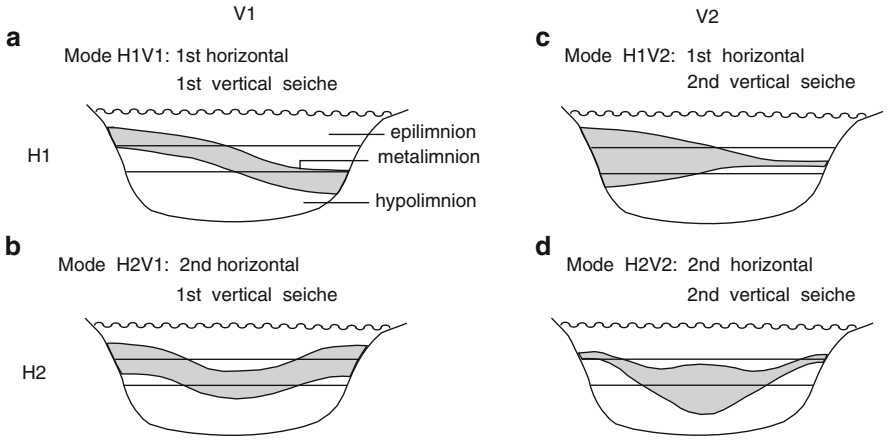

Fig. 16.1 Schematic illustration of various internal seiche modes in an enclosed basin with three homogeneous layers of different densities. The notation used to characterize the mode is of the form HmVn, characterizing the mth horizontal and nth vertical mode. The *shaded regions* illustrate snapshots of typical vertical displacements of the middle layer for the respective modes (after Münnich et al. [41], with changes and extensions)

16.1.1 Observations

Lake Alpnach is a small Alpine lake in Central Switzerland with hydrographical data as shown in the inset of Fig. 16.2. Two measuring campaigns were conducted in 1989 and 1992, respectively. In the 1989 campaign, time series of temperature at the positions M, N, P were recorded at 10 min intervals, and from time series of these, isotherm–depth–time series were interpolated. Selected isotherm–depth–time series, at M for (17°C, 9°C), at N and P for (17°C, 11°C) disclose dominant periodicities at 24 and 7.5 h, which are at times fairly isolated, at other instances intermixed. The 24-h period can also be seen in the wind measurements, but the 7.5-h periodicity is not so clearly seen in the wind data. Energy spectra of the wind and the mentioned selected isotherm–depth–time series disclose identifiable peaks at 24, 12 and 7.5 h with the 24-h signal being unanimously the strongest, followed by the 7.5-h and only afterwards the 12-h signal, see Fig. 16.3. Coherence and phase spectra have also been calculated; for the 24-h period, coherence is always high for the wind–isotherm pair, for pairs of isotherms at the same location as well as for isotherms at different moorings. Phase angle spectra for time-series pairs have also been done. With somewhat generous tolerance, these spectra indicate relations as summarized in the following tables:

	M	N	P
M	−	−	−
N		−	+
P			−

24 h

	M	N	P
M	+	−	−
N		+	+
P			+

7.5 h

	M	N	P
M	?	?	−
N		?	−
P			−

12 h

Here, a minus sign indicates that the two signals are in counter-phase, whilst a plus sign shows an in-phase relation. A question mark (?) means that phase information is not certain. For the 24-h period, isotherm–depth–time series of the selected isotherms at M (17°C, 9°C), N (17°C, 11°C) and P (17°C, 11°C) are in counter-phase as indicated by the negative sign in the diagonal. The vertical epilimnion and hypolimnion displacements are in opposite directions, characteristic for V2-behaviour. On the other hand, the isotherm–depth pairs (N17°C, M17°C), (P17°C, M17°C) show counter-phase relation, whilst (N17°C, P17°C) suggests in-phase behaviour. Because of the positions of M, N, P, this suggests H1-mode behaviour. Thus, the signal at the 24-h period is likely an H1V2 seiche.

The in-phase and counter-phase relations of the 7.5-h period are listed in the middle matrix of the above table, but the indicated claims are less convincing than for the 24-h period. They suggest in this case excitation of the H1V1 seiche, since phase angles between isotherm–depth pairs at the same position but different depths (MM, NN, PP) are all approximately zero, but positive, (+), suggesting V1-behaviour, and the pairs (MN, MP) are approximately ±180°, which is indicative of H1 behaviour, see Fig. 16.1.

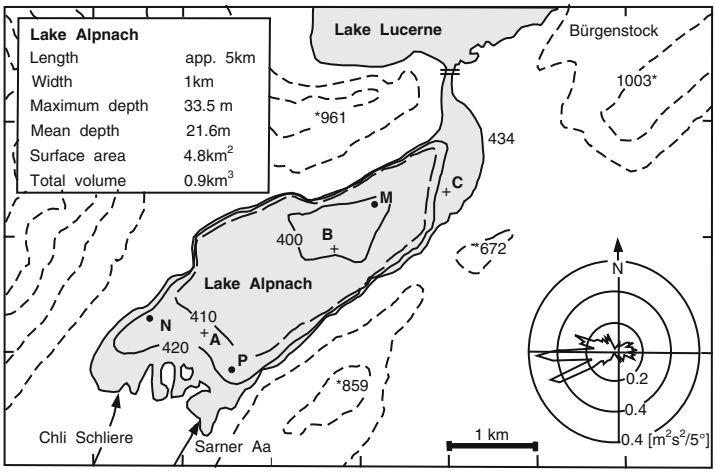

Fig. 16.2 Map of Lake Alpnach, a side basin of lake of the four cantons (Lake Lucerne). The insets show the hydrographical data (*upper left*) and the angular distribution of the squared wind speed recorded at mooring M. The map shows depth contours and the heights of the nearby mountains (peaks identified by *asterisks*). Two field campaigns were conducted: (1) in the summer 1989 (20 June–30 July) thermistor chains were moored at N, P and M with additional wind speed measurements at M. (2) In May 1992, a thermistor chain was moored at A and Anderaa current meters were installed close to the *bottom* at B and C from 8 to 22 May 1992. Adapted from [16, 41], with changes and extensions

The behaviour at the 12-h period is yet less clearly understood. The measurements reported by Münnich et al. [41] allow only inferences as given in the third matrix of the above table; the question marks show either no or weak and inconclusive information. Nevertheless, the authors claim H1V2 behaviour.

16.1.2 Seiche Analysis

The above description of the dynamical response of Lake Alpnach to wind forces and its interpretation as H1V1 and H1V2 behaviour is not very convincing, given the limited temperature data. A further scrutiny on the basis of model calculations is necessary. Münnich et al. [41] chose to do[2] this by approximating the lake geometry by a rectangular basin of constant depth and stratified in $n(=3)$ layers of constant depth. In this case, under the assumptions that the rotation of the Earth can be ignored and the motion is uni-directional in the long direction of the basin, the

[2] The authors present the analysis, which was already given by Longuet–Higgins in Mortimer [36] and by Heaps [17].

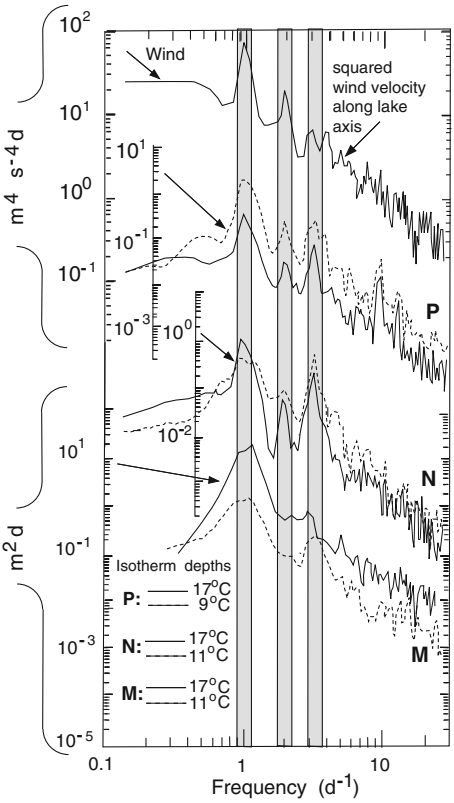

Fig. 16.3 Energy (power) spectra of the wind stress at mooring M and at the depths of the indicated isotherms at the moorings M, N, P. of Lake Alpnach. Adapted from [41], with changes

phase speeds and the periods of the HmVn-seiche are given by

$$c_n = \sqrt{g\lambda_n}, \;\; T_{m,n} = \frac{2L}{m\sqrt{g\lambda_n}}, \tag{16.1}$$

in which L is the length of the rectangle and λ_n are the eigenvalues of the n^{th} baroclinic mode. In the $(n = 3)$-case they show that

$$\lambda_{1,2} = \frac{1}{2H}\left\{\gamma \pm \left(\gamma^2 - 4\alpha H\right)^{1/2}\right\} + O(\varepsilon^2), \tag{16.2}$$

where

$$\begin{aligned} \gamma &= \varepsilon_{12}H_1H_2 + \varepsilon_{13}H_1H_3 + \varepsilon_{23}H_2H_3, \\ \alpha &= \varepsilon_{12}\varepsilon_{23}H_1H_2H_3, \\ \varepsilon_{ij} &= \frac{\rho_j - \rho_i}{\rho_j}, \qquad \varepsilon := \max_{i,j}(\varepsilon_{ij}). \end{aligned} \tag{16.3}$$

Epi-, meta- and hypolimnion depths are given by H_1, H_2, H_3, respectively, and $H = \sum_{i=1}^{n} H_i$. Münnich et al. chose for their corroboration of the (H1V1,

Table 16.1 Periods of the H1V1 and H1V2 seiche modes calculated with the three-layer rectangular basin model using different approximations for the stratification. H denotes the thickness of the respective layer. The length was 3,500 m (From [41])

Epilimnion		Metalimnion		Hypolimnion		Period [h]	
Temperature [°C]	H [m]	Temperature [°C]	H [m]	Temperature [°C]	H [m]	H1V1	H1V2
20	3	16	7	8	15	8.0	16.4
20	4	16	5	8	16	7.8	16.8
19.5	5	16	3	8.5	17	7.7	20.8
19.5	5.5	16	2.2	8.5	17.5	7.8	23.6

H1V2)-behaviour $L = 3{,}500$ m (the lake has a very shallow Southern end not consisting of two layers), $H = 25$ m, and varied the selection of H_i $(i = 1, 2, 3)$, constrained to $\sum_{i=1}^{3} H_i = H$, and found for a set of reasonable choices the values of the periods as listed in Table 16.1. It is evident that by varying the mean depth and thickness of the metalimnion, the period of the H1V1-mode depends chiefly on the mean depth, whilst that of the H1V2-mode reacts primarily to variations of the metalimnion thickness, but only unreasonably thin metalimnia bring the H1V2 periods close to the 24 h, suggested by the measurements.

To improve the model, i.e. to bring the theoretical (H1V1, H1V2) periods closer to the measured ones, two paths of improvement are possible. (1) Replacing the three-layer stratification with constant density in each layer by continuous stratification that is based on a mean density profile from thermistor records. This density profile is given in Fig. 16.4a with buoyancy frequency in Fig. 16.4b.[3] (2) Replacing the rectangular basin with constant depth also by a basin with realistic bathymetry.

Münnich's et al. [41] analysis is based on the adiabatic, Boussinesq approximated, linear wave equation in a steady (non-rotating) frame. In a constant depth basin, the boundary value problem for the vertical velocity component takes the form

$$\begin{aligned} &\frac{\partial^2}{\partial t^2}\nabla^2 w + N^2\nabla_H^2 w = 0, \\ &w(0) = w(-H) = 0, \end{aligned} \tag{16.4}$$

and reduces in two dimensions with

$$w(x, z, t) = W(z)\exp\left[i\left(kx - \omega t\right)\right] \tag{16.5}$$

to the eigenvalue problem

[3] The authors do not specify in their paper how these profiles were determined from the measured temperature time series of the thermistors in the thermistor chains during the June/July 1992 summer campaign.

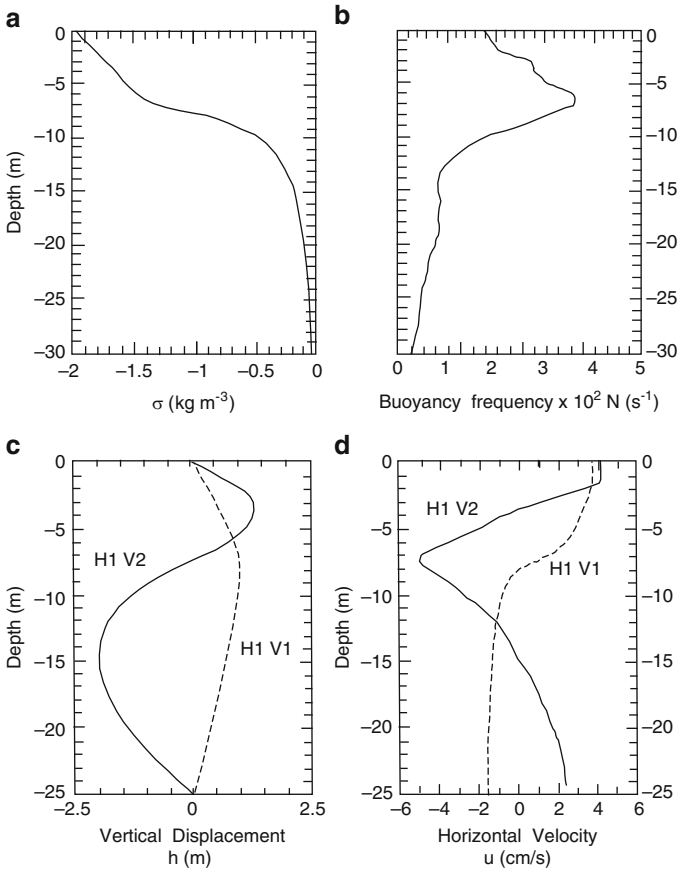

Fig. 16.4 Vertical profiles of density anomaly (**a**) and buoyancy frequency (**b**) as measured in Lake Alpnach with which the baroclinic vertical modes are computed using (16.6), showing the profiles for the vertical displacements (**c**) and horizontal velocities (**d**). Composed from graphs in Münnich et al. [41]. Copyright 2000 by the American Society of Limnology and Oceanography, Inc., reproduced with permission

$$\begin{aligned} &\frac{\mathrm{d}^2 W}{\mathrm{d}z^2} + \left(\frac{N^2(z)}{\omega^2} - 1\right) k^2 W = 0, \\ &W(0) = W(-H) = 0. \end{aligned} \tag{16.6}$$

$N(z)$ is the buoyancy frequency for the measurements shown in Fig. 16.4b. For chosen k, nontrivial solutions of (16.6) exist only for particular values of $\omega(k)$, and associated eigenfunctions are then given by $W_n(z)$. We look only for quantized solutions for which $2\pi/k$ must be an integer part of twice the length of the lake, $2L$. So, the horizontal mode is selected according to

$$k_m = m \times (\pi/L), \quad m = 1, 2, 3, \ldots \tag{16.7}$$

It follows, the H_mV_n-solution is given by ω_{mn}, from which $T_{m,n} = 2\pi/\omega_{mn}$ and $W_{m,n}(z)$ can be determined. Münnich et al. [41] chose, as before, $H = 25\,\text{m}$, $L = 3{,}500$ and then found[4]

$$\text{for the H1V1-mode, } T_{1,1} = 8.2\,\text{h},$$
$$\text{for the H1V2-mode, } T_{1,2} = 23.3\,\text{h}.$$

The corresponding vertical profiles of the vertical displacement and horizontal velocities are displayed as panels (c) and (d) in Fig. 16.4, and the profiles are scaled to have maximum values of 1 and 2 m, respectively.

It is interesting that no interpretation of the 12-h measured signal is given. We shall remark on this below. Here, it may be mentioned that the numerical values chosen for L and H are somewhat subjective and can be used to tune the results with measurements. The period $T_{m,n}$ scales linearly with L, and no rational procedure is available that would justify the selection $L = 3{,}500\,\text{m}$ for a lake of which the length is 5,500 m. This fact, of course, alters the purpose of the whole exercise, which looses a substantial part of its validation role. A more realistic procedure would in this case certainly require the solution of a multi-layer representation of the lake, in which the regions with fewer than the maximum number of layers would also be accounted for, as it was done for the three-layer model of the Lake of Lugano (see part B of the last chapter). Unfortunately, this was not done.

A careful analysis, either by improved calculations or by more detailed experiments was not performed. In the second field campaign, see [16], a thermistor chain was moored at position A (see Fig. 16.2) and current meters were deployed in the bentic boundary layer at B and C. Conspicuous measured periods in the isotherm depths and velocity time series disclose periods of 24 and 12 h, and are interpreted as V1 and V2 responses, respectively. No further scrutiny of the validity of this interpretation is provided. It is, therefore, concluded that a reliable interpretation of the internal wave signals of the thermistor chain and velocity data in Lake Alpnach is still lacking.

16.2 Internal Seiche Climate in Lake Banyoles, Catalonia (Spain)

Higher order baroclinic seiches are sometimes also excited together with higher order horizontal modes; if a lake consists of two (or more) nearly separated basins, then the interpretation of the periodic features in measured time series of typical parameters may be complicated by the fact that the conspicuous periodicities may be referred to individual basin characteristics or the characteristics of the entire lake. In what follows, we report on work performed by Roget et al. [45] that is based in parts on Roget's Ph.D. dissertation [44].

[4] By varying the profiles slightly, they found $T_{1,1} \in (7.7\text{–}8.8)\,\text{h}$ and $T_{1,2} \in (22.2\text{–}25.7)\,\text{h}$ and conclude that their results corroborate their physical interpretation.

16.2.1 Description of the Site

Lake Banyoles' morphometry is shown in Fig. 16.5; it consists of a small compact North and a bit larger oblong South basin. The South basin has a maximum depth of approximately 45 m; the North basin is less than 25 m deep, and the sub-basins are connected by a narrow throat which constrains the dynamical interaction. The evolution of the vertical temperature is that of a holomictic lake in temperate climates. More precisely, mixing starts in September and a month later the lake is unstratified and remains so until spring. In April, a gentle stratification develops, builds-up and is maintained for approximately half of the year. During summer, the temperature difference between the epilimnion and the hypolimnion is approximately 5°C, and the metalimnion occupies 5 m with the thermocline at approximately 7 m. From mid spring to early autumn, the thickness of the metalimnion represents about a third of the mean depth of the whole lake, which is equivalent to a fourth of the mean depth

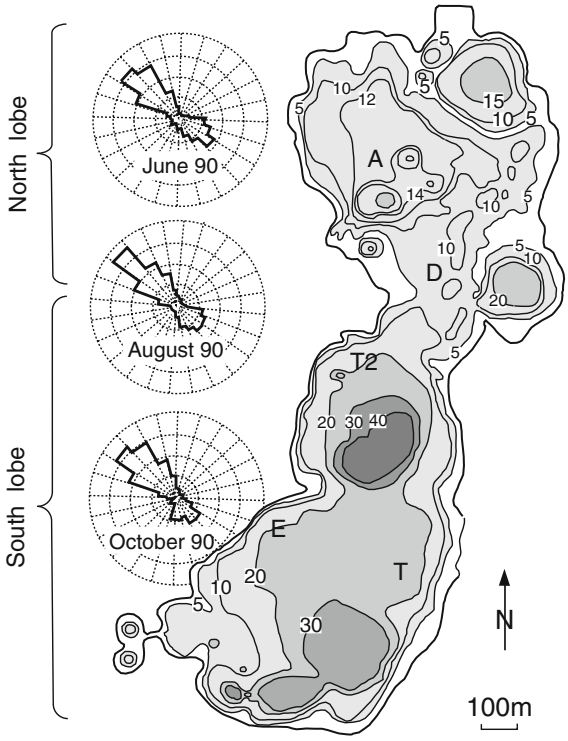

Fig. 16.5 Bathymetric map of Lake Banyoles, Catalonia, Spain, with measuring stations A, D, T2, E, T where data were recorded. The insets show also rosettes for the prevailing winds from SE during the summer time, here in June, August and October, 1990. Composed from figures of Roget et al. [45], with changes. Copyright 2000 by the American Society of Limnology and Oceanography, Inc., reproduced with permission

of the Southern lobe. The prevailing winds during the summer months (from April to October) blow from the SE directions and have speeds from 0.6 to 1.6 m s^{-1} (see insets in Fig. 16.5, which show wind rosettes for June, August and October 1990). This prevailing wind direction is approximately 45° off the NS main orientation of the lake and likely responsible for the excitation of both longitudinal and transverse oscillating baroclinic motions.

Aanderaa thermistor chains with a 1 m distance of the thermistors were deployed at the stations A, D, T2, E and T of Fig. 16.5. From the temperature–time series new time series of isotherm depths were constructed by linear interpolation where possible. A meteorological station on land, to the west of the lake, measured wind data 12 m above ground.

16.2.2 Methods of Computation and Data Analysis

Dismissing the Defant-type models [33, 38], who formulate the balances of mass and linear momentum in a two-layer cross-sectionally averaged version, Roget et al. [45] employed two models: (1) the TVDC (two-layered variable depth complete, see Chap. 11) and (2) the THVDC (three-layered variable depth complete, see part B in Chap. 15). The layers in these models are immiscible, each with constant density, and their interfaces are sharp material surfaces. The letter C in the acronyms TVDC and THVDC stands for 'complete' and indicates that in the numerical finite difference (FD) implementation the models resolve also those regimes of the lake where fewer than the maximum number of layers exist (i.e. one layer for TVDC and one or two layers for THVDC, see Fig. 15.23). The governing equations and the implementation of the transition conditions at the positions (from three to two layers or from two to one layer) as well as the treatment of boundary conditions along the lake shore are described in Part B of Chap. 15. The linear eigenvalue problem that emerges for the free oscillations appears in the FD approximation as a matrix eigenvalue problem for the eigenfrequencies (eigenperiods) and the corresponding eigenvectors, from which the seiche periods and the displacements of the free surface and the interface can be obtained. For a grid size of $40 \times 40\,\mathrm{m}^2$ the TVDC model with sharp thermocline at 8 m depth led to 687 cells and 1,157 unknowns, whence a $1{,}157 \times 1{,}157$ matrix.

The time series were operated on by using algorithms for the least square linear prediction and maximum entropy spectral analysis (MESA) by Barrondale and Erickson [5]. Frequency analysis was also done with fast Fourier transforms (FFT) and revealed the same reported results. The normalized cross-correlation function was used to compare data that were simultaneously recorded at different locations. Furthermore, low-pass and high-pass Chebychev filters were applied to some data to isolate the frequency band of interest. To this end the method of Trampe [53] was employed.

16.2.3 Results

It turned out that, owing to the narrow and shallow neck by which the two sub-basins are connected, the two lobes can dynamically be treated as independent for the FD implementation of both the TVDC and THVDC models. Data have also indicated that the internal dynamics of the South basin are more intense than those in the North basin; so, data of the South basin are better to analyze than those of the North basin. Moreover, when referring to the HmVn-seiche, then always the response of the South basin is meant. When discussing the modes of the whole lake, the acronym $(\mathrm{H}m\mathrm{V}n)_{\mathrm{wl}}$ will be used. The seiches of the North basin will not be separately analyzed.

16.2.3.1 Second Vertical Modes Combined with First and Second Horizontal Modes (H1V2, H2V2) of the Southern Lobe

Because of the relatively small mean depth of the South basin and the relatively thick metalimnion, the THVDC model is likely the simplest model that accounts for the V1 and V2 modes of the stratification. Thus, baroclinic seiches can be identified at the two interfaces between the middle-top and middle-bottom layers. If time series of the vertical displacements of these interfaces are in-phase (in counter-phase) then such behaviour is indicative of V1 (V2) response. Within the middle layer, there is a position where the vertical displacement of the V2 mode goes through zero. Here, the period of the V2 mode should not (or poorly) be visible.

In Fig. 16.6, the filtered vertical displacements of the 19.7, 18.2 and 17.6°C isotherms at station E (all three located at the upper edge, in the middle and at the lower edge of the metalimnion) are shown from 6 to 10 September 1991. The filters were low-pass for the 19.7 and the 17.6°C isotherms, and high pass for the 18.2°C isotherm-depth-time series, all with a cut-off frequency of $0.25\,\mathrm{h}^{-1}$. The figure shows that the 19.7 and 17.6°C isotherms disclose both an oscillation with 7 h period, and the oscillations for these time series are in counter-phase. On the other hand, the 18.2°C isotherm–depth–time series in the middle of the metalimnion shows a dominant oscillation with a period of approximately 4 h. A more refined identification by eye is not possible.

These periods can also be identified in Fig. 16.7, where MESA spectral analysis of the data from Fig. 16.6 is presented. A dominant peak of energy at about a frequency of $0.14\,\mathrm{h}^{-1}$ (period 7.4 h) is clearly seen in the spectra of the 19.7 and 17.6°C isotherms, but not of the intermediate 18.2°C isotherm. This is reminiscent of V2 behaviour. There is also an additional peak at $0.26\,\mathrm{h}^{-1}$ (period 3.8 h). This mode can also be shown to be in counter-phase with any of the isotherm-depth-time series between 7 and 9 m which also suggests the supposition of V2 mode behaviour. There are also other responses seen in the spectra of all three isotherm–depth–time series, e.g. the peak at $\sim$1.05 h, but these are not of concern here.

The two main modes shown in Figs. 16.6 and 16.7 can be reproduced by the THVDC model when considering the mean thermal structure of the lake during the

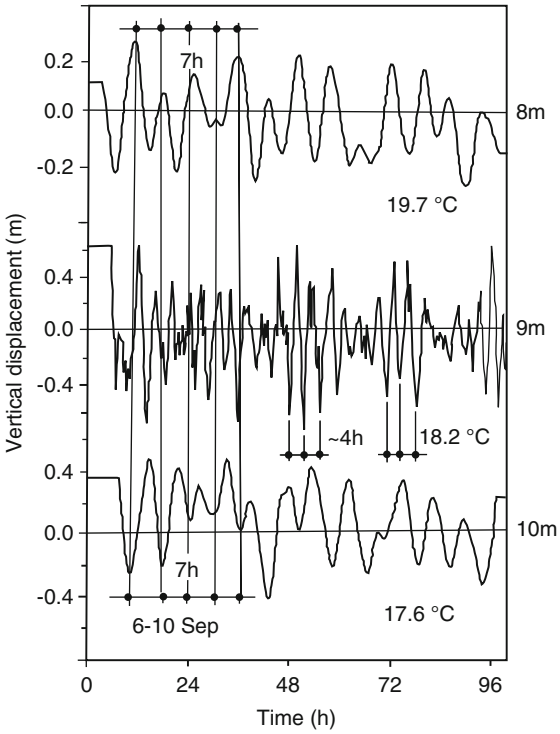

Fig. 16.6 Time series of filtered vertical displacements of the 19.7, 18.2 and 17.6°C isotherms at station E in Lake Banyoles, approximately at 8, 9 and 10 m below the surface. Periods of ∼7 and ∼4 h can be identified (From [45], with changes). Copyright 2000 by the American Society of Limnology and Oceanography, Inc., reproduced with permission

time at which the data were recorded. With the data given between 6 and 10 September 1991, the stratification of the THVDC model is as given in Table 16.2. For this, the H1V2 and H2V2 (corresponding to the $(H1V2)_{wl}$ and $(H5V2)_{wl}$ modes), predicted by the model have periods of 7.44 and 3.89 h, both of them longitudinal and very close to the peak periodicities in Figs. 16.6 and 16.7. The mode structure can be inferred from Fig. 16.8, where isolines of the elevation amplitudes at the upper and lower interfaces of the metalimnion are drawn; solid and dotted lines indicate counter phase behaviour.

Roget et al. [45] report also on V2 mode behaviour in Lake Banyoles when different stratification occurs through the summer. The authors say that the occurrence of V2 modes is a common situation, and report that in May 1990, at the beginning of the stratification period, waves of the 6 and 9 m isotherm depth with periods ∼22 and ∼11 h oscillated with counter-phase in the Southern lobe, and that these modes could also be reproduced by the THVDC model and represented H1V2 and H2V2 behaviour. In fact, depending on stratification, they verified that H1V2 and H2V2

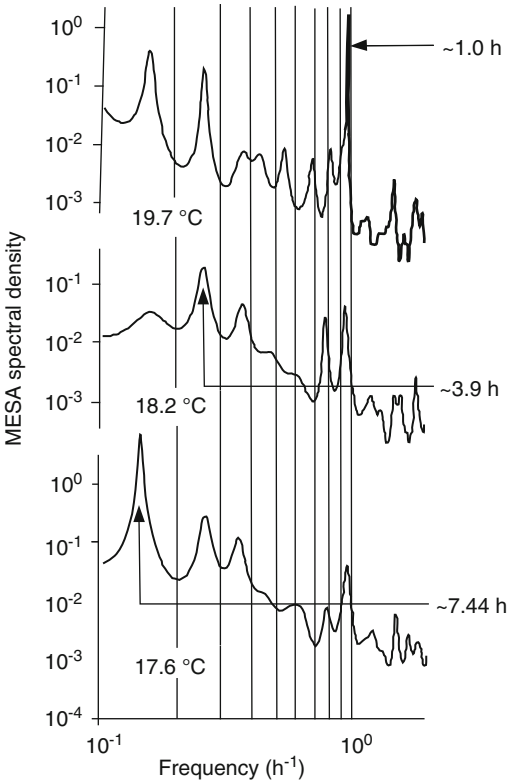

Fig. 16.7 MESA energy spectra of the time series of the depths of the isotherms 19.7, 18.2 and 27.6°C for 6–10 September 1991 from Fig. 16.6 (From [45]). Copyright 2000 by the American Society of Limnology and Oceanography, Inc., reproduced with permission

Table 16.2 Thicknesses and temperatures of the layers in the THVDC model

	Depth [m]	Temperature [°C]
Epilimnion	0–7	25.3
Metalimnion	7–12	19.0
Hypolimnion	12–25	17.9

behaviours have periods $T_{1,2} \in (7, 22)$ h and $T_{2,2} \in (11, 3.5)$ h that were observed between May and September, and a coupling with the wind was absent.

16.2.3.2 Transversal First Vertical Mode (H3V1) of the Southern Lobe

First and second vertical modes (V1, V2) were also simultaneously excited in Lake Banyoles. Here, however, emphasis is put on the fact that often the excited V1 mode is horizontally transverse. This was so on 25–26 October 1991, as can be deduced from Fig. 16.9, where the correlation function between the depth location of the 17.6 and the 20.5°C isotherm–depth–time series (at mean depths of 14.2 and 11.0 m, respectively) at station E (Fig. 16.5) is presented. This correlation function presents two different periods, one of ∼8 h and the other slightly larger than ∼1 h (this latter

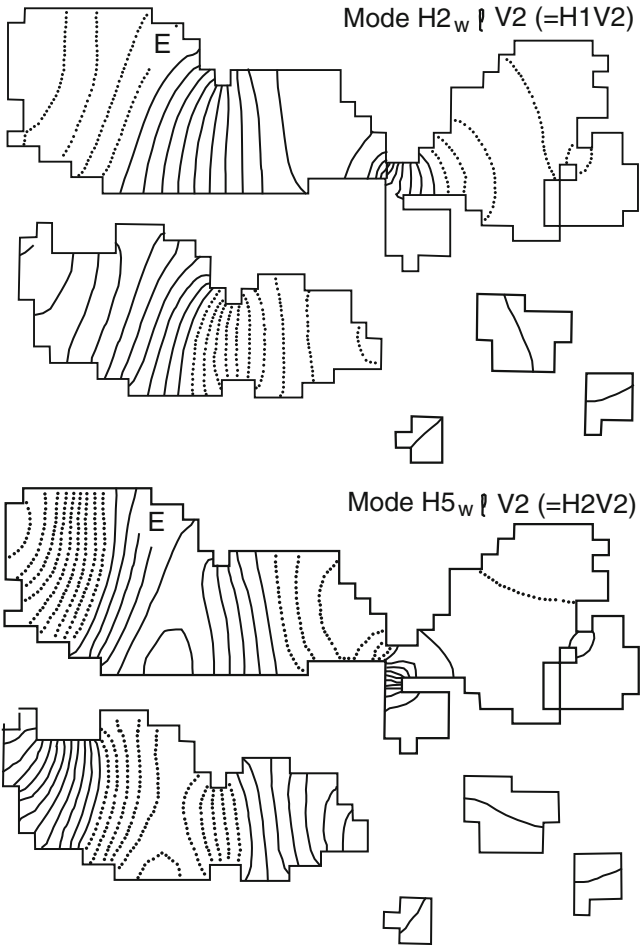

Fig. 16.8 Horizontal structure of the upper and lower interfaces of the metalimnion for the $(H2V2)_{wl}$ (H1V2) of the Southern lobe and $(H5V2)_{wl}$ (H3V2) of the Southern lobe modes in Lake Banyoles, predicted by the THVDC model. Station E where data were collected is also shown (From [45]). Copyright 2000 by the American Society of Limnology and Oceanography, Inc., reproduced with permission

period is also very clearly seen in the MESA energy spectra of Fig. 16.7. When the behaviour of the correlation function of this figure is considered only with respect to the period of ∼8 h (i.e. not considering the ∼1 h period), then, when there is no time shift, the correlation between the two considered isotherms is minimal; this is indication that the two time series are in counter phase at the 8 h period. Correspondingly, the THVDC model predicts for the stratification of the lake in this case a H1V2 response of the Southern lobe with a period of 8.28 h.

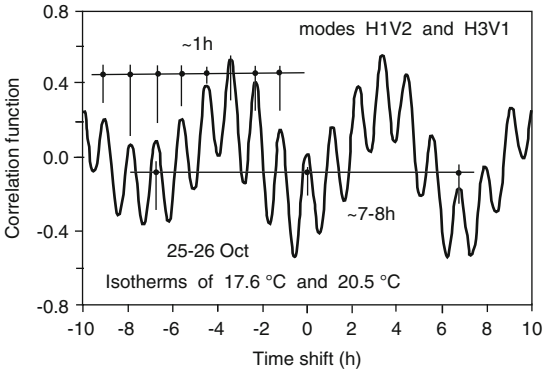

Fig. 16.9 Correlation function between the 17.6 and 20.5°C isotherms on 25–26 October 1991, showing periodicities of ∼7–8 h and ∼1 h in Lake Banyoles (From [45], with additions). Copyright 2000 by the American Society of Limnology and Oceanography, Inc., reproduced with permission

Considering the much shorter period of ∼1 h of the correlation function, a relative maximum is reached at zero shift, which corresponds to the maximum correlation of the oscillation of ∼1 h period. Therefore, the 17.6 and 20.5°C isotherms are oscillating in phase at this period. Moreover, Roget et al. [45] report, that this mode oscillates in phase at all depths where it was recorded, which is strongly reminiscent of V1 behaviour. For some unidentified cause, it is claimed that the THVDC model cannot reproduce this mode, but with the TVDC model a period of 1.14 h was obtained for the H3V1 mode of the Southern lobe.

The structure of the H3V1 mode of the Southern lobe corresponds to the $(H7V1)_{wl}$ mode of the whole lake, which is represented in Fig. 16.10. The amplitude values between two consecutive isolines of the vertical displacements of either the surface layer of the lake or the thermocline are indicated in brackets next to the respective referenced surface displacement and thermocline displacement. In Fig. 16.10, the velocity field for the $(H7V1)_{wl}$ mode is also shown when the amplitude of the seiche is assumed to be 1 m.

Roget [44] and Roget et al. [45] also looked at the whole lake seiche response when only the lowest baroclinic mode V1 was excited. These modes are not of higher order baroclinicity for which reason the reader is directed to the literature.

Complementary to the above analysis, it should also be emphasized that the computations were all performed with the effect of the rotation of the Earth ignored, $f = 0$. This may be questionable, in particular for the high mode $H7V1_{wl}$, for which Poincaré-type behaviour is to be expected. Unfortunately, this more appropriate approach was not pursued by Roget et al. [45].

16.2.3.3 Further Evidence of Higher Order Baroclinic Waves in Lakes

The preceding examples of higher order baroclinic waves were limited to small scale basins in which the effects of the rotation of the Earth could be, or was, ignored. If this rotation must be accounted for, then basin scale wave motions arise as V_n $(n = 1, 2, \ldots)$ baroclinic modes of (horizontal) Kelvin-type or Poincaré-type waves. Works focusing on these have also been published about Lake Biwa (Japan),

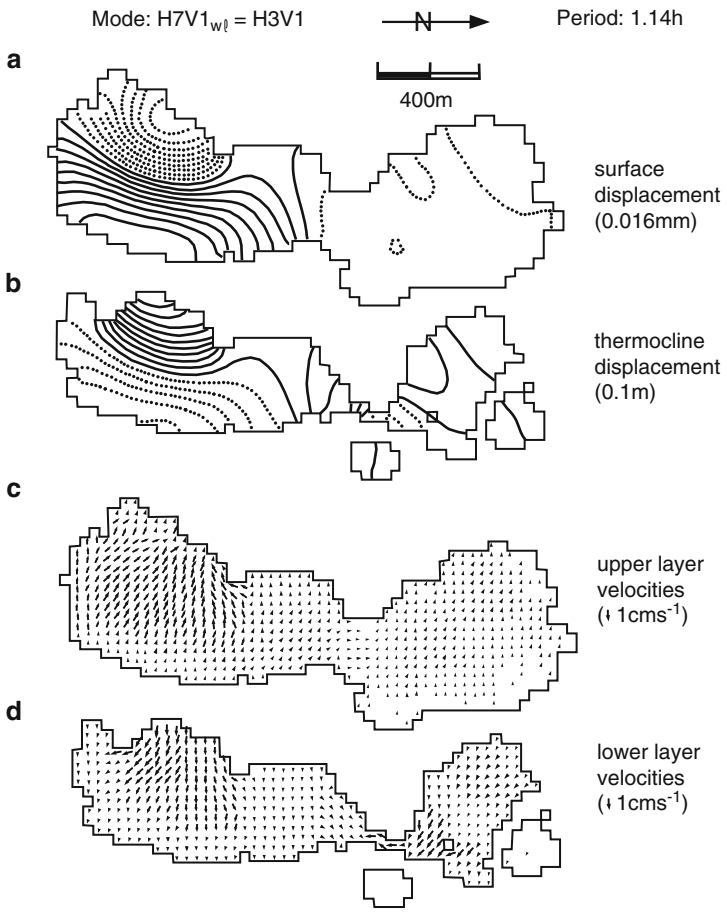

Fig. 16.10 Mode $(H7V1)_{wl}$ behaviour of the whole Lake Banyoles with period of 1.14 h. (**a**) surface displacement, (**b**) thermocline displacement, (**c**) upper layer velocities, (**d**) lower layer velocities (From [45]). Copyright 2000 by the American Society of Limnology and Oceanography, Inc., reproduced with permission

Kinneret (Israel) and Constance (Germany, Switzerland, Austria), see Imberger and associates.[5] These lakes have all sizes that the rotation of the Earth cannot be ignored for the internal wave dynamics, because the internal Rossby radii of deformation are smaller than typical horizontal lengths (generally expressed as the mean width of the basin). In what follows, we shall briefly report on evidence of higher order baroclinic responses and how these are identified in some of these works.

[5] Saggio and Imberger [46], Antenucci et al. [3], Antenucci and Imberger [1, 2], Boegman et al. [11, 12], Appt et al. [4], Shimizu et al. [50], Shimizu and Imberger [51, 52].

16.3 Internal Wave Weather in Stratified Lake Biwa

This title was essentially chosen by Saggio and Imberger [46], to characterize the internal dynamics which they observed in stratified Lake Biwa, Japan, during two field campaigns, called Lake Biwa Transport Experiment (BITEX) in 1992 when no typhoon occurred and in 1993 when three typhoons crossed the Island Honshu. Thermistor chains, deployed close to the Southern end of the North basin of the lake disclose Kelvin-type and Poincaré-type oscillations of several horizontal and vertical orders. The waves are characterized as (1) basin scale waves, i.e. seiches, (2) free gravity waves, not fully constrained by the lake boundaries and (3) small scale weakly non-linear internal waves.

16.3.1 Methodology and Overview of Field Results

16.3.1.1 Experiments

Figure 16.11 displays the lake bathymetry with the experiment station BN50. Five, fast-response, high resolution thermistor chains were deployed in 1992 and arranged as a cross with 20 m distance (see Fig. 16.11), and in 1993 along two straight lines before and after the typhoon on 4 September 1993 (some chains were destroyed during the typhoon). The thermistors of all chains were 1 m apart in the metalimnion and 5 m apart below it; they have an accuracy of 0.01°C with a resolution of 0.001°C. Isotherm–depth–time series were constructed from the temperature–time series by linear interpolation. Unfortunately, the close proximity of the five thermistor chains did not allow disclosure of the spatial structure of the measurements; thus, the following results are from time series averaged over all five chains only.

16.3.1.2 Model

The linear wave responses as seiches and free waves at small frequencies were modeled with simulations of the evolution of the wave dynamics by direct wind input using a three-dimensional model known as TRIM-3D, Casulli & Cheng (1992) [14]. This software is based on the Navier–Stokes equations in the Boussinesq and hydrostatic pressure assumptions, appropriate for the shallow water approximation. A semi-implicit finite difference scheme is used for the numerical solution; the gradient of the surface elevation in the momentum equation and the velocity in the free surface equation are treated implicitly, whilst the advective, Coriolis and viscous terms are treated explicitly; the convective and viscous terms are discretized in an Euler–Lagrange approach (ELA) to increase stability (see [13, 14] and volume 3 of this book series).

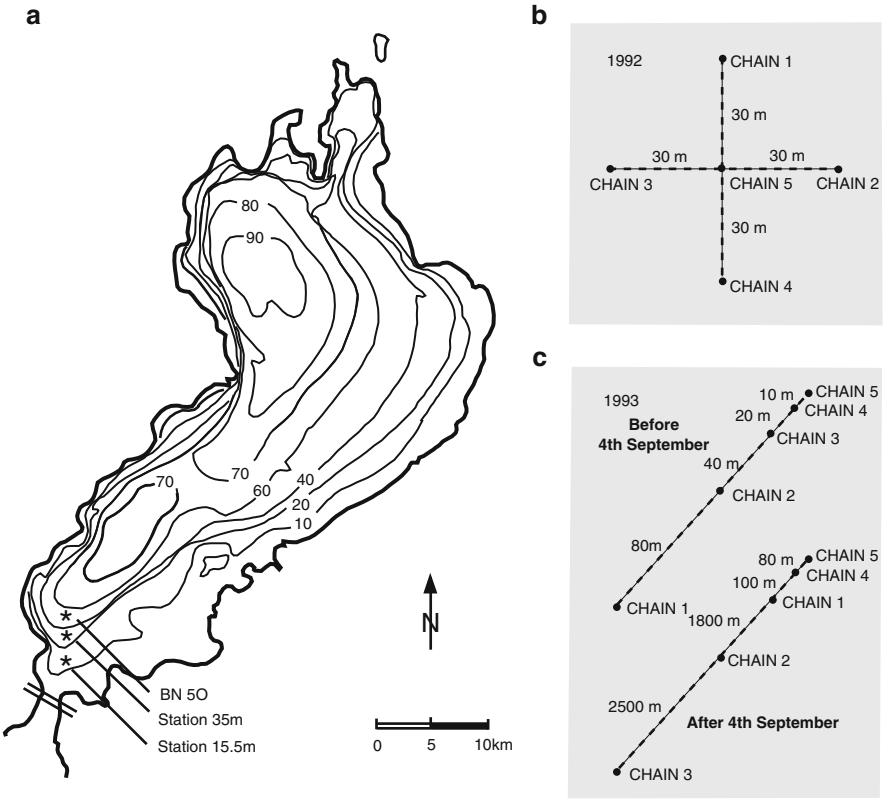

Fig. 16.11 (**a**) Lake Biwa bathymetry with location of sampling stations. The thermistor chains were deployed near station BN50 in a *star shaped* array in 1992 (**b**) and aligned in 1993 **(c)**. During the experiment in 1993 the stations were relocated as indicated in (**c**). Redrawn from Saggio and Iurberger [46]. Copyright 2000 by the American Society of Limnology and Oceanography, Inc., reproduced with permission

The model is applied to a *rectangular box* with constant depth.[6] So, Kelvin-type and Poincaré-type waves can be modeled, but not topographic (shelf) waves. The dimension of the box is 38 km × 12 km × 50 m, matches the North basin geometry, and the FD model is discretized horizontally by 500 m × 500 m cells and vertically by layers having 0.25 m thickness in the metalimnion and 4 m otherwise. A typical stratification (for 30 August 1993) was used as initial condition, and the model was started from rest. The uniform wind was applied with a quarter period sinu-

[6] The model was also used with the actual bathymetry of Lake Biwa and the measured winds during the experiment in 1993. The corresponding analysis is not reported by Saggio and Imberger [46] but was presented in a Ph.D. dissertation by Ogihara [42]. It is claimed also elsewhere in the manuscript that inferences from these results are less convincing. We have not had access to this work.

soidal increase in time, starting at zero velocity and culminating at $5\,m\,s^{-1}$, 48 h after wind set-up with abrupt secession afterwards. Computations were followed during 23 days, sufficiently long that the waves could adjust to the natural periods of the lake.

The computed surface elevations, temperature and horizontal and vertical velocities were stored at 1-h intervals for each grid, and spectra of isotherm depths and velocities were deduced at each grid point and then bandpass filtered around identified frequencies. This allowed identification of the associated isotherm–depth spectra and their modal shapes and evolutions.

16.3.1.3 Field Results

In what follows, we focus attention on basin scale response. The behaviour of the isotherms at BN50 is shown in Fig. 16.12, in panel (a) for 10–19 September 1992, in panel (b) from 24 August to 13 September 1993. The isotherm depth pattern was marked by a number of well defined features which we list here in abbreviated form (for details see [46]):

- A regular heaving of the whole metalimnion with a period of ∼2 days and ∼10 m amplitude is clearly visible.
- Superimposed on this is a surmised V2-mode response with a period of ∼6 days that modulated the buoyancy frequency in the metalimnion between 0.008 and 0.016 Hz.
- The sampling periods of isotherm depth spectra for the 1992 and 1993 campaigns (Fig. 16.13) show a discrete set of sampling periods of small frequency waves ranging from 2×10^{-6} to 4×10^{-5} Hz (6 d to 6 h).
- The first peak in the power spectra occurred in the hypolimnion at a frequency between 2×10^{-6} and 3×10^{-3} Hz. This smallest observed frequency is conjectured to coincide with the V2-mode response modulating the buoyancy frequency.
- The second peak is at the frequency 6×10^{-2} Hz and is the most energetic one in 1992/1993. This high amplitude 2-day oscillation is present in all isotherms over the entire depth with no sign change of the displacements of the different isotherm-time series. It is, therefore, reminiscent of V1 behaviour.
- There are further peaks at $(1.2, 1.7, 2.3) \times 10^{-5}$ Hz.

Following this regime, the spectra extend to 10^{-3} Hz with an energy fall-off at a rate of ω^{-2}. These correspond to the free wave response (see [46]). How do the numerical computations assist the above surmised inferences? Saggio and Imberger [46] write: 'In order to identify the type of wave present, the temperature and velocity fields generated by the model were band pass filtered at the main peaks of the spectra [...], see Fig. 16.14.[7] The most energetic wave (6×10^{-6} Hz)

[7] Figure 16.14 shows the spectra for the 13 and 19°C isotherm depths at BN50 obtained with the model, and representative for the centre of the metalimnion and the hypolimnion, respec-

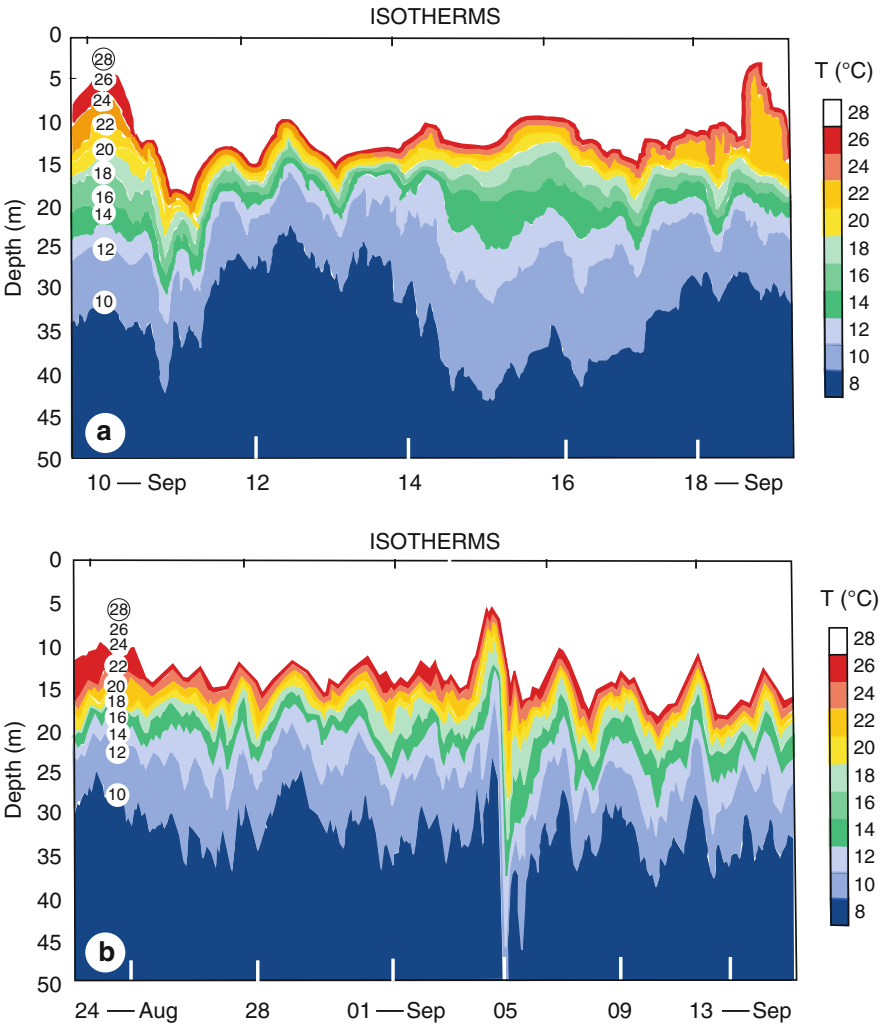

Fig. 16.12 Output from the thermistor chain BN50. The panels show isotherm depths at 2°C steps from the lake surface to the 50-m depth. The original 15-s sampling interval of the temperature records were smoothed to give a 10-min interval in the plots. (**a**) for BITEX 1992, (**b**) for BITEX 1993. Redrawn from [46] with loss of accuracy especially in the upper metalimnion. Copyright 2000 by the American Society of Limnology and Oceanography, Inc., reproduced with permission

was identified as a Kelvin-type wave with vertical mode one. This wave has forward velocities (same direction as the phase speed) under the wave crest, an exponential

tively. Peaks (i) and (ii) are reminiscent of V2 and V1 Kelvin-type behaviour, whilst (iii)–(v) are likely HmV1 ($m = 2, 3, 4$) responses. These interpretations are likely, because at peak (i) vertical velocities (displacements) in the centre of the metalimnion are small, but large at peak (ii).

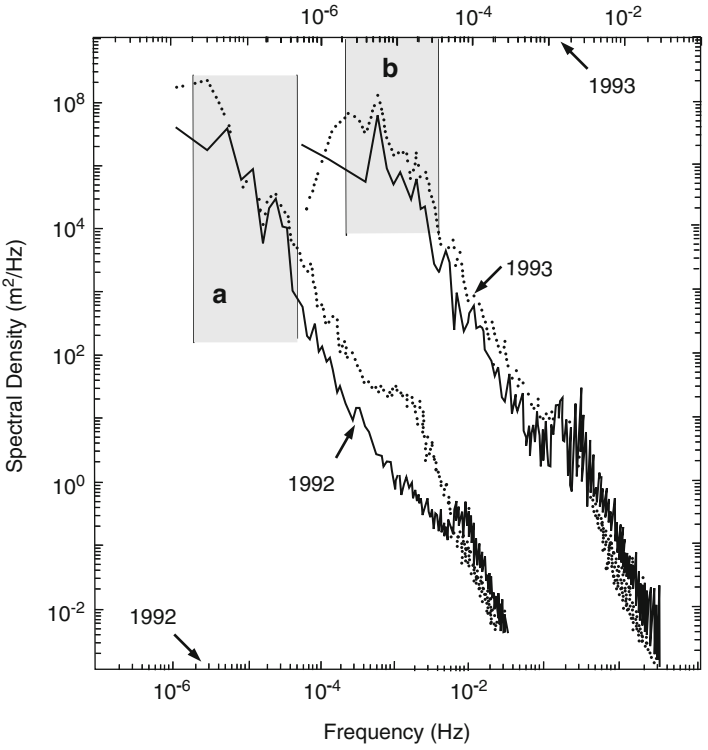

Fig. 16.13 Lake Biwa spectra of isotherm–depth–time series for the (**a**) 10-d record in 1992 and the (**b**) 21-d record in 1993. The 19°C isotherm (*solid line*) was at the centre of the metalimnion during these periods, whilst the 11°C isotherm (*dotted line*) was in the hypolimnion. The spectra were computed using the entire record and were smoothed in frequency domain to improve statistical confidence. The *shaded stripes* mark the (2×10^{-6} to 4×10^{-5} Hz) frequency regime. Adapted from two figures of [46], with changes

decay from the boundaries, and a sinusoidal oscillation along the boundaries [...]. Kanari [29] has previously identified such a first-mode Kelvin wave[8] in Lake Biwa. The next three main peaks in the spectra were identified as Poincaré waves with a vertical mode-one and horizontal modes two ($\omega = 1.2 \times 10^{-5}$ Hz), three ($\omega = 1.7 \times 10^{-5}$ Hz) and four ($\omega = 2.3 \times 10^{-5}$ Hz). Distinct from the Kelvin waves, Poincaré waves exhibit sinusoidal oscillations in both directions, normal and tangential to the boundaries. Higher order vertical modes were also observed in the model results, but their isolation was limited by the small amplitude of their vertical displacement. These consisted of a Kelvin wave with vertical mode-two and Poincaré waves. The spectra of different isotherms in the water column showed that

[8] Saggio and Imberger call Kelvin and Poincaré behaviour what we call Kelvin-type and Poincaré-type behaviour.

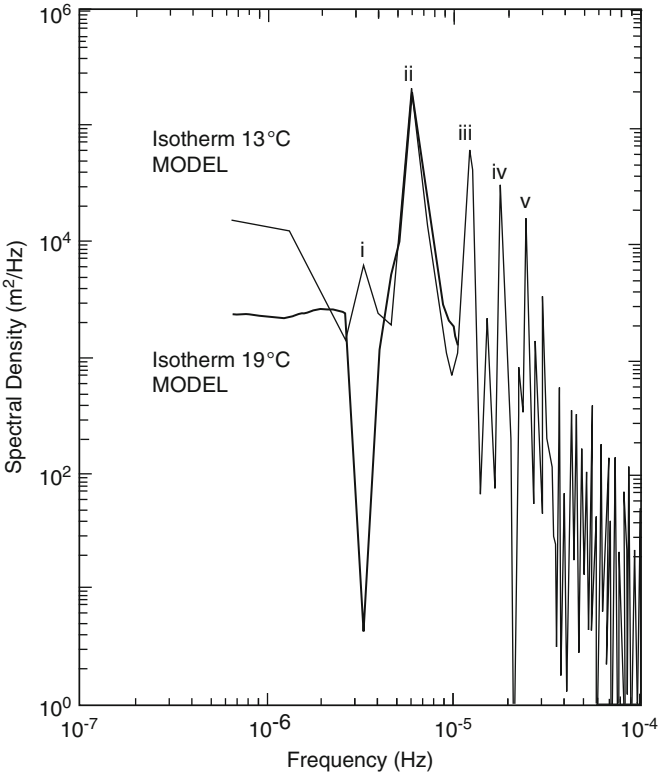

Fig. 16.14 Comparison of the spectra of the 13°C (*thin solid line*) and the 19°C (*heavy solid line*) isotherm–depth–time series generated by the numerical model. The identifiers (i) and (ii) correspond to V2-Kelvin waves, whilst (iii), (iv) and (v) identify HmV1 Poincaré waves for $m = 2, 3, 4$, see also Table 16.3. Extracted from [46]. Copyright 2000 by the American Society of Limnology and Oceanography, Inc., reproduced with permission

the Kelvin wave at frequency 3×10^{-6} Hz has high energy in the hypolimnion and no energy in the centre of the thermocline, suggesting a mode two vertical structure [...]. This wave probably corresponds to the long mode-two wave observed in Lake Biwa [...] but showing higher frequency in the model due to the simplified nature of the model bathymetry [42])'.

Saggio and Imberger [46] continue: '[...] The frequency of the long waves observed in the field data and numerical simulations were also estimated with the modal decomposition of the waves [...]. By considering only the mean stratification and dimension of Lake Biwa, the vertical modes [which] were calculated and the frequencies estimated by such a normal decomposition showed good agreement with our (the authors) observations (Table 16.3). Deviations of the frequencies obtained from the normal modal decomposition from the observed frequencies of a system under rotation only start to be significant for waves faster than the inertial frequency and waves with more horizontal mode structure, [32]'.

Table 16.3 Long waves in Lake Biwa (Inertial frequency 1.3×10^{-5} Hz, Rossby radius: 5.4 km). From Saggio and Imberger (1998) [46]

	Frequency (10^{-5} Hz)			Mode		
	Measured	Model	Modal decomp.	Vertical	Horizontal	Type
i	0.2	0.3	0.2	2	1	Kelvin
ii	0.6	0.7	0.7	1	1	Kelvin
iii	1.2	1.3	1.3	1	(2, 1)	Poincaré/wind
iv	1.7	1.9	2.0	1	(3, 1)	Poincaré
v	2.3	2.5	2.7	1	(4, 1)	Poincaré/wind

As described above, the long waves present in the isotherm displacement spectrum in Lake Biwa can be identified as a combination of several modes of Kelvin- and Poincaré-type waves, as summarized in Table 16.3.

To summarize: Saggio and Imberger [46] conclude: The band pass filtered time series at the main peaks of the spectra, obtained from the *computed* isotherm–depth–time series disclose the following results:

- The 6×10^{-6} Hz wave (the strongest!) can be interpreted as a V1 Kelvin-type wave,
- The next main peaks correspond to V1-modes:
  - Waves at 1.2×10^{-5} Hz are H2-Poincaré-type waves
  - Waves at 1.7×10^{-5} Hz are H3-Poincaré-type waves
  - Waves at 2.3×10^{-5} Hz are H4-Poincaré-type waves,
- Kelvin-type waves with V1 and V2 structure are also observed, but their amplitudes were relatively small. 'The spectra of different isotherms in the water column showed that the Kelvin wave at a frequency of 3×10^{-6} Hz has high energy in the hypolimnion and no (or, small) energy at the location of the thermocline, suggesting a V2-structure, [46].

These results have essentially been corroborated by refined analyses. First, a more detailed approach considering the bathymetry of the lake, the real wind data, and the inclusion of a parametric model for the free internal wave propagation was presented by Ogihara [42]. Second, a modal analysis has also been performed with correct V1 and V2 velocity distributions from which new energy peaks for the various horizontal modes were computed. All results are summarized in Table 16.3.

It is unfortunate that in the above interpretation of the BITEX campaigns of 1992/1993, a number of claims about the basin-scale mode behaviour are stated, but not explicitly demonstrated: they must be taken for granted. This holds, in particular, for the inferences drawn from the computations, claiming Kelvin and Poincaré-type behaviour, which, on the basis of the published document can not be corroborated. The amphidromic systems for these modes and the clockwise rotation (on the Northern hemisphere) of the horizontal projection of the velocity vector for Poincaré mode structures are elements that support Kelvin and Poincaré-type

behaviour. Similarly, the periodic contraction and expansion of the metalimnion are strong signs for a V2-mode behaviour, but not a full proof for it. When designing a field campaign, aiming at corroboration of higher order baroclinicity, much denser deployment of thermistor chains *and* current meters is necessary for the identification and isolation of V_n ($n > 2$) response.

16.4 Basin-Scale Wave Motion in Lake Constance

16.4.1 Morphology and Methodology

Lake Constance (Fig. 16.15), the second largest Alpine lake in Europe, consists of three basins, the main basin of Upper Lake Constance and Lake Überlingen, which together form the *Upper Lake Constance* (Obersee) and the *Lower Lake Constance* [4, 55]; the latter is dynamically decoupled from the others by the 5 km long River Rhine. Basic properties of the Upper Lake are listed in Table 16.4. The two basins 'Upper Lake' and 'Lake Überlingen' are connected at the sill of Mainau, where the depth of the thalweg reduces to 100 m. The seasonal stratification is primarily due to temperature, with mineralization having an effect only when temperatures are near 4°C [43]. The prevailing synoptic winds are from SW-W and NE. The former winds prevail during strong wind events that occur for 2–9 days per month and have a duration between 1 and 7 days, see [25]. A mountain ridge South of Lake Überlingen leads to less intense winds over Lake Überlingen when they blow from SW-W, see [56]. Periodically, föhn flows down from South along the Alpine Rhine valley and affects the dynamics of the Eastern basin [40].

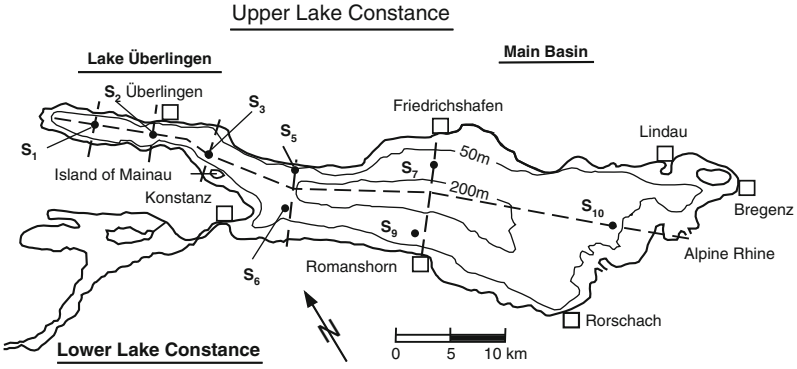

Fig. 16.15 Upper Lake Constance (47°39′N, 9°18′E) with locations of the lake diagnostic systems (LDSs) sampling stations of the 2001 field program (denoted by S_j, $j = 1, 2, 3, 5, 6, 7, 9, 10$) (From Appt et al. (2004) [4], with additions). Copyright 2000 by the American Society of Limnology and Oceanography, Inc., reproduced with permission

Table 16.4 Morphological properties of the upper Lake Constance

Upper lake (large basin)		Überlingen	
Total length 63 km			
Maximum width	14 km	Maximum width	4 km
Mean width	9.3 km	Mean width	2.3 km
Maximum depth	252 m	Maximum depth	184 m
Mean depth	101 m	Mean depth	84 m

Basin-scale internal waves in Upper Lake Constance are affected by the rotation of the Earth. The dimensionless number measuring this is the so-called Burger number S_i, which is the ratio of the (dominant) internal Rossby radius of deformation, $R_\mathrm{R} = c_i/f$ to the horizontal length scale $2L$,

$$S_i = \frac{c_i}{(2L)f}, \tag{16.8}$$

where c_i is the phase speed of the particular wave, f is the Coriolis parameter and L is a typical horizontal length of the basin under consideration [1]. For a two-layer system ($i = 1$),

$$c_1 = \sqrt{\frac{\rho_2 - \rho_1}{\rho_2} g \frac{H_1 H_2}{H_1 + H_2}}, \tag{16.9}$$

for upper (lower) layer densities ρ_1 (ρ_2) and layer depths H_1 (H_2), implying $c_1 \simeq 0.3\,\mathrm{m\,s^{-1}}$ or smaller, and $R_\mathrm{R}^{(1)} \leq 3{,}000\,\mathrm{m}$; furthermore, with L being the width of the basin as given in Table 16.4, one obtains

$$S_1 \simeq 0.6 \text{ (Upper Lake)}, \qquad S_1 \simeq 2.4 \text{ (Lake Überlingen)}.$$

It is also clear from the above formulae that the phase speed and, consequently, the Rossby radii and Burger numbers decrease with decreasing density difference $\Delta\rho = \rho_2 - \rho_1$ between the two layers. The H1V1-mode Kelvin-type basin-scale seiche has periods in the range between 90 and 120 h with typical isotherm–depth–displacement amplitudes of 5–10 m at the Western end of Lake Überlingen and less in the Eastern end of the main basin; it can adequately be modeled by the linear two-layer model [7, 10, 47, 55, 57]. The rotation of the pycnocline displacements counter-clockwise around the basin (on the Northern hemisphere) was documented by Hutter et al. [27], see Fig. 16.16.

Poincaré waves have periods less than the local inertial period of 16.3 h and the associated horizontal velocity fields propagate clockwise (on the Northern hemisphere), Mortimer [37, 39]. Appt et al. [4] also state that Poincaré-like V1-waves in the Upper Lake Constance have a more local character [55], with periods in autumn typically around 12 h in the central main basin [20, 23, 55], 9 h at the Western end

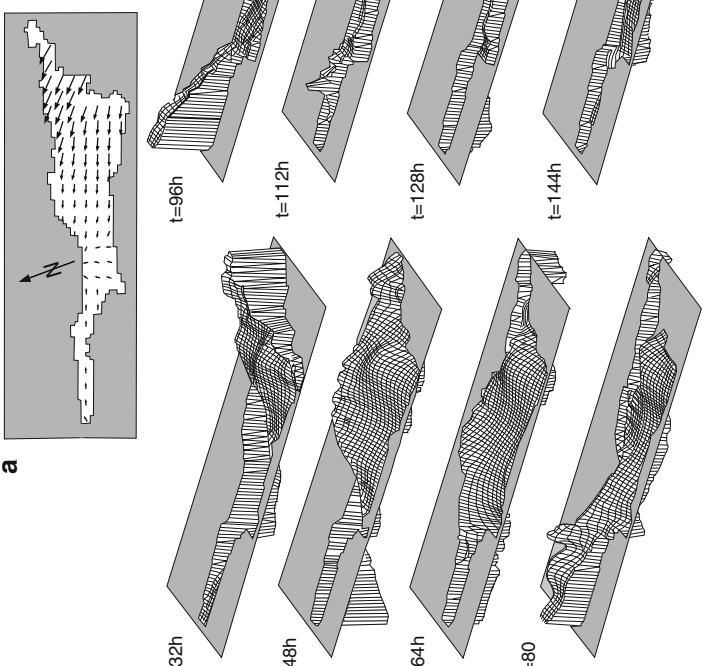

Fig. 16.16 Snapshots of the thermocline displacement obtained with the weakly nonlinear two-layer wave model for the upper lake Constance. The wind field of panel (**a**) was applied for the first 24 h of the model time and then abruptly stopped, generating a characteristic elevation of the internal interface, which is seen to travel essentially counter clockwise around Lake Constance. The stratification was such that the H1-seiche period is 144 h. (**a**) Wind field of a föhn storm selected from Serruya et al. [48]. (**b**) Snapshots of the layer interface at the time slices $t = (32 + n \times 16)$ h for $n = 1, 2, 7$. Adapted from Bauer et al. [6], with changes.

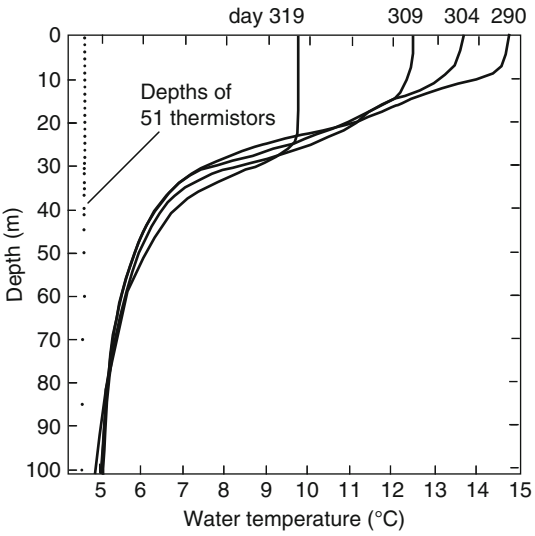

Fig. 16.17 Lake Constance: Vertical temperature profiles of daily averaged field data at station S_7. The time when each profile was taken is written on the *top* of that profile. Note the considerable cooling in the top layer as a consequence of the storm on day 310. *Dots* on the *left* show the depths of the thermistors in the thermistor chain (From Appt et al. (2004) [4]). Copyright 2000 by the American Society of Limnology and Oceanography, Inc., reproduced with permission

of the main basin [20, 55], and 4 h in Lake Überlingen [9, 23, 55]. Little seems to be known about basin-scale internal waves of higher vertical modes.

In the field experiment lasting from day 288 to 321, 15 October–17 November 2001, eight LDSs were deployed at the locations shown in Fig. 16.15. Each station was equipped with a 100 m thermistor chain and wind anemometers 2.4 m above the lake surface with 0.01°C absolute accuracy and 0.001°C resolution; thermistors were 0.75 m apart in the upper 30 m and at increasing intervals below. No current meters were deployed; so, rotational motions of the current under Poincaré or topographic waves can not be identified from measured data. The measuring period is divided into two sub-periods, the first lasting from 15 October until 10 November 2001, characterized by small winds and free surface temperature above 12°C (see Fig. 16.17), the second (from 11 to 17 November 2001), initiated by a strong WS-W wind event and accompanied by a dramatic drop of the air temperature to 4°C and a subsequent cooled and homogenized epilimnion layer with a temperature below 10°C (see Fig. 16.17).

Numerical simulations were performed with the Estuary and Lake Computer Model (ELCOM, code 1.5) of the Centre of Water Research, University of Western Australia, which has previously been shown to model successfully the baroclinic dynamics of stratified lakes, [22, 31]. The code solves the three-dimensional Navier–Stokes and scalar transport equations in the hydrostatic and Boussinesq approximations, [21]. The model was applied to the Upper Lake Constance with a finite

difference grid of mesh size 400 m × 400 m and coordinate axes parallel and transverse to the lake axis. Vertical grid sizes varied from 2.5 m in the surface layer to 34 m in the deepest part of the hypolimnion. At fixed boundaries free slip was imposed and the free surface was subject to wind shear and vanishing heat flow. As initial conditions, a horizontally uniform temperature profile, a horizontal free surface and zero velocity in the whole lake were imposed. Measured wind speeds were interpolated over the surface and transferred to velocities 10 m above the lake surface ($U_{w10} = 1.14U_{w2.4}$) with a quadratic drag law. The computed time series of density and velocities at each grid point were stored and later subjected to power spectral analysis as needed.

16.4.2 Interpretation of the Observations

In period I (15 October–10 November 2001), there were energy peaks

- At 90 h (3.066×10^{-6} Hz) in all stations, said to correspond to a H1V1 Kelvin-type seiche,
- At 12 h (2.3×10^{-5} Hz), particularly at stations S_7, S_9 and S_{10}, claimed to correspond to a V1-Poincaré-type mode,
- At 8 h (3.5×10^{-5} Hz), also reminiscent to a V1-Poincaré seiche.

Frequency spectra of the computed temperature-time series were constructed from the time series of the integrated potential energy $PE(t)$, per unit area, defined by

$$PE(t) = \int_0^{\mathcal{D}} gz\rho(z,t)\mathrm{d}z, \tag{16.10}$$

where integration is over the upper most $\mathcal{D} = 100$ m below the water surface. (At depths below 100 m the contribution to (16.10) is nearly a constant that does not affect the temporal variation of (16.10). Figure 16.18a shows PE-energy spectra from period I as explained in the figure legend at all stations with peaks at 90, 12 and 8 h, as solid lines, obtained from the observed data, and as dotted lines, computed with ELCOM for conditions as previously described. For small frequencies the basin-mode spectra coincide well with one another. Figure 16.18b shows the analogous results for period II after the storm on day 310 (10 November 2001).

Appt et al. [4] justify the above mentioned mode interpretation as follows: 'As for the Kelvin-type mode, the counter clockwise travel along the shore line is evident from the excursion of the metalimnion that is represented by the 9°C isotherm (Fig. 16.19a). The travel history is more clearly seen from band-passed PE variations shown in Fig. 16.19b, with the internal crest labeled 1–6 and internal troughs labeled a–e. The phase speed around the main basin, from station S_6 to station S_5, is almost constant [...]. Observed periods vary between 72 and 105 h with an average

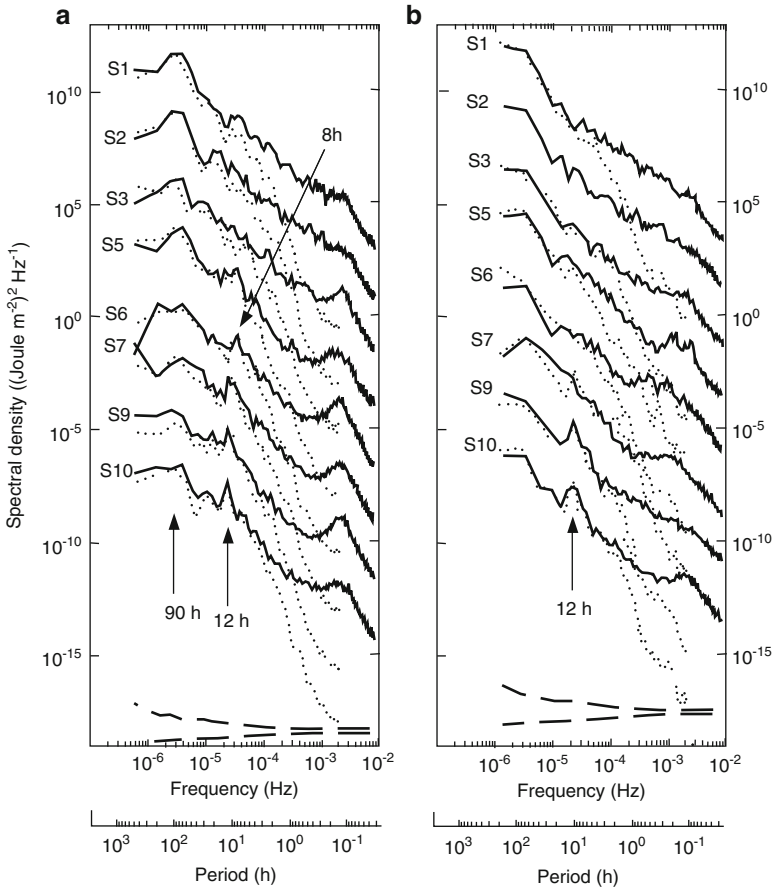

Fig. 16.18 Spectral analysis of field (*solid lines*) and simulated (*dotted lines*) data. (**a**) Spectra of PE for simulated data as well as for 1-min averaged field data of the interval days 288.0–310.0 for S_1, S_2, S_3, S_7 and S_9, days 293.0–310.0 for S_6 and S_{10}, as well as days 288.0–306.0 for S_5; (**b**) same as in panel (**a**) for period days 310.0–320.0 at all stations. Confidence at the 95% level is shown by the *dashed lines*. Coordinates are staggered between adjacent stations (From Appt et al. (2004) [4]). Copyright 2000 by the American Society of Limnology and Oceanography, Inc., reproduced with permission

of 90 h. The crests steepen when they pass station S_5 and enter Lake Überlingen through the contraction and over the sill of Mainau [...]'.

'The simulated Kelvin-type wave signal plotted in Fig. 16.19b (dashed lines) shows a delay of some hours. The wave attenuation during the calm period (crest 4 and troughs c and d) is stronger in the simulated than in the measured data (possibly due to the stepwise approximation of the real topography) and the period of 108 h, obtained with the ELCOM simulation, exceeds somewhat the 90 h period, most likely because of the effect of direct wind forcing [4]'.

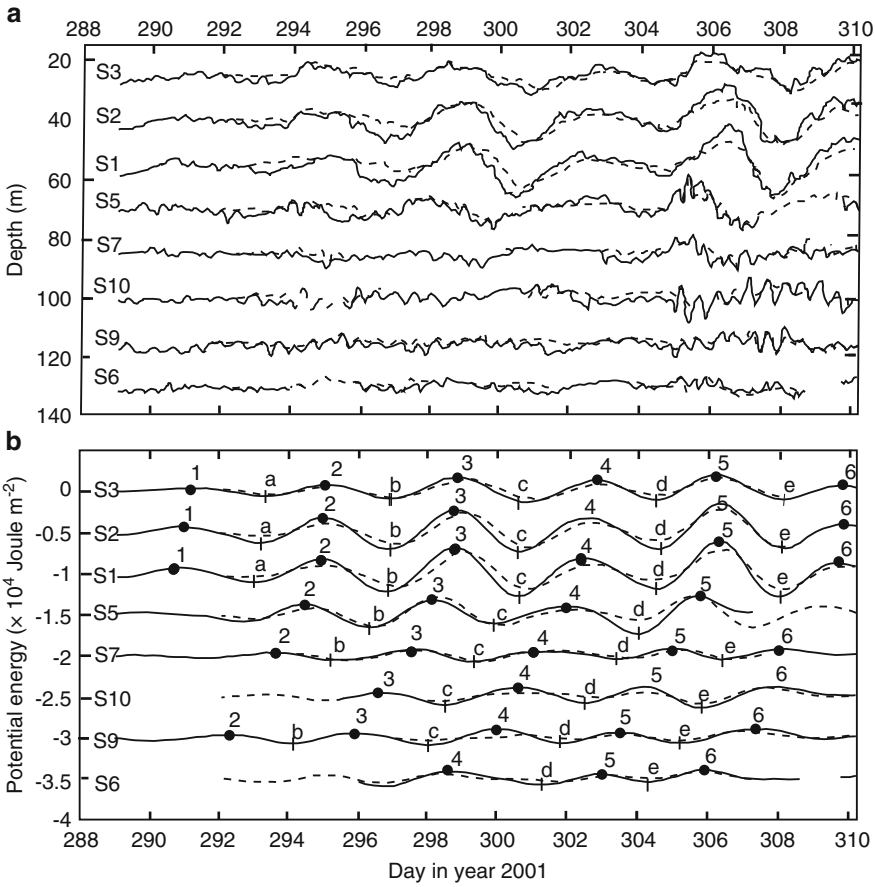

Fig. 16.19 Lake Constance: (**a**) Measured 9°C isotherms staggered at 15-m intervals. 10-min averaged field data (*solid lines*) and 4-min ELCOM model results (*dashed lines*). (**b**) Filtered time series of PE. The time series of PE are staggered with dots denoting the wave crests 1–6 and + denoting the wave troughs a–e (From Appt et al. (2004) [4]). Copyright 2000 by the American Society of Limnology and Oceanography, Inc., reproduced with permission

The identification of the second mode behaviour in the data and simulated time series looks as if Appt et al. [4] did find a needle in the haystack. The key to it must be the evolutions of rotary spectra of simulated isopycnal velocities in the range of periods below the inertial period of 16.3 h. Rotary spectra allow identification of Poincaré-type behaviour through the clockwise rotation of the horizontal velocity vector. Indeed, a rotary spectral analysis of *computed* vertical velocities at S_7 for the 9°C isotherm-depth-time series allowed separation of the 14 and 12 h response, see Fig. 16.20. The 14 h signal is claimed to be a V2 mode, whilst the 12 and 8 h signals are V1 modes. In the measured temperature records, the 14 h peak is, however, not clearly seen.

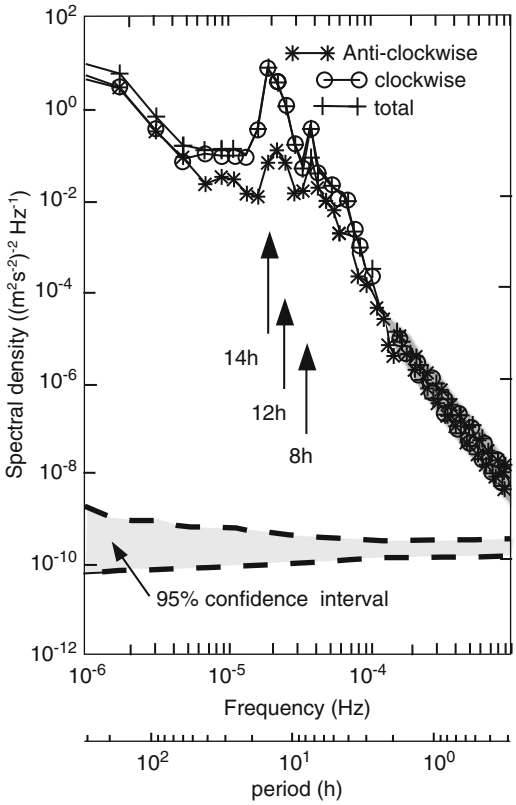

Fig. 16.20 Lake Constance: Rotary power spectra of isopycnal velocity, decomposed into clockwise and anti-clockwise rotating components of 9.0°C isopycnal velocity at S_7. Model data of the velocity field between day 293.0 and day 310.0. *Line markers* show Fourier frequency discretization with spectra smoothed in the frequency domain. Adapted from Appt et al. (2004) [4]. Copyright 2000 by the American Society of Limnology and Oceanography, Inc., reproduced with permission

Appt et al. [4] present data of the simulated velocity field at S_{10} (Fig. 16.21a) to disclose the vertical structure of the internal dynamics. 'The figure shows time series in three depths, in the epilimnion (10 m), metalimnion (30 m) and hypolimnion (60 m), respectively. Band-passed filtering of the simulated velocity field around the 12-h period (Fig. 16.21b) suggests a vertical mode-one structure of the oscillation, in a similar way, the 8-h oscillation in the western main basin, particularly at S_5 and S_6, was identified as an oscillation of vertical mode-one Poincaré-type (not shown [here]). The 14-h oscillation is dominant in the simulated velocity field of the main basin but not in the temperature signal [...]. Filtering the velocity around the 14-h period (Fig. 16.21c) suggests a vertical mode-2 structure at S_{10}. At other stations in the main basin, the vertical mode-two structure is not as clear, possibly indicating the involvement of even higher order modes'.

16.5 Closing Remarks

Internal waves of higher baroclinic order in basins on the rotating Earth have also been identified in other works dealing with stratified lakes. Antenucci et al. [3] report on the seasonal evolution of the basin-scale internal wave field in Lake Kinneret

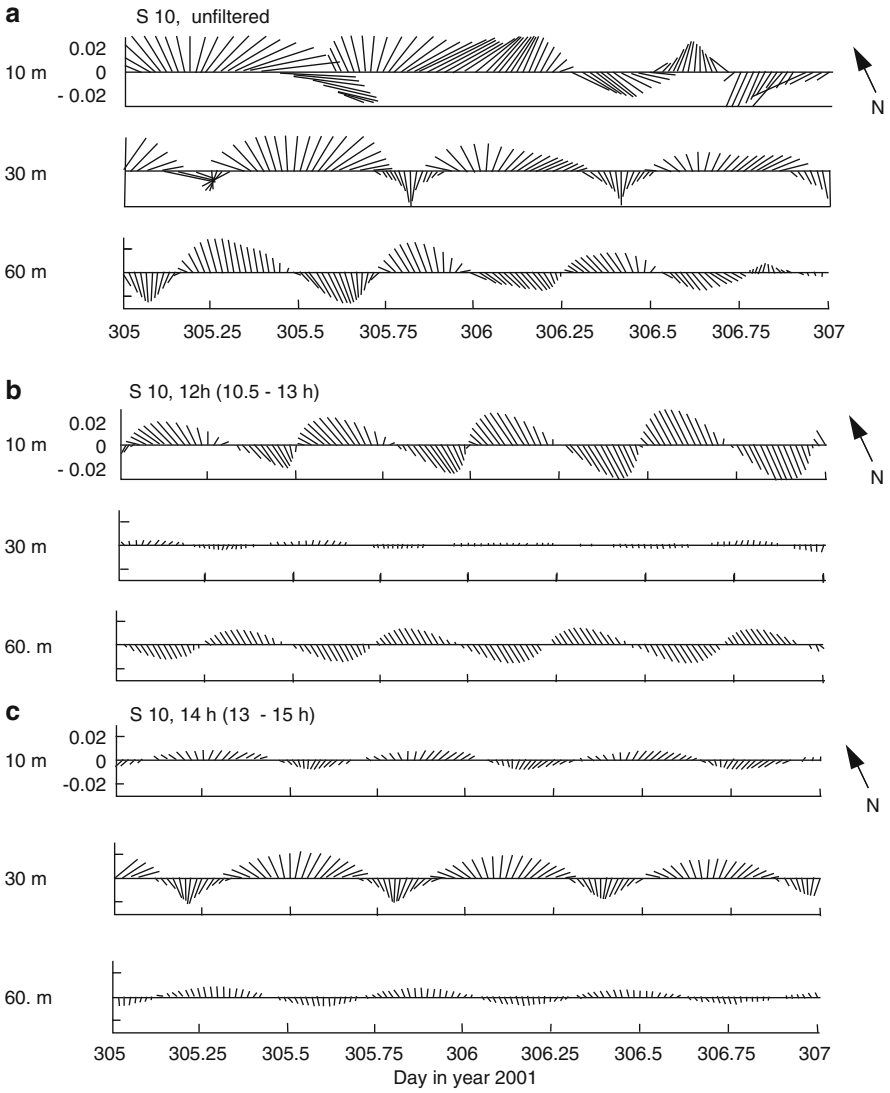

Fig. 16.21 Lake Constance: Simulated velocity field at S_{10}. Time series of horizontal velocity vectors from ELCOM simulation plotted for three depths: (**a**) unfiltered, (**b**) band-pass filtered (limits 10.5–13.0 h), (**c**) band-pass filtered (limits 13.0–15.0 h). The abscissa gives the day in 2001, ordinate is in $\mathrm{m\,s^{-1}}$ (From Appt et al. (2004) [4]). Copyright 2000 by the American Society of Limnology and Oceanography, Inc., reproduced with permission

(Israel) and identify V1 and V2 modes (as well as V3 modes, but less convincingly), as do MacIntyre et al. [35] about Lake Mono (USA). Furthermore, in a more principal study of internal waves in enclosed basins of compact convex shape Antenucci and Imberger [1] present a theoretical analysis of the distributions of the

potential and kinetic energies in circular and elliptical basins of constant depths. They formulate the linear inviscid normal mode equations in plane polar and elliptical coordinate systems for an arbitrary stratification and specialize it for a two and three layer system. Their guidelines are the single layer analogues, treated by Jeffreys [28] and Goldstein [15]. For convex-shaped basins, which somehow match the geometry of realistic basins, the solutions can be used to qualitatively estimate the mode behaviour. Antenucci and Imberger [1] do this by fitting an elliptical basin to Lake Kinneret (Israel) and other lakes, after their earlier analysis had used a circular basin geometry, [3]. In Chap. 13 internal waves in circular and elliptical basins with constant depths were studied in detail to which the reader is referred.

Free internal waves of very short wave lengths were also looked at by Antenucci and Imberger [1] and Boegman et al. [11, 12] for Lakes Kinneret (Israel) and Biwa (Japan). It is claimed that, among many traces of vertical mode-one, also mode-two waves were found. These appear to have been identified as byproducts of general studies of basin-scale modes; certainly, if systematically searched for in focused field campaigns, more detailed inferences, also identifying V_n-modes, $n > 2$, could be drawn.

In closing this chapter on higher order baroclinicity, we summarize by saying that in all cases, (A) the solitary internal waves travelling in a two-layer rectangular channel with diffusive interface in the laboratory, (B) the internal wave response of the Northern basin of Lake of Lugano, stratified by a thermocline at 10 m depth and a chemocline at 100 m depth, (C) the internal wave response of Lake Alpnach and Lake Banyoles, stratified by a metalimnion of finite thickness led to higher order wave response because of special conditions which triggered the generation of the higher order modes. Finally, (D) lakes with horizontal length scales of two or more internal Rossby radii of deformation develop basin scale seiching in which higher order baroclinicity is coupled with Kelvin and Poincaré-type horizontal behaviour. Lake Biwa in Japan and Lake Constance, bordering Southern Germany, Switzerland and Austria were used as illustrations demonstrating the complexities in this case.

In the channel experiments, the interaction of a V1 solution with an obstruction built into the lower layer led to the fission of this wave into reflected and transmitted waves, which turned out to be a combination of V1 and V2 (and possibly V3, V4) responses. Accurate reproduction of the sigmoidal density profile was important in the identification of these modes and the correct determination of the phase speeds.

In the seiche analysis of the Northern basin of Lake of Lugano, the modeling of the density profile by a three layer theoretical model was sufficiently accurate, given the observations from an earlier field campaign. Other, higher order baroclinic oscillations were not recognized or discovered.

In the first part of this chapter, Lake Alpnach and Lake Banyoles were scrutinized for higher order baroclinic response. Time-series of thermistors from chains deployed at various stations within the lakes and encompassing the epilimnion, metalimnion and hypolimnion were scrutinized, and measured periods were identified with computed eigenperiods from three-layer models. It was seen that the three layer approximation was not sufficiently accurate for adequate prediction of the V1

and V2 periods in Lake Alpnach, but for Lake Banyoles the THVDC model was sufficient to reproduce the surmised HmVn ($m \geq 2, n = 1, 2$) periods by the model.

In internal wave dynamics of lakes whose horizontal length scale extends over two or more internal Rossby radii, the vertical mode behaviour is coupled with the rotational effects exhibited by Kelvin and Poincaré-type horizontal seiche modes. Here, it became apparent that field campaigns ought to be conducted not only with synoptic temperature measurements, but also with current meter recordings of horizontal (and vertical) velocity components in the epi-, meta- and hypolimnion and moored close to shore (for capturing Kelvin-type behaviour) as well as off-shore (for capturing Poincaré-type behaviour). Moreover, accurate identification of seiche periods of higher vertical order often requires application of a theoretical model which resolves the vertical stratification better than simply with a two or three-layer model. Apart from a more accurate modeling of the phase speeds of the V1 and V2 modes, this also opens room for higher order baroclinicity with V_n, $n > 2$.

Interestingly, (1) the analysis transpired the suggestion to apply a multi-layer model ($n > 2$) when higher order baroclinic periods must be accurately determined, (2), the account of the regions with fewer layers than in the maximum layer regime is important, in particular, when shore areas are not steep, and (3), no HmVn ($n > 2$) modes were identified in any of the temperature time series of Lakes Alpnach, Banyoles, Biwa and Constance. No convincing examples are known to us where this would be the case.[9] It is, however, clear that an energy cascade to smaller wave lengths is necessary, if the transition to turbulence is occurring. This transfer takes place more likely via internal wave instabilities and wave overturning than by higher mode baroclinic wave fission.

References

1. Antenucci, J.P. and Imberger, J.: Energetics of long internal gravity waves in large lakes. *Limnol. Oceanogr.* **46**(7), 1760–1773 (2001)
2. Antenucci, J.P. and Imberger, J.: On internal waves near the high-frequency limit in an enclosed basin. *J. Geophys. Res*, **106**, C10, 22465–22474 (2001)
3. Antenucci, J.P., Imberger, J. and Saggio, A.: Seasonal evolution of the basin-scale internal wave field in a large stratified lake. *Limnol. Oceanogr.*, **45**, 1621–1638 (2000)
4. Appt, J., Imberger, J. and Kobus, H.: Basin-scale motion in stratified Upper Lake Constance. *Limnol. Oceanogr.*, **49**(4), 919–933 (2004)
5. Barrondale, I. and Erickson, R.: Algorithms for least-squares linear prediction and maximum entropy spectral analysis. Part 2: Fortran Program. *Geophysics*, **45**, 433–446 (1980)
6. Bauer, G., Diebels, S. and Hutter, K.: Nonlinear internal waves in ideal rotating basins. *Geophys. Astrophys. Fluid Dyn.*, **78**, 21–46 (1994)
7. Bäuerle, E.: *Die Eigenschwingungen abgeschlossener, zweigeschichteter Wasserbecken mit variabler Topographie*. Berichte aus dem Institut für Meereskunde, Kiel, **85**, 126p (1981)

[9] We interpret the claims of Antenucci and Imberger [1] and Boegman et al. [11] for Lake Biwa and Kinneret as (perhaps strong) indications, but not as proofs of their existence. The vertical resolution from temperature–time series of thermistor chains with much denser distribution of the thermistors with depth are necessary, to claim *with certainty* that V_n-modes with $n > 2$ can be isolated.

8. Bäuerle, E.: Internal free oscillations in the Lake of Geneva. *Ann. Geophysicae*, **3**, 199–206 (1985)
9. Bäuerle, E.: Transverse baroclinic oscillations in Lake Überlingen. *Aquatic Sci.*, **56**, 145–160 (1994)
10. Bäuerle, E., Ollinger, D. and Ilmberger, J.: Some meteorological, hydrological, and hydrodynamical aspects of Upper Lake Constance. *Arch. Hydrobiol. Sopec. Issues Adv. Limnol.*, **53**, 31–83 (1998)
11. Boegman, L. Imberger, J. Ivey, G.N. and Antenucci, J.P.: High-frequency internal waves in large stratified lakes. *Limnol.Oceanogr.*, **48**(2), 895–919 (2003)
12. Boegman, L. Ivey, G.N. and Imberger, J.: The energetics of large-scale internal wave degeneration in lakes. *J. Fluid. Mech.*, **531**, 159–180 (2005)
13. Casulli, V. and Cattani, E.: Stability, accuracy and efficiency of a semi-implicit method for three-dimensional shallow water flow. *Comput. Math. Applic.*, **27**, 99–112 (1994)
14. Casulli, V. and Cheng, R.T.: Semi-implicit finite difference method for three- dimensional shallow water flow. *Int. J. Numerical Methods Fluids*, **15**, 629–648 (1992)
15. Goldstein, S.: Tidal motion in rotating elliptical basins of constant depth. *Monthly Notices R. Atron. Soc. (Geophys. Supp.)*, **2**, 213–231 (1929)
16. Gloor, M., Wüest, A. and Münnich, M.: Benthic boundary mixing and resuspension induced by internal seiches. *Hydrobiologia*, **284**, 59–68 (1994)
17. Heaps, N.S.: Seiches in a narrow lake, uniformly stratified in three layers. *Geophys. Suppp. R. Astron. Soc.*, **5**, 134–156 (1961)
18. Heaps, N.S.: Development of a three-layered spectral model for the motion of a stratified shelf sea. I. Basic equations. In:*Physical Oceanography of Coastal and Shelf Seas* (ed.: B. Johns). Amsterdam Elsevier, 386–400 (1983)
19. Heaps, N.S.: Development of a three-layered spectral model for the motion of a stratified shelf sea. II. Experiments with a rectangular basin representing the Celtic Sea. In: *Physical Oceanography of Coastal and Shelf Seas* (ed.: B. Johns). Amsterdam Elsevier, 401–465 (1983)
20. Heinz, G.: Strömungen im Bodensee. Ergebnisse einer Messkampagne im Herbst 1993. *Mitt. Versuchsanstalt für Wasserbau, Hydrologie & Glaziologie an der ETH Zürich* (Ed.: D. Vischer), **135** (1995)
21. Hodges, B.R. and Dallimore, C.J.: *Estuary and lake computer model. ELCOM scence manual code (Version 1.5.)* Centre for Water Research, University of Western Australia (2001)
22. Hodges, B.R., Imberger, J., Saggio, A. and Winters, K.B.: Modeling basin-scale internal waves in a stratified lake. *Limnol. Oceanogr.*, **45**(4), 1603–1620 (2000)
23. Hollan, E.: Wind-induced motions in Lake Constance. *Bericht der AWBR*, **6**, 111–187 (1974)
24. Horn, W., Mortimer, C.H. and Schwab, D.J.: Wind-induced internal seiches in the Lake of Zürich observed and modelled. *Limnol. Oceanogr.*, **31**(6), 1230–1252 (1986)
25. Huss, E. and Stranz, D.: die Windverhältnisse am Bodensee. *Pure, Appl. Geophys.*, **81**, 323–56 (1970)
26. Hutter, K., Salvadè, G. and Schwab, D.J.: On internal wave dynamics in the Northern Basin of the Lake of Lugano. *Geophys. Astrophys. Fluid Dyn.*, **27**, 299–336 (1983)
27. Hutter, K., Bauer, G., Wang, Y. and Güting, P.: Forced motion response in enclosed lakes. In: *Amer. Geophys. Union, Coastal and Estuarine Studies. Physical Processes in Lakes and Oceans* (Ed.: J. Imberger), **54**, 137–166 (1998)
28. Jeffreys, H.: The free oscillations of water in an elliptical lake. *Proc. Lond. Math. Soc.*, **23**, 455–476 (1925)
29. Kanari, S.: The long internal waves in Lake Biwa. *Limnol. Oceanogr.*, **20**, 544–553 (1975)
30. LaZerta, B.D.: The dominating higher order vertical modes of the internal seiche in a small lake. *Limnol.Oceanogr.*, **25**(5), 846–854 (1980)
31. Laval, B., Imberger, J., Hodges, B.R. and Stocker, R.: Modeling circulation in lakes: Spatial and tempral variations. *Limnol. Oceanogr.*, **48**(3), 983–994 (2003)
32. LeBlond, P.H. and Mysak, L.A.: *Waves in the Ocean*. Elsevier Oceanogr. Ser., Elsevier Scientific Publ. Co., Amsterdam, Oxford. New York (1978, 1980)

33. Lemmin, U. and Mortimer, C.H.: Tests of an extension to internal seiches of Defant's procedure for determination of surface seiche characteristics in real lakes. *Limnol. Oceanogr.*, **31**(6), 1207–1231 (1986)
34. Lemmin, U., Mortimer, C.H. and Bäuerle, E.: Internal seiche dynamics in Lake Geneva. *Limnol. Oceanogr.*, **50**(1), 207–216 (2005)
35. MacIntire, S., Flynn, K.M., Jellison, R. and Romero, J.R.: Boundary mixing and nutrient fluxes in Mono Lake, California. *Limnol. Oceanogr.*, **44**, 512–529 (1999)
36. Mortimer, C.H.: The resonant responses of stratified lakes to wind. *Schweiz. Z. Hydrol.*, **15**, 94–151 (1953)
37. Mortimer, C.H.: Lake Hydrodynamics. *Mitt. Int. V. Theor. Angew. Limnol.*, **20**, 124–197 (1974)
38. Mortimer, C.H.: Strategies for coupling data collection and analysis with the dynamic modeling of lake motions. In: *Lake Hydrodynamics* (Eds. W.H. Graf and C.H. Mortimer), Elsevier, Amsterdam, 183–222E (1979)
39. Mortimer, C.H.: *Lake Michigan in Motion. Responses of an Inland Sea to Weather, Earth-Spin, and Human Activities*. The University of Wisconsin Press, 311 pp (2004)
40. Mühleisen, R.: Starkwinde an und auf dem Bodensee. *Meteorol. Rundschau*, **30**, 15–22 (1977)
41. Münnich, M., Wüest, A. and Imboden, D.M.: Observations of the second vertical mode of the internal seiche in an alpine lake. *Limnol. Oceanogr.*, **37**(8), 1705–1719 (1992)
42. Ogihara, Y.: *Internal Wave Energy Distribution*. Ph. D. Thesis, University of Western Australia (1998)
43. Ollinger, D.: *Modellierung von Temperatur, Turbulenz und Algenwachstum mit einem gekoppelten physikalisch-biologischen Modell*. Doctoral Disseratation, Ruprechts-Karls Univertiät Heidelberg (1999)
44. Roget, E.: *Internal Seiches and Baroclinic Currents in Lake Banyoles*. Ph. D. Thesis, Autonomous University, Barcelona, 287p (1992)
45. Roget, E., Salvadè, G. and Zamboni, F.: Internal seiche climatology in a small lake where transversal and second vertical modes are usually observed. *Limnol.Oceanogr.*, **42**(4), 663–673 (1997)
46. Saggio, A. and Imberger, J.: Internal wave weather in a stratified lake. *Limnol. Oceanogr.*, **43**(8), 1780–1795 (1998)
47. Schimmele, M.: *Anregung interner Seiches im Bodensee durch den Wind*. Doctoral dissertation, Ruprecht-Karls Universität Heidelberg (1993)
48. Serruya, S., Hollan, E. and Bitsch B.: Steady winter circulation in Lakes Constance and Kinneret driven by wind and main tributaries. *Archiv für Hydrobiologie*, Suppl. **70**(1), 33–110 (1984)
49. Stocker, K., Hutter, K., Salvadè, G., Trösch, J. and Zamboni, F.: Observations and analysis of internal seiches in the Southern Basin of Lake of Lugano. *Ann Geophysicae*, **5B**, 553–568 (1987)
50. Shimizu, K., Imberger, J. and Kumagai, M.: Horizontal structure and excitation of primary motions in a strongly stratified lake. *Limnol. Oceanogr.*, **52**(6), 2641–2655 (2007)
51. Damping mechanisms of internal waves in continuously stratified rotating basins. *J. Fluid. Mech.* **637**, 137–172 (2009)
52. Shimizu, K. and Imberger, J.: Energetics and damping of basin-scale internal waves in a strongly stratified lake. *Limnol. Oceanogr.*, **53**(4), 1574–1588 (2008)
53. Trampe, J.: *Principles of analog and digital frequency analysis*. Norwegian Institute of Technology (1981)
54. Wiegand, R.C. and Chamberlain, V.: Internal waves of the second vertical mode in a stratified lake. *Limnol. Oceanogr.* **32**(1), 29–42 (1987)
55. Wang, Y., Hutter, K. and Bäuerle, E.: Wind-induced baroclinic response of Lake Constance. *Annales Geophysicae*, **18**, 1488–1501 (2000)
56. Zenger, A., Anker, W., Ilmberger, J. and Münnich, K.-O.: Die Untersuchungen der Windverhältnisse im westlichen Teil des Bodensees und die Untersuchung von Landwinden auf Seebedingungen. *Meteorol. Rundschau.*, **42**, 42–51 (1990)
57. Zenger, A., Ilmberger, J., Heinz, G., Schimmele, M. and Münnich, K.-O.: Struktur der internen Seiches des Bodensees. *Wasserwirtschaft*, **79**, 616–623 (1989)

Chapter 17
Barotropic Oscillations in Lake Onega: A Lake of Complex Geometry[1]

17.1 Lake Morphology and First Interpretations of Water Level Measurements

The most simple model of a lake is a quadrilateral basin, i.e. a rectangular basin with constant depth and vertical walls along its four sides. Analysis of the barotropic or baroclinic linear shallow water equations without rotation revealed that the free oscillations occur in ordered modes. This will mean that the eigenperiods of these modes can be sequentially numbered according to their size and the corresponding eigenfunctions equally grow in complexity with the mode number, i.e. the function for the free surface elevation exhibits one, two, three, etc. modal lines. Such an 'orderly' response in the mode geometry is typical only for simple, equally orderly basin geometries. If the basin geometry is complex by its shoreline and/or bathymetry the eigenperiods are still countably infinite and orderable according to their size but the mode structures belonging to a certain eigenperiod can, in general, not be guessed. In particular, it is in such cases hardly possible to plan optimal sites for instrumentation without conducting computations ahead of time. The barotropic response of Lake Onega is such a case. Surface oscillation measurements were made since the 1960s of the last century with limnigraphs at various stations along the shores, and early interpretations were provided. However, only a whole-lake analysis yielded the necessary detailed information to interpret the measured data adequately.

We describe and interpret some features of the barotropic motion recorded by limnigraphs and current meters moored or fixed at various positions and depths in Lake Onega. The measurements were done by Russian limnologists in the mid to late 1960s and early 1970s and are reported by Malinina and Solntseva [6]. Spectral analyses of time series of water level and velocity records disclose conspicuous signals at periods of 13 h and smaller. These periods can be interpreted in terms of the eigenperiods of the barotropic, linearized shallow-water equations, applied to the

[1] This chapter is reproduced (with some changes) from Rudnev et al., Annales Geophysicae, 13, 893–906 (1995) [10]. © European Geosciences Union, reproduced with permission.

K. Hutter et al., *Physics of Lakes*, *Volume 2: Lakes as Oscillators*, Advances in Geophysical and Environmental Mechanics and Mathematics,
DOI 10.1007/978-3-642-19112-1_17, © Springer-Verlag Berlin Heidelberg 2011

complex basin system of Lake Onega. However, this interpretation is not so straightforward, first because the relatively complex geometry of the lake requires use of a finite difference representation of the shallow-water equations with high resolution. This implies that a very large matrix-eigenvalue problem must be solved, which, on standard PCs or workstations, is only possible with a sophisticated reduction of the matrix-eigenvalue problem to a form that allows accurate identification of but the few lowest order eigenfrequencies and corresponding modes. In the present situation, the ten lowest eigenfrequencies are reliably computed. A second reason for the difficulty in interpreting the observations is that the complex lake geometry gives rise to correspondingly complex mode structures of the pertinent seiches. They need to be rather well known in order for the recorded data to be adequately interpreted. As a consequence, thumb rules such as Merian's formula will not lead very far in this interpretation.

After Lake Ladoga, Lake Onega is the second largest European lake, situated in Karelia, in the north-west of Russia. Owing to its complicated geomorphometry and a fringed northern shoreline the lake differs from the other great lakes of the world [7]. There are five finger-like main bays extending north-westwards from the central part of the lake, and each possesses a number of small connected bays (see Fig. 17.1). The lake length, together with the length of the individual bays varies from 130 to 250 km. The average depth is 30 m, the maximum depth is 120 m, the surface area 9692.6 km^2 and the volume 291.2 km^3 [3]. After Stabrowskiy [19], who performed the first limnological study, the latest and most detailed investigation on surface seiches of Lake Onega was carried out and described by Malinina and Solntseva [6]. Figure 17.1 displays the lake shoreline together with the 20, 40 and 60 m isobaths. The various numbers and letters in the figure indicate shore positions and offshore locations where instruments were deployed. Some of these positions carry local names which are also indicated in the figure. We will use the names and symbol identifications interchangingly.

A summary of results from the observations reported by Malinina and Solntseva [6], are shown in Table 17.1. Conspicuous oscillation periods of the water-level-time series recorded at the different gauges are listed in columns 3–11 and labelled 'mode 1'–'mode 9', since Malinina and Solntseva surmised these periods to be the nine lowest modes of the lake's surface seiches. We emphasize that they are not: we will see that 'mode 1' is indeed the fundamental mode of the entire lake; however, 'mode 2', with period of 4 h 20 min is actually the third overtone, i.e. the fourth mode of the basin, and what is called 'mode 3' in Table 17.1 is probably mode 9 or mode 10 of the full barotropic lake response. All shorter periods in Table 17.1 probably belong to even higher order barotropic modes and have not become interpretable by our analysis. It is evident that an interpretation of the periods of Table 17.1 in terms of eigen oscillations of the lake must be taken with care.

That the complex lake form offers difficulties in the interpretation of the periods, can already be seen when it is attempted to attribute the 13-h period to the fundamental mode of the whole lake. Water-level fluctuations with this period were observed – i.e. discernible from water-level-time series – only in a single bay, the Povenetskiy bay, at the water-level stations 10, 12, 13 and nowhere else. The confusion about this

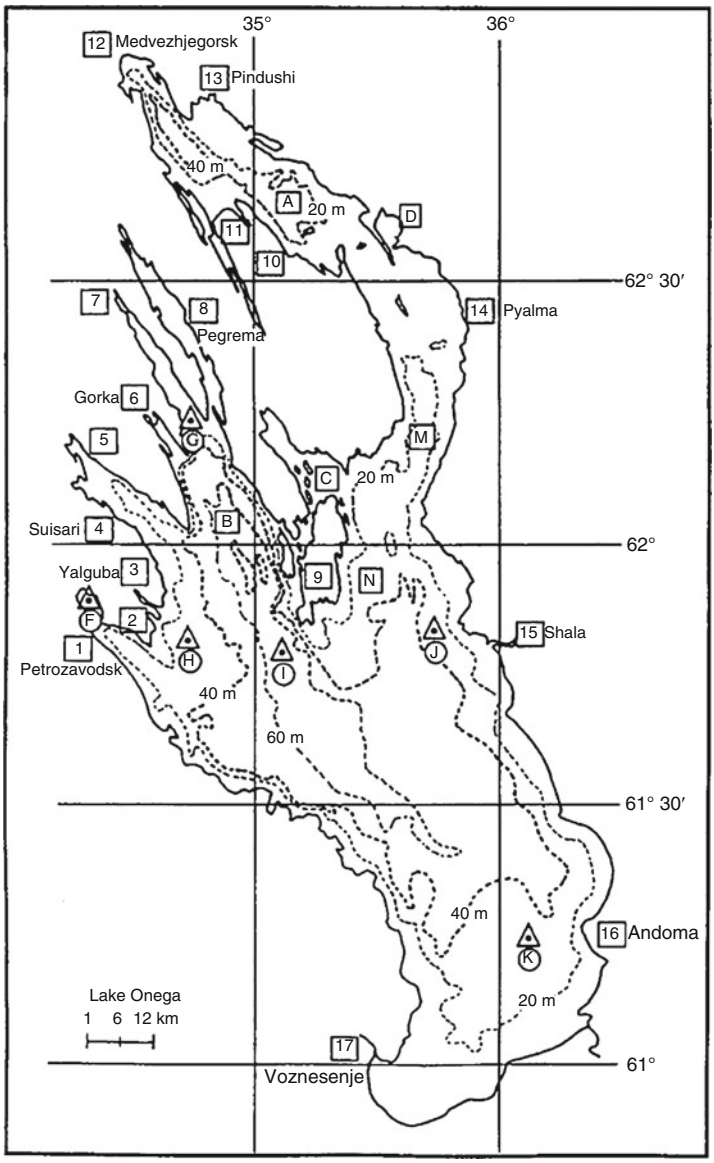

Fig. 17.1 Bathymetric chart of Lake Onega contoured in meters and showing the entire lake with 20, 40, 60 m contours. The numbered positions 1–17 show locations where limnigraphs were moored. Stations F, G, H, I, J and K, also marked by *triangles*, show positions where current-meters were moored. For ease of reference we give here a list of place names and their identification with symbols in the map. 1: Petrozavodsk Bay, 2: Ivanovskie Islands, 3: Yalguba, 4: Suisari, 5: Condopoga Bay, 6: Gorka, 7: Big Lizhma Bay, 8: Pegrema, 9: Big Klimenets Islands, 10: Sal Island, 11: Svyatuha, 12: Medvezhjegorsk, 13: Pindushi, 14: Pyalma, 15: Shala, 16: Andoma, 17: Voznesenje, A: Povenetskiy Bay, B: Big Onega Bay, C: Velikaya Bay, D: Chelmuzbskaya Bay, M: Zaonezhskiy Bay, N: Small Onega Bay (From Rudnev et al. [10]).

Table 17.1 Surface seiche periods observed at different positions of lake Onega (see Fig. 17.1) by level gauge recordings (Malinina and Solntseva [6]). The periods are given in hours and minutes and are identified as 1–9. These numbers identify table columns and do not indicate modes of the barotropic seiches

Point of observation		'Mode' Periods (in h and min)								
	Position	1	2	3	4	5	6	7	8	9
Medvezhjegorsk	12	13:20		2:16		1:02				
Pindushi	13	13:20		2:16		0:60				
Sal	10	13:20		2:20		0:58				
Svyatuha	11						0:44			
Pegrema	8			2:12						
Lizhma	7		4:20	2:15	1:20		0:44		0:14	
Gorka	6		4:15	3:10					0:18	
Condopoga	5		4:20	2:15		1:06		0:26		
Suisari	4					1:05		0:26		
Yalguba	3				1:22			0:20		
Petrozavodsk	1				1:30			0:22		
Pyalma	14		4:30			0:58		0:26	0:15	
Ivanovskie Island	2		4:18	2:15					0:18	0:10
B.Klimenets	9		4:25					0:22		0:08
Shala	15			2:15		0:59			0:12	
Andoma	16		4:20	2:30	1:12				0:16	
Voznesenje	17		4:20	2:30	1:22	0:60				

period emerged from a rough analysis with the Merian formula, $T = 2L/\sqrt{gH}$, where T is the period, L the length of the (rectangular) basin and H its constant water depth, which gave a 'theoretical' first-mode period of 8 h which, however, was not recorded (see Table 17.1). In this evaluation, $L = 250$ km was taken to be the length of the entire lake from the northern most point (position 12 in Fig. 17.1) to its southern end (about at position 17) and a mean depth of approximately 30 m is used. The interpretation of the entire lake basin as a rectangle being rather problematic, Malinina and Solntseva nevertheless 'stuck out their heads' and chose L to be twice the length of the right most arm ($= 122$ km) with the mean depth equal to 13.9 m, and obtained a period of 11.6 h. This choice positioned the nodal line by construction at the entrance of the right arm of the lake (Zaonezhskiy and Povenetskiy bays, which together form this arm). The southern, large basin then plays the role of the second half of the Merian-rectangle. However, since this basin is much larger, its water-level displacements in such a hypothetical fundamental mode are expected to be much smaller than those at the northern most tip of the Povenetskiy bay; this may serve as a possible explanation that the 13-h period could not be identified by eye from time series of water-level fluctuations taken at stations that were situated in the southern main basin, see [11–14].

There were also other attempts in identifying observed periods in Lake Onega by Merian's formula and its modification [5,9,11–14]. For instance, considering the Zaonezhskiy and Povenetskiy bays as a lake in isolation, and selecting $L = 122$ km, $h = 13.9$ m, the Merian formula yields 11.6 h for the fundamental period, which is,

perhaps, close to the observed 13 h. However, all these analyses are at best educated guesses. They may give a halfway satisfactory explanation of the fundamental mode, but certainly cannot explain any other observed period. A detailed analysis to that end appears to be mandatory and is attempted in the ensuing analysis.

17.2 Measured Water-Level Fluctuations and Water Currents at Isolated Points

The data that are closely analyzed here, are the level gauge records taken from the Malinina archives, collected in 1965. Figure 17.2 shows excerpts from these. Panel (a) shows a 720 h excerpt of the water-level fluctuations from 25 August to 23 September 1965 at positions 12 and 17, i.e. at the northern most point in the Povenetskiy bay and in the south-west corner of the large southern basin. By simply counting the maxima of the water-level-time series at position 12 between 100 and 300 h we find a period of approximately 11.8 h. A similar result is obtained by the corresponding minima for the water-level-time series at station 17, and the minima occur simultaneously with the maxima of the water fluctuations at station 12. In other words, the two time series at these periods exhibit a counter-phase relationship. Figure 17.2a also allows identification of periods of about 25 and 50 h, and certainly the water-level-time series at positions 12 and 17 also contain shorter period processes, but this analysis is best deferred until Fourier spectral plots are presented.

Water-level-elevation-time series at other locations were taken by Rudnev in the late 1980s and early 1990s. Figure 17.2b shows an 80-h episode from September 1990 of the water-level displacement at position 1 (see Fig. 17.1, at the northwest shore of the main basin), from which an 11.8-h period can be identified even more easily; shorter periods are discernible from a spectral analysis.

We also show two episodes from current measurements recorded at position F and J in the main basin taken in February 1987 and July 1989, respectively (for positions F and J, see Fig. 17.1). Graphs of the time series are displayed in Fig. 17.3a,b. They show the modulus of the velocity at F and J, plotted against time. The two episodes disclose physically two different processes. The time series at position 1 discloses a dominant process with a period of approximately 12 h complemented by less energetic motions at smaller periods. For the time series taken at position F, the dominant process has about a period of 4.2 h, and processes with larger and smaller periods are superposed on it with less energy.

The spectral analysis subtracts the best linear trend from the time series. To reduce leakage the resulting time series was processed with a spectral window and filters having lengths between 10 and 30%. Standard MESA technique of spectral analysis as described in Barrondale and Erickson [1] were used; technical details will therefore not be shown. We move directly to the discussion of the spectral plots shown in Figs. 17.4 and 17.5.

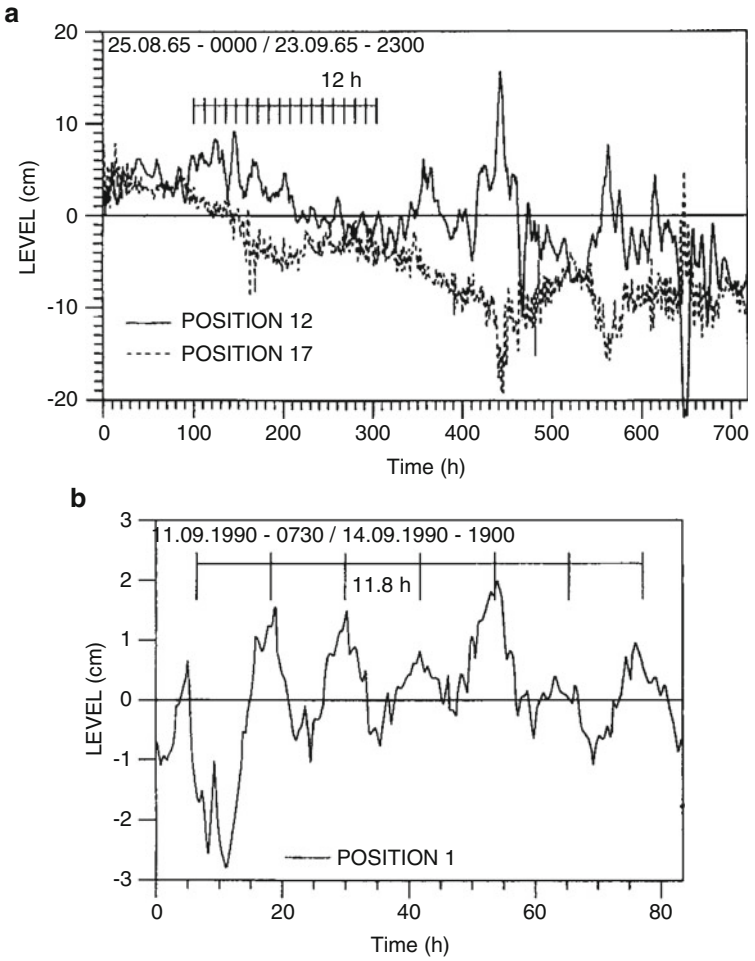

Fig. 17.2 Excerpts of time series for water elevation: (**a**) 720-h episode recorded at Medvezhjegorsk (position 12) and at Voznesenje (position 17) measured by Malinina, from 25 August 1965 (00 h 00 min) to 23 September 1965 (23 h 00 min). We have indicated eye-fitted oscillations of approximately a 12-h period; note the signals at the two stations are out of phase at this period. (**b**) Data recorded in Petrozavodsk Bay at position 1 from 11 September 1990 (7 h 30 min) to 14 September 1990 (19 h 00 min), recorded by a WLR-5 instrument. An 11.8-h periodic signal is indicated again (From Rudnev et al. [10]). ©Annales Geophysicae, European Geosciences Union, reproduced with permission

Figure 17.4 shows the energy densities against period (frequency) for four water-level-time series at positions 2, 12, 17 and 1 (Fig. 17.4a–d) the positions being identifiable from Fig. 17.1. The graphs are given in double logarithmic representation (to be energy conserving) and a high frequency cut-off at 5 cycles h^{-1} (corresponding to a period of 2 h) was employed (see the vertical dashed lines).

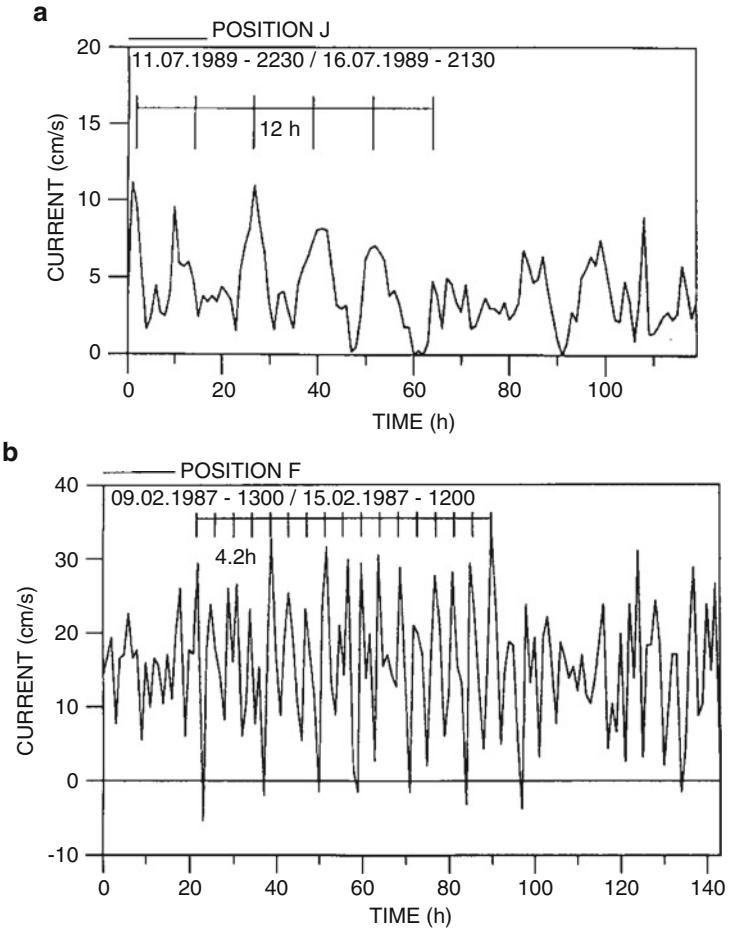

Fig. 17.3 Excerpts of time series of the current speed: (**a**) 120-h episode of a current–time series recorded by an ATSIT instrument at position J, at 10 m depth, from 11 July 1989 (22 h 30 min) to 16 July 1989 (21 h 30 min) with a period of 12 h. (**b**) 144-h episode of a current-time series recorded by the RCM-4 instrument in Solomenskiy Strait (position F) in Winter, from 9 February 1987 (13 h 00 min) to 15 February 1987 (12 h 00 min) with a period of app. 4.2 h. (We have no information about direction) (From Rudnev et al. [10]). © Annales Geophysicae, European Geosciences Union, reproduced with permission

Indicated is also the 95% confidence interval and the period of measurement for which the spectral analysis was performed (lower left corners of the graphs). Lastly, the small vertical strokes, numbered from 1 to 5 show the values of computed eigen-periods of the five lowest order barotropic modes for the whole Lake Onega to be described below. Figure 17.4b–d, show the spectra of the water-level-time series at positions 12, 17 and 1, also shown directly in Fig. 17.2. Similarly, Fig. 17.5 displays the energy spectra of the current-time series from episodes taken at positions K,

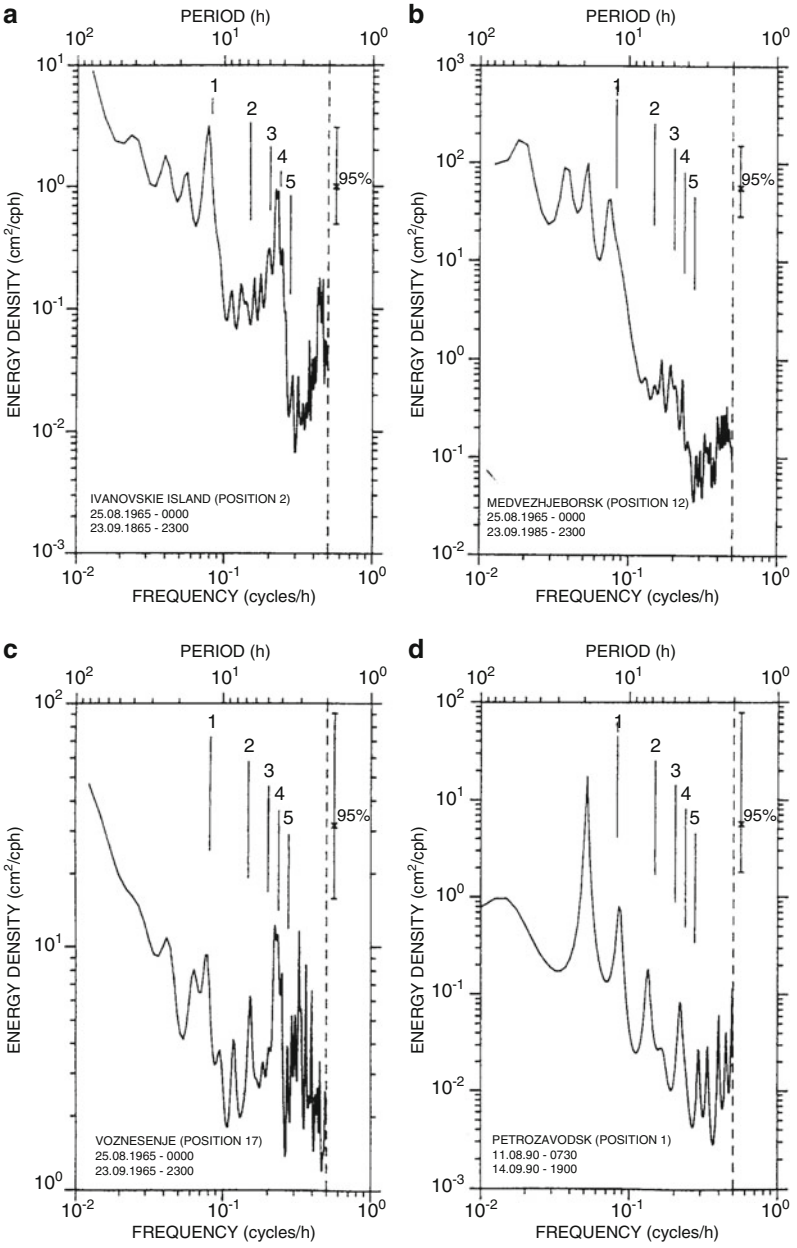

Fig. 17.4 Energy spectra of the water-elevation-time series in double logarithmic representation for positions 2, 12, 17 and 1 for episodes as indicated in the insets of each panel. Also shown are the 95% confidence intervals (*upper right corner*). The *dashed vertical line* indicates the higher frequency cut-off at 2-h period. The vertical strokes, numbered 1–5 indicate the periods (frequencies) of the five lowest seiche modes predicted by the model (From Rudnev et al. [10]). © Annales Geophysicae, European Geosciences Union, reproduced with permission

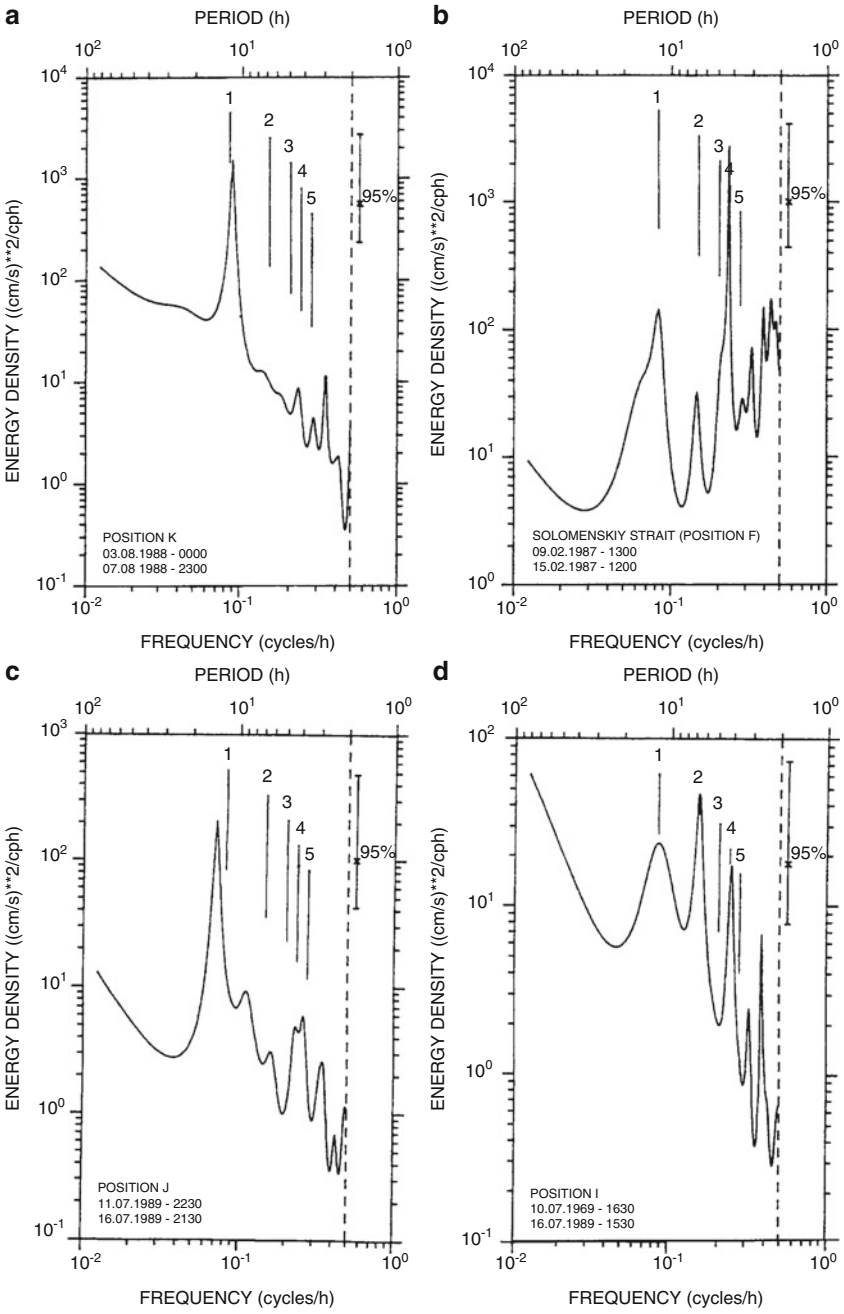

Fig. 17.5 Energy spectra of the current–speed–time series in double logarithmic representation for positions K, F, J, and I for episodes as indicated in the insets of each panel (see also caption of Fig. 17.4) (From Rudnev et al. [10]). © Annales Geophysicae, European Geosciences Union, reproduced with permission

F, J and I; the graphical display is the same as for Fig. 17.4, and Fig. 17.5b, c are the spectra of the time series from Fig. 17.3. We will return to these observational evidences when an attempt of interpretation of these observations is made.

17.3 The Barotropic Eigenvalue Problem

We use the homogeneous linearized shallow-water equations referred to a Cartesian coordinate system and ignore the rotation of the Earth and frictional effects (Hutter [2] or see Chap. 11, (11.17), in which $f = 0$ and H replaced by h). Thus

$$\frac{\partial \boldsymbol{u}}{\partial t} + g\nabla_H \zeta = 0, \tag{17.1}$$

$$\frac{\partial \zeta}{\partial t} + \nabla_H \cdot (\boldsymbol{u}h) = 0, \tag{17.2}$$

in which $\boldsymbol{u}$ is the 2-vector consisting of the Cartesian components u and v and ζ is the surface displacement; moreover ∇_H is the two-dimensional gradient operator, g the gravity constant and h the water depth. Equation (17.1) is the horizontal momentum equation, balancing the acceleration term with the horizontal pressure gradient; Coriolis effects are ignored. Alternatively, (17.2) is the vertically integrated mass balance. Equations (17.1) and (17.2) must be solved in the lake domain $\mathcal{D}$ subject to the boundary conditions of no water flow through the shore line,

$$\boldsymbol{u} \cdot \boldsymbol{n} = 0, \quad \text{along } \partial\mathcal{D}, \tag{17.3}$$

where $\boldsymbol{n}$ is the unit normal 2-vector along the shoreline.

When a harmonic time dependence is extracted, i.e. if $(\boldsymbol{u}, \zeta) = (\bar{\boldsymbol{u}}, \bar{\zeta}) \exp(i\sigma t)$, then (17.1) and (17.2) may be used to deduce the following eigenvalue problem for $\bar{\zeta}$:

$$\left.\begin{aligned} &\nabla_H \cdot (h\nabla_H \bar{\zeta}) + \frac{\sigma^2}{g}\bar{\zeta} = 0, && (x, y) \in \mathcal{D}, \\ &\nabla_H \bar{\zeta} \cdot \boldsymbol{n} = 0, && (x, y) \in \partial\mathcal{D}, \end{aligned}\right\}, \tag{17.4}$$

in which σ is the frequency to be determined as the eigenvalue of problem (17.4). To each σ_n belongs a corresponding eigenfunction $\bar{\zeta}_n$, here often simply referred to as the mode. Once $\bar{\zeta}_n$ is evaluated the velocity field is determined by

$$\bar{\boldsymbol{u}} = i\frac{g}{\sigma}\nabla_H \bar{\zeta}, \tag{17.5}$$

i.e. the velocity field leads the free surface elevations by $\pi/2$.

Let $\Omega = 0.73 \times 10^{-4}\,\mathrm{s}^{-1}$ be the angular velocity of the Earth and $\phi = 62°$ the mean latitude of the lake area; then $f = 2\Omega \sin\phi = 1.28 \times 10^{-4}\,\mathrm{s}^{-1}$ and the external Rossby radius of deformation becomes

$$R = \sqrt{gH/f^2} \cong 135\,\mathrm{km} \tag{17.6}$$

for $H = 10\,\mathrm{m}$. With a maximum width of approximately 80 km the effects of the rotation of the Earth are likely to be moderately small and will subsequently therefore be neglected. In any case, effects of the rotation of the Earth, if significant, will only be recognizable in the southern large basin.

Because of the complex geometry of the lake a finite difference net with constant mesh size requires fine resolution. Square elements were chosen with 1 km side length within a coordinate system of which the axes were oriented 30° counterclockwise from the WE and SN directions. Using a centred second order finite-difference representation this resulted in a rectangular net of 107×231 cells, of which 9,344 were activated with non-empty entries representing surface elevations. The matrix that emerges has the dimension $9{,}344 \times 9{,}344$. It implies that the corresponding matrix eigenvalue problem that follows from (17.4) is extremely large. Limitation in storage of the available computer prevented direct solution of the matrix eigenvalue problem. An approximate determination of the few lowest eigenmodes is warranted. The Lanczos [4], approximate method, explained in Paige [8] and Schwab [17] was used.

We shall outline the Lanczos procedure in detail in Appendix A, comprising Sect. 17.6 of this chapter. Here, it may suffice to explain its effects and workability. The procedure is to expand $\bar{\zeta}_n$ as

$$\bar{\zeta}_n = \sum_{i=1}^{NF} C_i^n W_i, \quad NF \to \infty, \tag{17.7}$$

where W_i are orthonormal functions, defined over the domain $\mathcal{D}$ that satisfy the boundary conditions $(17.4)_2$, i.e. $\int_{\mathcal{D}} W_i W_j \mathrm{d}A = \delta_{ij}$ and $\partial W_i / \partial \boldsymbol{n} = \mathbf{0}$ along $\partial\mathcal{D}$.

Substituting (17.7) into the eigenvalue equation $(17.4)_1$ yields the standard matrix-eigenvalue equation

$$\sum_{i=1}^{NF} A_{ji} C_i^n = \lambda_n C_j^n, \quad \lambda_n = -\frac{\sigma_n^2}{g}, \tag{17.8}$$

where

$$A_{ij} = \int_{\mathcal{D}} (W_j \nabla_H \cdot h \nabla W_i) \mathrm{d}A.$$

The advantage of the matrix-eigenvalue equation (17.8) as opposed to the corresponding eigenvalue problem that obtains from a direct discretization of problem (17.4) is that, by adequately choosing $W_i, i = 1, 2, \ldots, NF$ in the Lanczos procedure, the matrix $\boldsymbol{A}$ is symmetric and tridiagonal, in which case special eigenvalue solvers can be used. Solving (17.8) for the eigenvalues λ_n and the eigenvectors C_j^n determines, via $(17.8)_2$ the eigenfrequency σ_n of the original problem and via (17.7) the corresponding eigenfuction. The functions are constructed as shown

in Appendix A. This guarantees that $\boldsymbol{A} = \boldsymbol{A}^{\mathrm{T}}$ and that the functions $W_i, i = 1, 2, \ldots, NF$ are orthonormal in the sense that

$$\int_{\mathcal{D}} W_i W_j \mathrm{d}A = \delta_{ij}. \tag{17.9}$$

17.4 Numerical Results and Their Comparison with Observations

In what follows, we shall discuss the individual modes of the free barotropic oscillations of the basin and compare the results with those deduced from observations and described in Sect. 17.2.

A somewhat critical parameter is the truncation number NF of functions W_i. The few largest eigenfrequencies σ_n^2 can well be determined even with a relatively small number of W_i-functions. To guarantee a sufficiently accurate representation of the modal structure, NF must, however, be large. On the other hand, all W_i-functions must be stored on external devices to free the computer from unnecessarily occupied storage places. For $NF = 3{,}000$, the storage area occupied by the W_i-functions in double precision (8 Bytes real) is about 225 MB.

Analytically, all W_i-functions are orthogonal. However, due to the numerical determination of W_i truncation errors set in after a number of evaluations of W_i (e.g. $i = 50$) and W_{50+j} is not exactly orthogonal to $W_1, W_2, \ldots$. Schwab [17] proposed to test the structure of the free mode as constructed by (17.7) with the parameter

$$\varepsilon = \int_{\mathcal{D}} (\nabla_H \cdot h \nabla_H \bar{\zeta}_n - \lambda_n \bar{\zeta}_n)^2 \mathrm{d}A \Big/ \int_{\mathcal{D}} \zeta_n^2 \mathrm{d}A. \tag{17.10}$$

Analytically, ε is zero, but when the discretized version is calculated numerically, ε is a small number and tends to be large for spurious eigenvalues.

Table 17.2 collects the values of the periods of the first ten modes for three different values of the truncation number NF (equal to 1,000, 3,000 and 6,000, respectively). For $NF = 3{,}000$ the very small values of ε are also listed; the spurious periods with larger ε-values being ignored. It is seen that $NF = 1{,}000$ was too small, because with $NF = 3{,}000$ new eigenperiods emerged with small ε-values. $NF = 6{,}000$ did, however, not generate additional relevant periods in the period interval 12.14–2.22 h that were not obtained with $NF = 3000$. It was thus concluded that $NF = 3{,}000$ was also sufficient for the computation of the surface structure of the ten lowest order modes.

A somewhat critical point is the question of how much the eigenperiods change if the mean depth of the lake is varied. For $NF = 3{,}000$, results are shown in Table 17.3 when $h = 31.3 \pm 0.5$ m. One can see that the eigenperiods do change by 1.5–3.3%. We shall encounter differences of this order when comparing computed

Table 17.2 Periods of surface oscillations in Lake Onega as predicted by the model. Indicated are the mode numbers 1–10, the number NF of basis functions used in the Lanczos procedure ($NF = 1{,}000$, 3,000 and 6,000) and the value ε (for $NF = 3{,}000$) defined in (17.10) which gives an indication of how reliably the eigenperiods have been computed

Mode	T(h)	T[h]	ε	T[h]
	$NF = 1{,}000$	$NF = 3{,}000$	$NF = 3{,}000$	$NF = 6{,}000$
1	12.09	12.14	5.6e–29	12.14
2	6.62	6.74	9.2e–30	6.75
3	4.75	4.89	2.9e–34	4.90
4	4.18	4.19	3.0e–34	4.19
5		3.56	1.1e–30	3.56
6	2.88	2.92	1.1e–33	2.92
7		2.64	2.7e–33	2.65
8		2.50	3.7e–31	2.50
9	2.35	2.35	2.2e–33	2.35
10		2.22	1.6e–29	2.24

Table 17.3 Periods of surface oscillations in Lake Onega calculated for different mean depths of the lake for $NF = 3{,}000$

Mode	Calculated periods (h) $NF = 3{,}000$		
	$H = 30.8$ m	$H = 31.3$ m	$H = 31.8$ m
1	12.34	**12.14**	11.93
2	6.89	6.74	6.62
3	4.98	4.89	4.81
4	4.23	4.19	4.15
5	3.70	3.56	3.44
6	2.97	2.92	2.87
7	2.74	2.64	2.56
8	2.60	2.50	2.36
9	2.40	2.35	2.30
10	2.28	2.22	2.21

periods with measured ones. Not knowing the accuracy of the bathymetric charts, interpretation of the observations requires a certain flexibility in this regard.

Table 17.4 collects the periods, obtained from the solution of the eigenvalue problem (17.8), together with the observational periods as inferred from the spectra of the water-level and water-current-time series. The periods of the latter are taken from the spectral analysis and agree with the identifiable relative maxima in the spectra whose peaks are isolated and large enough to guarantee statistical confidence (see 95% confidence intervals in Figs. 17.4 and 17.5). Table 17.4 shows shaded and unshaded rows and thus anticipates a certain interpretation of the results. The rows corresponding to the computed barotropic free modes are all shaded and thus believed to find an interpretation, the unshaded rows show periods that need another interpretation for which we can presently only offer educated guesses.

Table 17.4 Surface seiche periods of Lake Onega, calculated by the model and observed by spectral analysis from measured data

Mode	Calculated periods [h]	Observed periods [h]									
		Level gauge						Current meter instruments			
		Pos. 2	Pos.12	Pos. 17	Pos. 1	Pos. F Winter	Pos.I	Pos. G	Pos. K Summer	Pos. H	Pos. J
		25.0	26.8	23.9	19.0					26.7	
		17.8	18.7	15.6							
1	12.1	12.8	13.3	12.9	11.8	12.0	12.1	12.5	11.8	14.8	13.8
				8.5	7.4			9.3		9.1	8.9
2	6.7		6.6	6.6		6.8	6.7			6.9	
		6.3	6.0							6.1	6.3
3	4.9	4.5	5.2	4.5	4.5			4.6			
4	4.2	4.3	4.4	4.3		4.2	4.1	4.0	4.3	4.2	4.3
5	3.6	3.4	3.5	3.7	3.4	3.5		3.3	3.4	3.7	3.8
6	2.9	3.2	3.1	3.1	3.0	3.0	3.1	3.0	2.9	3.0	2.9
				2.8							
7	2.6	2.7	2.6				2.6	2.7		2.5	
8	2.5	2.5	2.5	2.5	2.5	2.5					
9	2.4	2.4	2.4					2.4	2.4	2.3	2.4
10	2.2	2.2	2.2	2.2	2.2	2.3		2.2		2.2	

Mode 1. Figure 17.6 shows the structure of the fundamental mode. In Fig. 17.6a the level lines of the surface-elevation-amplitude distribution are shown; they are scaled to a maximum value 1.0; solid lines indicate elevation maxima, and dashed lines correspond to elevation minima. Thus, two water-level-time series from a point on one side and another on the other side of the (zero amplitude) nodal line are out of phase by 180°. This feature is perhaps better illustrated in the axonometric view of Fig. 17.6b which displays the surface elevation at the moment of its maximum. According to the model calculations the fundamental surface seiche has a period of 12.1 h with its maximum amplitude in the Povenetskiy Bay. The nodal line is located at the entrance of the Zaonezhskiy Bay, i.e. the entrance of the large north-eastern most channel; amplitudes grow as one moves northwards and reach their maximum at the northern end of the lake arm. In the central main basin, amplitudes of the water-surface elevations are small everywhere, so that one should not be surprised that early measurements from gauges at shore positions of the large basin hardly

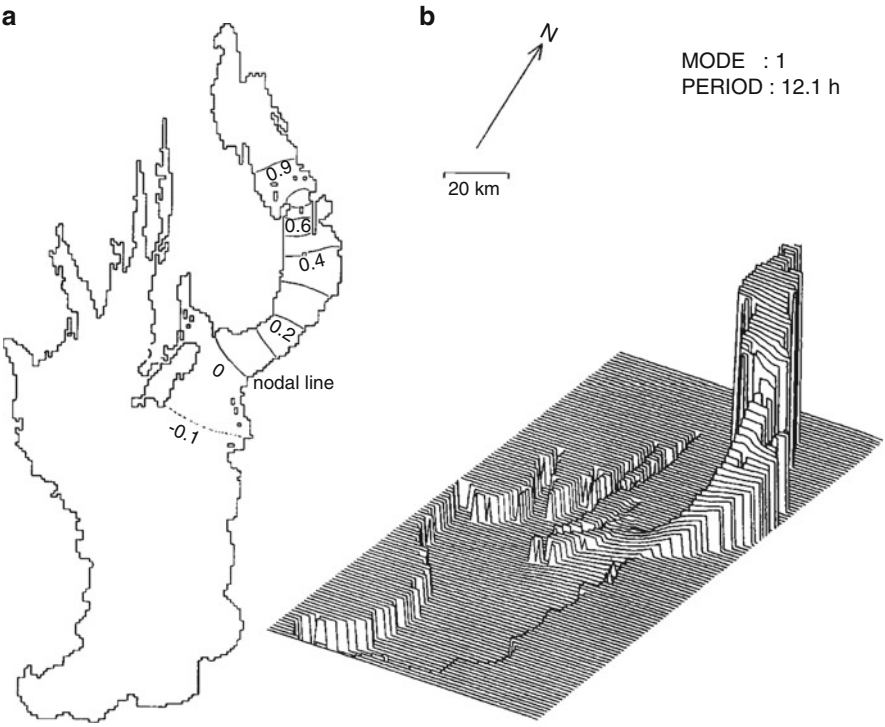

Fig. 17.6 Lake Onega: (**a**) Isolines of surface-elevation amplitudes for the fundamental mode with a period of 12.1 h. *Solid lines* and *dashed lines* indicate surface elevations which are in counter-phase relative to each other. The maximum is scaled to have the value 1 m; (**b**) Axonometric representation of the surface displacement distribution at the moment of extreme amplitudes for the same mode. The two representations are equivalent (From Rudnev et al. [10]). © Annales Geophysicae, European Geosciences Union, reproduced with permission

disclose the 12 h period. According to Malinina and Solntseva [6], oscillations with a 13 h period were only observed at stations 10, 12 and 13 in Povenetskiy Bay with amplitudes between 15 and 18 cm. Our results would imply that amplitudes with this period in the main basin would have been at most 2 cm. It is uncertain whether these were recordable by the water-level gauges used by Malinina and Solntseva.

Interpretation of the data in the vicinity of the fundamental mode period is hampered by the fact that the inertial period is 13.6 h. We emphasize, however, that ideally, the inertial motion does not generate surface displacements and thus only shows up in the velocity records; at a fixed position velocity vectors would rotate in the clockwise direction. Thus we interpret water-level oscillations at the 12-h period as true fundamental-mode response to the barotropic gravitational seiche.

The spectra for the water-level-time series at gauges 12 and 17 show peaks at 13.3 and 12.9 h (Table 17.4) with energies that are larger for the time series at gauge 12 than at gauge 17, in conformity with an interpretation as a fundamental mode signal (Fig. 17.4b,c). The two other spectra of surface elevation at gauges 1 and 2, both positions in the large basin, indicate energy maxima at 11.8 and 12.8 h with energy levels comparable to those at gauge 17 (compare Fig. 17.4a,c and d), again qualitatively corroborating first-mode response. The relatively small period of 11.8 h at gauge 1 could be explained with slow mean water-level fluctuations of approximately 1 m (see Table 17.3), but unfortunately, this is uncertain, as no records about mean water-level variations are available. Rudnev [11] and Rudnev and Petrov [13] attribute this discrepancy to many other effects such as inertial motion, set-up phenomena and coupling with internal waves [18], but do not justify these suspicions.

Interpretation of the current-meter data is more difficult because the observations of processes with a 12–13-h period are likely to be a mix of fundamental-mode response and inertial waves. The fundamental mode response can best be observed by current-meter data from instruments that are located close to the nodal line. However, current-meters were only moored at the locations indicated by the triangles in Fig. 17.1, and those closest to the nodal line are positions I and J. The spectra of these data are shown in Fig. 17.5c,d. At J the energetically significant period is at 13.8 h, and the peak is strong and narrow, suggesting that this signal corresponds primarily to inertial waves. A definite answer would require knowledge about the rotational properties of the velocity, information which we do not have. The spectral peak of the current meter at Station I is at 12.1 h and less strong and broader than at J. This allows the supposition, that this record is a mix between inertial wave and first-mode-barotropic-seiche response.

Current data recorded in the Solomenskiy Straight at position F (Fig. 17.1) close to the shore are significant because they were obtained in winter, when the lake was covered by ice and the wind action on the water masses absent. This also guaranteed absence of a possible barotropic baroclinic coupling of the recorded signals. Moreover, at a shore position inertial waves are unlikely to be active. The peak in the spectrum at the position is at 12.0 h (Fig. 17.5b) and relatively sharp and may thus be attributed to first-mode barotropic seiche behaviour.

Current time series were also recorded at positions G, K and H; spectral analyses of episodes showed maxima of the energy spectra at 12.5, 11.8 and 14.8 h. Since we have no information about the mean water-level, we can only muse about reasons of the differences, but will abstain from doing it.

Mode 2. Figure 17.7a, b displays the second mode of the lake. It possesses two nodal lines, the first approximately connecting the shore points 2 and 9 in Fig. 17.1, the other at the entrance of the Povenetskiy Bay. Water-level displacements are very small everywhere except in Big Onega Bay (in Fig. 17.1 the narrow and long northward-oriented channel at which station 8 is located). This behaviour in very well identifiable in the axonometric view of Fig. 17.7b. This oscillation has a period of 6.7 h and, surprisingly, has been recorded in the water-level gauges 12 and 17, but equally also in the velocity time series at F, I and H, although not in G, K and J. This period, however, was not recorded by the limnigraphs at 1 or 2 which lie close to the nodal line. This mode is obviously not detectable with a simple model except perhaps by assuming that Big Onega Bay forms an open half-channel for which the Merian period is $T = 4L/\sqrt{gH}$. With $L = 50$ km and $H = 7$ m this yields 6.6 h, very close to the 6.7 h.

Interesting as this result is, it has been obtained as an *a posteriori* fact, and we do not think that it is apparent at all. On the other hand, it now becomes understandable why this period is not listed in Table 17.1 and escaped early observations by Malinina and Solntseva [6]. With the less reliable measurements at that time we could at most only have hoped to see the 6.7-h period at gauge 8, but apparently it has not been seen in those records.

Mode 3. Figure 17.7c, d displays the structure of mode 3 with a computed period of 4.9 h. It also possesses two nodal lines (as mode 2 does), one at the entry of the right most large finger-like Zaonezhskiy bay, the second about half way within it and being responsible for the second resonance of the Povenetskiy Bay. Water-level amplitudes are large in this entire bay and reach a maximum in the Velikaya Bay (C in Fig. 17.1). Whereas the surface elevation amplitudes are large in this bay, they are only moderate in the main basin reaching their maximum here close to station 17.

Observations from limnigraphs corroborating this mode are the water-level-spectral peaks of the surface elevation records at positions 2, 12, 17 and 1 with periods 4.5, 5.2, 4.5 and 4.5 h and the velocity-spectral peak at position G with a 4.6 h period. These have an arithmetic mean of 4.7 h. To draw more conclusive inferences, cross-statistical analyses of simultaneous time series from different stations would be needed, but these have not been done.

Mode 4. The fourth mode with a computed period of 4.2 h is the main oscillation of the whole lake. Its structure is shown in Fig. 17.8; it possesses three nodal lines, one crossing the main basin from east to west, the second spanning the entrance of the channel north of the Big Klimenets Island and the third crossing the entrance of the Povenetskiy Bay in the eastern most arm. The second nodal line is continued in the narrow eastern most arm of Big Onega Bay. The axonometric representation of the surface elevation in Fig. 17.8b shows that the water levels of the southern most parts of the large basin are in-phase with those of the Zaonezhskiy Bay and the channel at Pegrema (location 8 in Fig. 17.1). On the other hand, they are in

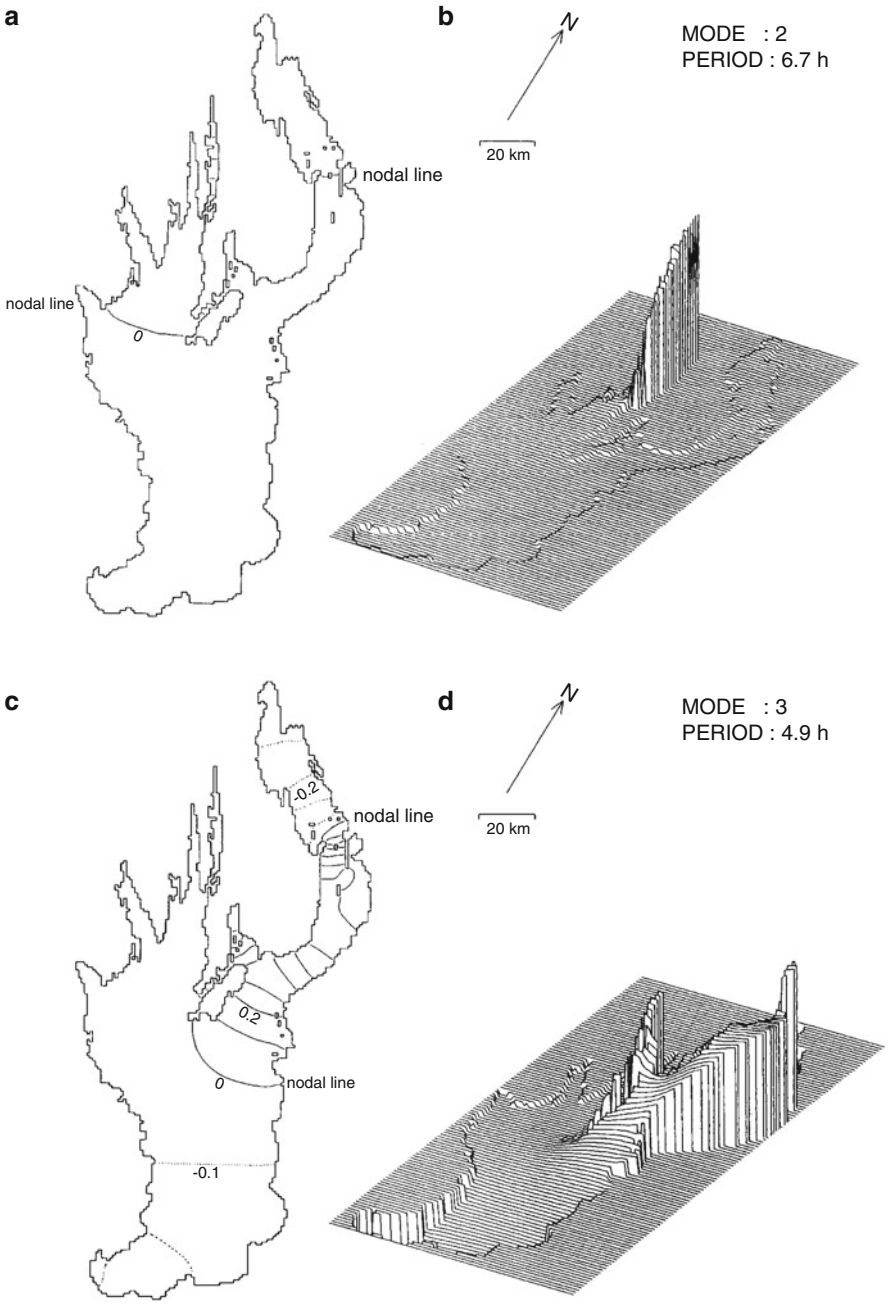

Fig. 17.7 Lake Onega: (**a**), (**b**). Same as Fig. 17.6 but for *mode* 2 with a period of 6.7 h and (**c**), (**d**) for *mode* 3 with a period of 4.9 h (From Rudnev et al. [10]). © Annales Geophysicae, European Geosciences Union, reproduced with permission

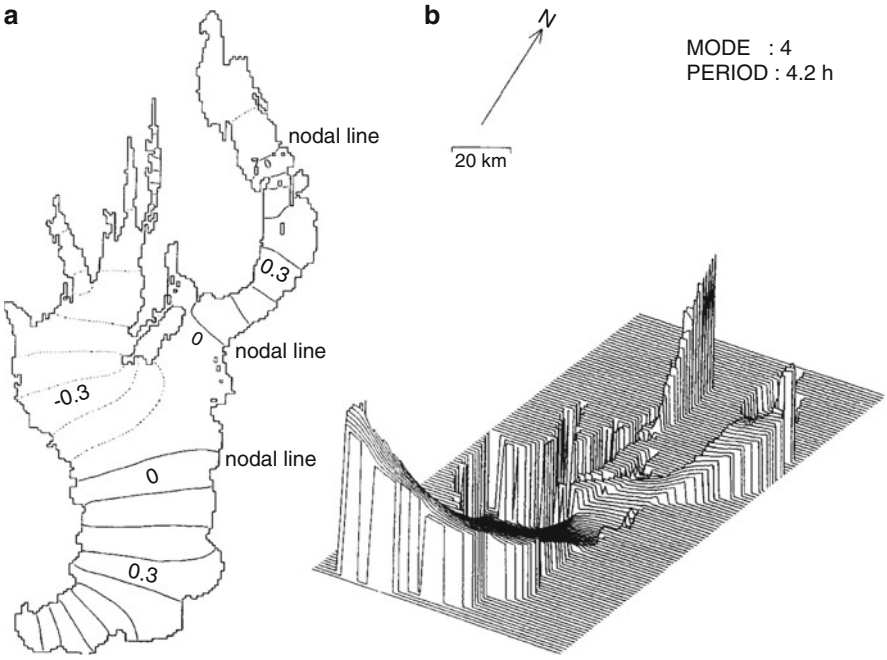

Fig. 17.8 Lake Onega: (**a**), (**b**). Same as Fig. 17.6 but for *mode* 4 with a period of 4.2 h (From Rudnev et al. [10]). © Annales Geophysicae, European Geosciences Union, reproduced with permission

counter-phase with the free surface elevations in the northern part of the main basin (Big Onega Basin) and those of Povenetskiy Bay. This mode is being confirmed by the early water-level measurements at many stations indicated in Fig. 17.1 as can be seen from Table 17.1. However, it is also confirmed by the surface and current measurements of Figs. 17.4 and 17.5, and it has also been identified in temperature measurements [12, 13].

Given the mode structure of Fig. 17.8 with its locations of the nodal lines, one should not be surprised that the 4.2-h period was not recorded at position 15 of Fig. 17.1, which is situated practically on the nodal line. Analogously, at the north tip of Big Klimenets Island the 4.2-h period should not be observed; to no surprise it was only seldom observed at its southern shore with an amplitude of less than 3 cm. The maximum amplitude is to be expected to occur at Voznesenje (position 17 in Fig. 17.1) with an amplitude about 4–5 times larger according to the distribution of the surface-level lines of Fig. 17.8a. Summer to autumn values are about 15 cm which fits these estimates well. Winter values are at 3–4 cm. Similarly, at position 7, in the north of Big Lizhma Bay, water-level amplitudes are 4.7 cm during summer (data from 1966 to 1968) and 8–42 cm in autumn.

Table 17.1, which summarizes data from Malinina and Solntseva [6] shows that this whole-lake mode is discernable at many locations around the lake. Positions

10, 11, 12, 13, but also 15 and 8, however, have apparently no discernable signal at this period. This is good news because all these positions are located where the surface-displacements lines of Fig. 17.8a indicate small to zero amplitudes. The spectral analysis of the level-gauge data (Fig. 17.4) show that oscillations with a 4.2-h period form the dominant signal at positions 2 and 17, while they are hardly detectable at 12, which is now understandable. The spectral analyses of the current data (Fig. 17.5): show large peaks at positions I and J (which are close to a nodal line!) but a small one at position K. At position F, in the Solomenskiy Straight, which connects the main basin of the lake with Lake Logmozero (not shown in Fig. 17.1), is the energetically strongest signal (see Fig. 17.5b). This is no surprise, as Salvadè and Zamboni [15] have shown for Lake of Lugano that, if a channel connects one lake basin with another basin, then the surface seiches lead to strong current oscillations in the channel whenever one of the adjoining basins is excited. All this is in full agreement with the model predictions.

Mode 5. This mode (see Fig. 17.9a) is essentially a bay resonance of the bay Velikaya Guba (C in Fig. 17.1) immediately to the north of Big Klimenets Island (9, in Fig. 17.1) with very small responses in the northern parts of the lake and nothing in the southern part of the main basin. The computed period is 3.6 h, but it does not seem to have been recorded in the early data collected by Malinina and Solntseva [6]. Our water level and current spectra show weak peaks with periods between 3.3 and 3.8 h (see Table 17.4 and Fig. 17.5). Unfortunately, neither water level nor current-meters were moored where the action is in this mode.

Mode 6. It appears to be the second whole-lake mode (see Fig. 17.9b), possesses five nodal lines and has a numerical period of 2.9 h. The early observations (Table 17.1) do not disclose this mode, the spectra of Figs. 17.4 and 17.5 show it clearly at position 1 (Fig. 17.4d) and, in the currents, at positions K, F, I and J (Fig. 17.5). The periods lie between 2.9 and 3.2 h with a mean of 3.0 h.

We have also found a coincidence between the computed periods attributed to modes 7–10 and periods in spectral peaks in Figs. 17.4 and 17.5. They cluster around 2.8 and 2.2 h.

Mode 7 and 8. These are essentially bay resonances (see Fig. 17.9c,d), so that it is no surprise that they are excited at positions 1, 2, 12 and 17 with low energies.

Modes 9 and 10. These are again whole lake responses (see Fig. 17.9e,f) which explains why their periods are better identifiable in the spectra than modes 7 and 8, see also Table 17.4. Obviously, mode identification is very difficult and the coordinations made in Table 17.4 are no more than suggestions. The signal at 2.2 h is particularly frequent (Table 17.4, mode 10) and, interestingly, a period of approximately 2.2 h has also been identified by Malinina and Solntseva [6], see Table 17.1 where it is attributed to ‘mode 3’.

The spectra displayed in Fig. 17.9 provide also clear indication why exact identification of higher order modes must be very difficult. The five modes 6–10 have eigenperiods between 2.9 and 2.2 h. They lie very close to one another and must, in measured time series, be very difficult to separate, unless data are collected simultaneously, have very high resolution and time series are relatively long. In a lake as large as Lake Onega this is hardly possible.

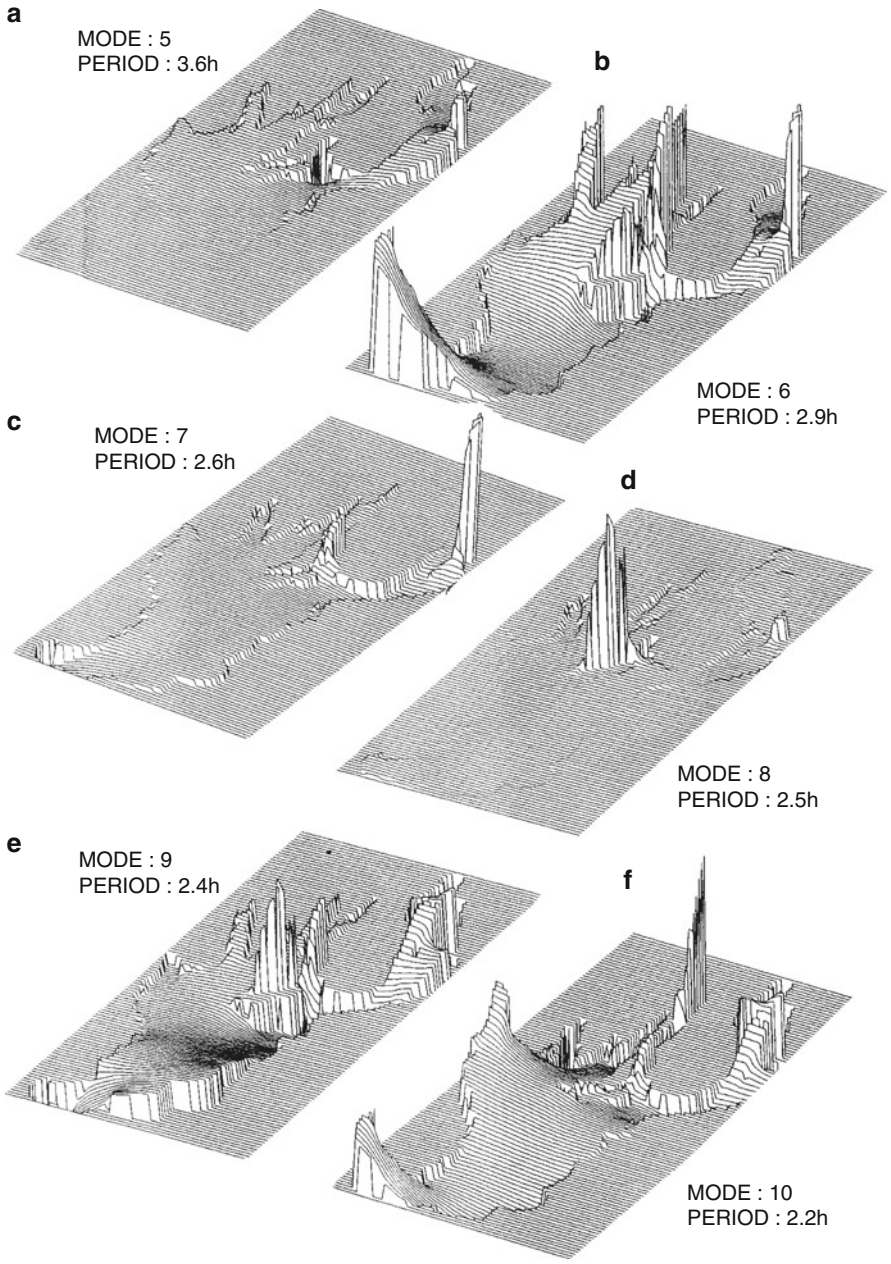

Fig. 17.9 Lake Onega: (**a**)–(**f**). Same as Fig. 17.6b, but (**a**) for mode 5 with a period of 3.6 h, (**b**) mode 6 with a period of 2.9 h, (**c**) mode 7 with a period of 2.6 h, (**d**) mode 8 with a period of 2.5 h, (**e**) mode 9 with a period of 2.4 h, (**f**) mode 10 with a period of 2.2 h (From Rudnev et al. [10]).

The spectra of the current-time series (Fig. 17.5 and Table 17.4) also show oscillations with a period of approximately 9 h. These signals are particularly strong at positions G and H. However, our free oscillation model does not explain this period. We can presently only guess what it might be: a topographic wave, an internal wave response or direct wind forcing.

Table 17.4 also lists periods of observed signals from the spectral analysis of the water level and current-time series that are longer than the barotropic response. These may also be interpreted as the 9-h signal. Finally, Table 17.1 lists a great number of very short periodic events with apparent periods of less and also larger than 1 h. These are likely higher order barotropic responses, perhaps local bay modes or transverse seiches. A careful study would be needed both observationally and computationally to identify them. Computations with the Lanczos procedure would require the choice of NF $\simeq$ 6,000 which is computationally not economical.

17.5 Concluding Remarks

An attempt has been made to interpret water-level fluctuations and current-time series from gauges positioned around and within Lake Onega in terms of the barotropic free seiches of the entire lake basin. The results demonstrate that this modelling attempt for studying the surface seiches of the lake has been successful. They allow interpretation of certain dominant oscillatory processes to be identified as eigenmodes of the lake but also give indications as to where, in later observational studies, limnigraphs should be positioned if certain modes want to be detected.

The analysis indicated very clearly that a naive interpretation using simple thumb rules (like, e.g. the Merian formula) is very dangerous. Most modes are being missed or misinterpreted, and those which could be explained, are *a posteriori* constructions (at least by us). Lake Onega is a perfect example of where only a full-scale analysis could explain the few observations that are available.

Naturally, the analysis is imperfect at several places (some of which we explicitly indicated). Better data should be available if certain inferences are to be founded on a better physical ground. A proper identification of modes of the external gravitational seiches would also require determination of phase differences of the oscillations from time series of station pairs. This requires simultaneous measurements at several gauges, which was not done. Furthermore, in the current-meter data, information was only available about the absolute value of the speed. A proper analysis would also require measurement of the direction. With such information, one could see how the water current at a certain location would rotate, and could therefore identify e.g. inertial modes and find out how significant the effects of the rotation of the Earth would indeed be in the external wave dynamics. Therefore, even though the analysis revealed many answers it also raises questions for further possible studies.

17.6 Appendix: The Lanczos' Procedure in Solving Symmetric Eigenvalue Problems

Consider the eigenvalue problem[2]

$$\begin{aligned} \nabla \cdot (h \nabla \zeta_n) &= \lambda_n \zeta_n \quad && (x, y) \in \mathcal{D}, \\ \nabla \zeta_n \cdot \boldsymbol{n} &= 0, && (x, y) \in \partial \mathcal{D}, \end{aligned} \tag{17.11}$$

where h is a positive function, $\mathcal{D} \subset \mathbb{R}^2$ and $\boldsymbol{n}$ is the unit normal vector exterior to $\partial \mathcal{D}$; $n = 1, 2, 3, \ldots$ is a counting index. This corresponds to (17.4) in the main text with

$$\lambda_n = -\frac{\sigma_n^2}{g}. \tag{17.12}$$

To show that λ_n is real and negative, and therefore that σ_n is real, multiply $(17.11)_1$, by ζ_n^*, the conjugate complex of ζ_n and integrate the resulting identity over $\mathcal{D}$. This process yields

$$\int_{\mathcal{D}} \zeta_n^* \nabla \cdot (h \nabla \zeta_n) \mathrm{d}a = \lambda_n \underbrace{\int_{\mathcal{D}} \zeta_n^* \zeta_n \mathrm{d}a}_{>0}. \tag{17.13}$$

The left-hand side can be rewritten as

$$\int_{\mathcal{D}} \nabla \cdot \{\zeta_n^* h \nabla \zeta_n\} \mathrm{d}a - \int_{\mathcal{D}} h (\nabla \zeta_n^* \cdot \nabla \zeta_n) \mathrm{d}a.$$

With the use of the divergence theorem and the boundary condition $(17.11)_2$ the first integral vanishes, so that (17.13) becomes

$$\lambda_n = -\frac{\displaystyle\int_{\mathcal{D}} h (\nabla \zeta_n^* \cdot \nabla \zeta_n) \mathrm{d}a}{\displaystyle\int_{\mathcal{D}} \zeta_n^* \zeta_n \mathrm{d}a}. \tag{17.14}$$

On the right-hand side, the numerator and denominator are both positive proving that $\lambda_n < 0$.

The eigenfunctions to two different counting indices are orthogonal and can be normalized such that

$$\int_{\mathcal{D}} \zeta_i \zeta_j \mathrm{d}a = \delta_{ij} \tag{17.15}$$

To show this, we write (17.11), as

[2] We follow Schwab [16]. In this appendix ∇ must be interpreted as the two-dimensional Nabla operator $\nabla := \nabla_H$.

$$\nabla \cdot (h\nabla\zeta_i) = \lambda_i \zeta_i,$$
$$\nabla \cdot (h\nabla\zeta_j) = \lambda_j \zeta_j,$$

multiply the first by ζ_j, the second by ζ_i, integrate the resulting identities over the domain $\mathcal{D}$ and subtract. This yields

$$\int_{\mathcal{D}} \{(\nabla \cdot (h\nabla\zeta_i))\zeta_j - (\nabla \cdot (h\nabla\zeta_j))\zeta_i\} \mathrm{d}a = (\lambda_i - \lambda_j) \int_{\mathcal{D}} \zeta_i \zeta_j \mathrm{d}a. \tag{17.16}$$

The integral on the left-hand side vanishes; to show this, we write

$$\int_{\mathcal{D}} (\nabla \cdot (h\nabla\zeta_i))\zeta_j \mathrm{d}a = \int_{\mathcal{D}} \nabla \cdot (\zeta_j h \nabla\zeta_i) \mathrm{d}a - \int_{\mathcal{D}} h\nabla\zeta_i \cdot \nabla\zeta_j \mathrm{d}a$$

$$= \int_{\partial\mathcal{D}} \zeta_j h \underbrace{\nabla\zeta_i \cdot \boldsymbol{n}}_{0} \mathrm{d}s - \int_{\mathcal{D}} h\nabla\zeta_i \cdot \nabla\zeta_j \mathrm{d}a = -\int_{\mathcal{D}} h\nabla\zeta_i \cdot \nabla\zeta_j \mathrm{d}a,$$

and an analogous expression holds for the second member on the left-hand side of (17.16). Therefore,

$$(\lambda_i - \lambda_j) \int_{\mathcal{D}} \zeta_i \zeta_j \mathrm{d}a = 0. \tag{17.17}$$

This is automatically satisfied for $i = j$, but for $\lambda_i \neq \lambda_j$ it implies the vanishing of the integral. Because the eigenfunctions ζ_i are determined up to a constant factor, they may be normalized such that $\int_{\mathcal{D}} \zeta_i^2 \mathrm{d}a = 1$. This proves (17.15).

The Lanczos procedure consists in transforming the eigenvalue problem (17.11) into a different eigenvalue problem by expanding ζ_n into a series of different functions that are suitably selected,

$$\zeta_n = \sum_{i=1}^{\infty} C_i^n W_i. \tag{17.18}$$

For all i the functions W_i are selected such that

$$(1) \quad \frac{\partial W_i}{\partial \boldsymbol{n}} = \boldsymbol{0}, \qquad \text{for } (x, y) \in \partial\mathcal{D} \qquad (2) \quad \int_{\mathcal{D}} W_i W_j \mathrm{d}a = \delta_{ij}. \tag{17.19}$$

Requirement (1) guarantees that the boundary conditions on ζ_n are automatically satisfied and (2) establishes the orthonormality of the W_i's. When applied to the discretized version of $(17.11)_1$, the Lanczos procedure results in a tridiagonal symmetric matrix with the same eigenvalues as the general matrix of $(17.11)_1$.

With (17.18), (17.11) becomes

$$\nabla \cdot \left\{ h\nabla \left(\sum_{i=1}^{\infty} C_i^n W_i \right) \right\} = \lambda_n \sum_{i=1}^{\infty} C_i^n W_i. \tag{17.20}$$

Multiplying both sides of this equation by W_j and integrating the resulting identity over $\mathcal{D}$ yields

$$\sum_{i=1}^{\infty} C_i^n \underbrace{\int_{\mathcal{D}} W_j \nabla \cdot (h \nabla W_i) \mathrm{d}a}_{=A_{ij}} = \lambda_n \sum_{i=1}^{\infty} C_i^n \underbrace{\int_{\mathcal{D}} W_i W_j \mathrm{d}a}_{\delta_{ij}}$$

or

$$\sum_{i=1}^{\infty} C_i^n A_{ij} = \lambda_n C_j^n. \tag{17.21}$$

This is an infinite set of homogeneous equations for the eigenvalues λ_n and the eigenvectors C_j^n. In practical applications one must truncate the summation and then obtains the matrix eigenvalue problem

$$\sum_{i=1}^{NF} C_i^n A_{ij} = \lambda_n C_j^n. \tag{17.22}$$

Once λ_n and $C_i^n (i = 1, 2, \ldots, NF)$ are known, σ_n follows from (17.12) and ζ_n from (17.18).

The matrix A_{ij} is symmetric. This can be shown as follows:

$$\begin{aligned} A_{ij} &= \int_{\mathcal{D}} W_j \nabla \cdot (h \nabla W_i) \mathrm{d}a = \underbrace{\int_{\mathcal{D}} \nabla \cdot (W_j h \nabla W_i) \mathrm{d}a}_{\substack{= 0 \text{ by divergence} \\ \text{theorem and } (17.19)_1}} - \int_{\mathcal{D}} h \nabla W_j \cdot \nabla W_i \mathrm{d}a \\ &= -\int_{\mathcal{D}} h \nabla W_j \cdot \nabla W_i \mathrm{d}a = A_{ji}. \end{aligned}$$

There remains to construct the functions W_i such that A_{ij} is a tridiagonal matrix. This is done by the following recurrence relation:

- Initialization:

$$W_0 = 0, \quad W_1, \quad \text{such that} \quad \partial W_1 / \partial \boldsymbol{n} = \mathbf{0}.$$

- Recurrence procedure

$$\begin{aligned} \alpha_i &:= \int_{\mathcal{D}} W_i \nabla \cdot (h \nabla W_i) \mathrm{d}a, \quad (\text{no sum over } i), \\ \hat{W}_{i+1} &:= (\nabla \cdot h \nabla - \alpha_i) W_i - \beta_i W_{i-1}, \\ \beta_{i+1} &:= \left(\int_{\mathcal{D}} \hat{W}_{i+1} \hat{W}_{i+1} \mathrm{d}a \right)^{1/2}, \\ W_{i+1} &:= \frac{1}{\beta_{i+1}} \hat{W}_{i+1}. \end{aligned} \tag{17.23}$$

If W_1 and $W_0 = 0$ are given, relations (17.23) define a recurrence relation to compute W_i, α_i and β_i. α_i are the diagonal elements of A_{ij} and β_i the first off-diagonal elements. To this end, a useful way of writing $(17.23)_2$ is

$$\begin{aligned} &\beta_{i+1}W_{i+1} = (\nabla\cdot h\nabla - \alpha_i)W_i - \beta_i W_{i-1}, \\ \text{or}\quad &\\ &\nabla\cdot h\nabla W_i = \alpha_i\cdot W_i + \beta_{i+1}W_{i+1} + \beta_i W_{i-1}, \end{aligned} \tag{17.24}$$

in which $(17.23)_4$ was used. If we multiply $(17.24)_2$ by W_j and integrate the emerging equation over $\mathcal{D}$, we generate the identity

$$\begin{aligned} &\int_{\mathcal{D}} W_j\nabla\cdot(h\nabla W_i)\mathrm{d}a \\ &\quad = \alpha_i\int_{\mathcal{D}} W_j W_i\,\mathrm{d}a + \beta_{i+1}\int_{\mathcal{D}} W_j W_{i+1}\mathrm{d}a + \beta_i\int_{\mathcal{D}} W_j W_{i-1}\mathrm{d}a. \end{aligned} \tag{17.25}$$

Letting $j = i$ in (17.25), we obtain

$$A_{ii} = \int_{\mathcal{D}} W_i\nabla\cdot(h\nabla W_i)\mathrm{d}a = \alpha_i, \tag{17.26}$$

since $W_i W_j$ are orthonormal. The first off-diagonal elements are obtained by letting $j = i-1$ in (17.25),

$$A_{(i-1)i} = \int_{\mathcal{D}} W_{i-1}\nabla\cdot(h\nabla W_i)\mathrm{d}a = \beta_i = A_{i(i-1)}. \tag{17.27}$$

Finally, by choosing $j = i-k, k = 2,3,\ldots$, the orthonormality of the W_i's implies that $A_{(i-k)i} = 0$. Thus, A_{ij} is indeed symmetric tridiagonal.

In summary, the Lanczos procedure for the solution to (17.11) consists of the following steps:

1. Selection of starting functions $W_0 = 0$ and W_1 such that $\partial W_1/\partial\boldsymbol{n} = \mathbf{0}$ at the boundary,
2. Application of the recurrence procedure (17.23) for the evaluation of α_i, β_i and W_i,
3. Solution of the linear homogeneous equations (17.22) for the eigenvalues λ_n and the eigenvectors C_i^n, and
4. Evaluation of the eigenvalues σ_n according to (17.12) and the eigenfunctions ζ_n according to (17.18).

In this solution procedure, the functions W_i are not needed for the solution of the eigenvalue problem (17.21) or (17.22) and can be externally stored once and for all. Furthermore, in the numerical implementation the recurrence procedure (17.23) is usually applied with centred difference formulas for the gradient operator and simple summation for the integrations. Analytically, all W_i are orthogonal according to

$(17.19)_2$. In practice, however, since all W_i are determined numerically, truncation errors set in and cause W_k, k large, not to be orthogonal to W_1. This implies that a large number of W_i-functions is required to resolve the modal structures, but the lowest eigenfrequencies are determined quite well at low truncation. Furthermore, at higher truncation the loss of orthogonality tends to cause spurious values of λ_i to appear. Schwab [17], proposed to test the structure of the free mode as constructed by (17.18) with the parameter

$$\varepsilon = \frac{\int_{\mathcal{D}} (\nabla \cdot (h \nabla \zeta_n) - \lambda_n \zeta_n)^2 \mathrm{d}a}{\int_{\mathcal{D}} \zeta_n^2 \mathrm{d}a}. \tag{17.28}$$

Analytically, ε is zero, but when the discretized version of (17.28) is calculated numerically, ε is some small number and tends to be larger for spurious eigenvalues.

References

1. Barrondale, I. and Erickson, R.E.: Algorithms for least-squares linear prediction and maximum entropy spectral analysis. *Geophysics*, **45(3)**, 420–432 (1980)
2. Hutter, K.: Fundamental Equations and Approximations. In: *Hydrodynamics of Lakes. CISM Courses and Lectures, No.286*, Springer, New York, 1–76 (1984)
3. Kaufmann ZS (ed.) Ekosistema Onezhskogo ozera i tendentsii ee izmenenija. Nauka Publ. House, Leningrad, 264 pp [Ecosystem of Lake Onega and tendency of its transformation, in Russian] (1990)
4. Lanczos, C.: An iteration method for the solution of the eigenvalue problem of linear differential and integral operators, *J. Res. Natl. Bur. Stand.*, **45**, 255–282 (1950)
5. Lifshits, V.H., Boyarinov, P.M. and Petrov, M.P.: Observations and spectral analysis of seiche currents in Lake Onega. In: *Ecological Studies of Lake Onega*, Petrozavodsk, 5–7 (in Russian) (1981)
6. Malinina, T. I. and Solntseva, N. O.: The seiches of Lake Onega. Water masses dynamics of Lake Onega. In: *"Nauka"*, Leningrad, 40–74, (1972) (in Russian)
7. Molchanov, I.V.: Lake Onega. In: *"Gidrometeoizdat"*, Leningrad, 208 p. (in Russian) (1946)
8. Paige, G.W.: Computational variants of the LANCZOS method for the eigenproblem, *J. Inst. Math. Appl.*, **10**, 373–381 (1972)
9. Petrov, M. P. and Lifshits, V. H.: *Spectral analysis of temperature oscillation in Petrozavodsk Bay of Lake Onega*, Petrozavodsk, 48–52 (in Russian) (1981)
10. Rudnev, S.F., Salvadè, G., Hutter, K. and Zamboni, F.: External gravity oscillations in Lake Onega. *Annales Geophys.*, **13**, 893–906 (1995)
11. Rudnev, S.F.: The interaction of seiches and inflow current in Lake Onega. In: *VINITI Ref. Jour., 2060-B89*, Petrozavodsk, 19 p. (in Russian) (1989)
12. Rudnev, S.F. and Petrov, M.P.: Internal wave dynamics in Lake Onega (Experiment Fjord-1, 1987). In: *VINITI Ref. Jour. 878-B90*, Petrozavodsk, 68 p. (in Russian) (1990)
13. Rudnev, S.F.: Internal wave dynamics in Lake Onega (Experiment Fjord-2, 1988). In *VINITI Ref. Jour. 2362-B90*, Petrozavodsk, 31 p. (in Russian) (1990)
14. Rudnev, S.F.: Internal wave dynamics in Lake Onega (Experiment Onega-89). In *VINITI Ref. Jour. 3872-B91*, Petrozavodsk, 80 p. (in Russian) (1991)
15. Salvadè, G. and Zamboni, F.: External gravity oscillations of the coupled basins of the Lake of Lugano. An explanation of the current oscillations in the channel at Melide. *Ann. Geophysicae*, **5B**(3), 247–254 (1987)

16. Schwab, D.J.: Internal free oscillations in Lake Ontario. *Limnol. Oceanogr.*, **22**, 700–708 (1977)
17. Schwab, D.J.: The free oscillations of Lake St. Clair. *Great Lakes Environment Research Laboratory, NOAA Techn. Mem. ERL GLERL-32* (1980)
18. Sirkes, Z.: Surface manifestations of internal oscillations in a highly saline lake (the Dead Sea). *Limnol. Oceanogr.*, **32 (1)**, 76–82 (1987)
19. Stabrowskiy, M.: Du phénomène des seiches: observations faites durant un séjour de sept années près du Lac Oniga. *Comp. Rend. Acad. Sci.*, **XLV**, Paris (1857)

Chapter 18
Observation and Analysis of Internal Seiches in the Southern Basin of Lake of Lugano[1]

18.1 Introductory Remarks, Lake Morphology

As mentioned already earlier in Chap. 15, Lake of Lugano is a lake system consisting of two large basins and a pond of much smaller size, all connected to one another. In fact, the discharge of the water masses is from the 15 km long Northern basin through the channel of Melide into the roughly S-shaped 17-km long Southern basin and from there through the 500-m long channel of Lavena into the small pond at Ponte Tresa, see Fig. 18.1. The barotropic response of the two large basins has been separately studied as has this response of the lake system as a whole. In the Southern basin, three limnigraphs, positioned at Riva San Vitale, Morcote and Agno, recorded in February 1982 water elevation oscillations with periods of 28 min and less, that could be identified with the eigenperiods of the surface seiches with amplitudes of less than 5 cm. In a further campaign in 1984, current meters were installed in the Channels of Melide and Lavena and it was found that two further longer periodic eigenoscillations were excited which were not discernible in the limnigraph records and could be interpreted as the eigenvalues of the barotropic oscillations of the lake system acting as a coupled (Helmholtz-type) resonator. The structure of the eigenmodes, i.e. the distribution of the surface elevation was relatively simple. As the eigenfrequencies (periods) increased (decreased) the eigenmodes went from simple to complex with the number of nodal lines increasing by one with each higher order mode. Qualitatively this behaviour is akin to that of a rectangular basin with constant depth, so that interpretation of the data by means of theoretical modelling is easy. Deviations of the eigenperiods and structures of the eigenfunctions from those of the rectangle are due to the bathymetry and nothing else.

This is not so for the dynamic response, where besides the geometry of the basin also the density structure affects the response of the lake to oscillations. If the stratification is only vertical, then the periods of the internal seiche oscillations are determined by both the bathymetry and the stratification, whilst the corresponding

[1] This chapter closely follows the article Stocker et al. [33]. When this paper was written Prof. C.H. Mortimer read its first version and, apart from correcting our English wording, gave advise for improvement.

K. Hutter et al., *Physics of Lakes*, *Volume 2: Lakes as Oscillators*, Advances in Geophysical and Environmental Mechanics and Mathematics,
DOI 10.1007/978-3-642-19112-1_18,

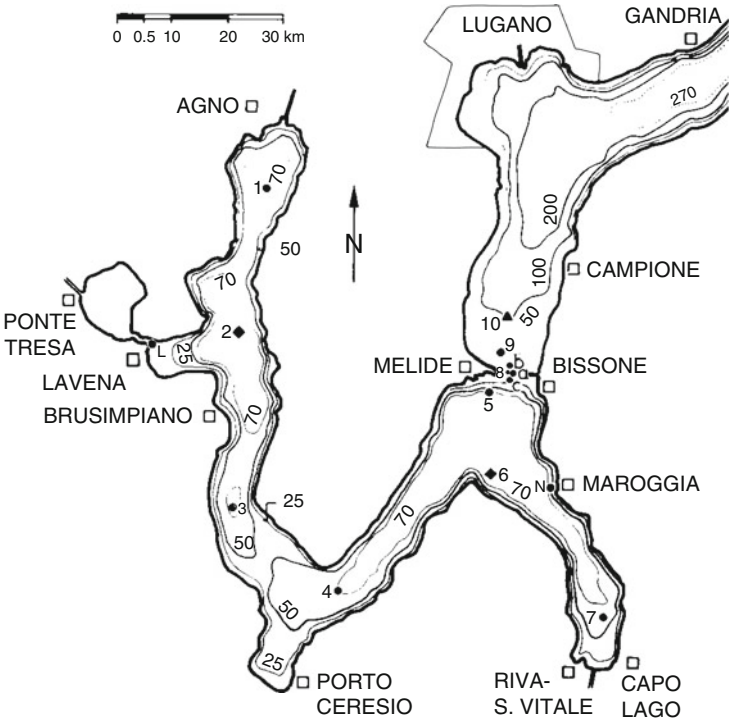

Fig. 18.1 Bathymetric chart of the Lake of Lugano contoured in metre and showing the entire Southern Basin, part of the Northern Basin, the lagoon at Ponte Tresa, and the connecting channels at Melide and Lavena. Symbols mark the positions of the following instruments: *filled circles*: moorings with a current meter in the epilimnion, and one in the hypolimnion, and a thermistor chain encompassing the thermocline; *diamonds*: meteorological buoys; *triangles*: positions with current meters, thermistor chains, and meteorological instruments (from Stocker et al. [33]), © European Geosciences Union, reproduced with permission)

mode structure is given by the lake geometry alone. In this chapter, this will be demonstrated particularly convincingly, since the vertical temperature or density profile changed during the measuring period by strong wind events. We report and interpret measurements taken in a field campaign in summer 1984 in the Southern basin of Lake of Lugano to study its internal wave dynamics. Thermistor chains were moored at seven different positions at depth encompassing the metalimnion with, generally, current meters above and below the thermocline and meteorological buoys at the three positions 2, 6 and 10 (Fig. 18.1). Over stretches of several days the wind was relatively mild so that isotherm depth time series exhibit amplitudes of 1–2 m and can be considered small, justifying application of the linear shallow water equations. However, strong wind events of 1–2 days duration also occurred; they changed the stratification by turbulent mixing and therefore also altered the internal dynamics after the storm relative to that prior to the storm.

The basin size of Lake of Lugano is such that the effects of the rotation of the Earth can safely be ignored for barotropic wave processes. For baroclinic oscillation this neglection is less convincing, especially if higher baroclinic modes[2] are excited. The observations, however, show that the higher baroclinic response is so small that it could not be discerned and, if present, was hidden in the 'noise' of the response to unstructured smaller scale phenomena.[3]

Displacements of isothermal surfaces from their equilibrium positions during and after wind stress were observed and have been documented for many lakes. We mention only a few: Lake Zurich [10, 18, 35–37]; Lake of Lugano, North Basin [12]; Lake Geneva [4, 14–17]; Lake Ontario [29]; Lake Constance [3, 9].[4] These lakes are rather simply structured; they are generally long and have fairly straight thalwegs. Wind stress in the long direction is likely to excite internal gravity waves of several mode orders and interpretation of these eigenoscillations in terms of a linear baroclinic two-layer model has been rather successful.

As Fig. 18.1 shows, the South basin is a long and narrow S-shaped basin of 19 km thalweg length, 1 km mean width and 60 m mean depth. Its maximum depth at position 2 is 90 m and its surface area is 20.3 km^2. In plan view it is divided into three legs. The first, from Agno to Porto Ceresio is directed towards South, the second, from Porto Ceresio to Melide points towards North-East and the third, from Melide to Riva San Vitale points towards South-East. The bathymetry, however, suggests a different subdivision. There are two sills, one North-West of Porto Ceresio, the other between Lavena and Agno, so that the bay at Agno, the stretch between the two sills and the nook between Porto Ceresio and Riva San Vitale, may in first order be regarded as separate units.

---

[2] What is meant here is the baroclinic response beyond the two-layer response. At mid summer stratification the epilimnion depth is 12 m. With a mean depth of 70 m and a relative density difference $\Delta\rho/\rho = 2.5 \times 10^{-3}$ and $f = 1.55 \times 10^{-5}$ (s^{-1}) for $\phi = 42°$, the two-layer internal, Rossby radius of deformation is

$$R_{\mathrm{int}}^{(2)} = \sqrt{g h_{\mathrm{eq}} \frac{\Delta\rho}{\rho}} \Big/ f = 3{,}559\,\mathrm{m}, \quad h_{\mathrm{eq}} = \frac{h_1 h_2}{h_1 + h_2}.$$

This is larger than the lake width almost everywhere. An analogous estimate for a three-layer model shows that

$$R_{\mathrm{int}}^{(3)} \simeq 1{,}000\,\mathrm{m},$$

which is slightly less than typical half-widths of the lake. So, the rotation of the Earth can be ignored.

[3] This statement is correct if the higher baroclinic modes due to the diffusive thermocline are meant and separate density interfaces due to chemically induced layering are not present. In Chap. 15 (Higher order baroclinicity (I)), it was shown that for the Northern basin of the Lake of Lugano large chemocline elevations occurred with only small amplitudes of the thermocline displacements. In the Southern basin of Lake of Lugano no separate chemocline was recorded.

[4] Similar measurements were also performed in lakes with more compact shapes, e.g. Lake Banyoles [26, 27]; Lake Biwa [20, 28]; Lake Kinneret [1, 2] and others.

In spite of this seemingly complex topography of the basin and surrounding alpine landforms, the first four modes of the basin response were found to be excited. Indeed, during storms, hypolimnetic water was sometimes forced into the North Basin against the mean flow through the Melide Channel. We describe and interpret some features of the internal motion recorded by instruments moored at various positions and depths in the Southern Basin of the Lake of Lugano. Measurements lasted from mid August to mid October 1984. Descriptions of the instruments, the mooring arrangements, data processing and first detailed interpretations were given in a report by Stocker and Salvadè [31]. At seven positions (1–7 in Fig. 18.1) in the South Basin and one position in the North Basin (9 in Fig. 18.1) current meters and thermistor chains were moored, generally with a current meter in the epilimnion, a second one in the hypolimnion and the 15 or 20 m long thermistor chain with 11 equidistant sensors in the thermocline. Additional current meters were also moored for 2 weeks in the channels at Melide (connecting the North- and South Basins, positions 8c) and Lavena (connecting the South Basin and the pond at Ponte Tresa, position L) and at Maroggia (South Basin, position N).

Meteorological data (wind, air temperature, solar irradiation) were recorded on buoys at positions 2, 6 (South Basin) and 10 (North Basin) with anemometers and temperature sensors at 2.6 and 5.4 m above the water level. Further wind data are available from the automatic meteorological station at Lugano of the Swiss Meteorological Service. The current- and anemometers recorded speed and direction every 10, 20 or 30 min and the thermistor chains recorded temperature every 20 or 30 min, respectively (see Table 18.1). Furthermore, in an attempt, to study the water exchange processes through the channel between the North- and South Basin in greater detail, current meters and thermistors were also moored in, and close to, the Channel of Melide (positions 8a and 8b) from February 1984 until May 1985.

18.2 State of Stratification and Wind Forces: 15 August–15 October 1984

The measuring interval is characterized by three episodes of relatively calm weather separated by two strong storms on 5–6 September and 1–2 October, respectively which led to thermocline erosion and descent.

Table 18.1 Mean thermocline depth and temperatures and mean epilimnion and hypolimnion temperatures of a two layer model during the indicated periods in 1984 as constructed from all temperature recordings

Period	Thermocline		Mean temperature	
	Depth [m]	Temperature [°C]	Epilimnion [°C]	Hypolimnion [°C]
14 August–5 September	8.6	15.9	20.6	6.6
7 September–30 September	12.2	12.3	16.4	6.2
3 October–16 October	14.5	10.5	13.9	6.0

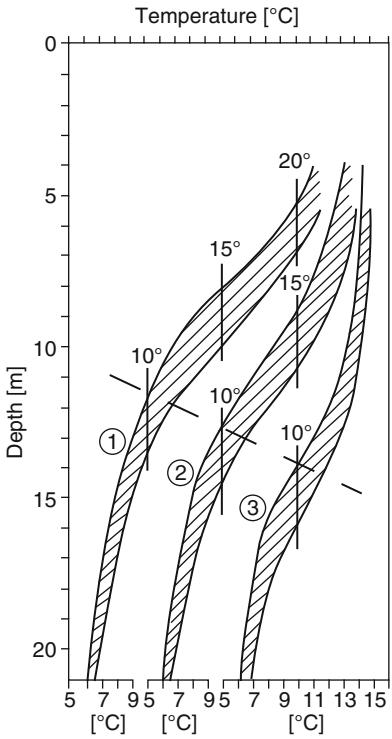

Fig. 18.2 Vertical profiles of temperature, °C, representing three 48 h intervals with differing stratification structure. The profiles 1, 2 and 3, respectively centred on 00.00 h MEZ on 30 August, 13 September and 9 October, are envelopes of the 48 h averaged profiles at all positions 1–7 (position 1 near the *upper* edge, 5 and 6 near the *bottom*, 2, 3, 4, and 7 in the *middle*). The *dashed line* indicates how the thermocline erodes during the measuring period (from [33]), © European Geosciences Union, reproduced with permission)

Temperature–time series, recorded at each mooring position at 11–13 different depths, therefore, yield different vertical temperature profiles for the three periods. Figure 18.2 shows the ranges of the temperature–depth relation during the three episodes into which the recorded temperatures fall at positions 1–7 when averages over 48 h are taken.

Table 18.1 lists the parameters of a two-layer approximation over all temperature measurements during the indicated periods. These were computed from the temperature profiles which lie in the middle of the dashed areas of Fig. 18.2 with smooth extrapolations to the surface. The temperature profile at position 1 is always at the upper edge of the shaded areas in Fig. 18.2, those of positions 5 and 6 at the lower edge, whilst those of positions 2, 3, 4 and 7 lie nearer to the middle. A possible reason for this could be differential deepening of the thermocline due to different wind exposure [13]. We believe that, at position 1, the colder river water entering at Agno dives down and thus pushes the thermocline upwards in that vicinity. At positions 5 and 6 the predominance of warm epilimnion waters flowing from the North- to the South Basin presses the thermocline downwards in its neighbourhood. The spread in the temperature profile is about 2 m or less, definitely less significant than the changes associated with the thermocline erosion produced by the storms and, in the last interval, surface cooling. The three subintervals require separate treatment, which will complicate the spectral analysis.

Wind, responsible for excitation of the internal seiche modes was applied, not only occasionally during storms, but also more regularly in diurnal wind impulses exhibiting a dominant NS component. On most days the anemometer at Lugano recorded wind from South in the early afternoon, which reversed at 20.00–21.00 MEZ ($= UTC + 1$) and remained northerly for the entire night. Wind-rosettes for all meteorological stations (Fig. 18.3) also show this NS channelling for strong winds with speeds $|\boldsymbol{v}| < 3\,\mathrm{ms}^{-1}$ except at position 2 where the preferred orientation is NW-SE. Weaker winds with $|\boldsymbol{v}| < 3\,\mathrm{ms}^{-1}$ have, however, in general much less directional preference. Position 6 is somewhat special as it is very close to the shore and thus shielded by the nearby mountains. This may explain why the expected SE component along the basin between Melide and Riva San Vitale is virtually absent. At any rate, the prevailing NS-wind is likely to excite one of the higher order internal gravity modes.

The direct response of the lake to the 5/6 September storm is illustrated in Figs. 18.4 and 18.5. With vectors of wind speed squared (proportional to wind stress), the stick diagram (Fig. 18.4a) displays the time variation of stress magnitude and direction at positions 6, 2, 10 and Lugano SMA. Figure 18.4b is a corresponding diagram for epilimnetic currents at positions 1, 2, 4–7.

Evidently the general wind at the SMA station was toward N from approximately 06.00 to 18.00 MEZ on 5 September and then turned towards S and stayed there until the storm ended in late afternoon, 6 September. Wind at positions 10 and 6 followed the same pattern. However, at station 2 the wind during the early part of the storm was towards SW; only in the second half did all stations indicate a wind stress generally directed southward. The response of the epilimnetic current to this event (Fig. 18.4b) was, however, complicated and confusing. At position 2, where epilimnion current and wind stress are expected to be uni-directional, they at first differed (compare time series on 5 September between 06.00 and 18.00 MEZ for wind and current). They later agree (in the second half of the storm, 5 September, 18.00 to 6 September, 12.00 MEZ) but deviated again afterwards. The current meter at position 2 seems to have been the only one that indicated an onset of a conspicuous oscillatory motion induced by the storm. Current records at the other moorings show slight direct responses to the storm between Agno and Porto Ceresio (positions 1, 2, 4); but directionally rather incoherent water currents are seen between Melide and Riva San Vitale (positions 5, 6, 7). This suggests that small gyres might have migrated past those instruments.

Easier to interpret is the Fig. 18.5 sequence of isotherm depth distributions, interpolated between positions 1, 4, 6, 7, which displays the internal motion along the thalweg. In the first part of the storm, when the wind was blowing towards N, isotherms at positions 1, 2 and 6 were lowered, while those at positions 3, 4 and 7 rose (Fig. 18.5a, b). Therefore, epilimnetic water must have been pushed from Porto Ceresio towards Agno and from Riva San Vitale towards Melide. This is corroborated in Fig. 18.4 at positions 1, 2 and 4 at 09:30 MEZ on 5 September, but not conclusively at position 7. Accompanying this setup was upwelling in the Melide and Porto Ceresio regions, clearly shown in panel (b). The compensating process was a downstroke of the hypolimnion isotherms at the lake ends (c and d at position

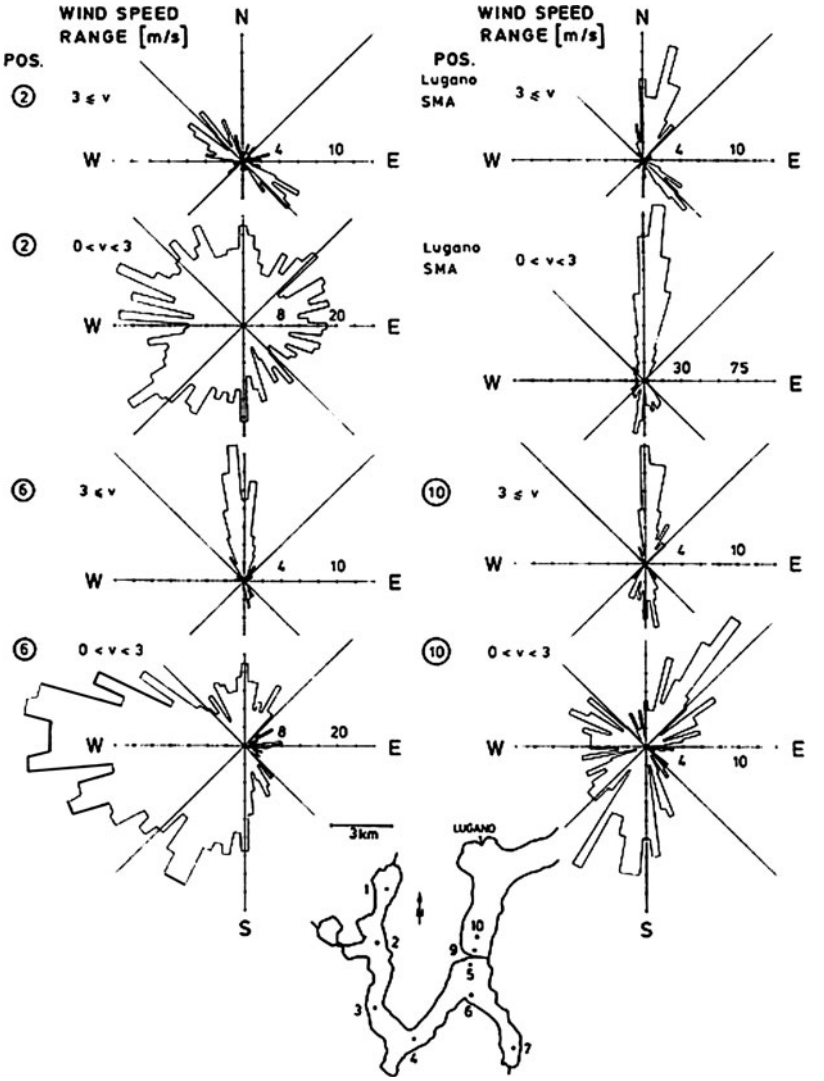

Fig. 18.3 Wind rosettes of the wind speed $|v| < 3\,\mathrm{ms}^{-1}$ and $|v| > 3\,\mathrm{ms}^{-1}$ at positions 2, 6, Lugano (SMA) and 10 (directions indicate where the wind is blowing from). Note that the scale of the frequency of occurrence differs for different positions and ranges of wind speed (from [33], © European Geosciences Union, reproduced with permission)

7 and less convincing at position 1, but strong in panels (c), (d) at 3). The accompanying drift of hypolimnetic water towards the Melide area enhanced the upwelling there (d, position 6). By this time the wind forcing had turned. Wind blew now for more than a full day from N. The onsetting internal motion was reorganized by the strong wind shear; and epilimnetic water was then consistently pushed along the

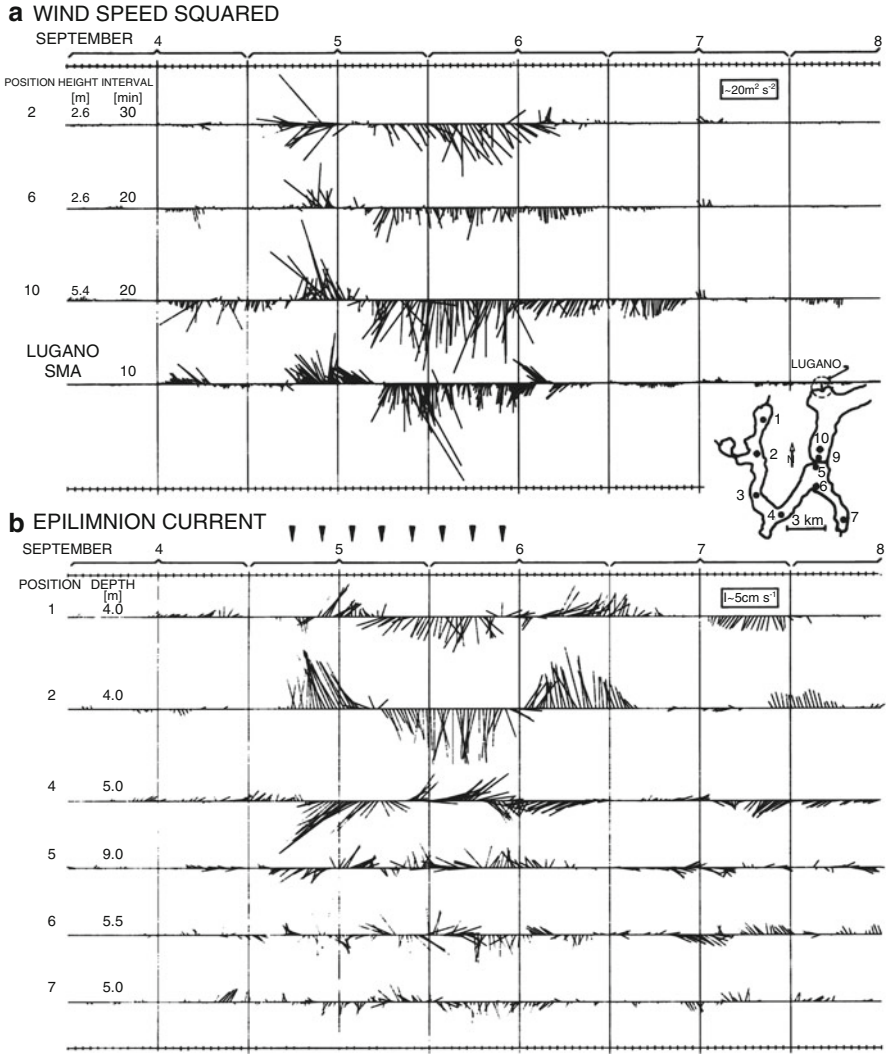

Fig. 18.4 Stick diagrams of: (**a**) wind speed squared $(u^2 + v^2)^{1/2}u$, $(u^2 + v^2)^{1/2}v$ at positions 2, 6, 10 and Lugano (SMA) from 4 to 8 September; and (**b**) half hour means of epilimnetic current at positions 1, 2, 4–7 during the same period. The sticks point towards the direction into which the wind blows or the water flows. Locations of the positions can be inferred from the inset. *Filled triangles* indicate the timing of the panels in Fig. 18.5 (from [33], © European Geosciences Union, reproduced with permission)

'channel' axis from Agno to Riva San Vitale. Correspondingly, the isotherm depth tilt, not yet evidenced in graph e, increased with time (f, g, h). The stick plots of epilimnetic current in Fig. 18.4b are consistent with this interpretation. The currents at positions 1 and 2 were towards S.

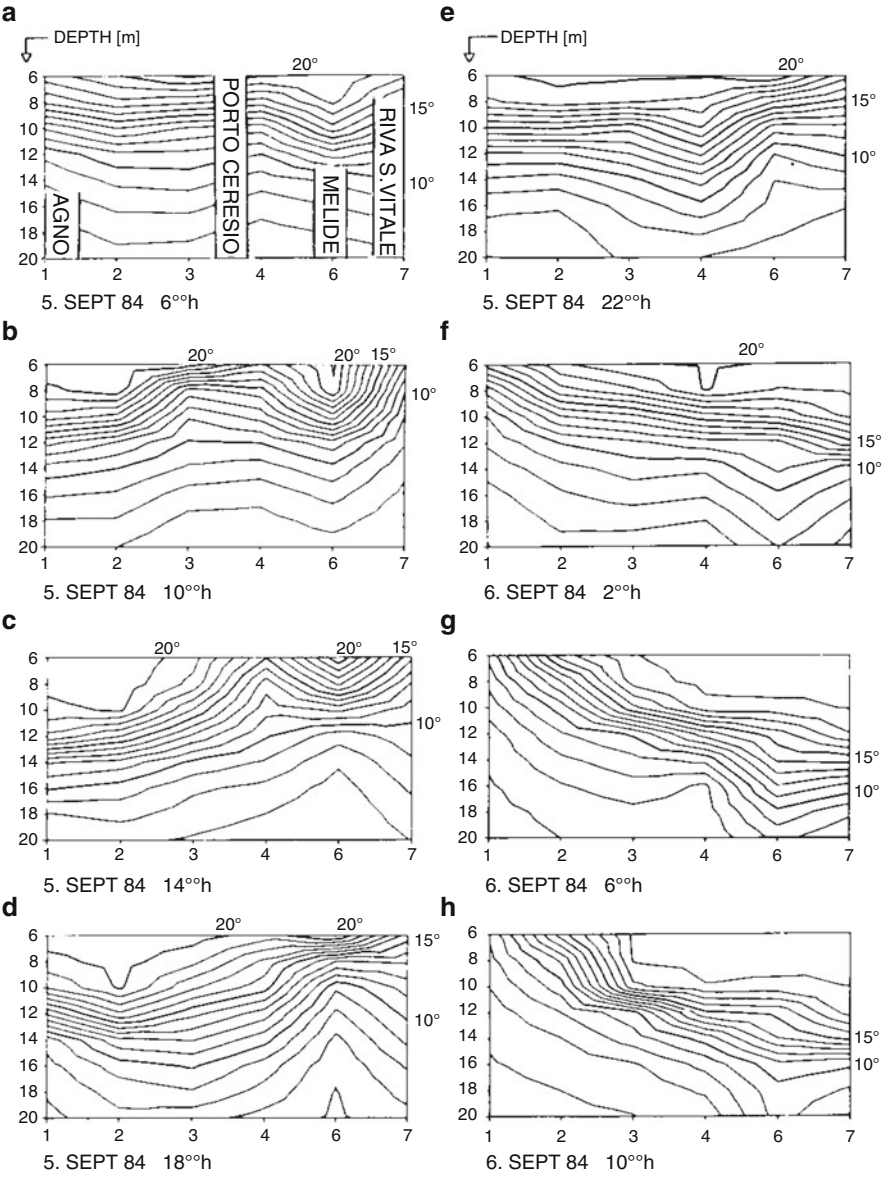

Fig. 18.5 Eight spatially interpolated 'distribution snapshots' of whole-degree isotherms (7° and above) along the unrolled thalweg at 4 h intervals from 5 September 06.00 h to 6 September 10.00 h, i.e. covering the storm illustrated in Fig. 18.4. The approximate positions of villages along the basin are indicated in (**a**) (see also Fig. 18.1) (from [33], © European Geosciences Union, reproduced with permission)

The current at position 4 was towards NE and towards S at position 7. At 12.00 MEZ on 6 September there was a current reversal at positions 1 and 2, even though the wind was still blowing, though less strongly, towards S. This backward swing is indicative of the ongoing internal oscillation, discussed in detail in the next section.

18.3 Internal Seiche Response: Variation in Isotherm Depth and Wind Stress

The data set from the 1984 field program contains temperature–time series from all 11 equidistant thermistors on chains at the seven moorings of the South Basin and from thermistors built into the current meters. Each series is used to construct interpolated isotherm–depth–time plots. Isotherm depths, indicative of vertical displacement of water particles within the metalimnion, are better suited for spectral analysis than are temperature–time series.

This procedure is standard ever since Phillips' [21] paper on spectra in a stratified undulating medium. In the following graphs, we plot hourly depth averages of the 12 or 8°C isotherms together with corresponding stick diagrams of hourly-averaged vectors of wind energy 2.6 m above the water surface. The 12 and 8°C isotherms correspond roughly to the thermocline depth and to a depth at the lower edge of the metalimnion, respectively. Episodes before, between, and after the two storms are selected for a separate study.

18.3.1 Internal Oscillations 25 August–5 September

(Figure 18.6, before the 5/6 September storm). The main features are:

1. The wind stresses at moorings 2 and 10 showed strong wind from N and S on 25 and 26 August due to adverse weather. Thereafter, a daily cycle persisted until 5 September when a strong storm commenced. The strong afternoon pulses, towards N at position 10 and NW at position 2, and the corresponding weak reverse wind at night are typical for lake-land wind behaviour. (The different directions (NW and SE) at 2 reflect a local response attributable to the channelling of the Magliasina Valley just NW of position 2.)
2. Isotherm–depth plots, which during the first two days are influenced by the adverse weather, show oscillations with approximate periods of 10, 12, 16 and 24 h. The latter period is probably a direct response to the daily wind pulse.
3. The 10-h oscillation before 29 August (indicated by narrow open arrows) is conspicuous in all isotherm depth records except at position 4. Scrutiny of phase relations between time series pairs, i.e. identification of simultaneous maxima and minima, leads us to infer the presence of nodal lines[5] (lines of zero amplitude

[5] This discussion is based on the assumption that effects of the rotation of the Earth can be ignored. In this case, static nodal lines replace the amphidromes.

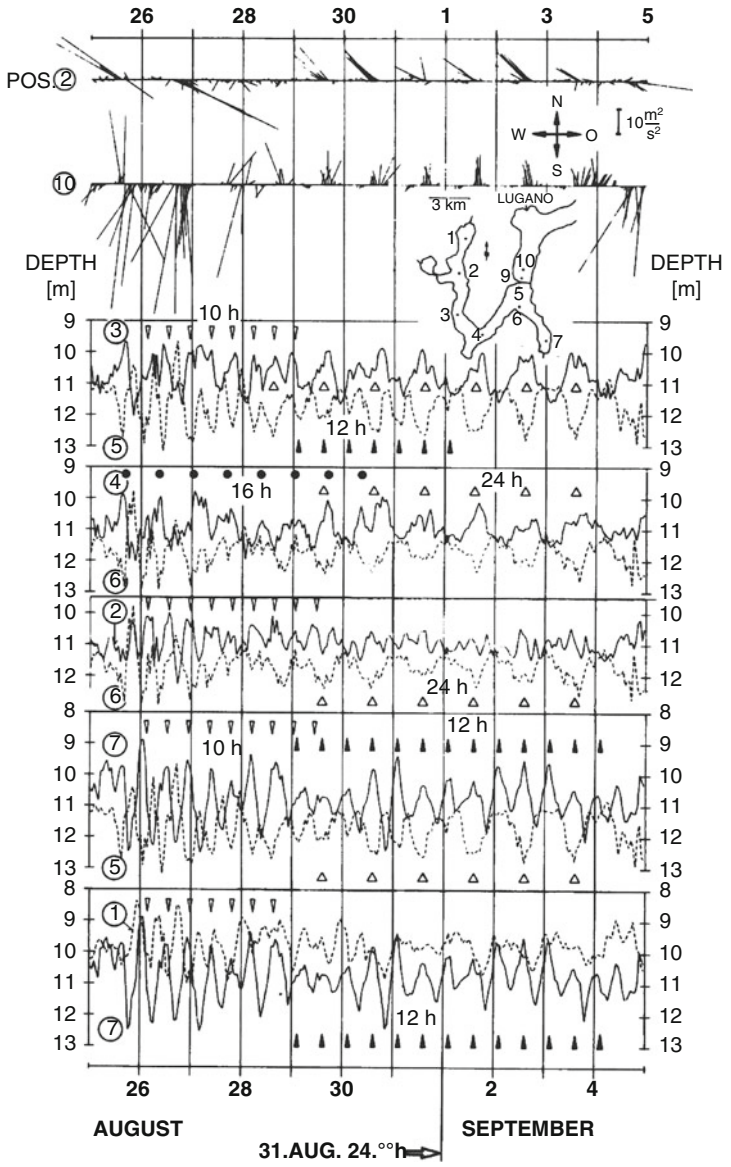

Fig. 18.6 Wind speed squared ($\sqrt{u^2 + v^2}(u, v)$ in $m^2\ s^{-2}$ as vector stick plots at positions 2,10), and fluctuations in depth of the 12°C-isotherm of seven positions (see insert) in the Southern Basin from 25 August to 5 September, 1984. Wind vector and isotherm depth plots are hourly averaged. The latter are grouped in selected pairs to display episodes of approximate counter-phase oscillations. Such episodes are marked by symbols repeated at the appropriate periodicity (△ 24 h, • 16 h, ▽ 10 h and ▲ 12 h) (from [33]).

between positions 1 and 2, 6 and 7 (or 5 and 7) and 3 and 6, and possibly at position 4. In Fig. 18.6, simultaneous pairs of maxima-minima are seen to arise in the combinations (1, 2), (1, 3), (2, 6), (3, 5), (3, 6), (5, 7), (6, 7) which suggests the mentioned locations of the nodal lines. To better identify the structure of this oscillation, the mean amplitude and variance at each position are computed and plotted in Fig. 18.7b along an unrolled thalweg, accounting thereby also of the counter-phase relations suggested by the positions of the nodal lines suggested above. Variances are indicated by (error) bars. Amplitudes were read from plots similar to Fig. 18.6, and the means and standard deviations were then computed. This is a rough but useful procedure. Position 4, where no oscillation with a 10-h period could be discerned, is marked by an open circle suggesting zero amplitude. The interpolated smooth curve describes an isotherm depth distribution of a third order longitudinal internal seiche mode.

4. The 16-h oscillation is only clearly discernable by eye in the isotherm–depth plot of position 4, and less convincingly at position 3. In both cases, the maxima and minima occur in phase. If it is further assumed that zero amplitudes for this oscillation are found in the vicinity of moorings 2, 5 and 6, it may be identified as the second internal seiche response. Fig. 18.7a supports such an identification.
5. The 12-h oscillation is only seen with a 180°-phase shift in the leg between Melide and Riva San Vitale (Fig. 18.7); but it persists at both stations for only 3 days. Otherwise, the 24-h signal persists for an entire week with considerable amplitude (Fig. 18.7d). Since the amplitude distribution in this case gives rise to two or three nodal lines, this motion cannot be interpreted as a free oscillation. It must be attributed to direct wind forcing.

In summary, the 16- and 10-h signals appear to be free internal oscillations of order 2 and 3. The fundamental mode (with one nodal line) is apparently absent; and the 12-h signal is inconclusive.

18.3.2 Internal Oscillations 7–30 September

(Post-storm behaviour, Fig. 18.8). As noted above, the 5–7 September storm led to partial thermocline erosion (Fig. 18.2), causing a descent to 12.2 m at a mean temperature of 12.3°C. The 12°C-isotherm now represents thermocline motion; and the 8°C-isotherm corresponds to the upper edge of the hypolimnion. A detailed data analysis of post-storm motions was carried out by Stocker and Salvadè [31]. Here we restrict ourselves to a summary of the main features. Figures 18.8 and 18.9 yield the following inferences:

1. The most conspicuous event in Fig. 18.8 is the storm on 5–6 September, which was followed by a long interval of fairly calm weather. At positions 2 and 6 no daily wind cycle can be recognized; only occasionally moderate winds are seen, from NW and N, respectively. Consequently, no diurnal periodicity in isotherm depth is seen at positions, 1–4, 6 and 7. The storm, however, did induce an extremely strong thermocline excursion of more than 10 m. That energy impulse

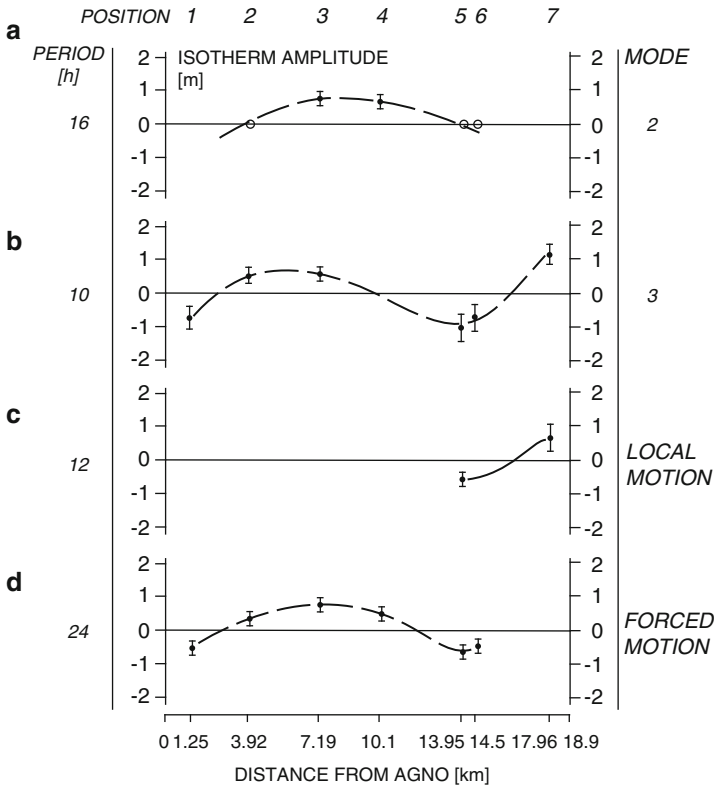

Fig. 18.7 Relative amplitudes of thermocline deflection along the unrolled thalweg during the oscillation episodes with different dominant periodicities, as displayed in Fig. 18.6 and tabulated below (Distance from Agno is also indicated in kilometre). The mean thermocline depth was 8.6 m and the mean epi- and hypolimnetic temperatures were 20.6 and 6.6°C, respectively. *Points* and *error bars* mark mean elevations and standard deviations (from [33]). © European Geosciences Union, reproduced with permission

Graph	Period [h]	Episode	Interpretation
a	16	26–30 August	Mode 2
b	10	26–28 August	Mode 3
c	12	29–31 August	Local motion
d	24	29 August–3 September	Forced motion

did not, however, lead to a non-linear large-amplitude surge travelling along the lake. Rather, upon the cessation of the storm, the lake reverted to small-scale oscillations with amplitudes of metalimnion–isotherm–depths of 1–2 m and predominant period of 38 h. Phase relations and amplitude estimates (Fig. 18.11a) suggest that this motion is the fundamental longitudinal internal seiche.

2. The 38-h oscillation could only be detected by eye in isotherm depth fluctuations in the hypolimnion. It was never clearly seen in plots of the 12°C- isotherm.

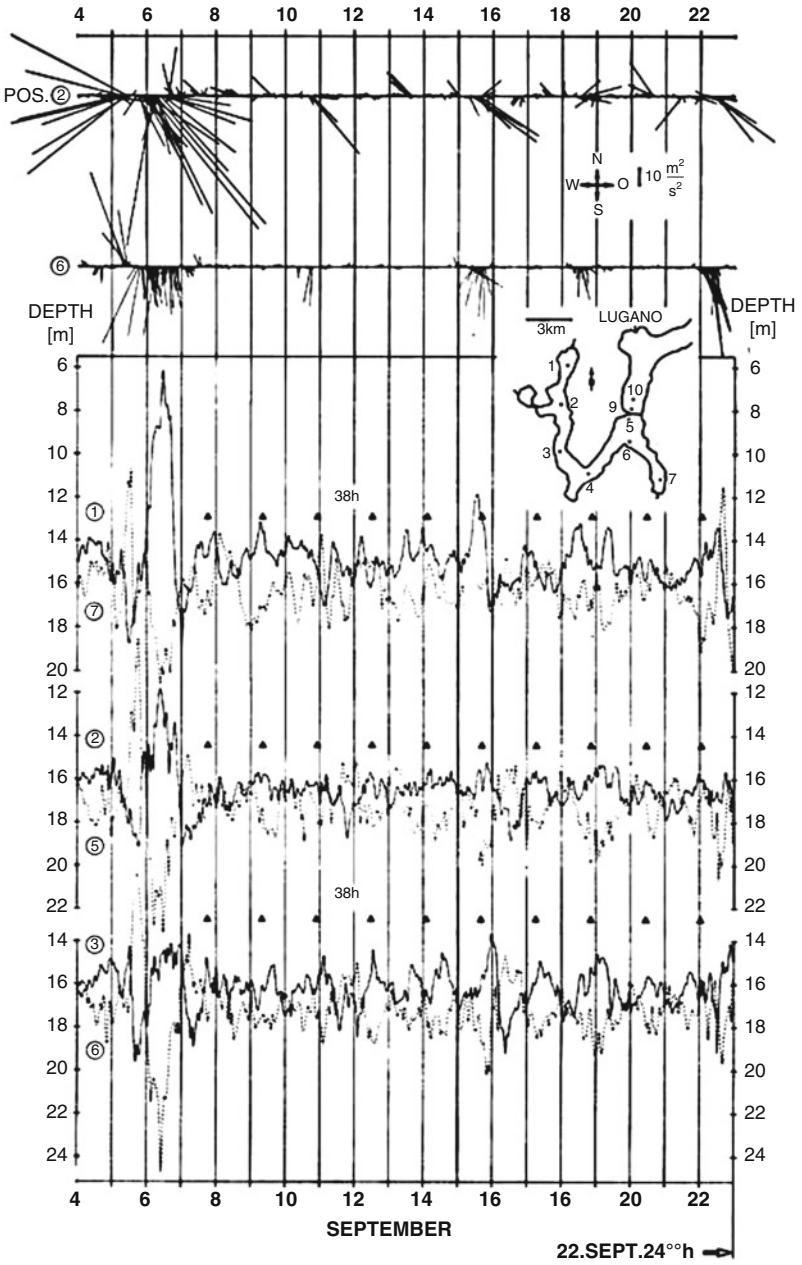

Fig. 18.8 Wind speed squared ($(u^2 + v^2)^{1/2}(u, v)$ in $m^2\,s^{-2}$ as vector stick plots at positions 2, 6) and fluctuations in depth of the 8°C-isotherm at six positions (see insert) in the Southern Basin, 4–22 September, 1984. Wind vectors and isotherm depths are hourly averaged; and the latter are plotted for the position pairs (1,7), (2,5) and (3,6). Note the dramatic storm of 5/6 September which generated very large thermocline excursions, that did, however, not generate a non-linear surge. Oscillations with a period of 38 h are marked by *full triangles* (from [33]).

3. Expansion of the time axis permits conspicuous signals to be detected with periods of 16, 12 and 10 h and, less convincingly, 24h. From 10 to 20 September, for example, the oscillations with a 16-h period (Fig. 18.9) was dominantly excited for 5 consecutive days. It was interrupted at 15 September but continued thereafter. Moreover, at positions 2 and 5, brief episodes can be seen with 10- and 24-h periods. Alternatively, from 21 September until 1 October (Fig. 18.10), oscillations with a 12-h period prevailed; and an episode with a 10-h period on 25/26 September was relatively short. Further scrutiny between 17 and 24 September (not shown here) discloses a predominance of the 10-h oscillation. Estimates of mean amplitudes and their variances are summarized in Fig. 18.11b–d. Evidently, from (b), with two nodal lines near positions 2, 5 and 6, a second mode structure can be inferred. For the two episodes of 12-h oscillation in (c), third mode behaviour is suggested. There are three nodal lines; but the inferred position of the middle node is different in the two episodes. The amplitude distribution, constructed for the 10-h oscillation, again differs for the two events in (d). There, an internal seiche of order four is the most likely interpretation.
4. The 10-h oscillations illustrated in Figs. 18.7 and 18.11 also appear to differ in showing mode-3 behaviour in Fig. 18.7, but mode-4 behaviour in Fig. 18.11. This interpretation can be tested by computation. It is plausible, because the mean stratification is different for the two episodes (Fig. 18.2).

In summary, the storm 5/6 September was able to excite the fundamental seiche mode and the three higher modes. Traces of the former are seen in time series of the isotherm depths below the thermocline, while the higher modes are more readily seen in depth fluctuations of the thermocline isotherms.

18.3.3 Internal Seiche After 3 October

After the storm on 1 and 2 October a thermocline of mean temperature 10.5°C lies at 14.5 m (Fig. 18.2, Table 18.2). After the storm, calm conditions prevailed until the end of the field program in mid-October. The 12°C-isotherm–depth plot discloses a dominant 12-h oscillation; and the amplitude distribution (Fig. 18.11e) corresponds to a fourth mode structure in contrast to that in Fig. 18.11d). The difference must again be attributed to the change in stratification (compare Fig. 18.2 and Table 18.2).

18.3.4 Harmonic Analysis

Based on inspection alone the foregoing analysis is approximate; but energy spectra demonstrate that the deductions were correct.

In the left- and right-hand portions of Fig. 18.12 we, respectively, present the energy spectra for the 11°C- and the 8°C- isotherm–depth fluctuations during the

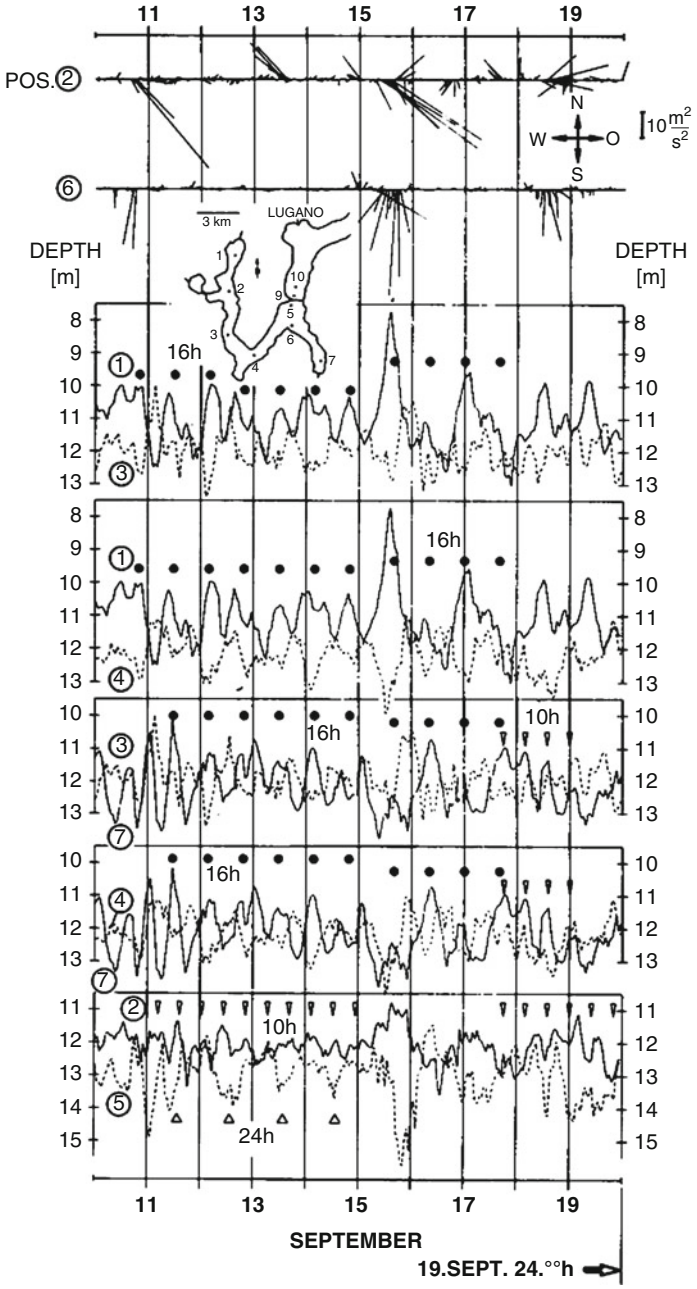

Fig. 18.9 Stick plot diagrams of hourly averaged wind speed squared $((u^2+v^2)^{1/2}(u,v)$ in $m^2\ s^{-2}$ at positions 2, 6) and 12°C isotherm–depth fluctuations in the Southern Basin, 10–20 September, 1984, plotted for the station pairs (1,3), (1,4), (3,7), (4,7) and (2,5). The dominant periodicities during oscillatory episodes are marked by symbols as in Fig. 18.6 (▽ 10 h, • 16 h, △ 24 h) (from [33]).

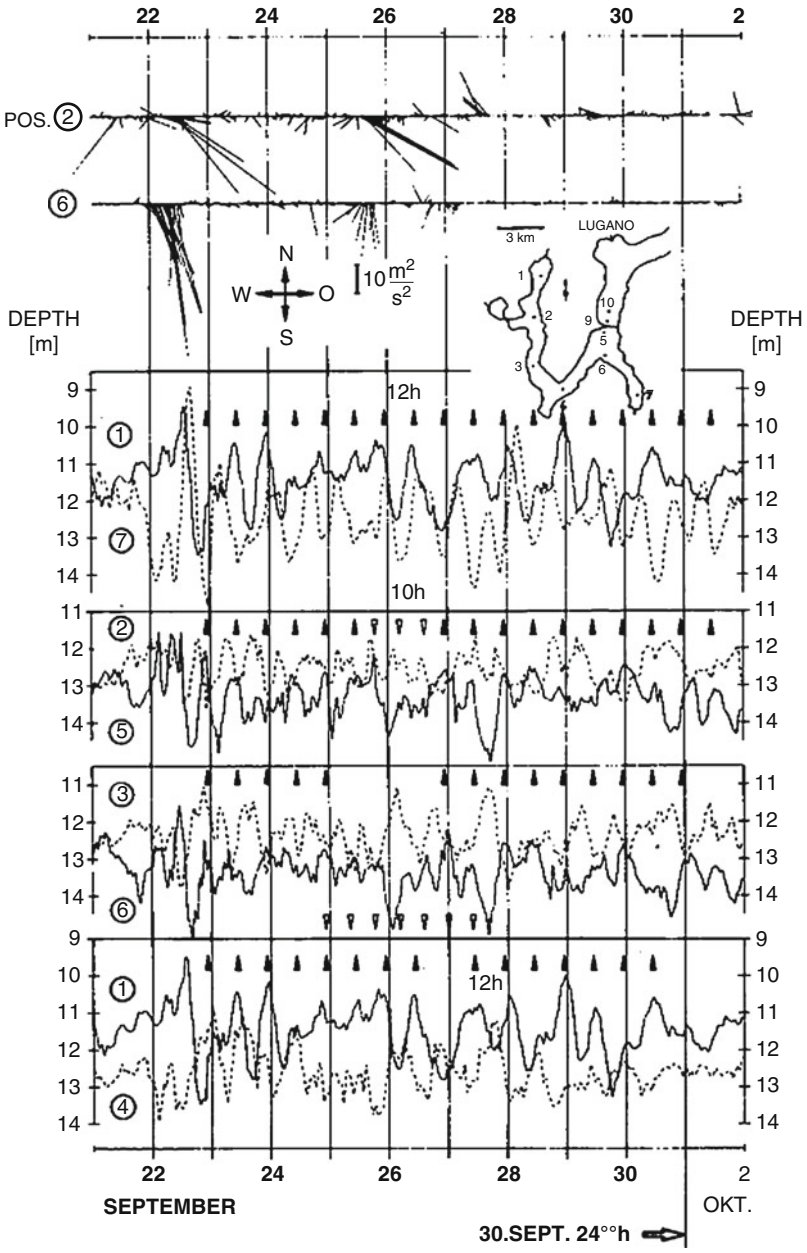

Fig. 18.10 Stick plot diagrams of hourly-averaged wind speed squared $((u^2 + v^2)^{1/2}(u, v)$ in $m^2\,s^{-2}$ at positions 2,6) and 12°C isotherm–depth–time series in the Southern Basin, 21 September–2 October, 1984, plotted for station pairs (1,7), (2,5), (3,6) and (1,4) (▽ 10 h and ▲ 12 h) (from [33]).

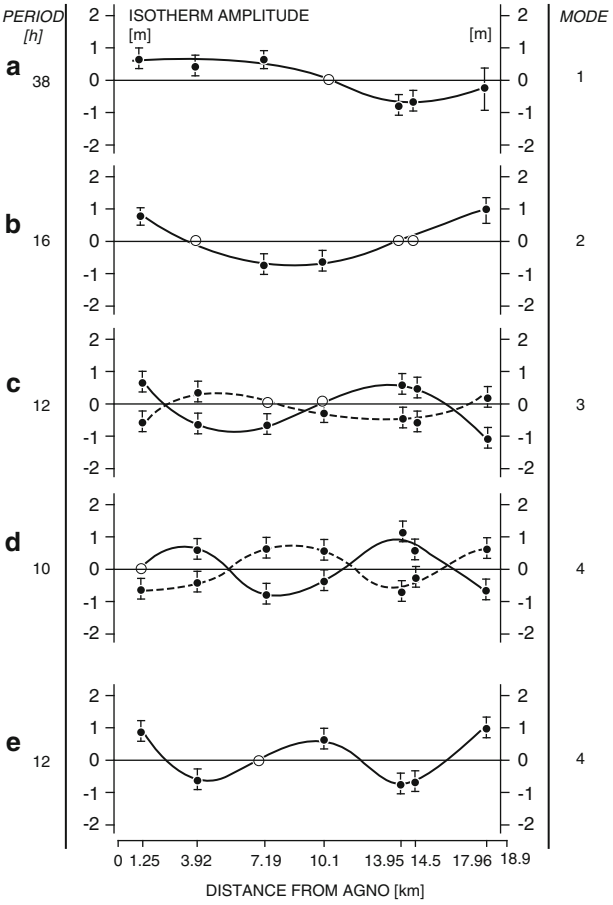

Fig. 18.11 Relative amplitudes of thermocline deflection along the unrolled thalweg (kilometre from Agno) during the oscillation episodes displayed in Figs. 18.8–18.10 and tabulated below. During episodes (**a**)–(**d**), 7–30 September, the mean thermocline depth was 12.2 m and the respective mean epi- and hypolimnetic temperatures were 16.4 and 6.2°C. For episode (**e**), 3–16 October, the corresponding values were 14.5 m, 13.9 and 6.0°C. *Points* and *error bars* mark the mean values and standard deviations (from [33]).

Graph	Period [h]	Isotherm [°C]		Interpretation
a	38	8	7–21 September	Mode 1
b	16	12	10–14 September	Mode 2
c	12	12	22−30 September 8−10 September (dashed)	Mode 3
d	10	8 12	24−27 September 17−21 September (dashed)	Mode 4
e	12	12	6–12 October	Mode 4

Table 18.2 Periods where spectral peaks of the isotherm depth energy density spectra arise, their accuracy, and associated mode numbers. The question marks indicate that the mode numbers are uncertain

Mode number	Period (h)	Accuracy (h)
1	37.2	± 1.3
2	17.4	± 0.7
3	12.1	± 0.2
4	10.2	± 0.2
5	6.6	± 0.3
?	4.5	± 0.2
?	3.9	± 0.2
?	3.1	± 0.2

middle interval 7 September to 2 October. The main features of the applied spectral analysis are elimination of a linear trend, tapering with a 'split cosine bell window' (10% on each side) and smoothening of the periodogram with a modified Daniell procedure [5]. With the thermocline at a mean depth of 12 m, the selected isotherms lie, respectively, about 1 and 4 m below it. In Fig. 18.12, log energy density (m^2/cph) is plotted against log frequency (cph) or period (h). Vertical lines, centred on peaks rising above background 'noise', are assigned periods and mode numbers as listed in Table 18.2. Mode number identification, from the model analysis described below, was also confirmed by cross-spectral analysis, but only up to the fifth mode. At higher mode orders the interseries coherence was too low. Furthermore, records from 7 moorings permit at most 6 nodes to be identified.

Figure 18.13 shows the phase structure of the 11 and 8°C-time series at the five longest periods and plotted for each position along the unrolled thalweg. The phases of the 11 and 8°C-isotherms are indicated by open circles and crosses, respectively. Absence of a spectral peak is shown by an open square and nodal lines, corresponding to a phase change of 180° are marked by open triangles. Circles and crosses have only been indicated when at that period the cross spectral analysis yielded a coherence above the 95% confidence limit. The results are strongly reminiscent of the indicated mode response (see right column in Fig. 18.13).

18.4 Model Predictions: The Two-Layered Variable-Depth Model

In order to model the internal free oscillations in the South Basin mathematically, the stratification is approximated by two immiscible layers of fluid with densities ρ_1 (upper layer) and ρ_2 (lower layer), $\rho_1 < \rho_2$. The model assumes that the lake domain is bordered by vertical walls such that the entire domain, where the two-layer model applies, consists of both, an epilimnion layer and a hypolimnion layer. The boundary of this domain is the intersection of the topography and the thermocline (the depth of discontinuity of the two layers) and will be referred to

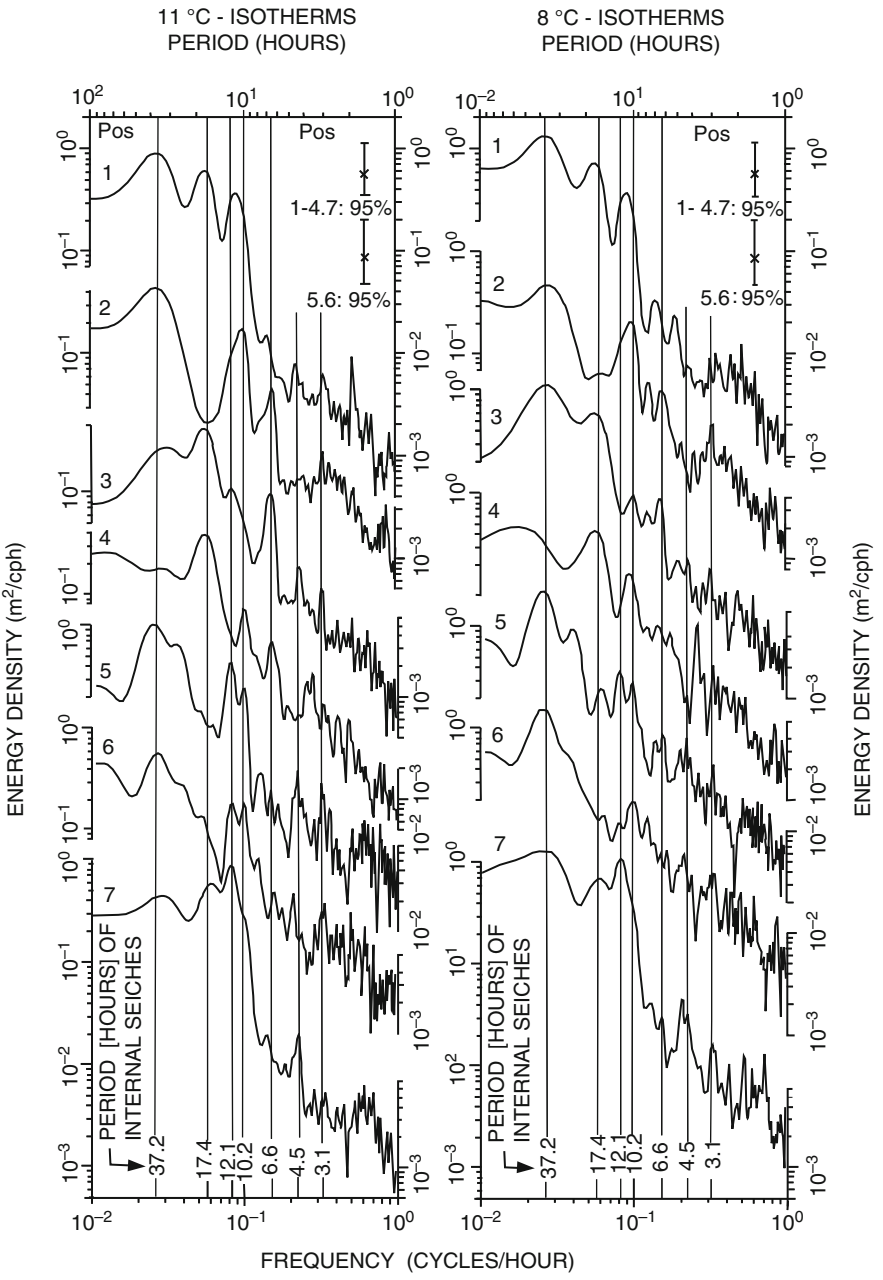

Fig. 18.12 Energy spectra of fluctuations of 11 and 8°C isotherm depths at positions 1–7 for the period 7 September 00.00 h to 2 October 00.00 h, 1984. Log energy density (m^2/cph) is plotted against log frequency (cph) or period (h). *Vertical lines* identify the periods of significant peaks. Confidence intervals are displayed at the *upper right* of the panels (from [33]).

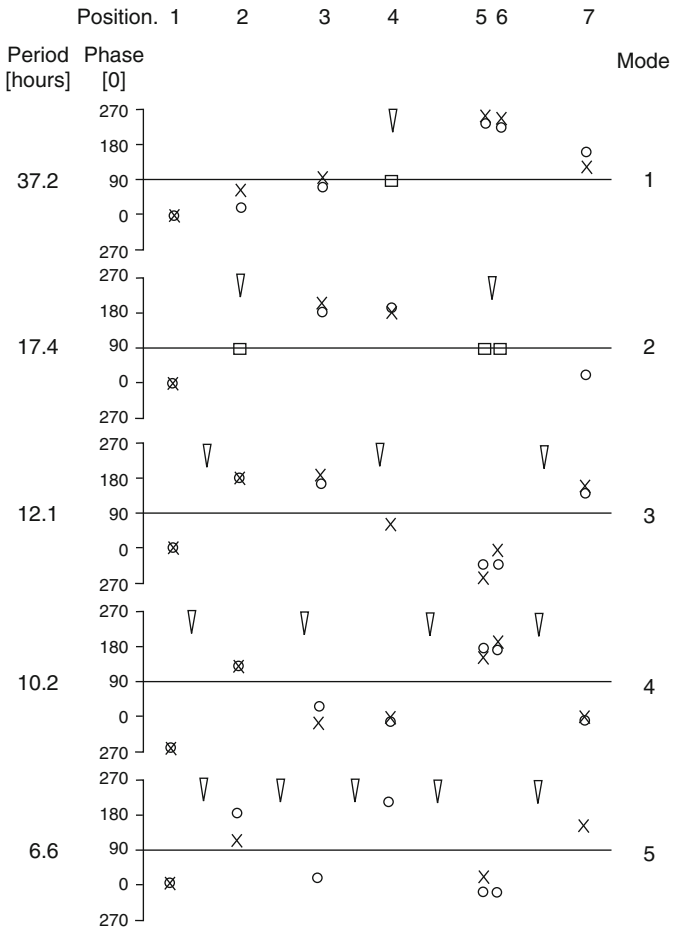

Fig. 18.13 Phase structures of the 11°C-(*open circles*) and 8°C-(*crosses*) isotherm–depth fluctuations at the computed periods of modes 1 through 4, plotted along the unrolled thalweg. Displayed are phase angles relative to position 1, for modes 1, 2, 3 and 5 and relative to position 7 for mode 4. Coherences of the phase estimates lie within 95% confidence limits, except for the 8°C-isotherm cases: position 5, mode 5; and position 3, mode 4. Absence of a spectral peak is marked by an *open square*. *Open triangles* mark locations where a jump in phase of 180°C is likely to arise (from [33]). © European Geosciences Union, reproduced with permission

as 'thermocline shore'. Introduction of this 'virtual' vertical wall ascertains that everywhere inside this shoreline two layers do exist. Clearly, the domain of the two-layered variable depth model (TVD) is smaller than the actual lake domain. This will make the periods of the internal gravity seiches somewhat smaller than if the full lake domain could be used, but for deep intermontane lakes the effects are

generally small and likely negligible. The TVD-model equations are[6]

$$\begin{aligned} \partial \boldsymbol{M}_1/\partial t - f\hat{\boldsymbol{k}} \times \boldsymbol{M}_1 &= -gh_1\nabla(\eta + \eta_2), \quad \partial\eta/\partial t + \nabla \cdot \boldsymbol{M}_1 = 0, \\ \partial \boldsymbol{M}_2/\partial t - f\hat{\boldsymbol{k}} \times \boldsymbol{M}_2 &= -gh_2\nabla(\delta\eta + \eta_2), \quad \partial\eta_2/\partial t + \nabla \cdot \boldsymbol{M}_2 = 0, \end{aligned} \tag{18.1}$$

in which

$\boldsymbol{M}_1 = h_1\boldsymbol{u}_1$	Vertically integrated transport in upper layer,
$\boldsymbol{M}_2 = h_2\boldsymbol{u}_2$	Vertically integrated transport in lower layer,
$\eta = \eta_1 - \eta_2$	
η_1	Free surface displacement,
η_2	Interface displacement,
$f \simeq 10^{-1}$	Coriolis parameter,
$\delta = \rho_1/\rho_2$	Density ratio,
$\varepsilon = 1 - \delta = (\rho_2 - \rho_1)/\rho_2$,	
$\hat{\boldsymbol{k}}$	Vertical unit vector,
g	Gravity acceleration.

Vectorial quantities have only two non-vanishing components and ∇ is the horizontal gradient operator. Equations (18.1) are to be solved over a common domain, defined by the intersection of the interface surface with the bottom topography. Via the Coriolis parameter these equations account for the effects of the rotation of the Earth. The condition of no mass flow through this 'thermocline shore' is

$$\boldsymbol{M}_i \cdot \boldsymbol{n} = \boldsymbol{0} \qquad (i = 1, 2), \tag{18.2}$$

where $\boldsymbol{n}$ is the two-dimensional, horizontal unit normal vector along the thermocline shore.

Equations (18.1) and (18.2) define an eigenvalue problem in a domain $\mathcal{D}_{ts}$ bounded by the 'thermocline shore' $\partial\mathcal{D}_{ts}$ which is smaller than the lake domain bounded by the true shore line $\partial\mathcal{D}_s$. The simplified approach is, of course, only applicable if the area and the volume of the water contained between the two boundaries are sufficiently small. For mountain lakes this requirement is generally tacitly assumed to be justified, but an analysis of the validity of the assumption has not been performed.

In this spirit the equations were used by Wang [39] to investigate the couplings of stratification and topography on the characteristics of coastal trapped waves on a rotating continental shelf of variable depth. He found that the low frequency response was characterized by topographic Rossby waves and internal Kelvin waves. Rao [25], used the equations for flat-bottomed rectangles, Schwab

[6] A TVDC-model, in which the epilimnion and hypolimnion layers are bounded by their own shore lines would improve on this, but this was not pursued here.

[29] and Bäuerle [4] applied them to uniform depth models of Lake Ontario and Lake Geneva and Bäuerle [3][7] employed them for variable depth models of rectangles and of Lake Constance. Hutter et al. [12] and Horn et al. [10] ignore the rotational effects in studies of the internal seiches of Lakes Lugano (North Basin) and Zurich. We will also set the Coriolis terms equal to zero here and thus ignore rotational effects.

In the Southern Lake of Lugano, the internal Rossby radius is somewhat larger than the width of the lake (see footnote on p. 317) so that the approximation $f = 0$ is reasonably justified. A direct coupling of rotational topographic Rossby waves with internal gravity waves is, however, unlikely since the periods of the former are 50 h and more (see [32] and Chaps. 19–21), while those of the gravity seiches are 38 h and less. This does not exclude per se the existence of topographic waves which were observed in the North Basin [19,38] but permits uncoupled treatment of rotational and gravitational effects. On the other hand, the main effects of rotation on the gravity modes is to cause a transverse slope of the interface which generates a pressure gradient in geostrophic balance with the longitudinal current. The effect on the frequency is small; that on the mode structure (Kelvin waves) cannot be corroborated with moorings positioned only along the thalweg as done in the 1984 field campaign.

When the rotation of the Earth is ignored, (18.1) can be combined to give the simpler system

$$\left.\begin{aligned} \partial^2\eta/\partial t^2 &= \nabla\cdot[gh_1\nabla(\eta+\eta_2)],\\ \partial^2\eta_2/\partial t^2 &= \nabla\cdot[gh_2\nabla(\delta\eta+\eta_2)] \end{aligned}\right\} \quad (x,y)\in\mathcal{D}_{ts}, \tag{18.3}$$

subject to the boundary conditions

$$\nabla\eta\cdot\boldsymbol{n} = \nabla\eta_2\cdot\boldsymbol{n} = 0, \qquad (x,y)\in\partial\mathcal{D}_{ts}. \tag{18.4}$$

Assuming time harmonic solutions

$$\eta = \bar{\eta}(x,y)\exp(i\sigma t), \quad \eta_2 = \bar{\eta}_2(x,y)\exp(i\sigma t),$$

in which σ is the frequency, the equations reduce to the eigenvalue problem

$$\left.\begin{aligned} -\sigma^2\bar{\eta} &= \nabla\cdot[gh_1\nabla(\bar{\eta}+\bar{\eta}_2)],\\ -\sigma^2\bar{\eta}_2 &= \nabla\cdot[gh_2\nabla(\delta\bar{\eta}+\bar{\eta}_2)], \end{aligned}\right\} \quad (x,y)\in\mathcal{D}_{ts},$$
$$\nabla\bar{\eta}\cdot\boldsymbol{n} = \nabla\bar{\eta}_2\cdot\boldsymbol{n} = 0,\ (x,y)\in\partial\mathcal{D}_{ts}. \tag{18.5}$$

Equations (18.5) are discretized on a rectangular grid of 250 × 250 m^2 squares, replacing the spatial derivatives with centred finite differences. Areas of the lake

[7] For these and further applications, see Chap. 14.

shallower than the thermocline depth have been eliminated from the grid. The resulting 328 cells led to a standard matrix eigenvalue problem of size 656×656 which was solved by routines described in Smith et al. [30] yielding eigenvalues $\sigma^{(\alpha)}$ ($\alpha = 1, 2, 3 \ldots$) and eigenvectors representing the grid point values of $\eta^{(\alpha)}$ and $\eta_2^{(\alpha)}$. Once these are determined the velocities in the two layers follow from

$$i\sigma \boldsymbol{u}_1 = -g\nabla(\eta + \eta_2), \qquad i\sigma \boldsymbol{u}_2 = -g\nabla(\delta\eta + \eta_2). \tag{18.6}$$

Interpretation. The stratification of the lake in the TVD-model is described by the thermocline depth and the relative density difference $\varepsilon = (\rho_2 - \rho_1)/\rho_2$. From the temperature and resistivity measurements of 13 positions within the lake, taken on 24 September and thus representative of the period from 7 to 30 September the relative density difference was determined once via mean two-layer temperatures and once via mean two-layer densities (Fig. 18.14). Bührer and Ambühl's [6] equation of state[8] was used. The two values for ε are

$$\varepsilon_I = 1.0184 \times 10^{-3}, \qquad \varepsilon_{II} = 1.168 \times 10^{-3},$$

with a relative difference of 13%, and the interface of the two layers is at 12 m for both cases. Table 18.3 assembles the computed periods of the ten lowest modes ($\alpha = 1, 2, \ldots, 10$) and compares these with the earlier estimates from inspection of the isotherm depth plots. The computed and observed periods show satisfactory agreement (maximum deviations of 15%, mode 2, $\varepsilon = \varepsilon_I$). Interestingly, the computation tends to overestimate the periods when $\varepsilon = \varepsilon_I$, but does not consistently underestimate them when $\varepsilon = \varepsilon_{II} > \varepsilon_I$. Estimates of the periods T, which the model would predict at different stratifications, is given by the following approximate formula (see [10])

$$T_I^2 \varepsilon_I h_I^* = T_{II}^2 \varepsilon_{II} h_{II}^*, \tag{18.7}$$

in which h_I^* and h_{II}^* are the equivalent depths in the two different stratifications i.e.

$$h_I^* = \{h_1 h_2/(h_1 + h_2)\}_I^{1/2}.$$

The reader can easily check that the computed periods in Table 18.3 satisfy relation (18.7).

Computations were also performed for the other two episodes with different mean stratification as indicated in Table 18.1. In Table 18.4, computed and observed periods are compared. The latter are estimated by inspection of isotherm–depth

[8] See Volume I, Chap. 10.

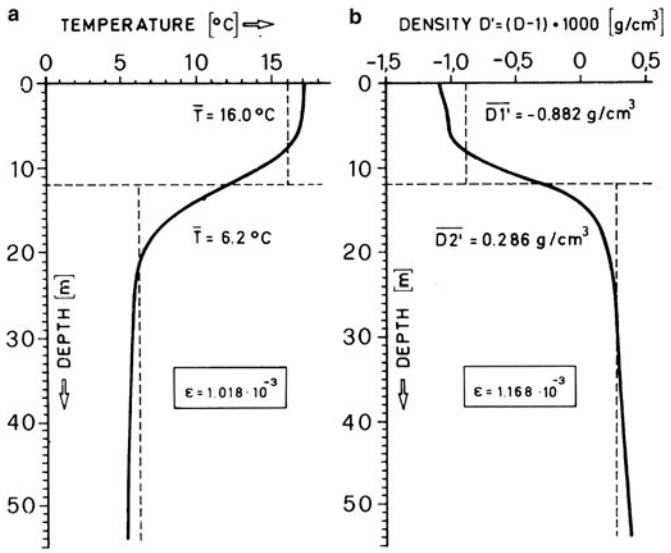

Fig. 18.14 (**a**) Temperature profile of 24 September 1984, determined as the mean of profiles taken at 13 different positions in the South Basin, and the two-layer approximation derived from it. (**b**) Mean density profile of 21 September 1984, determined from temperature and salinity profiles, and two-layer approximation derived from it (from [33]). © European Geosciences Union, reproduced with permission

Table 18.3 Computed and measured periods of the internal seiches in stratified Southern Lake of Lugano (7–30 September 1984)

Mode	Computed TVD-model		Observed from isotherm depth time series	
	$\varepsilon_I = 1.018 \times 10^{-3}$	$\varepsilon_{II} = 1.168 \times 10^{-3}$	Eye-fitted	Spectral analysis
	T [h]	T [h]	12°, 8°[a] T [h]	11°, 8°[a] T [h]
1	37.3	34.8	38	37.2 (±1.3)
2	19.2	18.0	16	17.4 (±0.7)
3	12.8	11.9	12	12.1 (±0.2)
4	11.5	10.8	10	10.2 (±0.2)
5	7.2	6.7		6.6 (±0.3)
6	6.3	5.9		
7	5.2	4.9		
8	5.0	4.7		4.5[b] (±0.2)
9	4.4	4.1		3.9[b] (±0.2)
10	4.2	4.0		3.1[b] (±0.2)

[a]Indicates chosen isotherm for the isotherm–depth–time series.
[b]Not classified.

plots. Spectra were not computed because time series are too short to guarantee statistical confidence for any period except those indicated in Table 18.4. Most significant in the above tables is the shift in the period of modes 3 and 4 when the stratification changes. The predictions of the periods from the observations are

Table 18.4 Computed and observed periods of the internal seiche modes of the stratified Southern Lake of Lugano for the indicated time. h_1 denotes the epilimnion depth

Time		14 August–5 September 1984		2 October–16 October 1984	
	Mode	TVD-model $\varepsilon = 1.842 \times 10^{-3}$ $h_1 = 8.6\,\text{m}$	Observed	TVD-model $\varepsilon = 0.720 \times 10^{-3}$ $h_1 = 14.5\,\text{m}$	Observed
		T [h]	T [h]	T [h]	T [h]
	1	32.2		41.5	
	2	16.4	16	21.4	
	3	10.9	10	14.2	
	4	9.9		12.8	12
	5	6.2		8.0	
	6	5.4		7.1	
	7	4.5		5.9	

	14 August–5 September	7 September–30 September	3 October–16 October
Mode			
3	10 h	12 h	–
4	–	10 h	12 h

and these agree satisfactorily with the computations. The TVD model also permits distribution of interface displacements and near epi- and hypolimnetic velocities to be displayed for each mode. Displacement amplitudes for the first four modes, scaled in percent of the maximum amplitude in each case, are presented in Fig. 18.15, in which the transitions between positive (solid) and negative (dotted) contours correspond to nodes (heavy lines). 'Observed' nodal lines, inferred from the above-described analysis of isotherm–depth-fluctuations, are shown as heavy dashed lines. Given the uncertainty of the locations of the latter, we must regard the agreement as satisfactory. The figure further discloses that the maximum deflections occur at Agno (modes 1 and 2) and at Riva San Vitale (modes 3 and 4), but it can also be shown that, for mode 5, the maximum arises at a mid-lake position near Brusimpiano (Fig. 18.1). Along the shore in Fig. 18.15 we also show in pairs the phases of the 11 and 8°C-isotherm–depth–time series at the respective mode period, except at those positions where amplitudes were too small to identify a phase. The expected jump of 180° when nodal lines are crossed is reasonably well achieved in all modes up to order 5. Figures 18.16 and 18.17 illustrate, for the first four modes, the distribution of the current fields in the upper and lower layers. Generally, the highest velocities are found in nodal regions and the lower currents are less and always opposed in direction to those in the upper layer. Exceptions occur. For instance mode 1, velocities are highest where the basin has its smallest width. Comparison with Fig. 18.15 shows that velocity maxima always coincide with locations where lines of constant amplitude of interface displacements are closest to each

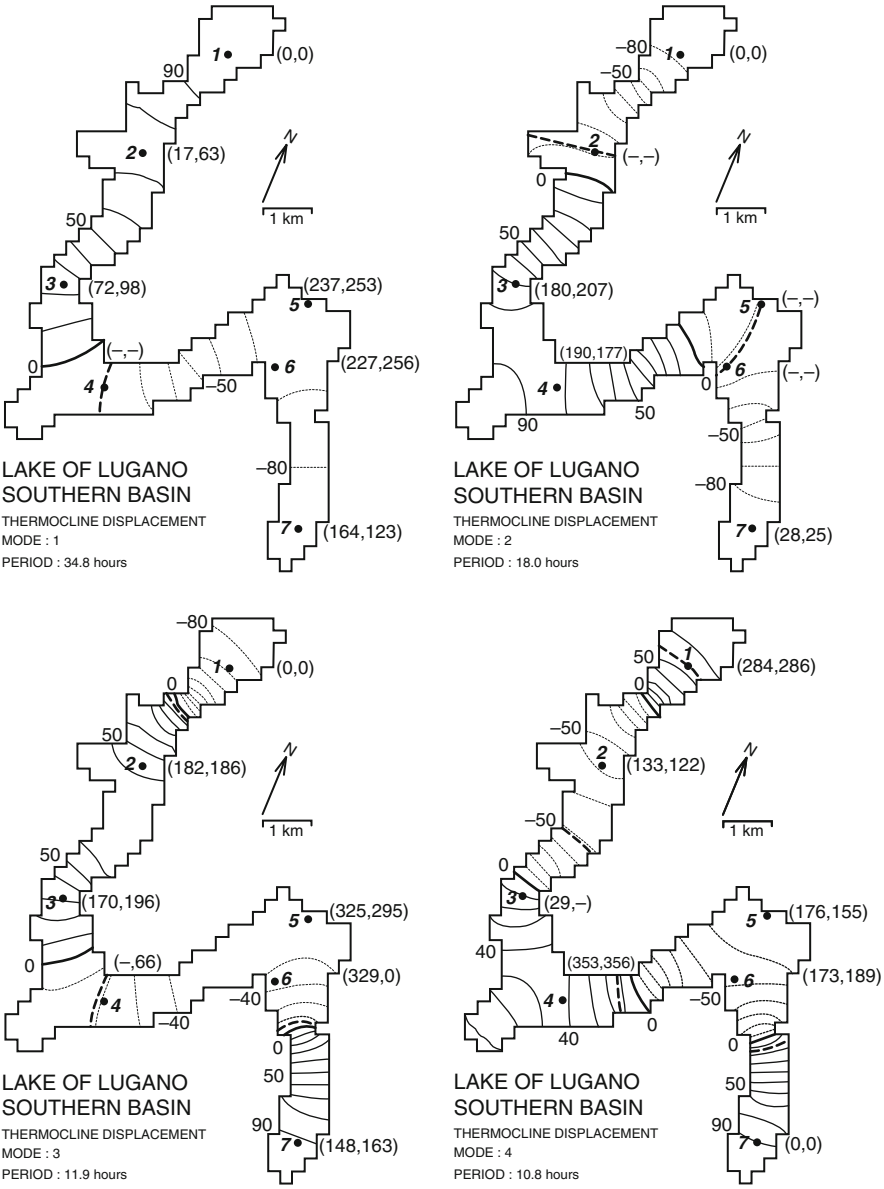

Fig. 18.15 Distributions, predicted by the TVD model described in the text, of interface elevations corresponding to the first four internal modes, relative to a maximum elevation of 100 in each case and with the upper and lower layer temperatures taken from Fig. 18.14a. Elevation contours (*thin lines*, *solid positive*, *dotted negative*) are drawn at 10% intervals. Also shown are mooring positions (*bold italic numbers*); computed periods; location of nodes (*heavy solid lines*) and 'observed' nodes (*dashed heavy lines*) and 'observed' phase angles (*bracketed paired numbers*, respectively, derived from analysis of 8 and 12°C-isotherm–depth fluctuations) relative to 0° at position 1 (modes 1–3) and position 7 (mode 4) (from [33]).

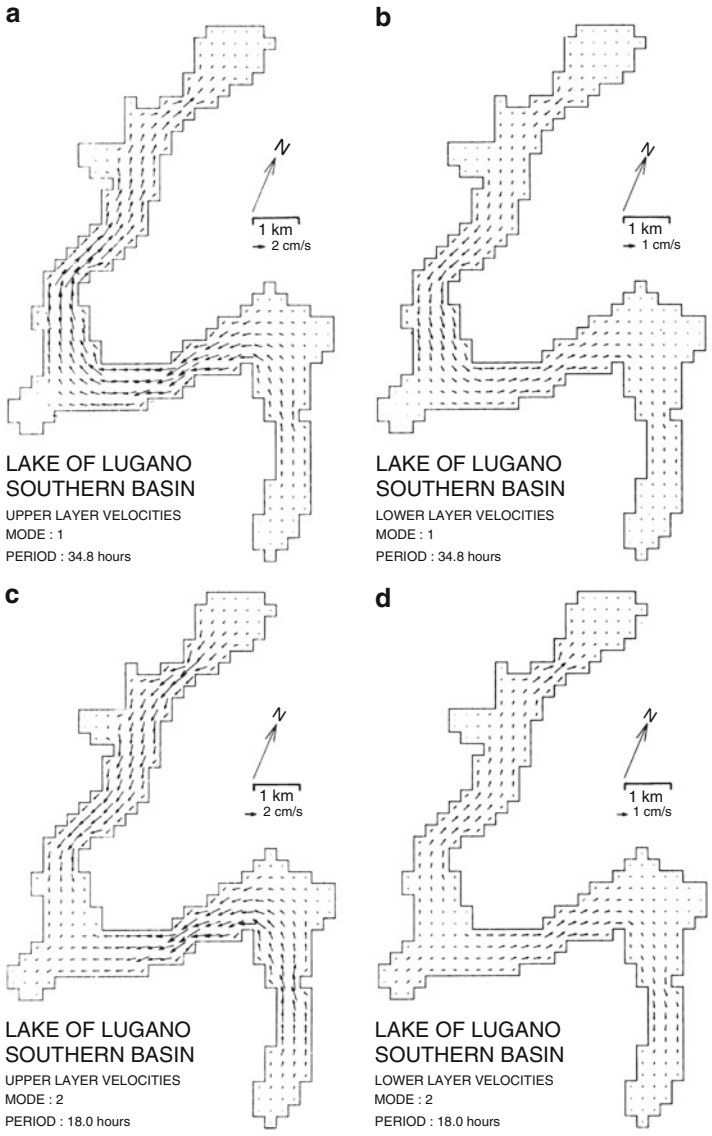

Fig. 18.16 TVD-model-predicted current vectors in the upper and lower layer corresponding to the internal seiches of modes 1 and 2, of which the elevation distributions are shown in Fig. 18.15. Vector lengths indicate maximum velocities (speed scale as indicated in the inset), attained in each case one quarter-period after the elevation maximum (from [33]).

	Upper layer	Lower layer
Mode 1	(**a**)	(**b**)
Mode 2	(**c**)	(**d**)

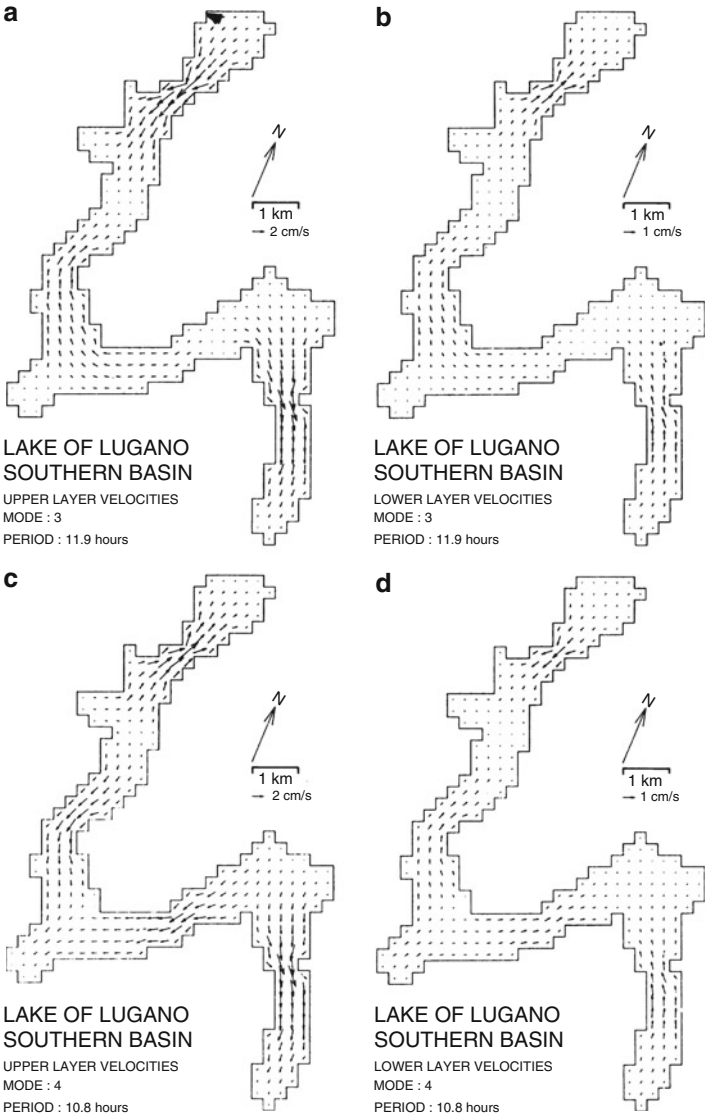

Fig. 18.17 Same as Fig. 18.16 but for modes 3 and 4 (from [33]). © European Geosciences Union, reproduced with permission

	Upper layer	Lower layer
Mode 3	(**a**)	(**b**)
Mode 4	(**c**)	(**d**)

other. Figures 18.16 and 18.17 also help to identify the moorings at which certain modes can best be inferred from velocity measurements.

18.5 Current Structure of the Internal Seiches

Isotherm motions are coupled with the current field in the entire basin. Therefore, inferences based on analysis of isotherm depths should also be deducible from current meter records. Such deductions are, however, more difficult and could often only be made with knowledge of isotherm behaviour. One difficulty arises because the speed threshold of the Aanderaa current meters is about 2.5 cm s^{-1}, while current directions are reliably recorded at lower speeds. Therefore, while complete records of *direction* were obtained from all moorings (except No.3 which failed) and in both layers, speed was rarely recorded in the hypolimnion; and there were episodes, sometimes lasting several hours, when speed was neither recorded in the epilimnion. This ruled out spectral or other statistical analysis of the whole current time series.

Figures 18.18a, b show the distributions of the water current directions in the epilimnion and hypolimnion, respectively. Evidently, the current in the epilimnion is dominantly oriented along the thalweg; such a preference is not seen in the hypolimnion, except at position 5 (Melide) where the epilimnetic current is towards W, while the hypolimnion current is towards E. The reason for this behaviour is not clear, but it may be due to the increased thickness of the epilimnion close to the channel, inducing a horizontal pressure gradient, which drives the epi- and hypolimnetic currents in opposite directions.

Whereas the TVD model predicts currents for the first four modes, which are predominantly longitudinally directed and always opposed in the two layers, the observed current directions show greater variability, particularly in the hypolimnion (Fig. 18.18b). To render visible any periodic behaviour which may be present in the current records, we have plotted (in Fig. 18.19) hourly averages of the longitudinal component at positions 1, 2, 4, 6 and 7 for the interval 26 August–5 September, i.e. that covered by the isotherm–depth plots in Fig. 18.6, p. 325. To assist comparison of the two figures we have repeated (in Fig. 18.19) the symbols which marked the presence of 24, 16, 12 and 10 h oscillations in Fig. 18.6. Whereas, in Fig. 18.6, those symbols generally coincided with elevation maxima or minima, in Fig. 18.19 they more often than not coincide with vanishing current. Such behaviour is to be expected from the model-predicted phase lag of one quarter cycle between maximum elevation and maximum current and is further confirmed by the along-thalweg amplitudes of isotherm displacement (dashed lines) and epilimnetic current (solid lines) in Fig. 18.20 for the interval 25 August–5 September. Excitation of the third mode is evident.

Similar analyses were also carried out on several episodes from the interval 7–30 September. These are summarized in Fig. 18.21. Evidently, there are episodes which permit identification of the internal seiche modes of order 2–4 from time series of the epilimnion current, and the mode identification agrees with that deduced from

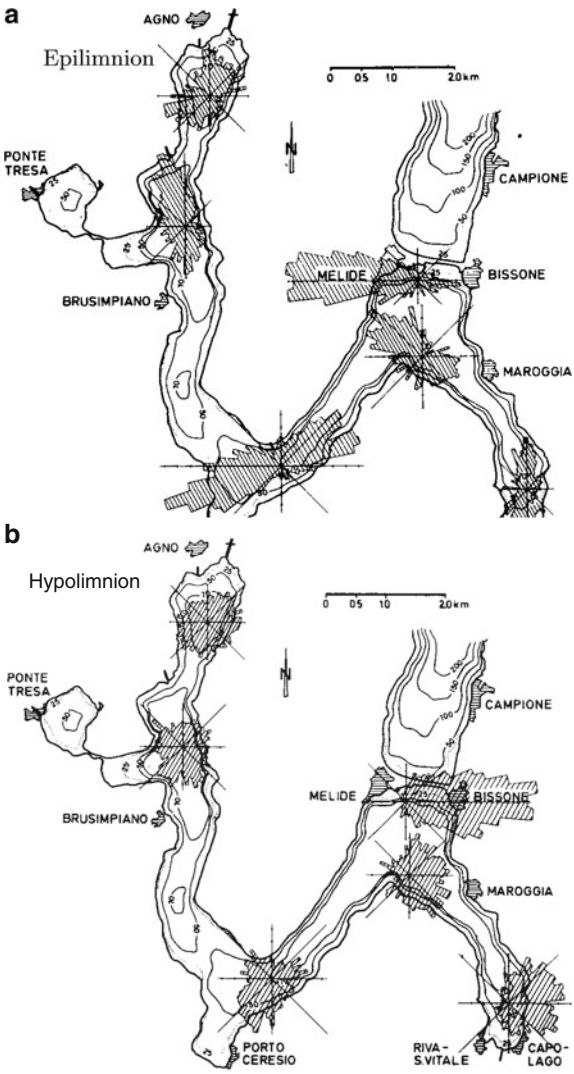

Fig. 18.18 (**a**) Water current rosettes illustrating the relative frequency of occurrence of the direction of the current in the epilimnion; (**b**) Same as Fig. 18.18a for the hypolimnion (from [33]). © European Geosciences Union, reproduced with permission

the isotherm–depth–time series. We have, however, not been able to detect by eye the fundamental internal seiche mode in those current records. This accords with the earlier finding that mode 1 was only revealed by the 8°C-isotherm, which is below the thermocline where currents are weak.

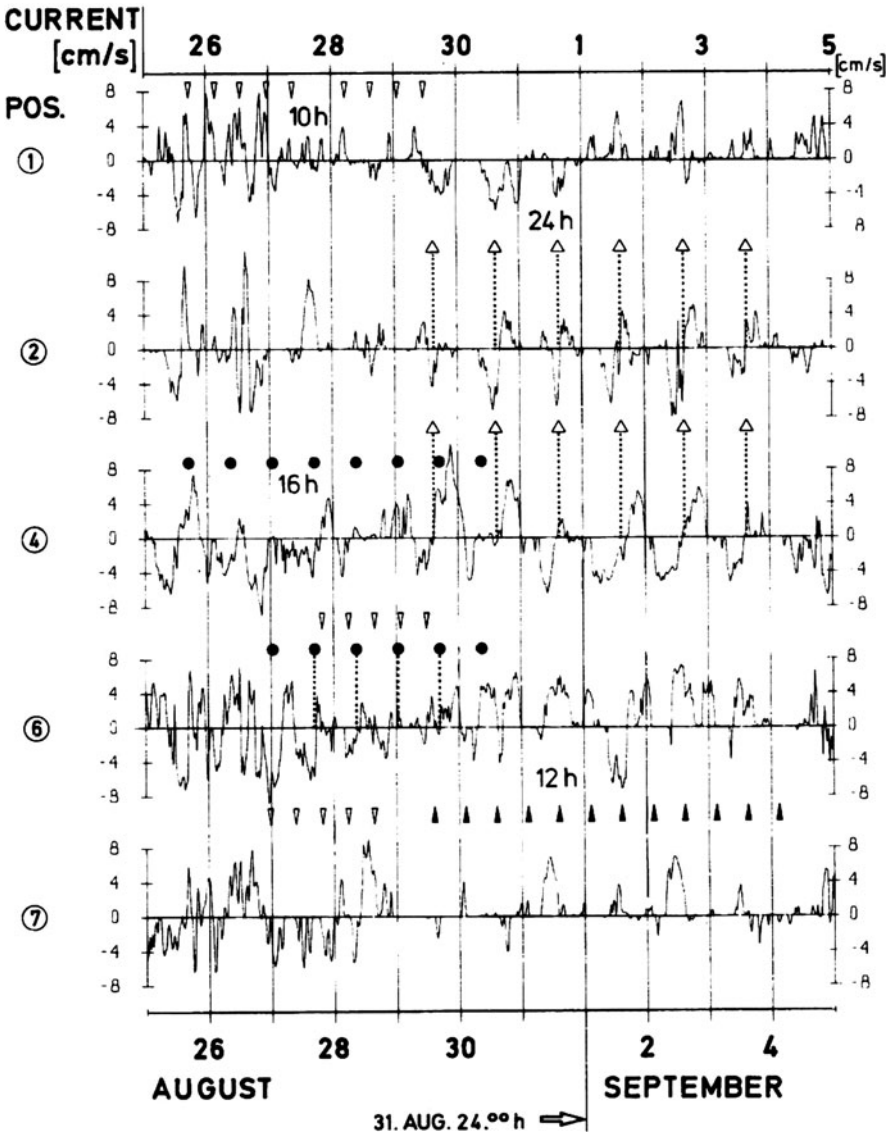

Fig. 18.19 Along thalweg components of the epilimnetic current in positions 1, 2, 4, 6 and 7. Positive direction is toward Agno. Symbols mark times when the 12°C-isotherms were near minima in Fig. 18.6. In Fig. 18.19, those symbols generally coincide with velocity zeros (see the 24 h episodes of positions 2 and 4 (△ 24 h, • 16 h, ▲ 12 h, ▽ 10 h)) (from [33]).

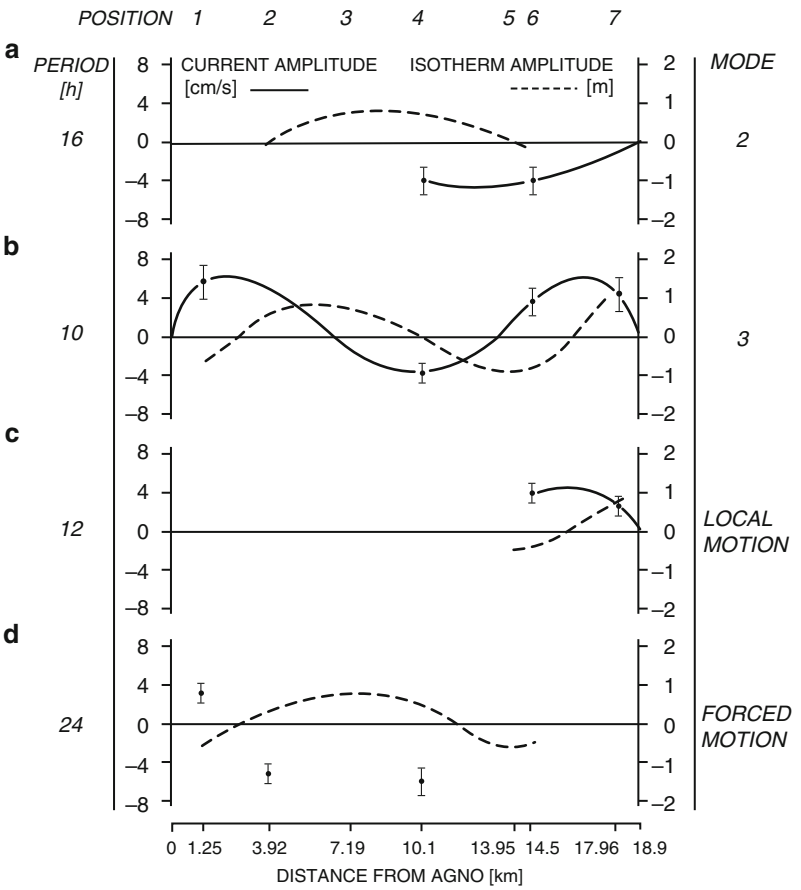

Fig. 18.20 Amplitude distribution, along the thalweg (kilometre from Agno) of the thalweg-component of the epilimnetic current during episodes of differing periodicity, as tabulated below. Amplitude means are plotted and standard deviations at the positions indicated, interpolated by *solid lines* which bring the velocity to zero at the basin ends. Plotted as *dashed lines* are the amplitude distributions of isotherm–depth oscillations illustrated in Fig. 18.7. Modes, their periods and the episodes from which the graphs have been constructed are:

Graph	Period (h)	Episode	Interpretation
a	16	26–30 August	Mode 2
b	10	26–29 August	Mode 3
c	12	29 August–3 September	Local motion
d	24	20 August–3 September	Forced motion

From [33].

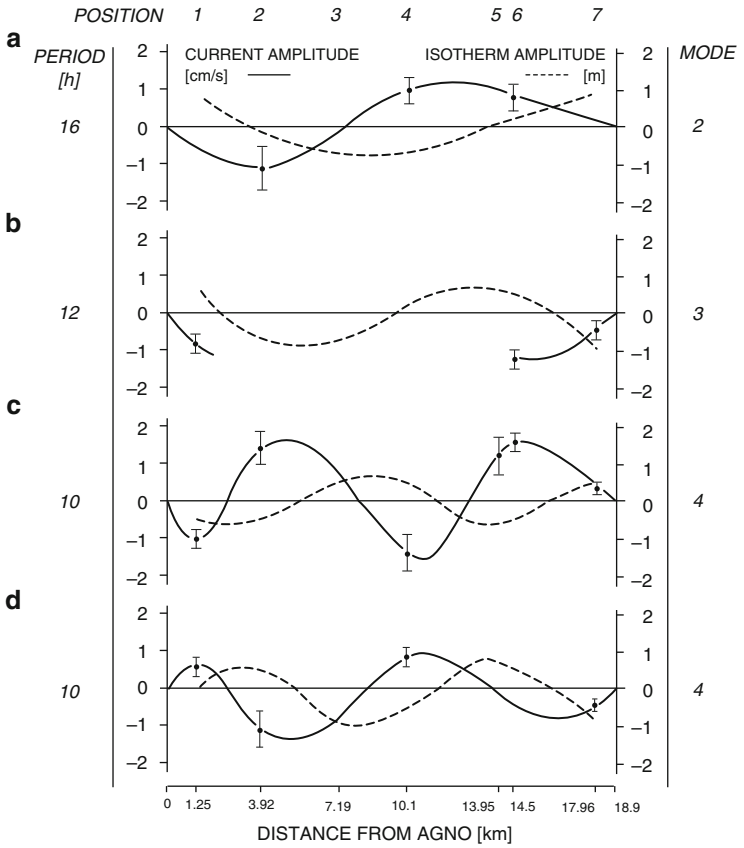

Fig. 18.21 Same as Fig. 18.20 but for the interval to 30 September and with isotherm–depth distributions (*dashed*) taken from Fig. 18.11. The episodes are:

Graph	Period (h)	Episode	Interpretation
a	16	10–14 September	Mode 2
b	12	23–30 September	Mode 3
c	10	10−11 September 17−18 September	Mode 4
d	10	24–27 September	Mode 4

From [33]. © European Geosciences Union, reproduced with permission.

18.6 Closing Remarks

18.6.1 Observed Features Not Reproduced by the TVD-Model

Flow features which are not reproduced in the TVD model are particularly visible at the basin ends (positions 1 and 7) and during episodes of 24 h forced oscillation (position 2). Typical for such episodes are currents which rotate so that existence of

large eddies must be assumed. For instance, the currents in the epi- and hypolimnion at positions 1 and 7 are often rotated relative to each other by a finite (but not constant) angle. Observations are insufficient to determine the cause.

Similarly, because the internal Rossby radius is of the order of the mean width of the basin, an effect of the rotation of the Earth on the gravity seiches should be noticeable in the form of Kelvin-wave behaviour. The main effect is to bring about a transverse slope of the interface which generates a pressure gradient in geostrophic balance with the longitudinal current. To be observable, this effect also requires records from at least two moorings across the channel.

The thermocline erosion that occurred during the two storms made the records unsuitable for statistical analysis of the whole measuring interval. It is of interest to note that, even though the storms generated extremely large amplitudes (up to 10 m change in isotherm depth), an internal surge was not generated. Soon after the initial set-up, the isotherm motion returned back to 'normal', i.e. to approximately 1 m amplitude. Parenthetically, we might mention that Mortimer and Horn [18] and Horn et al. [10] conclude that only a larger *downstroke* of the thermocline interacting with the bottom, can generate a surge. Perhaps greater depths near the ends of the North Basin, and the fact that the thermocline (although substantially deflected) does not approach the bottom closely enough (see Fig. 18.5h). This explains why no obvious surge is generated.

During the storm, when the wind direction was fairly constant, epilimnetic current directions were correlated with the wind at positions 1, 2 and 4, but not at positions 5–7. An analysis of forced, wind-induced currents is needed to shed light on the phenomenon.

It has already been noted that, in isotherm–depth records and their spectra, the fundamental (mode 1) internal seiche response is generally weaker than those of higher modes. This is due to external forcing. That mode 1 behaviour could be detected from 8°C, but not 12°C isotherm depth (the thermocline location), however, is not easily explicable. One likely reason may be a distortion of gravity waves by nonlinearity. Vertical displacement of water particles at the 8°C isotherm depth may be larger than that at the 12°C isotherm depth, as suggested by Thorpe's [34] analyses.

18.6.2 A Remark on the Generation of Topographic Waves

It is remarkable that no clear signal of long periodic processes (>50 h) was detected in the data, in contrast to an earlier study in the North Basin, where these processes were interpreted as topographic Rossby waves, see Chaps. 19–21 or Trösch et al. [38], Mysak et al. [19], Stocker and Hutter [32]. It is believed that their absence is due to (1) the varied topography and (2) the shallowness of the South Basin. Both facts work towards enhancing frictional effects. Long periodic processes, if excited, may be damped out before having lived a few cycles. It may indeed be the great depth and the uniform bathymetry which make such processes survive in the North Basin.

Table 18.5 Periods (in min) of the barotropic gravitational seiches in the North- and South Basins of Lake of Lugano, obtained with the classical channel model of Defant [7, 8], the extended channel model of Raggio and Hutter [22–24] and FE and FD models of Hutter et al. [11], Hutter [12]. Observed periods are from limnigraph stations at the lake shore for the North- and South Basins and from a current meter moored in the channel at Melide connecting the two basins [38]

Modality	Lake of Lugano (North Basin)					Lake of Lugano (South Basin)			Channel at Melide observation current meter measurements
	Channel model	Extended channel model	FE computation	FD computation	Observation	Modality	FE	Observation	
Coupled fundamental	–	–	–		110	Coupled fundamental	–	–	110
–						1	27.8	27.6	27.3
1	13.8	13.7	13.8	14.4	13.8	2	13.6	13.9	13.8
–					9.5	3	9.4	9.6	9.72
–						4	8.5	8.7	–
2	6.6	6.5	6.6	6.5	6.2				6.6
						5	5.7	5.8	–
3	5.0	5.0	5.1	4.6	5.1				5.1
4	–	3.7	3.8	3.7	–				

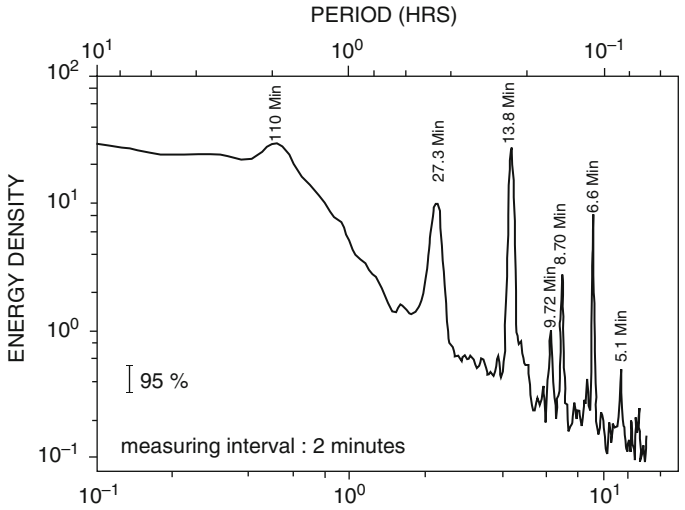

Fig. 18.22 Energy spectrum of the time series (from 13 September to 16 October 1984) of a current meter moored within the channel at Melide connecting the North- and South Basins of Lake of Lugano. The energy peaks identify the modes of the barotropic seiches in the two individual basins and the fundamental mode of the coupled system (from Trösch et al. [38]). © Schweiz. Z. Hydrologie, reproduced with permission

18.6.3 Barotropic–Baroclinic Coupling of the North- and South Basin

The North and South Basins of the Lake of Lugano are connected by the channel at Melide. All mean flow is from the North to the South Basin. During summer stratification, because the thermocline depth is below the channel bottom, the water exchange is dominated by epilimnion water. Detailed measurements of the current within the channel and in its immediate vicinity have shown that there are strong barotropic oscillations that force the water from the North- to the South Basin and vice versa. It is evident that the return current into the North Basin cannot be ignored [38]. Figure 18.22 shows an energy spectrum of current meter measurements conducted within the channel at Melide at 3 m depth, taken between 13 September and 16 October 1984 with a VAW Savonius rotor current meter[9] set at a 2 min measuring interval. Energy peaks can be identified as particular barotropic modes of the two basins, see Table 18.5. The high energy peak at 110 min can be interpreted as the fundamental mode of the co-oscillation of the two coupled basins. It is obvious that these significant oscillations forth and back between the two basins will influence the circulation dynamics of the stratified lake system. Because in a rigid lid model

[9] This is an instrument constructed by the workshop of the Versuchsanstalt für Wasserbau, Hydrologie and Glaziologie at ETH Zürich (VAW).

none of these signals would be reproduced, such models are likely inappropriate in the prediction of short term water motions.

Scrutiny of vertical velocity and temperature profiles also indicate that, under conditions of relatively strong winds from North, hypolimnetic water sloshes over from the South to the North Basin. This can be inferred from current profiles within the 5-m deep channel. These show unusually large shear with NS-flow at the top, but reversed at the bottom. Moreover, temperature profiles close to the channel in the North basin exhibit inversion brought about by the near-bottom return current. More detailed analysis of large-amplitude internal wave dynamics of the channel region is evidently necessary to account for the substantial depth variation of the basin profile and for the strong shear within the channel. It appears, therefore, likely that a fuller computational study of the wind induced circulation of the stratified Lake of Lugano will also require coupling of the two basins.

References

1. Antenucci, J.P., Imberger, J. and Saggio, A.: Seasonal evolution of the basin-scale internal wave field in a large stratified lake. *Limnol. Oceanogr.* **45**, 1621-1638 (2000)
2. Antenucci, J.P. and Imberger, J.: On internal waves near the high-frequency limit in an enclosed basin. *J. Geophys. Res.* **106**, C10, 22465-22474 (2001) *Limnol.Odeanogr.* **43**, (8), 1780-1795 (1998)
3. Bäuerle, E.: *Die Eigenschwingungen abgeschlossener, zweigeschichteter Wasserbecken mit variabler Topographie*. Berichte aus dem Institut für Meereskunde, Kiel, **85**, 126p (1981)
4. Bäuerle, E.: Internal free oscillations in the Lake of Geneva. *Ann. Geophysicae*, **3**, 199–206 (1985)
5. Bloomfield, P.: *Fourier analysis of time series: An introduction*. John Wiley, New York (1976)
6. Bührer, H. and Ambühl, H.A.: Die Einleitung von gereinigtem Abwasser in Seen. *Schweiz. Z. Hydrol.*, **37**(2), 347–369 (1975)
7. Defant, A.: *Physical Oceanography*. Vol I, Pergamon Press, New York, (1961)
8. Defant, A.: *Physical Oceanography* Vol II, Pergamon Press, New York, (1961)
9. Hollan, E. and Simons, T.J.: Wind-inuced changes of temperature and currents in Lake Constance. *Arch. Met. Geophys. Bioklim.*, **A 27**, 333–373 (1978)
10. Horn, W., Mortimer, C.H. and Schwab, D.J.: Wind-induced internal seiches in the Lake of Zürich observed and modelled. *Limnol. Oceanogr.*, **31**(6), 1230–1252 (1986)
11. Hutter, K., Raggio, G., Bucher, C., Salvadè, G. and Zamboni, F.: The surface seiches of Lake of Lugano. *Schweiz. Z. Hydr.*, **44**, 455-484 (1982)
12. Hutter, K., Salvadè, G. and Schwab, D.J.: On internal wave dynamics in the Northern Basin of the Lake of Lugano. *Geophys. Astrophys. Fluid Dyn.*, **27**, 299–336 (1983)
13. Imberger, J. and Parker, G.: Mixed layer dynamics in a lake exposed to spatially variable wind field. *Limnol. Oceanogr.*, **30**(9), 473–488 (1985)
14. Mortimer, C.H.: The resonant responses of stratified lakes to wind. *Schweiz. Z. Hydrol.*, **15**, 94–151 (1953)
15. Mortimer, C.H.: Lake Hydrodynamics. *Mitt. Int. V. Theor. Angew. Limnol.*, **20**, 124–197 (1974)
16. Mortimer, C.H.: Strategies for coupling data collection and analysis with the dynamic modeling of lake motions. In: *Lake Hydrodynamics* (Eds. W. H. Graf and C. H. Mortimer), Elsevier, Amsterdam, 183–222E (1979)
17. Mortimer, C.H.: Internal oscillatory response of Lac Léman to wind impulses during 1977/1978 compared with wave models in rotating channels of uniform depth. *Comm. Lab. Hydraul., Ecole Polytechnique Fédérale de Lausanne*, **50**, 1–89 (1983)

18. Mortimer, C.H. and Horn, W.: Internal wave dynamics and their implications for plankton biology in the Lake of Zürich. *Vierteljahresschr. Naturforsch. Ges., Zürich*, **137**, 299–318 (1982)
19. Mysak, L.A., Salvadè, G., Hutter, K. and Scheiwiller, T.: Topographic waves in a stratified elliptical basin with application in the basin of Lugano. *Phil. Trans. R. Soc. Lond. A*, **316**, 1–55 (1985)
20. Ogihara, Y.: *Internal Wave Energy Distribution* Ph. D. Thesis, University of Western Australia, (1998)
21. Phillips, O.M.: On spectra measured in an undulating layered medium. *J. Phys. Oceanogr.*, **1**, 1–16 (1971)
22. Raggio, G. and Hutter, K.: An extended channel model for the prediction of motion in elongated homogeneous lakes, Part I: Theoretical introduction. *J. Fluid Mech.*, **121**, 231–255 (1982)
23. Raggio, G. and Hutter, K.: An extended channel model for the prediction of motion in elongated homogeneous lakes, Part II: First order model applied to ideal geometry. Rectangular basins with flat bottom. *J. Fluid Mech.*, **121**, 257–281 (1982)
24. Raggio, G. and Hutter, K.: An extended channel model for the prediction of motion in elongated homogeneous lakes, Part III: Free oscillations in natural basins. *J. Fluid Mech.*, **121**, 283–299 (1982)
25. Rao, D.B.: Free internal oscillations in a narrow, rotating rectangular basin. *Mar. Sci. Directorate, Dept. Fish. Environ.*, Ottawa (Canada), MS-report 43, 391–398 (1977)
26. Roget, E.: *Internal Seiches and Barclinic Currents in Lake Banyoles*. Ph. D. Thesis, Autonomous Unuiversity, Barcelona, 287pp. (1992)
27. Roget, E., Salvadè, G. and Zamboni, F.: Internal seiche climatology in a small lake where transversal and second vertical modes are usually observed. *Limnol. Oceanogr.* bf 42 (4), 663-673 (1997)
28. Saggio, A. and Imberger, J.: Internal wave weather in a stratified lake. *Limnol. Oceanogr.*, **43**(8), 1780–1795 (1998)
29. Schwab, D.J.: Internal free oscillations in Lake Ontario. *Limnol. Oceanogr.*, **22**, 700–708 (1977)
30. Smith, B.T., Boyle, J.M., Garbow, B.S., Ikebe, Y., Klema, V.C. and Moler, C.B.: Matrix eigensystem routines.*Eispack guides. Lecture Notes in Computer Science*, **6**, Eds. G. Goos and J. Harmanis, Springer, Berlin, 387p. (1974)
31. Stocker, K. and Salvadè, G.: Interne Wellen im Luganersee. *Interner Bericht Nr. I/85 der Versuchsanstalt für Wasserbau, Hydrologie und Glaziologie an der ETH Zürich* (unpublished) (1986)
32. Stocker, K. and Hutter, K.: Topographic waves in rectangular basins. *J. Fluid Mech.*, **185**, 107–120 (1987)
33. Stocker, K., Hutter, K., Salvadè, G., Trösch, J. and Zamboni, F.: Observations and analysis of internal seiches in the Southern Basin of Lake of Lugano. *Ann. Geophysicae*, **5B**, 553–568 (1987)
34. Thorpe, S.A.: On the shape of progressive internal waves. *Phil. Trans. Roy. Soc. London*, **A 263**, 563–614 (1968)
35. Thomas, E.A.: Sprungschichtneigung im Zürichsee durch Sturm. *Schweiz. Z. Hydrol.*, **11**, 527–545 (1949)
36. Thomas, E.A.: Auffällige bilogische Folgen von Sprungschichtneigungen im Zürichsee. *Schweiz. Z. Hydrol.*, **12**, 5–23 (1950)
37. Thomas, E.A.: Sturmeinfluss auf das Tiefenwasser des Zürichsees im Winter. *Schweiz. Z. Hydrol.*, **13**, 5–23 (1951)
38. Trösch, J., Salvadè, G. and Stocker, K.: Die Eigenschwingungen der durch den Kanal im Damm von Melide gekoppelten Becken des Luganersees. *Schweiz. Z. Hydrol.*, **49**, 16–28 (1987)
39. Wang, D.P.: Coastal trapped waves in a baroclinic ocean. *J. Phys. Oceanogr.*, **5**, 326–333 (1975)

Chapter 19
Topographic Waves in Enclosed Basins: Fundamentals and Observations

19.1 Review of Early Work

In Sect. 11.2, the notions of first and second class waves were introduced. The former were said to be due to the action of the gravity force. These waves are therefore also called gravity waves. The latter are due to the rotation of the Earth and cease to exist when the frame of reference is inertial. These waves are alternatively also termed Rossby-, *vortex-, geostrophic* or *gyration-waves*, see Fig. 19.1. In a homogeneous fluid, subject to the rigid lid assumption and in the limit of the shallow water approximation the second class linearized waves are described by the differential equation

$$T[\Psi] = \frac{\partial}{\partial t} E[\Psi] + \mathcal{J}\left[\Psi, \frac{f}{H}\right] = 0, \tag{19.1}$$

in which

$$\begin{aligned} E[\Psi] &:= \nabla \cdot \left(\frac{\nabla \Psi}{H}\right), \\ \mathcal{J}\left[\Psi, \frac{f}{H}\right] &= \frac{\partial \Psi}{\partial x}\frac{\partial}{\partial y}\left(\frac{f}{H}\right) - \frac{\partial \Psi}{\partial y}\frac{\partial}{\partial x}\left(\frac{f}{H}\right). \end{aligned} \tag{19.2}$$

Ψ is the volume transport stream function, H the water depth and f the Coriolis parameter.[1] When the frame of reference is inertial ($f = 0$), then $T[\Psi] = 0$ reduces to $\partial E[\Psi]/\partial t = 0$. This implies that $E[\Psi]$ does not depend on time which

[1] For the derivation of (19.1), see Sect. 11.3 and for a first attempt of interpretation Sect. 9.2 of Chap. 9 in Volume I. An elegant derivation follows from the conservation law of barotropic potential vorticity, which requires (see (5.74)–(5.79) in Chap. 5 in Volume I of this book series)

$$\frac{\mathrm{d}\Pi_{bt}}{\mathrm{d}t} = \frac{\mathrm{d}}{\mathrm{d}t}\left(\frac{\zeta + f}{H}\right) = 0,$$

in which $\zeta = \omega_z = \partial v/\partial x - \partial u/\partial y = E[\Psi]$. Therefore,

K. Hutter et al., *Physics of Lakes*, *Volume 2: Lakes as Oscillators*, Advances in Geophysical and Environmental Mechanics and Mathematics,
DOI 10.1007/978-3-642-19112-1_19,

shows that second class waves cannot propagate in this case. Therefore, $H = const.$ and $f(x, y) \neq const.$ defines the planetary Rossby[2] waves, whilst $f = const.$ and $H(x, y) \neq const.$ defines the topographic Rossby waves, also simply called topographic waves (TWs). On the f-plane these only exist when the basin has variable bathymetry. We shall confine attention to this case.

The interest in topographic waves in the ocean arose from the conspicuous long periodic wave signals that were observed along the continental shelves of our oceans. In lakes, a considerable number of temperature and current observations in various lakes also disclosed pronounced oscillations with a characteristic period of a few days that could not be explained by (external or) internal gravity waves. Poincaré (1910) [34] was the first to point out the existence of such long periodic oscillations in a rotating circular basin with parabolic depth profile, and Lamb (1932) [26] gives the first analytic solution of these topographic waves. Much later, Birchfield and Hickie (1977) [5] considered the transient wind generation of the Lamb modes and demonstrated, how the gravity oscillations and the TWs modulate the seiche response by a slow rotation in the cyclonic sense of the pattern of coastal jets and return flow across the lake centre. Free circular basin solutions for second class waves have been found by Saylor et al. [35] and Saylor and Miller [36] and Wenzel [49]. An analytical method for determining second class modes in an elliptical paraboloid was prescribed by Ball [2] and Mysak [30], and Johnson [20] constructed solutions of TWs in an elliptical basin whose shoreline and depth contours form a family of confocal ellipses. Using a semi-analytic semi-numerical approach Stocker and Hutter [41–43] found solutions to the TW-equation in a rectangular basin with symmetric bathymetric chart and could identify three typical wave modes of the TW-equation: (1) basin wide modes with large wavelengths, (2) basin wide modes with shorter wavelengths and (3) bay modes, in which the major part of the energy is concentrated in a localized (bay) region. From this study sprang a series of localized TWs by Stocker and Johnson [45, 46].[3]

Most work on gyration waves is on barotropic TWs. However, these waves also exhibit a baroclinic coupling when they propagate in a stratified fluid. Mysak et al. [33] have shown that, in a two-layer basin of the size and depth scale of many intermontane lakes, barotropic TWs are only slightly affected by the interfacial motion. However, the interfacial oscillations are driven by the TWs. Thus, one can find the baroclinic TW-mode from the solution of the barotropic TW-equation subject to the

$$\frac{1}{H}\frac{\partial \omega_z}{\partial t} + \frac{\partial}{\partial x}\left(\frac{\omega_z + f}{H}\right)u + \frac{\partial}{\partial y}\left(\frac{\omega_z + f}{H}\right)v = 0,$$

which, after linearization, is equivalent to (19.1).

[2] For a biographical sketch see Fig. 19.1.

[3] There is a vast literature on TWs. A reference text may be LeBlond and Mysak [27] who treat primarily waves in the open ocean. A review, perhaps more adequate to the present topic is by Stocker and Hutter [42] and contains a large number of references pertaining to the propagation of TWs in closed or semi-closed basins. Relevant works are also by Stocker and Hutter [40, 43, 44] and Johnson [20–22], Willmott and Johnson [50], Johnson and Kaoullas [23] and others.

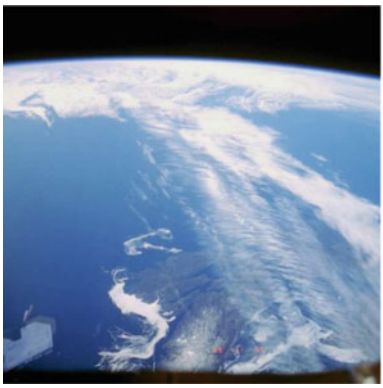

Fig. 19.1 Carl-Gustav Rossby (1898–1957), a Swedish-US meteorologist (portrait from http://www.villasmunta.it/Storia_della_meteorologia/) and in the left picture clouds along a jet stream over Canada (http://en.wikipedia.org/).

Carl-Gustav Rossby (28 December 1898, Stockholm; 19 August 1957, Stockholm) was a Swedish-US meteorologist who first explained the large-scale fluid motion in the atmosphere, (ocean and lakes) due to the rotation of the Earth. He was studying meteorology and oceanography from 1919 under Vilhelm Bjerknes in Bergen (Norway), in Leipzig and the Lindenberg Observatory in Brandenburg. In 1921, he returned to Stockholm to join the Swedish Meteorological–Hydrological Service where he participated in a number of oceanographic expeditions at Stockholm University. While ashore, between expeditions, he studied mathematical physics at Stockholm University. In 1925, Rossby moved to the United States and joined the US Weather Bureau in Washington, DC, where he worked on atmospheric turbulence. In 1928, he became Associate Professor at the Aeronautics Department (renamed soon later Meteorology Department) of the Massachusetts Institute of Technology, Boston, and additionally joined the Woods Hole Oceanographic Institution as a Research Associate. His major interests at this time included thermodynamics, mixing, turbulence and atmosphere–ocean interactions.

Rossby, after having assumed US citizenship in 1938, was appointed in 1940 the chairmanship of the Department of Meteorology of the University of Chicago. It is here, where he turned his attention to large-scale atmospheric motions, in particular the jet stream and large-scale planetary waves. During World War II he trained military meteorologists. In 1947, he returned to Sweden to become the founding director of the Institute of Meteorology in Stockholm, but he kept part-time his positions at Chicago and Woods Hole. From Stockholm, he renewed by visits his friendship with Prof. Hans Ertel in Berlin. Their cooperation led to the mathematical formulation of the so-called Rossby waves. In his later years, between 1954 and his death in 1958 Rossby championed the field of atmospheric chemistry.

Originally, only large-scale planetary waves on the β-plane in a constant thickness atmosphere were called Rossby waves. Today, any gyroscopic wave on a rotating frame tends to be named after Rossby as topographic Rossby waves, equatorial Rossby waves, planetary Rossby waves, etc.

The text is based on:

http://en.wikipedia.org.wiki/Carl-Gustav_Rossby.

mass flux condition through the lake shores yet is able to observe the wave from temperature measurements in the thermocline.

Identification of TW-signals in spectra of temperature and isotherm–depth–time series is difficult because their mode frequencies for enclosed basins are often clustered together with subinertial modal frequencies of gravity waves. This makes a clear separation of second class modes from their first class counterparts a challenging exercise not only of time-series analysis, but also of numerical identification of their eigenfrequencies and mode structures.

19.2 Some Observations and Proposed Interpretations

ln this section we describe a series of long periodic oscillations of temperature or current data indicating that the phenomenon which underlies these observations can probably be interpreted in terms of topographic waves. We heavily draw from two monographs by Stocker and Hutter [42] and Hutter [18]; both are out of print for more than a decade. Our approach is to present facts, including interpretations and to postpone detailed explanations in terms of models to later sections.

19.2.1 Lake Michigan

The analysis outlined here and the figures are due to Saylor et al. [35] and Huang and Saylor [13]. During spring, summer and fall 1976 current meters were deployed in Southern Lake Michigan as indicated in Fig. 19.2. Most of these current meters were positioned along the Eastern shore between Benton Harbor and Muskegon, but ten current meters were also deployed along a straight line connecting opposite points along the shores between Racine and Holland.

The bathymetry of the Southern Lake Michigan is simple and concise. An approximation of the topography by a circular basin with radial profile dependence, see Fig. 19.3, may not be an oversimplification of the situation at hand.

Figure 19.4 collects kinetic energy spectra of the Eastward (Fig. 19.4a) and Northward (Fig. 19.4b) velocity components (generally at the 25-m level) at the six stations indicated in Fig. 19.4. Vertical lines are drawn to accentuate the two conspicuous energy peaks at near inertial ($\sim$17 h) and near 4-day periods. Thus, the lake responds distinctly at these periods. This is further substantiated by the graphs presented in Fig. 19.5. They show a progressive vector diagram of the hourly averaged low-pass filtered current velocities from the 32-m depth current meter at station 11 (Fig. 19.5a) and coherence and phase difference between the East and North velocities from the same current meter (Fig. 19.5b).

The hodograph clearly reveals the oscillatory wave motion with a period of about 4 days, the rotation of the current vector being in a cyclonic (counterclockwise) direction for this station, which is in the centre of the lake basin. Coherence and

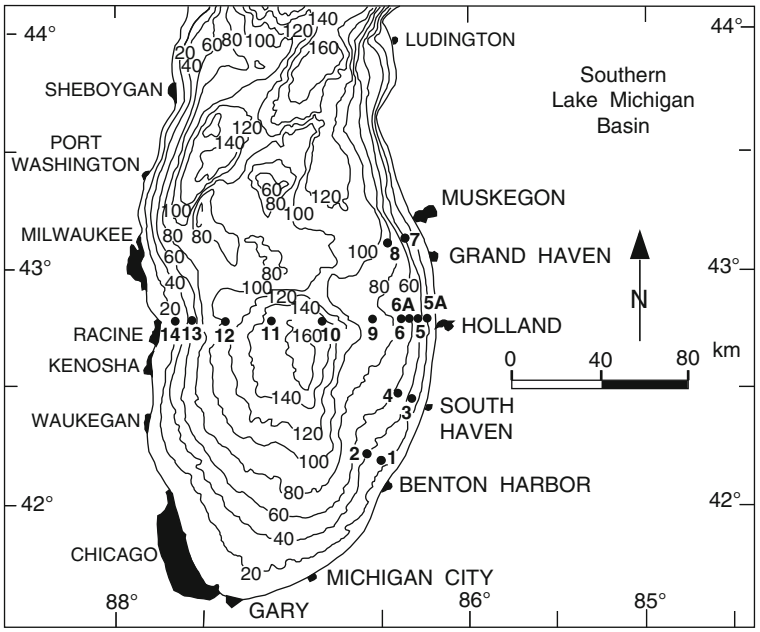

Fig. 19.2 Location map showing the bathymetry of Southern Lake Michigan and the positions of the 16 current meter moorings, adapted from Saylor et al. (1980) [35]. © American Meteorological Society, reprinted with permission

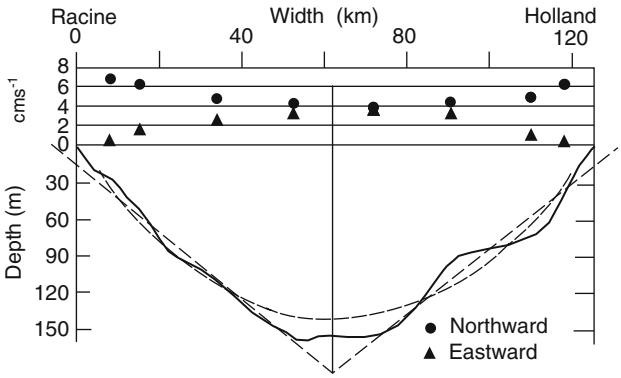

Fig. 19.3 Average amplitudes of the North and East velocity components for rotational oscillations on the southern Lake Michigan cross section during an episode of wave excitation, 1–15 July 1976. Basin approximations as a paraboloid or as an inverted cone that are referred to later are also shown, adapted from Saylor et al. (1980) [35]. © American Meteorological Society, reprinted with permission

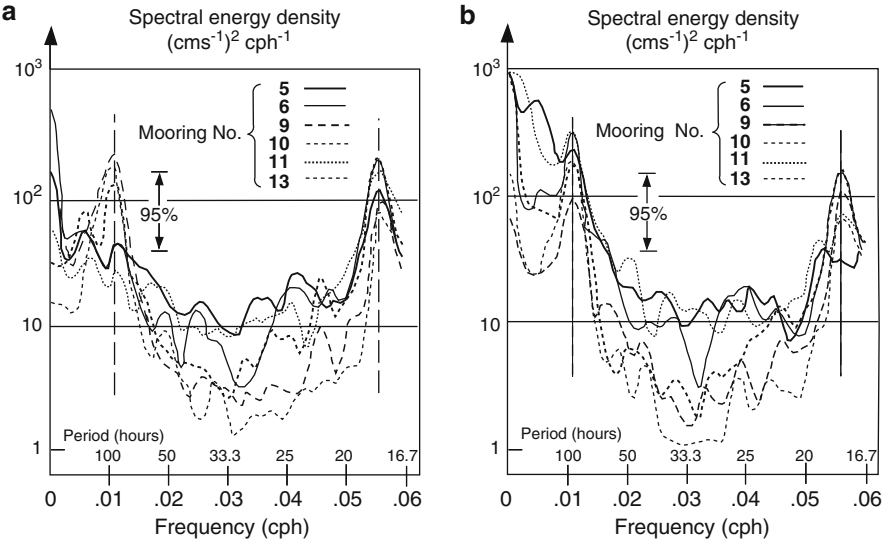

Fig. 19.4 (**a**) Kinetic energy spectra of the Eastward velocity component (u) recorded at the 25 m level at six stations in Southern Lake Michigan. *Vertical lines* are drawn to accentuate the two conspicuous energy peaks at near inertial and near 4-day periods. (**b**) as in (**a**), except for the Northward velocity component (v), adapted from [35]. © American Meteorological Society, reprinted with permission

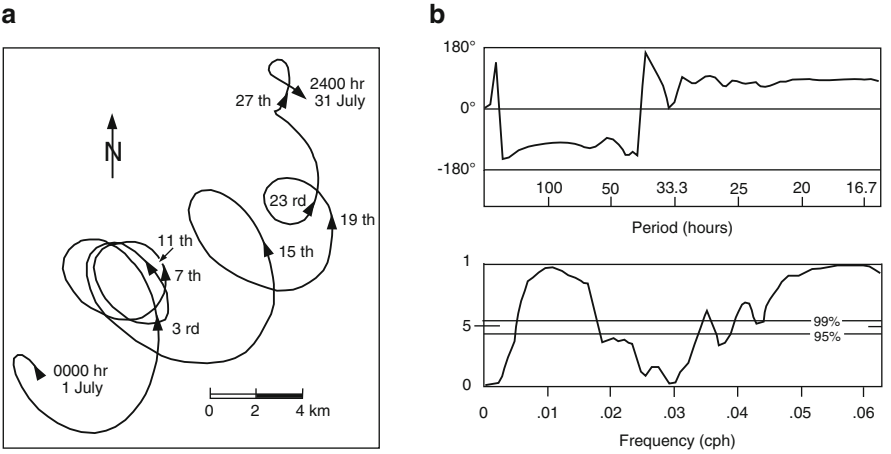

Fig. 19.5 (**a**) Hodograph of hourly averaged, lowpass filtered current velocities from the 32-m depth current meter at station 11 for the month of July 1976. (**b**) Coherence (lower) and phase between the East and North velocities at the 32 m level from station 11. Two broad areas of high coherence highlight the cyclonic rotating 4-day oscillation and the anti-cyclonic near inertial oscillation, adapted from [35]. © American Meteorological Society, reprinted with permission

Table 19.1 Eigenfrequencies (-periods) of the first three TW-modes computed according to (19.4) using $f = 2\pi/16.9\,\mathrm{h}$

Profile	q	$m=1$		$m=2$		$m=3$	
		f/ω	T [h]	f/ω	T [h]	f/ω	T [h]
	1	5	84.5	4	67.6	3	50.7
	2	7	118	5	84.5	4	67.6
	3	9	152	6	101	5	84.5
	∞	0	∞	0	∞	0	∞

phase plots in Fig. 19.5b for the East (u)- and North (v)-components for one current meter at position 11 accentuate this, as they show two highly correlated signals centred at the two indicated frequencies. At the 4-day period, the u-component leads the v-component by a phase angle of 90° which corresponds to a cyclonic rotation; at the near-inertial period the phase angle of the u-component lags that of the v-component by approximately 90°, indicating an anti-cyclonic oscillation.

Further scrutiny of the data shows that (1) the 4-day period motions are clockwise rotations at all stations except 10 and 11 in the centre of the lake, where they are counterclockwise and (2) currents at on-shore positions are primarily along-shore while those at off-shore stations may have appreciable amplitudes for both, the East- and North-components.

These observations can be interpreted in terms of free TWs in a circular basin with nearly conical profiles. For a depth profile of the form

$$H = H_0 \left(1 - \left(\frac{r}{a}\right)^q\right), \quad q > 0, \tag{19.3}$$

(H_0 is the maximum depth at the centre, a the radius of the circular basin and q a parameter characterizing the profile), Saylor et al. [35] deduce the frequency relation

$$\frac{f}{\omega} = \frac{3m + 2q}{m}. \tag{19.4}$$

Here, ω is the frequency, f the Coriolis parameter and $m = 1, 2, 3, \ldots$ the radial mode number. Values for the frequencies or periods are summarized in Table 19.1 and the streamline pattern of the vertically integrated transport for the lowest two modes is sketched in Fig. 19.6. The fundamental mode ($m = 1$) enjoys all properties of the observations mentioned above. In particular for the conical profile, its period is close to the observed 90 h period. Table 19.1 and (19.4), however, also show that for each mode the periods depend strongly on the topography, but not on the size of the basin (H_0 and a do not enter into the frequency relation). Moreover, the same period arises for different modes and different bathymetries, indicating that the mode *structure* is very important in interpreting observations.

In summary, the data analysis of the current meters and the interpretation of the observed periods and velocity rotations in terms of free topographic waves in a circular basin seem to be in harmony in the sense that no discrepancies were discovered.

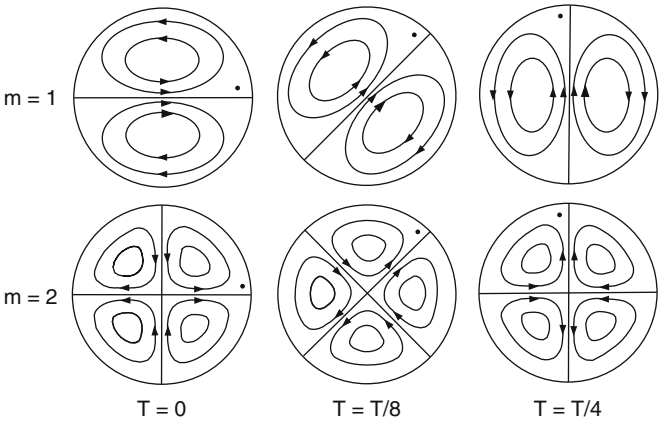

Fig. 19.6 Schematic sketch of the mass transport stream line patterns of the fundamental and first 'higher' mode plotted for three instances during a quarter period. During one cycle, the system of gyres rotates counterclockwise (on the northern hemisphere) around the basin (From [42]). © Springer, Berlin, reprinted with permission

19.2.2 Lake of Lugano (North Basin)

Southern Lake Michigan is a large and relatively shallow lake with a width of approximately 100 km, whereas Lake of Lugano is small (17 km long, approximately 2 km wide and 300 m deep).

In summer 1979, thermistor chains and current meters were positioned at various locations in the stratified Northern basin of Lake of Lugano. Only temperature-time series could be analyzed (for a detailed description see [19, 32, 33]). They disclose a moderate long-periodic signal with a period of app. 74 h.

Figure 19.7 shows the map of Lake of Lugano (North basin) with indicated stations where the wind and temperature (generally at the lower portion of the metalimnion) were measured in July/August 1979. Figure 19.8 summarizes wind data at stations 4 and 7 (top) and isotherm–depth–time series at the stations 1 and 8, 6 and 4 (lower part). These time series 'demonstrate a strong component of the motion with a period of perhaps 74 h (marked by circles ◔). To emphasize this wave the troughs of the isotherm depths have been brought into prominence by thick solid and dotted lines. The front arises first at station 4, propagates Southwards, reaches station 1 approximately 7 h later (indicated by the solid line connecting the troughs at Cassarate and Melide) and is 'reflected' at the Southern end of the lake. The 'reflected' wave passes through station 4 again (though split up into two smaller minima with an intermediate maximum, indicated by an arrow marked with an encircled 1), and after 37 h, can be recognized at station 8 with a conspicuous minimum (heavy dotted lines). It appears later at Cassarate, Melide and as a reflected wave at Cassarate (arrow marked by an encircled 2), Porlezza, etc.' [19]. The corresponding wave speed of approximately 12 cm s^{-1} is substantially lower than the wave speed of the

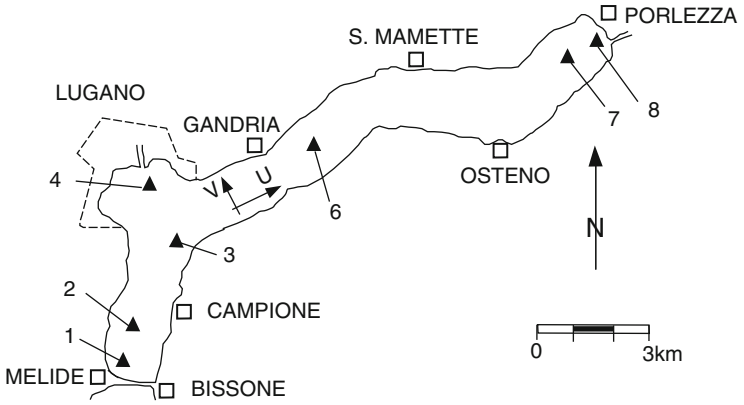

Fig. 19.7 Northern Lake of Lugano with indicated positions of moorings (1–8) equipped with anemometers, thermistor chains and current meters in the field campaign July–August 1979 (From [42]). © Springer, Berlin, reprinted with permission

internal gravity wave of the two-layer model; neither can it be explained as a higher order baroclinic Kelvin wave of, say, a three-layer model. Furthermore, *direct* wind forcing can be excluded as a likely cause of excitation [33]).

A statistical cross-correlation analysis of the temperature time series indicated for all station-pair-time series – except stations 3/8 – high coherence and strongly suggested a counter clockwise rotation of the wave signal around the basin.

Mysak et al. [33] have explained the 74-h oscillation and the anticlockwise propagation of the phase as the baroclinic trace of a barotropically driven TW. They explain all their observations (except the 'discrepancy' in the phase of the pair 3/8 of the mean temperature displacement function, which interrupts the anticlockwise increase of the phase difference) in terms of the fundamental mode of TW in an elliptical two-layer basin. The streamlines as constructed by [20] are sketched in Fig. 19.9.[4]

To round out this picture it must be mentioned that the TW-equation has been approximately and numerically solved by the finite element technique [47] with results which do not at all support the interpretation using elliptical TW. Trösch finds that solutions in the 65–95-h-period range are generally localized to the two narrow ends and the bay of Lugano. Figure 19.10 shows the streamline pattern of three such modes, having periods of 68.5, 80.5 and 91 h, respectively.

This was the state of conflicting interpretation of the same observations in the mid-1980s of the last century. It led Stocker and Hutter to a research activity of about 5 years duration and culminated in the finding that eigenmodes of the TW-equation in a closed basin with periods close to one another can be basin filling with small or large scale structures or they can be localized in relatively small bays.

[4] Mysak et al. [33, p. 52] list six arguments in support of the TW-model and only the above mentioned discrepancy in the phase relation against it.

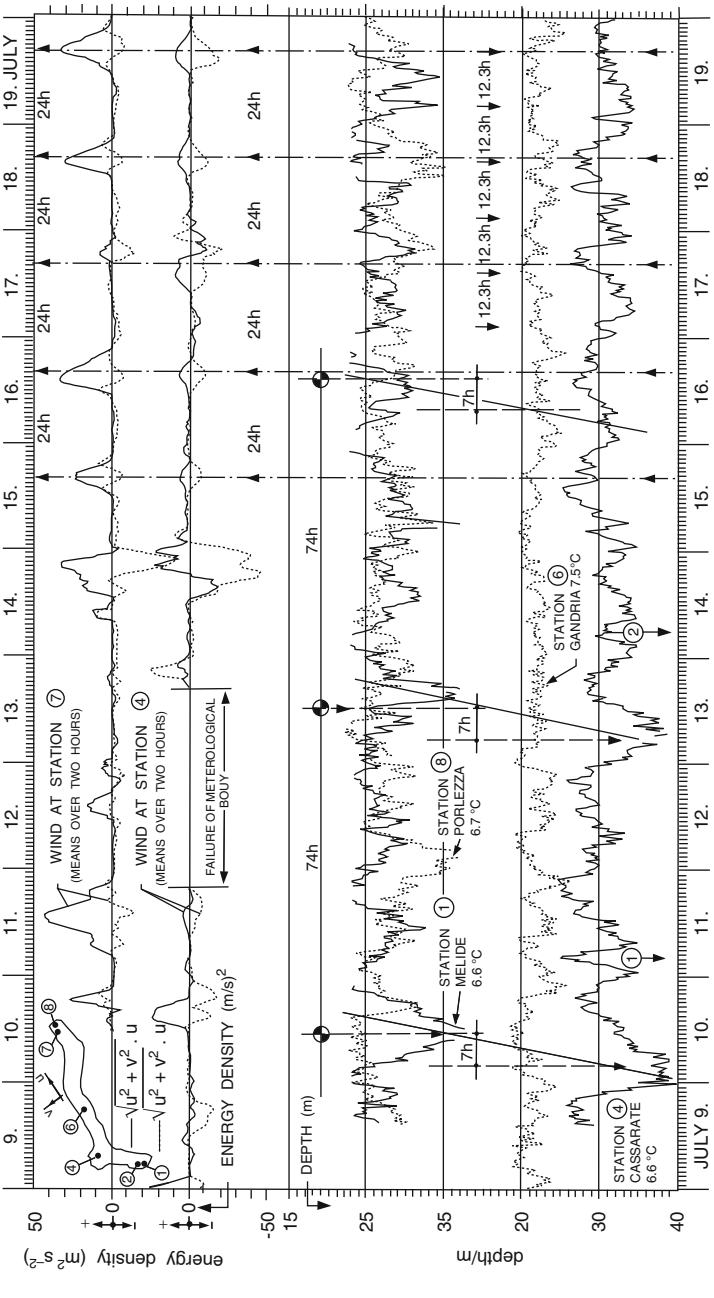

Fig. 19.8 Time series of 2 h means of the longitudinal and transverse components of the wind energy ($(u^2+v^2)^{1/2}u$, $(u^2+v^2)^{1/2}v$) with directions of u and v components as indicated in the *upper left corner* at the stations 7 (Porlezza) and 4 (Cassarate) and unfiltered time series of selected isotherm depths at the stations 1 (Melide, *top solid curve*), 8 (Porlezza, *dotted*, superposed on the Melide curve) and 4 (Cassarate, *solid curve*). Components of the motion with conspicuous periods are marked by special symbols: troughs in *heavy solid* and *dotted lines* and marked by *circles* ◒ are for 74 h; *triangles* for 24 h; *arrows* for 12 h. The time shown is from 9 to 19 July 1979 (From Hutter et al. [19]).

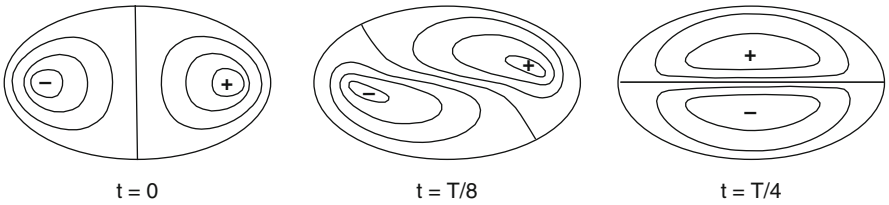

Fig. 19.9 Contours of the mass transport stream function of the fundamental mode for elliptical topographic waves (From Johnson (1987) [20]). © Taylor & Francis, http://www.informaworld.com, reprinted with permission

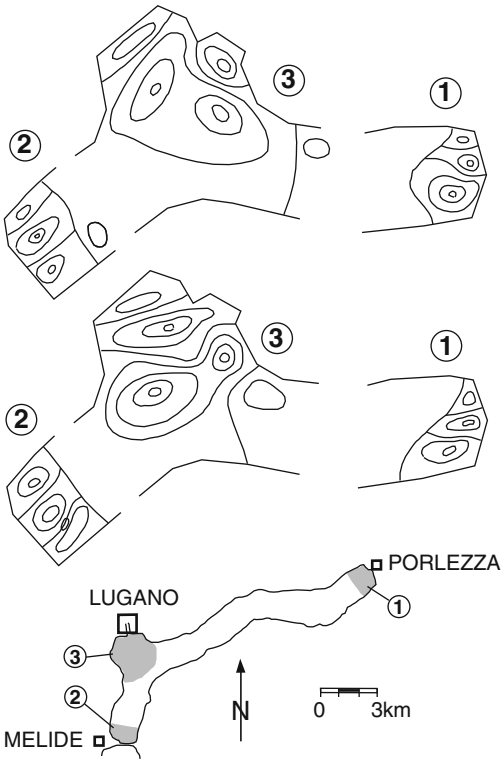

Fig. 19.10 Three modes of long periodic waves in Lake of Lugano obtained by the finite element technique. $\left.\begin{array}{l} T_1 = 68.5\ \text{h} \\ T_2 = 80.5\ \text{h} \\ T_3 = 91\ \text{h} \end{array}\right\}$ for $t = 0$ (above) and $t = T/4$ (below). From Trösch (1986) [47], with alterations. © National Cheng Kung University Press, Tainan, Taiwan, reproduced with permission

19.2.3 Other Lakes and Ocean Basins

Stocker and Hutter [42] present 10°C-isotherm–depth data at ten different moorings distributed in Lake Zurich and give evidence that the consistently observed high amplitudes in the period range 100–110 h give rise to the suspicion of a counter-clockwise propagation of an oscillating signal. Furthermore, rotary spectra of the water current at the positions and at depth show that near the 100 h period (1) the

rotation of the current vector at the mid-lake position is predominantly counter-clockwise, but (2) it is predominantly clockwise at some near-shore positions. This gives support for the suspicion that the 100 h signal could be a TW.

Csanady's [7] coastal strip model that is applied to Lake Ontario is based on Gill and Schumann's [9] shelf wave analysis, but describes a local near shore wave, which, in the 25 day period range in later work by Marmorino [28], is interpreted as a free TW. These waves are no basin wide response and therefore do not fall into the category dealt with in this chapter.

There is ample further evidence of vorticity generated flow features reminiscent of TW-behaviour. Saylor and Miller [36] also analyze time series of water currents from instruments moored in Lakes *Erie* and *Huron* at several offshore positions. They find for these lakes that in the period band of 85–125 h kinetic energy associated with anticlockwise (clockwise) rotation of the current vector is accumulated for 'mid-lake' (near-shore) mooring stations, suggesting a fundamental TW-mode.

Numerical studies of the wind-induced circulation in the *Baltic Sea* [25, 37, 39] and interpretation of infrared satellite imagery [24], indicate local current patterns with cyclonically rotating gyres that are reminiscent of TWs induced by winds.

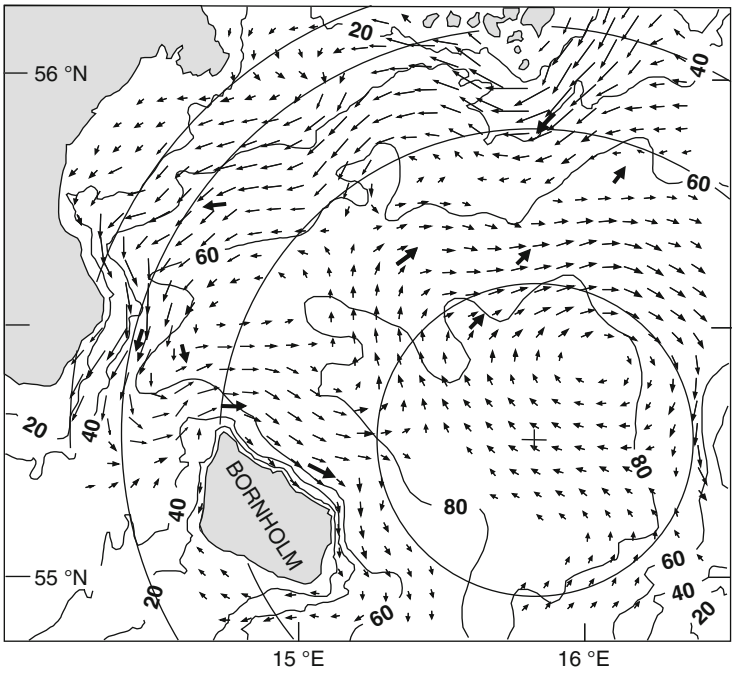

Fig. 19.11 Observed (*dark arrows*) and computed (*light arrows*) vertically integrated transports in the South–West Baltic Sea after a strong wind from the Northeast, i.e. from the upper right-hand corner (From Simons [37], with additions; see also [38]). © Wiley Blackwell, reproduced with permission

Figure 19.11 shows the observed and computed vertically integrated transport in the *Bornholm basin* located in the South-West Baltic Sea after a strong wind from the Northwest. This current pattern was established from a configuration of completely reversed flow before the onset of the wind, thus confirming the basic concept of large-scale vorticity generation by the interaction of wind stress and bottom slope. The figure also shows the topography and its approximation by a circular basin. Adopting this circular basin, Wenzel [49] demonstrates that there are good reasons to assume that the system of gyres is an excited higher mode of TWs with a period of approximately 5 days. Kielmann [24] reaches similar conclusions.

Similar vortex systems for the vertically integrated transport of the *Gulf of Bothnia* are also attributed to wind generated topographic response [25]. Bäuerle [3] models this gulf as a channel having a trench profile; he constructs numerical TW solutions having periods of 70–75 h, but abstains from a comparison of his results with observations.

We may conclude this brief overview with the following slightly simplified statements:

1. There exists a large amount of episodic and isolated observational evidence which suggests that long periodic oscillating responses in lakes and local areas of such basins *may* be explained in terms of TW-models.
2. Coherent temperature and current data covering an entire basin for a period of longer duration do not seem to be available in order to clearly identify the primary cause of the motion and to interpret the observations uniquely in terms of a model.
3. It appears that long periodic circulation features which are the immediate result of strong winds, can be explained by simple idealized or more realistic and complicated models and both yield very similar if not identical results. Long periodic features which are the direct result of a strong wind gust permit interpretation in terms of TWs.
4. On the other hand, inferences from simple (analytically accessible) models and more realistic (only numerically exploitable) models which attempt to explain basin-wide TW-behaviour are conflicting. Hence, interpretation of basin-wide long periodic oscillations remains an open problem, at least as long as one cannot assume with certainty that the numerically discretized models generate flows which are the approximation (in a well defined sense) of the original nondiscretized TW-equation to the real topography.

The above statements, which were made more than 20 years ago by Stocker and Hutter [42] are still correct today but verification by measurements is difficult. The reason is that *basin- and bay-filling TWs often have eigenfrequencies which are very close to each other, whereas their eigen-functions are far apart*. This fact suggests observationally that *it is very difficult to separate the different modes from synoptically taken data, whilst numerically high accuracy is needed to capture modes which are close to each other*. This is what we attempt to elucidate in this and the two following chapters.

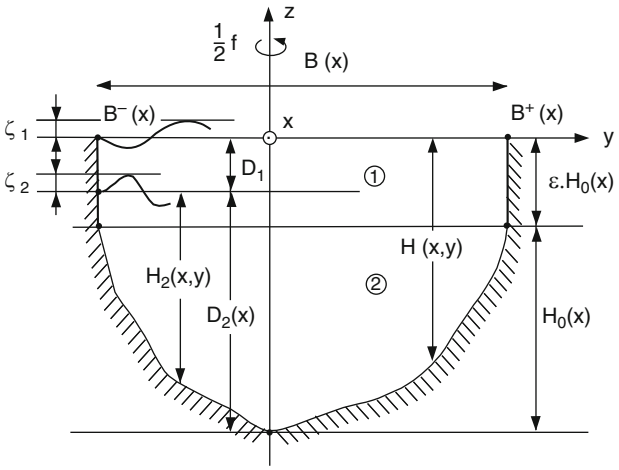

Fig. 19.12 Side view of a cross section of the two-layer lake in its natural coordinate system (x, y, z). *Upper* and *lower layer* variables are denoted by an index 1 or 2, respectively. The lake is within a rotating system of spatially constant angular velocity $(1/2)f$ (From [40]). © Versuchsanstalt für Wasserbau, Hydrologie und Glaziologie an der ETH Zürich, reproduced with permission

19.3 Baroclinic Coupling: The Two-Layer Model

Having discussed the purely barotropic topographic Rossby waves already, we proceed directly to their description in a stratified fluid and commence with a two-layer configuration.

Motions occur in both layers and are subject to a coupling by the thermocline. As we shall show later on, this coupling mechanism is weak in the sense that it is mainly one-way, i.e. the motion of the thermocline is driven by the barotropic transport. If the velocity fields in the two layers are unidirectional the motion is barotropic, if they are in opposite directions it is baroclinic.

The configuration of the lake and the notation is summarized in Fig. 19.12. Important in the depicted geometry are the vertical side walls that extend beyond the thermocline well into the hypolimnion. Application must, therefore, be limited to lakes with steep shores.

Lake topography varies in space only in the lower layer, i.e. the upper layer is confined by two vertical side walls, which must exceed the depth of the thermocline, so $H(\boldsymbol{x}) > D_1$ for all $\boldsymbol{x}$. We accept the varying thickness of the side walls with $\boldsymbol{x}$ because of analytical simplicity.

19.3.1 Two-Layer-Equations

Basic idea in obtaining a description of the physical behaviour of our system is to formulate equations which describe conservation of mass, momentum and energy

for the individual layers. Thermodynamic effects will be neglected in this study. The evolving nonlinear system is linearized by the assumption of small Rossby numbers. Furthermore, surface elevations ζ are thought to be small in comparison to the depth of the upper layer. Turbulence will be ignored but wind stress, distributed over the thin upper layer, and acting as a driving force will be considered. Under these approximations, the equations of motion in components of a Cartesian system take the forms (Mysak [31], p 87, Mysak et al. [33])

$$\begin{aligned} u_{1t} - f v_1 &= -g\zeta_{1x} + \tau^x/(\rho_1 D_1), \\ v_{1t} + f u_1 &= -g\zeta_{1y} + \tau^y/(\rho_1 D_1), \\ D_1(u_{1x} + v_{1y}) &= \zeta_{2t} - \underline{\zeta_{1t}}, \end{aligned} \tag{19.5}$$

$$\begin{aligned} u_{2t} - f v_2 &= -g\zeta_{1x} - g'(\zeta_{2x} - \underline{\zeta_{1x}}), \\ v_{2t} + f u_2 &= -g\zeta_{1y} - g'(\zeta_{2y} - \underline{\zeta_{1y}}), \\ (H_2 u_2)_x + (H_2 v_2)_y &= -\zeta_{2t}, \end{aligned} \tag{19.6}$$

where g' is the reduced gravity $g' = g(\rho_2 - \rho_1)/\rho_2$. Subscripts denote differentiation with respect to the subscript-variable. Everything that follows can be directly derived from (19.5)–(19.6).

19.3.2 Approximations

We will now transform the above equations and introduce further approximations which will make it apparent why the conservation law of potential vorticity is still a reasonable approximation for vorticity waves when barotropic–baroclinic coupling is present.

19.3.2.1 Rigid-Lid Approximation

It is known that to every wave type of the above system there exists an internal and an external variant. The periods of the latter are generally much smaller than those of the former and, by applying the rigid lid approximation, the external modes are impeded. This means, that compared to the interface elevation any surface elevation can be neglected, i.e. the underlined terms in (19.5) and (19.6) are ignored. With this, it follows from the mass conservations $(19.5)_3$ and $(19.6)_3$ that the quasi-solenoidal velocity field can be replaced by the stream function through which the components of the integrated transport are given by

$$-\psi_y = D_1 u_1 + H_2 u_2, \quad \psi_x = D_1 v_1 + H_2 v_2. \tag{19.7}$$

ψ is called the barotropic or *mass transport stream function*. Equations (19.5) and (19.6) can be transformed into a compact system in the variables ψ and $\zeta_2 \equiv \zeta$. Assuming a constant Coriolis parameter f the result reads

$$\nabla \cdot (H^{-1}\nabla\psi_t) + f(\nabla\psi \times \nabla H^{-1}) \cdot \hat{\boldsymbol{k}} = -g' D_1 (\nabla\zeta \times \nabla H^{-1}) \cdot \hat{\boldsymbol{k}} + \frac{1}{\rho_1}[\nabla \times (\boldsymbol{\tau} H^{-1}) + \frac{H}{D_1}\boldsymbol{\tau} \times \nabla H^{-1}] \cdot \hat{\boldsymbol{k}}, \quad (19.8)$$

$$H\nabla^2\zeta_t - \frac{H^2}{g' D_1 H_2}\mathcal{L}\zeta_t + \frac{D_1}{H_2}\nabla\zeta_t \cdot \nabla H - \frac{f D_1}{H_2}(\nabla\zeta \times \nabla H) \cdot \hat{\boldsymbol{k}} = \frac{1}{g' H_2}[\nabla(\mathcal{L}\psi) \times \nabla H] \cdot \hat{\boldsymbol{k}} - \frac{H}{\rho_1 g' D_1} f(\nabla \times \mathcal{L}\boldsymbol{\tau}) \cdot \hat{\boldsymbol{k}}, \quad (19.9)$$

where $\hat{\boldsymbol{k}}$ is a unit vector in the positive z-direction and the operator $\mathcal{L} = \partial_{tt} + f^2$ has been introduced.

Problem 19.1 *Derive (19.8) and (19.9) from (19.5) and (19.6) and show in the process of derivation that the formulae (19.10) below for the horizontal velocities can be derived.* ◆

Mysak et al. [33] give a detailed discussion of the physics of (19.8) and (19.9), which is now briefly summarized. In the absence of stratification ($g' = 0$) and wind forcing ($\boldsymbol{\tau} = \mathbf{0}$), (19.8) reduces to the conservation law of potential vorticity. Wind is the external force; the second term on the right-hand side of (19.8) may therefore be interpreted as the supply of potential vorticity due to wind action. Stratification ($g' \neq 0$) in a basin with variable topography ($\nabla H \neq \mathbf{0}$) couples the barotropic part of (19.8), namely its left-hand side, with the baroclinic processes. The first term on the right-hand side of (19.8) is, therefore, the production of potential vorticity due to baroclinicity; it represents the influence of the baroclinic effects on the barotropic motion.

By the same argument, (19.9) describes the influence of the barotropic processes (terms involving ψ) and the wind (terms involving $\boldsymbol{\tau}$) on the baroclinic motion. Ignoring these barotropic terms results in an equation describing internal waves with a phase speed

$$c_{\text{int}}^2 = g' D_1 H_2 / H.$$

When $\nabla H = \mathbf{0}$ the third and fourth term on the left-hand side vanish, and the equation describes classical internal Kelvin and Poincaré waves. Thus, (19.8) and (19.9) exhibit in general a two-way coupling, a baroclinic–barotropic coupling and a barotropic–baroclinic coupling the strengths of which must be estimated by a scale-analysis.

When deriving (19.8) and (19.9) from (19.5) and (19.6) the layer velocities can be expressed in terms of ψ and ζ. The expressions are

$$\mathcal{L}\boldsymbol{u}_1 = \frac{1}{H}\left[\hat{\boldsymbol{k}} \times \nabla(\mathcal{L}\psi) + H_2 g'(\nabla\zeta_t - f\hat{\boldsymbol{k}} \times \nabla\zeta) + \frac{H_2}{\rho_1 D_1}(\boldsymbol{\tau}_t - f\hat{\boldsymbol{k}} \times \boldsymbol{\tau})\right],$$
$$\mathcal{L}\boldsymbol{u}_2 = \frac{1}{H}\left[\hat{\boldsymbol{k}} \times \nabla(\mathcal{L}\psi) - D_1 g'(\nabla\zeta_t - f\hat{\boldsymbol{k}} \times \nabla\zeta) - \frac{1}{\rho_1}(\boldsymbol{\tau}_t - f\hat{\boldsymbol{k}} \times \boldsymbol{\tau})\right], \tag{19.10}$$

(see Problem 19.1) which are additively composed of three parts, i.e. a barotropic, a baroclinic and a wind force component. The first are the same (and unidirectional) in both layers, and the second are in opposite directions and add up to vanishing total transport, reminiscent of barotropic and baroclinic behaviour, respectively.

19.3.2.2 Low-Frequency Approximation

In (19.9), ζ appears with a third order time derivative. This means that (19.9) can contain three types of waves. In fact, a more precise analysis shows that there are two (internal) gravity waves and one topographic wave of which the latter has the longest period. Because we want to study here topographic waves, we will search for solutions of (19.8) and (19.9) with low frequency ω. For $\omega \ll f$ we may therefore neglect ω in comparison to f. Thus, $\mathcal{L}$ reduces to $\mathcal{L} \approx f^2$. Such an approximation, however, requires that periods are substantially greater than about 17 h (the inertial period corresponding to f at 45° latitude).

Parenthetically, we might also mention that this approximation holds only for lakes in which the internal seiche period (of a gravity or Kelvin wave) is considerably smaller than the period of topographic waves. Since the former increases with the lake dimension and the latter is size-invariant, the frequencies of gravity waves in larger lakes become of comparable order to those of topographic waves. For Lakes Zurich and Lugano the approximation is appropriate, for Lake Geneva or larger lakes it may be dubious, see Table 19.2.

The situation is nevertheless not as limiting as this statement might let us surmise, because we shall prove below that for many situations the baroclinic–barotropic coupling term on the right-hand side of (19.8) may safely be ignored. In this case, the TW-equation (19.8) uncouples from (19.9). Since also boundary conditions will be shown to be free of this baroclinic–barotropic coupling, solutions to the

Table 19.2 The gap between the eigenperiods of internal gravity and topographic waves depends on the lake dimension

Lake	Surface length [km]	Period of internal gravity waves [h]	Period of topographic waves [h]
Lugano	17.2[a]	≤28[a]	74[b]
Zurich	28[a]	≤45[a]	100[b]
Geneva	72[c]	≤78[d]	72–96[b]

[a]Hutter, 1983 [15] [b]Mysak, 1985 [31] [c]Graf, 1983 [10]
[d]Bäuerle, 1985 [4]

TW-problem can be obtained without solving the inertial gravity wave problem. The assumption $|\omega| \ll f$ need not necessarily be invoked.

19.3.3 Scale Analysis

Information about the orders of magnitude of the various coupling terms in (19.8) and (19.9) is obtained by constructing dimensionless counterparts of these equations via the introduction of scales.

19.3.3.1 Wind Forcing

The external forcing mechanism in (19.8) and (19.9) is the wind. To estimate its relative importance, consider the identity

$$\nabla \times (\boldsymbol{\tau} H^{-1}) + \frac{H}{D_1} \boldsymbol{\tau} \times \nabla H^{-1} \equiv H^{-1} (\nabla \times \boldsymbol{\tau}) + (\nabla H^{-1}) \times \boldsymbol{\tau} + \frac{H}{D_1} \boldsymbol{\tau} \times \nabla H^{-1}. \tag{19.11}$$

The first term on the right can be neglected in comparison to the others, because the atmospheric length scale is in general much larger than the lake dimensions. Such a statement is tantamount to ignoring spatial variations of wind stress over the domain of the lake. Further, comparing the last two terms it is seen that they differ by an order D_1/H which, in view of our basic assumption, is small (cf. Table 19.3). Consequently, only the last term of (19.11) survives. In a way, this is a strange result: As far as the barotropic contribution of the motion is concerned, only a lake with variable topography can be affected by the wind. This leads to the conclusion that the assumption on atmospheric length scales may be doubtful. Indeed, varying topography in the vicinity of a lake may play a significant role as it can modify regional winds with atmospheric length scales to local winds with smaller length scales. An example is the topography around Lake of Lugano; but experimental evidence for the wind stress curl to be significant is so far lacking.

19.3.3.2 Gratton's Scaling

Gratton [11] and Gratton and LeBlond [12] consider lake stratifications with $D_1 \ll D_2$, i.e. a thin upper layer lies on top of a deep hypolimnion. For this case they found that the baroclinic effect on the barotropic motion is of order D_1/D_2 smaller than the barotropic effect on the baroclinic motion. So, to order D_1/D_2 the coupling only arises as a forcing of the baroclinic motion by the barotropic mass transport.

Before we demonstrate this result let us point out its significance. The one-way coupling means that traces of the topographically induced motion can be observed

by measuring baroclinic quantities such as temperature-time series of thermistor chains, moored within the metalimnion. The description of the observations in Lakes of Lugano in Sect. 19.1 are based on such temperature-time series.

We now introduce the following set of nondimensional variables:

$$\begin{aligned} &\psi := \psi_0 \psi', \quad \zeta := \zeta_0 \zeta', \quad \boldsymbol{\tau} := \tau_0 \boldsymbol{\tau}', \\ &(x, y) := L(x', y'), \quad t := f^{-1} t', \\ &H := Dh' = (D_1 + D_2)h', \quad H_2 := D_2 h_2, \end{aligned} \tag{19.12}$$

where the primed variables are non-dimensional; L is a typical length scale of the considered waves (e.g. half the lake length). Higher wave modes, where cross variations are important, may require a (x, y)-scaling which is different for each spatial direction, but this will not be considered. With (19.12) we obtain the scaled equations as

$$\begin{aligned} &\nabla \cdot \left(h^{-1} \nabla \psi_t\right) + \left(\nabla \psi \times \nabla h^{-1}\right) \cdot \hat{\boldsymbol{k}} \\ &\quad = -C_1 \left(\nabla \zeta \times \nabla h^{-1}\right) \cdot \hat{\boldsymbol{k}} + \left(\frac{L D \tau_0}{f \rho_1 D_1 \psi_0}\right) \left(h \boldsymbol{\tau} \times \nabla h^{-1}\right) \cdot \hat{\boldsymbol{k}}, \end{aligned} \tag{19.13}$$

$$\begin{aligned} &\frac{1}{h} \left(\nabla^2 \zeta_t - \frac{L^2 h}{R_{\text{int}}^2 h_2} \mathcal{L} \zeta_t\right) - \frac{D_1}{D_2 h_2} \nabla \zeta_t \cdot \nabla h^{-1} + \frac{D_1}{D_2 h_2} \left(\nabla \zeta \times \nabla h^{-1}\right) \cdot \hat{\boldsymbol{k}} \\ &\quad = -C_2 h_2^{-1} \left(\nabla \psi \times \nabla h^{-1}\right) \cdot \hat{\boldsymbol{k}} - \frac{\tau_0 L}{\rho_1 g' D_1 \zeta_0} \frac{1}{h} \left(\nabla \times \mathcal{L} \boldsymbol{\tau}\right) \cdot \hat{\boldsymbol{k}}, \end{aligned} \tag{19.14}$$

where now $\mathcal{L} = \partial_{tt} + 1$ and the coupling coefficients are given by

$$C_1 = \frac{g' D_1 \zeta_0}{f \psi_0}, \qquad C_2 = \frac{f \psi_0}{g' D_2 \zeta_0} = \frac{D_1}{D_2} \cdot \frac{1}{C_1}, \tag{19.15}$$

and $R_{\text{int}} = g' D_1 D_2 / (D f^2)^{1/2}$ is the internal Rossby radius. Note that in (19.13) and (19.14) we have dropped the primes on the scaled (nondimensional) variables.

Let us now suppose that (19.13) and (19.14) are strongly coupled, i.e. that C_1 and C_2 are both $O(1)$. Then (19.15) implies that

$$\zeta_0 = O\left(\frac{f \psi_0}{g' D_1}\right) \quad \text{and} \quad \zeta_0 = O\left(\frac{f \psi_0}{g' D_2}\right), \tag{19.16}$$

and we observe that independent of the ψ_0-scale, $(19.16)_{1,2}$ are consistent only if $D_1/D_2 = O(1)$. Since we are concerned with the case $D_1 \ll D_2$, it follows that C_1 and C_2 cannot both be of order unity, i.e. that (19.13) and (19.14) are only weakly coupled. Suppose we assume that $(19.16)_1$ applies and thus choose

$$\frac{\zeta_0}{\psi_0} = \frac{f}{g' D_1} \tag{19.17}$$

as the scaling for the ratio ζ_0/ψ_0. Then $C_1 = 1$ and $C_2 = D_1/D_2 \ll 1$. Therefore, to $O(D_1/D_2)$, (19.14) reduces to

$$\left(\nabla^2 - \left(\frac{L}{R_{\text{int}}}\right)^2 \mathcal{L}\right)\zeta_t = -\frac{\tau_0 L}{\rho_1 g' D_1 \zeta_0}(\nabla \times \mathcal{L}\boldsymbol{\tau}) \cdot \hat{\boldsymbol{k}}, \tag{19.18}$$

where we have used $h/h_2 = 1 + O(D_1/D_2)$. Equation (19.18) is a wave equation forced by the wind stress curl, but the scale choice (19.17) leads to an unrealistically large value for the ζ_0 scale (about $\zeta_0 \leq 50$ m, which is several times the upper layer depth for most lakes[5]).

Hence, we are compelled to choose the scaling $(19.16)_2$ (Gratton's choice, which was based on data from the Strait of Georgia, British Columbia). Putting

$$\frac{\zeta_0}{\psi_0} = \frac{f}{g' D_2}, \tag{19.19}$$

we find $C_2 = 1$ and $C_1 = D_1/D_2 \ll 1$, We choose the ζ_0 scale by setting the coefficient of the wind stress term in (19.13) equal to unity, which gives

$$\psi_0 = \frac{L D \tau_0}{f \rho_1 D_1}. \tag{19.20}$$

Substituting (19.20) into (19.19) gives the scale ζ_0 in terms of the wind stress scale τ_0:

$$\zeta_0 = \frac{L D \tau_0}{\rho_1 g' D_1 D_2} = \frac{\psi_0 f}{g' D_2}, \tag{19.21}$$

which yields a realistic order of magnitude.[6] Using (19.20) and (19.21) in (19.13) and (19.14), we obtain, correct to $O(D_1/D_2)$

$$\nabla \cdot (h^{-1} \nabla \psi_t) + (\nabla \psi \times \nabla h^{-1}) \cdot \hat{\boldsymbol{k}} = (h\boldsymbol{\tau} \times \nabla h^{-1}) \cdot \hat{\boldsymbol{k}}, \tag{19.22}$$

$$(\nabla^2 - S^{-1}\mathcal{L})\zeta_t = -(\nabla \psi \times \nabla h^{-1}) \cdot \hat{\boldsymbol{k}} - (\nabla \times \mathcal{L}\boldsymbol{\tau}) \cdot \hat{\boldsymbol{k}}, \tag{19.23}$$

[5] With $f = 10^{-4}\,\text{s}^{-1}$, $g' = 0.02\,\text{ms}^{-2}$, $D_1 = 10\,\text{m}$, $D_2 = 270\,\text{m}$ and $\psi_0 = U \cdot L \cdot (D_1 + D_2) = 0.03 \cdot 10^4 \times 270\,\text{m}^3\,\text{s}^{-1}$, where U is a velocity scale (approximately $3\,\text{cm}\,\text{s}^{-1}$ for Lake of Lugano) and $L = 10^4$ m, one obtains $\zeta_0 = 40\,\text{m}$.

[6] With $f = 10^{-4}\,\text{s}^{-1}$, $g' = 0.02\,\text{ms}^{-2}$, $\psi_0 = 7 \times 10^4\,\text{m}^3\,\text{s}^{-1}$ and $D_2 = 270\,\text{m}$, (19.21) yields $\zeta_0 = 1\,\text{m}$. Alternatively, using $\tau_0 = \rho_{\text{air}} c_d U_w^2$ with $\rho_{\text{air}} = 1.29\,\text{kg}\,\text{m}^{-3}$, $c_d = 1.85 \times 10^{-3}$ (an average value for lakes during summer, see Simons [39], p. 92), and $U_w = 4\,\text{ms}^{-1}$, we find $\tau_0 = 0.038\,\text{Nm}^{-2}$ and hence according to (19.21), $\zeta_0 = 1.5\,\text{m}$ and according to (19.20), $U = \tau_0/(\rho_1 f D_1) = 3.8\,\text{cm}\,\text{s}^{-1}$. Both values are typical observations in Lake Zurich and Lake of Lugano, see Table 19.3.

as the appropriate non-dimensional equations for ψ and ζ. In (19.23), note that we have introduced the stratification parameter S (Burger number), defined as

$$S = (R_{\text{int}}/L)^2. \tag{19.24}$$

For the derivation of (19.23) it is important that $h_2 \neq 0$ (as illustrated in Fig. 19.12). If $h_2 = 0$, the third and fourth terms on the left side of (19.14) are not uniformly $O(D_1/D_2)$ and hence could not be neglected. If an elliptic paraboloid contained a two-layer fluid, then clearly $h_2 = 0$, where the interface touches the basin wall and (19.23) would not be valid. Thus, Ball's [2] solution[7] for second-class waves in an elliptic paraboloid could not be easily extended to the stratified case by our analysis.

The derivation of (19.22) and (19.23) follows Mysak et al. [33] but is more general in that the low frequency assumption has not been invoked and the wind stress curl has not been ignored. With these two additional assumptions $\mathcal{L}$ would be replaced by $\mathcal{L} = 1$ and the last term in (19.23) would be missing. As stated above these assumptions are not needed to achieve the decoupling of the barotropic motion from the baroclinic influence.

Substituting (19.12) and the scaling $(19.16)_2$ into (19.10) and using the scale $\psi_0 = ULD$, as before, we obtain the following formulae for the velocities:

$$\mathcal{L}\boldsymbol{u}_1 = \frac{1}{h}\left[\hat{\boldsymbol{k}} \times \nabla\mathcal{L}\psi + h_2\left((\nabla\zeta_t - \hat{\boldsymbol{k}} \times \nabla\zeta) + \frac{D_2}{D}(\boldsymbol{\tau}_t - \hat{\boldsymbol{k}} \times \boldsymbol{\tau})\right)\right], \tag{19.25}$$

$$\mathcal{L}\boldsymbol{u}_2 = \frac{1}{h}\left[\hat{\boldsymbol{k}} \times \nabla\mathcal{L}\psi - \frac{D_1}{D_2}\left((\nabla\zeta_t - \hat{\boldsymbol{k}} \times \nabla\zeta) + \frac{D_2}{D}(\boldsymbol{\tau}_t - \hat{\boldsymbol{k}} \times \boldsymbol{\tau})\right)\right]. \tag{19.26}$$

To $O(D_1/D_2)$ these can be approximated by

$$\mathcal{L}\boldsymbol{u}_1 = \frac{1}{h}\left[\hat{\boldsymbol{k}} \times \nabla\mathcal{L}\psi + h(\nabla\zeta_t - \hat{\boldsymbol{k}} \times \nabla\zeta + \boldsymbol{\tau}_t - \hat{\boldsymbol{k}} \times \boldsymbol{\tau})\right], \tag{19.27}$$

$$\mathcal{L}\boldsymbol{u}_2 = \frac{1}{h}\hat{\boldsymbol{k}} \times \nabla\psi. \tag{19.28}$$

Thus, for deep lakes, the lower layer current associated with topographic waves is essentially barotropic, whereas the upper layer current consists of a barotropic part, a baroclinic part and a contribution directly forced by the wind. Hence, we conclude that the current motions are generally surface intensified.

In Table 19.3, we collect some data pertinent to the above estimates. Values are given for the layer thickness and density difference of the summer stratification for three Swiss lakes from which Rossby radii, stratification parameters and typical values of the thermocline elevation can be computed. Accordingly, neglecting $O(D_1/D_2)$-terms is certainly justified for Lake of Lugano and still reasonable for

[7] This solution in an elliptic basin with parabolic bottom is constructed in Chap. 20, Sect. 20.3.3.

Table 19.3 Properties of some Swiss lakes

Lake	D_1 [m]	D_2^{mean} [m]	$D_2^{\max}$ [m]	$\frac{D_1}{D_2^{\text{mean}}}$	$\frac{\rho_2-\rho_1}{\rho_2}$	R_i [km]	Half length [km]	S^{-1}	ζ_0 [m]
Lugano	10[a]	183[a]	278[b]	0.055	$1.91 \cdot 10^{-3}$[a]	4.05	8.6	4.5	1.8[e]
Zurich	12[a]	52[a]	124[b]	0.231	$1.75 \cdot 10^{-3}$[a]	4.13	14	11.5	2.9[e]
Geneva	15[d]	153[d]	310[c]	0.098	$1.41 \cdot 10^{-3}$[d]	4.24	36	72.1	6.9[e]

a Hutter, 1984b [17], p. 78
b Hutter, 1983 [15], p. 1088
c Graf, 1983 [10], p. 64
d Bäuerle, 1984 [3]
e Computed using (19.21)

the other lakes. Moreover, the thermocline-elevation amplitude ζ_0 is smaller than D_1 in all three cases, a fact which gives some confidence in the scaling procedure.

19.3.4 Boundary Conditions

To solve (19.22) and (19.23) in some domain $\mathcal{D}$ for a given $\boldsymbol{\tau}$, we have to prescribe initial values for ψ and ζ and the boundary conditions on $\partial\mathcal{D}$. The first boundary condition which we impose is that the total mass flux normal to $\partial\mathcal{D}$ must vanish: in non-dimensional variables this can be written as $\hat{\boldsymbol{n}} \cdot (D_1\boldsymbol{u}_1 + D_2 h_2 \boldsymbol{u}_2) D^{-1} = 0$ on $\partial\mathcal{D}$, where $\hat{\boldsymbol{n}}$ is a unit vector perpendicular to $\partial\mathcal{D}$. On substituting for $\boldsymbol{u}_1$ and $\boldsymbol{u}_2$ from (19.25) and (19.26), this reduces to[8]

$$\hat{\boldsymbol{n}} \cdot (\hat{\boldsymbol{k}} \times \nabla\psi) = 0, \quad \text{on } \partial\mathcal{D}. \tag{19.29}$$

Since $\hat{\boldsymbol{n}} \cdot (\hat{\boldsymbol{k}} \times \nabla\psi) = (\hat{\boldsymbol{n}} \times \hat{\boldsymbol{k}}) \cdot \nabla\psi = \hat{\boldsymbol{s}} \cdot \nabla\psi$, where $\hat{\boldsymbol{s}}$ is a unit vector tangential to $\partial\mathcal{D}$, (19.29) implies $\partial\psi/\partial s = 0$ on $\partial\mathcal{D}$ and hence $\psi =$ constant on $\partial\mathcal{D}$. Thus, in a simply connected domain, without loss of generality, we take

$$\psi = 0, \quad \text{on } \partial\mathcal{D}. \tag{19.30}$$

Next we require $\hat{\boldsymbol{n}} \cdot \boldsymbol{u}_i = 0$ on $\partial\mathcal{D}$ for each layer i. Upon again using (19.25) and (19.26), together with (19.29), we find

$$\frac{\partial}{\partial n}\frac{\partial\zeta}{\partial t} - \frac{\partial\zeta}{\partial s} = -\frac{D_2}{D}(\hat{\boldsymbol{n}} \cdot \boldsymbol{\tau}_t - \hat{\boldsymbol{s}} \cdot \boldsymbol{\tau}) = -\hat{\boldsymbol{n}} \cdot \boldsymbol{\tau}_t + \hat{\boldsymbol{s}} \cdot \boldsymbol{\tau}, \quad \text{on } \partial\mathcal{D}, \tag{19.31}$$

to $O(D_1/D_2)$.

[8] These equations actually imply a statement regarding $\mathcal{L}'(D_1\boldsymbol{u}_1 + D_2 h_2 \boldsymbol{u}_2) \cdot \hat{\boldsymbol{n}}$ rather than the mass transport itself. However, if $\mathcal{L}g = 0$ along $\partial\mathcal{D}$ for all time, then necessarily $g = 0$ as well.

The boundary condition (19.29) applies, whether the simplifying assumptions $D_1 \ll D_2$ and $\omega^2 \ll f^2$ are imposed or not. Because (19.22) supposes D_1 to be small in comparison to D_2 we conclude that *the barotropic part of the motion can be determined without simultaneously also determining the baroclinic response*. However, if the corresponding barotropically driven baroclinic currents or thermocline elevations are to be determined, then (19.23) subject to the boundary condition (19.31) must also be solved. Since (19.23) is a forced wave equation, this by itself is a formidable problem. For *weak stratification* (S small) simplifications are possible. This is the case for most Swiss lakes (compare Table 19.3).

To introduce this additional simplification we note that our scales have been chosen such that dimensionless gradients are order unity. Hence, we expect ∇^2 to be $O(1)$ whereas S^{-1} is large. On the left-hand side of (19.23) we may thus ignore ∇^2 in comparison to $S^{-1}\mathcal{L}$, implying

$$\zeta_t = S\{\mathcal{L}^{-1}(\hat{\boldsymbol{k}} \times \nabla\psi) \cdot \nabla h^{-1} + (\nabla \times \boldsymbol{\tau}) \cdot \hat{\boldsymbol{k}}\}, \tag{19.32}$$

where $\mathcal{L}^{-1}$ is the inverse operator of $\mathcal{L}$. Equation (19.32) can be described as the *geometric optics approximation for* ζ. Along the shore $\partial\mathcal{D}$ we may assume a constant depth; then ∇h^{-1} is parallel to $\hat{\boldsymbol{n}}$, the unit normal vector along $\partial\mathcal{D}$, and the first term in the curly bracket vanishes.[9] With nonvanishing wind stress the emerging equation is not consistent with (19.31). For the *unforced* problem, however, (19.32) implies

$$\zeta(\boldsymbol{x}, t) = 0, \quad \text{along } \partial\mathcal{D},$$

which is consistent with (19.31) provided that the term $\partial^2\zeta/\partial n\partial t$ is ignored. This omission is justified in the low-frequency approximation.

We conclude: the geometric optics approximation is only consistent in the low-frequency limit. In all other cases, the baroclinic coupling should be computed with the full equations (19.22), (19.23) and (19.31).

19.4 Continuous Stratification

19.4.1 Modal Equations

The two-layer model can only nearly approximate the internal dynamics of a lake that permits a clear distinction of an epi- and a hypolimnion. It is important to investigate to which extent inferences from the pure barotropic or two-layer model of Sect. 19.3 can be carried over to a lake with continuous stratification. The oceanographic literature is rich in studies of low-frequency processes in a stratified medium. A general result, common to all studies, is that increasing the stratifica-

[9] Recall that $(\hat{\boldsymbol{k}} \times \nabla\psi) \cdot \nabla h^{-1} = 0$ for all times implies that $\mathcal{L}^{-1}\{(\hat{\boldsymbol{k}} \times \nabla\psi) \cdot \nabla h^{-1}\} = 0$.

tion increases the frequencies of the considered long-period motion. This has been shown by Wang and Mooers [48], Clarke [6] and Huthnance [14]. A review can be found in Mysak [29].

Here, in this section, our aim is to analyze, how and how strongly the individual baroclinic modes are coupled among each other and how the baroclinic part of the motion couples with the barotropic processes.

These equations are given below as (19.43) and (19.44). To derive them, we start from the continuity equation

$$\nabla \cdot \boldsymbol{v} = \nabla_H \cdot \boldsymbol{v}_H + \frac{\partial w}{\partial z} = 0 \tag{19.33}$$

and integrate it over depth to obtain

$$\begin{aligned} 0 &= \int_{-H}^{\zeta} \left(\nabla_H \cdot \boldsymbol{v}_H + \frac{\partial w}{\partial z} \right) \mathrm{d}z \\ &\overset{\text{Leibniz}}{=} \nabla_H \cdot \underbrace{\int_{-H}^{\zeta} \boldsymbol{v}_H \, \mathrm{d}z}_{:=\boldsymbol{V}} - \underbrace{[\boldsymbol{v}_H \cdot \nabla\zeta - w]_{z=\zeta}}_{=-\partial\zeta/\partial t} - \underbrace{[\boldsymbol{v}_H \cdot \nabla_H H + w]_{z=-H}}_{=0} \\ &= \frac{\partial \zeta}{\partial t} + \nabla_H \cdot \boldsymbol{V} = 0, \end{aligned}$$

which agrees with $(19.43)_1$ below. In the above, the bracketed terms are so identified because of the kinematic boundary conditions at the free and the basal surfaces. In a similar fashion, the horizontal components of the momentum equations are treated. To this end, we write the stress tensor as

$$\boldsymbol{t} = -p(z)\boldsymbol{I} + \boldsymbol{t}_{\mathrm{dyn}}, \tag{19.34}$$

in which $p(z)$ is the hydrostatic pressure, given by

$$p(z) = \underbrace{p_{\mathrm{atm}} + \rho_* g(\zeta - z)}_{p_e} + \underbrace{\rho_* g \int_z^{\zeta} \sigma(z') \, \mathrm{d}z'}_{p_i} \tag{19.35}$$

and p_e and p_i are the *external* and *internal* pressures, respectively. $\boldsymbol{t}_{\mathrm{dyn}}$ is the dynamic stress contribution, mostly due to turbulence; it will be decomposed as

$$\boldsymbol{t}_{\mathrm{dyn}} = \begin{pmatrix} -\rho_* \boldsymbol{\Gamma} & -\rho_* \boldsymbol{\gamma} \\ t_{13}\, t_{23} & t_{33} \end{pmatrix}, \quad \boldsymbol{\Gamma} = \begin{pmatrix} \Gamma_{11} & \Gamma_{12} \\ \Gamma_{21} & \Gamma_{22} \end{pmatrix}, \quad \boldsymbol{\gamma} = \begin{pmatrix} \gamma_{31} \\ \gamma_{32} \end{pmatrix}. \tag{19.36}$$

With (19.35) and (19.36), the horizontal momentum equation takes the form

$$\frac{\mathrm{d}\boldsymbol{v}_H}{\mathrm{d}t} + f\hat{\boldsymbol{k}} \times \boldsymbol{v}_H + \frac{1}{\rho_*}\nabla_H(p_e + p_i) + \nabla_H \cdot \boldsymbol{\Gamma} + \frac{\partial \boldsymbol{\gamma}}{\partial z} = \boldsymbol{0}, \tag{19.37}$$

in which

$$\begin{aligned}\frac{\mathrm{d}\boldsymbol{v}_H}{\mathrm{d}t} &= \frac{\partial \boldsymbol{v}_H}{\partial t} + (\nabla_H \boldsymbol{v}_H)\,\boldsymbol{v}_H + \frac{\partial \boldsymbol{v}_H}{\partial z} w + \underbrace{\left(\boldsymbol{v}_H \nabla_H \cdot \boldsymbol{v}_H + \boldsymbol{v}_H \frac{\partial w}{\partial z}\right)}_{=\boldsymbol{0}} \\ &= \frac{\partial \boldsymbol{v}_H}{\partial t} + \nabla_H \cdot (\boldsymbol{v}_H \otimes \boldsymbol{v}_H) + \frac{\partial}{\partial z}(\boldsymbol{v}_H w)\,. \end{aligned} \tag{19.38}$$

Substituting (19.38) in (19.37), rearranging the emerging equation and integrating this equation from $z = -H$ to $z = \zeta$ yields

$$\begin{aligned}\boldsymbol{0} &= \int_{-H}^{\zeta} \left\{ \frac{\partial \boldsymbol{v}_H}{\partial t} + f\hat{\boldsymbol{k}} \times \boldsymbol{v}_H + \frac{1}{\rho_*}\nabla_H(p_e + p_i) \right. \\ &\quad \left. + \nabla_H \cdot (\boldsymbol{v}_H \otimes \boldsymbol{v}_H + \boldsymbol{\Gamma}) + \frac{\partial}{\partial z}(\boldsymbol{v}_H w + \boldsymbol{\gamma}) \right\} \mathrm{d}z \\ &= \frac{\partial \boldsymbol{V}}{\partial t} + f\hat{\boldsymbol{k}} \times \boldsymbol{V} + \frac{\zeta + H}{\rho_*}\nabla_H p_e + \frac{1}{\rho_*}\int_{-H}^{\zeta} \nabla p_i \,\mathrm{d}z \\ &\quad + \nabla_H \cdot \int_{-H}^{\zeta} (\boldsymbol{v}_H \otimes \boldsymbol{v}_H + \boldsymbol{\Gamma})\,\mathrm{d}z + [\boldsymbol{\gamma} - \boldsymbol{\Gamma}\nabla\zeta]_{z=\zeta} - [\boldsymbol{\gamma} + \boldsymbol{\Gamma}\nabla H]_{z=-H} \\ &\quad - \boldsymbol{v}_H(\zeta) \underbrace{\left[\frac{\partial \zeta}{\partial t} + \boldsymbol{v}_H \cdot \nabla\zeta - w\right]_{z=\zeta}}_{=\boldsymbol{0}} - \boldsymbol{v}_H(-H) \underbrace{[\boldsymbol{v}_H \cdot \nabla H + w]_{z=-H}}_{=\boldsymbol{0}}. \end{aligned} \tag{19.39}$$

Here, the step from the first line to the remaining lines involved application of Leibniz' rule when interchanging the order of differentiation and integration. Moreover, the bracketed terms in the last line vanish in view of the kinematic boundary conditions on the free surface and the base. On the other hand, with

$$\boldsymbol{n} = \frac{(-\nabla\zeta, 1)}{\sqrt{1 + ||\nabla\zeta||^2}}, \quad \boldsymbol{t}_{\mathrm{dyn}}\boldsymbol{n} = \begin{pmatrix} -\rho_*\boldsymbol{\Gamma} & -\rho_*\boldsymbol{\gamma} \\ t_{13}\, t_{23} & t_{33} \end{pmatrix}, \begin{pmatrix} -(\nabla\zeta)^{\mathrm{T}} \\ 1 \end{pmatrix}$$

we may write at $z = \zeta(x, y, t)$

$$\frac{1}{\rho_*}\left(\boldsymbol{t}_{\mathrm{dyn}}\boldsymbol{n}\right)_H = \frac{\boldsymbol{\Gamma}\nabla\zeta - \boldsymbol{\gamma}}{\sqrt{1 + ||\nabla\zeta||^2}} = \frac{1}{\rho_*}\left(\boldsymbol{t}_{\mathrm{atm}}\boldsymbol{n}\right)_H = \frac{1}{\rho_*}\frac{\boldsymbol{\tau}_{\mathrm{wind}}}{\sqrt{1 + ||\nabla\zeta||^2}}$$

or

$$\frac{1}{\rho_*}\boldsymbol{\tau}_{\mathrm{wind}} = \boldsymbol{\Gamma}\nabla\zeta - \boldsymbol{\gamma}. \tag{19.40}$$

Analogously for the stress boundary condition at the basal surface,

$$-\frac{1}{\rho_*}\boldsymbol{\tau}_{\text{bottom}} = \boldsymbol{\Gamma}\nabla H + \boldsymbol{\gamma}. \tag{19.41}$$

If we now substitute (19.40) and (19.41) into (19.39), the bracketed terms in the second last line of (19.39) can be replaced by

$$\frac{1}{\rho*}\left(\boldsymbol{\tau}_{\text{bottom}} - \boldsymbol{\tau}_{\text{wind}}\right). \tag{19.42}$$

In summary, we therefore obtain from (19.34) and (19.39)–(19.41):

$$\frac{\partial\zeta}{\partial t} + \nabla\cdot\boldsymbol{V} = 0, \qquad \frac{\partial\boldsymbol{V}}{\partial t} + f\hat{\boldsymbol{k}}\times\boldsymbol{V} = -\frac{H+\zeta}{\rho*}\nabla p_e + \boldsymbol{F}, \tag{19.43}$$

in which ζ is the surface elevation, $\boldsymbol{V}$ the transport, $\hat{\boldsymbol{k}}$ a unit vector pointing upwards, ρ^* a constant reference density and

$$\begin{aligned} p_e &= p_{\text{atm}} + \rho^* g(\zeta - z),\\ \boldsymbol{F} &= -\frac{1}{\rho^*}\int_{-H}^{\zeta}\nabla p_i\,\mathrm{d}z - \nabla\cdot\int_{-H}^{\zeta}(\boldsymbol{v}\otimes\boldsymbol{v} + \boldsymbol{\Gamma})\,\mathrm{d}z + \frac{\boldsymbol{\tau}_{\text{wind}} - \boldsymbol{\tau}_{\text{bottom}}}{\rho^*},\\ p_i &= \rho^* g\int_z^{\zeta}\sigma(z')\mathrm{d}z' + p', \quad \sigma \equiv \frac{\rho_0 - \rho^*}{\rho^*}. \end{aligned} \tag{19.44}$$

This derivation follows Hutter [16], p. 18–21. Here, p_e is the external and p_i the internal pressure. The latter consists of the dynamic baroclinic pressure p' and the quasistatic baroclinic pressure due to the density anomaly $\sigma(z)$, which is referred to a reference profile of density $\rho_0(z)$ of a *stably stratified state* at rest. The hydrostatic pressure assumption has not been made in (19.44); this is important. The force $\boldsymbol{F}$ consists of a contribution of the baroclinic pressure p_i, a term involving advection ($\boldsymbol{v}\otimes\boldsymbol{v}$) and turbulent diffusion ($\boldsymbol{\Gamma}$), the wind stress and the bottom shear stress. In ensuing developments we ignore turbulent diffusion ($\boldsymbol{\Gamma} \simeq \boldsymbol{0}$) and advection ($\boldsymbol{v}\otimes\boldsymbol{v} \simeq \boldsymbol{0}$), omit bottom shear ($\boldsymbol{\tau}_{\text{bottom}} \simeq \boldsymbol{0}$) and spatial variations of the atmospheric pressure ($\nabla p_{\text{atm}} \simeq \boldsymbol{0}$) and neglect non-linear terms such as $\zeta\nabla\zeta$. If we also invoke the rigid-lid assumption and thus eliminate surface gravity waves, (19.43) and (19.44) reduce to

$$\begin{aligned} &\nabla\cdot(H\bar{\boldsymbol{v}}) = 0,\\ &\frac{\partial\bar{\boldsymbol{v}}}{\partial t} + f\hat{\boldsymbol{k}}\times\bar{\boldsymbol{v}} = -g\nabla\zeta - \frac{1}{\rho * H}\int_{-H}^{0}\nabla p'\,\mathrm{d}z + \frac{\boldsymbol{\tau}}{\rho^* H}, \end{aligned} \tag{19.45}$$

where $H\bar{\boldsymbol{v}} = \boldsymbol{V}$ has been introduced and where $\boldsymbol{\tau} = \boldsymbol{\tau}_{\text{wind}}$. In the next step we introduce the mass transport stream function ψ by setting

$$H\bar{u} = -\psi_y, \quad H\bar{v} = \psi_x \tag{19.46}$$

and eliminate $\nabla\zeta$ from $(19.45)_2$ by taking the curl of this equation. This transforms (19.45) to the single equation

$$\begin{aligned}\nabla\cdot\left(\frac{1}{H}\nabla\psi_t\right) + \mathcal{J}\left(\psi, \frac{f}{H}\right)\\ = -\frac{\partial}{\partial x}\left[\frac{1}{\rho^* H}\int_{-H}^{0}\frac{\partial p'}{\partial y}\,\mathrm{d}z\right] + \frac{\partial}{\partial y}\left[\frac{1}{\rho^* H}\int_{-H}^{0}\frac{\partial p'}{\partial x}\,\mathrm{d}z\right] + \nabla\times\left(\frac{\boldsymbol{\tau}}{\rho^* H}\right).\end{aligned} \tag{19.47}$$

This equation is analogous to (19.8). Notice that it involves no term due to the stratification of the state defined by $\rho_0(z)$. Baroclinic effects are all contained in the dynamic pressure p', but the terms involving p' may also describe deviations from the hydrostatic pressure distribution. We shall interpret p' as being due to baroclinic effects. Thus, in the absence of stratification and without wind forcing, (19.47) reduces to the conservation law of potential vorticity. Stratification and external winds (the terms of the right-hand side of (19.47)) act as supplies of potential vorticity. Thus, the first term on the right-hand side couples the barotropic part of (19.47) to the baroclinic processes. Our experience with the two-layer model suggests that this baroclinic coupling is small and can be ignored to lowest order. If this is correct, the barotropic motion can be fully determined from equations (19.45)–(19.47) by simply omitting the p'-dependent terms.

To complete the formulation we still need a system of equations that describes the baroclinic processes and is coupled to the barotropic motion. To deduce it let us consider the Boussinesq approximated adiabatic equations of motion (see e.g. Chap. 4, (4.235)–(4.237) in Volume I)

$$\begin{aligned} u_t - fv &= -\frac{1}{\rho^*}p'_x, & \rho'_t + \frac{\mathrm{d}\rho_0}{\mathrm{d}z}w &= 0,\\ v_t + fu &= -\frac{1}{\rho^*}p'_y, & w_t + \frac{g}{\rho^*}\rho' + \frac{1}{\rho^*}p'_z &= 0,\\ u_x + v_y + w_z &= 0, \end{aligned} \tag{19.48}$$

in which subscripts denote differentiation with respect to the subscripted variable. The first two of these are the horizontal momentum equations, the third expresses continuity, the fourth derives from the adiabatic heat equation, $\mathrm{d}T(\rho)/\mathrm{d}t = 0$. Finally, the last equation is the vertical momentum equation; if w_t were ignored, the hydrostatic pressure assumption would result from it.

The two equation sets, (19.47), describing the transport, and (19.48), representing the vertical details, suggest to split the velocity field into two parts,

$$(u, v) = (\bar{u}, \bar{v}) + (\tilde{u}, \tilde{v}), \tag{19.49}$$

such that the total transport of (u, v) is incorporated in the barotropic field and hence

$$\int_{-H}^{0} \tilde{u}\,\mathrm{d}z = \int_{-H}^{0} \tilde{v}\,\mathrm{d}z = 0. \tag{19.50}$$

Substitution of (19.49) in (19.48) and use of (19.45) yields the new set of equations

$$\begin{aligned}
&\tilde{u}_t - f\tilde{v} + \frac{1}{\rho^*}p'_x - \frac{1}{\rho^* H}\int_{-H}^{0} p'_x\,\mathrm{d}z = g\zeta_x - \frac{\tau_1}{\rho^* H},\\
&\tilde{v}_t + f\tilde{u} + \frac{1}{\rho^*}p'_y - \frac{1}{\rho^* H}\int_{-H}^{0} p'_y\,\mathrm{d}z = g\zeta_y - \frac{\tau_2}{\rho^* H},\\
&\tilde{u}_x + \tilde{v}_y + w_z = \frac{H_x}{H}\bar{u} + \frac{H_y}{H}\bar{v},\\
&\rho'_t + \frac{\mathrm{d}\rho_0}{\mathrm{d}z}w = 0,\\
&w_t + \frac{\rho'}{\rho^*}g + \frac{1}{\rho^*}p'_z = 0,
\end{aligned} \tag{19.51}$$

in which τ_1 and τ_2 are the x- and y-components of the wind stress. These have been written, so that the external wind forcing and the barotropic contributions of the motion appear on the right hand sides of the equations.

19.4.2 Spectral Decomposition of the Baroclinic Fields

We shall now demonstrate how (19.51) can be reduced to a set of spatially two-dimensional equations by using a vertical shape function expansion of the velocity, pressure and density fields. To this end, let us now introduce the following expansions of the baroclinic fields:

$$\begin{aligned}
\tilde{u}(x, y, z, t) &= \sum_{n=1}^{N} U_n(x, y, t)\phi_n\left(\frac{z}{H}\right),\\
\tilde{v}(x, y, z, t) &= \sum_{n=1}^{N} V_n(x, y, t)\phi_n\left(\frac{z}{H}\right),\\
w(x, y, z, t) &= \sum_{n=1}^{N} W_n(x, y, t)\Xi_n\left(\frac{z}{H}\right),\\
p'(x, y, z, t) &= \sum_{n=1}^{N} P_n(x, y, t)\psi_n\left(\frac{z}{H}\right),\\
\rho'(x, y, z, t) &= \sum_{n=1}^{N} R_n(x, y, t)\chi_n\left(\frac{z}{H}\right).
\end{aligned} \tag{19.52}$$

Here, $\{\phi_n, \Xi_n, \psi_n, \chi_n\}, n = 1, 2, 3, \ldots, N$ are treated as known and their determination will be explained below. To find the evolution equations for U_n, V_n, W_n, P_n and R_n the *Principle of Weighted Residuals* is used.[10] It essentially amounts to evaluating the integrals

$$\int_{-H}^{0} \delta\phi_m^M (19.51)_{1,2} \mathrm{d}z, \quad \int \delta\phi_m^C (19.51)_3 \mathrm{d}z, \quad \int \delta\phi_m^V (19.51)_{4,5} \mathrm{d}z,$$

for arbitrary weighting functions $\delta\phi_m^L$ $(L = M, C, V)$. Inserting (19.52) into these expressions, (19.51) can be reduced to the following spatially two-dimensional system of differential equations for the coefficient functions U_n, V_n, W_n, P_n and R_n (for details of the derivation see the Appendix at the end of this chapter).

$$\begin{aligned}
&A_{mn}^M \left(\frac{\partial U_n}{\partial t} - f V_n \right) - \frac{1}{\rho^*} \frac{\partial H/\partial x}{H} B_{mn} P_n + \frac{C_{mn}}{\rho^*} \frac{\partial P_n}{\partial x} = \left(g \frac{\partial \zeta}{\partial x} - \frac{\tau_1}{\rho^* H} \right) D_m^M, \\
&A_{mn}^M \left(\frac{\partial V_n}{\partial t} + f U_n \right) - \frac{1}{\rho^*} \frac{\partial H/\partial y}{H} B_{mn} P_n + \frac{C_{mn}}{\rho^*} \frac{\partial P_n}{\partial y} = \left(g \frac{\partial \zeta}{\partial y} - \frac{\tau_2}{\rho^* H} \right) D_m^M, \\
&A_{mn}^C \left(\frac{\partial U_n}{\partial x} + \frac{\partial V_n}{\partial y} \right) - K_{mn} \left(\frac{\partial H/\partial x}{H} U_n + \frac{\partial H/\partial y}{H} V_n \right) - L_{mn} \frac{W_n}{H} \\
&\quad = \left(\bar{u} \frac{\partial H/\partial x}{H} + \bar{v} \frac{\partial H/\partial y}{H} \right) (D_m^C - \delta\phi_m^C(\xi = 0)), \\
&E_{mn} \frac{\partial R_n}{\partial t} - \frac{\rho^* N_{\max}^2}{g} F_{mn} W_n = 0, \\
&G_{mn} \frac{\partial W_n}{\partial t} + \frac{g}{\rho^*} E_{mn} R_n + \frac{1}{\rho^* H} H_{mn} P_n = 0, \\
&\text{Summation over } n, \quad (m, n = 1, 2, 3, \ldots, N).
\end{aligned} \tag{19.55}$$

The last two of these equations can also be replaced by the second order (in time) equation

[10] We assume the reader to be familiar with the method of the *Principle of Weighted Residuals*, see e.g. Finlayson [8]. The principle or method of weighted residuals (MWR) is based on the following mathematical equivalence: Let $f(\boldsymbol{x})$ be a function or functional whose value vanishes for all $\boldsymbol{x} \in \mathcal{D} \subset \mathbb{R}^N$:

$$f(\boldsymbol{x}) = 0 \quad \text{for all } \boldsymbol{x} \in \mathcal{D} \subset \mathbb{R}^N. \tag{19.53}$$

Let, moreover, $\delta\phi_\alpha(\boldsymbol{x})$ be an arbitrary bounded function from a set $\{\delta\phi_\alpha, \alpha = 1, 2, \ldots\}$. Obviously, (19.53) implies

$$\int_{\mathcal{D}} \delta\phi_\alpha(\boldsymbol{x}) f(\boldsymbol{x}) \mathrm{d}\boldsymbol{x} = 0 \qquad (\alpha = 1, 2, \ldots). \tag{19.54}$$

If (19.54) holds for any complete set of $\delta\phi_\alpha$, then (19.54) also implies (19.53). This equivalence statement lies at the heart of the MWR.

$$G_{mn}\frac{\partial^2 W_n}{\partial t^2} + N_{\max}^2 F_{mn} W_n + \frac{H_{mn}}{\rho^* H}\frac{\partial P_n}{\partial t} = 0, \qquad (19.56)$$
$$\text{Summation over } n, \quad (m, n = 1, 2, 3, \ldots, N).$$

The various coefficient matrices are collected in Table 19.4. For (19.56) to hold true, E_{mn} must be invertible, which according to Table 19.4 is the case. The matrices $A^{\boldsymbol{M}}_{mn}$, etc., are all expressible in terms of the inner product

$$\langle f(\xi),\ g(\xi)\rangle = \int_0^1 f(\xi) g(\xi) \mathrm{d}\xi.$$

Furthermore, $\hat{N}^2$ in Table 19.4 is the normalized Brunt–Väisälä frequency

$$\hat{N}^2 = \frac{N^2(\xi; H)}{N_{\max}^2} = -\frac{\mathrm{d}\rho_0/\mathrm{d}z(\xi, H)}{|\ \mathrm{d}\rho_0/\mathrm{d}z\ |_{\max}}, \qquad \xi = \frac{z}{H} + 1.$$

Table 19.4 Matrix elements for the expansion of the field variables in terms of the flat-bottom buoyancy modes or Jacobi polynomials. $\langle a, b\rangle$ is the inner product $\int_0^1 ab\mathrm{d}\xi$, λ_n is the eigenvalue defined in (19.58)

Elmt	Definition	Buoyancy mode set	Jacobi polynomial set
A^L_{mn}	$\langle \delta\phi^L_m,\ \phi_n\rangle, L \in \{M, C\}$	$\lambda_n \delta_{mn}$	δ_{mn}
B_{mn}	$\langle \delta\phi^M_m,\ (\xi-1)\frac{\mathrm{d}\Phi_n}{\mathrm{d}\xi}\rangle -$ $\langle 1, (\xi-1)\frac{\mathrm{d}\psi_n}{\mathrm{d}\xi}\rangle\langle 1, \delta\phi^M_m\rangle$	$\langle \frac{\mathrm{d}\Xi_m}{\mathrm{d}\xi},\ (\xi-1)\frac{\mathrm{d}^2\Xi_m}{\mathrm{d}\xi^2}\rangle$	$0\ (n \le m),\ \ b_{n-1,m}\ (n > m)$
C_{mn}	$\langle \delta\phi^M_m, \psi_n\rangle - \langle 1, \psi_n\rangle\langle 1, \delta\phi^M_m\rangle$	$\lambda_n \delta_{mn}$	$\delta_{m,n-1}$
D^L_m	$\langle 1, \delta\phi^L_m\rangle$	0	0
E_{mn}	$\langle \delta\phi^V_m, \chi_n\rangle$	δ_{mn}	δ_{mn}
F_{mn}	$\langle \delta\phi^V_m, \hat{N}^2 \Xi_n\rangle$	δ_{mn}	$\langle G_{m-1}, \hat{N}^2 G_{n-1}\rangle$ $(= \hat{N}_0^2 \delta_{mn}$,cont. strat.)
G_{mn}	$\langle \delta\phi^V_m, \Xi_n\rangle$	$\langle \Xi_m, \Xi_n\rangle$	δ_{mn}
H_{mn}	$\langle \delta\phi^V_m, \frac{\mathrm{d}\psi_n}{\mathrm{d}\xi}\rangle$	$\lambda_n \delta_{mn}$	$0\ (n \le m),\ h_{n-2,m-1}\ (n > m)$
K_{mn}	$\langle (\xi-1)\frac{\mathrm{d}\phi_n}{\mathrm{d}\xi}, \delta\phi^C_m\rangle$ $-\delta\phi^C_m(0)\phi_n(0)$	$B_{mn} - \frac{\mathrm{d}\Xi_m}{\mathrm{d}\xi}\frac{\mathrm{d}\Xi_n}{\mathrm{d}\xi}\big\vert_0$	$0\ (n < m),\ b_{mn}(n \ge m)\} -$ $(-1)^{n+m} \cdot \sqrt{(2n+1)(2m+1)}$
L_{mn}	$\langle \frac{\mathrm{d}\delta\phi^C_m}{\mathrm{d}\xi}, \Xi_n\rangle$	$\lambda_n \delta_{mn}$	$h_{m-1,n-1}\ (n \le m),\ 0\ (n > m)$
M_m	$\langle 1, \psi_m\rangle$	0	δ_{1m}
N_m	$\langle 1, \psi_m\rangle - \psi_m(0)$	$-\frac{\mathrm{d}\Xi_m}{\mathrm{d}\xi}\big\vert_{\xi=0}$	$\delta_{1m} + (-1)^m\sqrt{2m-1}$

The first two of (19.55) derive from the horizontal momentum equations $(19.51)_{1,2}$, the third corresponds to the continuity equation $(19.51)_3$ and the fourth and fifth are obtained from the adiabaticity statement $(19.51)_4$ and the vertical momentum balance $(19.51)_5$. It is also evident that (19.55) constitute 5N equations for the 5N unknowns $\{U_n, V_n, W_n, P_n, R_n\}$, provided the barotropic quantities $\zeta, \bar{u}, \bar{v}$ are known. If they are not, (19.55) must be complemented by (19.45) which, with the use of (19.52), take on the form

$$\begin{aligned}
&\frac{\partial(H\bar{u})}{\partial x} + \frac{\partial(H\bar{v})}{\partial y} = 0,\\
&\frac{\partial \bar{u}}{\partial t} - f\bar{v} + g\frac{\partial \zeta}{\partial x} = -\frac{1}{\rho^*}\left(M_m \frac{\partial P_m}{\partial x} + N_m \frac{\partial H/\partial x}{H} P_m + \frac{\tau_1}{H}\right),\\
&\frac{\partial \bar{v}}{\partial t} + f\bar{u} + g\frac{\partial \zeta}{\partial y} = -\frac{1}{\rho^*}\left(M_m \frac{\partial P_m}{\partial y} + N_m \frac{\partial H/\partial y}{H} P_m + \frac{\tau_2}{H}\right).
\end{aligned} \tag{19.57}$$

The vectors $M_m, N_m (m = 1, 2, 3, \ldots, N)$ are also defined in Table 19.4.

It is our contention that, by accordingly selecting the shape functions, the barotropic modes and the baroclinic modes can almost completely be separated. This orthogonalization is exactly possible in stratified basins with constant depth; selecting the shape functions from this set will nearly achieve the uncoupling in the case of a variable bottom. Towards a motivation, consider (19.48) and ignore the vertical acceleration terms, i.e. restrict considerations to quasi-static pressure conditions. For this case (19.48) may be reduced to the single partial differential equation for w

$$N^2 \nabla^2 w + \left(\frac{\partial^2}{\partial t^2} + f^2\right)\frac{\partial^2 w}{\partial z^2} = 0.$$

Subject to the boundary conditions

$$w = 0, \quad \text{at } z = 0, -H,$$

we know that this equation permits separation of variable solutions $w(x, y, z, t) = W_n(x, y, t) Z_n(z)$, where $Z_n(z)$ satisfies the eigenvalue problem

$$\begin{aligned}
&Z_n''(z) + \frac{N^2(z)}{gH_n} Z_n(z) = 0, \quad -H < z < 0,\\
&Z_n = 0, \qquad\qquad\qquad\qquad z = -H, 0,
\end{aligned}$$

with the eigenvalue gH_n. Introducing the transformation $z = H(\xi - 1)$ this becomes

$$\begin{aligned}
&\frac{\mathrm{d}^2 Z_n(z)}{\mathrm{d}\xi^2} + \lambda_n \hat{N}^2(\xi; H) Z_n(\xi) = 0, \quad 0 < \xi < 1,\\
&Z_n(\xi) = 0, \qquad\qquad\qquad\qquad \xi = 0, 1,\\
&\lambda_n = \frac{N_{\max}^2 H^2}{gH_n},
\end{aligned} \tag{19.58}$$

where λ_n is the eigenvalue. This is the classical eigenvalue problem of internal waves in a basin of constant depth. It is selfadjoint, and so λ_n is real and positive for all $n = 1, 2, \ldots$; furthermore, the eigenfunctions form a complete set and can be normalized to satisfy the orthogonality relations

$$\langle \hat{N}^2(\xi; H) Z_m(\xi), \quad Z_n(\xi) \rangle = \delta_{mn}. \tag{19.59}$$

We conjecture that by selecting shape functions and weighting functions from this set or from derivatives of them we will achieve a weak coupling of the essentially barotropic-TW motion with the internal wave motion. The arguments are:

1. If we choose $\Xi_m = Z_m$ the vertical velocity profiles are those of the internal wave motion of a fluid with constant depth (Fig. 19.13). Actual boundary conditions at the bottom are not satisfied by these functions. This will result in a coupling of the different internal modes.
2. If we further select $\phi_m = \mathrm{d}\Xi_m/\mathrm{d}\xi$ we will exactly match the vertical distribution of the horizontal velocity profiles for internal waves in a basin with constant depth. To be consistent with (19.50) the function set $\{\phi_m\}$ must be orthogonal to the constant function. One can easily verify that

$$\langle 1, \phi_m \rangle = \langle 1, \frac{\mathrm{d}\Xi_m}{\mathrm{d}\xi} \rangle = \int_0^1 \frac{\mathrm{d}Z_m}{\mathrm{d}\xi}\, \mathrm{d}\xi = Z_m(1) - Z_m(0) = 0,$$

by virtue of the boundary condition in $(19.58)_2$.

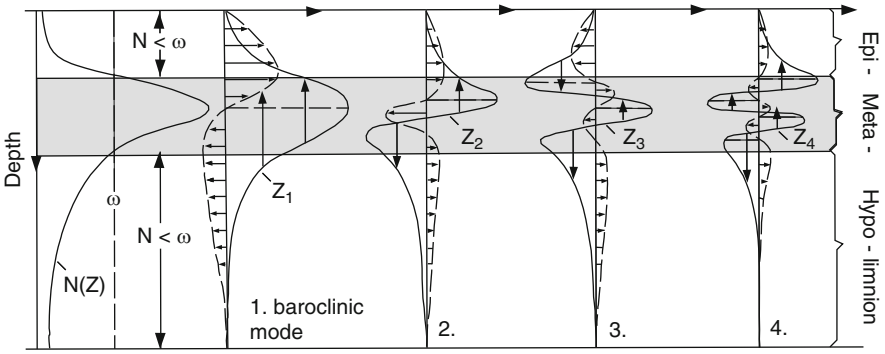

Fig. 19.13 Typical vertical distribution of the Brunt–Väisälä frequency N (*left*) and the four lowest baroclinic modes (qualitative). *Solid curves* show the distribution of the vertical velocity component, *dashed curves* indicate the distribution of the longitudinal velocity component (when $f = 0$), Most energy is usually concentrated in the first baroclinic mode, the exact distribution must, however, be determined by continuous profiles of horizontal velocities (from [16]).

3. The momentum equations $(19.48)_{1,2,5}$, the continuity equation $(19.48)_3$ and the adiabaticity equation $(19.48)_4$ now suggest that we should choose

$$\{\psi_m\} = \{\phi_m\} = \{\mathrm{d}\Xi_m/\mathrm{d}\xi\} \text{ and } \{\chi_m\} = \{\hat{N}^2\Xi_m\}.$$

4. We weigh the horizontal momentum equations with the same weighting function as the shape functions of the horizontal velocity. Similarly, the shape functions and the weighting functions in the continuity equation should be chosen from the same function set. This yields

$$\{\delta\phi_m^M\} = \{\delta\phi_m^C\} = \{\frac{\mathrm{d}\Xi_m}{\mathrm{d}\xi}\}.$$

Finally, the adiabatic equation and the vertical momentum equation then suggest that

$$\{\delta\phi_m^V\} = \{\Xi_m\}$$

With these choices the matrix elements can readily be calculated; they are listed in column 3 of Table 19.4. This table also gives the elements for an alternative selection of basis functions. Leading idea in postulating (19.59) was to incorporate into the function set as much as possible of the particular physics under consideration. Consequently, the complete function set was that of the eigenfunctions for buoyancy waves in a stratified basin of constant depth. From a computational point of view this approach implies that the eigenvalue problem (19.58) must be solved in advance in order to obtain the required basis functions Ξ_n. Alternatively, we could expand the functions $\tilde{u}, \tilde{v}, w, p$ and ρ in terms of special *orthogonal polynomials*. Indeed, the scalar product $\langle\theta, \psi\rangle = \int_0^1 \theta\psi\mathrm{d}\xi$ suggests the use of Jacobi polynomials $G_n(1, 1, \xi)$ (see [1]), which are orthonormal in the interval [0, 1] with respect to the weighting function 1 in the scalar product. They are defined by

$$\begin{aligned}
G_n(1,1,\xi) &= \frac{\sqrt{2n+1}}{n!}\sum_{k=0}^{n}(-1)^{n-k}\binom{n}{k}\frac{(n+k)!}{k!}\xi^k,\\
G_0 &= 1,\\
G_1 &= \sqrt{12}\left(\xi - \frac{1}{2}\right),\\
G_2 &= \sqrt{180}\left(\xi^2 - \xi + \frac{1}{6}\right), \ \ldots
\end{aligned}$$

and satisfy the orthogonality relations

$$\int_0^1 G_n G_m \mathrm{d}\xi = \langle G_n, G_m\rangle = \delta_{mn}.$$

Note that the constant function G_0 is the first basis function and all G_n for $n > 0$ are orthogonal to it, i.e. they span a vanishing vertical area. This is well in accord with condition (19.50). The derivative of G_{n+1} is a polynomial of degree n and can be expressed as a linear combination of $G_k, k = 1, 2, \ldots, n$. For later use we define

$$(\xi - 1)\frac{\mathrm{d}G_n}{\mathrm{d}\xi} \equiv \sum_{k=0}^{n} b_{nk} G_k,$$
$$\frac{\mathrm{d}G_{n+1}}{\mathrm{d}\xi} \equiv \sum_{k=0}^{n} h_{nk} G_k.$$

The advantage of this polynomial set is its easy accessibility that frees us from solving a problem oriented eigenvalue problem. Its likely disadvantage is a slower convergence in comparison to the 'physical set' of internal eigenfunctions

We now select

$$\left.\begin{aligned} \{\phi_m\} &= \{G_m\}, \\ \{\Xi_m\} = \{\psi_m\} = \{\chi_m\} &= \{G_{m-1}\}, \end{aligned}\right\} \quad m = 1, \ldots, N$$

and the weighting functions

$$\left.\begin{aligned} \{\delta\phi_m^M\} = \{\delta\phi_m^C\} &= \{G_m\}, \\ \{\delta\phi_m^V\} &= \{G_{m-1}\}, \end{aligned}\right\} \quad m = 1, \ldots, N.$$

The corresponding matrix elements are listed in column 4 of Table 19.4. We now see the distinct properties of the two alternative approaches: When non-hydrostatic terms are ignored an expansion in terms of buoyancy modes uncouples the individual baroclinic modes in (19.56). The barotropic–baroclinic coupling arises in the horizontal momentum equation $(19.55)_{1,2,3}$ and $(19.57)_{2,3}$ only in conjunction with topographic gradients. For a flat bottom all barotropic and baroclinic modes are uncoupled. On the other hand, the Jacobi set, even though it is more easily accessible, does not follow the physics so closely. Notice also that the buoyancy equations (involving E_{mn} and F_{mn}) are strongly coupled in this case whereas the coupling due to topography gradients in the horizontal momentum equations (involving B_{mn}) is weaker.

Summarizing the governing equations, we obtain *for an expansion in buoyancy modes*

$$\frac{\partial(H\bar{u})}{\partial x} + \frac{\partial(H\bar{v})}{\partial y} = 0,$$
$$\frac{\partial \bar{u}}{\partial t} - f\bar{v} + g\frac{\partial \zeta}{\partial x} = \underline{-\frac{1}{\rho^*}\frac{\mathrm{d}\Xi}{\mathrm{d}\xi}(0)\frac{\partial H/\partial x}{H}P_m} + \frac{\tau_1}{\rho^* H},$$

$$
\begin{aligned}
&\frac{\partial \bar{v}}{\partial t} + f\bar{u} + g\frac{\partial \zeta}{\partial y} = \underline{-\frac{1}{\rho^*}\frac{\mathrm{d}\Xi}{\mathrm{d}\xi}(0)\frac{\partial H/\partial y}{H}P_m} + \frac{\tau_2}{\rho^* H},\\
&\frac{\partial U_m}{\partial t} - fV_m + \frac{1}{\rho^*}\frac{\partial P_m}{\partial x} - \frac{1}{\rho^*}\lambda_m^{-1}B_{ml}\frac{\partial H/\partial x}{H}P_l = 0,\\
&\frac{\partial V_m}{\partial t} + fU_m + \frac{1}{\rho^*}\frac{\partial P_m}{\partial y} - \frac{1}{\rho^*}\lambda_m^{-1}B_{ml}\frac{\partial H/\partial y}{H}P_l = 0,\\
&\frac{\partial U_m}{\partial x} + \frac{\partial V_m}{\partial y} - \frac{W_m}{H} - \lambda_m^{-1}K_{ml}\left[\frac{\partial H/\partial x}{H}U_l + \frac{\partial H/\partial y}{H}V_l\right]\\
&\quad = \underline{-\lambda_m^{-1}\frac{\mathrm{d}\Xi_m}{\mathrm{d}\xi}(0)\left[\frac{\partial H/\partial x}{H}\bar{u} + \frac{\partial H/\partial y}{H}\bar{v}\right]},\\
&G_{mn}\frac{\partial^2 W_n}{\partial t^2} + N_{\max}^2 W_m + \frac{1}{\rho * H}\lambda_m\frac{\partial P_m}{\partial t} = 0,\\
&(m, n, l = 1, 2, 3, \ldots, N).
\end{aligned}
\tag{19.60}
$$

Boundary conditions which must be satisfied are

$$
\left.\begin{aligned}
&\bar{\boldsymbol{u}}\cdot\boldsymbol{n} = 0,\\
&\boldsymbol{U}_m\cdot\boldsymbol{n} = 0, \quad m = 1, 2, \ldots N,
\end{aligned}\right\} \text{ along the shore,} \tag{19.61}
$$

where $\boldsymbol{n}$ is the unit normal vector and it is assumed that the depth H does not vanish along the shore. The underlined terms in (19.60) describe the barotropic–baroclinic coupling. All these terms involve the gradient of H.

19.4.3 Scale Analysis

To estimate the significance of the barotropic–baroclinic coupling, let us non-dimensionalize equations (19.60). To this end we introduce the following scales and dimensionless variables:

$$
\begin{aligned}
&(x, y, H) = ([L]x^*, [L]y^*, [H]H^*),\\
&\zeta = [\zeta]\zeta^*, \quad t = [f^{-1}]t^*,\\
&(\bar{u}, \bar{v}, U_m, V_m) = [U](\bar{u}^*, \bar{v}^*, U_m^*, V_m^*),\\
&W_m = [W]W_m^*,\\
&P_m = [P]P_m^*,\\
&\boldsymbol{\tau}_{\text{wind}} = [\tau_{\text{wind}}]\boldsymbol{\tau}^*.
\end{aligned}
\tag{19.62}
$$

Bracketed quantities are orders of magnitude of the variables in question and variables having an asterisk are dimensionless. With (19.62), (19.60) becomes (asterisks are consistently omitted):

$$
\begin{aligned}
&\frac{\partial}{\partial x}(H\bar{u}) + \frac{\partial}{\partial y}(H\bar{v}) = 0,\\
&\frac{\partial \bar{u}}{\partial t} - \bar{v} + \mathbb{A}\frac{\partial \zeta}{\partial x} = \underline{-\mathbb{B}\frac{\mathrm{d}\Xi_m(0)}{\mathrm{d}\xi}\frac{\partial H/\partial x}{H}P_m} + \mathbb{C}\frac{\tau_1}{H},\\
&\frac{\partial \bar{v}}{\partial t} + \bar{u} + \mathbb{A}\frac{\partial \zeta}{\partial y} = \underline{-\mathbb{B}\frac{\mathrm{d}\Xi_m(0)}{\mathrm{d}\xi}\frac{\partial H/\partial y}{H}P_m} + \mathbb{C}\frac{\tau_2}{H},\\
&\frac{\partial U_m}{\partial t} - V_m + \mathbb{B}\frac{\partial P_m}{\partial x} - \mathbb{B}\lambda_m^{-1}B_{ml}\frac{\partial H/\partial x}{H}P_l = 0,\\
&\frac{\partial V_m}{\partial t} + U_m + \mathbb{B}\frac{\partial P_m}{\partial y} - \mathbb{B}\lambda_m^{-1}B_{ml}\frac{\partial H/\partial y}{H}P_l = 0,\\
&\frac{\partial U_m}{\partial x} + \frac{\partial V_m}{\partial y} - \mathbb{D}\frac{W_m}{H} - \lambda_m^{-1}K_{ml}\left[\frac{\partial H/\partial x}{H}U_l + \frac{\partial H/\partial y}{H}V_l\right]\\
&\quad = \underline{-\lambda_m^{-1}\frac{\mathrm{d}\Xi_m(0)}{\mathrm{d}\xi}\left[\frac{\partial H/\partial x}{H}\bar{u} + \frac{\partial H/\partial y}{H}\bar{v}\right]},\\
&\mathbb{E}G_{mn}\frac{\partial^2 W_n}{\partial t^2} + W_m + \mathbb{F}\lambda_m\frac{1}{H}\frac{\partial P_m}{\partial t} = 0,
\end{aligned}
\tag{19.63}
$$

where

$$
\begin{aligned}
&\mathbb{A} = \frac{g[\zeta]}{f[L][U]}, \qquad \mathbb{C} = \frac{[\tau]}{\rho^* f[H][U]}, \qquad \mathbb{E} = \frac{f^2}{N_{\max}^2},\\
&\mathbb{B} = \frac{[P]}{\rho^* f[L][U]}, \qquad \mathbb{D} = \frac{[L][W]}{[H][U]}, \qquad \mathbb{F} = \frac{f[P]}{\rho^*[H][W]N_{\max}^2}.
\end{aligned}
\tag{19.64}
$$

Choosing the scales according to[11]

$$
\begin{aligned}
&[L] = 10^4\,\mathrm{m}, && [H] = 10^2\,\mathrm{m}, && [\zeta] = 10^{-1}\,\mathrm{m},\\
&[f^{-1}] = 10^4\,\mathrm{s}, && [U] = 1\,\mathrm{ms}^{-1}, && [W] = 10^{-2}\,\mathrm{ms}^{-1},\\
&[P/\rho*] = 10^{-1}\,\mathrm{m}^2\,\mathrm{s}^{-2}, && [\tau/\rho*] = 10^{-2}\,\mathrm{m}^2\,\mathrm{s}^{-2}, && N_{\max}^2 = 10^{-3}\,\mathrm{s}^{-2},
\end{aligned}
$$

the orders of magnitude of (19.64) are

$$
\begin{aligned}
&\mathbb{A} = O(1), \qquad \mathbb{C} = O(1), \qquad \mathbb{E} = O(10^{-5}),\\
&\mathbb{B} = O(10^{-1}), \qquad \mathbb{D} = O(1), \qquad \mathbb{F} = O(1).
\end{aligned}
$$

[11] An estimate for $[P/\rho^*]$ is obtained as follows: Under hydrostatic conditions the last of (19.51) suggests that $[P/\rho^*] \sim (\Delta\rho/\rho)g[D]$, where $\Delta\rho/\rho$ is the density anomaly and $[D]$ a typical metalimnion thickness: Thus, with $\Delta\rho/\rho \sim 10^{-3}$ and $[D] \le 10\,\mathrm{m}$ this yields $[P/\rho^*] \le 10^{-1}\,\mathrm{m}^2\,\mathrm{s}^{-2}$, implying $\mathbb{B} \le 10^{-1}$.

Important in the following argument are only the values for $\mathbb{A}$, $\mathbb{B}$ and $\mathbb{C}$. Thus the barotropic–baroclinic coupling terms (underlined) in the momentum equations of the barotropic motion are small in comparison to the remaining terms of this equation, but this cannot be said about the baroclinic–barotropic coupling term (underlined) in the baroclinic continuity equation, because these terms do not contain a factor $\mathbb{B}$ while at least some of the remaining terms in the equation are order unity.[12] This argument demonstrates that the barotropic–baroclinic coupling is weak in the sense that to lowest order the barotropic motion is unaffected by the baroclinic processes. On the other hand, a baroclinic trace of the barotropic motion can be discerned, because to the same order of accuracy the barotropic flow serves as an input to the baroclinic response.

This is then the approximate solution procedure: We solve in a first step the TW-equation

$$\begin{aligned} &\nabla \cdot \left(\frac{\nabla \psi_t}{H} \right) + \mathcal{J}\left(\psi, \frac{f}{H} \right) = 0, \text{ in } \mathcal{D}, \\ &\psi = 0, \qquad\qquad\qquad\qquad\qquad \text{on } \partial\mathcal{D}, \end{aligned}$$

evaluate $\bar{u}$ and $\bar{v}$ according to (19.46) and substitute them into $(19.63)_6$.

The internal wave problem ($(19.63)_{4,5,6,7}$) is then solved in a second step. Structurally, this is analogous to the two-layer case studied before.

The above calculations have not been used in a concrete computation for the evaluation of the effects of the barotropic motion in the baroclinic motion due to TWs. However, the computations have nevertheless been useful from a viewpoint of measurements. The scale analysis has shown *for an arbitrary stratification* that *the barotropic–baroclinic coupling is weak in the sense that it is one-sided from the barotropic processes to the baroclinic processes, but not vice versa*. This implies that traces of TWs can be observed in isotherm–depth–time series and compared with solutions of the barotropic TW-equation. The solutions of the baroclinic part of the equations do not have to be determined to perform a comparison between theory and measured quantities.

19.5 Discussion

In this chapter, an introduction was given to topographic Rossby waves. The starting point was the linearized wave equation for barotropic oscillations in a rotating container of which the vertical motion of the free surface was suppressed by the rigid lid assumption. The emerging equation subject to the no flux boundary condition at the circular container wall was solved for a power law radial bathymetry profile. It led to the following qualitative results of the associated eigensolutions:

[12] This argument can even be made more forceful by recognizing that according to $(19.58)_3$ an estimate for H_1 is 10 m ($n = 1$) so that $\lambda_1 = 10^{-3} \times 10^4/10^2 = 10^{-1}$. Consequently, one baroclinic–barotropic coupling term is about a factor of 100 larger than the corresponding barotropic–baroclinic term.

- Countable subinertial eigenfrequencies, whose values depend significantly upon the bathymetric variation. With the variable depth profile tending to constant depth the eigenfrequency (-period) approaches zero (infinity).
- The eigenmodes, expressed as graphs of streamlines, consist of systems of gyres which rotate counter clockwise (on the N. H.) and may for elongated basins also structurally change within a period.
- The fundamental mode consists of a pair of gyres; its scrutiny showed that the horizontal velocity vector close to the container centre rotates counter clockwise (on the N. H.), whilst the horizontal velocity vector at points close to the shore rotates in the opposite direction.

These results are in conformity with observations of velocity measurements in Southern Lake Michigan.

A similar analysis for the Northern basin of Lake of Lugano indicated that whole basin eigenmodes may not be the sole qualitative structure of TW-modes in elongated basins. As shown by Trösch, whose finite element bay mode solutions contrasted with Mysak et al.'s elliptical whole-basin solutions, TW eigensolutions could also arise as bay resonances. It could not be decided, which of the two mode types were suggested by the Lake of Lugano data.

Analysis of the two-layer equations for a small depth epilimnion and a deep hypolimnion (Gratton scaling) showed that the barotropic–baroclinic scaling is one-sided in this case to the extent that the barotropic TW drives the baroclinic response and not vice versa. This implies that TW signals may be extracted from thermistor chain data. That this qualitative behaviour prevails for a general vertical density profile was corroborated by employing a spectral analysis based on the application of the principle of weighted residuals.

Appendix

In this Appendix, we demonstrate how (19.51) can be reduced to a set of spatially two-dimensional equations by using a vertical shape function expansion of the velocity, pressure and density fields as given in the formulae (19.52), in which $\{\phi_n, \Xi_n, \psi_n, \chi_n\}, n = 1, 2, N$ are a set of known functions of the independent variable z/H; through $H = H(x, y)$ they depend implicitly on x and y. It will be explained in the main text, from which function set they will be chosen. The coefficient functions U_n, V_n, W_n, P_n, R_n depend on the spatial horizontal coordinates only and on the time. It is our goal to use the *Principle of weighted residuals* to deduce field equations for these quantities.

Let $\langle\langle f_m, g_n\rangle\rangle$ and $\langle f_m, g_n\rangle$ be the following inner products:

$$\begin{aligned}\langle\langle f_m, g_n\rangle\rangle &= \int_{-H}^{0} f_m\left(\frac{z}{H}\right) g_n\left(\frac{z}{H}\right) \mathrm{d}z,\\ \langle f_m, g_n\rangle &= \int_{0}^{1} f_m(\xi) g_n(\xi) \mathrm{d}\xi.\end{aligned} \tag{19.65}$$

They can be connected by the transformation

$$z = H(\xi - 1), \qquad \mathrm{d}z = H\,\mathrm{d}\xi. \tag{19.66}$$

We mention that it would be more adequate to define $\langle\langle , \rangle\rangle$ as the integral from $z = -H$ to $z = \zeta$ and dropping terms involving ζ afterwards. This definition will be used in the transformation of (19.75) below.

With the aid of (19.65) and (19.66) the reader may easily deduce the following properties:

$$\begin{aligned}
\langle\langle f_m, g_n\rangle\rangle &= H\langle f_m, g_n\rangle,\\
\left\langle\left\langle \frac{\mathrm{d}f_m}{\mathrm{d}z}, g_n\right\rangle\right\rangle &= \left\langle \frac{\mathrm{d}f_m}{\mathrm{d}\xi}, g_n\right\rangle,\\
\left\langle\left\langle \frac{\partial f_m}{\partial x}, g_n\right\rangle\right\rangle &= -\frac{\partial H}{\partial x}\left\langle \frac{\mathrm{d}f_m}{\mathrm{d}\xi}(\xi-1), g_n\right\rangle,\\
\left\langle\left\langle \frac{\partial f_m}{\partial y}, g_n\right\rangle\right\rangle &= -\frac{\partial H}{\partial y}\left\langle \frac{\mathrm{d}f_m}{\mathrm{d}\xi}(\xi-1), g_n\right\rangle.
\end{aligned} \tag{19.67}$$

Consider now the momentum equations $(19.51)_{1,2}$ first. Substitute the expansions (19.52) for $\tilde{u}, \tilde{v}$ and p' and form the following inner products: $\langle\langle\ 19.51_{1,2},\ \delta\phi_m^M\rangle\rangle$; this yields

$$\begin{aligned}
&A_{mn}^M\left[\frac{\partial U_n}{\partial t} - fV_n\right] - \frac{1}{\rho_\star}\frac{\partial H/\partial x}{H}B_{mn}P_n + \frac{C_{mn}}{\rho_\star}\frac{\partial P_n}{\partial x}\\
&\quad = \left(g\frac{\partial \zeta}{\partial x} - \frac{\tau_1}{\rho_\star H}\right)D_m^M,\\
&A_{mn}^M\left[\frac{\partial V_n}{\partial t} + fU_n\right] - \frac{1}{\rho_\star}\frac{\partial H/\partial y}{H}B_{mn}P_n + \frac{C_{mn}}{\rho_\star}\frac{\partial P_n}{\partial y}\\
&\quad = \left(g\frac{\partial \zeta}{\partial y} - \frac{\tau_2}{\rho_\star H}\right)D_m^M, \qquad (m = 1, 2, 3, \ldots, N),
\end{aligned} \tag{19.68}$$

where

$$\begin{aligned}
A_{mn}^M &= \langle \delta\phi_m^M, \phi_n\rangle,\\
B_{mn} &= \left\langle \delta\phi_m^M, (\xi-1)\frac{\mathrm{d}\psi}{\mathrm{d}\xi}\right\rangle - \left\langle 1, (\xi-1)\frac{\mathrm{d}\psi_n}{\mathrm{d}\xi}\right\rangle\langle 1, \delta\phi_m^M\rangle,\\
C_{mn} &= \langle \delta\phi_m^M, \psi_n\rangle - \langle 1, \psi_n\rangle\langle 1, \delta\phi_m^M\rangle,\\
D_m^M &= \langle 1, \delta\phi_m^M\rangle.
\end{aligned} \tag{19.69}$$

Here and henceforth, functions carrying a prefix δ are weighting functions in the expansions (19.52). Moreover, in (19.68) summation over repeated indices n is understood. In an analogous manner, $(19.51)_{4,5}$ can be treated: the inner products $\langle\langle\ (19.51)_4, \delta\phi_m^V\rangle\rangle$ and $\langle\langle\ \ (19.51)_5, \delta\phi_m^V\rangle\rangle$ are formed and yield the equations

$$
\begin{aligned}
&E_{mn}\frac{\partial R_n}{\partial t} - \frac{\rho_\star N_{\max}^2}{g} F_{mn} W_n = 0,\\
&G_{mn}\frac{\partial W_n}{\partial t} + \frac{g}{\rho_\star} E_{mn} R_n + \frac{1}{\rho_\star H} H_{mn} P_n = 0,\\
&\qquad (m = 1, 2, 3, \ldots, N),
\end{aligned}
\tag{19.70}
$$

in which

$$
\begin{aligned}
&E_{mn} = \langle \delta\phi_m^V, \chi_n \rangle, \qquad G_{mn} = \langle \delta\phi_m^V, \Xi_n \rangle,\\
&F_{mn} = \langle \delta\phi_m^V, \hat{N}^2 \Xi_n \rangle, \; H_{mn} = \langle \delta\phi_m^V, \tfrac{\mathrm{d}\psi_n}{\mathrm{d}\xi} \rangle,
\end{aligned}
\tag{19.71}
$$

and where

$$
\hat{N}^2 = \hat{N}^2(\xi) = \frac{N^2(\xi)}{N_{\max}^2} = -\frac{\dfrac{\mathrm{d}\rho_0}{\mathrm{d}z}}{\left|\dfrac{\mathrm{d}\rho_0}{\mathrm{d}z}\right|_{\max}}. \tag{19.72}
$$

Clearly, in order that these relations are meaningful, the boundary conditions $p'(\xi = 1) = 0$ must be satisfied. Hence we must request

$$
\psi_n(\xi = 1) = 0. \tag{19.73}
$$

With our choice of ψ_n this condition will be nearly satisfied. Equations (19.70) can be combined to yield the single equation

$$
\begin{aligned}
&G_{mn}\frac{\partial^2 W_n}{\partial t^2} + N_{\max}^2 F_{mn} W_n + \frac{H_{mn}}{\rho_\star H}\frac{\partial P_n}{\partial t} = 0,\\
&\qquad (m = 1, 2, 3, \ldots, N).
\end{aligned}
\tag{19.74}
$$

Equations (19.68) and (19.74) are $3N$ equations for the unknowns U_n, V_n, P_n, W_n. The remaining N equations follow from the continuity equation $(19.51)_3$. Because kinematic boundary conditions at the upper and lower surfaces must be incorporated when employing the Principle of weighted residuals, we shall go into greater details. Forming $\langle\langle\, (19.51)_3, \delta\phi_m^C \rangle\rangle$, it follows that

$$
\begin{aligned}
&\langle\langle \tilde{u}_x, \delta\phi_m^C \rangle\rangle + \langle\langle \tilde{v}_y, \delta\phi_m^C \rangle\rangle + \langle\langle w_z, \delta\phi_m^C \rangle\rangle\\
&\quad = \left(\frac{H_x}{H}\bar{u} + \frac{H_y}{H}\bar{v}\right) \langle\langle 1, \delta\phi_m^C \rangle\rangle.
\end{aligned}
\tag{19.75}
$$

Using the definition of the inner product $\langle\langle , \rangle\rangle$, we may easily prove that.[13]

$$\begin{aligned}
\langle\langle \tilde{u}_x, \delta\phi_m^C \rangle\rangle &= \frac{\partial}{\partial x}\langle\langle \tilde{u}, \delta\phi_m^C \rangle\rangle - \left\langle\left\langle \tilde{u}, \frac{\partial \delta\phi_m^C}{\partial x} \right\rangle\right\rangle \\
&\quad - \tilde{u}\delta\phi_m^C\Big|_{z=\zeta} \frac{\partial \zeta}{\partial x} - \tilde{u}\delta\phi_m^C\Big|_{z=-H} \frac{\partial H}{\partial x}, \\
\langle\langle \tilde{v}_x, \delta\phi_m^C \rangle\rangle &= \frac{\partial}{\partial y}\langle\langle \tilde{v}, \delta\phi_m^C \rangle\rangle - \left\langle\left\langle \tilde{v}, \frac{\partial \delta\phi_m^C}{\partial y} \right\rangle\right\rangle \\
&\quad - \tilde{v}\delta\phi_m^C\Big|_{z=\zeta} \frac{\partial \zeta}{\partial y} - \tilde{v}\delta\phi_m^C\Big|_{z=-H} \frac{\partial H}{\partial y}, \\
\langle\langle \tilde{w}_z, \delta\phi_m^C \rangle\rangle &= -\langle\langle w, \delta\phi_{m_z}^C \rangle\rangle + w\delta\phi_m^C\Big|_{z=\zeta} - w\delta\phi_m^C\Big|_{z=-H}.
\end{aligned} \tag{19.76}$$

With these expressions the weighted continuity statement (19.74) takes the form

$$\begin{aligned}
&\frac{\partial}{\partial x}\langle\langle \tilde{u}, \delta\phi_m^C \rangle\rangle + \frac{\partial}{\partial y}\langle\langle \tilde{v}, \delta\phi_m^C \rangle\rangle \\
&- \left\langle\left\langle \tilde{u}, \frac{\partial \delta\phi_m^C}{\partial x} \right\rangle\right\rangle - \left\langle\left\langle \tilde{v}, \frac{\partial \delta\phi_m^C}{\partial y} \right\rangle\right\rangle - \left\langle\left\langle w, \delta\phi_{m_z}^C \right\rangle\right\rangle \\
&- \delta\phi_m^C(\zeta)\left(\left[u\zeta_x + v\zeta_y - w\right]_{z=\zeta} - \bar{u}\zeta_x - \bar{v}\zeta_y\right) \\
&- \delta\phi_m^C(-H)\left(\left[uH_x + vH_y - w\right]_{z=-H} - \bar{u}H_x - \bar{v}H_y\right) \\
&= \left(\frac{H_x}{H}\bar{u} + \frac{H_y}{H}\bar{v}\right)\langle\langle 1, \delta\phi_m^C \rangle\rangle.
\end{aligned} \tag{19.77}$$

This equation is written down in full in order to demonstrate incorporation of the boundary conditions. The term in brackets in the third line equals $-\partial\zeta/\partial t$ and that in the fourth line vanishes. After this substitution we may ignore the two terms involving $\partial\zeta/\partial t$ because the rigid-lid assumption is made. Finally, the non-linear term $\bar{u}\zeta_x, \bar{v}\zeta_y$ may be omitted because the non-linearities have consistently been dropped in earlier equations. Thus, (19.77) reduces to

$$\begin{aligned}
&\frac{\partial}{\partial x}\langle\langle \tilde{u}, \delta\phi_m^C \rangle\rangle + \frac{\partial}{\partial y}\langle\langle \tilde{v}, \delta\phi_m^C \rangle\rangle - \left\langle\left\langle \tilde{u}, \frac{\partial \delta\phi_m^C}{\partial x} \right\rangle\right\rangle \\
&- \left\langle\left\langle \tilde{v}, \frac{\partial \delta\phi_m^C}{\partial y} \right\rangle\right\rangle - \langle\langle w, \delta\phi_{m_z}^C \rangle\rangle \\
&= \left(\bar{u}H_x + \bar{v}H_y\right)\left[\frac{1}{H}\langle\langle 1, \delta\phi_m^C \rangle\rangle - \delta\phi_m^C(-H)\right].
\end{aligned} \tag{19.78}$$

[13] Here, we use the definition $\langle\langle f, g \rangle\rangle = \int_{-H}^{\zeta} fg\,\mathrm{d}z$.

Substituting the expansion (19.52) and making use of the formulae (19.67) at appropriate places yields the equation

$$A^C_{mn}\left[\frac{\partial U_n}{\partial x}+\frac{\partial V_n}{\partial y}\right]-K_{mn}\left[\frac{H_x}{H}U_n+\frac{H_y}{H}V_m\right]-L_{mn}\frac{W_n}{H}$$
$$=\left(\bar{u}\frac{H_x}{H}+\bar{v}\frac{H_y}{H}\right)\left[D^C_m-\delta\phi^C_m(\zeta=0)\right],\quad (m=1,2,3,\ldots,N),\ (19.79)$$

in which

$$\begin{aligned}A^C_{mn}&=\langle\delta\phi^C_m,\phi_n\rangle,\\ D^C_m&=\langle\delta\phi^C_m,1\rangle,\\ K_{mn}&=\left\langle(\xi-1)\frac{\mathrm{d}\phi_n}{\mathrm{d}\xi},\delta\phi^C_m\right\rangle-\delta\phi^C_m(0)\delta\phi^C_n(0),\\ L_{mn}&=\left\langle\Xi,\frac{\mathrm{d}\delta\phi^C_m}{\mathrm{d}\xi}\right\rangle.\end{aligned}\qquad (19.80)$$

This completes the derivation of the baroclinic equations. They are: (19.68), (19.74) and (19.79) and form $4N$ partial differential equations for the baroclinic variables U_n, V_n, W_n, P_n; needless to say that the barotropic quantities $\bar{u}, \bar{v}, \zeta$ are regarded as being prescribed or governed by (19.45) or (19.57) in the main text.

References

1. Abramowitz, M. and Stegun, I. A.: *Handbook of mathematical functions.* Dover (1972)
2. Ball, K. F.: Second class motions of a shallow liquid. *J. Fluid Mech.*, **23**, 545–561 (1965)
3. Bäuerle, E.: Topographic waves in the Baltic Sea. *Proc. XIV. Conf of Baltic Oceaographers, Gdynia* (1984)
4. Bäuerle, E.: Internal free oscillations in the Lake of Geneva. *Annales Geophysicae*, **3**, 199–206 (1985)
5. Birchfield, G. E. and Hickie, B. P.: The time dependent response of a circular basin of variable depth to wind stress. *J. Phys. Oceanogr.*, **7**, 691–701 (1977)
6. Clarke, A. J.: Observational and numerical evidence for wind-forced coastal trapped long waves. *J. Phys. Oceanogr.*, **7**, 231–247 (1977)
7. Csanady, G.: Topographic waves in Lake Ontario. *J. Phys. Oceanogr.*, **6**, 93–103 (1976)
8. Finlayson, B.A.: *The Method of weighted residuals and variational principles* Academic Press (1972)
9. Gill, A. E. and Schumann, E. H.: The generation of long shelf waves by the wind. *J. Phys. Oceanogr.*, **4**, 83–90 (1974)
10. Graf, W.: Hydrodynamics of the Lake of Geneva. *Schw. Z. Hydrol.*, **45**, 62–100 (1983)
11. Gratton, Y.: *Low frequency vorticity waves over strong topography.* Ph.D. Thesis, Univ. of British Columbia, 132 pp. (1983)
12. Gratton, Y. and LeBlond, P. H.: Vorticity waves over strong topography. *J. Phys. Oceanogr.*, **16**, 151–166 (1986)
13. Huang, J. C. K. and Saylor, J.H.: Vorticity waves in a shallow basin. *Dyn. Atmos. Oceans*, **6**, 177–196 (1982)

14. Huthnance, J. M.: On coastal trapped waves: Analysis and numerical calculation by inverse iteration. *J. Phys. Oceanogr.*, **8**, 74–92 (1978)
15. Hutter, K.: Strömungsdynamische Untersuchungen im Zürich- und Luganersee. *Schw. Z. Hydrol.*, **45**, 102–144 (1983)
16. Hutter, K.: Fundamental equations and approximations. In *Hydrodynamics of Lakes*. CISM **286**, edited by K. Hutter, 1–37, Springer, Wien-New York (1984a)
17. Hutter, K.: Mathematische Vorhersage von barotropen und baroklinen Prozessen im Zürich- und Luganersee. *Vierteljahreszeitschrift der Naturf. Ges.*, **129**, 51—92 (1984b)
18. Hutter, K.: Waves and oscillations in the ocean and in lakes. In: *Continuum mechanics in environmental sciences and geophysics* (K. Hutter, ed.). Springer Verlag Vienna. New York, 79–240 (1993)
19. Hutter, K., Salvadè, G. and Schwab, D. J.: On internal wave dynamics in the Northern basin of Lake of Lugano. *Geophys. Astrophys. Fluid Dyn.*, **27**, 299–336 (1983)
20. Johnson, E. R.: Topographic waves in elliptical basins. *Geophys. Astrophys. Fluid Dyn.*, **37**, 279–295 (1987a)
21. Johnson, E. R.: A conformal mapping technique for topographic wave problems. *J. Fluid Mech.*, **177**, 395–405 (1987b)
22. Johnson, E.R.: Topographic waves in open domains. Part I: Boundary conditions and frequency estimates. *J. Fluid Mech.*, **200**, 69–76 (1989)
23. Johnson, E. R. and Kaoullas, G.: Bay-trapped low-frequency oscillations in lakes. *Geophys. Astrophys. Fluid Dyn.*, **105**(1), 48–60 (2011)
24. Kielmann, J.: The generation of eddy-like structures in a model of the Baltic Sea by low frequency wind forcing (unpublished) (1983)
25. Kielmann, J. and Simons, T. J.: Baroclinic circulation models. In: *Hydrodynamics of lakes* CISM Lecture Notes, **286** (K. Hutter, ed.), 235-285, Springer Verlag, Vienna-New York (1984)
26. Lamb, H.: *Hydrodynamics*. 6th ed. Cambridge University Press (1932)
27. LeBlond, P. H. and Mysak, L. A.: *Waves in the Ocean*. Elsevier (1980)
28. Marmorino, G. O.: Lowfrequency current fluctuation in Lakes Ontario. *J. Geophys. Res.*, **84**, 1206–1214 (1979)
29. Mysak, L. A.: Recent advances in shelf wave dynamics. *Review of Geophysics and Space Physics*, **18**, 211–241 (1980)
30. Mysak, L. A. Topographic waves in lakes. In *Hydrodynamic of Lakes*, **CISM 286**, edited by K. Hutter, 81–128, Springer, Wien-New York. (1984)
31. Mysak, L. A. Elliptical topographic waves. *Geophys. Astrophys. Fluid Dyn.*, **31**, 93–135 (1985)
32. Mysak, L. A., Salvadè, G., Hutter, K. and Scheiwiller, T.: Lake of Lugano and topographic waves. *Nature*, **306**, 46–48 (1983)
33. Mysak, L. A., Salvadè, G., Hutter, K. and Scheiwiller, T.: Topographic waves in an elliptical basin with application to the Lake of Lugano. *Phil. Trans. R. Soc. London*, **A 316**, 1–55 (1985)
34. Poincaré, H.: *Théorie des marées. Leçon de mécanique céleste*, **3**, Paris (1910)
35. Saylor, J. H., Huang, J. S. K. and Reid, R. O.: Vortex modes in Southern Lake Michigan. *J. Phys. Oceanogr.*, **10**, 1814–1823 (1980)
36. Saylor, J. H. and Miller, G. S.: *Vortex modes of particular Great Lakes basins*, Great Lakes Environmental research Laboratory, Contribution, **394**, NOAA, Ann Arbor, Michigan USA (1983)
37. Simons, T. J.: Wind-driven circulations in the South-West Baltic. *Tellus*, **30**, 272–283 (1978a)
38. Simons, T. J.: Generation and propagation of downwelling fronts. J. Phys. Oceanogr., **8**, 571–581 (1978b)
39. Simons, T. J.: Circulation models of lakes and inland seas. *Can. Bull. Fish. Aquat., Sci.*, **203**, 1–146 (1980)
40. Stocker, T. and Hutter, K.: A model for topographic Rossby waves in channels and lakes. *Mitteilungen der Versuchsanstalt für Wasserbau, Hydrologie und Glaziologie, ETH, Zürich*, **76** (1985)
41. Stocker, T. and Hutter, K.: One-dimensional models for topographic Rossby waves in elongated basins on the f-plane. *J. Fluid Mech.*, **70**, 435–459 (1986)

42. Stocker, T. and Hutter, K.: Topographic waves in channels and lakes on the f-plane. *Lecture Notes on Coastal and Estuarine Studies* Nr 21, Springer Verlag, Berlin etc. 176 p (1987a)
43. Stocker, T. and Hutter, K.: Topographic Rossby waves in rectangular basins. *J. Fluid Mech.*, **185**, 107–120 (1987b)
44. Stocker, T. and Hutter, K.: Qualitative aspects of topographic waves in closed basins, gulfs and channels. In: *Modeling Marine Systems, I.* (A. M. Davies, ed.) CRC-Press, 255–289 (1990)
45. Stocker, T. and Johnson, E. R.: Topographic waves in open domains. Part II. Bay modes and resonances, *J. Fluid Mech.*, **200**, 77–93 (1989)
46. Stocker, T. and Johnson, E. R.: The trapping and scattering of topographic waves by estuaries and headlands. *J. Fluid Mech.*, **222**, 501–524 (1991)
47. Trösch, J.: Finite element calculation of topographic waves in lakes. *Proceedings of 4th International Conference on Applied Numerical Modeling, Tainan, Taiwan.* 1986. Edited Han-Min, Hsio, Yo Li Chon, Shu Yi Wang, ad Sheng Jii Hsien, Vol. 63 of *Science and Technology Series*, 307-311 (1986)
48. Wang, D. P. and Mooers C. N. K.: Coastal trapped waves in a continously stratified ocean. *J. Phys. Oceanogr.*, **6**, 853–863 (1976)
49. Wenzel, M.: *Interpretation der Wirbel im Bornholm becken durch topographische Rossby Wellen in einem Kreisbecken*. Diplomarbeit, Christian Albrechts Universität Kuel. 52 pp. (1978)
50. Willmott, A. J. and Johnson, E. R.: Topographic waves in a rotating stratifies basin *Geophy. Astrophys. Fluid Dynamics*, **45**, 71–87 (1989)

Chapter 20
Topographic Rossby Waves in Basins of Simple Geometry

20.1 Motivation

In the last chapter, topographic Rossby-waves on the f-plane were studied with emphasis of their mathematical description as extracted from the governing equations of fluid mechanics. Their possible observation by synoptic measurements was also discussed: they pertain to horizontal velocity and temperature-time series from moored thermistor chains and current recorders. It was shown by appropriately scaling the adiabatic Boussinesq approximated equations that in lakes with shallow epilimnion and deep hypolimnion – more specifically lakes which satisfy the so-called Gratton-scaling – the barotropic-baroclinic coupling is one-sided from the barotropic to the baroclinic TWs but not vice versa. In other words, if a topographic wave or a free or wind-induced oscillation in a lake, whose spectral component can be associated with a barotropic topographic wave mode, is acting in a lake, then this spectral component exerts a sizeable effect on the vertical baroclinic water movement which is (in principle) measurable in isotherm–depth–time series. Conversely, a baroclinic wave signal has a negligible influence on the barotropic TW response. This implies that for all those lakes whose geometry and stratification falls into the range of Gratton's scaling – most Alpine lakes satisfy this scaling – the spectral structure can be found from the spectral analysis of the TW-operator, yet observational inferences can be drawn not only from cross-correlation analyses of moored current meters but equally also from such analyses involving isotherm–depth or temperature–time series.

This fact, which was proved in the last chapter, is the reason why the study of solutions of the linear barotropic TW-equation is important, because it reveals insight into the physics of these processes. This is what shall be done in this chapter: Solutions to the barotropic TW-equation will be discussed for basins with various different geometries. By presenting an almanac of such solutions for circular and elliptic basins, for channels and shelf bathymetries, a first qualitative understanding of TW-modes is established. However, a deeper understanding can only be gained when rectangular basins with various bathymetries will have been studied in detail.

K. Hutter et al., *Physics of Lakes*, *Volume 2: Lakes as Oscillators*, Advances in Geophysical and Environmental Mechanics and Mathematics,
DOI 10.1007/978-3-642-19112-1_20,

20.2 Topographic Wave Equation in Curvilinear Orthogonal Coordinate Systems

Because in subsequent sections the TW-equation will be used when being referred to various coordinate systems, we shall first present it in an arbitrary orthogonal coordinate system.

20.2.1 Preparation

We restrict our considerations to *orthogonal* coordinate systems $\boldsymbol{x} = (x_1, x_2, x_3)$ which have the property that their metric tensor $\boldsymbol{g}$ has diagonal form, e.g. in $\mathbb{R}^3$

$$\boldsymbol{g} = \begin{bmatrix} J_1 & 0 & 0 \\ 0 & J_2 & 0 \\ 0 & 0 & J_3 \end{bmatrix}. \tag{20.1}$$

The arc element $\mathrm{d}\boldsymbol{l}$ can be expressed using

$$\mathrm{d}\boldsymbol{l} = \boldsymbol{g}\,\mathrm{d}\boldsymbol{x}, \tag{20.2}$$

where $\mathrm{d}\boldsymbol{x} = (\mathrm{d}x_1, \mathrm{d}x_2, \mathrm{d}x_3)$ is the increment vector and insertion of (20.1) into (20.2) yields

$$\mathrm{d}\boldsymbol{l} = (J_1 \mathrm{d}x_1, J_2 \mathrm{d}x_2, J_3 \mathrm{d}x_3). \tag{20.3}$$

Table 20.1 collects the components of the metric tensor for frequently used orthogonal coordinate systems.

We recall the TW-equation and the barotropic velocity field in the coordinate-invariant formulation

$$\frac{\partial}{\partial t}\left(\nabla \cdot \left(\frac{\nabla \psi}{H}\right)\right) + \hat{\boldsymbol{k}} \cdot \left(\nabla \psi \times \nabla \left(\frac{f}{H}\right)\right) = 0, \quad \boldsymbol{u} = \frac{1}{H}(\hat{\boldsymbol{k}} \times \nabla \psi), \tag{20.4}$$

Table 20.1 Coordinate systems often used in lake hydrodynamics

Coordinates	(x_1, x_2, x_3)	J_1	J_2	J_3	
Cartesian	(x, y, z)	1	1	1	
Cylindric	(r, ϕ, z)	1	r	1	
Elliptic	(ξ, η, z)	J	J	1	where $J = a(\sinh^2 \xi + \sin^2 \eta)^{1/2}$
Natural[a]	(s, n, z)	J	1	1	where $J = 1 - K(s) \cdot n$

[a] $K(s)$ is the curvature as a function of arc length s.

where $\hat{\boldsymbol{k}}$ is a unit vector acting in the direction against gravity. (For the derivation, see Sect. 11.3.) Defining the two operators

$$\begin{aligned} E[\psi] &:= \nabla \cdot \left(\frac{\nabla \Psi}{H} \right), \\ \mathcal{J}\left[\psi, \frac{f}{H} \right] &:= \hat{\boldsymbol{k}} \cdot \left(\nabla \psi \times \nabla \left(\frac{f}{H} \right) \right) = \frac{\partial \psi}{\partial x} \frac{\partial}{\partial y} \left(\frac{f}{H} \right) - \frac{\partial \psi}{\partial y} \frac{\partial}{\partial x} \left(\frac{f}{H} \right), \end{aligned} \tag{20.5}$$

Equation (20.4) may also be written as

$$T[\psi] := \frac{\partial}{\partial t} E[\psi] + \mathcal{J}\left[\psi, \frac{f}{H} \right]. \tag{20.6}$$

In $(20.5)_2$, x and y are Cartesian coordinates, whilst the representation involving $\hat{\boldsymbol{k}}$ is coordinate invariant.

To obtain these equations in the different coordinate systems the vector differential operators need be written in curvilinear coordinates. In the orthogonal coordinate system whose arc element has the form (20.3), the gradient-, divergence- and curl-operators are given by

$$\begin{aligned} \operatorname{grad} u &= \left(\frac{1}{J_1} \frac{\partial u}{\partial x_1}; \frac{1}{J_2} \frac{\partial u}{\partial x_2}; \frac{1}{J_3} \frac{\partial u}{\partial x_3} \right), \\ \operatorname{div} \boldsymbol{v} &= \frac{1}{J_1 J_2 J_3} \left(\frac{\partial}{\partial x_1}(J_2 J_3 v_1) + \frac{\partial}{\partial x_2}(J_1 J_3 v_2) + \frac{\partial}{\partial x_3}(J_1 J_2 v_3) \right), \\ \operatorname{curl} \boldsymbol{v} &= \frac{1}{J_1 J_2 J_3} \left[J_1 \frac{\partial}{\partial x_2}(J_3 v_3) - J_1 \frac{\partial}{\partial x_3}(J_2 v_2); \right. \\ &\qquad \left. J_2 \frac{\partial}{\partial x_3}(J_1 v_1) - J_2 \frac{\partial}{\partial x_1}(J_3 v_3); J_3 \frac{\partial}{\partial x_1}(J_2 v_2) - J_3 \frac{\partial}{\partial x_2}(J_1 v_1) \right], \end{aligned} \tag{20.7}$$

where $u = u(\boldsymbol{x})$ is a scalar and $\boldsymbol{v} = \boldsymbol{v}(\boldsymbol{x})$ is a vector in $\mathbb{R}^3$. A derivation can e.g. be found in Pearson [30].

Problem 20.1 *Using the above representations of the operators E and $\mathcal{J}$, and the* grad *and* div *operators in (20.7) show that in the orthogonal curvilinear coordinates x_1, x_2 one has*

$$\begin{aligned} E[\psi] &= \frac{1}{J_1 J_2} \left\{ \frac{\partial}{\partial x_1} \left(\frac{J_2}{J_1} \frac{1}{H} \frac{\partial \psi}{\partial x_1} \right) + \frac{\partial}{\partial x_2} \left(\frac{J_1}{J_2} \frac{1}{H} \frac{\partial \psi}{\partial x_2} \right) \right\}, \\ \mathcal{J}\left[\psi, \frac{f}{H} \right] &= \frac{1}{J_1 J_2} \left\{ \frac{\partial \psi}{\partial x_1} \frac{\partial}{\partial x_2} \left(\frac{f}{H} \right) - \frac{\partial \psi}{\partial x_2} \frac{\partial}{\partial x_1} \left(\frac{f}{H} \right) \right\}. \end{aligned} \tag{20.8}$$

Thus, $T[\psi] = 0$, expressed in any orthogonal curvilinear coordinate system, is given by

$$\frac{\partial}{\partial t}\left\{\frac{\partial}{\partial x_1}\left(\frac{J_2}{J_1}\frac{1}{H}\frac{\partial\psi}{\partial x_1}\right)+\frac{\partial}{\partial x_2}\left(\frac{J_1}{J_2}\frac{1}{H}\frac{\partial\psi}{\partial x_2}\right)\right\}$$
$$+\left\{\frac{\partial\psi}{\partial x_1}\frac{\partial}{\partial x_2}\left(\frac{f}{H}\right)-\frac{\partial\psi}{\partial x_2}\frac{\partial}{\partial x_1}\left(\frac{f}{H}\right)\right\}=0, \qquad (20.9)$$

provided the curvilinear coordinates x_1, x_2 are not time dependent. ◆

The TW-equation satisfies the following properties:

- Whenever $\mathcal{J}=0$, no waves can propagate. Any non-steady solution is due to the presence of the rotation of the Earth and the variation of the bathymetric profile.
- The boundary value problem

$$\begin{aligned} T[\psi] &= 0 \quad \text{in } \mathcal{D},\\ \psi &= 0 \quad \text{at } \partial\mathcal{D} \end{aligned} \qquad (20.10)$$

  is scale invariant, i.e. changing x, y by the scale $[L]$ and the depth by the scale $[H]$ leaves the equations (20.10) unchanged. This property is due to the rigid lid assumption; it holds as long as $[L]$ is small in comparison to the external Rossby radius $R=\sqrt{g[H]}/f\sim 500\,\text{km}$.
- The TW-equation is invariant under conformal mappings. Indeed, if $z=x+\mathrm{i}y$ and $w=u+\mathrm{i}v$ are complex valued and $z=z(w)$ is a holomorphic function, then

$$|\mathrm{d}z|^2=(\mathrm{d}x)^2+(\mathrm{d}y)^2=\left|\frac{\mathrm{d}z}{\mathrm{d}w}\right|^2((\mathrm{d}u)^2+(\mathrm{d}v)^2),$$

  implying $J_1=J_2$ in (20.9). This means that the TW-equation (20.9) is independent of the scale factors. This property was pointed out and used by Johnson [14, 15].

  This invariance property of the TW-operator under conformal mappings is a useful property, as a large number of solutions to special geometries can be generated from known solutions. This will be pointed out below in a number of occasions. In this way, exact solutions of the TW-equation in complex geometries can be constructed which may be used to test numerical software for the TW-operator. From a physical viewpoint this invariance property is, however, not as useful as one might surmise, because the bathymetry is equally transformed with the conformal mapping procedure. Moreover, the conformal mapping technique does not generate characteristically new solutions. For instance, a TW-mode with basin wide structure in one domain will be stretched and bent in the transformed domain, but it will still be basin-wide.

20.2.2 Cylindrical Coordinates

These coordinates are often used in problems which exhibit some rotational symmetry. The coordinates are (r, ϕ, z) which are related to the Cartesian system by the formulae

$$\begin{aligned} x &= r\cos\phi, \\ y &= r\sin\phi, \quad r \geq 0; \quad 0 \leq \phi \leq 2\pi \\ z &= z. \end{aligned}$$

The arc element is given by

$$\mathrm{d}\boldsymbol{l} = (\mathrm{d}r, r\mathrm{d}\phi, \mathrm{d}z),$$

as anticipated in Table 20.1. Applying (20.7) to (20.4) yields

$$\left(\frac{r}{H}\psi_{tr}\right)_r + \left(\frac{1}{rH}\psi_{t\phi}\right)_\phi + \psi_r\left(\frac{f}{H}\right)_\phi - \psi_\phi\left(\frac{f}{H}\right)_r = 0 \tag{20.11}$$

as the TW-equation in cylindrical coordinates. Then

$$\boldsymbol{u} = \left(-\frac{1}{Hr}\psi_\phi, \frac{1}{H}\psi_r\right).$$

20.2.3 Elliptical Coordinates

The coordinates of the elliptic cylinder system are (ξ, η, z), and for fixed z the lines $\xi = \text{const}$ are confocal ellipses whereas the lines $\eta = \text{const.}$ are hyperbolas, see Fig. 20.1. The parameter a denotes the position of the foci, and the Cartesian coordinates are calculated from (ξ, η, z) by

$$\begin{aligned} x &= a\cosh\xi\cos\eta, \\ y &= a\sinh\xi\sin\eta, \quad \xi \geq 0, \quad 0 \leq \eta \leq 2\pi \\ z &= z. \end{aligned} \tag{20.12}$$

The shore line of the elliptic basin is given by

$$\frac{x^2}{(a\cosh\xi_S)^2} + \frac{y^2}{(a\sinh\xi_S)^2} = 1,$$

which is an ellipse with the semi-axes A and B and an aspect ratio (width to length)

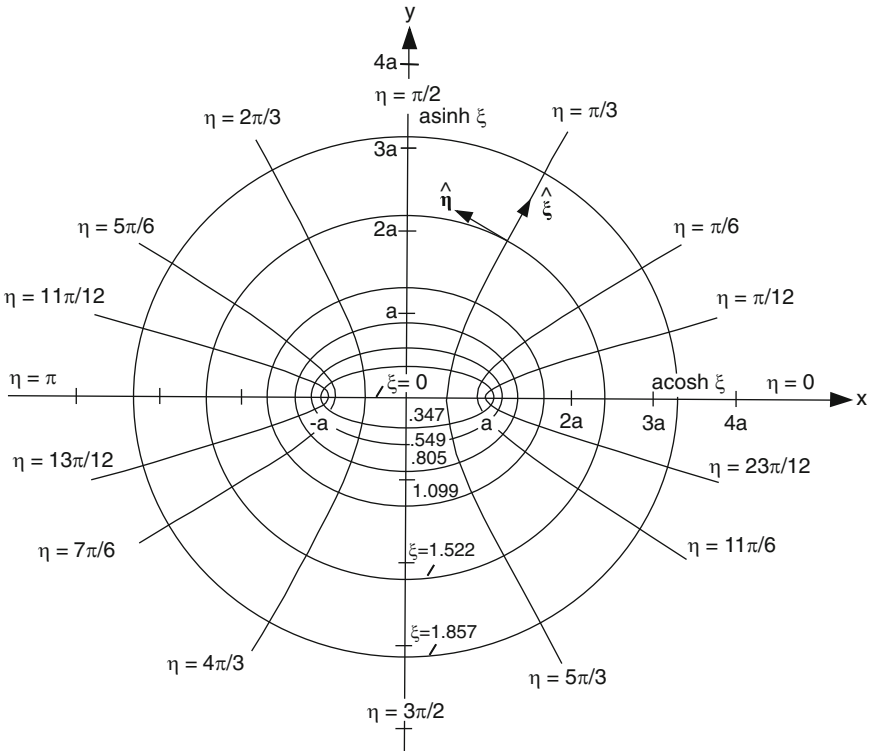

Fig. 20.1 Elliptic cylinder coordinates (ξ, η). The quantities $\hat{\boldsymbol{\xi}}$ and $\hat{\boldsymbol{\eta}}$ are unit vectors in the directions of increasing ξ and η. We refer to ξ and η as radial and angular coordinates, respectively (from [27]). © Taylor & Francis, http://www.informaworld.com, reproduced with permission

$$r = \frac{B}{A} = \frac{a \sinh \xi_S}{a \cosh \xi_S} = \tanh \xi_S. \tag{20.13}$$

The first two diagonal elements of the metric tensor are equal and read

$$J \equiv J_1 = J_2 = a(\sinh^2 \xi + \sin^2 \eta)^{1/2},$$

whilst

$$J_3 = 1.$$

Thus the TW-equation in elliptic coordinates takes the form

$$\left(\frac{1}{H}\psi_{t\xi}\right)_\xi + \left(\frac{1}{H}\psi_{t\eta}\right)_\eta + \psi_\xi \left(\frac{f}{H}\right)_\eta - \psi_\eta \left(\frac{f}{H}\right)_\xi = 0. \tag{20.14}$$

Due to the equality $J \equiv J_1 = J_2$ the equation for the stream function is independent of J so that, formally, the same equation as in a Cartesian system is obtained. However, the metric factor enters the formula for the velocity field

$$\boldsymbol{u} = \left(-\frac{1}{JH}\psi_\eta, \quad \frac{1}{JH}\psi_\xi \right). \tag{20.15}$$

20.2.4 Natural Coordinates

For the developments in subsequent sections we need the TW-equation also referred to a natural coordinate system. With this, it is particularly convenient to describe elongated and curved lake basins. We choose an orthogonal network which spans the elongated domain. The basis for it is an axis, which follows more or less the *thalweg*[1] of the lake. The arc length s along this axis forms the first coordinate of the system.

In view of the restriction to elongated narrow lakes it is possible to choose a straight n-axis; so, the system is curved only in the s-direction, see Fig. 20.2a. In order to define the lake domain uniquely in terms of these coordinates, the radius of curvature $R(s)$ must exceed half the width of the lake $B(s)$, $R(s) > B(s)/2$. Let

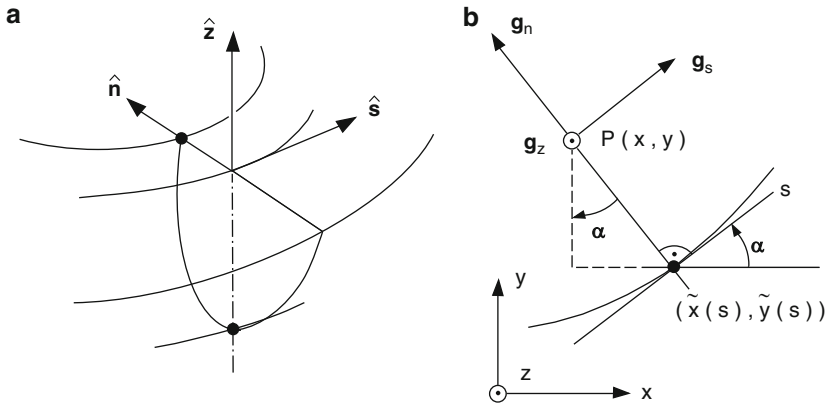

Fig. 20.2 (**a**) Natural coordinate system (s, n, z) in the lake basin with unit vectors $\hat{\boldsymbol{s}}$, $\hat{\boldsymbol{n}}$ and $\hat{\boldsymbol{k}}$. $\hat{\boldsymbol{n}}$ points to the positive centre of the curvature along s; (**b**) Basis vectors in the natural coordinate system (from Stocker and Hutter (1985) [37]). © Versuchsanstalt für Wasserbau, Hydrologie und Glaziologie an der ETH Zürich, reproduced with permission

[1] The thalweg of an elongated lake is the line which follows the deepest points of the basin cross sections. For simple shapes and simple bathymetries (ellipses with parabolic bottom surface, rectangles, etc.) the thalweg can readily be defined. For arbitrary basins the thalweg cannot be defined this way. In those cases, the lake axis is a line roughly defining the middle between opposite shores.

the lake axis be given by a parameter representation $(\tilde{x}(s), \tilde{y}(s))$ within a Cartesian system as shown in Fig. 20.2b. The coordinates of an arbitrary point P are then given by

$$x = \tilde{x}(s) - n\sin\alpha(s), \quad y = \tilde{y}(s) + n\cos\alpha(s),$$

provided the n-axis is chosen to be straight. The set of basis vectors $\boldsymbol{g}_s$, $\boldsymbol{g}_n$ and $\boldsymbol{g}_z$ at point P can be expressed in the form

$$\boldsymbol{g}_s = \left(\frac{\mathrm{d}x}{\mathrm{d}s}, \frac{\mathrm{d}y}{\mathrm{d}s}, 0\right), \quad \boldsymbol{g}_n = \left(\frac{\mathrm{d}x}{\mathrm{d}n}, \frac{\mathrm{d}y}{\mathrm{d}n}, 0\right), \quad \boldsymbol{g}_z = (0, 0, 1),$$

which is easily simplified to the form

$$\begin{aligned} \boldsymbol{g}_s &= (\ \tilde{x}' - nK\cos\alpha,\ \ \tilde{y}' - nK\sin\alpha,\ \ 0), \\ \boldsymbol{g}_n &= (\quad -\sin\alpha,\qquad \cos\alpha,\qquad 0), \\ \boldsymbol{g}_z &= (\qquad 0,\qquad\quad 0,\qquad\quad 1), \end{aligned}$$

using as definition for the curvature $K = \mathrm{d}\alpha/\mathrm{d}s$. With the aid of Fig. 20.3 it follows that the arc element $\mathrm{d}\boldsymbol{l}$ takes the form

$$\mathrm{d}\boldsymbol{l} = (J\,\mathrm{d}s, \mathrm{d}n, \mathrm{d}z), \quad J = 1 - Kn.$$

We finally obtain the TW-equation and the velocity field in natural coordinates as

$$\begin{aligned} &\left(\frac{1}{JH}\psi_{ts}\right)_s + \left(\frac{J}{H}\psi_{tn}\right)_n + \psi_s\left(\frac{f}{H}\right)_n - \psi_n\left(\frac{f}{H}\right)_s = 0, \\ &\boldsymbol{u} = \left(-\frac{1}{H}\psi_n, \frac{1}{JH}\psi_s\right), \end{aligned} \tag{20.16}$$

subject to the boundary condition $\psi = 0$ along the lake shore.

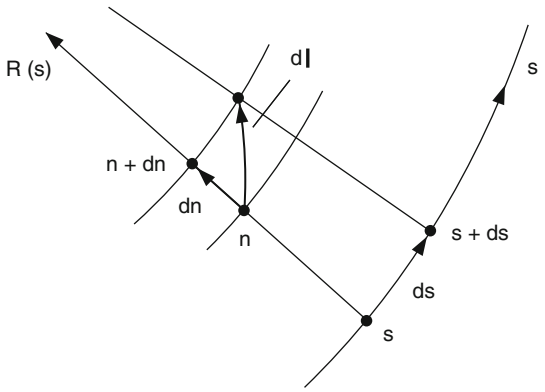

Fig. 20.3 Arc element in a natural coordinate system (from [37]).

20.2.5 Cartesian-Coordinate Correspondence Principle

It was mentioned that the TW-equation in elliptical coordinates is formally the same as that in Cartesian coordinates. Because also the boundary conditions of no flux are the same a correspondence principle can be applied to construct solutions in elliptical coordinates from those that are already known in Cartesian coordinates, of course, for the correspondence principle to apply the bathymetric functions in the two systems must also correspond. For instance, TW-solutions in hyperbolic channels can easily be deduced from corresponding solutions in straight channels and TWs in basins which are bounded by confocal ellipses and hyperbolas can be deduced from corresponding TW-solutions in rectangles.

Obviously, this correspondence principle follows from the invariance of the TW-operator under conformal mapping transformation. Indeed, the Cartesian-elliptic coordinate transformation is a conformal mapping.

20.3 An Almanac of Analytical Solutions

Having presented the TW-equation in the last section referred to several orthogonal coordinate systems, we proceed now to construct and physically interpret explicit solutions. The intention is to extract through this analysis the physical properties of TWs and to see in what respect the interpretations anticipated in the last chapter can be substantiated.

We shall discuss (1) circular basins with a topography being a function of the radial distance only (parabola, power-law), (2) elliptic basins with a parabolic bottom and an exponential shelf profile, (3) infinite channels and shelves and (4) TWs around an elliptical island. All these domains are characterized by the fact that the isobaths follow one coordinate line of the coordinate system, so that ordinary differential equations emerge. As a result the mathematical tool is solving two-point boundary-value problems.

20.3.1 Circular Basin with Parabolic Bottom

Following Lamb ([17] Sect. 212) we start our analysis of TWs in circular basins with the dimensionless equation (see also (11.24))

$$\nabla_H \cdot (h\nabla\zeta_t) + \mathcal{J}(h,\zeta) - \left(\frac{L}{R}\right)^2 \mathcal{L}\zeta_t = 0. \tag{20.17}$$

Because of the last term on the left-hand side, (20.17) describes TWs *and* gravity waves; the equation is scale dependent through this last term and allows in principle to estimate, how much barotropic gravity waves affect TWs. Here all quantities are

dimensionless except L and R, a typical length and the Rossby radius, respectively. In polar coordinates, (20.17) may be written as

$$(h\zeta_{rt})_r + \frac{1}{r}\left(\frac{h}{r}\zeta_{\theta t}\right)_\theta + \frac{h}{r}\zeta_{rt} + \frac{h_r}{r}\zeta_\theta - \frac{h_\theta}{r}\zeta_r - \left(\frac{L}{R}\right)^2 \mathcal{L}\zeta_t = 0, \qquad 0 < r < 1. \tag{20.18}$$

The boundary conditions (no mass flux at the outer boundary, finiteness of ζ at the origin) are

$$\zeta = \text{finite, at } r = 0; \qquad \zeta_r = 0, \text{ at } r = 1. \tag{20.19}$$

Consider a radial topography,

$$h = h(r) \tag{20.20}$$

and assume an azimuthal wave solution of the form

$$\zeta = Z(r)\exp[\mathrm{i}(m\theta - \sigma t)], \tag{20.21}$$

travelling counterclockwise around the basin; $\sigma = \omega/f$ is the dimensionless frequency and m the azimuthal wavenumber. With (20.20) and (20.21), the boundary value problem (20.18) and (20.19) assumes the form

$$\begin{aligned} &(hZ')' + \frac{h}{r}Z' - \left[\frac{m^2}{r^2}h + \frac{m}{\sigma}\frac{h'}{r} + \frac{1-\sigma^2}{(R/L)^2}\right]Z = 0, \quad 0 < r < 1, \\ &Z = \text{finite}, \quad r = 0; \quad Z' = 0, \quad r = 1. \end{aligned} \tag{20.22}$$

Primes denote differentiations with respect to r. From this equation the solutions presented by Lamb [17], Wenzel [42] and Saylor, Huang and Reid [34] can be obtained as special cases.

For the parabolic bottom profile,

$$h = 1 - r^2,$$

$Z(r)$ can be expressed in terms of a hypergeometric polynomial F ([17, Sect. 212], [1, 22])

$$Z(r) = A_{mj} r^m F(m + j;\ 1 - j;\ m + 1;\ r^2), \qquad m = 0, 1, 2, \ldots, \quad j = 1, 2, 3, \ldots, \tag{20.23}$$

in which A_{mj} is a free amplitude and σ satisfies the frequency relation

$$\frac{\sigma^2-1}{(R/L)^2}+\frac{2m}{\sigma}=2[2j(m+j-1)-m], \qquad (20.24)$$
$$m=0,1,2,\ldots,\ j=1,2,3,\ldots.$$

The frequency occurs in third order which corresponds to three wave types, two first class and one second class wave. Here, we concentrate on second class waves and will therefore exclude the case $m=0$. Equation (20.24) is then equivalent to

$$\frac{1}{\sigma}=\left\{\frac{2j(m+j-1)}{m}-1\right\}-\frac{\sigma^2-1}{2m(R/L)^2}.$$

The last term on the right-hand side represents the influence of the size effect via the external Rossby radius R and a length scale L. An order of magnitude for R is 500 km and an upper bound for L may be 200 km (Great Lakes), so $2(R/L)^2\geq 12$. The minimum value of the term in curly brackets is l, which suggests that the two first class modes entering via the size dependent term may be suppressed. Approximately, we may write, after neglection of the inertial motion ($\sigma=1$ for $j=1$) and transformation $n=j-2, n=0,1,\ldots$

$$\frac{1}{\sigma}=\frac{2(n+2)(m+n+1)}{m}-1, \qquad (20.25)$$
$$m=0,1,2,\ldots,\ n=0,1,2,3,\ldots,$$

We thus obtain the approximate frequencies and periods of Table 20.2. The real parts of the surface elevation ζ and the mass transport stream function ψ for the mode $(m,n)=(1,0)$ are given by

$$\begin{aligned}\zeta(r,t)&=Ar\left(1-\tfrac{3}{2}r^2\right)\cos(\theta-\sigma t),\\ \psi(r,t)&=Ar\left(1-r^2\right)\left(1-\sigma-\tfrac{3}{2}(1-3\sigma)r^2\right)\cos(\theta-\sigma t).\end{aligned} \qquad (20.26)$$

The streamlines of this solution and those of the (1,1)- and (2,0)- modes are sketched in Fig. 20.4. Mode structures are shown at $t=0,T/8,T/4$ (from top to bottom), where T is the period. The simplest fundamental mode has a period of 118 h and consists of two basin-wide gyres, a cyclonic and an anti-cyclonic vortex. The entire system of gyres rotates counterclockwise (on the N.H.) around the

Table 20.2 Frequencies and periods of TWs in a circular basin with parabolic bottom profile ignoring the size dependent term in (20.24) and computed with $f=2\pi/16.9\,\mathrm{h}$

m	$n=0$		$n=1$		$n=2$	
	σ	T [h]	σ	T [h]	σ	T [h]
1	0.143	118	0.0588	287	0.323	524
2	0.200	84.5	0.0909	186	0.0526	321
4	0.250	67.6	0.125	135	0.0769	220
∞	0.333	50.7	0.200	84.5	0.143	118

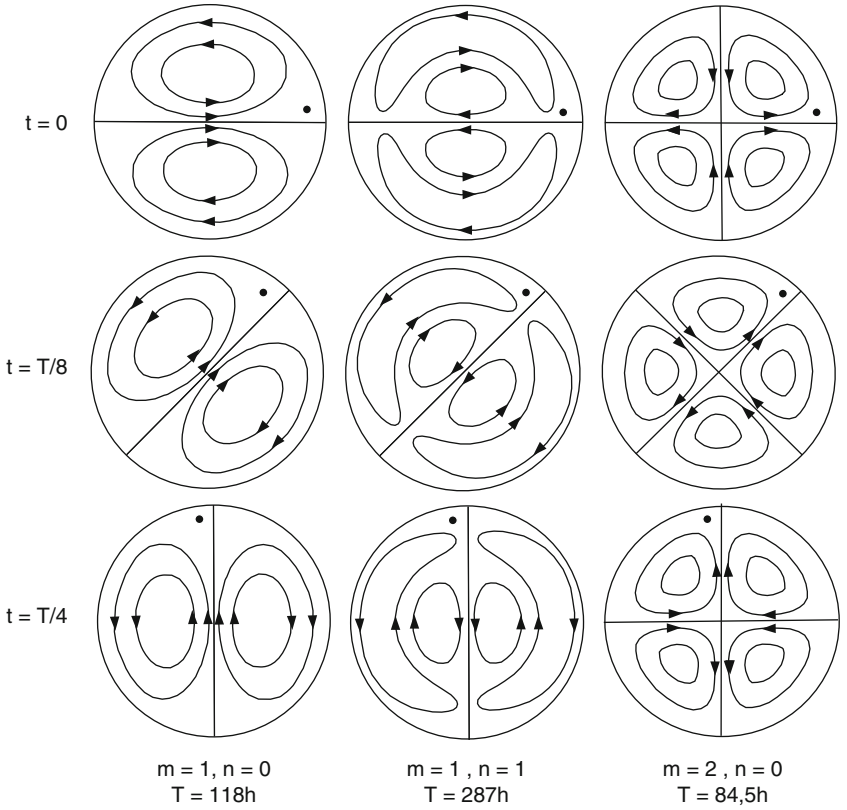

Fig. 20.4 Contour lines of the mass transport stream function of the three modes with the simplest wave structure. The gyres rotate anticlockwise (on the Northern hemisphere) around the basin (from [39]). © Springer, Berlin, reproduced with permission

basin. If we imagine a current meter positioned at the centre position, then it is seen from the streamlines in the three panels on the left that the current vector rotates in the anticlockwise direction in this motion. On the other hand, for a current meter, moored close to the shore line, one may infer from the same three panels that near shore currents rotate in the clockwise direction. This behaviour can also be corroborated by constructing the horizontal current tracks by progressive vector diagrams. This is exactly the current pattern described by Saylor et al. [34] in Southern Lake Michigan, but the period of 118 h is too large to fit the 100 h, inferred from the measurements. An improved fit to the observations can be obtained by adjusting the topography accordingly. This will be shown below.

The next mode (right column in Fig. 20.4) has a period of $T = 84.5$ h and four basin filling gyres which are separated by a pair of perpendicular straight lines which rotate cyclonically around the basin. It follows easily by inspection of Fig. 20.4 that the horizontal current in the centre of the basin must vanish. However, apart from

this 'stagnation point', the current rotates counterclockwise in the lake interior, but clockwise close to the shore circle. The four gyres have alternating orientation of rotation. From the complexity of the motion of this still rather simply structured current pattern it easily follows that identification of this mode from moored instruments must be difficult.

Complexity further increases for mode (1,1) in the middle column of Fig. 20.4. Now, $T = 287\,\mathrm{h}$, and besides one radial separation line, there exists also a separating circle. A double pair of counter rotating gyres circles cyclonically around the basin, performing a complete revolution in 287 h. At the lake centre the current rotates counterclockwise, whilst close to the outer shoreline this rotation is clockwise. Here, it must become very difficult to identify this current structure by field measurements.

In Lake Michigan, the mode structure that was observed is the (1, 0)-mode (Fig. 20.4, left column). It will now be shown that the period of this mode can be varied by accordingly changing the radial profile of the bathymetry.

20.3.2 Circular Basin with a Power-Law Bottom Profile

The following analysis is due to Saylor et al. [34] who investigated the influence of topography gradients on the periods of topographic wave motion. They used the profile

$$h(r) = (1 - r^q), \quad 0 \le r \le 1, \quad q > 0. \tag{20.27}$$

Varying the exponent q yields an entire sequence of profile geometries with strong and weak topography gradients. For $q = 1$ the radial depth profile is conical, for $q = 2$ it is parabolic, for $q > 2$ it becomes blunt and for $q \to \infty$ it approaches constant depth. On the other hand, for $0 < q \le 1$ the profile has a vertex at the centre and (except for $q = 1$) a convex curvature similar to the exponential profile often used in shelf wave analysis. With $\psi = \psi(r)\exp(\mathrm{i}(m\theta - \sigma t))$, use of the TW-equation in cylindrical coordinates, (20.11), and a trial solution

$$\psi(r) = Ar^m h^2(r), \tag{20.28}$$

(which satisfies the boundary conditions) the depth profile must fulfil the differential equation

$$h'' + \frac{3m + 2 - \frac{m}{\sigma}}{2r} h' = 0. \tag{20.29}$$

Equation (20.27) is compatible with this provided that

$$\sigma = \frac{m}{3m + 2q}, \tag{20.30}$$

Table 20.3 Topography effect on the dimensionless eigenfrequency of the three first modes in the model of Saylor et al. [34], according to (20.30) using $f = 2\pi/16.9\,\mathrm{h}$

Profile	q	$m=1$		$m=2$		$m=3$	
		f/ω	T [h]	f/ω	T [h]	f/ω	T [h]
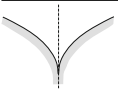	0.5	4	**67.6**	3.5	**59.2**	3.333	**56.3**
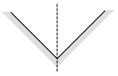	1.0	5	**84.5**	4	**67.6**	3	**50.7**
	2.0	7	**118.3**	5	**84.5**	4	**67.6**
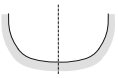	3.0	9	**152.1**	6	**101.4**	5	**84.5**
	∞	0	∞	0	∞	0	∞

which is the frequency–wavenumber relation for the prescribed topographic profile. Table 20.3 lists the frequencies for a sequence of topography parameters q and the wavenumbers $m = 1, 2, 3$. The table indicates that *the topography has a dominant effect on the periods*. The solutions

$$\psi(r) = Ar^m(1 - r^q), \quad \sigma = \frac{m}{3m + 2q}$$

embrace all those motions whose stream function ψ has no radial nodal circle. Hence, they contain in particular the solutions for the parabolic depth profile as shown in the left and right columns of Fig. 20.4.

The above solutions have been used to explain the observations in Southern Lake Michigan. Figure 19.3 in the last chapter displays the bathymetric profile for Southern Lake Michigan and power law profiles with $q = 1$ and $q = 2$ fit the mean bathymetry pretty well. According to Table 20.3, these two profiles yield mode periods of 84.5 and 118.3 h. A somewhat better fit is obtained with a profile $q = 1 + \varepsilon, \varepsilon = 0.35$ and yields $f/\omega = 5.7$ and $T = 96.3\,\mathrm{h}$.

Wenzel [42] made an attempt to interpret the wind-driven currents in the Bornholm basin of the Baltic Sea as obtained as a free TW (see Fig. 19.11 in the previous chapter). He inferred from Fig. 19.11 and his own computations that the free TW within the Bornholm basin must be between 11 and 14 days. Preliminary calculations indicated that the $(n, m) = (2, 2)$ mode will generate a period between 11 and 14 days. Wenzel approximated the mean bathymetry of the Bornholm basin with a radial depth profile parameterized as a tenth degree polynomial and computed the period for this (2, 2)-mode to be 12.6 days. The radial distribution of the free

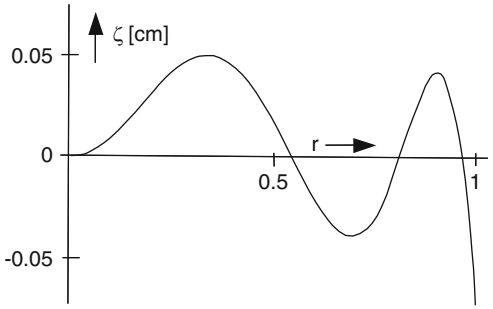

Fig. 20.5 Radial cross-section of the surface elevation of the (2,2)-mode in a circular basin with a depth profile represented by a polynomial of degree 10 (from [42])

surface elevation corresponding to Wenzel's polynomial of tenth degree is shown in Fig. 20.5.

20.3.3 Elliptic Basin with Parabolic Bottom

Most lakes are long in one direction and not well approximated by circles. It is interesting, therefore, to see how the periods and mode structures of TWs depend on the aspect ratio (i.e. the width to length ratio) of the basins.

We consider the TW-equation in dimensionless form and in Cartesian coordinates

$$\begin{gathered}(h^{-1}\Psi_{xt})_x + (h^{-1}\Psi_{yt})_y - h_x^{-1}\Psi_y + h_y^{-1}\Psi_x = 0, \quad \text{in}\mathcal{D}, \\ \Psi = 0, \quad \text{on} \quad \partial\mathcal{D},\end{gathered} \tag{20.31}$$

and choose a parabolic depth profile

$$h = \tfrac{1}{2}((1-a)x^2 + (1+a)y^2) - 1, \tag{20.32}$$

where $A(h) = \sqrt{2(h+1)/(1-a)}$ and $B(h) = \sqrt{2(h+1)/(1+a)}$ are the semi-axes of the elliptic depth-contours. These have all identical aspect ratios

$$r = \frac{B(h)}{A(h)} = \sqrt{\frac{1-a}{1+a}}, \quad a := \frac{1-r^2}{1+r^2}, \tag{20.33}$$

and the profile has a maximum depth $\mid h \mid_{\max} = 1$. The basin is bounded by the zero depth contour line, an ellipse with $A(0)$ and $B(0)$ as semi-axes.

The following analysis is due to Ball [3] . With (20.32) and the transformation

$$\psi = h^{-2}\Psi$$

it is straightforward to show that (20.31) takes the form

$$\begin{aligned} &4\psi_t + 3\big((1-a)x\psi_{xt} + (1+a)y\psi_{yt}\big) + h(\psi_{xxt} + \psi_{yyt}) \\ &\qquad + (1-a)x\psi_y - (1+a)y\psi_x = 0, \qquad \text{for } h < 0, \\ &\psi = \text{finite}, \qquad\qquad\qquad\qquad\qquad\quad \text{for } h = 0. \end{aligned} \tag{20.34}$$

Note that the boundary condition $\Psi = 0$ along $\partial\mathcal{D}$ necessarily requires that ψ is bounded on $\partial\mathcal{D}$. The velocities are given by

$$\begin{aligned} u &= -h^{-1}(h^2\psi)_y = -2h_y\psi - h\psi_y, \\ v &= h^{-1}(h^2\psi)_x = 2h_x\psi - h\psi_x. \end{aligned}$$

The advantage of the introduction of the stream function ψ is that (20.31) transforms into a differential equation with the following special property. Suppose, ψ is an even (odd) polynomial of degree N, then the differential equation (20.34) generates again an even (odd) polynomial of the same degree.

Taking advantage of this fact, we consider first a polynomial with degree $N = 0$, i.e. a constant ψ_{00} which obviously satisfies (20.34). This is a *simple steady gyre* with the velocity field

$$(u, v) = 2\psi_{00}(-(1+a)y, \ \ (1-a)x),$$

representing an elliptical rotation with constant vorticity $4\psi_{00}$. Maximum speeds are experienced along the shore-line.

More insight provides the choice of a homogeneous odd polynomial of degree $N = 1$, the *linear Ball-mode*:

$$\psi_1 = \psi_{10}(t)x + \psi_{01}(t)y. \tag{20.35}$$

Substitution into (20.34) yields the coupled system

$$\begin{aligned} (7-3a)\dot{\psi}_{10} + (1-a)\psi_{01} &= 0, \\ (7+3a)\dot{\psi}_{01} - (1+a)\psi_{10} &= 0, \end{aligned} \tag{20.36}$$

with $(\ \ )^{\cdot} \equiv \mathrm{d}/\mathrm{d}t$. Assuming a harmonic time evolution $e^{-\mathrm{i}\sigma t}$ for both coefficient functions, (20.36) allows nontrivial ψ_{10} and ψ_{01} if and only if[2]

$$\sigma^2 = \frac{1-a^2}{49-9a^2}. \tag{20.37}$$

[2] With $\psi_{ij} = \psi_{ij}^{(0)}\mathrm{e}^{-\mathrm{i}\sigma t}$ $(i, j = 0, 1)$, (20.36) can be transformed to a homogeneous linear system for $\psi_{ij}^{(0)}$ which possesses a solution provided that its determinant vanishes. Equation (20.37) makes this determinant to vanish.

Table 20.4 Frequencies and periods of the linear and quadratic Ball-modes for various aspect ratios r. The periods are calculated with $f = 2\pi/16.9\,\mathrm{h}$

r	a	Linear		Quadratic	
		σ	T [h]	σ	T [h]
1.0	0	0.143	118	0.200	84.5
0.67	0.385	0.134	126	0.190	88.8
0.50	0.600	0.118	143	0.173	97.7
0.33	0.800	0.091	185	0.139	121
0.1	0.980	0.031	542	0.051	335
0	1	0	∞	0	∞

This relation describes the dependence of the frequency on the aspect ratio parameter r (via a, see (20.33)). Table 20.4 lists the periods obtained with (20.37). Obviously, $a = 0$ recovers the solution for the circle with parabolic bottom profile. Smaller a results in smaller σ; consequently, the more elongated the ellipses become the larger will be the periods. In view of observational results for Lake of Lugano reported in Chap. 19, this is unfortunate as these lakes are long and narrow, and measurements point at oscillations with periods of 3–4 days. This is smaller than the 118 h obtained as a *lower* bound for the fundamental linear Ball mode.

The linearity of (20.35) implies that the line $\psi_1 = 0$ which separates vortices of different signs is a straight line which, owing to (20.36), rotates anticlockwise around the basin. Figure 20.6a shows the time evolution of this mode. The structure of the wave pattern i.e. the number of gyres is conserved in the course of a wave cycle. This is in accord with the wave patterns found in the circular basin.

To obtain the next higher mode, we select an even polynomial of degree $N = 2$.

$$\psi_2 = \psi_{00} + \psi_{20}x^2 + \psi_{11}xy + \psi_{02}y^2, \tag{20.38}$$

with the time dependent coefficient functions $\psi_{mn}(t)$. Equation (20.38) characterizes the *quadratic Ball-mode*. Substitution into (20.34) and equating equal powers of x and y, respectively, yields the system

$$\begin{aligned}
(11-7a)\dot{\psi}_{20} + (1-a)\dot{\psi}_{02} + 2(1-a)\psi_{11} &= 0,\\
10\dot{\psi}_{11} + (1-a)\psi_{02} - (1+a)\psi_{20} &= 0,\\
(11+7a)\dot{\psi}_{02} - (1+a)\dot{\psi}_{20} - 2(1+a)\psi_{11} &= 0,\\
2\dot{\psi}_{00} + \dot{\psi}_{20} - \dot{\psi}_{02} &= 0,
\end{aligned} \tag{20.39}$$

which allows periodic solutions proportional to $\mathrm{e}^{-\mathrm{i}\sigma t}$ provided that

$$\sigma\left(5\sigma^2\left(5-2a^2\right) - \left(1-a^2\right)\right) = 0.$$

Again, there is a steady solution $\sigma = 0$ and an oscillating solution with

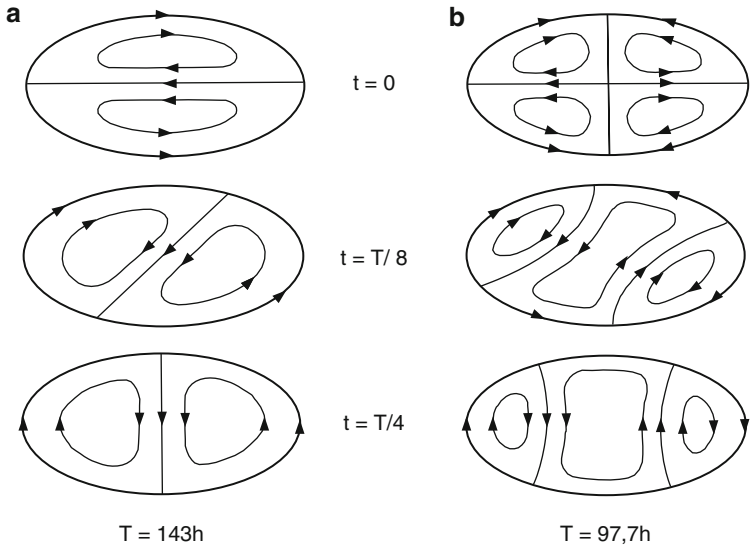

Fig. 20.6 Mass transport streamline patterns for the 'linear' (**a**) and 'quadratic' (**b**) mode of the TW-equation in an elliptic basin with parabolic bottom profile (from Ball (1965) [3]). © Cambridge University Press, reproduced with permission

$$\sigma^2 = \frac{1-a^2}{5(5-2a^2)}. \tag{20.40}$$

Table 20.4 collects frequencies and periods for several aspect ratios r. For a fixed aspect ratio the periods of the quadratic mode are smaller than those of the fundamental linear mode.

As (20.39) indicates, a steady solution must have

$$\psi_{11}^{st} = 0 \quad \text{and} \quad \psi_{02}^{st} = \frac{1+a}{1-a}\psi_{20}^{st},$$

and hence

$$\psi_2^{st} = \psi_{00} + A((1-a)x^2 + (1+a)y^2),$$

where ψ_{00} and A are constants. $\psi_{00} \neq 0,\ A = 0$ recovers the simple steady gyre whereas $\psi_{00} = 0,\ A \neq 0$ yields the steady second order solution

$$\Psi_2^{st} = h^2\psi_2^{st} = 2Ah^2(h+1). \tag{20.41}$$

This stream function vanishes along the boundary ($h = 0$) and at the centre $(x, y) = (0, 0)$ and is positive otherwise; furthermore, its value is constant along similar ellipses and assumes a maximum value along the ellipse with $h = -2/3$ between the centre and the shore line, Fig. 20.7a. The steady flow corresponding to

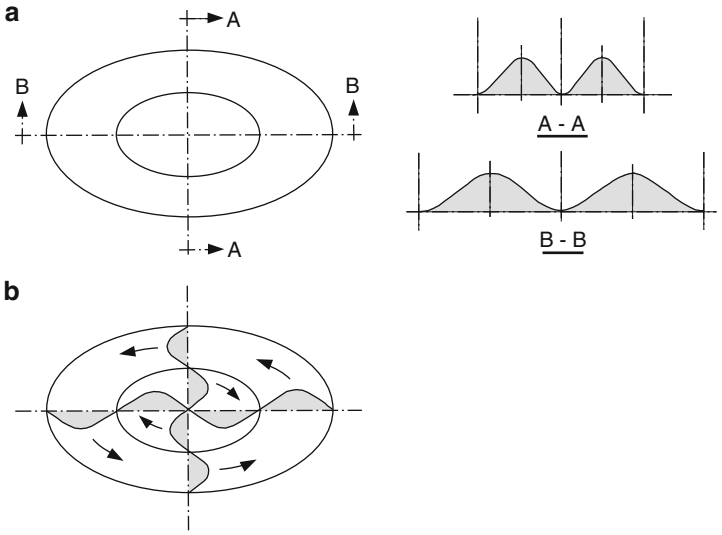

Fig. 20.7 (**a**) Distribution of the mass transport stream function and (**b**) of the associated velocity field of the 'quadratic' steady solution (20.41) (from [39]). © Springer, Berlin, reproduced with permission

the solution (20.41) is qualitatively indicated in Fig. 20.7b. An anticyclonic elliptical gyre in the centre is surrounded by an elliptical ring of cyclonically rotating fluid.

Oscillating solutions are obtained by constructing the eigenvector of (20.39) corresponding to the frequency given by (20.40). We quote Ball's result (real. part)

$$\Psi_2 = h^2\psi_2 = Ah^2\big[((1+a)(3-2a)y^2 - (1-a)(3+2a)x^2 + a)\sin\sigma t + (6(1-a^2)/5\sigma)xy\cos\sigma t\big]. \tag{20.42}$$

For $t = 0$ the nodal lines $\psi_2 = 0$ are the lines $x = 0$ and $y = 0$, whereas for $t > 0$ they are rotating hyperbolas (note that $0 < a < 1$). As illustrated in Fig. 20.6b the wave pattern starts with four gyres of which the two positive vortices merge together building three gyres in the basin for most part within a period. The structure of this mode is therefore *not conserved* during the cycle. This is a new phenomenon due to the influence of the aspect ratio parameter a, from [39].

20.3.4 Elliptic Basin with Exponential Bottom

20.3.4.1 Basin with Central Island

In the previous sections, TWs in circular and specific elliptical domains were discussed. Whereas the model of Saylor et al. [34] uncovered a conspicuous dependence

of the frequencies on the topography, Ball's model enabled investigation of the effect of the aspect ratio. In this section, we present models which account for both bathymetric parameters and therefore permit a more realistic modelling of the lake basin.

To introduce a topography parameter in an elliptical basin, Mysak [27] set out to study the TW-equation in elliptical coordinates (ξ, η). Basically, this was a generalization of Saylor's choice who studied a circular domain in polar coordinates and thus lost the possibility of incorporating into the analysis an aspect ratio parameter.

The derivation of the TW-equation in the elliptic coordinate system has already been given in (20.14); the result was

$$\begin{aligned} &(h^{-1}\psi_{\xi t})_\xi + (h^{-1}\psi_{\eta t})_\eta + \psi_\xi (h^{-1})_\eta - \psi_\eta (h^{-1})_\xi = 0, \\ &\qquad\qquad 0 < \xi < \xi_S,\ 0 \le \eta \le 2\pi, \\ &\psi = 0, \qquad\qquad \xi = \xi_S,\ 0 \le \eta \le 2\pi, \end{aligned} \tag{20.43}$$

where ξ and η are the radial and azimuthal coordinates, ξ_S is the elliptic shore-line. Note that the water depth $H = H_0 h$ has been scaled here with any convenient H_0, since the TW-equation is scale invariant. Note, moreover, that we have scaled time with f which is constant on the f-plane. Furthermore, ξ_S is related to the aspect ratio parameter r through

$$r = \frac{B}{A} = \frac{a \sinh \xi_S}{a \cosh \xi_S} = \tanh \xi_S . \tag{20.44}$$

The velocity field can easily be computed from the stream function ψ by means of the formulae

$$u_\xi = -(hJ)^{-1}\psi_\eta, \quad u_\eta = (hJ)^{-1}\psi_\xi, \tag{20.45}$$

and the definitions of a and the Jacobian J are listed in Table 20.1.

Consider now a topography with constant depth along lines of constant ξ (confocal ellipses), and hence has $h_\eta = 0$. For this case (20.43) is a differential equation with constant coefficients provided

$$h_\xi / h = \text{const} .$$

Therefore, we select an exponential depth-profile (shelf) of the form $h(\xi) = \exp(-b\xi)$, $b > 0$. Introducing the separation of variables solution

$$\psi(\xi, \eta) = F(\xi) \mathrm{e}^{\mathrm{i}(m\eta - \sigma t)}, \tag{20.46}$$

with integer $m > 0$, (2π-periodicity in η), and dimensionless frequency $\sigma = \omega / f$, (20.43) becomes

$$F'' + bF' + \left(\frac{mb}{\sigma} - m^2\right) F = 0, \qquad (\ )' = \frac{\mathrm{d}}{\mathrm{d}\xi}. \tag{20.47}$$

This second order ordinary differential equation requires two boundary conditions. No mass transport through the basin boundary ξ_S leads to

$$F(\xi_S) = 0. \tag{20.48}$$

To obtain the second boundary condition we consider an elliptic basin with a *central island* in the domain $0 \le \xi \le \xi_I$. Hence, an additional no-flux condition must hold at ξ_I,

$$F(\xi_I) = 0. \tag{20.49}$$

Mysak's choice was the limit of a barrier-like island $\xi_I = 0$; here ξ_I is retained as a further bathymetric variable. Equation (20.47) has the general solution

$$F(\xi) = \mathrm{e}^{-b\xi/2}(A \sin \lambda\xi + B \cos \lambda\xi), \tag{20.50}$$

with $\lambda^2 = mb/\sigma - m^2 - b^2/4$, and the trigonometric functions imply the frequency of the mth azimuthal mode to be bounded by

$$0 < \sigma_m < \frac{mb}{m^2 + \frac{b^2}{4}}. \tag{20.51}$$

The lower bound can be obtained by multiplying (20.47) with F and integrating the resulting equation from $\xi = \xi_I$ to $\xi = \xi_S$. This yields the Rayleigh quotient

$$\frac{mb}{\sigma} = \frac{\int_{\xi_I}^{\xi_S} (-F''F + m^2F^2)\mathrm{d}\xi - \frac{b}{2}\int_{\xi_I}^{\xi_S} \frac{\mathrm{d}}{\mathrm{d}\xi}(F^2)\mathrm{d}\xi}{\int_{\xi_I}^{\xi_S} F^2 \mathrm{d}\xi} = \frac{\int_{\xi_I}^{\xi_S} (F'^2 + m^2F^2)\mathrm{d}\xi}{\int_{\xi_I}^{\xi_S} F^2 \mathrm{d}\xi} > 0\,.$$

The boundary conditions (20.48) and (20.49) quantize the radial wavenumber λ such that[3]

$$\lambda = \frac{n\pi}{\xi_S - \xi_I}, \quad n = 1, 2, \ldots.$$

With this and the definition of λ we obtain the eigenfrequency as a function of the three bathymetric parameters ξ_S, ξ_I, b

[3] Equation (20.48) implies that $B = -A\tan(\lambda\xi_S)$, and then (20.49) yields $(\tan(\lambda\xi_I) - \tan(\lambda\xi_S)) = 0$, or $\tan(\lambda\xi_S) = \tan(\lambda\xi_I)$ so, $\lambda\xi_S = (\lambda\xi_I + n\pi)$, $n = 1, 2, \ldots$.

$$\sigma = \frac{mb}{m^2 + \frac{b^2}{4} + \left(\frac{n\pi}{\xi_S - \xi_I}\right)^2}. \tag{20.52}$$

Selecting the aspect ratio r determines ξ_S via (20.44). For the evaluation of the eigenfrequency (20.52) one then also needs ξ_I/ξ_S, (m,n) and b. Table 20.5 lists the eigenfrequencies for particular selections of values for these parameters, whilst the finite shoreline depth, $h(\xi_S) = 0.1$, and the depth at the island, $h(\xi_I) = 1$ are kept constant. $\xi_I/\xi_S = 0$ recovers the case studied by Mysak et al. [28]. It is seen in Table 20.5 that the influence of the aspect ratio on σ and T is very strong; frequencies decrease and periods increase with decreasing aspect ratio; moreover, for fixed aspect ratio but varied ξ_I the barrier island ($\xi_I = 0$, zero width but finite length) eigenperiods reach an upper bound for the latter case. Figure 20.8 displays contour lines for the stream functions ψ_{11} and ψ_{12} for the case of an elliptic basin with a barrier island. It is interesting to compare this figure with Fig. 20.6, which shows the corresponding Ball modes. For the (1, 1)-mode, the two oppositely rotating gyres move (on the N.H.) cyclonically around the basin (left column in Fig. 20.8), but the barrier island constrains their geometry considerably, particularly when the gyres move around the long ends of the basin. Close to the two focal points of the ellipse the streamlines are clustered together, which indicates large velocities. For the (2, 1)-mode, two counter rotating pairs of gyres rotate again cyclonically around the basin; None of these gyres merge together during a mode cycle, quite contrary

Table 20.5 Influence of the aspect ratio and relative island width on the eigenfrequencies and mode periods according to (20.52). The periods are calculated with $f = 2\pi/(16.2\,\text{h})$

r	ξ_S	ξ_I/ξ_S	b	$(m,n) = (1,1)$		$(m,n) = (2,1)$		$(m,n) = (2,2)$	
				σ	T[h]	σ	T[h]	σ	T[h]
		1/2	1.74	0.235	68.9	0.335	48.4	0.127	127.6
0.99	2.65	1/3	1.31	0.284	57.0	0.344	47.1	0.153	105.9
		0	0.87	0.335	48.4	0.311	52.1	0.177	91.5
		1/2	5.72	0.082	197.6	0.156	103.8	0.045	360.0
0.67	0.81	1/3	4.29	0.108	150.0	0.200	81.0	0.059	274.6
		0	2.86	0.156	103.8	0.269	60.2	0.085	190.6
		1/2	8.38	0.056	289.3	0.110	147.3	0.031	522.6
0.5	0.55	1/3	6.29	0.074	218.9	0.144	112.5	0.041	395.1
		0	4.19	0.110	147.3	0.204	79.4	0.060	270.0
		1/2	13.3	0.036	450.0	0.071	228.2	0.019	852.6
0.33	0.35	1/3	9.97	0.047	344.7	0.093	174.2	0.026	623.1
		0	6.64	0.071	228.2	0.137	118.2	0.039	415.4
		1/2	45.9	0.010	1620.0	0.021	771.4	0.006	2700.0
0.1	0.10	1/3	34.4	0.014	1157.1	0.027	600.0	0.008	2025.0
		0	22.9	0.021	771.4	0.041	395.1	0.011	1472.7

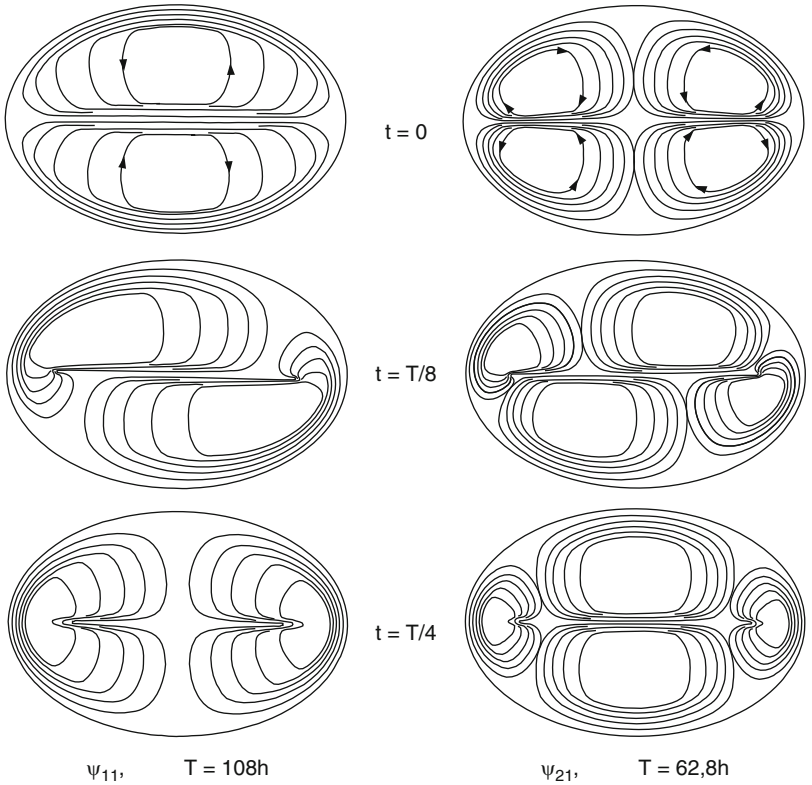

Fig. 20.8 Contours of the stream functions ψ_{11} and ψ_{21} for an elliptic basin with a barrier. The parameters are $\xi_S = 0.805$, $\xi_I = 0$, $b = 2.86$ (from [27]).

to the analogous case in the (2, 1)-mode of the Ball solution without an island, but an accumulation of contour lines of ψ also occurs here in the vicinity of the focal points. Hence, these points will be critical with respect to the velocity field.

Inserting the real part of (20.46) into (20.45) yields

$$u_\xi = \frac{1}{J} m \mathrm{e}^{b\xi/2} \sin\left(\lambda(\xi - \xi_I)\right) \sin(m\eta - \sigma t),$$
$$u_\eta = -\frac{1}{J} \mathrm{e}^{b\xi/2} [\lambda \cos\left(\lambda(\xi - \xi_I)\right) - \frac{b}{2} \sin\left(\lambda(\xi - \xi_I)\right)] \cos(m\eta - \sigma t),$$

with $J = a\sqrt{\sinh^2 \xi + \sin^2 \eta}$ and $\lambda = n\pi/(\xi_S - \xi_I)$. Indeed, for u_ξ, u_η the limits $(\xi_I, \eta) \to (\xi_I, \pi)$ or $(\xi_I, 0)$ do not exist for $\xi_I \to 0$.

20.3.4.2 Basin Without Island

The analysis which is outlined here extends the theory of the above Sect. 20.3.4.1 and is due to Mysak et al. [28] with corrections by Johnson [14].

It is characteristic of the elliptical coordinate system that the formulation of the boundary condition at the centre $\xi = 0$ is subtle. It is necessary to have both ψ and $\nabla\psi$ continuous 'across' $\xi = 0$,[4] in order that the velocity field takes physically meaningful values. Therefore, ansatz (20.46) is too restrictive to fulfil the extended boundary condition at the centre. The trial solution (20.46) is complemented by the contribution with negative integers $m < 0$. Thus following Johnson [14], we write

$$\psi(\xi,\eta) = F_1(\xi)\mathrm{e}^{\mathrm{i}(m\eta-\sigma t)} + F_2(\xi)\mathrm{e}^{\mathrm{i}(-m\eta-\sigma t)}, \quad m = 1,2,\ldots. \tag{20.53}$$

Again using the shelf profile $h(\xi) = \exp(-b\xi)$, $h_\eta = 0$, (20.43) is equivalent to the system

$$\begin{aligned} F_1'' + bF_1' + \left(\frac{mb}{\sigma} - m^2\right) F_1 &= 0, \\ F_2'' + bF_2' + \left(-\frac{mb}{\sigma} - m^2\right) F_2 &= 0, \end{aligned} \tag{20.54}$$

with $(\ )' = \mathrm{d}/\mathrm{d}\xi$ and the four boundary conditions

$$\begin{aligned} &F_1(\xi_S) = 0, \quad F_2(\xi_S) = 0, \\ &F_1(0) - F_2(0) = 0, \\ &F_1'(0) + F_2'(0) = 0. \end{aligned} \tag{20.55}$$

Equation $(20.55)_{2,3}$ express that ψ and ψ_η are continuous across the line $\xi = 0$. System (20.54) together with $(20.55)_{1,2}$ constitutes a well-posed boundary value problem of second order in the interval $[0, \xi_S]$, which can be solved in terms of exponential functions. Condition $(20.55)_3$ will select the eigenfrequencies.

Because of the form of (20.54) and (20.55) the radial functions can be taken as purely real, and it can be verified that the real solutions

$$\begin{aligned} F_1(\xi) &= \mathrm{e}^{-\frac{b}{2}\xi}\sin(\lambda_1(\xi_S - \xi)), \quad F_2(\xi) = \mathrm{e}^{-\frac{b}{2}\xi}\sinh(\lambda_2(\xi_S - \xi)), \\ \lambda_1^2 &= \frac{bm}{\sigma} - m^2 - \frac{1}{4}b^2, \qquad \lambda_2^2 = \frac{bm}{\sigma} + m^2 + \frac{1}{4}b^2, \end{aligned} \tag{20.56}$$

fulfil (20.54) and $(20.55)_{1,2}$. Equation $(20.55)_3$ eventually requires

$$\lambda_1 \cot \lambda_1\xi_S + \lambda_2 \coth \lambda_2\xi_S + b = 0, \tag{20.57}$$

[4] Clearly, in elliptical coordinates $\xi \geq 0$. Continuity of a quantity $\phi(\xi,\eta)$ 'across' $\xi = 0$ means $\lim_{\xi\downarrow 0}\phi(\xi, 2\pi - \eta) = \lim_{\xi\downarrow 0}\phi(\xi,\eta)$, $0 < \eta < 2\pi$.

Table 20.6 Eigenfrequencies and periods of the first four TW-modes in an elliptical basin with exponential bottom profile. The parameters are $\xi_S = 0.805$ and $b = 2.86$. The periods are calculated with $f = 2\pi/(16.2\,\mathrm{h})$

m	$n=1$		$n=2$		$n=3$		$n=4$	
	σ	T [h]	σ	T [h]	σ	T [h]	σ	T [h]
1	0.201	80.6	0.0541	299.4	0.0235	689.4	0.0130	1246.1
2	0.327	49.5	0.102	158.8	0.0458	353.7	0.0257	630.4
3	0.376	43.1	0.139	116.5	0.0659	245.8	0.0375	432.0
4	0.379	42.7	0.165	98.2	0.0830	195.2	0.0483	335.4

from which the eigenfrequencies can be calculated. Note that for sufficiently large m and σ, λ_1^2 in (20.56) becomes negative and F_1 takes the same form as F_2. The cotangent in (20.57) equally transforms into a coth, and then real eigenfrequencies are no longer allowed; σ is thus bounded according to (20.51). Equation (20.57) yields a countable set of eigenfrequencies for given topography parameter b and azimuthal wavenumber m and for each σ the inequalities

$$(n - \tfrac{1}{2})\pi < \lambda_1(\sigma)\xi_S < n\pi, \quad n = 1, 2, 3, \ldots$$

must hold. The upper and lower bounds in these inequalities exclude $\cot(\lambda_1\xi_S)$ and $\coth(\lambda_1\xi_S)$ from approaching infinity. Table 20.6 gives eigenfrequencies and eigenperiods calculated by Johnson [14] for $\xi_S = 0.805$ (ellipse with aspect ratio $r = 2/3$) and $b = 2.86$ (shore line depth $h(\xi_S) = 0.1$). It is seen that the periods decrease with increasing m and increase with increasing n. Figure 20.9 displays the streamline contours of the modes with $(m, n) = (1, 1), (2, 1)$ and $(1, 2)$. The patterns resemble those of Ball's model or Mysak's island model and modifications here are due to the different choice of the topography (with respect to Ball [3]) and of the central boundary condition (with respect to Mysak [28]). Note also that the different boundary conditions at the line connecting the foci compared to the corresponding Mysak-solution are responsible for the variable numbers of gyres in the (2, 1)-mode (displayed in the middle column of Fig. 20.9).

The influence on the fundamental mode of the variation of both bathymetric parameters ξ_S (via aspect ratio) and b (via shore line depth) is shown in Table 20.7. The influence due to topography is dominant.

Table 20.8 compares the eigenfrequencies and eigenperiods obtained with (20.52) for an elliptical basin with a barrier ($\xi_S = 0$ Mysak's solution [27] and without a barrier [14] and for different aspect ratios and shoreline depths. It is seen that the estimate is better for large aspect ratio and small shoreline depth. This latter behaviour was also observed with the circular basin with power law bathymetry, see Table 20.3. Indeed, for the elliptical basin with $h(\xi_S) = 1$, the basal topography would be flat and the period would be infinitely large.

In exactly this spirit, Johnson extended his elliptic model by choosing the profile

$$h(\xi) = \begin{cases} \mathrm{e}^{-b(\xi-\xi_B)}, & \xi_B \le \xi \le \xi_S, \\ 1, & 0 \le \xi \le \xi_B, \end{cases} \tag{20.58}$$

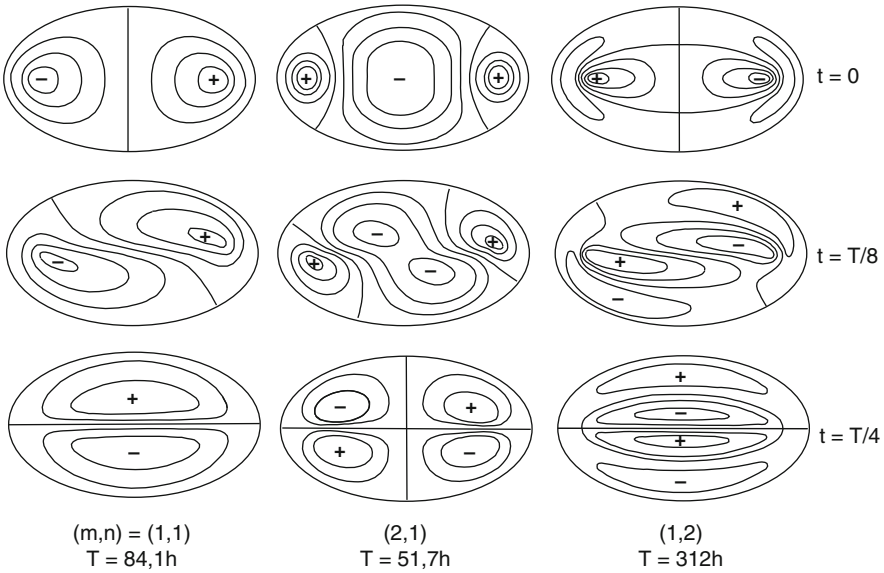

Fig. 20.9 Stream line contours of the three lowest modes in an elliptical lake with exponential bottom. The periods are calculated with $f = 2\pi/(16.9\,\mathrm{h})$ (from [14]). © Taylor & Francis, http://www.informaworld.com, reproduced with permission

Table 20.7 Bathymetry and aspect ratio effects on the frequency and period of the (1,1)-mode of the TW. The periods are calculated with $f = 2\pi/(16.2\,\mathrm{h})$

r	$h(\xi_S) = 0.1$		0.2		0.5		0.8	
	σ	T [h]	σ	T [h]	σ	T [h]	σ	T [h]
0.99	0.380	42.6	0.281	57.7	0.128	126.6	0.0422	383.9
0.67	0.201	80.6	0.158	102.5	0.0738	219.5	0.0270	600.0
0.50	0.143	113.3	0.113	143.4	0.0569	284.7	0.0197	822.3
0.33	0.0921	175.9	0.0732	221.3	0.0371	436.7	0.0129	1255.8
0.1	0.0270	600.0	0.0216	750.0	0.0110	1472.7	0.00384	4218.8

Table 20.8 Comparison of the eigenfrequencies and periods of the first TW-mode in an elliptical basin with a barrier and a basin without island. The periods are calculated with $f = 2\pi/(16.2\,\mathrm{h})$

r	$h(\xi_S) = 0.1$		σ	T [h]	$h(\xi_S) = 0.5$		σ	T [h]
	$\sigma_{\mathrm{barrier}}$	T_{barrier} [h]			$\sigma_{\mathrm{barrier}}$	T_{barrier} [h]		
0.99	0.335	48.2	0.380	42.6	0.108	150.0	0.128	126.6
0.67	0.156	103.8	0.201	80.6	0.052	311.5	0.078	207.7
0.50	0.110	147.3	0.143	113.3	0.037	437.8	0.057	284.2
0.33	0.071	228.2	0.092	176.1	0.024	675.0	0.037	437.8
0.1	0.021	771.4	0.027	600.0	0.007	2314.3	0.011	1472.7

which has a flat bottom in its centre. He shows that by increasing the central flat area but holding shoreline depth and aspect ratio of the basin fixed, the eigenperiod is increased. Given the past experience, this behaviour was to be expected.

We close this section by reporting an attempt of interpretation of basin wide wave signals in the 100–110-h period range for Lake Zurich as measured in a field campaign in August–September 1978 for a description of the low-frequency response, see [37]. Mysak et al. [28] made an attempt to interpret this signal by adjusting the thalweg of Lake Zurich to the elliptical basin with exponential depth profile. To cut a long story short, it was not possible to approximately match a period in the 100–110-h regime with the patched-up thalweg profile and (1, 1)-mode behaviour *and* simultaneously arrive with an aspect ratio for the ellipse that would nearly reproduce the slenderness of Lake Zurich; the ellipses always turned out to be too 'fat'. Thus, the long period oscillatory response of Lake Zurich remains an enigma.

20.3.5 Topographic Vorticity Waves in Infinite Domains

Second class vorticity waves were primarily studied to understand long period ocean waves. For many applications the ocean can be treated as an unbounded domain, as an infinite or half-infinite domain, a channel or gulf, the unbounded exterior of an island with various parameterizations of the bathymetry.[5] We present here a selection of solutions to illustrate the qualitative behaviour of the dispersion relation. From this study a great deal can be learned for the construction of solutions to the topographic wave equation in enclosed basins, e.g. rectangles or basins which are composed of several units, but essentially closed.

20.3.5.1 Straight Channel

Consider a straight, infinite channel with the Cartesian coordinate system as indicated in Fig. 20.10. With a depth profile $h(y)$ which is constant along the channel axis and a carrier-wave ansatz of the form

$$\psi = \psi(y)\mathrm{e}^{\mathrm{i}(kx-\sigma t)}, \quad \sigma = \omega/f$$

the TW-equation reduces to

$$(h^{-1}\psi')' - \left[\frac{k}{\sigma}(h^{-1})' + k^2 h^{-1}\right]\psi = 0, \tag{20.59}$$

in which $()' = \mathrm{d}/\mathrm{d}y$.

[5] A source where second class waves in the ocean are studied is LeBlond and Mysak [19]. Additional works are e.g. by Allen [2], Brink [5, 6], Djurfeldt [9], Gratton [10], Gratton and LeBlond [11], Huthnance [13], Koutitonsky [16], Lie [20], Lie and El-Sabh [21], Mysak [25, 26], Ou [29], Takeda [40] and others.

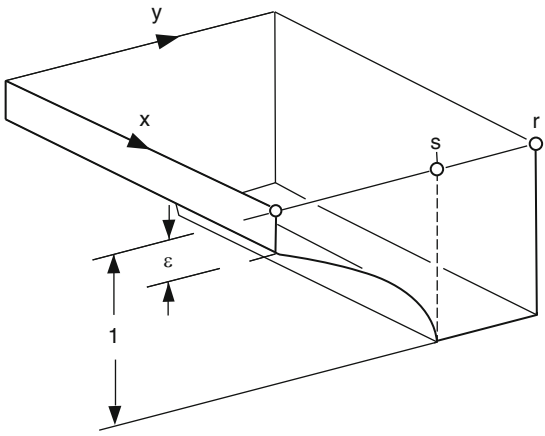

Fig. 20.10 Infinite channel with one-sided shelf. At the boundary points, 0, s, r the functions h and h' may not be continuous (from [39]).

Equation (20.59) is subject to the familiar no-flux conditions

$$\psi(0) = \psi(r) = 0. \tag{20.60}$$

Furthermore, at interior points we request that[6]

$$\begin{aligned} &[\![\psi]\!] = 0, \\ &[\![(\psi' - (k/\sigma)\psi)/h]\!] = 0, \end{aligned} \quad \text{at } \; y = s. \tag{20.61}$$

Equation $(20.61)_1$ means that the transport is continuous whereas $(20.61)_2$ follows by integrating (20.59) across the discontinuity:

$$\lim_{\epsilon \downarrow 0} \int_{s-\epsilon}^{s+\epsilon} \left\{ (h^{-1}\psi')' - \frac{k}{\sigma}(h^{-1})'\psi - k^2 h^{-1}\psi) \right\} \, \mathrm{d}y = 0,$$

$$\lim_{\epsilon \downarrow 0} \left\{ \left[h^{-1}\psi' - \frac{k}{\sigma} h^{-1}\psi \right]_{s-\epsilon}^{s+\epsilon} + \int_{s-\epsilon}^{s+\epsilon} \left[\frac{k}{\sigma} h^{-1}\psi' - k^2 h^{-1}\psi \right] \mathrm{d}y \right\} = 0.$$

Because h, ψ and ψ' are all bounded and continuous at $y = s$ and h is nonzero at $y = s$ the last integral vanishes in the limit as $\epsilon \downarrow 0$.

[6] $[\![\phi(y)]\!]$ at $y = s$ denotes the jump of the quantity ϕ defined by

$$[\![\phi(s)]\!] = \lim_{\epsilon \downarrow 0} (\phi(s+\epsilon) - \phi(s-\epsilon)).$$

20.3.5.2 Channel with One-Sided Topography

Consider the piecewise exponential depth profile (see Fig. 20.10)

$$\begin{aligned} h(y) &= \begin{cases} \epsilon \mathrm{e}^{by}, & 0 \le y \le s, \\ 1, & s \le y \le r, \end{cases} \\ b &= \frac{1}{s} \ln \frac{1}{\epsilon}. \end{aligned} \tag{20.62}$$

It renders (20.59) an ordinary differential equation with *constant* coefficient with the solution

$$\psi(y) = \begin{cases} \mathrm{e}^{by/2} \sin \lambda y, & 0 \le y \le s, \\ A \sinh(k(y-r)), & s \le y \le r. \end{cases} \tag{20.63}$$

Problem 20.2 *Show that the trial solution (20.63) satisfies the boundary conditions (20.60) and prove by substituting (20.63) into the differential equation that λ, k, σ and b must fulfill $(20.64)_2$. Prove, moreover, that the jump conditions then require $(20.64)_1$ to be satisfied. Thus, the dispersion relation is given by the following implicit form*

$$\begin{aligned} \frac{1}{\lambda} \tan s\lambda &= \frac{-1}{k \coth k(r-s) + \frac{b}{2}}, \\ \lambda^2 &= \frac{k}{\sigma} b - k^2 - \frac{b^2}{4}. \end{aligned} \tag{20.64}$$

◆

This is the dispersion relation of TWs in an infinite channel with one-sided topography. Figure 20.11 displays the left-hand side and right-hand side of $(20.64)_1$ as functions of λr. The left-hand side is independent of σ whereas the right-hand side is a double-valued relation of λ due to $(20.64)_2$. For frequencies lower than a critical value there exists a finite number of intersections (σ, λ) or (σ, k). This number increases stepwise with decreasing σ due to the periodicity of the tangent function. Note that λ^2 is only positive provided the signs of k and σ are the same. The dashed curve in Fig. 20.11 shows the left-hand side for $\lambda^2 < 0$, i.e. 'tan' is replaced by 'tanh'. For this case there are no intersections and hence no real pairs (σ, k) satisfying (20.64). This implies that phase propagation is into the positive x-direction for this configuration, which amounts to the well-known property of shelf waves on the Northern hemisphere ($f > 0$): the phase propagation is *right-bounded*.[7] Two limiting cases of this dispersion relation are of interest. These will be discussed now.

[7] Right-bounded means that the shallower region is to the right when looking into the direction of phase propagation.

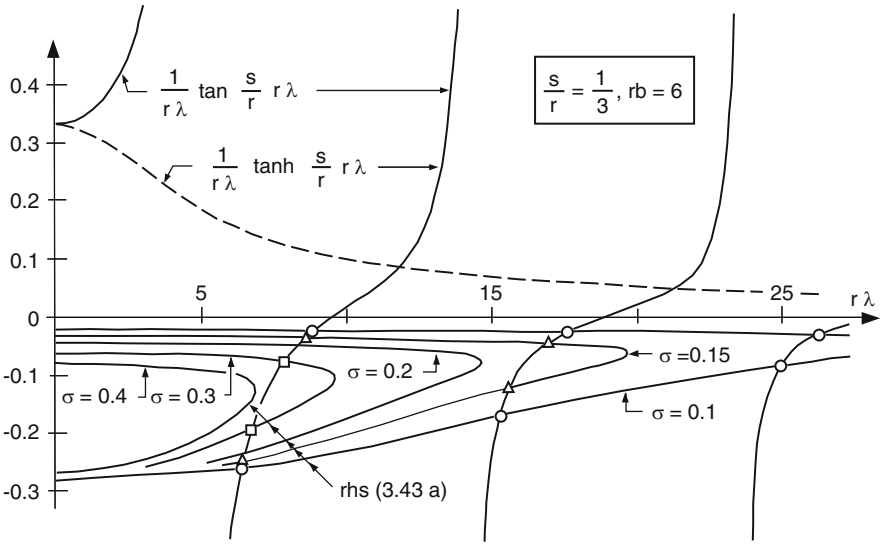

Fig. 20.11 Plot of the left-hand side and right-hand side of the implicit dispersion relation $\sigma(\lambda)$ or $\sigma(k)$ given in (20.64) for $s/r = 1/3$, $rb = 6$. The points (σ, λ) are indicated with $\square$, $\triangle$, $\circ$ (from [38]). © Versuchsanstalt für Wasserbau, Hydrologie und Glaziologie an der ETH Zürich, reproduced with permission

20.3.5.3 Shelf

A shelf is generally defined as a region which extends to infinity, $r \to \infty$. In this case (20.62) models the well known exponential shelf. Correspondingly, the dispersion relation reads

$$\frac{1}{\lambda} \tan s\lambda = -\frac{1}{k + b/2}, \tag{20.65}$$

and the result of Buchwald and Adams [7] is recovered. Figure 20.12 displays this dispersion relation for the first five modes. The shapes of these curves exhibit features which are typical of topographically trapped second-class waves: Firstly, long shelf waves are non-dispersive, i.e. as $k \to 0 \quad c_{gr} = \partial\sigma/\partial k \to c = \sigma/k > 0$. Phase and group velocity are the same. Secondly, when h'/h[8] is bounded, for $y \in [0, \infty)$ then $c_{gr} < 0$ for some range of $k > 0$. In other words, the dispersion relation $\sigma(k)$ possesses a maximum at $k = k_0$. For $k < k_0$, c and c_{gr} are both positive, and phase and energy propagate in the same direction; for $k > k_0$, c is still positive but c_{gr} is negative. Furthermore, $\sigma(k) \to 0$ as $k \to \infty$. These properties

[8] Because of its significance h'/h is often referred to as slope parameter $S \equiv h'/h$.

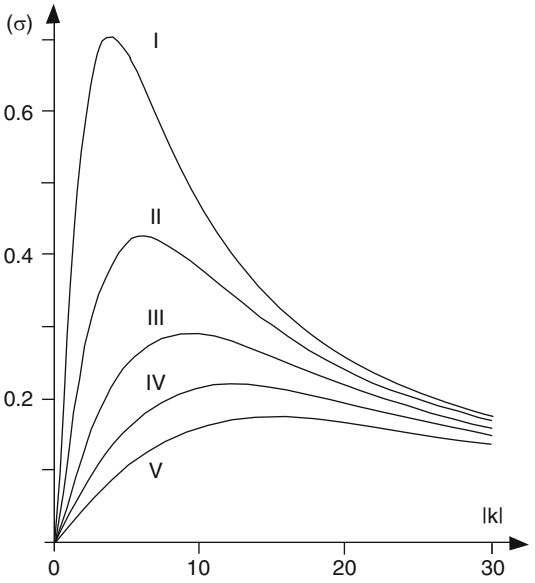

Fig. 20.12 Dispersion relation $\sigma(k)$ (20.65) for the first five modes on a shelf with $b = 5.4$ (from [7]). © Royal Soc. London, reproduced with permission

which hold in an infinite domain were proven by Huthnance [13] in a more general context.

The stream function in the shelf-wave limit takes the form

$$\psi(y) = \begin{cases} \mathrm{e}^{by/2} \sin \lambda y, & 0 \le y \le s, \\ \mathrm{e}^{bs/2} \sin \lambda s \cdot \mathrm{e}^{-k(y-s)}, & s < y. \end{cases}$$

It decays exponentially for $y > s$ and is essentially sinusoidal in the shelf domain.

20.3.5.4 Trench

A second simple case is obtained when $s \to r$. The dispersion relation (20.64) is then reduced to

$$\tan r\lambda = 0,$$

whence

$$\sigma = \frac{kb}{k^2 + \left[\dfrac{b^2}{4} + \left(\dfrac{n\pi}{r}\right)^2\right]}, \quad n = 1, 2, \ldots,$$

where the integer n denotes the mode of the wave. The stream function of the nth mode has $n - 1$ nodes across the channel. Long waves in this channel are non-dispersive with phase and group velocity

$$c = c_{gr} = \frac{b}{\frac{b^2}{4} + \left(\frac{n\pi}{r}\right)^2}, \quad \text{as } k \to 0.$$

For very short waves the frequency is inversely proportional to the wavenumber, $\sigma = b/k$, and phase and group velocity have opposite signs. The critical point (k_0, σ_0), where the group velocity vanishes is given by

$$(k_0, \sigma_0) = \left[\sqrt{\frac{b^2}{4} + \left(\frac{n\pi}{r}\right)^2}, \quad \frac{b}{2\sqrt{\frac{b^2}{4} + \left(\frac{n\pi}{r}\right)^2}} \right].$$

The critical frequency, σ_0, strongly depends on the topography parameter $b = h'/h$. The qualitative behaviour of the dispersion relation shown in Fig. 20.12 is typical and will again be encountered when we look for TW-solutions in rectangular basins.

20.3.5.5 Single-Step Shelf

We now demonstrate that boundedness of h'/h is important for the second of Huthnance's properties, namely existence of vanishing group velocity for finite $k_0 < \infty$. To this end consider the profile

$$h(y) = \begin{cases} d < 1, & 0 < y < s, \\ 1, & s < y < r. \end{cases} \tag{20.66}$$

This profile was used by Sezawa and Kanai [35], Snodgrass et al. [36] and Larsen [18] to explain edge waves and trapped long waves. Clearly, since $h' = (1-d)\delta(y-s)$ vanishes everywhere in $y \in (0, r)$ except at $y = s$, where h' is infinite, TWs only exist because of this singularity.

Problem 20.3 *Show that with (20.66) the differential equation (20.59) for TWs possesses the solution*

$$\psi(y) = \begin{cases} \sinh ky, & 0 \le y \le s, \\ A \sinh k(y-r), & s \le y \le r. \end{cases}$$

Show, moreover, that (20.61) imply the dispersion relation

$$\sigma = (1-d)\frac{\tanh ks \tanh k(r-s)}{d \tanh ks + \tanh k(r-s)}, \tag{20.67}$$

which is strictly convex. ◆

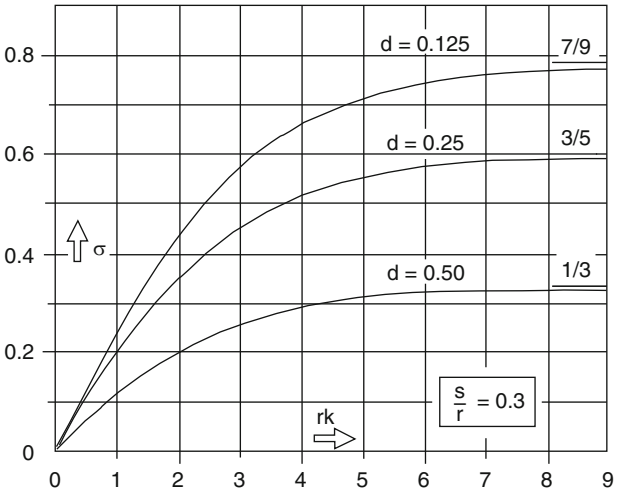

Fig. 20.13 Graph of the dispersion relation (20.67) for $s/r = 0.3$ and three values of d. Note $\sigma(rk)$ is monotone (from [39]). © Springer, Berlin, reproduced with permission

Figure 20.13 displays $\sigma(k)$ for different values of d, and we notice that these are *monotonically growing* functions of k. Indeed,

$$\sigma \to \frac{1-d}{1+d}\,, \quad \text{as} \quad k \to \infty,$$

$$\sigma \;\; \text{prop} \;\; k, \quad \text{as} \quad k \to 0,$$

and no critical wavenumber k_0 exists. Furthermore, *there is only one single fundamental TW mode*.

Shelf waves have also been analyzed for different topographies with $r \to \infty$. Reid [31] and Mysak [24] have investigated the finite width sloping shelf profile of Fig. 20.14a. The mass transport stream function can in this case be expressed in terms of Laguerre polynomials and dispersion curves are qualitatively as those shown in Fig. 20.13. However, there are now a countably infinite set of shelf modes because of the sloping portion of the shelf. Ball [4] on the other hand studied the exponential depth profile of Fig. 20.14b and finds dispersion curves for shelf waves which are qualitatively as those of Fig. 20.13, as would be expected since $h'/h \to \infty$ at $y = 0$. A similar study for escarpment-, trench-, shelf- and wedge waves was given by Djurfeldt [9].

In reality, channels have bathymetric gradients on both sides. From the results obtained so far, it can be concluded that in such a channel (e.g. with a parabolic depth profile) there will be TWs travelling along either sides of the channel each in a right-bounded way. The dispersion relation then consists of two branches (assume $\sigma > 0$), one for $k > 0$ representing those waves trapped to $y = 0$ and $k < 0$ for

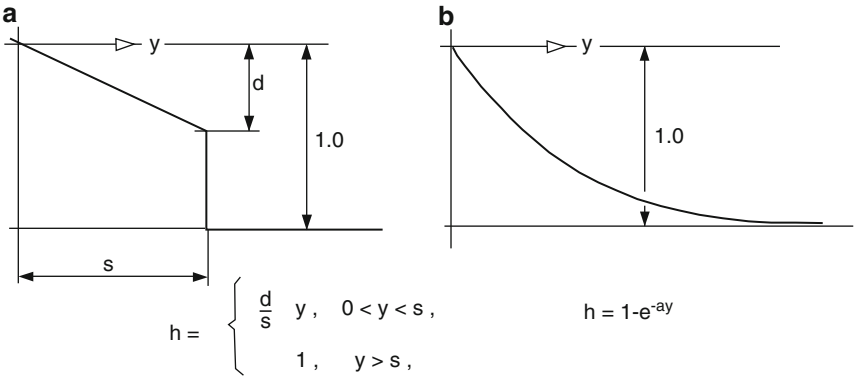

Fig. 20.14 (**a**) Finite width sloping shelf profile. (**b**) Exponential profile

those trapped to $y = r$. This, and the propagation of TWs in *curved* channels will be discussed in Chap. 21.

20.3.6 Elliptic Island in Infinite Space

Island-trapped shelf waves were studied by Mysak [23], Rhines [32], Saint-Guily [33], Buchwald and Melville [8] and Hogg [12]. All these authors solved the TW-equation in cylindrical coordinates, but used different representations of the topographic profile. Mysak used the finite width sloping profile of Fig. 20.14a (in which y is now the radial distance), Saint-Guily applied the parabolic depth profile, while Rhines [32], Buchwald and Melville [8] and Hogg [12] employed the power law

$$h(y) = \begin{cases} \mathrm{d}y^{\alpha}, & a < y < a + r, \\ 1, & y > a + r, \end{cases}$$

with $\alpha > 0$; a is the radius of the island. Solutions of the TW-equation in the exterior of an elliptical island were constructed by Stocker and Hutter [39].

The derivation of the relevant equations in elliptical coordinates ξ, η is given in Sect. 20.3.4. We assume the isobaths to follow confocal ellipses, so that $h = h(\xi)$. The shore of the island will be given by $\xi = \xi_I$, the contour line of the outer edge of the shelf by $\xi = \xi_E$. The TW-equation is given by $(20.43)_1$. With the separation of variables solution

$$\psi(\xi, \eta) = F(\xi)\mathrm{e}^{\mathrm{i}(m\eta + \sigma t)}, \quad m = 1, 2, 3, \ldots$$

(the + sign of σ is used because a right-bounded phase propagation is clockwise around the island) the boundary value problem becomes

$$\begin{aligned} &(h^{-1}F')' + (\tfrac{m}{\sigma}(h^{-1})' - m^2 h^{-1})F = 0, \quad \xi > \xi_I, \\ &F = 0, \qquad\qquad\qquad\qquad\qquad \text{at } \xi = \xi_I, \infty, \\ &[\![F]\!] = [\![F']\!] = 0, \qquad\qquad\qquad \text{at } \xi = \xi_E > \xi_I. \end{aligned} \tag{20.68}$$

With the exponential shelf profile

$$h(\xi) = \begin{cases} \mathrm{e}^{b(\xi-\xi_E)}, & \xi_I \le \xi \le \xi_E, \\ 1, & \xi_E \le \xi, \end{cases}$$

the solution of (20.68) satisfying the boundary conditions reads

$$F(\xi) = \begin{cases} \mathrm{e}^{b(\xi-\xi_E)/2} \sin(\lambda(\xi - \xi_I)), & \xi_I \le \xi \le \xi_E, \\ Ae^{-m\xi}, & \xi_E \le \xi, \end{cases}$$

with

$$\lambda^2 = \frac{mb}{\sigma} - m^2 - \frac{b^2}{4}.$$

The matching conditions at $\xi = \xi_E$ determine the constant A and yield the eigenvalue equation

$$\frac{1}{\lambda}\tan(\lambda(\xi_E - \xi_I)) = -\frac{1}{m + \frac{b}{2}}, \quad m = 1, 2, 3, \ldots. \tag{20.69}$$

This is exactly analogous to the dispersion relation (20.65) for TWs of a straight shelf, except that the 'wavenumber' m is quantized here due to the 2π-periodicity in η. Equation (20.69) is an example of an infinite domain with a discrete spectrum. Table 20.9 lists a selection of eigenfrequencies for various values of m, ξ_I, ξ_E and b.

Table 20.9 Eigenfrequencies of the ($m = 1, n = 1$), (2,1), (3,1), (1,2) modes of TWs around an elliptic island according to (20.69). r is the aspect ratio (width to length) of the island, A_E and A_I are the semi-axes of the elliptic shelf boundary, $A_E = \cosh \xi_E$, and of the island $A_I = \cosh \xi_I$, and b is a topography parameter such that $h(\xi_I) = 0.1$

r	ξ_I	A_E/A_I	b	Mode (m,n)			
				(1,1)	(2,1)	(3,1)	(1,2)
		2	3.30	0.232	0.358	0.405	0.006
0.99	2.65	3	2.09	0.317	0.408	0.399	0.088
		5	1.43	0.379	0.401	0.347	0.120
		2	2.48	0.285	0.396	0.410	0.076
0.5	0.549	3	1.69	0.354	0.410	0.374	0.105
		5	1.22	0.397	0.385	0.318	0.135
		2	1.88	0.336	0.411	0.388	0.096
0.1	0.100	3	1.38	0.384	0.398	0.341	0.123
		5	1.05	0.408	0.363	0.289	0.149

20.4 Application of Transformation Principles

Two principles or property theorems of the TW-operator were presented in this chapter, (1) the Cartesian-coordinate correspondence principle, see Sect. 20.2.5 and (2) the invariance of the TW-operator under conformal mappings. These properties can be used to construct solutions of the TW-equation in various different domains, provided of course, that the isobaths in one domain transform to the isobaths in the transformed domain. Such solutions, when being constructed analytically, can serve a good purpose when numerical software is tested for its accuracy in special problems. We shall illustrate the applicability of this method of solution below.

20.4.1 Hyperbolically Curved Channels

It was shown in Sect. 20.2.3 that the TW-operator, referred to elliptic coordinates of confocal ellipses and hyperbolas has the same form as the same operator referred to Cartesian coordinates.[9] The reason for this invariance is the fact that the mapping from Cartesian to confocal elliptic coordinates is conformal. Indeed, with $\mathsf{z} = \mathsf{x} + \mathrm{i}\mathsf{y}$ and $\zeta = \xi + \mathrm{i}\eta$, where i is the imaginary unit, $(20.12)_{1,2}$ can be written as

$$\mathsf{z} = a \cosh \zeta. \tag{20.70}$$

The Cartesian-correspondence principle can be used for constructing channel solutions if the channel shores follow confocal hyperbolas. Three such configurations, where topographically trapped waves may exist, are illustrated in Fig. 20.15. Panel (a) is a sketch of such a wave along a curved boundary; panel (b) shows a situation for a model in which a TW approaches an isthmus or an isolated basin and panel (c) illustrates a model for a curved channel. Provided the isobaths are confocal hyperbolas, the solutions for straight channels can directly be used to find the dispersion relation and mode structures for the TWs in these curved domains.

Consider the configuration of Fig. 20.16 in elliptical coordinates (ξ, η) and assume that in these coordinates $h = h(\eta)$. In this case, the TW-equation is given by (20.43). With the trial solution

$$\psi(\xi, \eta) = \begin{cases} F(\eta)\mathrm{e}^{\mathrm{i}(k\xi + \sigma t)}, & 0 \le \eta_L < \eta < \eta_R \le \pi, \\ G(\eta)\mathrm{e}^{\mathrm{i}(-k\xi + \sigma t)}, & \pi \le \bar{\eta}_R < \eta < \bar{\eta}_L \le 2\pi, \end{cases} \tag{20.71}$$

[9] See the transformation formulae (20.12) and Fig. 20.1 and compare the TW-equation in Cartesian, (20.5) and (20.6), and in elliptical (20.12) coordinates.

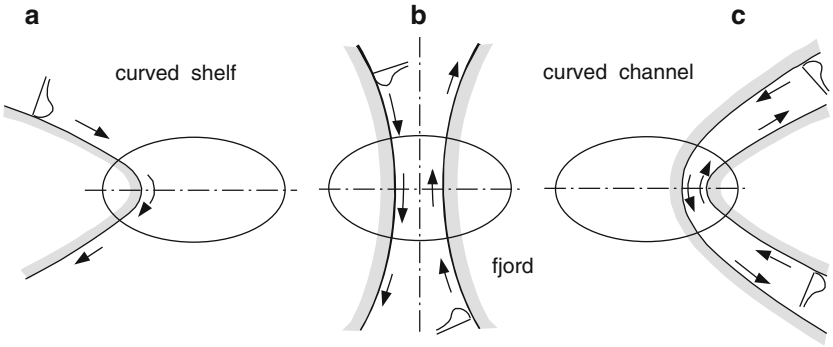

Fig. 20.15 Sketch of the propagation of trapped waves along a hyperbolically curved shelf (**a**) or channel (**b**, **c**) (from [39]). © Springer, Berlin, reproduced with permission

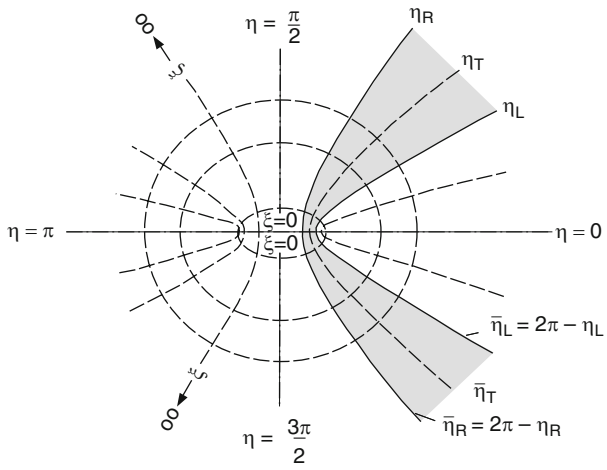

Fig. 20.16 Hyperbolically curved channel embedded in an elliptic coordinate system with shore lines following confocal hyperbolas (from [39]). © Springer, Berlin, reproduced with permission

the following boundary value problems for F and G emerge

$$\begin{aligned} &F'' - \frac{h'}{h}F' - \left(k^2 + \frac{h'}{h}\frac{k}{\sigma}\right)F = 0, && \eta_L < \eta < \eta_R, \\ &F = 0, && \eta = \eta_L, \eta_R \\ &G'' - \frac{h'}{h}G' - \left(k^2 - \frac{h'}{h}\frac{k}{\sigma}\right)G = 0, && 2\pi - \eta_R < \eta < 2\pi - \eta_L, \\ &G = 0, && \eta = 2\pi - \eta_R, 2\pi - \eta_L. \end{aligned} \tag{20.72}$$

Here, primes mean differentiations with respect to η, and η_L and η_R denote the values of η of the hyperbolas along the boundary shore lines; they may have values

Table 20.10 Coordinate domains and transformations for the two systems

Cartesian	Scaled	Elliptic
$0 \le x \le L \longrightarrow$ $\rho = x/L$	$0 \le \rho \le 1$	$\longleftarrow 0 \le \xi \le \xi_E$ $\rho = \xi/\xi_E$
$-\frac{1}{2}B \le y \le -\frac{1}{2}B \longrightarrow$ $\chi = y/B$	$-\frac{1}{2} \le \chi \le \frac{1}{2}$	$\longleftarrow \eta_L \le \eta \le \eta_R$ $\chi = \frac{\eta}{\eta_R - \eta_L} - \frac{\eta_R + \eta_L}{2(\eta_R - \eta_L)}$

from $0 \le \eta_L, \eta_R \le \pi$. Equation $(20.71)_1$ represents a wave traveling in the hyperbolic channel approaching the narrowest cross section from above and leaving it in the lower half plane. Alternatively, $(20.71)_2$ represents such a wave approaching the narrowest cross section from below and leaving it in the upper half plane. The two waves match smoothly at $\xi = 0$ provided that

$$\begin{aligned} \psi(0,\eta) &= \psi(0, 2\pi - \eta), \\ \frac{\partial \psi}{\partial \xi}(0,\eta) &= -\frac{\partial \psi}{\partial \xi}(0, 2\pi - \eta). \end{aligned} \qquad 0 \le \eta \le \pi. \tag{20.73}$$

These conditions are fulfilled if

$$G(\eta) = F(2\pi - \eta). \tag{20.74}$$

This is consistent with $(20.72)_{2,4}$. We now demonstrate that (20.72) is formally analogous to the two-point-boundary-value-problem in a *straight* channel. In order to fully apply the correspondence we transform the independent coordinates such that in the transformed coordinate the domain is the same as that for which the straight channel solution has been determined. Table 20.10 demonstrates the different coordinate domains and the transformations. The two-point-boundary-value-problems for the scaled Cartesian and the scaled elliptical system read[10]

$$\begin{aligned} F_s'' - \left(\frac{h'}{h}\right) F_s' - \left[\frac{B^2}{L^2} k_s^2 + \frac{B}{L}\left(\frac{h'}{h}\right)\frac{k_s}{\sigma}\right] F_s = 0, \\ F_c'' - \left(\frac{h'}{h}\right) F_c' - \left[\frac{(\eta_R - \eta_L)^2}{\xi_E^2} k_c^2 + \frac{\eta_R - \eta_L}{\xi_E}\left(\frac{h'}{h}\right)\frac{k_c}{\sigma}\right] F_c = 0, \end{aligned} \tag{20.75}$$

[10] An identical equation as that for F can also be obtained for G if

$$\chi = -\frac{1}{\eta_R - \eta_L}\eta - \frac{\eta_R + \eta_L}{2(\eta_R - \eta_L)} + \frac{2\pi}{\eta_R - \eta_L}$$

is chosen.

in which primes denote differentiations with respect to χ, and the subscripts s and c stand for 'straight' (Cartesian) and 'curved' (elliptic). These two problems are formulated in the same domain $[0 \le \rho \le 1, -\frac{1}{2} \le \chi \le \frac{1}{2}]$ and are identical if

$$k_s = \frac{(\eta_R - \eta_L)/\xi_E}{B/L} k_c. \tag{20.76}$$

The effect of curvature is, therefore, measured by the two aspect ratios, $(\eta_R - \eta_L)/\xi_E$ and B/L in the two coordinate systems. In order to determine $\sigma(k_c)$ it thus suffices to stretch the k-axis of the straight channel dispersion relation according to (20.76): Likewise, the eigenfunctions are obtained from the straight channel solutions by a stretching transformation. Notice that this approach incorporates an entire family of curved channel solutions. For instance $\eta_R = \pi - \eta_L$, $0 < \eta < \pi/2$ may be appropriate to model TWs close to the mouth of a fjord, while $\pi/2 < \eta_R < \eta_L < 0$ is appropriate to model curvature effects in channels. Along the thalweg hyperbola

$$\eta \equiv \eta_T = \frac{\eta_R + \eta_L}{2}$$

this curvature is given by

$$K(\xi) = \frac{-\cos \eta_T \sin \eta_T}{a(\cos^2 \eta_T \sinh^2 \xi + \sin^2 \eta_T \cosh^2 \xi)^{3/2}}$$

and its maximum is obtained for $\xi = 0$

$$K(0) = -\frac{\cos \eta_T}{a \sin^2 \eta_T}.$$

The behaviour of TWs in hyperbolic channels, however, depends on two parameters, the curvature K and a width parameter $\eta_R - \eta_L$.

20.4.2 Semi-Infinite Gulf and Patched-Up Elongated Basins

Let us recall the TW-mode analysis for an elliptical basin with exponential depth profile, see Sect. 20.3.4b. It was shown there, how the solutions of the two lowest modes for the elliptic basin were constructed. The formulae are given as (20.53)–(20.57) and the streamline contours are plotted for these modes in Fig. 20.9. The elliptical coordinates were denoted as ξ ('radial') and η ('azimuthal'). Johnson [15] constructed a conformal transformation which maps the interior of an ellipse into a semi-infinite strip in the (x, y)-domain. This mapping from (x, y) onto (ξ, η) is given by

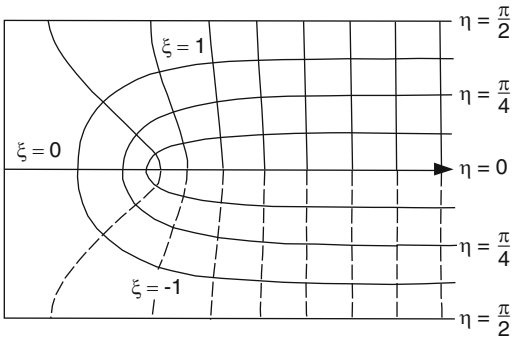

Fig. 20.17 Coordinate lines of the (ξ, η) system in the semi-infinite channel $|\ y\ | \leq \pi/2, x \geq 0$ (from Johnson (1987) [15]). © Cambridge University Press, reproduced with permission

$$\xi + \mathrm{i}\eta = \cosh^{-1}\left\{\frac{\sinh(x + \mathrm{i}y)}{\sinh a}\right\}. \tag{20.77}$$

It maps the semi-infinite channel $|\ y\ | < \pi/2, x \geq 0$ with a branch cut on $y = 0$, $x \geq a$ to the strip $0 \leq \eta \leq \pi/2, -\infty < \xi < \infty$, as shown in Fig. 20.17. For large $|\ \xi\ |$ the coordinate system (ξ, η) becomes Cartesian. With a depth profile $h(\eta)$ varying only with η, the channel has a constant depth along the thalweg $\eta = 0$. The boundary can be chosen at $\eta = \eta_S$ $(0 < \eta_S \leq \pi/2)$; this curve and all isobaths are smooth. Because (20.77) is conformal and $h_\xi \equiv 0$, the TW-equation takes the form (compare e.g. (20.43))

$$(h^{-1}\psi_{t\xi})_\xi + (h^{-1}\psi_{t\eta})_\eta + \psi_\xi(h^{-1}f)_\eta = 0 \tag{20.78}$$

and ψ vanishes on η_S and is smooth across the branch cut $\eta = 0$. We assume two oppositely traveling waves, viz.,

$$\psi = F_1(\eta)\cos(k\xi - \omega t) + F_2(\eta)\cos(k\xi + \omega t). \tag{20.79}$$

With this and the assumption that the depth depends only on η, one obtains from (20.78)[11] the ordinary differential equation

$$F'' - \left(\frac{h'}{h}\right)F' - \left[\pm\frac{k}{\sigma}\left(\frac{h'}{h}\right) + k^2\right]F = 0, \tag{20.80}$$

with $\sigma \equiv \omega/f$ for F_1 and F_2, respectively. Across the channel boundary $\eta = \eta_S$ the no-flux condition,

$$F_1(\eta_S) = F_2(\eta_S) = 0 \tag{20.81}$$

[11] The text below follows Stocker [38] with some minor changes.

is requested. Moreover, the stream function ψ must be smooth across the cut $\eta = 0$, implying

$$\begin{aligned} F_1(0) - F_2(0) &= 0, \\ F_1'(0) + F_2'(0) &= 0. \end{aligned} \tag{20.82}$$

The exponential depth profile (with flat interior)

$$h(\eta) = \begin{cases} \mathrm{e}^{-b(\eta-\eta_B)}, & \eta_B \le \eta \le \eta_S, \\ 1, & 0 \le \eta \le \eta_B \end{cases} \tag{20.83}$$

renders (20.80)–(20.83) a well-posed linear eigenvalue problem with constant coefficients. Equations (20.80)–(20.82) agree with (20.54) and (20.55), however, with the roles of the coordinates interchanged. The solutions, citing Johnson [15], read

$$\begin{aligned} F_1 &= \left[\cosh k\eta_B + \frac{\alpha_1}{k}\sinh k\eta_B\right]^{-1} \\ &\quad \times \begin{cases} \dfrac{\exp\left(-\frac{1}{2}b(\eta-\eta_B)\right)\sin\left(\lambda_1(\eta_S-\eta)\right)}{\sin\left(\lambda_1(\eta_S-\eta)\right)}, & (\eta_B \le \eta \le \eta_S) \\ \cosh\left(k(\eta-\eta_B)\right) - \frac{\alpha_1}{k}\sinh\left(k(\eta-\eta_B)\right), & (0 \le \eta \le \eta_B) \end{cases} \\ F_2 &= \left[\cosh k\eta_B + \frac{\alpha_2}{k}\sinh k\eta_B\right]^{-1} \\ &\quad \times \begin{cases} \dfrac{\exp\left(-\frac{1}{2}b(\eta-\eta_B)\right)\sinh\left(\lambda_2(\eta_S-\eta)\right)}{\sinh\left(\lambda_2(\eta_S-\eta_B)\right)}, & (\eta_B \le \eta \le \eta_S) \\ \cosh\left(k(\eta-\eta_B)\right) - \frac{\alpha_2}{k}\sinh\left(k(\eta-\eta_B)\right), & (0 \le \eta \le \eta_B) \end{cases} \end{aligned} \tag{20.84}$$

with

$$\begin{aligned} \lambda_1^2 &= \frac{kb}{\sigma} - k^2 - \frac{b^2}{4}, & \lambda_2^2 &= \frac{kb}{\sigma} + k^2 + \frac{b^2}{4}, \\ \alpha_1 &= \lambda_1 \cot\lambda_1(\eta_S-\eta_B) + b/2, & \alpha_2 &= \lambda_2 \cot\lambda_2(\eta_S-\eta_B) + b/2. \end{aligned} \tag{20.85}$$

The dispersion relation follows from $(20.82)_2$ and takes the form

$$0 = (\alpha_1 - \alpha_2)\left(1 + \tanh^2(k\eta_B)\right) + 2\frac{k+\alpha_1}{\alpha_2}k\tanh(k\eta_B). \tag{20.86}$$

Note that a channel with no flat central zone, i.e. $\eta_B = 0$, has the simpler dispersion relation

$$\alpha_1 - \alpha_2 = 0,$$

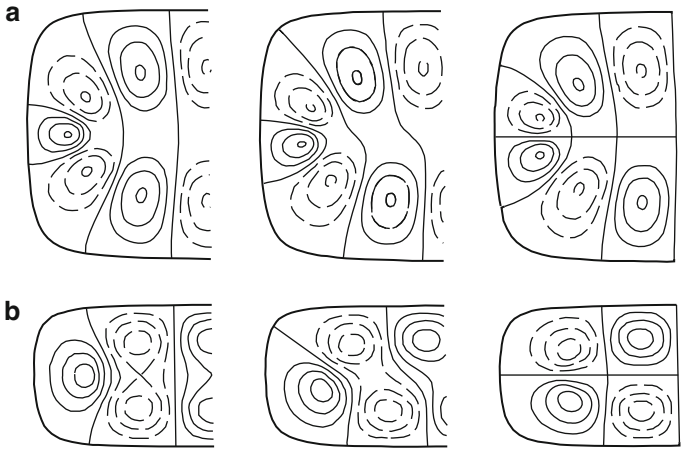

Fig. 20.18 Contours of the stream function of TWs in an semi-infinite channel. The parameters are $\eta_S = 1.5$, $\eta_B = 0.5$, $b = 1$ and (**a**) $a = \pi/4$, $k = 4$ and (**b**) $a = \pi/2$, $k = 1$ (from Johnson (1987) [15]).

its qualitative shape is given in Fig. 20.12. Due to the invariance principle under conformal mapping it is the same dispersion relation as in a straight infinite channel. More specifically, each frequency σ allows a short and a long topographic wave with their phases travelling from $\xi = \infty$ to $\xi = -\infty$. The energy of the long wave propagates into the same direction as the phase whereas it travels into the opposite direction for short waves.

Figure 20.18 displays contours of ψ in two semi-infinite channels. A right bounded wave propagating from infinity towards $\xi = 0$ follows the lines of constant f/h. This amounts to a complete reflection of wave energy as the reflected wave travelling towards $\xi \to -\infty$ has the same wavelength and amplitude. Hence, the energy of an incident wave is not distributed among other possible wave types but is transferred without loss to an outgoing wave with the same wavenumber. We shall encounter configurations with a different reflection behaviour in the next chapter.

The results for the semi-infinite channel can be applied to construct approximate solutions in elongated basins as proposed by Johnson [15]. As mentioned, the (ξ, η)-coordinate system approaches the Cartesian system for growing $|\xi|$ and x, respectively. A basin of length $2L$ can then be constructed by patching two semi-infinite channels at $\xi_L = L - \ln \sinh a$ together. The coordinate lines coincide there with an error of order $(\exp(-2L)\cosh^2 a)$ as can be seen from an expansion of (20.77) for $x \gg 1$. The stream function (20.79) must be continuous at $\xi = \xi_L$ implying that the periodicity condition $k = m\pi/(2\xi_L)$, $m = 1, 2, 3,$ holds. This selects the eigenfrequencies from the dispersion relation. Figure 20.19 shows plots of the $(m, n) = (1, 1), (1, 2)$ and $(2, 1)$ modes in the elongated basin of aspect ratio $1 : 6$.

The solutions qualitatively agree with those in the elliptical basins, see Figs. 20.6 and 20.9. A particular eigensolution is characterized by two mode numbers m and n.

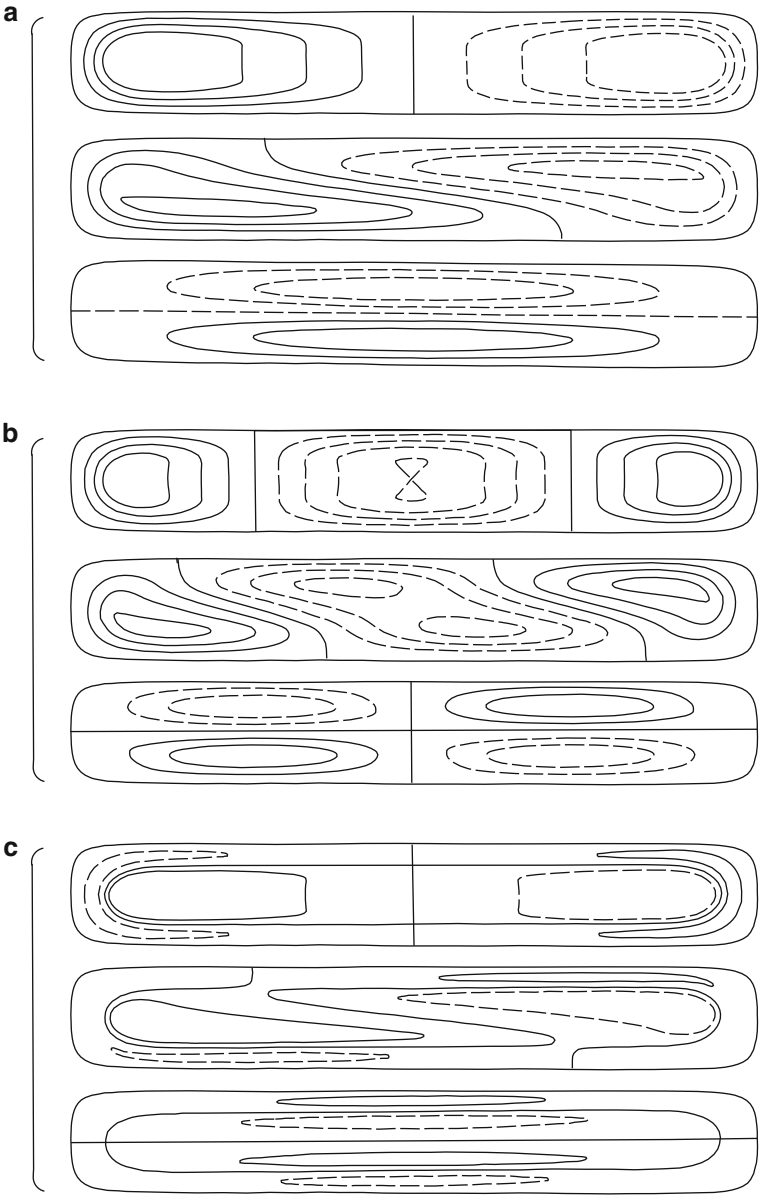

Fig. 20.19 Modes (1, 1), (2, 1) and (1, 2) in a basin with aspect ratio 1 : 6 and $\eta_S = 1.5$, $\eta_B = 0.5$, $b = 1$ and $a = \pi/2$. The frequencies are (**a**) $\sigma = 0.0511$ ($T = 331\,\mathrm{h}$), (**b**) $\sigma = 0.0966$ ($T = 175\,\mathrm{h}$), **(c)** $\sigma = 0.0258$ ($T = 655\,\mathrm{h}$) (from Johnson (1987) [15]).

The 'radial' mode number n governs the structure of the solution in the transverse η-direction and is incorporated in the dispersion relation (20.86). Modes with the same radial mode number lie on the same branch of the dispersion relation. Figure 20.12 gives a schematic impression of these branches and demonstrates that each radial mode number has its individual cut-off frequency above which only modes with smaller radial mode number can exist. The 'azimuthal' mode number m, defined by the periodicity condition, gives the structure in the ξ-direction and is related to the number of nodes along the long axis of the basin. We conclude, that the spectrum is ordered with respect to both mode numbers individually. The largest eigenfrequencies are expected from modes with $n = 1$ and $m = m_0$, where m_0 is an integer closest to the critical wave number k_0. Moreover, this critical mode number m_0 separates solutions with different properties. Modes with $0 < m < m_0$ have wave numbers $0 < k < k_0$, and, from the dispersion relation, $\partial\sigma/\partial k > 0$, see Fig. 20.12. Eigenmodes with increasing frequencies have increasing mode numbers and hence exhibit vortices with smaller spatial scale. The opposite is true when $m > m_0$. Since these two azimuthal mode types belong to the respective domains of the dispersion relation, they enjoy different physical properties. In the next chapter, these two and an additional modal type will further be discussed. There, the dispersion relation of freely propagating TWs again proves to be the key in understanding the structure of the spectrum of the TW-operator in enclosed domains.

The method of Johnson works with five bathymetric parameters to model the aspect ratio of a lake and, independently, the form of the lake ends satisfactorily. It is, therefore, a more general approach than the elliptic basin treated earlier though closely related to it as the latter is obtained by a conformal mapping, as well.

To use the above analysis in lake data interpretations, recall the discussion in the introductory section of Chap. 19, where controversial opinions about the interpretation of a 74 h signal in Lake of Lugano were reported. Mysak et al. [28] said that it was the response of the fundamental TW-mode, whilst Trösch [41] said, it was more likely a localized bay resonance. Johnson, on the other hand, demonstrates that a realistic choice of the bathymetric parameters, particularly that of the aspect ratio leads to periods of about $T = 300$ h and longer. He conjectures that a possible TW with a period of the order of 70 h must have a wave number of the order of the inverse aspect ratio of the basin. For a basin with the parameters of Fig. 20.19, e.g. the (20,1)-mode has $T = 87.2$ h. Modes with such large azimuthal mode numbers exhibit very small scale structure over the entire elongated basin, and it is questionable whether such a mode can persist in nature to produce a pronounced signal as in Lakes of Lugano and Zurich. The Lake of Lugano results by Trösch point at modes with a completely different modal structure which lack the property that they have a coherent wave motion in the entire domain (after Stocker [38]).

It will be shown in the next chapter that such localized modes indeed may exist.

20.5 Discussion

This chapter was devoted to the construction of analytical solutions of topographic waves in basins with simple variable bathymetry, the intention being to acquire knowledge of the structure of the wave modes in such basins. After presenting the TW-equation in arbitrary orthogonal coordinate systems (and their specialization in polar and elliptical coordinates) TW-solutions were constructed for circular and elliptical basins of which the topography varied only in the radial direction. Streamlines for the horizontal transport current showed gyres which, as a whole, rotate counterclockwise around the basin and eigenperiods depended heavily on the strength of the ∪-shape of the radial profile. For the circular basin, Fig. 20.4, and elliptic basin with an interior island, Fig. 20.8, the number of gyres would not change during a mode period but for elongated elliptical basins without island the number of gyres could change in the course of a period-time. Furthermore, the mode periods depended, apart from the bathymetry parameter, also upon the aspect ratio. The above modes are basin-filling and have large characteristic lengths of the order of, but less than a typical horizontal basin width.

These solutions contrast with TW-solutions in infinite domains, such as straight canals. For bathymetries, which vary only in the transverse direction and are continuous, the dispersion relation consists for each mode of a hump, see Fig. 20.12. For $\sigma \leq \sigma_0$ the phase and group velocities are both of the same sign, whilst for $\sigma \geq \sigma_0$ they have different signs, so that the energy and phase propagate into opposite directions, whilst for $\mathrm{d}\,\sigma/\mathrm{d}\,k_{|k_0} = 0$, i.e. at $\sigma = \sigma_0$, energy does not propagate at all. Existence of this energy characteristics with the largest real $\sigma = \sigma_0 < \infty$ is tied to the bathymetry being continuous. Also, for $\sigma < \sigma_0$ corresponding wave numbers are large, since $\mid \sigma \mid$ is small, whilst for $\sigma > \sigma_0$ the wave numbers are large and typical wavelengths small. Moreover, in the growing branch of the dissipation curve, $\mid k \mid < k_0$, frequencies grow with decreasing typical gyre diameter, whilst for $\mid k \mid > k_0$ frequencies decrease with decreasing gyre size. All this follows easily from the dispersion curves of Fig. 20.12.

Since the TW-operator is invariant under conformal mapping, TW-solutions obtained for one domain can easily be constructed also for any other domain which is the conformally mapped domain of any other domain for which a solution is already known. This transformation principle is applied to TW-solutions in hyperbolic channels, TWs around an elliptical island in an otherwise infinite channel and long rounded rectangles. Useful this method may be, it is limited by the fact that the topography must also be transformed; the transformed basins may then not represent realistic bathymetries. Even more distressing is the fact that with this method only solutions are found with the same characteristics as the solutions in the pre-image domain.

In the next chapter, characteristically new solutions will be sought and found!

References

1. Abramowitz, M. and Stegun, I. A.: *Handbook of mathematical functions.* Dover (1972)
2. Allen, J. S.: Coastal trapped waves in a stratified ocean. *J. Phys. Oceanogr.*, **5**, 300–325 (1975)
3. Ball, K. F.: Second class motions of a shallow liquid. *J. Fluid Mech.*, **23**, 545–561 (1965)
4. Ball, K. F.: Edge waves in an ocean of finite depth. *Deep Sea Res.*, **14**, 79–88 (1967)
5. Brink, K. H.: Propagation of barotropic continental shelf waves over irregular bottom topography. *J. Phys. Oceanogr.*, **10**, 765–778 (1980)
6. Brink, K. H.: A comparsion of long coastal trapped wave theory with observations of Peru. *J. Phys. Oceanogr.*, **12**, 897–913 (1982)
7. Buchwald, V. T. and Adams J. K.: The propagation of continental shelf waves. *Proc. Roy. Soc.*, **A305**, 235–250 (1968)
8. Buchwald, V. T. and Melville, W. K.: Resonance of shelf waves near islands. In *Lecture Notes in Physics*, **vol. 64**, edited by D.G. Provis and R. Radok, 202–205, Springer, New York (1977)
9. Djurfeldt, L.: A unified derivation of divergent second-class topographic waves. *Tellus*, **36A**, 306–312 (1984)
10. Gratton, Y.: *Low frequency vorticity waves over strong topography.* Ph.D. thesis, Univ. of British Columbia, 132 pp. (1983)
11. Gratton, Y. and LeBlond, P. H.: Vorticity waves over strong topography. *J. Phys. Oceanogr.*, **16**, 151–166 (1986)
12. Hogg, H. G.: Observations of internal Kelvin waves trapped round Bermuda. *J. Phys. Oceanogr.*, **10**, 1353–1376 (1980)
13. Huthnance, J. M.: On trapped waves over a continental shelf. *J. Fluid Mech.*, **69**, 689–704 (1975)
14. Johnson, E. R.: Topographic waves in elliptical basins. *Geophys. Astrophys. Fluid Dyn.*, **37**, 279–295 (1987a)
15. Johnson, E. R.: A conformal mapping technique for topographic wave problems. *J. Fluid Mech.*, **177**, 395–405 (1987b)
16. Koutitonsky, V. G.: *Subinertial coastal-trapped waves in channels with variable stratification and topography* PH.D. thesis, Marine Sciences Res. Center, State Univ. New York, Stony Brook (1985)
17. Lamb, H.: *Hydrodynamics*. 6th ed. Cambridge University Press (1932)
18. Larsen, J. C.: Long waves along a single-step topography in a semi-infinite uniformly rotating ocean. *J. Mar. Res.*, **27**, 1–6 (1969)
19. LeBlond, P. H. and Mysak, L. A.: *Waves in the Ocean*. Elsevier (1980)
20. Lie, H.-J.: Shelf waves on the exponential, linear and sinusoidal bottom topographies. *Bull: KORD1*, **5**, 1–8 (1983)
21. Lie, H.-J. and El-Sabh, M. I.: Formation of eddies and transverse currents in a two-layer channel of variable bottom: Applications to the lower St. Lawrence estuary. *J. Phys. Oceanogr.*, **10**, 1063–1075 (1983)
22. Miles, J. W. and Ball, F. K.: On free-surface oscillations in a rotating paraboloid. *J. Fluid Mech.*, **17**, 257–266 (1963)
23. Mysak, L. A.: On the theory of continental shelf waves. *J. Mar. Res.*, **25**, 205–227 (1967)
24. Mysak, L.A.: Edgewaves on a gently sloping continental shelf of finite width. *J. Mar. Res.*, **26**, 24–33 (1968)
25. Mysak, L. A.: Topographically trapped waves. *Ann. Rev. Fluid Mech.*, **12**, 45–76 (1980a)
26. Mysak, L. A.: Recent advances in shelf wave dynamics. *Review of Geophysics and Space Physics*, **18**, 211–241 (1980b)
27. Mysak, L. A.: Elliptical topographic waves. *Geophs. Astrophys. Fluid Dyn.*, **31**, 93–135 (1985)
28. Mysak, L. A., Salvadè, G., Hutter, K. and Scheiwiller, T.: Topographic waves in an elliptical basin with application to the Lake of Lugano. *Phil. Trans. R. Soc. London*, **A 316**, 1–55 (1985)
29. Ou, H. W.: On the propagation of the topographic Rossby waves near continental margins. Part 1: Analytical model for a wedge. *J. Phys. Oceanogr.*, **19**, 1051–1060 (1980)
30. Pearson, C. E.: *Handbook of Applied Mathematics*. VNR Company (1974)

31. Reid, R. O.: Effect of Coriolis force on edge waves. I: Investigation of the normal modes. *J. Mar. Res.*, **16**, 104–144 (1958)
32. Rhines, P. B.: Slow oscillations in an ocean of varying depth. *J. Fluid Mech.*, **37**, 161–205 (1969)
33. Saint-Guily, B.: Oscillations propres dans un bassin de profondeur variable: Modes de seconde classe. In *Studi in Onore di Giuseppe Aliverti*, 15–25. Instituto Universitario Navale di Napoli, Napoli, Italy (1972)
34. Saylor, J. H., Huang, J. S. K. and Reid, R. O.: Vortex modes in Southern Lake Michigan. *J. Phys. Oceanogr.*, **10**, 1814–1823 (1980)
35. Sezawa, K. and Kanai, K.: On shallow water waves transmitted in the direction parallel to a sea coast with special reference to long waves in heterogeneous media. *Bull. Earthquake Res. Inst. Tokyo*, **17**, 685–694 (1939)
36. Snodgrass, F. E., Munk, W. H. and Miller, G. R.: Long-period waves over California's continental borderland. I: Background spectra. *J. Mar. Res.*, **20**, 3–30 (1962)
37. Stocker, T. and Hutter, K.: A model for topographic Rossby waves in channels and lakes. *Mitteilungen der Versuchsanstalt für Wasserbau, Hydrologie und Glaziologie, ETH Zürich*, No **76**, 1–154 (1985)
38. Stocker, T.: Topographic waves, eigenmodes and reflections in lakes and semi-infinite channels. *Mitteilungen der Versuchsanstalt für Wasserbau, Hydrologie und Glaziologie, ETH Zürich*, No **93**, 1–170 (1987)
39. Stocker, T and Hutter, K.: Topographic waves in channels and lakes on the f-plane. *Lecture Notes on Ccoastal and Estuarine Studies*, Springer Verlag, Berlin etc., **21**, 1–178 (1987)
40. Takeda, H.: Topographically trapped waves over the continental shelf and slope. *J. Oceanogr. Soc. Japan*, **40**, 349–366 (1984)
41. Trösch, J.: Finite element calculation of topographic waves in lakes. *Proceedings of the 4th Internnatl. Conf. Applied Numerical Methods*, Tainan, Taiwan (1988)
42. Wenzel, M.: *Interpretation der Wirbel im Bornholm becken durch topographische Rossby Wellen in einem Kreisbecken*. Diplomarbeit, Christian Albrechts Universität Kiel. 52 pp. (1978)

Chapter 21
Topographic Waves in Basins with Complex Shapes and Complex Bathymetries

21.1 Conceptual Review

In the last two chapters, construction of analytical solutions to the topographic wave (TW)-equation in enclosed basins subject to the no-flux boundary condition was possible only for basins of simple geometries and simple bathymetries. The situations were generally such that the linear boundary value problems could be constructed and solved by the method of separation of variables leading to two-point-eigenvalue problems of ordinary differential equations with homogeneous boundary conditions, which could be expressed in terms of simple functions. However, unless the bathymetry was approximately expressible by very simple exponential or power law functions, the differential equations soon took forms, which were no longer expressible by common functions of mathematical physics, or the mathematical expressions for the solution would be so tedious to handle, that they are very likely better solved numerically. As an example, we presented the solutions of the few lowest order TW-modes in a circular basin with parabolic radial profile in terms of hypergeometric polynomials (see Chap. 20, formulae (20.23)). It is also known that the interior of a circle can be transformed by a conformal mapping onto the interior of a rectangle. This transformation involves, among others, elliptic integrals of the first kind. So, the solution in the rectangle will be a composition of hypergeometric polynomials and elliptic integrals of the first kind. Such solution techniques served their purposes in times prior to electronic computation. Today, more flexibility is demanded, such that mathematical expressions can be optimally matched to the realistic bathymetries. Indeed, we have so far not been able to describe *qualitatively* how TW-modes look like for a rectangular long basin even when its bathymetry is very simple. In fact it is claimed that an elongated basin of more general than rectangular or elliptical shape possesses also TW-modes which are *characteristically different* from those hitherto constructed. The identification of these other solutions is physically important; and it will solve the Lake of Lugano controversy explained in Chap. 19.

A hint that an elongated basin must at a certain frequency possess another basin-filling solution beyond the long wavelength solutions, e.g. expressed by the 'Ball'

K. Hutter et al., *Physics of Lakes*, *Volume 2: Lakes as Oscillators*, Advances in Geophysical and Environmental Mechanics and Mathematics,
DOI 10.1007/978-3-642-19112-1_21,

solutions, see Fig. 20.6, follows for a straight channel solution with exponential profile from Buchwald and Adams' [4] channel solution. For five transverse modes, its dispersion relation is displayed in Fig. 20.12. In these dispersion curves, to each value of σ, there exist two positive wavenumbers k; for the first in the regime of positive $\mathrm{d}\sigma/\mathrm{d}k > 0$, a typical wavelength of the TW-mode is *large*, whereas in the regime of negative $\mathrm{d}\sigma/\mathrm{d}k < 0$, the corresponding wavelength of the TW-mode is *small*. Whilst the number of gyres in a long enclosed basin is small in the former case, this number tends to be large in the latter case. This behaviour is to be expected also for enclosed basins.

There is even a third type of TW-modes in an enclosed basin, but it can with the present knowledge not easily be explained. Consider the analogue to the Taylor reflection problem in a semi-infinite gulf. In that problem, the reflection of a Kelvin wave at the end of a semi-infinite gulf can only be achieved by the addition of Poincaré waves with complex wave numbers and the same frequency such that the reflection condition is fulfilled *and* these Poincaré waves are exponentially evanescent (or oscillatory) as they move back to the gulf entrance. An analogous behaviour also exists for the TW-operator. The dispersion relation of TWs above the critical point σ of no energy propagation, $\mathrm{d}\sigma/\mathrm{d}k = 0$, allows complex valued wavenumbers for given real σ. These additional solutions, when adequately combined, can also form solutions which will be called *bay-modes* or *trapped modes* with large activity at the gulf end but exponentially negligible excitement far from it. From this we conclude that the TW-operator will allow long and short-length basin-filling modes plus bay modes whose excitation is restricted to boundary regions. The demonstration of this behaviour will be the major topic of this chapter.

The numerical method best suited to discover the above described behaviour is the method of weighted residuals (MWR) with an expansion of the transport stream function into a complete set of functions across the width of elongated basins multiplied with functions in the long direction of the basin. The presentation of this method and its use are the goals of this chapter.

21.2 The Method of Weighted Residuals

21.2.1 The Method of Weighted Residuals Applied to Topographic Waves

The MWR consists of a reduction of the dimension of the mathematical problem by a basis (shape) function expansion and is a variant of the *projection method*, the *spectral* or *modal* method and may also be considered a *generalized separation of variables procedure*. Its advantage is that despite of its numerical intent, the method permits analytical techniques to be pursued farther than with classical numerical approaches, such as finite difference or finite element methods.

There are several techniques by which the reduction of the dimensionality of a boundary value problem can be achieved and then approximately solved. One is to derive the governing equations from a *Variational Principle*. For the TW-equation this involves construction of a *functional* (Lagrangian) in terms of the mass transport stream function; the TW-equation is obtained as the Euler–Lagrange equation of this functional and the boundary condition would result from the natural boundary condition of the variation of the functional. Ripa [20] and Mysak [17] proceed this way. We use here (as we have done in Chap. 19 for the derivation of the governing equations of a continuously stratified lake) the MWR. Both methods, in their essentials, are described in Finlayson [7]. The MWR has already been applied to gravity waves by Raggio and Hutter [19], see Chap. 22, to topographic waves by Stocker and Hutter [23–25] and to two-phase turbidity currents by Scheiwiller et al. [22].

The MWR and the variational principle in the function expansion approach are related to the Method of Finite Elements (FE). One fundamental difference, however, consists in the fact that the domain of integration is not partitioned into a number of elements in which linear or higher order interpolation is performed. Rather than assuming the *local* functional dependence within an individual element and then minimizing some global measure, our model approach prescribes the *global* functional dependence along one dimension and maps the problem into the orthogonal subspace. This is achieved by a weighted integration of the equations along this dimension.

We consider the eigenvalue problem (20.16) formulated in the natural coordinate system shown in Fig. 21.1,

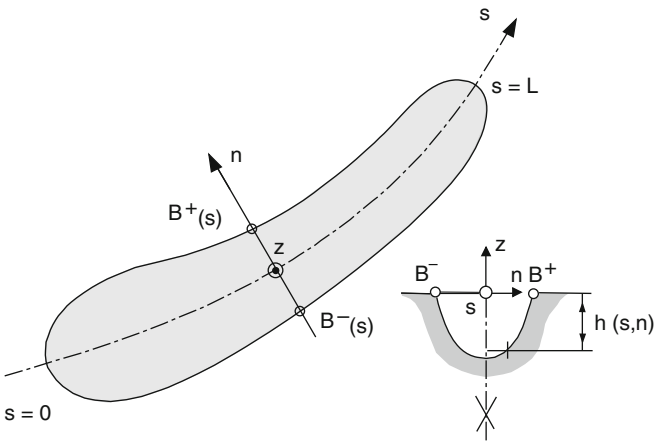

Fig. 21.1 Elongated lake and transverse section in a natural (s, n, z)-coordinate system. The thalweg axis ($n = 0$) may be a centre of symmetry and have curvature $K(s)$ (from Stocker (1987) [26]). © Versuchsanstalt für Wasserbau, Hydrologie und Glaziologie an der ETH Zürich, reproduced with permission

$$\begin{aligned} \mathbb{D}\psi &= 0, \quad \text{in} \quad \mathcal{D}, \\ \mathbb{B}\psi &= 0, \quad \text{in} \quad \partial\mathcal{D} \end{aligned} \tag{21.1}$$

with the definition of the (dimensionless) differential and boundary operators $\mathbb{D}$ and $\mathbb{B}$, respectively

$$\mathbb{D} \equiv \frac{1}{J}\left[-i\sigma\left[\frac{\partial}{\partial s}\left(\frac{h^{-1}}{J}\frac{\partial}{\partial s}\right)+\frac{\partial}{\partial n}\left(h^{-1}J\frac{\partial}{\partial n}\right)\right]+\frac{\partial h^{-1}}{\partial n}\frac{\partial}{\partial s}-\frac{\partial h^{-1}}{\partial s}\frac{\partial}{\partial n}\right], \tag{21.2}$$

$$\mathbb{B} \equiv 1.$$

$\sigma \equiv \omega/f$ is the non-dimensional frequency and $J = 1 - Kn$, where K is the curvature of the thalweg.

Let $\{P_\alpha(s,n)\}$ be a complete set of basis functions indexed by α, in terms of which the mass transport stream function $\psi(s,n)$ is expanded,

$$\psi(s,n) = \sum_{\alpha=1}^{N} P_\alpha(s,n)\,\psi_\alpha(s) \equiv P_\alpha\psi_\alpha. \tag{21.3}$$

Each basis function is weighted by a residue function $\psi_\alpha(s)$ which is assumed not to depend on the transverse coordinate n. All functional dependence on n is now incorporated in the preselected basis functions, a general form of separation. Expansion (21.3) represents the exact solution for a separable problem provided the basis functions are appropriately selected. For non-separable systems as (21.2) generally is, and for an arbitrary set $\{P_\alpha\}$ with $N < \infty$, the expansion is merely an approximation. Clearly, fast convergence is anticipated so that truncation of (21.3) for very small N may furnish a sufficiently accurate solution. The integration of (21.1) with an arbitrary bounded weighting function $\delta\phi(s,n)$ over the lake domain and along the shoreline, respectively, leads to the integral formulations

$$\begin{aligned} \int_D (\mathbb{D}\psi)\,\delta\phi\,\mathrm{d}a &= 0, \\ \oint_{\partial D} (\mathbb{B}\psi)\,\delta\phi\,\mathrm{d}l &= 0. \end{aligned} \tag{21.4}$$

If (21.4) holds for any weighting function, this is equivalent to (21.1) owing to the fundamental lemma of the Calculus of Variation [5]. Expanding also the weighting function in terms of the complete set $\{Q_\beta\}$, viz.

$$\delta\phi(s,n) = \sum_{\beta=1}^{N} Q_\beta(s,n)\,\delta\phi_\beta(s) \equiv Q_\beta\,\delta\phi_\beta,$$

and inserting (21.3) and this expansion into (21.4) yields

$$\begin{aligned} \int_{\mathcal{D}} (\mathbb{D}\, P_\alpha \psi_\alpha)\; Q_\beta\; \delta\phi_\beta \,\mathrm{d}a &= 0, \\ \oint_{\partial\mathcal{D}} (\mathbb{B}\, P_\alpha \psi_\alpha)\; Q_\beta\; \delta\phi_\beta \,\mathrm{d}l &= 0. \end{aligned} \tag{21.5}$$

Summation over doubly repeated Greek indices is understood. The integration over the lake domain $\mathcal{D}$ can be split up into two integrations over either coordinates using $\mathrm{d}a = J\,\mathrm{d}n\mathrm{d}s$ for the area element in the natural coordinate frame. Further, the trivial form of the boundary operator $\mathbb{B} \equiv 1$ suggests the special choices

$$P_\alpha\left(s, B^{\pm}\right) = 0, \qquad Q_\beta\left(s, B^{\pm}\right) = 0, \qquad \text{for all} \qquad \alpha, \beta \tag{21.6}$$

such that the only contribution to $(21.5)_2$ arises from the ends of the lake. Since the weighting functions are arbitrary, (21.5) can be replaced by

$$\left.\begin{aligned} \int_{n=B^-}^{n=B^+} (\mathbb{D}\, P_\alpha \psi_\alpha)\; J\; Q_\beta \,\mathrm{d}n &= 0 \\ \psi_\alpha(s)\;|_{s=0,L} &= 0 \end{aligned}\right\} \alpha, \beta = 1, \ldots, N. \tag{21.7}$$

The residue functions ψ_α depend only on s and are therefore extracted from the integration by carefully accounting for the effect of the differential operator $\mathbb{D}$ on $\psi_\alpha(s)$. On substituting (21.2) into (21.7), we obtain

$$\begin{aligned} 0 = \int_{B^-}^{B^+} \Bigg[-i\sigma \Bigg\{ \underbrace{\frac{\partial}{\partial s}\left[\frac{h^{-1}}{J}\frac{\partial}{\partial s}(P_\alpha\psi_\alpha)\right]}_{(1)} + \underbrace{\frac{\partial}{\partial n}\left[h^{-1}J\frac{\partial}{\partial n}(P_\alpha\psi_\alpha)\right]}_{(2)} \Bigg\} \\ + \underbrace{\frac{\partial h^{-1}}{\partial n}\frac{\partial}{\partial s}(P_\alpha\psi_\alpha)}_{(3)} - \underbrace{\frac{\partial h^{-1}}{\partial s}\frac{\partial}{\partial n}(P_\alpha\psi_\alpha)}_{(4)} \Bigg] Q_\beta \,\mathrm{d}n, \end{aligned} \tag{21.8}$$

where summation over the repeated index α is understood. Using judiciously integration by parts in the individual terms, (21.8) can be written in the form

$$\left.\begin{aligned} \mathbb{M}_{\beta\alpha}\psi_\alpha &= 0 \\ \psi_\alpha &= 0 \end{aligned}\right\} \alpha, \beta = 1, \ldots, N \left\{ \begin{aligned} &0 < s < L, \\ &s = 0, L, \end{aligned} \right. \tag{21.9}$$

in which $\mathbb{M}_{\beta\alpha}$ is the following ordinary matrix differential operator

$$\begin{aligned}\mathbb{M}_{\beta\alpha} = &- i\sigma\left[M^{00}_{\beta\alpha}\frac{\mathrm{d}^2}{\mathrm{d}s^2} + \left(\frac{\mathrm{d}M^{00}_{\beta\alpha}}{\mathrm{d}s} + M^{10}_{\beta\alpha} - M^{01}_{\beta\alpha}\right)\frac{\mathrm{d}}{\mathrm{d}s}\right.\\ &\left. + \left(\frac{\mathrm{d}M^{10}_{\beta\alpha}}{\mathrm{d}s} - M^{11}_{\beta\alpha} - M^{22}_{\beta\alpha}\right)\right] - \left(M^{20}_{\beta\alpha} + M^{02}_{\beta\alpha}\right)\frac{\mathrm{d}}{\mathrm{d}s}\\ &- \left(\frac{\mathrm{d}M^{20}_{\beta\alpha}}{\mathrm{d}s} + M^{12}_{\beta\alpha} - M^{21}_{\beta\alpha}\right) \qquad (\alpha,\beta = 1,\ldots,N). \quad (21.10)\end{aligned}$$

The matrix elements $M^{ij}_{\beta\alpha}$ represent quadrature formulae in the transverse direction, explicitly:

$$\begin{aligned}
M^{00}_{\beta\alpha} &= \int h^{-1}J^{-1}P_\alpha Q_\beta \mathrm{d}n,\\
M^{10}_{\beta\alpha} &= \int h^{-1}J^{-1}\frac{\partial P_\alpha}{\partial s}Q_\beta \mathrm{d}n, \quad M^{01}_{\beta\alpha} = \int h^{-1}J^{-1}P_\alpha\frac{\partial Q_\beta}{\partial s}\mathrm{d}n,\\
M^{20}_{\beta\alpha} &= \int h^{-1}\frac{\partial P_\alpha}{\partial n}Q_\beta \mathrm{d}n, \qquad M^{02}_{\beta\alpha} = \int h^{-1}P_\alpha\frac{\partial Q_\beta}{\partial n}\mathrm{d}n, \qquad (21.11)\\
M^{11}_{\beta\alpha} &= \int h^{-1}J^{-1}\frac{\partial P_\alpha}{\partial s}\frac{\partial Q_\beta}{\partial s}\mathrm{d}n, \quad M^{22}_{\beta\alpha} = \int h^{-1}J^{-1}\frac{\partial P_\alpha}{\partial n}\frac{\partial Q_\beta}{\partial n}\mathrm{d}n,\\
M^{12}_{\beta\alpha} &= \int h^{-1}\frac{\partial P_\alpha}{\partial s}\frac{\partial Q_\beta}{\partial n}\mathrm{d}n, \qquad M^{21}_{\beta\alpha} = \int h^{-1}\frac{\partial P_\alpha}{\partial n}\frac{\partial Q_\beta}{\partial s}\mathrm{d}n.
\end{aligned}$$

For the derivation of (21.9)–(21.11) from (21.8), see the Appendix to this chapter.

The individual components $M^{ij}_{\beta\alpha}$ in (21.11) are known functions of s and depend on the topography of the lake, h, on the metric of the natural coordinate system, $J(s,n)$, on the shape of the lake shore, $B^{\pm}(s)$, and on the sets of basis functions $\{P_\alpha(s,n)\}$ and $\{Q_\beta(s,n)\}$.

Notice that (21.9) is only meaningful as long as all entries of the matrices (21.11) are bounded. Since J and J^{-1} are both regular, this means that the basis functions P_α and Q_β must be chosen such that the combinations $h^{-1}\,P_\alpha\,Q_\beta$, $h^{-1}\,(\partial P_\alpha/\partial s)\,Q_\beta$, etc. arising in (21.11) are integrable. For $h>0$ no difficulties arise, however, when $h = 0$ along the shore the functions P_α, Q_β must be taken from a set of which the nearshore behaviour is dictated by that of h. This is a drawback of this method and restricts it essentially to profiles with finite shore depth.

Equation (21.9) form a system of coupled one-dimensional differential equations that replace the single two-dimensional boundary-value problem (21.1). These two formulations are presumed to be equivalent provided (1) the sets of basis functions are complete in $[B^-, B^+]$ and (2) $N = \infty$. The selected order N of the system sets a natural bound to the variability of the approximate solution as well as to its quality. At a first glance the MWR seems to leave us with a more complicated task. Finite-difference calculations, however, have indicated numerical difficulties such as slow convergence, particularly for complicated topographies and for large

wavenumbers [2]. Moreover, this version of the MWR is very well suited to the identification of long and short wavelength basin-filling modes as well as bay modes in enclosed elongated basins and therefore draws a parallel to the corresponding behaviour of gravity modes in rotating enclosed basins.

21.2.2 Symmetrisation

It is now assumed that the physical configurations exhibit symmetry with respect to the axis $n = 0$. This symmetrisation is also suggested by the fact that TW-solutions for the stream function in circular and elliptical basins change repeatedly their symmetry with respect to the lake axis.[1] This suggests to build the solution by pairs of symmetric and skew-symmetric functions. Therefore, the functions P_α, Q_α, J and J^{-1} are symmetrised by introducing the decompositions

$$\begin{aligned} f(s,n) &= f^+(s,n) + f^-(s,n), \\ f^+(s,n) &= f^+(s,-n), \\ f^-(s,n) &= -f^-(s,-n), \end{aligned} \tag{21.12}$$

in which

$$\begin{aligned} f^+(s,n) &= \frac{1}{2}(f(s,n) + f(s,-n)), \\ f^-(s,n) &= \frac{1}{2}(f(s,n) - f(s,-n)). \end{aligned} \tag{21.13}$$

This decomposition is applied to the matrix elements $M^{ij}_{\beta\alpha}$ in (21.11); the important result here is

$$\begin{aligned} M^{00}_{\beta\alpha} &= M^{00++}_{\beta\alpha} + M^{00--}_{\beta\alpha} + M^{00-+}_{\beta\alpha} + M^{00+-}_{\beta\alpha} \quad (\alpha,\beta = 1,\ldots,N) \\ &= \int h^{-1}(J^{-1})^+ P^+_\alpha Q^+_\beta \,\mathrm{d}n + \int h^{-1}\,(J^{-1})^+ P^-_\alpha Q^-_\beta \,\mathrm{d}n \\ &\quad + \int h^{-1}\,(J^{-1})^- P^-_\alpha Q^+_\beta \,\mathrm{d}n + \int h^{-1}(J^{-1})^- P^+_\alpha Q^-_\beta \,\mathrm{d}n, \\ M^{20}_{\beta\alpha} &= M^{20-+}_{\beta\alpha} + M^{20+-}_{\beta\alpha} \\ &= \int h^{-1}\,\frac{\partial P^-_\alpha}{\partial n}\, Q^+_\beta \,\mathrm{d}n + \int h^{-1}\,\frac{\partial P^+_\alpha}{\partial n}\, Q^-_\beta \,\mathrm{d}n \end{aligned} \tag{21.14}$$

[1] If in Fig. 20.6 the long axis is identified with the s axis, it is seen that for $t = 0$ the mass transport stream function ψ is skew-symmetric and for $t = T/4$ it is symmetric.

with analogous expressions for $M^{22}_{\beta\alpha}$ and $M^{02}_{\beta\alpha}$, respectively. It has been assumed above that $h^- = 0$ (symmetric depth profile), and the integration is from $B^- = -\frac{1}{2}B(s)$ to $B^+ = \frac{1}{2}B(s)$. Because the basis functions P_α and Q_β are decomposed according to (21.12) and (21.13), the expansion (21.3) of the solution $\psi(s,n)$ must be replaced by

$$\psi(s,n) = P^+_\alpha(s,n)\,\psi^+_\alpha(s) + P^-_\alpha(s,n)\,\psi^-_\alpha(s), \tag{21.15}$$

where the $\pm$ superscripts on ψ_α indicate merely affiliation to the individual $P^\pm_\alpha$. In vector notation, the stream function reads

$$\boldsymbol{\psi} = (\psi^+_1, \ldots, \psi^+_N; \quad \psi^-_1, \ldots, \psi^-_N) = (\boldsymbol{\psi}^+; \boldsymbol{\psi}^-), \tag{21.16}$$

and the matrices (21.14) take the forms

$$\boldsymbol{M}^{00} = \begin{bmatrix} \boldsymbol{M}^{00++} & \boldsymbol{M}^{00-+} \\ \boldsymbol{M}^{00+-} & \boldsymbol{M}^{00--} \end{bmatrix}, \quad \boldsymbol{M}^{20} = \begin{bmatrix} \boldsymbol{0} & \boldsymbol{M}^{20-+} \\ \boldsymbol{M}^{20+-} & \boldsymbol{0} \end{bmatrix}, \quad \text{etc.}$$

With this notation the differential equations (21.9) read

$$\left(-i\sigma \begin{bmatrix} \mathbb{M}^{++} & \mathbb{M}^{-+} \\ \mathbb{M}^{+-} & \mathbb{M}^{--} \end{bmatrix} + \begin{bmatrix} \boldsymbol{0} & \mathbb{N}^{-+} \\ \mathbb{N}^{+-} & \boldsymbol{0} \end{bmatrix}\right) \begin{pmatrix} \boldsymbol{\psi}^+ \\ \boldsymbol{\psi}^- \end{pmatrix} = 0, \tag{21.17}$$

with the matrix operators $\mathbb{M}$ and $\mathbb{N}$ of which the particular form is unimportant in the ensuing arguments.

The coupling of the solution vectors $\boldsymbol{\psi}^+$ and $\boldsymbol{\psi}^-$ is induced by the off-diagonal operators $\mathbb{M}^{-+}$, $\mathbb{M}^{+-}$ and $\mathbb{N}^{-+}$, $\mathbb{N}^{+-}$, respectively. The former are due to curvature and vanish when $K = 0$.[2] The latter originate from the vector product $\hat{\boldsymbol{k}} \cdot \nabla\psi \times \nabla\,(f/H)$ and express the effect of the Coriolis force. The restriction to only symmetric basis functions reduces (21.17) to two decoupled equations. This obviously corresponds to the claim that both terms of the sum of the TW-equation be individually zero. On imposing the boundary condition this implies $\psi \equiv 0$, a result claimed already in Chap. 19. It suggests that the approximate system requires a set of basis functions containing both symmetric and antisymmetric functions if qualitatively correct results are to emerge.

21.3 Topographic Waves in Infinite Channels

TWs in infinite channels have been studied previously, and their treatments have been presented in Chaps. 19 and 20 on the basis of analytical solutions. Numerical solutions for two sided topographies and the application of the finite difference

[2] This is so, since $J = 1 - Kn$, $J^+ = 1$, $J^- = -Kn$ and evaluation of $\mathbb{M}^{-+}$ and $\mathbb{M}^{+-}$ according to (21.11) makes only those contributions survive which involve J^-.

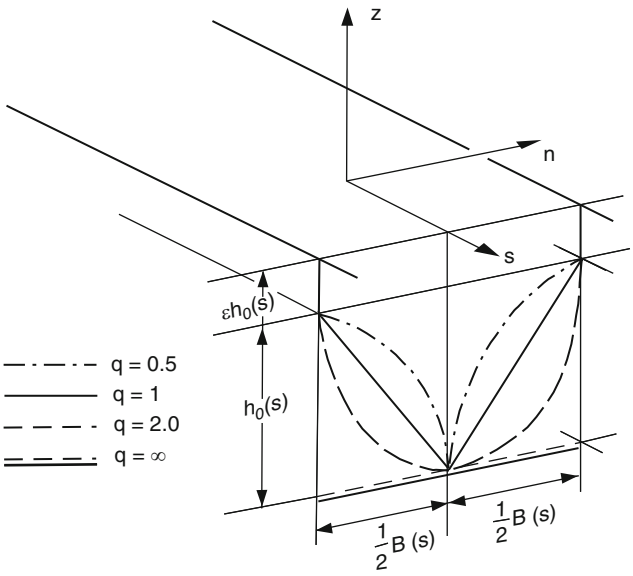

Fig. 21.2 Cross-sectional depth profiles of a symmetric channel

method were presented by Gratton [9], Gratton and LeBlond [10] and Bäuerle [2]. We reproduce here the solution procedure by Stocker and Hutter [23–25, 27], because this solution method has turned out to be particularly apt in elucidating the physics and, in particular, because of the parallels to the mode behaviour of gravity waves in rotating enclosed basins.

21.3.1 Basic Concept

The suitability of the approximate model equations (21.9) deduced with the MWR is now tested using a straight, infinite and symmetric channel with a topography of the form[3]

$$h(s,n) = h_0(s)\left(1+\epsilon-\left|\frac{2n}{B(s)}\right|^q\right), \tag{21.18}$$

where ϵ is a sidewall and q a topography parameter, see Fig. 21.2, which provides the possibility of modelling both concave ($q > 1$) and convex ($q < 1$) transverse depth profiles. The sidewall parameter ϵ has been introduced in order that all matrix elements (21.11) take finite values. The complete sets of basis functions $\{P_\alpha\}$ and

[3] This profile is the same as that used by Saylor et al. [21] for the circular basin, simulating the dynamics of Southern Lake Michigan, see Chaps. 19 and 20.

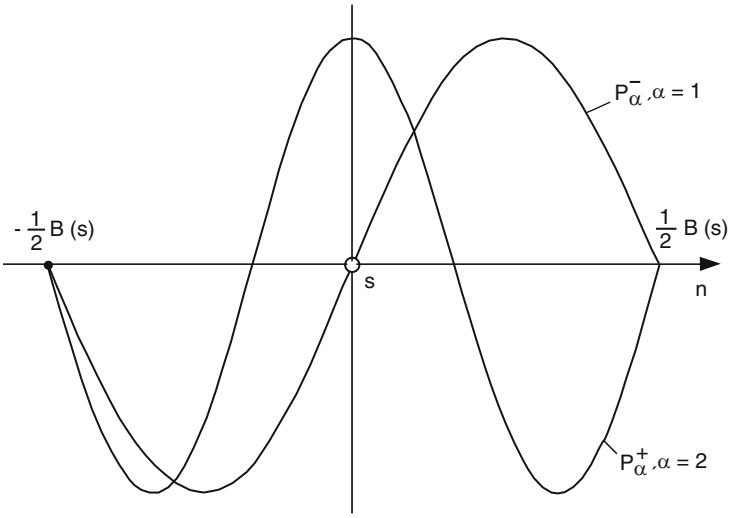

Fig. 21.3 Symmetric and skew-symmetric basis functions

$\{Q_\beta\}$ will be chosen to be identical (Galerkin procedure) with the symmetric and skew-symmetric parts given by, see Fig. 21.3;

$$\begin{aligned} P_\alpha^+(s,n) &= \cos\left(\pi\left(\alpha-\frac{1}{2}\right)\frac{2n}{B(s)}\right), \\ P_\alpha^-(s,n) &= \sin\left(\pi\alpha\frac{2n}{B(s)}\right), \end{aligned} \quad (\alpha = 1,\ldots,N). \tag{21.19}$$

Here, P_α^+ and P_α^- arise in pairs; N, thus, characterizes a model consisting of $2N$ basis functions. These satisfy the boundary conditions (21.6) along the shoreline $n = \pm\frac{1}{2}B(s)$. Substituting (21.18) and (21.19) into (21.11) and assuming $B(s)$ to be constant[4] it is seen that

$$\begin{aligned} &M_{\beta\alpha}^{00} = Bh_0^{-1}K_{\beta\alpha},\ M_{\beta\alpha}^{22} = B^{-1}h_0^{-1}K_{\beta\alpha}^{22}, \\ &M_{\beta\alpha}^{20} = h_0^{-1}K_{\beta\alpha}^{20}, \quad M_{\beta\alpha}^{02} = h_0^{-1}K_{\beta\alpha}^{02}, \end{aligned} \tag{21.20}$$

while the elements with the superscripts 10, 01, 11, 12 and 21 all vanish.

The dimensionless matrix elements $K_{\alpha\beta}^{ij}$ depend on ϵ and q and straightforward calculation leads to the expressions for these:

[4] This assumption is not necessary and the operator $\mathbb{M}$ for $\partial B/\partial s \neq 0$ is given in [23].

$$
\begin{aligned}
K_{\beta\alpha}^{00++} &= \int h_\star^{-1} \cos\left(\pi\left(\alpha-\frac{1}{2}\right)y\right)\cos\left(\pi\left(\beta-\frac{1}{2}\right)y\right)\mathrm{d}y,\\
K_{\beta\alpha}^{00--} &= \int h_\star^{-1} \sin(\pi\alpha y)\ \sin(\pi\beta y)\mathrm{d}y,\\
K_{\beta\alpha}^{22++} &= 4\pi^2\left(\alpha-\frac{1}{2}\right)\left(\beta-\frac{1}{2}\right)\int h_\star^{-1}\sin\left(\alpha\left(\alpha-\frac{1}{2}\right)y\right)\\
&\quad\times\sin\left(\pi\left(\beta-\frac{1}{2}\right)y\right)\mathrm{d}y,\\
K_{\beta\alpha}^{22--} &= 4\pi^2\alpha\beta\int h_\star^{-1}\cos(\pi\alpha y)\cos(\pi\beta y)\,\mathrm{d}y,\\
K_{\beta\alpha}^{20+-} &= -2\pi\left(\alpha-\frac{1}{2}\right)\int h_\star^{-1}\sin\left(\pi\left(\alpha-\frac{1}{2}\right)y\right)\sin(\pi\beta y)\,\mathrm{d}y,\\
K_{\beta\alpha}^{20-+} &= 2\pi\alpha\int h_\star^{-1}\cos(\pi\alpha y)\cos\left(\pi\left(\beta-\frac{1}{2}\right)y\right)\mathrm{d}y,\\
K_{\beta\alpha}^{02+-} &= 2\pi\alpha\int h_\star^{-1}\cos\left(\pi\left(\alpha-\frac{1}{2}\right)y\right)\cos(\pi\beta y)\,\mathrm{d}y,\\
K_{\beta\alpha}^{02-+} &= -2\pi\left(\beta-\frac{1}{2}\right)\int h_\star^{-1}\sin(\pi\alpha y)\sin\left(\pi\left(\beta-\frac{1}{2}\right)y\right)\mathrm{d}y
\end{aligned}
\tag{21.21}
$$

with $h_\star = 1+\epsilon-y^q$; the integration is meant to be from $y=0$ to $y=1$. Numerical evaluation of these integrals for selected values of $q=(0.5,2.5)$ and $\varepsilon=(0.05,01)$ can easily be performed with any commercial software. Results are listed for the more general case that $B(s)\neq$ *constant* in tables by Stocker and Hutter [23]. With (21.21), (21.10) takes the form

$$
\begin{aligned}
\mathbb{K}\equiv Bh_0\mathbb{M} = -i\sigma\Bigg[&B^2\boldsymbol{K}^{00}\frac{\mathrm{d}^2}{\mathrm{d}s^2}-B^2\left(h_0^{-1}\frac{\mathrm{d}h_0}{\mathrm{d}s}\right)\boldsymbol{K}^{00}\frac{\mathrm{d}}{\mathrm{d}s}-\boldsymbol{K}^{22}\Bigg]\\
&-B\left(\boldsymbol{K}^{20}+\boldsymbol{K}^{02}\right)\frac{\mathrm{d}}{\mathrm{d}s}+B\left(h_0^{-1}\frac{\mathrm{d}h_0}{\mathrm{d}s}\right)\boldsymbol{K}^{20}.
\end{aligned}
\tag{21.22}
$$

This operator has constant coefficients whenever the depth-profile is constant or exponential with respect to the basin axis. For an infinite channel, however, we prefer $h_0=$ constant. Let us take a solution of the form

$$
\boldsymbol{\psi}=(\boldsymbol{\psi}^+;\boldsymbol{\psi}^-)=\mathrm{e}^{\mathrm{i}ks/L}(c_1,\ldots,c_N;c_{N+1},\ldots,c_{2N})=\mathrm{e}^{\mathrm{i}ks/L}\boldsymbol{c}
\tag{21.23}
$$

with a dimensionless complex-valued wavenumber k; $\mathrm{Im}(k)\neq 0$ is meaningful in semi-infinite and finite channels, and a length L is then appropriate. With (21.22), (21.23) and $h_0=$ const. the symmetrized form of (21.9) reduces to a system of algebraic equations

$$
\left.
\begin{aligned}
\boldsymbol{C}\boldsymbol{c}&=\boldsymbol{0},\\
\boldsymbol{C}&=\begin{bmatrix}\sigma\left((rk)^2\boldsymbol{K}^{00++}+\boldsymbol{K}^{22++}\right) & -(rk)\left(\boldsymbol{K}^{20-+}+\boldsymbol{K}^{02-+}\right)\\ -(rk)\left(\boldsymbol{K}^{20+-}+\boldsymbol{K}^{02+-}\right) & \sigma\left((rk)^2\boldsymbol{K}^{00--}+\boldsymbol{K}^{22--}\right)\end{bmatrix},
\end{aligned}
\right\}
\tag{21.24}
$$

in which the aspect ratio parameter $r = B/L$ has been introduced. Notice that r and k enter only through the product rk, suggesting that solutions for $r = 1$ only need to be constructed. $\boldsymbol{C}$ is a $(2N \times 2N)$-matrix and depends on σ and k. Equation $(21.24)_1$ admits a non-trivial solution vector $\boldsymbol{c}$ if

$$\det \boldsymbol{C}(\sigma, k) = 0, \tag{21.25}$$

forming the *dispersion relation* $\sigma(k)$ for topographic Rossby waves in a straight infinite channel. It is a polynomial equation of order $2N$ in $(rk)^2$ with real coefficients. For each frequency a Nth order model, therefore, yields $4N$ wavenumbers counting complex conjugates and pairs having opposite signs.

Let k_γ $(\gamma = 1, \ldots, 4N)$ be a root of (21.25) corresponding to a frequency σ and $\boldsymbol{c}_\gamma$, $(c_{\alpha\gamma})$ the associated eigenvector (component) of (21.24). A general channel solution $\psi(s, n, t)$ can then be written as

$$\psi(s, n, t) = \mathrm{e}^{-\mathrm{i}\sigma f t} \sum_{\gamma=1}^{4N} \mathrm{e}^{\mathrm{i}k_\gamma s/L} d_\gamma \left[\sum_{\alpha=1}^{N} P_\alpha^+(s, n) c_{\alpha\gamma} + \sum_{\alpha=N+1}^{2N} P_{\alpha-N}^-(s, n) c_{\alpha\gamma} \right], \tag{21.26}$$

in which solutions belonging to individual k's occur in a linear combination by an arbitrary complex vector $\boldsymbol{d}$, (d_γ). The MWR offers sufficient freedom in modelling the channel topography, because improved accuracy can be obtained by higher-order models, and convergence is expected.

21.3.2 Dispersion Relation

Solutions of (21.25) may be plotted schematically for a first-order model, $N = 1$, in a $(\mathrm{Re}(k), \mathrm{Im}(k), \sigma)$-coordinate system, see Fig. 21.4. This is a model which uses one symmetric and one skew-symmetric basis function of the form (21.19) and is of lowest possible order. Its graph is symmetric with respect to both axes $\mathrm{Re}(k) = 0$ and $\mathrm{Im}(k) = 0$. Three regimes 1, 2, 3 can be distinguished where the wavenumbers k take real, complex and purely imaginary values, respectively. Table 21.1 gives the periods at which the individual regimes join for different topography and sidewall parameters. In regime 1 all wavenumbers k are real and, therefore, represent physically possible channel solutions. Evidently in regime 1, there exists for each frequency a long and a short wave. This is typical of Rossby waves and has also been observed for *shelf waves* in Chap. 20, provided the slope parameter $S = h'/h$ was bounded in the domain. This is so also for channels: in other words it can be proven that existence of a wavenumber $|k| = |k_0| < \infty$ such that $c_g = \mathrm{d}\sigma/\mathrm{d}k = 0$ is guaranteed only if h'/h is bounded everywhere across the channel width.[5] At this

[5] A proof for this is given by Stocker and Hutter [27] in their Appendix C; it involves WKB perturbation procedures, see e.g. [3]. An example with infinite h'/h is given in Chap. 20. In the

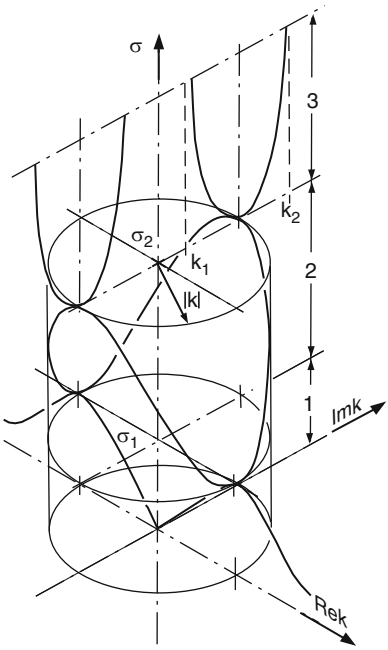

Fig. 21.4 Schematic plot of the complex dispersion relation for an infinite channel with $\varepsilon = 0.05$ and $q = 0.5$ and in a first-order model. In regime 1, k is real; in regime 2, it is complex with constant modulus; and in regime 3, k is purely imaginary, taking asymptotic values k_1 and k_2 and for large σ (from [26]). © Versuchsanstalt für Wasserbau, Hydrologie und Glaziologie an der ETH Zürich, reproduced with permission

Table 21.1 Periods and corresponding wavenumbers in a first-order model, which separate the regimes, depending on topography and sidewall parameters q and ε, respectively. The period T is calculated using $T = 16.9\,\mathrm{h}/\sigma$ corresponding to 45° latitude. At T_1 no wave energy is transported; T_2 separates requires 2 and 3

q	T_1 [h]		T_2 [h]		$\lvert k\rvert$	
	$\varepsilon = 0.05$	$\varepsilon = 0.10$	$\varepsilon = 0.05$	$\varepsilon = 0.10$	$\varepsilon = 0.05$	$\varepsilon = 0.10$
0.5	52.8	58.3	10.5	11.8	6.6	5.9
1.0	60.5	64.3	13.2	14.4	6.9	6.2
2.0	83.0	88.2	22.0	22.6	6.8	6.3
5.0	174.0	199.0	58.2	61.8	6.1	5.8

critical wavenumber no energy is transported along the channel. This corresponds roughly to wavelengths of about one channel width or less, and the periods are listed in Table 21.1. It is also worth noting that $\mathrm{Re}(k)$ can have both signs. This is in contrast to planetary Rossby waves which are due to the β-effect [11] or Rossby waves on the continental shelf [14], the reason being that here h'/h changes sign in the channel. So, such configurations enable topographic Rossby waves to propagate in *both* directions. In either case, as an effect of the Coriolis force, the structure of the wave on the Northern hemisphere is right-bounded with respect to the direction of phase propagation. The dispersion relation (21.25) contains only even powers of

single-step shelf, there is no maximum of σ for finite k: $\mathrm{d}\sigma/\mathrm{d}k = 0$ is only reached for $k \to \infty$. An analogous case occurs when the bathymetry is of multi-step shape.

σ such that (21.25) is independent of the sign of σ. It is convention that the sign of f (positive on the Northern hemisphere) determines the sign of the nondimensional frequency σ.

The structure of the stream function depends upon the frequency range. Small frequencies (regime 1) favour periodic patterns along the channel. Waves with intermediate frequencies of order 1 (regime 2) have a mixed periodic-exponential structure and do not represent possible solutions in an infinite channel. At frequencies $\sigma > 1$ (regime 3) the solutions grow or decay exponentially. For later use, the union of the three regimes of the dispersion relation in Fig. 21.4 will be called a *mode unit*.

The second-order model furnishes 8 wavenumbers to each frequency and its dispersion relation consists of two interlocking mode units, see Fig. 21.5. Thus, there are now two branches with real, complex and imaginary k, respectively. The relative size of the mode units and their spatial positions within the (k, σ)-coordinate system depend crucially upon the topography. The cylindrical surface of the first-order model degenerates to the smaller bell-shaped surface, i.e. its radius now depends on the frequency. The second mode unit forms an outer shell, which here has the form of a cone. Physically possible solutions for the infinite channel exist in regime 1 for both mode units and in regime 2 only for the first mode unit. The qualitative shape of the dispersion relation for an Nth-order model can be guessed from

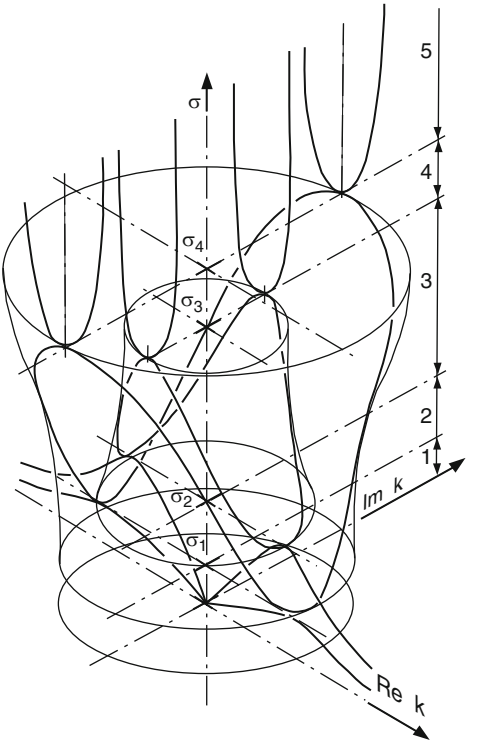

Fig. 21.5 Schematic plot of the complex dispersion relation $\sigma(k)$ for an infinite channel with $\varepsilon = 0.05$ and $q = 0.5$ in a second-order model. Five regimes with respect to σ can be differentiated (from [26]). © Versuchsanstalt für Wasserbau, Hydrologie und Glaziologie an der ETH Zürich, reproduced with permission

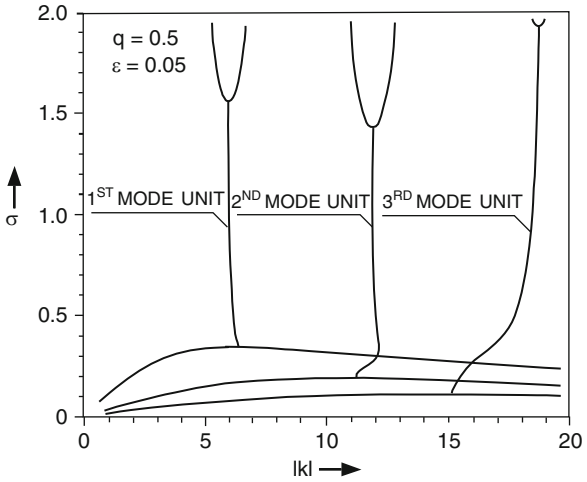

Fig. 21.6 Modulus k of the third-order-dispersion relation for an infinite channel, $q = 0.5, \varepsilon = 0.05$ (from [26]). © Versuchsanstalt für Wasserbau, Hydrologie und Glaziologie an der ETH Zürich, reproduced with permission

Figs. 21.4 and 21.5. The modulus $|k|$ is plotted for a third-order model in Fig. 21.6, demonstrating clearly the addition of the next mode unit.

Summarizing and extrapolating, we state:

- The dispersion relation of an Nth order model consists of N mode units each of which has 3 regimes, in which wavenumbers are real, complex or imaginary.
- Solutions for infinite channels, which are physically meaningful, can only be constructed for wavenumbers k which are real. Therefore, when h'/h is bounded, there exist maximum frequencies, for which channel solutions may occur (see Table 21.1). At these maxima energy cannot propagate; for smaller k's group and phase velocities are unidirectional, for larger k's they are antidirectional.
- In domains, which are of finite extent also in the s-direction (lakes), solutions can be constructed with real, complex or imaginary wavenumbers k. Their spatial dependence is either periodic, periodic exponential or exponential.
- From this point of view, lake solutions occur for all $\sigma \in (0, \infty)$. However recall, that the low-frequency approximation, $\omega^2 \ll f^2$, was made, for the barotropic TW-equation to be valid. Therefore, physical applications of results $|\sigma| > 1$ may be dubious.

These properties are tied to the existence of a finite $k = k_0$, where the purely real dispersion relation branches off to become complex.

The performance of the MWR approximation is best tested when results obtained with increasing mode-units are compared against an exact solution. Figure 21.7 displays such a comparison, the exact solution being constructed for a channel with constant $h_0 = 1$, exponential shores and a region with constant depth (see insets in

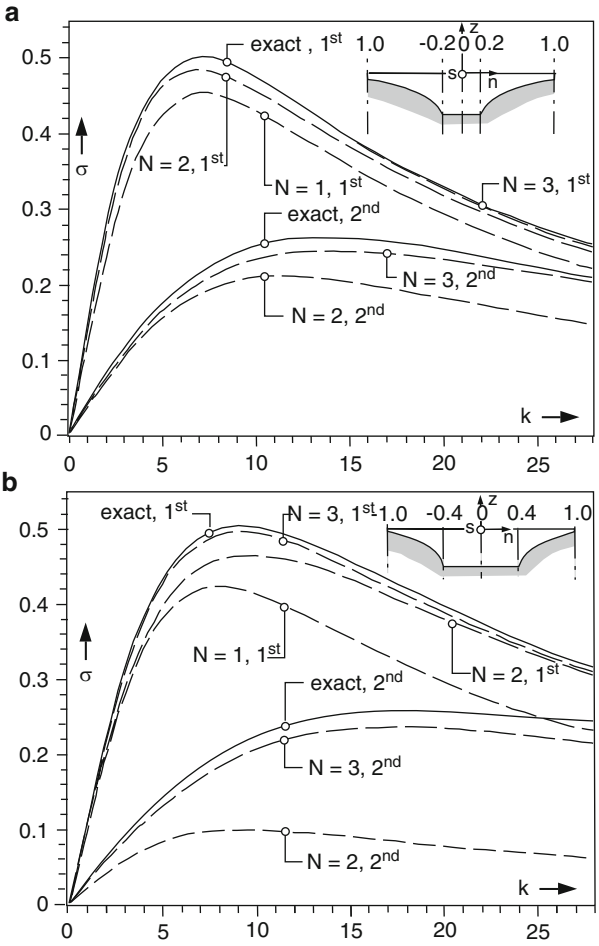

Fig. 21.7 Comparison of the dispersion relation $\sigma(k)$ of the exact solutions in a piecewise exponential channel (see inset) with the MWR solutions for $N = 1$–3 and the two first modes (from [27]). © Springer, Berlin, reproduced with permission

both panels for the bathymetric profiles).[6] The exact dispersion curves are shown for the first and second mode (solid lines), and approximate MWR-dispersion curves are shown for $N = 1, 2, 3$ mode units (dashed lines). The convergence of the approximate dispersion curves for $N = 1, 2, 3$ to the exact solutions is clearly seen; this convergence is faster for shallow slopes than for steep slopes, and obviously higher order models are required for modes $N \geq 3$.

[6] In the three regimes the differential equation for the transverse variation of the stream function has constant coefficients and the solutions in the three regimes are patched together by requesting continuity of ψ and $\partial\psi/\partial n$, see the straight channel solution in Chap. 20.

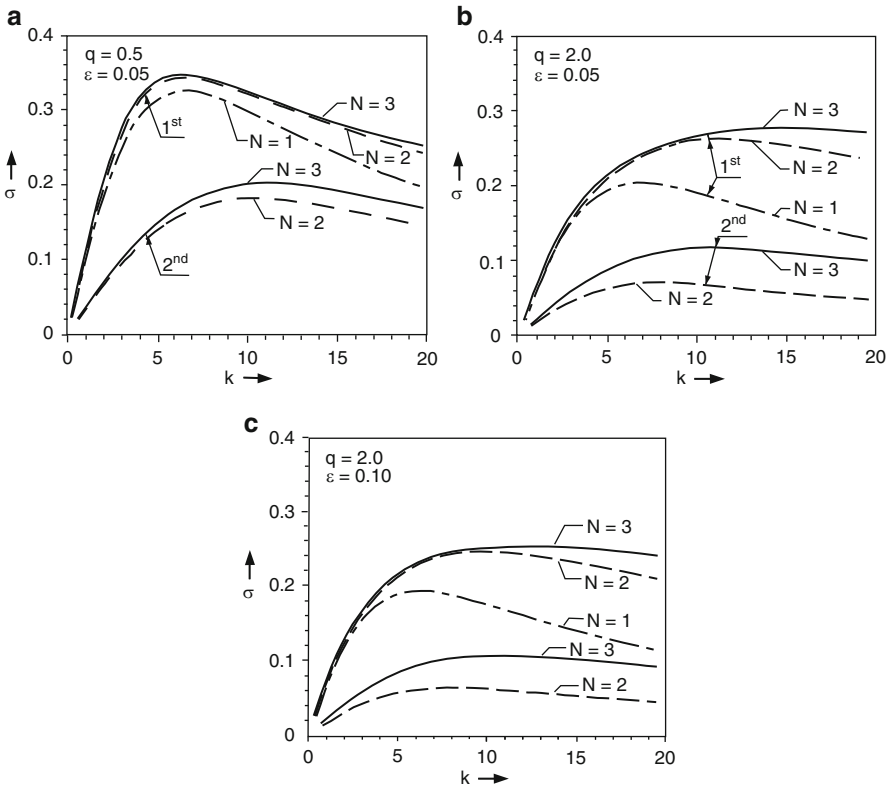

Fig. 21.8 Convergence of the different modes, increasing the order of the model from $N = 1$–3 for convex ($q = 0.5$) and concave ($q = 2.0$) topography and two side-wall parameters, $\varepsilon = 0.05$ and $\varepsilon = 0.10$ (from [27]). © Springer, Berlin, reproduced with permission

Figures 21.8 show MWR-solutions for the first and second mode for $N = 1$–3 and different values of q and ε. Comparison of panels (a) and (b) shows that convergence with growing N is faster for $q = 0.5$ than $q = 2.0$. This is unfortunate, because the larger q-values correspond to more realistic bathymetries. On the other hand, comparison of panels (b) and (c) suggests that variations of ε are of lesser influence on the dispersion curves. This same qualitative behaviour is also seen in panels (b) and (c), where dispersion curves are shown for a second order model for $q = 2$ and $\varepsilon = 0.05, \varepsilon = 0.1$. Evidently, the dispersion relation reacts more sensitively to changes in q than changes in ε.

In summary, the above results suggest that the order of approximation of the MWR-method must at least be one to two mode units larger than the number of modes which one wishes to consider in a computation of 'quasi-standing' channel solutions of the TW-equation.

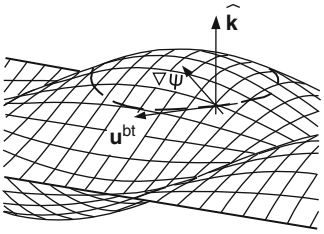

Fig. 21.9 Explaining the anticyclonic barotropic velocity field on a convex stream function surface (from [26]). © Versuchsanstalt für Wasserbau, Hydrologie und Glaziologie an der ETH Zürich, reproduced with permission

21.3.3 Channel Solutions

Equation (21.26) represents a general solution in a straight, infinite channel with arbitrary cross-section. ψ is a complex-valued function and so, both real and imaginary parts are physically reasonable solutions. However, as can be easily shown, they differ only by a spatial or temporal phase shift. We recall the identities

$$\mathrm{Im}(z) \equiv \mathrm{Re}(-\mathrm{i}z), \quad z \in \mathbb{C}, \qquad -\mathrm{i} \equiv \mathrm{e}^{-i\cdot\pi/2}, \tag{21.27}$$

and obtain from (21.26)

$$\mathrm{Im}\left(\psi(s,n,t)\right) = \mathrm{Re}\left(\mathrm{e}^{-\mathrm{i}\cdot\pi/2}\psi(s,n,t)\right) = \mathrm{Re}\left(\psi(s,n,t+T/4)\right).$$

Therefore, the complete information about the solution ψ is already obtained when considering $\mathrm{Re}(\psi)$ alone.

Before discussing the solutions in detail, however, a qualitative argument is shown by which the stream function is related to the barotropic velocity field according to (see (20.4))

$$\boldsymbol{u}^{bt} = \frac{1}{h}\left(\hat{\boldsymbol{k}} \times \nabla\psi\right). \tag{21.28}$$

It follows from this, that the deeper the channels are, the weaker the velocities will be. Further, convex stream function surfaces are connected with anti-cyclonic velocity cells (Fig. 21.9), and the steeper the ψ-surfaces are the stronger will be the velocities in these cells.

Rather than considering general solutions such as (21.26) we investigate solutions to particular wavenumbers.

Figures 21.10–21.12[7] display perspective views and contour lines of $\mathrm{Re}(\psi)$ in a straight infinite channel for a third order model. The n-axis has been stretched by a

[7] Only snapshots of the first quarter period are shown. The panels can easily be extended by recognizing that cells with the same parity at $t = 0$ and viewed as a 'dumbbell' rotate cyclonically.

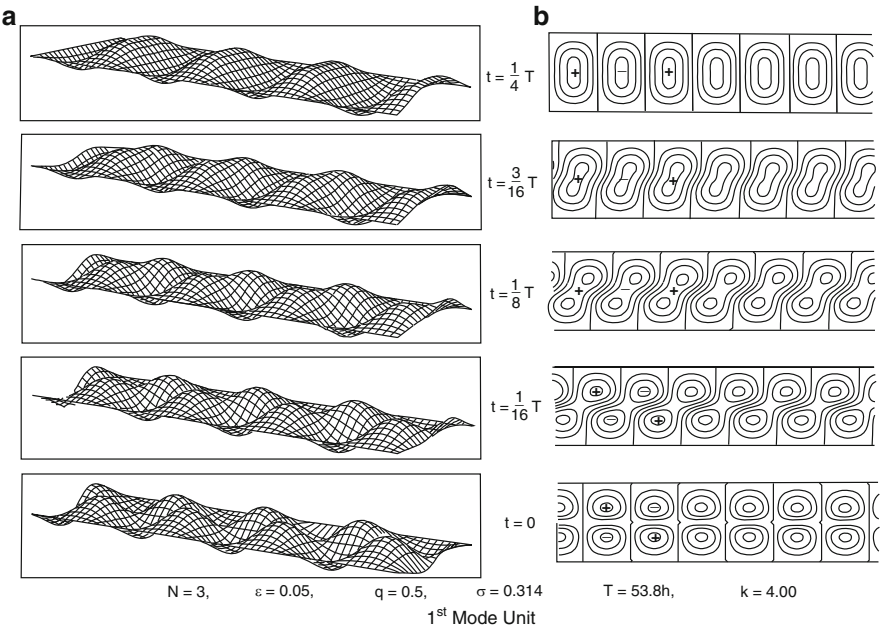

Fig. 21.10 (**a**) Time sequence of the stream function surface in steps of 1/16 T in a channel $-1/2B \leq n \leq 1/2B, 0 \leq s \leq 6Lr$ and aspect ratio $r = 1$. Note that the phase motion in the domains $n > 0$ and $n < 0$ is right bounded. (**b**) Time sequence of lines of constant ψ relative to 90% of the maximum value at each time step. The cellular structure of cyclonic (+) and anticyclonic (−) vortices is clearly visible. Composed from figures in Stocker and Hutter [23]. © Versuchsanstalt für Wasserbau, Hydrologie und Glaziologie an der ETH Zürich, reproduced with permission

factor of 1.5 to make the transverse structure more visible. The lines of constant ψ are chosen such that all inner most lines correspond to 90% of the maximum ψ value in each time step. Thus, the lines of different time steps cannot be used for amplitude comparison. The pattern consists of two right-bounded topographic waves evolving from the superposition of the solutions $\psi(\sigma, k)$ and $\psi(\sigma, -k)$. Each mode shows its own characteristic cross-channel behaviour. The cells rotate anticlockwise; with proceeding time they split and merge again together, which reflects the varying balance between the symmetric and skew-symmetric aspects of the motion. As would be expected, the complexity of the system of gyres increases with the mode number. Whereas these properties are shown above for a third order model, they have been computed also for a first and second order model by Stocker and Hutter [23]. This is a rewarding result as it demonstrates that the MWR-approximation has led to the qualitatively correct results already at its lowest order.

Stocker and Hutter [27] have studied the properties of the wave solution both for the transport stream function ψ and the velocity and have found the following results:

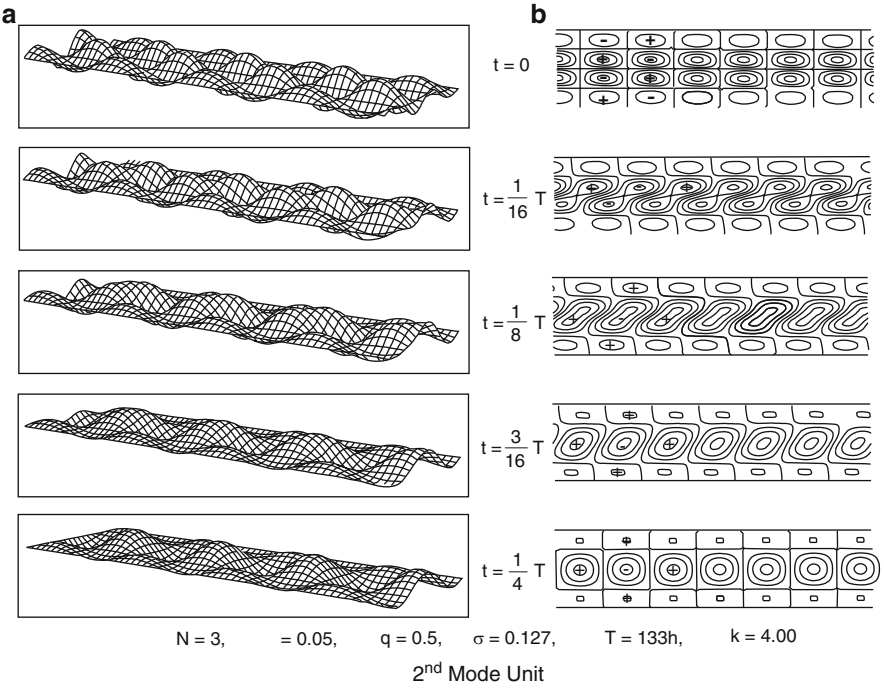

Fig. 21.11 (**a**) Time sequence of the stream function surface in steps of 1/16 T in a channel $-1/2B \leq n \leq 1/2B, 0 \leq s \leq 6Lr$ and aspect ratio $r = 1$. Note that the phase motion in the domains $n > 0$ and $n < 0$ is right bounded. (**b**) Time sequence of lines of constant ψ relative to 90% of the maximum value at each time step. The cellular structure of cyclonic (+) and anticyclonic (−) vortices is clearly visible. Composed from figures in [23]. © Versuchsanstalt für Wasserbau, Hydrologie und Glaziologie an der ETH Zürich, reproduced with permission

- With increasing number of the functions used in the MWR-approximation the wave activity is becoming more and more shore bound.
- The wave activity is also closer to shore when the wave number is increased.
- The same is observed when the bathymetric profile changes from convex ($q = 0.5$) to concave ($q = 2$).
- These behaviours also apply for the transport stream function and the velocity.
- The parameter ε has a rather small effect on the distribution of the velocities and stream function.

These results suggest, first, that the choice of the trigonometric basis functions may not be the optimal selection of orthogonal functions for the use of the MWR. Another set, which weighs boundary regions higher than interior regions, may be better. Second, the results can help in selecting mooring sites in channels or in elongated lakes when basin-filling topographic waves are to be detected by velocity recordings. When these positions are close to shore (say $0.1B$ offshore, $B =$ basin

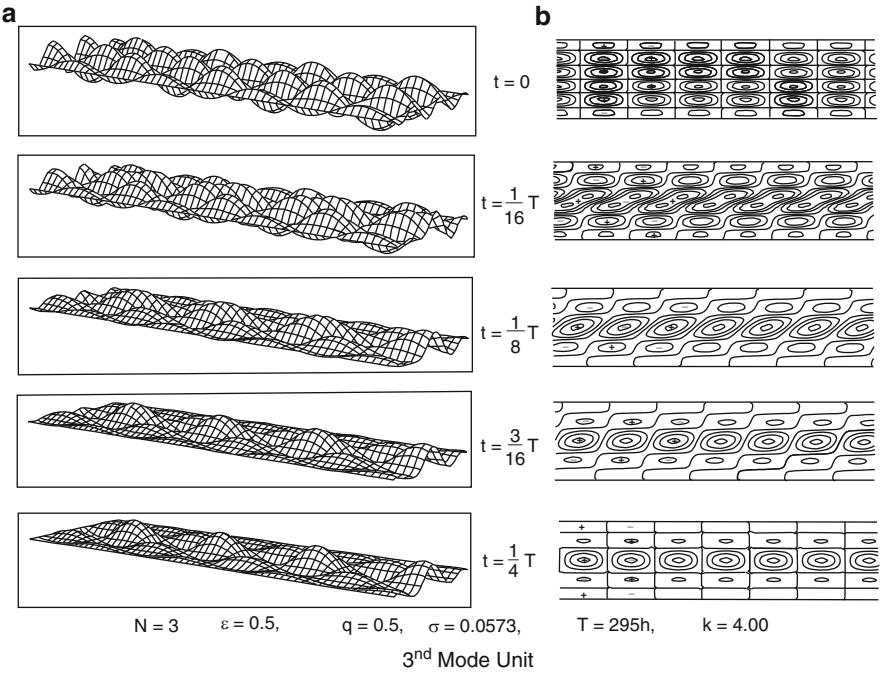

Fig. 21.12 (**a**) Time sequence of the stream function surface in steps of 1/16 T in a channel $-1/2B \leq n \leq 1/2B, 0 \leq s \leq 6Lr$ and aspect ratio $r = 1$. Note that the phase motion in the domains $n > 0$ and $n < 0$ is right bounded. (**b**) Time sequence of lines of constant ψ relative to 90% of the maximum value at each time step. The cellular structure of cyclonic (+) and anticyclonic (–) vortices is clearly visible. Composed from figures in [23]. © Versuchsanstalt für Wasserbau, Hydrologie und Glaziologie an der ETH Zürich, reproduced with permission

width) then the clockwise rotating velocities can be recorded and may be attributed to mode-1 TW-motion.

We close this section on TWs in infinite channels by a few remarks on TW-propagation in straight channels by others. Instead of applying the MWR to the TW-equation, one can start with the trial solution for propagating (and not quasi-standing) waves, given by

$$\psi(x, y) = F(y)\exp\left(\mathrm{i}(kx - \omega t)\right)$$

and then obtains the two-point-boundary-value problem for the cross channel variation

$$\frac{\mathrm{d}^2F}{\mathrm{d}y^2} - \frac{\mathrm{d}h/\mathrm{d}y}{h}\frac{\mathrm{d}F}{\mathrm{d}y} - \left(k^2 - \frac{\mathrm{d}h/\mathrm{d}y}{h}\frac{k}{\sigma}\right)F = 0 \qquad -y_1 < y < y_2,$$

$$F = 0 \qquad y = y_1, y_2. \tag{21.29}$$

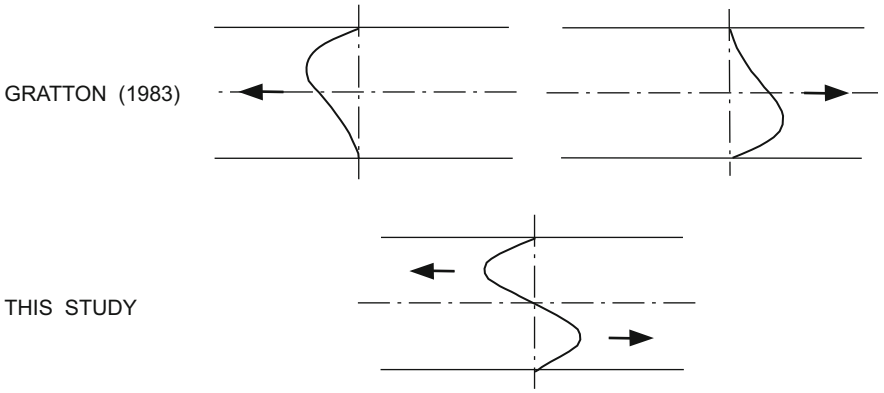

Fig. 21.13 Topographic waves propagating in an infinite channel with cross-topography, by Gratton [9] and Stocker and Hutter (this study). Both exhibit right-bounded waves. Gratton has separate solutions, but here they area a combination of the two (from [23]). © Versuchsanstalt für Wasserbau, Hydrologie und Glaziologie an der ETH Zürich, reproduced with permission

Gratton [9], Gratton and LeBlond [10] and Bäuerle [2] proceed this way and solve (21.29) for different channel topographies, whilst Lie [15] and Djurfeldt [6] and Takeda [33] perform shelf wave analyses ($y_2 \to \infty$). Gratton [9] and Gratton and LeBlond [10] investigate channels with linear asymmetric or symmetric parabolic depth profile ($y_1 = -y_2$) and find solutions of two forms: Exact solutions are expressible in hypergeometric (so-called) Kummer functions and approximate 'small-slope' solutions, for which h is treated as constant except when being differentiated. These solutions have a hump close to the right shore (on the Northern Hemisphere) when looking into the direction of propagation and decay exponentially to zero when the other (left) shore is approached. This formulation yields right bounded waves, propagating in both directions along the channel axis, see Fig. 21.13. A linear superposition of two waves propagating in the $+s$ and $-s$ directions yields a quasi-standing wave as constructed here with the MWR-method, which is more flexible than Gratton and LeBlond's method.

Bäuerle [2] solves the two-point-boundary-value problem (21.29) by using standard Finite Difference (FD) methods and repeats results obtained by the MWR and then compares his results with those obtained by using the FD-method. We show here only one result, quoting from Bäuerle [2] and Stocker and Hutter [27]. Figure 21.14 compares the dispersion relations for $\varepsilon = 0.05$ and $q = 0.5, 1, 2, 5$ as determined with the FD technique using 401 mesh points across the channel and the MWR using a third order model. According to this figure, the $N = 3$ MWR-results only differ appreciably from the FD-results for $q = 5$ and $k > 10$. For large k and large q, it was already mentioned before, that a higher than $n = 3$ MWR-model is required to achieve accurate results.

In conclusion: No advantage of the FD-method over the MWR-method seems to emerge from this analysis, since extremely small mesh size is required to reproduce

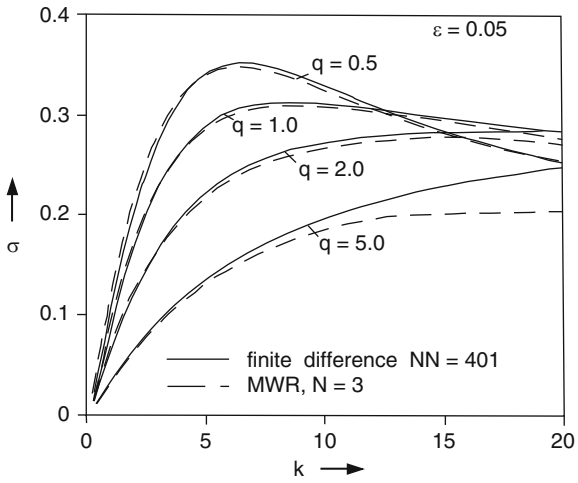

Fig. 21.14 Comparison of the dispersion curves calculated by the finite difference (*solid*) and MWR-technique (*dashed*) (from [2]). © Versuchsanstalt für Wasserbau, Hydrologie und Glaziologie an der ETH Zürich, reproduced with permission

the same accuracy as achieved by the MWR-method with only three mode units. An analogous critique also holds for Gratton and LeBlond's analytical solution, [27].

21.4 Topographic Waves in Rectangular Basins

In the preceding TW-analyses, solutions to the TW-equation were found, which describe basin-filling wave motions e.g. in circular and elliptical basins with symmetric bathymetries. Solutions, which were constructed for channels with bathymetric profiles varying only across the channel width, were also obtained, but none of these solutions provided any hints as to the interpretation of the long periodic (60–100 h) signals in Lake of Lugano as basin-filling and localized dynamical features, respectively. In fact, up to now, no localized TW-mode was discovered in the solutions presented so far. In this section, we shall make a significant step towards an affirmative answer of this still unsolved problem.

21.4.1 Crude Lake Models

A lake model is called *crude*, if in the natural coordinates (s, n) its topography varies only in the transverse direction n. For such a model, it is straightforward to extend the results obtained for infinite channels. As there exist $4N$ independent solutions in a channel for an Nth order model, they may be superposed such that the resulting solution also fulfills the boundary conditions on the s-axis, i.e. $s = 0$ and $s = L$. These must be satisfied for all $\psi_\alpha^\pm$ in order that the combination $\psi(s, n, t)$ in (21.26) obeys the requirement

$$\psi(s, n, t) = 0 \qquad s = 0, L \tag{21.30}$$

for all times. If all frequencies are below the critical frequency, see Figs. 21.4–21.6, (21.30) together with (21.26) implies

$$\begin{aligned}
\psi_+^{\alpha}|_{s=0} &= 0 \;\rightarrow\; \sum_{\gamma=1}^{4N} c_{\alpha\gamma} d_\gamma = 0, && \alpha = 1,\ldots,N,\\
\psi_-^{\alpha-N}|_{s=0} &= 0 \;\rightarrow\; \sum_{\gamma=1}^{4N} c_{\alpha\gamma} d_\gamma = 0, && \alpha = n+1,\ldots,2N,\\
\psi_+^{\alpha}|_{s=L} &= 0 \;\rightarrow\; \sum_{\gamma=1}^{4N} \mathrm{e}^{\mathrm{i}k_\gamma} c_{\alpha\gamma} d_\gamma = 0, && \alpha = 1,\ldots,N,\\
\psi_-^{\alpha-N}|_{s=0} &= 0 \;\rightarrow\; \sum_{\gamma=1}^{4N} \mathrm{e}^{\mathrm{i}k_\gamma} c_{\alpha\gamma} d_\gamma = 0, && \alpha = n+1,\ldots,2N.
\end{aligned} \tag{21.31}$$

Recall that the coefficients $c_{\alpha\gamma}$ are functions of the frequency σ. By defining a $(4N \times 4N)$-matrix $D_{\alpha\gamma}(\sigma)$, such that

$$\begin{aligned}
D_{\alpha\gamma} &= c_{\alpha\gamma}, && \alpha = 1,\ldots,2N,\\
D_{\alpha\gamma} &= \mathrm{e}^{\mathrm{i}k_\gamma} c_{\alpha-2N,\gamma}, && \alpha = 2N+1,\ldots,4N,
\end{aligned} \qquad \gamma = 1,\ldots,4N, \tag{21.32}$$

the boundary conditions (21.31) assume the compact form

$$D_{\alpha\gamma} d_\gamma = 0, \qquad \alpha,\gamma = 1,\ldots,4N. \tag{21.33}$$

Non-trivial lake solutions require that[8]

$$\det \boldsymbol{D}(\sigma) = 0, \tag{21.34}$$

which is the equation determining the eigenfrequency in the lake. Having found an eigenfrequency σ with (21.34), the lake solution can readily be calculated by determining the eigenvector d_γ from (21.33) and evaluating ψ from (21.26). Both, real and imaginary parts of ψ are solutions; however, for simplicity only one of them will be considered. Calculations showed that the eigenfrequency σ could be evaluated from (21.34) with appreciable accuracy. Calculating, in a second step, the eigenvector d_γ by a Gauss algorithm (backward substitution from a left-right decomposition of $\boldsymbol{D}$ caused serious difficulties insofar as some of the thus constructed eigenfunctions showed dissatisfaction of the boundary conditions. This is characteristic of numerically stiff systems and occurs particularly in cases, when zeros have to be evaluated which are connected with large derivatives. In these cases the calculation of the zero of a nonlinear function exhibits good and fast convergence although

[8] It turns out that all solutions of (21.34) satisfy $\sigma < \sigma_0$, where σ_0 is the critical frequency. This is a posteriori proof that (21.31) is justified.

the function value at the root may be far from zero. Special integrators of ordinary differential equations must be used.

Computations show that frequencies (periods) decrease (increase) appreciably, when the topography parameter q increases. This effect is demonstrated in Tables 21.2–21.4. The first compares the lowest eigenfrequencies for models of order $N = 1$–3. There is always a pair of eigenfrequencies differing from each other by less than 1% (but only one of the pairs is shown in Table 21.2). The second Table 21.3 shows the first eigenfrequencies computed by a second order model for various aspect ratios $r = B/L$ (width/length) and results indicate that eigenfrequencies are robust (stiff) against changes in r, but change considerably with variations of q. Table 21.4 shows the eigenperiods (in hours) of a second order model with $\varepsilon = 0.05$ and proves that pairwise appearing periods are very close to one another, so close to each other that their separation by measurement is certainly out of reach.

The form of the dispersion relation $\sigma(k)$ also implies that modes with higher periods have higher modal structure in the s-direction, because to a given period the two wave numbers are far apart; so, in a particular solution it is not possible to arrange the eigenfrequencies in a strict order which would be connectable with the modal structure. This seems to be intrinsic of second class wave motion, since already Ball [1] has not found such a connection even in an exact analytical solution, see Fig. 20.9.

Table 21.2 First eigenfrequencies σ for $r = 0.5$ and $\epsilon = 0.05$ in a crude lake model. There is always a pair of eigenfrequencies differing from each other by less than 1% and the table shows only one of them. $N = 1, 2, 3$ indicates the order of the model, from [27]

2 : 1 basin	$N = 1$	$N = 2$	$N = 3$
$q = 0.5$	0.314	0.335	0.337
	0.292	0.316	0.317
	0.264	0.293	0.295
$q = 2.0$	0.198	0.260	0.274
	0.186	0.254	0.271
	0.169	0.246	0.267
$q = 5.0$	0.087	0.167	0.208
	0.081	0.163	0.206
	0.073	0.158	0.202

Table 21.3 The first eigenfrequencies in a second-order model for various aspect ratios r and topography parameters $q, \epsilon = 0.05$. Question marks indicate computational difficulties, from [27]

q	$r = 0.5$	$r = 0.4$	$r = 0.3$	$r = 0.2$
0.5	0.335	0.337	0.339	0.341
1.0	0.303	0.304	0.304	0.305?
2.0	0.260	0.260	0.261	0.261
5.0	0.167	0.167	0.167	0.168?

Table 21.4 Six lowest eigenperiods (in hours) of a second order model (45° latitude) with $\varepsilon = 0.05$ for four different values of the bathymetry parameter q and three values of the aspect ratio r. The *vertical dashed lines* separate pairs of periods which lie close together, from [23]

q	r	Periods [h]					
	0.5	50.0	50.5	53.5	53.6	62.5	62.7
0.5	1.0	53.7	53.8	62.9	63.3	74.1	74.7
	2.0	63.8	64.6	87.6	88.4	106	108
	0.5	59.8	59.9	63.1	63.2	71.7	71.8
1.0	1.0	57.6	57.6	63.5	63.7	72.2	72.5
	2.0	64.5	64.7	84.1	84.4	108	109
	0.5	68.7	68.7	89.7	89.7	122	122
2.0	1.0	66.5	66.5	71.9	72.0	80.2	80.3
	2.0	72.4	72.5	91.6	91.7	116	117
	0.5	107	107	156	157	422	423
5.0	1.0	111	112	124	124	139	140
	2.0	112	112	140	140	176	178

21.4.2 The Role of the Aspect Ratio

A rectangular basin of aspect ratio $r \neq 1$ gives rise to differentiate between crude lake models with inverse aspect ratios $r < 1$ and $r > 1$, as shown in Fig. 21.15. In panel (a) of this figure the orthogonal function expansion is in the transverse direction and ODE-integration in the long direction; in panel (b), the two roles are interchanged. It is expected that with the MWR, two different eigenmodes at the same frequency will be selected. To verify this, note that the dispersion relation depends on the product rk implying $\sigma = \sigma(rk)$. Thus, when plotted as a function of k only, dispersion relations $\sigma(k)$ with different aspect ratios emerge from each other by a stretching transformation along the k-axis. Figure 21.16 illustrates this effect qualitatively. Increasing r means that, for fixed σ, the waves have smaller wave numbers and, therefore, exhibit within a given distance along the s-direction fewer troughs and fewer crests. This property provides a hint towards an answer of the following questions:

- What is the domain of the aspect ratio $r < 1$ or $r > 1$, for which reasonable approximate topographic wave solutions are obtained which allow comparison with earlier studies, such as Ball [1] or Mysak [16]?
- Under which situations must the cases $r < 1$ and $r > 1$ be applied? Can one decide by any means whether a lake favours one over the other?

The answer to the first question has already been sketched above. It follows from the aspect ratio dependence of the dispersion relation that the lower the aspect ratio is, the higher will be the modal structure in the s-direction. This feature can be seen in Fig. 21.17 for the lowest eigenperiods in the first order model. On the left, $r < 1$, the two wave numbers which correspond to a given σ lie far apart; the stream function is composed of a long wave and a short wave component. The

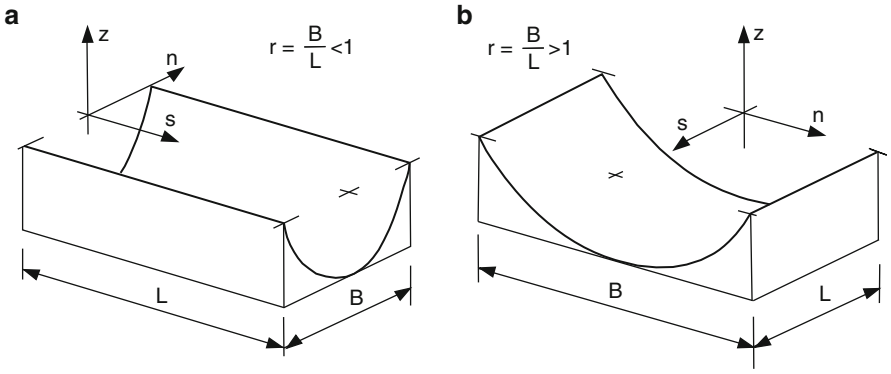

Fig. 21.15 Lake geometry for (**a**) $r < 1$ and (**b**) $r > 1$. For $r < 1$ the lake has a cross topography with a constant thalweg-depth, whereas for $r > 1$ there is no cross topography but a variable thalweg depth (from [23]). © Versuchsanstalt für Wasserbau, Hydrologie und Glaziologie an der ETH Zürich, reproduced with permission

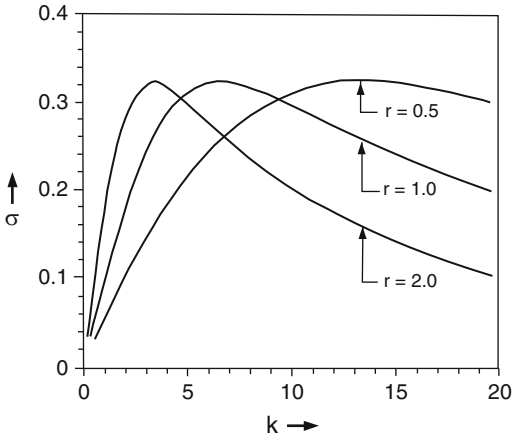

Fig. 21.16 Dispersion relation $\sigma(k)$ for different aspect ratios r, retaining the value of the other parameters N, ε, q (from [23]). © Versuchsanstalt für Wasserbau, Hydrologie und Glaziologie an der ETH Zürich, reproduced with permission

structure of the closed basin mode is therefore rich. This fact prevents the occurrence of ground modes[9] of TWs. On the right $r > 1$, the two wave numbers are much smaller such that the stream function is composed only of 'long' wave components; the modal structure of the basin solution is simple or fundamental. This type of solution, obtained in a first order model, resembles globally the structure of exact, fundamental close basin solutions such as those of Ball [1] or Mysak [16].

Stocker and Hutter [23] and Stocker [26] have shown results for crude lake models of order 1 and 2 and found the distressing results that basin-filling solutions in the rectangle did qualitatively not look like the exact solution, e.g. in long ellipses.

[9] *Ground, gravest* or *fundamental* mode: Mode, whose stream function has the least possible structure over the lake domain.

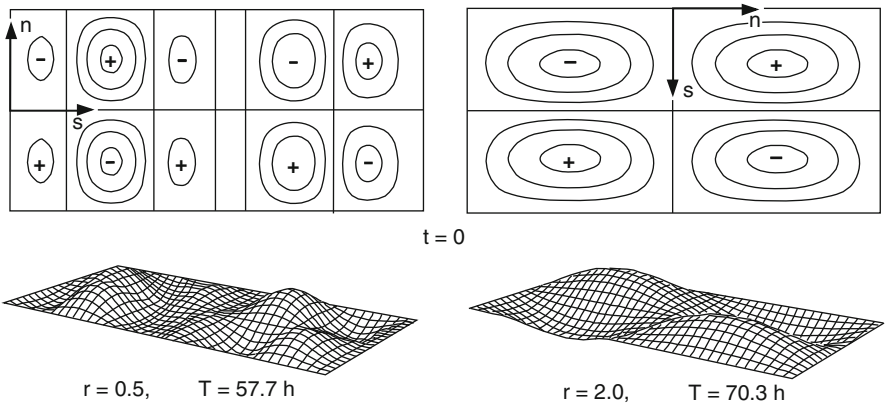

Fig. 21.17 Comparison of the modal structure for an aspect ratio $r < 1$ and $r > 1$, respectively. The parameters are selected as $N = 1, q = 0.5$, time $t = 0$ (from [23]). © Versuchsanstalt für Wasserbau, Hydrologie und Glaziologie an der ETH Zürich, reproduced with permission

Very simple mode structures with global phase propagation were not found. This is no surprise, however. The rectangular basin with vertical end walls has isotrophs (lines of constant f/H) which are not continuous at the end boundaries $s = 0$ and $s = L$. So, TWs which oscillate along isotrophs cannot follow such lines to the other lake side at the long ends of the rectangle. Moreover, when raising the order of approximation from $N = 1$ to $N = 2$ the 'improved' flow pattern seems to move further away from the structure which one saw for $N = 1$ and found promising.

The obvious idea to amend this situation is likely the introduction of a smooth bathymetry at the two lake ends. Stocker and Hutter [27] introduced a variable thalweg depth $h_0(s)$ such that $h_0'(s)/h_0 = \textit{constant}$ (this requires exponential depth profiles $h_0(s)$ at the two long ends) with a possible constant depth h_0 for $s_1 < s < \ell - s_2$. However, it is as easy to design bathymetries which are smooth and vary with s and n.

21.4.3 Lake Model with Non-constant Depth Along Its Thalweg

21.4.3.1 Numerical Method

Consider a rectangle of width B and length L which has the depth profile

$$h(s,n) = h_0(s)\left(1 + \epsilon - \left|\frac{2n}{B}\right|^q\right), \qquad 0 \le s \le L, \quad -\frac{1}{2}B \le n \le \frac{1}{2}B, \tag{21.35}$$

with constant ϵ and $0 < q < \infty$. This bathymetry possesses a finite shore depth $\epsilon h_0(s)$, which is necessary to have $(\partial h/\partial n)/h$ bounded everywhere. It was

demonstrated in Sect. 21.2 how the boundary value problem (21.1)-(21.2) was transformed to a new *one-dimensional* problem for the coefficient functions $\psi_\alpha^{\pm}(s)$. The result was

$$\begin{aligned} \mathbb{K}\boldsymbol{\psi}(s) &= \mathbf{0}, \qquad 0 < s < L, \\ \boldsymbol{\psi}(s) &= \mathbf{0}, \qquad s = 0, L, \end{aligned} \tag{21.36}$$

in which

$$\begin{aligned} \boldsymbol{\psi} &= (\psi_1^+, \ldots, \psi_N^+; \psi_1^-, \ldots, \psi_N^-) = (\boldsymbol{\psi}^+; \boldsymbol{\psi}^-), \\ \mathbb{K} &= -i\sigma \left[B^2 \boldsymbol{K}^{02} \frac{\mathrm{d}^2}{\mathrm{d}s^2} - B^2 \left(h^{-1} \frac{\mathrm{d}h}{\mathrm{d}s} \right) \boldsymbol{K}^{00} \frac{\mathrm{d}}{\mathrm{d}s} - \boldsymbol{K}^{22} \right] \\ &\quad - B(\boldsymbol{K}^{20} + \boldsymbol{K}^{02}) \frac{\mathrm{d}}{\mathrm{d}s} + B \left(h^{-1} \frac{\mathrm{d}h}{\mathrm{d}s} \right) \boldsymbol{K}^{20} \end{aligned} \tag{21.37}$$

with the $\boldsymbol{K}$-matrices defined in (21.21). Here and henceforth $h = h_0$, and it has been assumed that the operator $\mathbb{K}$ has coefficients which depend on the variable s through an arbitrary thalweg depth $h(s)$. Furthermore, the symmetrized form of $\mathbb{K}$ is obtained by using (21.21) to express the $\boldsymbol{K}$'s in symmetrized form. For the numerical solution we transform (21.36) to a *real, first-order* system. Introducing

$$\boldsymbol{\Psi} \equiv \left(\mathrm{Re}\boldsymbol{\psi}^+, \mathrm{Re}\boldsymbol{\psi}^-, \mathrm{Re}\dot{\boldsymbol{\psi}}^+, \mathrm{Re}\dot{\boldsymbol{\psi}}^-, \mathrm{Im}\boldsymbol{\psi}^+, \mathrm{Im}\boldsymbol{\psi}^-, \mathrm{Im}\dot{\boldsymbol{\psi}}^+, \mathrm{Im}\dot{\boldsymbol{\psi}}^- \right), \tag{21.38}$$

with $()^{\cdot} \equiv \mathrm{d}/\mathrm{d}s$ and substituting $s' \equiv s/L$, $\mathrm{d}/\mathrm{d}s' = L\mathrm{d}/\mathrm{d}s$ we obtain after dropping primes

$$\begin{aligned} \frac{\mathrm{d}}{\mathrm{d}s}\boldsymbol{\Psi} &= \boldsymbol{A}(s)\boldsymbol{\Psi}, \; 0 < s < 1, \\ \boldsymbol{B}\boldsymbol{\Psi} &= 0, \qquad s = 0, 1. \end{aligned} \tag{21.39}$$

This system has dimension $8N$; $\boldsymbol{B}$ is a constant diagonal matrix with $B_{ii} = 1$ for $i = 1, \ldots, 2N$ and $i = 4N + 1, \ldots, 6N$ and else $B_{ii} = 0$. The matrix $\boldsymbol{A}$ can be split into a part which is independent of s and another part proportional to the slope parameter S

$$S(s) \equiv h_0^{-1} \frac{\mathrm{d}h_0}{\mathrm{d}s}, \tag{21.40}$$

explicitly

$$\boldsymbol{A}(s) = \boldsymbol{C} + S(s)\boldsymbol{D}.$$

The matrices $\boldsymbol{C}$ and $\boldsymbol{D}$ take the forms (the subscripts R and I stand for real and imaginary parts)

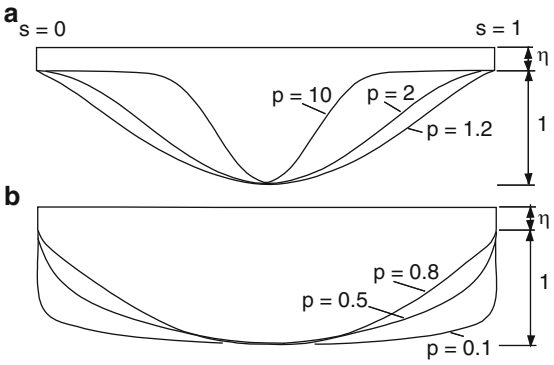

Fig. 21.18 Thalweg profiles (21.43) for different values of the exponent p. For $p > 1$ slopes at the lake ends are zero, (**a**), when $p < 1$ they are infinite, (**b**) (from [26]). © Versuchsanstalt für Wasserbau, Hydrologie und Glaziologie an der ETH Zürich, reproduced with permission

$$\boldsymbol{C} = \begin{bmatrix} \boldsymbol{C}_\mathrm{R} & -\boldsymbol{C}_\mathrm{I} \\ \boldsymbol{C}_\mathrm{I} & \boldsymbol{C}_\mathrm{R} \end{bmatrix}, \quad \boldsymbol{D} = \begin{bmatrix} \boldsymbol{D}_\mathrm{R} & -\boldsymbol{D}_\mathrm{I} \\ \boldsymbol{D}_\mathrm{I} & \boldsymbol{D}_\mathrm{R} \end{bmatrix} \tag{21.41}$$

with the $(4N \times 4N)$-submatrices[10]

$$\boldsymbol{C}_\mathrm{R} = \begin{bmatrix} 0 & 1 \\ \frac{1}{r^2}(\boldsymbol{K}^{00})^{-1}\boldsymbol{K}^{22} & 0 \end{bmatrix}, \boldsymbol{C}_\mathrm{I} = \frac{1}{\sigma}\begin{bmatrix} 0 & 0 \\ 0 & \frac{1}{r}(\boldsymbol{K}^{00})^{-1}(\boldsymbol{K}^{20} + \boldsymbol{K}^{02}) \end{bmatrix},$$

$$\boldsymbol{D}_\mathrm{R} = \begin{bmatrix} 0 & 0 \\ 0 & 1 \end{bmatrix}, \qquad \boldsymbol{D}_\mathrm{I} = \frac{1}{\sigma}\begin{bmatrix} 0 & 0 \\ -\frac{1}{r}(\boldsymbol{K}^{00})^{-1}\boldsymbol{K}^{20} & 0 \end{bmatrix}, \tag{21.42}$$

and the aspect ratio $r = B/L$. The matrices (21.42) are independent of s and need be calculated only once during the integration for $s \in [0, 1]$.

Solutions of the two-point-boundary value problem (TPBVP) (21.39) were constructed numerically for the profile (Fig. 21.18)

$$h_0(s) = \eta + \sin^p(\pi s), \tag{21.43}$$

here with $p = 2$. η and p are parameters; $\eta > 0$ guarantees that the depth is never zero and the exponent p could be varied such that the longitudinal variation of the depth is more or less concentrated at the long ends of the lake. The slope parameter $S(s)$ is easily calculated from (21.43); one obtains

$$S(s) = \frac{p\pi \sin^{p-1}(\pi s)\cos(\pi s)}{\eta + \sin^p(\pi s)}. \tag{21.44}$$

[10] The entries 0 and 1 in these matrices are to be interpreted as $2N \times 2N$ matrices.

For $p > 1$ and $\eta > 0$, $S(s)$ vanishes at the lake ends, which is a numerical advantage. When $0 < p < 1$ the slope parameter is not finite at $s = 0$ and $s = 1$. In order to keep $S(s)$ finite everywhere, (21.43) could be replaced by

$$h_0(s) = \begin{cases} \eta + bs, & 0 \le s \le \hat{s}, \\ \sin^p(\pi s), & \hat{s} \le s \le 1 - \hat{s}, \\ \eta + b(1-s), & 1 - \hat{s} \le s \le 1, \end{cases} \tag{21.45}$$

in which, for a given shore-slope b, η and $\hat{s}$ can be calculated such that h and h' are continuous at $s = \hat{s}$. With this choice $S(s)$ is finite everywhere and for all $p > 0$. The lake model now consists of two sidewall parameters ϵ and η (or alternatively ϵ and the shore-slope b) and a longitudinal and transverse topography parameter p and q, respectively. It is easy to see that with the choices (21.35) and (21.45) the isotrophs f/H are now smooth throughout the entire rectangular basin.

Equation $(21.39)_1$ allows the formal integration

$$\boldsymbol{\Psi}(s) = \exp\left(\int_0^s \boldsymbol{A}(\hat{s})\mathrm{d}\hat{s}\right)\boldsymbol{\Psi}(0) \equiv \boldsymbol{E}(s)\boldsymbol{\Psi}(0). \tag{21.46}$$

Equation $(21.39)_2$ implies

$$\begin{aligned} \boldsymbol{\Psi}(0) &= (0, \dot{\boldsymbol{\psi}}_R(0); 0, \dot{\boldsymbol{\psi}}_I(0)), \\ \boldsymbol{\Psi}(1) &= (1, \dot{\boldsymbol{\psi}}_R(1); 1, \dot{\boldsymbol{\psi}}_I(1)), \end{aligned} \tag{21.47}$$

in which $\dot{\boldsymbol{\psi}}_R$, $\dot{\boldsymbol{\psi}}_I$ are the real and imaginary parts of $\dot{\boldsymbol{\Psi}}$, respectively, and the symmetrization has been dropped for convenience of ensuing arguments. Formally, $\boldsymbol{E}(s)$ in (21.46) is a matrix valued function. At the basin end, it can be written as

$$\boldsymbol{E}(1)|_{s=1} = \begin{bmatrix} \boldsymbol{E}_{11} \cdots \boldsymbol{E}_{14} \\ \vdots \qquad\quad \vdots \\ \boldsymbol{E}_{41} \cdots \boldsymbol{E}_{44} \end{bmatrix}. \tag{21.48}$$

Note that $\boldsymbol{E}(1)$ is a function of the frequency σ via (21.46) and (21.42) and the $\boldsymbol{E}_{ij}$ are $(2N \times 2N)$-matrices. For each initial vector of the form

$$\boldsymbol{\Psi}_j(0) = (\underbrace{0, 0, \ldots, 0}_{(j-1)}, 1, \underbrace{0, 0, \ldots, 0}_{(8N-j)}), \quad \begin{matrix} 2N+1 \le j \le 4N, \\ 6N+1 \le j \le 8N, \end{matrix} \tag{21.49}$$

the corresponding vector $\boldsymbol{\Psi}_j(1)$ is computed using a discretized form of (21.39), see below. From (21.46) and (21.47) it then easily follows that the solution $\boldsymbol{\Psi}_j(1)$ corresponding to the jth initial vector $\boldsymbol{\Psi}_j(0)$ is the jth column of the matrix $\boldsymbol{E}(1)$. Equation $(21.47)_2$ eventually requires

$$\begin{bmatrix} \boldsymbol{E}_{12} & \boldsymbol{E}_{14} \\ \boldsymbol{E}_{32} & \boldsymbol{E}_{34} \end{bmatrix} \begin{bmatrix} \dot{\boldsymbol{\Psi}}_{\mathrm{R}}(0) \\ \dot{\boldsymbol{\Psi}}_{\mathrm{I}}(0) \end{bmatrix} = 0, \tag{21.50}$$

which allows derivation of the equation which determines the *eigenfrequency* in this lake basin. It takes the form

$$\det \begin{bmatrix} \boldsymbol{E}_{12} & \boldsymbol{E}_{14} \\ \boldsymbol{E}_{32} & \boldsymbol{E}_{34} \end{bmatrix} = 0. \tag{21.51}$$

It remains to select the integration routine for the $4N$ initial-value problems $(21.39)_1$ with initial data as shown in (21.49). This choice depends on how the matrix is available. Here $\boldsymbol{A}$ can be computed for all $s \in [0, 1]$; the fourth order Runge–Kutta scheme (or higher order multi-step forward integration technique can be used.[11] We discretize the integration interval $[0, 1]$ into M equidistant increments of length $d = 1/M$. The $\boldsymbol{\Psi}_{i+1}$ at the position s_{i+1} within the interval is then given by

$$\begin{aligned} \boldsymbol{\Psi}_{i+1} &= \boldsymbol{\Psi}_i + d\hat{\boldsymbol{\Psi}}, \\ \hat{\boldsymbol{\Psi}} &= \tfrac{1}{6}(\boldsymbol{K}_1 + 2\boldsymbol{K}_2 + 2\boldsymbol{K}_3 + \boldsymbol{K}_4), \\ \boldsymbol{K}_1 &= \boldsymbol{A}(s_i)\boldsymbol{\Psi}_i, \\ \boldsymbol{K}_2 &= \boldsymbol{A}\left(s_i + \frac{d}{2}\right)\left(\boldsymbol{\Psi}_i + \boldsymbol{K}_1\frac{d}{2}\right), \\ \boldsymbol{K}_3 &= \boldsymbol{A}\left(s_i + \frac{d}{2}\right)\left(\boldsymbol{\Psi}_i + \boldsymbol{K}_2\frac{d}{2}\right), \\ \boldsymbol{K}_4 &= \boldsymbol{A}(s_i + d)(\boldsymbol{\Psi}_i + \boldsymbol{K}_3 d). \end{aligned}$$

With this scheme the local error is of order d^5. When $\boldsymbol{A}(s)$ is only defined at discrete points the method of Adams or other multistep methods may be preferable, see [32] or any other book on ODE integration.

The actual computation uses shooting, the shooting parameter being the frequency σ and the penalty function being the determinant (21.51).

21.4.3.2 New Types of Topographic Waves

The first step in finding the TW-modes in a rectangle is the determination of the eigenfrequencies σ from (21.51), which are real and can be ordered according to their sizes. Back-substitution into (21.50) then yields the associated initial values for $(\dot{\psi}_{\mathrm{R}}(0), \dot{\psi}_{\mathrm{I}}(0))^{\mathrm{T}}$ and, in turn via (21.47), $\boldsymbol{\Psi}(s)$ in (21.46), $\boldsymbol{\psi}$ in $(21.47)_1$, $(21.47)_2$ and, eventually, the stream function $\psi(s, n; \sigma)$ in (21.26) associated with

[11] The fundamental single-step forward integrator is the Euler-Cauchy scheme. It reads $\psi_{i+1} = \psi_i + dA(s_i)\psi_i$ and the local error is order d^2; therefore the method is only slowly converging.

this frequency. Arranging the frequencies according to their sizes does not, as already mentioned before, order the modes according to their structure. Moreover, by increasing the order of accuracy (by increasing the number N of mode units) additional 'eigenfrequencies' are obtained; those obtained for smaller N are not simply slightly shifted. This is understandable, since the larger transverse variability makes the system more flexible and opens room for additional eigenfrequencies and associated modes. However, this also raises the question how physically realistic the determined eigenfrequencies and associated modes are. This fact calls at least for very accurate numerical methods.

We investigate the spectrum of TWs in a second and third order model. The basin is rectangular with an aspect ratio $r = 0.5$, a parabolic cross section ($q = 2.0$) and a thalweg varying as a $(\sin)^2$ according to (21.43). Figures 21.19 and 21.20 display a selection of modes from the spectrum of a second and third order model, respectively. It is apparent that in the period interval from 35–140 h (corresponding to 45° latitude) a large variety of *qualitatively* different eigenmodes can be detected. According to the complexity of their modal structure we distinguish *three types of eigenmodes*.

Type 1 is the well known modal pattern described by all exact models of topographic waves in enclosed basins. It is akin to Ball's solutions [1] and therefore called *Ball-type*. Both, the linear ($\sigma = 0.155$) and the quadratic ($\sigma = 0.213$) Ball-modes (Fig. 21.20) occur in the spectrum and additional eigenmodes are identified as type 1. All exact models for which solutions have been constructed so far, have shown qualitatively similar solutions. Generally, type 1 modes consist of a few large-scale vortices moving counterclockwise around the basin, and the water in the whole basin underlies this wave motion. The rectangular basin, however, appears to sustain also two new types, which so far were unnoticed in other models.

Type 2, with only a few candidates in this frequency interval, can be called *bay-type*. Wave motion is mostly trapped to the long ends of the lake; very weak activity is experienced in the lake centre and along its long sides. The pattern shows one or a few mid-scale gyres which do not propagate along the entire isobaths (lines of constant f/H) but are rather trapped in the bays. This type arises above the cut-off frequency σ_0 of any mode unit, see Fig. 21.21; and thus embraces contributions with complex wavenumbers. The amplitudes of these modes are exponentially evanescent in space which makes it understood why bay-type solutions do exist for enclosed basins. The fact that there are eigenmodes with frequencies $\sigma > \sigma_0$ is a new result. These modes were neither detected by the analytic models nor by the crude lake model presented in the previous section.[12]

Type 3, eventually, appears most frequently in the spectrum. In contrast to type 2, all wave activity is now trapped along the long boundaries of the basin and consists of a large number of small-scale vortices. The pattern is very similar to that found in straight infinite channels; type 3 is thus named *channel-type*. Along the long

[12] Their determination is very difficult even with high-accuracy integrators. In order to obtain patterns with $|\psi(s,n)| = |\psi(1-s,n)|$ the eigenfrequency need be known up to a relative error of 10^{-7}.

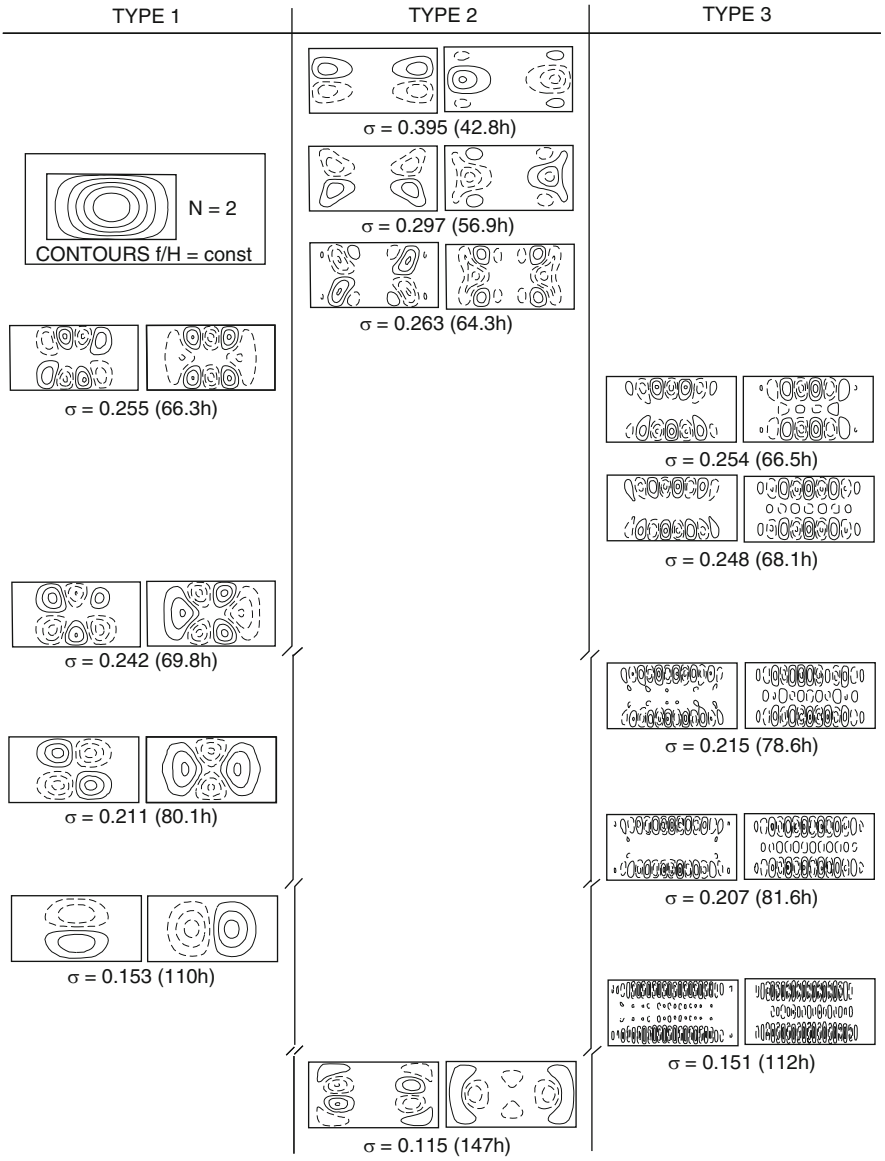

Fig. 21.19 Selection through the spectrum containing eigenmodes of a second order model. The contour lines of ψ are plotted for times $t = 0$ (*left*) and $t = 1/4T$ (*right*). Three types of solutions can be distinguished and cuts of the *vertical lines* indicate further modes not shown here. The parameters are : $N = 2, r = 0.5, q = 2.0, \varepsilon = 0.05, \eta = 0.01$ (from [26, 28]).

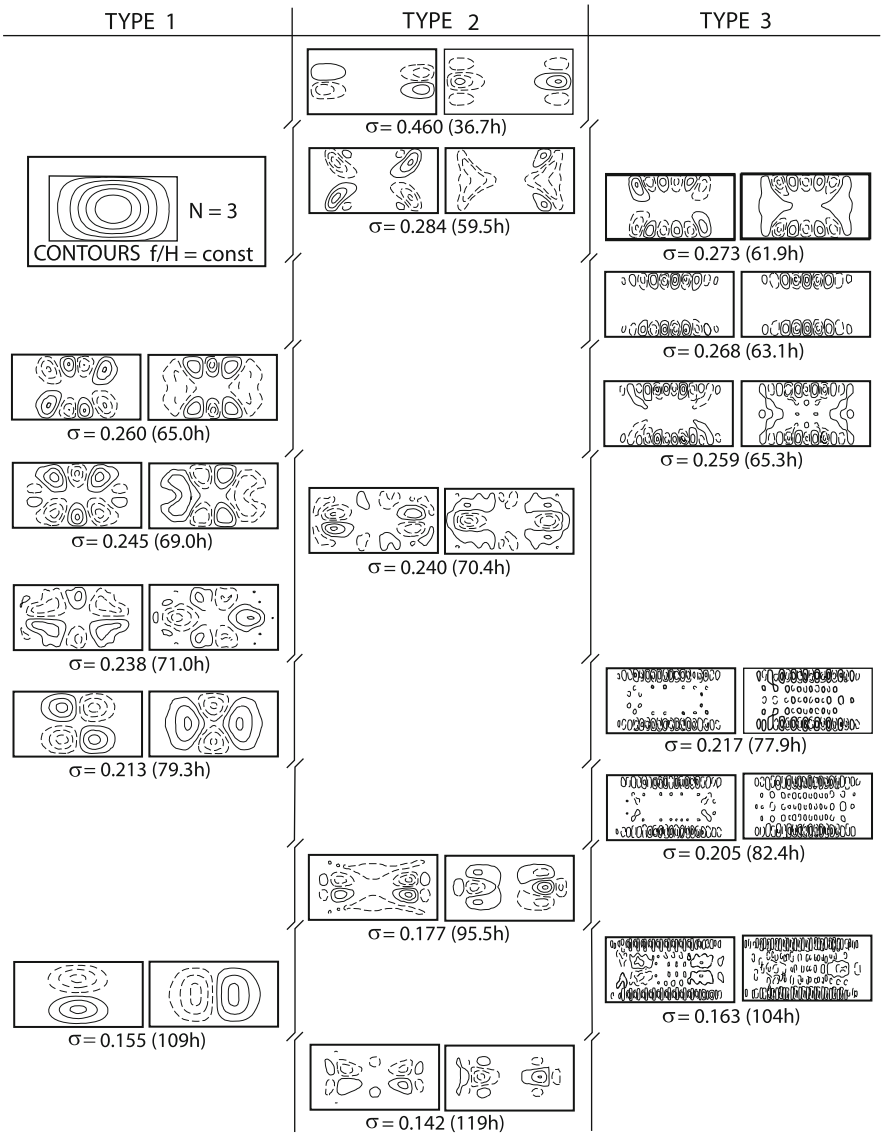

Fig. 21.20 Same as Fig. 21.19 for a third order model $N = 3$ (from [26, 28]). © American Meteorological Society, reproduced with permission

sides two seemingly non-interacting beat-patterns are observed. They originate from reflection of wave energy in the bays and a corresponding wavenumber shift.

The modal structure of the different types can be explained with the help of the Rossby dispersion relation in Fig. 21.21. Type 1 enjoys the property that increasing σ brings about more complex structure since it consists primarily of modes

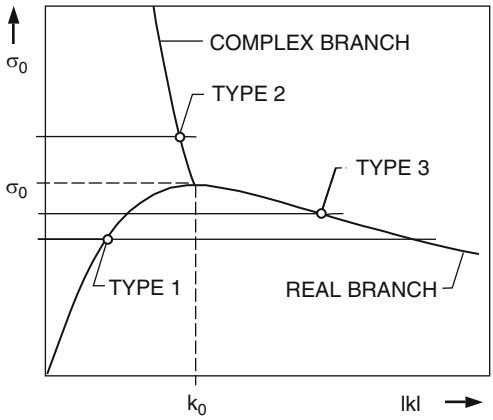

Fig. 21.21 Schematic plot of one mode unit of the dispersion relation of topographic waves in a channel with parabolic transverse depth profile. A Nth order model consists of N mode units (from [26]). © Versuchsanstalt für Wasserbau, Hydrologie und Glaziologie an der ETH Zürich, reproduced with permission

with wavenumbers $k < k_0$. For $k < k_0 \quad \partial\sigma/\partial k > 0$ and so the wavelengths of the contributing modes decrease with growing σ. Type 3, the channel-type, on the other hand, reveals the opposite property: the scale of the wave pattern gradually decreases with decreasing frequency. Type 3 solutions are mostly made up of modes with $k > k_0$. In this range, $\partial\sigma/\partial k < 0$ and consequently the wavelengths decrease with decreasing σ, c.f. Figs. 21.19 and 21.20.

The fact that topographic waves in a rectangular basin occur as bay-trapped modes casts light on the results of Trösch [35]. These seemed to entirely contradict the applicability of analytic models to real basins as anticipated in Sec. 19.2.3 and Fig. 19.10. Each mode is trapped to one of the bays and does not seem to influence the rest of the basin. The few trapped vortices exhibit roughly the scale of the bay. The rectangular basin, a much simpler configuration than Lake of Lugano, reveals equally bay-type modes *together* with the known Ball-type solutions; in the interested period range the latter were not found by Trösch [35]. This model, therefore, links these two different approaches and demonstrates that the propagation of topographic waves in enclosed basins cannot merely be described by those analytically determined modes of exact models that were so far constructed. It is in principle possible and remains to be proved or disproved that type-2 modes also exist in ellipses with parabolic or exponential bottom profiles and that these modes have a period of the same order of magnitude as those above. It is seen that many further questions still need to be answered to fully understand the behaviour of TWs in enclosed basins. Two facts have, however, transpired: Firstly, the smoothness of the isobaths is essential in enabling global TW-features and, secondly, careful numerical solution procedures are needed to find bay-type modes.

21.4.3.3 Convergence and Parameter Dependence

The quality of approximation strongly depends on the type of wave considered. Ball-type modes have large-scale vortices, and a good representation of these modes

with comparatvely few basis functions is expected. High orders of expansions are therefore not needed and fast convergence is observed. By contrast channel-type solutions consist of small-scale modes with large wavenumbers. Convergence is slow for large wavenumbers and this must equally be expected for type 3 modes.

Table 21.5 collects results of a convergence test for the same configuration as in Figs. 21.19 and 21.20. Type 1 shows convergence for both, eigenfrequency and stream function; similar but considerably slower convergence is found for types 2 and 3. For type 2 it is particularly difficult to determine the correct distribution of the stream function along the axis, as small changes in the eigenvalue result in relatively large changes of the eigenfunction. Thus, high resolution and small step sizes in the numerical integration procedure are needed. Since for ODE's high accuracy integrators exist, the channel method allows for some compromise; this at least explains the superiority of the MWR in comparison to some other numerical procedures.

Table 21.6 collects the dependence of σ on the aspect ratio and transverse topography for the solutions that correspond to Ball's quadratic mode. As expected from the behaviour of the dispersion relation in a straight infinite channel, the slope of the transverse topography has a dominant influence on the values of the eigenfrequency. Steeper profiles ($q = 5.0$) lower the eigenfrequencies. An equal but weaker effect on Ball-type modes is experienced when the aspect ratio is decreasing. Table 21.6 demonstrates that these modes are much more governed by the transverse depth profile than by the aspect ratio. All this is in line with results obtained from the crude lake model.

Tables 21.7 and 21.8 investigate the influence of the two bathymetric parameters q and r on the three types of basin solutions. Again the topography effect is seen

Table 21.5 Convergence properties of the eigenfrequencies in a 2:1 basin with $q = 2.0, \epsilon = 0.05$, $\eta = 0.01$. *Stars* indicate plotted modes in Figs. 21.19 and 21.20

Type	$N = 1$	$N = 2$	$N = 3$
1, Ball-type	0.143	0.153⋆	0.155⋆
	0.181	0.211⋆	0.213⋆
	0.195	0.255⋆	0.260⋆
2, bay-type	–	0.297⋆	0.314
	–	0.263⋆	0.284⋆
	–	0.115⋆	0.240⋆
3, channel-type	0.151	0.254⋆	0.273⋆
	0.142	0.248⋆	0.268⋆
	0.11	0.215⋆	0.253⋆

Table 21.6 Topography q and aspect ratio r influencing the eigenfrequency of the quadratic Ball-mode. The parameters are $N = 2, \epsilon = 0.05, \eta = 0.01$. The question mark indicates uncertain numerical output

Ball quadratic	$r = 0.5$	$r = 0.4$	$r = 0.3$
$q = 1.0$	0.267	0.250	0.219
$q = 2.0$	0.211	0.195	0.170
$q = 5.0$	0.140	0.123	?

Table 21.7 Topography effect on the frequency of the three wave types. The parameters are as in Table 21.6

$r = 0.5$	Ball-type	Bay-type	Channel-type
$q = 1.0$	0.200	0.299	0.250
$q = 2.0$	0.153	0.263	0.232
$q = 5.0$	0.097	0.175	0.153

Table 21.8 Aspect ratio effect on the frequency of the three wave types. The parameters are as in Table 21.6.

$q = 2.0$	Ball-type	Bay-type	Channel-type
$r = 0.5$	0.153	0.263	0.232
$r = 0.4$	0.139	0.267	0.251
$r = 0.3$	0.118	0.269	0.258

to be more influential. By going from a triangular depth profile ($q = 1.0$) to a very steep U-shaped profile ($q = 5.0$) the eigenfrequencies diminish by up to a factor of 2. As far as the topography effect is concerned, the three types react the same way, yet Ball-type modes are more sensitive to an increase of q.

Table 21.8 demonstrates that basins with a smaller aspect ratio sustain Ball-type waves with decreased eigenfrequencies. This decrease is over-proportional as it is enhanced for smaller aspect ratios. By contrast, bay- and channel-type solutions show an opposite behaviour. Decreasing the aspect ratio increases the eigenfrequency; this time the response is under proportional and for bay-type solutions the dependence of σ or r is very small.

21.4.3.4 Bay-Type Modes

The occurrence of bay-trapped modes in enclosed basins raises further questions concerning the properties of solutions of the eigenvalue problem (20.4).

When the aspect ratio of the basin is decreased the bay vortices of these models lie farther and farther apart and we wonder whether these isolated gyres become uncoupled. Two points seem to be remarkable in this context. First, basins with no symmetry seem to sustain decoupled bay modes as in Fig. 21.15b. Second, with our procedure it is very difficult to determine the parity[13] of these solutions with respect to the long axis of the basin. In this regard, very fine resolution is needed to obtain reliable solutions. The basic problem is to bring numerical information through the 'dead' zone in the centre of the domain. This suggests to consider again semi-infinite channels and to ask the question of a possible existence of *bay-trapped modes*. A partial answer is given in the following section.

[13] $\psi(s,n)$ has positive or negative parity with respect to s when $\psi(s,n) = \psi(1-s,n)$ or $\psi(s,n) = -\psi(1-s,n)$, respectively.

21.4.4 Current Patterns

In the preceding sections, the flow patterns of TW-modes in enclosed basins were graphically displayed by plotting values of the transport stream function and transport stream lines for consecutive time slices. Complementary information can be obtained by drawing particle trajectories which show the excursion of material particles in their motion. Once the stream function for TWs is determined, the vector $\hat{\boldsymbol{k}} \times \nabla\psi$ determines the vertically integrated velocity and $\hat{\boldsymbol{k}} \times \nabla\psi/h$ the velocity field, constant with depth. If we trace the motion of a fluid particle whose position at an initial time $t = 0$ is at $\boldsymbol{x}(0)$, then its trajectory is given by $\boldsymbol{x}(t)$, where

$$\frac{\mathrm{d}\boldsymbol{x}(t)}{\mathrm{d}t} = \boldsymbol{u}(\boldsymbol{x}(t), t) \qquad \boldsymbol{u}(\boldsymbol{x}(t), t) = \frac{1}{h}\hat{\boldsymbol{k}} \times \nabla\psi(\boldsymbol{x}(t), t). \tag{21.52}$$

In the present study, all fields have harmonic time dependence and, hence, the tip of a field vector describes an ellipse.[14] This ellipse will be called *transport ellipse* (for the transport vector $\hat{\boldsymbol{k}} \times \nabla\psi$) or *current ellipse* (for the velocity vector $\hat{\boldsymbol{k}} \times \nabla\psi/h$). In harmonic oscillations, these ellipses can be nearly identified with the fluid particle motion and therefore provide a realistic picture of the motion.

The trajectory follows from (21.52) by integration, viz.,

$$\boldsymbol{x}(t) = \boldsymbol{x}(0) + \int_0^t \boldsymbol{u}(\boldsymbol{x}(t'), t')\mathrm{d}t', \tag{21.53}$$

which is an integral equation for $\boldsymbol{x}(t)$, since $\boldsymbol{x}(t)$ arises explicitly as well as implicitly in the integrand function. Equations (21.52) and (21.53) are equations written in the Eulerian description. It is advantageous to write them in the so-called Lagrangean description. Let $u_L(\boldsymbol{x}(0), t)$ be the Lagrangean velocity field, i. e., the velocity at time t of the particle, which was at $\boldsymbol{x}(0)$ at time $t = 0$,

$$\boldsymbol{u}_L(\boldsymbol{x}(0), t) = \boldsymbol{u}(\boldsymbol{x}(t), t). \tag{21.54}$$

Then, (21.53) takes the form

$$\boldsymbol{u}_L(\boldsymbol{x}(0), t) = \boldsymbol{u}\left(\int_0^t \boldsymbol{u}_L(\boldsymbol{x}(0), t')\mathrm{d}t' + \boldsymbol{x}(0), t\right). \tag{21.55}$$

For short times, one may expect that

$$\left|\left|\int_0^t \boldsymbol{u}_L(\boldsymbol{x}(0), t')\mathrm{d}t'\right|\right| \ll ||\boldsymbol{x}(0)||\,, \tag{21.56}$$

[14] This concerns the linear *theory* but not the real trajectory of a fluid particle in a periodic oscillation because such a particle is always exposed to nonlinear advection (Stokes drift).

so that a Taylor series expansion of the right-hand side of (21.55) yields

$$\boldsymbol{u}_L(\boldsymbol{x}(0),t) = \boldsymbol{u}(\boldsymbol{x}(0),t) + \boldsymbol{u}_s(\boldsymbol{x}(0),t) + \ldots, \tag{21.57}$$

in which $\boldsymbol{u}_s(\boldsymbol{x}(0),t)$ is the so-called *Stokes drift velocity* given by

$$\begin{aligned}\boldsymbol{u}_s(\boldsymbol{x}(0),t) &= (\text{grad}\,(\boldsymbol{u}(\boldsymbol{x}(0),t))) \cdot \int_0^t \boldsymbol{u}_L(\boldsymbol{x}(0),t')\mathrm{d}t' \\ &\simeq (\text{grad}\,(\boldsymbol{u}(\boldsymbol{x}(0),t))) \cdot \int_0^t \boldsymbol{u}(\boldsymbol{x}(0),t')\mathrm{d}t',\end{aligned} \tag{21.58}$$

where in the second line the approximation $\boldsymbol{u}_L(\boldsymbol{x}(0),t) = \boldsymbol{u}(\boldsymbol{x}(t),t) \simeq \boldsymbol{u}(\boldsymbol{x}(0),t)$ has been made. With (21.54) and (21.57) the trajectory (21.53) may be written as

$$\boldsymbol{x}(t) = \boldsymbol{x}(0) + \int_0^t \boldsymbol{u}(\boldsymbol{x}(0),t')\mathrm{d}t' + \int_0^t \boldsymbol{u}_s(\boldsymbol{x}(0),t')\mathrm{d}t' \tag{21.59}$$

with an error of $\mathcal{O}(\boldsymbol{u}^2)$. With the periodic velocity field of the form

$$\boldsymbol{u}(\boldsymbol{x},t) = \text{Re}[(\exp(\mathrm{i}\omega t)U(x)] = (\text{Re}U)\cos(\omega t) - (\text{Im}U)\sin(\omega t) \tag{21.60}$$

the net displacement after one period, T, can be written as

$$\begin{aligned}\boldsymbol{x} - \boldsymbol{x}(0) &= \text{Re}U \int_0^{\mathrm{T}} \cos(\omega t)\mathrm{d}t + \text{Im}U \int_0^{\mathrm{T}} \sin(\omega t)\mathrm{d}t \\ &\quad + \int_0^{\mathrm{T}} [(\text{grad}\,\text{Re}U)\cos(\omega t) + (\text{grad}\,\text{Im}U)\sin(\omega t)] \\ &\qquad \times \left[\frac{\text{Re}U}{\omega}\sin(\omega t) - \frac{\text{Im}U}{\omega}\cos(\omega t) + \frac{1}{\omega}\text{Im}U\right]\mathrm{d}t \\ &= \frac{\pi}{\omega^2}\left[\text{grad}\,(\text{Im}U)\text{Re}U - \text{grad}\,(\text{Re}U)\text{Im}U\right],\end{aligned} \tag{21.61}$$

in which $T = 2\pi/\omega$ was used. In the integrations of (21.61) only the terms with $\sin^2(\omega t)$ and $\cos^2(\omega t)$ survive; these terms define the Stokes drift.

If we restrict considerations to purely linear terms, then $\boldsymbol{u}_s$, defined in (21.58) may be ignored, so that (21.59) reduces to

$$\boldsymbol{x}(t) = \boldsymbol{x}(0) + \int_0^t \boldsymbol{u}(\boldsymbol{x}(0),t')\mathrm{d}t'),$$

which, in view of (21.60), takes the form

$$\boldsymbol{x}(t) = \boldsymbol{x}(0) + \frac{1}{\omega}\boldsymbol{u}\left(\boldsymbol{x}(0), t - \frac{1}{4}T\right) + \frac{1}{\omega}\mathrm{Im}U. \tag{21.62}$$

The trajectory is, therefore, basically the scaled trace of the Eulerian velocity vector.

Stocker [26] plotted the transport ellipses and depth integrated Stokes drifts for the three types of modes: Ball-modes, bay-modes and channel-modes. The transport fields only being determined to within a constant factor (the TW-equation is linear and homogeneous), the current ellipses and integrated Stokes drift in Figs. 21.22 and 21.23 are accordingly scaled to show the flow pattern optimally.

The 'fundamental' Ball-mode in Fig. 21.22a is characterized by a central area of counterclockwise rotation with non-vanishing velocity at the centre. This centre is surrounded by a region of clockwise rotating thinner ellipses. This behaviour essentially also prevails for the other Ball-modes (not shown here) and no 'radial nodal line': counter clockwise rotating current vectors in the central area and clockwise rotating currents near the long shores and practically vanishing currents close to the long ends. Panel (b) of Fig. 21.22 shows the transport ellipses for a bay mode. Here, TW-activity is concentrated at the long ends of the rectangular basin, and the region in the middle is characterized by weak activity. The transport ellipses are traversed clockwise close to shore and anticlockwise about a distance $B/2$ from the long ends, where B is the breadth of the rectangle. The polarization of the current varies considerably with position, can be nearly circular and almost linear at positions which are not too far apart from one another. This behaviour is also seen in bay modes not shown here. The stream function and transport ellipses of a typical channel mode are plotted in panel (c) of Fig. 21.22. The displayed pattern is typical for all channel modes; there are bands of active dynamics along the long sides of the basin and very weak activity, if any, in the vicinity of the lake axis. The currents rotate clockwise near shore and anticlockwise further away from the long shores, but only about half towards the middle line of the basin.

The closed ellipses in Fig. 21.22 mimic the fluid particle trajectories if their motion were governed by a strictly linear theory. These ellipses, however, are not stationary; their midpoints also experience a drift, which is due to the nonlinear advective terms in the momentum equation and is approximately described by the Stokes drift. Figure 21.23 shows the depth integrated Stokes drift, and panels (a)–(c) correspond with the analogous panels in Fig. 21.22. It is the property of the Ball-mode in panel (a) of Fig. 21.23, that the counterclockwise propagating gyres produce a net drift in the clockwise direction. This rotation is strong in the middle of the basin and weak nearer to the shores, but (not shown here) moves closer to the boundaries and may even be complemented by a weak counterclockwise gyre in the centre for higher order bay modes. For bay-modes (panel (b)) the Stokes-drift is strong along the shores of the bays with activity, and, as a whole, mimic a left-bounded motion against the propagation of the phase. For the channel modes, the Stokes-drift is typically as shown in panel (c) of Fig. 21.23. The drift is strong only very close to the long boundaries of the rectangle and left-bounded, i.e. against the

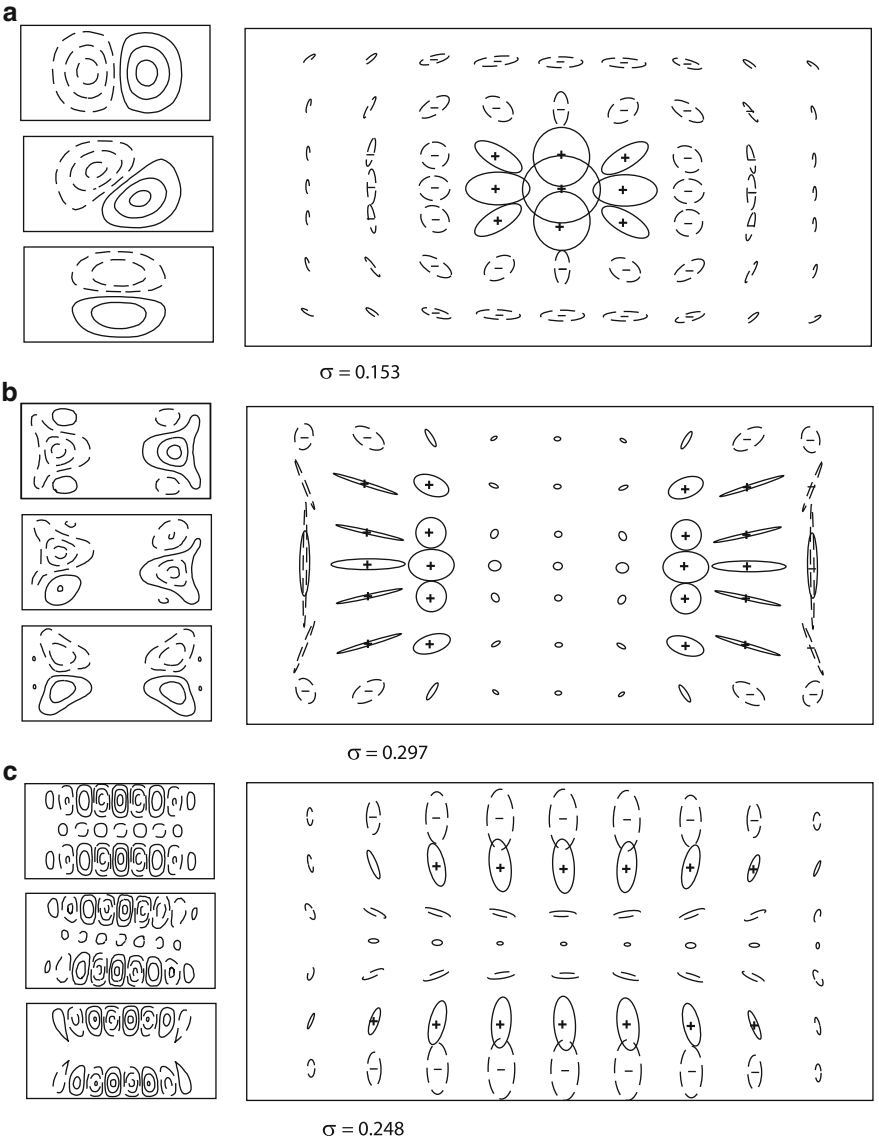

Fig. 21.22 Stream function and transport ellipses for the fundamental Ball-mode, (**a**), a typical bay-mode, (**b**), and a typical channel-mode (**c**). The small frames on the left show contours of the stream functions for $t = 0$ (*bottom*), $t = T/8$ (*middle*) and $t = T/4$ (*top*). Transport ellipses are *dashed* (*solid*) for (counter) clockwise rotating transport vectors. The parameters are $N = 2, r = 0.5, \varepsilon = 0.05$. Composed from [26, 29]. © CRC-Press, reproduced with permission

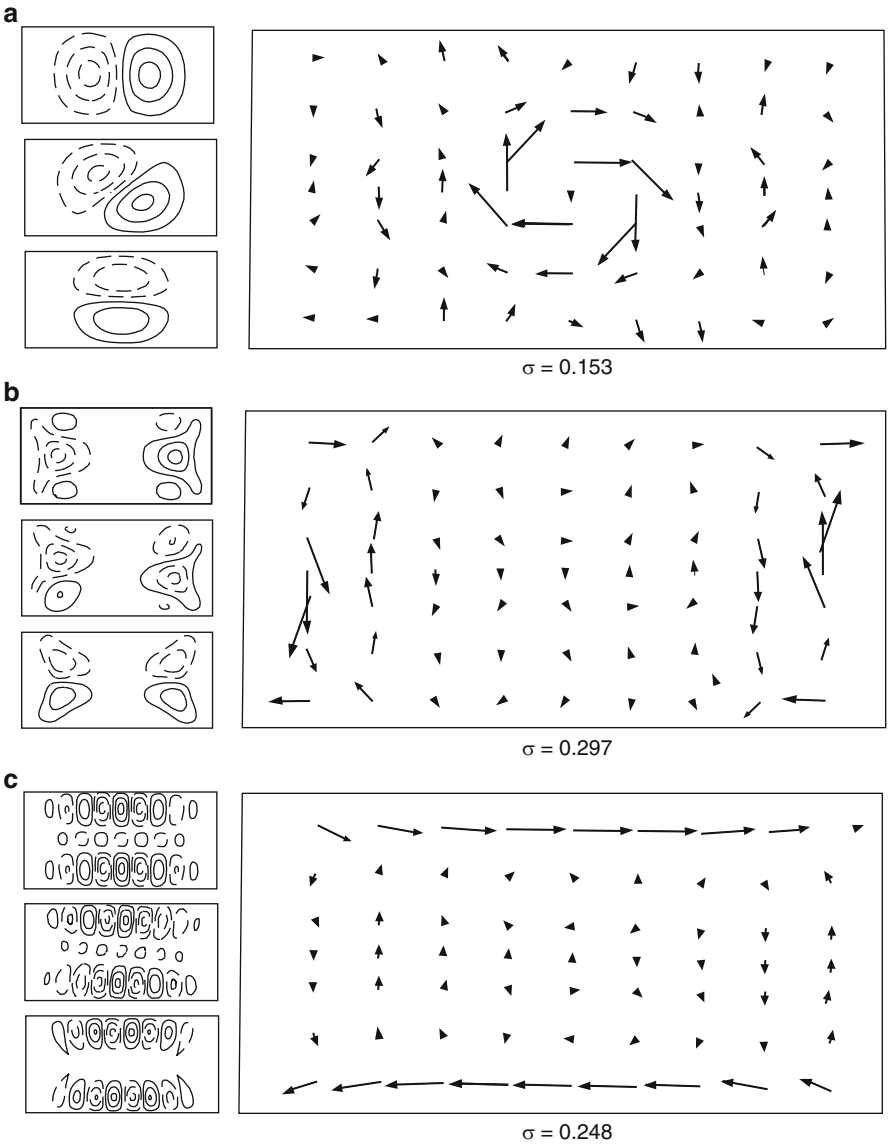

Fig. 21.23 Depth-integrated Stokes drift during one period for the Ball-, bay- and channel modes shown in Fig. 21.22. The parameters are the same as those used for Fig. 21.22. Composed from [26,29]. © CRC-Press, reproduced with permission

propagation of the phase. Everywhere else the drift is small and essentially negligible in the lake middle. The Stokes-drift in all three mode types exhibits a motion, which is essentially clockwise around the basin (on the N. H.). However, it differs for different mode-types. Ball-type modes are strong in a nearly circular vortex in the centre of the basin. Bay- and channel-type modes show a straight drift current along the short and long sides of the basin, respectively. In interpretations of velocity data, this may help in the identification of the mode selection.

21.5 Curved Channels

21.5.1 The Method of Weighted Residuals for Lakes with Curved Thalwegs

Many intermontane lakes, such as, e.g. Lake of Lugano possess curved lake axes with curvature so large that its neglection in the governing equations is not automatically justified. For these situations the MWR must be applied in its full generality. The corresponding equations in the natural coordinates following the thalweg[15] have been derived in Sect. 21.2 of this chapter and in the Appendix. The curvature is incorporated in the Jacobian J

$$J(s,n) = 1 - K(s)n, \tag{21.63}$$

where s is the arc length measured along the thalweg, n is the length coordinate measured across the basin and $K(s)$ is the thalweg curvature, which, in general, is a function of s. In the ensuing analysis, it will be assumed that symmetrization is possible. The formulae in Sect. 21.2 require expressions for $J(s)$ and $J^{-1}(s)$; so, in view of the symmetry of the chosen bathymetry (21.18), one easily may deduce the symmetric and skew-symmetric parts of J and $(J)^{-1}$ as follows

$$\begin{aligned} J^+ &= 1, \qquad (J)^- = -Kn, \\ (J^{-1})^+ &= \frac{1}{1-K^2n^2}, \qquad (J^{-1})^- = \frac{Kn}{1-K^2n^2}. \end{aligned} \tag{21.64}$$

[15] A definition of the thalweg is not unique for a real lake and its choice in reality must be determined with care. Without imposing symmetry requirements, we may simply choose an arbitrary line following more or less the approximate middle line in the long direction of the lake. Such a choice then determines the direction across the lake, n, for every s and $B^+(s)$ and $B^-(s)$. When a symmterization in the sense that $B^+(s) = B(s)/2$ and $B^-(s) = B(s)/2$ is attempted, then the selection of the s-axis can only be determined by trial and error. In both cases, islands and complex shorelines with small bays may disrupt the construction, and in extreme cases may make the use of the MWR impossible.

These expressions enter the matrix elements (21.11) and (21.14). As can be seen from these formulae, the matrices $(M^{ij}_{\beta\alpha})^{++}$, $(M^{ij}_{\beta\alpha})^{+-}$, etc., are functions of s through the integrand functions (21.64) and the width function $B(s)$, but they can in a numerical solution attempt of TWs for a lake be stored as preliminary information prior to any explicit computation.

In the ensuing analysis, we consider lake domains of which the thalweg is composed of disjoint segments with constant curvature and also constant width B. The matrix elements $(K^{ij}_{\beta\alpha})^{++}$, $(K^{ij}_{\beta\alpha})^{+-}$, etc., evaluated for the bathymetry

$$h(s,n) = h_0(s)\left(1+\varepsilon-\left|\frac{2n}{B(s)}\right|^q\right), \tag{21.65}$$

defined in $(21.19)_1$ and (21.21) must newly be computed for non-zero, but constant curvature. Recalculating the matrix elements $(K^{ij}_{\beta\alpha})^{++}$, $(K^{ij}_{\beta\alpha})^{+-}$, etc., by introducing the variable $y = (2\pi/B)n$ and the dimensionless curvature

$$\kappa = \tfrac{1}{2}KB \tag{21.66}$$

yields

$$\begin{aligned}
K^{00}_{\beta\alpha} &= K^{00++}_{\beta\alpha} + K^{00--}_{\beta\alpha} + K^{00-+}_{\beta\alpha} + K^{00+-}_{\beta\alpha}\\
&= \int h^{-1}\left(\frac{1}{1-\kappa^2y^2}\right)\cos\left(\pi\left(\alpha-\frac{1}{2}\right)y\right)\cos\left(\pi\left(\beta-\frac{1}{2}\right)y\right)\mathrm{d}y\\
&\quad+\int h^{-1}\left(\frac{1}{1-\kappa^2y^2}\right)\sin(\pi\alpha y)\sin(\pi\beta y)\,\mathrm{d}y\\
&\quad+\int h^{-1}\left(\frac{\kappa y}{1-\kappa^2y^2}\right)\sin(\pi\alpha y)\cos\left(\pi\left(\beta-\frac{1}{2}\right)y\right)\mathrm{d}y\\
&\quad+\int h^{-1}\left(\frac{\kappa y}{1-\kappa^2y^2}\right)\cos\left(\pi\left(\alpha-\frac{1}{2}\right)y\right)\sin(\pi\beta y)\,\mathrm{d}y,\\
K^{22}_{\beta\alpha} &= K^{22++}_{\beta\alpha} + K^{22--}_{\beta\alpha} + K^{22-+}_{\beta\alpha} + K^{22+-}_{\beta\alpha}\\
&= 4\pi^2\left(\alpha-\frac{1}{2}\right)\left(\beta-\frac{1}{2}\right)\int h^{-1}\sin\left(\pi\left(\alpha-\frac{1}{2}\right)y\right)\sin\left(\pi\left(\beta-\frac{1}{2}\right)y\right)\mathrm{d}y\\
&\quad+4\pi^2\alpha\beta\int h^{-1}\cos(\pi\alpha y)\cos(\pi\beta y)\,\mathrm{d}y\\
&\quad+4\pi^2\alpha\left(\beta-\frac{1}{2}\right)\int h^{-1}(\kappa y)\cos(\pi\alpha y)\sin\left(\pi\left(\beta-\frac{1}{2}\right)y\right)\mathrm{d}y\\
&\quad+4\pi^2\left(\alpha-\frac{1}{2}\right)\beta\int h^{-1}(\kappa y)\sin\left(\pi\left(\alpha-\frac{1}{2}\right)y\right)\cos(\pi\beta y)\,\mathrm{d}y,
\end{aligned} \tag{21.67}$$

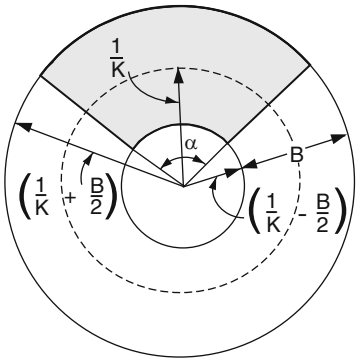

Fig. 21.24 Closed basin formed as a wedge with opening angle α of an annulus. The thalweg is given as the circle with radius $1/K = const.$, and the boundaries are formed by the circles with radii $1/K \pm B/2$, respectively, and the radial cross sections at the azimuth o and α

with $h = 1 + \varepsilon - y^q$, and the integration is from $y = 0$ to $y = 1$. The matrices $K^{20}_{\beta\alpha}$, $K^{02}_{\beta\alpha}$ remain unchanged when compared with (21.21).

Because the natural coordinate system can only be defined, if the radius of curvature exceeds half the local width, we have $\kappa < 1$, implying that all integrals in (21.67) are well defined.

Let us now construct solutions of the free TWs in a wedge of an annulus having mean constant radius $1/K$. Then the radii of the inner and outer circle of the annulus are given by $1/K \pm B/2$, respectively, see Fig. 21.24. The crude-lake assumption will also be made so that $h_0(s) = \text{const.} = 1$. In the following, the 'continuous' dispersion relation will be discussed; only quantized points of it will be actual solutions of the TW-mode with azimuthal wave length corresponding to $\alpha/m, m = 1, 2, \ldots$, where α is the wedge angle. This continuous dispersion relation is not realistic either for the full annulus because its periodicity is $\alpha = 2\pi$.

We now assume a carrier-wave ansatz of the form

$$\boldsymbol{\psi} = (\boldsymbol{\psi}^+; \boldsymbol{\psi}^-) = \mathrm{e}^{\mathrm{i}ks/L}(c_1, \ldots, c_N; c_{N+1}, \ldots, c_{2N}) = \mathrm{e}^{\mathrm{i}ks/L}\boldsymbol{c}. \tag{21.68}$$

The operator equation $\mathbb{K}\boldsymbol{\psi} := Bh_0\mathbb{M}\boldsymbol{\psi} = \boldsymbol{0}$ may, thus, be written as

$$\boldsymbol{C}\boldsymbol{\psi} = (\boldsymbol{C}_1 + \boldsymbol{C}_2)\boldsymbol{\psi} = \boldsymbol{0}, \tag{21.69}$$

in which

$$\boldsymbol{C}_1 = \begin{bmatrix} \sigma\left((rk)^2\boldsymbol{K}^{00++} + \boldsymbol{K}^{22++}\right) & -(rk)\left(\boldsymbol{K}^{20-+} + \boldsymbol{K}^{02-+}\right) \\ -(rk)\left(\boldsymbol{K}^{20+-} + \boldsymbol{K}^{02+-}\right) & \sigma\left((rk)^2\boldsymbol{K}^{00--} + \boldsymbol{K}^{22++}\right) \end{bmatrix},$$
$$\boldsymbol{C}_2 = \begin{bmatrix} 0 & \sigma\left((rk)^2\boldsymbol{K}^{00-+} + \boldsymbol{K}^{22-+}\right) \\ \sigma\left((rk)^2\boldsymbol{K}^{00+-} + \boldsymbol{K}^{22+-}\right) & 0 \end{bmatrix}. \tag{21.70}$$

Obviously, $\boldsymbol{C}$ depends on the frequency and on (rk), where $r = 1$ may be chosen as long as the continuous dispersion relation is looked at. The dispersion relation

follows from (21.70) as the requirement

$$\det \boldsymbol{C}(\sigma, k) = 0. \tag{21.71}$$

Inspection of (21.67) shows that $\boldsymbol{C}_2 = \boldsymbol{0}$ when $K = 0$. In that case, (21.71) is a polynomial equation of order $2N$ in $(rk)^2$, already studied for straight channels. For non-vanishing K (21.71) is a polynomial equation of order $4N$ in (rk), and $+rk$ and $-rk$ are no longer simultaneous solutions. The dispersion relation does no longer exhibit the mirror symmetry with respect to the k-axis. As a result of the non-vanishing curvature, we can now differentiate between the inner and outer streamlines. Likewise, the critical points (k_0, σ_0) at which $\partial\sigma/\partial n = 0$ will be different for $k < 0$ and $k > 0$. Furthermore, it is straightforward to see from (21.67) and (21.70) that

$$\sigma(\kappa, k) = \sigma(-\kappa, -k), \tag{21.72}$$

which includes the special case $\kappa = 0$. Moreover, we have now replaced K by κ according to (21.66).

21.5.2 Dispersion Relation

Stocker [26] calculated the continuous dispersion relation. He writes: 'Figure 21.25 shows the dispersion relation (21.71) of a third order model for the first two mode units. For $\kappa = 0$ the symmetry with respect to the vertical is visible whereas for $\kappa > 0$ it is broken. For a given frequency all wave numbers are shifted to the right which implies that curvature shortens waves for $\kappa > 0$ whereas they become longer for $\kappa < 0$. Recalling that the solution $\boldsymbol{\psi}$ is proportional to $\exp(\mathrm{i}(kx - \omega t)$ and $\boldsymbol{\psi}$ is right bounded, it follows that the waves travelling along the inner (outer) shore line are longer (shorter) than for $\kappa = 0$.[16]

Furthermore, the critical point (k_0^+, σ_0^+) in the domain $\kappa > 0$ is translated to lower frequencies and larger wavenumbers, and the opposite is true for (k_0^-, σ_0^-) in the domain $k < 0$. Consequently, there exists a frequency range $\sigma_0^+ < \sigma < \sigma_0^-$, where only waves with $k < 0$ can propagate. These are trapped along the inner shore line. If there existed eigenfrequencies in this range for a closed basin, their modal structure would exhibit a particular pattern with wave motion primarily at the inner shore line [...]. Table 21.9 lists the boundaries of these frequency ranges. For increasing curvature the values of σ_0^- and σ_0^+ lie farther and farther apart; this effect is weak for steep topographies.

Note, that from an observational point of view the difference is very small, e.g. $T_0^- = 57\,\mathrm{h}$ and $T_0^+ = 63\,\mathrm{h}$ for $q = 2$ and $\kappa = 0.2$, a difference that is unlikely to be detectable by field observations.

[16] The same is true when $\kappa < 0$ or the coordinate system is chosen such that s points into the opposite direction. It is a consequence of the general property (21.72).

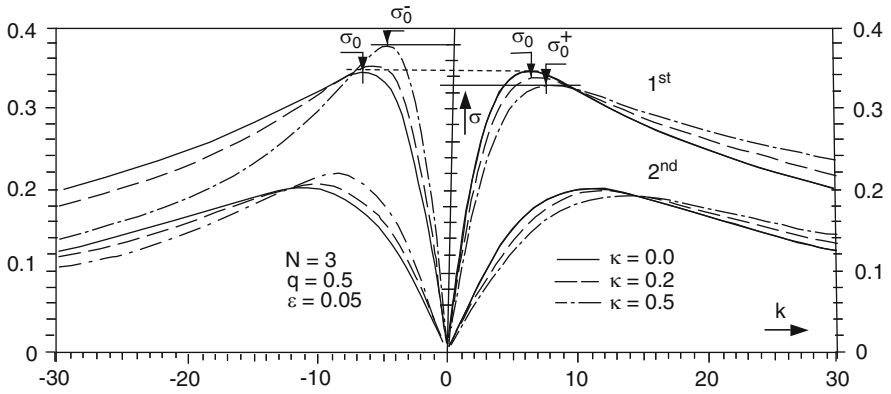

Fig. 21.25 Dispersion relation of a third order model for various values of curvature. The parameters are $N = 3, q = 0.5, \varepsilon = 0.05$ (from [29]). © CRC-Press, reproduced with permission

Table 21.9 Frequencies $\sigma_0^{\pm}$ for $k \gtrless 0$ where $\partial\sigma/\partial k = 0$ for different values of the curvature κ and topography q. The parameters are $N = 3$, $\varepsilon = 0.05$, first mode unit, from [26]

q		$\kappa = 0$	$\kappa = 0.2$	$\kappa = 0.5$
	σ_0^-	0.2745	0.2799	0.2947
2.0	σ_0^+	0.2745	0.2708	0.2669
	$\Delta\sigma$	0	0.0091	0.0278
	σ_0^-	0.2081	0.2111	0.2188
5.0	σ_0^+	0.2081	0.2059	0.2033
	$\Delta\sigma$	0	0.0052	0.0155

Table 21.10 Wavenumbers $k_0^{\pm}$ corresponding to Table 21.9, from [26]

q		$\kappa = 0$	$\kappa = 0.2$	$\kappa = 0.5$
	k_0^-	−14.9	−12.1	−7.83
2.0	k_0^+	14.9	17.8	21.9
	$k_0^+ - \lvert k_0^- \rvert$	0	5.7	14.1
	k_0^-	−17.7	−14.6	−9.83
5.0	k_0^+	17.7	20.7	25.1
	$k_0^+ - \lvert k_0^- \rvert$	0	6.1	15.3

On the other hand, for increasing κ and q the difference of the wavenumbers increases. These properties are also displayed in Fig. 21.26. Two mode units of the dispersion relation are given for different values of topography and curvature parameters. The results support the findings listed in Tables 21.9 and 21.10. In Fig. 21.27, the frequency $\sigma(\lambda)$ is plotted as a function of the wavelength $\lambda = 2\pi/k$. As surmised above, short wavelengths are hardly influenced by κ, whereas long waves experience strong curvature effects.

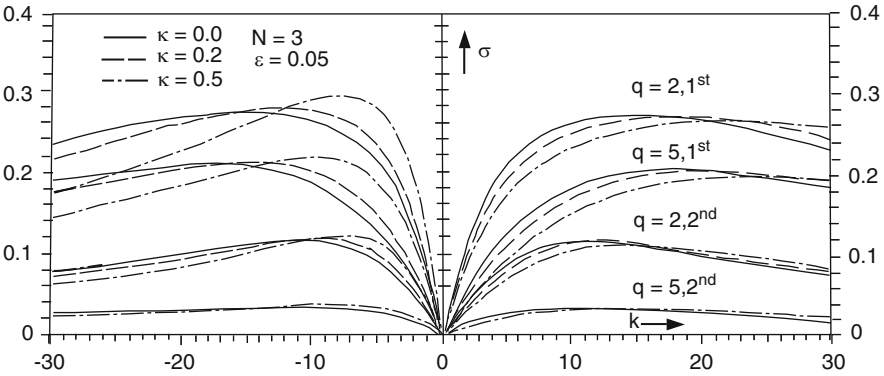

Fig. 21.26 Curvature and topography effect on the dispersion relation (from [29]). © CRC-Press, reproduced with permission

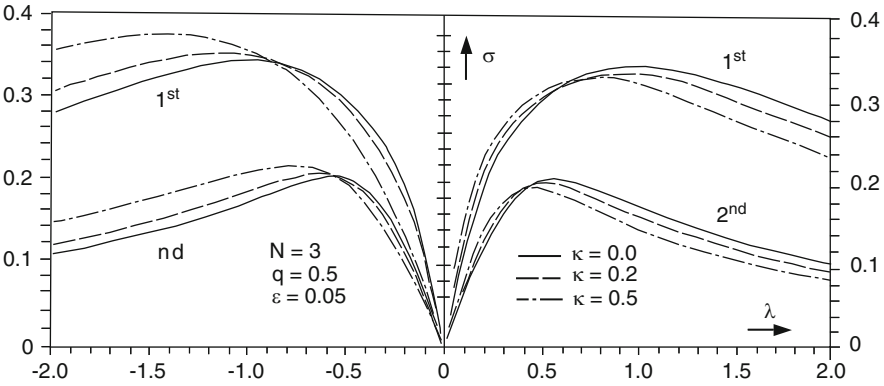

Fig. 21.27 Dispersion relation as a function of the wavelength $\lambda = 2\pi/k$. Short waves are not influenced by the curvature (from [26]). © Versuchsanstalt für Wasserbau, Hydrologie und Glaziologie an der ETH Zürich, reproduced with permission

21.5.3 TW-Wave Modes in Wedges of Annuli with Smooth Bathymetry

In this section, results will be presented on TW-modes, which are the analogues to the TW-modes in rectangles having smooth isotrophs as treated in Sect. 21.4.3. We follow closely Stocker [26] and Stocker and Hutter [29]. TW-modes in such basins also exhibit Ball-, bay- and channel-type modes, however, these are on occasion considerably modified. Moreover, additional modes may exist which were not found for rectangles; their frequencies lie in the interval $\sigma \in [\sigma_0^+, \sigma_0^-]$ of Fig. 21.25. The bathymetry will be chosen as in (21.65), where the dimensionless arc length is given by

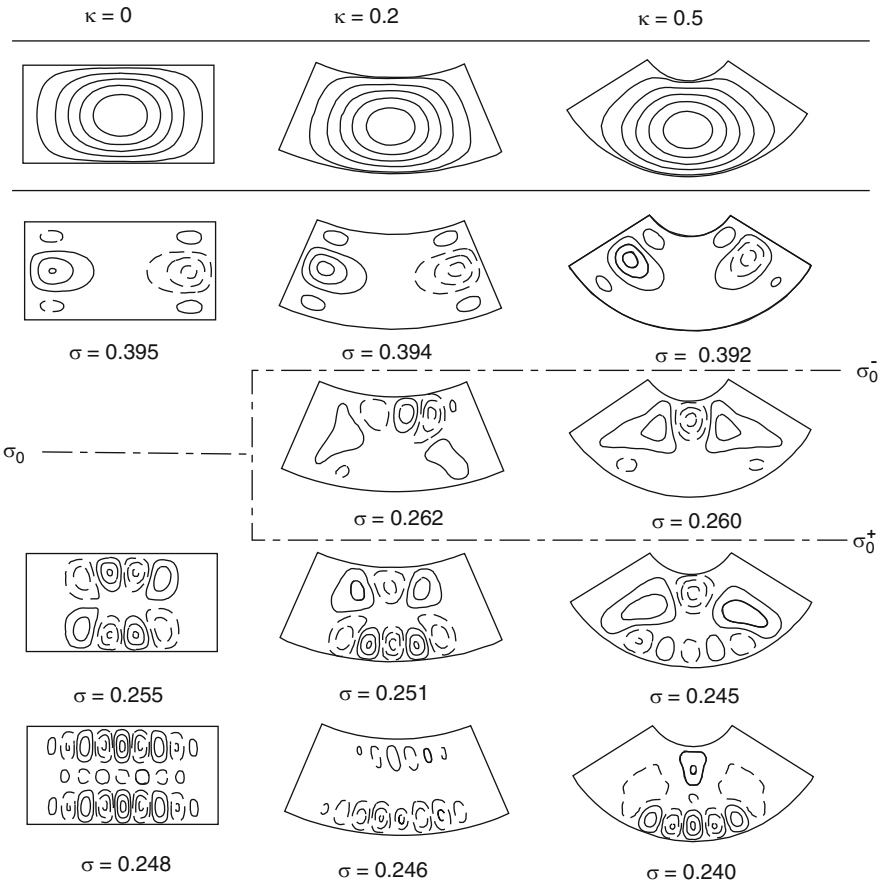

Fig. 21.28 Comparison of eigenmodes in *straight* and *curved* basins, their lines of constant depth are shown in the *top row*. The modes are ordered for decreasing frequency and the continuation is given in Fig. 21.29. The cut-off frequency σ_0 splits in the case of curvature, building an interval $[\sigma_0^+, \sigma_0^-]$ in which the modes show uncommon patterns. The parameters are $N = 2, r = 0.5, q = 2, \varepsilon = 0.05, \eta = 0.01, M = 100$ (from [26, 29]). © CRC-Press, reproduced with permission

$$s = \frac{1}{\kappa}\xi, \qquad \xi \in [0,1], \qquad \kappa = \frac{KB}{2}$$

with $|\kappa| \in [0,1)$ and $h_0(s)$ as selected in (21.43). The integration procedure is the same as that for rectangular basins in Sect. 21.4.3, the only difference being that the matrices $K^{ij}_{\alpha\beta}$ must now be computed according to the formulae (21.67). For the integration along the channel axis from $s = 0$ to $s = 1$ the fourth order Runge–Kutta method was used with a discretisation of the interval $s \in [0,1]$ in M equidistant elements of length $d = 1/M$. Satisfying the boundary conditions at $s = 0$ and $s = 1$ yields an eigenvalue equation analogous to (21.51).

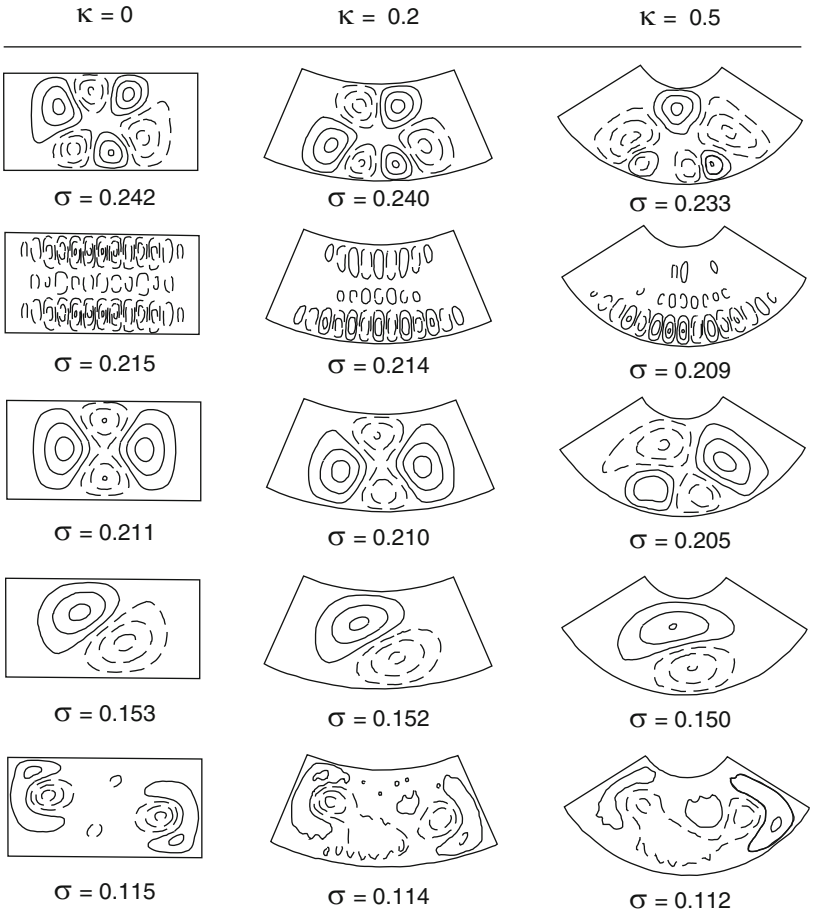

Fig. 21.29 Same as Fig. 21.28 for different frequencies (from [26,29]). © CRC-Press, reproduced with permission

The inferences drawn from the continuous dispersion relation showed that the symmetry $\sigma(+k) = \sigma(-k)$ is broken and replaced by (21.72); for $\kappa > 0$ all wavenumbers belonging to a given frequency are shifted to more positive values. As a consequence, TWs propagating along the inner (outer) shore line are longer (shorter) than for straight channels. Moreover, there exists a frequency interval $[\sigma_0^+, \sigma_0^-]$ such that free TWs are restricted to the inner shore line. These symmetry breakings manifest themselves in the streamline and current patterns of the TWs. Stocker [26] writes: 'Figures 21.28 and 21.29 show corresponding eigenmodes for different values of the curvature, ordered according to frequency. Generally, curvature does not alter the eigenfrequency very much. Deviations of the eigenfrequencies for a strongly curved basin ($\kappa = 0.5$) from the values in the straight lake are throughout less than 5%. Eigenfrequencies decrease with increasing curvature. There is little

hope to detect experimentally any effect of curvature on the eigenfrequency. The stream function pattern, on the other hand, shows more pronounced modification.

The Ball-modes clearly demonstrate (increased gyre scales close to the inner shore). Although the total number of vortices remains constant when increasing κ from $\kappa = 0$, the number of gyres along the inner shore decreases in favor of that along the outer (shore). Along with this, the inner (gyres) become larger.

As could be expected in advance, the stream function of the bay-modes ($\sigma = 0.395$ and $\sigma = 0.115$)[17] is hardly altered in the curved basin. Mainly modes, which consist of wave motion over the whole curved domain, will be influenced by this change of geometry.

The channel-modes demonstrate remarkable changes. By increasing the curvature, the wave motion is significantly attenuated in the region towards the centre of the curvature. For $\kappa = 0.5$ (an extreme case), the eigenmode only consists of a trail of waves trapped along the outer shore line.

In the critical interval $I = [\sigma_0^+, \sigma_0^-]$, there are indeed eigenfrequencies which exhibit the conjectured structure. Few large scale vortices are trapped at the inner boundary of the basin. In Fig. 21.19, one finds a bay mode with an eigenfrequency very close to but above σ_0. This mode is not shown in Fig. 21.28 for $\kappa = 0$ because, strictly, the modes for $\kappa = 0.2$ and $\kappa = 0.5$ with $\sigma \in I$ have no limit for $\kappa \downarrow 0$, and it is not clear whether and how a possible eigenmode could be constructed right at $\sigma = \sigma_0$. Thus, solutions for $\kappa > 0$ with $\sigma \in I$ are structurally new. In the course of one cycle, the vortices do not propagate around the basin but rather remain trapped in the domain $n > 0$.

21.6 Reflection of Topographic Waves

In the preceding section, it was shown, on the basis of phenomenology, i.e. appropriate selection of the bathymetry, that three types of TW-modes exist in rectangular basins: Long periodic large wavelength basin-filling (Ball)-modes, long-periodic short wavelength basin-filling channel-modes and bay-modes which are localized at the long ends of the rectangle. All three were heuristically explained with the aid of the dispersion relation, see Figs. 21.4 and 21.4. Ball- and channel-type modes must have frequencies in the domain of purely real wave numbers; for the channel-modes the phase and group velocities are in the same direction, $c_{\mathrm{ph}} \uparrow\uparrow c_{\mathrm{gr}}$ whilst they are in opposite directions, $c_{\mathrm{ph}} \downarrow\uparrow c_{\mathrm{gr}}$, for the Ball-modes. For bay-modes, the frequency must be complex-valued and lie above the critical cut-off frequency σ_0 for which $\partial\sigma/\partial k|_{\sigma_0} = 0$. Moreover, it was shown that for 'crude lake models', i.e. lakes with vertical walls at their long ends, bay-modes could not be shown to exist. This lack of a surmised TW-mode was suspected to be due to the discontinuity of the isotrophs

[17] The modes $\sigma > \sigma_0^-$ for $\kappa = 0.2$ and $\kappa = 0.5$ are obtained by shooting from both ends, $s = 0$ and $s = L$.

at the vertical walls of the end cross sections; indeed, once a lake topography with a smooth connection of the level lines on the long sides of the rectangle was selected, bay modes of TWs were found. It was further suspected that bay modes would also exist in a semi-infinite channel. Such a suspicion was based on the fact that the dispersion relation has a complex valued regime, which assigns to a frequency above σ_0, complex valued wave numbers, leading to stream function selections, which are exponentially evanescent as one moves away from the bay region. This behaviour is reminiscent of Taylor's reflection problem of a Kelvin wave at the end of a semi-infinite gulf ([34], see Chap. 12.)

In this section, the above suspected behaviours will all essentially be substantiated. In doing so, we shall follow the works of Stocker which is contained in [26, 27, 29–31].

21.6.1 Reflection at a Vertical Wall

Consider a semi-infinite channel with $s \geq 0$ and its end wall at $s = 0$. A wave entering this channel from $s = \infty$ is moving in the negative s-direction and, therefore, has $\exp(\mathrm{i}(\sigma t + ks))$ as its harmonic representation with real $\sigma < \sigma_0$ and real wavenumber k. For the energy moving *into* the channel, the possible wave numbers of an incident mode to a given $\sigma < \sigma_0$ are shown in Fig. 21.30 for a third order model. If k is negative, $k < 0$, then $c_{\mathrm{ph}} \uparrow\uparrow c_{\mathrm{gr}}$, and typical scales of the incident wave are large; if k is positive, $k > 0$, then $c_{\mathrm{ph}} \uparrow\downarrow c_{\mathrm{gr}}$, and typical scales of the incident wave are small. A reflection of an incident wave can in our MWR only be achieved when it is superposed with several or all waves having the same frequency (but different wavenumbers). The incident wave and at least one reflected wave have real k and the remaining modes must have

$$\mathrm{Im}(k) \geq 0 \tag{21.73}$$

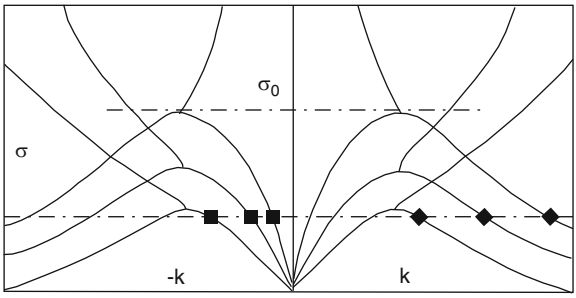

Fig. 21.30 Dispersion relation $\sigma(|k|)$ of a third order model in an infinite channel. Possible incident modes with group velocity into the negative s-direction are indicated by *filled square* for $c_{\mathrm{ph}} \uparrow\uparrow c_{\mathrm{gr}}$ and by *filled diamond* for $c_{\mathrm{ph}} \downarrow\uparrow c_{\mathrm{gr}}$. Above the cut-off frequency σ_0 all wavenumbers are complex (from [26, 27]).

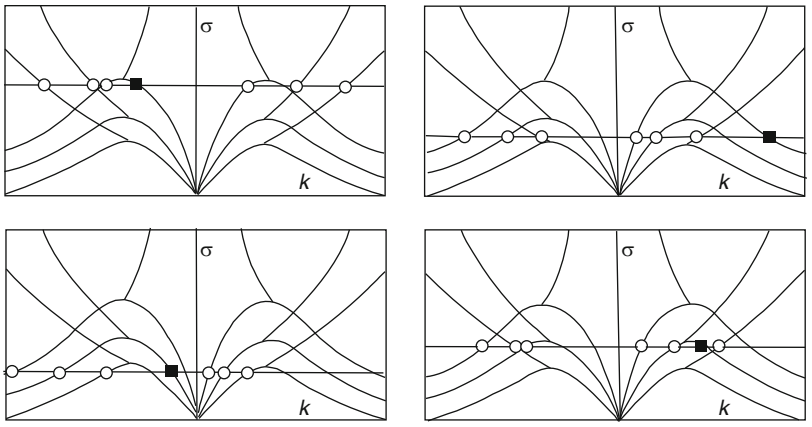

Fig. 21.31 Selection of possible incident (■) and reflected (○) modes in a semi-infinite channel (from [27]). © Springer, Berlin, reproduced with permission

to be exponentially evanescent as $s \to \infty$. With this, the superposition and determination of the compound solution is unique and consists of one incident mode and $2N$ reflected modes. This argument relies on the fact that the real branch of the dispersion relation has domains of $k > 0$ where $\partial\sigma/\partial k < 0$ and $\partial\sigma/\partial k > 0$. It also makes use of the existence of a complex branch of the mode units. Examples of this selection are shown in Fig. 21.31. Full squares mark the k-values for the incident wave, whilst open circles give the corresponding k-values for the reflected waves; in the real branches, they all have outgoing group velocities and of the four possibilities in the complex branches only those with $\mathrm{Im}(k) \geq 0$ evanesce exponentially for $s \to \infty$.

Recall that a general wave in a straight infinite channel has the form (21.26). If we renounce from explicitly distinguishing between P_α^+ and P_α^- with $\alpha = 1, \ldots, N$ and use for simplicity only P_α with $\alpha = 1, \ldots, 2N$, then the general solution reads

$$\psi = \sum_{\gamma=1}^{2N} \left(d_\gamma \exp\left(\mathrm{i}k\gamma s\right) \sum_{\alpha=1}^{2N} c_{\alpha\gamma} P_\alpha \right), \tag{21.74}$$

in which the harmonic time dependence of (21.26) has been dropped and the summation over γ is from $\gamma = 1$ to $\gamma = 2N$ (and not $\gamma = 4N$ because of the constraint (21.73)). A solution representing wave reflection is then given by

$$\psi = \psi_{\mathrm{in}} + \psi_{\mathrm{out}} = \sum_{\alpha=1}^{2N} \psi_\alpha = \exp\left(\mathrm{i}k_i s\right) \sum_{\alpha=1}^{2N} c_{\alpha i} P_\alpha + \sum_{\gamma=1}^{2N} \left(d_\gamma \exp\left(\mathrm{i}k_\gamma s\right) \sum_{\alpha=1}^{2N} c_{\alpha\gamma} P_\alpha \right), \tag{21.75}$$

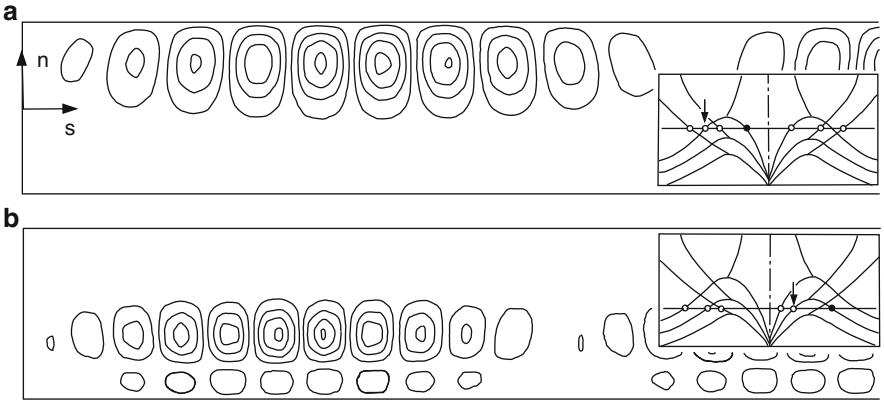

Fig. 21.32 ψ-contour lines of a reflection of TWs at a vertical wall. The insets explain the composition of the reflection pattern with incident wave (•) and reflected wave (∘). The selected parameters are $N = 3, \varepsilon = 0.05$, for (**a**) $q = 1.0, \sigma = 0.305$ and (**b**) $q = 0.5, \sigma = 0.202$ (from [27]). © Springer, Berlin, reproduced with permission

with the unknown vector d_γ. The coefficients $c_{\alpha i}$ are known if the frequency σ and corresponding wavenumber k_i of the incident wave are prescribed. They are computed with the methods of Sect. 21.5. Analogously, to each of the wavenumbers $k_\gamma(\sigma)$ of the reflected waves the corresponding $c_{\alpha\gamma}$ can be computed.[18] Hence, $k_i, k_\gamma, c_{\alpha i}(\alpha, \gamma = 1, \ldots, 2N)$ are known. Imposing the no-flux condition $\psi_\alpha = 0$ at $s = 0$ yields the linear system

$$\sum_{\gamma=1}^{2N} c_{\alpha\gamma} d_\gamma = -c_{\alpha i}, \qquad \alpha = 1, \ldots, 2N, \tag{21.76}$$

in which d_γ and $c_{\alpha i}$ are vectors of length $2N$ and $c_{\alpha\gamma}$ is a $(2N \times 2N)$-matrix. Due to the orthogonality of the set P_α and the modes belonging to different wavenumbers k_γ the matrix $c_{\alpha\gamma}$ is regular and (21.76) can be inverted.

Figure 21.32a displays the reflection pattern for a wave belonging to the first mode unit with both phase and group velocities directed towards the wall. Alternatively, incident phase and group velocities may have different directions as in the second-mode response of Fig. 21.32b. It was found that the largest portion of the reflected energy lies in the mode with the corresponding wavenumber belonging to the same branch of the dispersion relation (indicated by arrows in the insets of Fig. 21.32). Consequently, wave activity remains primarily at the side of the inci-

[18] The computation proceeds as follows: For given $\sigma < \sigma_0$ one solves the determinant equation (21.25) for all k and eliminates from this set those with $\mathrm{Im}(k) < 0$. One of the real k's is k_{in}, all others define the real k_{out}. For each of the admissible k's (all real k_{out} and of the complex valued ones those with $\mathrm{Im}(k) > 0$), we solve (21.24) for $c_{\alpha\gamma}$.

dent wave. The result is a beat pattern with its first 'calm' area at approximately $2\pi B/|k_{\text{in}} - k_{\text{out}}|$ away from the wall. If k_{in} and k_{out} differ markedly from each other, rather local and small-scale patterns emerge. Channel-type solutions for rectangles as e.g. displayed in Fig. 21.32 can be interpreted in this spirit as a superposition of two nearly independent reflection patterns, which are induced by the two vertical walls. Since the discontinuous depth lines prevent wave energy from changing the side in the channel, there are no simple reflection patterns to be expected that occupy the whole channel.

21.6.2 *Reflection at a Gulf End with Continuous Depth Lines But Discontinuous Slope Parameter*

To substantiate these statements, Stocker [26] looked at a semi-infinite channel with exponential shore at its end. He employed the bathymetry according to (21.35) with

$$h_0(s) = \begin{cases} \varepsilon \left(1 + \dfrac{1}{\varepsilon}\right)^{s/s_0} & , \; 0 < s < s_0 \\ (1+\varepsilon), & s > s_0, \end{cases} \tag{21.77}$$

so that $h_0'(s)/h_0 = \ln[(1 + 1/\varepsilon)^{1/s_0}]$ is constant. The isobaths at the gulf end are now $\subset$-shaped. Dropping a time dependent factor, $\exp(-\mathrm{i}\sigma t)$, the solution then takes the form[19]

$$\psi = \begin{cases} \psi^0 = \displaystyle\sum_{\Gamma=1}^{4N} d_\Gamma \mathrm{e}^{\mathrm{i}k_\Gamma s} \sum_{\alpha=1}^{2N} c_{\alpha\Gamma}^{\text{ex}} P_\alpha, & 0 < s < s_0, \\ \psi^\infty = \mathrm{e}^{\mathrm{i}k_i s} \displaystyle\sum_{\alpha=1}^{2N} c_{\alpha i} P_\alpha + \sum_{\gamma=1}^{2N} d_\gamma \mathrm{e}^{\mathrm{i}k_\gamma s} \sum_{\alpha=1}^{2N} c_{\alpha\gamma} P_\alpha, & s_0 < s, \end{cases} \tag{21.78}$$

where k_i is the incident wavenumber, $\{k_\Gamma\}_1^{4N}$ is the whole set of wavenumbers and $\{k_\gamma\}_1^{2N}$ is the restricted set with $\mathrm{Im}(k) \geq 0$ and the group velocity directed away from the end wall, all corresponding to σ. Superscripts 0 and ∞ denote the domains $0 < s < s_0$ and $s_0 < s$, respectively. $c_{\alpha\Gamma}^{\text{ex}}$ is the $(2N \times 2N)$-matrix coresponding to (21.26) but for the case $h'/h = s_0 = \text{const.} \neq 0$. The stream function ψ must

[19] In this representation, $\sigma < \sigma_0$ is prescribed as the frequency of the incoming wave. To this frequency belong real and complex valued wavenumbers of the N mode units. For $s < s_0$ these wavenumbers $k_\Gamma (\Gamma = 1, \ldots, 4N)$ and the matrix $c_{\alpha\Gamma}^{\text{ex}}$ are determined from equations analogous to (21.25) and (21.24) with the matrices $(K_{\beta\alpha}^{ij})^{\pm}$ evaluated for $h_0'/h_0 = \ln[(1 + 1/\varepsilon)^{1/s_0}]$. Analogously, for $s > s_0$, k_γ and $c_{\alpha\gamma}$ are similarly obtained from (21.25) and (21.24), where h_0'/h_0 now vanishes.

be continuous and differentiable at $s = s_0$ and vanish at $s = 0$. Thus, for $\alpha = 1, \ldots, 2N$[20]

$$\begin{aligned}
\psi_\alpha^0|_{s=0} &= 0 &&: \quad c_{\alpha\Gamma}^{\mathrm{ex}} d_\Gamma = 0, \\
\psi_\alpha^0|_{s=s_0} &= \psi_\alpha^\infty|_{s=s_0} &&: \quad \mathrm{e}^{\mathrm{i}k_\Gamma s_0} c_{\alpha\Gamma}^{\mathrm{ex}} d_\Gamma = c_{\alpha\gamma} \mathrm{e}^{\mathrm{i}k_\gamma s_0} d_\gamma + c_{\alpha i} \mathrm{e}^{\mathrm{i}k_i s_0}, \\
\frac{\partial}{\partial s} \psi_\alpha^0|_{s=s_0} &= \frac{\partial}{\partial s} \psi\alpha^\infty|_{s=s_0} &&: \mathrm{i}k_\Gamma \mathrm{e}^{\mathrm{i}k_\Gamma s_0} c_{\alpha\Gamma}^{\mathrm{ex}} d_\Gamma = \mathrm{i}k_\gamma \mathrm{e}^{\mathrm{i}k_\gamma s_0} c_{\alpha\gamma} d_\gamma + \mathrm{i}k_i c_{\alpha i} \mathrm{e}^{\mathrm{i}k_i s_0},
\end{aligned} \tag{21.79}$$

with the $6N$ unknowns and must be satisfied. This can be written as

$$\begin{bmatrix} c_{\alpha\Gamma}^{\mathrm{ex}} & 0 \\ c_{\alpha\Gamma}^{\mathrm{ex}} \mathrm{e}^{\mathrm{i}k_\Gamma s_0} & -c_{\alpha\gamma} \mathrm{e}^{\mathrm{i}k_\gamma s_0} \\ \mathrm{i}k_\Gamma c_{\alpha\Gamma}^{\mathrm{ex}} \mathrm{e}^{\mathrm{i}k_\Gamma s_0} & -\mathrm{i}k_\Gamma c_{\alpha\gamma} \mathrm{e}^{\mathrm{i}k_\gamma s_0} \end{bmatrix} \begin{bmatrix} d_\Gamma \\ d_\gamma \end{bmatrix} = \begin{bmatrix} 0 \\ c_{\alpha i} \mathrm{e}^{\mathrm{i}k_i s_0} \\ \mathrm{i}k_i c_{\alpha i} \mathrm{e}^{\mathrm{i}k_i s_0} \end{bmatrix}, \tag{21.80}$$

and the vectors d_Γ and d_γ are determined by inverting (21.80).

Figure 21.33 shows solutions ψ for a composed channel; two significant differences to Fig. 21.32 are observed. Now, there is wave activity also in the oposite half of the channel corresponding to the negative of the incident wavenumber. This amounts to a weak *leakage of wave energy* by reflection into the other channel domain (Fig. 21.33a). However, probably owing to the non-smoothness of the isobaths at s_0 it is comparatively weak and most of the reflected wave activity remains on the incident side.

Figure 21.33b shows a reflection pattern of lower frequency, k_{in} and k_{out} lie farther apart and, therefore, more local and complicated structures result. Moreover, at the beginning of the reflecting shelf ($s \approx s_0$) *wave intensification* is observed. These specific results demonstrate that the global wave pattern is very sensitive to the basin shape and the depth profile at the channel end.

However, these results still do not explain the distinction of TWs into three different basin types as suggested in Sect. 21.4.3. We would like to have these explained e.g. as special cases of three different reflection patterns.

21.6.3 Reflection at a Channel End with Continuous Depth Lines and Continuous Slope Parameter

This section closely follows the analysis outlined in Sect. 21.4.3 and is due to Stocker [26]. The procedure is, however, more complicated than there, since the solution must be constructed in an *open* domain.

[20] We now omit the summation signs over $\Gamma = 1, 2, \ldots, 4N$ and $\gamma = 1, 2, \ldots, 2N$.

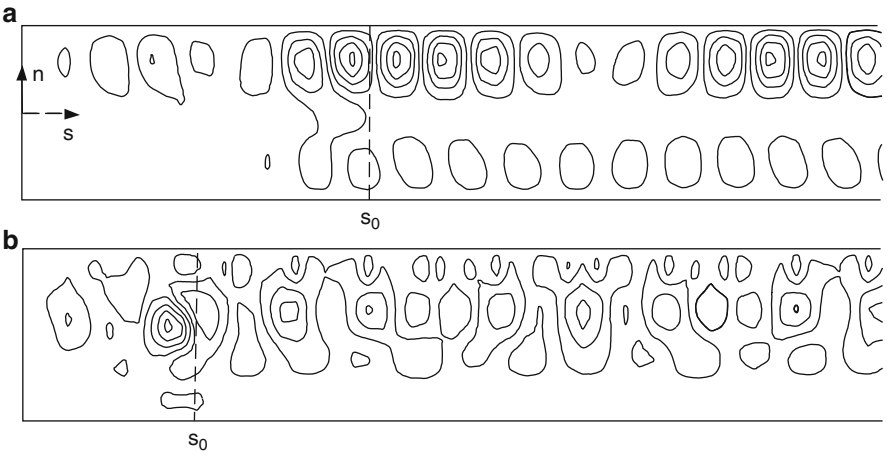

Fig. 21.33 Reflection pattern in a composed channel. For $0 < s_0$ the depth varies exponentially along the axis whereas it is constant for $s > s_0$. This connects the isobaths of both channel domains $n > 0$ and $n < 0$ and enables wave energy to leak into the opposite domain in the course of reflection. The selected parameters are $\epsilon = 0.05$, for (**a**) $N = 2, q = 2.0, \sigma = 0.260, s_0 = 2.0$ and (**b**) $N = 3, q = 0.5, \sigma = 0.200, s_0 = 1.0$ (from [27]). © Springer, Berlin, reproduced with permission

21.6.3.1 Numerical Method

We now replace h_0 in (21.77) by

$$h_0(s) = \begin{cases} \eta + \sin^2\left(\dfrac{\pi s}{2s_0}\right), & 0 < s < s_0, \\ 1 + \eta, & s_0 < s. \end{cases} \tag{21.81}$$

This profile is smooth at s_0 and the slope parameter $S(s) \equiv h^{-1}\mathrm{d}h/\mathrm{d}s$ takes the form

$$S(s) = \begin{cases} \dfrac{\pi \sin(\pi s/s_0)\cos(\pi s/s_0)}{s_0(\eta + \sin^2(\pi s/2s_0))}, & 0 < s < s_0, \\ 0, & s_0 < s, \end{cases} \tag{21.82}$$

The solution $\boldsymbol{\Psi}$ in the two domains is given by

$$\boldsymbol{\Psi} = \begin{cases} \boldsymbol{\Psi}^0 = \exp\left(\displaystyle\int_0^s \boldsymbol{A}(\hat{s})\mathrm{d}\hat{s}\right)\boldsymbol{\Psi}^0(0) = \boldsymbol{E}(s)\boldsymbol{\Psi}^0(0), & 0 < s < s_0, \\ \boldsymbol{\Psi}^\infty = \boldsymbol{\Psi}_i^\infty + \displaystyle\sum_{\gamma=1}^{2N} \boldsymbol{\Psi}_\gamma^\infty \boldsymbol{D}_\gamma, & s_0 < s, \end{cases} \tag{21.83}$$

where (21.38) and (21.46) have been used. $\boldsymbol{\Psi}_i^{\infty}$ is the incident mode with wavenumber k_i and, in real notation, has the form

$$\boldsymbol{\Psi}_i^{\infty} = (\mathrm{Re}\boldsymbol{\psi}_i, \mathrm{Re}\dot{\boldsymbol{\psi}}_i, \mathrm{Im}\boldsymbol{\psi}_i, \mathrm{Im}\dot{\boldsymbol{\psi}}_i), \tag{21.84}$$

which is a vector with $8N$ components; one such component, e.g. $(\mathrm{Re}\boldsymbol{\Psi}_i)_\alpha$ is given by $\mathrm{Re}\exp(\mathrm{i}k_i s)c_{\alpha i}P_\alpha$ (no sum over α). If $\boldsymbol{D}_\gamma$ and $\boldsymbol{\Psi}_\gamma^{\infty}$ are also separated into real and imaginary parts, they have the form[21]

$$\Psi_\gamma^{\infty} = \left[\begin{array}{c|c} \mathrm{Re}\,\boldsymbol{\psi}_\gamma & \mathrm{Im}\,\boldsymbol{\psi}_\gamma \\ \mathrm{Re}\,\dot{\boldsymbol{\psi}}_\gamma & \mathrm{Im}\,\dot{\boldsymbol{\psi}}_\gamma \\ \hline \mathrm{Im}\,\boldsymbol{\psi}_\gamma & \mathrm{Re}\,\boldsymbol{\psi}_\gamma \\ \mathrm{Im}\,\dot{\boldsymbol{\psi}}_\gamma & \mathrm{Re}\,\dot{\boldsymbol{\psi}}_\gamma \end{array}\right], \quad \boldsymbol{D}_\gamma = \left[\begin{array}{c} D_{\mathrm{R}\gamma} \\ D_{\mathrm{I}\gamma} \end{array}\right]. \tag{21.85}$$

As was the case for the incident wave, $\boldsymbol{\psi}_\gamma$ consists of $2N$ components, each of which has the form

$$(\boldsymbol{\psi}_\gamma)_\alpha \equiv \mathrm{e}^{\mathrm{i}k_\gamma s}c_{\alpha\gamma}P_\alpha, \quad (\dot{\boldsymbol{\psi}}_\gamma)_\alpha \equiv \mathrm{i}k_\gamma \mathrm{e}^{\mathrm{i}k_\gamma s}c_{\alpha\gamma}P_\alpha$$

(no sum over α), $\alpha = 1, 2, \ldots, 2N$, and wavenumbers are restricted such that $\mathrm{Im}k_\gamma \geq 0$.

Representation (21.83) has $8N$ real unknowns, $\boldsymbol{\Psi}^0(0) = (0, \dot{\boldsymbol{\psi}}_{\mathrm{R}}^0(0); 0, \dot{\boldsymbol{\psi}}_{\mathrm{I}}^0(0))$ and $\boldsymbol{D}_\gamma$. These are determined with the help of the matching condition at $s = s_0$, viz.

$$\boldsymbol{\Psi}^0\big|_{s=s_0} = \boldsymbol{\Psi}^{\infty}|_{s=s_0} : \boldsymbol{E}(s_0)\boldsymbol{\Psi}^0(0) = \boldsymbol{\Psi}_i^{\infty} + \sum_\gamma \boldsymbol{\Psi}_\gamma^{\infty}\boldsymbol{D}_\gamma,$$

or more precisely,

$$\left[\begin{array}{cc|c} \boldsymbol{E}_{12} & \boldsymbol{E}_{14} & \\ \vdots & \vdots & -\boldsymbol{\Psi}_\gamma^{\infty} \\ \boldsymbol{E}_{42} & \boldsymbol{E}_{44} & \end{array}\right] \left[\begin{array}{c} -\dot{\boldsymbol{\psi}}_{\mathrm{R}}^0(0) \\ -\dot{\boldsymbol{\psi}}_{\mathrm{I}}^0(0) \\ \boldsymbol{D}_\gamma \end{array}\right] = \left[\begin{array}{c} -\boldsymbol{\Psi}_i^{\infty} \\ \\ \end{array}\right], \tag{21.86}$$

and the calculation of the $\boldsymbol{E}_{ij}$'s is described in the text below (21.49). The computational scheme therefore requires first, numerical integration by e.g. a Runge–Kutta method to obtain the $\boldsymbol{E}_{ij}$'s and second, an algebraic procedure to calculate both $\boldsymbol{\Psi}_\gamma^{\infty}$ and, for a preselected incident wavenumber k_i, the corresponding $\boldsymbol{\Psi}_i^{\infty}$.

[21] The extended formulations (21.85) do not contain more information than the form (21.38) and only account for the characteristics of the complex multiplication. Capital subscripts R and I denote real and imaginary parts, respectively.

21.6.3.2 Reflection Patterns

We learn from (21.83) that $2N + 1$ modes are superposed which make up the solution $\boldsymbol{\Psi}^{\infty}$ far away from the reflecting zone. It is of particular interest to determine the reflection coefficients R_γ corresponding to the individual modes with wavenumber k_γ. Usually, these are calculated with the help of an energy argument: R_γ then is proportional to the averaged total energy contained in mode k_γ. However, any attempt to draw inferences concerning the energy content of the TW-motion is ambiguous when considerations are restricted to a barotropic formulation. This is so, because the averaged velocity field does not account for the energy content due to vertical velocity variations and therefore is always a *lower bound*. Hence, we propose another procedure. The measure of 'strength' of the contributing modes is selected by scaling the maximum value of the modulus of the stream function ψ_γ with the maximum value of that of the incident mode ψ_i. More precisely, we define R_γ as

$$R_\gamma \equiv \frac{\max_{n\in[B^+,B^-]}\left|(D_{\mathrm{R}_\gamma} + \mathrm{i}D_{\mathrm{I}_\gamma})\sum_{\alpha=1}^{2N} c_{\alpha\gamma}P_\alpha(n)\right|}{\max_{n\in[B^+,B^-]}\left|\sum_{\alpha=1}^{2N} c_{\alpha i}P_\alpha(n)\right|}. \tag{21.87}$$

We have calculated the reflection coefficients R_γ for a second and a third order model. The former has already revealed remarkable results which are demonstrated in Fig. 21.34. It shows R_γ of the two possible[22] reflected modes as functions of the frequency. The reflected modes are induced by the incident mode ■ which has $c_{\mathrm{gr}} \uparrow\uparrow c_{\mathrm{ph}}$ towards $s = 0$.

When solving (21.86) two cases have to be considered. If $\sigma > \sigma_0$ there exist no modes which are periodic in space, i.e. $\mathrm{Im}k \neq 0$ for all k. Consequently we cannot define an incident mode as in (21.83). Setting $\boldsymbol{\Psi}_i^{\infty} = \mathbf{0}$, (21.86) allows a non-trivial solution if

$$\det\left[\boldsymbol{E}(s_0), -\boldsymbol{\Psi}_\gamma^{\infty\mathrm{T}}\right] = 0. \tag{21.88}$$

On the other hand, when $\sigma < \sigma_0, \boldsymbol{\Psi}_i^{\infty} \neq \mathbf{0}$ and (21.86) is invertible provided the determinant does not vanish.

Calculations have shown that there are indeed real frequencies $\sigma > \sigma_0$ satisfying (21.88). Consequently, there exists a *discrete spectrum for* $\sigma > \sigma_0$ and a *continuous spectrum for* $\sigma < \sigma_0$. The contour lines of the stream function (21.83) for different frequencies are also plotted in Fig. 21.34. We call the waves which belong to the discrete spectrum *bound states* of TWs in the semi-infinite channel whereas waves for $\sigma < \sigma_0$ are *free states* of the system. This terminology is very appealing and obviously applies here well as inspection of the stream functions in Fig. 21.34 reveals.

[22] A possible reflected mode has $c_{\mathrm{gr}} = \partial\sigma/\partial k$ directed away from $s = 0$, i.e. towards $s = +\infty$ and $\mathrm{Im}\,k = 0$.

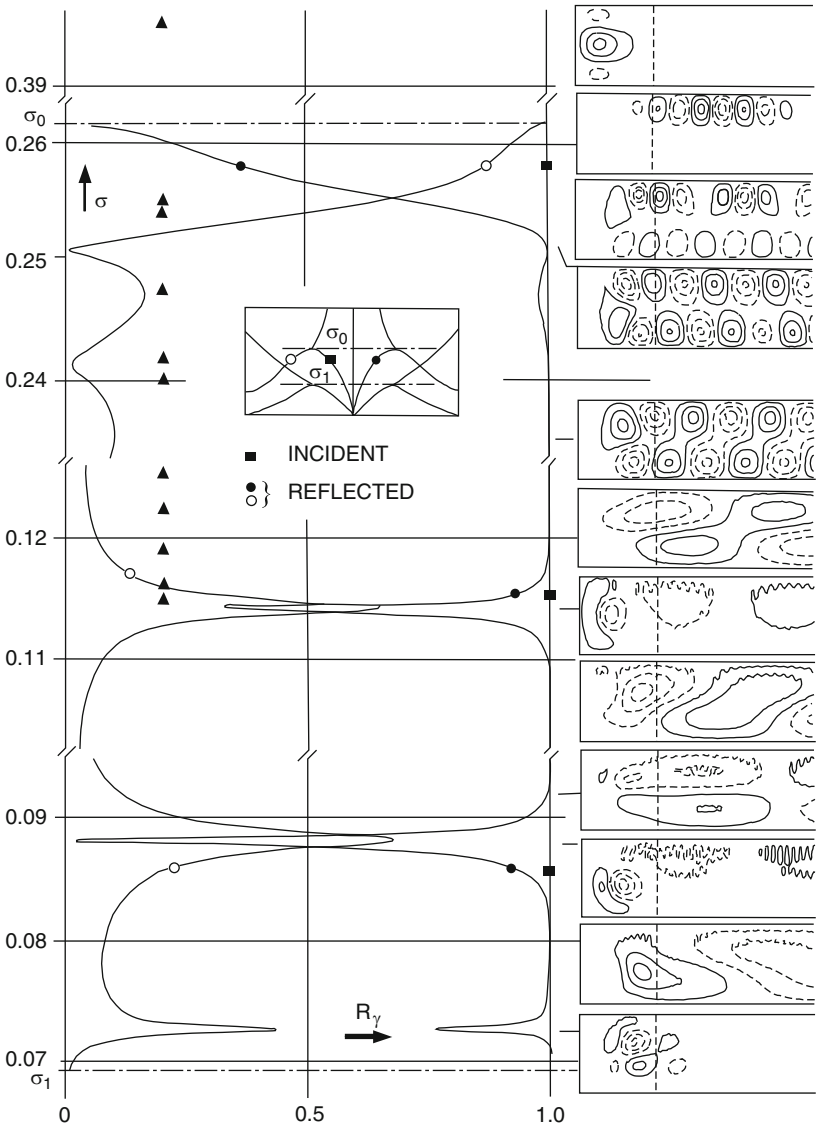

Fig. 21.34 Reflection coefficients and stream function patterns in subdomains of the frequency interval $[\sigma_1, \sigma_0]$ of the two reflected modes • and ∘, respectively. The coefficients of the incident mode ■ is scaled to 1 and both c_{gr} and c_{ph} are directed towards the reflecting wall. ▲ indicate lake solutions for $\sigma > 0.11$ corresponding to Fig. 21.19. The inset explains the position of the modes within the dispersion relation and the parameters are $N = 2$, $r = 1$, $q = 2$, $\epsilon = 0.05$, $\eta = 0.01$, $s_0 = 1$ (*dashed line*), $M = 50$ for $\sigma > 0.2$ and $M = 200$ for $\sigma \leq 0.2$ (from [26, 27]).

The bound states must be identified with the type 2 waves (bay-modes) found in the improved lake model in Sect. 21.4.3. Indeed, the frequencies $\sigma = 0.395$ are the same and when ignoring in the rectangle the stream function at the far end $s = 1$ the mode structures are alike, see Fig. 21.19. We, therefore, conclude that the occurrence of the bay-mode in the rectangular basins for $\sigma > \sigma_0$ is due to two trapped bound states of TWs in either lake bay at $s = 0$ and $s = 1$. The stream function of this mode consists of $2N$ modes k_γ with $\operatorname{Im} k_\gamma > 0$ for $s > s_0$ and is spatially evanescent. The longer a lake basin is, the weaker will be the coupling of the bound modes in the respective bays. The two additional bay-modes shown in Fig. 21.19 at $\sigma = 0.297$ and $\sigma = 0.263$ are also originating from bay-trapped topographic waves not shown in Fig. 21.34.

The fact that the TW-equation (20.4) has a discrete spectrum above $\sigma > \sigma_0$ consisting of bound states resolves the seeming controversy formulated in Sect. 21.4.1. In particular, in elongated lakes with very steep transverse topography ($q \leq 10$ for Northern Lake of Lugano as determined by Bäuerle [2]) this new result is of importance. Let us estimate the frequency of the quadratic Ball-mode of the elongated Northern Lake of Lugano. The basin is $17km$ long and has an approximate width of 1.5 km. This gives an aspect ratio of $r = 1.5/17 \approx 0.088$. Using (20.33) and (20.40) yields the estimate

$$\sigma \approx 0.049, \qquad T \approx 350\,\mathrm{h}. \tag{21.89}$$

Recall that the topography of the lake has a markedly steeper profile than the parabolic profile used in the Ball-model. Due to the conspicuous topography effect, (21.89) is certainly an overestimate for σ. Periods would therefore have to be expected to be even longer. Measurements, however, indicate a distinct signal at around 74 h, clearly far above the cut-off frequency for this basin. The following interpretation is thus put forward, and it seems reasonable that the 74 h-signal could be the trace of a *bay-trapped topographic* wave of one of the bays at Melide, Lugano or Porlezza, see Fig. 19.10. A further argument supporting this interpretation is the fact that spectral peaks of temperature time series of moorings at the Melide end (see Fig. 19.7) have this maximum at periods which are generally slightly larger than 74 h; alternatively, the corresponding peak for the Porlezza mooring is at a slightly smaller period (compare Figs. 19.7–19.10). The difference could be interpreted as being due to independent bound modes that are generated by the different topographies at the two lake ends. The FE-results of Trösch [35] support this interpretation, see Fig. 19.10. Mysak et al. [17], however, also list limited facts which conflict with this view. Giving a final answer would require data which would uncover the spatial structure much more clearly.

Starting from σ_0 and decreasing σ we observe that the wave pattern undergoes considerable alterations which corresponds to changes in the relative strength of the two reflected modes. More precisely, as $R_\circ$ decreases $R_\bullet$ increases. For $\sigma < 0.25$ $R_\circ$ oscillates weakly whilst gradually decreasing and $R_\bullet \geq 0.98$. This can be verified by considering the associated stream functions. For $0.254 \leq \sigma < \sigma_0$, the reflected wave mainly consists of the $\circ$-mode. What evolves is a *beat pattern* at the same

channel-side where the incident mode is located. The increase of $R_\bullet$ manifests itself as a growing *leakage* of wave activity into the opposite channel side, because the $\bullet$-mode has $k = -k_i$. For $0.120 \leq \sigma \leq 0.254$ $R_\bullet$ is dominant, and this is clearly visible in the wave patterns. The dispersion relation has $\partial\sigma/\partial k > 0$ for this reflected mode and consequently, increasing wavelengths accompany decreasing frequencies. At $\sigma = 0.115$ a remarkable *resonance* is discovered: Two coinciding peaks give rise to a local minimum and maximum for $R_\bullet$ and $R_\circ$, respectively. Looking at the wave pattern suggests that this again is a bay-trapped mode. Contrary to the trapped modes with $\sigma > \sigma_0$ which are true bound states, this mode has also a non-vanishing periodic contribution in $s > s_0$. The pattern is, however, a bay-mode or type-2 wave because the characteristic structure is due to the modes with $\mathrm{Im}\, K_\gamma > 0$ belonging to the *second* mode unit which still has a complex branch for $\sigma_1 < \sigma < \sigma_0$ (see inset).

The resonance $\sigma = 0.115$ coincides with an eigenfrequency in the closed basin as indicated with filled triangles. The structure agrees well with that shown in Fig. 21.19. Below the resonance the component $R_\bullet$ dominates again and large-scale TWs are observed. There is a further resonance at $\sigma = 0.088$. It also resembles second mode structure, and it also has a non-vanishing periodic contribution in $s > s_0$, as does the bay mode with $\sigma = 0.115$. This is due to the activation of the real wavenumber in the interval $\sigma_1 < \sigma < \sigma_0$. Contrary to the bound mode at $\sigma = 0.395$, those modes at $\sigma = 0.115$ and $\sigma = 0.088$ are triggered by a true reflection mechanism of an incoming wave that is reflected. So physically these are true resonances at bays which only exist because they are energetically fed from the incoming wave.

For $\sigma < \sigma_1$ all modes have $\mathrm{Im}\, K_\gamma = 0$ in this second order model and no further bay-modes can be expected. Instead of this, contributions of the real branch belonging to the second mode unit are possible. Figure 21.35 displays the reflection coefficients for the frequency interval $[0.052, \sigma_1]$. All reflection coefficients change smoothly and, as expected, no resonances occur. For $0.063 < \sigma < \sigma_1$ $R_\triangledown$ belonging to the second mode unit is dominant (see inset for an explanation of the symbolic subscripts). For lower frequencies the influence of the second mode unit is comparatively weak. Comparison of Figs. 21.34 and 21.35 reveals, that close to the critical frequencies σ_0 and σ_1 energy is distributed among several modes, whereas for other frequencies most of the reflected energy is contained in the $\bullet$-mode. This is the mode with the negative of the incident wavenumber.

So far, we have studied the reflections of TWs, when the incident wavemode $\blacksquare$ belongs to the first mode unit and has $c_{\mathrm{ph}} \uparrow\uparrow c_{\mathrm{gr}}$ towards the reflecting zone. We also investigated the situation for an incident mode with $c_{\mathrm{ph}} \downarrow\uparrow c_{\mathrm{gr}}$. For this case, the graph of Fig. 21.34, qualitatively looks the same except that the curves $R_\circ$ and $R_\bullet$ are interchanged. The position of the two conspicuous resonances is unchanged.

Figure 21.36 collects the results of importance. The incident mode with $c_{ph} \downarrow\uparrow c_{gr}$ has its wave crests at the opposite side of the channel. Energy is propagating towards s_0 whereas the phase propagates away from it. These two cases distinguish two different types of reflection patterns, type 1 and type 3. Type 1 has a large scale structure with increasing wavelengths for decreasing σ. Conversely, type 3 exhibits a small-scale pattern which is intensified for decreasing frequencies. The

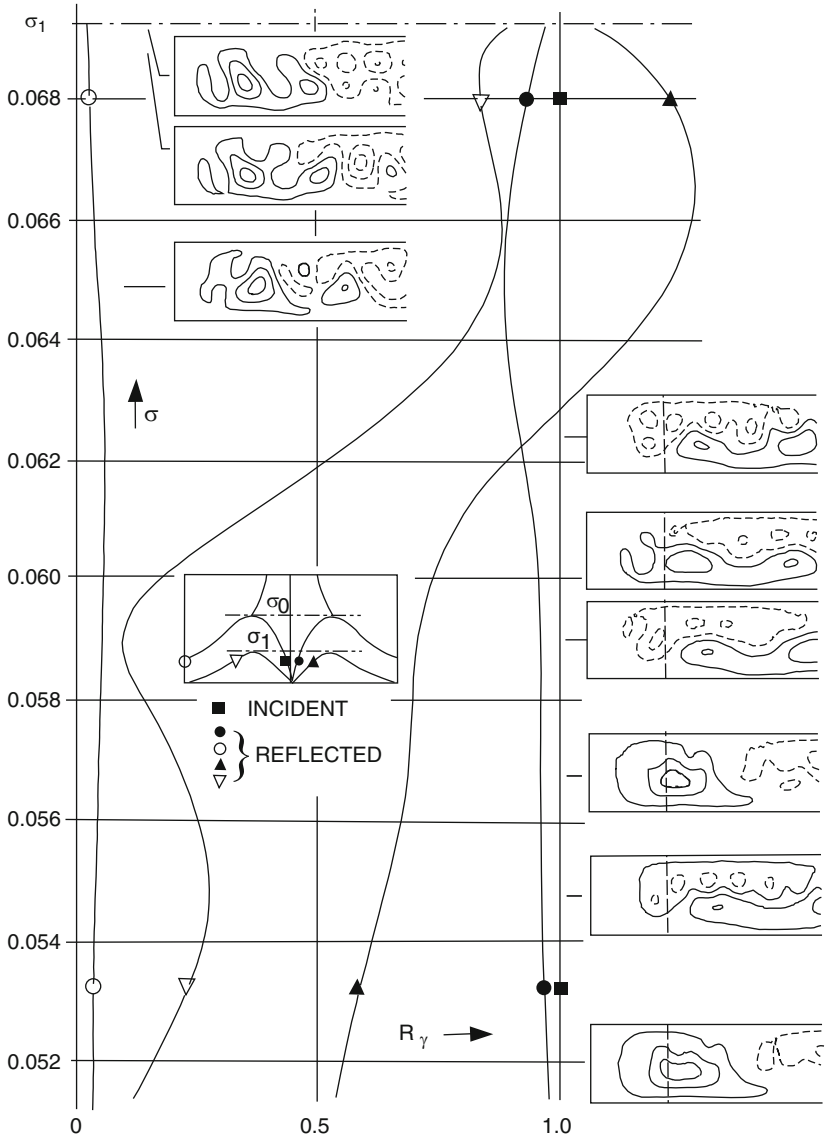

Fig. 21.35 Reflection coefficients and stream function patterns for $0.052 \leq \sigma < \sigma_1$ for the four reflected modes. The coefficient $R_{\blacksquare}$ of the incident mode is scaled to 1. The parameters are as in Fig. 21.34 and the inset explains the modes (from [26]). © Versuchsanstalt für Wasserbau, Hydrologie und Glaziologie an der ETH Zürich, reproduced with permission

distinction of these types and their individual properties agree with the classification suggested in Sect. 21.4.3. There, we only were able to make the distinction plausible by phenomenological arguments. We now have discovered a *physical* explanation for the occurrence of bay-modes, Ball-modes and channel modes in enclosed basins. Comparing Figs. 21.36 with 21.19 makes it clear:

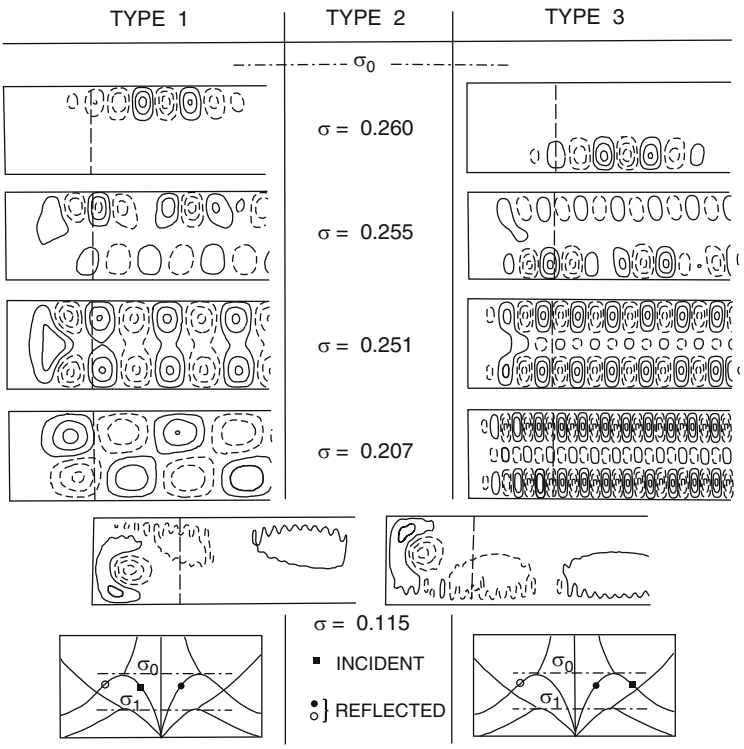

Fig. 21.36 Reflection patterns indicated by an inicident wave with $c_{\mathrm{ph}} \uparrow\uparrow c_{\mathrm{gr}}$ (type 1) and $c_{\mathrm{ph}} \downarrow\uparrow c_{\mathrm{gr}}$ (type 3), respectively. The mode at the resonance $\sigma = 0.115$ constitutes type 2. The parameters are as in Fig. 21.34 (from [26]). © Springer, Berlin, reproduced with permission

1. The type 1-modes or Ball-modes originate form a sequence of reflections at the lake ends which are induced by an incident wave with $c_{\mathrm{ph}} \uparrow\uparrow c_{\mathrm{gr}}$. For an appropriately selected frequency, i.e. eigenfrequency, the pattern is not evanescent in time and a Ball-mode survives.
2. The basin solutions classified as type 2 or *bay-modes* are due to the conspicuous resonances observed in Fig. 21.34. As Fig. 21.36 demonstrates the structure in the bay is only weakly influenced by the incident mode.
3. Finally, the *channel-modes* or type 3-waves of Fig. 21.36 can be explained as the result of a sequence of reflections at the lake ends which are induced by a mode with $c_{\mathrm{ph}} \downarrow\uparrow c_{\mathrm{gr}}$. Contrary to the Ball-modes, the spatial scale decreases with decreasing frequency.

These results justify and strengthen the statements which were made in Sect. 21.4.3. They provide a more precise and broader understanding of TWs in channels and lakes. It is now clear that the models to which (some) exact solutions were presented in Sect. 20.3 do not exhibit the complete variability of TWs in basins but provide us only with Ball-mode solutions. These often do not suffice for a

reliable interpretation of field measurements. As the model of Mysak et al. [31] has shown, the ellipse which could model the 74 h-signal had a far too large aspect ratio. This discrepancy seems to be removed if the signal is interpreted as a bay-trapped mode with a frequency that exceeds the cut-off frequency for the particular basin. On the other hand, what has been conjectured at the end of Sect. 21.4 is now made clear in a quantitative manner. The existence of three distinctly different wave types is a natural consequence of the typical dispersion relation of topographic Rossby waves. The conspicuous eigenmodes in the rectangular basin can be understood in terms of *reflections* of TWs at either shore-zone. Depending on the structure of the incident wave the corresponding type is established. All parameter dependencies are explicable with the help of this correspondence.

In elongated lakes, the quantities determining the TW-features may, perhaps be listed as follows:

First, the *transverse depth-profile* fixes the frequency range, in which solutions can be expected. We draw this inference from the conspicuous topography dependence of the frequency illustrated in, e.g. Fig. 21.14 and Tables 19.1, 20.3, 20.5, 20.7, 21.1–21.3, 21.6, 21.7. The larger topography gradients for a fixed maximum depth are, the lower will be the frequencies. Therefore, σ is strongly influenced by $h^{-1}|\nabla h|$. Second, the form of the *lake ends* is of particular importance as far as the structure of the solution is concerned. This determines whether a Ball-, bay- or channel-type wave will occur. Third, it should not be forgotten that TWs are wind-generated. Depending on the scale of the exciting force the lake basin will respond differently. Small-scale driving forces will preferably excite bay-modes or channel-modes whereas large-scale wind forces may produce Ball-modes.

21.7 Bay Modes and Resonances

The computations performed in the previous section suggested for the chosen bathymetries that normal modes of the TW-operator can be divided into two types: *basin wide modes*, for which the wave activity is spread through the entire gulf region and *bay modes*, for which the motion is highly localized. In this section our intention is to corroborate these findings and to deepen their understanding. In fact, we wish to show that for a shelf zone at the end of a semi-infinite flat gulf, topographic waves are trapped. More specifically, a countable infinite set of bay modes exists in this case, of which the energy does not radiate away from the bay. The motion away from the bay is exponentially evanescent as one moves farther away from the shelf.

If the bathymetry in the semi-infinite channel is generalized to consist of a one-sided shelf and a bay with oblique bottom contours, the modal response of the TW-operator is more complex. ‘Whereas the spectrum of the flat channel is purely discrete, channels with transverse topography exhibit compound spectra consisting of a continuous and a possibly empty, discrete part. The former contains an infinite set of resonances, each of which can be attributed to a point in the discrete spectrum

of the flat channel. Resonances can thus be considered as leaky bay modes' [30]. They have a strong wave activity in the bay region and non-negligible, moderate, oscillating activity in the channel. Some of these leaky wave modes may be exponentially evanescent; a single oscillating one suffices to characterize the bay mode as leaking. The analogy may be overstretched, but it is tempting to recall here the Taylor reflection analysis (Chap. 12, Sect. 12.5) of a Kelvin wave at the end of a semi-infinite gulf, where the reflection properties were characterized as being complete or incomplete, respectively, depending upon whether the reflected modes were all exponentially evanescent or at least one was oscillating.

We demonstrate these properties with chosen bathymetric profiles, which allow the construction of exact solutions.

21.7.1 The Boundary Value Problem for TWs in a Semi-Infinite Gulf with Exponential Bathymetry

Consider Cartesian coordinates, x, y, and a semi-infinite gulf, $(x, y) \in [0, \infty) \cup [0, 1]$, of which the dimensionless scaled water depth is defined by

$$h(x, y) = \begin{cases} \exp(2b(x-\ell))\exp(2c(y-1)), & 0 \le x \le \ell, \\ \exp(2c(y-1)), & x > \ell, \end{cases} \tag{21.90}$$

in which b, c and ℓ are constants. Figure 21.37 displays the isobaths for this topography.

We wish to solve the boundary value problem (21.2) which, in Cartesian coordinates, takes the form

$$\begin{aligned} \nabla \cdot (h^{-1}\nabla \Psi_t) + \hat{\boldsymbol{k}} \cdot (\nabla\Psi \times \nabla h^{-1}) = 0, \quad & \text{in } \mathcal{D}, \\ \Psi = 0, \quad & \text{on } \partial\mathcal{D}, \end{aligned} \tag{21.91}$$

where Ψ is the volume (mass) transport stream function, h is the scaled water depth, ∇ is the horizontal gradient operator, $(\cdot)_t$ denotes differentiation of $(\cdot)$ with respect to time and $\hat{\boldsymbol{k}}$ is a unit vector, pointing vertically upwards. It is assumed that $\mathcal{D}$ is simply connected, so that $\Psi = 0$ along $\partial\mathcal{D}$ expresses tangency of the velocity field along the domain boundary. We wish to solve (21.91) when the bathymetric profile is given by (21.90).

Problem 21.1 *Let Ψ be complex valued (the real and imaginary parts are then physically acceptable solutions) and choose*

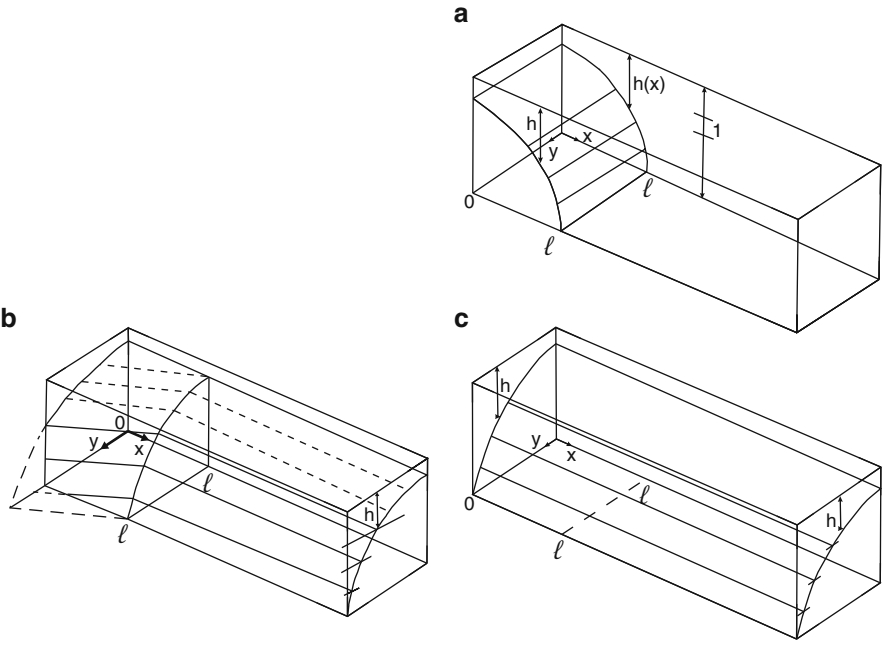

Fig. 21.37 Views of the bathymetry (21.90) for the cases (**a**) $b > 0, c = 0$; (**b**) $b > 0, c > 0$ and (**c**) $b = 0, c > 0$

$$\Psi = \exp(-i\sigma t)\psi, \qquad \left(\sigma = \frac{\omega}{f}\right). \tag{21.92}$$

By substituting (21.92) into (21.91) and choosing h according to (21.90), show that the eigenvalue problem (21.91) takes the form

$$\begin{gathered}\psi_{xx} + \psi_{yy} - 2\beta\psi_x - 2\gamma\psi_y = 0, \\ \beta = \left\{\begin{matrix} b + \dfrac{ic}{\sigma} \\ \dfrac{ic}{\sigma} \end{matrix}\right\}, \quad \gamma = \left\{\begin{matrix} c - \dfrac{ib}{\sigma} \\ c \end{matrix}\right\}, \quad \begin{matrix} 0 \le x \le \ell \\ \ell < x \end{matrix} \Bigg\} (x, y) \in [0, \infty) \cup [0, 1], \\ \psi = 0, \quad \{y = (0, 1), x > 0\}; \quad \{y \in [0, 1], x = 0\}.\end{gathered} \tag{21.93}$$

By selecting

$$\psi = \exp(\beta x + \gamma y)\phi(x, y), \tag{21.94}$$

show, moreover, that $\phi(x, y)$ satisfies the boundary value problem

$$\left.\begin{aligned} &\phi_{xx} + \phi_{yy} + \kappa^2\phi = 0, \\ &\kappa^2 = \begin{cases} (b^2 + c^2)\left(\dfrac{1}{\sigma^2} - 1\right), & 0 \le x \le \ell, \\ c^2\left(\dfrac{1}{\sigma^2} - 1\right), & x > \ell, \end{cases} \end{aligned}\right\} (x, y) \in [0, \infty) \cup [0, 1], \tag{21.95}$$

$$\phi = 0, \quad \{y = (0, 1), x > 0\}; \{y \in [0, 1], x = 0\}$$

◆

This formulation is incomplete, because the far field condition for $x \to \infty$ is not yet imposed. We shall request that the kinetic energy remains bounded as $x \to \infty$. It can be shown that this requires

$$\nabla\phi \cdot \nabla\phi^* < \infty \qquad \text{as } x \to \infty, \tag{21.96}$$

where ϕ^* is the conjugate complex of ϕ. Furthermore, it is to be expected that the solutions in the bay region ($0 \le x \le \ell$) and in the far region ($x > \ell$) are separate and must be patched together by requesting continuity of ϕ and ϕ_x. Figure 21.38 gives a sketch of the formulation of the problem.

21.7.1.1 Solutions in $x \in [0, \ell]$

We call this the bay area and seek a separation of variables solution of the form

$$\phi_n = A(x)\sin(n\pi y), \qquad (n = 1, 2, \ldots). \tag{21.97}$$

It satisfies the boundary conditions at $y = (0, 1)$. Substituting (21.97) into the differential equation $(21.95)_1$ yields the ordinary differential equation

$$\frac{\mathrm{d}^2 A}{\mathrm{d}x^2} + (\kappa^2 - (n\pi)^2)A = 0, \tag{21.98}$$

in which the coefficient of A is either positive or negative, depending on n. If it is negative, then

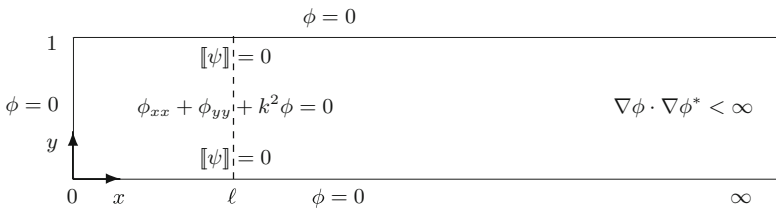

Fig. 21.38 Sketch of the boundary value problem for ϕ to be solved, when h is given by (21.90). $[\![f]\!] = f(x - \ell + \varepsilon) - f(x - \ell - \varepsilon)$, $0 < \varepsilon << 1$

$$A = a_n \sinh(\alpha_n x) \quad \text{and} \quad A = b_n \cosh(\alpha_n x)$$

are fundamental solutions, provided that[23]

$$\alpha_n^2 = (n\pi)^2 - (b^2 + c^2)\left(\frac{1}{\sigma^2} - 1\right). \tag{21.99}$$

However, we must have $b_n \equiv 0$ to satisfy the boundary condition at $x = 0$. It follows that

$$\phi_n^b = a_n \sinh(\alpha_n x)\sin(n\pi y), \qquad (n = 1, 2, 3, \ldots) \tag{21.100}$$

are 'bay' solutions, of which n is the transverse mode number; the α_n's are either real or purely imaginary; in the latter case the functions $\sinh(\alpha_n x)$ are replaced by $\sin(\hat{\alpha}_n x), \hat{\alpha}_n^2 = -\alpha_n^2$.

21.7.1.2 Solution in $x \in [0, \infty)$

We call this the channel area and seek again separation of variables solutions of the form

$$\phi_n^c = \mathcal{D}_n^c(x)\sin(n\pi y), \qquad (n = 1, 2, 3, \ldots), \tag{21.101}$$

which satisfies the side boundary conditions $\phi_n^c = 0$ at $y = (0, 1)$. Substituting (21.101) into (21.95) yields

$$\frac{\mathrm{d}^2\mathcal{D}^c}{\mathrm{d}x^2} - \underbrace{\left[(n\pi)^2 - c^2\left(\frac{1}{\sigma^2} - 1\right)\right]}_{-\lambda^2}\mathcal{D}^c = 0. \tag{21.102}$$

With the trial solution $\mathcal{D}^c = \exp(\lambda x)$ this equation implies

$$\begin{aligned}\lambda^{\pm} &= \pm \mathrm{i}\left[c^2\left(\frac{1}{\sigma^2} - 1\right) - (n\pi)^2\right]^{1/2} \\ &= -\mathrm{i}\frac{c}{\sigma} + \mathrm{i}\left\{\frac{c}{\sigma} \pm \left[c^2\left(\frac{1}{\sigma^2} - 1\right) - (n\pi)^2\right]^{1/2}\right\}.\end{aligned}$$

Defining the longitudinal wave number as

$$k_n = \left\{\frac{c}{\sigma} \pm \left[c^2\left(\frac{1}{\sigma^2} - 1\right) - (n\pi)^2\right]^{1/2}\right\} \tag{21.103}$$

[23] Note that b and b_n are distinct quantities.

we may now write

$$\phi_n^c = d_n \exp\left(-\mathrm{i}\frac{c}{\sigma}x + \mathrm{i}k_n x\right)\sin(n\pi y). \tag{21.104}$$

The dispersion relation (21.103) can, alternatively, also be written as

$$\sigma = \frac{2ck}{k^2 + c^2 + (n\pi)^2}. \tag{21.105}$$

With these definitions, k is the wavenumber in the x direction of the stream function ψ.

Propagating modes with transverse mode number n are possible provided that λ^2, defined in (21.102) is positive, i.e. if

$$0 < \sigma < \sigma_n := \frac{c}{[c^2 + (n\pi)^2]^{1/2}}. \tag{21.106}$$

σ_n is the cut-off frequency of the nth transverse mode. If $\sigma > \sigma_n$, then the modes decay exponentially with x.

21.7.2 The Flat Channel

The above solutions in the bay and channel regions are exact and only need to be patched together at $x = \ell$ by requesting that the stream function ψ and the velocity are continuous across the line $x = \ell$. We shall demonstrate this first for a semi-infinite domain with a flat channel section, i.e. $c = 0$. Clearly, there are no propagating waves in the channel section, because, according to (21.106) $\sigma_n = 0$, and in view of (21.103), $k_n = -\mathrm{i}n\pi$ for an exponentially evanescent solution as $x \to \infty$,

$$\phi_n^c = d_n \exp(-n\pi x)\sin(n\pi y). \tag{21.107}$$

In the bay region the solution is given by (21.100) with

$$\alpha_n^2 = (n\pi)^2 - b^2\left(\frac{1}{\sigma^2} - 1\right). \tag{21.108}$$

The solution for ψ, (21.94), can be written as

$$\psi = \begin{cases} \displaystyle\sum_{n=1}^{\infty} a_n \psi_n^b = \exp\left(bx - \mathrm{i}\frac{b}{\sigma}y\right) \\ \qquad\qquad \times \displaystyle\sum_{n=1}^{\infty} a_n \sinh(\alpha_n x)\sin(n\pi y), \quad 0 \le x \le \ell, \\ \displaystyle\sum_{n=1}^{\infty} d_n \psi_n^c = \sum_{n=1}^{\infty} d_n \exp(-n\pi x)\sin(n\pi y), \quad x > \ell, \end{cases} \tag{21.109}$$

with α_n as given in (21.108). (21.109) is an exact solution of the TW-equation (21.91) in the semi-infinite channel, if the stream function and the velocity are continuous across the line $x = \ell$. This continuity requirement determines the constants a_n and d_n via the equations

$$\begin{aligned}
&\exp\left(b\ell - \mathrm{i}\frac{b}{\sigma}y\right)\sum_{n=1}^{\infty} a_n \sinh(\alpha_n \ell)\sin(n\pi y) = \sum_{n=1}^{\infty} d_n \exp(-n\pi x)\sin(n\pi y),\\
&\exp\left(b\ell - \mathrm{i}\frac{b}{\sigma}y\right)\sum_{n=1}^{\infty} a_n\big(b\sinh(\alpha_n\ell) + \alpha_n\cosh(\alpha_n\ell)\big)\sin(n\pi y) \qquad (21.110)\\
&\quad = \sum_{n=1}^{\infty} d_n(-n\pi)\exp(-n\pi\ell)\sin(n\pi y).
\end{aligned}$$

Multiplying equations (21.107) each with

$$\int_0^1 \mathrm{d}y \exp\left(\mathrm{i}\frac{b}{\sigma}y\right)\sin(m\pi y) \qquad (21.111)$$

and using the orthogonality of the trigonometric functions

$$\int_0^1 \sin(m\pi y)\sin(n\pi y)\mathrm{d}y = \frac{1}{2}\delta_{mn}, \qquad (21.112)$$

gives the system

$$\begin{aligned}
\frac{1}{2}\exp(b\ell)a_m\sinh(\alpha_m\ell) &= J_{mn}d_n\exp(-n\pi\ell),\\
\frac{1}{2}\exp(b\ell)a_m\left(b\sinh(\alpha_m\ell) + \alpha_m\cosh(\alpha_m\ell)\right) &= J_{mn}d_n(-n\pi)\exp(-n\pi\ell),
\end{aligned} \qquad (21.113)$$

in which

$$\begin{aligned}
J_{mn} &:= \int_0^1 \exp\left(\mathrm{i}\frac{b}{\sigma}y\right)\sin(m\pi y)\sin(n\pi y)\mathrm{d}y\\
&= \frac{2}{\pi}\tau(-1)^{m+n}\frac{mn}{[(m+n)^2-\tau^2][\tau^2-(m-n)^2]}\\
&\quad\times\left\{\sin(\pi\tau) + \mathrm{i}\left(\cos(\pi\tau) - (-1)^{m+n}\right)\right\}, \quad \tau := \frac{b}{\pi\sigma},
\end{aligned} \qquad (21.114)$$

(see Gradshteyn and Ryzhik [8]). Combining (21.113) leads to the following countable infinite matrix vector equation

$$\begin{aligned}
&D_{mn}\exp(-n\pi\ell)d_n = 0,\\
&D_{mn} := (b + \alpha_m\coth(\alpha_m\ell) + n\pi)J_{mn},
\end{aligned} \qquad (21.115)$$

which has a non-trivial solution if

$$\det(\boldsymbol{D}) = 0. \tag{21.116}$$

To solve (21.115), (21.116) numerically, the summation over n must be restricted to $n = 1, 2, \ldots, N$. Because of the completeness of the trigonometric functions, increasing N guarantees convergence of the solution. Once a frequency is determined from (21.116), (21.115) allow determination of the constants d_n ($n = 1, 2, \ldots, N$) (modulo a multiplicative constant) and then in a further step, using $(21.113)_1$, evaluation of a_m ($m = 1, 2, \ldots, N$), again modulo a multiplicative constant).

Stocker and Johnson [30] state that the eigenvalues of the exact problem (21.91) are real, and experience has shown that this seems also to be true for the approximate problem with finite N. They show that $N = 4$ is generally sufficient to have 4–5 significant figures of the eigenfrequencies of the $(n, m) = (1, 1), (1, 2), (2, 1), (2, 2)$ modes securely determined; whilst $N = 7$ seems to suffice to obtain the coefficients a_j ($j = 1, 2, 3, 4$) accurately determined.

Figure 21.39 displays the stream functions for the first four eigenmodes at $t = 0$ and $t = T/4$, where T is the period. Substantial wave activity is restricted to the bay region; outside the bay, the stream function is exponentially small.

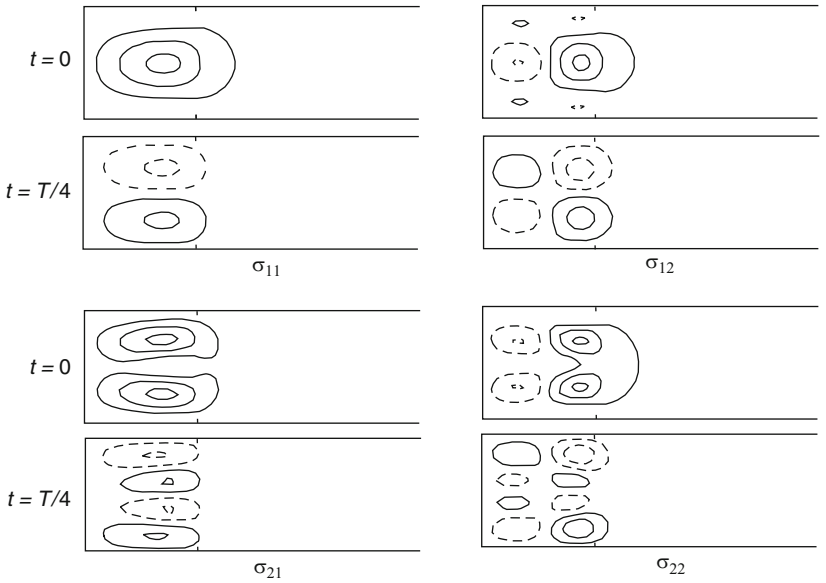

Fig. 21.39 Stream function ψ of the first four eigenfrequencies in a flat semi-infinite channel with a shelf bay zone. The solutions are bay modes with all wave activity trapped in the bay zone and Ψ is exponentially evanescent for $x > \ell$. Here, $b = \ell = 1$ and $N = 6$ (after [30]).

21.7.3 Channel with Shelf Topography

We now consider a semi-infinite gulf with bathymetry (21.90) and $c \neq 0$. It follows, according to (21.106) that the cut-off frequencies σ_n are non-zero and so for $\sigma < \sigma_1$ topographic waves carry energy both towards and away from the bay. For $\sigma > \sigma_1$, however, bay modes are possible. The spectrum is *discrete* (or empty) above σ_1 and *continuous* below it.

Let N_R be an integer > 1 characterizing the cut-off frequency σ_{N_R} according to (21.106). In view of (21.103), there are thus $2N_R$ propagating modes in the channel; N_R modes have group speed which carry energy away from the bay. The remaining ones carry energy towards the bay; and anyone of these can be selected as an incident wave. With these preliminary remarks we are now able to construct the general solutions begun in Sect. 21.7.1 and the application of the continuity requirements for ψ at $x = \ell$. This is summarized in Problem 21.2.

Problem 21.2

1. *Show that in view of (21.94) and (21.100) the general solution for ψ in the bay region $x \in [0, \ell]$ is given by*

$$\psi = \sum_{j=1}^{\infty} a_j \psi_j^b$$
$$= \exp(\beta x + \gamma y) \sum_{j=1}^{\infty} a_j \sinh(\alpha_j x) \sin(j\pi y), \quad 0 \leq x \leq \ell. \quad (21.117)$$

2. *Let ψ_i^c be the incident wave in the channel portion of the gulf. For definiteness, restrict attention to an incident wave of transverse order* 1. *(Similar results are obtained for other incident modes.) Show that the general solution for ψ in $x \in [\ell, \infty)$ is given by*

$$\psi = \psi_i^c + \sum_{=1}^{\infty} d_j \psi_j^c = \exp(cy)\exp(ik_i x)\sin(\pi y)$$
(incident wave)
$$+ \exp(cy) \sum_{j=1}^{N_R} r_j \exp(ik_j x) \sin(j\pi y)$$
(reflected oscillating modes)
$$+ \exp(cy) \sum_{j=N_R+1}^{\infty} d_j \exp(ik_j x) \sin(j\pi y)$$
(reflected exp. evanescing modes), (21.118)

in which

$$k_i = \frac{c}{\sigma} + \left[c^2\left(\frac{1}{\sigma^2} - 1\right) - \pi^2\right]^{1/2},$$

$$k_j = \begin{cases} \dfrac{c}{\sigma} - \left[c^2\left(\dfrac{1}{\sigma^2} - 1\right) - (j\pi)^2\right]^{1/2}, & j \le N_{\mathrm{R}}, \\ \dfrac{c}{\sigma} + i\left[(j\pi)^2 - c^2\left(\dfrac{1}{\sigma^2} - 1\right)\right]^{1/2}, & j > N_{\mathrm{R}}, \end{cases} \tag{21.119}$$

where r_j and d_j are arbitrary coefficients characterizing the amplitude of the jth mode. The last two terms on the right-hand side of (21.118) can also be combined together as

$$\exp(cy)\sum_{j=1}^{\infty} d_j \exp(ik_j x)\sin(j\pi y) \tag{21.120}$$

with $r_j \equiv d_j$ for $j \le N_{\mathrm{R}}$ if (21.119) is observed.

◆

The compound solution (21.117)–(21.120) for the transport stream function in the rectangular semi-infinite gulf does not satisfy yet the continuity requirements $[\![\psi]\!]=0$, $[\![\psi_x]\!] = 0$ at $x = \ell$. These conditions yield

$$\begin{aligned} &\exp(\beta\ell + \gamma y)\sum_{j=1}^{\infty} a_j \sinh(\alpha\ell)\sin(j\pi y) \\ &\quad = \exp(cy)\exp(\mathrm{i}k_i\ell)\sin(\pi y) + \exp(cy)\sum_{j=1}^{\infty} d_j \sum_{j=1}^{\infty}\exp(\mathrm{i}k_j\ell)\sin(j\pi y), \\ &\exp(\beta\ell + \gamma y)\sum_{j=1}^{\infty} a_j \left(\beta\sinh(\alpha_j\ell) + \alpha_j\cosh(\alpha_j\ell)\right)\sin(j\pi y) \\ &\quad = \exp(cy)\mathrm{i}k_i\exp(\mathrm{i}k_i\ell)\sin(\pi y) + \exp(cy)\sum_{j=1}^{\infty} d_j \mathrm{i}k_j\exp(\mathrm{i}k_j\ell)\sin(j\pi y), \end{aligned} \tag{21.121}$$

in which notation (21.118) has been replaced by (21.120). Multiplying both (21.121) with $\exp(-\gamma y)\sin(m\pi y)$ and integrating the emerging equations from $y = 0$ to $y = 1$ and then applying the orthogonality condition of the trigonometric functions results in the equation pair

$$\begin{aligned}
&\tfrac{1}{2}\exp(\beta\ell)a_m \sinh(\alpha_m\ell) = \exp(\mathrm{i}k_i\ell)J_{m1} + J_{mj}\exp(\mathrm{i}k_j\ell)d_j,\\
&\tfrac{1}{2}\exp(\beta\ell)a_m\,(\beta\sinh(\alpha_m\ell) + \alpha_m\cosh(\alpha_m\ell))\\
&\qquad = \mathrm{i}k_i\exp(\mathrm{i}k_i\ell)J_{m1} + J_{mj}\mathrm{i}k_j\exp(\mathrm{i}k_j\ell)d_j.
\end{aligned} \tag{21.122}$$

Here, summation over j from $j = 1$ to $j = \infty$ is understood and J_{mj} is given in (21.114). Eliminating a_m from (21.122) by substituting the first into the second equation yields the following infinitely large inhomogeneous system of equations for α_m:

$$\begin{aligned}
&\{\exp(\mathrm{i}k_i\ell)[\beta + \alpha_m\coth(\alpha_m\ell) - \mathrm{i}k_j]J_{mj}\}d_j\\
&\quad = \exp(\mathrm{i}k_j\ell)[\mathrm{i}k_j - \beta - \alpha_m\coth(\alpha_m\ell)]J_{m1},
\end{aligned} \tag{21.123}$$

which is truncated to order $j = N$, when a numerical solution is sought. Because of the inhomogeneous structure of (21.123) a solution is constructed by selecting a value for σ of the incident wave, evaluating the wave numbers (21.119) of the channel solutions, determining J_{mj} for $m \le N$, $j \le N$, and then solving (21.123) for d_j, $j = 1, 2, \ldots, N$; this will also fix a_m, $m = 1, 2, \ldots, N$. These solutions define the continuous spectrum and describe the reflection of incoming waves of prescribed frequency at the gulf end. There are also bound solutions of (21.122) or (21.123) with vanishing incident wave and thus $d_j = 0$ for all $j \in [0, \infty)$. In this case the linear system (21.123) becomes homogeneous, and the eigenfrequencies emerge from the condition

$$\det\{\exp(\mathrm{i}k_j\ell)[\mathrm{i}k_j - \beta - \alpha_m\coth(\alpha_m\ell)]J_{m1}\} = 0. \tag{21.124}$$

Together with the associated a_m's these define the true bay solutions (21.117).

21.7.3.1 Bay Modes

Recall from (21.106) that for the transverse mode-1 behaviour here, all modes will be exponentially evanescent in the channel and trapped to the bay, provided that

$$\sigma > \sigma_1 = \frac{c}{(c^2 + \pi^2)^{1/2}}.$$

Of interest is, how many modes exist, if the transverse order is n. Stocker and Johnson [30] show, on the basis of work by Johnson [12], and for the selected bathymetry (21.90), how this number can be estimated. If $N_B(n)$ is the number of bay modes of transverse order n, these authors show that

$$\text{int}\left\{\ell\left(\frac{b^2}{c^2}+1-n^2\right)^{1/2}\right\} \le N_{\text{B}}(n) \le \text{int}\left\{\frac{1}{2}+\ell\left(\frac{b^2}{c^2}+1-n^2\right)^{1/2}\right\}, \tag{21.125}$$

where 'int' denotes the integer part of the number in braces. When the bounds coincide, (21.125) determines $N_{\text{B}}(n)$ exactly, else it gives upper and lower estimates differing by unity. The total number of bay modes is obviously

$$N_{\text{B}} = \sum_{n=1}^{\infty} N_{\text{B}}(n). \tag{21.126}$$

If the channel is flat ($c = 0$), then $\sigma_n = 0$ for all n, and all bay modes are trapped, and their number is infinite, corresponding to a doubly infinite set of bay modes. For $c > 0$, the number is finite and may even be zero, if c is so large that the upper bound of (21.125) is zero.

Stocker and Johnson show transport streamlines for modes $(1, 1)$, $(1, 2)$, and $(2, 1)$ for $c = 0.3$ and $c = 1$, see Fig. 21.40. For $c = 0.3$, formula (21.125) yields $6 \le N_{\text{B}} \le 8$, of which three are shown. For $c = 1$, $N_{\text{B}} = 1$ and $b = \ell = 1$, only the fundamental bay mode is present. For $c \ge 1.55$, no bay modes occur. The transport streamlines have the tendency to follow the isobaths (which on the f plane agree with the isotrophs).

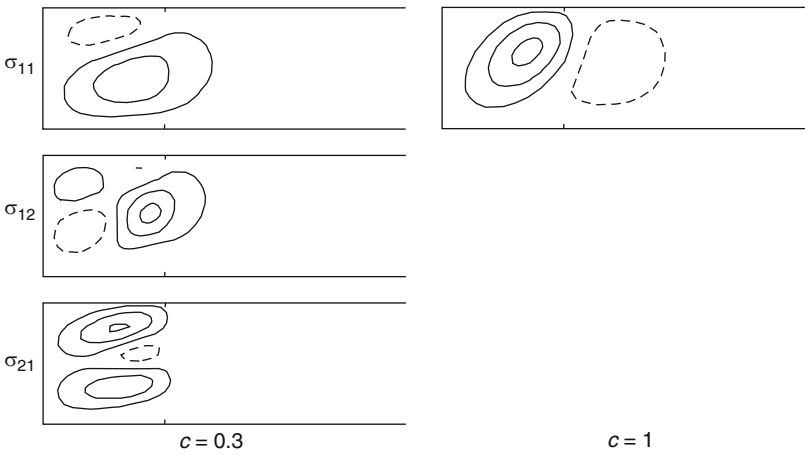

Fig. 21.40 Stream line contours of the first three bay modes ($c = 0.3$) and the single bay mode ($c = 1$). Computations were performed for $b = \ell = 1$ and $N = 6$, according to Stocker and Johnson [30]. © Cambridge University Press, reproduced with permission

21.7.3.2 Reflections

Existence of traveling (incoming and reflected) waves requires the frequency of the incoming wave ψ_i^c to be below the cut-off frequency of the transverse mode-1: $0 < \sigma < \sigma_1$. These modes are obtained by constructing solutions to the inhomogeneous system (21.123). For $\sigma_{j+1} < \sigma < \sigma_j$, the reflected transverse energy is distributed onto j different transverse modes. The relative importance to these modes can be determined by calculating the fluxes of kinetic energy associated with each of them. Stocker and Johnson [30] compute for the present gulf bathymetry the positive reflection coefficients R_j per incident energy flux and find

$$R_j = \frac{c - \sigma k_j}{\sigma k_i - c} |d_j|, \qquad j \le N_{\mathrm{R}}, \tag{21.127}$$

satisfying (21.119) and subjected to the constraints

$$\sum_{j=1}^{N_{\mathrm{R}}} R_j = 1. \tag{21.128}$$

Figure 21.41 displays R_j against the frequency for $b = \ell = c = 1$ and $N = 6$. For these, the cut-off frequencies are

$$\sigma_1 = 0.3033, \quad \sigma_2 = 0.1572, \quad \sigma_3 = 0.1055.$$

The figure shows that for $\sigma_2 < \sigma < \sigma_1$, only mode-1 reflected waves exist ($R_2 = R_3 = 0$), whilst for $\sigma_3 < \sigma < \sigma_2$ both mode-1 and mode-2 reflected waves are excited. For $\sigma < \sigma_3$ very small excitement of reflected mode-3 waves also exist. In the interval $0.10 < \sigma < 0.16$, mode-1 and mode-2 reflections co-exist with varied intensity. Figure 21.42 shows streamline plots for the indicated dimensionless frequencies. For $\sigma = 0.300$, the bay zone is negligibly excited (on the streamline plot no bay-trapped streamline is shown for the chosen ψ-values), whilst the channel section exhibits quasi-steady mode-1 response. 'For $\sigma_2 < \sigma < \sigma_1$ a beat pattern prevails in the channel part arising from a superposition of the incident wave with wave number k_i and the only reflected mode-1, both of identical transverse order [...]. As the wave length of the incident wave becomes shorter (for decreasing σ) wave activity in the bay is enhanced. For $\sigma < \sigma_2$, wave motion in the channel consists of several transverse modes. (Obviously), the reflection behaviour of the semi-infinite channel strongly depends on the frequency of the incident wave. This mode has the characteristic lenth scale $2\pi/k_i$, which interacts with the 'resonator' (the bay) of length scale $b\ell/c$' [30].

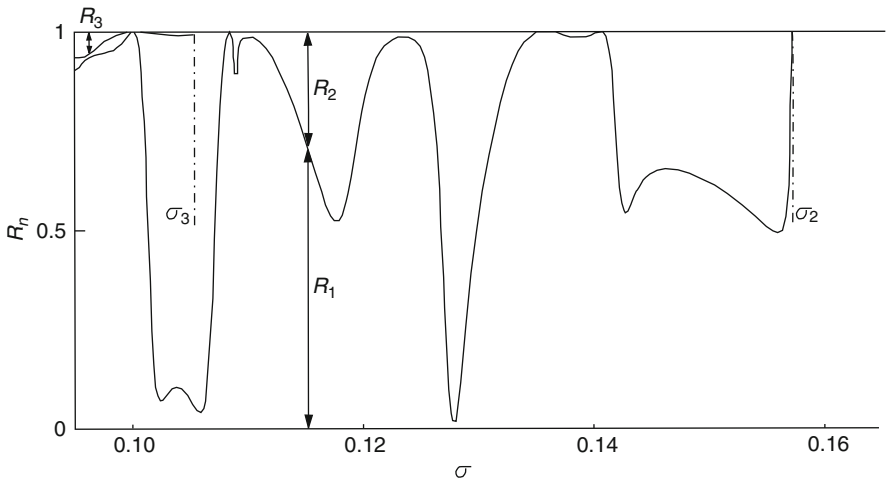

Fig. 21.41 Reflection coefficients R_j as functions of the frequency, determined for $b = c = \ell = 1$ and $N = 6$ (from [30]). © Cambridge University Press, reproduced with permission

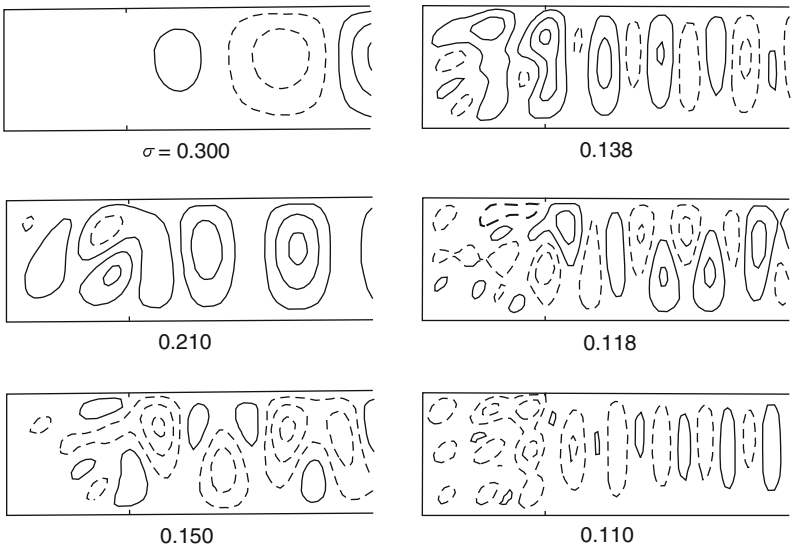

Fig. 21.42 Transport stream lines for ψ for decreasing frequencies in the continuous spectrum. The parameters are as in Fig. 21.41 (from [30]). © Cambridge University Press, reproduced with permission

21.7.3.3 Leaky Bay Modes

Resonances in the continuous spectrum were reported in the last Sect. 21.6.3, see e.g. Fig. 21.34, and were called there leaky bay modes. They can physically be identified here as modes with large kinetic energy of the incoming and reflected waves. Stocker and Johnson [30] computed the depth integrated energy density over one period and over the bay zone and plotted the logarithm of this energy as a function of the incident frequency in the interval $0.095 < \sigma < 0.24$, see Fig. 21.43a. Peaks in this figure are identified with frequencies of the modes $(m, n) = (1, 2), \ldots, (4, 2)$. The six panels in Fig. 21.43b show the stream line patterns for the six modes $(2, 1)$, $(2, 2)$, $(3, 1)$, $(3, 2)$, $(3, 3)$ and $(4, 2)$. Evidently, the bay energy exhibits a conspicuous resonance at $\sigma = 0.203$, but this resonance is not exhibited in the reflection coefficient (not shown here). At $\sigma = 0.222$, a further weak resonance is visible. The other panels of Fig. 21.43b also demonstrate higher wave activity in the bay than in the channel, but at varied relative strengths. Moreover, the graphs indicate that each resonance can be associated with a pair of mode numbers according to the structure of the wave motion in the bay zone.

'It has, (thus), been demonstrated above that the spectrum of the topographic wave equation in the semi-infinite channel can consist of a discrete and a continuous spectrum. Solutions associated with the discrete spectrum are trapped in the bay zone – they are true bay modes whereas solutions of the continuous part are free states: incoming wave energy is reflected. Increasing the cut-off frequency of the channel region, i.e. increasing c, causes a decrease in the number of true bay modes. This is nicely illustrated in Fig. 21.44, in which the bay mode frequencies are displayed as functions of the topography parameter c. The dashed dotted lines indicate the cut-off frequencies of the individual transverse modes. For $\sigma > \sigma_1$ true bay modes evolve. It is evident that, owing to the different functional dependencies of σ_n and σ_{mn} with respect to c, the lines of σ_{mn} cross the lines of the cut-off frequencies σ_n for increasing c. Once σ_1 is crossed a true bay mode becomes a resonance in the continuous spectrum. Moreover, once σ_{mn} crosses σ_n, the resonance may become weak, because the mode with the same transverse mode number n is now propagating in the channel. This is indicated by the dashed lines in the figure. Therefore, each resonance in the continuous spectrum can be associated to a true bay mode, i.e. a solution of the discrete spectrum of the simple bay mode with $c = 0$. Hence, with increasing c (or decreasing $b\ell$) true bay modes do not vanish but rather emerge as resonant states in the continuous spectrum [and then form leaky bay modes]', after [30].

One disadvantage, perhaps, of the computations performed by Stocker and Johnson [30] is the rather artificial bathymetry (21.90), which is geometrically far from realistic basin profiles. Johnson and Kaoullas [13] presented computations for a more realistic, however, still 'academic' bathymetry. Their isobaths (at 0.1 intervals) for the lake-end model are as shown in Fig. 21.45a. The profile across the breadth of the channel is for very large $x > 0$ as shown in Fig. 21.45b and the profile has zero derivatives of all orders with respect to x at $x = 0^+$. So. A shallow shelf of constant depth H_0 can extend the bay zone for $-d < x < 0^-$. As already men-

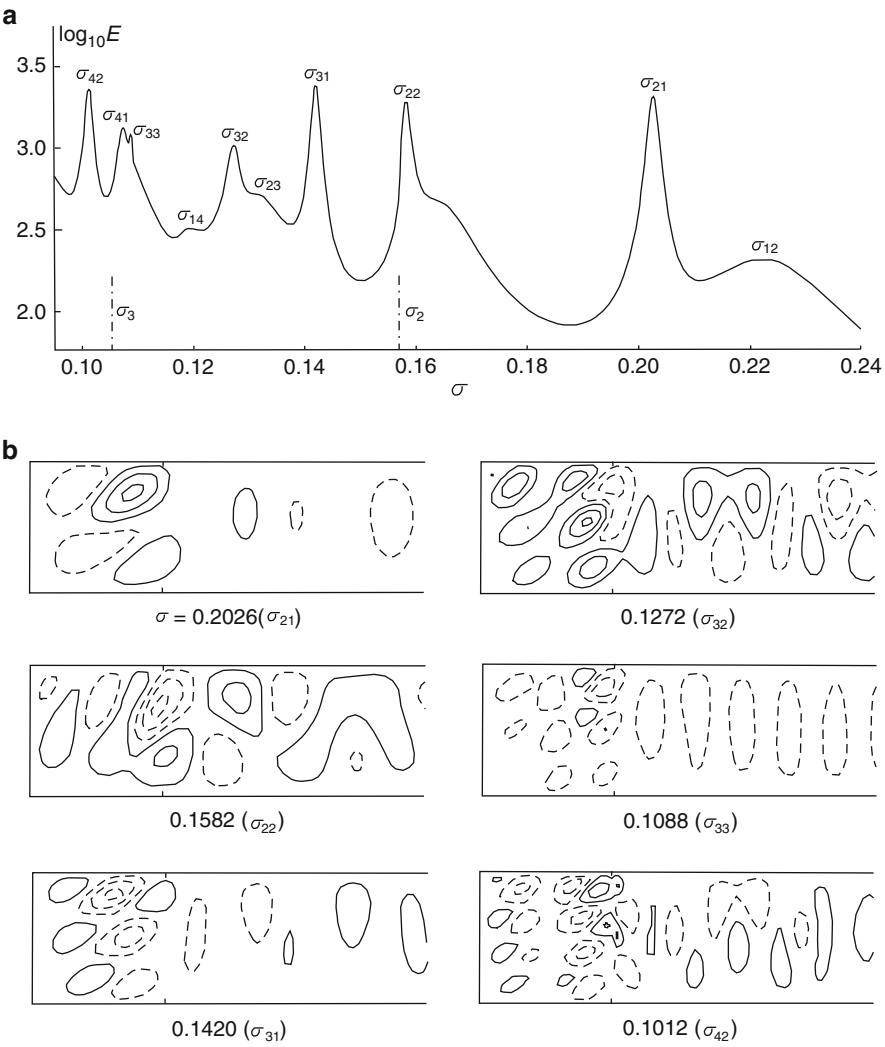

Fig. 21.43 (**a**) Energy in the bay plotted against the dimensionless frequency in the interval $0.095 < \sigma < 0.24$. (**b**) Streamlines at resonances corresponding to panel (**a**). Parameters are $b = \ell = c = 1, N = 6$ (from [30]). © Cambridge University Press, reproduced with permission

tioned, the TW-equation does not support trapped bay modes when $d = 0$, because its solution is constructed by conformal mapping from solutions of the TW-equation in an infinite channel with rectilinear topography. However, Johnson and Kaoullas [13] show that with non-vanishing d a discrete spectrum of modes emerges, which can be interpreted as true bay modes, but further interpretation of resonances and leaky bay modes is not provided.

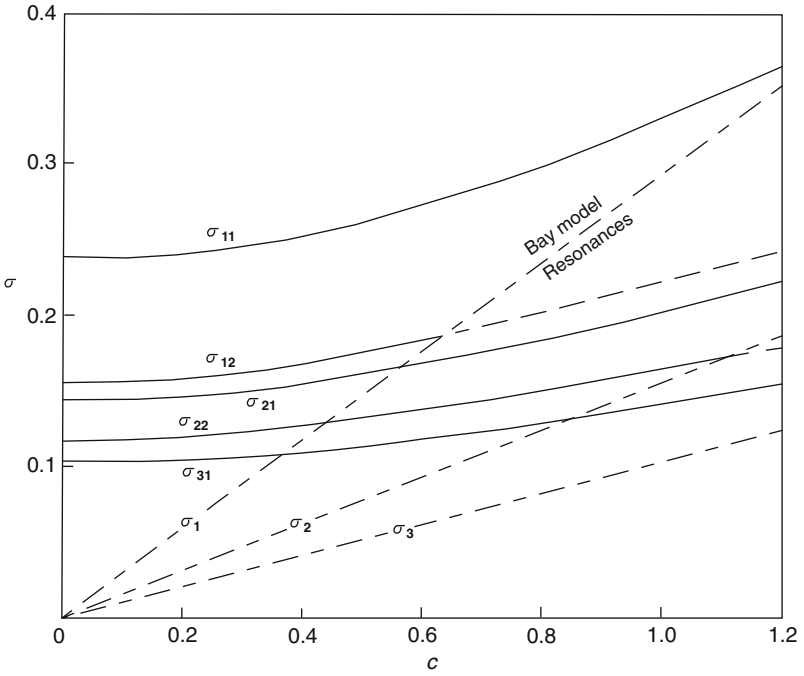

Fig. 21.44 Frequencies of bay modes and resonances as functions of the channel topography. For increasing c, the bay modes (*solid curves*) undergo transition to resonances. Thus, each resonance in the continuous spectrum with $\sigma < \sigma_1$ corresponds to a bay mode of the discrete spectrum for $c = 0$ (from [30]). © Cambridge University Press, reproduced with permission

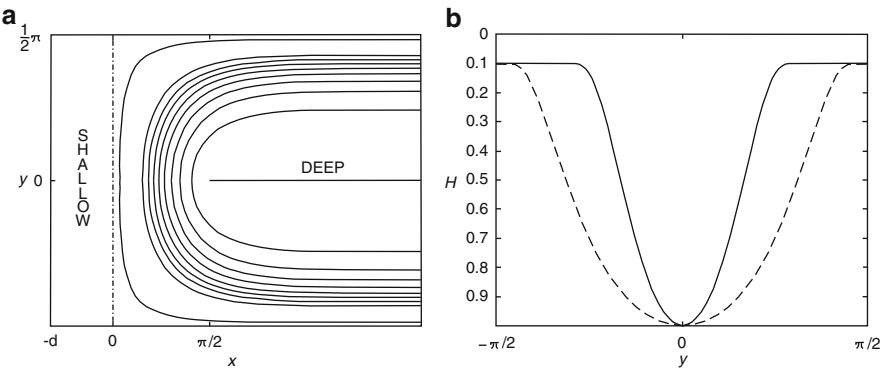

Fig. 21.45 (**a**) Isobaths (at 0.1 intervals) for the semi-infinite rectangular basin. For $x > 0$ the bathymetry has shelf structure as in panel (**b**). The shallow shelf for $-d < x < 0$ has constant depth smoothly joining the profile for $x > 0$. (**b**) Bathymetric profile in the y-direction for large $x > 0$ showing two different side shelves, composed from figures of [13]. © Taylor & Francis, http://www.informaworld.com, reprinted with permission

Table 21.11 Characterization of the spectrum of TW in infinite channel. After [30]

	Structure of domain	Discrete spectrum	Continuous spectrum
1.	Lake basin, domain closed	Countable infinite	Empty
2.	Bay zone connected with flat open domain	Countable infinite	Empty
3.	Open domain: bay and adjacent channel or shelf with cutoff σ_1	Finite for $\sigma > \sigma_1$	$0 < \sigma < \sigma_1$, infinite number of resonances
4.	As 3 with σ_1 large	Empty	$0 < \sigma < \sigma_1$, infinite number of resonances
5.	No bay zone or bay conformally equivalent to channel	Empty	$0 < \sigma < \sigma_1$ no resonances

21.7.3.4 Summary

In this section, TWs were studied in a semi-infinite gulf with a bay zone and a channel region with a bathymetric profile (21.90), which either had an exponentially varying topography of the bay and a flat channel bed or vice versa or a combination of the two. Analytical solutions of the TW-equation to the combined case were constructed and specialized for the different cases.

For an exponential shelf at the gulf end, but otherwise a flat ($c = 0$) channel, TWs cannot radiate away from the bay nor propagate into the channel: waves are trapped. The given exponential bathymetry sustains a countable infinite set of bay modes, which have exponentially evanescent 'tails' as one move away from the bay. The spectrum of the eigenfrequencies is discrete. These solutions corroborate findings obtained in earlier sections of this chapter.

When $c \neq 0$, i.e. when besides the bay shelf also the channel possesses a shelf at one (or both of its) sides, the number of bay modes is finite and of the order $b\ell/c$, thus reflecting an interplay of the bathymetry (b, c) with the geometry (ℓ) of the domain. Channels with such transverse bathymetry give rise to a compound spectrum, consisting of a continuous and a discrete, possibly empty, part. The former contains an infinite set of resonances, each of which can be attributed to a corresponding point in the discrete spectrum of the flat channel, so that resonances can be interpreted as leaky bay modes. Table 21.11 summarizes these findings.

Stocker and Johnson have also studied the trapping and scattering of topographic waves at estuaries and headlands [31].

21.8 Concluding Discussion

In this chapter the question, how the controversial interpretations of long period wave signals observed in Lake of Lugano should or could be interpreted, found an answer based on the physics of TW-reflection. This explanation was given

by constructing TW-modes in rectangular basins with an approximate numerical technique that is based on the MWR and employs an expansion of the mass transport stream function in terms of sets of shape functions which are symmetric and skew-symmetric with respect to the long basin axis. The constructed solutions are not exact but approximate, and convergence of the numerical solutions to the unknown exact solution was surmised and observed, but not mathematically proved. This is a disadvantage and may be taken up by mathematicians as a challenge.

The solution process, however, demonstrated properties of the TW-equation, which are physically convincing. TW-modes were found as follows:

- In rectangular lakes basin-filling eigenstates were found with gyres having characteristic diameters, which are comparable in size to the basin dimension or somewhat smaller. These are the so-called Ball-*modes*.
- Basin-filling modes also exist with gyres of small characteristic diameters, smaller than the rectangle's semi-breadth and rather regularly arranged along the long sides of the basin. These are the so-called *channel-modes*.
- Provided the bathymetry exhibits smooth variation – i.e. there are no vertical end walls – *bay-modes* do also exist; these are solutions which show appreciable wave activity close to the long ends of the rectangle, and the wave signals evanesce as one moves away from the lake end towards the opposite long end.

It was suspected that the bay modes would be the manifestation of *bound states* in a semi-infinite gulf and that the bay mode in a rectangle would simply not 'see' the other far end of the long rectangular lake. This was corroborated by the construction of such bay modes in a semi-infinite gulf. These solutions needed to be composed of waves, reflected at the gulf end, which all are exponentially evanescent as one moves infinitely far away from the gulf end. Solutions with this property were constructed in the sense that they are eigenstates of the formulated eigenvalue problem using the MWR technique.

A crucial element in the physical understanding of the above classification of the different modes of TWs is the form of the dispersion relation, which became physically transparent, because of the application of the MWR. The mode units in Figs. 21.4 and 21.5 show two versions of the dispersion relation of the *MWR-approximated* first and second order model, not the exact dispersion relation of the TW-equation. These approximate dispersion relations with their increasing complexities with growing order of approximation are the ultimate cause for the existence of the Ball-, channel- and bay-modes as well as the bound states in a semi-infinite gulf.

- The double valuedness of the real branch of the dispersion relation in form of Fig. 20.12 led to an interpretation of Ball- and channel-modes. Ball-modes have phase and energy propagating into the same direction, whilst channel-modes have phase and energy move in opposite directions. This immediately follows from the real branch of the first order dispersion graph Fig. 21.4.
- The complex domain of the dispersion relation generates wave modes which are exponential, either growing or evanescing in the space coordinate. Solutions in domains where for fixed (real) σ some wave numbers are real and others are

complex, their superposition can explain how wave activity may be restricted to certain preferred regions, either primarily on one side of the rectangle and less on the other, or with comparable energy on either side of the rectangle, depending on bathymetry. Or their combination is such that bay modes are formed.

The construction of such solutions closely resembles the superposition of Kelvin and Poincaré waves in gravity wave modes in rectangles or a semi-infinite gulf as described by Taylor in his seminal paper of 1920 [34]. The exact bathymetry is very crucial for the generation of the mode types, which may exist in a lake. It was proved that $h^{-1}|\text{grad}\, h|$, where h is the water depth, needs to remain bounded in order that a double-valued real branch of the $\sigma(k)$-relation emerges. Thus, TWs in artificial reservoirs with vertical steps in the bathymetry are not fully covered by this theory. The assumption, however, that $h^{-1}|\text{grad}\, h|$ remains bounded, is an acceptable assumption for natural basins.

The MWR-based approximate solution technique, based on orthogonal curvilinear coordinates has also explained how the three different solution types in rectangular basins change if these rectangles are 'bent' into wedges of annuli. The graphs of dispersion curves are now dependent on the curvature of the lake axis. Waves traveling clockwise or counter clockwise around the inner or outer shore follow dispersion curves, which are now different from one another, see Fig. 21.25. Quantitatively, the three mode types are preserved, but curved basins can exhibit solutions which do not exist in straight rectangular basins. The very narrow frequency band where these solutions exist, however, makes it not likely that they can be observed.

The above summary pertains to TWs in their formulation as linear waves emerging from the shallow water equations. The analysis suggests that when $h^{-1}|\nabla h|$ or the wavenumber k is large or when the mode number is high, the stream function is either shore trapped or may oscillate rather violently in space: In other words, typical wavelengths are rather small, while associated periods remain large. These are circumstances at which nonlinear terms become significant. The nonlinear barotropic TW-equation can in this case be derived from the conservation law of potential vorticity and its analysis would be interesting.

The above study has essentially ignored discussion of all difficulties that were encountered when determining TW-modes. The corresponding eigenvalue problem often has eigenfrequencies, which are clustered close to one another so that their separation requires very accurate root finders, since otherwise some solutions may be lost. Moreover, when $h^{-1}|\nabla h|$ takes locally large values, the ordinary differential equation becomes stiff which also requires accurate ordinary differential integrators. This eigenvalue clustering is even more critical when the full linearized equation is studied, including gravity and topographic mode-frequencies. In such situations, the corresponding stream functions can hardly be separated.

Other imperfections of the MWR solution approach are as follows:

- The expansion into pairs of symmetric and skew-symmetric functions has only been pursued to $N = 3$ pairs and has not been further explored to search for convergence properties of the numerical method. This should be done before examples are computed for more complex lake geometries and lake bathymetries.

- Only then the MWR should be applied to real lakes e.g. Lake of Lugano or Lake Zürich or other lakes for which data are available.
- In the three chapters dealing with TWs, no study was conducted in which the role played by the wind on the generation of TWs was looked at. Measured typical wind events show periods in Lakes Zürich and Lugano of approximately 24 and 80–110 h. It is still unknown how much these signals are transferred to the water motion as direct wind forcing and as whole basin topographic wave response. Such an analysis, e.g. would shed light on the three bay modes seen in Lake Lugano, which in the computations by Trösch [35] were attributed to three different modes and in the interpretation of Mysak et al. [18] as one single whole basin mode.
- To answer such questions requires field campaigns with much higher resolution of data, i.e. many more deployed thermistor chains and current meters than are generally affordable in field campaigns.

21.9 Appendix

Consider the integral expression (21.8)

$$0 = \int_{B^-}^{B^+} \Bigg[-i\sigma \Bigg\{ \underbrace{\frac{\partial}{\partial s}\left[\frac{h^{-1}}{J}\frac{\partial}{\partial s}(P_\alpha \psi_\alpha)\right]}_{(1)} + \underbrace{\frac{\partial}{\partial n}\left[h^{-1} J \frac{\partial}{\partial n}(P_\alpha \psi_\alpha)\right]}_{(2)} \Bigg\} + \underbrace{\frac{\partial h^{-1}}{\partial n}\frac{\partial}{\partial s}(P_\alpha \psi_\alpha)}_{(3)} - \underbrace{\frac{\partial h^{-1}}{\partial s}\frac{\partial}{\partial n}(P_\alpha \psi_\alpha)}_{(4)} \Bigg] Q_\beta \, \mathrm{d}n .$$

In the evaluation of the individual terms in this expression the Leibniz' rule of integration will be used at appropriate places:

$$\int_{B^-}^{B^+} \frac{\partial F}{\partial s} G \, \mathrm{d}n = \int_{B^-}^{B^+} \frac{\partial}{\partial s}(F\,G)\,\mathrm{d}n - \int_{B^-}^{B^+} F \frac{\partial G}{\partial s}\,\mathrm{d}n$$

$$= \frac{\partial}{\partial s}\int_{B^-}^{B^+} F\,G\,\mathrm{d}n - (F\,G)\Big|_{B^+} \cdot \frac{\partial B^+}{\partial s} + (F\,G)\Big|_{B^-} \cdot \frac{\partial B^-}{\partial s} - \int_{B^-}^{B^+} F \frac{\partial G}{\partial s}\,\mathrm{d}n,$$

where F and G are arbitrary, differentiable functions of s and n.

With these preliminaries the terms (1)–(4) can be evaluated. The rule of transformation is to remove differentiations of the topography h as far as possible, which can be achieved by integration by parts:

Term (1):

$$
\begin{aligned}
(1) &= \int \frac{\partial}{\partial s}\left(\frac{h^{-1}}{J}\frac{\partial}{\partial s}\left(P_\alpha\,\psi_\alpha\right)\right) Q_\beta\,\mathrm{d}n \\
&= \frac{\partial}{\partial s}\int \frac{h^{-1}}{J}\frac{\partial}{\partial s}\left(P_\alpha\,\psi_\alpha\right) Q_\beta\,\mathrm{d}n - \int \frac{h^{-1}}{J}\frac{\partial}{\partial s}(P_\alpha\psi_\alpha)\frac{\partial Q_\beta}{\partial s}\mathrm{d}n \\
&= \frac{\partial}{\partial s}\left[\psi_\alpha\int \frac{h^{-1}}{J}\frac{\partial P_\alpha}{\partial s}Q_\beta\mathrm{d}n + \frac{\partial\psi_\alpha}{\partial s}\int \frac{h^{-1}}{J}P_\alpha Q_\beta\mathrm{d}n\right] \\
&\quad -\psi_\alpha\int \frac{h^{-1}}{J}\frac{\partial P_\alpha}{\partial s}\frac{\partial Q_\beta}{\partial s}\mathrm{d}n - \frac{\partial\psi_\alpha}{\partial s}\int \frac{h^{-1}}{J}P_\alpha\frac{\partial Q_\beta}{\partial s}\mathrm{d}n \\
&= \psi_\alpha\left[\frac{\partial}{\partial s}\int \frac{h^{-1}}{J}\frac{\partial P_\alpha}{\partial s}Q_\beta\mathrm{d}n - \int \frac{h^{-1}}{J}\frac{\partial P_\alpha}{\partial s}\frac{\partial Q_\beta}{\partial s}\mathrm{d}n\right] \\
&\quad +\frac{\partial\psi_\alpha}{\partial s}\left[\int \frac{h^{-1}}{J}\frac{\partial P_\alpha}{\partial s}Q_\beta\mathrm{d}n + \frac{\partial}{\partial s}\int \frac{h^{-1}}{J}P_\alpha Q_\beta\mathrm{d}n\right. \\
&\quad \left.-\int \frac{h^{-1}}{J}P_\alpha\frac{\partial Q_\beta}{\partial s}\mathrm{d}n\right] + \frac{\partial^2\psi_\alpha}{\partial s^2}\int \frac{h^{-1}}{J}P_\alpha Q_\beta\mathrm{d}n,
\end{aligned}
$$

Term (2):

$$
\begin{aligned}
(2) &= \int \frac{\partial}{\partial n}\left[h^{-1}J\frac{\partial}{\partial n}(P_\alpha\psi_\alpha)\right]Q_\beta\mathrm{d}n \\
&= -\int h^{-1}J\frac{\partial}{\partial n}(P_\alpha\psi_\alpha)\frac{\partial Q_\beta}{\partial n}\mathrm{d}n \\
&= -\psi_\alpha\int h^{-1}J\frac{\partial P_\alpha}{\partial n}\frac{\partial Q_\beta}{\partial n}\mathrm{d}n,
\end{aligned}
$$

Term (3):

$$
\begin{aligned}
(3) &= \int \frac{\partial h^{-1}}{\partial n}\frac{\partial}{\partial s}(P_\alpha\psi_\alpha)Q_\beta\mathrm{d}n \\
&= -\int \frac{\partial}{\partial n}\left(\frac{\partial}{\partial s}(P_\alpha\psi_\alpha)Q_\beta\right)h^{-1}\mathrm{d}n \\
&= -\psi_\alpha\int h^{-1}\frac{\partial}{\partial n}\left(\frac{\partial P_\alpha}{\partial s}Q_\beta\right)\mathrm{d}n - \frac{\partial\psi_\alpha}{\partial s}\int h^{-1}\frac{\partial}{\partial n}(P_\alpha Q_\beta)\mathrm{d}n,
\end{aligned}
$$

Term (4):

$$
\begin{aligned}
(4) &= -\int \frac{\partial h^{-1}}{\partial s}\frac{\partial}{\partial n}(P_\alpha\psi_\alpha)Q_\beta\mathrm{d}n \\
&= -\frac{\partial}{\partial s}\int h^{-1}\frac{\partial}{\partial n}(P_\alpha\psi_\alpha)Q_\beta\mathrm{d}n + \int h^{-1}\frac{\partial}{\partial s}\left(\frac{\partial}{\partial n}(P_\alpha\psi_\alpha)Q_\beta\right)\mathrm{d}n
\end{aligned}
$$

$$= -\frac{\partial\psi_\alpha}{\partial s}\int h^{-1}\frac{\partial P_\alpha}{\partial n}Q_\beta \mathrm{d}n - \psi_\alpha\frac{\partial}{\partial s}\int h^{-1}\frac{\partial}{\partial s}\int h^{-1}\frac{\partial P_\alpha}{\partial n}Q_\beta \mathrm{d}n$$
$$+ \psi_\alpha\int h^{-1}\frac{\partial}{\partial s}\left(\frac{\partial P_\alpha}{\partial n}Q_\beta\right)\mathrm{d}n + \frac{\partial\psi_\alpha}{\partial s}\int h^{-1}\frac{\partial P_\alpha}{\partial n}Q_\beta \mathrm{d}n.$$

We may remark that the process of this evaluation is more complex when the basis functions are not restricted by the condition that they vanish along the shore, because further integration by parts is necessary in that case. Equation (21.7) thus takes the form

$$\begin{aligned}
0 = &- i\sigma\left[\frac{\partial^2\psi_\alpha}{\partial s^2}\left[\int\frac{h^{-1}}{J}P_\alpha Q_\beta \mathrm{d}n\right]\right.\\
&+ \frac{\partial\psi_\alpha}{\partial s}\left[\int\frac{h^{-1}}{J}\frac{\partial P_\alpha}{\partial s}Q_\beta \mathrm{d}n + \frac{\partial}{\partial s}\int\frac{h^{-1}}{J}P_\alpha Q_\beta \mathrm{d}n - \int\frac{h^{-1}}{J}P_\alpha\frac{\partial Q_\beta}{\partial s}\mathrm{d}n\right]\\
&+ \psi_\alpha\left[\frac{\partial}{\partial s}\int\frac{h^{-1}}{J}\frac{\partial P_\alpha}{\partial s}Q_\beta \mathrm{d}n - \int\frac{h^{-1}}{J}\frac{\partial P_\alpha}{\partial s}\frac{\partial Q_\beta}{\partial s}\mathrm{d}n\right.\\
&\qquad\left.\left. - \int h^{-1}J\frac{\partial P_\alpha}{\partial n}\frac{\partial Q_\beta}{\partial n}\mathrm{d}n\right]\right]\\
&+ \frac{\partial\psi_\alpha}{\partial s}\left[-\int h^{-1}\frac{\partial P_\alpha}{\partial n}Q_\beta \mathrm{d}n - \int h^{-1}P_\alpha\frac{\partial Q_\beta}{\partial n}\mathrm{d}n\right]\\
&+ \psi_\alpha\left[\int h^{-1}\frac{\partial P_\alpha}{\partial n}\frac{\partial Q_\beta}{\partial s}\mathrm{d}n - \int h^{-1}\frac{\partial P_\alpha}{\partial s}\frac{\partial Q_\beta}{\partial n}\mathrm{d}n - \frac{\partial}{\partial s}\int h^{-1}\frac{\partial P_\alpha}{\partial n}Q_\beta \mathrm{d}n\right],
\end{aligned}$$

and the integrals are understood as $\int_{B^-}^{B^+}\ldots$. This expression can be written as

$$\left.\begin{aligned}\mathbb{M}_{\beta\alpha}\psi_\alpha &= 0\\ \psi_\alpha &= 0\end{aligned}\right\}\ \alpha,\beta = 1,\ldots,N\ \begin{cases}0 < s < L,\\ s = 0, L,\end{cases}$$

in which $\mathbb{M}_{\beta\alpha}$ is the following ordinary matrix differential operator

$$\begin{aligned}
\mathbb{M}_{\beta\alpha} = &- i\sigma\left[M^{00}_{\beta\alpha}\frac{\mathrm{d}^2}{\mathrm{d}s^2} + \left(\frac{\mathrm{d}M^{00}_{\beta\alpha}}{\mathrm{d}s} + M^{10}_{\beta\alpha} - M^{01}_{\beta\alpha}\right)\frac{\mathrm{d}}{\mathrm{d}s}\right.\\
&\left. + \left(\frac{\mathrm{d}M^{10}_{\beta\alpha}}{\mathrm{d}s} - M^{11}_{\beta\alpha} - M^{22}_{\beta\alpha}\right)\right] - \left(M^{20}_{\beta\alpha} + M^{02}_{\beta\alpha}\right)\frac{\mathrm{d}}{\mathrm{d}s}\\
&- \left(\frac{\mathrm{d}M^{20}_{\beta\alpha}}{\mathrm{d}s} + M^{12}_{\beta\alpha} - M^{21}_{\beta\alpha}\right)\qquad(\alpha,\beta = 1,\ldots,N).
\end{aligned}$$

in which the matrix elements are given as stated in (21.11).

References

1. Ball, F. K.: Second class motions of a shallow liquid. *J. Fluid Mech.*, **23**, 545–561 (1965)
2. Bäuerle, E. 1986. Eine Untersuchung über topographische Wellen in einem Kanalmodell. In: Vischu D (ed) *Mitteilungen der Versuchsanstalt für Wasserbau, Hydrologie und Glaziologie, ETH-Zürich*, **No. 83**, p 65 (1986)
3. Bender, C.M., Orszag, S.A. *Advanced mathematical methods for scientists and engineers*. Springer Verlag, Berlin, etc. 593p. (1999)
4. Buchwald, V. T. and Adams, J. K.: The propation of continental shelf waves. *Proc. Roy. Soc.*, **A305**, 235–250 (1968)
5. Courant, R. and Hilbert, D.: *Methoden der mathematischen Physik I, II*. Springer Verlag (1967)
6. Djurfeldt, L.: A unified derivation of divergent second-class topographic waves. *Tellus*, **36A**, 306–312 (1984)
7. Finlayson, B. A.: *The Method of Weighted Residuals and Variational Principles.* Academic Press (1972)
8. Gradshteyn, I. S. and Ryzhik, I. M: *Table of Integrals, Series and Products* Academioc Press New York, London 1086 pp (1965)
9. Gratton, Y. : *Low frequency vorticity waves over strong topography.* Ph.D. thesis, Univ. of British Columbia, 132p. (1983)
10. Gratton, Y. and LeBlond, P. H.: Vorticity waves over strong topography. *J. Phys. Oceanogr.*, **16**, 151–166 (1986)
11. Holton, J. R.: *An Introduction to Dynamical Meteorology*. 2nd ed., Academic Press (1979)
12. Johnson, E. R.: Topographic waves in open domains. Part 1: Boundary conditions and frequency estimates *J. Fluid Mech.*, **200**, 69–76 (1989)
13. Johnson, E. R. and Kaoullas, G.: Bay-trapped low frequency oscillations in lakes *Gephys. Astrophys. Fluid Dyn.*, **105**(1), 48–60 (2011)
14. LeBlond, P. H. and Mysak, L. A.: *Waves in the Ocean*. Elsevier (1980)
15. Lie, H.-J.: Shelf waves on the exponential, linear and sinusoidal bottom topographies. *Bull. KORD I.*, **5**, 1–8 (1983)
16. Mysak, L. A.: Topographic waves in lakes. In: *Hydrodynamic of Lakes*, **CISM 286**, edited by K. Hutter, 81–128, Springer, Wien-New York (1984)
17. Mysak, L. A.: Elliptical topographic waves. *Geophys. Astrophys. Fluid Dyn.*, **31**, 93-135 (1985)
18. Mysak, L. A., Salvadè, G., Hutter, K. and Scheiwiller, T.: Topographic waves in an elliptical basin with applications to the Lake of Lugano. *Phil. Trans. Roy. Soc. London.* **A 316**, 1–55 (1985)
19. Raggio, G. and Hutter, K.: An extended channel model for the prediction of motion in elongated homogeneous lakes. *J. Fluid Mech.*, **121**, 231–299 (1982)
20. Ripa, P.: Normal modes of a closed basin with zopography. *J. Geophys. Res.*, **83**, 1947–1957 (1978)
21. Saylor, J. H., Huang, J. S. K. and Reid, R. O.: Vortex modes in Southern Lake Michigan. *J. Phys. Oceanogr.*, **10**, 1814–1823 (1980)
22. Scheiwiller, T., Hutter, K. and Hermann, F.: Dynamics of powder snow avalanches. *Annales Geophysicae*, **5B**(6), 569–588 (1986)
23. Stocker T. and Hutter K.: A model for topographic Rossby waves in channels and lakes. *Mitteilungen der Versuchsanstalt für Wasserbau, Hydrologie und Glaziologie, ETH Zürich*, No. 76. (1985)
24. Stocker, T. and Hutter, K.: One-dimensional models for topographic Rossby waves in elongated basins on the f-plane. *J. Fluid Mech.*, **170**, 435–459 (1986)
25. Stocker, T: and Hutter, K.: Topographic Rossby waves in rectangular basins. *J. Fluid Mech.*, **185**, 107–120 (1987)
26. Stocker, T: *Topographic Waves, Eigenmodes and Reflections in Lakes and Semi-infinite Channels* Mitt. Versuchsanstalt für Wasserbau, Hydrologie und Glaziologie an der ETH Zürich, Nr 93 (Ed.: D. Vischer) 170p. (1987)

27. Stocker, T. and Hutter, K.: *Topographic waves in channels and lakes on the f-plane*. Lecture Notes on Coastal and Estuarine Studies. **21**, 1–178. Springer Verlag, Berlin, etc. (1987)
28. Stocker, T: A numerical study of topographic waves in semi-infinite channels. *J. Phys. Oceanogr.*, **18**, 609–618 (1988)
29. Stocker, T. and Hutter, K.: Qualitative aspects of topographic waves in closed basins, gulfs and channels. In: *Modeling Marine Systems* (Ed.: A. M. Davies). CRC-Press, Boca Baton, Fl., USA, 255–289 (1990)
30. Stocker, T. and Johnson, E.R.: Topographic waves in open domains. Part 2. Bay modes and resonances *J. Fluid Mech.*, **200**, 77–93 (1989)
31. Stocker, T. and Johnson, E.R.: The trapping and scattering of topographic waves by estuaries and headlands. *J. Fluid Mech.*, **222**, 501–524 (1991)
32. Szidarovszky, F. and Yakowitz, S.: *Principles and Procedures of Numerical Analysis*. Plenum Press, New York (1978)
33. Takeda, H.: Topographically trapped waves over the continental shelf and slope. *J. Oceanogr. Soc. Japan*, **40**, 349–366 (1984)
34. Taylor G. I.: Tidal oscillations in gulfs and rectangular basins. *Proc. London Math. Soc.*, **Ser. 2**, 148–181 (1920)
35. Trösch, J.: Finite element calculation of topographic waves in lakes. *Proceedings of 4th International Conference on Applied Numerical Modeling*, Tainan, Taiwan (1984)

Chapter 22
A Class of Chrystal-Type Equations

22.1 Motivation

This chapter is concerned with the derivation of an approximate system of equations for slender fluid bodies using free-surface hydrodynamics on the rotating Earth. Early methods of computing free oscillations or wind-forced responses of oblong lakes or ocean basins assume exclusively uniaxial motion of the water in the long direction of the lake. Consistent derivation of the governing equations from the balances of mass and momentum requires that the rotation of the Earth is ignored. These traditional methods of calculating free oscillations are the channel approximations, of which the classical example is the set of Chrystal equations [4, 5] for barotropic motions. In the linear approximation the corresponding two-layer channel equations can also be derived. They yield the V1Hm modes[1] of a 2-layered fluid with free surface, subject to the neglect of the effects of the rotation of the Earth.

In situations when the rotation of the Earth cannot be ignored, we have seen in Chap. 14,[2] that imposition of Kelvin wave dynamics on the channel solution may be employed to approximately construct the positively (counterclockwise on the N.H.) rotating modes appearing in such basins (see [8]). However, the solution depends on the chosen location of the lake axis, which a priori is not unique. One may be tempted to select this axis as the projection into the horizontal plane of the thalweg, but this selection is based on *geometric* reasoning, whereas Kelvin waves are governed by rotational *dynamics*. Therefore, the corrections of the channel solutions depend on an a posteriori patching of the lake axis, such that the amphidromic structure fits elevation data of the free surface at the shore stations best. This is obviously unsatisfactory. Moreover, Rao and Schwab [30] note: 'Even though the imposition of Kelvin wave dynamics on the channel solution gives very satisfactory results for the lowest mode, its validity for the higher modes breaks down both qualitatively

[1] By 'V1Hm' a baroclinic seiche mode is characterized which is of vertical mode 1 and horizontal mode m. For elongated basins Hm is sometimes replaced by Lm.

[2] Compare Figs. 14.1 and 14.2, panels (a), (b) and the different distributions of the co-tidal lines around the amphidromic points in the L1 and L2 modes, in Fig. 14.1 constructed by Kelvin wave dynamics, in Fig. 14.2 by the two-dimensional finite difference method of the tidal equations.

K. Hutter et al., *Physics of Lakes*, *Volume 2: Lakes as Oscillators*, Advances in Geophysical and Environmental Mechanics and Mathematics,
DOI 10.1007/978-3-642-19112-1_22, © Springer-Verlag Berlin Heidelberg 2011

and quantitatively. The Kelvin-wave hypothesis leads to amphidromic systems all of which rotate in the counterclockwise direction on the Northern Hemisphere' [30]. Yet, there is ample demonstration in Lake Michigan and Lake Superior, reported by Mortimer and Fee [20] and for internal waves in Lake Überlingen by Bäuerle (see [1] or Chap. 14 Sect. 14.4), in Lake Biwa by Shimizu et al. [32] and others that in these basins both positively and negatively propagating amphidromic systems are possible.

'It is clear then that a satisfactory treatment of seiches [and other dynamical processes] in an arbitrary basin requires an attack on the two-dimensional (and when including viscosity effects, three-dimensional) problem. Such models [. . .] are based on particular forms of the tidal operator; the discretization makes explicit use of the two dimensionality of the region of solution for which the classical channel equations break down, because the basins are not elongated' [26], or the channels may be strongly curved that the assumption of a straight channel axis may break down and the Chrystal equations themselves may have to be replaced by an equation set that is based on curvilinear coordinates.

'We develop an extended channel model for *curved, elongated rotating basins*, which not only accounts for the curvature of the axis, but also simulates the characteristic behaviour of waves in rotating basins without excessive computational efforts. The aim is thereby twofold. Firstly, a systematic, rational procedure is sought, by which a series of channel models is obtained. For free oscillations the emerging channel theory should improve on the classical Chrystal equation, allowing for positive and negative amphidromic systems. Secondly, the extended models are regarded as *approximations*, by which the spatially two- or three-dimensional equations of fluid motion are replaced by a one-dimensional set of equations to predict the fluid motion with reasonable accuracy. Here, the *minimum effort* is sought that *suffices* to predict the motion of the original problem with reasonable accuracy' [26].

In what follows, we shall present in a first part the approach by which the extended class of Chrystal models is derived from the general three-dimensional formulation of hydrodynamics. These equations are formulated relative to a curvilinear coordinate system, which has as principal coordinate an axis of the channel-like lake, which allows development of such a channel model but reduces the 'element of subjectivity' in prescribing the channel axis. This major axis is complemented by two axes forming an orthogonal system. The channel model will be derived by the method of weighted residuals (MWR) in a similar way as this was done for topographic Rossby waves in Chaps. 19–21. Accordingly, each field variable (velocities, surface elevation and interface elevation for the 2-layer equations) will be expanded in a set of functions of the cross-sectional coordinates and unknown fields, which will only depend on time and the longitudinal spatial coordinate along the lake axis. By truncating this sum of products at a certain number of terms, a hierarchy of models is established; it is assumed and must be corroborated that increasing the number of terms will also increase the accuracy of the solution generated by the hierarchy of the models. We shall demonstrate the construction of these models for the linear baroclinic field equations. The simplest solutions for a lake with a straight

major axis will generate the classical Chrystal equations, but already spatially one-dimensional equations for curved basins need correction as do effects of the rotation of the Earth.

In a second part of this chapter, 'a first-order channel model for fluid motion in long homogeneous lakes, as derived in detail in the first part will be presented. This model describes the motion with the aid of spatially one-dimensional boundary value problems and is deduced by truncating the hierarchy of equations to the lowest and first-order terms only. Various wave solutions of the governing equations applied to rectangular basins are presented. It is shown that for moderate rotation speeds of the Earth and for elongated basins of a homogeneous fluid the main features of gravitational oscillations are predicted by the model. Kelvin- and Poicaré-type waves are shown to exist. Moreover, conditions of complete and incomplete reflections of Kelvin waves and free oscillations are discussed. The results corroborate the suitability of the model as far as wave motion in rectangular basins is concerned, but equally elucidate the physics behind them, which is less transparent when attacked with the full theory' [27].

In the last part of this chapter, we shall illustrate the computational procedure by applying it to a real lake with an arbitrary number of shape functions.

22.2 Traditional Chrystal-Type Equations

22.2.1 Homogeneous Lakes

Consider a long lake for which a straight lake axis can reasonably be defined. Suppose homogeneous, i.e. barotropic conditions and assume small displacements of the free surface and small velocities, so that non-linear terms can be ignored.

Let $S(x)$ and $B(x)$ be the cross section and the width of the lake at the free surface, measured perpendicular to the lake axis; x is the coordinate measured along the lake axis which is not curved. Let, moreover, $u(x,t)$ be the 'barotropic' velocity in the x-direction and uniform over the cross section. Let $\zeta(x,t)$ be the free surface displacement, equally independent of the transverse coordinate across the lake.

If two parallel cross sections are a distance $\mathrm{d}x$ apart, then the volume flow of water through the two cross sections and into the small volume between the two cross sections at time t is given by

$$(Su)(x,t) - (Su)(x+\mathrm{d}x,t). \tag{22.1}$$

If the water is density preserving (which we assume), expression (22.1) must balance the increase of volume between the two cross-sections,

$$B(x)\frac{\partial \zeta}{\partial t}\mathrm{d}x. \tag{22.2}$$

Equating the above two relations, using Taylor series expansion in the second term of (22.1) and taking the limit of the resulting equation as $\mathrm{d}x \to 0$, then yields

$$B(x)\frac{\partial \zeta(x,t)}{\partial t} + \frac{\partial}{\partial x}\left((Su)(x,t)\right) = 0, \tag{22.3}$$

which (modulo a factor ρ) is the mass balance equation.

The balance equation of linear momentum can be treated in an analogous fashion. The momentum in the x-direction between the two cross sections is given by $\rho Su\mathrm{d}x$. So,

$$\frac{\partial(Su)}{\partial t}\mathrm{d}x \tag{22.4}$$

is the increase of momentum per unit time and unit mass within the volume bound by the two cross-sections. The fluxes of momentum through the cross sections at x and $x + \mathrm{d}x$ are given by

$$(\rho Su^2)(x,t), \qquad (\rho Su^2)(x+\mathrm{d}x,t).$$

These advective terms will be ignored here, because they are quadratic in u, but could be accounted for if so desired. So, the time rate of change of momentum per unit mass is approximately given by (22.4). According to Newton's Second Law it must be balanced by the forces acting on the cross-sectional increment. If friction is ignored, the contributions to the horizontal forces are the hydrostatic pressures exerted on the cross-sectional areas and the mantle surface formed by the topography, see Fig. 22.1a, which shows a lake element between x and $x+\mathrm{d}x$. The pressure is zero at the free surface and grows linearly with depth. On the cross-section at x the cross-sectional contribution of the pressure force acts in the positive x-direction; on the cross-section at $x + \mathrm{d}x$ it acts in the negative x-direction; on the mantle surface, it is perpendicular to this surface, but its components in the x-direction

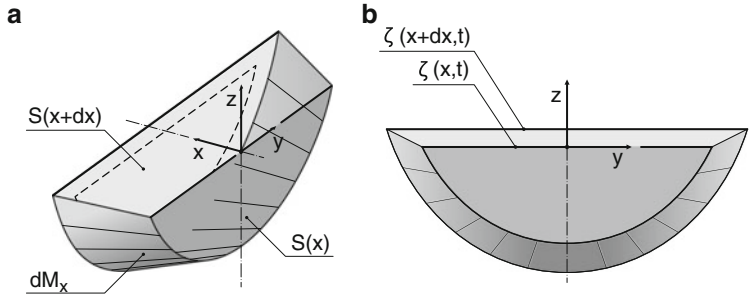

Fig. 22.1 Explaining the derivation of (22.5). (**a**) Lake increment cut at x with cross section $S(x,t)$, free surface elevation $\zeta(x,t)$ and at $x + \mathrm{d}x$ with cross-section $S(x+\mathrm{d}x,t)$ and free surface elevation $\zeta(x+\mathrm{d}x,t)$ and mantle surface increment $\mathrm{d}M(x+\mathrm{d}x,t)$. (**b**) $S(x,t)$, $S(x+\mathrm{d}x,t)$ and projection $\mathrm{d}M_x$ of mantle surface $\mathrm{d}M$ onto the (y,z)-plane at $x + \mathrm{d}x$

are in each point reduced by the projection of the mantle-surface increment onto the cross-sectional area at $x + \mathrm{d}x$, perpendicular to x. The combined effect in the x-direction of the pressures on the cross-section at x and the mantle surface between x and $x + \mathrm{d}x$ is as if the cross section at x were the projected area onto the cross-section at $x + \mathrm{d}x$ of $S(x,t)$ plus that of the mantle surface $\mathrm{d}M_x$ (the projection of $\mathrm{d}M$), see Fig. 22.1. Subtracting this contribution from the total pressure force at $x + \mathrm{d}x$ and employing Taylor series expansion yields the resultant pressure force in the x-direction

$$-gS(x)\frac{\partial\zeta(x,t)}{\partial x}\mathrm{d}x, \tag{22.5}$$

where g is the gravity constant and a constant factor ρ has been dropped as in (22.3) already. The minus sign expresses the fact that the resulting pressure points for positive $\partial\zeta/\partial x$ into the negative x-direction.

Equating (22.4) and (22.5) and dropping in the emerging relation the common factor $S(x)$ yields

$$\frac{\partial u}{\partial t} + g\frac{\partial\zeta}{\partial x} = 0. \tag{22.6}$$

Equations (22.3) and (22.6) together form the so-called Chrystal equations for a homogeneous elongated straight lake. The unknowns are the vertical surface displacement $\zeta(x,t)$ and the cross-sectional averaged longitudinal barotropic velocity $u(x,t)$. Boundary conditions for which (22.3) and (22.6) must be solved, require the longitudinal velocity to vanish at the long ends of the lake, so that

$$u(0,t) = 0 \quad \text{and} \quad u(L,t) = 0, \tag{22.7}$$

where the two lake ends are at $x = 0$ and $x = L$. Equations (22.3), (22.6) and (22.7) form the free eigenvalue problem for u and ζ.

For later use, let us write (22.3) and (22.6) also as the following alternative system:

$$\begin{aligned} B(x)\frac{\partial\zeta}{\partial t} + \frac{\partial}{\partial x}(Su) &= 0, \\ \frac{\partial}{\partial t}(Su) = -gS\frac{\partial\zeta}{\partial x} &= 0, \end{aligned} \tag{22.8}$$

in which $Su = M$ is the total momentum over the cross-section.

It is often regarded as advantageous to eliminate ζ between (22.3) and (22.6). This process leads to the single second order differential equation

$$\frac{\partial^2 u}{\partial t^2} = g\frac{\partial}{\partial x}\left\{\frac{1}{B}\frac{\partial}{\partial x}(Su)\right\}. \tag{22.9}$$

This is the famous Chrystal equation, dating back to 1904–1905 [4,5]. The equation can be put into standard form by the transformations

$$\tilde{u} = Su, \qquad \tilde{x} = \int_0^x B(\xi)\mathrm{d}\xi \tag{22.10}$$

to yield

$$\frac{\partial^2 \tilde{u}}{\partial t^2} = g\sigma \frac{\partial^2 \tilde{u}}{\partial \tilde{x}^2}, \qquad \sigma(x) = B(x)S(x), \tag{22.11}$$

subject to the boundary conditions

$$\tilde{u}(0,t) = \tilde{u}(\tilde{L},t) = 0, \qquad \tilde{L} = \int_0^L B(\xi)\mathrm{d}\xi. \tag{22.12}$$

Equations (22.11) and (22.12) form the standard eigenvalue problem for a standing wave in a long non-rotating lake with straight lake axis. Tacitly, it is also assumed that the transverse variations of ζ and u can be ignored.

This simple channel model has been prepared for computations by hand by Defant as early as 1918 [7], see also [9]. The calculation of periods and structures of surface seiches in basins of irregular shapes has produced results (e.g. see Marcelli [19], Caloi [3], Servais [31] and others), which agree with observations surprisingly well in view of its relative simplicity. For barotropic processes the rotation-free Chrystal equations are certainly an acceptable approximation in small elongated lakes, but for medium size to large lakes (Great Lakes, ocean basins and large fjords) the account of the rotation of the Earth should not be ignored. As extension of the works of Defant [8] and Rao and Schwab [30] an improved procedure beyond Kelvin wave dynamics is warrantable.

22.2.2 Two-Layer Channel Model

Let us again consider a long lake for which a straight lake axis can be defined, and assume two-layered conditions with an epilimnion of constant density ρ_1 and constant thickness H_1 and a hypolimnion with constant density $\rho_2 > \rho_1$ and variable thickness $H_2(x, y)$. Their interface between the two layers is identified with the thermocline. The width of the still free surface will be denoted by $B_1(x)$, and that at the still thermocline, $B_2(x)$, is generally different from $B_1(x)$. The cross-sectional area of the epilimnion at rest is bounded by the free surface, the still thermocline and the segments of the (straight) lines at the lake boundary connecting the two; it will be denoted by $S_1(x)$. Similarly, the cross-sectional area of the hypolimnion is bounded by the still thermocline separating the epi- and hypolimnion and the bottom surface and will be denoted by $S_2(x)$. Other cross-sectional quantities of the geometry can also be defined and will be introduced at need. They are known functions of the coordinate x. When the lake is in motion, e.g. in a seiche, the free surface and the thermocline will move and the actual values for the widths and the cross-sectional areas will, consequently, also alter but the changes in B_1, B_2 and S_1, S_2 due to this motion will be ignored.

Consider next two parallel cross sections which are a distance dx apart from one another. Assume that the longitudinal velocities within the epi- and hypolimnion are only functions of the longitudinal coordinate, $u_{1,2} = u_{1,2}(x)$. Similarly, the vertical displacements of the free surface, ζ_1, and the thermocline, ζ_2 are equally only assumed to be functions of x and time t, $\zeta_{1,2} = \zeta_{1,2}(x,t)$; they are small in comparison to the equilibrium thickness, $\|\zeta_1\| \ll H_1$, $\|\zeta_2\| \ll H_1$. It is obvious, the latter assumption is somewhat critical and likely not satisfied during and immediately after storms. The assumption is, however, needed if linear equations are to be derived.

If changes of cross-sectional areas due to $\zeta_{1,2}$ are ignored, then the volume balance (mass balance divided by a constant density) for the volume in the epilimnion between the neighbouring cross-sections is given by

$$[S_1(x)u_1(x,t) - S_1(x+\mathrm{d}x,t)u_1(x+\mathrm{d}x,t)] = B_1(x)\frac{\partial\zeta_1}{\partial t}\mathrm{d}x - B_2(x)\frac{\partial\zeta_2}{\partial t}\mathrm{d}x. \tag{22.13}$$

Using Taylor series expansion in the second term on the left-hand side of (22.13) and thereby dropping higher order terms of dx transforms the above equation in the limit as $\mathrm{d}x \to 0$ into

$$B_1(x)\frac{\partial\zeta_1}{\partial t} - B_2(x)\frac{\partial\zeta_2}{\partial t} + \frac{\partial}{\partial x}\left(S_1(x)u_1\right) = 0. \tag{22.14}$$

This is the mass balance equation for the epilimnion layer. An analogous computation for the bottom layer gives

$$B_2(x)\frac{\partial\zeta_2}{\partial t} + \frac{\partial}{\partial x}\left(S_2(x)u_2\right) = 0. \tag{22.15}$$

To derive the x-component of the momentum balance, note that the time rates of change and the flux contribution of the x-momentum in a slice of the lake between x and $x + \mathrm{d}x$ are given by

$$\begin{cases} \dfrac{\partial}{\partial t}\left(\left(\rho_1 S_1 u_1\right)(x,t)\right) + \dfrac{\partial}{\partial x}\left(\left(\rho_1 S_1 u_1^2\right)(x,t)\right)\Big\}\,\mathrm{d}x, & \text{in the epilimnion,} \\ \left\{\dfrac{\partial}{\partial t}\left(\left(\rho_2 S_2 u_2\right)(x,t)\right) + \dfrac{\partial}{\partial x}\left(\left(\rho_2 S_1 u_2^2\right)(x,t)\right)\right\}\,\mathrm{d}x, & \text{in the hypolimnion.} \end{cases} \tag{22.16}$$

Henceforth, the non-linear convective terms will be ignored. When also neglecting the forces due to viscous effects, the only force contributions are due to the hydrostatic pressure

$$p(z) = \begin{cases} \rho_1 g(z+\zeta_1), & -\zeta_1 \le z \le H_1 - \zeta_2, \\ \rho_1 g(H_1 + \zeta_1 - \zeta_2) + \rho_2 g(\bar{z} + \zeta_2), & -\zeta_2 \le \hat{z} \le H_2(x,y). \end{cases} \tag{22.17}$$

Following the arguments offered for the barotropic case (see Fig. 22.1) and the derivation of (22.5) for the pressure force on an epilimnion lake slice of length dx, the x-component of the pressure force is obtained as

$$-\left\{\rho_1 g S_1(x)\frac{\partial\zeta(x,t)}{\partial x}\right\}\mathrm{d}x. \tag{22.18}$$

Similarly, for the pressure force on a lake element of the hypolimnion, one gets

$$-\left\{\rho_1 g S_2(x)\frac{\partial\zeta_1(x,t)}{\partial x}+(\rho_2-\rho_1)g S_2(x)\frac{\partial\zeta_2(x,t)}{\partial x}\right\}\mathrm{d}x. \tag{22.19}$$

Therefore, the linearized x-momentum equations read:

- In the epilimnion,

$$\frac{\partial}{\partial t}\left((S_1u_1)(x,t)\right)=-gS_1(x)\frac{\partial}{\partial x}\left(\zeta_1(x,t)\right), \tag{22.20}$$

- In the hypolimnion,

$$\begin{aligned}\frac{\partial}{\partial t}\left((S_2u_2)(x,t)\right)=-\Bigg\{&\frac{\rho_1}{\rho_2}gS_2(x)\frac{\partial}{\partial x}\left(\zeta_1(x,t)\right)\\&+\frac{\rho_2-\rho_1}{\rho_{2)}}gS_2(x)\frac{\partial}{\partial x}\left(\zeta_2(x,t)\right)\Bigg\}.\end{aligned} \tag{22.21}$$

Equations (22.14), (22.15), (22.20) and (22.21) together form a two-layered channel model for elongated basins stratified in two layers. They can also be written as

$$\begin{aligned}&B_1(x)\frac{\partial\zeta_1}{\partial t}-B_2(x)\frac{\partial\zeta_2}{\partial t}+\frac{\partial M_1}{\partial x}=0,\\&B_2(x)\frac{\partial\zeta_2}{\partial t}+\frac{\partial M_2}{\partial x}=0,\\&\frac{\partial M_1}{\partial t}=-gS_1(x)\frac{\partial\zeta_1}{\partial x},\\&\frac{\partial M_2}{\partial t}=-(1-\varepsilon)gS_2(x)\frac{\partial\zeta_1}{\partial x}+g\varepsilon S_2(x)\frac{\partial\zeta_2}{\partial x},\end{aligned} \tag{22.22}$$

with

$$M_1:=S_1u_1,\quad M_2:=S_2u_2,\quad \varepsilon:=\frac{\rho_2-\rho_1}{\rho_2}. \tag{22.23}$$

Recall that Charney [2] constructed a formal one-layer analogue to the two-dimensional tidal equations representing pure barotropic and pure baroclinic responses of the two-layer system with constant depth, see Chap. 11 , Sect. 11.4. The analogous one-layer model is (22.8) or

$$\begin{aligned} B_\alpha \frac{\partial \zeta_\alpha}{\partial t} + \frac{\partial M_\alpha}{\partial x} &= 0, \\ \frac{\partial M_\alpha}{\partial t} &= -g S_\alpha \frac{\partial \zeta_\alpha}{\partial x}, \end{aligned} \tag{22.24}$$

with

$$M_\alpha = M_1 + \nu_\alpha M_2, \quad B_\alpha \zeta_\alpha = B_1 \zeta_1 + B_2(\nu_\alpha - 1)\zeta_2. \tag{22.25}$$

and yet unknown B_α and S_α. Using (22.25) in (22.24) yields the following chain of identities:

$$\begin{aligned} \frac{\partial M_\alpha}{\partial t} &= -g \left\{ S_1 \frac{\partial \zeta_1}{\partial x} + (1-\varepsilon)\nu_\alpha S_2 \frac{\partial \zeta_1}{\partial x} - \varepsilon \nu_\alpha S_2 \frac{\partial \zeta_2}{\partial x} \right\} \\ &= -g \left\{ (S_1 + (1-\varepsilon)\nu_\alpha S_2) \frac{\partial \zeta_1}{\partial x} - \varepsilon \nu_\alpha S_2 \frac{\partial \zeta_2}{\partial x} \right\} \\ &\overset{*}{=} -g \frac{\partial}{\partial x} \left\{ (S_1 + (1-\varepsilon)\nu_\alpha S_2)\, \zeta_1 - \nu_\alpha \varepsilon S_2 \zeta_2 \right\} \\ &\overset{!}{=} -g S_\alpha \frac{\partial \zeta_\alpha}{\partial x} \\ &= -g \left\{ \frac{S_\alpha}{B_\alpha} B_1 \frac{\partial \zeta_1}{\partial x} + B_2 \frac{S_\alpha}{B_\alpha} (\nu_\alpha - 1) \frac{\partial \zeta_2}{\partial x} \right\}. \end{aligned} \tag{22.26}$$

It is at the step $\overset{*}{=}$ where the cross-sectional areas must be constant. Moreover, at $\overset{!}{=}$ a formal one-layer model is requested. Comparing the expressions in lines 3 and 5 of (22.26) yields

$$\begin{aligned} S_1 + (1-\varepsilon)\nu_\alpha S_2 &= \frac{S_\alpha}{B_\alpha} B_1, \\ -\nu_\alpha \varepsilon S_2 &= B_2 \frac{S_\alpha}{B_\alpha} (\nu_\alpha - 1), \end{aligned} \tag{22.27}$$

in which S_α / B_α and ν_α are still unknown. Eliminating S_α / B_α between $(22.27)_1$ and $(22.27)_2$ leads to the following quadratic equation:

$$\nu_\alpha^2 + \frac{S_1 - (1-\varepsilon)S_2 + \varepsilon S_2 (B_1/B_2)}{(1-\varepsilon)S_2} \nu_\alpha - \frac{S_1}{S_2} \frac{1}{1-\varepsilon} = 0. \tag{22.28}$$

Since $0 < \varepsilon \ll 1$ is small of $\mathcal{O}(10^{-3})$ we solve it for $\varepsilon \to 0$ and then obtain

$$\nu_\alpha^2 + \left(\frac{S_1}{S_2} - 1 \right) \nu_\alpha - \frac{S_1}{S_2} = 0. \tag{22.29}$$

It has the solutions

$$\nu_{(o)}^{\text{ext}} = 1, \quad \nu_{(o)}^{\text{int}} = -\frac{S_1}{S_2}, \tag{22.30}$$

where the index $(\cdot)_{(o)}$ indicates the zeroth order approximation. With this approximation the modes take the following forms:

- *Barotropic mode*

$$\begin{aligned}
&\nu_{\text{ext}} = 1,\\
&M_{\text{ext}} = M_1 + M_2 = S_1 u_1 + S_2 u_2,\\
&B_{\text{ext}}\zeta_{\text{ext}} = B_1\zeta_1 \quad \rightarrow \quad B_{\text{ext}} = B_1 \quad \Longrightarrow \quad \zeta_{\text{ext}} = \zeta_1, \qquad (22.31)\\
&\zeta_2 \text{ is not determined, see, however (22.34) below,}\\
&S_{\text{ext}} = S_1 + S_2 =: S,
\end{aligned}$$

  all with $\mathcal{O}(\varepsilon)$-errors.
- *Baroclinic mode*

$$\begin{aligned}
&\nu_{\text{int}} = -\frac{S_1}{S_2},\\
&M_{\text{int}} = M_1 - \frac{S_1}{S_2}M_2 = S_1 u_1 - S_1 u_2 = S_1(u_1 - u_2),\\
&B_{\text{int}}\zeta_{\text{int}} = B_1\zeta_1 - B_2\frac{S_1 + S_2}{S_2}\zeta_2, \qquad (22.32)\\
&\rightarrow B_{\text{int}} \stackrel{!}{=} B_1 \quad \Longrightarrow \quad \zeta_{\text{int}} = \zeta_1 - \frac{S_1 + S_2}{S_2}\frac{B_2}{B_1}\zeta_2,\\
&S_{\text{int}} = \frac{B_2}{B_1}\frac{S_1 S_2}{S_1 + S_2}\varepsilon \left(= S^{\text{int}}_{\text{equiv}}\right),
\end{aligned}$$

  again all with $\mathcal{O}(\varepsilon)$-errors.

These relations are all analogous to corresponding relations for the equivalent depth models in the tidal theory (see Chap. 11, (11.95)–(11.104)). The analogy with these is, however, only complete in the sense that $S_{1,2}$ here correspond to $H_{1,2}$ there, if $B_1 = B_2$. If $B_1 \neq B_2$, then, apart from S_1/S_2 also B_1/B_2 will influence the results. This is generally the restriction that is tacitly assumed in realistic calculations.

Inverting (22.31) and (22.32) yields

$$\begin{aligned}
M_1 &= \frac{S_1}{S_1 + S_2}\left(M_{\text{ext}} + \frac{S_2}{S_1}M_{\text{int}}\right) + \mathcal{O}(\varepsilon),\\
M_2 &= \frac{S_2}{S_1 + S_2}\left(M_{\text{ext}} - M_{\text{int}}\right) + \mathcal{O}(\varepsilon),\\
\zeta_1 &= \zeta_{\text{ext}} + \mathcal{O}(\varepsilon),\\
\zeta_2 &= -\frac{B_1}{B_2}\frac{S_2}{S_1 + S_2}\left(\zeta_{\text{int}} - \zeta_{\text{ext}}\right) + \mathcal{O}(\varepsilon).
\end{aligned} \qquad (22.33)$$

Suppose now that $M_{\text{int}} = 0, \zeta_{\text{int}} = 0$ (no baroclinic motion). Then (22.33) implies

$$\begin{aligned} &\frac{M_1}{S_1} = u_1 = \frac{M_{\text{ext}}}{S_1 + S_2} = \frac{M_2}{S_2} = u_2, \\ &\zeta_1 = \zeta_{\text{ext}}, \quad \zeta_2 = \frac{B_1}{B_2}\frac{S_2}{S_1 + S_2}\zeta_{\text{ext}}. \end{aligned} \tag{22.34}$$

These formulae imply that the velocities are the same, $u_1 = u_2$; moreover,

$$\frac{\zeta_2}{\zeta_1} = \frac{B_1}{B_2}\frac{S_2}{S_1 + S_2}, \tag{22.35}$$

which means that the interface displacement is smaller than the free surface displacement by the factor (22.35). All this is analogous to the results also obtained in Chap. 11.

If we take instead $M_{\text{ext}} = 0, \zeta_{\text{ext}} = 0$ (no barotropic motion) then (22.32) together with (22.25) and (22.27) implies

$$\begin{aligned} &M_1 = \frac{S_2}{S_1 + S_2} M_{\text{int}} = -M_2, \\ &\zeta_1 = [\mathcal{O}(\varepsilon\zeta_{\text{int}})], \quad \zeta_2 = -\frac{B_1}{B_2}\frac{S_2}{S_1 + S_2}\zeta_{\text{int}}. \end{aligned} \tag{22.36}$$

Here, the longitudinal momentum fluxes in the two layers are equally large but are in opposite directions, and the free surface displacement is $\mathcal{O}(\varepsilon\zeta_{\text{int}})$, which is a very small fraction of the interface displacement.

Equation (22.22) describe the dynamics of the full two-dimensional channel model and correspond to the Chrystal equations treated earlier in this chapter. Effects of the rotation of the Earth are ignored; the equations can, therefore, only represent a physically adequate model for narrow elongated lakes of which the width is generally smaller than the internal Rossby radius of deformation. We are not aware that this model has been applied by limnologists in practice. However, the equivalent-depth variant, characterized by (22.32), has been applied by Lemmin and Mortimer [17] in a simplified form in which $B_1 = B_2 = B$ and $S_{1,2}$ are replaced by suitably chosen depths $H_{1,2}$ essentially corresponding to $S_{1,2}/B =: H_{1,2}^{\text{LM}}$, where LM stands for Lemmin-Mortimer. With this choice

$$\frac{S_1}{S_2} = \frac{H_1}{H_2} \quad \text{and} \quad \frac{S_{1,2}}{S_1 + S_2} = \frac{H_{1,2}^{\text{LM}}}{H_1^{\text{LM}} + H_2^{\text{LM}}}.$$

Lemmin and Mortimer essentially solve (22.24) for the internal waves

$$\begin{aligned} &B_1\frac{\partial\zeta_{\text{int}}}{\partial t} + \frac{\partial M_{\text{int}}}{\partial x} = 0, \\ &\frac{\partial M_{\text{int}}}{\partial t} = -g\left(S_{\text{int}}^{\text{equiv}}\right)\frac{\zeta_{\text{int}}}{\partial x} \end{aligned} \tag{22.37}$$

for harmonic excitations

$$M_{\text{int}} = M_{\text{int}}^{(o)} \exp(\mathrm{i}\omega t) \quad \zeta_{\text{int}} = \zeta_{\text{int}}^{(o)} \exp(\mathrm{i}\omega t)$$

and subject to the no-flux conditions at $x = 0$ and $x = L$. This transforms (22.37) to the following eigenvalue problem

$$\begin{aligned} &\frac{\mathrm{d}^2 M_{\text{int}}^{(o)}}{\mathrm{d}x^2} + \left(\frac{B_1 \omega^2}{S_{\text{int}}^{\text{equiv}}}\right) M_{\text{int}}^{(o)} = 0, \quad 0 \le x \le L \\ &M_{\text{int}}^{(o)} = 0, \quad \text{at } x = 0,\ x = L. \end{aligned} \tag{22.38}$$

22.2.2.1 Application

The likely earliest applications of interval oscillations in lakes are Wedderburn's studies of temperature to Loch Earn and Loch Ness [36–38]. The two layer equivalent depth model for elongated lakes in the channel approximation and when the effects of the rotation of the Earth can be ignored were applied to eight different basins by Lemmin and Mortimer [17]: Lake Geneva, Loch Ness, Lake Zurich, Lake of Lugano, Lake Zug, Windermere (north and south basins) and Lake Baldegg. Lemmin and Mortimer [17] used Defant's [7,9] one-dimensional procedure designed for computations by hand of barotropic seiches by replacing the water depth by the equivalent depth

$$H_{\text{eq}} = \frac{\rho_2 - \rho_1}{\rho_2} \frac{H_1 H_2}{H_1 + H_2}.$$

It is well known and has first been demonstrated by Charney [2] that equivalent depth models are strictly only correct for basins of constant depth.[3] Moreover, Lemmin and Mortimer defined their lake axis as the thalweg of the lake bathymetry, which are generally curved, but used equations which Defant[4] derived for straight lake axes; however, the authors state that comparisons between channel solutions using the straight axis-approximation and solutions of the two-dimensional shallow water equations suggest that the errors in applying the 'two-layer Defant procedure' (TDP) to real channels and basins of variable cross section are not large'.

In all their eight examples Lemmin and Mortimer base their computations on the replacement of the realistic measured stratification (obtained from the temperature profiles) by judiciously selecting two layers with constant densities. The interface is selected by them at the depth of maximum density gradient. This determines H_1 and the length L of the interfacial thalweg at rest. At the ends of the thalweg, impermeable barriers are erected, ignoring the dynamics of the water masses beyond

[3] See Sect. 11.4.3. In the above computation the analogous result was demonstrated, requiring here constant cross-sections.

[4] For a biographical sketch see Fig. 22.2.

these end cross sections. The choice of H_1 influences the possible choices of H_2 (and the layer temperatures θ_1 and θ_2). Lemmin and Mortimer state that the best of their choices was to choose as H_2 the mean depth of the sub-basin bounded by the interface and the bottom.

Only for Lake Zurich detailed results of mode periods and isotherm-depth-time series at several stations, distributed over the entire lake were available in 1985, which allowed a detailed comparison of the computational results with measured data. We, therefore, restrict the presentation of this comparison to Lake Zurich and refer the reader for all other examples to [17]. Observations of isotherm displacements and currents (and corresponding spectra) were made during an intensive measuring campaign in August–September 1978 with 31 instruments moored at various stations and depths [10, 13]. 'Also available for comparison are the results from a more elaborate two-layered model [11] based on a two-dimensional grid fitted to the basin topography' [11], using a TVD model. The two-layered Defant procedure (TDP) was applied based on $H_1 = 12m$ and $\theta_1 = 18°\text{C}$ and $\theta_2 = 6°\text{C}$, and the 26 stations of Fig. 22.3 have been constructed in conformity with the bathymetry parameterization used in [11].

The structures predicted by the two methods are compared, for the first three modes in Fig. 22.4 and the observed and predicted periods are as shown in Table 22.1.

'The TDP periods are about 10% less than the Schwab model periods which are in good agreement with those observed [...]. The first three modes (44, 25, and 17 h) could be clearly identified, with the first dominant. Signals from higher modes did not clearly emerge. However, the two-layer parameters in the above comparison were fitted to the mean temperature profile for the whole of August and September [13]. At the time when internal seiching was most evident (during September), a more realistic two-layer fit corresponds to the θ_1, θ_2 values 16°C, 6°C, and $H_1 =$ 15 m. With those values, TDP yielded somewhat longer periods [...] which come closer to the observed periods [...].

For the Lake Zurich first and second mode structures (Fig. 22.4), the two models predict (TDP, dots; Schwab, lines) very similar interface elevation distributions and nodal positions; agreement is less close for the third mode. The TDP-predicted maximum current speeds (dots in Fig. 22.4b) for the first and second modes are distinctly less than those predicted by Schwab's model: The TDP estimates are averages for each cross-section, while the Schwab model's values are calculated for grid points near the thalweg where speeds are above the section average. The apparent closer agreement between dots and lines for the third mode is spurious because, as Fig. 22.4 shows, the Defant procedure over-predicts interface displacement in that case. It will also be noted that, whereas the TDP estimates of current speed fall to zero at the two designated end sections, 2 and 26, the Schwab-predicted values do not. This is because the Schwab model does not truncate the basin at those two end sections.

The vertical lines surmounted by circles in Fig. 22.4 are relative, approximate estimates of the 'observed' along-thalweg interface elevations and relative current speeds at the moorings indicated by numbers. Those estimates were derived from

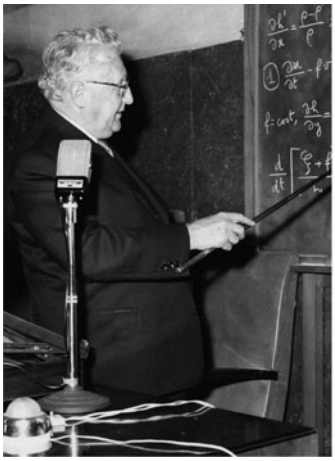

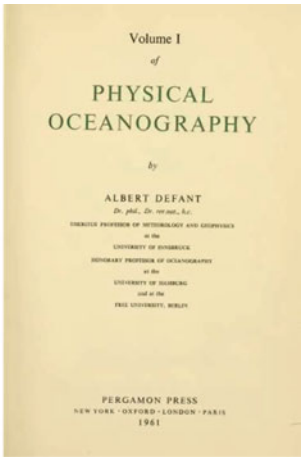

Fig. 22.2 Albert Joseph Maria Defant (1884–1974), an Austrian meteorologist and oceanographer (photo from Koertge, ed). New Dictionary of Scientific Biography. © 2008 Gale, a part of Cengage Learning, Inc. Reproduced with permission) and front cover of his book 'Physical Oceanography' (1961).

Born in Trento on 12 July 1884, Albert Joseph Maria Defant was educated in Innsbruck, Austria where he studied mathematics, physics, meteorology and geophysics and received from its university the Ph. Degree with distinction with a dissertation on the 'Distribution of the droplet size in rain'. His first regular job early 1907 was Assistant at the 'Directorate for Meteorology and Geodynamics' in Vienna, of which he took on the head position in 1909. In the same year he had also passed his Habilitation degree. His collaboration with Prof. J. Hahn brought him also the co-editorship of the 'Meteorologische Zeitschrift' at this young age of 25 years.

Defant's rich research activities centred both around observation and theory in many fields such as solar radiation, dynamic meteorology, physics of the atmosphere and air-electricity. His fundamental contributions on atmospheric circulation and exchange processes of heat and his practical experience with synoptic weather observations led to several books and expository articles on weather and weather forecast, 1918, revised 1926, 'Atmosphärenkunde', 1923, and 'Statik und Dynamik der Atmosphäre', 1928, in the Encyclopedia of Earth Science and the Handbook of Experimental Physics, respectively.

Between 1919 and 1926 Defant was Professor of Cosmic Physics at the University of Innsbruck. In his courses on all aspects of geophysics he also lectured on oceanography. Already earlier, he had been concerned with lake surface oscillations and ocean tides. This work, for that time rather mathematical, brought him an invitation of participation in oceanographic expeditions in the North Sea and Germany's Atlantic Expedition with the research vessel 'Meteor', 1925–1927, whose leadership he took over in fall 1925 after the sudden death of Professor A. Merz. He also led the whole exploitation of the data material of that expedition. 1927 Defant accepted an invitation as Professor of Oceanography at the University Berlin and Director of the Museum of Marine Sciences in Berlin. He was holding these positions also during World War II.

Defant's numerous articles on theoretical oceanography are very broad in scope and perspectives and cover the thermohaline structure of the ocean and its variation, ocean circulation and turbulence and meromixis. In 1929 the 'Dynamische Ozeanographie' appeared and in 1931 'Die Physik des Meeres' was published in the 'Handbuch der Experimentalphysik'. From this the 2-volume treatise 'Physical Oceanography' sprang, which he largely wrote from his lectures in 1943 to meteorologists of the German Army. In November 1945, Defant returned as Professor of Meteorology and Geophysics to Innsbruck, where he formally retired in 1955. He held visiting positions at the Scripps Institution of Oceanography in La Jolla, USA, 1949–1950, and was Visiting Professor at the University of Hamburg 1951/1952 and 1955/1956 each during the winter months.

Albert Defant was Dr. honoris causa of the Free University Berlin and member of Academies of Sciences of Vienna, Berlin, Halle, Göttingen, Helsinki and Oslo and honorary member of several international scientific societies. He has been a leading meteorologist and can well be regarded as one of the founders of physical oceanography. He died on 24 December 1974.

Text based on: F. Steinhauser: Zum Gedenken an Albert Defant Arch Met Geophys Biokl Ser A 24, 385–388 (1975).

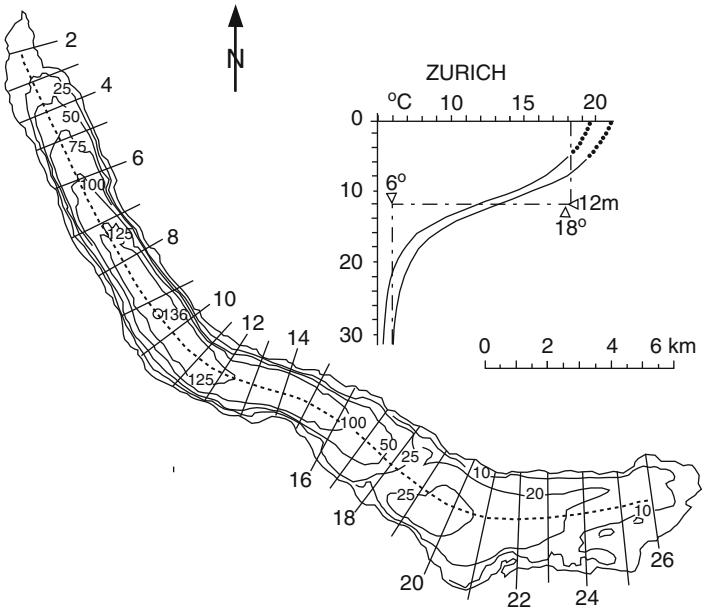

Fig. 22.3 Bathymetric chart of Lake Zurich with depth contours in meters and the interface thalweg line of length 27.2 km shown *dotted*. Indicated are also cross-sections 2–26 for which the epi- and hypolimnion areas were determined on the basis of the lake's bathymetry for the TDP. The temperature profiles mark the envelope of average profiles at 11 moorings in August–September 1978, from [17]. © Am. Soc. Limnol. and Oceanogr., reproduced with permission

spectral analyses (reported in [11]), in which the square roots of spectral peak heights (proportional to amplitude estimated for the first two modes only) were normalized relative to 100 cm s^{-1} at mooring 5 (for currents) and were entered, with attention to sign, in Fig. 22.4. The agreement between those approximate estimates and the model results for first mode elevation is good, perhaps surprisingly so, when one recalls that temperature fluctuations at each mooring (the basis for the spectra) are proportional to isotherm depth fluctuations only if the vertical temperature gradient is the same at each sensor. The agreement for second mode elevation and first mode current is not close' [17].

Lemmin and Mortimer [17] did apply Kelvin wave dynamics in the Lake Geneva internal mode analysis. This lake is the broadest of their eight examples for which the influence of the Earth's rotation is considerable. Following Defant [8] they calculate the resulting transverse tilt in each cross-section on the basis that it is linear and proportional and changing with the difference in section averaged current speed in the upper and lower layer. They find in this case that the interface-elevation maximum for the first mode progresses counterclockwise around the basin once in the corresponding seiche period. They also concede that this linear slope of the thermocline is 'hardly acceptable'. Below it will be shown that the selection of the thalweg as a reference is more critical in a model which does not allow various transverse modalities to be incorporated.

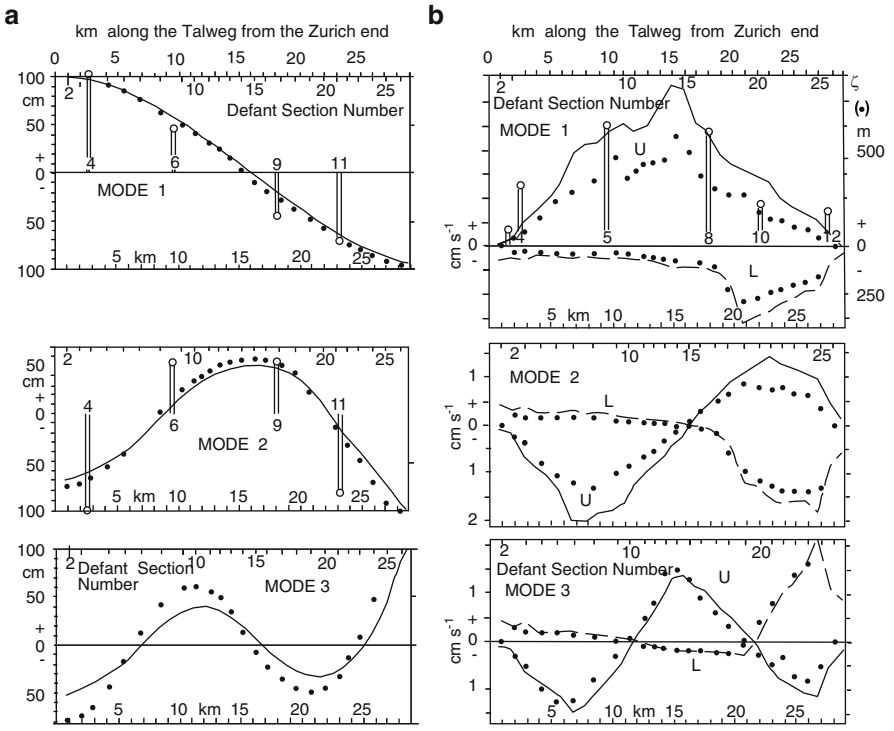

Fig. 22.4 Lake Zurich. Prediction by the TDP (*dots*) compared with those (*lines*) by Schwab's two dimensional model (in [11]). (**a**) Along thalweg interface elevations ζ_i for modes 1–3, normalized in each case to 100-cm maximum. (**b**) Horizontal displacements ξ and maximum current speeds u for modes 1–3 in the upper and lower layers, U and L. The current speed maxima occur $\frac{1}{4}$ cycle after the maximum elevations shown in panel (**a**). Periods are given in Table 22.1. *Vertical double lines* in panel (**a**) are approximate estimates of relative 'observed' interface elevation at four moorings spaced along the thalweg (modes 1 and 2, normalized to 100 cm at mooring 4) derived from spectra of temperature fluctuations at thermocline depth (as described by Horn et al. [11]). Corresponding estimates in panel (**b**) (first mode only, normalized to 2.5 cm s^{-1} at mooring 5, are for current speed derived from current spectra, from [17]. © Am. Soc. Limnol. and Oceanogr., reproduced with permission

Table 22.1 Periods of stratified Lake Zurich for the baroclinic modes of two layer models using the Defant integration procedure (TDP) of the two-layer equivalent depth (TED)-channel model and the two-dimensional two-layer variable depth (TVD) model and as measured in the August–September 1978 field campaign with sources stated in the last column

	Periods [h]			
	Mode	Mode 2	Mode 3	Source
TDP	40.3	21.3	15.2	[17]
TED	44.8	23.8	17.1	[13]
Measured	44.0	25.0	17.0	[11, 13, 21]

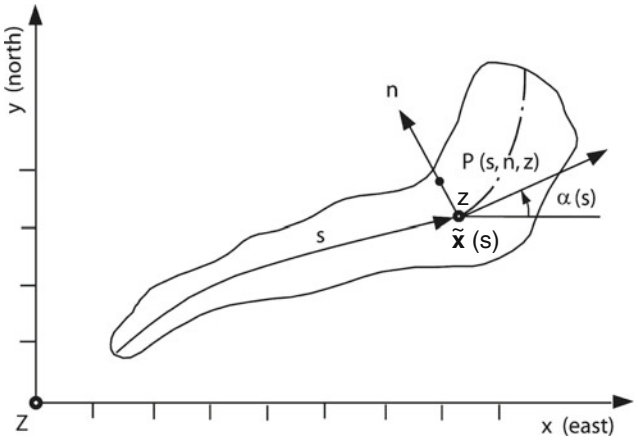

Fig. 22.5 Definition of the (s, n, z) coordinate system

22.3 Extended Channel Models: Governing Equations

In the remainder of this chapter, we shall restrict considerations to homogeneous elongated lakes. In particular, we shall be concerned with the dynamics of an incompressible fluid with free surface in a steady rotating basin. More general situations can also be handled, but are not dealt with here for reasons of avoiding arithmetic complexities. We follow closely Raggio and Hutter [26–28]. In addition, we shall restrict the analysis to linear processes in which displacements and velocities are small.

Let Ω denote the domain of the lake and $\partial\Omega$ its boundary consisting of the free surface $\partial\Omega_\sigma$ and the bottom boundary $\partial\Omega_n$. A first step in deducing a hierarchy of equations for barotropic motions is the presentation of the dynamical equations of balances of mass and linear momentum in a curvilinear coordinate system. Thus, we select within the undisturbed lake surface a curved lake axis and complement this axis by two other axes, one horizontal and one vertical, see Fig. 22.5. There is some element of subjectivity in the selection of the long axis; it may follow the projection of the thalweg of the lake into the horizontal plane, or may (roughly) equally divide the lake width, measured perpendicular to the axis. Beyond this choice, however, there will be no other subjective steps in the derivation of the model equations. The curve parameter on the axis is denoted by s, the coordinate, measured horizontally by n and that on the vertical axis by z, which is positive upwards (counter gravity).

Let $\boldsymbol{x}$ be a point in $\mathbb{R}^3$; referred to a Cartesian basis $\{\boldsymbol{i}, \boldsymbol{j}, \boldsymbol{k}\}$ it possesses the components (x, y, z). Let, moreover, $\boldsymbol{x} = \tilde{\boldsymbol{x}}(s)$ describe the lake axis. A point $\boldsymbol{x}$, which is sufficiently close to the lake axis (it will soon become clear how close this must be) can then uniquely be defined as (see Fig. 22.5)

$$\boldsymbol{x} = \tilde{\boldsymbol{x}}(s) - n\sin(\alpha), \quad \boldsymbol{y} = \tilde{\boldsymbol{y}}(s) + n\cos(\alpha), \quad z = z, \tag{22.39}$$

where

$$\tan(\alpha) = \frac{\mathrm{d}\tilde{y}/\mathrm{d}s}{\mathrm{d}\tilde{x}/\mathrm{d}s} \tag{22.40}$$

and α is the 'slope angle' of the lake axis relative to the $\boldsymbol{i}$-direction. The expression

$$K(s) = \frac{\mathrm{d}\alpha}{\mathrm{d}s} = \tilde{y}''\tilde{x}' - \tilde{x}''\tilde{y}' \tag{22.41}$$

is the local curvature and

$$\begin{aligned} \boldsymbol{g}_1 &= \boldsymbol{g}_s = \left(\frac{\mathrm{d}\,\tilde{\boldsymbol{x}}}{\mathrm{d}\,s} - Kn\cos(\alpha), \frac{\mathrm{d}\,\tilde{\boldsymbol{y}}}{\mathrm{d}\,s} - Kn\sin(\alpha), 0\right), \\ \boldsymbol{g}_2 &= \boldsymbol{g}_n = (-\sin(\alpha), \cos(\alpha), 0), \\ \boldsymbol{g}_3 &= \boldsymbol{g}_z = (0,0,1) \end{aligned} \tag{22.42}$$

are the *natural* base vectors from which via

$$g_{ij} = \boldsymbol{g}_i \cdot \boldsymbol{g}_j = \begin{pmatrix} (1-Kn)^2 & 0 & 0 \\ 0 & 1 & 0 \\ 0 & 0 & 1 \end{pmatrix} \tag{22.43}$$

the metric tensor ensues. Its Jacobian J is given by

$$J^2 := g := \det(g_{ij}) = (1 - K(s)n)^2. \tag{22.44}$$

Thus, the curvilinear coordinates can describe a point in space uniquely, as long as J does not change sign. This restricts points to regions where $n \leq 1/K(s)$ and constrains lake regions to points for which $|n| < 1/K(s)$ for all $s \in [s_0, s_1]$, where s_0 and s_1 identify the two long lake ends. This condition also defines the slenderness for which the above curvilinear coordinate setting is meaningful.

It is customary in applications to problems of physics not to express vectors and tensors in terms of the natural basis vectors $\{\boldsymbol{g}_i, i = 1,2,3\}$, but in terms of the orthonormal basis

$$\boldsymbol{e}_i := \frac{\boldsymbol{g}_i}{||\boldsymbol{g}_i||}, \quad \text{(no summation over } i\text{)} \quad ||\boldsymbol{e}_i|| = 1. \tag{22.45}$$

So, if $\boldsymbol{a}$ is a vector, then one has the two representations

$$\boldsymbol{a} = a_j^{(n)} \boldsymbol{g}_j = a_j \boldsymbol{e}_j, \tag{22.46}$$

where summation is understood over doubly repeated indices; $a_j^{(n)} (j = 1,2,3)$ are called the *natural* components, whereas $a_j (j = 1,2,3)$ are the *physical* components of the vector $\boldsymbol{a}$ referred to the curvilinear orthonormal basis $\{\boldsymbol{e}_1, \boldsymbol{e}_2, \boldsymbol{e}_3\}$.

In the ensuing analysis the balance laws of mass and linear momentum are the necessary basic laws of concern. They will be written below in their point (=local) forms for a density preserving (incompressible) fluid in the curvilinear coordinates introduced above. They can be shown to take the forms:

- Balance of mass

$$\frac{1}{J}\frac{\partial v_s}{\partial s}+\frac{\partial v_s}{\partial n}+\frac{\partial v_s}{\partial z}-\frac{K}{J}v_n=0, \tag{22.47}$$

- Balances of linear momentum

$$\begin{aligned}
&\rho\left[\frac{\partial v_s}{\partial t}+\frac{v_s}{J}\frac{\partial v_s}{\partial s}+v_n\frac{\partial v_s}{\partial n}+v_z\frac{\partial v_s}{\partial z}-\frac{K}{J}v_sv_n\right]+\frac{1}{J}\frac{\partial p}{\partial s}-\rho f v_n\\
&\quad-\left(\frac{1}{J}\frac{\partial T^E_{ss}}{\partial s}+\frac{\partial T^E_{sn}}{\partial n}+\frac{\partial T^E_{sz}}{\partial z}\right)+\frac{K}{J}\left(\frac{K'n^2}{J}T^E_{ss}+2T^E_{sn}\right)=0,\\
&\rho\left[\frac{\partial v_n}{\partial t}+\frac{v_s}{J}\frac{\partial v_n}{\partial s}+v_n\frac{\partial v_n}{\partial n}+v_z\frac{\partial v_n}{\partial z}+\frac{K}{J}v_s^2\right]+\frac{\partial p}{\partial n}+\rho f v_s\\
&\quad-\left(\frac{1}{J}\frac{\partial T^E_{sn}}{\partial s}+\frac{\partial T^E_{nn}}{\partial n}+\frac{\partial T^E_{nz}}{\partial z}\right)+\frac{K}{J}\left(J^2T^E_{ss}-T^E_{nn}\right)=0,\\
&\rho\left[\frac{\partial v_z}{\partial t}+\frac{v_s}{J}\frac{\partial v_z}{\partial s}+v_n\frac{\partial v_z}{\partial n}+v_z\frac{\partial v_z}{\partial z}\right]+\frac{\partial p}{\partial z}+\rho g\\
&\quad-\left(\frac{1}{J}\frac{\partial T^E_{sz}}{\partial s}+\frac{\partial T^E_{nz}}{\partial n}+\frac{\partial T^E_{zz}}{\partial z}\right)+\frac{K}{J}T^E_{nz}=0.
\end{aligned} \tag{22.48}$$

Equation (22.47) is a statement for a scalar quantity, and (22.48) represents the three physical components of Newton's law in the s-, n- and z-directions, respectively. Notation is rather self-evident: $\rho, \boldsymbol{v}, p, \boldsymbol{T}^E$ and g are the density, velocity, pressure, Cauchy stress deviator (the extra stress tensor) and the gravity constant; K is the curvature, $K' := \mathrm{d}K/\mathrm{d}s$ its derivative with respect to s and f the (first) Coriolis parameter. We do not present a detailed derivation of (22.47) and (22.48), since this is standard; the interested reader may consult Raggio [24].

Equations (22.47) and (22.48), must be complemented by phenomenological statements for the extra stress $\boldsymbol{T}^E$, which enters the equations, if viscous or turbulent effects are significant. In the general theory, we shall leave $\boldsymbol{T}^E$ unspecified and choose $\boldsymbol{T}^E = \boldsymbol{0}$ when an ideal fluid is in focus.

To solve the field equations, *boundary* and *initial* conditions must be prescribed. As for boundary conditions, kinematic and dynamic conditions apply. Let

$$F := \begin{cases} \hat{\zeta}(s,n,t)-z=0, & \text{on } \partial\Omega_\sigma,\\ H(s,n)-z=0, & \text{on } \partial\Omega_n \end{cases} \tag{22.49}$$

describe the free and basal surfaces, respectively; we have chosen the hat to identify functions only defined on the free surface. With the wind traction components in

the s- and n-directions, t_s^*, t_n^*, and the atmospheric pressure p_{atm} the kinematic and dynamic boundary conditions on $\partial\Omega_\sigma$ read

$$\frac{\partial\hat{\xi}}{\partial t}+\frac{1}{J}\frac{\partial\hat{\xi}}{\partial s}v_s+\frac{\partial\hat{\xi}}{\partial n}v_n-v_r=0, \tag{22.50}$$

$$\begin{aligned}
&\frac{1}{J}(-p+T_{ss}^E)\frac{\partial\hat{\xi}}{\partial s}+T_{sn}^E\frac{\partial\hat{\xi}}{\partial n}-T_{sz}^E=-t_s^*l_\xi,\\
&\frac{1}{J}T_{sn}^E\frac{\partial\hat{\xi}}{\partial s}+(-p+T_{nn}^E)\frac{\partial\hat{\xi}}{\partial n}-T_{nz}^E=-t_n^*l_\xi,
\end{aligned} \tag{22.51}$$

$$\frac{1}{J}T_{sz}^E\frac{\partial\hat{\xi}}{\partial s}+T_{zn}^E\frac{\partial\hat{\xi}}{\partial n}-(-p+T_{zz}^E)=+p_{\mathrm{atm}}^*l_\xi,$$

at $z=\hat{\xi}(s,n,t)$ with

$$l_\xi\equiv\left[1+\frac{1}{J^2}\left(\frac{\partial\hat{\xi}}{\partial s}\right)^2+\left(\frac{\partial\hat{\xi}}{\partial n}\right)^2\right]^{1/2}=1+\mathcal{O}(\hat{\xi}^2). \tag{22.52}$$

Equation (22.50) expresses the fact that $\partial\Omega_\sigma$ is material, and (22.52) are the three components expressing continuity of the surface traction.

At the bottom boundary, the kinematic condition $(22.49)_2$ and a viscous sliding law imply the relations

$$0=\frac{1}{J}\frac{\partial H}{\partial s}v_s+\frac{\partial H}{\partial n}v_n-v_z, \tag{22.53}$$

$$\begin{aligned}
v_s&=-\frac{R}{l_H}\left\{\frac{1}{J}T_{ss}^*\frac{\partial H}{\partial s}+T_{sn}^*\frac{\partial H}{\partial n}-T_{sz}^*\right\},\\
v_n&=-\frac{R}{l_H}\left\{\frac{1}{J}T_{sn}^*\frac{\partial H}{\partial s}+T_{nn}^*\frac{\partial H}{\partial n}-T_{nz}^*\right\},\\
v_z&=-\frac{R}{l_H}\left\{\frac{1}{J}T_{sz}^*\frac{\partial H}{\partial s}+T_{zn}^*\frac{\partial H}{\partial n}-T_{zz}^*\right\},
\end{aligned} \tag{22.54}$$

at $z=H(s,n)$, in which

$$\boldsymbol{T}^*=\boldsymbol{T}^E-(\boldsymbol{n}\cdot\boldsymbol{T}^E\boldsymbol{n})\boldsymbol{I},\quad l_H=\left[1+\frac{1}{J^2}\left(\frac{\partial H}{\partial s}\right)^2+\left(\frac{\partial H}{\partial n}\right)^2\right]^{1/2}. \tag{22.55}$$

Here, $\boldsymbol{n}$ is the unit normal vector pointing into the exterior of the lake region and R is a friction coefficient, which may depend on bed roughness, tangential and normal tractions, etc. The boundary condition includes with $R=0$ the no-slip condition and automatically satisfies the kinematic condition $\boldsymbol{v}\cdot\boldsymbol{n}=0$. $R\to\infty$ necessarily

requires $\boldsymbol{T}^E = \mathbf{0}$; so, a viscous sliding law at the bottom can, strictly, only be introduced if the extra stress tensor does not identically vanish. A similar remark also holds for wind stress, as can be seen from (22.52). Finally, (22.50)–(22.55) have been written down in the curvilinear coordinates, details of which are given in [24].

A complete formulation also requires *initial conditions* for the fields $\boldsymbol{v}$ and ζ. These are stated as

$$\boldsymbol{v} = \boldsymbol{v}^{**}(s, n, z), \qquad \zeta = \zeta^{**}(s, n). \tag{22.56}$$

The functions $\boldsymbol{v}^{**}(s, n, z)$ and $\zeta^{**}(s, n)$ are not arbitrary as they should conform with the balance laws and boundary conditions. As the equations are written for a density preserving material, the initial velocity field must also be solenoidal, $\operatorname{div}(\boldsymbol{v}^{**}) = 0$. The trivial fields $\boldsymbol{v}^{**} \equiv \mathbf{0}$, $\zeta^{**} \equiv 0$ satisfy all these requirements automatically.

22.4 Method of Weighted Residuals

The purpose of a one-dimensional model, which replaces the three-dimensional model, is to obtain a computationally more easily accessible description of the processes in a physical system than the full two-dimensional or three-dimensional original problem. Scientists, however, take different attitudes to view such lower dimensional problems. On the one hand, one regards the lower dimensional equations as a physical model, which explicitly takes into account the slenderness of the bodies. The dimensionally reduced set of evolution equations are then manifestations of a structurally more complex material system at the lower spatial dimension than the original problem. On the other hand, one regards the lower dimensional formulation as a numerical approximation technique, in which the eliminated space variables are accounted for by function expansions. Both approaches are embedded in the more general Principle or *MWR*.

Technically, the MWR is based on a complex version of the following simple

Fundamental Theorem of Weighted Residuals: *Let $f(x)$ be a function or a functional and assume that*

$$f(x) = 0, \quad \forall x \in \mathcal{I} = [a, b]. \tag{22.57}$$

So, $f(x)$ is simply the zero function in $\mathcal{I}$. Given any non-vanishing function $g(x)$, it is a trivial fact that (22.57) also implies

$$\int_a^b f(x)g(x)\mathrm{d}x = 0, \qquad \forall x \in \mathcal{I}. \tag{22.58}$$

Conversely, assume now that (22.58) holds for all $g(x)$ defined in $\mathcal{I}$. Then (22.58) implies (22.57). ■

Proof. The step $\Longrightarrow$ is trivial, nothing must be proved. The step $\Longleftarrow$ is more difficult, but since (22.58) holds for all g, we choose $g(x) = \delta(x - y)$, where δ is the Dirac-delta function. With this choice we obtain

$$\int_a^b f(x)\delta(x-y)\mathrm{d}x = f(y), \qquad \forall (x,y) \in \mathcal{I}. \tag{22.59}$$

□

The only, perhaps difficult point in this proof is the claim (22.59). It is proved in any elementary book on generalized functions; see also the following footnote.[5]

The MWR can be applied to almost any initial boundary value problems. The essential idea is as follows: Let $\boldsymbol{R}_\Omega = \boldsymbol{0}$ be the set of field equations defined over Ω and let $R_{\partial\Omega_\alpha} = 0$ $(\alpha = 1, 2, \ldots, \nu)$ be the associated boundary conditions, of which each holds at the part $\partial\Omega_\alpha$ of the total boundary. In the present context $\boldsymbol{R}_\Omega = \boldsymbol{0}$ stands for (22.47) and (22.48), written here in vector form; moreover, with $\nu = 2$, $\partial\Omega_1 = \partial\Omega_\sigma$, $\partial\Omega_2 = \partial\Omega_n$, the statement $\boldsymbol{R}_{\partial\Omega_\alpha} = \boldsymbol{0}$ represents (22.50)–(22.55). Note also that the number of components in $\boldsymbol{R}_\Omega$ and $\boldsymbol{R}_{\partial\Omega_\alpha}$ need not be the same, and the domains of their definition are different, which explains the use of the subscripts). $\boldsymbol{R}_\Omega$ and $\boldsymbol{R}_{\partial\Omega}$ both are now elements of functions which play the role of $f(x)$ in the simple example in (22.57) of the fundamental theorem.

Next, corresponding functions g must be selected. It is customary to use a prefix δ as identifier for weighting functions and to call these functions $\delta\boldsymbol{w}_\Omega$ and $\delta\boldsymbol{w}_{\partial\Omega_\alpha}$, respectively. We form the scalar products,

$$\boldsymbol{R}_\Omega \cdot \delta\boldsymbol{w}_\Omega \quad \text{and} \quad \boldsymbol{R}_{\partial\Omega_\alpha} \cdot \delta\boldsymbol{w}_{\partial\Omega_\alpha}, \tag{22.60}$$

and then integrate these over the domains of their definition and add all these integrals. Upon this addition one obtains

$$\delta I = \int_\Omega \boldsymbol{R}_\Omega \cdot \delta\boldsymbol{w}_\Omega \mathrm{d}\Omega + \sum_\alpha \int_{\partial\Omega_\alpha} \boldsymbol{R}_{\partial\Omega_\alpha} \cdot \delta\boldsymbol{w}_{\partial\Omega_\alpha} \mathrm{d}(\partial\Omega_\alpha). \tag{22.61}$$

[5] A plausible choice for g would be

$$g = \begin{cases} 0, & |x-y| > \varepsilon/2, \\ 1/\varepsilon, & |x-y| < \varepsilon/2. \end{cases}$$

With this choice we obtain

$$\int_{y-\varepsilon/2}^{y+\varepsilon/2} f(x)\frac{1}{\varepsilon}\mathrm{d}x = f(y) + \mathcal{O}(\varepsilon^2) \underbrace{\longrightarrow}_{\varepsilon \to 0} f(y).$$

.

The MWR now requests that

$$\delta I = 0, \qquad \forall \{\delta \boldsymbol{w}_{\Omega}, \delta \boldsymbol{w}_{\partial\Omega_\alpha}\}. \tag{22.62}$$

Mathematicians call this the weak form of the original boundary value problem. In the above, the δ-symbol was used as a reminder that the weighting functions are arbitrary; however, the quantity I by itself is not defined in general. Furthermore, the two dots '$\cdot$' in the integrals (22.61) represent inner products, but over different function spaces.

Problem 22.1 *By making the selections*

$$(a) \quad \delta \boldsymbol{w}_{\Omega} \neq \boldsymbol{0}, \quad \delta \boldsymbol{w}_{\partial\Omega_\alpha} = \boldsymbol{0},$$

$$(b) \quad \delta \boldsymbol{w}_{\Omega} = \boldsymbol{0}, \quad \delta \boldsymbol{w}_{\partial\Omega_\alpha} \neq \boldsymbol{0},$$

the reader may show that using the fundamental theorem, (22.62) implies

$$(a) \quad \boldsymbol{R}_{\Omega} = \boldsymbol{0}, \quad (b) \quad \boldsymbol{R}_{\partial\Omega_\alpha} = 0, \quad \forall \alpha. \qquad \blacklozenge$$

From now on, we are primarily involved with judicious manipulations of (22.62). This equation will now be the basis for the approximation to deduce the spatially one-dimensional model.

The field equations $\boldsymbol{R}_{\Omega} = \boldsymbol{0}$ and boundary conditions $\boldsymbol{R}_{\partial\Omega_\alpha} = \boldsymbol{0}$ contain a set of independent variables (e.g. velocities). Let us collectively denote these variables by $\mathfrak{x}$. These variables and the weighting functions $\delta \boldsymbol{w}_{\Omega}, \delta \boldsymbol{w}_{\partial\Omega_\alpha}$, henceforth collectively denoted by $\delta \boldsymbol{w}$, are functions of the spatial coordinates and of time, in this case s, n, z, t. In an attempt to deduce a spatially one-dimensional set of equations these functions are now product decomposed as

$$\begin{aligned} \mathfrak{x} &= \sum_{i=1}^{N} \phi_i \mathfrak{x}_i = \boldsymbol{\phi} \cdot \mathfrak{x}, & \delta \boldsymbol{w} &= \sum_{i=1}^{N} \psi_i \delta \mathsf{w}_i = \boldsymbol{\psi} \cdot \delta \mathbf{w}, \\ \mathfrak{x}(s,n,z,t) &= \boldsymbol{\phi}(n,z) \cdot \mathfrak{x}(s,t), & \delta \boldsymbol{w}(s,n,z,t) &= \boldsymbol{\psi}(n,z) \cdot \delta \mathbf{w}(s,t), \end{aligned} \tag{22.63}$$

where ϕ_i and ψ_i generate sets of linearly independent known functions, called *shape, basis* or *trial functions*, and the $\mathfrak{x}_i$ and $\delta \mathsf{w}_i$ constitute sets of unknown ($\mathfrak{x}_i$) and arbitrary ($\delta \mathsf{w}_i$) functions. The shape functions, $\boldsymbol{\phi}$ and $\boldsymbol{\psi}$, are chosen to depend on those spatial variables – here n, z – which one wishes to eliminate in the process of construction of the lower-dimensional model equations. The sets $\boldsymbol{\phi}$ and $\boldsymbol{\psi}$ may be constructed from products of polynomials, trigonometric functions or other appropriate functions of a complete function set; in principle they could also vary with s without violation of the general developments, but here this will not be pursued. Furthermore, one may choose $\boldsymbol{\phi} = \boldsymbol{\psi}$, which corresponds to a Galerkin procedure.

If the representations (22.63) are substituted into (22.61) and (22.62), then integrations over Ω and $\partial\Omega_\alpha$ can be split into cross-sectional integrals over the

coordinates n, z, followed by an integration along the axis. Because $\boldsymbol{\phi}$ and $\boldsymbol{\psi}$ are known, integrations over n and z can be performed explicitly. Structurally, (22.62) then takes the form

$$\delta I = \int_{s_1}^{s_2} \langle \mathbf{A}(\mathfrak{x}), \delta \mathbf{w} \rangle \mathrm{d}s = 0, \tag{22.64}$$

in which $\langle\ ,\ \rangle$ is a bilinear form, and integration is along the lake axis from $s = s_1$ to $s = s_2$. Since $\delta \mathbf{w}$ is arbitrary, (22.64) implies, in view of the fundamental theorem of the MWR,

$$\mathbf{A}(\mathfrak{x}(s,t)) = \mathbf{0}, \tag{22.65}$$

which is the approximate set of spatially one-dimensional equations. In view of the truncation N of the product decomposition of (22.63) equation $\mathbf{A}(s,t) = \mathbf{0}$ forms N evolution equations (partial differential equations in s and t). Different values of N define different orders of approximations of the model. Technically, in the process of construction of (22.64) certain volume integrals may be transformed to surface integrals using Green's theorem, but physical arguments must suggest which of the global representations should be regarded as the appropriate ones. This difficulty will further be explained below.

Specifically, application of the above MWR-procedure to the initial value problem in Sect. 22.2, the field equations (22.47) and (22.48) and boundary equations (22.50)–(22.55) are scalarly multiplied with weighting functions, which we select as follows:

$\delta\lambda_1$ for mass balance equation, $\delta \boldsymbol{v}_1$ for momentum balance equation,	in Ω
$\delta\lambda_2$ for kinematic boundary condition at the free surface, $\delta \boldsymbol{v}_2$ for the stress boundary condition at the free surface,	on $\partial\Omega_\sigma$
$\delta\lambda_3$ for the kinematic boundary condition at the basal surface, $\delta \boldsymbol{v}_3$ for the basal sliding law,	on $\partial\Omega_n$.

In symbolic notation we thus have

$$\sum_{\alpha=1}^{6} \delta I_\alpha = 0, \tag{22.66}$$

with

$$\begin{aligned} \delta I_1 &= \int_{t_1}^{t_2} \mathrm{d}t \iiint_\Omega \mathrm{div}\boldsymbol{v}\,\delta\lambda_1 \mathrm{d}V, \\ \delta I_2 &= \int_{t_1}^{t_2} \mathrm{d}t \iiint_\Omega \left\{ \rho \frac{\mathrm{d}\boldsymbol{v}}{\mathrm{d}t} + \mathrm{grad}\, p - \mathrm{div}\, \boldsymbol{T}^E - \rho \boldsymbol{f} \right\} \cdot \delta \boldsymbol{v}_1 \mathrm{d}V, \end{aligned} \tag{22.67}_1$$

$$\delta I_3 = \int_{t_1}^{t_2} \mathrm{d}t \iint_{\partial\Omega_\sigma} \left\{ \frac{\partial F_\zeta}{\partial t} + \mathrm{grad}\, F_\zeta \cdot \boldsymbol{v} \right\} \delta\lambda_2 \mathrm{d}a,$$

$$\delta I_4 = \int_{t_1}^{t_2} \mathrm{d}t \iint_{\partial\Omega_\sigma} \{(-p\mathbf{1} + \boldsymbol{T}^E)\boldsymbol{n} - \boldsymbol{t}^*\} \cdot \delta\boldsymbol{v}_2 \mathrm{d}a, \qquad (22.67)_2$$

$$\delta I_5 = \int_{t_1}^{t_2} \mathrm{d}t \iint_{\partial\Omega_n} \frac{\mathrm{grad}\, F_H}{||\mathrm{grad}\, F_H||} \cdot \boldsymbol{v}\delta\lambda_3 \mathrm{d}a,$$

$$\delta I_6 = \int_{t_1}^{t_2} \mathrm{d}t \iint_{\partial\Omega_n} \left\{ \boldsymbol{T}^*\boldsymbol{n} + \frac{1}{R}\boldsymbol{v} \right\} \cdot \delta\boldsymbol{v}_3 \mathrm{d}a,$$

where $\mathrm{d}V$ is a volume element in the domain Ω, and $\mathrm{d}a$ a surface element on the surface Ω. Integrations over time from $t_1 \le t \le t_2$ arise because our physical problem is an initial boundary value problem. Conceptually, these time integrations are important. In actual calculations they do not play a role, however, and will henceforth be omitted.

22.5 Derivation of a Hierarchy of Channel Equations for Barotropic Motions in Lakes

To derive the spatially one-dimensional model for water motion in rotating basins a shape function expansion, is selected, in which the dimensions of $\boldsymbol{\phi}$ and $\boldsymbol{\psi}$ are chosen to coincide (same values of N!); this is necessary to yield a determinate system. With the same shape function for each variable and each weighting function, we thus may write

$$\begin{aligned}
(v_s, v_n, v_z) &= \boldsymbol{\phi} \cdot (\mathbf{v}_s, \mathbf{v}_n, \mathbf{v}_z), \\
\hat{\zeta} &= \hat{\boldsymbol{\phi}} \cdot \boldsymbol{\zeta}, \\
(\delta v_s, \delta v_n, \delta v_z, \delta\lambda_1) &= \boldsymbol{\psi} \cdot (\delta\mathbf{v}_s, \delta\mathbf{v}_n, \delta\mathbf{v}_z, \delta\boldsymbol{\lambda}_1) \\
(\delta\lambda_2, \delta\lambda_3) &= \hat{\boldsymbol{\psi}} \cdot (\delta\boldsymbol{\lambda}_2, \delta\boldsymbol{\lambda}_3)
\end{aligned} \qquad (22.68)$$

with $\boldsymbol{\phi} = \boldsymbol{\phi}(n, z)$, $\boldsymbol{\psi} = \boldsymbol{\psi}(n, z)$, $\hat{\boldsymbol{\phi}} = \hat{\boldsymbol{\phi}}(n)$ and $\hat{\boldsymbol{\psi}} = \hat{\boldsymbol{\psi}}(n)$.[6]

[6] We use in (22.68) the dot to denote the scalar (inner) product between two vectors in $\mathbb{R}^N$. An alternative 'matrix-vector notation' is $\boldsymbol{\phi}^{\mathrm{T}}\mathbf{v}_s, \ldots$, where $\boldsymbol{\phi}^{\mathrm{T}}$ is the transpose of $\boldsymbol{\phi}$. We shall not use this second variant.

22.5.1 Mass Balance

By way of illustration, let us begin by transforming δI_1 into a form suitable for a one-dimensional description of the water motion. The steps of computations are shown in the following chain of identities:

$$\begin{aligned}
\delta I_1 &= \int_{t_1}^{t_2} \mathrm{d}t \iiint_{\Omega} \mathrm{div}\boldsymbol{v}\delta\lambda_1 \mathrm{d}V = \int_{t_1}^{t_2} \mathrm{d}t \int_{s_0}^{s_1} \mathrm{d}s \iint_{Q} \mathrm{div}\,\boldsymbol{v}\delta\lambda_1 J\,\mathrm{d}n\mathrm{d}z \\
&= \int_{t_1}^{t_2} \mathrm{d}t \int_{s_0}^{s_1} \mathrm{d}s \iint_{Q} \delta\boldsymbol{\lambda}_1 \cdot \boldsymbol{\psi} \left\{ \frac{1}{J}\frac{\partial v_s}{\partial s} + \frac{\partial v_n}{\partial n} + \frac{\partial v_z}{\partial z} - \frac{K}{J} v_n \right\} J\,\mathrm{d}n\mathrm{d}z \\
&= \int_{t_1}^{t_2} \mathrm{d}t \int_{s_0}^{s_1} \mathrm{d}s\delta\boldsymbol{\lambda}_1 \cdot \left\{ \iint_{Q} \boldsymbol{\psi} \otimes \boldsymbol{\phi}\,\mathrm{d}n\mathrm{d}z \frac{\partial \mathbf{v}_s}{\partial s} \right. \\
&\quad + \left[\iint_{Q} \boldsymbol{\psi} \otimes \boldsymbol{\phi}_{,n} J\,\mathrm{d}n\mathrm{d}z - K \iint_{Q} \boldsymbol{\psi} \otimes \boldsymbol{\phi}\,\mathrm{d}n\mathrm{d}z \right] \mathbf{v}_n \\
&\quad \left. + \iint_{Q} \boldsymbol{\psi} \otimes \boldsymbol{\phi}_{,z} J\,\mathrm{d}n\mathrm{d}z\,\mathbf{v}_z \right\} = 0.
\end{aligned} \tag{22.69}$$

Here, $\otimes$ is the exterior product: $(\boldsymbol{\psi} \otimes \boldsymbol{\phi})_{ij} = \psi_i \phi_j$ for all $i, j = 1, 2, \ldots, N$ and $\boldsymbol{\phi}_{,n} = \partial\boldsymbol{\phi}/\partial n$, and $\boldsymbol{\phi}_{,z} = \partial\boldsymbol{\phi}/\partial z$. In the first line of (22.69), the volume integral is split into integrations over the cross-section Q and along the lake axis. This is achieved by writing $\mathrm{d}V = J\mathrm{d}s\mathrm{d}n\mathrm{d}z$. In the second line the divergence operator, expressed in the curvilinear coordinates of Sect. 22.3 is substituted and the weighting function $\delta\lambda_1 = \delta\boldsymbol{\lambda}_1 \cdot \boldsymbol{\psi}$ is expressed in terms of a truncated shape function expansion. An analogous expansion is subsequently used for v_s, v_n, v_z by writing $v_s = \boldsymbol{\phi} \cdot \mathbf{v}_s$, etc. Observe that the cross-sectional integrals are all done over integrand functions which are known functions. It is therefore easy to see that (22.69) can be written as

$$\delta I_1 = \int_{t_1}^{t_2} \mathrm{d}t \int_{s_0}^{s_1} \mathrm{d}s\delta\boldsymbol{\lambda}_1 \cdot \left\{ \mathbf{C}^{(0)} \frac{\partial \mathbf{v}_s}{\partial s} + (\mathbf{C}^{(1)}_{\phi_n} - K\mathbf{C}^{(0)}\mathbf{v}_n - \mathbf{C}^{(1)}_{\phi_z}\mathbf{v}_z \right\}, \tag{22.70}$$

where the easily identifiable coefficient matrices are collectively given in Appendix 22.A. If we were to require that $\delta I_1 = 0$, which is mathematically a possible choice (prove this!) one could conclude, by employing the principal theorem of the MWR that the expression in braces should vanish. However, even though such an assignment is mathematically correct, it does not yield the global physical mass balance.

Remedy can be found by recalling that, when integrating the continuity equation for a density preserving fluid over depth, boundary terms enter through the application of Leibniz' rule in interchanging differentiations and integrations; these boundary terms can be simplified with the aid of the kinematic boundary conditions, see e.g. the derivation of (11.12) in Chap. 11.

Inspection of (22.66) and (22.67) shows that $\delta I_1, \delta I_3$ and δI_5 represent the balance law of mass in Ω and the kinematic boundary conditions on $\partial\Omega_\sigma$ and $\partial\Omega_n$, respectively. It is, therefore, tempting to try the combination $\delta(I_1 + I_3 + I_5)$ and to set

$$\delta I_1 + \delta I_3 + \delta I_5 = 0. \tag{22.71}$$

It is a straightforward exercise to demonstrate that admissible weighting functions do indeed exist, which reduce (22.66) to (22.71). Evaluation of (22.71) follows computations analogous to those performed in (22.70); they are, however, more difficult. In order not to distract the reader from the main ideas, this calculation is relegated to Appendix 22.B. Here, we state the result which follows from (22.71):

$$\hat{\mathbf{Z}}^{(1)} \frac{\partial \boldsymbol{\zeta}}{\partial t} + \frac{\partial}{\partial s}\left(\mathbf{C}^{(0)}\mathbf{v}_s\right) - \mathbf{C}^{(1)}_{\psi_n}\mathbf{v}_n - \mathbf{C}^{(1)}_{\psi_z}\mathbf{v}_z = \mathbf{0}, \tag{22.72}$$

where the coefficient matrices are defined in Appendix 22.A. This equation, indeed, resembles the structure of a kinematic equation, but it is a statement concerning vectors of the shape function expansion of the velocity field; and it also involves the vertical velocity component through $\mathbf{v}_z$. This entails the derivation of a set of equations for $\mathbf{v}_z$ in terms of $\mathbf{v}_s$ and $\mathbf{v}_n$. In the classical linear formulations the vertical velocity does not arise.[7]

The missing equation is obtained from the requirement $\delta I_5 = 0$ in (22.65). A selection of weighting functions for $\sum_{\alpha=1}^{6} \delta I_\alpha = 0$ in (22.67) which yields $\delta I_5 = 0$ is permissible and implies the statement

$$\begin{aligned}
&\int_{\partial\Omega_n} \frac{\operatorname{grad} F_H}{||\operatorname{grad} F_H||} \cdot \boldsymbol{v}\, \delta\lambda_3 \mathrm{d}a \\
&= \int_{\partial\Omega_n} \left(\frac{1}{J}\frac{\partial H}{\partial s} v_s + \frac{\partial H}{\partial n} v_n - v_z\right) \delta\lambda_3 \frac{\mathrm{d}a}{l_H} \\
&= \int_{s_0}^{s_1} \mathrm{d}s \left\{ \int_{B-}^{B+} \frac{\partial H}{\partial s} v_s \mathrm{d}n + \int_{B-}^{B+} J \frac{\partial H}{\partial n} v_n \mathrm{d}n - \int_{B-}^{B+} J v_z \mathrm{d}n \right\}_{z=H} \delta\lambda_3 \\
&= \int_{s_0}^{s_1} \mathrm{d}s \delta\boldsymbol{\lambda}_3 \cdot \left\{ \int_{B-}^{B+} \frac{\partial H}{\partial s} \boldsymbol{\psi} \otimes \boldsymbol{\phi}\, \mathrm{d}n \mathbf{v}_s + \int_{B-}^{B+} J \frac{\partial H}{\partial n} \boldsymbol{\psi} \otimes \boldsymbol{\phi}\, \mathrm{d}n \mathbf{v}_n \right. \\
&\quad \left. - \int_{B-}^{B+} J \boldsymbol{\psi} \otimes \boldsymbol{\phi}\, \mathrm{d}n \mathbf{v}_z \right\}_{z=H} = 0,
\end{aligned} \tag{22.73}$$

or in view of the definitions in Appendix 22.A

$$\mathbf{H}^{(0)}_s \mathbf{v}_s + \mathbf{H}^{(1)}_n \mathbf{v}_n - \mathbf{H}^{(1)} \mathbf{v}_z = \mathbf{0}. \tag{22.74}$$

[7] We will see below that also the momentum equations in the s- and n-directions contain $\mathbf{v}_z$.

The basal surface equation $F_H = H(s,n) - z = 0$ leads to

$$\begin{aligned} \text{grad}\, F_H &= \left(\frac{1}{J}\frac{\partial H}{\partial s}, \frac{\partial H}{\partial n}, -1 \right) \\ ||\text{grad}\, F_H|| = l_H &:= \left\{ \frac{1}{J^2}\left(\frac{\partial H}{\partial s}\right)^2 + \left(\frac{\partial H}{\partial n}\right)^2 + 1 \right\}^{1/2} \end{aligned} \tag{22.75}$$

and explains the expression in the first line of (22.73). The formula for the basal surface increment

$$\mathrm{d}a = J l_H \, \mathrm{d}n\mathrm{d}s \tag{22.76}$$

then explains the second line of (22.73). This, via shape-function expansions of $\boldsymbol{v}$ and $\delta\lambda_3$, then leads to the remainder of (22.73). The various steps have transformed an integration over the basal surface into a succession of integrals over the width of the cross-section from $n = B^-$ to $n = B^+$ and over the channel axis. The result, (22.74), is an algebraic equation relating the velocity components.

22.5.2 Momentum Balance

The experience gained with the derivation of the global balance of mass, (22.71) makes one to suppose that global momentum balance cannot follow from a statement $\delta I_2 = 0$. Such a requirement will not incorporate the stress boundary condition at the free surface and the sliding condition at the base. It turns out that the combination

$$\delta I_2 + \delta I_4 + \delta I_6 = 0. \tag{22.77}$$

will generate the global form of the momentum balance. Computations analogous to those presented above will then generate the spatially one-dimensional equations representing balance of momentum. The detailed calculations are very lengthy and tedious and therefore will not be presented. The result of (22.77) is

$$\begin{aligned} &\rho_{(0)}\Big\{ \mathbf{C}^{(1)}\frac{\partial \mathbf{v}_s}{\partial t} + \mathcal{E}^{(0)}\left(\frac{\partial \mathbf{v}_s}{\partial s} \otimes \mathbf{v}_s - K\mathbf{v}_s \otimes \mathbf{v}_n \right) \\ &\quad + \mathcal{E}_n^{(1)}\mathbf{v}_s \otimes \mathbf{v}_n + \mathcal{E}_z^{(1)}\mathbf{v}_n \otimes \mathbf{v}_z - f\mathbf{C}^{(1)}\mathbf{v}_n \Big\} \\ &\quad + \rho_{(0)} g \hat{\mathbf{C}}^{(0)}\frac{\partial \boldsymbol{\zeta}}{\partial s} + \mathbf{p}_s^{*(0)} - \mathbf{w}_s^{*(1)} - \mathbf{R}^{(1)}\mathbf{v}_s + \mathbf{J}_s = \mathbf{0}, \end{aligned} \tag{22.78}$$

$$\begin{aligned} &\rho_{(0)}\Big\{ \mathbf{C}^{(1)}\frac{\partial \mathbf{v}_n}{\partial t} + \mathcal{E}^{(0)}\left(\frac{\partial \mathbf{v}_n}{\partial s} \otimes \mathbf{v}_s + K\mathbf{v}_s \otimes \mathbf{v}_s \right) \\ &\quad + \mathcal{E}_n^{(1)}\mathbf{v}_n \otimes \mathbf{v}_n + \mathcal{E}_z^{(1)}\mathbf{v}_n \otimes \mathbf{v}_z + f\mathbf{C}^{(1)}\mathbf{v}_s \Big\} \\ &\quad + \rho_{(0)} g \hat{\mathbf{C}}_{\phi_n}^{(1)}\boldsymbol{\zeta} + \mathbf{p}_n^{*(1)} - \mathbf{w}_n^{*(1)} + \mathbf{R}^{(1)}\mathbf{v}_n + \mathbf{J}_n = \mathbf{0}. \end{aligned} \tag{22.79}$$

'In these expressions, quantities written as bold script capital letters are third-order tensors in N dimensions; hence,

$$(\boldsymbol{\mathcal{E}}\mathbf{a} \otimes \mathbf{b})_i = \mathcal{E}_{ijk} a_j b_k,$$

with $i, j, k = 1, 2, \ldots, N$. Equation (22.78) corresponds to the momentum balance in the s-direction, and (22.79) is that in the n-direction. An equation for the third component is incorporated in (22.78) and (22.79) as the hydrostatic pressure assumption $p = \rho\, g(\hat{\zeta}(s, n, t) - z)$ has been used. The unknown field variables are $\mathbf{v}_s, \mathbf{v}_n, \mathbf{v}_z$ and $\boldsymbol{\zeta}$. The various indexed coefficients $\mathbf{C}$, $\mathbf{R}$ and $\boldsymbol{\mathcal{E}}$ are known when the bathymetry is prescribed and when the shape functions are selected, all of which are defined in Appendix 22.A. The quantities carrying asterisks are the driving forces due to the wind and the atmospheric pressure gradient. These terms are also expressible as cross-sectional integrals, and are known when wind stress and atmospheric pressure gradients are prescribed. The terms in curly brackets are the accelerations in the longitudinal and transverse directions, those involving the $\boldsymbol{\mathcal{E}}$'s are nonlinear and represent advection, and terms involving f account for the Coriolis effects. The first two terms in the second lines comprise all external forces, namely the pressure gradient due to surface elevation, atmospheric pressure and wind; together they constitute the geostrophic balance. The term involving the matrix $\mathbf{R}^{(1)}$ accounts for bottom friction. It can consistently only be accounted for in a fluid that permits non-trivial viscous or turbulent stresses, of which the effect is collectively represented by $\mathbf{J}_s$ and $\mathbf{J}_n$. For completeness these quantities are defined in Appendix 22.A. For a particular closure model they must be given in terms of the independent field variables [26].

22.5.3 Summary

The above partial differential equations (22.72), (22.74), (22.78) and (22.79) comprise a system of four vector equations for the four N-vectors $\mathbf{v}_s, \mathbf{v}_n, \mathbf{v}_z, \boldsymbol{\zeta}$. They are analogous to the basic equations (22.47), (22.48), (22.50)–(22.55), but unlike these, they represent the global behaviour of the motion as a consequence of the smoothing or averaging process over the cross-sections of the lake achieved by expanding the variables in the weighted residual expressions. 'Equation (22.72) is the analogue of the continuity equation in which the kinematic boundary conditions at the free and bottom surfaces are built in. Equation (22.74) is the global form of the bottom boundary condition, expressing the tangency of the flow at the bottom. The remaining two equations (22.78) and (22.79) represent the two horizontal components of the momentum equations in which external driving forces are incorporated. It should, finally, also be mentioned that with the definitions listed in Appendix 22.A the validity of the equations is restricted to small elevations of the free surface.

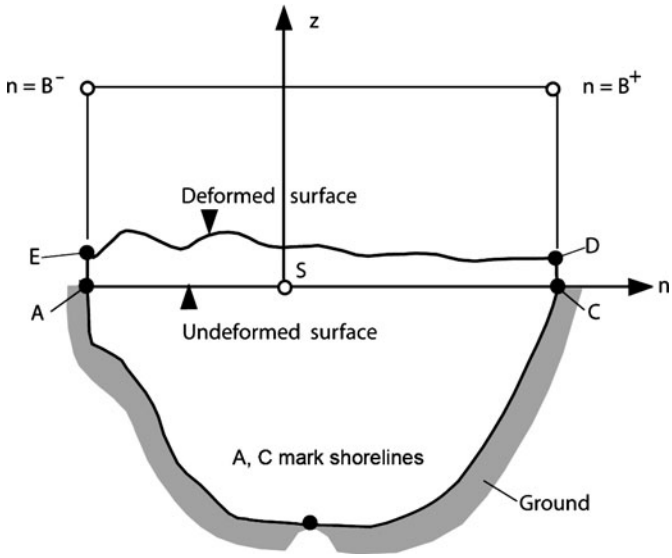

Fig. 22.6 Cross-section, idealized to illustrate the neglecting of AE and CD, from [26]. © Cambridge University Press, reproduced with permission

In fact, it is assumed that shorelines do not change under motion. This amounts in Fig. 22.6 to the identification of the points A with E and C with D.

The spatially one-dimensional differential equations for the field variables $\mathbf{v}_s$, $\mathbf{v}_n$, $\mathbf{v}_z$ and $\boldsymbol{\zeta}$ must be complemented by closure conditions relating the macroscopic stress components with the variables $\mathbf{v}_s$, $\mathbf{v}_n$, $\mathbf{v}_z$ and by boundary conditions. These are partly interrelated, because the closure condition determines the order of the differential equation. For an inviscid fluid model with vanishing viscous stress (22.72), (22.74), (22.78) and (22.79) are of first order in $\mathbf{v}_s$, $\mathbf{v}_n$ and $\mathbf{v}_z$; the latter can be regarded as being eliminated from (22.79). Hence, using N shape functions for the variables, $3N$ boundary conditions must be prescribed. From (22.79) it is seen that the term involving $\partial \mathbf{v}_n / \partial s$ only arises in a formulation accounting for convective acceleration terms. Hence the number of boundary conditions depends on whether the term $\boldsymbol{\mathcal{E}}^{(0)} \partial \mathbf{v}_n / \partial s \otimes \mathbf{v}_s$ is kept or not. If it is not, then $2N$ boundary conditions suffice; one may then require no flow through the end cross-sections. Hence the s-component of the physical velocity must vanish, which implies $\mathbf{v}_s = \mathbf{0}$ at $s = s_1$ and $s = s_2$, where s_1 and s_2 are the values of the arc length at the beginning and the end of the channel axis. When all convective terms are kept, N further conditions must be added.

Finally, to complete the initial-value problem, initial conditions for $\mathbf{v}_s$, $\mathbf{v}_n$, $\mathbf{v}_z$ and $\boldsymbol{\zeta}$ must be prescribed' [26].

22.6 Low-Order Channel Models for Curved Rotating Elongated Lakes

In this section, we present preliminary calculations regarding gravity waves in rotating basins of inviscid fluids. The intention is to test the usefulness of the general model derived in the last section. In particular, we would like to see whether such simplified models would in any way reasonably describe the water motion in elongated narrow basins. It is hoped that with increased refinement, the approximate model will equally more and more closely approximate reality. It will, among other things, be shown that free oscillations in a zeroth-order model reduce to the Chrystal equations. This will elucidate the assumptions behind the limitations of these equations and identify the necessary alterations for their improvement. A first-order model, in which the field variables are expanded in terms of two shape functions, is already sufficiently general to correctly predict waves in rotating basins, indeed we shall show later on that Kelvin, inertial and Poincaré waves are correctly predicted as are the reflection conditions in semi-infinite gulfs or in rectangles. The first-order model equally allows correct prediction of propagating and standing waves in ring-shaped annuli.

For the simplest model *zeroth-order model for arbitrarily curved, narrow basins* the expansions (22.63) are restricted to one single term, $\phi = \psi = 1$, representing a mean value of the variable over the cross-section or over the basin width. Of the governing equations (22.72), (22.74), (22.78), (22.79), the transverse momentum equation (22.79), however, is not needed when longitudinal motions are considered, and the bottom boundary condition (22.74) is merely a prediction equation for the vertical velocity component, which can be determined a posteriori if so desired. Hence, only (22.72), (22.78) are relevant. Under these restrictions they take the forms[8]

- Continuity equation:

$$\mathsf{Z}^{(1)}\frac{\partial \zeta}{\partial t} + \frac{\partial}{\partial s}\left(\mathsf{C}^{(0)} v_s\right) = 0. \tag{22.80}$$

- Longitudinal momentum equation:

$$\rho_0 \left\{ \mathsf{C}^{(1)}\frac{\partial v_s}{\partial t} + \mathcal{E}^{(0)}\left(\frac{\partial v_s}{\partial s} v_s - K v_s v_n\right) - f\,\mathsf{C}^{(1)} v_s \right\}$$

$$+ \rho_0 g \hat{\mathsf{C}}^{(0)}\frac{\partial \zeta}{\partial s} + p_s^{(0)*} - w_s^{(1)} + \mathsf{R}^{(1)} v_n = 0. \tag{22.81}$$

[8] In (22.80)–(22.82), the variables v_s, v_n, $w_s^{(1)}$, $w_n^{(1)}$ and $p_s^{(0)}$, $p_n^{(1)}$ should be written in sanserif type to conform with the MWR notation. However, they correspond to the variables in the Chrystal equations for which sanserif type was not introduced.

- Transverse momentum equation:

$$\rho_0 \left\{ \mathsf{C}^{(1)} \frac{\partial v_n}{\partial t} + \mathcal{E}^{(0)} \left(\frac{\partial v_n}{\partial s} v_s + K v_s v_n \right) + f \mathsf{C}^{(1)} v_s \right\} - p_n^{(1)*} - w_n^{(1)} + \mathsf{R}^{(1)} v_n = 0. \tag{22.82}$$

It further follows under these limiting conditions that $\mathcal{E}^{(0)} = \mathsf{C}^{(0)}$ and $\hat{\mathsf{C}}^{(0)} = \mathsf{C}^{(0)}$. Therefore, only two cross-sectional coefficients, $\mathsf{C}^{(0)}$ and $\mathsf{C}^{(1)}$ occur; these and $\mathsf{Z}^{(1)} = B$ enter (22.80)–(22.82), where B is the channel width at the lake surface. These equations contain the channel curvature explicitly in the non-linear convective terms. Curvature is, however, not neglected when nonlinear advective terms are omitted.

22.6.1 Non-rotating Basins

When rotation is neglected the transverse momentum equation separates from the longitudinal momentum equation and the continuity equation. If one introduces the mean atmospheric pressure across the channel width according to

$$p^*_{\text{atm}} = \rho_0 g \zeta^*(s,t) \tag{22.83}$$

so that

$$p_s^{*(0)} = \iint_Q \frac{\partial p^*_{\text{atm}}}{\partial s} \mathrm{d}n\mathrm{d}z = \rho_0 g \mathsf{C}^{(0)} \frac{\partial \zeta^*}{\partial s}, \tag{22.84}$$

the linearized equations (22.80) and (22.81) take the forms

$$\begin{aligned} &\mathsf{C}^{(1)} \frac{\partial v_s}{\partial t} + \mathsf{C}^{(0)} g \frac{\partial \zeta}{\partial s} + \frac{\mathsf{R}^{(1)}}{\rho_0} v_s = \frac{w_s^{(1)}}{\rho} - g \mathsf{C}^{(0)} \frac{\partial \zeta^*}{\partial s}, \\ &\mathsf{Z}^{(1)} \frac{\partial \zeta}{\partial t} + \frac{\partial}{\partial s} \left(\mathsf{C}^{(0)} v_s \right) = 0, \end{aligned} \tag{22.85}$$

from which on eliminating ζ, one may deduce

$$\begin{aligned} &\frac{\partial^2 v_s}{\partial t^2} + \frac{\mathsf{R}^{(1)}}{\rho_0 \mathsf{C}^{(1)}} \frac{\partial v_s}{\partial t} - \frac{g \mathsf{C}^{(0)}}{\mathsf{C}^{(1)}} \frac{\partial}{\partial s} \left[\frac{1}{\mathsf{Z}^{(1)}} \frac{\partial}{\partial s} \left(\mathsf{C}^{(0)} v_s \right) \right] \\ &= \frac{1}{\rho_0 \mathsf{C}^{(1)}} \frac{\partial w_s^{(1)}}{\partial t} - \frac{g \mathsf{C}^{(0)}}{\mathsf{C}^{(1)}} \frac{\partial^2 \zeta^*}{\partial s \partial t}. \end{aligned} \tag{22.86}$$

For a canal with constant cross-section this equation has the form

$$\frac{\partial^2 v_s}{\partial t^2} + 2b \frac{\partial v_s}{\partial t} - c^2 \frac{\partial^2 v_s}{\partial s^2} = P(s,t), \tag{22.87}$$

where

$$2b := \frac{\mathsf{R}^{(1)}}{\rho_0}\mathsf{C}^{(1)}, \qquad c^2 := \frac{g(\mathsf{C}^{(0)})^2}{\mathsf{C}^{(1)}\mathsf{Z}^{(1)}},$$
$$P := \frac{1}{\rho_0 \mathsf{C}^{(1)}}\frac{\partial w_s^{(1)}}{\partial t} - g\frac{\mathsf{C}^{(0)}}{\mathsf{C}^{(1)}}\frac{\partial^2 \zeta^*}{\partial s \partial t}. \tag{22.88}$$

In the above so-called telegraph equation (22.87), c is the *phase velocity* of the shallow water wave and b the *damping coefficient*, while P is the atmospheric driving term. It is the wave equation of a damped oscillator with forcing term P.

For free oscillations ($P = 0$) solutions of (22.87) are of the form

$$v_s = V_0 \sin\left(\frac{n\pi s}{L}\right) \exp\left\{-bt \pm \mathrm{i}\sqrt{\frac{n^2\pi^2}{L^2} - b^2}\; t\right\}. \tag{22.89}$$

For rectangular cross-sections of width B and depth H and a straight channel the definitions of $\mathsf{C}^{(i)}(i = 0, 1)$ and $\mathsf{Z}^{(1)}$ imply

$$c^2 = g\frac{(BH)^2}{B(BH)} = gH, \qquad b = \frac{1}{2}\frac{(B+2H)}{\rho_0 BH}R \tag{22.90}$$

and, therefore,

$$\omega = \left\{\frac{n^2\pi^2}{L^2}gH - \left(\frac{1}{2}\frac{(B+2H)R}{\rho_0 BH}\right)^2\right\}^{1/2}. \tag{22.91}$$

The frequency of free oscillations is thus reduced by wall friction.

For the frictionless case ($b = 0$) and with

$$P = uF''(s - ut), \tag{22.92}$$

where u is the wave speed and F'' the second derivative of F with respect to its argument, (22.87) implies the solution

$$v_s = \frac{u}{u^2 - c^2}F(s - ut). \tag{22.93}$$

Resonance occurs when

$$u = c = \left(\frac{g(\mathsf{C}^{(0)})^2}{\mathsf{Z}^{(1)}\mathsf{C}^{(1)}}\right)^{1/2} (= \sqrt{gH}, \text{for a rectangular cross-section}). \tag{22.94}$$

The above equations (22.85) also reproduce the Chrystal equations. Indeed, ignoring basal friction ($\mathsf{R}^{(1)} = 0$) and the driving terms (the right hand side in $(22.85)_1$), yields

$$\frac{\partial^2 v_s}{\partial t^2} = g\frac{\mathsf{C}^{(0)}}{\mathsf{C}^{(1)}}\frac{\partial}{\partial s}\left[\frac{1}{\mathsf{Z}^{(1)}}\frac{\partial}{\partial s}\left(\mathsf{C}^{(0)}v_s\right)\right]. \tag{22.95}$$

For a straight lake axis we have $\mathsf{C}^{(1)} = \mathsf{C}^{(0)}$ and $\mathsf{Z}^{(1)} = B$, where $B = B^+ + B^-$, and (22.95) is identical to (22.9). Therefore, the zeroth-order model without friction and straight lake axis reproduces *exactly* the Chrystal equation [4,5]. However, when the lake axis is curved, (22.95) does not exactly reproduce the Chrystal equations, because $\mathsf{C}^{(1)}$ and $\mathsf{Z}^{(1)}$ are curvature dependent. In this case, (22.95) is formally of *Chrystal-type*, which means that equation (22.95) is of the same structure as (22.9). Motivated by the transformation (22.10), we now introduce the transformation

$$\tilde{u} = \mathsf{C}^{(0)}v_s, \qquad \tilde{s} = \int_0^s \mathsf{Z}^{(1)}(\xi)\mathrm{d}\xi. \tag{22.96}$$

It brings (22.95) to the form

$$\frac{\partial^2 \tilde{u}}{\partial t^2} = g\sigma\frac{\partial^2 \tilde{u}}{\partial \tilde{s}^2}, \qquad \sigma := \frac{(\mathsf{C}^{(0)})^2\mathsf{Z}^{(1)}}{\mathsf{C}^{(1)}}, \tag{22.97}$$

in which, now, σ is curvature dependent. Equation (22.97) is formally equal to (22.11), the classical Chrystal equation.[9] The advantage of (22.97) is that the element of subjectivity in selecting the channel axis is eliminated, for the value of the coefficient σ is accordingly adjusted by the Jacobian. The analysis also clearly demonstrates the conditions for which an equation with the same structure as the Chrystal equation is obtained: the rotation of the Earth around its axis is ignored and shape functions are independent of the cross-sectional coordinates.

22.6.2 A First-Order Model Accounting for the Rotation of the Earth

It is not difficult to show that a zeroth-order model does not lead to a physically meaningful description if the effects of the rotation of the Earth are incorporated in the model [24]. To account for this rotation it is vital that variations of the field variables transverse to the lake axis are accounted for. On the other hand, variations of the field variables in the z-direction are absent in a frictionless model. If as shape function expansions so-called *Cauchy series*

[9] In the works of Raggio [24] and Raggio and Hutter [26] the coefficient σ is incorrectly stated.

$$\begin{aligned}\mathfrak{x} &= \sum_{k=0}^{N}\sum_{\ell=0}^{M} n^k z^\ell \left[\mathfrak{x}_{(k,\ell}(s,n)\right] = \phi^{k,\ell}\mathfrak{x}_{k\ell},\\ \delta\mathbf{w} &= \sum_{k=0}^{N}\sum_{\ell=0}^{M} n^k z^\ell \left[\{\delta \mathsf{w}_{(k,\ell}(s,n)\right] = \phi^{k,\ell}\delta \mathsf{w}_{k\ell}\end{aligned} \tag{22.98}$$

with $\phi_{k\ell} = \psi_{k\ell}$ (Galerkin) are used, then the lowest order model accounting for transverse variability is given by $M = 0$ and $N = 1$. The general equations which emerge in this case for arbitrary values of M and N are given by Raggio and Hutter [24, 26]. Moreover, the model in which $M = N = 1$ is referred to as being *first-order in all variables*. These variables are $\zeta^{(0)}$, $\mathsf{v}_s^{(0,0)}$, $\mathsf{v}_n^{(0,0)}$, $\zeta^{(1)}$, $\mathsf{v}_s^{(1,0)}$ and $\mathsf{v}_n^{(1,0)}$, and six equations can be deduced from (22.72), (22.78), (22.79), but (22.74) is superfluous, because it is merely a prediction equation for v_z. Omitting the second index in $\mathsf{v}_s^{(0,0)}$ etc., as simply being mute, and introducing the vector

$$\mathbf{y} = \left(\zeta^{(0)}, \mathsf{v}_s^{(0)}, \mathsf{v}_n^{(0)}, \zeta^{(1)}, \mathsf{v}_s^{(1)}, \mathsf{v}_n^{(1)}\right)^{\mathrm{T}} \tag{22.99}$$

the equation describing the free motion can be written as

$$\mathbf{A}\mathbf{y} = \mathbf{0}, \tag{22.100}$$

where

$$\mathbf{A}[\cdot] = \left[\begin{array}{cc:c:ccc} \mathsf{Z}_{10}\dfrac{\partial()}{\partial t} & \dfrac{\partial \mathsf{C}_{00}()}{\partial s} & 0 & \mathsf{Z}_{11}\dfrac{\partial()}{\partial t} & \dfrac{\partial \mathsf{C}_{01}()}{\partial s} & 0 \\ g\mathsf{C}_{00}\dfrac{\partial()}{\partial s} & \mathsf{C}_{10}\dfrac{\partial()}{\partial t} & -f\mathsf{C}_{10}() & g\mathsf{C}_{01}\dfrac{\partial()}{\partial s} & \mathsf{C}_{11}\dfrac{\partial()}{\partial t} & -f\mathsf{C}_{11}() \\ \hdashline 0 & f\mathsf{C}_{10}() & \mathsf{C}_{10}\dfrac{\partial()}{\partial t} & g\mathsf{C}_{10}() & f\mathsf{C}_{11}() & \mathsf{C}_{11}\dfrac{\partial()}{\partial t} \\ \mathsf{Z}_{11}\dfrac{\partial()}{\partial t} & \dfrac{\partial C_{01}()}{\partial s} & -\mathsf{C}_{10}() & \mathsf{Z}_{12}\dfrac{\partial()}{\partial t} & \dfrac{\partial C_{02}()}{\partial s} & -\mathsf{C}_{11}() \\ gC_{01}\dfrac{\partial()}{\partial s} & \mathsf{C}_{11}\dfrac{\partial()}{\partial t} & -\mathsf{C}_{11}() & g\mathsf{C}_{02}\dfrac{\partial()}{\partial s} & \mathsf{C}_{12}\dfrac{\partial()}{\partial t} & -f\mathsf{C}_{12}() \\ 0 & f\mathsf{C}_{11}() & \mathsf{C}_{11}() & g\mathsf{C}_{11}() & f\mathsf{C}_{12}() & \mathsf{C}_{12}\dfrac{\partial()}{\partial t} \end{array}\right], \tag{22.101}$$

the coefficients being defined as

$$\begin{aligned}\mathsf{C}_{mj}(s) &= \int_{B-}^{B+} H(n,s)(1-Kn)^m n^j \,\mathrm{d}n,\\ \mathsf{Z}_{mj}(s) &= \int_{B-}^{B+} (1-Kn)^m n^j \,\mathrm{d}n,\end{aligned} \tag{22.102}$$

valid for an arbitrary channel with bathymetry $z = -H(s,n)$ [14, 26, 28]. The first and fourth row in (22.101) are continuity statements, the second and fifth row describe momentum balance in the longitudinal direction and the third and sixth row express momentum balance in the transverse direction. 'The orders of the rows and columns of the operator **A** have been selected such that, as one deletes rows and columns from the lower right of the operator **A**, other channel models which are zeroth-order in some and first-order in other variables, are obtained. Thus, a hierarchy of models with decreasing complexity may be deduced. For instance, the upper left 2×2 matrix corresponds to the zeroth-order model discussed above (equivalent to the extended Chrystal equation); the next extension to the 3×3-matrix would be a full zeroth-order model, but it is meaningless because there is no transverse pressure gradient produced by transverse variation of surface elevation, which does not occur (such a variation is necessary to obtain geostrophic balance). The model corresponding to the upper left 4×4 matrix is first-order in the surface elevation but zeroth-order in the velocities. This model would be the simplest version for which the effect of the rotating basin is reasonably accounted for. The remaining 5×5 and 6×6 models also include transverse variations in the velocity field. Clearly, in a model involving first-order terms the unidirectional zeroth-order motion is coupled with the remaining equations describing transverse variation of the field variables. A decoupling can only be achieved if all entries to the right of column 2 in rows 1 and 2 are zero. Non-dimensionalizing (22.100) with (22.101) by introducing appropriate scales shows that coupling results from, in general, three separate causes. One is due to the Coriolis parameter, the second is due to curvature along the channel axis and a third can be traced to 'asymmetry' of the cross-sections', from [27].

Boundary conditions to which (22.100) are subjected may be zero mass flux through the channel ends, implying $\mathbf{v}_s = \mathbf{0}$ at $s = s_0$ and $s = s_1$, corresponding to

$$\mathbf{B_c y} = \mathbf{0}, \quad \text{at } s = (s_0, s_1), \qquad \mathbf{B_c} = \begin{bmatrix} 0 & 0 & 0 & 0 & 0 & 0 \\ 0 & 1 & 0 & 0 & 0 & 0 \\ 0 & 0 & 0 & 0 & 0 & 0 \\ 0 & 0 & 0 & 0 & 0 & 0 \\ 0 & 0 & 0 & 0 & 1 & 0 \\ 0 & 0 & 0 & 0 & 0 & 0 \end{bmatrix}. \tag{22.103}$$

Two important special cases of the operator **A** emerge for straight channels ($K(s) = 0$) with constant cross-section of uniform depth (rectangles) and for ring shaped basins ($K(s) \equiv const.$) with constant depth. For straight rectangles with width B and depth H cross-sectional coefficients are found from (22.102) as

$$\begin{aligned} &\mathsf{C}_{m0} = BH, \quad \mathsf{C}_{m1} = 0 \quad \mathsf{C}_{m2} = \frac{BH^3}{12}, \quad (m = 0, 1), \\ &\mathsf{Z}_{10} = B, \quad \mathsf{Z}_{11} = 0, \quad \mathsf{Z}_{12} = \frac{B^3}{12}, \end{aligned} \tag{22.104}$$

and the operator $\mathbf{A}$ becomes $\mathbf{A}_{\mathrm{s}}$ (s for straight), where

$$\mathbf{A}_{\mathrm{s}} = \begin{array}{c} \begin{array}{cccccc} \zeta^{(0)} & \mathsf{v}_s^{(0)} & \mathsf{v}_n^{(0)} & \zeta^{(1)} & \mathsf{v}_s^{(1)} & \mathsf{v}_n^{(1)} \end{array} \\ \left[\begin{array}{cc:cccc} \frac{1}{H} g \frac{\partial}{\partial t} & g \frac{\partial}{\partial s} & 0 & 0 & 0 & 0 \\ g \frac{\partial}{\partial s} & \frac{\partial}{\partial t} & -f & 0 & 0 & 0 \\ \hdashline 0 & f & \frac{\partial}{\partial t} & g & 0 & 0 \\ 0 & 0 & -g & \frac{B^2}{12} \frac{g}{H} \frac{\partial}{\partial t} & \frac{B^2}{12} g \frac{\partial}{\partial s} & 0 \\ 0 & 0 & 0 & \frac{B^2}{12} g \frac{\partial}{\partial s} & \frac{B^2}{12} \frac{\partial}{\partial t} & -\frac{B^2}{12} f \\ \hdashline 0 & 0 & 0 & 0 & \frac{B^2}{12} f & \frac{B^2}{12} \frac{\partial}{\partial t} \end{array}\right] \end{array}. \tag{22.105}$$

For a *ring* with outer and inner radii r_a and r_i, we may define with $R_m = \frac{1}{2}(r_a + r_i)$, $B = (r_a - r_i)$ the mean radius $(K) = R_m^{-1}$ and the channel width, respectively. With these and the abbreviations

$$d := \frac{1}{R_m} \frac{B^2}{12} = \frac{1}{R_m} e, \quad e := \frac{B^2}{12} \tag{22.106}$$

the operator $\mathbf{A}$ becomes $\mathbf{A}_{\mathrm{R}}$ (R for ring) and has the form

$$\mathbf{A}_{\mathrm{R}} = \begin{array}{c} \begin{array}{cccccc} \zeta^{(0)} & \mathsf{v}_s^{(0)} & \mathsf{v}_n^{(0)} & \zeta^{(1)} & \mathsf{v}_s^{(1)} & \mathsf{v}_n^{(1)} \end{array} \\ \left[\begin{array}{cc:cccc} \frac{\partial}{\partial t} & H \frac{\partial}{\partial s} & 0 & -d \frac{\partial}{\partial t} & 0 & 0 \\ g \frac{\partial}{\partial s} & \frac{\partial}{\partial t} & -f & 0 & -d \frac{\partial}{\partial t} & fd \\ \hdashline 0 & f & \frac{\partial}{\partial t} & g & -fd & -d \frac{\partial}{\partial t} \\ -d \frac{\partial}{\partial t} & 0 & -H & e \frac{\partial}{\partial t} & eH \frac{\partial}{\partial s} & dH \\ 0 & -d \frac{\partial}{\partial t} & fd & eg \frac{\partial}{\partial s} & e \frac{\partial}{\partial t} & -fe \\ \hdashline 0 & -fd & -d \frac{\partial}{\partial t} & -gd & +fe & e \frac{\partial}{\partial t} \end{array}\right] \end{array}. \tag{22.107}$$

The above special forms, (22.105) and (22.107) are particularly apparent because they make the couplings of the motion evident. The dashed lines in the operators $\mathbf{A}_{\mathrm{s}}$ and $\mathbf{A}_{\mathrm{R}}$ facilitate the physical interpretations. For $\mathbf{A}_{\mathrm{s}}$ the zeroth-order equations

decouple from the first-order equations if the rotation of the Earth is ignored ($f = 0$). In this case longitudinal and transverse motions are independent of each other. For $\mathbf{A}_{\mathrm{R}}$, however, zeroth- and first-order equations are coupled owing to both the rotation of the Earth *and* centripetal accelerations. Setting $f = 0$ isolates the effects of the latter from the former. The structure of (22.107) shows that a true zeroth-order model as exemplified in the last subsection for non-rotating basins is likely inappropriate because transverse variations of $\boldsymbol{\zeta}$ and $\mathbf{v}$ are only consistently accounted for at the first (and higher) order levels.

22.7 Gravity Waves in Channels and Lakes of Rectangular Cross Section on the Rotating Earth

A significant result of the first-order model is the demonstration that all essential features of gravitational oscillations – Kelvin-, Poincaré-, inertial waves and their reflection properties – are approximately reproduced. This will in this section be demonstrated. We shall restrict attention to straight canals, gulfs and rectangles for which the geometric curvature of the channel axis vanishes. The governing differential equation in this case is

$$\mathbf{A}_{\mathrm{s}}\mathbf{y} = \mathbf{0} \tag{22.108}$$

with $\mathbf{A}_{\mathrm{s}}$ given in (22.105). This system is particularly transparent because it makes the couplings of the zeroth- and first-order terms evident. The rotation of the frame of reference genuinely couples the zeroth-order model (described by the upper left (2×2)-matrix in (22.105) with the higher-order terms of the full system). The subsequent analysis is based on a detailed exploitation of system (22.105) and follows [27].

22.7.1 Free Oscillations in a Non-rotating Rectangle

When $f = 0$, the full first-order system $\mathbf{A}_{\mathrm{s}}\mathbf{y} = \mathbf{0}$ falls into three independent subsystems, which are described by

- The upper left (2×2)-matrix for the variables $\zeta^{(0)}$, $v_s^{(0)}$, the classical Chrystal equations,
- The middle (3×3)-matrix for the variables $v_n^{(0)}$, $\zeta^{(1)}$, $v_s^{(1)}$, and
- The single lower-right element for the variable $v_n^{(1)}$.

Problem 22.2 *Show that standing-wave solutions of these three systems with velocity components v_s, which vanish at $s = 0$ and $s = L$ have the forms*

$$\begin{aligned}
\zeta^{(0)} &= A_1 \cos\left(\frac{k_1\pi}{L}s\right)\cos(\omega_1 t),\quad \zeta^{(1)} = A_4 \cos\left(\frac{k_2\pi}{L}s\right)\cos(\omega_2 t),\\
v_s^{(0)} &= A_2 \sin\left(\frac{k_1\pi}{L}s\right)\sin(\omega_1 t),\quad v_s^{(1)} = A_5 \sin\left(\frac{k_2\pi}{L}s\right)\sin(\omega_2 t),\\
v_n^{(0)} &= A_3 \cos\left(\frac{k_2\pi}{L}s\right)\sin(\omega_2 t),\quad v_n^{(1)} = A_6 \cos\left(\frac{k_3\pi}{L}s\right)\sin(\omega_3 t),
\end{aligned} \tag{22.109}$$

in which k_1, k_2, k_3 possess integer values, and $A_1, \ldots, A_6$ are amplitudes and $\omega_1, \omega_2, \omega_3$ are frequencies. Prove, moreover, that substitution of (22.109) into the three systems leads to three linear homogeneous systems of equations. They lead to the dispersion relations

$$\begin{aligned}
\omega_1 &= \sqrt{gH}\frac{\pi k_1}{L} = \omega_{1\text{Chrystal}}, \qquad \omega_3 = 0,\\
\omega_2 &= \sqrt{gH}\frac{\pi k_2}{L}\left[1 + \frac{12}{\pi^2}\left(\frac{L}{k_2 B}\right)^2\right]^{1/2} \simeq \omega_{2\text{Chrystal}}\left[1 + 1.2\left(\frac{L}{k_2 B}\right)^2\right]^{1/2}
\end{aligned} \tag{22.110}$$

and amplitudes

$$\begin{aligned}
A_1 &= \sqrt{\frac{H}{g}}A_2, \quad A_3 = -\frac{L}{\pi k_2}A_5,\\
A_4 &= \sqrt{\frac{H}{g}}\left[1 + \frac{12}{\pi^2}\left(\frac{L}{k_2 B}\right)^2\right]^{1/2} A_5, \quad A_6 = 0.
\end{aligned} \tag{22.111}$$

The combined solution, therefore, takes the form

$$\begin{aligned}
\zeta = \zeta^{(0)} + n\zeta^{(1)} &= \sqrt{\frac{H}{g}}\left\{A_2 \cos\left(\frac{k_1\pi}{L}s\right)\cos(\omega_1 t)\right.\\
&\quad \left. + n\left[1 + \frac{12}{\pi^2}\left(\frac{L}{k_2 B}\right)^2\right]^{1/2} A_5 \cos\left(\frac{k_2\pi}{L}s\right)\cos(\omega_2 t)\right\}\\
v_s = v_s^{(0)} + nv_s^{(1)} &= A_2 \sin\left(\frac{k_1\pi}{L}s\right)\sin(\omega_1 t) + nA_5 \sin\left(\frac{k_2\pi}{L}s\right)\sin(\omega_2 t),\\
v_n = v_n^{(0)} + nv_n^{(1)} &= -\frac{L}{\pi\, k_2}A_5 \cos\left(\frac{k_2\pi}{L}s\right)\sin(\omega_2 t).
\end{aligned} \tag{22.112}$$

◆

Note that two of the six amplitudes, here A_2 and A_5, are free; and owing to $\omega_3 = 0$ the corresponding amplitude A_6 of v_n vanishes. Because of the linear dependence of ζ and v_s on n the model gives rise to the possibility of anti-symmetric surface elevation. It must be, and indeed is, accompanied with transverse mass flux as seen from $(22.112)_3$. Boundary conditions at the canal shore are not matched; however,

this is no surprise for the unbiased shape functions which were selected do not automatically satisfy the boundary conditions.

The understanding of the above solution profits from its comparison with the solution of the two-dimensional field equations as constructed in Volume I, Chap. 7, Sect. 3 for $f = 0$. This comparison has led to the following inferences:

- Whereas the exact solution consists of terms in which any order of sinusoidal variation of the fields in the transverse direction may occur, (22.110) and (22.112) only allow the lowest order transverse mode to be taken into account. When restricting the two-dimensional solution to this mode, it reveals the longitudinal frequency ω_1 exactly (!). However, the transverse frequency ω_2 differs in the second term of the bracket under the square root sign in (22.110). In the exact two-dimensional shallow-water-standing-wave solution the transverse frequency is given by

$$\omega_2^{\mathrm{cl}} = \sqrt{gH}\frac{k_2\pi}{L}\left[1+\left(\frac{L}{k_2 B}\right)^2\right]^{1/2},$$

so that

$$\frac{\omega_2}{\omega_2^{\mathrm{cl}}} = \left\{\frac{1+\frac{12}{\pi^2}\left(\frac{L}{k_2 B}\right)^2}{1+\left(\frac{L}{k_2 B}\right)^2}\right\}^{1/2}. \tag{22.113}$$

- As for velocities and surface elevation, comparison of the two-dimensional solutions and (22.112) reveals that *the latter are derivable from the former by a Taylor series expansion of all functions of the transverse coordinate n, restricting the expanded representations to zeroth- and first-order terms*.
- Higher-order models using Cauchy series with more terms will improve on this Taylor series expansion, but still violate shore boundary conditions. Shape functions which satisfy the shore boundary conditions, will make the convergence in the transverse direction more uniform, perhaps generate even exact solutions for the two-dimensional equations. Indeed, by selecting the shape functions

$$\begin{aligned}
&\left[\sin\left(\frac{k\pi}{B}n\right), \sin\left(\frac{k\pi}{B}n\right), \cos\left(\frac{k\pi}{B}n\right)\right] \text{ for } (\zeta, v_s, v_n)\ (k = 1,3,5,\ldots),\\
&\left[\cos\left(\frac{k\pi}{B}n\right), \cos\left(\frac{k\pi}{B}n\right), \sin\left(\frac{k\pi}{B}n\right)\right] \text{ for } (\zeta, v_s, v_n)\ (k = 2,4,6,\ldots),
\end{aligned} \tag{22.114}$$

  the *exact* two-dimensional solutions for the rectangular basin with flat bottom are obtained for the kth mode of transversely symmetric and skew-symmetric surface elevation, respectively, and a model with an infinite number of trigonometric terms will provide the exact two-dimensional solution for all modes.
- It is somewhat surprising that the selection of one single shape function per variable was sufficient to model a particular mode. This is no longer so when $f \neq 0$ the reason being that in rotating basins neighbouring points move in a 'counter-phase fashion', requiring at least a 'two-degrees-of-freedom' description for at least one variable.

22.7.2 *Kelvin-Type Waves in an Infinitely Long Rectangular Straight Canal*

The classical tidal equations permit wave solutions for which $v_n = 0$ and v_s and ζ are exponentially evanescent in the direction perpendicular and to the left (on the northern hemisphere) of the direction of wave propagation. The operator equation (22.108) with $\mathbf{A}_s$ given by (22.105) does not permit a solution with $v_n^{(0)} = v_n^{(1)} = 0$. Hence, exact reproduction of Kelvin waves is not possible with the full first-order equations. However, a subsystem, in which the last row and column of $\mathbf{A}_s$ are dropped (this corresponds to ignoring $v_n^{(1)}$) possesses solutions of the form

$$(\zeta^{(0)}, v_s^{(0)}, v_n^{(0)}, \zeta^{(1)}, v_s^{(1)}) = (Z_0, U_0, V_0, Z_1, U_1)\, F(\kappa\, s - \omega\, t), \tag{22.115}$$

where F is any smooth function, Z_0, U_0, V_0, Z_1, V_1 are amplitudes, κ is the wavenumber and ω is the frequency.

Problem 22.3 *By substituting (22.115) into the (5×5)-reduction of (22.105), prove that*

$$\begin{aligned} c &= \frac{\omega}{\kappa} = \sqrt{gH}, \\ \zeta &= \zeta^{(0)} + n\zeta^{(1)} = \sqrt{\frac{H}{g}}\left(1 \mp n\frac{f}{c}\right) U_0 F(\kappa\, s \mp \omega\, t), \\ v_s &= v_s^{(0)} + n v_s^{(1)} = \pm\left(1 \mp n\frac{f}{c}\right) U_0 F(\kappa\, s \mp \omega\, t), \\ v_n &= 0, \end{aligned} \tag{22.116}$$

in which upper (lower) signs correspond to waves travelling in the positive (negative) direction of s. ◆

Comparing (22.116) with the classical Kelvin wave solution, we note that

- Equation (22.116) reproduces the phase speed of the classical Kelvin wave exactly (!);
- Longitudinal velocity v_s and surface elevation ζ decay linearly with distance perpendicular to and to the left of the propagation direction;
- This decay rate nf/c is the linear approximation of the exponential decay rate, $\exp(\pm nf/c)$, of the classical Kelvin wave;
- The solution (22.116) corresponds exactly to the solution constructed by the so-called Kelvin-wave-dynamics approach, in which the transverse variations of v_s and ζ are constructed with a geostrophic balance (see e.g. Defant's 1953-construction of the surface seiches of Lake Michigan, see also Mortimer's discussion in Chap. 14, Sect. 14.4). As explained there, a patching of the co-tidal lines with measured phases leaves some flexibility in the determination of the 'best solution', but requires observations for the prediction. This flexibility here

does not exist and the patching of co-tidal lines is unnecessary. Improvement of a solution can be obtained by increasing the order of the model.

Quasi-standing Kelvin-like wave solutions are constructed by adding a forward (upper sign) and a backward (lower sign) solution (22.116) and assuming that $F(\cdot) = \cos(\cdot)$,

$$\begin{aligned} \zeta &= \sqrt{\frac{H}{g}} U_0 \left\{ \cos(\kappa\, s) \cos(\omega\, t) - n \frac{f}{c} \sin(\kappa\, s) \sin(\omega\, t) \right\}, \\ v_s &= U_0 \left\{ \sin(\kappa\, s) \sin(\omega\, t) - n \frac{f}{c} \cos(\kappa\, s) \cos(\omega\, t) \right\}. \end{aligned} \tag{22.117}$$

Notice that there is no position $s = s_1$ for which v_s would vanish for all n and all time t. Qualitatively, this is exactly the situation encountered by Taylor [34] when trying to solve the reflection of a Kelvin wave at the closed end of a half-open gulf. The solution (22.117) enjoys the following properties (compare also Chap. 12. Sect. 12.2 and formula (12.12)):

- For $n = 0$ and $s = (2j + 1)\pi/(2\kappa)$, $j = 1, 2, \ldots, \zeta$ vanishes for all time. These are the *amphidromes* at which the surface experiences no elevation for all time.
- For $n = 0$ and $s = j\pi/\kappa$, $j = 1, 2, \ldots$, (these are the points on the centre line between two amphidromic points), the velocity v_s vanishes at all time.
- At times $t = j\pi/\omega$, $j = 1, 2, \ldots$, the surface elevation ζ (velocity v_s) is symmetrically (anti-symmetrically) distributed across the channel width with maximum velocities arising at the shore lines at positions midway between the amphidromic points. Similarly, for $t = ((2j + 1)\pi/(2\omega))$, $j = 1, 2, \ldots, \zeta$ is anti-symmetrically, while v_s is symmetrically distributed across the channel.
- Lines of *constant elevation amplitudes* – the so-called *co-range lines* – are given by

$$\cos^2(\kappa\, s) + \left(n \frac{f}{c} \right)^2 \sin^2(\kappa\, s) = \text{const.}, \tag{22.118}$$

  which agrees with the corresponding equation of the exact theory [see (12.13)] if in the latter a one-term Taylor series expansion is performed in the transverse direction.
- Lines of *constant phase* – the so-called *co-tidal lines* are described instead by

$$\tan\phi = -\text{cotan}(\kappa\, s) \Big/ \left(n \frac{f}{c} \right) = \text{const.}, \tag{22.119}$$

  which are easily seen to radiate out from the amphidromic points.

These properties are all qualitatively as the corresponding properties of the standing Kelvin waves of the full two-dimensional tidal operator. They differ quantitatively from those because of the restriction to the linear terms in the transverse coordinate n.

22.7.3 Wave Solutions of the Full First-Order System: Poincaré-Like Waves

We now return to the full system $\mathbf{A}_{\mathrm{s}}\mathbf{y} = \mathbf{0}$ with $\mathbf{A}_{\mathrm{s}}$ given by (22.105) and seek travelling solutions of the form

$$\begin{aligned}(\zeta^{(0)}, v_s^{(0)}, \zeta^{(1}, v_s^{(1)}) &= (Z_0, U_0, Z_1, U_1)\cos(\omega t \pm \kappa s),\\ (v_n^{(0)}, v_n^{(1)} &= (V_0, V_1)\sin(\omega t \pm \kappa s).\end{aligned} \tag{22.120}$$

Problem 22.4 *By substituting (22.120) into (22.108) with* $\mathbf{A}_{\mathrm{s}}$ *given by (22.105), show that a linear system* $\mathbf{Bz} = \mathbf{0}$ *emerges with*

$$\mathbf{z} = (Z_0, U_0, Z_1, U_1, V_0, V_1)^{\mathrm{T}}, \tag{22.121}$$

$$\mathbf{B} = \left[\begin{array}{cc:cccc} -\dfrac{\omega}{H} & \mp\kappa & 0 & 0 & 0 & 0 \\ \mp g\kappa & -\omega & -f & 0 & 0 & 0 \\ \hdashline 0 & f & \omega & g & 0 & 0 \\ 0 & 0 & -\dfrac{12}{B^2} & -\dfrac{\omega}{H} & \mp\kappa & 0 \\ 0 & 0 & 0 & \mp g\kappa & -\omega & -f \\ 0 & 0 & 0 & 0 & f & \omega \end{array}\right]. \tag{22.122}$$

This system possesses non-trivial solutions if $\det\mathbf{B} = 0$. *Show that this equation is given by*

$$\mathcal{F} := \sigma^6 - [\bar{\mu}^2 + 2(\gamma^2+1)]\sigma^4 + [\bar{\mu}^2(\gamma^2+1) + (\gamma^2+1)^2]\sigma^2 - \bar{\mu}^2\gamma^2 = 0, \tag{22.123}$$

where

$$\left.\begin{aligned}\sigma &= \frac{\omega}{|\kappa|\sqrt{gH}} = \frac{\omega L}{\pi\sqrt{gH}},\\ \bar{\mu}^2 &= \frac{12}{|\kappa|^2 B^2} = \frac{12}{\pi^2}\left(\frac{L}{B}\right)^2 = \frac{12}{\pi^2}\mu^2,\\ \gamma &= \frac{f}{|\kappa|\sqrt{gH}} = \frac{fL}{\pi\sqrt{gH}}\end{aligned}\right\} \quad \kappa = \frac{\pi}{L}, \quad \mu = \frac{L}{B}. \tag{22.124}$$

◆

'In the above, μ^{-1} is the aspect ratio and $\sigma, \bar{\mu}$ and γ are, respectively, dimensionless frequency, transverse wavenumber and rotational speed, all normalized with the longitudinal wavenumber κ. Two parameters thus govern the dispersion relation. The aspect ratio describes the ratio of transverse to longitudinal wavelengths. For $\mu = 1$ both are the same, and the motion has no prevailing direction. For $\mu > 1$ the elongated nature of the motion must evolve and become more and more pronounced as μ is increased. This suggests that if the channel model is meaningful, real behaviour should be better and better approximated with increasing μ. The second parameter in the dispersion relation, γ, is a dimensionless measure of the rotation speed. According to its definition it grows with increasing f and L and with decreasing H. For homogeneous water bodies and realistic values of $f, \gamma < 1$; for reasons explained later we shall, however, also consider values of γ between 1 and 20. Once the frequency relation (22.123) is exploited, the free amplitudes $Z_0, U_0, V_0, Z_1, U_1, V_1$ can be determined; when this is done the combined solution has the form

$$\begin{aligned} v_s &= v_s^{(0)} + n v_s^{(1)} \\ &= \frac{-V_0}{\omega^2 - gH\kappa^2} \left\{ f\omega \pm \tau^2 \kappa\, gH \frac{1}{1 - [(f/\omega)^2]^*} n \right\} \cos(\omega t \pm \kappa s), \\ v_n &= v_n^{(0)} + n v_n^{(1)} \\ &= V_0 \left\{ 1 \mp \left[\kappa f gH\omega \frac{1}{(\omega^2 - f^2)(\omega^2 - gH\kappa^2)} \tau^2 n \right]^* \right\} \sin(\omega t \pm \kappa s), \\ \zeta &= \zeta^{(0)} + n\zeta^{(1)} = \frac{-V_0 H}{\omega^2 - gH\kappa^2} \left(\mp \kappa f - \tau^2 \omega n \right) \cos(\omega t \pm \kappa s), \end{aligned} \tag{22.125}$$

where for reasons of further comparison the abbreviation

$$\tau^2 = \frac{\omega^2 - f^2 - gH\kappa^2}{gH} \tag{22.126}$$

has been used. This solution may be contrasted with the Poincaré [23] solutions of the tidal operator. There are two classes of such solutions. In the limit as $f \to 0$ one class has transversely anti-symmetric, and the other symmetric, surface elevation. When expanding these solutions into Taylor series of n and truncating at the lowest-order terms, the 'anti-symmetric' solution reveals (22.125) except for the terms indicated by $[\ldots]^*$. But these turn out to be small when exploiting the frequency relation for practical values of the rotation speed, and hence can be ignored. The 'symmetric' solution is not approximated by (22.125), but this is no surprise, for in the limit $f \to 0, \zeta$ in (22.125) is odd in the transverse coordinate', after [27].

It still must be demonstrated that the approximate dispersion relation (22.123), which has three double roots (for forward and backward motion), gives accurate values for the frequency–wavenumber relation for all waves characterizing rotating systems. Moreover, since energy propagates with the group velocity, sufficient agreement of the latter in the two formulations should also be obtained.

To derive an explicit formula for the group velocity, note that the dispersion relation (22.123) can, in dimensional form, be written as $\mathcal{F}(\omega, \kappa) = 0$. It then follows that

$$\frac{\partial \mathcal{F}}{\partial \omega} \mathrm{d}\omega + \frac{\partial \mathcal{F}}{\partial \kappa} \mathrm{d}\kappa = 0 \quad \Longrightarrow \quad c_{\mathrm{gr}} = \frac{\mathrm{d}\omega}{\mathrm{d}\kappa} = -\frac{\partial \mathcal{F}/\partial \kappa}{\partial \mathcal{F}/\partial \omega}. \tag{22.127}$$

When writing the dispersion relation in this form and then performing the indicated differentiations and non-dimensionalizing the result, it can be shown that

$$\begin{aligned} &\frac{c_{\mathrm{gr}}}{\sqrt{gH}} = \frac{1}{\sigma} \alpha_{\mathrm{gr}}, \\ &\alpha_{\mathrm{gr}} = \frac{\sigma^2[2\sigma^2 - (\bar{\mu}^2 + 2(1+\gamma^2))] + \bar{\mu}^2\gamma^2}{\sigma^2[3\sigma^2 - 2(\bar{\mu}^2 + 2(1+\gamma^2))] + \bar{\mu}^2(1+\gamma^2) + 1}. \end{aligned} \tag{22.128}$$

This equation should approximately describe the group velocity for all channel waves with phase speeds satisfying (22.123).

The above approximate group velocity (22.128) must be compared with the group velocity of the classical two-dimensional theory.

- For classical Kelvin *waves* (see Sect. 12.2 in Chap. 12) the computations proceed as follows:

$$\begin{aligned} &\mathcal{F} \equiv \omega^2 - gH\kappa^2 \quad \Longrightarrow \quad \sigma_{\mathrm{cl}}^2 - 1 = 0, \\ &\frac{\partial \mathcal{F}}{\partial \kappa} = -2gH\kappa, \quad \frac{\partial \mathcal{F}}{\partial \omega} = 2\omega \quad \Longrightarrow \quad c_{\mathrm{gr}}^{\mathrm{cl}} = gH\frac{\kappa}{\omega} = \sqrt{gH}, \\ &\frac{c_{\mathrm{gr}}^{\mathrm{cl}}}{\sqrt{gH}} = \frac{1}{\sigma} \quad (= 1, \text{ since } \sigma_{\mathrm{cl}} = 1). \end{aligned} \tag{22.129}$$

- For classical Poincaré *waves* (see Sect. 12.4 in Chap. 12) we obtain

$$\begin{aligned} &\mathcal{F} \equiv \omega^2 - f^2 - gH(\lambda^2 + \kappa^2) = 0, \quad \Longrightarrow \quad \sigma_{\mathrm{cl}}^2 - \mu^2 - \gamma^2 - 1 = 0, (*) \\ &\frac{\partial \mathcal{F}}{\partial \kappa} = -2gH\kappa, \quad \frac{\partial \mathcal{F}}{\partial \omega} = 2\omega \quad \Longrightarrow \quad c_{\mathrm{gr}}^{\mathrm{cl}} = \sqrt{gH}, \\ &\frac{c_{\mathrm{gr}}^{\mathrm{cl}}}{\sqrt{gH}} = \frac{1}{\sigma_{\mathrm{cl}}} \quad (\text{where } \sigma_{\mathrm{cl}} \text{ is a solution of } (*)). \end{aligned} \tag{22.130}$$

  Here, λ is the transverse wavenumber such that $\mu^2 := (\lambda/\kappa)^2 = (L/B)^2$ with longitudinal (L) and transverse (B) wave lengths.
- Classical Sverdrup *waves* are special Poincaré waves with constant crests in one spatial direction. If this is the longitudinal direction (22.130) yields

$$\begin{aligned} &\sigma_{\mathrm{cl}}^2 - \mu^2 - \gamma^2 = 0, (+) \\ &\frac{c_{\mathrm{gr}}}{\sqrt{gH}} = \frac{1}{\sigma_{\mathrm{cl}}} \quad (\text{where } \sigma_{\mathrm{cl}} \text{ is a solution of} (+)). \end{aligned} \tag{22.131}$$

Table 22.2 Dispersion relation and group velocity for the classical tidal equations

Wave type	Dispersion relation	Group velocity
Kelvin	$\sigma_{\rm cl}^2 - 1 = 0$	$\dfrac{1}{\sigma_{\rm cl}}$
Poincaré	$\sigma_{\rm cl}^2 - \mu^2 - \gamma^2 - 1 = 0$	$\dfrac{1}{\sigma_{\rm cl}}$
Sverdrup	$\sigma_{\rm cl}^2 - \mu^2 - \gamma^2 = 0$	$\dfrac{1}{\sigma_{\rm cl}}$
Inertial	$\sigma_{\rm cl}^2 - \gamma^2 = 0$	0

- For *inertial waves* (see Sect. 12.3 in Chap. 12)

$$\begin{aligned} \mathcal{F} \equiv \omega^2 - f^2 = 0 \quad &\Longrightarrow \quad \sigma^2 - \gamma^2 = 0, \\ \frac{\partial \mathcal{F}}{\partial \kappa} = 0, \quad \frac{\partial \mathcal{F}}{\partial \omega} = 2\omega \quad &\Longrightarrow \quad c_{\rm gr}^{\rm cl} = 0. \end{aligned} \tag{22.132}$$

These results are summarized in Table 22.2.

The dispersion relation (22.123) and the group velocity formula (22.128) have been analyzed numerically. In view of the above results the dimensionless frequency σ and the correction factor for the group velocity, $\alpha_{\rm gr}$, should be plotted as functions of the aspect ratio $\mu = L/B$ when γ is held fixed and when γ is varied but μ is held fixed. Results are displayed in Figs. 22.5 and 22.6 for Kelvin-, Poincaré- and inertial-type waves. Solid lines show the results for the first-order approximate channel model, dashed lines display the results for the classical two-dimensional tidal theory. The three different solutions can be interpreted, respectively, as a Poincaré-type, Kelvin-type and inertial-type wave. To identify these interpretations, note that (Fig. 22.7a)

$$\left.\begin{array}{ll} \sigma \to \mu & \text{for Poincaré-type waves,} \\ \sigma \to 1 & \text{for Kelvin-type waves,} \\ \sigma \to \gamma & \text{for inertial-type waves.} \end{array}\right\} \quad \text{as } \mu \to \infty.$$

Similarly, (Fig. 22.7b)

$$\left.\begin{array}{ll} \alpha_{\rm gr} \to 1 & \text{for Poincaré-type waves,} \\ \alpha_{\rm gr} \to 1 & \text{for Kelvin-type waves,} \\ \alpha_{\rm gr} \to \gamma & \text{for inertial-type waves.} \end{array}\right\} \quad \text{as } \mu \to \infty.$$

By inspection we also see from (22.125) that for Kelvin-type waves $v_n/v_s \sim \omega^2 - gH\kappa^2$, which must be a very small number, implying that v_n is small in comparison to v_s. (A more detailed study shows in addition that the terms in (22.125) carrying an asterisk are negligible.)

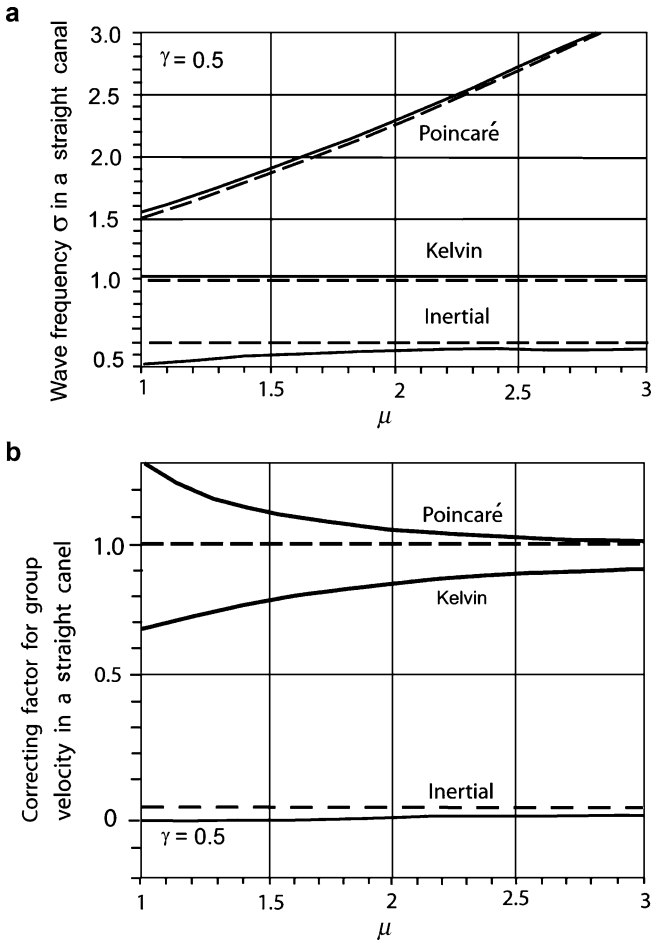

Fig. 22.7 (**a**) Dimensionless frequency σ in a straight rectangular channel as obtained from (22.123), plotted against $\mu = L/B$, for $\gamma = f/(\kappa\sqrt{gH}) = 0.5$. *Dashed lines* are for the dispersion relation of the exact two-dimensional tidal operator. (**b**) Dimensionless correction factor $\alpha_{\rm gr}$ in a straight rectangular channel plotted against μ for $\gamma = 0.5$. *Dashed lines* correspond to exact results, from [27]. © J. Fluid Mech., Cambridge University Press, reproduced with permission

Figure 22.8 displays σ and $\alpha_{\rm gr}$ as functions of the dimensionless rotation speed for $\gamma \in [0.1, 3]$ and for $\mu = 0.4$. Again, Poincaré-type, Kelvin-type and inertial-type wave solutions can be differentiated. According to Raggio and Hutter [27] 'Fig. 22.8 indicates further that, qualitatively, exact and approximate frequency curves are close (to one another...). The structure of the frequency curves for Kelvin- and inertial-type waves near $\gamma = 1$ is of some interest. As γ increases, a Kelvin-type wave at small values of γ becomes inertial-type at large values of γ, and vice versa. The frequency curves of the approximate dispersion relation do not cross, but only nearly touch each other. This will be called a 'kissing mode'. This

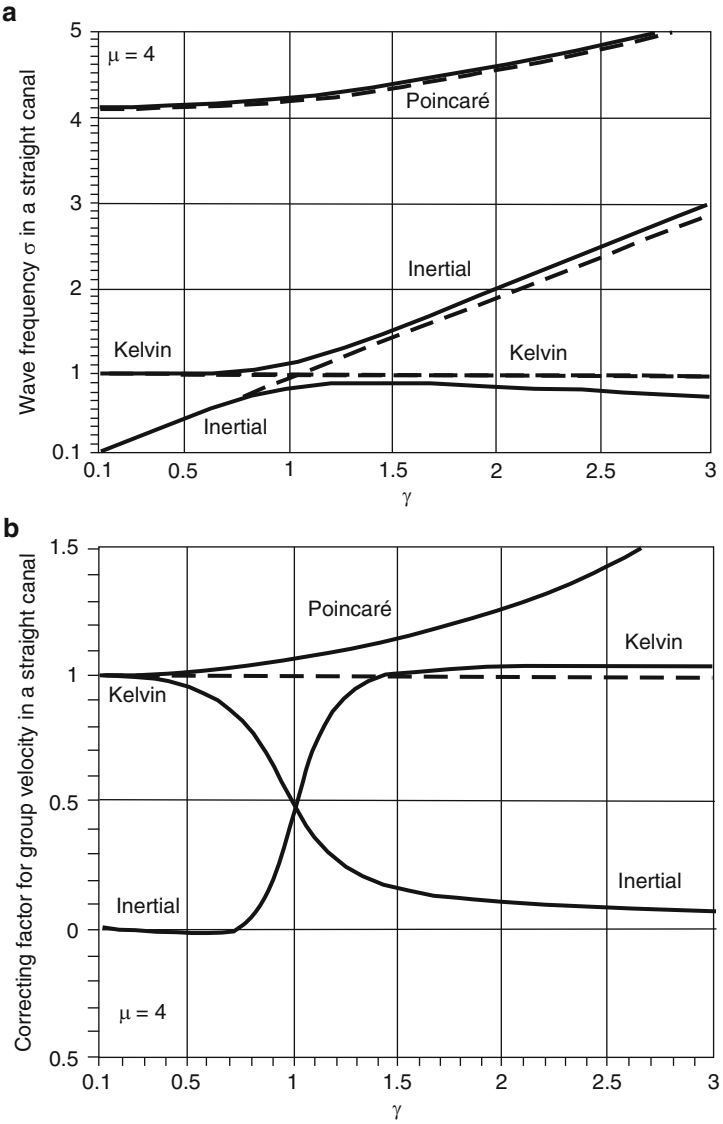

Fig. 22.8 (**a**) Dimensionless frequency σ in a straight rectangular channel as obtained from (22.123) plotted against $\gamma = f/(\kappa\sqrt{gH})$ for $\mu = 4$. Solid lines are those of the channel model, dashed lines correspond to the exact tidal operator. (**b**) Dimensionless correcting factor $\alpha_{\rm gr}$ for the group velocity in a straight rectangular channel plotted against $\gamma = f/(\kappa\sqrt{gH})$ for $\mu = 4$. The dashed lines at $\alpha_{\rm gr} = 1, 0$ correspond to the respective values of the two-dimensional tidal operator, from [27].

was found to be the location where the corresponding group velocities are poorly predicted (Fig. 22.8b). Further reasons for the existence of this transition zone can be found (below).

In Fig. 22.8b, the group-velocity correcting factor α_{gr} is plotted for the same three waves; dashed lines indicate the values of the corresponding values for the exact theory. Group velocities for Poincaré waves are only predicted accurately for rotation speeds $\gamma < 1$, approximately, and those for Kelvin-type and inertial-type waves are poor when $\gamma \simeq 1$. This is exactly the region of the 'kissing mode' in Fig. 22.8a. The results of Fig. 22.8a indicate that for the given value of μ and the range of values for γ Poincaré-type waves appear to be reasonably well predicted. This is borne out very clearly in Fig. 22.9a, b, which shows plots of the dimensionless Poincaré frequency as a function of γ and μ, respectively. Calculations were performed for

$$0 < \gamma < 20, \quad 1 < \mu < 20.$$

$\gamma = 0$ means no rotation or an infinitely deep basin, $\gamma = 20$ is an upper bound when a two-layer model (e.g. the two-layer equivalent depth model of Csanady [6]) is considered, in which a reduced gravity constant and a reduced depth are introduced to calculate the thermocline displacements. For homogeneous lakes γ is certainly less than 1.

The discrepancies between exact and approximate frequencies grow with increasing γ, yet relative errors $|(\sigma - \sigma_{\mathrm{cl}})|$ stay below 10^{-1} and are extremely small when $\gamma < 1$. Frequencies and therefore speeds for Poincaré waves being well predicted does not imply that group velocities for these waves are also obtained accurately. Exact and approximate dimensionless group velocities are given by (22.128) and Table 22.2, respectively, in which σ must obey the dispersion relations listed in Table 22.2 and (22.123), respectively. Results are displayed in Fig. 22.10a, where solid lines correspond to the dimensionless group velocity of the approximate model and symbols stand for that of the exact theory. For $\gamma \leq 1$ agreement is fair unless μ is about unity and slightly larger, and relative errors $|c_{\mathrm{gr}}^{(\mathrm{cl})} - c_{\mathrm{gr}}|/|c_{\mathrm{gr}}^{(\mathrm{cl})}|$ are small (Fig. 22.10b). On the other hand, for $\gamma = 10$ the approximate group velocity has a pole, approximately at $\mu = 8$. The location of this pole is obtained from (22.128) by setting $\alpha_{\mathrm{gr}} = \infty$. In the classical (exact) formulation it does not arise, implying that large relative errors must evolve from the application of the channel model in the neighbourhood of these points. This is corroborated in Fig. 22.10b.

The above considerations, together with further scrutiny of the dispersion relation of the full first-order model operating in rectangular basins [...] indicates that the extended channel theory for the tidal operator based on a two-term Cauchy-series expansion predicts frequency–wavenumber relations accurately enough, provided that (1) the longitudinal wavelength is about twice as large (or lager) than the width of the channel, (2) rotational speeds γ (defined in (22.124)) stay below unity. This indicates that the model should *not* be used for a two-layer model with reduced

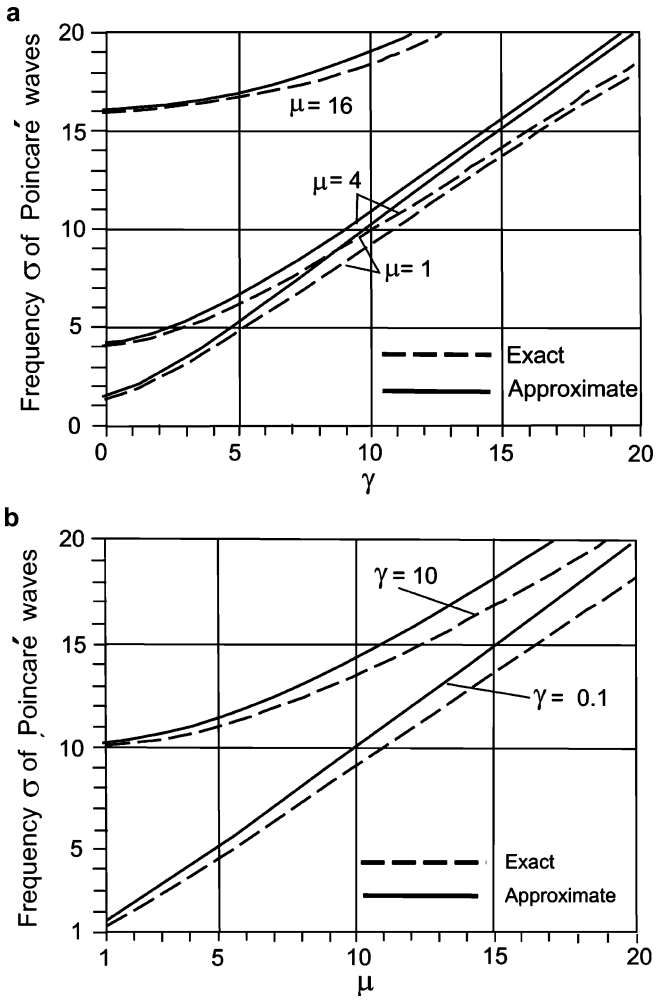

Fig. 22.9 (**a**) Dimensionless Poincaré-type frequency plotted against $\gamma = f/(\kappa\sqrt{gH})$ for various values of $\mu = L/B$. *Solid lines* correspond to the channel model, *dashed lines* are for the two-dimensional tidal operator. (**b**) Dimensionless frequency σ of the Poincaré-type waves plotted against μ for various values of γ. *Solid lines* are for the channel model, *dashed lines* for the two dimensional tidal operator, from [27]. © J. Fluid Mech., Cambridge University Press, reproduced with permission

height and density as proposed in the equivalent depth models. In such a mode rotational speeds are larger than unity, and group velocities and hence energy-propagation speeds are incorrectly predicted, as we have just seen above. On the other hand, calculations with higher-order models indicate that these poles might be removed to locations outside the practical range of the parameters' from [27].

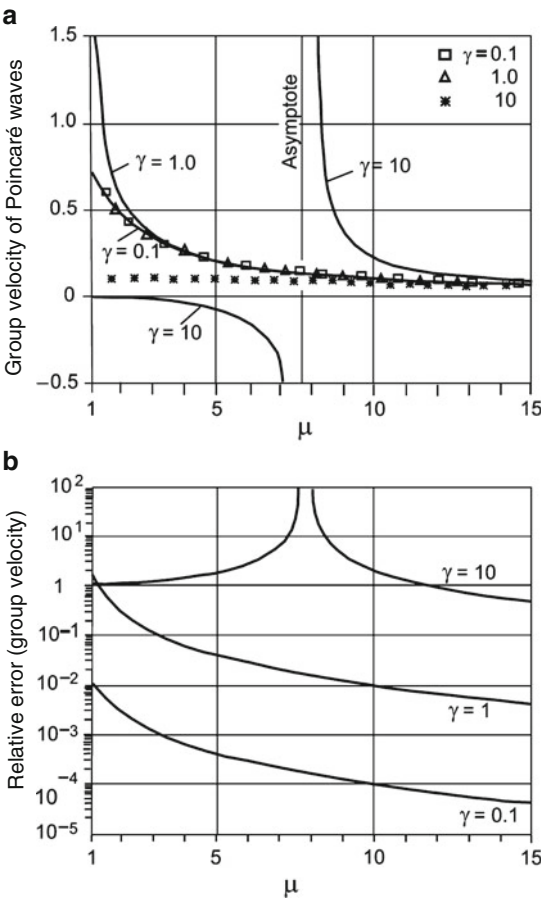

Fig. 22.10 (**a**) Dimensionless group velocity of Poincaré-type waves for the two-dimensional theory and the channel model, plotted against μ for $\gamma = (0.1, 1, 10)$. *Solid lines* correspond to results of the channel model; *Symbols* indicate group velocities of the two-dimensional tidal operator. (**b**) Relative error of the group velocity of Poincaré-type waves when calculated according to the classical and approximate models, respectively, from [26]. © Cambridge University Press, reproduced with permission

22.7.4 Reflection of Kelvin-Type Waves at a Barrier of a Half-Open Rectangular Canal and Free Oscillations in Rectangles

Reflections of Kelvin waves at a barrier and tidal oscillations in long rectangles of the two-dimensional tidal equations were treated in Chap. 12, Sects. 12.5 and 12.6. It was demonstrated there that for quasi-standing Kelvin waves no position along the channel axis does exist of which the axis-parallel velocity component would vanish for all positions across the channel at all time. To obtain a reflection with vanishing longitudinal velocity at a certain cross-section the forward and backward progressing waves had to be combined with an infinite number of Poincaré waves of the same frequency. In a particular solution these Poincaré waves are exponential or oscillatory in the direction of the channel axis. The reflection at a wall is called *complete* if all involved Poincaré waves are exponentially evanescent away from the

wall and then the solution has boundary layer character; the reflection is *incomplete* if some of them are oscillatory. The solution of this problem for the two-dimensional tidal operator is due to Taylor [34].

To allow for exponential decay of the involved fields, as one moves away from the barrier for the first-order model, it will now be assumed that

$$\begin{aligned}(\zeta^{(0)}, v_n^{(0)}, v_s^{(1)}) &= (Z_0, C_1, B_1)\exp(-\lambda\, s)\cos(\omega\, t),\\ (v_s^{(0)}, \zeta^{(1)}, v_n^{(1)}) &= (A_1, Z_1, D_1)\exp(-\lambda\, s)\sin(\omega\, t),\end{aligned} \tag{22.133}$$

in which λ may be complex valued. Depending on the sign of the real part of λ, these fields decay exponentially as one moves into the $\pm s$-direction. Substituting (22.133) into (22.108) with $\mathbf{A}_s$ given by (22.105) yields a homogeneous linear system of equations for $\zeta^{(0)}, \ldots, v_n^{(1)}$ of which the characteristic equation agrees with (22.123) if the substitution $\lambda = \mathrm{i}\kappa$ is made. For values of λ satisfying this equation, the combined solution (22.133) has the form

$$\begin{aligned}v_s &= A_1\exp(-\lambda\, s)\left\{\sin(\omega\, t) + n\,\lambda\omega\frac{\lambda^2 gH + \omega^2 - f^2}{f(f^2-\omega^2)}\cos(\omega\, t)\right\},\\ v_n &= A_1\exp(-\lambda\, s)\left\{\frac{\lambda^2 gH + \omega^2}{gf}\cos(\omega\, t) - n\lambda\frac{\lambda^2 gH + \omega^2 - f^2}{f^2-\omega^2}\sin(\omega\, t)\right\},\\ \zeta &= A_1\exp(-\lambda\, s)\left\{-\frac{\lambda H}{\omega}\cos(\omega\, t) + n\frac{\lambda^2 gH + \omega^2 - f^2}{gf}\sin(\omega\, t)\right\},\end{aligned} \tag{22.134}$$

in which A_1 is a constant amplitude.

22.7.4.1 Reflection at a Barrier

We have already seen when constructing quasi-steady Kelvin-type waves of the (5×5)-system in (22.117) that there is no position $s = s_1$ with no motion v_s for all n and t. The same inferences can also be drawn for the (6×6)-system with the solutions (22.125). However, on adding (22.117) (or (22.125)) to (22.134), positions of vanishing v_s-velocities can be found. This will be shown here for the simpler system (22.117). Considering a semi-infinite gulf, conditions of reflection at a barrier $s = s_1$ are

$$v_s^{\mathrm{Kelvin}}(s_1) + v_s^{\exp}(s_1) = 0, \tag{22.135}$$

where v_s^{Kelvin} is given by (22.117) and $v_s^{\exp}$ by (22.134). Equation (22.135) is an identity involving $\sin(\omega t)$ and $\cos(\omega t)$ in a linear combination of which the coefficients must separately vanish; this yields

$$A_1 = -U_0\exp(\lambda\, s_1)\sin(\kappa\, s_1),$$

$$\tan(\kappa\, s_1) = -\frac{\exp(-\lambda\, s_1)}{\sqrt{gH}\lambda\omega\dfrac{\lambda^2 gH + \omega^2 - f^2}{f^2(f^2-\omega^2)}}. \tag{22.136}$$

The first relates the amplitudes of v_s^{Kelvin} and v_s^{exp} (once s_1 is known), the second affords for given ω and κ at a barrier located at $s = s_1$ evaluation of λ and s_1 from (22.123) (in which κ is replaced by $-\mathrm{i}\lambda$). The compound wave is obtained when (22.117) and (22.134) are added together. With $c^2 = gH$, it reads[10]

$$\begin{aligned}
v_s &= U_0\Big\{[\sin(\kappa\, s) - \exp(-\lambda(s-s_1))\sin(\kappa\, s_1)]\sin(\omega\, t) \\
&\quad - n\left[\frac{f}{c}\cos(\kappa\, s) + \exp(-\lambda(s-s_1))\sin(\kappa\, s)\omega\frac{\lambda^2 c^2 + \omega^2 - f^2}{f(f^2-\omega^2)}\right]\cos(\omega\, t)\Big\}, \\
v_n &= U_0 \exp(-\lambda(s-s_1))\sin(\kappa\, s_1)\left\{\frac{\lambda^2 c^2 + \omega^2}{gf}\cos(\omega\, t)\right. \\
&\quad \left. - n\lambda\frac{\lambda^2 c^2 + \omega^2 - f^2}{f^2-\omega^2}\sin(\omega\, t)\right\}, \\
\zeta &= U_0\sqrt{\frac{H}{g}}\Big\{\left[\cos(\kappa\, s) - \exp(-\lambda(s-s_1))\frac{\lambda\, c}{\omega}\sin(\kappa\, s_1)\right]\cos(\omega\, t) \\
&\quad - n\left[\frac{f}{c}\sin(\kappa\, s) + \exp(-\lambda(s-s_1))\frac{\lambda^2 c^2 + \omega^2 - f^2}{fc}\sin(\kappa\, s_1)\right]\sin(\omega\, t)\Big\}.
\end{aligned} \tag{22.137}$$

'As is evident, a Kelvin wave propagating along one side of a half-open rectangular basin cannot always be regularly reflected as a *proper* Kelvin wave (propagating along the other side and in the opposite direction), because far distant from the barrier as $s \to \pm\infty$ the exponential solution has true exponential behaviour only when the real part of λ differs from zero, for which this contribution is asymptotically small. This corresponds to Taylor's problem, but our approximate analysis is very much simpler than was his. Frequency ranges for which the exponential decay in (22.137) occurs lead to solutions with boundary-layer structure and the reflection is *complete*. If λ is imaginary, there is no exponential decay, and a forward-moving Kelvin wave cannot be reflected as a backward-moving Kelvin wave, an incomplete reflection.

To determine the frequency ranges where solutions with boundary-layer character may exist, we renormalize the quantities (22.124) with $\bar{\mu}$, and introduce

[10] In the original paper [27], the third formula is in error.

$$\bar{\sigma} = \frac{\sigma}{\bar{\mu}} = \frac{\omega B}{\sqrt{12gH}},$$

$$\bar{\kappa}^2 = \frac{1}{\bar{\mu}^2} = \frac{1}{12}\pi^2 \left(\frac{b}{L}\right)^2 = \frac{\kappa^2}{(12/B)^2} = -\frac{\lambda^2}{(12/B)^2}, \tag{22.138}$$

$$\bar{\gamma} = \frac{\gamma}{\bar{\mu}} = \frac{fB}{\sqrt{(12gH)}}.$$

The dimensionless frequency $\bar{\sigma}$ is a parameter which involves the essential quantities characterizing the reflection, namely the width B (instead of the longitudinal wavelength L, which has less physical relevance since the channel is semi-infinite), the depth H of the channel, and the frequency of the wave' [27]. $\bar{\gamma}$ is a differently scaled rotation speed and $\bar{\kappa}$ is scaled as in (22.124).

Problem 22.5 *Rewrite the dispersion relation (22.123) in terms of the new scales (22.138) and show that, viewed as an equation for $\bar{\kappa}$, it can be written as*

$$A\bar{\kappa}^4 + E\bar{\kappa}^2 + C = 0, \tag{22.139}$$

$$A = \bar{\sigma}^2, \quad E = (2\bar{\sigma}^2 - 1)(\bar{\gamma}^2 - \bar{\sigma}^2),$$

$$C = \bar{\sigma}^2 \left(\bar{\sigma}^2(\bar{\sigma}^2 - 1 - 2\bar{\gamma}^2) + \bar{\gamma}^2(1 + \bar{\gamma}^2)\right). \tag{22.140}$$

So, for given frequency $\bar{\sigma}$ and given rotation speed $\bar{\gamma}, \bar{\kappa}$ can be determined from (22.139), which, alternatively, gives λ; boundary layer solutions emerge when $\bar{\kappa}$ has a non-vanishing imaginary part. To see when this happens, note that solutions of (22.139) for $\bar{\kappa}$ are given by

$$\bar{\kappa}^2 = \frac{-E \pm \sqrt{E^2 + 4AC}}{2A} = \frac{-E \pm \sqrt{D}}{2A}, \tag{22.141}$$

where the discriminant

$$D = \left(4\bar{\gamma}^2 + 1\right)\bar{\sigma}^4 - 2\bar{\gamma}^2\left(2\bar{\gamma}^2 + 1\right)\bar{\sigma}^2 + \bar{\gamma}^2 \tag{22.142}$$

can be regarded as a bi-quadratic equation for $\bar{\sigma}$. Verify (22.142) and show that its positive roots, $D = 0$, are given by

$$\bar{\sigma}_1 = \frac{\bar{\gamma}}{4\bar{\gamma}^2 + 1}, \quad \bar{\sigma}_2 = \bar{\gamma}. \tag{22.143}$$

(Negative roots need not be evaluated; they correspond to the same oscillation.) ◆

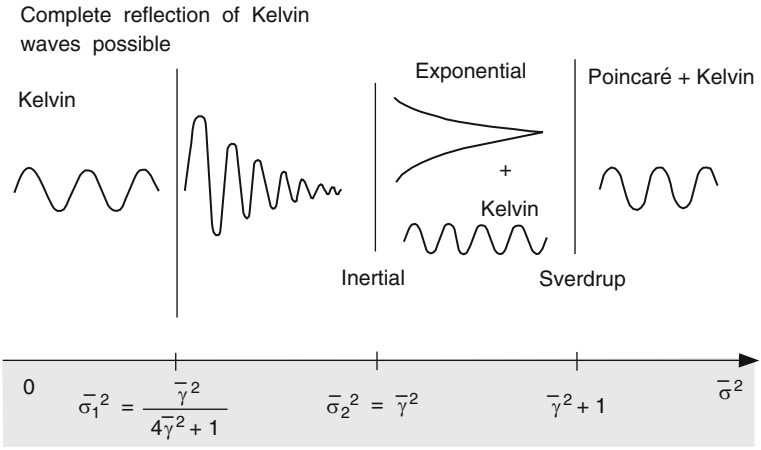

Fig. 22.11 Wavenumber $\bar{\kappa}$ in the frequency range for the first-order channel model, from [27]. © Cambridge University Press, reproduced with permission

So, for positive $\bar{\sigma}$

$$D \begin{cases} > 0 & (\bar{\sigma} < \bar{\sigma}_1, \bar{\sigma} > \bar{\sigma}_2), \\ = 0 & (\bar{\sigma} = \bar{\sigma}_1, \bar{\sigma} = \bar{\sigma}_2), \\ < 0 & (\bar{\sigma}_1 < \bar{\sigma} < \hat{\sigma}_2). \end{cases} \tag{22.144}$$

For $\bar{\sigma}_1 < \bar{\sigma} < \bar{\sigma}_2$, the characteristic equation (22.139) possesses four complex roots $\kappa_{1,2,3,4}$; therefore, the solution (22.134), viewed as functions of s have oscillatory exponential character as one moves away from the barrier. Figure 22.11 illustrates this in the second left sketch. This situation corresponds to complete reflection.

Consider next the two isolated points on the frequency axis where the discriminant vanishes. For $\bar{\sigma} = \bar{\sigma}_2 = \bar{\gamma}$, $D = E = 0$ and consequently $\kappa_{1,2,3,4} = 0$; no wave propagates along the s-axis. Scrutiny of (22.125) shows that ζ is very small in this case while v_s is not. The corresponding wave is therefore of inertial type. For $\bar{\sigma} = \bar{\sigma}_1, E > 0$, and therefore $\kappa^2 > 0$ so that κs is real; waves are purely oscillatory.

Raggio and Hutter continue: 'The above relates to the interval $\bar{\sigma}_1 \leq \bar{\sigma} \leq \bar{\sigma}_2$ as shown in Fig. 22.11. Three different wave types have already been encountered. For $\bar{\sigma} = \bar{\sigma}_1$, incomplete reflection arises; when $\bar{\sigma}_1 < \bar{\sigma} < \bar{\sigma}_2$, complete reflection is possible and when $\bar{\sigma} = \bar{\sigma}_2 = \bar{\gamma}$ no wave propagates. It is advantageous to interrupt the discussion here and to complement Fig. 22.11 with Fig. 22.12. It shows for given frequency $\bar{\sigma}$ in the range $0 < \bar{\sigma} < 2$ and for given rotation speed $\bar{\gamma} = 0.5$ real and imaginary parts of $\bar{\kappa}$ as obtained by exploiting both frequency relations, (22.139) of the channel approximation and the corresponding exact frequency relations of Table 22.2 (written in terms of the overbarred quantities). Because we are only interested in the reflection properties of (22.137), and since $\bar{\kappa}$ and λ are related

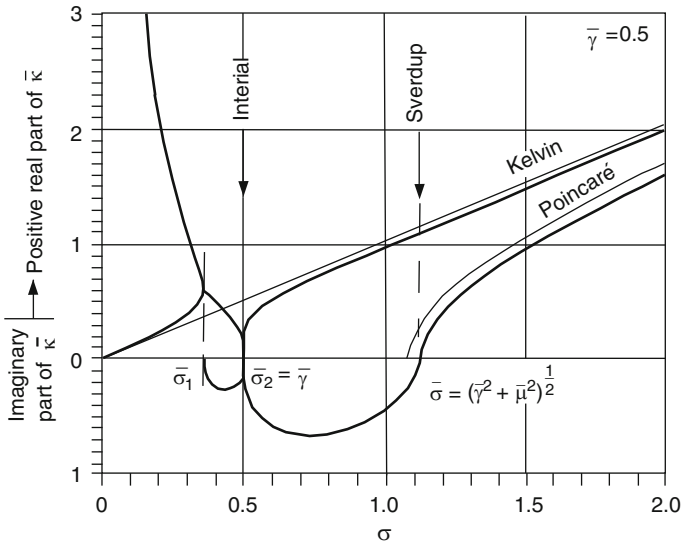

Fig. 22.12 Wavenumber $\bar{\kappa}$ in the frequency range $\bar{\sigma} \in [0, 2.0]$. Either two real (of a total of four) roots or a positive real and a negative imaginary part of the four complex roots are plotted. *Thick lines* correspond to the channel approximation, *thin lines* to the two-dimensional tidal operator. Inertial and Sverdrup wave motions are well predicted by the model, as is the superinertial branch $\bar{\sigma} > \bar{\gamma}$, from [27]. © Cambridge University Press, reproduced with permission

by $(22.138)_2$ it suffices to plot either two real parts of $\bar{\kappa}$ (of all four real roots) or else when $\bar{\kappa}s$ is complex one positive real part and one negative imaginary part. This is done in Fig. 22.12. A real $\bar{\kappa}$ (imaginary λ) will correspond to a purely oscillating solution, and a conjugate complex $\bar{\kappa}$ will give rise to exponentially decaying (positive imaginary part) oscillatory behaviour. The classical Kelvin- and Poincaré-type waves, obtained from Table 22.2 and $(22.138)_2$, are plotted as thin lines and inertial-and Sverdrup-type waves are marked as the points for which $\bar{\kappa} = 0, \bar{\sigma} = \bar{\gamma}$ and $\bar{\sigma} = (\bar{\mu}^2 + \bar{\gamma}^2)^{1/2}$. Thick solid lines correspond to the channel solution using the two-term Cauchy-series expansion. It is seen that in the subinertial range $\bar{\sigma} \leq \bar{\sigma} < \bar{\gamma}$ the exact theory and the channel model lie far apart. This is a first indication that difficulties might arise with the channel approximation for wave motions at subinertial frequencies.

It still remains to discuss the case for which $D > 0$ in (22.142). According to the lemma of Vieta applied to the parabola (22.139) one has

$$\bar{\kappa}_1^2 + \bar{\kappa}_2^2 = \frac{(2\bar{\sigma}^2 - 1)(\bar{\sigma}^2 - \bar{\gamma}^2)}{\bar{\sigma}^2}, \tag{22.145}$$

$$\bar{\kappa}_1^2 \bar{\kappa}_2^2 = \bar{\sigma}^2(\bar{\sigma}^2 - 1 - 2\bar{\gamma}^2) + \bar{\gamma}^2(1 + \bar{\gamma}^2), \tag{22.146}$$

where $\bar{\kappa}_1^2$ and $\bar{\kappa}_2^2$ are the two roots of (22.139). Some cases have to be distinguished. For $\bar{\sigma} < \bar{\sigma}_1$ the right-hand sides of (22.145) and (22.146) are positive,[11] so all $\bar{\kappa}s$ assume real values and all waves with frequencies $\bar{\sigma}^2 \leq \bar{\gamma}^2/(4\bar{\gamma}^2 + 1) = \bar{\sigma}_1^2$ are purely oscillatory. Two of these waves can be interpreted to have Kelvin character; the other two are due to the mathematical approximation of the channel model and have no physical interpretation. This follows from Fig. 22.12, which shows that two wavenumbers are close to those of the classical Kelvin waves, but it can also be inferred from a careful analysis of the velocities and surface elevations $(22.134)_3$ that correspond to these solutions.

The superinertial domain $\bar{\sigma} > \bar{\sigma}_2 = \bar{\gamma}$ separates into two subdomains as follows. For $\bar{\sigma}^2 = \bar{\mu}^2 + \bar{\gamma}^2, \bar{\kappa}_1^2 + \bar{\kappa}_2^2 > 0, \bar{\kappa}_1^2\bar{\kappa}_2^2 = 0$. Thus, there are two solutions where the $\bar{\kappa}s$ are positive, representing two oscillatory solutions and two solutions where no wave propagates in the direction of the channel axis, since the $\bar{\kappa}s$ vanish. The first is of Kelvin-type, the latter represents Sverdrup waves. For $\bar{\sigma}^2 > \bar{\mu}^2 + \bar{\gamma}^2$ the right-hand sides of (22.145) and (22.146) are positive, and the emerging waves are thus oscillatory. These waves are Poincaré- and Kelvin-type and have no boundary-layer structure (see Fig. 22.11). As is evident from Fig. 22.12, the classical solutions and the approximations are close.

Finally, for $\bar{\sigma}_2^2 < \bar{\sigma}^2 < \bar{\mu}^2 + \bar{\gamma}^2$, since $\bar{\kappa}_1^2\bar{\kappa}_2^2 < 0$, but $\bar{\kappa}_1^2 + \bar{\kappa}_2^2 > 0$, the two $\bar{\kappa}$'s are real and two are imaginary, giving rise to exponential and/or purely oscillatory solutions with Kelvin behaviour (Figs. 22.9 and 22.10). The latter figure clearly shows where Kelvin- and Poincaré-type waves are reasonably predicted by the channel model. The shift between the exact Poincaré solution and that of the channel model is due to the use of Cauchy expansions. Also, the superinertial ($\bar{\sigma} < \bar{\gamma}$) Kelvin branch deviates more and more from the exact Kelvin wave as $\bar{\sigma}$ decreases, approaching $\bar{\gamma}$, where the inertial motion obtains. As $\bar{\sigma}$ is further decreased there appears in the model a domain of exponential-type behaviour which is not exhibited by the two-dimensional equations; this points at a limitation of the channel model. For even smaller frequencies Kelvin-type behaviour is recovered, but a second oscillatory solution branch appears with no physical significance. Figure 22.12 also brings out very clearly the reflection properties of Kelvin waves. For $\bar{\sigma}^2 > (\bar{\mu}^2 + \bar{\gamma}^2)$ a reflected Kelvin wave will be essentially of Poincaré-type, since it will have a Poincaré component. For frequencies below the Sverdrup frequency, a Kelvin wave will, however, be essentially reflected as a Kelvin wave, since the reflected wave is either Kelvin-type or exponential-type.

A modification of Fig. 22.11, more appealing and better suited for a comparison with results from numerical solutions of the tidal equations, and valid for $\mu = 5$, is given in Fig. 22.13. The solid lines correspond to $\sigma^2 = [\gamma^2\bar{\mu}^2/(4\gamma^2 + \bar{\mu}^2), \gamma^2, \gamma^2 + \bar{\mu}^2]$ and separate the four different domains introduced above. As far as reflection of a progressing wave is concerned, only two physically significant domains need be distinguished, the Poincaré and Kelvin modes, as indicated. The domain 'Poincaré

[11] The analytical proof of this has not been successful; however, numerical evaluation of the right-hand sides of (22.145) and (22.146) for realistic values of $\bar{\gamma}^2$ and $\bar{\sigma} = (\bar{\sigma}_1 - \varepsilon)$ yields the stated result.

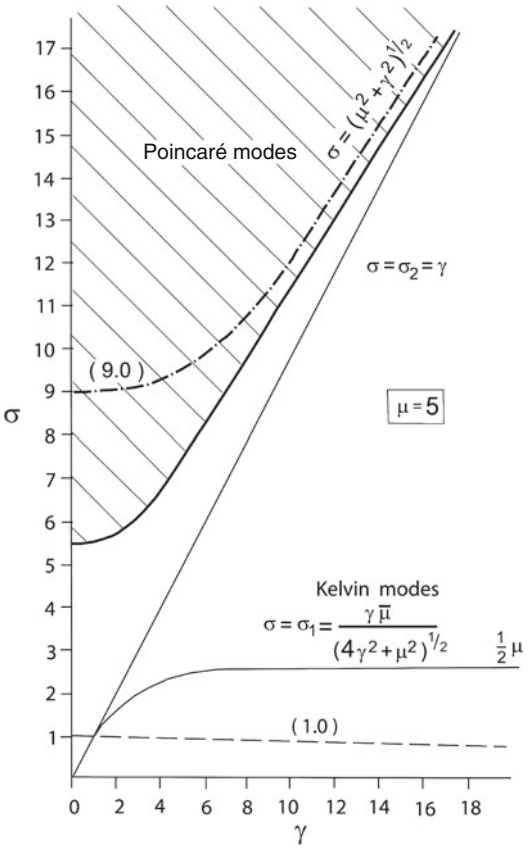

Fig. 22.13 Zones for characteristic eigenmode types. In the hatched area, modes have Poincaré character, in the *unhatched area* they are of Kelvin-type. The *dashed line* represents the first Kelvin mode in an *enclosed rectangle*. It has one amphidromic point and is the lowest transversely antisymmetric mode; it is thus denoted by (1, 0). The *dot-dashed line* (9, 0) represents the first Poincaré mode arising in enclosed rectangular basins, from [27]. © Cambridge University Press, reproduced with permission

modes' is so indicated despite the possibility of Kelvin solutions (see Fig. 22.11) because incoming Kelvin-type waves are reflected by Poincaré-type waves so that the total wave exhibits Poincaré structure. Similarly, for frequencies smaller than the Sverdrup frequency of the channel model, Kelvin waves are reflected by Kelvin waves or exponential type solutions, resulting in Kelvin-like behaviour. Figure 22.13 may be used to estimate whether certain oscillations arising in a basin are of Kelvin- or Poincaré-type. Depending on the value of γ an oscillation of given prescribed frequency may be Poicaré-type in a short and deep channel-like basin but become Kelvin-type as the channel becomes longer and more shallow as γ increases. Such estimates may be helpful in *a priori* estimates to decide whether a certain eigenmode of a basin gives rise to both cyclonic and anti-cyclonic amphidromic systems' after [27].

22.7.4.2 Rectangular Basins

Eigenfrequencies of barotropic seiches in rectangular basins of constant depth can, in principle, be determined by superposition of quasi-standing Kelvin and/or

Poincaré waves with semi-wave lengths of an integer fraction of L and exponential solutions comprising reflections at two barriers. This implies that v_s, v_n and ζ will involve $\exp(-\lambda s)$ and $\exp(+\lambda s)$ to match the no-flow condition through the two lake ends. Since the exponential function will appear with positive and negative arguments, it is advantageous to use the hyperbolic functions $\cosh(\lambda s)$ and $\sinh(\lambda s)$ instead and to place the origin of the coordinate system in the middle of the rectangle with length L and width B. A trial solution for (22.108) that replaces the boundary layer solution then takes the form

$$\begin{aligned} \zeta_{(0)} &= Z_0 \cosh(\lambda s)\cos(\omega t), & \zeta_{(1)} &= Z_1 \sinh(\lambda s)\sin(\omega t), \\ v_s^{(0)} &= U_0 \sinh(\lambda s)\sin(\omega t), & v_s^{(1)} &= U_1 \cosh(\lambda s)\cos(\omega t), \\ v_n^{(0)} &= V_0 \sinh(\lambda s)\cos(\omega t), & v_n^{(1)} &= V_1 \cosh(\lambda s)\sin(\omega t). \end{aligned} \tag{22.147}$$

The trigonometric functions are chosen here such that (22.108) with $\mathbf{A}_s$ given in (22.105) can identically be satisfied. Similarly, the selection of the hyperbolic functions has been chosen to yield an anti-symmetric elevation profile.

Substitution of (22.147) into (22.105) and (22.108) yields

$$\mathbf{B}_\square \mathbf{y}_\square = \mathbf{0} \tag{22.148}$$

with

$$\mathbf{y}_\square = (Z_0, U_0, V_0, Z_1, U_1, V_1)^{\mathrm{T}}$$

$$\mathbf{B}_\square = \left[\begin{array}{cc|ccc|c} -\frac{\omega}{H} & \lambda & 0 & 0 & 0 & 0 \\ \lambda g & \omega & -f & 0 & 0 & 0 \\ \hline 0 & f & -\omega & g & 0 & 0 \\ 0 & 0 & -\frac{12}{B^2} & -\frac{\omega}{H} & \lambda & 0 \\ 0 & 0 & 0 & \lambda g & -\omega & -f \\ \hline 0 & 0 & 0 & 0 & f & \omega \end{array}\right]. \tag{22.149}$$

Note the similarity of $\mathbf{B}_\square$ with $\mathbf{B}$ given in (22.122). The homogeneous linear system (22.148), (22.149) possesses non-trivial solutions for $Z_0, \ldots, V_1$ if $\det \mathbf{B}_\square = 0$, i.e.

$$\sigma^6 - [\bar{\mu}^2 + 2(\gamma^2 - \bar{\lambda}^2)]\sigma^4 + [\bar{\mu}^2(\gamma^2 - \bar{\lambda}^2) + (\gamma^2 - \bar{\lambda}^2)^2]\sigma^2 + \bar{\mu}^2\bar{\lambda}^2\gamma^2 = 0, \tag{22.150}$$

where

$$\begin{aligned} \sigma &:= \frac{\omega L}{\pi\sqrt{gH}}, & \bar{\mu}^2 &:= \frac{12}{\pi^2}\left(\frac{L}{B}\right)^2, \\ \gamma &:= \frac{fL}{\pi\sqrt{gH}}, & \bar{\lambda} &:= \frac{\lambda L}{\pi}. \end{aligned} \tag{22.151}$$

Problem 22.6 *For frequencies satisfying the dispersion relation (22.150) determine* $Z_0, \ldots, V_1$ *from (22.148) and (22.149) and with these the functions (22.147). Show that the first-order solution for* v_s, v_n, ζ *then becomes*

$$
\begin{aligned}
v_s &= A_1 \left\{ \sinh(\lambda s)\sin(\omega t) + n\lambda \frac{\omega}{f} \frac{\lambda^2 gH + \omega^2 - f^2}{\omega^2 - f^2} \cosh(\lambda s)\cos(\omega t) \right\}, \\
v_n &= A_1 \left\{ \frac{\lambda^2 gH + \omega^2}{\omega f} \sinh(\lambda s)\cos(\omega t) \right. \\
&\quad \left. - n\lambda \frac{\lambda^2 gH + \omega^2 - f^2}{\omega^2 - f^2} \cosh(\lambda s)\sin(\omega t) \right\}, \qquad (22.152) \\
\zeta &= A_1 \left\{ \frac{\lambda H}{\omega} \cosh(\lambda s)\cos(\omega t) + n \frac{\lambda^2 gH + \omega^2 - f^2}{gf} \sinh(\lambda s)\sin(\omega t) \right\},
\end{aligned}
$$

where A_1 *is a free amplitude. The above expressions (22.152) represent indeed standing waves, but they cannot satisfy the boundary conditions*

$$
v_s = 0, \quad at \quad s = \pm \tfrac{L}{2}, \qquad (22.153)
$$

since no location s *can be found for which* v_s *would vanish for all* n *and all* t*. A further, non-exponential solution must be found such that (22.152) plus this further solution allow satisfaction of (22.153). Such solutions have been constructed in (22.112) for Kelvin-type waves of the* (5×5)*-system and in (22.125) for Kelvin- and Poincaré-type waves of the* (6×6)*-system. We shall here present the solution for the simpler system (22.112). Using the superscript* $(\cdot)^{\text{Kelvin}}$ *for (22.112) and* $(\cdot)^{\text{hyp.}}$ *for (22.152), the boundary condition (22.153) takes the form*

$$
v_s^{\text{Kelvin}}(\pm \tfrac{L}{2}, n, t) + v_s^{\text{hyp.}}(\pm \tfrac{L}{2}, n, t) = 0. \qquad (22.154)
$$

◆

If one substitutes v_s from $(22.152)_1$ and $(22.112)_2$ into (22.154), an equation of the form

$$
(\cdot)\sin(\omega t) + [\cdot]\cos(\omega t) = 0 \quad \forall t
$$

emerges, which must hold for all time, implying $(\cdot) = 0, [\cdot] = 0$. This yields

$$
\begin{aligned}
A_1 &= -U_0 \frac{\sin\left(\frac{1}{2}\kappa L\right)}{\sinh\left(\frac{1}{2}\lambda L\right)}, \\
&\gamma^2(\sigma^2 - \gamma^2)\tanh(\tfrac{1}{2}\pi\bar{\lambda}) + \sigma\bar{\lambda}(\bar{\lambda}^2 + \sigma^2 - \gamma^2)\tan(\tfrac{1}{2}\pi\sigma) = 0,
\end{aligned} \qquad (22.155)
$$

where U_0 is the free amplitude of the Kelvin solution (22.112). With $(22.155)_1$ the compound solution of the first-order problem can be expressed as

$$
\begin{aligned}
v_s &= U_0 \Bigg\{ \left[\sin(\kappa\, s) - \frac{\sin\left(\frac{1}{2}\kappa L\right)}{\sinh\left(\frac{1}{2}\lambda\, L\right)} \sinh(\lambda\, s) \right] \sin(\omega\, t) \\
&\quad - n \left[\frac{f}{c} \cos(\kappa\, s) + \lambda \frac{\omega}{f} \frac{\sin\left(\frac{1}{2}\kappa L\right)}{\sinh\left(\frac{1}{2}\lambda L\right)} \frac{\lambda^2 c^2 + \omega^2 - f^2}{\omega^2 - f^2} \cosh(\lambda\, s) \right] \cos(\omega\, t) \Bigg\}, \\
v_n &= -U_0 \frac{\sin\left(\frac{1}{2}\kappa\, L\right)}{\sinh\left(\frac{1}{2}\lambda\, L\right)} \Bigg\{ \frac{\lambda^2 c^2 + \omega^2}{\omega f} \sinh(\lambda\, s) \cos(\omega\, t) \\
&\quad - n\lambda \frac{\lambda^2 c^2 + \omega^2 - f^2}{\omega^2 - f^2} \cosh(\lambda\, s) \sin(\omega\, t) \Bigg\}, \qquad (22.156) \\
\zeta &= U_0 \sqrt{\frac{H}{g}} \Bigg\{ \left[\cos(\kappa\, s) - \frac{\lambda\, c}{\omega} \frac{\sin\left(\frac{1}{2}\kappa\, L\right)}{\sinh\left(\frac{1}{2}\lambda\, L\right)} \cos(\lambda\, s) \right] \cos(\omega\, t) \\
&\quad - n \left[\frac{f}{c} \sin(\kappa\, s) - \frac{\lambda c^2 + \omega^2 - f^2}{fc} \frac{\sin\left(\frac{1}{2}\kappa\, l\right)}{\sinh\left(\frac{1}{2}\lambda\, L\right)} \sinh(\lambda\, s) \right] \sin(\omega\, t) \Bigg\},
\end{aligned}
$$

in which $c^2 = gH$. In this solution, the dispersion relation (22.150) and $(22.155)_2$ together determine the eigenfrequency σ and the decay parameter $\bar{\lambda}$.

Numerical solutions of (22.150) and $(22.155)_2$ have been calculated, and a selection of results is given in Fig. 22.14. This figure displays the first eigenfrequency σ as a function of the rotational speed γ for a square and for rectangles of length 4, 5 and 16 times their width. The curve for $\mu = 5$ corresponds to the dashed line in Fig. 22.13. This mode has one amphidromic point and is the lowest-order transversely anti-symmetric solution, and is thus denoted by the symbol (1, 0). Results have also been obtained for higher-order modes; for mode (9, 0) these are shown in Fig. 22.13. It may also be recognized that for elongated rectangular basins the (1, 0) eigenfrequency is fairly insensitive to the rotational speed. The inertial mode is also shown for completeness, for it is also an eigenfrequency of the system. It is also noteworthy in this connection to recognize that the co-phase lines of a Poincaré-type mode may rotate in the clockwise direction which is typical for Poincaré behaviour. (Recall that Kelvin wave dynamics needed to assume that the co-phase lines are all moving in the counterclockwise direction.) Therefore, the first-order theory reproduces all essential features of the two-dimensional tidal theory qualitatively correctly. We shall see that higher-order models also improve the accuracy of the prediction.

It is not the intention here to explore the channel approximation fully for rectangular cross sections. One could, for instance complement Fig. 22.14 with similar plots for higher frequencies and could further treat the reflection problem using (22.125) rather than (22.112). This would lead to results which would demonstrate better agreement with the exact results and would simply provide an alternative to the work of Rao [29], compare also Chap. 12, Sect. 12.6. Rather, the intention was to search for the conditions of validity of the channel model for its use in real natural elongated basins. As far as rectangles are concerned, limitations of applicability have been found, indicating that the channel model is likely to be

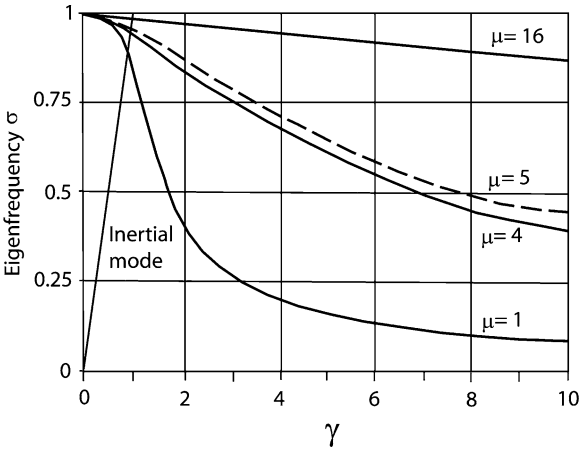

Fig. 22.14 First eigenfrequency σ for a square and rectangles of length 4, 5 and 16 times their width, plotted against the rotation speed γ, from [27]. © Cambridge University Press, reproduced with permission

a valid approximation for superinertial frequencies, but may be problematic for motions at frequencies below the inertial frequency. Since superinertial frequencies are the domain of gravitational motions, and rotational modes are subinertial, it is concluded that the channel approximation will predict gravitational modes reasonably well.

22.8 Ring-Shaped Basins with Constant Depth

22.8.1 Solutions of the Two-Dimensional Tidal Equation

Solutions to the frictionless tidal equations in polar coordinates have been constructed by Lord Kelvin [16]. For circular basins they are discussed by Lamb [18] and Howard [12]. Also other interesting situations can be found in Pnuelli and Pekeris [22].

If (r, θ) are polar coordinates and $(v_r,\ v_\theta)$ the radial and azimuthal physical velocity components, the boundary value problem for free barotropic oscillations for a ring-shaped basin takes the form

$$\left.\begin{aligned} &\frac{\partial v_r}{\partial t} + f v_\theta + g\frac{\partial \zeta}{\partial r} = 0, \\ &\frac{\partial v_\theta}{\partial t} - f v_r + g\frac{1}{r}\frac{\partial \zeta}{\partial \theta} = 0, \\ &\frac{\partial \zeta}{\partial t} + \frac{1}{r}\left\{\frac{\partial}{\partial r}(r v_r H) + \frac{\partial}{\partial \theta}(v_\theta H)\right\} = 0, \end{aligned}\right\} \begin{aligned} &r \in (r_i, r_a), \\ &\theta \in (\theta_1, \theta_2), \end{aligned} \tag{22.157}$$

$$\begin{aligned} v_r &= 0, \quad \text{at } r = r_a, \quad r = r_i, \quad \theta \in [\theta_1, \theta_2], \\ v_\theta &= 0, \quad \text{at } \theta = \theta_1, \quad \theta = \theta_2, \quad r \in [r_i, r_a]. \end{aligned} \tag{22.158}$$

Here, r_i and r_a denote the inner and outer radii of the ring and (θ_1, θ_2) bound the sector of the ring. If v_r, v_θ, ζ are proportional to $\exp(\mathrm{i}\omega t)$, the amplitude functions (carrying a tilde) must satisfy the equations

$$\begin{aligned} \nabla^2\tilde{\zeta} + \frac{\omega^2 - f^2}{gH}\tilde{\zeta} &= \frac{\partial^2\tilde{\zeta}}{\partial r^2} + \frac{1}{r}\frac{\partial\tilde{\zeta}}{\partial r} + \frac{1}{r^2}\frac{\partial^2\tilde{\zeta}}{\partial\theta^2} + \frac{\omega^2 - f^2}{gH}\tilde{\zeta} = 0, \\ \tilde{v}_r &= \frac{g}{\omega^2 - f^2}\left(\mathrm{i}\omega\frac{\partial}{\partial r} - f\frac{1}{r}\frac{\partial}{\partial\theta}\right)\tilde{\zeta}, \\ \tilde{v}_\theta &= \frac{g}{\omega^2 - f^2}\left(f\frac{\partial}{\partial r} + \mathrm{i}\omega\frac{1}{r}\frac{\partial}{\partial\theta}\right)\tilde{\zeta}, \end{aligned} \tag{22.159}$$

with the no-flux boundary conditions

$$\begin{aligned} f\frac{\partial\tilde{\zeta}}{\partial r} + \frac{\mathrm{i}\omega}{r}\frac{\partial\tilde{\zeta}}{\partial\theta} &= 0, \quad \text{at } \theta = \theta_1, \theta_2, \\ \mathrm{i}\omega\frac{\partial\tilde{\zeta}}{\partial r} - \frac{f}{r}\frac{\partial\tilde{\zeta}}{\partial\theta} &= 0, \quad \text{at } r = r_a, r_i. \end{aligned} \tag{22.160}$$

In the above, H is the water depth and ∇^2 the two-dimensional Laplace operator.

'Solutions[12] of (22.159)$_3$, (22.160) with period 2π for θ have separation form $\tilde{\zeta} = Z(r)\exp(\mathrm{i}\kappa\theta), \kappa = 0, \pm1, \pm2, \ldots$,where κ is positive (negative) for a wave progressing in the negative (positive) direction of θ; they are given by

$$Z(r) = \begin{cases} \bar{\beta}_1 J_\kappa(kr) - \hat{\beta}_1 Y_\kappa(kr), \; k^2 = \dfrac{\omega^2 - f^2}{gH} > 0, \\ \beta_2 I_\kappa(kr) - \hat{\beta}_2 K_\kappa(kr), \; k^2 = \dfrac{\omega^2 - f^2}{gH} < 0, \end{cases} \tag{22.161}$$

in which $J_\kappa, Y_\kappa, (I_\kappa, K_\kappa)$ are the (modified) Bessel functions of the first and second kind. The β-coefficients are determined by satisfying the boundary conditions (22.160) at $r = r_i, r_a$. This yields the dispersion relation

$$\bar{\alpha}_1\hat{\beta}_1 - \hat{\alpha}_1\bar{\beta}_1 = 0. \tag{22.162}$$

[12] This text is taken from Raggio and Hutter [14, 24].

in which

$$\left.\begin{aligned}\bar{\alpha}_1 &= \omega\, k\, r_i\, J'_\kappa(k\, r_i) - f\kappa\, J_\kappa(k\, r_i),\\ \hat{\alpha}_1 &= \omega\, k\, r_i\, Y'_\kappa(k\, r_a) - f\kappa\, Y_\kappa(k\, r_i),\\ \bar{\beta}_1 &= A_1(\omega\, k\, r_a J'_\kappa(k\, r_a) - f\kappa\, J_\kappa(k\, r_a)),\\ \hat{\beta}_1 &= A_1(\omega\, k\, r_a Y'_\kappa(k\, r_a) - f\kappa\, Y_\kappa(k\, r_a)).\end{aligned}\right\} \quad k^2 > 0 \qquad (22.163)$$

Primes indicate differentiation with respect to the argument. When $k^2 < 0$, J_κ and Y_κ in (22.163) must be replaced by I_κ and K_κ and the argument by $\sqrt{|k^2|}r_a$ and $\sqrt{|k^2|}r_i$..

The ensuing comparison with the channel model is simplified when the abbreviations

$$\begin{aligned} a &= \frac{B}{2R_m} < 1, \quad R_m = \tfrac{1}{2}(r_a + r_i), \quad B = (r_a - r_i),\\ m &= \kappa\left(1 + \frac{f}{\omega}\right) = \kappa\left(1 + \frac{R_m f/\sqrt{gH}}{R_m\omega/\sqrt{gH}}\right) = \kappa\left(1 + \frac{\gamma}{\sigma}\right), \qquad (22.164)\\ q &= k\, R_m = \sigma^2 - \gamma^2 \end{aligned}$$

are introduced; a is an aspect ratio, a measure for the curvature and the narrowness of the ring. For $a = 0$ the straight channel is obtained and $a = 1$ corresponds to the full circle (excluding the origin). With (22.164) the dispersion relation becomes

$$\begin{aligned} &\frac{q(1+a)J_{\kappa-1}(q(1+a)) - mJ_\kappa(q(1+a))}{q(1+a)Y_{\kappa-1}(q(1+a)) - mY_\kappa(q(1+a))}\\ &\quad = \frac{q(1-a)J_{\kappa-1}(q(1-a)) - mJ_\kappa(q(1-a))}{q(1-a)Y_{\kappa-1}(q(1-a)) - mY_\kappa(q(1-a))}, \quad k^2 > 0. \qquad (22.165) \end{aligned}$$

For non-rotating basins and small a, using Taylor series expansions, this equation was explored by Johns and Hamzah [15]. Notice that the dispersion relation is not invariant under the transformation $\kappa \to -\kappa$, implying that frequencies corresponding to wave trains progressing in the positive and negative direction of θ are different from each other, if the wavenumber $|\kappa|$ is the same in the two situations. On the other hand, two waves travelling in opposite directions at the same frequency possess different wavenumbers.

In circular basins, Poincaré-, Kelvin- and inertial-type waves in an annular basin possess a radial component, since (22.159) and (22.160) do not allow solutions for which the radial velocity component would vanish for all $r \in [r_i, r_a]$. They can be distinguished from Poincaré-type waves because their amplitude falls off rapidly away from the boundary and they move in the direction of rotation. The exploitation of (22.165) will be discussed together with the corresponding equation of the channel model.

22.8.2 First-Order Channel Model

Consider

$$\mathbf{A}_{\mathrm{R}}\mathbf{y} = \mathbf{0} \quad \text{with} \quad \mathbf{y} = (\zeta^{(0)}, v_\theta^{(0)}, v_s^{(0)}, \zeta^{(1)}, v_\theta^{(1)}, v_s^{(1)}), \tag{22.166}$$

where $\mathbf{A}_{\mathrm{R}}$ is given in (22.107). Two separate solutions will be presented of which the first allows approximate construction of Kelvin-type waves and the second gives the full treatment including Poincaré- and inertial-type waves.

22.8.2.1 Kelvin-Type Waves

Even though Kelvin-type waves in curved channels cannot be characterized by vanishing transverse velocity, these velocity components cannot become large in narrow channels, since they must vanish at the side boundaries. By way of approximating the true solution we may nevertheless set $v_n^{(0)} = v_n^{(1)} = 0$ and then find an approximate solution from the appropriate combination of the six equations (22.166). Thus, assuming solutions of the form

$$\mathbf{y} = (Z_0, U_0, 0, Z_1, U_1, 0)F(s \pm ct), \tag{22.167}$$

where c is a phase speed, six equations for four unknowns are obtained. Setting $v_n^{(0)} = v_n^{(1)} = 0$ corresponds effectively to ignoring transverse momentum balance; the dispersion relation is obtained by considering only those four equations which correspond to zeroth and first order mass and longitudinal momentum balances. When the determinant of the corresponding system of equations is set to zero, the following expression for the frequency or phase speed is obtained:

$$\sigma^2 = \frac{c^2}{gH} = \frac{\omega^2/\kappa^2}{gH} = \frac{1}{\left(1 \pm \frac{a}{\sqrt{3}}\right)^2}. \tag{22.168}$$

There are two values of c (or σ) depending on whether the wave is progressing in the clockwise (positive sign) or anticlockwise (negative sign) direction. The two frequencies lie above and below the Kelvin frequency of a straight channel and approach the latter as $a \to 0$. Whereas the frequency relation was derived using balance relations of mass and longitudinal momentum, but ignoring transverse momentum balance, the amplitudes in (22.167) can only be found by combining the two mass balance equations with the two zeroth-order momentum equations. Here, lowest order transverse momentum balance is accounted for. This allows to assign the necessary weight to the quasi-geostrophic balance. 'Solving' the equations in this way gives for the longitudinal velocity and the surface elevation

$$
\begin{aligned}
v_s &= U_0 \left\{ 1 \pm n \frac{f}{c}\sigma^2 \left[-\frac{1+\frac{a^2}{3}}{1 \mp \sigma^2 d \frac{f}{c}\left(1-\frac{a^2}{3}\right)} \right.\right. \\
&\quad \left.\left. + \frac{a^2}{3} \frac{1+\frac{a^2}{3}}{1 \mp \sigma^2 d \frac{f}{c}\left(1-\frac{a^2}{3}\right)} \right] - \frac{n}{R_m} \right\} F(s \mp ct), \\
\zeta &= \pm \sqrt{\frac{H}{g}} U_0 \left\{ \sigma \mp d \frac{f}{c} \frac{1}{\sigma} \frac{1+\frac{a^2}{3}}{1-\sigma^2 d \frac{f}{c}\left(1-\frac{a^2}{3}\right)} \right. \\
&\quad \left. - n \frac{f}{c}\sigma^2 \frac{1+\frac{a^2}{3}}{1-\sigma^2 d \frac{f}{c}\left(1-\frac{a^2}{3}\right)} \right\} F(s \mp ct).
\end{aligned}
\tag{22.169}
$$

Besides the aspect ratio a second parameter, df/c, has entered whose order of magnitude is 10^{-5} or smaller, justifying (22.169) in the limit $df/c \to 0$. This property indicates how the approximate and rather ad-hoc procedure of obtaining (22.168), (22.169) can be made more rigorous, if desired, by an asymptotic analysis in which $\mathbf{y} = (Z_0, U_0, 0, Z_1, 0) F(s \pm ct)$ is assumed, first-order transverse momentum is neglected and solutions of the emerging homogeneous system of equations is sought in the limit $df/c \to 0$. The resulting approximate solution is (22.168) and (22.169).

Notice, finally, that by combining a clockwise and anticlockwise moving wave (22.169) with F replaced by $\cos(\cdot)$ or $\sin(\cdot)$, a Kelvin amphidromy can be deduced,

$$
\begin{aligned}
v_s = \frac{U_0}{2} \big\{ & \cos(\kappa\, s) \left[(A^+ + A^-) \cos(\omega\, t) \cos(\Delta\omega\, t) \right. \\
& \left. + (A^+ - A^-) \sin(\omega\, t) \sin(\Delta\omega\, t) \right] \\
& - \sin(\kappa\, s) \left[(A^+ + A^-) \cos(\omega\, t) \sin(\Delta\omega\, t) \right. \\
& \left. + (A^+ - A^-) \sin(\omega\, t) \cos(\Delta\omega\, t) \right] \big\},
\end{aligned}
\tag{22.170}
$$

in which

$$
\omega = \tfrac{1}{2}(\omega^+ + \omega^-) \quad \text{and} \quad \Delta\omega = \tfrac{1}{2}(\omega^+ - \omega^-). \tag{22.171}
$$

$A^{\pm}(n)$ denotes the bracketed term in $(22.169)_1$, when the upper and lower signs apply. In the limit as $R_m \to \infty$ ($a \to 0$), $\Delta\omega \to 0$, $\omega \to \sqrt{gH}\kappa$ and (22.170) agrees with (22.117), identical with the straight channel Kelvin amphidromy. There is no position $s = s_1$ for which v_s would vanish for all n and t. Qualitatively this corresponds to the situation encountered by Taylor [34] when trying to solve the reflection problem of a Kelvin wave in a half open gulf. Solving the reflection problem would correspond to constructing boundary layer solutions of $\mathbf{A}_{\mathrm{R}}\mathbf{y} = \mathbf{0}$, but (22.170) is nonetheless physically meaningful in a closed ring (lake with an island), if the periodicity condition $\kappa\, R_m = l, l = 1, 2, 3, \ldots$, is applied. From (22.167) this yields corresponding eigenfrequencies

$$\omega_l^{\pm} = \frac{\sqrt{GH}\, l}{R_m} \frac{1}{1 \pm \frac{a}{\sqrt{3}}}. \tag{22.172}$$

22.8.2.2 Wave Solution of the Full First-Order System

For the full (6×6)-system of equations solutions of the form

$$\mathbf{y} = \mathbf{y}_0 \exp\left(\mathrm{i}(\kappa\, s + \omega\, t)\right) \tag{22.173}$$

yield again a homogeneous system of equations for the amplitude $\mathbf{y}_0$ with ω as eigenvalue for given κ. The evaluation of the characteristic equation and the determination of eigensolutions is very elaborate, but routine and little can be learned from the presentation of the analysis. We confine attention here to a comparison of the dispersion relation of the exact theory, (22.165) and that resulting from (22.166). Substituting (22.173) into (22.166) and setting the determinant of the emerging system of equations equal to zero yields

$$\begin{aligned}
&\{(1-\nu^2)^3 + 2\nu^2\}\sigma^6 - \left\{2\gamma^2\{(1-\nu^2)^3 + \nu^2\} - 2\nu^4 + \frac{(1-\nu^2)^2}{\nu^2}\right\}\sigma^4 \\
&+ \{2\gamma\{(1-\nu^2)^2 + \nu^2\}\}\sigma^3 + \left\{\gamma^4(1-\nu^2)^3 + \gamma^2\frac{(1-\nu^2)^2}{\nu^2} - \nu^4 - \nu^2 - 2 + \frac{1}{\nu^2}\right\}\sigma^2 \\
&+ \{\gamma^3(\nu^2 - 1 - 2\nu^4) + 2\gamma(1-\nu^2)\}\sigma - \gamma^2\frac{(1-\nu^2)^2}{\nu^2} = 0.
\end{aligned} \tag{22.174}$$

in which

$$\nu^2 = \frac{1}{3}a^2, \quad \sigma = \frac{\omega}{\kappa\sqrt{gH}}, \quad \gamma = f\kappa\sqrt{gH}. \tag{22.175}$$

The dispersion relation thus has the form $f(\sigma, \gamma, a) = 0$. It was solved numerically, and results were compared with those obtained from the exact relations (22.165). In a first set of calculations the aspect ratio was given the fixed value $a = 0.5$ and γ was varied between 0 and 3. For a homogeneous water body we certainly have $\gamma < 1$, but $\gamma > 1$ includes the case of the baroclinic mode of a two layer system with reduced height and density (this is the TED-model). Figure 22.15 shows the results for $0 < \gamma < 0.55$. The solid lines represent the real solutions to the channel model dispersion relation, representing Poincaré-, Kelvin- and inertial-type wave motions. The inertial type motion is also a solution. Each of the clockwise and anti-clockwise motions leads to pairs of frequencies. Figure 22.15 contains also results for the approximate solution of a straight channel (shown as dashed lines). These were obtained from the dispersion relation of straight channels but can also be deduced by exploring (22.174) in the limit $a \to 0$ ($\nu \to 0$). Except for the Poincaré-type

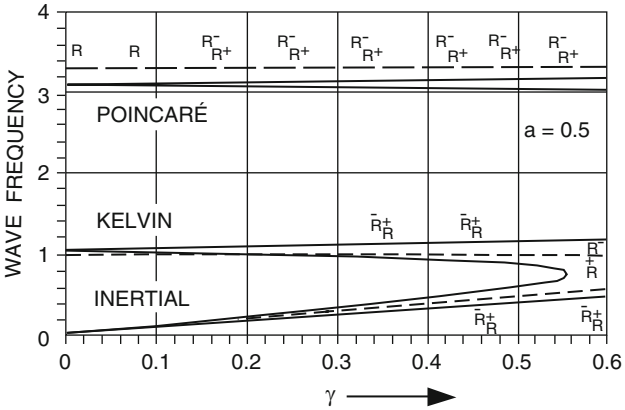

Fig. 22.15 Dimensionless free wave frequency σ in a ring shaped channel, plotted against the rotation speed $\gamma = f/(\kappa\sqrt{gH})$ between 0 and 0.55 for the aspect ratio $a = B/(2R) = 0.5$. *Solid lines* represent the approximate solutions. *Dashed lines* show the approximate solutions ignoring the curvature. The solutions of the two-dimensional tidal operator are indicated by the letters R^+ and R^-, the former for the counterclockwise travelling wave, the latter for a clockwise motion (R if the difference of the two is not visible on the graph), from [14]. © Springer, reproduced with permission

wave these approximate solutions lie between the two ring solutions. Figure 22.15 also contains the results of the two-dimensional theory (22.165). These solutions are indicated by the letters R^+, R and R^-, the former for counterclockwise rotating waves, the latter for a clockwise motion, and R if the difference of the two is not visible on the graph.

For Kelvin-type waves the approximate and exact solutions agree reasonably well; for Poincaré-type waves differences are larger, but relative errors stay below 12%. Because the straight channel solution also has a relative error of comparable magnitude compared with the corresponding two-dimensional solution, we should not conclude that the straight channel solution is superior for the description of curved channels. The results, however, clearly indicate that, as far as frequencies are concerned, the straight channel equations appear to be sufficiently accurate. But when curvature is included, the channel model shares with the two-dimensional theory the property of giving frequency pairs of each type of wave. Similar results are also shown in Fig. 22.16, but now for $0 < \gamma < 3$. For values of γ larger than 3 no special behaviour occurs. In the transition zone near $\gamma = 1$, two frequency solutions cannot be real for a given wave number κ. This is no surprise since in this region there can be purely oscillating solutions in the straight channel, which was already observed for rectangles. Figure 22.17 displays the same results for a fixed rotational speed $\gamma = 0.5$ and values of the aspect ratio between 0 and 1. Approximate frequencies are insufficiently accurate for basins approaching the full circle, $a = 1$. Further calculations indicate that the smaller γ the better the approximation.

Summarizing these findings, we conclude that the channel approximation in ring shaped basins is reasonable as long as the aspect ratio a and the rotation speed γ

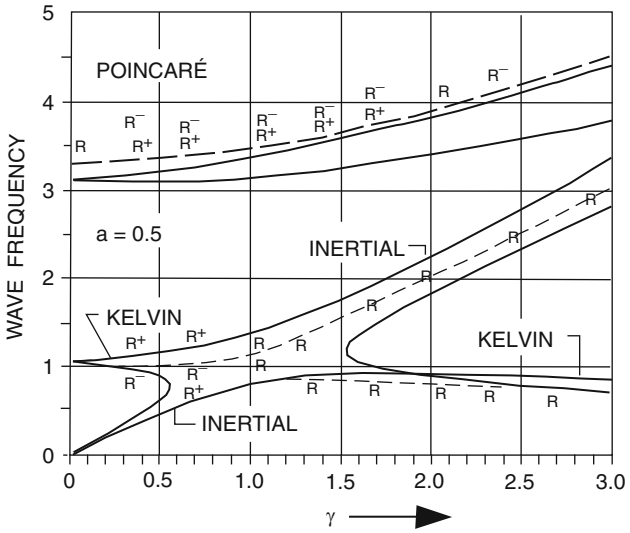

Fig. 22.16 Dimensionless free wave frequency σ in a *ring shaped canal*, plotted against the rotation speed $\gamma \in [0, 3]$ for the aspect ratio $a = 0.5$, from [14]. © Springer, reproduced with permission

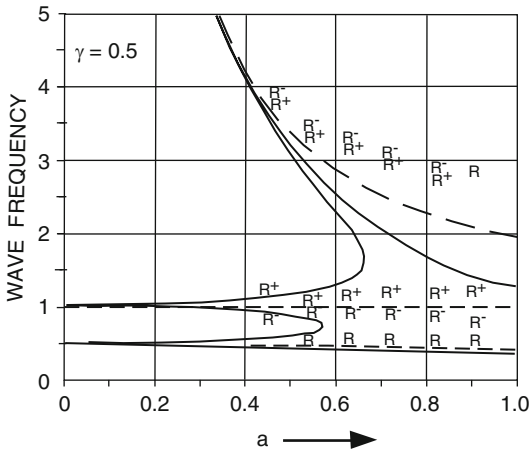

Fig. 22.17 Dimensionless free wave frequency σ in a *ring shaped canal*, plotted against the aspect ratio $a \in [0, 1]$, for the rotation speed $\gamma = 0.5$. For further explanation see also Fig. 22.15, from [14]. © Springer, reproduced with permission

are both smaller than 0.5. Under these restrictions the influence of the curvature of the channel is negligible, however. *To the oceanographers or limnologists this may serve as an* a posteriori *proof for their common procedure when blindly applying the Chrystal equation (valid in Cartesian coordinates) to a curvilinear system of coordinates.*

22.9 Higher Order Chrystal-Type Models Applied to Free Oscillations in Natural Basins

In the previous two sections our attention was focused on the performance of a first-order model to tidal oscillations. It was shown that the essential features exhibited by the two-dimensional tidal theory were reproduced by the first-order channel model: Kelvin-, Poincaré- and inertial-type waves; reflection of such waves at a barrier of a canal and characteristic solutions in elongated closed rectangles and rings of constant depth. Here we wish to complement this analysis by presenting results of a numerical study of gravitational oscillations in natural elongated basins. Our view is to treat the channel model of order N as a hierarchic system of approximations of which the increasing degree of order will provide better and better approximations of the characteristic motion of the two-dimensional field equations. The basic references are [24, 25, 28].

22.9.1 The Nth Order Two-Point Boundary-Value Problem for Barotropic Forced or Free Oscillations

The governing equations of the Nth order channel model have been presented in (22.72), (22.78) and (22.79). They hold in that form for 'arbitrary' shape function expansions of the unknown fields. When the non-linear convective terms and the non-linear terms due to the curvilinear coordinate system are ignored, these equations take the forms

$$\begin{aligned}
\rho_0 \left\{ \mathbf{C}^{(1)} \frac{\partial \mathbf{v}_s}{\partial t} - f \mathbf{C}^{(1)} \mathbf{v}_n + g \hat{\boldsymbol{C}}^{(0)} \frac{\partial \boldsymbol{\zeta}}{\partial s} \right\} + \mathbf{R}^{(1)} \mathbf{v}_s + \mathbf{p}_s^{*(0)} - \mathbf{w}_s^{*(1)} &= \mathbf{0}, \\
\rho_0 \left\{ \mathbf{C}^{(1)} \frac{\partial \mathbf{v}_n}{\partial t} + f \mathbf{C}^{(1)} \mathbf{v}_s + g \hat{\mathbf{C}}_{\phi_n}^{(1)} \boldsymbol{\zeta} \right\} + \mathbf{R}^{(1)} \mathbf{v}_n + \mathbf{p}_n^{*(1)} - \mathbf{w}_n^{*(1)} &= \mathbf{0}, \\
\hat{\mathbf{Z}}^{(1)} \frac{\partial \boldsymbol{\zeta}}{\partial t} + \frac{\partial}{\partial s} \left(\mathbf{C}^{(0)} \mathbf{v}_s \right) - \mathbf{C}_{\phi_n}^{(1)} \mathbf{v}_n - \mathbf{C}_{\phi_z}^{(1)} \mathbf{v}_z &= \mathbf{0}, \\
\mathbf{H}_s^{(0)} \mathbf{v}_s + \mathbf{H}_n^{(1)} \mathbf{v}_n - \mathbf{H}^{(1)} \mathbf{v}_z &= \mathbf{0}.
\end{aligned} \tag{22.176}$$

Here, $\mathbf{v}_s, \mathbf{v}_n, \mathbf{v}_z$ are unknown vector quantities in $\mathbb{R}^N$, representative of the velocity components in the longitudinal, transverse and vertical directions of the curvilinear coordinate system (s, n, z), and $\boldsymbol{\zeta}$ characterizes the surface elevation. The coefficient matrices are known functions of position s and are defined in Appendix 22.A, and vector quantities carrying an asterisk are those due to atmospheric pressure and wind forces, also defined in Appendix 22.A. The physical fields v_s, v_n, v_z, ζ are related to $\mathbf{v}_s, \mathbf{v}_n, \mathbf{v}_z$ and $\boldsymbol{\zeta}$ by the shape function expansions

$$v_s = \boldsymbol{\phi} \cdot \mathbf{v}_s, \quad \ldots \quad \zeta = \boldsymbol{\phi} \cdot \boldsymbol{\zeta} \tag{22.177}$$

and the dimension of $\mathbf{v}_s, \ldots$ or $\boldsymbol{\phi}$ defines the order of the model.

Equations $(22.176)_{1,2}$ represent the longitudinal and transverse momentum equations, $(22.176)_3$ derives from the mass balance equation (see Sect. 22.5.1) and $(22.176)_4$ stems from the kinematic surface condition at the bottom surface. For an Nth order model (22.176) is a system of $3N$ partial differential equations and N algebraic equations for $\mathbf{v}_s, \mathbf{v}_n, \mathbf{v}_z$ and $\boldsymbol{\zeta}$. The remaining variables carrying an asterisk are prescribed external forces. For large N computational efforts are likely large, but this disadvantage of the channel model is partly compensated as a steady process and a periodic process (based on a Fourier transformation) will alter the partial differential equations in the variables s and t into ordinary differential equations and the boundary value problem into a two-point boundary-value problem for a set of ordinary differential equations for which secure integrators exist. Thus, by writing for each function in (22.176) $\mathbf{f} = \mathbf{f}_0 \exp(\mathrm{i}\omega t)$ with complex valued amplitude vector $\mathbf{f}_0$, the following complex-valued set of equations emerges (the subscript $(\cdot)_0$ is now dropped)

$$\begin{gathered}
\mathbf{D}\frac{\mathrm{d}\mathbf{y}}{\mathrm{d}s} + \mathbf{B}\mathbf{y} + \mathbf{C}\mathbf{x} = \mathbf{l}_s^*, \\
\mathbf{E}\mathbf{y} + \mathbf{A}\mathbf{x} = \mathbf{l}_n^*, \\
\mathbf{x} = (\mathbf{v}_n, \mathbf{v}_z)^{\mathrm{T}}, \quad \mathbf{y} = (\mathbf{v}_s, \boldsymbol{\zeta})^{\mathrm{T}}, \\
\mathbf{l}_s^* = \frac{1}{\rho}(\mathbf{w}_s^{*(1)} - \mathbf{p}_s^{*(0)}, \mathbf{0})^{\mathrm{T}}, \quad \mathbf{l}_n^* = \frac{1}{\rho}(\mathbf{w}_n^{*(1)} - \mathbf{p}_n^{*(1)}, \mathbf{0})^{\mathrm{T}},
\end{gathered} \tag{22.178}$$

where $\mathbf{x}, \mathbf{y}, \mathbf{l}_{s,n}^*$ are complex valued vectors in $\mathbb{R}^N$ and

$$\begin{aligned}
\mathbf{D} &= \begin{pmatrix} \mathbf{0} & g\hat{\mathbf{C}}^{(0)} \\ \mathbf{C}^{(0)} & \mathbf{0} \end{pmatrix}, \\
\mathbf{B} &= \begin{pmatrix} \mathbf{R}^{(1)} + \mathrm{i}\omega\mathbf{C}^{(1)} & \mathbf{0} \\ \frac{\partial \mathbf{C}^{(0)}}{\partial s} & \mathrm{i}\omega\mathbf{Z}^{(1)} \end{pmatrix}, \\
\mathbf{C} &= \begin{pmatrix} f\mathbf{C}^{(1)} & \mathbf{0} \\ \mathbf{C}_{\psi_n}^{(1)} & \mathbf{C}_{\psi_z}^{(1)} \end{pmatrix} = \begin{pmatrix} \mathbf{C}_1 & \mathbf{0} \\ \mathbf{C}_{\psi_n}^{(1)} & \mathbf{C}_{\psi_z}^{(1)} \end{pmatrix},
\end{aligned} \tag{22.179}$$

$$\begin{aligned}
\mathbf{A} &= \begin{pmatrix} \mathbf{R}^{(1)} + \mathrm{i}\omega\mathbf{C}^{(1)} & \mathbf{0} \\ \mathbf{H}_n^{(1)} & -\mathbf{H}^{(1)} \end{pmatrix} = \begin{pmatrix} \mathbf{A}_1 & \mathbf{0} \\ \mathbf{H}_n^{(1)} & -\mathbf{H}^{(1)} \end{pmatrix}, \\
\mathbf{E} &= \begin{pmatrix} f\mathbf{C}^{(1)} & g\hat{\mathbf{C}}_{\phi_n}^{(1)} \\ \mathbf{H}_s^{(0)} & \mathbf{0} \end{pmatrix}
\end{aligned} \tag{22.180}$$

are complex valued matrices.

Equations $(22.178)_{1,2}$ consist of two subsystems, a first-order ordinary differential equation for the vector quantity $\mathbf{y} = (\mathbf{v}_s, \boldsymbol{\zeta})^{\mathrm{T}}$ and an algebraic system relating $\mathbf{y}$ with $\mathbf{x} = (\mathbf{v}_n, \mathbf{v}_z)^{\mathrm{T}}$. The matrices $\mathbf{A}, \mathbf{B}, \mathbf{C}, \mathbf{D}, \mathbf{E}$ are expressible in terms of the

coefficient matrices of the original system (22.176) and the vectors $\mathbf{l}_s^*$ and $\mathbf{l}_n^*$ are known for prescribed harmonically exciting external forces. For an Nth order model the vectors $\mathbf{x}$ and $\mathbf{y}$ have $2N$ complex-valued components and so, $\mathbf{A}$, $\mathbf{B}$, $\mathbf{C}$, $\mathbf{D}$, $\mathbf{E}$ have dimension $(2N \times 2N)$.

The physically relevant boundary condition is no-flux through the channel ends, $v_s = 0$, which implies via the shape function expansion $v_s = \boldsymbol{\phi} \cdot \mathbf{v}_s = 0$, $\forall\, n \in [B^-, 0] \cup [0, B^+]$ and at $s = 0$ and $s = L$ that $\mathbf{v}_s = \mathbf{0}$. In terms of the variable $\mathbf{y}$ this is expressible as

$$[\mathbf{I}, \mathbf{0}]\mathbf{y} = \mathbf{H}\,\mathbf{y} = \mathbf{0} \quad \text{at } s = 0 \text{ and } s = L, \tag{22.181}$$

where $\mathbf{I}$ and $\mathbf{0}$ are $(N \times N)$ unit and zero matrices, respectively. The two-point boundary-value problem is now given by (22.178) and (22.181).

'The above formulation is general for no assumptions regarding the number of terms occurring in the expansion of the variables have thus far been invoked. Explicit calculations are, however, restricted to the same number of shape functions for all variables and to shape functions which only vary in the transverse direction. These restrictions may be justified by the fact that, firstly, all seiche models based on the linear tidal equations operate on this level [...], secondly, for storm surges one is mainly interested in surface elevations rather than the vertical velocity distribution and, thirdly, such a procedure can be generalized to a multi-layer system' [24]. With this choice $\boldsymbol{\phi} = \boldsymbol{\phi}(n)$ and $\mathbf{C}^{(1)}_{\psi_z} = \mathbf{C}^{(1)}_{\phi_z} = \mathbf{0}$ in (22.179) and (22.180). The kinematic boundary condition $(22.176)_4$ is then separated from the remaining equations and transforms into a prediction equation for the vertical velocity component, once the horizontal velocity components are known. This means that the coupling between the differential equations $(22.178)_2$ is only by the transverse velocities $\mathbf{v}_n$. This is seen explicitly, if the first N equations of the $2N$ equations $(22.178)_2$ are written down, viz.,

$$[f\mathbf{C}^{(1)} \;\; g\mathbf{C}^{(1)}_{\phi_n}]\mathbf{y} + [\mathbf{A}_1]\mathbf{v}_n = \frac{1}{\rho_0}\left(\mathbf{w}_n^{*(1)} - \mathbf{p}_n^{*(1)}\right), \tag{22.182}$$

which does *not* involve $\mathbf{v}_z$. Notice that in the frictionless case as here, the matrix $\mathbf{A} = \mathrm{i}\omega\mathbf{C}^{(1)}$, where in a Galerkin procedure $\mathbf{C}^{(1)} = \iint_Q HJ\boldsymbol{\phi} \otimes \boldsymbol{\phi}\, \mathrm{d}n$, which is a positive definite matrix. Therefore, $\mathbf{A}^{-1}$ exists and (22.182) implies

$$\underbrace{\mathbf{v}_n}_{N} = -\underbrace{\underbrace{\mathbf{A}_1^{-1}}_{N\times N}\underbrace{[f\mathbf{C}^{(1)} \;\; g\mathbf{C}^{(1)}_{\phi_n}]}_{N\times 2N}\underbrace{\mathbf{y}}_{2N}}_{N} = \underbrace{\underbrace{\mathbf{A}_1^{-1}}_{N\times N}\underbrace{\frac{1}{\rho_0}\left(\mathbf{w}_n^{*(1)} - \mathbf{p}_n^{*(1)}\right)}_{N}}_{N}, \tag{22.183}$$

where the dimensions of the individual terms are indicated beneath the braces. Now, since $\mathbf{D}$ is also non-singular for non-vanishing cross-sections, $(22.178)_1$ can be written as

$$\frac{\mathrm{d}\,\mathbf{y}}{\mathrm{d}\,s} + \mathbf{D}^{-1}\mathbf{B}\,\mathbf{y} + \mathbf{D}^{-1}\begin{pmatrix} \mathbf{C}_1\mathbf{v}_n \\ (\mathbf{C}^1_{\psi_n}\mathbf{v}_n \end{pmatrix} = \mathbf{D}^{-1}\,\mathbf{I}^*_s. \tag{22.184}$$

This equation is uncoupled from $\mathbf{v}_z$ only because the matrices are independent of z.[13] It is now clear that substitution of (22.183) into (22.184) transforms the boundary value problem (22.178), (22.181) into the following so-called standard form

$$\left.\begin{aligned} \mathbf{y}'(s) &= \mathbf{F}(s,\omega)\mathbf{y}(s) + \mathbf{g}^*(s,\omega), \\ \mathbf{H}\,\mathbf{y}(0) &= \mathbf{0}, \\ \mathbf{H}\,\mathbf{y}(L) &= \mathbf{0}, \end{aligned}\right\} \quad \text{with } \mathbf{H} = (\mathbf{I}\ \mathbf{0}), \tag{22.185}$$

where

$$\begin{aligned} \mathbf{F}(s,\omega) &= -\mathbf{D}^{-1}(s)\left\{\mathbf{B} - \begin{bmatrix} \mathbf{C}_1\mathbf{A}_1^{-1}[\mathbf{C}^{(1)} & g\mathbf{C}^{(1)}_{\phi_n}] \\ \mathbf{C}^{(1)}_{\phi_n}\mathbf{A}_1^{-1}[\mathbf{C}^{(1)} & g\mathbf{C}^{(1)}_{\phi_n}] \end{bmatrix}\right\} \\ \mathbf{g}^*(s,\omega) &= \mathbf{D}^{-1}\left\{(\mathbf{I}^*_s)_{2N} - \begin{bmatrix} \mathbf{C}_1\mathbf{A}_1^{-1}\,(\mathbf{I}^*_n)_N \\ \mathbf{C}^{(1)}_{\phi_n}\mathbf{A}_1^{-1}\,(\mathbf{I}^*_n)_N \end{bmatrix}\right\} \end{aligned} \tag{22.186}$$

or, as can be shown,

$$\begin{aligned} \mathbf{F}(s,\omega) &= -\mathbf{D}^{-1}(s)\left[\mathbf{B}(s,\omega) - \mathbf{C}_1(s)\mathbf{A}_1^{-1}(s,\omega)\mathbf{E}(s)\right], \\ \mathbf{g}^*(s,\omega) &= \mathbf{D}^{-1}(s)\left[\mathbf{I}^*_s - \mathbf{C}(s)\mathbf{A}_1^{-1}(s,\omega)\mathbf{I}^*_n\right]. \end{aligned} \tag{22.187}$$

In the above, $(\mathbf{I}^*_{s,n})_{2N}$ is the $2N$-vector $(\mathbf{I}^*_{s,n})_{2N} = ((\mathbf{I}^*_{s,n})_{2N}\ \ \mathbf{0})^{\mathrm{T}}$ with N zeros in the last N components. Moreover, since (22.185) is complex valued, and because the matrices $\mathbf{A}$, $\mathbf{B}$, $\mathbf{C}$, $\mathbf{D}$, $\mathbf{E}$ have only a limited number of elements with real and imaginary parts, it is computationally advantageous not to work with (22.185), but with its associated system in which real and imaginary parts are separated. It should also be noticed that (22.185) is written as an inhomogeneous problem. For the homogeneous case, $\mathbf{g}^* = \mathbf{0}$; the problem then consists of solving for the eigenvalues and associated eigenfunctions. From a practical point of view, only the lowest eigenvalues and eigenfunctions are of interest, since they are the most likely ones to be exited; we shall focus attention on these below.

To see how the complex-valued two-point boundary-value problem is transformed into a real valued formulation, let us separate in (22.185) the real and imaginary parts, denoted by $\mathbf{f}_{\mathrm{R}}$ and $\mathbf{f}_{\mathrm{I}}$, as follows:

$$\begin{aligned} \mathbf{y}'_{\mathrm{R}} + \mathrm{i}\mathbf{y}'_{\mathrm{I}} &= (\mathbf{F}_{\mathrm{R}} + \mathrm{i}\mathbf{F}_{\mathrm{I}})(\mathbf{y}_{\mathrm{R}} + \mathrm{i}\mathbf{y}_{\mathrm{I}}) + \mathbf{g}^*_{\mathrm{R}} + \mathrm{i}\mathbf{g}^*_{\mathrm{I}} \\ &= (\mathbf{F}_{\mathrm{R}}\mathbf{y}_{\mathrm{R}} - \mathbf{F}_{\mathrm{I}}\mathbf{y}_{\mathrm{I}}) + \mathbf{g}^*_{\mathrm{R}} + \mathrm{i}(\mathbf{F}_{\mathrm{I}}\mathbf{y}_{\mathrm{R}} + \mathbf{F}_{\mathrm{R}}\mathbf{y}_{\mathrm{I}}) + \mathbf{g}^*_{\mathrm{I}}, \end{aligned} \tag{22.188}$$

[13] In particular, $\mathbf{C}^{(1)}_{\psi_z} = \mathbf{0}$ reduces $\mathbf{C}$ to the $(N \times 2N)$-form $(\mathbf{C}\ \ \mathbf{0})$ with N zero column vectors of length $2N$, so that $\mathbf{v}_z$ drops out from the third term on the left-hand side of (22.184).

or in matrix-like notation

$$\begin{pmatrix} \mathbf{y}'_{\mathrm{R}} \\ \mathbf{y}'_{\mathrm{I}} \end{pmatrix} = \begin{pmatrix} \mathbf{F}_{\mathrm{R}} & -\mathbf{F}_{\mathrm{I}} \\ \mathbf{F}_{\mathrm{I}} & \mathbf{F}_{\mathrm{R}} \end{pmatrix} \begin{pmatrix} \mathbf{y}_{\mathrm{R}} \\ \mathbf{y}_{\mathrm{I}} \end{pmatrix} + \begin{pmatrix} \mathbf{g}^*_{\mathrm{R}} \\ \mathbf{g}^*_{\mathrm{I}} \end{pmatrix}. \tag{22.189}$$

Boundary conditions must now also fall on real and imaginary parts of $\mathbf{v}_{\mathrm{s}}$ and obviously take the forms

$$\begin{pmatrix} \mathbf{H} & \mathbf{0} \\ \mathbf{0} & \mathbf{H} \end{pmatrix} \begin{pmatrix} \mathbf{y}_{\mathrm{R}} \\ \mathbf{y}_{\mathrm{I}} \end{pmatrix} = \begin{pmatrix} \mathbf{0} \\ \mathbf{0} \end{pmatrix}, \quad \text{for } s = 0,\ s = L, \tag{22.190}$$

where $\mathbf{H} = (\mathbf{I}\ \mathbf{0})$. Relations (22.189) and (22.190) are of the same form as (22.185) and (22.181); the only difference is that they consist of $4N$ real valued equations instead of $2N$ equations. Indeed, with the notation

$$\begin{aligned} &\mathbf{F} = \begin{pmatrix} \mathbf{F}_{\mathrm{R}} & -\mathbf{F}_{\mathrm{I}} \\ \mathbf{F}_{\mathrm{I}} & \mathbf{F}_{\mathrm{R}} \end{pmatrix}, \quad \mathbf{H} = \begin{pmatrix} \mathbf{H} & \mathbf{0} \\ \mathbf{0} & \mathbf{H} \end{pmatrix}, \\ &\mathbf{y} = \begin{pmatrix} \mathbf{y}_{\mathrm{R}} \\ \mathbf{y}_{\mathrm{I}} \end{pmatrix}, \quad \mathbf{g}^* = \begin{pmatrix} \mathbf{g}^*_{\mathrm{R}} \\ \mathbf{g}^*_{\mathrm{I}} \end{pmatrix}, \quad \mathbf{y} = \begin{pmatrix} \mathbf{y}_{\mathrm{R}} \\ \mathbf{y}_{\mathrm{I}} \end{pmatrix} \end{aligned} \tag{22.191}$$

relations (22.189) and (22.190) take the forms

$$\begin{aligned} &\mathbf{y}'(s) = \mathbf{F}(s,\omega)\mathbf{y}(s) + \mathbf{g}^*(s,\omega), && 0 < s < L, \\ &\mathbf{H}\,\mathbf{y} = \mathbf{0} && s = 0 \text{ and } s = L, \end{aligned} \tag{22.192}$$

which is formally the same as (22.185).

22.9.2 Integration Procedure

The *shooting method* may be applied to the above linear boundary value problem (22.192) by superposition of the independent solutions, which satisfy the boundary conditions $(22.192)_2$ at $s = 0$. The solution may be expressed as

$$\mathbf{y}(s) = \sum_{i=1}^{2N} \mathbf{u}_i(s)\, c_i + \mathbf{w}^*(s), \tag{22.193}$$

where the vectors $\mathbf{u}_i(s)$ of dimension $2N$ are linearly independent solutions of the homogeneous system

$$\mathbf{u}'_i = \mathbf{F}(s,\omega)\,\mathbf{u}_i(s). \tag{22.194}$$

The solutions are constructed by integrating $(22.192)_1$ with $\mathbf{g}^* = 0$ as an initial value problem subject to the homogeneous initial conditions $(22.192)_2$ at $s = 0$.

These independent solutions are for instance obtained by selecting for the components of $\boldsymbol{\zeta}_{\mathrm{R}}$ and $\boldsymbol{\zeta}_{\mathrm{I}}$ the values 0 except at the ith position where e.g. the value '1' is selected. This yields $2N$ independent functions $\mathbf{u}_i(s)$. The vector $\mathbf{w}^* = (\mathbf{w}^*_{\mathrm{R}}, \mathbf{w}^*_{\mathrm{I}})^{\mathrm{T}}$ is a particular solution of the inhomogeneous differential equations (22.192), also subject to the boundary conditions at $s = 0$. The c_i are constants of superposition, and may be determined from the second boundary condition

$$\mathbf{H}\,\mathbf{y}(L) = \mathbf{H}(\mathbf{U}(L)\mathbf{c} + \mathbf{w}^*(L)) = \mathbf{H}\mathbf{U}(L)\mathbf{c} + \mathbf{H}\,\mathbf{w}^*(L) = \mathbf{0}, \tag{22.195}$$

where $\mathbf{U}$ is the $(4N \times 2N)$-matrix[14] with column vectors $\mathbf{u}_i$, and $\mathbf{c}$ is the vector of the free constants c_i. If the matrix $\mathbf{H}\,\mathbf{U}(L)$ is non-singular, the unknown vector $\mathbf{c}$ may be determined from (22.195) and the solution may be computed from (22.193).

Formally, for the case of free oscillations the inhomogeneous solution is $\mathbf{w}^* = \mathbf{0}$; consequently, (22.195) has only non-trivial solutions provided the $(2N \times 2N)$-matrix $\mathbf{H}\,\mathbf{U}$ is singular. The criterion for this is $\det(\mathbf{H}\,\mathbf{U}) = 0$ and will, for a lake of length L yield a discrete frequency spectrum and associated eigenfunctions. The latter are obtained by calculating $\mathbf{c}$ (modulo a free amplitude (say for $\zeta^{(0)}$)) and re-substituting the result in (22.193).

'The above procedure to determine the complementary functions $\mathbf{u}_i (i = 1, \ldots, N)$ and to evaluate the eigenfrequency from a singularity condition of the system $\mathbf{H}\,\mathbf{U}(L, \omega)\mathbf{c} = \mathbf{0}$ would work perfectly, were it not for the numerical properties of the matrix $\mathbf{F}$ in (22.191). Numerical calculations for realistic values of ω show that the spectral width of the matrix $\mathbf{F}$ is generally large, and furthermore, increases with increasing number of shape functions. As a result, complementary functions lie far apart; although they are theoretically linearly independent, they are numerically (nearly) dependent, making the system (22.195) computationally ill-conditioned.

The situation is, however, well known to numerical analysts. A way of overcoming the difficulties is to divide the interval $[0, L]$ into subintervals that are sufficiently small so that the complementary solutions within each subinterval cannot lie too far apart at the end of the subinterval; at the end of each subinterval the complementary vector $\mathbf{c}$ is transformed by a Gram-Schmidt orthogonalization procedure, and integration is continued with this new orthogonalized initial vector. This process is continued until the other end $s = L$ is reached, where the second boundary condition is satisfied',[28]. This integration procedure is known in numerical analysis as the *initial-value approach coupled with orthonormalization* and excellent software packages exist with the aid of which the integration can be implemented. In our analysis the SUPPORT package [33] was used.

[14] It is a property of the complex differential equations (22.185) and their real valued counterpart (22.192) that only N solutions $\mathbf{u}_i(s)$ of the homogeneous system $(22.194)_1$ must be determined. Watts et al. [35] prove that it is necessary to integrate only half of the equations to obtain the necessary set of base functions for the problem. The reason for this is that the first N columns of base solutions have the form $(\mathbf{U}_{\mathrm{R}}, \mathbf{U}_{\mathrm{I}})$ and the last N columns of the set have the form $(\mathbf{U}_{\mathrm{I}}, \mathbf{U}_{\mathrm{R}})$, which is not a linear combination of the first N columns.

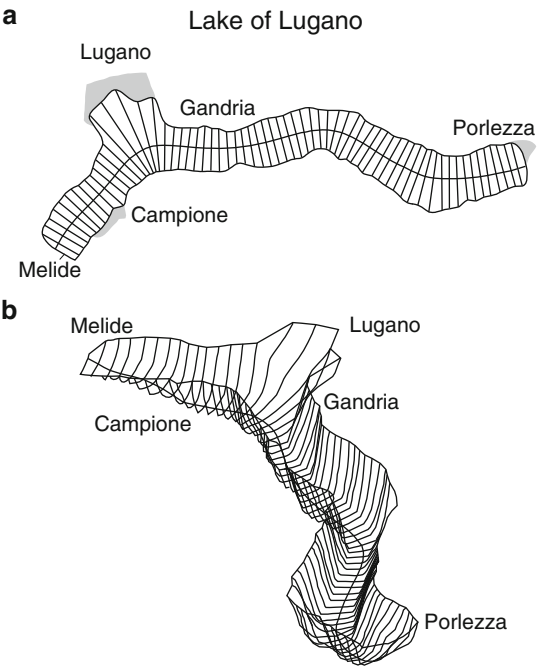

Fig. 22.18 Top (**a**) and perspective (**b**) view of the northern basin of Lake of Lugano with selected cross sections and thalweg for the computations of the barotropic seiches with the Nth-order channel model. The lake is 17 km long, has mean width of 1.5 km, minimum and maximum widths of 1 and 3 km, respectively, and mean and maximum depths of 175 and 287 m, respectively, from [28]. © Cambridge University Press, reproduced with permission

22.9.3 Barotropic Seiches of the Northern Basin of Lake of Lugano

Let us apply the above channel model to the barotropic free seiche oscillations of the northern basin of Lake of Lugano. Figure 22.18 displays in panel (a) the top view and in panel (b) an axonometric representation, both with chosen cross sections indicated; the figure caption lists the typical morphological parameters.

Numerical results should depend on the choice of the shape functions; the following results are based on a four term Cauchy-series expansion $\boldsymbol{\phi} = \{1, n, n^2, n^3\}$. Remarks on the significance of different shape-function choices will be made below. They will be presented for the first four modes, and these will be compared with those obtained from a finite-element representation of the two-dimensional tidal equations. The computations were performed by Raggio [24] for the finite-element computations with a code due to Hamblin (personal communication).

A partial verification of the computed four modes $H_1, \ldots, H_4$ of the surface seiches was possible on the basis of limnigraphs of the Swiss Hydrological Service, which were erected at shore positions Campione, Lugano and Porlezza (see Fig. 22.18) in August 1979. Time series from the registered surface elevations for late afternoon of 9 August to after midnight of 10 August 1979 (see Fig. 22.19) were subjected to spectral analysis and revealed the three spectra of Fig. 22.20. The eigenfrequencies of the four lowest-order computed and four lowest-order measured gravitational modes are shown in Table 22.3. The two computational models yield

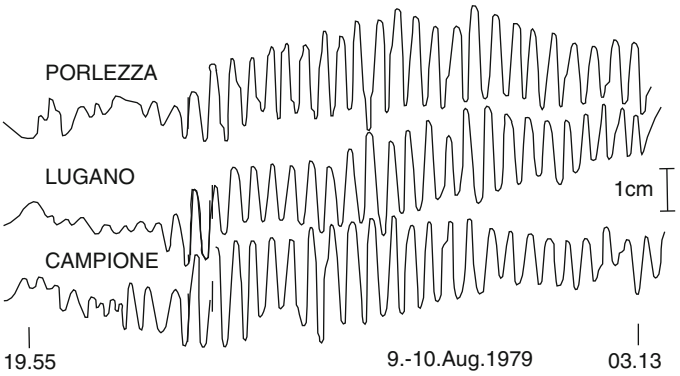

Fig. 22.19 Surface elevation time series at the stations of Campione, Lugano and Porlezza for the strongly wind forced episode from 9 August 19.55 h to 10 August 03.33 h 1979, from Raggio [24], reproduced with permission

Table 22.3 Eigenfrequencies of the four lowest gravitational surface seiches for the northern basin of Lake of Lugano as obtained with the finite element model, the channel model with 4 Cauchy-terms as shape functions and as inferred from the frequency spectra of the surface elevation time series of the limnigraphs installed in Campione, Lugano and Porlezza

Mode	Finite element model		Channel model		Spectral analysis[a]	
	Frequency ($\times 10^{-1}$)	Period [min]	Frequency ($\times 10^{-1}$)	Period (min)	Frequency ($\times$10−1)	Period [min]
1	0.0755	**13.9**	0.0765	**13.7**	0.074	14.0
2	0.158	**6.6**	0.161	**6.5**	0.165	**6.3**
3	0.206	**5.1**	0.210	**5.0**	0.210	**5.0**
4	0.287	**3.8**	0.280	**3.7**	–	–

[a]Inferred from Fig. 22.20

practically the same eigenfrequencies ω (or periods $= 2\pi/\omega$), and for the three lowest modes they agree reasonably well with the corresponding frequencies (periods) inferred from the locations of the spectral peaks in Fig. 22.20. Even though this comparison does not provide evidence that the structures of the computed eigenfunctions could also closely agree with those of the real lake, it is commonly claimed that the measured frequencies correspond to computed seiche modes.

'Figure 22.21a–d displays for the channel model the co-range and co-tidal lines of the four lowest eigenmodes of the basin. When $\zeta = \zeta_0 \exp(\mathrm{i}(\omega t - \beta))$ the former are the lines of constant real ζ_0 and the latter those of constant β. The normalization of both is arbitrary; ζ is normalized so as to give the maximum amplitude the value 100 units. The equidistance of the co-range lines is equal to 10 units, and the co-tidal lines are represented for the values $\beta = 0, 0.1, 179.9, 180, 180.1$ and $359.9°$ [...]. Inspection of the co-tidal lines indicates that all amphidromes rotate in the counterclockwise direction. The motion in the lake is consequently of Kelvin-type.

The lowest mode has a single amphidromic point roughly at the middle of the lake. Co-tidal lines are strongly bundled in the cross-channel direction.

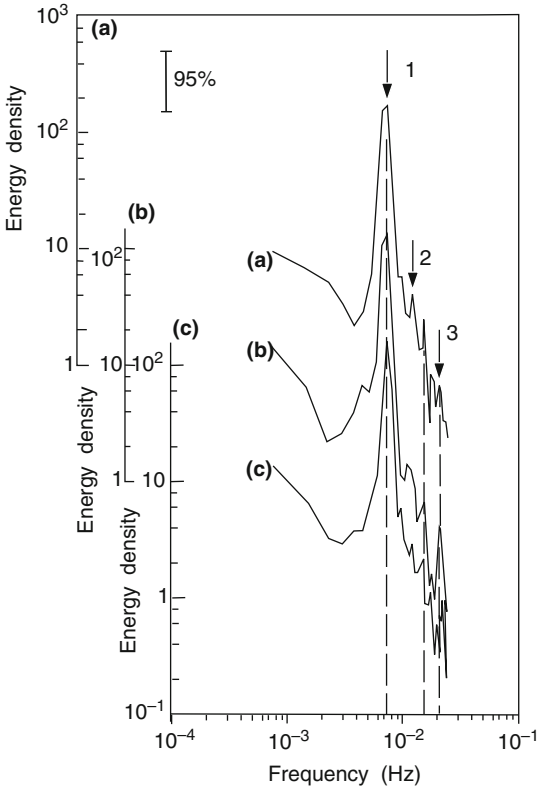

Fig. 22.20 Power spectra of the surface elevation oscillations for the limnigraph stations Campione (**a**), Lugano (**b**) and Porlezza (**c**). Energy density $= 0.36 \times 10^{\text{ordinate}}$ in $\text{m}^2\,\text{s}^{-1}$. The *arrows* marked by 1, 2, 3 indicate the first three eigenfrequencies of the lake as in column 6 of Table 22.3, from [28]. © Cambridge University Press, reproduced with permission

The longitudinal structure of the oscillation is manifested by this bundling, and because co-range lines all join points of opposite shores. This behaviour persists even in the vicinity of the bay of Lugano (the shallow wide portion of the lake close to Lugano). The preference for longitudinal behaviour persists for the second mode, even though an amphidromic point is situated near the Bay of Lugano. The third and fourth mode exhibit still mainly longitudinal behaviour, but in the Bay of Lugano surface elevations now show a strong gradient transverse to the main channel direction, as there are now co-range lines connecting points on the same shoreline' [28].

'A more challenging test of the suitability of the channel model than a frequency comparison is obtained by comparing the eigenmode structures with those based on the finite element model. Figure 22.22 shows the corresponding amphidromic systems for mode 1 and mode 4, based on the finite element representation using triangular elements with quadratic shape functions. Bearing in mind that contour plots for the channel model were produced with a contour-plot program while those for the finite-element calculations were drawn by hand, agreement must be regarded as excellent. It should further be noticed that the finite-element grid used was too

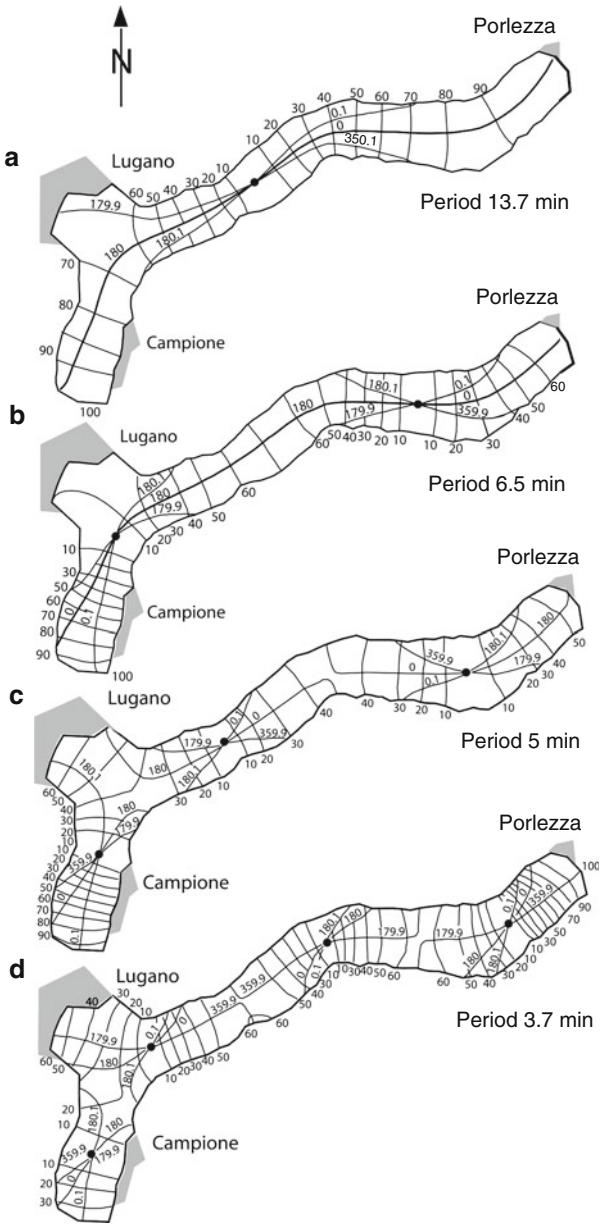

Fig. 22.21 Amphidromic systems for the first H_1 (**a**), second H_2 (**b**), third H_3 (**c**) and fourth H_4 (**d**) gravitational modes for the northern basin of Lake of Lugano, computed with the fourth-order channel model, using Cauchy series for the shape functions, redrawn from figures of [28].

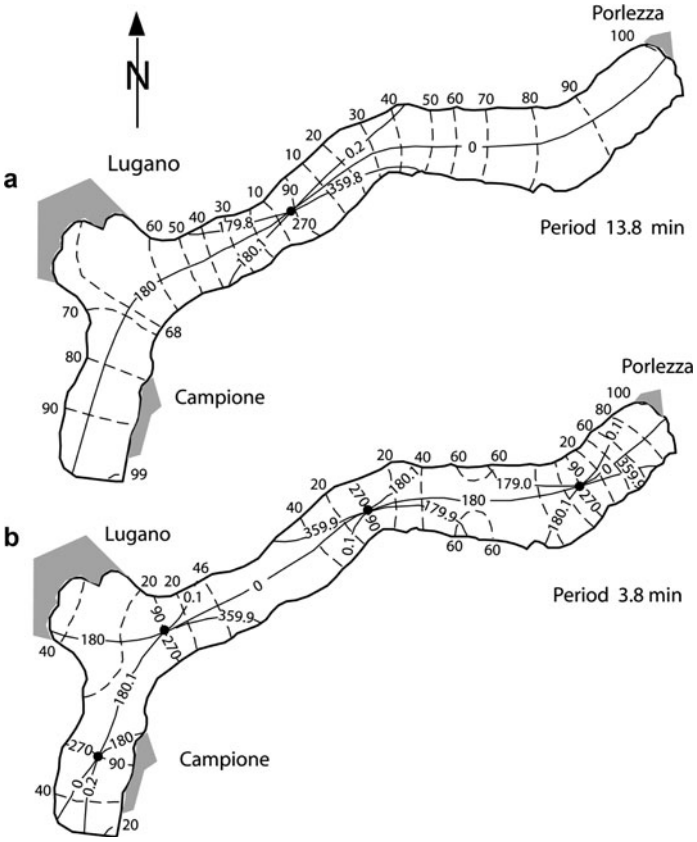

Fig. 22.22 Amphidromic systems for the first H_1 (**a**) and fourth H_4 (**b**) gravitational mode as computed with the finite element presentation of the tidal equations, redrawn from figures of [28]. © Cambridge University Press, reproduced with permission

coarse for the spatial resolution of the fifth and higher modes; in contrast, the fifth mode was reproduced without any difficulty with the channel model' [28].

Further tests regarding the accuracy of the model were undertaken when varying the number of terms considered in the Cauchy-series expansion. 'Calculations show broadly that, for each mode, increasing the number of shape functions incorporated in the model will decrease the difference in subsequent eigenfrequencies, presumably to an asymptotic value. The eigenfrequencies obtained with one to four shape functions, the difference between them, and extrapolated values for each mode are listed in Table 22.4. It is evident that the one-term model allows determination of the eigenfrequencies with sufficient accuracy for surface seiches. Structurally, the one-term model, corresponding to the Chrystal model, shows purely longitudinal standing waves with four nodal lines. The two-term model exhibits the onset of transverse oscillation in the vicinity and within the Bay of Lugano. This behaviour becomes more pronounced with increasing number of shape functions. Nonetheless,

Table 22.4 Eigenfrequencies for the northern basin of Lake of Lugano for the first and fourth gravitational modes using one, three and four Cauchy terms as shape functions and an extrapolated value

Number of	Mode 1×10^{-2} Hz		Mode 4×10^{-1} Hz	
shape functions	Frequency	Differences	Frequency	Differences
1	0.768063		0.287213	
		0.0016		0
2	0.766446		0.287213	
		0.0018		0.0063
3	0.764672		0.280926	
		0.0004		0.0009
4	0.764257		0.280017	
Extrapolated	0.762877		0.277845	

the results suggest that from the structure of the eigenmodes of such an elongated lake it appears to be sufficient to work with a two-term model to describe surface seiches properly' [28].

The above results and those obtained in previous sections prove the suitability of the model equations. They clearly provide a rational procedure which replaces the Kelvin wave dynamics approach which left some subjective element in the selection of the channel axis. It made measurements of surface elevations at shore stations necessary to patch the co-range lines and the amphidromic points optimally. Furthermore, an analysis of forced motions, see [24,25,28], indicated clearly a conspicuous sensitivity of the results with respect to the shape function choice and the limitation of the model to gravitational modes. Subinertial frequencies, the domain of topographic Rossby waves could not clearly be identified. They have been dealt with in Chaps. 19–21.

Shape functions different from Cauchy series 'may be selected from physically meaningful assumptions of the particular phenomenon one would like to simulate or from considerations regarding a minimization of the computational effort. The latter suggests the use of orthogonal families, generated by inner products of the form

$$(P_i, P_j) = \begin{cases} \int_a^b w(n) P_i(n)\, P_j(n) = ||P_i|| & (i = j), \\ 0 & (i \neq j), \end{cases} \tag{22.196}$$

in which P_i and P_j are two members of the family and w is a weighting function. Orthogonal polynomial families are computationally particularly advantageous, since they can be constructed with three-terms recursive formulae.

The idea is to select shape functions ϕ_i that diagonalize a particular submatrix in (22.178) and are thus orthogonal with respect to that inner product. Raggio [24,25] shows that the most convenient choice is to make the matrix

$$C_{ij}^{(1)} = \int_{B^-}^{B^+} JH(n)\phi_i(n)\phi_j(n)\mathrm{d}n, \tag{22.197}$$

diagonal or equal to the unit matrix (see (22.178)). Within the class of polynomial families the ϕ_i must be numerically evaluated. With $\phi_j = \sum_{\nu=0}^{3} a_\nu(s) n^\nu$ this amounts to the evaluation of the coefficients a_ν along the channel axis, [28]. Considerable expenditure of cpu time is saved and accuracy of numerical result is gained.

It should also be pointed out that the channel model has been found suitable in the range of gravitational modes where the currents are essentially irrotational and driven by pressure gradients caused by differences in the surface elevation of the lake. Below the inertial frequency the motion is basically non-divergent, rotational and not primarily dependent on the surface elevation distribution but rather on depth variation [28]. This is the domain of topographic waves and has extensively been dealt with in Chaps. 19–21.

Appendix 22.A

In this appendix, we list the definitions of the cross-sectional coefficients, load and stress resultants, which complement the dynamical equations in Sect. 22.5. Q denotes the cross-section erected perpendicular to the lake axis, generally in the present, deformed configuration but in the linear approximation dealt with here taken in the undeformed reference state. $H(s,n) = z$ denotes the depth function, and $n = B^{\pm}$ are the transverse coordinates of the shore lines. Commas followed by an index, say $()_{,j}$, denote partial derivatives with respect to the variable following the comma, and shape functions carrying a hat are functions of n only. We follow [26].

Cross-Sectional Coefficients

$$
\begin{aligned}
\mathbf{C}^{(m)} &= \iint_Q J^m \boldsymbol{\psi} \otimes \boldsymbol{\phi}\, \mathrm{d}n\mathrm{d}z, \\
\mathbf{C}^{(m)}_{\phi_j} &= \iint_Q J^m \boldsymbol{\psi} \otimes \boldsymbol{\phi}_{,j}\, \mathrm{d}n\mathrm{d}z \quad (j = n, z), \\
\mathbf{C}^{(m)}_{\psi_j} &= \iint_Q J^m \boldsymbol{\psi}_{,j} \otimes \boldsymbol{\phi}\, \mathrm{d}n\mathrm{d}z, \quad (j = n, z), \\
\hat{\mathbf{C}}^{(m)} &= \iint_Q J^m \boldsymbol{\psi} \otimes \hat{\boldsymbol{\phi}}\, \mathrm{d}n\mathrm{d}z, \\
\hat{\mathbf{C}}^{(m)}_{\phi_j} &= \iint_Q J^m \boldsymbol{\psi} \otimes \hat{\boldsymbol{\phi}}_{,j}\, \mathrm{d}n\mathrm{d}z \quad (j = n, z), \\
\mathbf{H}^{(m)} &= \int_{B^-}^{B_+} J^m \boldsymbol{\psi} \otimes \boldsymbol{\phi}\, \mathrm{d}n \quad (z = H(s,n)),
\end{aligned}
$$

$$
\begin{aligned}
\mathbf{H}_s^{(m)} &= \int_{B-}^{B+} J^m H_{,s} \boldsymbol{\psi} \otimes \boldsymbol{\phi} \, \mathrm{d}n \quad (z = H(s,n)), \\
\mathbf{H}_n^{(m)} &= \int_{B-}^{B+} J^m H_{,n} \boldsymbol{\psi} \otimes \boldsymbol{\phi} \, \mathrm{d}n \quad (z = H(s,n)), \\
\mathbf{Z}^{(m)} &= \int_{B-}^{B+} J^m \boldsymbol{\psi} \otimes \boldsymbol{\phi} \, \mathrm{d}n \quad (z = \zeta(s,n,t)), \\
\hat{\mathbf{Z}}^{(m)} &= \int_{B-}^{B+} J^m \boldsymbol{\psi} \otimes \hat{\boldsymbol{\phi}} \, \mathrm{d}n\mathrm{d}z, \quad (z = \zeta(s,n,t)), \\
\boldsymbol{\mathcal{E}}^{(m)} &= \iint_Q J^m \boldsymbol{\psi} \otimes \boldsymbol{\phi} \otimes \boldsymbol{\phi} \, \mathrm{d}n\mathrm{d}z, \\
\boldsymbol{\mathcal{E}}_{,j}^{(m)} &= \iint_Q J^{(m)} \boldsymbol{\psi} \otimes \boldsymbol{\phi}_{,j} \otimes \boldsymbol{\phi} \, \mathrm{d}n\mathrm{d}z \quad (j = n, z), \\
\hat{\boldsymbol{\mathcal{E}}}^{(m)} &= \int_{B-}^{B+} J^m \boldsymbol{\psi} \otimes \hat{\boldsymbol{\phi}} \otimes \boldsymbol{\phi} \, \mathrm{d}n\mathrm{d}z \quad (z = \zeta(s,n,t)), \\
\hat{\boldsymbol{\mathcal{E}}}_{,j}^{(m)} &= \int_{B-}^{B+} J^m \boldsymbol{\psi} \otimes \hat{\boldsymbol{\phi}}_{,j} \otimes \boldsymbol{\phi} \, \mathrm{d}n\mathrm{d}z \quad (z = \zeta(s,n,t), \, j = n, z).
\end{aligned}
\tag{22.A1}
$$

These quantities are purely geometric. Analogously, the *macroscopic bottom-friction coefficient* is mainly a function of the geometry of the basin:

$$
\mathbf{R}^{(m)} = \int_{B-}^{B+} \frac{J^m}{\mathsf{R}} \boldsymbol{\psi} \otimes \boldsymbol{\phi} \, l_H(s,n) \mathrm{d}n \quad (z = H(s,n)), \tag{22.A2}
$$

where $l_H(s,n)$ is defined in (22.55).

Load Resultants

Let $t_\alpha^*(\alpha = s,n)$ be the wind stress components and p_{atm}^* the atmospheric pressure. We then define the *macroscopic wind load* and *macroscopic atmospheric pressure gradients* as follows:

$$
\begin{aligned}
\mathbf{w}_\alpha^{*(m)} &= \int_{B-}^{B+} J^m \boldsymbol{\psi} t_\alpha^* \mathrm{d}n \quad (z = \zeta(s,n,t), \quad \alpha = s,n), \\
\mathbf{p}_\alpha^{*(m)} &= \iint_Q J^m \boldsymbol{\psi} \frac{\partial p_{\mathrm{atm}}^*}{\partial \alpha} \, \mathrm{d}n\mathrm{d}z \quad (\alpha = s,n).
\end{aligned}
\tag{22.A3}
$$

Stress Resultants

These arise only when internal friction is accounted for. The two quantities $\mathbf{J}_s, \mathbf{J}_n$, arising in (22.78) and (22.79) have the form

$$\begin{aligned}\mathbf{J}_s &= -\mathbf{p}_s^{\mathrm{T}} - \frac{\partial \mathbf{T}_{11}^{(0)}}{\partial s} + \mathbf{T}_{11s}^{(0)} + \mathbf{T}_{11s}^{(-1)} + \mathbf{T}_{12n}^{(1)} + \mathbf{T}_{13z}^{(1)} + K\mathbf{T}_{12}^{(0)},\\ \mathbf{J}_n &= -\mathbf{p}_n^{\mathrm{T}} - \frac{\partial \mathbf{T}_{12}^{(0)}}{\partial s} + \mathbf{T}_{22n}^{(1)} + \mathbf{T}_{23z}^{(1)} + K(\mathbf{T}_{11}^{(2)} - 2\mathbf{T}_{22}^{(0)})\end{aligned} \tag{22.A4}$$

and the stress resultants are of two types, namely the *macroscopic turbulent surface pressure*

$$\left.\begin{aligned}\mathbf{p}_s^{\mathrm{T}} &= \int_{B-}^{B+} \boldsymbol{\psi}(T_{ij}^E n_i n_j)\frac{\partial H}{\partial s}\mathrm{d}n,\\ \mathbf{p}_n^{\mathrm{T}} &= \int_{B-}^{B+} J\boldsymbol{\psi}(T_{ij}^E n_i n_j)\left[1 + \left(\frac{\partial H}{\partial n}\right)^2\right]^{1/2}\mathrm{d}n,\end{aligned}\right\} \quad (z = H(s,n)) \tag{22.A5}$$

and the *macroscopic stress resultants*

$$\begin{aligned}\mathbf{T}_{ij}^{(m)} &= \iint_Q J^m \boldsymbol{\psi} T_{ij}^E \mathrm{d}n\mathrm{d}z,\\ \mathbf{T}_{ij\alpha}^{(m)} &= \iint_Q J^m \boldsymbol{\psi}_{,\alpha} T_{ij}^E \mathrm{d}n\mathrm{d}z, \quad (\alpha = n, z),\\ \mathbf{T}_{ijs}^{(m)} &= \iint_Q \frac{\partial J}{\partial s} J^m \boldsymbol{\psi} T_{ij}^E \mathrm{d}n\mathrm{d}z.\end{aligned} \tag{22.A6}$$

The atmospheric pressure and wind-stress terms are

$$\left.\begin{aligned}\mathsf{w}_{\alpha(i,j)}^{*(m)} &= \int_{B-}^{B+} J^m n^i \zeta^j(s,n,t) t_\alpha^* \mathrm{d}n,\\ \mathsf{p}_{\alpha(i,j)}^{*(m)} &= \iint_Q J^m n^i z^j \frac{\partial p_{\mathrm{atm}}^*}{\partial \alpha}\mathrm{d}n\mathrm{d}z,\end{aligned}\right\} \quad (\alpha = s, n), \tag{22.A7}$$

and the turbulent stress terms $\mathsf{J}_{(i,j)}$ are

$$\begin{aligned}\mathsf{J}_{i,j}^s &= -\mathsf{p}_{s(i,j)}^{\mathrm{T}} - \frac{\partial \mathsf{T}_{11(i,j)}^{(0)}}{\partial s} + K'K\mathsf{T}_{11(i+2,j)}^{(-1)} + i\mathsf{T}_{12(i-1,j)}^{(1)} - K\mathsf{T}_{12(i,j)}^{(0)}\\ &\quad + j\mathsf{T}_{13(i,j-1)}^{(1)},\\ \mathsf{J}_{i,j}^n &= -\mathsf{p}_{n(i,j)}^{\mathrm{T}} - \frac{\partial \mathsf{T}_{12(i,j)}^{(0)}}{\partial s} + i\mathsf{T}_{22(i,j)}^{(1)} + j\mathsf{T}_{23(i,j)}^{(1)} + K(\mathsf{T}_{11(i,j)}^{(2)} - 2\mathsf{T}_{22(i,j)}^{(0)}),\end{aligned} \tag{22.A8}$$

with

$$\left.\begin{aligned}
\mathsf{p}^{\mathrm{T}}_{s(i,j)} &= \int_{B^-}^{B^+} n^i H^j(s,n)\frac{\partial H(s,n)}{\partial s}(T^E_{kl}n_k n_l)\mathrm{d}n,\\
\mathsf{p}^{\mathrm{T}}_{n(i,j)} &= \int_{B^-}^{B^+} J n^i H^j(s,n)\left[1+\left(\frac{\partial H}{\partial n}\right)^2\right]^{1/2}(T^E_{kl}n_k n_l)\mathrm{d}n,\\
\mathsf{T}^{(m)}_{kl(i,j)} &= \iint_Q J^{(m)} n^i z^j T_{kl}\mathrm{d}n\mathrm{d}z,
\end{aligned}\right\}\quad \begin{aligned}&k,l=1,2,3,\\ &i=1,2,\ldots,N,\\ &j=1,2,\ldots,M.\end{aligned} \tag{22.A9}$$

Appendix 22.B

In this appendix, we derive the global form of the continuity equation with incorporated boundary conditions; it expresses mass balance in one-dimensional form. To this end, the following preliminary calculations are needed.

Let $F(s,n,z,t)\equiv 0$ be the equation defining the boundary $\partial\Omega$ of the domain Ω as introduced in the main part of this chapter; let, moreover, $\mathrm{d}\boldsymbol{a}$ be the vectorial surface element perpendicular to $\partial\Omega$. Elementary vector calculus and differential geometry then shows that in the (s,n,z)-coordinate system one has

$$\begin{aligned}
\mathrm{d}\boldsymbol{a} &= \left(-\frac{\partial F}{\partial s},-J\frac{\partial F}{\partial n},J\right)\mathrm{d}n\mathrm{d}s = \mathrm{d}\boldsymbol{a}_s+\mathrm{d}\boldsymbol{a}_l,\\
\mathrm{d}\boldsymbol{a}_s &= \left(-\frac{\partial F}{\partial s},0,0\right)\mathrm{d}n\mathrm{d}s = -(1,0,0)\mathrm{d}a'_s\mathrm{d}s = \boldsymbol{n}_s\mathrm{d}a_s,\\
\mathrm{d}\boldsymbol{a}_l &= \left(0,-\frac{\partial F}{\partial n},1\right)J\mathrm{d}n\mathrm{d}s = (0,n_{l_2},n_{l_3})\mathrm{d}a'_l J\mathrm{d}s = \boldsymbol{n}_l\mathrm{d}a_l,\\
\mathrm{d}a &= ||\mathrm{d}\boldsymbol{a}|| = Jl\,\mathrm{d}n\mathrm{d}s = \mathrm{d}a'\mathrm{d}s,\\
l &= \left[1+\left(\frac{\partial F}{\partial n}\right)^2+\frac{1}{J^2}\left(\frac{\partial F}{\partial s}\right)^2\right]^{1/2} = ||\mathrm{grad}\,F||.
\end{aligned} \tag{22.B1}$$

Here, $\mathrm{d}a_s$ is the algebraic surface element of the projection of the mantle element $\mathrm{d}\boldsymbol{a}$ into the cross-sectional plane (see Fig. 22.23), $\boldsymbol{n}_s$ and $\boldsymbol{n}_l$ are unit vectors along the negative s-direction and perpendicular to the cross-sectional periphery but within the cross-sectional plane. Thus, $\mathrm{d}a_l = \mathrm{d}a'_l J\mathrm{d}s$, with $\mathrm{d}a'_l = (1+(\partial F/\partial n)^2)^{1/2}$, is the algebraic area element projected on a cylindrical surface that is parallel to s and sweeps out the periphery of the cross-section. Also, depending on the choice of the surfaces $\partial\Omega_\sigma$ and $\partial\Omega_n$, respectively, we write l as l_H and $l_\zeta = 1+\mathcal{O}(\zeta^2)$, respectively, consistently ignoring $\mathcal{O}(\zeta^2)$-terms. This assumption implies that the boundary changes AE and CD in Fig. 22.6 are ignored.

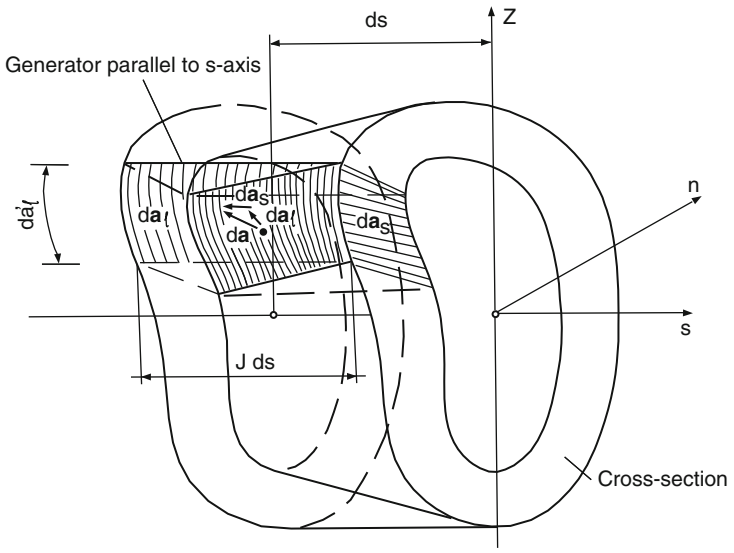

Fig. 22.23 Channel-like element of length ds with surface element d$\boldsymbol{a}$ on its mantle surface. Projections of this element into the cross-section and onto the cylindrical surface are shown by the lightly *shaded areas*, from [26]. © Cambridge University Press, reproduced with permission

We also need the following formulae:

$$\begin{aligned}
\frac{\partial}{\partial s}\iint_Q f\,\mathrm{d}n\mathrm{d}z &= \iint_Q \frac{\partial f}{\partial s}\mathrm{d}n\mathrm{d}z + \oint_{\partial Q} f\,\mathrm{d}a'_s,\\
\iint_Q \frac{\partial f}{\partial n}\mathrm{d}n\mathrm{d}z &= \oint_{\partial Q} f n_{l_2}\mathrm{d}a'_l,\\
\iint_Q \frac{\partial f}{\partial z}\mathrm{d}n\mathrm{d}z &= \oint_{\partial Q} f n_{l_3}\mathrm{d}a'_l.
\end{aligned} \tag{22.B2}$$

The first is based on the Reynolds transport theorem if s is interpreted as time and the remaining two expressions follow from the Gauss law. Q denotes the cross-section and ∂Q its periphery. With these preliminary calculations it is now straightforward to derive the global form of the mass-balance equation. In a first step we transform δI_1 in (22.65),

$$\begin{aligned}
\iiint_\Omega \mathrm{div}\,\boldsymbol{v}\delta\lambda\mathrm{d}V &= \int_{s_0}^{s}\delta\boldsymbol{\lambda}\cdot\left\{\iint_Q \boldsymbol{\psi}\left(\frac{1}{J}\frac{\partial v_s}{\partial s}+\frac{\partial v_n}{\partial n}+\frac{\partial v_z}{\partial z}-\frac{K}{J}v_n\right)J\,\mathrm{d}n\mathrm{d}z\right\}\mathrm{d}s\\
&= \int_{s_0}^{s}\delta\boldsymbol{\lambda}\cdot\left\{\iint_Q \boldsymbol{\psi}\frac{\partial v_s}{\partial s}\mathrm{d}n\mathrm{d}z+\iint_Q \boldsymbol{\psi}\frac{\partial v_n}{\partial n}J\,\mathrm{d}n\mathrm{d}z\right.\\
&\quad\left.+\iint_Q \boldsymbol{\psi}\frac{\partial v_z}{\partial z}J\,\mathrm{d}n\mathrm{d}z-K\iint_Q \boldsymbol{\psi}v_n\mathrm{d}n\mathrm{d}z\right\}\mathrm{d}s.
\end{aligned} \tag{22.B3}$$

The first three inner most cross-sectional integrals can be transformed with the aid of (22.B2) so that (22.B3) may be written as

$$\int_{s_0}^{s} \delta\boldsymbol{\lambda} \cdot \Big\{ \Big[\frac{\partial}{\partial s} \Big(\iint_Q \boldsymbol{\psi} v_s \mathrm{d}n\mathrm{d}z \Big) - \oint_{\partial Q} \boldsymbol{\psi} v_s \mathrm{d}a'_s \Big] + \Big[\oint_{\partial Q} \boldsymbol{\psi} J v_n n_{l_2} \mathrm{d}a'_l - \iint_Q \frac{\partial \boldsymbol{\psi}}{\partial n} J v_n \mathrm{d}n\mathrm{d}z + K \iint_Q \boldsymbol{\psi} v_n \mathrm{d}n\mathrm{d}z \Big] + \Big[\oint_{\partial Q} \boldsymbol{\psi} J v_z n_{l_3} \mathrm{d}a'_l - \iint_Q \frac{\partial \boldsymbol{\psi}}{\partial z} J v_z \mathrm{d}n\mathrm{d}z \Big] - K \iint_Q \boldsymbol{\psi} v_n \mathrm{d}n\mathrm{d}z \Big\} \mathrm{d}s, \quad (22.B4)$$

or, after rearranging terms,

$$\begin{aligned} \iiint_\Omega \operatorname{div} \boldsymbol{v} \delta\lambda \mathrm{d}V = \int_{s_0}^{s} \delta\boldsymbol{\lambda} \cdot \Big\{ & - \oint_{\partial Q} \boldsymbol{\psi} v_s \mathrm{d}a'_s + \oint_{\partial Q} \boldsymbol{\psi} J v_\beta n_{l\beta} \mathrm{d}a'_l \\ & + \frac{\partial}{\partial s} \Big(\iint_Q \boldsymbol{\psi} v_s \mathrm{d}n\mathrm{d}z \Big) \\ & - \iint_Q \Big(\frac{\partial \boldsymbol{\psi}}{\partial n} J v_n + \frac{\partial \boldsymbol{\psi}}{\partial z} J v_z \Big) \mathrm{d}n\mathrm{d}z \Big\} \mathrm{d}s \quad (\beta = n, z), \end{aligned} \quad (22.B5)$$

in which summation over Greek indices is understood. To eliminate the contour integrals, consider the weighted residual expressions δI_3 and δI_5 for the kinematic boundary conditions $(22.67)_{3,5}$. Set $\delta\lambda_3 = \delta\lambda_2$, which is permissible, and form $\delta I_3 + \delta I_5 = 0$; this yields

$$\begin{aligned} 0 &= \iint_{\partial\Omega_\sigma} \frac{1}{||\operatorname{grad} F_\xi||} \frac{\mathrm{d}F_\xi}{\mathrm{d}t} \delta\lambda_2 \mathrm{d}a + \iint_{\partial\Omega_n} \frac{1}{||\operatorname{grad} F_H||} \frac{\mathrm{d}F_H}{\mathrm{d}t} \delta\lambda_3 \mathrm{d}a \\ &= \iint_{\partial\Omega} \frac{1}{||\operatorname{grad} F||} \frac{\mathrm{d}F}{\mathrm{d}t} \delta\lambda_2 \mathrm{d}a \\ &= \iint_{\partial\Omega} \frac{1}{||\operatorname{grad} F||} \frac{\partial F}{\partial t} \delta\lambda_2 \mathrm{d}a + \iint_{\partial\Omega} \boldsymbol{v} \cdot \frac{\operatorname{grad} F}{||\operatorname{grad} F||} \delta\lambda_2 \mathrm{d}a \\ &= \iint_{\partial\Omega} ||\operatorname{grad} F||^{-1} \frac{\partial F}{\partial t} \delta\lambda_2 \mathrm{d}a - \iint_{\partial\Omega} |\boldsymbol{v} \delta\lambda_2 \cdot \mathrm{d}\boldsymbol{a}, \end{aligned} \quad (22.B6)$$

in which the sign change in the last term follows since $\operatorname{grad} F / ||\operatorname{grad} F||$ is the inward unit normal vector. Splitting the surface element $\mathrm{d}\boldsymbol{a}$ into the two perpendicular surface elements $\mathrm{d}\boldsymbol{a}_s$ and $\mathrm{d}\boldsymbol{a}_l$ yields

$$\iint_{\partial\Omega} ||\text{grad } F||^{-1} \frac{\partial F}{\partial t} \delta\lambda_2 \mathrm{d}a - \iint_{\partial\Omega} \boldsymbol{v}\delta\lambda_2 \cdot \mathrm{d}\boldsymbol{a}_s - \iint_{\partial\Omega} \boldsymbol{v}\delta\lambda_2 \cdot \mathrm{d}\boldsymbol{a}_l$$
$$= \iint_{\partial\Omega} ||\text{grad } F||^{-1} \frac{\partial F}{\partial t} \delta\lambda_2 \mathrm{d}a - \iint_{\partial\Omega} \boldsymbol{v} \cdot \boldsymbol{n}_s \delta\lambda_2 \cdot \mathrm{d}a_s - \iint_{\partial\Omega} \boldsymbol{v} \cdot \boldsymbol{n}_l \delta\lambda_2 \mathrm{d}a_l$$
$$= \int_{s_0}^{s} \left\{ \oint_{\partial\Omega} ||\text{grad } F||^{-1} \frac{\partial F}{\partial t} \delta\lambda_2 \mathrm{d}a' + \oint_{\partial\Omega} v_s \delta\lambda_2 \mathrm{d}a'_s - \oint_{\partial\Omega} v_\beta n_{l\beta} \delta\lambda \, J \mathrm{d}a'_l \right\} \mathrm{d}s,$$

or, after expansion of the weighting functions $\delta\lambda_2$,

$$\oint_{\partial\Omega} ||\text{grad } F||^{-1} \frac{\mathrm{d}F}{\mathrm{d}t} \delta\lambda_2 \mathrm{d}a$$
$$= \int_{s_0}^{s} \delta\boldsymbol{\lambda}_2 \cdot \left\{ \oint_{\partial\Omega} \boldsymbol{\psi} ||\text{grad } F||^{-1} \frac{\partial F}{\partial t} \mathrm{d}a' + \oint_{\partial Q} \boldsymbol{\psi} v_s \mathrm{d}a' \right.$$
$$\left. - \oint_{\partial Q} \boldsymbol{\psi} v_\beta n_{l\beta} \delta\lambda J \mathrm{d}a'_l \right\} \mathrm{d}s. \tag{22.B7}$$

When the expressions (22.B5) and (22.B7) are added together it is seen that the contour integrals cancel, so that the equation $\delta I_1 + \delta I_3 + \delta I_5 = 0$ implies

$$\int_{s_0}^{s} \delta\boldsymbol{\lambda} \cdot \left\{ \int_{B^-}^{B^+} \boldsymbol{\psi} \otimes \boldsymbol{\phi} J \mathrm{d}n \frac{\partial \boldsymbol{\zeta}}{\partial t} + \frac{\partial}{\partial s} \left(\iint_Q \boldsymbol{\psi} \otimes \boldsymbol{\phi} \, \mathrm{d}n\mathrm{d}z \mathbf{v}_s \right) \right.$$
$$\left. - \iint_Q \frac{\partial \boldsymbol{\psi}}{\partial n} \otimes \boldsymbol{\phi} J \mathrm{d}n\mathrm{d}z \mathbf{v}_n - \iint_Q \frac{\partial \boldsymbol{\psi}}{\partial z} \otimes \boldsymbol{\phi} J \mathrm{d}n\mathrm{d}z \mathbf{v}_z \right\} \mathrm{d}s = 0,$$

or since $\delta\boldsymbol{\lambda}$ is arbitrary, and in view of the definitions in Appendix A,

$$\hat{\mathbf{Z}}^{(1)} \frac{\partial \boldsymbol{\zeta}}{\partial t} + \frac{\partial}{\partial s} \left(\mathbf{C}^{(0)} \mathbf{v}_s \right) - \mathbf{C}^{(1)}_{\psi_n} \mathbf{v}_n - \mathbf{C}^{(1)}_{\psi_z} \mathbf{v} = \mathbf{0}. \tag{22.B8}$$

This is the form of the global mass balance equation. In the main text it corresponds to (22.67).

References

1. Bäuerle, E.: Tranverse baroclinic oscillations in Lake Überlingen *Aquatic Sciences*, **56**, 145–149 (1994)
2. Charney, J. G.: Generation of oceanic currents by wind *J. Marine Research*, **14**, 477–498 (1955)
3. Caloi, P.: Free oscialltions in the Lago di Garda [in Italian] *Arch. Meteorol. Geophys. Bioklimatol.* Ser **A7**, 434–465 (1954)
4. Chrystal, G.: Some results in the mathematical theory of seiches. *Proc. Royal Soc. Edinburgh*, **25**, 328–337 (1904)
5. Chrystal, G.: Some further results in the mathematical theory of seiches. *Proc. Royal Soc. Edinburgh*, **25**, 637–647 (1904)

6. Csanady, G. T.: Reesponse of large stratified lakes to wind. *J. Phys. Oceanogr.* **2**(1), 3–13 (1972)
7. Defant, A.: Neuere Methoden zur Ermittlung der Eigenschwingungen (Seiches) von abgeschlossenen Wassermassen (Seen, Buchten, usw.) *Ann. Hydrogr. Berlin*, **46**, 78–85 (1918)
8. Defant, F.: Theorie der Seiches des Michigansees und ihre Abwandlung durch Wirkung der Corioliskraft. *Arch. Meteorol. Geophys. Bioklimatol.* Ser. A **6**, 218–241 (1953)
9. Defant, A.: *Physical Oceanography*. Vol I, Pergamon Press, New York, (1961)
10. Horn, W.: Physikalisch-limnologische Untersuchungen in Schweizer Seen. *Wasser, Energ, Luft*, **9**, 276–284 (1980)
11. Horn, W., Mortimer, C. H. and Schwab, D. J.: Wind-induced internal seiches in Lake Zurich observed and modeled. *Limnol. Oceanogr.* **31**, 1232–1254 (1986)
12. Howard, L. N.: *Lectures on fluid dynamics* In: Notes on the 1960-Summer Study Program in geophysical fluid dynamics (Spiegel, E. A., ed.), Vol. 1, Woods Hole, Mass (1960)
13. Hutter, K.: Strömungsdynamische Untersuchungen im Zürich- und Luganersee. Ein Vergleich von Feldmessungen und Resultaten theoretischer Modelle *Scweiz. Z. Hydrol.* **45**, 101–144 (1983)
14. Hutter, K. and Raggio, G.: A Chrystal-Model describing gravitational barotropic motion in elongated lakes *Arch. Met. Geophys. Biokl.* Ser. A, **31**, 361–378 (1982)
15. Johns, B. and Hamzah, A. M. O.: On the seiceh motion in curved lakes. *Cambridge Philos. Soc.* **66**, 607–615 (1969)
16. Kelvin, Lord (William Thomson): On the gravitational oscillations of rotating water. *Proc. Roy. Soc. Edinburth*, **10**, 92–100 (1879); reprinted in *Phil. Mag.* **10**, 109–116 (1880)
17. Lemmin U. and Mortimer C. H.: Test of an extension to internal seiches of Defant's procedure for determination of surface seiche characteristics in real lakes. *Limnol.Oceanogr.* **31**(6), 1207–1231 (1986)
18. Lamb, H.: *Hydrodynamics* 6th editioin Cambridge University Press (1932)
19. Marcelli, L.: The seiches of Lago di Lugano [in Italian]. *Publ. Ist. Naz. Geofis., Roma. Ann. Geofis*, **1**, 454 (1948)
20. Mortimer, C. H. and Fee. E. J.: Free surface oscillation and tides of Lakes Michgan and Superior. *Phil. Trans. Roy. Soc.*, London **A 281**, 1–61 (1976)
21. Mortimer, C. H. and Horn, W.: Internal wave dynamics and their implication for plankton biology in the Lake of Zurich. *Vierteljahresschr. Naturforsch. Ges. Zürich*, **127**, 299–318 (1982)
22. Pnuelli, A. and Pekeris, C. L.: Free tidal oscillations in rotation flat basins of the form of rectangles and sectors of circles. *Proc. Roy. Soc*., London, **A263**, 149–171 (1968)
23. Poincaré, H.: *Lećons de mécanique Céleste, 3, Thwórie de Marées,* 1910 Gauthier-Villars
24. Raggio, G. M.: *A channel model for a curved elongated homogeneous lake*. Ph. D. Dissertation Swiss Federal Inst. Techn., Zurich. Diss. No 6742, pp. 222 (1980)
25. Raggio, G.: On the Kantorovich technique applied to the tidal equations in elongated lakes. *Computational Physics*, **46**(1), 43–53 (1982)
26. Raggio, G., and Hutter, K.: An extended channel model for the prediction of motion in elongated homogeneous lakes. Part 1. Theoretical introduction. *J. Fluid Mech.* **121**, 231–255 (1982a)
27. Raggio, G., and Hutter, K.: An extended channel model for the prediction of motion in elongated homogeneous lakes. Part 2. First-order model applied ti ideal geometry: rectangular basins with flat bottom *J. Fluid Mech.* **121**, 257–281 (1982b)
28. Raggio, G., and Hutter, K.: An extended channel model for the prediction of motion in elongated homogeneous lakes. Part 3. Free oscillations in natural basins *J. Fluid Mech.* **121**, 283–299 (1982c)
29. Rao, D. B.: Free gravitational oscillations in a narrow rotating rectangular basin. *J. Fluid Mech.* **25**, 523–555 (1966)
30. Rao, D. B and Schwab, D. J.: Two-dimensional normal modes in arbitrary enclosed basins on the rotating Earth: Applications to Lakes Ontario and Superior. *Phil. Trans. Roy. Soc., London*, **A 281**, 63–96 (1976)

31. Servais, F.: Etude théoretique des oscillations libres (seiches) du Lac Tanganika. *Explor. Hydrobiol. Tanganika* **2** *Fac. 3. Inst. R. Sci. Nat. Belg.* 113 p. (1957)
32. Shimizu, K, Imbergert, J. and Kumagai, M.: Horizontal structure and excitation of primary motions in a strongly stratified lake *Limnolo. Oceanogr.*, **52**(6), 2641–2655 (2007)
33. Scott, M. R. and Watts, H. A.: A computer code fortwo-point boundary value problem via orthogonalization. *Sandia Laboratories, Albuquerque*, Sandia-report-78-1501 (1979)
34. Taylor, G. I.: Tidal oscillations in gulfs and basins *Proc. London Math. Soc.* Series 2, XX, 148–181 (1972)
35. Watts, H. A., Scott, M. R. and Lord, M. E.: Solving complex valued differential systems. *Sandia Laboratories, Albuquerque*, report 78-1501 (1979)
36. Wedderburn, E. M.: The temperature of the fresh-water lochs of Scotland, with special reference to loch Ness *Trans. Royal Soc. Edinburg*, **45**, 407–489 (1907)
37. Weddderburn, E. M.: The temperature seiche. Hydrodynamical theory oftemperature oscillationsd in lakes *Trans. Royal Soc. Edinburg*, **47**, 628–684 (1911)
38. Weddderburn, E. M.: Temperature observations in Loch Earn. With afurther contribution to the hydrodynamical theory of the temperature seiche. *Trans. Royal Soc. Edinburg*, **48**, 629–695 (1912)

Name Index

K. Hutter et al., *Physics of Lakes*, *Volume 2: Lakes as Oscillators*, Advances in Geophysical and Environmental Mechanics and Mathematics,
DOI 10.1007/978-3-642-19112-1, © Springer-Verlag Berlin Heidelberg 2011

Lake Index

K. Hutter et al., *Physics of Lakes*, *Volume 2: Lakes as Oscillators*, Advances in Geophysical and Environmental Mechanics and Mathematics,
DOI 10.1007/978-3-642-19112-1,

Subject Index

K. Hutter et al., *Physics of Lakes*, *Volume 2: Lakes as Oscillators*, Advances in Geophysical and Environmental Mechanics and Mathematics,
DOI 10.1007/978-3-642-19112-1, © Springer-Verlag Berlin Heidelberg 2011